

ADVANCES IN ASTRONOMY

Robotic Astronomy

Guest Editors: Alberto J. Castro-Tirado, Joshua S. Bloom,
Lorraine Hanlon, and Taro Kotani





Robotic Astronomy

Advances in Astronomy

Robotic Astronomy

Guest Editors: Alberto J. Castro-Tirado, Joshua S. Bloom,
Lorraine Hanlon, and Taro Kotani



Copyright © 2010 Hindawi Publishing Corporation. All rights reserved.

This is a special issue published in volume 2010 of "Advances in Astronomy." All articles are open access articles distributed under the Creative Commons Attribution License, which permits unrestricted use, distribution, and reproduction in any medium, provided the original work is properly cited.

Editorial Board

Cesare Barbieri, Italy
Edwin Bergin, USA
Joshua S. Bloom, USA
Elias Brinks, UK
Michael Brotherton, USA
Giovanni Carraro, Italy
Alberto J. Castro-Tirado, Spain
Michael Disney, UK
Nye Evans, UK
Maurizio Falanga, Switzerland
Duncan Forbes, Australia
Andrew Fruchter, USA
Boris Gaensicke, UK
John Gizis, USA
Paul Goldsmith, USA
Jonathan Grindlay, USA
Martin Hardcastle, UK

Dean Hines, USA
Dieter Horns, Germany
Ivan Hubeny, USA
John Hughes, USA
Wing Huen Ip, Taiwan
Zeljko Ivezic, USA
Rob Ivison, UK
Valentina Klochkova, Russia
Gregory Laughlin, USA
Myung Gyoon Lee, South Korea
Karen Leighly, USA
Geraint Lewis, Australia
Jeffrey Linsky, USA
Mario Mateo, USA
Fulvio Melia, USA
Ronald Mennickent, Chile
David Merritt, USA

Zdzislaw E. Musielak, USA
Valery Nakariakov, UK
Jerome Orosz, USA
George Pavlov, USA
Juri Poutanen, Finland
Somak Raychaudhury, UK
William Reach, USA
Jerome Rodriguez, France
Peter Roming, USA
Ata Sarajedini, USA
Regina Schulte-Ladbeck, USA
Ravi Sheth, USA
Roberto Turolla, Italy
Gary Wegner, USA
Paul J. Wiita, USA
Edward L. Wright, USA

Contents

Robotic Astronomy, Alberto J. Castro-Tirado
Volume 2010, Article ID 824731, 1 page

Robotic Autonomous Observatories: A Historical Perspective, Alberto Javier Castro-Tirado
Volume 2010, Article ID 570489, 8 pages

Robotic Systems for Meteor Observing and Moon Impact Flashes Detection in Spain, José M. Madiedo, Josep M. Trigo-Rodríguez, José L. Ortiz, and Nicolás Morales
Volume 2010, Article ID 167494, 5 pages

AROMA (AGU Robotic Optical Monitor for Astrophysical Objects), Ichiro Takahashi, Kosuke Tsunashima, Takayuki Shiraki, Toru Kojima, Atsumasa Yoshida, and Yujin E. Nakagawa
Volume 2010, Article ID 214604, 5 pages

T35: A Small Automatic Telescope for Long-Term Observing Campaigns, Susana Martín-Ruiz, Francisco J. Aceituno, Miguel Abril, Luis P. Costillo, Antonio García, José Luis de la Rosa, Isabel Bustamante, Juan Gutierrez-Soto, Héctor Magán, José Luis Ramos, and Marcos Ubierna
Volume 2010, Article ID 869810, 7 pages

FRAMThe Robotic Telescope for the Monitoring of the Wavelength Dependence of the Extinction: Description of Hardware, Data Analysis, and Results, Michael Prouza, Martin Jelínek, Petr Kubánek, Jan Ebr, Petr Trávníček, and Radomír Šmída
Volume 2010, Article ID 849382, 5 pages


Converting from Classical to Robotic Astronomy: The Lowell Observatory 0.8-m Telescope, Marc W. Buie
Volume 2010, Article ID 130172, 12 pages

The OAdM Robotic Observatory, Josep Colomé, Ignasi Ribas, Xavier Francisco, Kevin Casteels, David Fernández, Jordi Isern, Xavier Palau, and Jordi Torra
Volume 2010, Article ID 183016, 8 pages

Autonomous Observations in Antarctica with AMICA, Gianluca Di Rico, Maurizio Ragni, Mauro Dolci, Oscar Straniero, Angelo Valentini, Gaetano Valentini, Amico Di Cianno, Croce Giuliani, Demetrio Magrin, Carlotta Bonoli, Favio Bortoletto, Maurizio D'Alessandro, Leonardo Corcione, and Alberto Riva
Volume 2010, Article ID 728470, 7 pages

The NMSU 1 m Telescope at Apache Point Observatory, Jon A. Holtzman, Thomas E. Harrison, and Jeffrey L. Coughlin
Volume 2010, Article ID 193086, 9 pages

Three Years of Experience with the STELLA Robotic Observatory, Thomas Granzer, Michael Weber, and Klaus G. Strassmeier
Volume 2010, Article ID 980182, 9 pages



“Pi of the Sky” Detector, Katarzyna Małek, Tadeusz Batsch, Henryk Czyrkowski, Mikołaj Ćwiok, Ryszard Dąbrowski, Wojciech Dominik, Grzegorz Kasprowicz, Ariel Majcher, Agnieszka Majczyna, Lech Mankiewicz, Krzysztof Nawrocki, Robert Pietrzak, Lech W. Piotrowski, Maria Ptasińska, Małgorzata Siudek, Marcin Sokołowski, Janusz Użycki, Piotr Wawer, Roman Wawrzaszek, Grzegorz Wrochna, Marcin Zaremba, and Aleksander F. Żarnecki
Volume 2010, Article ID 194946, 9 pages

Design, Manufacturing, and Commissioning of BIRCAM (Bootes InfraRed CAMera), Alberto Riva, Paolo Conconi, Alberto Javier Castro-Tirado, Filippo Zerbi, Ronan Cunniffe, Martin Jelinek, and Stanislav Vitek
Volume 2010, Article ID 760416, 8 pages

Robotic and Non-Robotic Control of Astrophysical Instruments, Gerd Küveler, Van Dung Dao, Axel Zuber, and Renzo Ramelli
Volume 2010, Article ID 620424, 6 pages

The Photometry Pipeline of the Watcher Robotic Telescope, A. Ferrero, L. Hanlon, R. Felletti, J. French, G. Melady, S. McBreen, P. Kubánek, M. Jelínek, B. McBreen, P. Meintjes, J. Calitz, and M. Hoffman
Volume 2010, Article ID 715237, 5 pages

The Data Reduction Pipeline of the Hamburg Robotic Telescope, Marco Mittag, Alexander Hempelmann, José Nicolás González-Pérez, and Jürgen H. M. M. Schmitt
Volume 2010, Article ID 101502, 6 pages

High-Speed and Wide-Field Photometry with TORTORA, G. Greco, G. Beskin, S. Karpov, S. Bondar, C. Bartolini, A. Guarnieri, and A. Piccioni
Volume 2010, Article ID 268501, 8 pages

Automated Detection of Short Optical Transients of Astrophysical Origin in Real Time, Marcin Sokołowski, Katarzyna Małek, Lech W. Piotrowski, and Grzegorz Wrochna
Volume 2010, Article ID 463496, 11 pages

Transient Detections and Other Real-Time Data Processing from MASTER-VWF Wide-Field Cameras, Evgeny Gorbovskoy, Kirill Ivanov, Vladimir Lipunov, Victor Kornilov, Alexander Belinski, Nikolaj Shatskij, Dmitry Kuvshinov, Nataly Tyurina, Pavel Balanutsa, Vadim Chazov, Artem Kuznetsov, Petr Kortunov, Andrey Tlatov, Alexander Parkhomenko, Vadim Krushinsky, Ivan Zalozhnyh, Alexander Popov, Taisia Kopytova, Sergey Yazev, and Alexander Krylov
Volume 2010, Article ID 917584, 17 pages

The Data Big Bang and the Expanding Digital Universe: High-Dimensional, Complex and Massive Data Sets in an Inflationary Epoch, Meyer Z. Pesenson, Isaac Z. Pesenson, and Bruce McCollum
Volume 2010, Article ID 350891, 16 pages

Multiple Depth DB Tables Indexing on the Sphere, Luciano Nicastro and Giorgio Calderone
Volume 2010, Article ID 524534, 11 pages

The REM Observing Software, Mauro Stefanon, Stefano Covino, Dino Fugazza, Emilio Molinari, Francesco D'Alessio, Giuseppe Malaspina, Luciano Nicastro, Vincenzo Testa, Gino Tosti, and Fabrizio Vitali
Volume 2010, Article ID 976890, 9 pages

REM: Automatic for the People, Emilio Molinari, Stefano Covino, Francesco D'Alessio, Dino Fugazza, Giuseppe Malaspina, Luciano Nicastro, Mauro Stefanon, Vincenzo Testa, Gino Tosti, and Fabrizio Vitali
Volume 2010, Article ID 253675, 7 pages

PiMan: System Manager of the “Pi of the Sky” Experiment, Krzysztof Nawrocki, Maria Ptasińska, Marcin Sokołowski, Janusz Użycki, and Marcin Zaremba
Volume 2010, Article ID 560378, 9 pages

The Software for the Robotization of the TROBAR Telescope, Mauro Stefanon
Volume 2010, Article ID 785959, 4 pages

RTS2The Remote Telescope System, Petr Kubánek
Volume 2010, Article ID 902484, 9 pages

Identification and Analyses in Optical Light of Gamma-Ray Sources with Astronomical Archival Plates, René Hudec and Miloš Klíma
Volume 2010, Article ID 618975, 6 pages

Detection of GRBs and OTs by All-Sky Optical and SID Monitors, R. Hudec, M. Spurny, M. Krizek, P. Pata, R. Slosiar, M. Rerabek, and M. Klima
Volume 2010, Article ID 428943, 8 pages

Scheduling in Targeted Transient Surveys and a New Telescope for CHASE, Francisco Förster, Nicolás López, José Maza, Petr Kubánek, and G. Pignata
Volume 2010, Article ID 107569, 8 pages

Wide and Fast: Monitoring the Sky in Subsecond Domain with the FAVOR and TORTORA Cameras, Sergey Karpov, Grigory Beskin, Sergey Bondar, Adriano Guarnieri, Corrado Bartolini, Giuseppe Greco, and Adalberto Piccioni
Volume 2010, Article ID 784141, 8 pages

Protocols for Robotic Telescope Networks, Alain Klotz
Volume 2010, Article ID 496765, 8 pages

Making Preliminary GRBs Real-Time Astronomical Reports, Sebastián Castillo-Carrión and Alberto Javier Castro-Tirado
Volume 2010, Article ID 102831, 8 pages

Double-Station Automatic Video Observation of the Meteors, Stanislav Vítek, Pavel Koten, Petr Páta, and Karel Fliegel
Volume 2010, Article ID 943145, 4 pages

Automated Observations of the Earthshine, P. R. Goode, S. Shoumko, E. Pallé, and P. Montañés-Rodríguez
Volume 2010, Article ID 963650, 5 pages

The STELLA Robotic Observatory on Tenerife, Klaus G. Strassmeier, Thomas Granzer, Michael Weber, Manfred Woche, Emil Popow, Arto Järvinen, Janos Bartus, Svend-Marian Bauer, Frank Dionies, Thomas Fechner, Wilbert Bittner, and Jens Paschke
Volume 2010, Article ID 970306, 11 pages

Monitoring of X-Ray Sources in the Optical Spectral Region, Vojtěch Šimon
Volume 2010, Article ID 382936, 12 pages

Robotic Astronomy with the Faulkes Telescopes and Las Cumbres Observatory Global Telescope, Fraser Lewis, Rachel Street, Paul Roche, Vanessa Stroud, and David M. Russell
Volume 2010, Article ID 873059, 4 pages

Robotic Monitoring of Gravitationally Lensed Quasars, Luis J. Goicoechea, Vyacheslav N. Shalyapin, and Aurora Ullán
Volume 2010, Article ID 347935, 7 pages

BART: The Czech Autonomous Observatory, Martin Nekola, René Hudec, Martin Jelínek, Petr Kubánek, Jan Štrobl, and Cyril Polásek
Volume 2010, Article ID 103986, 5 pages

Four Years of Real-Time GRB Followup by BOOTES-1B (20052008), Martin Jelínek, Alberto J. Castro-Tirado, Antonio de Ugarte Postigo, Petr Kubánek, Sergey Guziy, Javier Gorosabel, Ronan Cunniffe, Stanislav Vítek, René Hudec, Victor Reglero, and Lola Sabau-Graziati
Volume 2010, Article ID 432172, 10 pages

MASTER Prompt and Follow-Up GRB Observations, Nataly Tyurina, Vladimir Lipunov, Victor Kornilov, Evgeny Gorbovskoy, Nikolaj Shatskij, Dmitry Kuvshinov, Pavel Balanutsa, Alexander Belinski, Vadim Krushinsky, Ivan Zalozhnyh, Andrey Tlatov, Alexander Parkhomenko, Kirill Ivanov, Sergey Yazev, Peter Kortunov, Anatoly Sankovich, Artem Kuznetsov, and Vladimir Yurkov
Volume 2010, Article ID 763629, 6 pages

Recent GRBs Observed with the 1.23 m CAHA Telescope and the Status of Its Upgrade, Javier Gorosabel, Petr Kubánek, Martin Jelínek, Alberto J. Castro-Tirado, Antonio de Ugarte Postigo, Sebastián Castillo-Carrión, Sergey Guziy, Ronan Cunniffe, Matilde Fernández, Nuria Huélamo, Víctor Terrón, Nicolás Morales, José Luis Ortiz, Stefano Mottola, and Uri Carsenty
Volume 2010, Article ID 701534, 8 pages

Gamma-Ray Bursts in the Era of Rapid Followup, C. G. Mundell, C. Guidorzi, and I. A. Steele
Volume 2010, Article ID 718468, 14 pages

Master Robotic Net, Vladimir Lipunov, Victor Kornilov, Evgeny Gorbovskoy, Nikolaj Shatskij, Dmitry Kuvshinov, Nataly Tyurina, Alexander Belinski, Alexander Krylov, Pavel Balanutsa, Vadim Chazov, Artem Kuznetsov, Petr Kortunov, Anatoly Sankovich, Andrey Tlatov, A. Parkhomenko, Vadim Krushinsky, Ivan Zalozhnyh, A. Popov, Taisia Kopytova, Kirill Ivanov, Sergey Yazev, and Vladimir Yurkov
Volume 2010, Article ID 349171, 6 pages

Taiwan Automated Telescope Network, Dean-Yi Chou, Ming-Tsung Sun, Javier Fernandez Fernandez, Li-Han Wang, Antonio Jimenez, Alexander Serebryanskiy, and Shuhrat Ehgamberdiev
Volume 2010, Article ID 125340, 4 pages

Astrobiology with Robotic Telescopes at CAB, Luis Cuesta, M. Teresa Eibe, Aurora Ullán, Antonio Pérez-Verde, and Jorge Navas
Volume 2010, Article ID 278207, 6 pages

A Path to the Stars: The Evolution of the Species, Fabrizio Vitali, Guido Chincarini, Mario Zannoni, Stefano Covino, Emilio Molinari, Stefano Benetti, Carlotta Bonoli, Favio Bortoletto, Enrico Cascone, Rosario Cosentino, Francesco D'Alessio, Paolo D'Avanzo, Vincenzo De Caprio, Massimo Della Valle, Alberto Fernandez-Soto, Dino Fugazza, Enrico Giro, Demetrio Magrin, Giuseppe Malaspina, Lech Mankiewicz, Raffaella Margutti, Ruben Mazzoleni, Luciano Nicastro, Alberto Riva, Marco Riva, Ruben Salvaterra, Paolo Spanò, Monica Sperandio, Mauro Stefanon, Gino Tosti, and Vincenzo Testa
Volume 2010, Article ID 187269, 14 pages

From TORTORA to MegaTORTORAResults and Prospects of Search for Fast Optical Transients, Grigory Beskin, Sergey Bondar, Sergey Karpov, Vladimir Plokhhotnichenko, Adriano Guarnieri, Corrado Bartolini, Giuseppe Greco, Adalberto Piccioni, and Andrew Shearer
Volume 2010, Article ID 171569, 9 pages

Fast Universal Spectrophotopolarimeter for Robotic Telescopes, Vladimir Plokhhotnichenko, Grigory Beskin, Sergey Karpov, Sergey Bondar, Vjacheslav de-Boer, Alexandre Lioubetski, and Dmitry Badjin
Volume 2010, Article ID 109681, 6 pages

HexasphereRedundantly Actuated Parallel Spherical Mechanism as a New Concept of Agile Telescope, Michael Valasek, Josef Zicha, Martin Karasek, and Rene Hudec
Volume 2010, Article ID 348286, 6 pages

The Role of Ground-Based Robotic Observatories in Satellite Projects, R. Hudec
Volume 2010, Article ID 594854, 10 pages

Photometry and Low Dispersion Spectroscopy with ESA *Gaia*, René Hudec, Vojtěch Šimon, and Lukáš Hudec
Volume 2010, Article ID 781421, 7 pages

Editorial

Robotic Astronomy

Alberto J. Castro-Tirado

*Instituto de Astrofísica de Andalucía (IAA-CSIC), Departamento de Física Estelar, Glorieta de la Astronomía s/n,
P.O. Box 03004, 18080 Granada, Spain*

Correspondence should be addressed to Alberto J. Castro-Tirado, ajct@iaa.es

Received 28 April 2010; Accepted 28 April 2010

Copyright © 2010 Alberto J. Castro-Tirado. This is an open access article distributed under the Creative Commons Attribution License, which permits unrestricted use, distribution, and reproduction in any medium, provided the original work is properly cited.

The number of automatic astronomical facilities worldwide continues to grow, and the level of robotisation, autonomy, and networking is increasing as well. This has a strong impact in many astrophysical fields, like the search for extrasolar planets, the monitoring of variable stars in our Galaxy, the study of active galactic nuclei, the detection and monitoring of supernovae, and the immediate followup of high-energy transients such as gamma-ray bursts.

Most manuscripts published in this special issue are the fruit of the I Workshop on Robotic Autonomous Observatories held in Málaga (Spain) on May 18–21, 2009. The main focus of the workshop dealt with the new and existing astronomical facilities whose goal is to observe a wide variety of astrophysical targets with no (or very little) human interaction. The workshop became an international forum for researchers to summarise the most recent developments and ideas in the field, with a special emphasis given to the technical and observational results obtained within the last five years.

Torremolinos (Málaga) was the perfect place for hosting the workshop with pleasant early Summer temperatures and the possibility of swimming in the Mediterranean sea at any time, as the conference room at Hotel Camino Real was only 200 m away. Moreover, the lack of Internet access in the conference room was a real advantage (rather than a disadvantage as initially thought), and the participants could really concentrate and actively participate in the talks, without having the possibility of checking emails and so on (they had to leave the conference room if they wanted to do so). And twelve kilometres away, the 3,000-year-old Málaga Town, which is bidding for the title of 2016 European Capital of Culture, was the perfect companion, with its magnificent view from the Gibralfaro castle surroundings during the conference dinner.

The workshop was organized by both the Instituto de Astrofísica de Andalucía of the Spanish Research Council (IAA-CSIC) and the Department of System Engineering and Automatics at Universidad de Málaga (UMA) with support from the Spanish Ministry of Science and Technology (through Project AYA2009-06301-E). We want to thank the members of the Scientific Organizing Committee (SOC): C. Akerlof, M. Boer, A. J. Castro-Tirado (chair), A. García-Cerezo (cochair), L. Hanlon, R. Hudec, T. Kotani, L. Mankiewicz, F. M. Sánchez-Moreno, and F. Zerbi for arranging an excellent scientific programme, and we express our gratitude to the members of the Local Organizing Committee (LOC): S. Castillo, J. Gorosabel, S. Guziy, M. Jelínek, P. Kubánek, V. Muñoz-Fernández, C. Pérez del Pulgar, M. Pérez-Ramírez, and T. J. Mateo-Sanguino. Together with the Torremolinos and Málaga Town Halls and the Patronato de Turismo de la Costa del Sol, they made of the staying of the 80 participants in Málaga an unforgettable experience.

We appreciate Hindawi's support in order to help with the refereeing process (thanks are to the four Guest Editors: J. Bloom, A. J. Castro-Tirado, L. Hanlon, and T. Kotani and all anonymous referees) as well as for the very careful edition of this special issue.

We also thank Irina Guziy for designing the nice workshop announcement poster. And we are very much indebted to María Eva Alcohado-Feltström who worked as the unpaid workshop secretary in order to achieve a perfect organization, becoming "again" the beloved wife of one of us (Alberto J. Castro-Tirado) after the workshop's end.

Alberto J. Castro-Tirado

Review Article

Robotic Autonomous Observatories: A Historical Perspective

Alberto Javier Castro-Tirado

Instituto de Astrofísica de Andalucía (IAA-CSIC), Glorieta de la Astronomía s/n, 18008 Granada, Spain

Correspondence should be addressed to Alberto Javier Castro-Tirado, ajct@iaa.es

Received 22 July 2009; Accepted 29 January 2010

Academic Editor: Lorraine Hanlon

Copyright © 2010 Alberto Javier Castro-Tirado. This is an open access article distributed under the Creative Commons Attribution License, which permits unrestricted use, distribution, and reproduction in any medium, provided the original work is properly cited.

This paper presents a historical introduction to the field of Robotic Astronomy, from the point of view of a scientist working in this field for more than a decade. The author discusses the basic definitions, the differing telescope control operating systems, observatory managers, as well as a few current scientific applications.

1. Introduction

Early designs of what can be considered precursors to robots started in the First Century A.D. in Byzantium, Alexandria, and other places, but the first automatons called “robots” appeared in 1921 following the name of “robot” by the Czech writer Karel Čapek who took it from his brother Josef [1]. See Figure 1. Years later (1941), Isaac Asimov coined the word “Robotics” [2] for the science and technology of robots, and their design, manufacture, and application.

But what is a robot? Hereby the author introduces some widely accepted definitions.

Robot: A mechanical system that executes repetitive pre-programmed remote tasks with good accuracy with human assistance. Example: Industrial robotic arm.

Teleoperated Robot: A mechanical system that executes various remote tasks with good accuracy and whose behaviour can be dynamically modified with human assistance. Example: Submarine research robots.

Autonomous Robot: A mechanical system which executes various remote simple tasks with good accuracy and is able to adapt itself to changes during the task execution without any kind of human assistance. Example: Rovers devoted to planetary research.

Intelligent Robot: An automatic device which is capable of performing many complex tasks with seemingly human intelligence.

The first attempts to robotize telescopes were developed by astronomers after electromechanical interfaces to computers became common at observatories. Computer control is the most powerful technique for research today, but computer systems are inherently low voltage and are very susceptible to electrical noise. Thus putting electromechanical devices under computer control was particularly challenging. Early examples were expensive, had limited capabilities, and included a large number of unique subsystems, both in hardware and software. This contributed to a lack of progress in the development of robotic telescopes early in their history, but the situation was going to change rapidly.

Similarly, the abovementioned definitions can be extended to Robotic Astronomical Observatories (following the consensus reached after 1 hour of discussion amongst the 80 participants who attended the “Workshop in Robotic Autonomous Observatories,” held in Málaga (Spain) on May 18–21, 2009) as follows.

Automated Scheduled Telescope [Robot]: A telescope that performs pre-programmed observations without immediate help of a remote observer (e.g., avoiding an astronomer moving of the mount by hand).

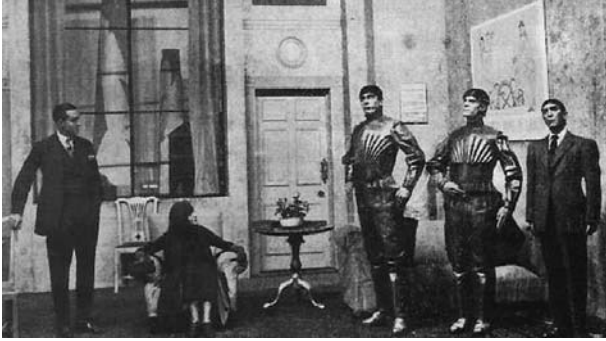


FIGURE 1: A scene in Čapek's play *Rossum's Universal Robots* (1921) showing three *robots*, adapted from [4].

Remotely Operated (remote) Telescope [Teleoperated Robot]: A telescope system that performs remote observations following the request of an observer.

Robotic Autonomous Observatory [Autonomous Robot]: A telescope that performs various remote observations and is able to adapt itself to changes during the task execution without any kind of human assistance (e.g., weather monitoring; the system must not endanger a human!).

Robotic Intelligent Observatory [Intelligent Robot]: A robotic observatory in which decisions will be taken by an artificial intelligent system. The next step forward!

2. Robotic Autonomous Observatories: A Brief History

In the light of the abovementioned facts and definitions, we can establish the following approximate chronology.

2.1. 1968–1975: The Automated Scheduled Telescopes. The history of robotic telescopes is closely related to the development of automated photoelectric telescopes (APTs). The first one was built by A. C. Code and some of his associates at the University of Wisconsin. A prototype was built by A. Code by the mid 1960s and operated for two or three nights before failing. Once repaired, it operated for other few nights, and was used by B. Millis for gathering data on Cepheids for his Dissertation. In 1968, they used one of the first minicomputers, a DEC PDP-8 with 4 K of RAM, for controlling a 0.2 m reflector telescope with a photometer placed at the prime focus (see Figure 2). The instrument was identical to the one used in the Orbiting Astrophysical Observatory Program: Code envisioned the use of telescopes in the space and later became codirector of the Space Telescope Science Institute. The instrument was used to measure a fixed sequence (from punched paper tape) of bright stars throughout the night to determine the nightly extinction for the larger telescopes [3] and can be considered the first automated scheduled telescope.

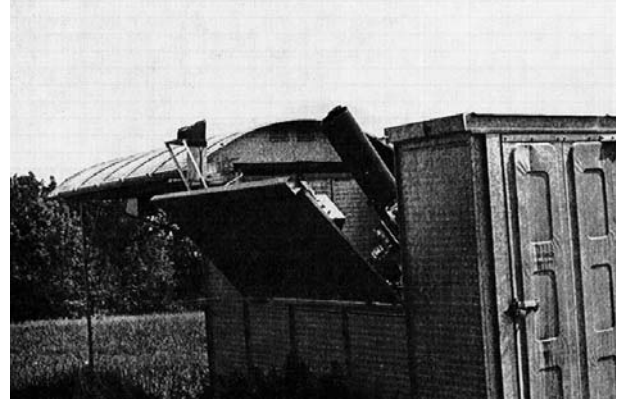


FIGURE 2: The first computer-controlled telescope ever built, at University of Wisconsin, 1968, adapted from [3].

By the same time (c.1968), the 50-inch B&C telescope in Kitt Peak was automated ... for one night: the system was too complex and not reliable enough. A 0.15 m f/8 Cassegrain telescope was the next one to be automated in 1970 [5]. All together, they paved the way and several publications on the field were already available by 1975 [6–8].

2.2. 1975–1984: The Remotely Operated Telescopes. In 1975, a 0.75 m telescope was fully automated allowing remote operation via a microwave link [9] and in 1976–1977 the Big Telescope Alt-azimuthal 6 m telescope in Caucasus [10] and the Wyoming InfraRed Observatory 2.3 m telescope [11] became the first large telescopes to be controlled by a computer. In the late 1970s an IBM 1800 was used by G. Henry and K. Kissell for automated photometry whereas the 0.9 m Indiana University telescope was computerized by K. Honeycutt et al. See also [12].

Following previous works in late 1970s and early 1980s, the first system which executed repetitive predefined tasks was achieved on the night of 13 of October 1983, when Boyd and Genet run the Phoenix T1 0.25 m diameter telescope in Boyd's backyard observatory in Phoenix, Arizona [13]. Boyd and Genet watched the telescope automatically find center and make UBV photometric measurements on star after star and finally went to bed. The telescope ran successfully all night, and almost every clear night for the next quarter century. It was recently retired. Also in 1983, M. Bartels computerized a small telescope using a Commodore 64 computer.

Two years later (1985), a book by Trueblood and Genet was a landmark engineering study in the field [14]. One of this book's achievements was pointing out many reasons, some quite subtle, why telescopes could not be reliably pointed using only basic astronomical calculations. The concepts explored in this book share a common heritage with the telescope mount error modelling software called *Tpoint*, which emerged from the first generation of large automated telescopes in the 1970s, notably the 3.9 m Anglo-Australian Telescope (Figure 3).

2.3. 1984–2000: The Era of Autonomous Robotic Observatories. The Carlsberg Meridian Circle (0.18 m diameter) in



FIGURE 3: The 3.9 m Anglo-Australian Telescope is one of the first ones which made use of *Tpoint*, adapted from [15].

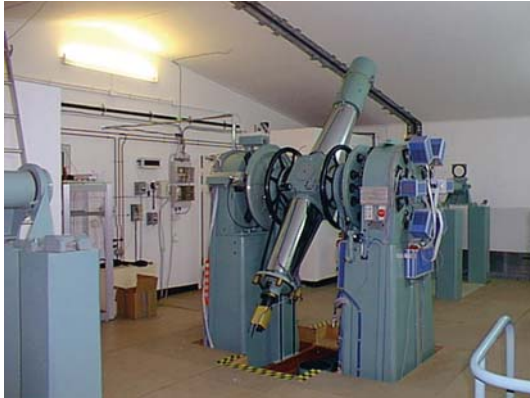


FIGURE 4: The Carlsberg Meridian Circle in La Palma was amongst the first automated telescopes, something achieved in 1984. It was until recently operated jointly by the Copenhagen University Observatory, the Institute of Astronomy, Cambridge, and the Real Instituto y Observatorio de la Armada en San Fernando (ROA); however it is now run solely by the ROA. Image was kindly provided by ROA.

La Palma (Canary Islands, Spain) was jointly automated by Copenhagen University Observatory (Denmark) and the Real Instituto y Observatorio de la Armada en San Fernando (Spain) and became in 1984 one of the very first autonomous observatories [16]; see Figure 4.

The first automated telescopes in autonomous observatories were able to start on a preprogrammed sequence of photometric measurements if the sky was clear. This was the case of the Automated Photoelectric Telescope (APT) service, a computer-driven system in Mount Hopkins (U.S.) which

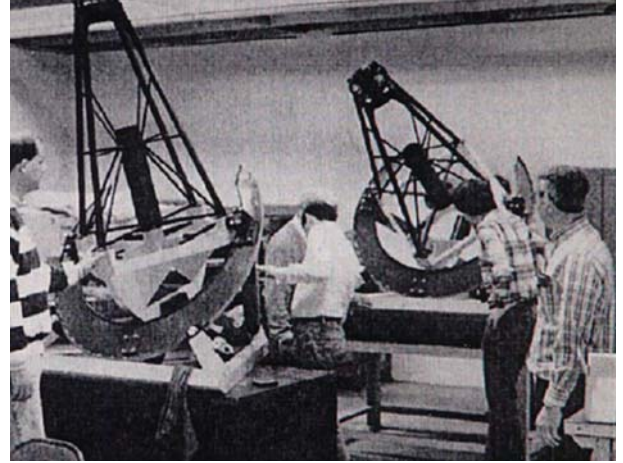


FIGURE 5: Early APT units.

knew when the Sun set and checked for rain snow, and so forth [17]. See Figure 5.

The Fairborn 10 T2 0.25 m APT began operations in early 1984 in Fairborn, Ohio, and was moved in early 1986 to the Fred Lawrence Whipple Observatory (FLWO) on Mount Hopkins in southern Arizona, which was operated jointly by the Harvard Smithsonian Center for Astrophysics and the University of Arizona. It was relocated in 1996 to Fairborn Observatory's new site at 1675 m in the Patagonia mountains near Washington Camp, Arizona. Operation of the Fairborn 0.25 m APT [18] was supported by FLWO (during its tenure on Mount Hopkins), Fairborn Observatory, and Tennessee State University. Until 2001 (16 years), the telescope was dedicated primarily to long-term photometric monitoring of semiregular pulsating variable stars and was decommissioned in 2007. Nowadays the TSU group has built 13 instruments including a 2 m class telescope.

In 1987-88 Genet managed to control a telescope with commands sent over internet. In 1988 M. Bartels used an IBM 286 AT to control Alt/Az devices. The same year Gray computerized an equatorial mount and Taki described a two-star Alt/Az alignment routine [19].

Thus, the first robots were telescopes with an absolute positioning control and guiding systems. Observatories with automatic weather stations were gradually being introduced in astronomical observatories.

The Berkeley Automated Imaging Telescopes (0.5 m and 0.76 m diameter telescopes) were used at the astronomy department's Leuschner Observatory in 1992 and 1994 for detailed monitoring of transient objects and for conducting the Leuschner Observatory Supernova Search (LOSS). The 0.76 m Katzman Automated Imaging Telescope (KAIT) in Lick Observatory (Figure 6) saw first light in 1998 and is still working nowadays and has proven to be very successful in the search for nearby supernovae [20].

The Perugia University Automated Imaging Telescope (0.4 m diameter; see Figure 7) in Italy started monitoring blazars in 1992 [21], nearly simultaneously with the 0.8 m Catania Automatic Photoelectric Telescope [22]. The

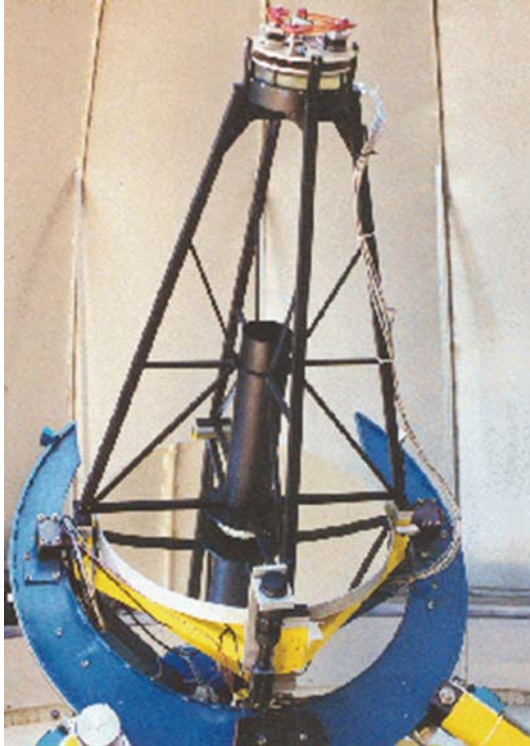


FIGURE 6: The 0.76 m KAIT telescope, adapted from [28].

Bradford Robotic Telescope (UK) has been operating via the web since 1993 and accepts requests from anyone and could be considered as one of the first instruments entirely devoted to educational purposes [23]. The 0.5 m $f/1$ Automated Patrol Telescope [24] run by the University of South Wales (Australia) and the University of Iowa Robotic Telescope Facility (0.37 m diameter Rigel telescope at Winer Observatory in AZ [25]) joined later (1994). The second one was devoted to undergraduate education and independent research projects.

In 1997, one of the first robotic amateur observatories achieved first light: the Hanna City Robotic Observatory, which made use of a 0.2 m Schmidt-Cassegrain telescope [26]. And at about the same time, the CWRU Nassau station 0.9 m telescope was probably among the first professional-class instrument publicly available over the internet [27].

And by the end of the 1990s the number of automated telescopes (mostly professional ones) increased substantially with many of them devoted to gamma-ray burst (GRB) followup observations: GROSCE (1993, a wide-field lens system prototype which later gave rise to ROTSE, in the U.S. [29]), LOTIS (1996, a wide-field lens system in Lawrence Livermore Laboratory in the U.S. [30]), ROTSE (1998, a wide-field lens system starting in Los Alamos National Laboratories, U.S. [31]), BOOTES (1998, starting initially with a 0.2 m telescope and a wide-field lens system located in south Spain [32]), TAROT (1998, a robotic 0.25 m telescope in France [33]), and BART (2000, a 0.2 m telescope wide-field system in Czech Republic [34]).



FIGURE 7: The 0.4 m Automatic Imaging Telescope of Perugia University, adapted from [42].



FIGURE 8: The RAPTOR array of wide-field lenses in LANL (U.S.), adapted from [43].

During this decade, several global networks of automated telescopes were proposed by several scientists [35–41]. Although none of them became a reality, their ideas inspired others for the next decade.

2.4. 2001-Present: The Era of Robotic Autonomous Observatories Networks. A plethora of robotic autonomous observatories (hereafter RAOs) had first light in the first decade of the 21st century: RAPTOR (2002, an array of wide-field lenses of different diameter [44] in the U.S.; see Figure 8), REM (2003, a 60 cm robotic nIR telescope in Chile [45]), and many others which we cannot discuss here and are quoted in [46].

They were joined as well by the first global networks: ROTSE-III (four 0.45 m telescopes in Australia, Namibia, Turkey, and U.S.), BOOTES (four 0.60 m telescopes in New Zealand, Russia, and two in south Spain, with one devoted to optical/near-IR wavelengths), TAROT (two 0.25 m telescopes in France and Chile), MASTER (several 0.20–0.35 m wide-field instruments across Russia [47]), ROBONET (three 2.0 m telescopes in Hawaii, Australia, and Canary Islands [48]), and MONET (two 1.2 m telescopes in the U.S. and South Africa [49]).



FIGURE 9: The robotic telescopes of the world, adapted from [46].

How are RAOs distributed worldwide? The number of RAOs on Earth is increasing with more than 100 so far of which nearly 80% are in Europe and in the U.S. (see Figure 9). It is strange why there are no robotic instrumentations in some of the best astronomical locations in the North Hemisphere like Mount Maidanak (Uzbekistan), Khurel Togoot (Mongolia), or San Pedro Mártir (México).

3. Science and Technology with Robotic Autonomous Observatories

3.1. Wide Range of Scientific Research Areas. Many scientific fields are benefiting from the use of Robotic Autonomous Observatories. For instance, the Lincoln Near-Earth Asteroid Research (LINEAR) 1 m telescope was used starting in 1998 for detecting and cataloging near-Earth asteroids—also referred to as near-Earth objects (NEOs)—that threaten the Earth. By 2009, 226,000 asteroids, 2019 NEOs, and 236 comets had been discovered [50]. Later on, the Moving Object and Transient Event Search System (MOTESS) started as an amateur project in the early 2000s and discovered hundreds of asteroids and a few comets by using the drift-scan imaging technique. This project was later used to search for variable stars in 300 sq. deg down to $R = 19$ [51].

Further Galactic searches for variable objects have been carried out with the ROTSE-III and BOOTES networks of robotic telescopes (see Figure 10), amongst many others. Besides ROTSE-III successful searches for GRB afterglows, BOOTES and ROBONET are both being used for followup observations of GRB and microlensing events.

The Perugian AIT was mainly dedicated to the automatic optical variability monitoring of blazars [52], as well as BART. ROTSE-III has been also used for SN searches and many of the RAOs have also been partially devoted to the followup of transient events like supernovae or GRB afterglows.

An exhaustive list describing the main achievements of RAOs worldwide is beyond the scope of this manuscript. Instead we report the scientific use of RAOs (Table 1) with the number of instruments as a function of the telescope diameter in Table 2.

3.2. Telescope Control Operating Systems. Two kinds are available: *Commercial automatization systems* (like TCS by Optical Mechanics for apertures in the range 0.4–1 m) which

TABLE 1: Scientific use of RAOs (adapted from [46]).

Description	Percentage
Gamma-ray bursts	22.1%
Service observations	15.0%
Education	14.3%
Photometric monitoring	10.0%
All-sky surveys	8.6%
Exoplanet searches	7.9%
Supernovae search	7.1%
Asteroids	5.7%
Spectroscopy	2.9%
Astrometry	2.9%
AGN, Quasars	2.9%
Microlensing	0.7%
Other uses	5.7%

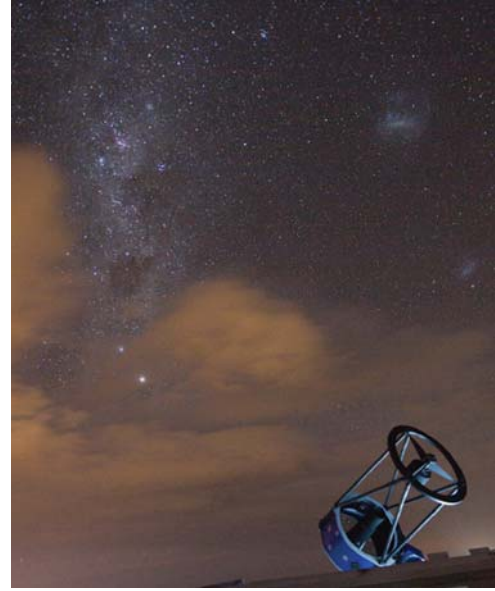


FIGURE 10: The Yock-Allen 0.6m Robotic Telescope at the BOOTES-3 astronomical station in Blenheim (New Zealand) with the Alpha and Beta Centauri, the Southern Cross, and Magellanic Clouds in the background. Photo courtesy of Dietzel.

TABLE 2: Range of RAO's main instrument apertures (adapted from [46]).

Description	Number	Percentage
≤ 0.25 m	77	44.3%
$0.25 \text{ m} < \text{aperture} \leq 0.50$ m	37	23.0%
$0.50 \text{ m} < \text{aperture} < 0.75$ m	14	8.6%
$0.75 \text{ m} < \text{aperture} < 1.00$ m	17	9.8%
$1.00 \text{ m} < \text{aperture} < 1.25$ m	7	4.0%
> 1.25 m	18	10.3%

can be either Open or Closed source and *specific control systems* (like the one for the 10.4 m GTC telescope at La Palma, Figure 11).

3.3. Observatory Managers. There are several observatory managers already available.

ATIS (Automatic Telescope Instruction Set). It is designed initially in 1984 by Boyd et al. (Arizona) and expanded over the years [53]; ATIS allows many options for real time, low-level AI type of control for both aperture photometry, and CCD imaging. The overall system includes provisions for weather sensors, observatory control, and so forth.

OCAAS (Observatory Control and Astronomical Analysis Software). It was originally developed starting in 1993 by Downey and Mutel [54]. In 2001, the software was purchased by Torus Technologies of Iowa City, Iowa. In late 2002, Torus was purchased by Optical Mechanics, Inc., and the updated OCAAS package was renamed as TALON and released under the GPL.

AUDELA. It is developed by Klotz et al. (Toulouse, France), starting in 1995 [55]. Open source code. Linux/Windows.

ASCOM. It is designed in 1998, by B. Denny (USA), as an interface standard for astronomical equipment, based on MS's Component Object Model, which he called the Astronomy Common Object Model [56]. Mostly used by amateur astronomers, has been also used by professionals. Windows. Widely used in SN, MP searches.

RTS2. The Robotic Telescope System version 2. is being developed by Kubánek et al., (Ondřejov/Granada) starting in 2000 [57, 58]. Open source code. Linux/Windows (command line and graphical interface foreseen). Widely used in GRB searches.

INDI. The Instrument Neutral Distributed Interface (INDI) was started in 2003 [59]. In comparison to the Microsoft Windows centric ASCOM standard, INDI is a platform independent protocol developed by E. C. Downey (USA). Open source code. Not so widely spread as the upper layer interface was not done.

Open- or Close-Loop Systems. In an *open-loop* system, a robotic telescope system points itself and collects its data without inspecting the results of its operations to ensure that it is operating properly. An open-loop telescope is sometimes said to be operating on faith, in that if something goes wrong, there is no way for the control system to detect it and compensate.

A *closed-loop* system has the capability to evaluate its operations through redundant inputs to detect errors. A common such input would be the capability of evaluating the system's images to ensure that it was pointed at the correct field of view when they were exposed.

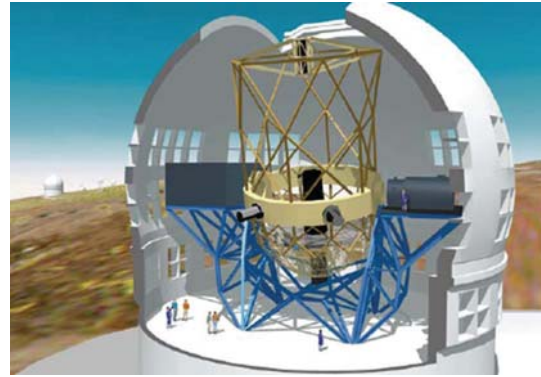


FIGURE 11: The Spanish 10.4 m GTC telescope in La Palma, Canary Islands. Courtesy of GRANTECAN.

4. Massive Data Production and Data Analysis

Until all of the data are analyzed, the robotic observations are worthless. Are all researchers prepared to handle the huge data flow? For instance, the data production of fast imager devices attached to a robotic telescope, could be as high as ~ 2 TB/night.

Archiving the data is also most essential. In this era, new generations of powerful tools are being built that rely on reaching transparently across the Internet to query remote services. In order to provide a truly useful service, RAOs should make their data archive available to such tools. The International Virtual Observatory Alliance (IVOA) [60] exists to develop interoperability standards, and RAOs should develop our archive access portal in accordance with those standards [61, 62].

Automatic pipelines able to deliver reliable data products written by capable analysts and computer programmers are a must in order to deliver the data products timely [63, 64]. The real-time analysis of the data is mandatory if we want to fully exploit the data and to be able to alert other observatories for followup observations (see, e.g., [65]).

5. Education and Public Outreach

An important mission of any robotic telescope could be the possibility of using a fraction of its time for education and public outreach purposes. In this respect, Robotic telescopes can be operated in two ways:

- (i) Direct Mode: remote control with the user directly controlling the telescope using a web/IP cam checking also for weather conditions, and so forth,
- (ii) Service Mode: where the user requests and observation is taken by the telescope and returned at a later date. Often called queue scheduling.

In Direct Mode, one person has control of the telescope, although others can watch the system operating. The observer receives the image as soon as the telescope has made the observation. This is most essential in case of real-time demonstrations.

In Service Mode, each person adds his request to the "input pool". The queue-scheduling computer system then sorts and grades the requests according to the observing details and weather conditions. It aggregates similar requests and creates an observing schedule that it passes to the telescope system. When the observation has been made, an email should be automatically sent to the user who made the request giving details of the location of the image file(s).

6. The Future Beyond 2010: The Era of Intelligent Robotic Astronomical Networks

This is the following step, where human assistance in the taking of decisions will be placed by an artificial intelligent system. This is starting to be developed nowadays [66].

Where to get next? With some instruments already planned for Antarctica [67], the far side of the moon is very promising, where straylight and electromagnetic interference are at minimum. Then new drives operating at 1 revolution per month under 1/6th gravity will need to be designed. Telescope-drive engineers and scientists will go on.

7. Conclusions

Since 1984, robotic telescopes have opened a new field in Astrophysics in terms of optimizing the observing time. Most of the existing one-hundred facilities can be considered autonomous robotic observatories (RAOs) with some of them being able to provide prereduced data.

Archiving the data in VO standards and timely analysis (in real-time if possible!) by specific pipelines is not available in most of them, which seriously compromises the new developments of the future intelligent robotic observatories (the next step forward).

In any case, the big advantage of RAOs is that they can be placed in remote locations where human life conditions will be hostile: Antarctica now [68] and the Moon (why not?) in the near future.

Acknowledgments

The author is very much indebted to R. Genet and P. Abrahams for the very useful suggestions regarding the early times. He also benefited from discussions with R. Cuniffe, J. Gorosabel, S. Guziy, F. Hessman, M. Jelínek, P. Kubánek, and A. de Ugarte Postigo. This work was supported by Spanish Ministry of Science and Technology's projects AYA 2004-01515, AYA 2007-63677, and AYA 2009-14000-C03-01.

References

- [1] K. Čapek, *R.U.R. (Rossum's Universal Robots)*, Dover, 1921, translated into English in 2001 by P. Selver and N. Playfair.
- [2] I. Asimov, "Liar !". *ASTOUNDING Science Fiction*, May 1941 Issue, reprinted by Cambridge University Press, 1977.
- [3] J. F. McNall, J. L. Miedaner, and A. D. Code, "A computer-controlled photometric telescope," *Astronomical Journal*, vol. 73, pp. 756–761, 1968.
- [4] <http://www.umich.edu/~engb415/literature/pontee/RUR/RURsmry.html>.
- [5] R. H. Lee, R. M. MacQueen, and W. G. Mankin, "A computer-controlled infrared eclipse telescope," *Applied Optics*, vol. 9, no. 12, pp. 2653–2657, 1970.
- [6] E. W. Dennison, "Computer control of large telescopes," in *Proceedings of Conference on Large Telescope Design*, R. M. West, Ed., ESO/CERN Conference, p. 363ff, Geneva, Switzerland, 1971.
- [7] E. W. Dennison, "Recent computer installations at the hale observatories," in *Automation in Optical Astrophysics*, H. Seddon and M. J. Smyth, Eds., Proceedings of IAU Colloq. 11, p. 8ff, Publ. R. Obs., Edinburgh, UK, 1971.
- [8] L. B. Robinson, "On-line computers for telescope control and data handling," *Annual Review of Astronomy and Astrophysics*, vol. 13, pp. 165–185, 1975.
- [9] S. A. Colgate, E. P. Moore, and R. Carlson, "A fully automated digitally controlled 30-inch telescope," *Publications of the Astronomical Society of the Pacific*, vol. 87, pp. 565–575, 1975.
- [10] <http://w0.sao.ru/Doc-en/Telescopes/bta/descrip.html>.
- [11] R. D. Gehrz and J. A. Hackwell, "Exploring the infrared universe from Wyoming," *Sky & Telescope*, vol. 55, pp. 466–473, 1978.
- [12] D. Skillman, "Running a telescope with a microcomputer," *Sky & Telescope*, vol. 61, p. 71, 1981.
- [13] R. M. Genet, "Introduction to automatic photoelectric telescopes (APTs)," *International Amateur-Professional Photoelectric Photometry Communication*, no. 25, pp. 1–25, 1986.
- [14] M. Trueblood and R. Genet, *Microcomputer Control of Telescopes*, Willmann-Bell, Richmond, Va, USA, 1985.
- [15] <http://upload.wikimedia.org/wikipedia/commons/thumb/8/8c/Aat.jpg/250px-Aat.jpg>.
- [16] L. Helmer and L.V. Morrison, "Carlsberg automatic meridian circle," *Vistas in Astronomy*, vol. 28, pp. 505–518, 1985.
- [17] S. Baliunas, L. J. Boyd, R. M. Genet, D. S. Hall, and S. Criswell, "Automatic photoelectric telescope III the Mount Hopkins site," *International Amateur-Professional Photoelectric Photometry Communication*, no. 22, p. 47, 1985.
- [18] R. Genet, L. J. Boyd, K. E. Kissell, D. L. Crawford, and D. S. Hall, "The automatic photoelectric telescope service," *Publications of the Astronomical Society of the Pacific*, vol. 99, pp. 660–667, 1987.
- [19] T. Taki, "A new concept in computers-aided telescopes," *Sky & Telescope*, vol. 77, p. 194, 1989.
- [20] A. V. Filippenko, W. D. Li, R. R. Treffers, and M. Modjaz, "The lick observatory supernova search with the Katzman automatic imaging telescope," in *Small-Telescope Astronomy on Global Scales*, vol. 246 of ASP Conference Series, pp. 121–130, Astronomical Society of the Pacific, San Francisco, Calif, USA, 2001.
- [21] G. Tosti, S. Pascolini, and M. Fiorucci, "The Perugia University automatic observatory," *Publications of the Astronomical Society of the Pacific*, vol. 108, no. 726, pp. 706–713, 1996.
- [22] M. Rodonó, G. Cutispoto, A. F. Lanza, and S. Messina, "The Catania automatic photoelectric telescope on Mt. Etna: a systematic study of magnetically active stars," *Astronomische Nachrichten*, vol. 322, no. 5–6, pp. 333–342, 2001.
- [23] J. Baruch, "Bradford robotic telescope: education & public outreach: journey into space," *Astronomy & Geophysics*, vol. 48, no. 4, pp. 4.27–4.28, 2007.
- [24] M. C. B. Ashley, <http://www.phys.unsw.edu.au/~mcba/apt/>.
- [25] <http://phobos.physics.uiowa.edu/>.
- [26] <http://www.mtco.com/~jgunn/>.
- [27] <http://astroweb.case.edu/history.shtml>.

- [28] <http://astro.berkeley.edu/~bait/kait.html>.
- [29] C. W. Akerlof, M. Fatuzzo, B. Lee, et al., "Gamma-ray optical counterpart search experiment (GROCE)," in *Proceedings of the 2nd Workshop on Gamma-Ray Bursts*, vol. 307 of *AIP Conference Proceedings*, pp. 663–666, Huntsville, Ala, USA, 1994.
- [30] H. S. Park, E. Ables, S. Barthelmy, et al., "Super-LOTIS/LOTIS/LITE: prompt GRB followup experiments," in *GAMMA 2001; Gamma-Ray Astrophysics 2001*, vol. 587 of *AIP Conference Proceedings*, pp. 181–184, 2001.
- [31] C. W. Akerlof, R. L. Kehoe, T. A. McKay, et al., "The ROTSE-III robotic telescope system," *Publications of the Astronomical Society of the Pacific*, vol. 115, no. 803, pp. 132–140, 2003.
- [32] A. J. Castro-Tirado, J. Soldán, M. Bernas, et al., "The burst observer and optical transient exploring system (BOOTES)," *Astronomy and Astrophysics Supplement Series*, vol. 138, no. 3, pp. 583–585, 1999.
- [33] M. Böer, M. Bringer, A. Klotz, et al., "TAROT: observing gamma-ray bursts 'in progress,'" *Astronomy & Astrophysics*, vol. 138, pp. 579–580, 1999.
- [34] M. Jelinek, P. Kubánek, R. Hudec, M. Nekola, M. Topinka, and J. Strobl, "BART-burst alert robotic telescope," in *The Astrophysics of Cataclysmic Variables and Related Objects*, vol. 330 of *ASP Conference Series*, p. 481, 2005.
- [35] F. R. Querci and M. Querci, "The Network of Oriental Robotic Telescopes (NORT)," *African Skies* 2, 18, 1998.
- [36] E. Budding, "Globalizing observations: prospects and practicalities," in *Stellar Photometry—Current Techniques and Future Developments*, C. J. Butler and I. Elliott, Eds., IAU Colloquium 136, p. 257, Cambridge University Press, 1993.
- [37] D. L. Crawford, "GNAT: global network of automated telescopes," in *Automated Telescopes for Photometry and Imaging*, vol. 28 of *ASP Conference Series*, p. 111, 1992.
- [38] D. L. Crawford, "Some GNAT issues," in *Robotic Observatories*, M. F. Bode, Ed., p. 77, John Wiley & Sons and Praxis, New York, NY, USA, 1995.
- [39] F. R. Querci, M. Querci, S. Kadiri, and Z. Benkhaldoun, "Network of Oriental Robotic Telescopes," in *Symposium: Robotic Telescopes: Current Capabilities, Present Developments, and Future Prospects for Automated Astronomy*, G. W. Henry and M. Drummond, Eds., vol. 79 of *ASP Conference Series*, Flagstaff, Ariz, USA, June 1995.
- [40] F. R. Querci, M. Querci, and S. Kadiri, "A complementary Network to GNAT: an Arabian and French Project for automated photometric stations," in *Robotic Observatories, Held in Kilkenny (Ireland), July, 1992*, B. P. Hines and M. F. Bode, Eds., p. 85, Praxis and John Wiley & Sons, New York, NY, USA, 1995.
- [41] F. R. Querci and M. Querci, "Robotic telescopes and networks: new tools for education and science," *Astrophysics and Space Science*, vol. 273, no. 1–4, pp. 257–272, 2000.
- [42] <http://astro.fisica.unipg.it/osserv.htm>.
- [43] <http://www.raptor.lanl.gov/>.
- [44] W. T. Vestrand, K. N. Borozdin, S. P. Brumby, et al., "The RAPTOR experiment: a system for monitoring the optical sky in real time," in *Advanced Global Communications Technologies for Astronomy II*, vol. 4845 of *Proceedings of the SPIE*, pp. 126–136, 2002.
- [45] F. M. Zerbi, G. Chincarini, G. Ghisellini, et al., "REM telescope, a robotic facility to monitor the prompt afterglow of gamma ray bursts," in *Instrument Design and Performance for Optical/Infrared Ground-Based Telescopes*, vol. 4841 of *Proceedings of the SPIE*, pp. 737–748, 2002.
- [46] F. Hessman, "Robotic telescope projects," <http://www.astro.physik.uni-goettingen.de/~hessman/MONET/links.html>.
- [47] V. M. Lipunov, V. G. Kornilov, A. V. Krylov, et al., "The master mobile astronomical system. Optical observations of gamma-ray bursts," *Astrophysics*, vol. 48, no. 3, pp. 389–399, 2005.
- [48] <http://www.astro.ljmu.ac.uk/RoboNet/>.
- [49] <http://monet.uni-goettingen.de/>.
- [50] <http://www.ll.mit.edu/mission/space/linear/>.
- [51] A. L. Kraus, E. R. Craine, M. S. Giampapa, W. W. G. Scharlach, and R. A. Tucker, "The first MOTESS-GNAT variable-star survey," *Astronomical Journal*, vol. 134, no. 4, pp. 1488–1502, 2007.
- [52] <http://astro.fisica.unipg.it/PGblazar/tabella2000.htm>.
- [53] R. M. Gener, L. J. Boyd, and D. S. Hayes, "Automatic Small Telescope Operations," in *New Directions in Spectrophotometry*, A. G. Davis Philip, D. S. Hayes, and S. J. Adelman, Eds., L. Davis Press, Schenectady, NY, USA, Las Vegas, Nev, USA, March 1988.
- [54] E. C. Downey and R. L. Mutel, "The university of Iowa automated telescope facility," in *Astronomical Data Analysis Software and Systems V*, G. H. Jacoby and J. Barnes, Eds., vol. 101 of *ASP Conference Series*, p. 380, 1996.
- [55] http://www.audela.org/english_audela.php.
- [56] <http://ascom-standards.org/>.
- [57] P. Kubánek, M. Jelinek, J. French, et al., "The RTS2 protocol," in *Advanced Software and Control for Astronomy II*, A. Bridger and N. M. Radziwill, Eds., vol. 7019 of *Proceedings of the SPIE*, pp. 70192S-1–70192S-12, 2008.
- [58] <http://rts2.org/>.
- [59] <http://www.indilib.org/>.
- [60] <http://www.ivoa.net/>.
- [61] <http://www.ivoa.net/Documents/SIA/>.
- [62] <http://www.ivoa.net/Documents/latest/CharacterisationDM.html>.
- [63] P. Ballester, P. Biereichel, A. Kaufer, M. Kiekebusch, and H. Lorch, "CLIP: bridging pipelines to instrument control software," in *Astronomical Data Analysis Software and Systems*, vol. 394 of *ASP Conference Series*, pp. 577–580, 2008.
- [64] C. Rit , R. Slijkhuis, P. Rosati, et al., "Production of previews and advanced data products for the ESO science archive," in *Astronomical Data Analysis Software and Systems*, vol. 394 of *ASP Conference Series*, pp. 605–608, 2008.
- [65] D. L. Starr, J. S. Bloom, and N. R. Butler, "Real-time transient classification and broadcast pipeline," in *Astronomical Data Analysis Software and Systems*, vol. 394 of *ASP Conference Series*, pp. 609–612, 2008.
- [66] R. R. White, S. M. Evans, W. T. Vestrand, M. S. Warren, J. A. Wren, and P. R. Wozniak, "Thinking telescopes and the future astronomical meta-network," *Astronomische Nachrichten*, vol. 327, no. 8, pp. 758–762, 2006.
- [67] M. Busso, G. Tosti, F. Roncella, et al., "The IRAIT project infrared astronomy from Antarctica," *EAS Publications Series*, vol. 14, pp. 181–186, 2005.
- [68] M. C. B. Ashley, M. G. Burton, J. S. Lawrence, and J. W. V. Storey, "Robotic telescopes on the Antarctic plateau," *Astronomische Nachrichten*, vol. 325, no. 6, pp. 619–625, 2004.

Research Article

Robotic Systems for Meteor Observing and Moon Impact Flashes Detection in Spain

José M. Madiedo,¹ Josep M. Trigo-Rodríguez,^{2,3} José L. Ortiz,⁴ and Nicolás Morales⁴

¹ *Facultad de Ciencias Experimentales, Universidad de Huelva, Avenida de las Fuerzas Armadas S/N, 21071 Huelva, Spain*

² *Institut d'Estudis Espacials de Catalunya, Gran Capità 2-4, Ed. Nexus, 08034 Barcelona, Spain*

³ *Institut de Ciències de l'Espai-CSIC, Campus UAB, Facultat de Ciències, Torre C5-p2., 08193 Bellaterra, Spain*

⁴ *Instituto de Astrofísica de Andalucía-CSIC, Camino Bajo de Huetor 50, 18080 Granada, Spain*

Correspondence should be addressed to José M. Madiedo, madiedo@uhu.es

Received 28 June 2009; Accepted 21 September 2009

Academic Editor: Alberto J. Castro-Tirado

Copyright © 2010 José M. Madiedo et al. This is an open access article distributed under the Creative Commons Attribution License, which permits unrestricted use, distribution, and reproduction in any medium, provided the original work is properly cited.

A robotic observatory has been setup in the south-west of Spain with the aim to study meteoroids interacting with the Earth's atmosphere and meteoroids impacting on the Moon's surface. This is achieved by using an array of high-sensitivity CCD video cameras and three automated Schmidt-Cassegrain telescopes. We summarize here the main characteristics of this new facility.

1. Introduction

Since November 2008 a new robotic observatory is being setup by the University of Huelva in the environment of the Doñana National Park, in the south-west of Spain. Most of the systems in this astronomical observatory operate within the framework of the Spanish Meteor Network (SPMN), which is an interdisciplinary project dedicated to study meteoroids streams and the interaction of these particles of interplanetary matter with the Earth's atmosphere. Climate conditions in this area provide over 320 clear nights per year, which makes this location ideal for this research project. One of the systems we use for this purpose is based on a network of video stations located in different places in Spain. These employ an array of high-sensitivity CCD video cameras to monitor the night sky. The first two of these stations in Spain were setup in Andalusia by the University of Huelva in during 2006, and one more video station was setup by the same university in this region in 2007 [1]. Since then, these systems have been improved with the development of dedicated software for automation and data reduction. In fact, software development has been one of our more intensive and productive areas since 2006, and several packages with a total of over 500.000 C++ code lines have been written. The configuration and characteristics of these

video devices have been also improved continuously. This has resulted in a significant advance that has been made in the latest video station setup by the above-mentioned astronomical observatory in 2009, as in this case the meteor detection system is fully autonomous, although it is flexible enough to allow for in situ or remote operation when necessary. This is the first robotic video CCD station for meteor observing that has been installed in Spain.

On the other hand, an automated system for lunar impact flashes detection has been setup in collaboration with IAA-CSIC. This is based on three telescopes that monitor the impact of meteoroids on the surface of the Moon. An important synergy is expected from the results recorded by both systems.

2. Robotic Meteor Observing Station

The University of Huelva is a pioneer in the development of fixed and mobiles video CCD stations for meteor observing in Spain. Thus, the first two of these stations operating in this country were setup by this institution in Andalusia in 2006 and one more video station was setup by the same university during 2007 [1–3]. During the last three years significant data have been obtained in collaboration with other SPMN video stations that have been setup later on [3–6].



FIGURE 1: Images of the control room and some of the high-sensitivity CCD video cameras operating from the astronomical observatory setup by the University of Huelva.

Our new CCD video station is coordinated with the three above-mentioned ones and with several more SPMN stations that were setup later on in other locations in this country [1–3]. However, in this case the observing station has been configured to work in an autonomous way. It started operation in April 2009 and employs an array of 12 high-sensitivity Watec and Mintron CCD video cameras (Watec Corporation, Japan; Mintron Enterprises Co., Japan). Seven of them monitor the night sky and the other five operate during daytime (Figure 1). Nocturnal cameras are also endowed with holographic diffraction gratings (1000 grooves per millimeter) for obtaining meteor spectra. Fast aspherical lenses ($f0.8$) are attached to these cameras to maximize image quality and detect meteors as faint as magnitude $+2/+3$ without using image intensifiers. Their focal length ranges from 3.8 to 6 mm. Thermoelectric coolers are also attached to the cameras when operation temperature is above 25 degrees Celsius in order to improve the signal/noise ratio. The images taken by each camera at 25 fps with a resolution of 720×576 pixels are continuously sent to a PC computer through a video capture card. The computers run a software package (UFOCapture, by SonotaCo, Japan) that automatically registers meteor trails and stores the corresponding video sequences on hard disk. This software includes time information on every video frame according to the current computer time. Each

computer is automatically synchronized every 5 minutes with two redundant time servers that employ a GPS antenna. This allows us to measure time in a precise way (about 0.01 sec.) along the whole meteor path. The video cameras and the 12 personal computers that control the observing station are automatically switched on and off at predefined times, so that the system can operate without human intervention.

Once the observing session is over, one of the software packages developed in our observatory scans every video file in order to identify very bright events (mag. -12 or brighter) and, if one of these is detected, an email is automatically sent to an operator. Another software also developed by the observatory automatically sends all the video files recorded during the observing session to an FTP server, from where they can be downloaded later on for data reduction. The astrometric measurements are then introduced into our recently developed Amalthea software that has been tested with Network software, which provides the equatorial coordinates of the meteors with a typical astrometric accuracy of about 0.01° [7]. By the method of the intersection of planes, we reconstruct the trajectory and length of the meteor in the Earth's atmosphere for those events that have been simultaneously registered from at least two observing stations. Time information needed for the calculation of the initial velocity, average velocity, and deceleration is directly obtained from the video sequences. The orbital parameters

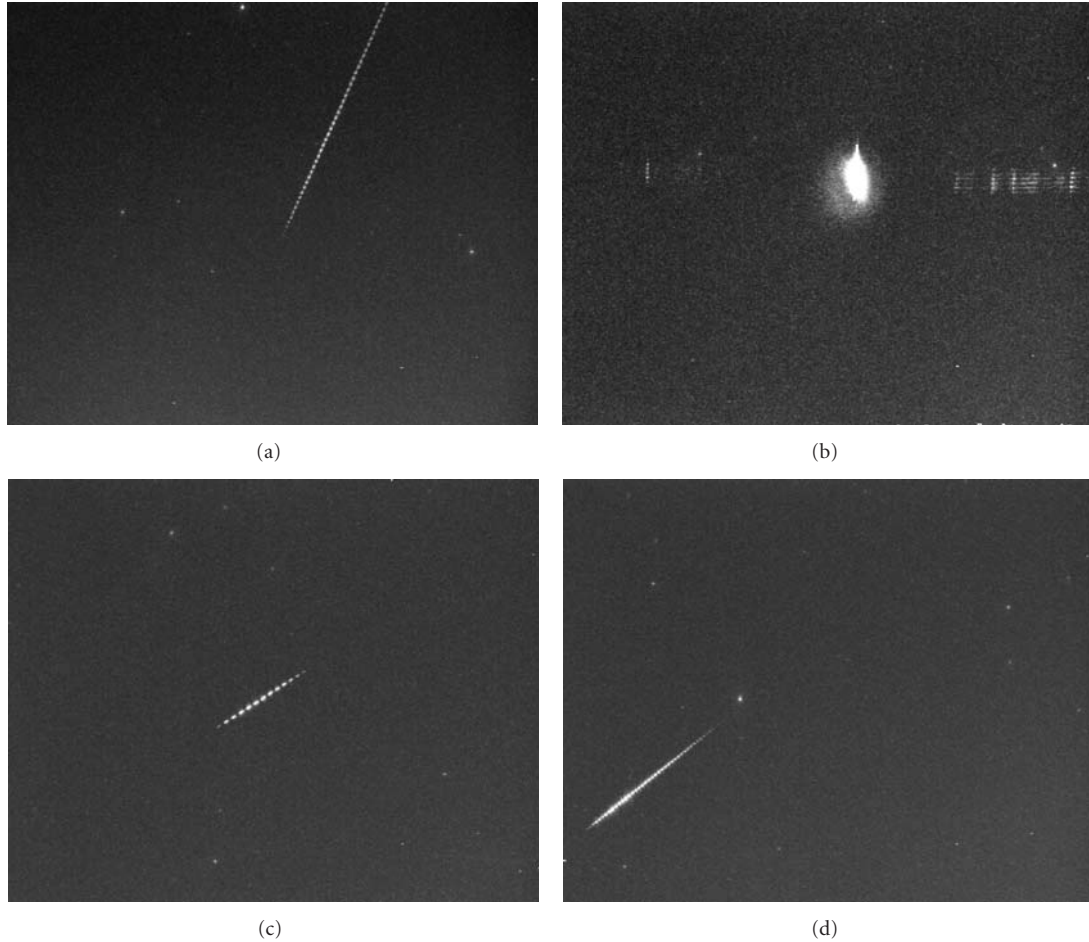


FIGURE 2: Low resolution mages of four of the meteors recorded by the robotic video CCD station. (a) Mag. 0 Virginid meteor registered on April 11, 2009 at 3 hours 37 minutes 34 ± 0.01 s UTC. (b) Mag. -8 Lyrid fireball registered on April 23, 2009 at 3 hours 24 minutes 07.49 ± 0.01 s UTC. The emission spectrum can also be noticed on this image. (c) Mag. -1 sporadic meteor registered on April 27, 2009 at 4 hours 05 minutes 54.12 ± 0.01 s UTC. (d) Mag. -2.5 Alpha-Bootid meteor registered on April 28, 2009 at 0 hour 36 minutes 51.52 ± 0.01 s UTC.

of the corresponding meteoroid can be also obtained with Amalthea. For meteors brighter than mag. -6 , the diffraction gratings attached to the video cameras operating during the night allow us to record the corresponding emission spectrum, which is also analyzed by the same software package in order to obtain information about the chemical composition of these particles. The parent bodies can be determined by means of our ORAS (ORbital Association Software) program, which employs several orbital similarity criteria to obtain this information [8–11].

Over 1200 meteor trails have been registered by this robotic video station during its first month of operation. Most of them are double-station events also registered from our video station in Sevilla, which is located at about 70 km from the new observatory. Figure 2 shows some of these events.

This new video station can be also remotely controlled by means of a standard web interface when necessary, as the different systems have been connected to a high-speed internet line (10 gigabit Ethernet). On the other hand, a high capacity UPS allows the observing station to keep on

working during over six hours in the event of a power failure. If the UPS also fails or its batteries run out of energy, the operation of the video station is automatically resumed when power is available again. This is done thanks to a proper BIOS configuration of the computers connected to the video cameras and to a software package (called MetStationONOFF) that has been developed in this observatory to accomplish this task.

3. Impact Flashes Detection System

Two automated 14-inch SC telescopes have been setup in the astronomical observatory to monitor the impact of meteoroids on the surface of the Moon (Figure 3). High-sensitivity Watec CCD video cameras working at 25 fps and with a resolution of 720×576 pixels have been attached to them in order to record the faint flashes produced by these impacts. A third 11-inch SC telescope will be also used from Sevilla, at about 70 km from the other two. This array of telescopes is intended to monitor the same area of the dark region of the Moon when the illuminated fraction of



FIGURE 3: Image of one of the two 14-inch SC telescopes integrating the impact flashes detection system.

our natural satellite ranges from 0 to 60%. By using several telescopes at the same time we can discard flashes produced by other sources, such as cosmic rays, space debris, satellites, and so forth [12]. The system has just been installed and is ready to start operation. It can be controlled in situ or remotely via a high-speed Internet connection.

The MIDAS software has been recently developed in our observatory to automatically identify lunar impact flashes produced by meteoroids. It allows for fast real time processing of the images obtained by the CCD video cameras attached to the telescopes. These images are sent from the cameras to the computers by means of a video capture card. The software also allows us to analyze video sequences previously recorded on hard disk or other media. GPS time inserters include time information on every video frame in order to measure time with a precision of about 0.01 second. These frames are continuously analyzed to identify the flashes, calculate the corresponding selenographic coordinates of the impact, and estimate which is the likely origin (meteoroid shower and radiant) of the meteoroid. A photometric analysis is also performed in order to estimate the mass of the impactor.

Our software can also identify if a given flash has been produced by a meteoroid impacting on the Moon's surface and, so, if it must be analyzed or, on the contrary, if a flash has been produced by an artefact on the CCD of the corresponding video camera and, so, it has to be discarded. Thus, when a telescope detects an event it communicates with the other telescopes in the system via TCP/IP network protocol (up to 256 telescopes could be connected in this way by means of MIDAS). The other telescopes may then confirm or not if they have detected the same event. If the event is confirmed, it is automatically stored in a database for further processing. On the contrary, the event is ignored.

Although this system is fully operative and the impact flashes detection task works in an autonomous way thanks to the MIDAS software, further developments are necessary in order to achieve a fully robotic operation. Thus, for instance, some issues related to the improvement of lunar tracking must be solved.

This technique is very useful to provide valuable information about the flux of large meteoroids reaching the Earth [12]. It has the advantage that the area covered by the telescopes monitoring the surface of the Moon is much larger than the area covered by the systems that register the interaction of meteoroids with the Earth's atmosphere. Anyway, an important synergy is expected from the data recorded by both systems. Of special interest is, for instance, the identification of common events that would allow us to establish the possible existence of clusters of large meteoroids that might be impacting on the Moon and also producing very bright fireballs in the Earth's atmosphere that could give rise to meteorites.

4. Conclusions

A significant improvement has been made in our meteor network by setting up an autonomous CCD video station for meteor detection in the environment of the Doñana National Park, in the south-west of Spain. This has been mainly achieved thanks to several software packages that have been developed in our observatory since 2006. Software development has been also a very active task in the field of lunar impact flashes detection and a program called MIDAS, which is capable of real-time image processing, is available for this. An important synergy is expected from the results obtained by the lunar impacts detection system, which uses the Moon as a detector of meteoroids, and the meteor observing station, which uses the Earth's atmosphere for this purpose. Of special interest is, for instance, the detection of common events that might reveal the existence of associated meteoroids that could give rise to impacts on the Moon and also to very bright fireballs in our atmosphere or even to meteorite falls. These systems will also provide more accurate data related to the flux of interplanetary matter reaching the Earth. Optimal climate conditions in this area of Spain where the observatory is located (over 320 clear nights per year) will play an important role in this research.

Acknowledgment

The first author thanks IAA-CSIC for the support received to setup the Moon impact flashes detection devices.

References

- [1] J. M. Madiedo and J. M. Trigo-Rodríguez, "Multi-station video orbits of minor meteor showers," *Earth, Moon and Planets*, vol. 102, no. 1–4, pp. 133–139, 2007.
- [2] J. M. Trigo-Rodríguez, J. M. Madiedo, A. J. Castro-Tirado, et al., "Spanish meteor network: 2006 continuous monitoring results," *WGN, Journal of the International Meteor Organization*, vol. 35, no. 1, pp. 13–22, 2006.
- [3] J. M. Trigo-Rodríguez, J. M. Madiedo, J. Llorca, et al., "The 2006 orionid outburst imaged by all-sky CCD cameras from Spain: meteoroid spatial fluxes and orbital elements," *Monthly Notices of the Royal Astronomical Society*, vol. 380, no. 1, pp. 126–132, 2007.

- [4] J. M. Trigo-Rodríguez, E. Lyytinen, D. C. Jones, et al., “Asteroid 2002NY40 as a source of meteorite-dropping bolides,” *Monthly Notices of the Royal Astronomical Society*, vol. 382, no. 4, pp. 1933–1939, 2007.
- [5] J. M. Trigo-Rodríguez, J. M. Madiedo, I. P. Williams, et al., “The outburst of the κ -Cygnids in 2007: clues about the catastrophic break up of a comet to produce an Earth-crossing meteoroid stream,” *Monthly Notices of the Royal Astronomical Society*, vol. 392, no. 1, pp. 367–375, 2008.
- [6] J. M. Trigo-Rodríguez, J. M. Madiedo, I. P. Williams, et al., “Observations of a very bright fireball and its likely link with comet C/1919 Q2 Metcalf,” *Monthly Notices of the Royal Astronomical Society*, vol. 394, no. 1, pp. 569–576, 2009.
- [7] J. M. Trigo-Rodríguez and J. M. Madiedo Earth, “Determination of meteoroid orbits and spatial fluxes by using high-resolution all-sky CCD cameras,” *Earth, Moon, and Planets*, vol. 102, no. 1–4, pp. 231–240, 2008.
- [8] R. B. Southworth and G. S. Hawkins, “Statistics of meteor streams,” *Smiths Control Astrophysics*, vol. 7, pp. 261–285, 1963.
- [9] J. D. Drummond, “A test of comet and meteor shower associations,” *Icarus*, vol. 45, no. 3, pp. 545–553, 1981.
- [10] G. Valsecchi, T. Jopek, and C. Froeschlé, “Meteoroid stream identification: a new approach. I. Theory,” *Monthly Notices of the Royal Astronomical Society*, vol. 304, no. 4, pp. 743–750, 1999.
- [11] P. Jenniskens, “Meteoroid streams that trace to candidate dormant comets,” *Icarus*, vol. 194, no. 1, pp. 13–22, 2008.
- [12] J. L. Ortiz, F. J. Aceituno, J. A. Quesada, et al., “Detection of sporadic impact flashes on the Moon: implications for the luminous efficiency of hypervelocity impacts and derived terrestrial impact rates,” *Icarus*, vol. 184, no. 2, pp. 319–326, 2006.

Research Article

AROMA (AGU Robotic Optical Monitor for Astrophysical Objects)

Ichiro Takahashi,¹ Kosuke Tsunashima,¹ Takayuki Shiraki,¹ Toru Kojima,¹ Atsumasa Yoshida,¹ and Yujin E. Nakagawa²

¹ Department of Physics and Mathematics, Aoyama Gakuin University, 5-10-1 Fuchinobe, Sagamihara, Kanagawa 229-8558, Japan

² Institute of Physical and Chemical Research, 2-1 Hirosawa, Wako, Saitama 351-0198, Japan

Correspondence should be addressed to Ichiro Takahashi, itakahashi@phys.aoyama.ac.jp

Received 30 June 2009; Accepted 23 October 2009

Academic Editor: Taro Kotani

Copyright © 2010 Ichiro Takahashi et al. This is an open access article distributed under the Creative Commons Attribution License, which permits unrestricted use, distribution, and reproduction in any medium, provided the original work is properly cited.

We are developing and operating the automatic telescope *Aoyama Gakuin University Robotic Optical Monitor for Astrophysical objects* (AROMA) in the Sagamihara Campus of Aoyama Gakuin University. AROMA is composed of two observational equipments, AROMA-N and AROMA-W. AROMA-N is a 30-cm aperture telescope system for rapid follow-up observations of the optical afterglow of gamma-ray bursts. Automatic analysis pipeline for AROMA-N has been developed and is working. The other observational equipment AROMA-W is a wide-field observation system using multiple digital single-lens reflex cameras. It covers a large FOV of about $35^\circ \times 25^\circ$. AROMAW provides photometric data in four bands with a limiting V magnitude of about 12-13 mag. Software to analyze massive image data automatically is being developed. We plan to monitor the luminosities of all the stars in the FOV of AROMA-W, detect optical transients, and trigger a follow-up observation with AROMA-N. We report on the development status and observational results of AROMA.

1. Introduction

There are various Optical Transients (OTs) which can be observed from ground based telescopes. Supernovae and novae are surveyed by various telescopes, and have increased the number of discoveries every year. Some Gamma-Ray Bursts (GRBs) are bright in optical [1]. In GRB 080319B, the brightest prompt optical emission that peaked at a visual magnitude of 5.3 was discovered during the burst [2]. Certain X-ray transients also have been observed not only in X-rays but also in optical. Microquasar V4641 Sgr can usually be observed with magnitude of 12 in optical. It lightened up to $m = 9$ correlated with X-rays in 1999. After that, a small-scale outburst is observed almost every year [3, 4]. The Tago event, a nearby gravitational microlensing event, displayed brightening up to 8 mag [5]. Comets and meteors also contribute to OTs. As for these phenomena, we cannot easily predict when and where they occur. To observe them before the onset, it is necessary to monitor the sky with a wide field

of view and a high observational efficiency. Today these wide field cameras, utilizing CCDs and the commercial camera lenses, designed for this purpose have been established and are already in operations (e.g., WIDGET [6], Pi of the sky [7], MASTAR-VWF-4 [8], and RAPTOR 16 [9]). While these observational equipments are expensive, we are developing a low cost wide-field observation device AROMA-W that uses digital single-lens reflex cameras (DSLRs).

2. AROMA

We are developing and operating *Aoyama Gakuin University Robotic Optical Monitor for Astrophysical objects* (AROMA). AROMA is set up in the Sagamihara Campus of Aoyama Gakuin University (Latitude = 35.566° and Longitude = 139.403°). It is composed of two kinds of remote observation systems, AROMA-N and AROMA-W. Figure 1 is photographs of two equipments of AROMA.

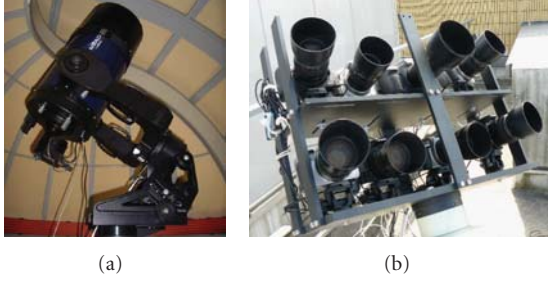


FIGURE 1: AROMA-N (a) and AROMA-W (b).

AROMA-N is a rapid follow-up telescope for astronomical transients. For GRB optical afterglows, this system autonomously makes rapid follow-up observations within tens of seconds based on positional information from satellites such as *Swift*. AROMA-N currently consists of a Schmidt-Cassegrain telescope with 30.5 cm aperture (MEADE LX200GPS-30), a Peltier cooled CCD camera (SBIG ST9-XE), and multiple standard filters (Clear, B, V, R and I). The limiting magnitude is typically about 17 mag in the Clear-band (in 100 s at 3σ level). Automatic analysis pipeline is being developed in order to search for optical afterglows.

AROMA-W monitors the sky with a wide field of view. It has been developed since 2005. We have assembled the device and are starting initial operation now. The performance and the development of AROMA-W are described in the following sections.

3. AROMA-W

3.1. Instrumentation. AROMA-W consists of multiple DSLRs on an equatorial mount. The cameras used are one Canon EOS 5D with a EF200mm F2.8 USM and seven EOS 350Ds (EOS D Rebels) with EF100mm F2.0 USMs. Because their prices are about 1/10 compared with CCD cameras, a lot of those reserves can be prepared. As a result, they can easily exchange without a loss of the observation time even when they suffered from troubles in system such as a shutter failure. These cameras are set up in a purpose-built mount and put on equatorial mount “EM-400 Temma2”. The cameras and the equatorial mount are operated remotely. The shutters of the cameras are controlled by the pulse from the DIO (Digital I/O) board in a Personal Computer (PC) so that the exposure of each camera is synchronized. The acquired data are transferred to PCs by USB every one frame. Since it takes time if the data of all cameras are transferred to one PC at a time, they are allotted with three PCs. The equatorial mount is controlled by the PC and will follow the field of view of the GRB observation satellites (e.g., *Swift*, *Fermi*). Figure 2 shows the schematic of AROMA-W system.

3.2. Multiple Bands Observation. The optical filters are placed on the image sensor of a DSLR along with a Bayer arrangement which has an alternating arrangement of three primary color red, green, and blue (here we call R' , G'

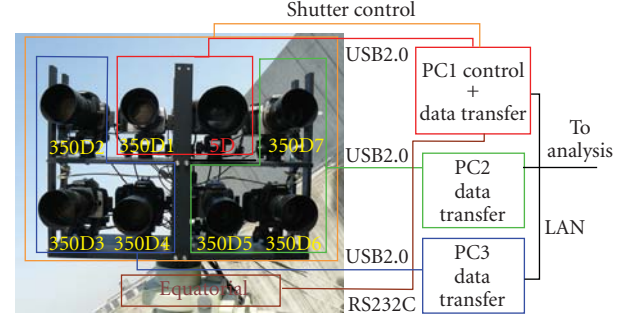


FIGURE 2: The schematic of AROMA-W system. Each camera and the equatorial mount are controlled by PC1. The observational data are acquired individually by the three PCs and forwarded to an analysis machine through LAN.

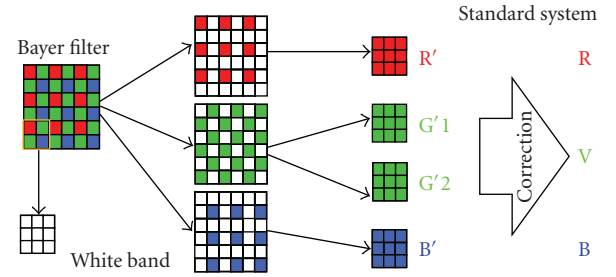


FIGURE 3: The schematic of the Tri-color imaging. Red, two, green, and blue filters are placed along with a Bayer arrangement on the image sensor. The W band image is made by adding the four images.

and B') [10]. Simultaneous multiple-band observations are achieved by reading the data of these filters individually (Tri-color imaging). W band data which represent brightness information is obtained by adding the three-color data. Since the digital cameras employ R' , G' and B' filters which differ a little from the standard system (R , V , and B), the relation between our filter system and the standard system has been investigated by observing the same objects with various magnitude ranges simultaneously by both well-calibrated AROMA-N and AROMA-W. Then, a relative photometry between the filters was performed and magnitude relations (i.e., $R-R'$, $V-G'$, and $B-B'$) are obtained. For example, the relations for EOS 5D are well fitted by a linear function; $R = (0.88 \pm 0.02)R' - (3.1 \pm 0.3)$, $B = (0.93 \pm 0.02)B' - (0.2 \pm 0.3)$ and $V = (0.90 \pm 0.01)G' - (2.8 \pm 0.2)$, where the quoted errors are 68.3% confidence levels. 350D also has a similar linearity. The standard system photometry with DSLRs can be done by correcting it according to this linearity. Figure 3 shows the schematic of the Tri-color imaging.

3.3. Field of View. The large field of view (FOV) of AROMA-W consists of that of the multiple cameras to make a mosaic image. An EOS 5D with an EF200mm F2.8 USM has a FOV of $10.2^\circ \times 6.8^\circ$, and a 350D with an EF200mm F2.8 USM has that of $13^\circ \times 9^\circ$. A wide FOV of $35^\circ \times 25^\circ$ is covered with eight

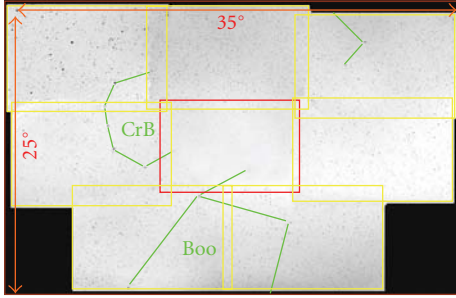


FIGURE 4: The AROMA-W FOV. This is a combined image of 20 frames of W band exposed for 30 s. The mosaic image shows the data taken by all eight cameras, in which the red rectangle displays the FOV of 5D and the yellow FOVs of 350Ds.

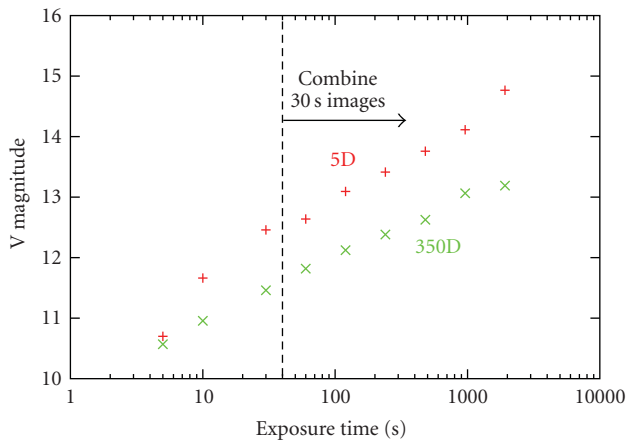


FIGURE 5: The summary of W band limiting magnitude with 5D and 350D. In the right side of the dashed line, the exposure time becomes long by combining the frames. There is a difference of about one magnitude between 5D and 350D.

cameras at a time. Figure 4 shows an image of the AROMA-W FOV. The view of the 5D is arranged at the center, and the views of 350D are arranged in the surroundings.

3.4. Limiting Magnitude. The limiting magnitudes of each filter were investigated for all digital cameras. The AROMA site is near Tokyo, and the sky background condition is not so good. The 3σ limiting magnitudes of EOS 5D (20 s exposure, winter data) are $R = 12.1$, $V = 12.8$ and $B = 13.5$. Those of 350D are $R = 11.9$, $V = 12.3$, and $B = 13.4$. Figure 5 shows the summary of W band limiting magnitude with 5D and 350D. This implies that our new system can detect GRB optical flashes like GRB 990123 with ~ 9 magnitude and GRB 080319B with ~ 5.3 magnitude. It is known that supernovae can be very bright in optical and X-ray band. Since the time scale of their decay is tens of days, and the optical peak is about 12–13 mag (V band), AROMA-W can detect such a peak with a few minutes exposure. Some X-ray novae also can be detected with the sensitivity of AROMA-W. Generally, after an X-ray nova is detected with X-ray detectors, observations in the optical band are conducted.

If an extensively large FOV monitor observation, such as those possibly by AROMA-W, is running during almost all the night, a detection in optical could be made in advance of X-rays. For example, V4641 Sgr becomes bright almost every year and it became as bright as 9 mag. in September, 1999. Moreover, sensitivity limits of AROMA-W are also appropriate to detect the large amplitude flares of BL-LACs and OVV (optically violent variable) quasars.

4. Real-Time Analysis of AROMA-W

We are developing the real-time analysis pipeline for AROMA-W. The data will be analyzed automatically in parallel with observations. Basic processes of the pipeline are as follows. First, the data of AROMA-W are transmitted from Compact Flash (CF) in the DSLRs to the analysis PCs via the transfer PCs. The dead time between frames can be shortened to about 3 seconds by transferring data while a following frame is exposed. When data are transmitted to the analysis PCs, the image processing is started. The RAW data are converted to FITS, and then the data reduction is processed; subtracting dark noise and correction of flat pattern, after those, resolving data into tri-colors and positional corrections are performed. Next, the main analysis starts; detection of *astronomical objects* and comparison with star catalogs (mainly USNO B1.0) follow. About 2000 to 5000 objects are detectable from the data of each camera. By comparing photometry data of these stars with the previous frame data, brightening OTs and fading stars are searched. Light curves of magnitude and flux ratio are obtained for all the objects within the AROMA FOV by the differential photometry. The variability of each light curve is investigated at certain interval, and if it exceeds a certain threshold, it is recorded and/or triggers an alert automatically. The development of the pipeline has progressed to produce light curves until now. The rejection algorithm of the false events will be added to the current software in the future. By monitoring light curves continuously, variable stars and transient objects (GRB, SNe, X-ray novae, etc.) will become detectable. Furthermore, an unexpected brightening and variability may also be detectable.

5. Test Observation

We have tested the performance to detect variable stars several times so far by using the analytical pipeline described in the previous section. Figure 6 shows examples of variable stars' light curves which were detected by the real-time analysis. Various variable stars are detected automatically during the test, though the observation time is short. However, there is still a problem in the detection program. Tracks of airplanes and double star, and so forth are misidentified as OTs.

6. Conclusions

In order to observe OTs of GRBs, SNe, X-Ray novae, variable stars, and so forth, we are developing AROMA-W:

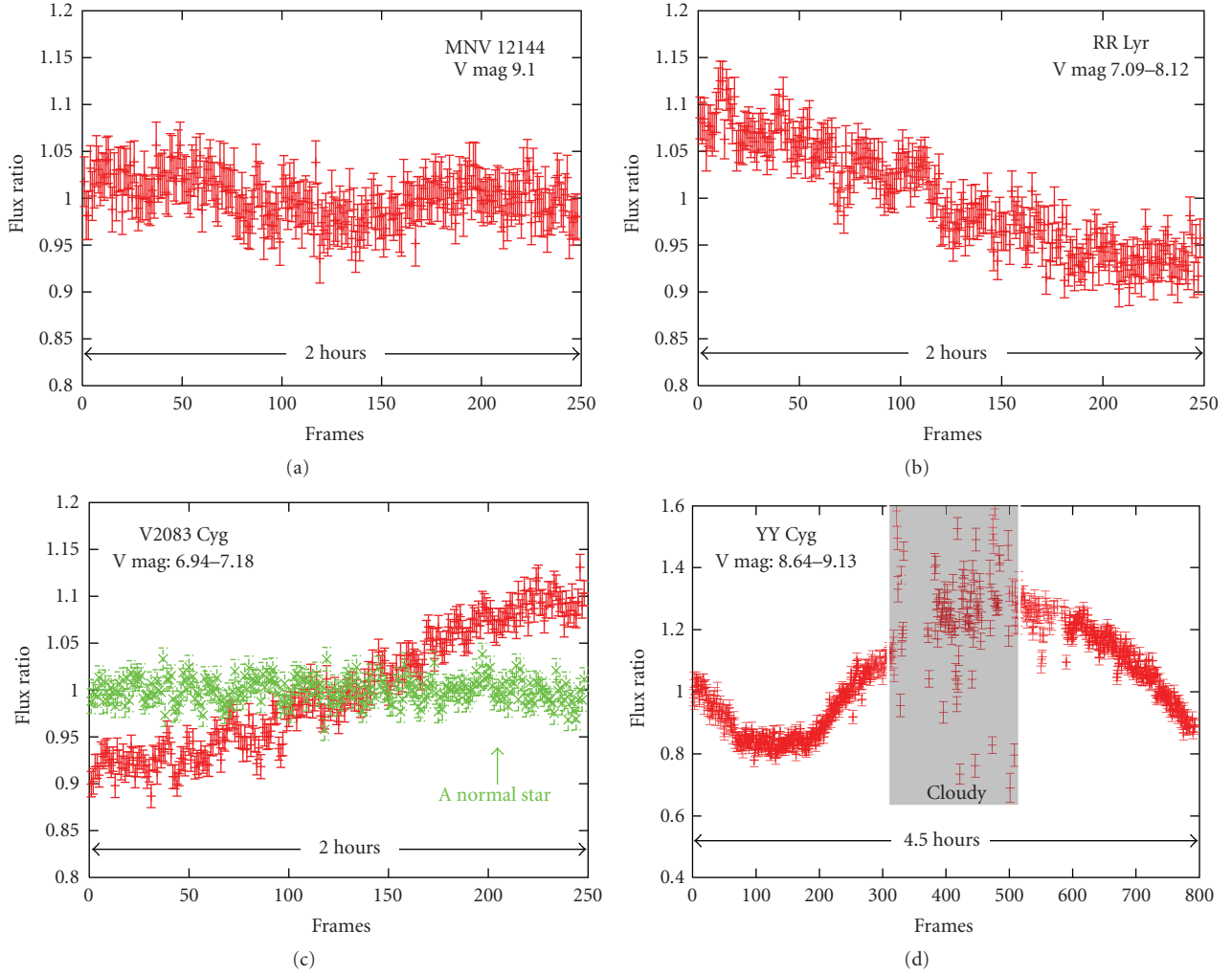


FIGURE 6: Examples of variable star's light curves which were detected by real-time analysis. In the panel of V2083, the light curve of a nearby usual star is plotted in green. Unfortunately, it became cloudy partly during the observation of YY Cyg; this part is colored in gray.

the full-time wide-field observation system using multiple digital single-lens reflex cameras. AROMA-W can detect stars with brightness down to 12–13 mag in the field of view of $35^\circ \times 25^\circ$ with an exposure time of 20 s. We are currently developing a real-time analysis pipeline, which will work in parallel with the observation. It detects OTs and makes the light curves. The test observation by AROMA-W was done, and some already-known variable stars have been detected automatically.

The next steps we foresee are the followings:

- (i) starting main observations of AROMA-W,
- (ii) improving analytical pipeline,
- (iii) building the data archive,
- (iv) setting up the AROMA website,
- (v) coordinating observation of AROMA-W and AROMA-N,

- (vi) aiming at real-time detection of OTs by AROMA-W to reporting it promptly to various telescopes worldwide.

References

- [1] J. Van Paradijs, P. J. Groot, T. Galama, et al., “Transient optical emission from the error box of the γ -ray burst of 28 February 1997,” *Nature*, vol. 386, pp. 686–689, 1997.
- [2] J. L. Racusin, S. V. Karpov, M. Sokolowski, et al., “Broadband observations of the naked-eye γ -ray burst,” *Nature*, vol. 455, pp. 183–188, 2008.
- [3] M. Uemura, R. E. Mennickent, and R. Ishioka, “Rapid optical fluctuations in the black hole binary V4641 sagittarii,” *Publications of the Astronomical Society of Japan*, vol. 54, pp. 95–101, 2002.
- [4] M. Uemura, et al., “Optical observation of the 2003 outburst of a black hole X-ray binary, V4641 Sagittarii,” *Publications of the Astronomical Society of Japan*, vol. 56, pp. 823–829, 2004.
- [5] A. Fukui, F. Abe, K. Ayani, et al., “Observation of the first gravitational microlensing event in a sparse stellar field: the

- tago event,” *The Astrophysical Journal*, vol. 670, pp. 423–427, 2007.
- [6] T. Tamagawa, K. Torii, M. Matsuoka, et al., “Spectral analysis of 35 GRBs/XRFs observed with HETE-2/FREGATE,” *New Community of Ichthus Mission Church*, vol. 28, pp. 771–774, 2005.
- [7] M. Sokolowski, et al., “ Investigation of astrophysical phenomena in short time scales with “Pi of the Sky” apparatus,” <http://grb.fuw.edu.pl/>.
- [8] <http://apollo.sai.msu.ru/>.
- [9] <http://www.raptor.lanl.gov/>.
- [10] B. E. Bayer, US patent no. 3,971,065, July 1976.

Research Article

T35: A Small Automatic Telescope for Long-Term Observing Campaigns

Susana Martín-Ruiz,¹ Francisco J. Aceituno,¹ Miguel Abril,¹ Luis P. Costillo,¹ Antonio García,¹ José Luis de la Rosa,¹ Isabel Bustamante,^{1,2} Juan Gutierrez-Soto,¹ Héctor Magán,^{1,3} José Luis Ramos,¹ and Marcos Ubierna^{1,4}

¹ Instituto de Astrofísica de Andalucía (CSIC), Camino Bajo de Huétor, 50. 18008 Granada, Spain

² Parque de las Ciencias, Avda de la Ciencia s/n, 18006 Granada, Spain

³ Centro Astronómico Hispano Alemán, C/ Jesús Durbán Remón 2-2, 04004 Almería, Spain

⁴ SENER Ingeniería y Sistemas S.A., Avda. Zugazarte, 56. Las Arenas, 48930 Bizkaia, Spain

Correspondence should be addressed to Susana Martín-Ruiz, susana@iaa.es

Received 30 June 2009; Accepted 29 December 2009

Academic Editor: Lorraine Hanlon

Copyright © 2010 Susana Martín-Ruiz et al. This is an open access article distributed under the Creative Commons Attribution License, which permits unrestricted use, distribution, and reproduction in any medium, provided the original work is properly cited.

The T35 is a small telescope (14") equipped with a large format CCD camera installed in the Sierra Nevada Observatory (SNO) in Southern Spain. This telescope will be a useful tool for the detecting and the studying of pulsating stars, particularly, in open clusters. In this paper, we describe the automation process of the T35 and also show some images taken with the new instrumentation.

1. Introduction

At the beginning, the main motivation for carrying out the T35 project was the search for and the study of pulsational behaviour of variable stars in open clusters. The role of open clusters, as stellar associations with a common origin, is fundamental in Asteroseismology. The physical properties shared by the members of a cluster—distance, reddening, age, and metallicity—provide us with very stringent constraints on the models, complementing the information obtained from the oscillation frequencies of the pulsating stars. Exhaustive studies on the incidence of variability and its behaviour, especially on pulsators located in the lower part of the Instability Strip (γ Doradus, δ Scuti, or solar-type variables), helps us to know better about some of the fundamental parameters (Teff, log g, chemical composition and rotational velocity) of these stars.

A previous systematic survey in search of γ Doradus variability in different open clusters with different metallicities and ages was performed between the years 1995 and 2000 [1–3]. More than 340 nights of observation

at Sierra Nevada Observatory (SNO) (Granada, Spain), using photoelectric photometry in the Strömgren-Crawford system, were used to carry out this study. Nine γ Doradus were found amongst the 41 variable stars detected in a sample of 175 members distributed among the 10 open clusters applying two methods based on different statistical tests to classify our light curves. The main outcomes were that the probability of finding γ Doradus stars increases if the sample is restricted to AF-type stars (effective temperature between 6900 and 7200 K), luminosity class IV–V (stars in the main sequence), and solar-type metallicity ($Z = 0.02$) and also that this probability was not bounded to the age of the cluster but to its metallicity, contradicting the theories published by other authors. Although our results were very fruitful due to the high precision of our uvby β measurements, that is, less than two thousands of magnitude, the number of member stars and clusters studied in the sample was small with the addition of entailing an enormous observational effort. Therefore, we needed a telescope of only modest aperture (30–40 cm) to reach the desired S/N in a reasonable time.



FIGURE 1: Dome of the T35 telescope.

With this telescope it is possible to perform long-term observations of variable stars. Continuous observations in time as well as long-time baseline campaigns are essential to the study of variable stars, including binary systems and pulsating stars. It is very difficult to allocate long duration observing sessions on large telescopes.

The process of automation of the T35 has involved efforts in hardware, software, and mechanics. A general block diagram of the final system is shown in Figure 3, which is described in detail in the next sections.

2. T35 Setup

The T35 telescope (Figure 1) is located at the Loma de Dílar (2896 m altitude), near the central building of Sierra Nevada Observatory (Granada, Spain). Before this 14'' telescope was installed, the dome housed a different instrument, and therefore, first we had to restore and adapt the structure to our new instrumentation.

The 14'' Schmidt-Cassegrain telescope (35.56 cm) is a Celestron CGE-1400. The telescope is equipped with an SBIG STL-11000 CCD Camera with a KAI-11000M CCD detector (4008×2762 pixels $\times 9 \mu\text{m}$). Figure 2 shows both instruments. The field of view is 31.70×21.14 arcmin with a scale of 0.2475 arcsec per pixel. The camera has an internal self-guiding camera Texas Instruments TC-237H (657×495 pixels $\times 7.4 \mu\text{m}$) and an internal filter wheel with standard UBVR Johnson—Cousins filters.

Since the beginning, the aim of our project was to install a telescope in order to perform long-term photometric observing campaigns. Owing to the fact that the OSN is a high mountain observatory where adverse weather conditions happen frequently, the T35 telescope had to work in remote mode with the greatest grade of autonomy. To date we are working to get this objective and hope to robotize the system in the near future.

Regardless of whether the mode of operation, fundamental requirements of pointing and tracking as well as a minimum precision in the photometric measurements are necessary. Table 1 shows these basic parameters necessary for our objectives and those ones achieved in our telescope.



FIGURE 2: The telescope and CCD Camera.

TABLE 1: Values of pointing, tracking and photometric accuracy necessary for our scientific objectives and those achieved in the T35 telescope.

	Scientific objectives	Achieved values
Pointing	Better than 5' of arc	10' of arc
Tracking	0'' of arc in several min	1.''3 of arc in 2 minutes
Photometric accuracy	1-2 thousandth of mag	5-6 thousandth of mag

The photometric accuracy, the 5-6 thousands of magnitudes have been obtained observing a variable star during a nonphotometric night, taking the frames with binning 3×3 , and using faint comparison stars. Best outcomes, less than 2 mmag, can be achieved if the atmospheric conditions as well as the observing parameters (integration time, binning, etc.) are optimum. Respect to the tracking accuracy, it can be improved using the internal self-guiding camera but the small size of chip does not often allow us to find a bright star in the camera field of view. In order to solve this problem, an external autoguiding system is being implemented. To obtain a higher value of pointing accuracy is more complicated. The typical pointing values have been obtained using around 30 stars located in different positions in the sky. The telescope pointed out 10' of arc in 23% of the cases. To accurately point to objects, first we preformed the alignment procedure described in the telescope manual using two known stars. Although the telescope was aligned properly, a pointing model was created to improve even more the pointing precision. This model has been made using the application *TPoint* which works quite well with the telescope control programme *TheSky Astronomy Software*. Although the observed target falls inside the field of view of the camera, its position can be corrected by the user at the beginning of the observation.

The T35 telescope has been supported with funding from the Marie Curie Reintegration Grant "Detection and Survey of pulsating Star in Open Clusters: a step forwards in Asteroseismology" (MERG-CT-2004-513610) funded from the European Commission's Sixth Framework and from

the Spanish project “Participación española en la misión espacial CoRoT” (ESP2004-03855-C03-01).

3. Control System

As mentioned above, the objective of this project was to automate and control remotely the movement of telescope and dome. The dome control system, in particular, is required to implement the following functions:

- (1) continuous reading and updating of Azimuth (Az),
- (2) ability to move to an absolute position, from 0 to 359 degrees,
- (3) ability to move to a relative position (\pm xxx degrees),
- (4) ability to move to a prefixed park position,
- (5) management of a zero cross-reference position for loss of steps error detection,
- (6) ability to modify remotely the constants of operation (park position, inertia constant, zero-cross position, etc.),
- (7) measurements of consumption, and ability to detect a malfunction of the system through measurement of anomalous values.

As can be seen in Figure 3, both telescope and dome can be controlled locally from a notebook or a conventional PC installed inside the dome (Telescope Control System, hereafter TCS). However, the control of the system in usual operation is performed from one of the user computers in the main building of the observatory.

Regarding hardware elements, in this application both commercial (zero cross-sensor, encoder, and dome motor) and in-house developments (consumption measurement card, dome controller) have been used.

With respect to software, at least two programs were needed for this application, one to run on the Dome Controller (DC) and another on the TCS or user computer. Apart from these, an engineering program was also developed for technical purposes.

The main mechanical works were related to the design and fabrication of adaptors for the integration of the different elements in the dome, in order to assure a proper reading of the encoder and the zero cross-sensor minimizing loss of steps.

In the next sections, the main tasks, elements, and programs developed for this application are discussed in more detail.

3.1. Hardware. The user interface and main control of both telescope and dome are provided by TCS, which is connected to the Internet in order to allow the system to be controlled remotely. In practice, the system is controlled from the main user computer on the T90 console. The TCS is connected via RS-232C to the telescope and the DC.

The DC, developed specifically for this application, is based on a PIC18F458 microcontroller, in which we had experience from previous projects as regards programming

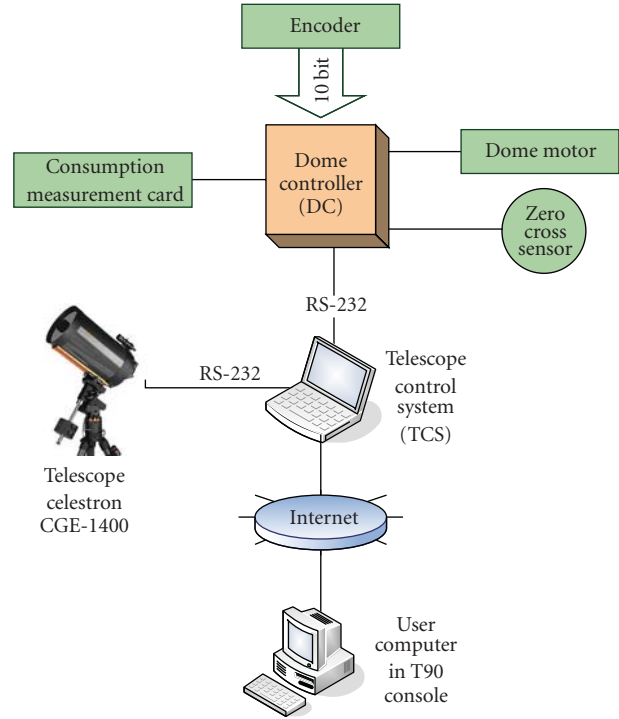


FIGURE 3: General block diagram of the system.

and developing [4]. There exist several commercial modules for control of small and medium-sized domes. However, the solution chosen was based on a modular system designed in the *Instituto de Astrofísica de Andalucía* and used in previous projects. This solution presents several advantages over a commercial system. An in-house design is well known and documented, and therefore, it is easier to maintain. It allows for an exact adaption to particular requirements at a low price. The heart of the system, the microcontroller PIC18F458, can be easily programmed in high-level languages using different tools supplied by the manufacturer or third party providers. Finally, the design's modularity made it compatible and interchangeable with other modules used in our institution. These factors can make this DC attractive for other telescopes, provided that their requirements are similar to those of our system. In fact, the advantages associated to this in-house developed system (modularity, ease of programming, and price) can result in interest for other institutions, not only to develop their own dome controller, but also other systems whose requirements are affordable by the PIC18F458 microcontroller.

As can be seen in Figures 3, 4 and 5, the DC reads the dome position from an absolute Gray encoder with a resolution of 10 bits (Hohner, model CS10-81310311-1024). A zero cross sensor allows for loss of steps error detection. The system also employs a consumption reading card, used to detect and prevent breakdowns due to ice on the dome or malfunction of the motor.

In addition to the reading of the encoder and the zero cross-sensor, the DC performs actions on the dome motor. The DC uses a driver card for adaption of the control signals

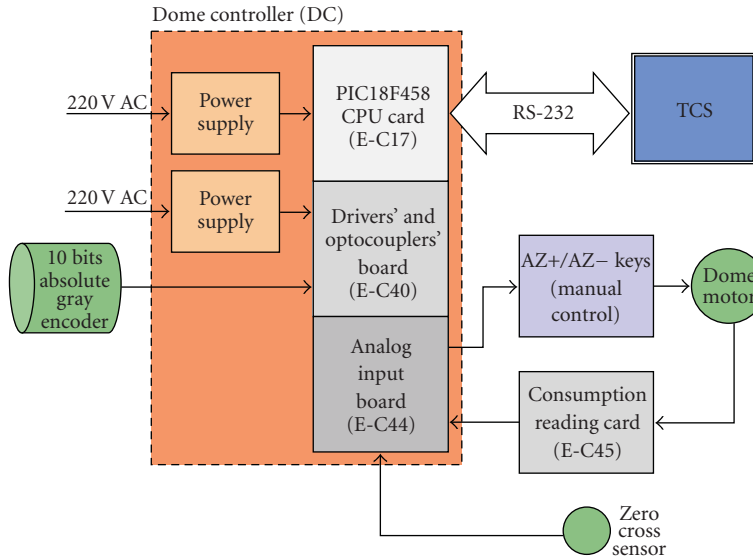


FIGURE 4: Connections among the different elements used in the dome control.

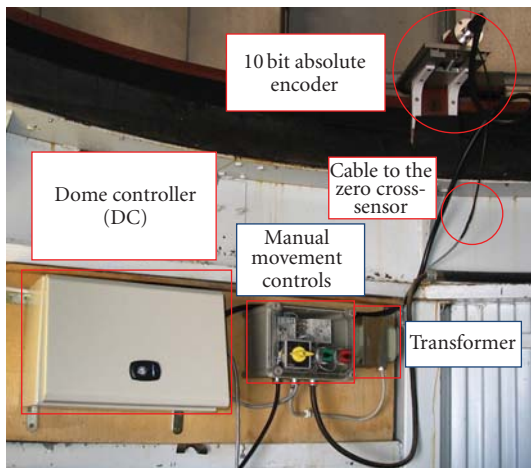


FIGURE 5: Photograph showing part of the system hardware. Red text show elements developed and described in this work.

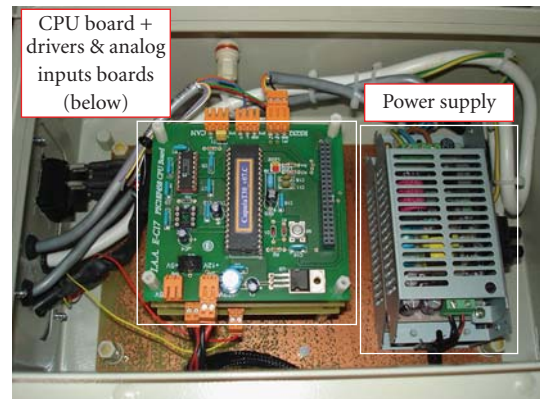


FIGURE 6: Interior of the Dome Controller (DC), showing its different boards and elements.

to the levels needed for acting on the dome motor. In order to facilitate the use of the previous operating hardware, the DC acts in parallel with buttons AZ+ and AZ−, which allow for manual movement of the dome. Consequently, there is no need for flipping between a manual and an automatic mode of operation. Figures 3 to 6 show a general block diagram of the system and some pictures of its hardware implementation.

3.2. Software. The Control Software of this automatic telescope is based on the ASCOM (Astronomy Common Object Model) standards. The telescope, the CCD camera, and the filter wheel are ASCOM compliant, so the manufacturers provide the corresponding ASCOM driver interfaces.

Regarding the DC, a program for the 18F458 micro-controller has been developed. The source code has been

written in C, using a PICC compiler integrated in the MPLAB environment. The program handles the acquisition of data from the absolute encoder, zero cross-sensor, and consumption reading card. In response to the read values, it calculates the dome target position and generates the necessary signals for the control of the motor. DC and TCS are connected through an RS-232 link, using control commands and data packets in accordance with a protocol defined by the authors and described in the next section.

The ASCOM Platform includes an application called ASCOM Dome Control Panel, which is a simple dome control “middleware”. It provides a uniform and consistent interface, regardless of the actual hardware and connections used. In our application, it was necessary to develop a driver that translates the ASCOM Dome interface to our software RS-232 commands (see Section 3.2.2 below).



FIGURE 7: Graphic user interface of the engineering program developed for technical purposes.

Although dome control is usually performed through the ASCOM Dome interface, an additional engineering program has been developed in LabVIEW (see Figure 7). This program will not be running during the usual operation of the system. It only needs to be executed eventually when a closer monitoring of the control and data packets is desired. This result is useful when trying to fix a breakdown, checking the correct operation, or implementing new features in the system. As can be seen, the graphic interface displays all the information about the dome status and allows for sending all the control commands. In the upper right corner it displays the present position of the dome, which is updated continuously with the values read from the encoder. In addition to the different buttons that perform the various commands, there is a command line available where a user can write directly the command in the format shown in Table 2. In order to detect interrupts and failures in the communication, all the traffic in the RS-232 link is monitored in the upper right line. Error conditions and zero crosses are also displayed using a pair of LEDs and a text window, where the type of error is displayed.

3.2.1. Communication Protocol. Communication between TCS and DC is bidirectional, messages structured according to the following format:

<STX><command><arguments><CR><LF><ETX>

where <STX>, <CR>, <LF> and <ETX> are the next ASCII control characters:

<STX>: Start of transmission (hexadecimal: 02h)

<ETX>: End of Transmission (03h)

<LF>: Line Feed (0Ah)

<CR>: Carriage Return (0Dh)

In order to make visualization of messages easier, both commands and arguments are written in ASCII. <command> has a fixed length of 4 bytes, while <argument> is variable, depending on the command. Table 2 lists all the messages used in the communication, showing the fields <command><argument> but not the control characters. As can be seen, in many of these, <argument> consists of the present or target azimuth, which appear in the table as xxx.

3.2.2. ASCOM Dome Driver. ASCOM is a platform that utilizes a standard interface between astronomic devices and their control software. Any device supplied with an ASCOM driver can be controlled by any ASCOM compliant software. In our application, every element supplied with the telescope (CCD, filter wheel, and the telescope itself) included an ASCOM driver. Thus, the main effort in development had to be focused on the dome controller. From the software development point of view, the main task consisted of programming a dynamic link library (DLL) for Windows. Any language suitable for developing Windows objects (COM) can be used. In this application we used C++, in a Microsoft Visual C++ 6.0 compiler.

As we have seen before, communication between the TCS and DC is achieved through a serial link based in the RS-232 standard. Thus, it was also necessary to integrate a serial communication library in the project. We chose for this purpose a freeware code *Serial Communication for WIN32, nonevent driven version* [5] performing the modifications needed to meet our requirements and to follow our serial message format.

TABLE 2: Description of messages used in the communication between TCS and DC.

Messages from TCS to DC	
Message	Meaning
AZABxxx	Absolute movement to azimuth xxx
AZR+xxx	Relative movement (+xxx or -xxx degrees)
AZR-xxx	
PARK	Movement to the PARK position
STOP	Stops dome movement if it is in motion
¿AZ?	Requires present azimuth, status, EEPROM content, motor consumption.
¿ST?	
¿EE?	
¿CO?	
AOFF	Auto messages disabled
A_AZ	Auto azimuth, auto consumption, auto zero cross messages enabled.
A_CO	
A_ZE	
CPARxxx	TCS sends new values for park position, zero cross position, zero margin constant, inertia constant.
CZERxxx	
CZEMxxx	
CINExxx	
Messages from DC to TCS	
FIN!xxx	Last command executed, dome stopped at azimuth xxx.
¿ZE!xxx	Zero cross detected at azimuth xxx
¿AZ!xxx	Present azimuth, status, EEPROM contents, consumption. These messages are sent in response to ¿AZ? ¿ST? ¿EE? ¿CO? or as automatic information, if the corresponding option is enabled.
¿ST!	
¿EE!	
¿CO!	
PAR!xxx	Confirmation of new values for park position, zero position, zero margin or inertia constant, sent by TCS through commands CPARxxx, CZERxxx, CZEMxxx and CINExxx.
ZER!xxx	
ZERM!xxx	
INE!xxx	
ERR!	Error message. The type of error is codified in the <argument> field.

Once developed this ASCOM driver, the dome could be controlled through any ASCOM compliant software, like *MaxIm DL*, *TheSky Astronomy Software*, or *ACP Observatory Control*. ASCOM platform also provides a small software packet for dome control, called *ASCOM DOME Control Panel*, which is the one we used in our application.

4. First Results

After installing the new instrument, some spectacular images of some objects in the sky were taken. Figures 8 and 9 show images of the IC434 bright red emission nebula around the Horsehead and of the M42 Great Nebula of Orion. The first one is a BVR median combination of 20×60 seconds of exposures and the second image is a combination of 5×60 seconds of exposures through BVI filters. Other images can be seen in the web site http://www.osn.iaa.es/T35/galeria_img.html.



FIGURE 8: IC 434 and M42 images obtained by using the T35 telescope.



FIGURE 9: IC 434 and M42 images obtained by using the T35 telescope.

Recently, we have carried out several photometric observing campaigns. The IC4756 and NGC7243 open clusters as well as two eclipsing binary systems, HIP7666 and V994Her, were observed during the summer and winter of 2008. This data is being reduced and the results will be published soon.

5. Conclusions

We have attained to install and automate a 14'' telescope system in order to perform long-term photometric campaigns. Although the telescope presented some problems of pointing and tracking during the first observations, the behaviour of the telescope and dome control was quite optimum. Both parameters improved fairly when a telescope pointing model was used. The new external autoguiding system will increase the tracking precision considerably.

The control of the telescope system has been performed through standard ASCOM commands. A simple system based on microprocessor has been designed and implemented allowing the control of the nonstandard dome using

ASCOM compliant software. Therefore, due to its reliability, this system is being adapted to the two other domes of the SNO.

The control of both telescope and dome can be performed locally or remotely, with the latter being the usual mode of operation. The possibility of controlling the system from the facilities of *Instituto de Astrofísica de Andalucía*, in the town of Granada, implies an important logistic advantage and considerable time saving.

Acknowledgments

We would like to acknowledge the staff in SNO for his technical, logistic, and human support. The first author thanks Juan Gutiérrez-Soto for his help with the data reductions and Victor Costa, Rafael Garrido, José Luis Ortiz, and Lourdes Verdes- Montenegro for their useful support.

References

- [1] S. Martín-Ruiz, “ γ Doradus-type variability in Open Clusters,” Ph.D. thesis, Granada University, 2000.
- [2] S. Martín and E. Rodríguez, “Search for γ Doradus variable stars in the Pleiades cluster,” *Astronomy and Astrophysics*, vol. 358, no. 1, pp. 287–298, 2000.
- [3] S. Martín, “Survey in search of variable stars in open clusters,” in *Interplay of Periodic, Cyclic and Stochastic Variability in Selected Areas of the H-R Diagram*, C. Sterken, Ed., vol. 292 of *ASP Conference Series*, pp. 58–64, 2003.
- [4] L. P. Costillo, J. M. Ibáñez, B. Aparicio, and A. J. García, “SNOWS: Sierra Nevada observatory weather system,” in *Advanced Software and Control for Astronomy*, vol. 6274 of *Proceedings of SPIE*, Orlando, Fla, USA, May 2006.
- [5] T. Schneider, 2001, <http://www.tetraedre.com/advanced/serial.php>.

Research Article

FRAM—The Robotic Telescope for the Monitoring of the Wavelength Dependence of the Extinction: Description of Hardware, Data Analysis, and Results

Michael Prouza,¹ Martin Jelínek,² Petr Kubánek,^{2,3} Jan Ebr,¹
Petr Trávníček,¹ and Radomír Šmída¹

¹ Institute of Physics, Academy of Sciences of the Czech Republic, 182 21 Praha 8, Czech Republic

² Instituto de Astrofísica de Andalucía (IAA-CSIC), 18008 Granada, Spain

³ GACE, Image Processing Laboratory, University of Valencia, 6980 Paterna (Valencia), Spain

Correspondence should be addressed to Michael Prouza, prouza@fzu.cz

Received 24 August 2009; Accepted 2 December 2009

Academic Editor: Alberto J. Castro-Tirado

Copyright © 2010 Michael Prouza et al. This is an open access article distributed under the Creative Commons Attribution License, which permits unrestricted use, distribution, and reproduction in any medium, provided the original work is properly cited.

FRAM—F/(Ph)otometric Robotic Atmospheric Monitor is one of the atmospheric monitoring instruments at the Pierre Auger Observatory in Argentina. FRAM is an optical telescope equipped with CCD cameras and photometer, and it automatically observes a set of selected standard stars. Primarily, FRAM observations are used to obtain the wavelength dependence of the light extinction. FRAM telescope is also able to observe secondary astronomical targets, and namely the detection of optical counterparts of gamma-ray bursts has already proven to be successful. Finally, a wide-field CCD camera of FRAM can be used for rapid monitoring of atmospheric conditions along the track of particularly interesting cosmic ray showers. The hardware setup of the telescope, its software system, data taking procedures, and results of analysis are described in this paper.

1. Introduction

The FRAM telescope is a part of the Pierre Auger Observatory (PAO) [1], which is currently the largest detector of the ultra-high energy cosmic rays (ultra-high energy cosmic rays (UHECRs) are defined as having their energy higher than 10^{18} eV.). The finished southern site of the PAO is located in Mendoza province in Argentina, close to the Andes mountain range, and in the vicinity of the town Malargüe (69° W, 35° S, 1400 m a.s.l.).

For the correct determination of the properties of the cosmic ray showers, it is necessary to have precise knowledge about the immediate status of the atmosphere. Therefore, there is a whole range of different atmospheric monitoring instruments at the PAO. The main task of the FRAM telescope is the continuous monitoring of the wavelength dependence of the atmospheric extinction. FRAM works as an independent, RTS2-driven [2], fully robotic system, and it performs a photometric calibration of the sky on various UV-to-optical wavelengths using a 0.2 m telescope

and a photoelectric photometer. As a primary objective, FRAM observes a set of chosen standard stars. From these observations, it obtains instant extinction coefficients and the extinction wavelength dependence. The instrument was installed during 2005 and after some optimizations it is routinely taking data since June 2006.

The main advantage of the system is a fast measurement—data for one star in all filters are usually obtained in less than five minutes. In comparison to Central Laser Facility (CLF) (the CLF is a laser with calibrated output, located approximately in the center of the detector array. The CLF automatically fires a set of shots every 15 minutes, and it is being observed by all the fluorescence detector telescopes. The analysis of the CLF signal is then used to determine the actual atmospheric conditions.) [3] or lidars (four lidars (a name originally derived from Light Detection And Ranging) are currently in operation at the Pierre Auger Observatory, each one is situated close to the one of four fluorescence detector buildings. Lidar shoots calibrated laser signal in the air and then



FIGURE 1: Original configuration FRAM telescope and its enclosure during sunset at the Los Leones site.

observes the backscattered signal with high-time resolution. From the analysis of the intensity of this returned signal it is then possible to determine the amount of scatterers (and specifically of aerosols) in different heights above the ground.) [4], the other advantage of FRAM is that its measurements are completely non-invasive, that is, producing no light that could affect the data acquisition of the fluorescence detector (FD). Furthermore, some of the stars are well calibrated and nonvariable standard light sources with precisely known and tabulated intensities in various filters, thus allowing straightforward comparison with measurements done using the same set of filters. On the other hand, the main disadvantage of this instrument is its limited capability of only integral measurements through the whole atmosphere.

2. Instrument Setup

The telescope has its own enclosure made of laminated glass fiber epoxy with inner iron frame. The enclosure is located about 30 meters from the building of the fluorescence detector at Los Leones (see Figure 1), on the southern edge of the Pierre Auger Observatory array and about 13 kilometers from the town of Malargüe in Mendoza province in Argentina (69° W, 35° , altitude 1400 m).

2.1. Original Setup. As a primary instrument, we used a 20 cm Cassegrain-type telescope with an Optec SSP-5A photometer and with integrated 6-position filter slider. Effective telescope focal length was 2970 mm and focal ratio $\sim 1:15$. The system was further equipped with an electronic focuser Optec TCF-S. This Crayford-style motorized focuser was installed in secondary Cassegrain focus and the photometer was attached to its moving end. A beam-splitting dichroic mirror was installed behind the focuser. The red and infrared light was reflected into narrow-field pointing CCD camera (Starlight XPress MX716) and ultraviolet and visible light passed through the mirror into the photometer.

Narrow-field pointing CCD camera had a resolution of 752×580 pixels and field of view of $7' \times 5'$. It was primarily

TABLE 1: FRAM filter characteristics.

Filter position	Filter name	λ_{centre} (nm)	Filter FWHM (nm)
0	Dark	—	—
1	<i>U</i>	360	70
2	<i>u</i>	350	38
3	<i>v</i>	411	19
4	<i>b</i>	467	18
5	<i>y</i>	547	23

used for the fine centering of the targeted star into a field of view of the photometer, which had only $1'$ in diameter.

Photometer Optec SSP-5A is a high-precision stellar single channel photometer. A Fabry lens projects an image of the primary mirror onto the cathode of photomultiplier (PMT). The Hamamatsu R6358 PMT was selected for our setup, because of extended spectral response from 185 nm to 830 nm. A Fabry lens is of B270-type glass that has enhanced UV-transmission. This still somewhat cuts down the transmission below 350 nm, but does not adversely affect the transmission of any of the used filters. For star measurements, we use the set of four Strömberg uvby filters and Johnson *U* filter (see Table 1 for filter characteristics).

Atop the telescope was installed wide-field CCD camera—Finger Lake Instrumentation (FLI) MaxCam CM8 with Carl Zeiss Sonnar 200 mm $f/2.8$ telephoto lens. This CCD camera uses Kodak KAF 1603 ME chip with 1536×1024 pixels, thus assuring $240' \times 160'$ field of view. The effective diameter of the lens is 57 mm and the limiting magnitude under optimum conditions reached $R \sim 15.0$ for a 30-seconds exposure. This wide-field CCD camera was primarily dedicated for astrometry. A median astrometric error for bright objects (signal to noise ratio > 7) and 120-second exposure is about $0.5''$ (i.e., about $1/20$ of WF camera pixel).

The mount was a commercially available Losmandy G-11, which used the standard GEMINI GOTO system equipped with two servomotors with relative optical encoders.

2.2. Upgrade in Summer 2009. The FRAM system was significantly upgraded in July 2009. The mount was replaced with Software Bisque Paramount ME German equatorial mount, that is, equipped with MKS 4000 dual-axis DC servomotor control system. The telescope was replaced with the commercially available $12''$ Meade LX200 Schmidt-Cassegrain telescope.

Furthermore, the pointing narrow-field CCD camera was replaced for a second FLI MaxCam CM8 camera (1536×1024 pixels), and the dichroic mirror was replaced with the small prism (off-axis guider optical element) that reflects part of the light from the telescope to the photometer, but which is not obscuring the field of view of the narrow-field camera. Therefore, both photometer and narrow field camera now receive full spectra of the light that is being observed by the telescope.

Finally, the wide-field camera was equipped with the FLI filter wheel CFW-2 with the set of Johnson-Coussins UBVRI filters. This will allow us to perform comparative studies of the wavelength dependence of the extinction from photometric and wide-field CCD measurements.

Due the presence of the corrector plate in the new Schmidt-Cassegrain telescope, the new setup has very constrained spectral sensitivity below 400 nm. It is questionable if we will be able to produce any good-quality results with photometer using Johnson *U* or Strömberg *u* filters (see also Table 1).

Currently (August 2009), the new setup is still in its commissioning stage, and no observation results are available. All the results presented in Section 6 were obtained with the original telescope setup.

3. Software

The system is driven by RTS2, or Remote Telescope System, 2nd Version, software package [2]. RTS2 is an integrated package for remote telescope control under the Linux operating system. It is designed to run in fully autonomous mode, selecting targets from a database table, storing CCD image and photometer metadata to the database, processing images and storing their identified coordinates in the database. RTS2 was developed and is maintained under open-source license in collaboration with robotic telescope projects of BART, BOOTES, and WATCHER [5].

4. Observed Targets and Observation Schedule

FRAM is primarily designed to provide the atmospheric extinction model. The data for this model are collected by the photometer with the help of both CCD cameras. The observation targets are selected bright (brighter than 6.5 mag) standard stars from the photometric catalogue of Perry et al. [6] that features star measurements in the Strömberg *uvby* photometric system [7]. Currently, we are using about 25 stars in the selection that are located at suitable declinations and homogeneously distributed over the right ascension.

The target cycle begins with a slew to the position followed by a short WF camera exposure to check the pointing accuracy. The position of the photometer aperture within WF camera's image is well known, so if the initial pointing is not satisfactory, a correction could be made. This image also serves as a test of atmospheric conditions: target may be canceled, if the necessary conditions are not met (clouds or fog resulting in no image astrometry).

After the star of interest was successfully centred within the WF aperture, a control exposure with the NF CCD camera is done. The star is identified as the brightest source in the field of view and, if needed, the mount position is corrected again and the star is moved to the centre of photometer aperture. The photometer then does two sequences of measurements per filter of interest. Each sequence typically consists of five 1-second integrations to obtain the signal value and its variance in each filter.

Simultaneously, both CCD cameras take exposures, so that pointing may be improved in real-time. The WF camera provides also a measurement in set of Johnson-Coussins UBVRI filters. The complete set of measurements is then stored in the structure of PSQ database.

5. Optical Follow-Ups of Gamma-Ray Bursts

The RTS2 software system was originally developed especially for the search of optical transients of gamma-ray bursts. This software system was significantly modified to achieve FRAM main aims in atmospheric monitoring; however, it is still very easy to activate special observation mode for optical transients. The main computer of the system receives in such case the alerts about detected gamma-ray bursts via network, slews there and makes images of the given sky region.

This alert system was activated on FRAM in late 2005, and already during January 2006 a very successful observation was made. An extraordinarily bright prompt optical emission of the GRB 060117 was discovered and observed with a wide-field CCD camera atop the telescope FRAM from 2 to 10 minutes after GRB. Optical counterpart identified in our images was characterized by rapid temporal flux decay with slope exponent $\alpha \propto 1.7 \pm 0.1$ and with a peak brightness of 10.1 mag in Bessel *R* filter. Later observations by other instruments set a strong limit on the optical and radio transient fluxes, unveiling an unexpectedly rapid further decay. We presented more details in [8].

6. Calibration and Results

Our main goal is to provide the so-called Angstrom exponent γ , which is often used for parametrization of wavelength (λ) dependence of aerosol optical depth τ_A : $\tau_A(\lambda) = \tau_{A0} \cdot (\lambda_0/\lambda)^\gamma$, where λ_0 is the reference wavelength and τ_{A0} is the aerosol optical depth measured for this wavelength [9]. Moreover, the Johnson *U* filter has almost the same central wavelength as have the lasers used for measurement of vertical aerosol optical depth (VAOD) at CLF [3] and at lidar stations [4]. The integral value of VAOD ($h = \infty$) in *U* filter thus can be used for direct cross-checks with these instruments.

We analyzed our database of photometer counts since June 2006, when the telescope achieved a stable mode of operation, until December 2008.

Using the available analysis of the CLF data, we initially selected a set of very clear ("Rayleigh") nights, when no aerosols (or only negligible amounts of aerosols) were observed by the CLF instrument. We used these data for calibration of FRAM photometer. Under the assumption of presence of no aerosols, we fitted the dependence of difference of observed and tabulated magnitudes on airmass. The resulting dependence should be linear and the fit parameters characterize both the extinction and the instrument properties. The slope for clear nights should be in agreement with the computed expectations for the Rayleigh scattering, and the value of the intercept defines the conversion of the instrumental magnitude. The knowledge of the real observed magnitudes then allowed us to directly compute the

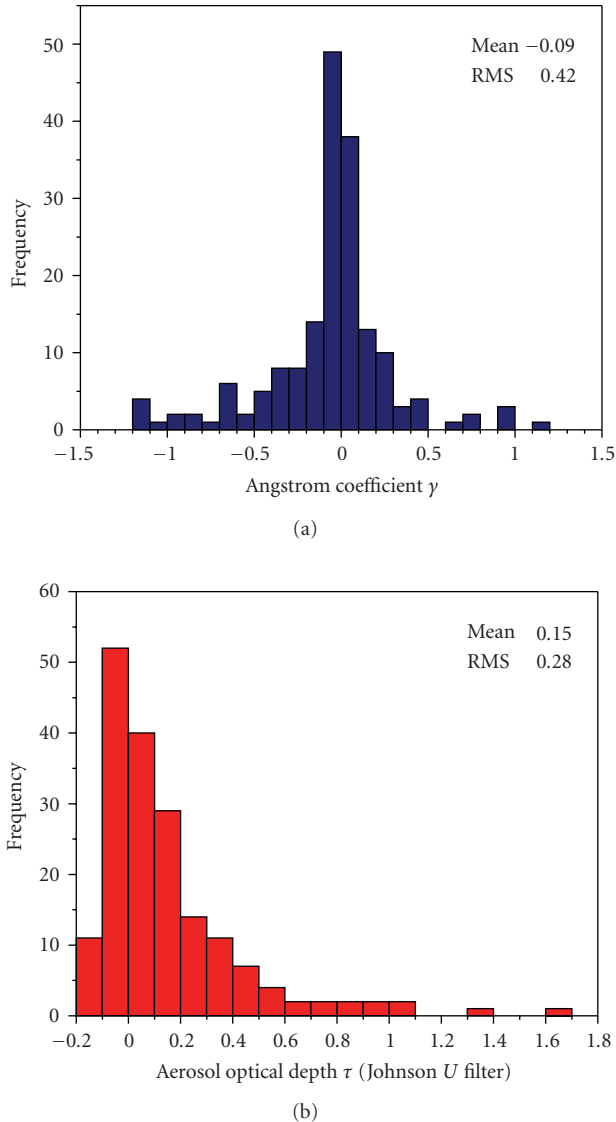


FIGURE 2: Histograms of measured distribution of Angstrom coefficient γ (a) and of integral aerosol optical depth τ (b) for all data obtained from June 2006 until December 2008. Quality cuts from wide-field camera and photometer were applied as described in the text.

extinctions for our whole database, including all other (i.e., non-Rayleigh) nights. After that, we converted extinction expressed in magnitudes into total optical depth and then subtracted molecular Rayleigh part, using model from [10].

For the analysis of the aerosol extinction wavelength dependence, we used only-high quality data. For our selection, we required that three following conditions were fulfilled simultaneously. First, the limiting magnitude of the wide-field camera images was higher than 13 (clear sky). Second, the fluctuations in the number of detected stars in the wide-field camera images were smaller than 30% between individual images. The third cut is then on the fluctuations of the photometer readings. If the fluctuations were higher than square root of the signal (e.g., due to strong wind), the measurement was also not used.

For the standard star measurements (see Figure 2), we obtained a preliminary mean value of $\gamma = -0.1 \pm 0.4$ that is, lower than the results from HAM instrument ($\gamma = 0.7 \pm 0.5$) [11]; however, 1σ limits of both instruments are overlapping.

Moreover, FRAM $\gamma = -0.1$ is in good agreement with theoretical expectations for the atmosphere in desert-like environment of the Argentinian pampa ($\gamma \sim 0$) [12], where coarse-grain particles prevail.

Acknowledgments

The authors from the Institute of Physics in Prague (M. Prouza, J. Ebr, P. Trávníček and R. Šmída) would like to acknowledge the support from the Academy of Sciences of the Czech Republic (AV0Z10100502 and AV0Z10100522) and from the Ministry of Education, Youth and Sports of the Czech Republic (MSMT-CR; projects LA08016, LC527, 1M06002, and MSM0021620859). The collaborators from Spain (M. Jelínek and P. Kubánek) were supported by the Grant of the Spanish Ministry of Science and Innovation (AYA 2007-063677). Finally, all authors acknowledge the ARAE group at IAA-CSIC for its support.

References

- [1] J. Abraham, P. Abreu, M. Aglietta, et al., “Operations of and future plans for the Pierre Auger observatory,” in *Proceedings of the 31st International Cosmic Ray Conference (ICRC ’09)*, Lodz, Poland, July 2009.
- [2] P. Kubánek, M. Jelínek, S. Vitek, et al., “RTS2: a powerful robotic observatory manager,” in *Advanced Software and Control for Astronomy*, vol. 6274 of *Proceedings of SPIE*, Orlando, Fla, USA, May 2006.
- [3] B. Fick, M. Malek, J. A. J. Matthews, et al., “The central laser facility at the Pierre Auger observatory,” *Journal of Instrumentation*, vol. 1, no. 1, Article ID P11003, 17 pages, 2006.
- [4] S. Y. BenZvi, R. Cester, M. Chiosso, et al., “The Lidar system of the Pierre Auger observatory,” *Nuclear Instruments and Methods in Physics Research, Section A*, vol. 574, no. 1, pp. 171–184, 2007.
- [5] P. Kubánek, M. Jelínek, S. Vitek, et al., “Status of robotics telescopes driven by RTS2 (BART, BOOTES, FRAM and Watcher),” *Nuovo Cimento B*, vol. 121, no. 12, pp. 1501–1502, 2006.
- [6] C. L. Perry, E. H. Olsen, and D. L. Crawford, “A catalog of bright UVBY beta standard stars,” *Publications of the Astronomical Society of the Pacific*, vol. 99, pp. 1184–1200, 1987.
- [7] B. Strömgren, “Two-dimensional spectral classification of F stars through photoelectric photometry with interference filters,” *Vistas in Astronomy*, vol. 2, pp. 1336–1346, 1956.
- [8] M. Jelínek, M. Prouza, P. Kubánek, et al., “The bright optical flash from GRB 060117,” *Astronomy and Astrophysics*, vol. 454, no. 3, pp. L119–L122, 2006.
- [9] J. Abraham, P. Abreu, M. Aglietta, et al., “Upper limit on the cosmic-ray photon fraction at EeV energies from the Pierre Auger observatory,” *Astroparticle Physics*, vol. 31, no. 6, pp. 399–406, 2009.
- [10] A. Bucholtz, “Rayleigh-scattering calculations for the terrestrial atmosphere,” *Applied Optics*, vol. 34, no. 15, pp. 2765–2773, 1995.
- [11] S. Y. BenZvi, M. Bohacova, B. Connolly, et al., “New method for atmospheric calibration at the Pierre Auger observatory

using FRAM, a robotic astronomical telescope,” in *Proceedings of the 30th International Cosmic Ray Conference (ICRC '07)*, Merida, Mexico, July 2007.

- [12] T. F. Eck, B. N. Holben, J. S. Reid, et al., “Wavelength dependence of the optical depth of biomass burning, urban, and desert dust aerosols,” *Journal of Geophysical Research D*, vol. 104, no. 24, pp. 31333–31349, 1999.

Research Article

Converting from Classical to Robotic Astronomy: The Lowell Observatory 0.8-m Telescope

Marc W. Buie

Southwest Research Institute, 1050 Walnut Street, Suite 300, Boulder, CO 80302, USA

Correspondence should be addressed to Marc W. Buie, buie@boulder.swri.edu

Received 3 June 2009; Accepted 2 December 2009

Academic Editor: Alberto J. Castro-Tirado

Copyright © 2010 Marc W. Buie. This is an open access article distributed under the Creative Commons Attribution License, which permits unrestricted use, distribution, and reproduction in any medium, provided the original work is properly cited.

The Lowell Observatory 0.8-m (31-in) Telescope was augmented by the addition of a robotic mode of operation in early 2001. This system executes any predetermined sequence of observing instructions without supervision. Described herein is a general description of the system, lessons learned from the conversion, and a few general algorithms for focusing, collecting twilight flat field images, and scheduling standard star observations.

1. Introduction

The power and value of autonomous observing has long been recognized in the amateur astronomy community while adoption has been slow at professional observatories. In January 2001 I converted the Lowell Observatory 0.8-m telescope from a classically-operated manual telescope to a robotic facility. At that time the telescope was poorly utilized and deemed unimportant enough to permit my experimenting with the system. The perception was that such a conversion and subsequent robotic operation was either dangerous to the hardware or disruptive to the operation of the telescope—a fear that was not realized. Since 2001 roughly 1/3 of the time was scheduled as classical observing and the rest operated in a robotic mode.

The ground rules for the conversion were (1) classical observations must still be possible without any changes in operation or procedures and (2) instrument changes had to continue to be supported. The project was further constrained by the lack of development funds and minimal technical staff support. This constraint led to a very frugal development path with minimal changes to the existing system. The new mode became operational and scientifically useful in March 2001 and immediately caused this telescope to be the most heavily used of any of the Lowell Observatory facilities. During this period of operation the system had to be modified to work with two different cameras as well as a total changeout of the dome control system.

In this paper the design objectives and constraints involved in moving this telescope from classical hands-on observing to robotic hands-off observing are summarized. The observing queue system and two camera systems will be discussed along with changes needed in telescope control. I also present some of the non-obvious algorithmic components of the system as lessons learned that may be useful to other projects. Also discussed are safety issues common to systems of this type. At the end I will present a brief synopsis of the types of observations carried out by this system since its implementation.

2. System Overview

This system was created to permit autonomous collection of images at the Lowell Observatory 0.8-m telescope on Anderson Mesa. The primary goal was to provide a means for collecting data without requiring an observer to be present. This approach makes data collection much more cost-effective in circumstances where a large number of nights are needed to yield a single useful result. For example, collecting a lightcurve of Pluto (period ~6.4 days) within one apparition requires a large number of nights to create a final composite lightcurve. Any type of survey or monitoring observation is also very well suited to this system.

Figure 1 is a flowchart showing the principal hardware subsystems, computers, software and the communication

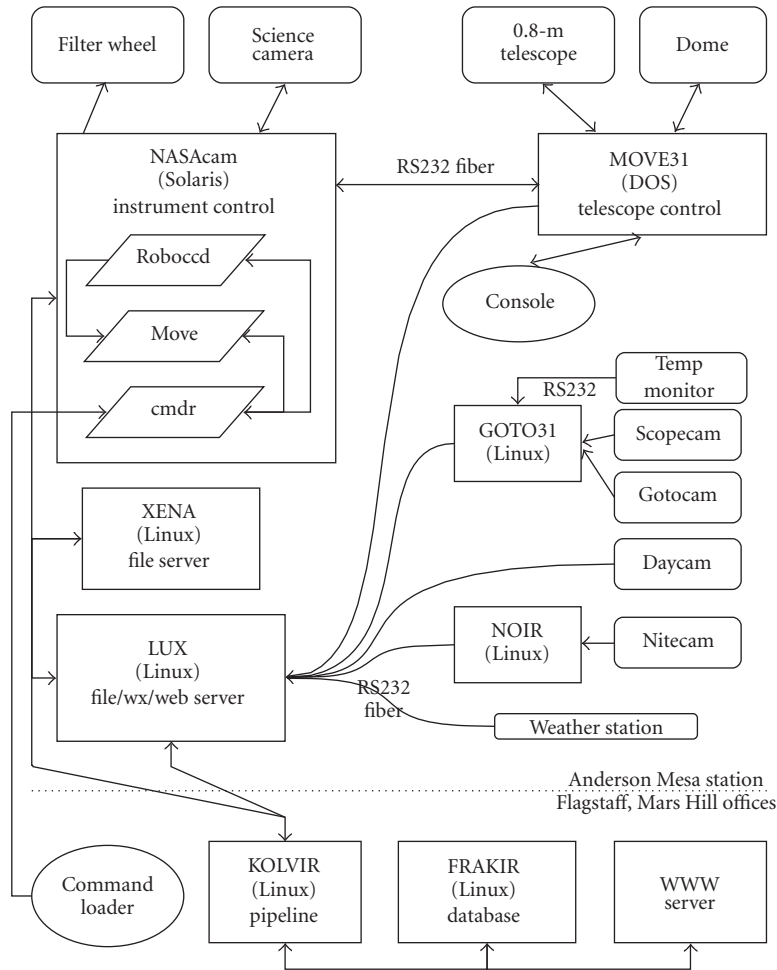


FIGURE 1: System overview; see text for details.

paths between them. The bulk of the figure describes systems in place at the Anderson Mesa Station where the telescope is situated. At the very bottom of the diagram a few machines are shown that are located at the main observatory office 20 km away. In this diagram, all of the rectangles depict specific computers (9 total). The rounded rectangles stand for specific hardware. The parallelograms show processes that are always running while the system is active. Ovals indicate where user input can enter into the system. All computers communicate at each site via a 100 Mbs ethernet LAN, typically using NFS for communications but occasionally using rsync, scp, or direct TCP/IP sockets. Communication between sites is provided by a dedicated T1 link but this link is not required for the system to run and collect data.

3. Hardware

This section describes the hardware used by the robotic system. A photograph of the facility exterior is shown in Figure 2. The white building on the left houses the telescope and telescope control computer. The low brown building houses a traditional control room and a computer room.



FIGURE 2: 31" dome and control building.

3.1. Telescope. The telescope is a 0.8-m closed-tube reflecting telescope with a single instrument port at the cassegrain focus. The output beam is $f/15$ with a focal plane scale of 17.5 arcsec/mm. The scale is poorly matched to modern CCD detectors requiring the use of a focal reducer to achieve a



FIGURE 3: 31" telescope and PCCD camera.

more useful field of view. The telescope tube is constructed of aluminum and as a result has a very strong shift in focus position with changing temperature. Figure 3 shows the telescope with the first generation CCD system.

The facility already had a sophisticated observatory control system that was the result of decades of local software and hardware development. The control program, named MOVE31, is written in FORTRAN with a small amount of assembly code and operates on an MSDOSv6.2 computer. The telescope has three digital stepper motors, one each for the Right Ascension and Declination axes and one for moving the secondary mirror for focus control. Position knowledge comes from relative encoders. Initially only the focus mechanism had a home switch for calibrating its absolute location. More recently a pair of switches was added to provide a home location from which to restore pointing in case of error. However, all of the startup and observing strategies grew out of the environment where loss of pointing meant the loss of a night and subsequent on-site effort to recover. The english yoke mount imposes a north declination limit of roughly 60° beyond which the telescope cannot point. There is a slight protrusion of the north pier that the telescope can track into. With classical observing one can work around this protrusion and extend the declination coverage. For robotic observing the northern limit was made more conservative so that the protrusion can never be reached. However, the limit is implemented in the scheduling software, not in the telescope control program.

The telescope has had a variety of positional limit switches over the years. All of the switches work well at normal tracking rates. The protections are not as effective while the telescope is slewing. As a result, the robotic system was forced to take on a larger pointing limit responsibility than it should. Over the years there was only one critical failure where the telescope was driven into the north pier, breaking the drive coupler that was designed to fail in such cases, protecting the drive motor and gears.

3.2. Dome. The telescope is protected from weather by an Ash dome. It uses high-power a/c motors operated via computer controlled relays for rotation and for opening and

closing the two-part dome slit. The dome slit has a long upper panel that is lifted up and over the top of the dome when open. It also has a short lower panel that drops down below the bottom of the dome. Opening or closing the dome takes roughly 3 minutes. The telescope mirror becomes vignetted below 18° altitude.

Power to the dome slit motors is provided by a bus-bar contact that is engaged over a 5° range in dome azimuth. To open and close the dome one must successfully stop on the correct position before the open/close operation will work. The original dome encoding system was handled with a friction wheel drive relative encoder and the power contact was wired to act as a fiducial switch. This system required elaborate software to maximize the likelihood of closing the dome in case of problems. In later years the dome encoding system was replaced by a bar code scanner providing an absolute position every degree, greatly simplifying the calibration process and making for considerably more reliable operation with much simpler software. Over the years there have been a few instances where a failure occurred and the dome was not properly closed at the end of the night. Procedurally this has led to a policy that someone always verify that the dome is closed after sunrise.

Dome control during the night is handled completely by the MOVE31 computer once automatic dome control is enabled. A minor software modification was required for robotic observing such that notification of the completion of a slew had to wait for the telescope *and dome* to both reach their final position. With classical observing an observer would know from the noise of the dome motion that the system was not ready.

3.3. Science Camera. The robotic system was originally developed with a thermoelectrically cooled Photometrics CCD system (PCCD) and a 3 : 1 focal reducer. The detector was 576×384 and had a pixel scale of 1.2 arcsec/pixel for a field of view of 11.5×7.7 arcmin. The focal reducer had a slight pupil ghost centered on the detector so the prime location for placing a single source was offset by a quarter of the FOV from the actual center of the device. This offset thus required better than about 3 arcmin pointing from a slew to ensure successful target acquisition. Full-frame readout time and saving the data to disk for this detector was 8 seconds. The shutter was a commercial two-leaf system that was not particularly fast. Photometrically accurate exposures had to be longer than 3 seconds but the system could take useful exposures as short as 0.002 seconds. The shorter exposures were not useful for science data but came in handy for other operational support modes. The thermoelectric cooling restricted exposure times to 5 minutes or less and the system required dark-frame calibrations.

The camera system also included an integrated 10-position filter wheel that provided fast cycling between filters and reliable knowledge of the state of the filter wheel. The wheel could only move in one direction and stepping by one position took less than one second. The worst case was for moving backward by one position which require moving forward by 9 positions and took about 3 seconds. Any time

a motion crossed the fiducial the controller would stop at the fiducial, recalibrate and then then move on to the final destination. Thus, observing with any two-filter pattern (e.g., alternating between *B* and *V*) would lead to a verification of filter position knowledge and a recalibration once per pattern. The typical observing pattern for this system put a lot of cycles on the filter wheel. Twice during the robotic usage of this camera the system wore out a critical part but the recalibration strategy and error logs gave several months notice before total failure.

The performance of the original system was limited by its plate scale, FOV, high-readnoise, low QE, and ultimately wore out and was removed from service in July 2005. A new camera was constructed for the telescope that was based on a custom focal reducer matching the CCD to the plate scale of the telescope. The initial CCD was a Loral detector that was thinned by M. Lesser of Steward Observatory. This batch of devices is prone to delamination and combined with a slow vacuum leak in the dewar this detector never collected science grade data even though it was in service for 9 months. By January 2007 a replacement CCD was put in service. This camera is known as NASAcam, so named for the source of the funds that made the camera possible.

NASAcam is built around an EEV 2048 × 2048 device. It has a image scale of 0.45 arcsec/pixel for a 15 arcmin field of view. The nominal gain is $2.15e^-/\text{DN}$ and a read-noise of $6.2e^-$. Lower read-noise was possible from this system but this setting was a compromise between readout time and readout noise. The full-frame read and store time is roughly 9 seconds. The detector is cooled by a Cryotiger closed-cycle refrigerator that maintains a regulated temperature of -113°C , sufficient to completely eliminate dark-current. The system is intended to run full time, providing a long-term stable environment for the detector. This system has two 10-position filter wheels. The filter wheel system is a little slower than that for PCCD. The shortest move takes just under 3 seconds while the longest move requires about 9 seconds.

The requirements for adapting this system to a new camera are relatively modest. The most critical is the availability of a Linux or Solaris driver. The only other requirement for efficient operation is the ability to read out a portion of the image with the expectation that the readout time is much faster for small subframes. System performance is also improved if the image last read is available to the application at some memory location.

3.4. Support Cameras. An essential element of this system are cameras to provide on-site visual feedback. Four cameras based on inexpensive surveillance camera hardware are used to monitor daytime sky conditions (DAYcam), nighttime sky conditions (NITEcam), the sky at the current telescope location (GOTOcam), and a view of the telescope and dome (SCOPEcam).

DAYcam is the simplest of all the cameras. The camera is a D-Link DCS-1000 and is a self-contained color video camera and web server. The stock lens was replaced with a 3.8 mm fixed-aperture fixed-focus lens that provided a field

of view of about 90° . This camera is housed inside a north-west facing window to protect it from the weather. Every 2 minutes a picture is sent via FTP to a central network location. These images are managed and culled by simple Perl scripts that file them by day and delete images taken when the sun is below -5° altitude when the sky is too dark for this camera. The pointing of the camera is set so that the sun and moon can never pass through the field of view. These color images are required for times when you cannot discern between high thin cirrus and a photometric sky without seeing the color of the sky. The data rate from this camera is about 4 Mb/day.

NITEcam provides information about clouds at night, even when there is no moonlight. To accomplish this, I used a Watec 903 K b/w video camera that has a $1/3''$ CMOS CCD detector with a minimum lux rating of 0.0002 lux. In comparison, DAYcam only works down to 2.5 lux. The camera is mated to a Computar HG3808AFCS-HSP video-mode auto-iris lens, focal length 3.8 mm, with a maximum aperture of $f/0.8$. The lens settings are set to full average brightness control. At night, the natural signal from the camera with the moon down does not yield a very useful image though it's not bad once you have illumination from the Moon. To grab the video, I use a Hauppauge WinTV-GO card mounted in an old surplus Pentium 200 Mhz computer running RedHat 7.3. The camera is located in the same window bay as DAYcam and also avoids looking at the sun and the moon. The setup of the Watec camera is automatic electronic shutter control on, hi-AGC on, and AGC on (AGC = automatic gain control). During the day an image one frame per minute is collected and saved. The night-time sensitivity is enhanced by coadding 200 individual video frames and then subtracting a predetermined dark/bias image thus increasing the sensitivity by a factor of 10. This sensitivity is sufficient to detect unilluminated clouds in silhouette against the dark night sky (no moon). The software also has some automatic gain logic that keeps the image in range on brighter nights. This camera provides full-time images of the sky and generates about 19 Mb of data per day.

SCOPEcam is a stock b/w CCTV camera that provides a classical observer with a remote real-time view of the telescope and dome while observing in the control room. To support robotic observing, the signal was split and routed to a computer with another WinTV video capture card. The camera is not sensitive enough to provide useful images at night with natural lighting so the MOVE31 computer turns on a 5 W red light in the dome whenever the telescope is slewing (or by explicit command). However, during the day it is immediately obvious if the dome is open even just a centimeter. The most important role this camera plays is in verifying that the dome is closed at the end of the night. This camera is also useful for debugging failures during robotic observing. To minimize the amount of data collected from this camera, images are saved only when something either moves (e.g., telescope slews) or if the lighting changes dramatically (e.g., a light is turned on). The data flow from this camera is extremely variable but averages to roughly 9 Mb per day.

The final camera, GOTOCam, has the same hardware and software as NITEcam except the camera lens. This image features a pixel scale of roughly 3 arcmin and a field of view of 14×10 degrees and is boresighted with the telescope. This camera makes it possible to recover pointing by positioning a bright star at a location that is known to be coincident with the science detector. These images also can be used to decide if data are affected by clouds. In practice, this data stream is rarely used and is marginally worth implementing. Images are collected only when the dome is open so the data rate is variable. On a clear night the camera generates roughly 40 Mb of data.

3.5. Environment Data. On-site weather conditions are collected with a Davis Instruments weather station. Special modification were made to increase the length of the sensor leads and to add some protection against lightning. The unit is connected to the logging computer via an RS232 fiber link. This station provides absolute barometric pressure, outside air temperature and relative humidity, dewpoint temperature, and wind speed and direction. Real-time information is available via socket communication and archival information is stored in text files. The weather data is primarily used to support predicting the weather conditions for the upcoming night and if it will be safe to open the telescope dome but it is not required in order to run the system. The local weather forecasts and satellite imagery is also used to support the nightly weather decision. In the early days this data was also used to estimate the focus position for the telescope at the beginning of the night.

With the development of NASAcam came an opportunity to improve the knowledge of the immediate telescope environment. The single most critical piece of missing information was the temperature of the telescope tube. To get accurate temperatures we used an OMEGA D5111 module that supports four temperature sensors (AD590) and has an RS232 port. One sensor was glued to the primary mirror (but done so that it could be removed when the mirror gets realuminized). One sensor is attached to the exterior of the telescope tube. Finally, there is one sensor dangling in the air at about the same height as the average position of the primary mirror. The tube temperature works well enough to predict the telescope focus position to within about $30 \mu\text{m}$ (focus operation has a typical step size of $6 \mu\text{m}$).

The telescope temperature data also provides information related to image quality. As expected, the mirror is often warmer than the ambient air. Surprisingly, the telescope tube was found to be significantly colder than the air and is just as detrimental to image quality as a hot mirror. The painted aluminum telescope tube radiatively couples to the night sky and over-cools during the night. This problem was easily fixed by wrapping the telescope in a loose layer of aluminized mylar. This simple solution broke the radiative link and afterward the tube was seen to track the air temperature very well. The seeing definitely improved as a result of this simple fix. At this point, the image quality is now limited by the quality of telescope tracking since there is no auto-guider.

4. Software

The basic design of the system is a collection of independent processes that share as little information as possible. Also deeply rooted in the system design is that all operations are unsupervised. That means there is no graphical display of any data, there are no real-time monitoring windows peeking into system processes, and queue manipulation is limited to adding commands or removing everything. Lastly, the software is designed to be running all the time. A specific effort was made to avoid forking and multi-threaded code for an easier path to reliable software. This coding constraint also led to the decision to use message queues for inter-process communication rather than TCP/IP sockets. The message queues provide a very simple and fast communication method but do require that all of the tightly coupled processes be running on the same computer. Communication via TCP/IP, where needed, is accomplished by adding a separate trivial process that accepts a socket connection and passes them along to a message queue.

Central to the very first versions of the system was the concept of event and anomaly logging in all of the programs. Every operation that can generate a system error (e.g., opening a file) will write a time-stamped system error message to a log file. Other informative messages about logical operations or decisions are included in the log as needed. This system has had its share of anomalies and software errors over the years. It is usually not practical to debug a problem by replicating the actions. These log files have been an essential and 100% effective tool for fixing the software without the need for error replication.

4.1. *cmdr*—Observing Queue. The top level controlling process is *cmdr* and it maintains a large FIFO of commands and passes them along, one at a time, to the appropriate agent for execution. If the FIFO becomes empty the system becomes idle. The *cmdr* daemon gets its commands over a inter-process communication (IPC) channel from the interactive program *send*. In many cases, this process has no knowledge of the consequences of any command and there is no concept of a time limit on any command. The communication protocol is to send a command via IPC channel to the appropriate agent, listen for optional information messages from the agent, and log the termination and time of execution when the completion message is returned. Information messages and command completions are logged with a timestamp as they are received. Commands consists of a single line of text. Single word lines are queue control commands. Everything else is a single character that is associated with either an external agent or a type of internal command followed by the command intended for the agent. There are four such categories defined: t: telescope commands, c: camera commands, f: file to be executed, and s: synchronization or timing commands.

The “file” command is really a special category since *cmdr* never actually sees such a command. Commands are give to *send* before being sent to *cmdr*. If *send* sees a file command it will process that file and send the commands

found in the file. Therefore, loading a full night's observing is usually a matter of loading the one file that contains all the commands. Any command that is itself a file command is expanded until nothing but non-file commands are sent. Thus a script for a night can appear to have relatively few commands, most of them file commands, that will be expanded into a very long list of actual commands that will occupy the fifo. All memory of the original organization of the files and commands is lost in the fifo other than the sequential order of execution. For this reason, no tools were developed to inspect the queue since it would be very hard to relate to the original script.

4.2. *move*—Telescope Communication and Control. The telescope and its dome are operated by a stand-alone computer (MOVE31 which refers to the computer and the control program) that maintains full knowledge and control of the telescope and the dome. This system supports a set of commands that can be sent via an RS232 serial port. All commands return an explanatory code upon completion. Some commands return instantly and some take as long as 3-4 minutes to complete.

The move process encapsulates all of the knowledge and idiosyncrasies of the MOVE31 system thus providing a clean commanding interface. This process takes care of preparing and sending the command and then waiting for the response. It also is aware of how long commands should take and imposes an appropriate length timeout period in case of errors. This process logs all activities, successful and unsuccessful, but any time there is a error the incident is also reported via email. Telescope failure codes are rare and always treated as a serious problem. A great deal of effort was expended to ensure that all errors are meaningful and worthy of response and intervention. Additional informational messages are also sent when the daemon is started or stopped and whenever the dome is opened or closed. This process also maintains an approximation of the telescope and dome state. It does so by querying the telescope every two seconds for its status and then parsing and saving that information. If another process wants to know the telescope state, the answer is returned instantly from the most recent query. This periodic query is not logged unless there is an error (such as a garbled ASCII string response or complete lack of response).

The move daemon listens to its own IPC channel for commands. There are three defined command sources, (1) primary command channel (usually from *cmdr*), (2) secondary command/query channel (*roboccd*), and (3) backdoor command/query channel (*movecmd*). The secondary channel is used to get the telescope status information to be saved along with each data frame. This channel is also used for pointing updates, small telescope offsets, and focus commands that are generated from the camera. The backdoor channel is used exclusively for testing or recovering from failures.

4.3. *roboccd*—CCD Camera Operation and Control. The CCD camera and filter wheels are controlled with the *roboccd* daemon. Image data is saved via NFS to a disk

served by XENA. Exposure durations are controlled by a hardware timer in the CCD electronics and the start time is taken from the system clock which is maintained by *ntpd*. Status information on the current state of *ntp* is recorded with each image. The *roboccd* daemon listens on its own IPC channel for commands from *cmdr*. Telescope focus is adjusted automatically for each filter based on differential focus offsets known for each filter. This program performs a few standard calculations on every image: (1) the mean and standard deviation of the background, (2) location and signal level of the maximum in the image, (3) instrumental magnitude, FWHM, and centroid location of the maximum. Quite a few decisions can be made that affect data collection with this limited knowledge. This information is recorded to the data headers and it is also sent to the log files on LUX. Thus it is possible to eavesdrop on the data collection process and get a reasonable idea of how things are progressing.

4.4. *Synchronization.* Timing and synchronization operations are handled internally by *cmdr* and are unusual to see in a classical observing system. Normally, all of these functions are performed implicitly by the observer as the night progresses. The following section lists the available synchronization commands

lst HH:MM:SS: Pause until the local sidereal time passes HH:MM:SS.

pause HH:MM:SS: Pause for the indicated length of time.

time HH:MM:SS: Pause until the UT time passes HH:MM:SS.

sun-above D.d: Wait while the Sun is above D.d degrees altitude. Used for sunset timing.

sun-below D.d: Wait while the Sun is below D.d degrees altitude. Used for sunrise timing.

pos-above D.d HH:MM:SS DD:MM:SS: Wait while the position (α, δ) is above D.d degrees altitude.

pos-below D.d HH:MM:SS DD:MM:SS: Wait while the position (α, δ) is below D.d degrees altitude.

The *lst* and *time* commands cannot pause for longer than 12 hours. If the time is within 12 hours in the past, the condition is considered to have been met. Of these commands, the *lst* and *sun-below/above* commands are the most heavily used. These commands permit building surprisingly flexible observing scripts that can be used night after night and year after year. They also make it possible to write good scripts that do not need to know exactly how long everything takes. In general, the best scripts will have a small amount of deadtime in the night to allow for timing variations in the actual schedule. A well honed full-night script will usually be scheduled within a few minutes of the full duration of the usable night.

4.5. *Predefined File Commands.* There are a collection of predefined command files that encapsulate operations that are used every night. By using these files, centralized changes

and improvements can be made that will automatically be incorporated into future nightly observing plans. The *alopen* script takes care of waking up the telescope, updating the clock on the telescope computer, opening the dome, turning on dome and telescope tracking, setting the file name for the data to be taken that night, and enabling the dead-man timer. Some operations benefit from reading out a small fraction of the science array. The file *acqsubar* sets the size of the sub-array for target acquisition to a 3 arcmin square in the center of the CCD. A second file is *focsubar* and is used to set the size of the sub-array for focusing at 80 arcsec square. In addition to speeding up these operations, reading a sub-array greatly reduces the chance for confusion from nearby sources or cosmic ray strikes. At the start of a new robotic run the telescope coordinates must be verified. A set of 12 *bigacqXX* files are defined (XX is the right ascension for the target star) that perform a full-field acquisition on a very bright star and updates the pointing. Accurate focusing is handled by a 24 scripts, *focusXX-25*, where XX is the right ascension of the focus star. All stars are at a declination of $+25^\circ$. Each script has a star $V=7-8$ that has nothing brighter within 3 arcmin. This brightness gives a good signal-to-noise ratio image in one second. These scripts include all the operations to slew to the star, take the data, and adjust the focus accordingly.

Most observing programs on this system strive to collect absolute photometry requiring the use of all-sky photometric standard stars. The list of Landolt standards [1–3] includes areas that provide two or more standard stars at the same time and spaced at roughly one-hour intervals on the sky. There are separate command files for these fields with different combinations of filters such as *BV* or *VRI*. These files contain the target pointing needed to place the stars on the field and also contain the relevant exposure times needed for optimal signal-to-noise ratio images.

At the end of the night, the system must be properly stowed. This is also the best time to take calibration frames for this telescope. There are commands for shutting down the telescope either with or without taking calibration data. Each of these also includes an instruction that marks data collection complete for that night.

5. Essential Algorithms

This project involved some algorithmic development and testing that were not obvious prior to starting. This section describes the most important of these lessons learned with the hope they will be useful in other systems.

5.1. Flat Field Collection. An essential calibration operation is the collection of flat field images for which I generally use twilight sky images. The challenge of collecting twilight flats is that the illumination level is constantly changing, affecting the exposure time needed. The system has the most recent mean background signal level making it easy to adjust before the next image. When taking a set of flats for any filter there are seven control parameters for the command and the default value is shown in parentheses: number of frames

desired (20), the highest signal level permitted for a usable flat (*maxgood* = 43000), the highest signal level permitted for the optimal flat (*maxbest* = 28000), lowest signal level permitted for the optimal flat (*minbest* = 18000), lowest signal level permitted for a usable flat (*mingood* = 10000), maximum exposure time allowed (*maxexp* = 20 seconds), and minimum exposure time allowed (*minexp* = 2 seconds). These default parameters are the result of optimizing against the dynamic range of the detector, readout time, speed of the shutter blades, and sensitivity of the detector and filter combination. The dawn flat steps are as follows.

- (1) Move telescope to the “Chromey” spot [4] and turn on tracking.
- (2) Take a single bias frame with a 200×200 sub-frame in the center of the CCD. This signal level is the zero-illumination reference value.
- (3) Take a 0.002 second exposure with a 200×200 sub-frame. If the signal level is too high no flats are possible and the operation terminates.
- (4) Take a one second metering exposure with a 200×200 sub-frame until the signal would be above *minbest* with a *maxexp* exposure time. If still too dark, wait for a minute before trying this step again.
- (5) Calculate exposure time. First compute the time need to have the signal level be *minbest* but no longer than *maxexp* and no shorter than *minexp*. This new time will predict a new signal level. If the predicted level is less than *mingood* or greater than *maxgood* quit taking images and log an error that the desired number of frames was not reached.
- (6) Take an image and save it. Exit when the desired number of frames have been taken.
- (7) Offset the telescope 20 arcsec to the east and go back to step 5.

The control settings allow optimization for the largest number of frames in the shortest time with a useful signal level. The number of frames is more important than the number of photons collected. The current system can get flats on 2 filters per twilight with 20 frames per filter. Dusk flats are vastly inferior to dawn flats for this instrument and telescope and are very rarely used. Generally collecting flats for a given filter once a week is sufficient.

5.2. Focus Determination. An automated system must be able to find the best telescope focus without user intervention. A completely general automatic focus algorithm that assumes nothing at the start proved impossible. As implemented, the telescope must be within $100 \mu\text{m}$ of proper focus to ensure success. In the early days it was common to interactively determine an approximate focus at the start of a new run. After sufficient operational history was reached this step was dropped in favor of a temperature based initial predictor. The focus shift between the end of the previous night and the start of a new night is larger than $100 \mu\text{m}$. Therefore, at the start of each night the initial focus value is set based on the current tube temperature and the known trend of focus versus temperature.

The automatic focusing procedure is based on a series of images, changing focus for each, with a default step size

of $10\ \mu\text{m}$, starting 9 steps below the current focus value and ending 9 steps above. Using the default 1-second exposure time this sequence takes roughly 80 seconds. The default step size is normally used only for the first focus of the night. After the initial focus, the step size is reduced to $6\ \mu\text{m}$ to get a more accurate focus. However, the sequence always includes $-90\ \mu\text{m}$ at the start and $+90\ \mu\text{m}$ at the end. These flanking focus settings ensure that the sweep always sees an image that must be out of focus. For each image a figure of merit (FOM) is calculated that is the value of the peak pixel signal divided by a small-aperture integrated signal. The best focus is the one with the largest FOM. However, the best FOM must be at least twice the worst FOM. If not, the sequence is flagged as indeterminant and the focus is left at its original position. This safeguard protects against taking focus data when there is no real data (e.g., clouds, bad pointing). Every focus run is recorded in a special focus log file that is designed to be machine readable and record all of the information available to the data collection program (except for the actual images). In this way, refinements to the focus algorithm can be tested against a very large dataset of past focus runs to ensure that any algorithmic change truly leads to an improvement in operation.

Table 1 shows an example focus sequence. The table shows the focus position, the FWHM of the brightest pixel (in pixels), the peak signal (above background), total flux in a 5-pixel radius aperture, and the FOM. The initial setting was $5520\ \mu\text{m}$, taken with a V filter, at $\alpha = 19 : 57 : 52.8$, $\delta = +24 : 29 : 18$, hour angle = E00 : 14 : 44, airmass = 1.02, tube temperature = 19.7°C . Best focus was found to be at $5562\ \mu\text{m}$ (shown in italics). This method has proven to be very fast and exceptionally robust. When conditions are bad it will refrain from making a change to focus. When conditions are excellent it gives the best focus subject to the chosen step size. Under conditions of poor seeing it will still give a good answer. Other common techniques such as long-exposure images (>30 seconds), functional fitting to FWHM versus focus, and minimum in FWHM were all attempted but had conditions under which they failed and reached a decision that made things worse.

5.3. Target Acquisition. Data quality and ease of reduction is considerably enhanced by accurate target acquisition. This system provides three different acquisition strategies depending on the pointing accuracy needed.

Blind acquisition refers to the simplest method of target acquisition. In this case, the telescope is commanded to the desired coordinates and data collection begins without any attempt to verify the pointing. The raw pointing accuracy of the telescope after a new pointing model determination is less than 10 arcsec ($1\ \sigma$) across the entire sky. Fortunately, it is easy to do better and this mode is generally used only for things like setting up for twilight flats.

A *self-referencing acquisition* is used if the target position happens to be the position of a point source with no other brighter objects within 3 arcmin. Generally this is only used on sources that are in the range of magnitude 6–9. In this case the acquisition consists of the following steps.

TABLE 1: Focus sweep.

Focus (μm)	FWHM (pixels)	Peak (DN)	Flux (DN)	FOM
5430	8.9	3619	$5.11\text{e} + 05$	0.0071
5466	8.7	5537	$7.13\text{e} + 05$	0.0078
5472	8.2	4564	$6.98\text{e} + 05$	0.0065
5478	8.5	4437	$7.25\text{e} + 05$	0.0061
5484	7.4	6452	$7.36\text{e} + 05$	0.0088
5490	7.6	6429	$7.29\text{e} + 05$	0.0088
5496	7.7	7707	$7.48\text{e} + 05$	0.0103
5502	6.3	10073	$7.62\text{e} + 05$	0.0132
5508	7.4	7206	$7.50\text{e} + 05$	0.0096
5514	7.3	6341	$7.46\text{e} + 05$	0.0085
5520	7.0	7535	$7.50\text{e} + 05$	0.0100
5526	5.4	13066	$7.53\text{e} + 05$	0.0174
5532	5.1	13832	$7.58\text{e} + 05$	0.0183
5538	5.6	11557	$7.50\text{e} + 05$	0.0154
5544	4.8	16368	$7.50\text{e} + 05$	0.0218
5550	5.4	12246	$7.44\text{e} + 05$	0.0165
5556	4.9	15461	$7.46\text{e} + 05$	0.0207
<i>5562</i>	<i>4.4</i>	<i>19354</i>	<i>$7.65\text{e} + 05$</i>	<i>0.0253</i>
5568	4.7	17501	$7.55\text{e} + 05$	0.0232
5574	5.7	11007	$7.48\text{e} + 05$	0.0147
5610	5.9	11352	$7.45\text{e} + 05$	0.0152

- (1) Slew the telescope to the nominal coordinates.
- (2) Take a short exposure (typically 1 second) with the 3-arcmin acquisition field setting.
- (3) If the brightest source in the image is too weak or has a FWHM less than 1.5 pixels the acquisition is aborted.
- (4) Given a good image, the telescope performs the small offset needed to put the source in the center of the CCD.
- (5) After the offset is completed the telescope pointing is updated to match the known coordinates of the source.

A *local-reference acquisition* is used when the desired pointing does not coincide with an actual target or if the target is too faint. In this case, acquisition becomes a two step process. First, a self-referencing acquisition is done on the nearest 8-9 magnitude star. This leaves the telescope nearby with very accurate coordinates. From there the final step is a blind acquisition of the requested position. If the local reference star is within a few degrees this method will get to within 1-2 arcsec of the desired location. The extra time for the local reference is generally quite small (<10 seconds).

5.4. Scheduling Standard Stars. Thinking about how to write software to build a night's observing session led to more than a few interesting revelations. One of the core lessons was how much more universal a timeline of observations is when it is laid out relative to the local sidereal time (LST). Using LST to schedule observations of standard stars is particularly effective since the airmass is known and constant for a given LST. Common practices developed with single-channel photoelectric photometry recommend observations of standards periodically spaced through the night that

TABLE 2: Standard star observing blocks.

LST	Horz	Low Field	High Field	Extra Field
00:47	west	SA112	SA114 (1.40)	
01:46	west	SA113	PG0231 (1.17)	SA114 (1.72)
02:18	west	PG2213	PG0231 (1.15)	SA114 (2.03)
02:48	west	SA114	PG0231 (1.15)	
03:23	east	Rubin149	PG0231 (1.17)	
04:14	east	M67	SA95 (1.22)	
05:00	west	SA92	SA95 (1.27)	
05:10	east	PG0918	Rubin149 (1.48)	
05:55	east	SA101	Rubin149 (1.33)	PG0918 (1.86)
06:47	east	PG1047	PG0918 (1.50)	
06:53	west	PG0231	Rubin149 (1.24)	SA95 (1.71)
07:57	west	SA95	M67 (1.11)	
09:54	east	PG1323	PG1047 (1.26)	
11:26	west	Rubin149	PG1047 (1.23)	
12:04	east	PG1633	PG1323 (1.49)	
13:29	west	M67	PG1323 (1.38)	SA101 (2.02)
13:33	west	PG0918	PG1323 (1.38)	
14:00	west	SA101	PG1323 (1.40)	
14:38	east	SA110	PG1633 (1.25)	
14:53	west	PG1047	PG1323 (1.50)	
16:39	east	SA112	PG1633 (1.10)	SA110 (1.41)
16:58	west	PG1323	PG1633 (1.11)	
17:36	east	SA113	SA110 (1.27)	SA112 (1.77)
18:14	east	PG2213	SA110 (1.22)	
18:35	east	SA114	SA110 (1.21)	
20:49	east	SA92	SA112 (1.22)	
21:08	west	PG1633	SA112 (1.22)	
22:14	east	PG0231	SA114 (1.21)	
22:48	west	SA110	SA114 (1.20)	SA112 (1.42)
23:49	east	SA95	PG0231 (1.50)	

are taken at a wide range in airmass. Standards for CCD photometry are much more effective if fields containing two or more standard stars are used. The Landolt standard fields mentioned in Section 4.5 are a set of 15 fields equally spaced along the equator. The choices were also influenced by requiring high-quality standards with a range of star color in the field.

Given this list of fields it is a simple matter to compute for each field the two LSTs when it is at 2.5 airmasses. At each LST, compute the airmass and hour angle of all the other fields. From this list, keep the field closest to the meridian that is on the same side of the meridian as the high airmass field at that time. These two fields are a low/high airmass field pair. Some of the pairs have a third well-placed field that is intermediate in airmass. The extra field is optional but if included will improve the quality of the calibrations. Table 2 provides a list of calibration opportunities ordered by LST for 35° north or south latitude. The column labeled “Horz” is short for horizon and indicates if the first field is rising in the east or setting in the west. The “Low Field” column is the shortened name of the field always at an airmass of 2.5. The

“High Field” is the field nearest the meridian. An extra field is also included if appropriate. The value in parentheses is the field’s airmass at this LST.

These fields and the temporal framework greatly simplify the process of sequencing a night either interactively or with software. For a given night you first eliminate all opportunities that do not fall within the observing window. Next, remove all sets involving fields that are too close to the moon ($<30^\circ$ for this system). As the science program is built for the night add these calibrations to the timeline at roughly a two hour spacing taking special care to put a calibration as close as possible to the start and end of the night.

5.5. Pointing Model. All telescopes, whether used robotically or classically, are much more effective when they can accurately point to a desired location on the sky. Most, if not all, telescopes use some method to map from raw telescope coordinates to sky coordinates and is used to take out systematic errors introduced by the mechanical system. The Lowell Observatory telescopes use the Wyoming analytic model [5] for this mapping. Robotic systems are particularly effective at collecting data needed to derive such maps and involves taking a set of images over the entire accessible sky. An astrometric solution for the image reveals the actual pointing while the header records where the telescope thought it was pointing. The current pointing model is removed from the header coordinates to provide the original raw telescope coordinates. These pairs of values can then be used to refine the pointing model. A normal pointing run is a grid of about 120 points uniformly spread over the sky and takes about 3 hours to collect. A regular pattern in either hour angle and declination or altitude and azimuth should be avoided since they often generate excess data at either the pole or the zenith. The improved data quality made possible by robotic means made it possible to find systematic limitations in the Wyoming model when applied to the Lowell telescopes. This telescope turns out to need three additional terms in the pointing model where the new independent variables are (1) hour angle, (2) hour angle times declination, and (3) hour angle squared. The addition of these three terms reduced the pointing error from a few arc-minutes to a few arc-seconds.

6. Safety

An unattended system has a very different risk profile to one where there are always on-site personnel. The differences between the two modes can often be subtle and yet surprisingly important. A significant challenge in developing this autonomous mode was in recognizing these differences and reducing or eliminating risk through software, hardware, and good safety practices. First and foremost is the need to maintain a safe environment for technical personnel that are on site from time to time for repairs or routine maintenance. The second priority is to safeguard the hardware.

6.1. Personnel Safety. The only risk posed by this system to personnel is through the moving components (telescope and

dome) that are influenced by computer control. Minimizing these risks therefore involves controlling when and how the computer can move the telescope. It is set by policy that the nighttime is the province of the system and going into the dome should be done in consultation with the cognizant observing supervisor. During the day, the system is supposed to be idle and if not, the activities must be cleared through the technical staff. A policy statement has provided sufficient protection since the staff are rarely onsite unless there is a problem in which case everyone is involved anyway. Most of the accommodations for safety are surprisingly transparent to the staff. For instance, the system was built to tolerate power failures during the day, a common step during maintenance. It is unlikely that the facility is a completely safe environment but the goal was to make sure the new mode of operation did not add any risk that was not already present.

6.2. Hardware Safety. The nature of working with hardware is that it does not always work as expected. Considerable attention was paid to protecting the telescope and dome from harm. Despite best efforts in software no system can be 100% reliable and understood by its software and notification is the last line of defense in case of error. Any error generated by the telescope is treated as a serious problem. In the early days there was a daemon that collected error notification requests and pass them along to a pager. It resent the page every 10 minutes until confirmation ensuring that someone saw the message. After a couple of years the spectrum of system errors changed enough that any error was unlikely to have a meaningful remedy during the night. With that realization the pager was retired and all notifications were relegated to email.

The telescope has a safety feature known as the dead-man timer. This is a mode, activated at night for robotic observing only, that causes the MOVE31 computer to keep track of command activity. Each time a command is received the time is reset to 0. If the timer reaches two hours the telescope will automatically stow, shut down tracking, and close the dome. This is largely a protection against a catastrophic failure of cmdr, the computer it runs on, or the RS232 communication link.

The most important design philosophy for hardware safety is that the system must not assume anything. Most, if not all, errors can be traced back to an assumption being made in software. For instance, the telescope control software (MOVE31) used to assume that if it was not commanding the dome it could not be moving. When faced with a hardware problem such as a stuck power relay to the dome rotation motor this assumption becomes part of the problem. Clearly, there was little harm in having the system occasionally poll the dome position while stationary and if it were seen to move it would throw an error. In this case there is nothing the software can do directly but sending an email messages vastly increases the chances that someone can intervene and deal with the problem.

The other important lesson learned is that errors, once seen, do not go away and must be understood and fixed, never deferred for later. In most cases the log files permit

reconstructing all elements of the problem and allow tracing through the software to find the problem. In cases where this was not possible it invariably led to finding some error condition that was not properly logged. By adding new logging code such problems can eventually be solved.

The final safety issue for the hardware relates to the weather. In the case of Anderson Mesa, the problem is not too difficult since the weather conditions rarely change on a timescale short compared to a night. A weather forecast in the afternoon can generally be relied on to indicate if there will be precipitation or fog during the night. If there is a chance of either, the telescope is not opened at all. This site does not suffer from problems caused by high winds during a workable night. All of these weather issues mean that there is no need for real-time decision making based on current weather conditions. A go/no-go decision just before sunset is sufficient to eliminate weather related risks.

7. Routine Operation

A typical night is handled by a single script that is intended to fill the entire night. Hand generated scripts are only feasible if the same observing pattern is used night after night. Machine generated scripts are much less prone to error and can change from night to night.

The night always starts with a command to wait for the sun to set. Once that happens, the dome is opened and all the housekeeping steps needed to bring the telescope and camera to an operational state are executed. If the night is the first robotic night a full-frame pointing verification is performed very early during twilight. Next, wait for the sun to get 9° below the horizon and then do a first focus update. Every focus command is preceded by a synchronization command that keeps the command from executing too early. At this point the system is ready to begin observing. Science observations are interspersed with the necessary focus (once an hour) and standard star observations (every two hours).

At the end of the night twilight flats and bias frames are collected, if desired. The flat field command begins after the sun reaches an altitude of -9° . Once flats are collected the dome is closed, the telescope is parked, and then bias frames are collected. With PCCD, darks were also taken after the dome was closed and before the bias frames were taken. If no flats are taken the system usually still waits until the sun reaches -9° altitude and then shuts down. This timing marker makes it easy to spot wasted time in the schedule. At the very end a marker file is written with the data to indicate that data collection has ceased for the night. Once that marker propagates to the pipeline processing computers the night can be processed.

8. Example Data

8.1. Pluto Lightcurve Monitoring. The project that led to the development of robotic observing is lightcurve monitoring of Pluto. Figure 4 shows one example lightcurve from 2000 [6] in the last year before the robotic system was functional. The project requires a complete lightcurve each year to

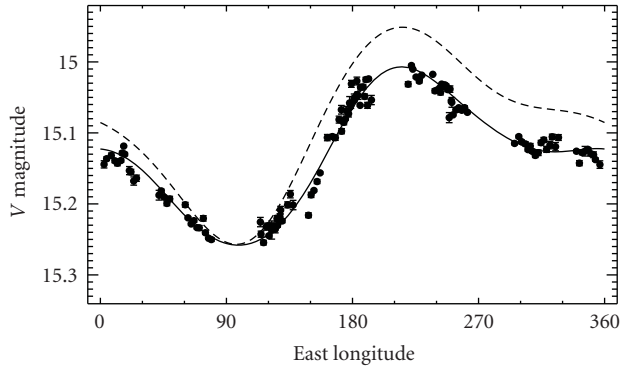


FIGURE 4: Lightcurve of Pluto in March-July 2000. The rotation period of Pluto is roughly 6.4 days and requires many nights to obtain a complete lightcurve. The points with error bars are the result of 35 nights of observation and nearly 1000 individual images. The solid curve is a 4-term Fourier series fit to the lightcurve. For comparison the lightcurve from 1986 is shown (dashed line).

document the system brightness during the current period of rapid change in the illumination geometry. The amount of effort required to collect data like this became prohibitively expensive for a long-term project.

8.2. Deep Ecliptic Survey Calibration. The Deep Ecliptic Survey [7–9] was an observational project to discover 1000 new trans- and ultraneptunian objects. The project used wide field imaging cameras on the Kitt Peak Mayall 4-m telescope and the Cerro Tololo Blanco 4-m telescope to survey the sky within 5° of the ecliptic. The robotic system has been working on calibrating those images by obtaining absolute photometry over most of this ecliptic zone. The survey has over 1300 primary fields and 1200 secondary fields that need supporting photometry requiring roughly 250 photometric nights to complete. This work is nearing completion and already has a photometric database of 515,000 observations from the first generation (PCCD) camera and 3.2 million observations from the current (NASAcam) camera. This observing project is supported by a dedicated single-purpose scheduling program that keeps track of which fields have already been done and builds a complete night of observations in a few seconds.

8.3. Astrometry. The current camera is an excellent instrument for making astrometric observations. The optical prescription was optimized to minimize image quality (PSF) variations over the field of view. There is a barely measurable quadratic distortion term required for fitting an astrometric control network to the images. In all cases, the astrometry from this system is limited by the quality of the supporting astrometric catalogs. To date, this system has been used to collect astrometry in support of occultation predictions, asteroid orbit improvement, and even astrometry of the background stellar field that the New Horizons spacecraft will see as it approaches Pluto in 2015. Often these astrometric observations can be slipped into the observing sequence with minimal disruption and with little advanced warning.

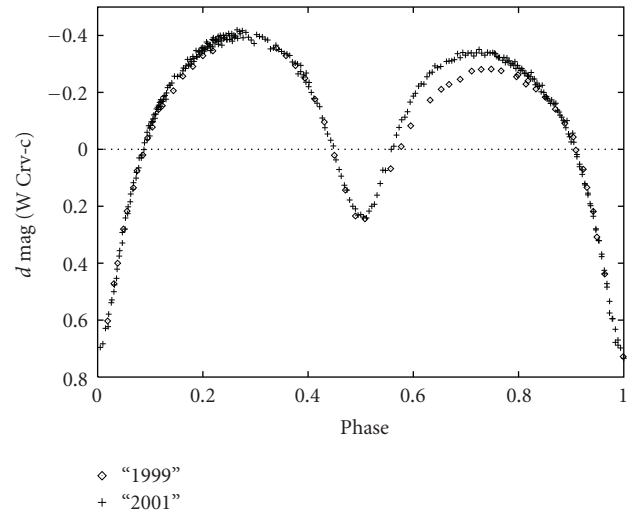


FIGURE 5: Lightcurve of W Corvi in 1999 and 2001 with the 0.8-m telescope. The 1999 data (diamonds) were taken with a classically operated CCD system in V . The 2001 data (+) were taken with the PCCD camera and the robotic system in $BVRI$ (only V data are shown). Figure used with permission from Odell [10].

8.4. Asteroid Lightcurves. A few test observations were taken to investigate the utility of this system for collecting asteroid lightcurves and near-earth asteroids in particular. The system supports observations of moving targets and is especially good at nearby targets where the topocentric corrections during the night are large.

8.5. Variable Stars. The simplest observations of all are photometric observations of variable stars where the photometry can be done relative to field stars. These can be done on non-photometric nights for which there is more time available than is typically used. Figure 5 shows a lightcurve of W Corvi collected with this system [10]. The fast filter wheel makes it very easy to collect multi-color observations of systems like this as well. As with all of the example projects, reducing the cost of data collection makes it much easier to collect long time base observations where the scientific breakthrough comes from a lifetime of monitoring rather than a single night of data.

8.6. Education. This system was used for a test project with the University of Hawaii to involve students in secondary education. This project made time available for students, typically in support of science fair projects, where the student picks a targets and an observing pattern. The data are collected on their behalf, calibrated, and sent to the teachers and students involved. The cost of supporting these educational projects is trivially small but has a profound impact on the students that are involved. We have worked together to build the process by which students can directly request the observations that feed into an automated scheduler but there has been insufficient funding thus far to complete this project.

9. Summary

Here are some of the benefits of this autonomous observing system:

- (i) Greatly reduced costs of data collection
- (ii) Fatigue free “observer”
- (iii) Much, much less prone to data collection errors
- (iv) Perfect data headers (simplifies reductions)
- (v) Zero-cost dawn twilights that improved data quality
- (vi) Extensible to much more elaborate observational patterns
- (vii) Eliminates all decision-related dead-time during the night.

In many ways this mode is the lifeblood for small telescopes everywhere. Robotic operation can maintain the scientific relevance of smaller apertures in cases where observing operations costs dominate.

Acknowledgments

This work was supported in part by NASA grants, NAG5-13380, NAG5-12229, NNG06-GI23G, NAG5-12835, NNX09-AB43G. Thanks to the technical staff at Lowell Observatory for their dedication to the Observatory telescopes. Special thanks to Larry Wasserman for his help above and beyond the call of duty on special modifications to the telescope control software that made this project a productive reality. David Tucker and REU student Brian Keeney helped with the early prototyping work on this project. Peter Collins was invaluable during the conversion process to NASAcam and also helped with crucial debugging and system oversight and monitoring.

References

- [1] A. U. Landolt, “UBV photoelectric sequences in the celestial equatorial selected areas,” *Astronomical Journal*, vol. 78, pp. 959–981, 1973.
- [2] A. U. Landolt, “UBV RI photometric standard stars around the celestial equator,” *Astronomical Journal*, vol. 88, pp. 439–460, 1983.
- [3] A. U. Landolt, “UBV RI photometric standard stars in the magnitude range $11.5 < V < 16.0$ around the celestial equator,” *Astronomical Journal*, vol. 104, no. 1, pp. 340–371, 1992.
- [4] F. R. Chromey and D. A. Hasselbacher, “The flat sky: calibration and background uniformity in wide-field astronomical images,” *Publications of the Astronomical Society of the Pacific*, vol. 108, no. 728, pp. 944–949, 1996.
- [5] E. J. Spillar, D. Dumbrell, G. L. Grasdalen, and R. R. Howell, “The Wyoming infrared observatory telescope software system,” *Publications of the Astronomical Society of the Pacific*, vol. 105, pp. 616–624, 1993.
- [6] M. W. Buie and W. M. Grundy, “Continued evolution in the lightcurve of Pluto,” *Bulleting of the American Astronomical Society*, vol. 32, p. 1083, 2000.
- [7] R. L. Millis, M. W. Buie, L. H. Wasserman, J. L. Elliot, S. D. Kern, and R. M. Wagner, “The Deep Ecliptic Survey: a search for Kuiper belt objects and Centaurs—I: description of methods and initial results,” *Astronomical Journal*, vol. 123, no. 4, pp. 2083–2109, 2002.
- [8] M. W. Buie, R. L. Millis, L. H. Wasserman, et al., “Procedures, resources and selected results of the Deep Ecliptic Survey,” *Earth, Moon and Planets*, vol. 92, no. 1–4, pp. 113–124, 2003.
- [9] J. L. Elliot, S. D. Kern, K. B. Clancy, et al., “The Deep Ecliptic Survey: a search for Kuiper belt objects and Centaurs—II: dynamical classification, the Kuiper belt plane, and the core population,” *Astronomical Journal*, vol. 129, no. 2, pp. 1117–1162, 2005.
- [10] A. P. Odell, *International Bulletin Variable Stars* no. 5514, 2001.

Research Article

The OAdM Robotic Observatory

Josep Colomé,^{1,2} Ignasi Ribas,^{1,2} Xavier Francisco,¹ Kevin Casteels,¹ David Fernández,³ Jordi Isern,^{1,2} Xavier Palau,⁴ and Jordi Torra^{1,3}

¹ Institut d'Estudis Espacials de Catalunya (IEEC), Gran Capità 2-4 (Edifici Nexus), 08034 Barcelona, Spain

² Institut de Ciències de l'Espai (CSIC-IEEC), Torre C-5 Parell, Zona planta, Facultat Ciències, Universitat Autònoma de Barcelona, 08193 Bellaterra, Spain

³ Departament d'Astronomia i Meteorologia, Institut de Ciències del Cosmos (UB-IEEC), Universitat de Barcelona, Av. Diagonal 647, 08028 Barcelona, Spain

⁴ Fundació Joan Oró, Travessera de les Corts 272, 08014 Barcelona, Spain

Correspondence should be addressed to Josep Colomé, colome@ieec.cat

Received 2 July 2009; Accepted 24 September 2009

Academic Editor: Alberto J. Castro-Tirado

Copyright © 2010 Josep Colomé et al. This is an open access article distributed under the Creative Commons Attribution License, which permits unrestricted use, distribution, and reproduction in any medium, provided the original work is properly cited.

The Montsec Astronomical Observatory (OAdM) is a small-class observatory working in fully unattended control, due to the isolation of the site. Robotic operation is, then, mandatory for its routine use. We present a description of the general control software and several software packages developed. The general control software protects the system specially at the identified single points of failure and makes a distributed control of any subsystem.

1. Introduction

During the coming months, the OAdM will begin routine operations working in fully unattended operation. The telescope and instrumentation finished their commissioning phases and are now being operated on a robotic supervised manner (astronomers are present at the observatory in case human intervention is required) for a six-month testing period. The primary guideline of the project is to guarantee the robotic operation of the observatory in order to carry out astronomical observations. The design and development processes were focused on ensuring a reliable and efficient system while working in this operational mode.

2. Observatory Description

2.1. Site. The OAdM is located at an altitude of 1570 m at the Montsec mountain, 50 km South of the central Pyrenees and 50 km North of the city of Lleida (Catalonia, Northeastern Spain).

Site testing campaigns were conducted during three years, with measurements of air stability, transparency, and weather conditions, and showed the high-quality night sky

of the Montsec mountain. Light pollution in the OAdM was found to be very low, with a night sky brightness at the zenith as low as $22.0 \text{ mag arcsec}^{-2}$ in the Johnson visual band (V), and between $21.5\text{--}20.6 \text{ mag arcsec}^{-2}$ at a height 45° above the horizon. Concerning the weather conditions, humidity is below 80% (90%) during 64% (77%) of the time (resulting in 81% of useful astronomical nights). Night temperatures are in the range from $(-10)\text{--}(-5)^\circ\text{C}$ in winter to $20\text{--}25^\circ\text{C}$ in summer. The mean wind speed is usually below 15 m s^{-1} and the sky is cloudless for 84% of the time. Recent measurements using a Robotic Differential Image Motion Monitor (DIMM, [1]) have confirmed these results: a median seeing of $0.86''$ was obtained from five months of data, better than $0.7''$ during 32% of the time.

2.2. Instrumentation. The OAdM is endowed with a 0.8 m telescope called TJO, standing for Joan Oró Telescope. It was supplied by Optical Mechanics Inc. and installed in March 2004. The 6.15 m dome was manufactured by Baader Planetarium GmbH and is fully automatic. The only current instrument is a 2048×2048 ProLine Finger Lakes Instrumentation CCD camera, with a CCD42-40 Marconi back illuminated chip with a pixel size of $13.5 \mu\text{m}$,

and a FOV at the Cassegrain focus of 12.4×12.4 arcmin (0.36 arcsec pixel⁻¹). The telescope is also equipped with an automatically controlled 12-position filter wheel, and the 5 filters of the Johnson-Cousins photometric system (U, V, B, R, I). Several instruments for environment monitoring are acquiring data continuously: two weather stations, a GPS antenna, a storm detector, and so forth. External communication necessary for remote supervision and control is provided by a radio link antenna with 10 Mbps bandwidth.

A complex software (SW) architecture, with several newly developed applications, manages all observatory operations. Basic telescope and dome control is conducted through the TALON SW (described in Section 5.1).

As complementary instrumentation, an all-sky CCD camera is working to detect bolides and meteors. As a mid-term objective, its images will be used to generate cloud maps that will allow the selection of clear areas of the sky.

2.3. Science Case. The OAdM scientific program will be comprehensive, embracing the observation of stellar variability, solar-type stellar activity, exoplanets, follow-up of novae and supernovae, Solar System bodies, and transient phenomena. The Observatory will offer time to the astronomical community via a Time Allocation Committee (TAC). Moreover, the robotic design will carry an important flexibility in the night scheduling, which will allow to react rapidly to observational alerts related to GRBs, new supernovae, and so forth. The participation to the networks of robotic observatories will be considered to carry out, for example, observations that require a dense time coverage.

2.4. Project Technological Scope. There are numerous advantages in operating an astronomical observatory using a robotic control instead of human attendance. These have been widely described in publications [2] over the last decade and will not be discussed here. The OAdM was designed from the beginning with a concept in mind: ensuring a reliable, secure, and efficient system while working in robotic mode. This mode of operation implies complex technology that is not commonly used in classical ground-based observatories, but rather in space observatories or some industrial applications. Its use has been extended today to ground-based observatories thanks to the evolution of hardware (HW) and SW capabilities and motivated by the clear advantages it offers in terms of time optimization to maximize the scientific return. But, achieving reliable operations is still an issue for most of these facilities that must be adapted to work on remote site locations and at extreme environment conditions.

The robotization level of an observatory is given by the confidence reached in responding to environment changes and by the required human interaction due to possible alarms. These two points establish a level of human attendance to ensure low risk at any time. Human attendance diminishes as robotization level increases, and that includes all the processes involved in observatory operations. Many situations should be automatically solved by a highly robo-

tized observatory: reacting correctly to critical errors or bad environment conditions, giving a response to external or internal alarms, making real-time evaluation of the images acquired, adapting the scheduling observations to current conditions, and so forth. The OAdM has been designed to achieve this high level of robotic control, just to be serviced once per month.

Single Points of Failure and Redundancies. Unattended observatories have to emulate human response to all those events that perturb the normal workflow. Any decision must be planned at the design phase. The malfunctioning of any HW or SW element must be detectable and a suitable response must be provided to ensure reliability and safety. Special attention must be paid to those points that could cause damage to critical parts of the system.

The dome shutter has been identified as the most critical point for the safety of the telescope, which is the core element at the observatory. Any error on its response would be fatal if it happened during a storm; so, special care has been put on dome control. See Section 4 for more details.

The specific environment at each site also introduces particular requirements. An observatory must have a planned response to any weather variable, for example, that could have an effect on the correct performance of the system or the quality of the acquired data. Instrument safety and working efficiency depend on a good response to environment conditions. The reliability of weather data is, then, the second critical point. That is the reason why there are several weather sensors with redundancies (see Section 6). All sensors are revised and calibrated periodically.

3. Initial Setup

The core element for the robotic operation at OAdM was the OMI telescope and its control SW (TALON) that at the time of purchase guaranteed reliable unattended control. After a poor installation by the manufacturer, which implied subsequent extensive efforts to reach working condition, we realized that a number of aspects should be improved and new features to be added to achieve a reliable, safe, and efficient robotic control. The system provided by the manufacturer, for example, did not have an application to control a dome nor any redundancy in case the main dome control channel failed; just a predefined small number of environment sensors could be connected, without the possibility of adding a redundant weather station, a storm detector, . . . In addition, a simple automatic queue scheduling was used to sort the observations before the beginning of the night, without real-time response capability to any kind of alarm. Except for the poor initial installation, the original setup of telescope and SW enabled low-level robotic observatory control, but that was in a much more limited manner than anticipated in the project.

We describe in the following sections the HW and SW elements, distributed in work packages, focusing the attention to unsolved aspects found during the implementation phase.

4. WP Dome

The dome was manufactured by the company Baader Planetarium GmbH. It is an automatic dome of 6.15 m diameter that receives from the telescope electronics the control commands, based on TTL protocol, to synchronize their movements and to open and close the shutter.

A redundant control of shutter closing (developed by Insercad Electronica S.L.) was installed in order to reduce the risk at this single point of failure. It uses a dedicated extremely robust computer to run this parallel control in case the main control subsystem crashes. A UNIX based application sends a shutter close order to the dome control electronics when it happens. It is done through an electronic board specially designed to manage signals coming from the telescope and from the redundant system.

Power is supplied using a dedicated UPS unit, whose load and battery charge values are automatically monitored.

5. WP Telescope

The TJO telescope has an equatorial fork mount. The instrumentation is placed at the Cassegrain focus. A segmented mirror cover protects the primary mirror from dust when the telescope is stowed. All these elements are automatically controlled and a standard pointing accuracy of about 10 arcsec over the entire sky is achieved. The electronics used to handle all the aspects of each axis of motion (Right Ascension (RA), Declination, focus and filter wheel) are the Clear Sky Institute Motion Controller (CSIMC) boards, distributed by OMI. A network of five CSIMC boards (four of them placed on the telescope mount) is used to communicate the devices for the axis movement control with the computer through an RS232 connection with only one of the boards, which serves as a gateway node. These standalone boards have the following features: communication with motor controllers, reception of a closed loop stepper axis encoder data and an open loop stepper axis, control of two limit switches and one home and several “user definable” opto-isolated I/O. RA, declination, dome rotation axis, and focus linear axis are closed loops, while filter wheel is an open loop stepper axis. Mirror covers aperture and shutter aperture and azimuth slew movements of the dome are computer controlled, through the CSIMC boards, too. The CCD camera uses a USB connection linked with the computer for the SW control of cooling, shutter aperture, and image acquisition and processing.

5.1. TALON. The basic equipment supplied by the telescope manufacturer included TALON, based on C and shell scripting programming, that enables the control of different elements to automatically manage astronomical observations, and which is now a GNU license SW. The HW elements controlled by TALON are the following: telescope, roof/dome, CCD camera, weather station, and UPS unit. Two of its applications (MKSCH and TELSCHED) can be used to create a list of objects to observe and to generate an observation schedule for the following night, based on simple queue scheduling. And, finally, it also has applications for image reduction and image photometric and astrometric

analysis. Robotic operations could be carried out using this SW, but the risk level would be high and it would imply a continuous human supervision. Solutions to integrate TALON in a more general structure that makes a reliable and safe global control have been found and developed.

6. WP Housekeeping

Housekeeping is the most critical aspect when considering the safety in robotic operations. It involves real-time environment knowledge and HW reliability, aspects that have been dealt at the OAdM with the appropriate equipment.

The use of just a weather station would be suitable for most observatories, but it is insufficient for a robotic one. A special effort has been made to have, at least, as many sensors as the number of environment variables to monitor. For those variables most critical for the observatory safety, redundancies are mandatory. Among the available sensors, there is a Davis weather station, used as a main weather data supplier, a second weather station (Campbell Scientific) used for data validation, a rain detector (Eigenbrodt IRSS 88), an opto electronic sensor for establishing the start and end of precipitation, a storm detector (INGESCO, Previstorm) that measures the variation of the electrostatic field and has four switches that configure different ways of automatically open electric lines to disconnect instrumentation in case of high risk of electric storms, and a cloud sensor (Boltwood Cloud Sensor II) that derives the fraction of cloud cover by comparing the temperature of the sky to the ambient ground level temperature. The information obtained with these sensors increases security, but a tool to manage the data and the generated alarms is required (see Section 8).

Internet communications and power supply are two more elements to take into account when facing the safety of the observatory. A radio link antenna of 10 Mbps bandwidth is used for external communication. It connects the observatory with the Anella Científica (Scientific Ring), a high-speed communications network (2 Gbps bandwidth) managed by CESCA (the Supercomputing Center of Catalonia), that connects universities and research centers in Catalonia. The network is connected to RedIRIS, the Spanish research network. Through RedIRIS, it reaches the most advanced international research networks. Continuous monitoring of the internet connection is done by CESCA that activates an alarm protocol when it breaks. Network monitoring is also done locally at the observatory, and an alarm manager is in charge of the execution of an alarm protocol if necessary.

6.1. Power and Electronics. The reliability of the power supply and the protection of signals against induced current and perturbations were also a matter of concern. The use of several UPS, SW controlled switches and electric insulation (optocouplers) increased the power supply security and its stability and reliability. The observatory is equipped with instruments to ensure a continuous supply of energy and to avoid any unforeseen distortion or power outage. They are mandatory due to the site isolation and the characteristics of the local weather, with a frequent occurrence of lightning

during storms, specially on Summer. The initial design of the building considered the installation of two lightning rods, a deep connection to ground, and the above mentioned storm detector for lightning protection. But some events showed that more protection and filtering was needed: voltage peaks produced by induced current at the communication wires, perturbation of the communication signal due to proximity of power lines, random power outages, and so forth.

Three UPS units, using double-conversion online technology (level 9, the maximum level of protection, with batteries always connected to an inverter, so no power transfer switches are necessary) were installed to supply power to the equipment that is very sensitive to power fluctuations and requires electrical isolation: astronomical instrumentation, sensors, computers, and dome. These UPSs allow a typical backup time of 15–30 minutes and have the capability to execute a computer controlled switching off.

Protection elements were installed at all electronic connections when communication between components required a cable length above 3–5 m. Commercial solutions were used for standard serial ports and network connectors, and optocouplers elements were implemented for the rest.

Reduction of noise at communication wiring was achieved by using optocouplers or fiber optic cables. Electrical noise was a big concern for dome encoder signals, because the cable transmitting this signal was very close to dome azimuth and shutter motors. These three-phase AC motors produce current voltage peaks when movement starts, which caused false signals and frequent encoder damaging. The use of a new encoder with high noise interference immunity designed for industrial applications (Hengstler Incremental Shaft Encoders, type RI30) in combination with fiber optic wiring drastically reduced the noise and corrected the position detection problem.

And, finally, different grounding for physically linked components caused a distortion of electric signals. This could only be solved by electric insulation.

7. WP Data Storage and Backup

Data storage and backup policy was designed and implemented to handle the data and assure a safe storage for raw images, extracted data, and logging information.

The maximum data rate produced by the TJO is 8 GB per day. On-site and off-site backups are conducted daily, using Redundant Arrays of Independent Disks (RAID) that provide redundancy and high reliability.

Images stored are compressed using the Rice algorithm. It is 2–3 times faster than GZIP or Hcompress, compresses an image of a factor of 3, 1.4 times better than GZIP, and headers for all extensions are still visible in compressed images [3].

8. WP Systems Control

Observatory control is based on a distributed task scheme executed using several computers. The distribution of applications in four subsystems (see Figure 1) implements a top-down control structure that manages the workflow of the

observatory. Almost all the SW acquired and developed is running on a UNIX platform, which is more stable and reliable than other operating systems.

8.1. Environment Control System (ECS). The main scope of this system is to provide a set of tools to monitor the conditions (environment, HW, SW applications, power supply, etc.) of the observatory and to manage and generate alarms according to these conditions.

The ECS is able to provide a reliable control mechanism ensuring that when the conditions become (un)suitable for observation, all the systems involved in it are able to act accordingly. The system provides the following features.

- (i) Constant monitoring of weather conditions: temperature, wind, relative humidity, atmospheric pressure, cloud cover, approaching storms, rain, and so forth.
- (ii) Information about the monitored elements: it serves this data to clients.
- (iii) Alarm generation and management: alarms are generated and managed according to defined criteria. These alarms are designed per observation setup (different location or different configuration) as each one may have different observation requirements. The same ECS can be used for several observatories at the same site, but each one needs a different alarm manager. An infrastructure for more than one alarm generator is provided. Alarms are generated when: an observation should start or should not continue, the system should shut down, and so forth.
- (iv) Reliability: ECS is critical. The developed SW has been designed to execute a reliable response when an alarm is triggered. The ECS is self-controlled, thanks to the distributed task scheme.

As it can be seen in Figure 2, the ECS is composed of two main internal elements and many external elements. The two internal blocks are as follows.

- (i) Environment monitor (EM): all the environment sensors are connected to this part, which serves all the environmental data to the other elements of the system using a server-client architecture. It reads the data collected and sends it to the clients that are connected over the network. The main feature is to provide a “generic” format and structure for the weather and environmental data collected from many different sensors. Usually each sensor has its own protocol or data format and this increases the complexity of a system managing data from various sensors. With this EM, every client that is connected will receive a common data structure with the different values collected. This approach yields a reduction of the overhead for these clients and a simpler implementation. In terms of portability, once this package is installed at a new observatory, there is just one part to be adapted. It corresponds to the lowest-level part: the driver framework. It has to be adapted just when different kinds of sensors are used,

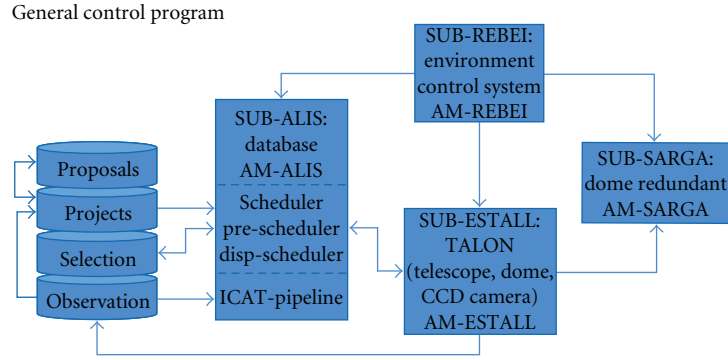


FIGURE 1: OAdM general control diagram.

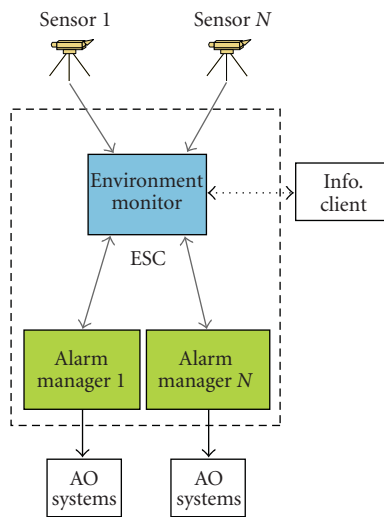


FIGURE 2: Main elements composing the ECS. The external blocks are: the sensors where data are collected, the different clients that request weather data to the EM, and the different systems that need to receive the alarms. AO stands for Astronomical Observatory.

because each sensor normally has its own application programming interface (API) and/or data stream. This application is implemented using Mono, C #, and C/C++.

- (ii) Alarm manager (AM): this element generates and manages alarms according to the status check it makes of HW and SW elements and the data values received from the EM. There can be as many AMs as needed and there should be at least one per facility. In the case of the OAdM, there are several AMs, as it is described next (Section 8.2). AMs are coded in JAVA and use XML configuration files.

8.2. Alarm Managers. This block is included in the ECS. It is described in a different section because it has critical relevance in the observatory management safety.

As the EM, it also has a server-client architecture, where one or more AM servers and AM clients are running

per facility located at the same site. At OAdM, there is a distribution of AMs, each one running on a different computer, which identifies a subsystem. They all have the same generic routines, and a configuration file defines which ones are applicable at a particular subsystem and must be activated.

Here follows a list of subsystems and a description of the routines running at their associated AMs.

- (i) SUB-ESTALL: This subsystem includes the control of all the HW involved in the observation process: telescope, CCD camera, and dome. The AM responds to an incorrect behavior of anyone of these instruments.
- (ii) SUB-ALIS: Subsystem in charge of data management and backup, pipeline, and scheduling routines. It is installed on the server.
- (iii) SUB-REBEI: The EM is running on this computer. The AM checks if this application is running correctly.
- (iv) SUB-SARGA: Subsystem in charge of the dome redundant control application. Environment alarms and any detected problem at the SUB-ESTALL subsystem activate a shutter close order sent by the AM.

SUB-REBEI and SUB-SARGA are the most critical subsystems and must work with a high level of confidence, as justified in Section 2.4. Two extremely robust computers (low dissipation CPU, modest amount of RAM memory, Flash memory with a Linux distribution, no hard disk, etc.) are used for that purpose.

Finally, a description of routines common to all the AMs is given.

- (i) Environment: Every subsystem is continuously checking the environment conditions and activates a protocol when critical values are detected. For weather data registered by redundant sensors, a validation routine is running to decide if any sensor is not working properly or has lost calibration. The response given by the AM to a weather alarm depends on the HW each subsystem controls.
- (ii) Network control: Every subsystem monitors both local and remote network services. When an error is

detected in any subsystem, the other AMs evaluate the risk and decide which protocol must be executed.

- (iii) Power: each UPS is constantly being monitored by the AMs. When they detect an error on power supply network, every subsystem AM responds with a shutdown of all the HW it controls if necessary. An automatic restart is also defined to ensure the correct sequence when switching on the subsystems.

AM uses broadcasting to inform all the AMs at other subsystems when an alarm appears.

8.3. Interfaces. Software interfaces between all the applications have been developed to integrate new packages with the commercial ones, in order to have a software suite that manages the whole observatory in a consistent manner.

A GUI to remotely control and monitor the observatory status is under designing phase.

Proposal Handling and Data Management. A new proposal is submitted in two phases. In Phase 1, proposers submit a scientific justification and observation summary for review. The Telescope Allocation Committee (TAC) recommends a list of programs with associated priorities to the TJO for preliminary approval and implementation. A technical assessment is the last step in this phase to determine the feasibility of the proposal and its final approval. In Phase 2, investigators with approved Phase 1 proposals provide complete details of the observations in their proposed observing program. This allows the TJO to conduct a technical feasibility review, and to schedule and obtain the current observations.

A web-based proposal submission tool stores all the information in the database. Information is accessible then by the TAC to evaluate the proposals and by the automatic scheduler.

The images and the extracted data stored at the observatory archive are easily accessed using a web interface. The user can download the data identified with his/her proposal code after logging in a private area of the observatory web page.

9. WP Database

The OAdM database (DB) is structured using a relational model. It is characterized by the presence of a common attribute used as a key identifier to link information about the same entry that is stored in different tables. The management system used is MySQL, widely deployed and regarded as being fast. The database is then updated by different applications using an ORM (Object-Relational Mapping) and SQL queries.

The optimal structure of a DB depends on the natural organization of the application data, and on the application requirements (which include transaction rate (speed), reliability, maintainability, scalability, and cost). For the OAdM observatory, different levels are identified following these criteria (see Figure 3). The list of levels is detailed below,

according to the global control design and the specific applications that interact with each one. They are sorted from high (Proposals and Projects) to low (Selection and Observation) level of human interaction.

- (i) Proposals: General information included in the first phase proposal submission (proposal identifier, investigator data, target list and scientific justification, date of submission, etc.). New entries are generated through a web user interface, acceptance date is updated manually after the submission to the observatory TAC, the proposal identifier is automatically created and date of completion and status are updated automatically.
- (ii) Projects: Specific information of the submitted proposal (phase 2 proposal submission, as described at Section 8.3), including observational data and scheduling constraints (detector to use, filters, exposure times, number of iterations, period between iterations, environment conditions, etc.). It also includes the number of present successful observations, which is automatically updated. The entries of this DB are accessed by the scheduler after validation by the observatory staff.
- (iii) Selection: Temporary list of targets extracted from the Projects DB according to their possibility of observation following defined criteria. This list is generated by the scheduler application and is used as input information for the dispatch scheduler (Section 10).
- (iv) Observation: Entries generated by the application that manages image acquisition when an observation is executed. There is an entry per observation, that includes: proposal and target identifiers, date and time of observation, calibration and analysis status, storage directory and filenames (raw image and analysis results), image quality report (seeing, S/N,...), error flags, and quality average (average value to decide if an image fulfills user requirements). This table is used for the calibration and analysis tool (Section 11) to decide which images have to be treated and to know where the results obtained on that process are stored.

A project is finished when the number of successful observations is equal to the number of the required iterations. And when all the projects included within the same proposal are executed, the proposal is considered completed and a notification is automatically sent to the proposal PI.

10. WP Scheduler

The scheduler main task is the time optimization and it has a direct effect on the scientific return achieved by an observatory. Then, it is the core SW application for a robotic facility and it is required to be fast and reliable.

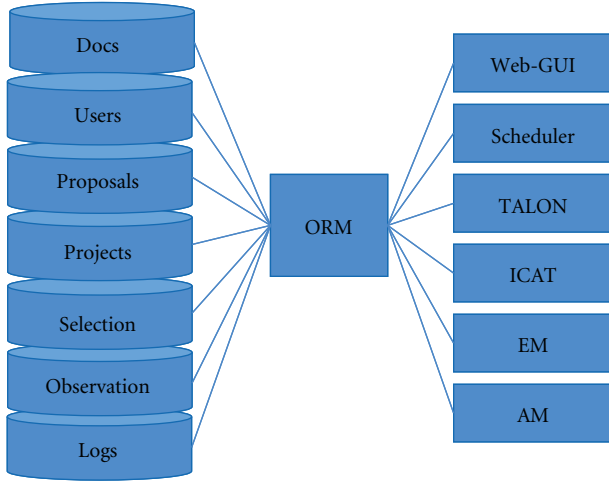


FIGURE 3: OAdM DB.

The OAdM scheduling is separated in two parts.

- (i) Pre-scheduling: It makes a temporary selection of objects according to their possibility of observation from those projects approved by the TAC. The selection is done before the beginning of the night following these selection criteria: height above horizon is positive at some moment during the night; night date is included in the defined observation window; moon brightness and distance fulfill user requirement, and so forth.
- (ii) Dispatch-scheduling: A dispatch scheduling is executed any time a target observation is over and a new one must be scheduled. It is done in real time according to current environment conditions and the set of priorities. The application uses the selected objects at the pre-scheduling process as input information and executes an algorithm that calculates the figure-of-merit of each object. Then, the object with the highest merit value is scheduled. A general definition of a merit function is

$$m(t) = \sum_i \alpha_i \cdot f_i(t), \quad (1)$$

where $f_i(t)$ functions and their associated weight α_i describe the different effects that contribute to increase or reduce of the global merit $m(t)$ per object. Among these effects, we consider

- (a) observing conditions: height above horizon, moon brightness and distance from the moon, best time in case observation is not required at the meridian, period between iterations, distance from previous target, proposal priority,
- (b) environment conditions: seeing, photometric conditions,
- (c) proposal history: a term to ensure a balance between the observation time spent to different proposals that have the same priority.

The definition of the dispatch scheduling algorithm is under study. Other works with a similar approach to this problem can be found in literature [4, 5].

11. WP Data Processing—The IEEC Calibration and Analysis Tool (ICAT)

Reliable and fast data calibration and analysis software is crucial to treat automatically the vast amount of images obtained at a robotic observatory. The ICAT software has been developed as a tool for robotic observatories with the objective of managing astronomical images to extract relevant scientific information in real time.

ICAT is based on Perl scripting to control program flux and manage image files. It is executed together with UNIX shell, NOAO-IRAF scripts, and CFITSIO library routines. When doing the installation of this SW, a few parameters must be set up according to the system: minimum number of calibration images to use, image header keywords, analysis parameters (crowding boundary,...), and so forth. After that, the reduction is automatic. It has been designed to be easily adapted to be used at other observatories setup.

Its general characteristics are: automatic management and treatment of FITS images according to database input information (Section 9), high accuracy photometric and astrometric data extraction and real-time execution. Although automatic execution is its main functionality, user-controlled execution is also available, using a web interface (written in PHP) and enabling the controller to modify a few parameters to adjust the reduction process to different criteria. Two kinds of reductions are executed automatically.

- (i) On-the-fly reduction: done after each observation in order to identify if the image has the required quality; the obtained information is then used by the scheduler program to decide which object to observe next.
- (ii) Final reduction: done during the day, includes obtaining final master calibration images before calibrating and analyzing the astronomical images in order to improve the data quality obtained.

11.1. Reliable and Fast Data Calibration and Analysis SW. Three packages are used for different purposes according to their capabilities: NOAO-IRAF, calibration and analysis SW, DAOPHOT [6] reliable PSF photometry package, and SExtractor [7] fast and good precision analysis SW, using flexible aperture photometry.

- (i) Calibration: NOAO-IRAF packages are used to combine raw astronomical images with processed bias, dark, and flat images.
- (ii) Analysis: Two different SW packages are used depending on image crowding in order to obtain good photometric quality with a minimum time of execution. ICAT, after a fast analysis using SExtractor, defines a density function on each image and identifies the crowded areas. The DAOPHOT

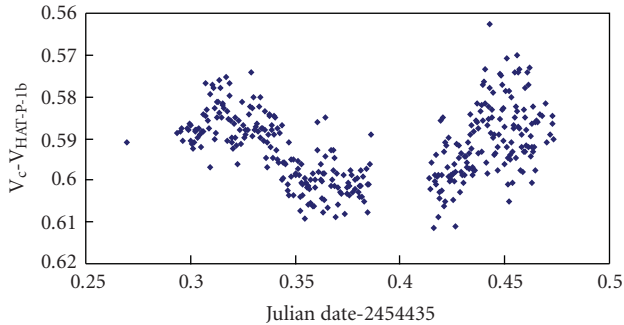


FIGURE 4: Transit light curve of the HAT-P-1b exoplanet obtained using the ICAT pipeline. 360 images were taken on November 30, 2007 at the OAdM, with the Johnson V filter. Calibration images were also taken and used for image correction. This figure also shows the instrumentation quality: a photometric dispersion of 0.4% is obtained at flat parts of the curve. Flat-fielding errors and scintillation are the main contributions to this dispersion, which is expected to be reduced up to a 0.2% when calibration tasks are finished. In contrast, the photon noise shows to have a smaller effect. The increasing noise at the end of the observation is because of the low altitude of the target. The gap during the transit was produced by an interruption of the observation sequence.

package is then applied to those areas to obtain PSF photometry using an improved selection of stars for the PSF matching function calculation. Non-crowded areas are analyzed using SExtractor. Astrometric and photometric data for the totality of the objects in the entire image is then a combination of the data obtained with SExtractor and DAOPHOT.

12. Conclusions

The OAdM is designed to be an unattended small-class observatory, and HW and SW features respond to this aim. Early results obtained during the commissioning phase have shown that robotic operations can already be carried out with proper management of the risks. No human intervention is required during an entire night process, but the reliability of the system is still to be improved. Packages in charge of enhanced safety, those included at the ECS, are being developed at the moment. The other tools that complement robotic operations and enable the reduction of human attendance are also under development, except for the ICAT-pipeline that has already been finished and tested with the calibration and analysis of several photometric exoplanet transit observations (see Figure 4). Its capabilities for an efficient and reliable extraction of scientific data have been proved. The OAdM is expected to start high-level robotic operations in a few months.

Acknowledgments

The authors wish to thank all who have contributed to the development of this project. The OAdM project is supported by the Catalan government and led by its local official institution: the Consorci del Montsec. Research

institutes and universities have actively contributed with scientific and technical supervision and manpower to the development of the project: the Institute for Space Studies of Catalonia (IEEC), the University of Barcelona (UB), the Technical University of Catalonia (UPC), the Spanish Research Council, (CSIC) and the Joan Oró Foundation (FJO).

References

- [1] J. Aceituno, "A new robotic DIMM for Calar Alto Observatory," *CAHA Newsletter*, vol. 04b, 2004.
- [2] K. G. Strassmeier, G. Hasinger, R. P. Kudritzki, N. O. Weiss, and H. W. YorkeK, "Third potsdam think shop on robotic astronomy," *Astronomische Nachrichten*, vol. 325, 2004.
- [3] W. P. Pence, R. Seaman, and R. L. White, "Lossless astronomical image compression and the effects of noise," *Publications of the Astronomical Society of the Pacific*, vol. 121, no. 878, pp. 414–427, 2009.
- [4] T. Granzer, "What makes an automated telescope robotic?" *Astronomische Nachrichten*, vol. 325, no. 6–8, pp. 513–518, 2004.
- [5] S. N. Fraser and I. A. Steele, "Robotic telescope scheduling: the Liverpool Telescope experience," in *Optimizing Scientific Return for Astronomy through Information Technologies*, vol. 5493 of *Proceedings of SPIE*, pp. 331–340, June 2004.
- [6] P. B. Stetson, "DAOPHOT—a computer program for crowded-field stellar photometry," *Publications of the Astronomical Society of the Pacific*, vol. 99, pp. 191–222, 1987.
- [7] E. Bertin and S. Arnouts, "SExtractor: software for source extraction," *Astronomy and Astrophysics Supplement*, vol. 117, no. 2, pp. 393–404, 1996.

Research Article

Autonomous Observations in Antarctica with AMICA

Gianluca Di Rico,¹ Maurizio Ragni,¹ Mauro Dolci,¹ Oscar Straniero,¹ Angelo Valentini,¹ Gaetano Valentini,¹ Amico Di Cianno,¹ Croce Giuliani,¹ Demetrio Magrin,² Carlotta Bonoli,² Favio Bortoletto,² Maurizio D'Alessandro,² Leonardo Corcione,³ and Alberto Riva³

¹ INAF—Osservatorio Astronomico di Teramo, 64100 Teramo, Italy

² INAF—Osservatorio Astronomico di Padova, 35122 Padova, Italy

³ INAF—Osservatorio Astronomico di Torino, 10025 Pino Torinese (TO), Italy

Correspondence should be addressed to Gianluca Di Rico, dirico@oa-teramo.inaf.it

Received 24 June 2009; Revised 30 December 2009; Accepted 11 February 2010

Academic Editor: Alberto J. Castro-Tirado

Copyright © 2010 Gianluca Di Rico et al. This is an open access article distributed under the Creative Commons Attribution License, which permits unrestricted use, distribution, and reproduction in any medium, provided the original work is properly cited.

The Antarctic Multiband Infrared Camera (AMICA) is a double channel camera operating in the 2–28 μm infrared domain (KLMNQ bands) that will allow to characterize and exploit the exceptional advantages for Astronomy, expected from Dome C in Antarctica. The development of the camera control system is at its final stage. After the investigation of appropriate solutions against the critical environment, a reliable instrumentation has been developed. It is currently being integrated and tested to ensure the correct execution of automatic operations. Once it will be mounted on the International Robotic Antarctic Infrared Telescope (IRAIT), AMICA and its equipment will contribute to the accomplishment of a fully autonomous observatory.

1. Introduction

In the recent years, great attention has been paid to the new possibilities opened from the exploitation of Antarctica for astronomical observations. A large number of advantages come out from the peculiar characteristics of this remote land and, at the same time, new stations are rising in the inner region of the continent, known as Antarctic Plateau. Among themis *Concordia*, one of the most advanced and organized permanent bases, which was built at Dome C within a French-Italian collaboration.

Taking advantage of the presence of this station, an ambitious goal is going to be achieved, consisting in the installation of a fully autonomous observatory, constituted by IRAIT [1] and the scientific equipment of AMICA [2]. IRAIT is a 0.8 m, F/22 Cassegrain with two Nasmyth foci, built within an Italian-Spanish collaboration among the University of Perugia, the University of Granada (DFTC), and the Institut d'Estudis Espacials de Barcelona (IEEC). Its mechanics has been mounted during the 2008-09 summer campaign while the assembly of the remaining components,

the mirrors alignment, and the integration of the camera system will be accomplished starting from the 2009-10 summer.

Main scientific tasks of AMICA are both the characterization of the Dome C sky for infrared astronomy and the observation of a large variety of astrophysical objects, among them not only the AGB and post-AGB stars, the star forming regions in our and nearby galaxies, but also RR-lyrae, nearby brown dwarf, heavily-obscured supernovae and Solar System bodies. Finally, Survey mode observations will be performed for interesting regions of the southern sky (e.g., the Large and the Small Magellanic Clouds).

The robotization of the whole system is a necessary condition due to the extreme climate conditions, as a result of which human activities are reduced and essentially stopped during the Antarctic winter (mainly because of the unavailability of efficient communication means and the total absence of personnel and supplies transport). On the other hand, the instrumentation needs reliable solutions to deal with such peculiar environment, to avoid the damage of the components, and to minimize any safety risk.

2. The Antarctic Scenario

In this section, we give a brief overview of pros and cons of the Antarctic environment from both a scientific and technological point of view. These considerations have led to the development of AMICA and to the adoption of the solutions discussed afterwards.

2.1. Sky Properties. Essential requirements for observations at infrared wavelengths are the low-sky emission and the high-atmospheric transmission. As reported in the literature, first estimations of these properties in Antarctica and in particular in the inner Plateau are highly promising [3, 4]. The extremely low temperatures (with an annual mean of about -55°C) reduce the thermal emission from the sky and prevent the atmosphere from containing high amount of water vapor. Since the most absorption is dominated by this component, near infrared bands ($2\text{--}5\ \mu\text{m}$) are wider than those in a temperate site and new windows open up in the mid-infrared (beyond $15\ \mu\text{m}$), which cannot be accessed elsewhere [5]. Other important advantages come out from the low level of aerosols and dust, the high stability of the atmosphere, the high percentage of cloud-free time, and the elevation of the site ($3250\ \text{m}$). For these reasons, a substantial increment of the resulting sensitivity is expected, obtaining, for a given primary mirror size, the same performance of a several times larger telescope, with lower construction and management costs.

2.2. Polar Condition. Further important characteristics have to be considered about the location of Dome C. Its near-Pole latitude (75°S) allows to perform longer and uninterrupted observations in a maximum field of circumpolar sources (particularly interesting for the presence of peculiar regions such as the Magellanic Clouds and the Galaxy Center), even at zenithal angles normally unfavorable for temperate sites. Finally, thanks to the excellent IR properties of the sky, daily duty-cycle of 100% is probably achievable for wavelengths beyond $4\ \mu\text{m}$, where observations can be carried out even with sunlight.

2.3. The Extreme Environment. Unfortunately, the site location and the environmental conditions that are responsible for the great advantages underlined above make it very difficult to operate conventional instrumentation. Main troubles rise out from the temperature and pressure values.

Low Temperature. The first problem to face concerns the low temperatures (down to -80°C during wintertime). Despite they provide an efficient passive cooling (dramatically reducing the instrumental emission that at infrared wavelengths could overcome the sky flux), the electronic and mechanical systems are dangerously exposed to the risk of damage and malfunction. The investigation of suitable solutions for components that have to inevitably work outdoors and the insulation of devices with limited operating conditions are very critical aspects. In fact, they require the development of custom elements accurately tested in climatic chamber, to

simulate the environment in which they will be operated and stored.

Low Pressure. Because of the low pressure ($\sim 640\ \text{mbar}$ at Dome C), the efficiency of the conduction and the convection of the air is significantly reduced, hence increasing the possible overheating of insulated electronics. This problem has been frequently reported during experiments performed in past Antarctic campaigns [6]. For this reason, a thermal study of dissipating elements and a careful distribution of hot spots inside the cabinets are fundamental prerogatives for an efficient active conditioning system.

Temperature and pressure are also responsible for the limited human activities, in particular during winter, when the difficulty to operate outdoors becomes prohibitive.

2.4. Logistic Facilities. The presence of the Concordia base ensures the availability of a large number of facilities for the permanence of the personnel, the visiting researchers, and the hosted scientific experiments. However, some relevant restrictions need to be considered:

- (i) the total amount of electrical supply that can be provided by the station generators is $200\ \text{kW}$ (shared among all scientific and logistic needs);
- (ii) satellite links are normally used for fax and voice connections. Data transfer is very limited in time and speed ($\sim 64\ \text{kbps}$) and used mainly for text emails. Some improvements are under study to provide a broad-band data connection;
- (iii) the site can be reached by plane from the Italian “Mario Zucchelli” coastal station after a 5-hours flight, or by ground from the French coastal station “Dumont d’Urville”, through a two-week oversnow traverse (protecting the equipment from jolts, vibrations, thermal shocks, and low temperatures);
- (iv) the low availability of operators inside the base and total isolation for about 8-9 months during wintertime are also to be considered.

3. AMICA Equipment

AMICA is a multiband camera provided with two detectors. A InSb 256×256 CRS-463 Raytheon array and an Si:As 128×128 DRS Tech. array are used for imaging in the NIR ($2\text{--}5\ \mu\text{m}$) and MIR ($7\text{--}28\ \mu\text{m}$) regions, with a set of KLMNQ filters. A complete equipment provides all the necessary support to the camera operation. To perform safe and unattended observations in such peculiar conditions, it is necessary to meet all environmental, cryogenic, and functional requirements, paying attention to failures in recovery and maintenance. After solving a large number of issues, the development of the control system is currently at its final stage. This is focused on the integration of the camera with all hardware and software subsystems and the verification of the correct execution of automatic procedures that will be cooperatively carried out with IRAIT.

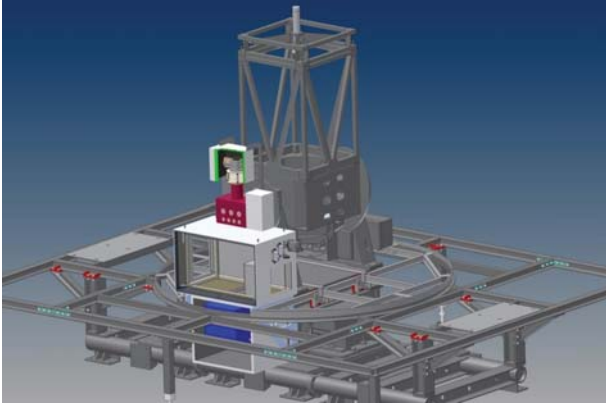


FIGURE 1: 3D rendering of the AMICA equipment mounted at the IRAIT fork. Most of the instrumentation is enclosed in thermal conditioned boxes (white) while the cryostat (red) is mounted at the telescope focus. Two small cabinets contain the cryocooler cold head and some vacuum system components. The box below encloses the LCU, the read-out electronics, controllers, and camera auxiliary devices. The cryocompressor (blue) is mounted below the rotating floor while the M2 wobbling system (light grey) is mounted at the IRAIT top ring.

3.1. Hardware Layout

3.1.1. Modularity and Subsystems. The compact configuration allows the whole system to corotate with the telescope fork (Figure 1). All the instrumentation, except for the front-end electronics (bias and clock filters, video signals preamplifier) are thermally controlled in separate insulated boxes. They have been designed to be easily mounted and transported by cranes used at Dome C. As shown in Figure 2, the components distribution has been carefully studied (taking into account thermal and size constraints) in order to ensure as much as possible their easy access and a fast replacement in case of malfunction. A schematic description of the AMICA control system (hardware layout and data connection) is shown in Figure 3.

The detectors control electronics (ACQ) has been developed cooperatively by INAF's departments (Padova, Teramo, Torino) and the Skytech Srl manufacturer [7]. It allows a pixel exposure time down to $0.7 \mu\text{sec}$ (16 bit ADC, up to 8 Mpx s^{-1}) with a minimum frame time of 2.9 msec for the MIR channel. It is composed of a digital programmable sequencer (PMC) installed in the cPCI Local Control Unit (LCU), optically connected through a 1.2 Gbaud fiber link with a separated rack. This hosts three further subunits: the SPC board provides the detectors clocks, while two DCS boards are used for the biases generation and for the correlated multisampling of the video signals.

Since mid-infrared observations require fast chopping techniques using the wobbling secondary mirror (M2) of IRAIT (with frequency of 2–10 Hz and a frame rate up to 300 fps for the AMICA+IRAIT configuration), the coadding and the sky subtraction of raw frames are performed in real-time mode during exposures, directly triggered through TTL

lines by the PMC or (for redundancy) through a TCP/IP command interface.

The IRAIT M2 subsystem has been manufactured by the Spanish NTE SA, which has also built a driver for the motion of the tertiary mirror (M3), in order to alternatively feed both the Nasmyth foci of the telescope. They have been tested to successfully operate down to -80°C , with the M2 driver being able to perform fast and accurate pointing during chopping (up to 10 Hz) and off-axis imaging. The M2 driver, in particular, has been fully integrated with the camera control system, in order to evaluate the overall accuracy and repeatability of the instrument, the settling time and the correct execution of automatic operations (e.g., observing modes configuration, focusing, etc.) during realistic simulations.

A multilevel thermal control ensures the continuous monitoring and the conditioning of the instrumentation placed inside the boxes. In fact, besides the Environmental Control System (ECS, a high-level software application), a Programmable Logic Controller (PLC) is devoted to the management of a large number of analog and digital devices (resistors, temperature and humidity probes, fans and contactors) to provide a low level active control of the conditions inside the cabinets. It can operate both autonomously (during outages of activity in which all other devices could be turned off) and cooperatively with the software running on the LCU. Moreover, the PLC is in charge of the boot and the shutdown of each component of the system (following well-defined safety procedures). Finally, a low-level passive electronics has been distributed inside the boxes to keep the minimum safe temperature in case of failure of all active systems.

As discussed above, because of the high air rarefaction, not only the low temperatures, but also the low heat dissipation from electrical elements could seriously damage the instrumentation. For this reason, two cooling systems have been installed, composed of pipes passing through the boxes in which the forced ventilation (periodically alternated in direction) allows the internal environment to indirectly exchange the exceeding heat with the external one, avoiding thermal shocks (that could be induced by a direct exposure to the outside air) and the entrance of highly dangerous ice crystals.

3.2. Software Layout. The AMICA Control Software (ACSW) is an agent-based cooperative system, modeled under the principles of the OO Programming (C++, Java), using the graphical notation of the Unified Model Language (UML).

3.2.1. Architecture. The observatory operation is managed by the IRAIT OCS (Observatory Control System), which detains the observations scheduler and the weather control, retrieving information about all subsystems activity (e.g., busy status during acquisition, intensive backup, maintenance operations, etc.) as well as alarms due to dangerous events (low temperature inside the boxes, overheatings, malfunctions, etc.).

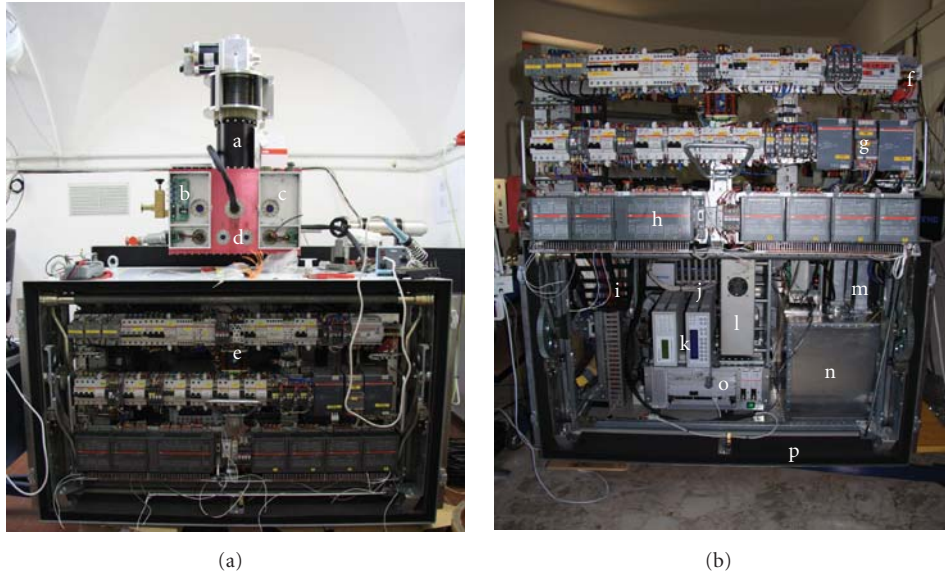


FIGURE 2: AMICA and the main thermal-conditioned box containing most of its equipment: (a) cryocooler head, (b) and (c) front-end electronics, (d) cryostat, (e) removable electrical panel (open on the right), (f) multimeter, (g) 24 V redundant power supply, (h) PLC with analog and digital I/O expansions, (i) turbo-molecular vacuum pump, gauges and electromagnetic valve, (j) Ethernet switch and MOXA converters, (k) Lakeshore controllers, (l) read-out electronics, (m) heat dissipation system, (n) rotary pump, (o) LCU, (p) insulating plastazote layer and alucor panels.

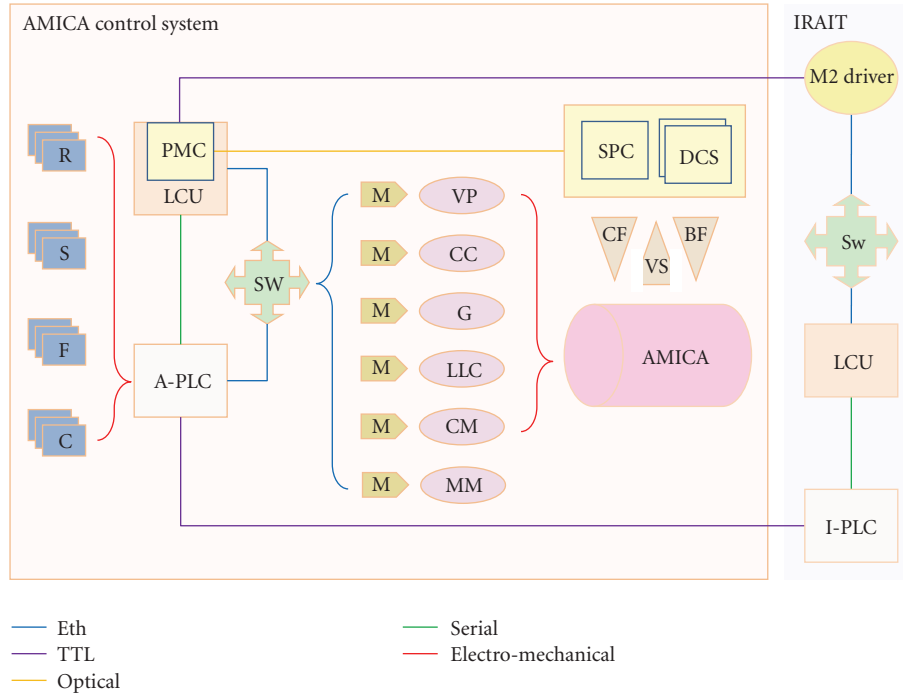


FIGURE 3: Hardware layout and data connections of the AMICA control system. The A-PLC manages resistors, sensors, fans, and contactors (R, S, F, C) for the local environment control. A mutual heartbeat monitoring with the telescope PLC (I-PLC) is ensured by TTL lines. Auxiliary devices (vacuum pump, cryocooler, gauges, temperature controllers, cryomotors and multimeters-VP, CC, LC, CM, MM) are accessed by the LCU through serial/Ethernet MOXA converters. Clock and bias filters and video signal amplifiers (CF, BF, VS) are directly connected to the read-out electronics (SPC and DCS boards). This is linked (by the optical fiber) with the LCU in which a PMC board drives the M2 wobbling system through TTL lines. All the local control units and the Ethernet devices belong to the same LAN, extended by switches (Sw), and remotely connected to the base through cables and a redundant WiFi point-to-point link.

The ACSW architecture (Figure 4) descends directly from the underlying modular hardware, with the aim to reduce the complexity level and to better identify all tasks that have to be assigned to each single- or multithread process. This distribution has led to the development of a multiprocess system that allows to reduce the possibility of critical failures that could compromise the operation of all software modules (ACS, ECS, DCS, SCS, and AAA, described below). Each subsystem is then controlled by one or more processes, which communicate through TCP/IP sockets, pipes, or files.

The entry-point for the telescope scheduler is the Activity Control System (ACS), a server application that retrieves through a TCP/IP connection the required parameters to perform scheduled observations. It creates and dispatches macrocommands to the cooperative agents, managing and monitoring their activities and restarting them in case of unexpected hangs. Both telemetries and scientific data are periodically stored in a remote server inside the Concordia base, hosting a relational (MySQL) database and the image archive. Then, all data are preserved until they are shipped to European partners.

A real-time active control of the environment inside the insulated cabinets and the maintenance of the correct cryogenic conditions inside the cryostat are provided by the ECS. Since it operates cooperatively with the PLC (driving its activity), it can monitor the thermal, electrical, and operational status of all the components of the AMICA hardware equipment. Moreover, camera auxiliary devices like heaters (for detectors thermal stability), temperature probes, cryomotors, the vacuum system, and the cryocooler are indirectly managed by the ECS through their controllers (each of them being connected to the LAN by means of Serial/Eth MOXA converters). During the operation, the ECS collects all telemetry data and notices the ACS about the status of the system, giving the green light to the observations or asking to wait for the achievement of suitable operating conditions. Each dangerous event is therefore signaled to the ACS and in case of high safety risks, the ECS automatically takes the control of the system.

If it is not possible to recover its status, all unnecessary operations are stopped, turning off the corresponding devices and leading the environmental control to the PLC.

The configuration of the observing modes is operated by the Chopper Control System (CCS) that communicates with the IRAIT M2 subsystem through the LAN. It controls and verifies the correct position of M2 during acquisition (correcting for possible offsets) and supports the automated focusing procedures. It also monitors the subsystem activity gathering information on its thermal status and logging the ongoing operations.

The acquisitions are managed by the Detector Control System (DCS). It verifies the correct setting of the parameters (bias, clocks, T_{exp} , N_{img} , etc.), interfacing the read-out electronics through a further application (SCS) dedicated to the accumulation of the incoming raw frames (storing coadded and sky-subtracted images in a real-time process and filtering bad frames acquired during the motion of M2). In addition, raw data could be also saved for an offline analysis of the M2 driver operation. Moreover, the

DCS performs their descrambling, generating final FITS files, while a first preprocessing of the resulting images is initially obtained using the package SExtractor. It is used to estimate centroids, ellipticities, and FWHMs of sources detected over the field and to obtain a preliminary pixels statistics, thus allowing the optimization of the observing parameters and of the focus quality, and the detection of bad images.

Finally, a remote Java web application (AMICA Activity Analyzer) is under development. Running on the control room workstation inside the base, it will provide statistics based on stored telemetry data for each component of the system, ensuring a full remote access to the instrumentation for local operators.

4. Aspects of the AMICA Control System

Generally, different levels of robotization can be distinguished for a system, depending on the capability to perform unattended operations, to resume its status after unexpected errors and to make use of some sort of intelligence to optimally operate for long-lasting periods (without human interaction). When all these properties coexist in such a system, it is usually referred to as “fully autonomous”.

On the basis of these considerations, and taking into account the Antarctic conditions, a robotic observatory as that formed by IRAIT and AMICA must necessarily be fully autonomous. Although the requirements on scheduler flexibility are less severe, thanks to the near-Pole condition and the possibility to observe throughout the year with a daily duty-cycle of 100% for wavelengths beyond $4\mu\text{m}$ (Section 2.2), further issues have to be addressed for an “Antarctic” system.

4.1. Reliability and Test Activity. The robustness and reliability of the AMICA instrumentation have been the first point to be considered during its design. After a careful analysis of the environment properties and the possible risks that could arise from such a climate, a great attention has been paid to the choice of suitable devices available from the industrial automation market. In fact, the development of custom Antarctic-proof instrumentation would have had otherwise so strict requirements (more similar to those used in space engineering) that the total cost of the project would not been sustainable, thus losing all the advantages that had motivated the project itself. For this reason, all components have been selected in order to ensure the maximum resistance to the Antarctic conditions in terms of vibrations and shocks resistance, operating and storage ranges for temperature, pressure and humidity values. In addition, several thermal studies have been carried out about the materials and the thickness of the boxes insulating layer to minimize changes of their internal temperature. Has a thermal configuration that will maintain about $+20^{\circ}\text{C}$ inside the cabinets with an external temperature of -60°C (winter average temperature), and with an average thermal input given by the dissipated heat from the operating electronics of about 750 W been considered suitable. Thanks to this

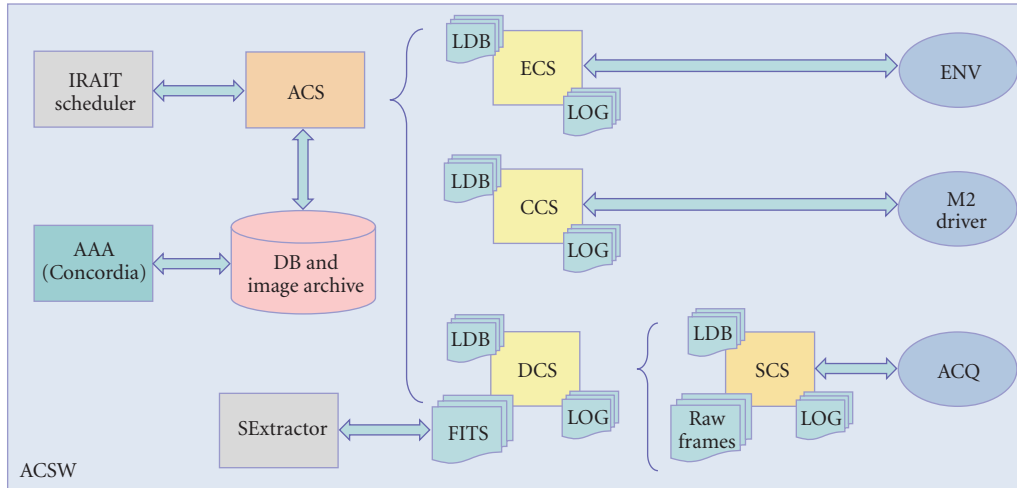


FIGURE 4: A deployment diagram showing the relationships among software and hardware modules in the run-time system. The ACS communicates with the IRAIT scheduler and manages four software modules (ECS, CCS, DCS, SCS) interfacing the hardware subsystems. A telemetry database and an image archive are maintained at the Concordia base, where a further application (AAA) monitors the whole system.

insulation, a low-level thermal control is able to maintain with a low-power consumption, the internal temperature of the boxes between the storing range of values of the critical components (~ 0 – 50°). This estimation has been confirmed performing realistic simulations on the behavior of insulated, warmed boxes, through a climatic chamber built at INAF-Teramo (ANTARES-Antarctic Environment Simulator). It allows to reproduce climate conditions worse than those occurring at Dome C ($T_{\min} = -93.4^\circ\text{C}$, $P \sim 600$ mbar, $RH \sim 5\%$) in a $\sim 200\ell$ volume. Thanks to these simulations, several effects have been studied as for example the wind chill effect induced by fans activation, the bias voltages drift with temperature, the failure of Buna O-ring vacuum seals below -43°C , and so forth.

Constraints on the total available space and instrumentation accessibility have led to the design of a very compact, complete, and modular system, paying attention to the logistic facilities (e.g. total power consumption, mounting and dismounting procedures).

Moreover, redundancy of critical components has been applied when possible, in particular for power supplies and electrical and data connections (TTLs, Ethernet, etc.), to continue operating even in case of damaging of any system element.

Despite the great attention that has been paid to the achievement of a highly reliable system, experiences in past Antarctic campaigns have highlighted the importance to provide each instrumentation with spares of sensible components. For this reason most of the elements constituting the AMICA equipment have been duplicated.

Multiple levels of control will ensure the instrumentation safety. Hardware devices and software systems will cooperate to achieve and maintain suitable conditions inside the AMICA conditioned boxes. In addition, all activities will be further monitored both through the LAN and

the mutual exchange of “heartbeat” signals among programmable devices (i.e., LCUs and PLCs) belonging to the camera and the telescope subsystems.

Finally, several long tests on the control software have been performed, with the aim to prevent Single Points of Failure (SPOF), thus allowing the recovery of possible malfunctions and successfully executing all system tasks (acquisition and chopping management, image preprocessing, data storing, environment conditioning, remote monitoring, etc.).

4.2. Future Work. The development of the whole control system is at its final stage. All hardware subsystems have been separately tested, while the preliminary release of the control software allows to automatically execute (simulated) scheduled observations. Next steps will consist of the integration of the ECS module and the verification of the reliability of the thermal control, cooling the insulated boxes down to Antarctic temperatures.

Improvements in the DCS are required for the accomplishment of the preprocessing pipeline, while further issues will be addressed to optimize the interaction between IRAIT and AMICA. Finally, the Activity Analyzer will be endowed with graphs and diagrams showing real-time information on the system activity and providing statistics that will be used to detect deviations from the expected behavior and to prevent malfunctions.

5. Conclusions

The excellent atmospheric properties of Dome C for infrared astronomy allow to achieve better observing performances than any observing temperate site. Despite these exceptional

advantages, several difficulties arise from its extreme environment. The AMICA project takes up the great challenge of the development of a highly reliable Antarctic instrumentation. For this reason, suitable and innovative solutions provide the necessary conditions to its robotization. After the conclusion of the integration stage and further test activities, the camera and its equipment will be shipped to Dome C for the accomplishment of the fully autonomous observatory.

References

- [1] G. Tosti, G. Nucciarelli, M. Bagaglia, et al., “The International Robotic Antarctic Infrared Telescope (IRAIT),” in *Ground-based and Airborne Telescopes*, vol. 6267 of *Proceedings of SPIE*, Orlando, Fla, USA, May 2006, 62671H.
- [2] O. Straniero, M. Dolci, A. Valentin, et al., “AMICA: the first camera for near- and mid-infrared astronomical imaging at Dome C,” *EAS Publications Series*, vol. 25, pp. 215–220, 2007.
- [3] J. S. Lawrence, “Infrared and submillimeter atmospheric characteristics of high Antarctic Plateau sites,” *The Publications of the Astronomical Society of the Pacific*, vol. 116, no. 819, pp. 482–492, 2004.
- [4] V. P. Walden, M. S. Town, B. Halter, and J. W. V. Storey, “First measurements of the infrared sky brightness at Dome C, Antarctica,” *The Publications of the Astronomical Society of the Pacific*, vol. 117, no. 829, pp. 300–308, 2005.
- [5] M. G. Burton, J. S. Lawrence, M. C. B. Ashley, et al., “Science programs for a 2-m class telescope at Dome C, Antarctica: PILOT, the pathfinder for an International Large optical telescope,” *Publications of the Astronomical Society of Australia*, vol. 22, no. 3, pp. 199–235, 2005.
- [6] R. Briguglio, G. Tosti, M. Busso, et al., “Small IRAIT: telescope operations during the polar night,” in *Observatory Operations: Strategies, Processes, and Systems*, vol. 7016 of *Proceedings of SPIE*, p. 12, Marseille, France, June 2008.
- [7] F. Bortoletto, D. Magrin, and C. Bonoli, “Control system for the AMICA infrared camera,” in *Ground-based and Airborne Instrumentation for Astronomy I*, vol. 7014 of *Proceedings of SPIE*, p. 10, Marseille, France, June 2008.

Research Article

The NMSU 1 m Telescope at Apache Point Observatory

Jon A. Holtzman, Thomas E. Harrison, and Jeffrey L. Coughlin

Department of Astronomy, MSC 4500, New Mexico State University, P.O. Box 30001, Las Cruces, NM 88003, USA

Correspondence should be addressed to Jon A. Holtzman, holtz@nmsu.edu

Received 15 June 2009; Accepted 12 January 2010

Academic Editor: Alberto J. Castro-Tirado

Copyright © 2010 Jon A. Holtzman et al. This is an open access article distributed under the Creative Commons Attribution License, which permits unrestricted use, distribution, and reproduction in any medium, provided the original work is properly cited.

We describe the New Mexico State University (NMSU) 1 m telescope located at the Apache Point Observatory (APO), and in particular, its robotic mode of operation. Some of the issues we have encountered may be of interest to others developing similar facilities. This telescope provides a good example of the possibilities of locating a moderate-sized university robotic research telescope at a major observatory. We find that this mode of operation provides a significant amount of productive science data on a relatively small budget.

1. Introduction

Many universities and colleges operate, or have an interest in operating, small to medium aperture telescopes with a primary goal of using them for research. In contrast with a primarily educational goal, it is preferred that research telescopes be located at a site with dark skies and good seeing. Since such sites are often not available at a campus location, telescopes often need to be situated at more remote locations. However, this can make them more difficult to be used on a nightly basis, given travel requirements. It can also be a challenge for small departments to supply observers on a nightly basis, especially if there is little or no budget to pay for observers and/or travel.

New Mexico State University operates a one-meter (1 m) telescope at the Apache Point Observatory in southern New Mexico; the site is shown in Figure 1, and the telescope in Figure 2. To fully utilize the telescope, that is, obtain data on essentially all clear nights, a robotic mode of operation was developed. In this paper, we describe our system and discuss how the robotic mode is implemented. While our system does not include anything especially complex, it did take a significant amount of time to work through all of the associated computer and hardware issues, and we hope that outlining these here will be useful to others who are considering implementation of a robotic telescope, to alert them to various issues and possible solutions.

The NMSU/APO 1 m may be different from other telescopes operated by small departments in remote locations as it is located at a major observatory. The benefits of having a robotic telescope at an established observatory location are significant, as we will discuss below, and we suggest that this is a productive setup to consider for small telescopes, as there can be benefits for both the operator of the small telescope and the observatory.

2. Hardware

2.1. Telescope. The telescope is a 1-meter-diameter, alt-az telescope, situated in a small, elevated dome. It was constructed in the early 1990s; the telescope design and construction was provided by the Autoscope Corporation. The optical design is a Ritchey-Chretien, with a system focal ratio of F/6 and a F/2.5 primary mirror. The primary mirror is supported laterally through the central hole and from behind on a nine-point static support system. The secondary mirror has three motorized actuators that allow piston and tilt motions. The telescope originally implemented a single Nasmyth focus, but a new rotating tertiary mount was recently purchased from Astronomical Consultants and Equipment (ACE) to allow instrumentation at both Nasmyth foci; tertiary rotation is motorized and computer controlled. Currently, an instrument derotator is only available at one of the Nasmyth ports.



FIGURE 1: The NMSU 1 m dome at Apache Point Observatory in New Mexico. The larger enclosure in the background is the ARC 3.5 m telescope.

2.2. Instruments. The primary instrument is a direct imaging camera at the primary Nasmyth focus. The current camera uses a 2048×2048 thinned, backside-illuminated E2V CCD, made available through a collaboration with the Los Alamos National Lab; the 13.5 micron pixels subtend ~ 0.46 arcseconds on a side, providing a 15.7-arcminute field-of-view. The chip is located in an IR labs LN2 dewar, and was installed by Astronomical Research Cameras (ARC), who also provided a shutter and the CCD control hardware. The dewar has a hold time of at least 12 hours in its sideways orientation. The location on the Nasmyth port allows a vacuum-jacketed hose to be permanently connected to a 50-liter LN2 dewar that is located below the telescope; there is a commandable cryogenic valve installed in the line.

A filter wheel system, built by ACE, is located in front of the shutter, and holds either 10 2-inch square filters or 6 3-inch square filters, depending on what filter wheel is installed. A guider module was also constructed by ACE that has a dual-stage arrangement to allow for a pickoff mirror to be moved radially in the field, along with an independent focus motion for the guide camera. The guide camera itself was purchased from Finger Lakes Instruments (FLI), and uses a 1024×1024 thinned, backside-illuminated E2V CCD in a thermoelectrically cooled camera.

Several years ago, funding was obtained from the National Science Foundation via their PREST program, primarily to enable the use of the second Nasmyth port and to construct a new instrument for it. This is a simultaneous 6-color single-object photometer, which uses a series of dichroics with a combination of avalanche photo-diodes and photomultiplier tubes to provide high speed, photon-counting photometry simultaneously in the UBVRIJ passbands; only a single target can be observed at a given time through a physical aperture of size ~ 15 arcseconds. This instrument is presently being commissioned.

2.3. Building and Dome. The dome is a ~ 15 -foot-diameter dome made by Ash Domes. As purchased, it featured motorized dome rotation and motorized control of the upper



FIGURE 2: The NMSU 1 m alt-az telescope. The Nasmyth port with the CCD camera being on the left.

dome slit. We modified the system to allow for motorized control of the lower dome slit as well, and the original Auto-scope observatory control hardware implemented computer control of the dome motors.

The building has louvers to improve ventilation that are hydraulically opened and can be controlled by applying or removing power.

To facilitate remote/robotic operation, most of the telescope systems are powered through an Ethernet-connected power strip, which allows power to be turned off and on via either HTTP or SNMP Internet control. In addition, three USB web cameras are situated in the dome to allow some degree of external monitoring. Four thermal probes are situated in the dome and are attached to web-accessible controllers.

2.4. Telescope and Camera Control. The telescope pointing system, secondary actuators, dome control, filter wheel, and guider stage locations are controlled by a single x86 computer located in a rack inside the dome. Motor control and position sensing are implemented through several Oregon Micro Systems motor control cards and a separate dome encoder card. The azimuth and altitude axes are controlled by motors, but also have separate encoders; the derotator axis only has motor positioning. All three axes have magnetic home sensors. The filter wheel and guider stages are operated with stepper motors. Dome rotation and slit operation are controlled via relays; the slit has built-in limit switches to kill power when it reaches the fully open and closed positions.

The science camera control is handled by a Linux computer in the main APO computer room; communication with the camera is achieved through a fiber optic connection. The guide camera is controlled by the same computer; since it uses a native USB connector, a fiber-USB converter kit was obtained to allow it to be controlled from the remotely

located computer. This interface is also used to control the webcams.

2.5. Performance. The telescope performance is adequate but not outstanding. With a pointing model implemented, we have achieved about 20-arcsecond rms pointing, but in practice, the pointing tends to be worse than this. The pointing performance is affected by imperfections in the drive surfaces, occasionally slippage of the motors, and temperature variations. Tracking is adequate for short exposures, but noticeable degradation is often seen in exposures of more than a few minutes, so guiding is generally required.

The image quality has been disappointing. While we have seen images with 1.2 arcseconds FWHM, typical images are between 1.75 and 2.5 arcseconds. The cause for this has been difficult to track down, but is likely due to a combination of dome seeing, imperfect alignment of the optics and placement of the focal plane, and tracking issues. We hope to understand and improve these issues at some point, but we have mostly concentrated our efforts on science programs for which the current performance is adequate to meet the scientific goals. This has been an important criterion for the choice of scientific programs to be executed; we choose ones that are appropriate for the telescope performance and the robotic mode of operation.

2.6. Maintenance and Support. We generally do not schedule any dedicated maintenance time on the telescope. In practice, we attempt to do visual checks and minor maintenance whenever we happen to be visiting the site for commissioning new capabilities at the telescope, resolving problems, or observing with another telescope. Large maintenance items, such as aluminization of the mirrors, are scheduled in coordination with the APO site staff, and we draw on their considerable expertise for the removal of the primary mirror and the recoating, which has been done at the nearby National Solar Observatory. Due to the time and support required, primary mirror aluminization has only been done a few times, with 5–10 years between aluminizations. Several years ago, we realuminized the secondary and the tertiary and had them overcoated with an Al/SiO₂ coating by Optical Surface Technologies to minimize the need for realuminization of these mirrors.

Of course, various hardware and software issues have arisen in the course of long-term operation, from system failures, aging of components, or the development of some previously unseen condition. The location of the telescope at APO greatly facilitates relatively rapid resolution of simple problems. Several site personnel have accumulated significant knowledge about the operation of the telescope systems and can often provide quick solutions to our problems, or at the very least, knowledgeable eyes that can report conditions and issues with the telescope. If significant issues develop, we generally send personnel from NMSU to attempt to resolve them.

Another key support item provided by APO is that they arrange for a regular supply of LN₂ to the site. As part of our support agreement, our large LN₂ dewar below this telescope is regularly checked, and replaced when needed (roughly

every two weeks). The availability of LN₂ allows us to operate our science detector without significant dark current.

Locating the telescope at APO also provides greater security for the telescope, as there are personnel on site 24 hours a day, 365 days a year.

Another advantage of the location at a major observatory site is that APO has a backup generator in case of a utility power outage, with automatic switchover occurring within a few seconds. Thus, even if the utility power fails, there is still power to continue the operation, or to close the dome if conditions require it. Within the 1 m dome, we also have systems on a UPS to avoid issues with short power glitches.

We contribute a small share of the total observatory budget to account for the floor space we use, electricity, access to facilities, and general site operations. Between this base contribution and typical cost-reimbursable site assistance, we generally spend about \$15 K/year on the telescope. Any costs associated with failed or aging hardware are in addition to this. Still, we feel that this is a very economical way to operate a 1 m telescope.

We note that there are benefits to the observatory. Albeit small, any contribution to the overall budget helps. Scientifically, several coordinated programs have been carried out between the 1 m and the 3.5 m, enhancing the productivity of each. The 1 m also provides a capability for photometric calibration of observations taken with the 3.5 m under nonphotometric conditions.

3. Software

The telescope control software is written in C++ and runs on a DOS platform. It was initially developed by Autoscope but has undergone substantial subsequent modification. The telescope control software handles low-level communication with the hardware. Software was obtained for this computer to allow Ethernet connectivity via TCP/IP, which provides a means to send commands from other computers on the network and to update the software remotely. Software updates can be achieved without any action on site by rebooting the computer via the remote power control; after loading the network drivers, the startup file on the DOS computer transfers a copy of the telescope control program from a disk on a Linux machine via TFTP, and then runs it, so software updates are accomplished simply by copying a file to the Linux command machine. This is very useful for adding minor features to the telescope control software without having to go to the site.

The science and guide cameras, as well as the web cameras, are controlled by a Linux computer using internally developed C software, with device drivers and software libraries provided by the camera manufacturers, or as part of the kernel for the webcams. The camera software receives updates from the telescope, so telescope information is placed in image headers. The computer is also synchronized with an Internet time source, so that the time when the shutter is opened is put in the header with an accuracy of better than a second.

The science camera software includes a temperature monitor that triggers an associated autofill system. When the CCD temperature rises above some preset value, a command is sent to open the cryogenic valve to the large LN₂ dewar for a preset amount of time. If this happens while observing is in progress, the telescope is appropriately stopped and restarted, however, the normal mode for robotic operation is to automatically do a fill shortly before sunset, since the hold time of the dewar is sufficient to make it through a full night without refilling.

The set point of the guide camera is automatically modified throughout the night based on an ambient temperature reading, since the thermoelectric coolers can only reach some fixed temperature differential from the ambient. This is not much of an issue for the guide camera, but we note it because it was very useful for our old science camera that was thermoelectrically cooled; this feature allowed us to operate at one of a few preset possible temperatures (depending on the ambient), rather than always running at maximum cooling, which would result in temperature drifts. Thus, we were able to construct libraries of dark frames at the few allowed operating temperatures.

The high-level control of the telescope and instruments and the robotic operation are handled by a Linux computer located in the main APO operations building. In principle, this computer could be located anywhere, but we locate it at APO to keep it behind the site firewall to limit access to the telescope. The basic software is relatively simple: there is a master control program that accepts text commands either from the keyboard or from a pipe on the control computer. The control program relays the command to programs running on the telescope computer or the instrument computer, depending on the command, which execute the command and return a success status. Once status has been returned, the next command is processed.

While no specific telescope/instrument commanding protocol was used for the telescope and camera software, it would be trivial to implement a standard command set if desired.

The robotic operation is enabled by sending commands over a pipe on the command computer. Any scripting software can be used to generate such commands. We have implemented our robotic control using the image processing package XVISTA, which has many built-in astronomical image processing routines, internal variables, and flow control, along with the capability to construct basic command procedures for stringing together multiple tasks.

The entire suite of control programs is run on a virtual desktop on the command computer. This allows checking on the progress of observations from any remote location that has the capability to view remote virtual desktops over the Internet.

4. Robotic Operation

The telescope is operated robotically more than 95% of the time, with the nonrobotic time being used for engineering. The robotic mode requires a person only to implement an observing list with observing priorities, as described below,

and to start the system at some point during the day. For safety precautions, we usually attempt to look at the system remotely by webcam during initialization, and again in the morning to insure proper dome closure and stowing of the telescope, but this monitoring is not required by the robotic system.

4.1. Weather Conditions and Enclosure Control. A critical issue for a robotic telescope is weather monitoring and associated protection of the telescope. The location of a telescope at a major observatory site facilitates this enormously. We cooperated with the observatory to install a mechanical sensor on the shutter of the ARC 3.5 m telescope that is located at APO, and the status of this sensor is broadcast over the local network once per minute. The software on the telescope computer continually listens for these broadcasts, and if it receives a “3.5 m dome closed” broadcast, or if it fails to receive a “3.5 m dome open” broadcast (indicating that something in the system/network is broken), then the dome shutter is automatically commanded to close and the telescope is stowed.

This is a simple system that takes advantage of the presence of the 3.5 m observing specialists on site, who have experience in judging weather conditions, without requiring any specific action of them. Of course, this system means that if the 3.5 m closes for any reason other than weather, the 1 m will also close, but this is a relatively rare occurrence and a small price to pay for simple protection of the telescope. For extended shutdowns, we also have the capability to switch over to monitoring the status of the SDSS 2.5 m telescope.

Of course, the potential for failure lies with the dome hardware itself; if the dome fails to close when commanded, there is the potential for exposure to weather. In fact, we have had issues with the failure of the dome slit system, so this can be a real issue. Within the past year, we have rewired the system, and it now works much more reliably (actually, it has not yet failed). At this time, a sensor on the 1 m dome slit has not been installed. While this would probably be a good idea, it is not totally trivial because of the dome rotation and the lack of available slip ring connections. We do ask the observatory staff to do a visual check if possible and notify us if anything unusual is seen, such as an open dome when other domes are closed. If all else fails, it is straightforward for site staff to close the dome manually. We also typically take a quick look at a webcam image each morning which quickly shows whether the dome is closed via the amount of light present. However, we stress that no actions by people are actually required by the robotic system, they are just implemented as basic safety precautions.

To avoid issues if the telescope computer fails or crashes, the hardware is wired with a watchdog circuit so that if the software does not regularly reset it, the dome will automatically close.

Aside from potential damage to the telescope from weather exposure, our biggest fear is a dome slit failure leading to direct sunlight shining on the mirror and associated fire/burning potential. To provide some extra insurance against this possibility, the telescope is routinely parked pointing to the NW, and the dome parked pointing to the N,

so that the dome slit is not lined up with the primary mirror and both the dome and the telescope point in a direction where the sun will never be seen.

4.2. Startup. For normal operation, the observing software can be started at any time. The telescope and dome are initialized by moving them to home sensors for which the position has been determined. Although not required, we usually do this task with remote personnel monitoring the web cameras to insure that things are operating normally. The system robotically commands a fill of LN2 camera dewar shortly before sunset to insure that the automatic filling of the dewar, as triggered by the temperature monitor, does not occur in the middle of the night.

After the initializations, the telescope simply waits until sunset and a notification that the 3.5 m telescope is open. At this point, the 1 m dome slit is automatically opened. The dome louvers are also opened and a fan is started to facilitate dome ventilation.

4.3. Instrument Calibration. Once the telescope is opened, the local time is checked and compared to local sunset and twilight. If the dome has been opened sufficiently before twilight, it is automatically pointed to the east, and a series of twilight sky flat-field exposures through all of the filters is initiated. The twilight flats start with the lowest throughput filters and successively proceed to flats in filters with higher transmission. The camera software takes a flat field, analyzes the brightness level, and commands a subsequent exposure with an exposure time that will provide high signal-to-noise data, accounting for a fading of the twilight sky brightness with time. It continues taking these until a requested number of good flats are obtained, after which it proceeds to the next filter. If the sky is too bright for any exposure with $t \geq 1$ s to succeed, it waits a minute and tries again. No exposure longer than 30 s is allowed, and no more than 3 such exposures are allowed, so that the entire twilight is not used up in observations of one filter. The telescope is automatically dithered by 30 arcseconds between exposures to aid in the removal of any stars that might appear.

This system works very well, and if the telescope is opened shortly after sunset, we routinely are able to get three high S/N flat fields in all of our ten filters in a single twilight.

4.4. Telescope Pointing and Focus. Once it is sufficiently dark, the telescope pointing and focus are adjusted. For pointing, a catalog of bright stars is consulted, and the telescope is commanded to one at a reasonable azimuth and altitude. A short image is taken, the brightest object is located, the telescope is offset to center the object, and the telescope position is subsequently adjusted to match the expected position of the star. To aid in automatic data reduction, we like to have the actual pointing match the commanded pointing as closely as possible, so we generally repeat this quick pointing correction before the exposure sequence of every new object we observe during the night, since it takes less than a minute.

Focus is probably the most challenging aspect of our robotic observing. To achieve this, we find an intermediate

brightness star ($V \sim 11$) from the USNO-A2.0 catalog and slew to it. The ambient temperature is checked and an estimated focus is determined from a temperature-focus relation that we have accumulated over time. A coarse focus run is commanded, and the master commanding software reads in the images.

A variety of image quality statistics, including the FWHM of the image, are computed for the stars in the images. After substantial experimentation, the statistic that seems to yield the best focus reliably is to compute the ratio of the peak pixel value to the integrated flux in a synthetic aperture around a star, and to associate the best focus with the image that has the maximum value of this ratio. The FWHM can be misleading because hot spots in significantly out-of-focus images can return small FWHM. The ratio of peak-to-total is also robust against changes in transparency during the focus run.

To insure against fluctuations in seeing, we use a minimum exposure time of several seconds, and thus the motivation for avoiding very bright stars. Once the best image has been found, we repeat the sequence using a finer focus run. If the best focus is found on either end of the focus run, we repeat another focus run shifting the range by half the width of the previous run. This generally leads to a reasonable focus value within a few iterations. While we have experimented with fitting a parabola to the derived FWHM values and determining the focus value of the minimum, we have found that it is more robust to just do a relatively fine focus run and adopt the focus value of the best image, as this avoids issues with the parabolic fit being corrupted by one or more bad images or measurements.

Unfortunately, we have found that substantial focus drift occurs with our telescope, especially within the first several hours of the night as the telescope is cooling to the ambient temperature (our dome often gets quite warm during the day). As a result, we generally redo a focus run before every object, since it is usually accomplished in less than 5 minutes (and often less than 2 minutes); if we are near focus, often only a single fine focus run leads to a new focus setting. For objects that are observed for a long period of time, we have developed an autofocus routine that can be run during exposure sequences; this is described below.

4.5. Observing Program. The basic scripting for robotic operations is simple, yet surprisingly flexible. A list of priority-sorted objects is constructed for a list of priority-sorted programs. When the telescope is ready to observe an object, it simply starts at the top of the list and chooses the first acceptable object. The flexibility comes into play when determining which objects are acceptable. The input files allow constraints on acceptable UT time and date (for time critical observations), airmass range, starting hour angle (to avoid starting objects as they are sinking into the west), and moon phase/distance. If an object meets all of the constraints, the desired observing sequence is performed. The observing sequence is defined by the number of cycles to perform a desired number of exposures of a specified exposure time per filter. An option also allows for a sequence of increasing exposure times per filter if a larger dynamic

range is required. A parameter specifies whether an initial pointing adjustment and/or focus run should be done before the observing sequence starts. Another parameter specifies whether guiding is desired.

Once an object has been selected, pointing and focus corrections and guide star acquisition are done if requested. After this setup, the observing sequence is run to completion, the object is marked as having been observed, and the next object to observe is found by starting at the top of the list again. A given object can be reobserved by specifying a maximum number of times to be observed (along with a minimum amount of time between observations), or by a flag requesting continuous observations so long as the observing constraints are met. Generally, most objects fall in the class of either requiring a single observation or requiring perpetual observations, although we occasionally have objects which are observed at some particular cadence, that is, once every several hours.

To keep exposures from extending outside the observability windows, and to provide the maximum likelihood that high priority objects will be observed as soon as they are observable, the general strategy is to try to keep the observing sequences as short as feasible, but allow for objects to be repeated, as this allows the list to be checked frequently. Selecting an object from the list only takes between a few seconds and a minute, so not much time is lost by doing this on a cadence of half an hour or so. If the same object is reselected for observing, the script proceeds straight to the observing sequence, without any pointing check, focus, or guide star reacquisition; guiding is continued while checking the list, and not stopped until the telescope is commanded to slew to a new target.

We have found that this scheme covers a large fraction of desired observations. For some special cases, some additional complexity is required, and we have developed several special modes, for example, for elevating the priority of a series of observing sequences if certain conditions are met. For example, one mode triggers a series of dithered exposures of a target once it becomes observable. Another mode switches the science camera into a subframe readout, which allows for a higher cadence of observations.

As previously noted, if the telescope computer determines that the 3.5 m dome is closed, it automatically closes the dome and stows the telescope, independently of any commanding software. The command software checks the telescope status after every exposure, and if it sees that the telescope has been closed, it immediately exits the observing sequence and restarts the initial loop of waiting for the 3.5 m to report open. If the telescope is subsequently reopened, the observing sequence proceeds as before, starting again at the top of the observing list to check for the highest priority object, since the previously observed object may no longer be available.

4.6. Focus Monitoring. As previously noted, the telescope experiences significant focus changes, especially in the first few hours of the night. While focus can be tracked using focus runs done before each new object, if the desired target is to be followed for a long time, then focus runs will

not occur. While it is possible to force focus runs after a desired time interval, some monitoring programs prefer a continuous stream of data without interruptions.

To accommodate this, we developed a method for performing focus tracking without interruption of science observations by using our guide camera. To do so, the guider determines image quality as well as image position for each guider image, which are generally taken every few seconds. To account for seeing variations, a series of measurements is averaged over a period of several minutes; this is an adjustable parameter. After the baseline is established, the internal focus on the guider is moved by a small amount. To avoid any image degradation because of the possibility that a focus change will move the star slightly, the guider focus is only allowed to move between science exposures. Another series of exposures is taken, and if the average image quality is better, then the telescope focus is adjusted by the amount corresponding to the guider focus offset (again, only between exposures), and the latest guide series is adopted as the baseline series. The guider offset is maintained so that if further moves in the same direction are required, they will be made after the next series. If a guider series is worse than the baseline series, then the guider offset is returned to nominal and a new baseline series is made to keep track of potential seeing changes, after which a guider offset is made in the opposite direction. The whole procedure continues, keeping the same sign of guider test offsets as long as image quality is improving, and reversing the sign of the test offsets if a previous test offset made things worse.

The procedure does a reasonable job of tracking focus changes. Of course, a key assumption is that the guider focus tracks the focus in the science camera. This is an issue for an offset guider on an alt-az telescope, because the guider is moving in the focal plane as the telescope tracks in image rotation. Thus, if the rotator change is large over the time span of a long image sequence, incorrect adjustment of focus can occur if the system is not well aligned, that is, if the guide focus changes with the rotator position.

4.7. End of the Night. After each exposure, the time is checked, and if morning twilight has arrived, science exposures are stopped and the telescope is slewed to the west for a morning sequence of flat-field exposures, done in reverse order from the evening sequence. After these have been completed, the telescope and dome are stowed, and the dome slit and louvers are closed.

As previously noted, shutdown is automatically forced immediately at any time during the night when the 3.5 m telescope is not reporting an open condition. Twilight is not an exception, so occasionally the flat fields sequence is interrupted if the 3.5 m closes early, but this is a small price to pay for the overall safety that the system normally insures; we could turn off the 3.5 m slaving during flats, but we prefer to be conservative.

4.8. Photometric Calibration. Certain science programs require absolute photometric calibration, which can be achieved by observations of photometric standard stars, but only on totally clear nights. We have not implemented

a method to automatically determine if a night is photometric, but instead we manually set a flag if the weather forecast appears to predict a good chance of a photometric night, and elevate the priority of the photometric programs accordingly.

If the photometric flag is set, then the system automatically intersperses observations of standard stars with the science program observations. This is done by setting a minimum time interval between observations of standard stars for stars at low and high airmass. We have compiled a list of fields, spread around the sky, with photometric standards, choosing fields with multiple standard stars where possible. After opening and performing initial pointing and focus, a specified number of fields are observed at low (1–1.3) airmasses and high (1.55–2) airmasses; we usually observe two fields at each. Science exposures then proceed as normal, but after each science exposure sequence has completed, the script determines whether the minimum amount of time between observations of standards has elapsed. If so, then another set of standards is observed. We generally set things to observe a pair of low airmass fields every hour or so (the minimum is set to one hour, but a science exposure sequence must be completed before the time is checked) and a pair of high airmass fields every two to three hours. With multiple standards per field, this provides a large number of standard star observations per photometric night.

4.9. Targets of Opportunity. We have developed software to allow for relatively quick response to the target of opportunity observations, in particular to respond to gamma-ray burst alerts from the GCN. To accomplish this, we run a separate program on the telescope command computer which listens to GCN alerts via socket communications. If an alert is received, the position is parsed, an ALERT command is sent to the command program, a flag is set to indicate that an alert was received, and a line is automatically added to an alert target file with the new object for subsequent high-priority normal observing after the ALERT sequence (discussed next) is completed.

The alert flag is continually checked both between exposures and during the photon collection process, and if the flag gets set during an exposure, the exposure is immediately interrupted and control returned to the command program. At this point, ALERT commands have priority over all others. The ALERT command slews the telescope to the desired location and immediately starts a preprogrammed observing sequence. To minimize the slew time, the rotator is not slewed to the default north-up position, so the image orientation will be not standard (but is recorded in the image headers). Our default sequence consists of five sets of short exposures (10, 10, 20, 40, 60 s) through each of IRVBU filters, followed by five sets of exposures twice as long, for a total of about one hour of observing. These exposure times were chosen in an attempt to provide broadband spectral information for relatively bright bursts.

After the ALERT sequence is completed, the telescope returns to its normal mode of operation, but usually we make the file with alert targets the highest priority, so that the preprogrammed ALERT sequence is followed by a set of longer exposures as specified in the alert target file. The

virtue of shifting to the normal target file is that this does a normal image acquisition, including acquiring a guide star. The ALERT sequence exposures are done without guiding, in an effort to get to the target as quickly as possible. This is not such a big problem for image quality, as the exposures are short, but does lead to image drift throughout the sequence. After an hour has passed, we feel that it is worth taking a few minutes to refocus and acquire a guide star before proceeding with longer exposures.

The main limitation of the response time to alerts is the time required to rotate the dome, which moves at about 4 degrees per second. Thus, very rapid response (less than tens of seconds) is not possible unless the telescope happens to be pointed by chance at a location near the alert position, but response within a minute is feasible.

5. Data Analysis

We have developed automatic data reduction for several types of programs, which enables a quick-look capability useful for determining whether observations have been successful or not. This helps to set up observations for subsequent nights. Many of these routines have been developed in the XVISTA image processing environment. However, we have found that many users prefer to do their own data reduction, so we also make the raw data available.

5.1. Differential Photometry. Our most common type of observing program is monitoring of variable stars. Data analysis for such programs generally consists of doing differential photometry between the variable object and one or more reference stars in the field after basic instrument calibrations are done. The procedure is relatively straightforward because the same field is observed over and over again.

We have implemented automated data reduction for such fields during the morning immediately following the data acquisition using our own custom software. During the robotic observations, log files are created for each program and object that are observed; these files list the sequence numbers of the observations in each filter. After the observing for the night is complete, the data and the log files are automatically transferred to a computer on the NMSU campus. A cron job runs every morning that sees what programs and objects were observed, and starts a data reduction script accordingly. Each of the data files is read in and basic calibration (flat fielding and a shutter shading correction) is done. The coordinates are read from the header and small corrections are determined using routines from the WCSLIB package, or by simply looking in the expected vicinity of a bright star to find where it actually lies; this latter technique is used for fields where there are too few stars to reliably determine the pointing via the WCSLIB routines. For each frame, coordinates of the variable star and other stars in the field are then transformed into pixel positions, centroids are computed around these positions, and aperture photometry is performed. The data files are merged with previous data files for the object, and plots are created for the light curves which are placed on a web page for easy inspection, along with links to the data files. The software can

be requested to notify one or more users by email when data for particular programs have been obtained, and the email provides links to the web page with the data plots and files.

Under certain circumstances, for example, coordination of observations with other facilities, we have run cron jobs to transfer data and attempt reductions during the night. If real-time data reduction was to become a priority, it would be straightforward to set things up to do reduction within several minutes of obtaining the data.

5.2. All Sky Photometry. We have also developed scripts for automated reduction of standard star photometry on nights when that is obtained. Again, the log files provide a method for automated software to know whether such data were obtained. If so, then the stars are automatically found and photometered, and photometric solutions, allowing for extinction, transformation, and zeropoint terms are determined for each filter. Plots are constructed showing residuals of the observed from the standard photometry as a function of magnitude, airmass, color, and time, which provide a quick means to determine whether the night was indeed photometric and whether there are any bad observations that are affecting the fit.

6. Scientific Programs

The telescope has been used for a number of different scientific programs. As previously mentioned, many of these involve monitoring of variable stars, which is a classic usage of a robotic telescope. Some examples include:

- (i) cataclysmic variables (Szkody et al. [1]; Harrison et al. [2]; Osborne et al. [3]; Mason et al. [4]),
- (ii) X-ray binaries (McNamara et al. [5]),
- (iii) eclipsing binaries (Stempels et al. [6]; Irwin et al. [7]; Hebb et al. [8]; Hoffman et al. [9]),
- (iv) δ Scuti stars (Hoffman et al. [10]),
- (v) M dwarfs: flare stars and a general sample to measure the flaring rate on typical stars (Hilton et al. [11]),
- (vi) brown dwarfs (Gelino et al. [12]),
- (vii) exoplanet transits (Coughlin et al. [13]).

Other productive uses have been rapid, multicolor followup of GRB 061126 (Perley et al. [14]), support of HST astrometry via photometric observations of parallax reference stars to help to estimate their distance (Benedict et al. [15]; Bean et al. [16]), monitoring of Saturn's moons during the opposition of 2005 (Miller et al. [17]), and support of several supernovae discovery and monitoring programs.

By agreement with the National Science Foundation as part of our PREST grant, we make a fraction of time available to the general astronomical community. We have been doing this on an informal basis, choosing programs where there is collaborative interest with NMSU personnel (to allow more time to be spent on the projects) and, most importantly, projects that are well suited to the

performance and robotic mode of operation of the telescope. Interested parties are encouraged to look at the information at <http://nmsu1m.apo.nmsu.edu/1m/obstime.html>.

7. Conclusion

We have described the hardware and software systems of the NMSU 1 m telescope located at the Apache Point Observatory. The telescope has been run almost exclusively in a robotic mode for ten years; the experience gained in this time may be of interest to others who are developing similar systems.

We have found that having a small robotic research telescope located at a major observatory site offers a number of advantages. The availability of site personnel for weather monitoring, which we have implemented for our telescope without requiring any direct action on the part of the site staff, and maintenance and repair is a significant benefit. Another advantage is a relatively low cost of operation for a large number of on-sky hours in a good observing site.

Acknowledgment

We would like to acknowledge the support of the staff of the Apache Point Observatory, whose cooperation and knowledge have made the development and operation of our facility possible. We also want to acknowledge the financial support of the National Science Foundation through their PREST program under Grant AST-0519398.

References

- [1] P. Szkody, A. P. Linnell, R. K. Campbell, et al., "GALEX, optical, and infrared light curves of MQ dra: UV excesses at low accretion rates," *The Astrophysical Journal*, vol. 683, pp. 967–977, 2008.
- [2] T. E. Harrison, S. B. Howell, M. E. Huber, et al., "Modeling the remarkable multiwavelength light curves of EF eridanus: the detection of its irradiated brown dwarf-like secondary star," *The Astronomical Journal*, vol. 125, pp. 2609–2620, 2003.
- [3] H. L. Osborne, T. E. Harrison, J. J. Johnson, and S. B. Howell, "Determining the masses and evolution of CVs through ellipsoidal variations," *Revista Mexicana de Astronomia y Astrofisica: Serie de Conferencias*, vol. 20, p. 250, 2004.
- [4] E. Mason, S. B. Howell, P. Szkody, T. E. Harrison, J. A. Holtzman, and D. W. Hoard, "Time-resolved, multi-color photometry and spectroscopy of virgo 4 (OU vir): A high orbital inclination, short orbital period dwarf nova," *Astronomy and Astrophysics*, vol. 396, no. 2, pp. 633–640, 2002.
- [5] B. McNamara, J. Norwood, T. E. Harrison, J. A. Holtzman, R. Dukes, and T. Barker, "Monitoring the mass accretion rate in scorpius X-1 using the optical Johnson B Filter," *The Astrophysical Journal*, vol. 623, pp. 1070–1075, 2005.
- [6] C. Stempels, L. Hebb, G. Stassun, et al., "The pre-main-sequence eclipsing binary ASAS J052821+0338.5," *Astronomy and Astrophysics*, vol. 481, no. 3, pp. 747–755, 2008.
- [7] J. Irwin, S. Aigrain, S. Hodgkin, et al., "The monitor project: JW 380—a 0.26-, 0.15- M_{\odot} , pre-main-sequence eclipsing binary in the Orion nebula cluster," *Monthly Notices of the Royal Astronomical Society*, vol. 380, no. 2, pp. 541–550, 2007.

- [8] L. Hebb, R. F. G. Wyse, G. Gilmore, and J. A. Holtzman, "Photometric monitoring of open clusters. II. A new M dwarf eclipsing binary system in the open cluster NGC 1647," *The Astronomical Journal*, vol. 131, pp. 555–561, 2006.
- [9] D. I. Hoffman, T. E. Harrison, B. J. McNamara, W. T. Vestrand, J. A. Holtzman, and T. Barker, "The case for third bodies as the cause of period changes in selected Algol systems," *The Astronomical Journal*, vol. 132, pp. 2260–2267, 2006.
- [10] D. I. Hoffman, T. E. Harrison, B. J. McNamara, and J. A. Holtzman, "Masses and Pulsational Modes of δ Scuti Stars in Eclipsing Systems," in *Proceedings of the 214th American Astronomical Society Meeting*, Pasadena, Calif, USA, June 2009.
- [11] E. J. Hilton, S. Hawley, N. Ule, et al., "Flare Rates on M Dwarfs," in *Proceedings of the 214th American Astronomical Society Meeting*, Pasadena, Calif, USA, June 2009.
- [12] C. R. Gelino, M. S. Marley, J. A. Holtzman, A. S. Ackerman, and K. Lodders, "L dwarf variability: I-band observations," *Astrophysical Journal*, vol. 577, no. 1 I, pp. 433–446, 2002.
- [13] J. L. Coughlin, G. S. Stringfellow, A. C. Becker, M. Lopez-Morales, F. Messalira, and T. Krajci, "New observations and a possible detection of parameter variations in the transits of gliese 436b," *The Astrophysical Journal*, vol. 689, pp. L149–L152, 2008.
- [14] D. A. Perley, J. S. Bloom, N. R. Butler, et al., "The troublesome broadband evolution of GRB 061126: does a gray burst imply gray dust?" *The Astrophysical Journal*, vol. 672, pp. 449–464, 2008.
- [15] G. F. Benedict, B. E. McArthur, and M. W. Feast, "Hubble Space Telescope fine guidance sensor parallaxes of galactic cepheid variable stars: period-luminosity relations," *The Astronomical Journal*, vol. 133, pp. 1810–1827, 2007.
- [16] J. L. Bean, B. E. McArthur, G. F. Benedict, et al., "The mass of the candidate exoplanet companion to HD 33636 from Hubble Space Telescope astrometry and high-precision radial velocities," *The Astronomical Journal*, vol. 134, pp. 749–758, 2007.
- [17] C. Miller, et al., in preparation.

Research Article

Three Years of Experience with the STELLA Robotic Observatory

Thomas Granzer, Michael Weber, and Klaus G. Strassmeier

Division of Telescope Control & Robotics, Astrophysical Institute Potsdam (AIP), An der Sternwarte 16, 14482 Potsdam, Germany

Correspondence should be addressed to Thomas Granzer, tgranzer@aip.de

Received 30 June 2009; Revised 1 November 2009; Accepted 18 January 2010

Academic Editor: Joshua S. Bloom

Copyright © 2010 Thomas Granzer et al. This is an open access article distributed under the Creative Commons Attribution License, which permits unrestricted use, distribution, and reproduction in any medium, provided the original work is properly cited.

Since May 2006, the two STELLA robotic telescopes at the Izaña observatory in Tenerife, Spain, delivered an almost uninterrupted stream of scientific data. To achieve such a high level of autonomous operation, the replacement of all troubleshooting skills of a regular observer in software was required. Care must be taken on error handling issues and on robustness of the algorithms used. In the current paper, we summarize the approaches we followed in the STELLA observatory.

1. Introduction

STELLA is a fully autonomous robotic observatory with two 1.2 m az-alt telescopes located at the Izaña observatory in Tenerife, Spain [1, 2]. STELLA-I is a classical f/8 Cassegrain-type telescope, equipped with a swiveling M3 mirror to make both Nasmyth foci available. STELLA-II is a highly specialized telescope with the single purpose to feed as much light as possible into an on-axis fiber. It has a single spherical mirror at f/1.95. At F1, a field corrector matches the PSF to the fiber entrance f-ratio and additionally provides a field of view of roughly 2 arcmin around the fiber. For acquisition and guiding, STELLA-II features an auxiliary, 15 cm refracting telescope. STELLA-I currently feeds the STELLA Echelle spectrograph (SES, see [3]), but in late 2009 the new wide-field imaging photometer (WiFSIP) should be operated on this telescope. STELLA-II is currently in a testing phase.

Both telescopes are truly robotic telescopes in the sense that they autonomously react to changing weather conditions, including operation of the telescope sheltering building. The object selection is not based on a single, prescribed sequence, but is always constructed dynamically, making fast reaction easy (see Section 2). Internet connection is only necessary for data retrieval and upload of new targets to the target pool, both of which can be achieved with considerable low bandwidth. Remote observing is possible but has so far never been necessary for normal scientific observations.

In the next sections, a step-by-step receipt of how a human observer has been replaced by individual pieces of software is presented.

2. Scheduling Observations

Different to classic observatories, robotic observatories in general and STELLA especially, do not divide the available observing time into different time slices and dedicate these to single users. All targets are active at any time, allowing for observing campaigns that span months and, quite usually, even years. An overview on the different projects conducted at STELLA might help to mitigate the scheduling requirements. One of the key projects on the spectroscopic telescope is the investigation of stellar magnetic activity on a handful of stars. The rotational period defines the time scale at which a couple of, say, twenty observations should occur, at intervals as regular as possible. The usability of a single observation highly depends on all the other observations occurring around it. Only if a high phase coverage could be achieved, the individual observation must be useful. Consequentially, the scheduling algorithm must be able to adjust the priority of such an observing project. Once started, it should be assured that it can also finish in time. If in doubt, refrain from starting the project at all. What comes to ease here is the general insensitiveness to the starting point of such programs, and the only focus lies on a proper phase coverage.

Studying highly phase critical phenomena like the Blazhko effect in RR Lyrae star requires the observations to be timed exactly around certain, well-known phases. Here, no freedom in choosing the starting point is possible, but observations do not need to be clumped especially close together.

Observations of radial velocity curves of δ Cephei stars or extrasolar planets relax that even further. Here you aim at good phase coverage, but the spacing between individual observations does hardly matter.

Objects with a prior unknown periods should be scheduled such that no bias is introduced on subsequent period determination.

The final class of targets is those that introduce no special timing or periodicity but rather yield the highest importance if observed at optimal conditions—optimal can refer to certain astronomic conditions, like no moon-light pollution or minimum airmass (easily to predict) or certain seeing requirements (difficult to predict).

Algorithms that deal with optimized scheduling are not confined to robotic telescopes alone. Basically all robotic processes face similar problems (e.g., [4]). Very different approaches to the scheduling problem exist in the literature; those relevant to robotic telescopes will be discussed briefly.

2.1. Queue Scheduling. Queue scheduling is the simplest approach possible, but also the least flexible. A superior process, most likely a human, defines a schedule for the upcoming observing period (not too long to make reaction to bad weather periods possible, not too short to gain advantage of the automated observing process). On observation start, the queue is loaded into the system and followed task by task. A coupling with additional constraints (target must be above a certain height; target may only be observed within an hour of the scheduled time) may allow for a limited degree of flexibility, which make queue scheduling apt for single-task surveillance projects.

2.2. Critical-Path Scheduling. A scheduling algorithm that splits a single task, like an entire observing campaign, into different, atomic, subtasks with various dependencies amongst each other is known as critical-path scheduling (e.g., [5]). It can be seen as the mathematical description of a Gantt chart and is mainly used in huge construction projects, where the main focus lies on the dependency between individual subtasks. Still, the main task of scheduling the different task relative to each other remains and such critical-path scheduling is seldom used in robotic astronomy.

2.3. Optimal Scheduling. An optimal schedule describes the particular flow of observations that allows the maximization of the scientific return measured according to a predefined metrics like shutter-open time. The high number of possible permutations of N targets, $p(N) \propto N!$, makes any algorithm a highly demanding one. In particular, unpredictable changes in environmental conditions break the optimal schedule, and a recalculation is necessary. At ground-based observatories, an optimal scheduling schema is difficult to implement due

to unforeseen changes in weather conditions. The Hubble Space Telescope, however, uses a software package called SPIKE [6] that delivers an optimal schedule for 14-day periods. Attempts to use the same algorithm on ground-based facilities, for example, with the Very Large Telescope [7] or the Subaru telescope [8] have yielded some success in producing guidelines for night astronomers.

2.4. Dispatch Scheduling. The algorithm that schedules targets in real time, always according to the current (observational) conditions, is known as dispatch scheduling. From the entire pool of targets available, the algorithm calculates a per-target merit, picking then the target with the highest yield.

$$m(t) = \sum_i w_i \cdot f_i(t). \quad (1)$$

The summation is done over individual merits $f_i(t)$, with different weights w_i for a particular merit. A balanced choice on the individual weights and merits allows for a very capable scheduling algorithm. This approach allows easy reaction on changing weather conditions and at the same time optimizes target scheduling for distinct side goals. However, it has no predictive capabilities in the sense that the currently top-rated observation will be done, regardless of an even higher yield possible in the future. Nevertheless, this approach is probably suited best for ground-based telescopes as the reaction to changing weather conditions is algorithm-inherent. Dispatch scheduling is thus used in many robotic telescope (e.g., [9]). On the STELLA observatory it is applied in a somewhat modified approach to compensate for the bad long-time behavior, see.

$$m(t) = \prod_i v_i \cdot s_i(t) \cdot \sum_j w_j \cdot g_j(t). \quad (2)$$

Here, the s_i 's, weighted with constant factors v_i , allow long-term modification of target selection (i.e., over several nights), while the g_j 's are mainly used for short-term scheduling, that is, over the course of a given night. On STELLA, the target itself defines which merits it may use. This is similar to setting all weights on all nonspecified merits to zero but allows easier adaptation to new observing strategies: new merits may be added at any time, given that they are available at run time. Out of convenience, all s_i 's and g_j 's are limited within $0 \leq s_i(t), g_j(t) \leq 1$, but merits exceeding one are allowed by adjustment of the weights. Generally, three sets of weights for all s_i 's and g_j 's are available, reflecting the three principal priority levels: level A for high-priority targets; all observations requested for a single target must be completed to allow scientific conclusions. Level B indicates mid-priority targets. Observing strategy is best-effort based, with (currently) a high likelihood of all observations to be completed. The lowest priority, C, is designed for targets that either add some scientific value, if observed, or for low-priority targets in large surveys. As a matter of fact, targets within this priority class are mostly observed during partly clouded nights, when targets in higher priority bins fail.

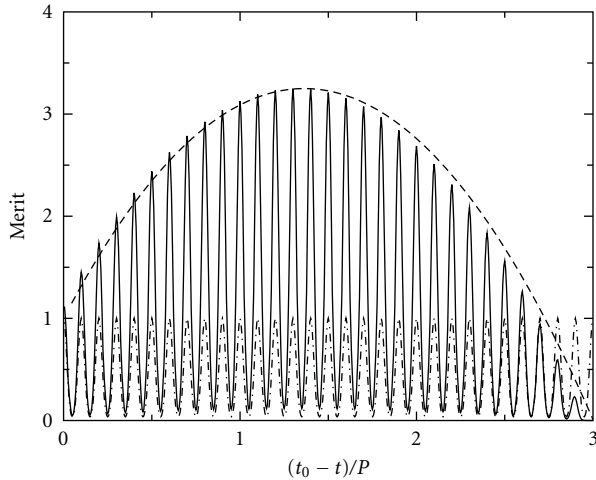


FIGURE 1: A combination of a long-term increasing and decreasing amplitude function (dashed line) with a high-frequency phase-selection wave (dotted-dashed line) to build a selection merit adequate for scheduling Doppler-imaging targets (thick line).

From the vast possibilities that the different combinations of weights and merits allow, only a few possible setups are currently implemented on STELLA. Large surveys on different targets have a pure airmass merit that peaks at one on the target's culmination and drops to zero at the apparent horizon, which lies between 5° and 30° . Depending on the priority class, the weights are $w_j = 1, 0.67, 0.33$ (A, B, C). Once observed *successfully*, their toggle-merit $s_i(t)$ drops to zero. Surveys, where targets should be revisited after a certain, maybe target-dependent, period have an s_i that starts at one, drops to zero on a successful observation, and linearly regains its top value of one after the specified period.

Targets that need observation strictly at specific phases utilize a so-called phase merit, that is the sum of normalized Gaussian centered at the requested phases. Targets that provide no phase zero point are scheduled according to their first successful observation. Again the weights read as $w_j = 1, 0.67, 0.33$ (A,B,C). In the basic form, where only strict phasing, but not the evolved time span matters, the single s_i is constructed such that it starts at $1/N$, where N is the number of phases requested. As the number n of phases successfully observed increases, s_i follows $s_i = (1 + n)/N$. The accompanying weight v_i equals $v_i = N$, leading to a gentle increase in total merit from one to N once the target has been started.

The most ambitious scheduling is done for objects that need a couple of phases observed within a few periods. At STELLA Doppler-imaging targets, these periods are in the range of several days, leaving you 2-3 weeks to complete a target. The merit is constructed in the following way. We start with an s_1 that peaks around the opposition of the target, mathematically a normalized Gaussian with an FWHM of three periods. Once such a target is successfully observed for the first time, a second s_2 gets activated, which is a parabola fit through points $1/v_2$, the reciprocal of the weight at the starting time and through zero after some multiple of the

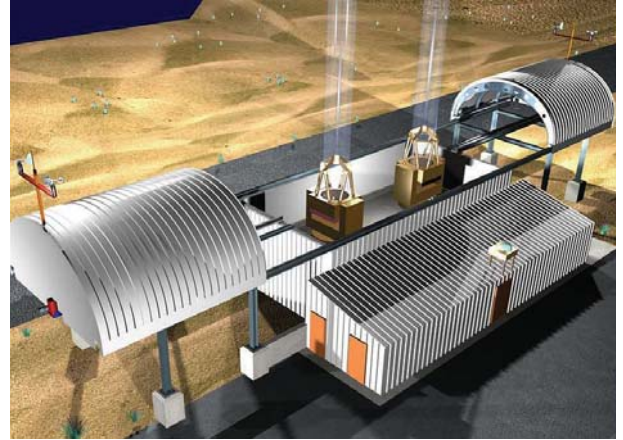


FIGURE 2: The layout of the STELLA building with the two roll-off roof halves. The building can be closed independently of the telescopes' positions. This allows for faster closing times, and, even more importantly, it allows for shutdown also in case of telescope movement failures.

period, default after $t = 3P$. Additionally, a time until the maximum is reached can be specified. In addition with the beforementioned phase merit, a complex merit functions like the one depicted in Figure 1 are reached. Some more details can be found in [10].

3. How to Carry out a Robotic Observation

When a target has been selected by the scheduling process, all the individual subtasks for that particular target have to be carried out—in parallel whenever possible, strictly sequential if dependencies between the subtasks exist. Parallelizing many tasks can save valuable observing time, on STELLA, read-out of the scientific CCD takes place while the telescope already slews to the next target. In pretty exactly half of the cases, the next target is already acquired and closed-loop guiding has commenced, when the read-out finishes.

STELLA houses a spectroscopic and an imaging telescope, thus the individual subtasks for a single observation differ quite substantially, nevertheless the general idea of splitting an observation into subtasks with the possibility to execute them in parallel or sequentially stays the same. In STELLA, we implemented a generic sequencing schema, which is described in detail in [11]. There we also explain how targets can define their own observing sequence and how a template sequence is constructed. In this paper, however, we want to focus more on the individual subtasks and their implementation, particularly pointing out that the solutions have been chosen for robustness rather than high accuracy. In the description, we follow the principle time line of an astronomic observation, starting by judging the overall weather situation, followed by pointing and focusing of the telescope, then acquiring of a target, followed by closed-loop guiding during the scientific exposure. These sections apply particularly to the fiber-fed instrument Stella-I. Tasks only

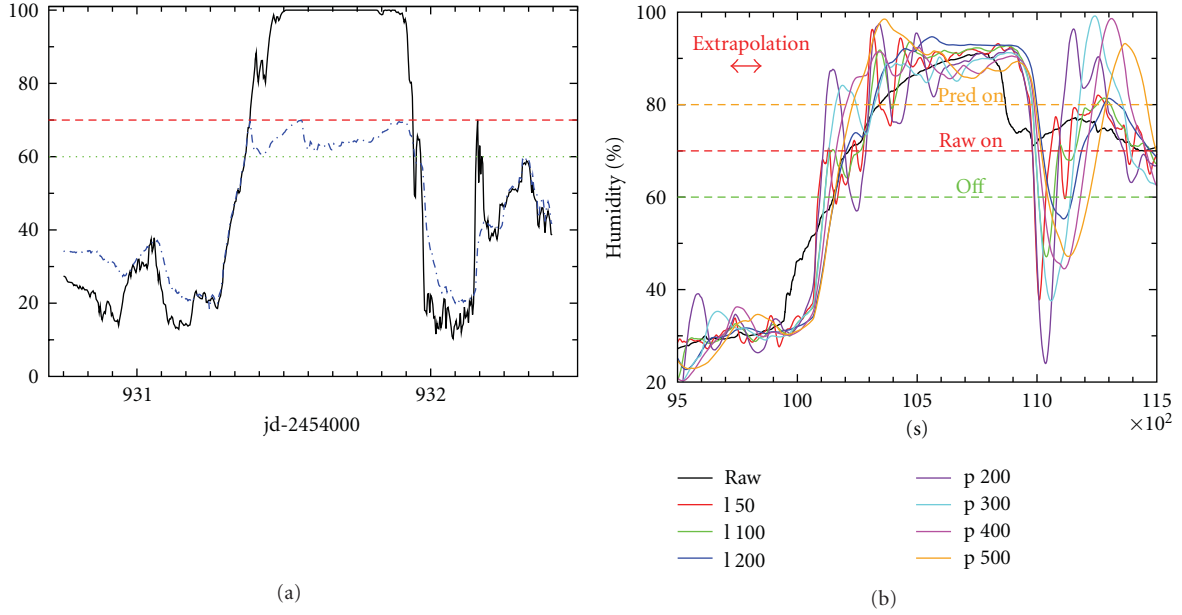


FIGURE 3: (a) The response of the environment system to the outside humidity (thick line). When a level of 70% on the rising edge is passed, the roofs are closed (note that the bay humidity, dot-dashed, stays roughly constant thereafter. Reopening of the building is allowed, once the humidity has dropped below 60% and remained at that level for at least two hours. (b) Prediction of inversion layer breakdowns. The thick line is the measured relative humidity. The 100-second extrapolations of various extrapolators are superimposed onto the true measurement. The true development of the humidity could be foreseen by all of the extrapolators. Note the delayed onset of the humidity rise of the extrapolated to the true values. The extrapolation could not predict that a sharp rise will *start* to occur, but the goal to predict the *height* of the humidity rise is well matched.

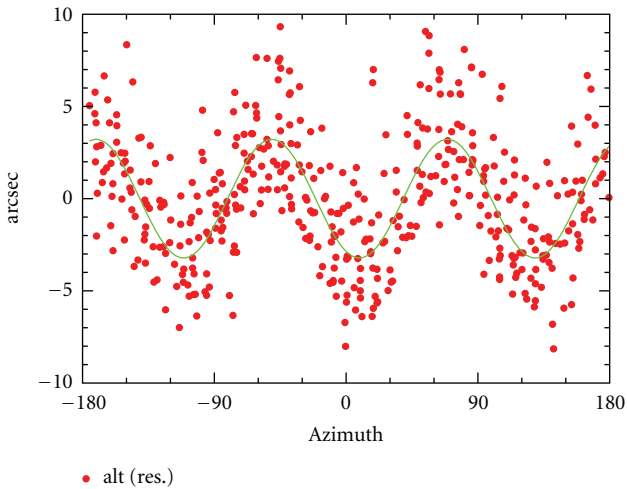


FIGURE 4: The RMS of the elevation pointings after a classical pointing model has been applied compared to the true offsets. The RMS varies at an amplitude of $\approx 3''$, at a wavenumber $k = 3$, reminiscent of the tripod mounting of the telescope.

required for the imaging telescopes Stella-II follow in the next Section 4.

3.1. Protecting the Telescope in Harsh Weather Conditions. Protecting the telescope from the outside during bad weather conditions is one of the task that an autonomous observatory

has to fulfill with the highest possible reliability. Needless to say that it is better to lose some observing time at unstable weather conditions than to risk damage to the telescope or the instrumentation due to high humidity, rain, high wind, or, particularly cumbersome in Tenerife, dust. The STELLA observatory is laid out as a building with a roll-off roof with two, elliptically shaped roof halves driven by crane motors. Opening and closing of the roof is possible in any position of the two telescopes; see Figure 2. As an additional security mechanism, a simple watchdog system that automatically closes the roof in case of computer crashes is used. Systems where the telescope has to be moved to a certain position before the closing of the roof can commence should be avoided whenever possible, as it leaves the instruments in an unprotected state if the telescope, for whatever reason, cannot be turned.

In standard, that is, unattended operation mode, the meteorological readings of two independent weather stations decide on the opening or closing of the roof. All sensors considered critical (precipitation, humidity, temperature, and wind speed) are available at either station, with the redundancy allowing for operation of the observatory even in case of failure of one of the stations. The building control acts completely independent from all other systems and had been installed even before the telescopes was put in place. In almost eight years of building operation, it never failed to protect the telescope.

The decision-making process for the open/close roof process relies on the current reading of the four critical

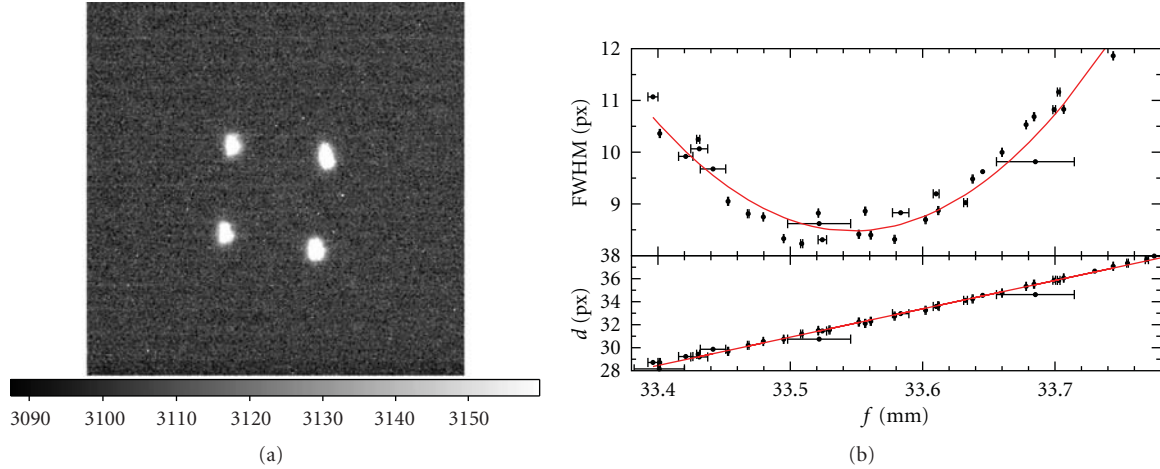


FIGURE 5: (a) The image of a single star with the focus pyramid introduced into the beam. Possible errors in the center-of-gravity determination of the four image centers do not hamper the focussing accuracy due to the high sensitivity of the subimages' distances on the focus position. (b) The calibration curve used to convert the pyramid's subimage distances to the focus applied. (a) shows the measured FWHM of a star without the pyramid in the optical beam as a function of focus position (distance of the secondary mirror to M1). (b) shows the average distance of the four subimages in pixel with the pyramid inside the optical beam. This calibration has been done at a very early time in the commissioning of the telescope, when the telescope control system was still unstable in attaining certain focus positions. This is visible as the sometimes huge error bars in the focus position.

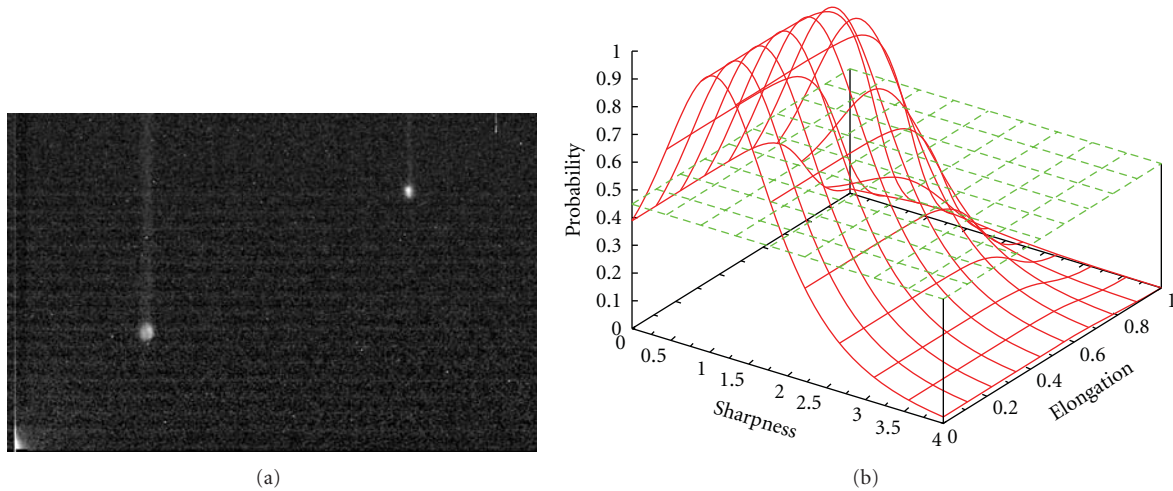


FIGURE 6: (a) A typical first image during the acquire phase. The image of the star through the beam splitter is the brighter spot to the left the fainter image to the right is the image from the mirror around the fiber entrance. The read-out stripes result from the shutter-less design. (b) The probability function used for identifying stars from their measured image elongation (y , to the back) and sharpness (x , to the right). The green, constant level at a probability of 0.446 is the threshold above which stars are identified. The two-dimensional function in red was derived by a manual training of the acquire system on 100 different images.

sensors, as well as on the history of their measures. A solar-height sensor is a purely calculated sensor but enters just like another critical sensor. Combining two or more sensors in the decision making turned out to be not necessary.

Most of the critical sensors act as Schmidt-triggers; they toggle their weather state on two values, depending on the general direction of the past measures. Toggling from one state into the other is additionally delayed by a sensor-dependant retard time, during that the sensor's reading must stay in the new state, otherwise toggling does not occur.

Typically, this retard time is two seconds or four read cycles if toggling to the bad weather state—its main purpose is to filter out erroneous readings of a sensor. Toggling to the good weather state is more depending on the site characteristics. For Izaña, humidity toggles to bad at 70% the clear toggle is set at 60% Wind speed toggles at 20 m/s and 10 m/s, respectively, temperature at -2°C and $+1^{\circ}\text{C}$. Precipitation has just an on/off state, thus zero is considered no rain, one is considered raining. A brightness sensor toggles at 3000 lx and 10000 lx. It is mainly a guard against wrong-posed solar height calculations.

We apply a retard time of two hours for a humidity event, four hours for a rain event, and twenty minutes for a high wind-gust event. This principle is depicted in Figure 3(a), for reaction on the humidity.

Early on, the exposed location of the Tenerife site, just above the inversion layer, demanded for the capabilities to predict inversion layer breakdowns. For that, the course of the humidity is examined in more detail and a prognosis for the next 100 seconds—the closing time of the roofs—is derived from it; see Figure 3(b). Different time bases and either linear or parabolic extrapolation are used for the near-future humidity development. Only if at least six out of seven extrapolators predict a humidity above 80%—compared to the normal toggle of 70%—, the roofs close.

3.2. Pointing the Telescope. For a reliable object acquisition, a good initial pointing of the telescope is desirable. For that, a stable mount is inevitable. To compensate for the small optical and mechanical misalignments of even the most precise telescope mounts, a mathematical model known as the pointing model is used to bring the initial pointing errors down to less than a few arc seconds. STELLA uses the classical pointing model, which describes only effects of misalignment of an otherwise perfect mount. The corrections to the azimuth (A) and the elevation (E), namely, ΔA and ΔE , are modeled according to (3). A_0 and E_0 are constant offsets; the two angles A_N and A_E describe the tilt of the telescope's azimuth axis to the true vertical in the northern and eastern direction, respectively. N_{PAE} describes the nonperpendicularity between the telescope's altitude and azimuth axis. B_{NP} is the nonperpendicularity between the telescope's altitude axis and the optical axis, while T_F is the tube flexure

$$\begin{aligned}\Delta A &= A_0 - B_{NP} \sec E + N_{PAE} \tan E + A_N \cos A \tan E \\ &\quad + A_E \sin A \tan E, \\ \Delta E &= E_0 - A_N \sin A + A_E \cos A + T_F \cos E.\end{aligned}\tag{3}$$

Ignoring the constant offset A_0 and E_0 , the highest absolute values are for $T_F = 49''$ and for B_{NP} and N_{PAE} at $B_{NP} = 28''$ and $N_{PAE} = 32''$, but note also the discussion on pointing models in [12]. One specific effect of the mount of the STELLA telescopes is depicted in Figure 4; the tripod-mooring of the telescope mount has its resemblance in a 120° , wavelength modulated RMS in the elevation pointing corrections.

3.3. Focusing with a Focus Pyramid. Different solutions for focusing a telescope exist. On Stella-I, we tried to aim at a fast and reliable procedure. We decided to equip the telescope with the so-called focus pyramid, which can be rotated into the optical beam. It splits the light of a point-source, that is, of stars, into four individual subimages, whose distances are a direct measure of the focus; see Figure 5. Once calibrated, a single measurement of the subimages' distances suffices to determine the focus.

3.4. Acquiring the Target. Currently, Stella-I is fiber-feeding an Echelle spectrograph [3]. Thus target acquisition must be done at a precision of less than an arc second. During integration, an adapter unit allows permanent position control down to subarc second levels. This adapter unit hosts a gray beam splitter that diverts 4% of the target light onto a guiding camera. The region just around the fiber entrance is imaged with a mirror onto the same guiding camera, leading to a second image at a varying offset from the direct beam splitter image; see Figure 6(a). The guiding camera has a shutter-less design to minimize the number of moving parts in the system. The read-out strips inherent to such a design are dealt with in the acquisition software. For details of the optical layout of the acquire unit, please refer to [1].

Once the telescope has been moved to the target position, an image of the entire guider's field of view (2.1×1.5 arcmin) is taken; see Figure 6(a). The image is bias-subtracted and a truncated Gaussian filter is applied to it. Similar to DAOfind [13], the resulting image is used to detect star candidates. Their sharpness and their elongation are validated against a two-dimensional probability function, shown in Figure 6(b). If no stars are found, the initial acquire is repeated up to five times with gradually increased exposure times. Once an ensemble of stars has been identified, their positions are matched to the UCAC2 [14] catalog and the shift to the current telescope's position is determined. After the first successful shift, this procedure is repeated using a much smaller window centered around the mirrored fiber entrance to finally reach an offset of less than $1.5''$. This relatively large offset is necessary because image motion induced by atmospheric turbulence at short exposure times can amount to an RMS in the target position of up to $0.5''$.

3.5. Closed-Loop Guiding on the Target Star. Once the star has been successfully acquired, the closed-loop guiding system starts. Its only aim is to keep the *direct* image of the target star as close to the *mirrored* fiber entrance position as possible. The target star's brightness defines the exposure time during the guiding phase; it is adjusted to get a stellar signal at a S/N ratio of $S/N \approx 5$. The read-out time of the guider window limits the exposure time to 500 milliseconds. Typically, 3000 guider frames are taken during a one-hour integration. A combined frame of all individual guider frames can be seen in Figure 7. This combined frame is also used to measure the light loss at the fiber entrance by aperture photometry of the two stellar images.

Due to atmospheric image motion, wind shake, and intrinsic telescope oscillations, not every offset measured should be applied directly to the telescope. In STELLA, a split approach is used. First, five offsets are averaged. If the average offset is less than the standard deviation, or if it is less than the expected image motion induced by the atmosphere, it is set to zero. This average offset is split into azimuth and altitude and is fed into two PID controls (from Proportional-Integral-Derivative; for an introduction to PID refer to [15]). The output of the PIDs is then applied to the telescope. During commissioning, three distinct weather situations have been identified, each triggering the use of



FIGURE 7: The combined image of ≈ 1200 guiding frames on 51 Peg, total exposure time 20 minutes. The bright image to the left is the position of the star as imaged through the beam splitter the fainter image to the right is the light spilled over the fiber entrance and reflected back onto the guider camera. Guiding is done exclusively at the brighter image. Aperture photometry of the combined frame is used to measure the amount of light lost, here 32%.

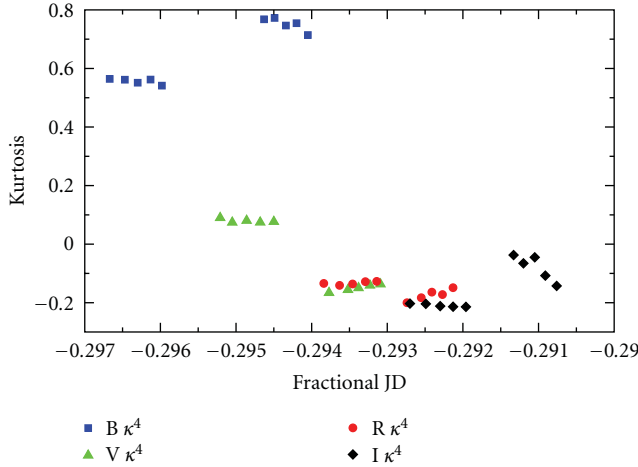


FIGURE 8: The kurtosis of the ADU statistics versus fractional JD of sky flats taken at the Mont Sec observatory during dusk twilight, five days apart. The different symbols refer to the different Johnson-Cousins filters B, V, R, and I. Within each night, the kurtosis stays remarkably constant, allowing for immediate identifications of flats affected by cosmics or clouds. The kurtosis offset in the blue filters visible between the two nights is probably caused by different efficiency in the light-straying process in Earth's atmosphere.

a different parameter set. In normal mode, a proportional term of $P = 0.3$ for altitude and $P = 0.4$ for azimuth is used. The integral constant I equals $I = 0$, and for the derivative term D , $D_{az} = 0.05$ and $D_{alt} = 0.02$ are used. The bad-seeing mode, effective when the seeing is worse than $1.5''$, has a reduced $P_{az} = 0.2$, $P_{alt} = 0.15$, and no D or I term. In high-wind mode for wind speeds $v > 7$ m/s, the number of individual offsets averaged increases from five to 20, therefore acting on a much slower time scale. P is thus relatively high, $P_{az} = 0.3$, $P_{alt} = 0.25$, and a low I term of $I = 0.05$ is introduced. D stays at zero.

4. The Imaging Telescope STELLA-II

Different to the spectroscopic telescope, commissioning on the imaging telescope is just beginning. What follows are first results and insights gained, but far from being backed by years-long experience as in the spectroscopic case. Nevertheless, we want to address a few problems and their possible solutions in high-precision robotic photometry. For a more detailed description on the capabilities of the

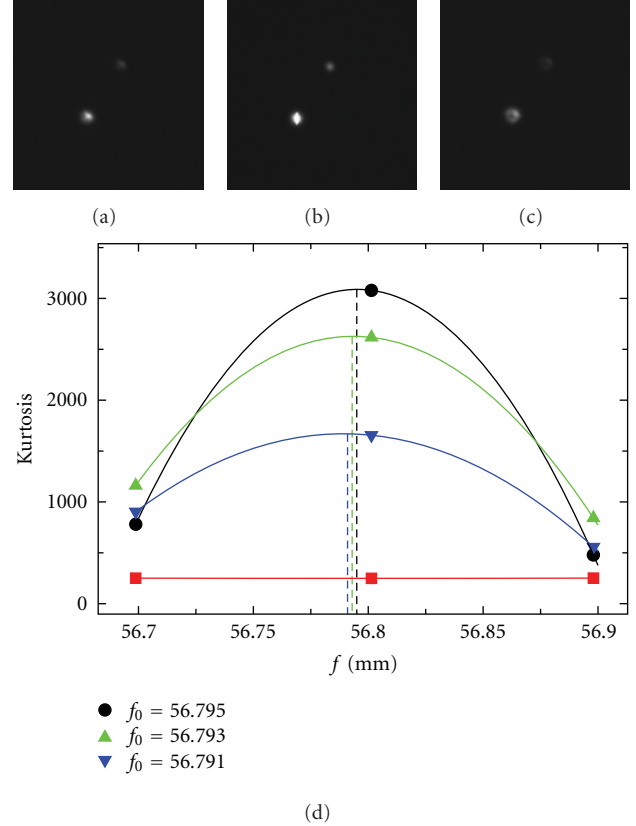


FIGURE 9: The kurtosis of the ADU statistics on three images taken with WiFSIP during precommissioning on Robotel, at the Astrophysical Institute in Potsdam. All three quadrants of the imaging CCD with bright stars in them show a peaking kurtosis close to the best focus position. The one flat line is the kurtosis in quadrant 1, which was essentially free of stars. The small inserts on top are tiny windows around two bright stars in the field at the different focus positions.

Wide Field STELLA Imaging Photometer (WiFSIP), see, for example, [16].

4.1. Ensuring High-Quality Flat Fielding. We do not intend to equip the STELLA building with a flat-fielding screen. The time of twilights will be used to obtain sky flats. The total number of 21 filters available in WiFSIP makes it impossible to obtain twilight flats on all filters each night. The individual filter will be grouped together according to their filter system

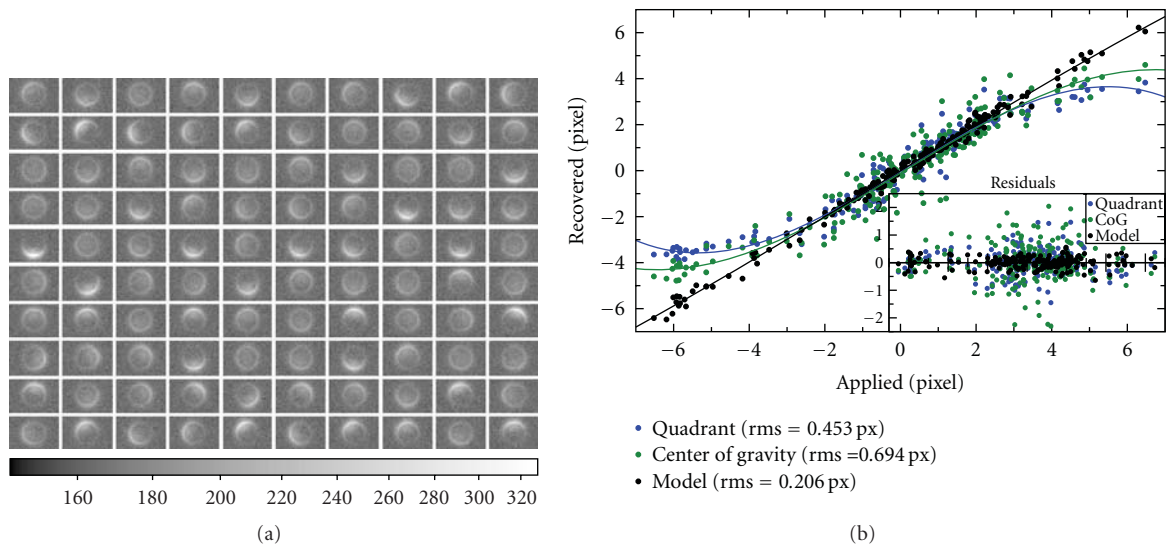


FIGURE 10: (a) Sequence of artificial images of an $R = 8''$ star on the fiber viewing Unibrain 520b camera on Stella-II, exposure time set to 1 second. Pixel scale is 0.13 arcsec/pixel the diameter of the pinhole is 2.8 arc seconds. The seeing was set to 1 arcsec. (b) Recovering of the shift of the center of the star relative to the center of the pinhole, for the image sequence to the left. Center of gravity uses first image moments the quadrant method compares the ADU sum in the left-to-right and up-to-down image segments. These two methods do not deliver a true shift, but only a shift direction. For clarity, the direction has been scaled to match the true offset. Direct modeling of the star plus pinhole recovers the true shift and allows to estimate the light loss and seeing, but requires relatively high S/N levels.

(Sloan, Strömgren, Johnson-Cousins), and flats in single, but entire groups should be obtained in a single twilight. Two main drivers will define which group of flats will be chosen, the time passed since the last calibration of the filter group, and the likeliness of science observations with filters of that group in the upcoming night.

Following the text book, we start with the filter of the shortest central wavelength on dusk twilight and with the red filter on dawn twilight. Small-window test exposures are taken in rapid succession until the average ADU level in the read-out window suggests an exposure time in the allowed range -0.2 to 5 seconds. The Bonn shutter of the instrument allows for such very short exposures. On OmegaCam, a similar shutter is reported by [17] to deliver equally exposed images at exposure times down to 0.1 second.

To minimize the effect of sky-brightness gradients, the telescope is pointed to the anti solar azimuth and five degrees away from the zenith. This region in the sky is the one with the lowest, sometimes even vanishing sky brightness gradient; see [18]. Additionally, the camera will be rotated by 180° after half of the individual exposures. Exposure times are gradually changed to keep the average exposure level as constant as possible.

The quality of the flat-field image is assessed via ADU statistics, with particular focus on higher-order moments. In Figure 8, the kurtosis of the ADUs for five sky flats, taken in Johnson-Cousins BVRI at two different days, is plotted. The flats are from the Mont Sec robotic observatory [19], separated by five days. Though the average ADU level dropped from almost 50000 to below 30000, the kurtosis, or, equivalent the fourth central moment, stayed remarkably constant. Cosmics show up in the kurtosis as high values. Higher moments than the kurtosis works even better in

detecting cosmics but also probes the arithmetic accuracy of the CPU.

4.2. Focusing Using Statistical Moments. On the imaging telescope, no auxiliary focusing unit like a focus pyramid will be present. The plan is to use a twofold approach. Depending on the temperature of the telescope structure, a focus position will be estimated. At this estimated focus position together with offsets at ± 0.05 mm, three images of a field close to the celestial North pole (or maybe of Polaris itself, this will be decided during on-site commissioning) will be taken, and the kurtosis of the images will be analyzed. Figure 9 shows the anticipated procedure; the focus will be found at the point maximizing the kurtosis of the image. We hope that this procedure is superior to directly minimizing the FWHM of stellar images.

5. Future Plans

In spring 2010, the spectrograph-feeding fiber will be moved from Stella-I to the second STELLA telescope. The light coupling occurs at F1, leaving no place for a large acquire field. Acquiring will be done using a piggy-back auxiliary telescope, a 15 cm refracting telescope equipped with a shutter-less, uncooled guiding camera. Again, details on the optical layout can be found in [2].

5.1. Guiding on Spilled-over Light. The main acquiring and guiding system will be built around the current acquire and guiding logic, but with one additional complexity. Due to unavoidable, relative bending of the auxiliary telescope to the main telescope, guiding with the auxiliary telescope alone

will not be sufficient. Additionally, we will use the light spilled over on the fiber entrance as a secondary guiding signal. This light will be caught on a fast read-out Unibrain 520b video camera. This camera comes with an electronic shutter, allowing for exposure times lower than 1 ms and up to 65 seconds. Furthermore, the gain of the CCD can be adjusted quasicontinuously from 2.8 to 0.11. This extreme range will suffice to guide on stars as bright as zeroth magnitude down to, say, 12^m . First tests of the camera on Robotel allowed to estimate the quantum efficiency (QE) of the entire system to $\text{QE} \approx 0.15$. Using artificial images, see Figure 10, we tested three algorithms to recover the shift of the stellar image with respect to the center of the pinhole: Center of gravity (CoG, based on image moments), quadrant weights (QWs), where the total ADUs in the left-to-right and up-to-down sectors have been compared to give a correction direction, and direct modelling of the star plus pinhole. Only direct modelling returns a true shift; CoG and QW can only deliver the principal direction of the correction. As guiding is done in a PID environment anyhow, this shortcoming does hardly matter as it is compensated by a proper choice of the proportional term.

The results of all three methods are shown in Figure 10(b). Basically all of the three methods could be used to retrieve the original shift. The higher robustness favors CoG and QW over direct modelling, while the latter delivers as a side product also information on light loss and stellar FWHM. Consequentially, we will use CoG during the guiding process and model the star plus pinhole on the combined frame to extract the additional information on light loss and seeing.

References

- [1] K. G. Strassmeier, T. Granzer, M. Weber, et al., "The STELLA robotic observatory," *Astronomische Nachrichten*, vol. 325, no. 6–8, pp. 527–532, 2004.
- [2] K. G. Strassmeier, "STELLA: two new robotic telescopes for binary-star research," *Astrophysics and Space Science*, vol. 304, no. 1–4, pp. 397–400, 2006.
- [3] M. Weber, T. Granzer, K. G. Strassmeier, and M. Woche, "The STELLA robotic observatory: first two years of high-resolution spectroscopy," in *Advanced Software and Control for Astronomy II*, A. Bridger and N. M. Radziwill, Eds., vol. 7019 of *Proceedings of SPIE*, p. 70190L, 2008.
- [4] M. Pinedo, *Scheduling: Theory, Algorithms, and Systems*, Prentice-Hall, Upper Saddle River, NJ, USA, 1995.
- [5] C. Hendrikson and T. Au, *Project Management for Construction: Fundamental Concepts for Owners, Engineers, Architects, and Builders*, Prentice-Hall, 1989.
- [6] M. Giuliano, "Achieving stable observing schedules in an unstable world," in *Astronomical Data Analysis Software and Systems VII*, R. Albrecht, R. N. Hook, and H. A. Bushouse, Eds., vol. 145 of *ASP Conference Series*, p. 271, 1998.
- [7] A. M. Chavan, G. Giannone, D. Silva, T. Krueger, and G. Miller, "Nightly scheduling of ESOs very large telescope," in *Astronomical Data Analysis Software and Systems VII*, R. Albrecht, R. N. Hook, and H. A. Bushouse, Eds., vol. 145 of *ASP Conference Series*, p. 255, 1998.
- [8] T. Sasaki, G. Kosugi, R. Hawkins, J. A. Kawai, and T. Kusumoto, "Observation scheduling tools for Subaru telescope," in *Optimizing Scientific Return for Astronomy through Information Technologies*, P. J. Quinn and A. Bridger, Eds., vol. 5493 of *Proceedings of SPIE*, pp. 367–372, 2004.
- [9] S. N. Fraser, "Scheduling for Robonet-1 homogenous telescope network," *Astronomische Nachrichten*, vol. 327, no. 8, pp. 779–782, 2006.
- [10] T. Granzer, "What makes an automated telescope robotic?" *Astronomische Nachrichten*, vol. 325, no. 6–8, pp. 513–518, 2004.
- [11] T. Granzer, "Generic control of robotic telescopes," in *Advanced Software, Control, and Communication Systems for Astronomy*, L. Hilton and G. Raffi, Eds., vol. 5496 of *Proceedings of SPIE*, pp. 667–678, 2004.
- [12] K. G. Strassmeier, K. Agabi, L. Agnoletto, et al., "Telescope and instrument robotization at Dome C," *Astronomische Nachrichten*, vol. 328, no. 6, pp. 451–474, 2007.
- [13] P. B. Stetson, "DAOPHOT—a computer program for crowded-field stellar photometry," *Publications of the Astronomical Society of the Pacific*, vol. 99, p. 191, 1987.
- [14] N. Zacharias, S. E. Urban, M. I. Zacharias, et al., "The second US naval observatory CCD astrograph catalog (UCAC2)," *Astronomical Journal*, vol. 127, no. 5, pp. 3043–3059, 2004.
- [15] A. Visioli, *Practical PID Control*, Springer, Berlin, Germany, 2006.
- [16] K. G. Strassmeier, T. Granzer, M. Weber, et al., "The STELLA robotic observatory on Tenerife," *Advances in Astronomy*, vol. 2010, Article ID 970306, 11 pages, 2010.
- [17] K. Reif, G. Klink, P. Müller, and H. Poschmann, "The OmegaCam shutter," in *Scientific Detectors for Astronomy*, P. Amico, J. W. Beletic, and J. E. Beletic, Eds., Astrophysics and Space Sciences Library, 2004.
- [18] F. R. Chromey and D. A. Hasselbacher, "The flat sky: calibration and background uniformity in wide-field astronomical images," *Publications of the Astronomical Society of the Pacific*, vol. 108, no. 728, pp. 944–949, 1996.
- [19] J. Colomé, D. Fernández, J. Isern, et al., "Robotic design of the Montsec astronomical observatory," *Astronomische Nachrichten*, vol. 325, no. 6–8, p. 658, 2004.

Research Article

“Pi of the Sky” Detector

**Katarzyna Małek,¹ Tadeusz Batsch,² Henryk Czyrkowski,³ Mikołaj Ćwiok,³
Ryszard Dąbrowski,³ Wojciech Dominik,³ Grzegorz Kasprowicz,⁴ Ariel Majcher,²
Agnieszka Majczyna,² Lech Mankiewicz,¹ Krzysztof Nawrocki,² Robert Pietrzak,⁵
Lech W. Piotrowski,³ Maria Ptasińska,⁶ Małgorzata Siudek,⁶ Marcin Sokołowski,²
Janusz Użycki,² Piotr Wawer,⁵ Roman Wawrzaszek,⁵ Grzegorz Wrochna,²
Marcin Zaremba,⁶ and Aleksander F. Żarnecki³**

¹ Center for Theoretical Physics Polish Academy of Sciences, Al. Lotników 32/46, 02-668 Warsaw, Poland

² The Andrzej Soltan Institute for Nuclear Studies, Hoza 69, 00-681 Warsaw, Poland

³ Institute of Experimental Physics, University of Warsaw, Hoza 69, 00-681 Warsaw, Poland

⁴ Institute of Electronic Systems, Warsaw University of Technology, Nowowiejska 15/19, 00-665 Warsaw, Poland

⁵ Space Research Center Polish Academy of Sciences, Bartycka 18A, 00-716 Warsaw, Poland

⁶ Faculty of Physics, Warsaw University of Technology, Koszykowa 75, 00-662 Warsaw, Poland

Correspondence should be addressed to Katarzyna Małek, malek@cft.edu.pl

Received 29 June 2009; Accepted 27 October 2009

Academic Editor: Taro Kotani

Copyright © 2010 Katarzyna Małek et al. This is an open access article distributed under the Creative Commons Attribution License, which permits unrestricted use, distribution, and reproduction in any medium, provided the original work is properly cited.

“Pi of the Sky” experiment has been designed for continuous observations of a large part of the sky, in search for astrophysical phenomena characterized by short timescales, especially for prompt optical counterparts of Gamma Ray Bursts (GRBs). Other scientific goals include searching for novae and supernovae stars and monitoring of blazars and AGNs activity. “Pi of the Sky” is a fully autonomous, robotic detector, which can operate for long periods of time without a human supervision. A crucial element of the detector is an advanced software for real-time data analysis and identification of short optical transients. The most important result so far has been an independent detection and observation of the prompt optical emission of the “naked-eye” GRB080319B.

1. Introduction

“Pi of the Sky” is a robotic telescope designed to perform observations in autonomous mode, without any human supervision. The detector has been designed mainly to search for the optical prompt emission of the Gamma Ray Bursts (GRBs) which can possibly occur during or even before gamma emission. The standard approach to look for optical afterglow associated with GRBs is to wait for satellite alerts distributed by the GCN network (The Gamma Ray Burst Coordinates Network) [1] and move the telescope to start observations of the target as fast as possible [2]. However, this approach causes an unavoidable delay of the optical observations with respect to the GRB event and it does not allow for catching the optical emission from the source exactly at the moment or before the GRB explosion.

The “Pi of the Sky” apparatus design and operation strategy is based on a different philosophy: it assumes a continuous observation of a large fraction of the sky, which increases the chances that a GRB will occur in the observed area.

The full “Pi of the Sky” system will consist of 2 sites separated by a distance of ~ 100 km. Each site will consist of 16 highly sustainable, custom-designed survey CCD cameras. Pairs of cameras work in coincidence and observe the same field of view. The whole system is capable of continuous observation of about 2 steradians of the sky, which roughly corresponds to the field of view of the Swift BAT instrument [3].

Before construction of the full system, the necessary hardware and software tests were performed using a prototype. It has been located in the Las Campanas Observatory in Chile since June 2004. It consists of two specially designed

CCD cameras observing the same $20^0 \times 20^0$ field of view with a time resolution of 10 seconds. During the past 4 years, the control software and analysis algorithms have been regularly developed, to improve the overall system performance and the sustainability, as well as flash and nova-like stars recognition algorithms. In 2008, the prototype indeed automatically recognized and observed the prompt optical emission from the famous “naked-eye” GRB080319B. This detection and subsequent observations have confirmed that the idea of the “Pi of the Sky” detector allows for the efficient search for prompt optical counterparts of GRBs.

2. Inspiration

It is commonly acknowledged that Bogdan Paczyński was one of the greatest minds of the contemporary astrophysics. One of the least discussed aspects of his remarkable personality is his ability to motivate and inspire other people to pursue research in the directions which he himself considered interesting. Professor Paczyński strongly supported the application of small robotic telescopes to study astrophysical phenomena, with ASAS [4] and HAT [5] being perhaps the best examples of how right he was.

In the beginning of 2000s, Paczyński was visiting Warsaw from time to time. His seminars attracted attention not only of astrophysicists but also of people from other branches of physics. This is how a small group of particle physicists came across Paczyński’s idea that small robotic telescopes may play an important role in solving perhaps the most intriguing astrophysical mystery of that time, namely, the nature of Gamma Ray Bursts. It did not take long before, after some discussions, we realized that indeed, apart from different sources of input signals—stars instead of particles—the general architecture of a wide-field, all-sky fast optical transients detector would resemble very much what we are accustomed to in particle physics experiments. Moreover, as self-triggering would give such a detector precious independence on satellite information, it was taken into account from the very beginning in the design. Here the proper strategy for searching of a GRB optical emission, like for a needle in a hay stack, could be based on a multilevel trigger scheme well-known from particle physics experiments searching for rare events, which could be, for example, footprints of creation of a new particle.

We started R&D work armed with modest grants from Professor Paczyński and the Polish Ministry of Science. Soon it becomes obvious that with money we had we could only dream about buying detector components from a shelf; so we decided to build the detector from the scratch on our own. As it has been demonstrated by the future development, this decision was right and has proved to be the key to success of the whole project. We did not only build, for example, CCD cameras for less money but also could design these cameras with features which later turned out to be crucial. Like a submarine crew which takes part in the final construction of their boat in order to know every piece of its mechanism, we know every element of our detector and in case of some failure, which is unavoidable during a long operation period,

we can come with an effective work-around strategy. There is also no way to overestimate gains stemming from detailed knowledge of software, including drivers for all devices, which were home-written as well.

What started as a small project soon became a larger enterprise because the news spread out and more students came, interested in taking part in a new project. Although key elements have been built by full-time professionals, a lot of, for example, software has been written by students coming to us for master thesis, and so forth. Participation in our project became a challenge for the best young people studying around, and that development turned out to be quite an asset as well.

In the meantime, other groups, motivated by GRB observations, develop their own robotic systems. BOOTES [6], RAPTOR [7], REM [8], ROTSE [9], MASTER [10, 11], TORTORA [12], WIDGET [13], WFOC [14], and so forth presented unique, technologically advanced designs. Robotic follow-up telescopes and wide-field survey systems have become part of the mainstream astronomy.

Gamma Ray Bursts were discovered more than 40 years ago. Studies of these unusual phenomena are based on data collected by gamma detectors located on satellites as well as by optical and IR ground telescopes. It is widely accepted that GRBs are associated with extremely energetic explosions in distant galaxies. It is almost certain that bursts are due to collapsing massive stars or merging of two neutron stars [15]. The most interesting piece of GRB’s puzzle is the nature of the central engine, that is, the place where gravitational energy is converted into burst energy in timescales of milliseconds. The detailed mechanism of the central engine is still unknown. It is certain that multiwavelength observation of prompt emission can reveal hints which eventually will allow us to construct a robust theory of the central engine mechanism or mechanisms. It is hard to imagine other types of detectors which can serve this mission, but robotic, wide field, all-sky like “Pi of the Sky” telescope.

3. “Pi of the Sky” Final System

The most important ingredient of our strategy for independent search for optical counterparts of GRBs and other fast optical transients is the self-triggering capability. This strategy has been tested and developed using the prototype telescope located in the Las Campanas Observatory. Tests of the real-time flash recognition algorithms revealed that the most common background sources are flashes due to cosmic rays hitting the CCD and near-Earth flashes from the Sun light reflections from satellites. For efficient search for prompt optical counterparts of GRBs we have designed a system consisting of two mirror sites. In order to reduce the background flashes, mirror sites should be located at a distance ~ 100 km and their cameras should observe pairwise the same field of view. The reflections from satellites could then be identified and removed by their parallax, and cosmic rays can be eliminated by analyzing the coincidence on both cameras. A schematic view of the final system is shown on Figure 1. Here one site consists of 16 CCD cameras installed on four parallactic mounts [2].

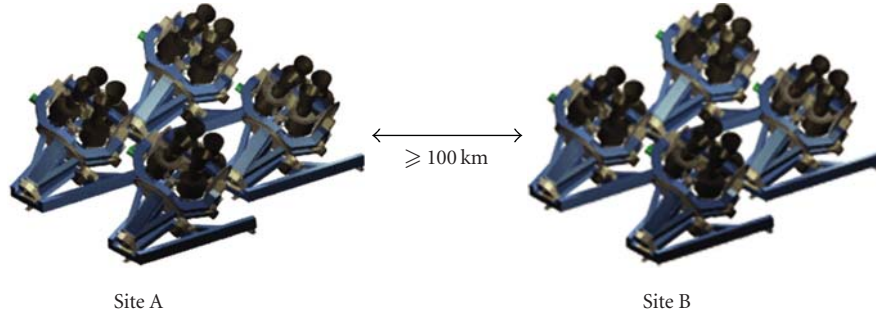


FIGURE 1: Schematic view of the final “Pi of the Sky” detector.

In order to ensure full control over the detector design and construction, we have decided to build custom-design CCD cameras. STA0820 $2k \times 2k$ CCD chips with 2 dual-stage outputs have been selected because of their relatively low price and satisfactory price/performance ratio. The pixel size is $15 \times 15 \mu m^2$. The readout frequency, gain, CCD temperature, mechanical shutter, and other parameters are remotely controlled via Ethernet or USB2.0 interface. The CCD is cooled with a two-stage Peltier module up to 40 degrees below the ambient temperature. EF CANON lenses with the focal length $f = 85$ mm and $f/d = 1.2$ have been chosen as the optical system. With this setup, one camera covers a field of view of approximately $20^\circ \times 20^\circ$, with pixel size corresponding to 36 arcsec on the sky. The final system will cover ~ 2 steradians that correspond approximately to the field of view of the BAT instrument on board the Swift satellite [3].

Following the FoV of the Swift detector, “Pi of the Sky” can detect optical counterparts of GRBs at the very beginning and during the gamma emission, or even before it. No time is needed for repointing the telescope to the coordinates from GCN. The dead time which arises from the decision process and signal propagation from the satellite to the GCN and from the GCN to a ground instruments is eliminated as well. Small, fast follow-up telescopes can minimize the delay arising from inertia, but the problem of the delay time due to the signal propagation cannot be solved in this way. Even a very fast reaction to a GCN alert cannot guarantee the detection of the prompt emission. Hence our primary strategy is to continuously follow, if possible, the FoV of Swift. Moreover, this strategy allows us to observe or determine the upper limit for a precursor in the optical band.

The system is in the final construction phase now. Most of parallactic mounts and cameras have already been completed and hardware as well as software is being assembled and tested now. We plan to begin the installation of the final system by the end of 2009.

4. Prototype

The prototype was installed in Las Campanas Observatory (LCO) in Chile. Regular observations started in June 2004. The place was selected because of very good and stable weather conditions (Figures 2 and 3).

Design of the prototype detector follows the assumption that it should be a scalable version of the final detector. It consists of 2 CCD cameras on a common parallactic mount. It is just a small version of the final instrument and apart from performing regular observations, it serves for testing both hardware and software solutions. From the very beginning, the prototype as well as the final instrument has been designed to operate in autonomous mode, with minimum human supervision, although remote control via Internet is possible as well. It is clear that a robotic system must be very reliable. This goal has been accomplished with the help of the special diagnostic software, which monitors continuously the system performance in the autonomous operation mode, detects problems, if any, and reacts to them. Every software module which controls a piece of hardware writes status file every 60 seconds. This file contains all important information about the current state of the module and also contains information if any problem was self-detected by this particular module. Another script is checking all status files every 5 minutes and is able to automatically identify the problem in a single status file or combine information from several files. In case such problem is detected, certain repairing action is undertaken to fix the problem. In addition, the appropriate information is sent to the mobile phone of a person in charge. Interestingly enough, the diagnostic software is practically 100% effective in solving encountered problems, a performance which was never achieved before by humans. System sustainability has been also increased by hardware redundancy and careful, flexible system configuration avoiding choke points.

Cameras monitor the sky taking 10 seconds exposures with 2-second readout time at the readout speed of 2 Mpixel/second. The limiting magnitude for a single frame is 12^m and rises to approximately 13.5^m for a frame stacked from 20 exposures. This rather short magnitude range is a price paid for wide field observations. With the 10 second time resolution and 2 second readout time, one camera collects from 2 to 3 thousand frames per night, depending on the time of the year. With such a large number of opening cycles, a really heavy-duty shutter is a must. We have designed a special, mechanically durable shutter, which can sustain about 10^7 opening cycles. It corresponds to a few years of continuous operation. The shutter is based on voice-coil principle used, that is, to control read-write

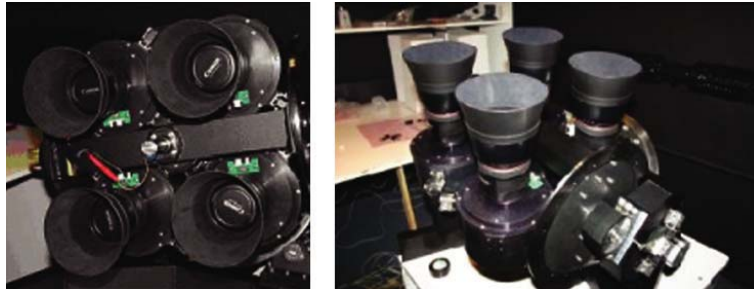


FIGURE 2: “Pi of the Sky” mount with 4 cameras.



FIGURE 3: “Pi of the Sky” prototype located in the ASAS dome, Las Campanas Observatory, Chile.

heads in hard disks. Such construction results in lack of friction between diaphragm and its support as a key factor in shutter’s durability. In addition, before the shutter hits the bumper while opening or closing, the voice-coil is actuated by precisely adjusted pulse with negative sign. Such electronic brake slows down speed of the shutter and reduces the stresses to the mechanism. Since May 2009 one of the CCD cameras has been equipped with the R-band filter in order to facilitate absolute calibration of measurements.

Because of the field of view which is smaller than for the final telescope, the prototype cameras follow, for most of the time, the center of the Swift’s BAT FoV. When the Swift FoV is not visible from LCO, an alternative target like the INTEGRAL FoV or some other interesting object from the special target list is chosen automatically. The system also reacts automatically to GCN alerts. When the target from the received GCN alert is located outside the current FoV, the system moves telescope towards the alert position and starts taking exposures. The software takes decision about repointing automatically. It also sends an information to the person in charge every time when detector reacts to a GCN alert and moves to the GRB’s position.

In the normal observing mode images are analyzed on-line in order to find optical transients, possibly optical counterparts of GRBs. An algorithm searching for short optical flashes by comparing a new image with the stack of recently taken frames has been developed. The algorithm design resembles multilevel triggering system known from high-energy physics experiments.

Twice a night, at the beginning and at the end, a systematic all-sky scans are performed in order to search for transients with a longer timescale. During one scan the

system collects three 10 second images for each of about 30 predefined fields, which are observed each time. Systematic observations of the whole visible sky are important for investigation of objects with variability timescale from hours to days and longer. Hence, an off-line algorithm searching the scan observations for novae, supernovae, and other optical transients not associated with GRBs has been developed and tested as well [16].

5. Results

5.1. Optical Counterparts of GRBs

5.1.1. Prompt Optical Observation of GRB 080319B. On March 19, 2008 the “Pi of the Sky” prototype observed the prompt optical emission from long-duration gamma ray burst GRB080319B [17]. It was later measured that the burst occurred at the redshift $z = 0.937$ [18]. Luckily, this was the second burst that night. At 5:45 UT the Swift satellite detected an intense pulse of gamma rays (GRB 080319A). The determined position was sent via GCN and ground experiments moved to follow-up optical observations of this burst. The “Pi of the Sky” prototype also started observing that object. Less than 30 minute later, at 6:12:49 UT, the BAT detector was triggered by gamma emission from another GRB. This moment is marked $T = 0$ for GRB 080319B. The position of the burst was distributed over GCN and the “Pi of the Sky” system received it at 6:13:06 UT. Fortunately, the angular distance between GRB 080319A and GRB 080319B was only about $\sim 11.8^\circ$ and so it was just small enough for the second burst to occur in the FoV of the “Pi of the Sky” detector. The “Pi of the Sky” telescope had continuously

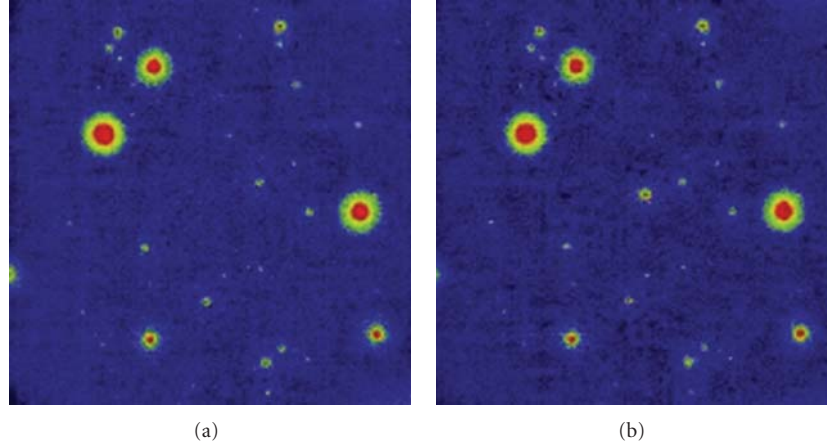


FIGURE 4: Optical counterpart of GRB 080319B taken by “Pi of the Sky” prototype detector. The prompt optical emission is clearly visible on the right image, taken during the gamma emission at 06:14:03 UT. The prompt emission is no more detectable on the left image, taken 10 minutes after the burst.

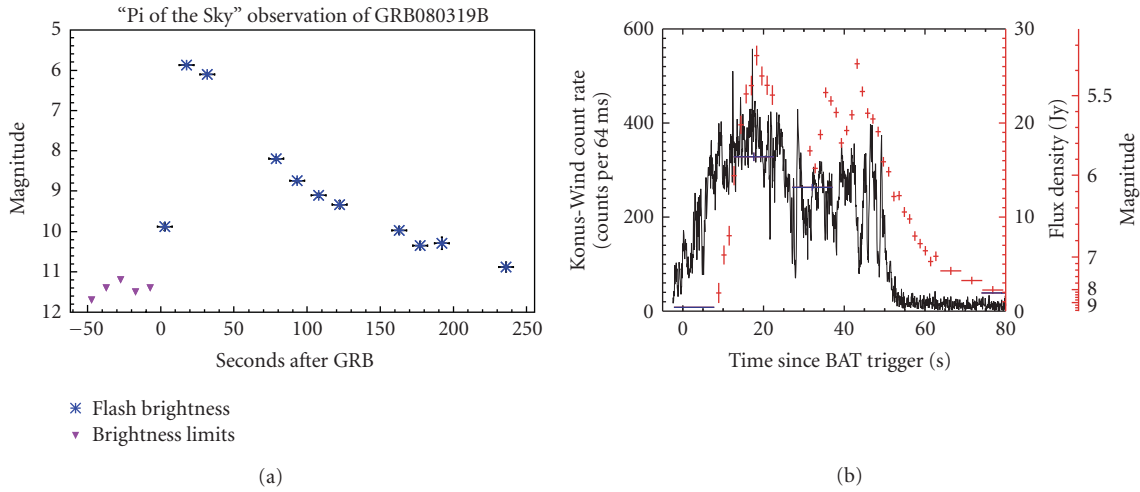


FIGURE 5: Light curve of GRB 080319B prompt emission. (a) shows “Pi of the Sky” measurements alone. (b) (taken from Racusin et al. [18]) shows the “Pi of the Sky” (blue), “TORTORA” (red), and Wind-Konus (black) data.

observed this area for more than 23 minutes before the burst, pointing to the first GRB position. 2 seconds before BAT was triggered by the second burst, at 6:12:47 UT, the detector started a new 10 second exposure. The burst recognition algorithm automatically detected a new object [17]. The prompt optical emission from GRB 080319B was bright enough to be observed by the “Pi of the Sky” prototype for more than 4 minutes (Figures 4 and 5). As it is well known now, the optical flash was so strong that for about 40 seconds it could even be seen with a naked eye, without any instruments. For this reason the GRB 080319B burst is generally known as the “naked-eye burst.”

Early optical observations during the very first tens of seconds from the beginning of the gamma emission, together with later data that cover wavelengths from radio to gamma rays, are shown on Figure 6. These observations challenged many existing models of GRB emission and demonstrated usefulness of wide-field detectors, capable of continuous

monitoring of large parts of the sky. In practice such systems are probably the only choice to observe the prompt optical emission from the gamma ray bursts in a systematic way.

The most unexpected result coming from the analysis of the prompt emission of GRB 080319B was the flux density difference between optical and gamma-ray spectrum (Wind-Konus data [19]) appointed during the first three 10 second intervals centred at T_0+3 s, T_0+17 s, and T_0+32 s. As is turned out, the optical flux from the flash detected by “Pi of the Sky” prototype was ~ 10000 larger than the extrapolation of the flux density of the gamma emission (Konus-Wind data, Figure 7). The Konus-Wind data have been extrapolated to the optical domain using the best-fit Band function [9]. Such a bright optical component suggests that optical photons are emitted in a different mechanism than γ ray emission. An interpretation has been proposed that optical emission arises from synchrotron emission and the high-energy gamma emission comes from a synchrotron self-Compton process.

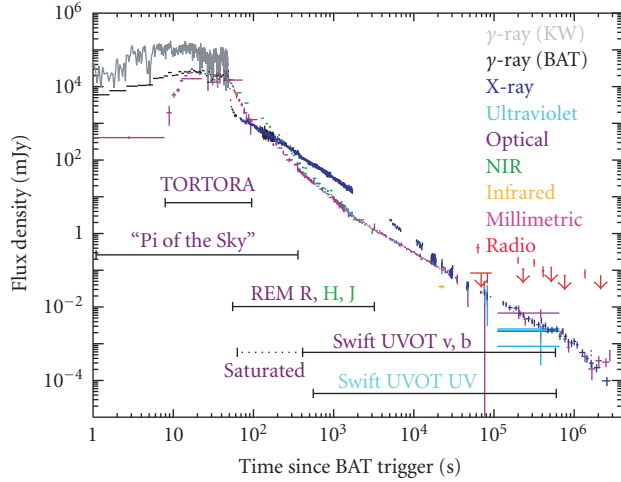


FIGURE 6: Light curves of GRB 080319B, including radio, millimetric, infrared, NIR, optical, ultraviolet, X-ray, and gamma ray flux densities. The original light curve was taken from Racusin et al. [18]. Bars with names of different instruments show timescales of different observations.

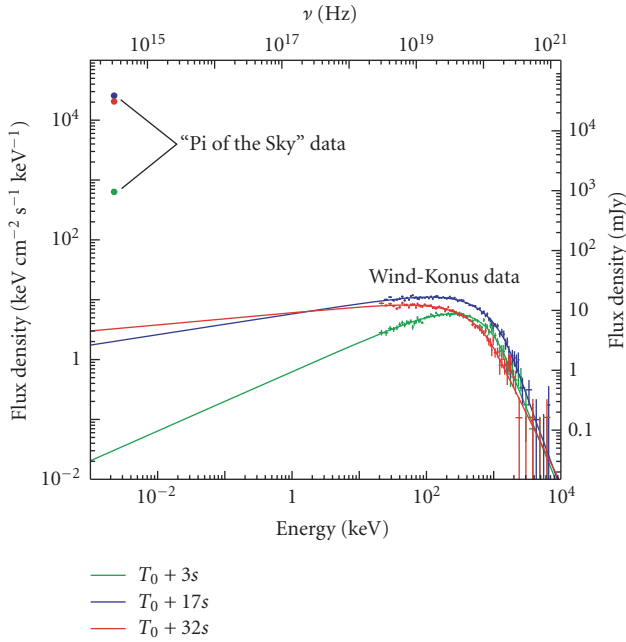


FIGURE 7: Spectral Energy Distribution of the prompt emission of GRB 080319B [18].

This interpretation implies the existence of a third, harder, spectral part, GeV component. Unfortunately, this third component remained undetected in case of GRB080319B. However, more than one year later the ground experiment TUPI [20] detected the first GeV emission from GRB 090315.

Based on GRB080319B measurements, new models of a GRB have been considered [18, 21–25]. Observations of this unique GRB continued for weeks afterwards, following fading afterglow, and provided important clues to understanding of a mechanism of the GRB emission.

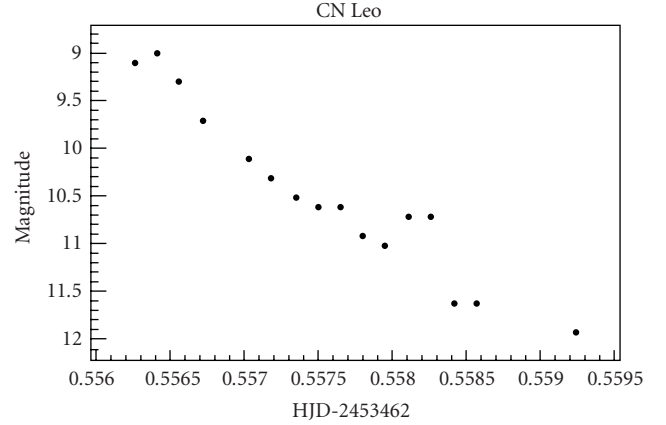


FIGURE 8: Outburst of CN Leo star (02.04.2005). On the image taken before the outburst, the star was not visible. During a few seconds its brightness raised by a factor of 100 and then faded away during several minutes.

5.1.2. Other Observations of GRBs. The “Pi of the Sky” prototype has been active from 2004.07.01 to 2005.08.07 and from 2006.06.01 till now, with 10-month break due to maintenance of CCD cameras. As of 2008.06.05 different gamma-ray satellites observatories detected a total of 404 gamma ray burst with known positions. The “Pi of the Sky” detector could observe only 81 of them, that is, only those which occurred during local nighttime, on the southern hemisphere, with sufficiently high altitude above the horizon and during good weather conditions. Table 1 summarizes statistics of the “Pi of the Sky” observations of these events.

In 77 cases, when GRBs occurred outside “Pi of the Sky”’s FoV, the system repointed to the burst position after receiving an alert from the GCN. Four GRBs occurred inside the FoV of the prototype but only in the case of GRB 080319B an optical transient was detected. In addition, upper limits of magnitude for 14 optical counterparts for GRBs set by “Pi of the Sky” have been published as GCN Notes.

5.2. Optical Flashes. Since June 2004 the basic software of the “Pi of the Sky” telescope has been regularly developed and tested in order to improve both on-line and off-line transient-detection algorithms. During this period the prototype detected more than 200 short optical flashes in a single frame and 7 flashes visible in two frames. It is very likely that most of flashes visible in a single frame are sunlight reflexes from satellites, which have not been recognized by our algorithms. Optical flashes visible for more than 1 frame are unlikely to be satellite images, because staying for more than 10 second in a single pixel would require very high orbit, which contradicts their high brightness. However, no coincidence with any satellite GRB trigger was detected. Two of them were recognized as flashes of astrophysical origin. The first one was identified as the outburst of CN Leo flare star ($\alpha = 10:56:29$, $\delta = +07:00:53$) on 2005.04.02 (Figure 8), and the second one as the optical counterpart of GRB 080319B.

TABLE 1: Statistic of “Pi of the Sky” observations.

Apparatus off	North hemisphere	Daytime	Below horizon	Clouds	Outside FOV	Inside FOV
19	35	196	57	16	77	4

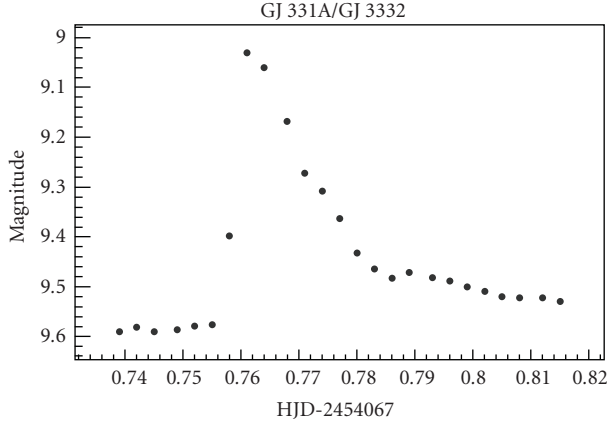
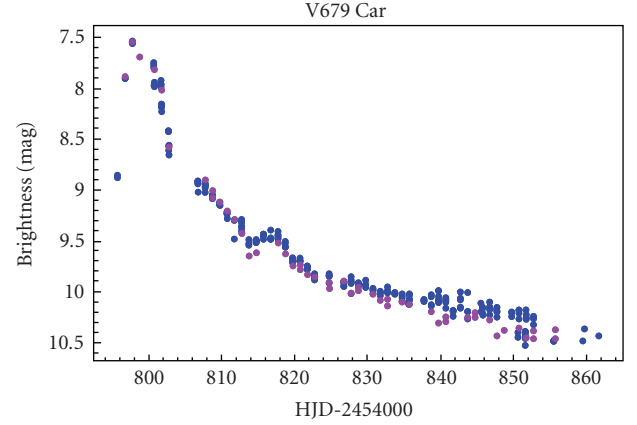


FIGURE 9: During the night 27/28.11.2006 the “Pi of the Sky” automatically detected outburst of a flare star GJ3331A/GJ3332 ($\alpha = 05:06:50$, $\delta = -21:35:06$). Each point on the light curve corresponds to a sum of 20 images, 10 second exposure each.

5.3. Optical Flares. A separate off-line algorithm has been developed in order to search for outbursts of flare stars. The algorithm gets light curves of stars from the database and looks for significant increase of brightness (Figure 9). The algorithm is still being developed and tested. As for 05.06.2009, the “Pi of the Sky” apparatus has detected seven optical flares.

5.4. Novae Stars. Identification algorithm for novae uses the data collected during all-sky scans as an input. The algorithm does not try to determine the parameters of novae but simply looks for a new object in the data. The algorithm requires that the new object is visible on two or more single 10 second images taken one by one. All selected events must be detected on images taken by both cameras. The next condition is that the new object is not present in the TYCHO2 database [16]. The final analysis is taking into account a few more technical conditions, introduced to increase background rejection efficiency of the algorithm. All the selected events are sent to Warsaw for examination of their light curves and visual inspection of sequences of images taken before and during the new object detection. Such algorithm gives good results as far as search for novae and other variable stars and planetoids is concerned. The most impressive results were discoveries of two dwarf novae and one classical nova and the identification of V5115 Sgr in our database. The first dwarf nova 1RXS J023238.8-371812, most likely a WZ Sge type dwarf nova, was discovered in mid-September 2007 [26]. Two months later “Pi of the Sky” algorithm identified another WZ Sge type dwarf nova: WZ Sge type in Hydra constellation (VSX J111217.4-353828) [27]. In November 2008 classical nova Nova in Carina (V679 Car) [28] was



• Pi aver
• Pi scan

(a)



(b)

FIGURE 10: (a) shows a light curve of V679 Car. Data are taken from the “Pi of the Sky” database. Blue points denote measurements taken during all-sky scans and violet points from regular observations. (b) shows an optical image of the V679 Car (indicated by an arrow) taken by Alain Maury, Steve Barnes, Caisey Harlinton, and Stephane Guisard on December 1, 2008.

automatically detected as well. A light curve of V679 Car is shown on Figure 10.

5.5. Catalog of Variable Stars. A catalog of variable stars with periods from 0.1 to 10 days identified in the “Pi of the Sky” data was published in [29]. Light curves of 925 201 stars observed during the period 2004-2005 were analyzed by a variability search algorithm to find variable stars. The AoV method [30] was used to determine periods and reject stars with false variability. Classification based on the shape of light curves was performed by a visual inspection. The catalog consists of 725 variable stars. Most of them are eclipsing binaries of W UMa type.

Analysis of data collected during 2006-2007 has been performed as well [31]. We have selected about 3000 stars for further analysis. We are currently working on visual inspection of light curves and types of variability determination for these stars.

5.6. Public Databases. Data acquired during the “Pi of the Sky” observations are reduced and only light curves of stars are stored in the database. Two public databases containing star’s measurements from 2004–2005 and 2006–2007 have been created so far, with observations from 2007–2008 being analyzed just now. These databases contain all measurements taken by the “Pi of the Sky” detector. The first database covers VII.2004–VI.2005 and contains about 790 mln measurements for about 4.5 mln objects. The second database covers period V.2006–XI.2007 and includes about 1002 mln measurements for about 10.8 mln objects. A dedicated web interface has been developed to facilitate public access to databases of the “Pi of the Sky” project. The interface allows to search for stars by magnitude, coordinates, and other parameters and to view a light curve of a selected star [32]. Public databases are available on the “Pi of the Sky” web page <http://grb.fuw.edu.pl/pi/>.

5.7. Minima of Binary Stars. Several binaries observed by the “Pi of the Sky” were analyzed in order to determine times of their minima using the method of Kwee and van Woerden [33]. The web access to the database with individual times of minima is available at <http://www.as.ap.krakow.pl/miniauto/>.

6. Conclusions

We have described the design, philosophy, construction and the prototype performance of the “Pi of the Sky” robotic wild-field telescope. The “Pi of the Sky” has indeed been operating in the fully autonomous mode, practically without any human supervision for about a year, 3 years after the prototype installation in the Las Campanas Observatory in Chile. The key element behind this achievement has been development of special diagnostic software which supervises the system and reacts to problems which appear during system operation.

High sustainability of the “Pi of the Sky” instrument has allowed us to concentrate on gathering and analysis of data. The dedicated software performs an on-line search for optical transients. The successful detection of a prompt GRB emission during the night of March 19, 2008 has shown that the software is indeed capable of identifying an optical counterpart of a GRB prior to the satellite alert distributed by the GCN. In addition, we have presented results of searches for flare stars, novae, and other optical transients, which are performed off-line.

The full “Pi of the Sky” system, currently in the completion and testing phase, will consist of 2 mirror sites with 12 or 16 CCD cameras each. We plan to begin installation of the final system by the end of 2009.

Acknowledgments

The authors are very grateful to G. Pojmański for access to the ASAS dome and sharing his experience with them. They would like to thank the staff of the Las Campanas for their help during the installation of the apparatus. This work was

financed by the Polish Ministry of Science in 2005–2009 as a research project. They are grateful to A. Pollo for careful reading of the manuscript.

References

- [1] S. D. Barthelmy, et al., “The GRB Coordinates Network (GCN): a status report,” in *Gamma-Ray Bursts: 4th Huntsville Symposium*, C. A. Meegan, R. D. Preece, and T. M. Koshut, Eds., AIP Conference Proceedings, pp. 99–103, American Institute of Physics, Woodbury, NY, USA, September 1998.
- [2] A. Burd, M. Cwiok, H. Czyrkowski, et al., “Pi of the Sky— all-sky, real-time search for fast optical transients,” *New Astronomy*, vol. 10, no. 5, pp. 409–416, 2005.
- [3] N. Gehrels, G. Chincarini, P. Giommi, et al., “The Swift gamma-ray burst mission,” *Astrophysical Journal*, vol. 611, no. 2, pp. 1005–1020, 2004.
- [4] G. Pojmański, “The all sky automated survey. Catalog of variable stars. I. 0 h–6 h quarter of the Southern Hemisphere,” *Acta Astronomica*, vol. 52, no. 4, pp. 397–427, 2002.
- [5] G. Bakos, R. W. Noyes, G. Kovács, K. Z. Stanek, D. D. Sasselov, and I. Domsa, “Wide-field millimagnitude photometry with the HAT: a tool for extrasolar planet detection,” *Publications of the Astronomical Society of the Pacific*, vol. 116, no. 817, pp. 266–277, 2004.
- [6] A. J. Castro-Tirado, J. Soldán, M. Bernas, et al., “The burst observer and optical transient exploring system (BOOTES),” *Astronomy and Astrophysics Supplement Series*, vol. 138, no. 3, pp. 583–585, 1999.
- [7] W. T. Vestrand, P. R. Wozniak, J. A. Wren, et al., “A link between prompt optical and prompt γ -ray emission in γ -ray bursts,” *Nature*, vol. 435, no. 7039, pp. 178–180, 2005.
- [8] F. M. Zerbi, G. Chincarini, M. Rodono, et al., “REM—Rapid Eye Mount. A fast slewing robotized telescope to monitor the prompt Infra-red afterglow of GRBs,” in *Gamma-Ray Bursts in the Afterglow Era*, ESO Astrophysics Symposia, Springer, London, UK, October 2000.
- [9] C. Akerlof, R. Balsano, S. Barthelmy, et al., “Observation of contemporaneous optical radiation from a γ -ray burst,” *Nature*, vol. 398, no. 6726, pp. 400–402, 1999.
- [10] V. M. Lipunov, A. V. Krylov, V. G. Kornilov, et al., “MASTER: the mobile astronomical system of telescope-robots,” *Astronomische Nachrichten*, vol. 325, no. 6–8, pp. 580–582, 2004.
- [11] MASTER project, <http://observ.pereplet.ru/>.
- [12] S. Karpov, “Wide and fast monitoring the sky in subsec domain,” these proceedings.
- [13] T. Tamagawa, F. Usui, Y. Urata, et al., “The search for optical emission on and before the GRB trigger with the WIDGET telescope,” *Nuovo Cimento della Societa Italiana di Fisica C*, vol. 28, no. 4–5, pp. 771–774, 2005.
- [14] A. Pozanenko, et al., “Wide field optical camera for search and investigation of fast cosmic transients,” in *Gamma-Ray Bursts: 30 Years of Discovery: Gamma-Ray Burst Symposium*, vol. 727 of AIP Conference Proceedings, pp. 757–760, American Institute of Physics, Melville, NY, USA, 2004.
- [15] P. Meszaros, “Gamma-ray bursts,” *Reports on Progress in Physics*, vol. 69, pp. 2259–2322, 2006.
- [16] K. Malek, L. Mankiewicz, L. W. Piotrowski, and M. Sokolowski, “All sky scan analysis algorithm for Pi-of-the-Sky

- project,” in *Photonics Applications in Astronomy, Communications, Industry, and High-Energy Physics Experiments 2006*, vol. 6347 of *Proceedings of SPIE*, October 2006, 63470Q.
- [17] M. Sokolowski, et al., “Prompt optical observations of GRBs with “Pi of the Sky” system,” in *GAMMA-RAY BURST: Sixth Huntsville Symposium*, vol. 1133 of *AIP Conference Proceedings*, pp. 306–311, 2009.
 - [18] J. L. Racusin, S. V. Karpov, M. Sokolowski, et al., “Broadband observations of the naked-eye γ -ray burst GRB 080319B,” *Nature*, vol. 455, no. 7210, pp. 183–188, 2008.
 - [19] R. L. Aptekar, D. D. Frederiks, S. V. Golenetskii, et al., “Konus-W gamma-ray burst experiment for the GGS Wind spacecraft,” *Space Science Reviews*, vol. 71, no. 1–4, pp. 265–272, 1995.
 - [20] C. E. Navia, “Muons enhancements at sea level from solar flares of small scale,” in *Proceedings of the 29th International Cosmic Ray Conference*, B. Sripathi Acharya, S. Gupta, P. Jagadeesan, et al., Eds., vol. 1, pp. 181–184, Tata Institute of Fundamental Research, Pune, India, August 2005.
 - [21] K. Toma, X.-F. Wu, and P. Mészáros, “An up-scattered cocoon emission model of Gamma-Ray Burst high-energy lags,” *The Astrophysical Journal*, vol. 707, no. 2, pp. 1404–1416, 2009.
 - [22] K. Asano and T. Terasawa, “Slow heating model of gamma-ray burst: photon spectrum and delayed emission,” *Astrophysical Journal*, vol. 705, no. 2, pp. 1714–1720, 2009.
 - [23] S. B. Cenko, et al., “The collimation and energetics of the brightest Swift Gamma-Ray bursts,” submitted to *The Astrophysical Journal*.
 - [24] S. B. Pandey, A. J. Castro-Tirado, M. Jelinek, et al., “Multi-wavelength observations of the GRB 080319B afterglow and the modeling constraints,” *Astronomy and Astrophysics*, vol. 504, no. 1, pp. 45–51, 2009.
 - [25] G. Ghisellini, M. Nardini, G. Ghirlanda, and A. Celotti, “A unifying view of gamma-ray burst afterglows,” *Monthly Notices of the Royal Astronomical Society*, vol. 393, no. 1, pp. 253–271, 2009.
 - [26] AAVSO Special Notice 72, “1RXS J023238.8-371812 rapid fading,” October 2007.
 - [27] AAVSO Special Notice 87, “New WZ Sge variable in Hya,” January 2008.
 - [28] AAVSO Special Notice 136, “Possible Nova in Car,” November 2008.
 - [29] A. Majczyna, M. Nalezyty, M. Biskup, et al., “The catalog of short periods stars from the “Pi of the Sky” data,” *New Astronomy*, vol. 13, no. 6, pp. 414–417, 2008.
 - [30] A. Schwarzenberg-Czerny, “On advantage in using analysis of variance for period determination,” *Monthly Notices of the Royal Astronomical Society*, vol. 241, pp. 153–165, 1989.
 - [31] A. Majczyna, M. Nalezyty, M. Siudek, et al., “Variable stars classification based on photometric data from the “Pi of the Sky” project,” in *Photonics Applications in Astronomy, Communications, Industry, and High-Energy Physics Experiments 2009*, vol. 7502 of *Proceedings of the SPIE*, 2009.
 - [32] M. Biskup, K. Małek, L. Mankiewicz, M. Sokołowski, and G. Wrochna, “Web interface for star databases of the “Pi of the Sky” experiment,” in *Photonics Applications in Astronomy, Communications, Industry, and High-Energy Physics Experiments 2007*, vol. 6937 of *Proceedings of the SPIE*, December 2007, 693706.
 - [33] W. Ogloza, et al., “Times of minima observed by “Pi of the Sky”,” *Information Bulletin on Variable Stars*, vol. 1, p. 5843, 2008.

Research Article

Design, Manufacturing, and Commissioning of BIRCAM (Bootes InfraRed CAMera)

Alberto Riva,¹ Paolo Conconi,² Alberto Javier Castro-Tirado,³ Filippo Zerbi,² Ronan Cunniffe,⁴ Martin Jelinek,³ and Stanislav Vitek⁵

¹ INAF—Osservatorio Astronomico di Torino, Strada Osservatorio, 20, 10025 Pino Torinese, Italy

² INAF—Osservatorio Astronomico di Brera, Via Emilio Bianchi, 46, 23807 Merate, Italy

³ IAA—Instituto de Astrofísica de Andalucía (CSIC), Camino Bajo de Huétor, 50, 18008 Granada, Spain

⁴ Blackrock Castle Observatory (Cork Institute of Technology), Castle Road, Mahon, Cork, Ireland

⁵ Department of Radio Engineering, Faculty of Electrical Engineering, Czech Technical University in Prague, Technická, 2, 166 27, Praha, Czech Republic

Correspondence should be addressed to Alberto Riva, riva@oato.inaf.it

Received 30 June 2009; Accepted 23 November 2009

Academic Editor: Joshua S. Bloom

Copyright © 2010 Alberto Riva et al. This is an open access article distributed under the Creative Commons Attribution License, which permits unrestricted use, distribution, and reproduction in any medium, provided the original work is properly cited.

This paper covers the various aspect of design, manufacturing and commissioning of the infrared camera BIRCAM, installed at BOOTES-IR, the 60 cm robotic infrared telescope at Sierra Nevada Observatory (OSN, Granada, Spain). We describe how we achieved a quality astronomical image, moving from the scientific requirements.

1. Introduction

Fast pointing robotic telescopes for transient detections have decades of tradition in astronomy. However, the first successful attempt to extend their coverage to the IR band is REM (Rapid Eye Mount) installed in 2003 at La Silla Observatory and currently still in operation. REM was conceived as the ground-based complement of the satellite SWIFT [1, 2].

Well beyond its original purposes, REM is today serving the Italian Community as a long-term monitoring facility for variable stars, AGNs, Supernovae and many other types of programs that need IR observations. Moreover, it invalidated the equation “IR equal to large telescope” and opened to a number of projects such as BOOTES-IR with its infrared camera BIRCAM.

BIRCAM is an astronomical infrared camera, installed on the Spanish BOOTES-IR telescope (Observatorio de Sierra Nevada, Granada, Spain) and is designed for the Gamma Ray Burst afterglow observations, as the original REMIR camera installed on REM.

2. General Overview of BIRCAM

BIRCAM (Bootes-IR CAMera) is a near infrared camera working in the 1–2.3 microns wavelength range. It is installed at one of the Nasmyth foci of the BOOTES-IR.

The design of the camera is strictly joined with its telescope. Indeed, they have as primary objective the acquisition of images of the GRB early afterglows.

Observations at infrared wavelengths are of great importance in astronomy. One of the most known advantages concerns the observation of the distant universe. Due to red-shift, distant objects have their spectral features moved toward higher wavelengths. If one wants to compare the rest-spectrum of a nearby galaxy in the V band (500–600 nanometers) with a galaxy at $z = 3$, he will have to observe the latter between 2000 and 2400 nanometers, that is, in the infrared region. Furthermore if the Lyman break (912 Ångströms) is redshifted to the upper limit of the visible region ($z \sim 7-8$), the object is detectable only in the infrared.

Further advantage of the infrared band with respect to the visible is the reduced absorption of the radiation by the

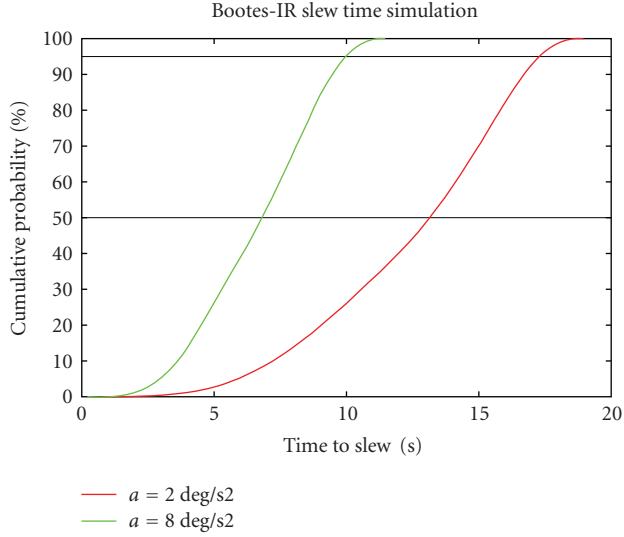


FIGURE 1: Simulation of slews times for Bootes-IR.

interstellar medium. Indeed the absorption in the classical V band is about one order of magnitude greater than the absorption in the K band. Hence any observation of sources in dusty areas such as galactic centers, clouds, and so forth, benefits of being carried out in infrared instead of visible.

Moreover, every astronomical source for which the thermal blackbody emission is relevant, if cold, will emit in the infrared band. These objects are typically brown dwarfs, planets, protostars, low mass stars.

The telescope-camera system is similar to the REM project, installed in Chile (La Silla) [3]. Both telescopes are in communication with the mission satellite SWIFT [4], that is, able to detect and give the position of a GRB within 10 seconds with a precision of 3 arcminutes. They also follow up other sources of trigger such as INTEGRAL and GLAST.

The REM telescope is able to point the source in 30–45 seconds with a field of 10 arcminutes squared. Instead, BOOTES-IR is able to point the source in 10–20 seconds with a field of 12 arcminutes squared.

The coordination between the satellite and the two telescopes located in different parts of the earth leads to the coverage of large number of the GRB within the first minute after their detection. Both telescopes are provided with a simultaneous covering of visible and near infrared wavelength range.

Two other currently active near infrared instruments in the GRB detection are: PAIRITEL [5] and GROND [6]. BOOTES-IR presents two main advantages with respect to those two instruments: the position and the speed. Indeed BOOTES-IR is situated at more than 70° in longitude compared to these two instruments. This allows observations of GRB when it is day over PAIRITEL and GROND. Regarding the speed, BOOTES-IR is faster than GROND, and this fact is essential in the observation of the first minutes after the SWIFT trigger. This can lead to a detection for faint afterglows or a catching for eventual flashes.

In order to understand how the camera has been designed we need to briefly describe the characteristics of the

TABLE 1: Basic parameters for 1024×1024 pixels HgCdTe, Hawaii-1, Rockwell detector.

Parameter	Measured value	Units
Die size	<400	mm^2
Integration capacity	1.0×10^5	carriers
Integration capacitance	18 – 35	fF
Signal Conversion Gain	3.6 – 4.8	V/e^-
Output Signal Excursion	0.4 – 1	V
Minimum Read Noise	<10	e^-
Dynamic Range	Up to 10^4	V/V
Maximum data rate	<1	MHz
Maximum Slew rate	400	nsec
Peak D* @ min Qb	$>1 \times 10^{14}$	Jones
Power dissipation	≤ 1	mW

telescope. Built by ASTELCO GmbH (Munich, Germany), this telescope is a 0.6 m Ritchey-Chrétien working with a focal number of f/8. Its direct drives were designed to allow it to slew at a maximum acceleration of 8° per second, with a maximum speed of 20° per second, being capable of pointing any part of the sky within 20 seconds. In other words, 50% of slews ends within 6.8 seconds and 95% slews within 10 seconds, see Figure 1. It has two Nasmyth foci, one of which is occupied by both the near infrared and optical cameras. Currently the second Nasmyth is not used, although future instrumentation is foreseen.

The infrared camera is equipped with a 1024×1024 pixels HgCdTe detector (Hawaii-1, Rocwell), sensible from 0.9 to $2.5 \mu\text{m}$. It has a pixel size of $18.5 \mu\text{m}$, four outputs, $<10 \text{ e}^-$ read noise, up to 1 MHz data rate per output, low power dissipation, $<0.1 \text{ e}^-/\text{sec}$ dark current at 78 K, 3.4 to $6.8 \mu\text{V/e}^-$ signal conversion gain. In Table 1 we report a summary of relevant detector data. The controller is a Skytech CTR-A1700 CCD with a 4-channel video board customised for infra-red (CDS-A100.2.00).

The pixel scale is $0.7''$, providing a field of view of $12' \times 12'$. Dithering of the images is achieved by using a rotating tilted-window (dithering wedge), placed in front of the camera, which displaces the image in a circular pattern. This allows us to later correct the sky background present in NIR images.

The electronic system that is responsible to acquire photons and translate them into readable signals has been designed and built by SKYTECH Electronic Technologies (La Spezia, Italy). The cooling down of the detector, based on a bath of liquid nitrogen, and the cryomechanical system has been designed and built by the Italian company RIAL Vacuum S.p.A. (Parma, Italy).

The optical path was designed in cooperation by P. Conconi and A. Riva, elements were procured from two companies, OptoTL (Saint-Petersburg, Russia), and Laboratorio Ottico Colombo (Rovagnate, Italy).

Finally, the integration of each subsystem and the characterization of the optomechanical properties of the camera was carried out under responsibility of A. Riva in the framework of gOlem laboratories (INAF, Merate, Italy).

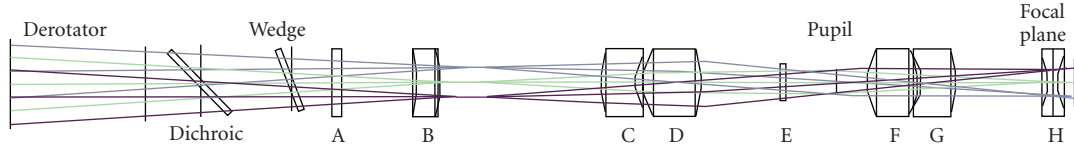


FIGURE 2: Optical layout of BIRCAM.

TABLE 2: Basic data of each lens. Note that the radii are expressed positive or negative because referred to a common coordinate system.

Name	Material	Thickness (mm)	Radius 1 (mm)	Radius 2 (mm)	Diameter (mm)
Entrance window (A)	CaF ₂	6.00	infinite	Infinite	60.00
First lens (B)	SFTM-16	14.00	86.04	69.05	50.80
1st collimator lens (C)	SFTM-16	20.00	−69.05	−28.00	50.80
2nd collimator lens (D)	CaF ₂	35.00	−32.68	59.64	50.80
1st camera lens (F)	CaF ₂	30.00	−38.76	38.76	50.80
2nd camera lens (G)	SFTM-16	20.00	28.00	69.05	50.80
Field flattener (E)	CaF ₂	6.00	37.00	−37.00	50.80

The following paragraphs contain a description of some interesting issues related to the various phases of the project.

3. Optical Design: The Answer to the Scientific Requirements

The optical system of the camera is completely transmissive, composed by optical elements of two materials: the CaF₂ (calcium fluoride) as crown, and SFTM-16 (O'Hara glass) as flint.

In Figure 2, we show the final raytracing of the camera. The first surface in the figure represents the Derotator, a mechanical flange that compensates the field rotation at Nasmyth focus. It is essentially the mechanical interface that the telescope offers to both the visible and near infrared cameras. Between the derotator and the first element of the camera (A), there are other two optical elements: the Dichroic with the function of separate the visible light from the infrared, and the Wedge that rotate along the optical axis with the function to move the viewed field at different positions on the detector. The function of the wedge is basically the dithering of the image to increase the signal to noise ratio. [7]

The first optical element of the camera is the entrance window (labelled with letter A). It is a CaF₂ disk of 60 mm of diameter and 6 mm of thickness. Before reaching the first focal position, the beam encounters the first SFTM-16 lens (B). This lens acts like a FPAL (Focal Plane Adaption Lens), and reduces the curvature of the field and the astigmatism. It is designed in order to simplify the design of the collimator. The elements labelled with C and D are the crown/flint couple that compose the collimator. Indeed their function is to form a parallel beam where the filter position (E) and the pupil stop are located.

After the pupil, there is another couple of crown/flint glasses (F and G) with the function of reforming a focalized beam, usually called camera. The last element before the focal plane is the field flattener (H). The final equivalent focal ratio

of the system is 9.35. In Table 2 we report the basic data of each lens belonging to BIRCAM.

Following the experience of REMIR camera (the Infrared camera on REM telescope) we adopted a unconventional solution for the size of the lenses. Indeed looking at the shape of most of the lenses, specially the doublets of collimator and camera, it is possible to notice that they are thicker than the lenses usually adopted in astronomical instrumentation. The choice of such large thickness is one of the most interesting features of this design. All the lenses (from B to H in Figure 2) are placed in a optical bench with a V shaped machining (see Figure 6). The combination between the precision in the cylindrical shape of each lens and the precision in the milling of the V, is a guarantee on the precision on the aligning of each lens with respect to the optical bench, and in second analysis it guarantees a good aligning between each lens.

This feature is strongly helpful in cryogenic system because the cool down process, with its related differential shrinking between each material, does not affect the global alignment of the optical train. The only attention to be paid during the manufacturing of each lens is the over-sizing of each element proportional to its coefficient of thermal expansion (CTE).

3.1. Dichroic. Special attention has been put on the design and procurement of the dichroic. It does not belong to the camera structure but it has strong effects on the final image on the detector. It is essentially a CaF₂ disk tilted by 45° along the optical axis. Its function is to separate the electromagnetic spectrum coming from the telescope into two beams. It operates both in transmission and in reflection. Due to the special interferential coating, it is able to transmit the infrared radiation and reflect the visible one. The design of the dichroic coating was done via the FilmStar32 software.

Since the visible path is materialized after a reflection it is basically undistorted, on the other hand the infrared path crosses the dichroic and the wavefront is consequently modified. From the point of view of the infrared camera the

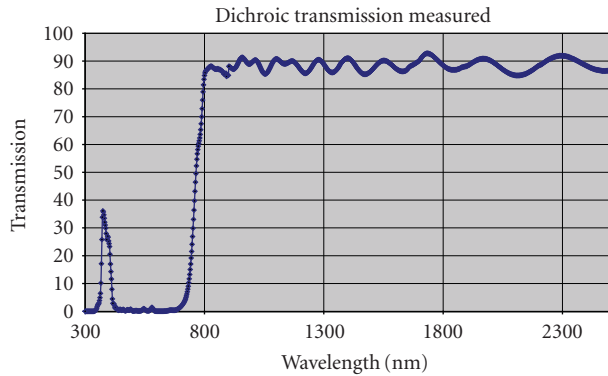


FIGURE 3: Transmission measured on final coating of the dichroic.

dichroic is essentially a plane parallel plated tilted by 45° and that implies an introduction some amount of astigmatism distortion. Following the same reasoning and looking at Figure 2, it seems that the dithering wedge acts in the same way. This effect (smaller because introduced by an angle of 20°) appears along the direction perpendicular to the tilt axis, which rotates around the optical axis. The astigmatism introduced by the dichroic is instead greater and always displaced in the same direction. In order to correct the aberration introduced, the dichroic is designed with a back cylindrical surface (concave radius of 12800 mm). The axis of the cylinder is parallel to the tilt axis.

In Figure 3 we show the final output of the dichroic coating transmission measured with a spectrophotometer available within gOlem laboratories (Merate, Italy). As requested by the final user, the transmission band starts around 800 nm, in order to include the possibility of using inside the infrared camera an UKIRT z-filter filter (central wavelength 877 nm, FWHM 95 nm, cut-on 830 nm, cut-off 925 nm).

4. Cryomechanical System

One of the features of the Nasmyth focus, during a tracked observation, is the fact that the field observed by the telescope rotates around its central point. In Bootes-IR telescope case, the problem is resolved installing a mechanical system (a derotator) that counter-rotate the mechanical interface on the mounting flange of the Nasmyth focus. This fact allows BIRCAM camera, mounted on such flange, to point at the same field, avoiding any error introduced on the images and avoiding complicate calculation on the astrometry of each acquisition. The rotation of the camera is equivalent to the field rotation at the Nasmyth focus, compensating for the change of the parallactic angle during the observation. For a fast telescope-camera project, any loss of time implies a delay on the final image, and degradation on the scientific performances.

A peculiarity of this project consists in the cooling system. It is essentially based on liquid nitrogen. Liquid nitrogen offers the possibility to avoid any further mechanism loaded at the Nasmyth focus mounting. The price to be paid for this advantage consists in the complexity of the pipe scheme on

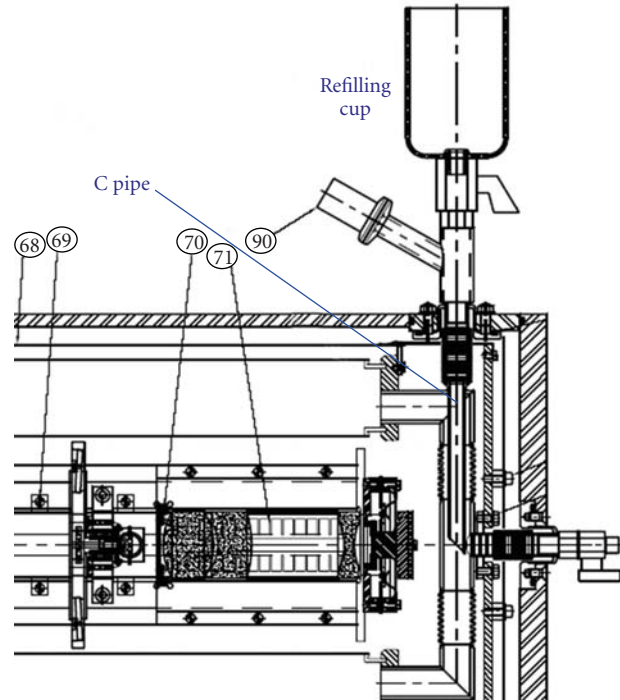


FIGURE 4: Scheme of the refilling mechanism in order to prevent leak of nitrogen during the derotation.

the loading part of the refilling system in order to compensate the rotation of the dewar, shown in Figure 4 and described below.

The camera is designed to be refilled manually every 24 hours, with the possibility of an upgrade with an automatic system. This choice fixes some constraints upon the mechanical design and production. The first and obvious implication is the presence of a tank for the storage of the liquid nitrogen. This tank is at cryogenic temperatures ($77\sim 80$ K) and it has to be placed in a vacuum vessel in order to reduce the thermal contact and the condensation of air in order to maximize the duration of the liquid form of nitrogen, and hence the cooling power.

As described above it is almost impossible to have a tank completely insulated from air if it needs a feeding pipe. Another complication given by the presence of a tank of liquid nitrogen is related to the evaporation of the nitrogen itself. The volume ratio between the gas form and the liquid form of nitrogen is about 700, so it is strictly necessary to provide the tank with a venting system. This system is complicated by the rotation of the telescope. It implies that the gaseous form of nitrogen needs to have a continuous outlet regardless of the orientation of the tank. The best solution for these cases is to have a tank with the volume doubled with respect to the filling capacity, with several outlets that stand on top of the liquid in every position of the camera. It also implies to have a system that closes the outlet that time by time stands on the bottom of the liquid and would leak nitrogen.

The solution adopted for this camera is a tank with a C-shaped pipe with outlet on top and bottom of the tank. The C present a valve on the rotational axis of the tank, which

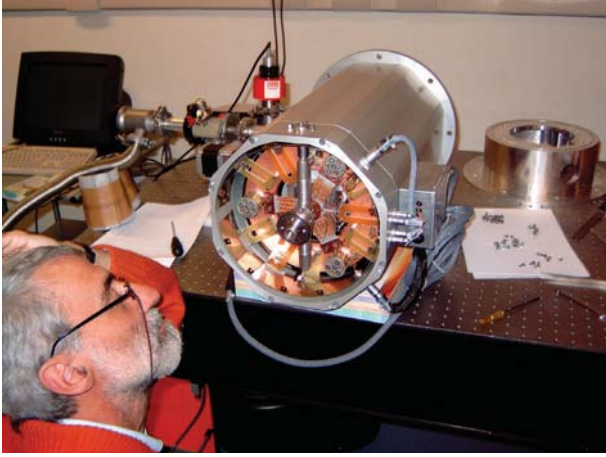


FIGURE 5: BIRCAM electronic, fiberglass, C-pipe during the assembling phase.

helps during the refilling operation, because once the tank is half-filled, the exceeding nitrogen exits the tank through the valve pointing out the end of refilling.

As mentioned before, there is another complication due to the refilling channel. In Figure 4 we show a representation of the tank scheme. It is possible to notice the refilling cup on the right with an asymmetric displacement respect to the rotational axis of the camera. The cup is connected to the axis of the tank trough a needle, that prevent any radial leak of liquid nitrogen once the camera is rotated and the cup is downside. Nevertheless, both the axial valve and the radial valve have a closing system. The overpressure due to the evaporation of the nitrogen is prevented through a valve, that gets the gas from the axial position.

5. Integration

The integration took place in gOlem facilities (Merate, Italy). Once the optical pieces, the mechanical pieces and the electronic pieces were delivered. Integration implied aligning of optical elements on the bench, characterization of the entire system under the cryo-mechanical point of view. At this stage the detector system was not part of the integration activities. This because, contractually, the camera did not include the delivery and the characterization of any scientific detector. The development of the control electronics was carried out through a multiplexer, a device that simulates the electrical scheme of the science detector. This caused problems in the verification of the accuracy of the alignment of the camera. Indeed, as described before, the optical train is designed in order to function at cryogenic temperature with infrared sources. This feature implies that the quality of the design (mechanical, optical, electronic and cryogenic) can be verified under these conditions only with the final detector.

Fortunately the multiplexer is sensitive to the visible light. Hence by means of a laser lighted in the train is possible to have an idea of the projection of a star source on the detector.

A further analysis of the system was performed through an interferometer available in our laboratories. We essentially

put the camera as a single element in the nominal focal position of the instrument, having as output the global quality of the system. One of the limits of this way of measuring was in the power of the testing source, heavily absorbed by the number and the materials of the lenses of the camera.

The most important result of these tests was that the tolerances given by the system, and in particular by the shape of the lenses and the spacers between them, was highly within the limits of the goals set for this camera.

In following Figures 4 and 5 we show some snapshot of the integration phases.

6. Tests

During the integration phase various problems were encountered. The most important fact was related to the liquid nitrogen consumption. The initial calculation carried out by RIAL technicians, and the constraints about the total space available between the telescope and the dome, lead to the dimensioning of the capacity of the nitrogen tank in order to reach autonomy of 24 hours. In the early integration tests, this goal was fully accomplished as can be seen from Figure 7. In successive characterizations tests, the performance of BIRCAM decreased until a minimum autonomy of 12 hours.

The investigation of the problem was conducted through successive steps. The philosophy in setting up the successive tests was aimed in excluding step by step any possible source of the problem.

We will not describe here all tests done in one year of trials. We will summarize below the most interesting.

- (i) Leak test: we measured any possible vacuum leak with specific helium-based leak-detector. This type of dewar is sensitive to wrong positioning of sealing o-rings.
- (ii) Weight test: one of the probable cause of the low autonomy could be the formation of ice inside the tank. The measure of weight of BIRCAM during the first filling operation shown that the real load of nitrogen was compliant with the design.
- (iii) Extra radiation: one of the possible agents that increased the consumption could be an increased amount of radiation going in the camera through the entrance window. The measure with the window and with an aluminium disk was substantially the same.
- (iv) Wrong shielding: some modification on original radiation shield suggested the possibility that the new configuration increased the radiation between the external and internal part of dewar.
- (v) Extra current: the multiplexer adopted for electronic test was operated in a different configuration with respect to the science detector, increasing the nitrogen consumption.
- (vi) Thermal simulation: we simulated via Finite Elements Analysis (FEA) software the consequence of an unwanted thermal bridge between the dewar and the shield.



FIGURE 6: Assembling of lenses and spacers on the V-cave of the optical bench.

- (vii) Shield configuration: we added and removed reflective layers of thermal shield in order to evaluate the radiation contribution.
- (viii) Tank pressure: we tried different values of pressure inside the nitrogen tank in order to evaluate if nitrogen vapours could contribute to the global thermal balance.

All tests helped in understanding and improving the performances, but at the current date the 24-hour limits is not reached. So improvements were achieved but not allowing to solve the main problem. We stated that the problem stands in the dimensioning of the tank. Future upgrades (now under study) could be developed expanding the tank with an additional stage. We show in Figure 8 as example the temperature and pressure graphs for one of the intermediate test.

7. Commissioning

After the phase of testing and setting up, the camera was accepted and delivered to Granada (IAA) Laboratories to undergo the phase of the final integration. In this phase, carried out by R. Cunniffe and A. Riva, the substitution of the multiplexer with the final scientific detector, the 1024×1024 pixels HgCdTe, Hawaii (Rockwell, Thousand Oaks, CA, USA) was operated. This task was completed using the clean room and the optical equipment of the IAA. This allowed to perform a further test in visible light, using the residual sensitivity to visible light (laser beam) of the Scientific Detector. In addition we performed an infrared light test, using a pinhole placed in front of the camera, with a common candle as light source.

After a obvious phase of tuning of the electronic readout devices, the camera, in April 2008 was able to be installed at the Nasmyth focus of BOOTES-IR. This stage was dedicated to the setup of the Linux software dedicated to this experiment. Indeed the SKYTECH company provided only a Windows version with the capability to read only one

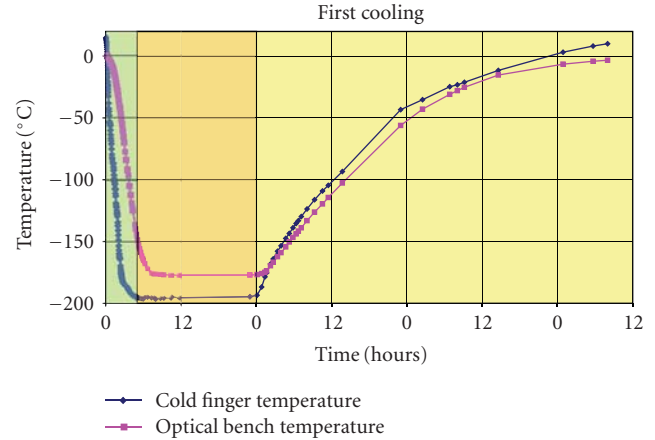


FIGURE 7: Graph of the temperatures during a complete cycle of cooling down and warm up on BIRCAM. Cold finger is located behind the detector. Optical bench sensor is located next B lens in Figure 2. The first part (first band, about 5 hours) is the cooling down phase, the second part (second band, until first 24 hours) is the stationary cold phase, the last one (about two days and half) is the warm up phase.

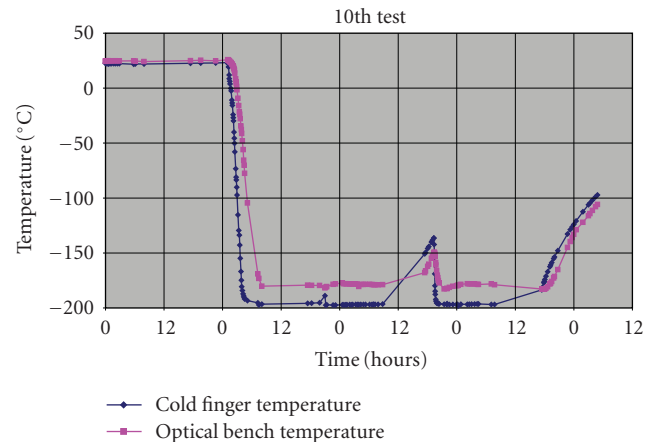


FIGURE 8: Temperature graph of a laboratory intermediate test of endurance. After the first cooling down, the camera was maintained at low temperature with successive refilling. The little bump in the middle of the plateau reflects a lack of refilling (night time).

of the four quadrant in a single exposure. The final tuning of Linux is still to be completed, however the 16th October 2008 the BIRCAM + BOOTES-IR teams obtained the first scientific light in J band of the well known M82 galaxy, shown in Figure 10.

The first light images were taken with an experimental software package and have shown that many things have to be solved yet. The estimate of a limiting magnitude of one of these images is $J \sim 16$ for a 3×60 seconds exposures.

8. Lessons Learned

As stated at the beginning the BIRCAM project was followed end-to-end from the design to the final integration and

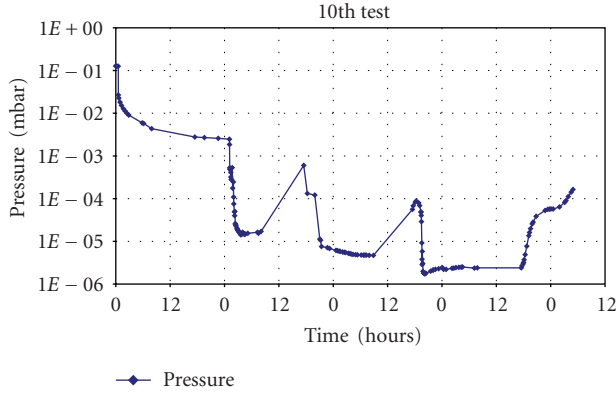


FIGURE 9: Pressure graph of intermediate test of endurance. This graph refers to a different test respect to the previous. The first part is the pumping of the system with a turbomolecular (two stages) pump, the second part (after first 24 hours) is the cooling down phase. Intermediate bumps reflect the end of the nitrogen in the fuel tank (again night time).

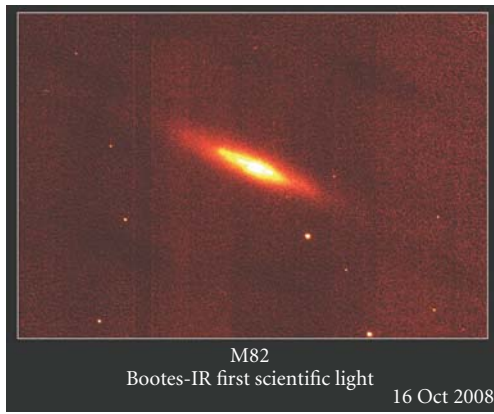


FIGURE 10: First scientific image of BIRCAM at BOOTES-IR telescope.

testing. During each phase of the project, we had the great opportunity of learning some important lessons about this kind of infrared camera for small telescope.

Most obvious and generically related to any astronomical instrument is that it is produced in a single unit (or at most a few). This fact marks a difference between astronomical instruments devices of mass production or from the prototype production. With the mass production, we concentrate on the statistics of possible failures and weak points of the series of machines. While building a prototype instead we concentrate more on enabling technologies more than on the functions of the final product.

If we look deep into BIRCAM project, we learned some lessons.

- (i) Coordination between the telescope team and the camera team is essential in order to avoid unpredicted constraints (like for instance the space available between the telescope and the dome).

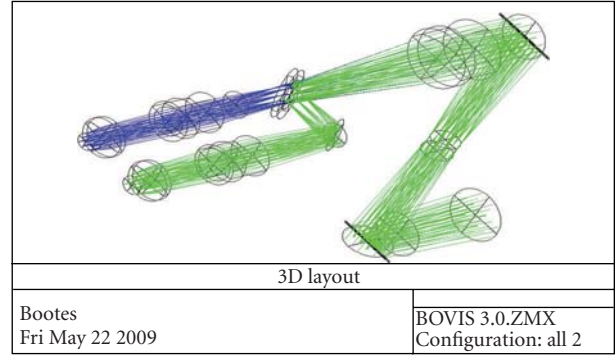


FIGURE 11: Schematic view of the future visible arm of BOOTES-IR.

- (ii) The system engineering of the project must be kept into a scientific institution and not outsourced to industry. These kind of instruments needs an adequate amount of time dedicated to tests and optimizations.
- (iii) Every constraint parameter must be carefully overdimensioned where possible. For instance, if the nitrogen consumption should be daily-based, the designer needs to assume some contingency parameter in dimensioning the tank capacity (i.e., doubled).

In particular, electronic subsystem problems taught us the following:

- (i) Due to the lack of the science detector, a specific work package must be allocated for the tuning of bias and offset values of the electronic acquiring system.
- (ii) The cabling is essentially fragile and it implies a great care during each operation of mounting and dismounting of the camera; on the other hand the thermal mass of the cabling induces a mechanical constraint on the deploy of the cables, increasing the probability to make some dangerous bends in the cables themselves. Specific care must be kept in the design phase, introducing where possible the option to disconnect cables between the dewar and the detector board.
- (iii) Due to the complexity of windows-based and Linux-based systems, specific attention must be kept in design the software. Where possible, a dedicated team should simulate and optimize the acquisition process in both systems.

9. The Optical Arm

Our team is now working to the new instrument that completes the BOOTES-IR telescope. As its “cousin” REM, this telescope has a visible arm [8]. The aim of this arm is to extend the field of monitoring at the visible range of the GRB afterglow. The visible arm will be fed by the transmission of the Dichroic in Figure 1. A preliminary study of the arm foresee a fold mirror that drives the light into a collimator. This collimator produce a beam that can be

split into two arms through another dichroic that can divide the light into two arms, a $B + V$ and a R . In the conceptual study, these two arms are foreseen to hit the same detector, a CCD $2\text{ k} \times 4\text{ k}$ like the commercial ones, into two quadrants following previous studies [9].

The cost evaluation and the optimization of the optical elements is now argument of study of the Italo-Spanish working group.

10. Conclusions

The conclusion of this phase of the project is the beginning of the next phase. We strongly believe that such instrumentation require a lot of care and needs a strong team well coordinated. The next step stands in giving to the Spanish Astronomical Community, and more in general to the Astronomical community a new modern and powerful observing facility, possibly joined to the already existing network of the GRB community, and the robotic and remote telescopes community.

Acknowledgments

The authors need to make a special thank to the collaborators that physically made the camera: M. Canetti and A. Battocchio from RIALVACUUM, M. Gemma and A. Carbone from SKYTECH, G. Colombo and all their collaborators; the REM team for the filters providing, Favio Bortoletto for his valuable and decisive support in solving big electronic troubles. The authors thank F. Aceituno, C. Cárdenas, S. Castillo, J. Gorosabel, S. Guziy, P. Kubánek, T. Mateo Sanguino, J. C. del Toro and last but not least A. de Ugarte Postigo for the support during various phase of manufacturing and testing. This development was supported by Spanish Ministry of Science and Technology's projects AYA 2004-01515 and AYA 2007-63677.

References

- [1] F. M. Zerbi, G. Chincarini, G. Ghisellini, et al., "The REM telescope: detecting the near infra-red counterparts of Gamma-Ray Bursts and the prompt behavior of their optical continuum," *Astronomische Nachrichten*, vol. 322, no. 5-6, pp. 275–285, 2001.
- [2] S. Covino, F. M. Zerbi, G. Chincarini, et al., "The multi-frequency robotic facility REM: first results," *Astronomische Nachrichten*, vol. 325, no. 6–8, pp. 543–548, 2004.
- [3] F. M. Zerbi, G. Chincarini, G. Ghisellini, et al., "The REM telescope: detecting the near infra-red counterparts of Gamma-Ray Bursts and the prompt behavior of their optical continuum," *Astronomische Nachrichten*, vol. 322, no. 5-6, pp. 275–285, 2001.
- [4] N. Gehrels, G. Chincarini, P. Giommi, et al., "The Swift Gamma-Ray burst mission," *Astrophysical Journal*, vol. 611, no. 2, pp. 1005–1020, 2004.
- [5] J. S. Bloom, et al., "Autonomous observing and control systems for PAIRITEL, a 1.3 m infrared imaging telescope," in *Astronomical Data Analysis Software and Systems XV*, vol. 351 of *ASP Conference Series*, p. 751, San Francisco, Calif, USA, 2006.
- [6] J. Greiner, W. Bornemann, C. Clemens, et al., "GROND—a 7-channel imager," *Publications of the Astronomical Society of the Pacific*, vol. 120, no. 866, pp. 405–424, 2008.
- [7] F. Vitali, F. M. Zerbi, G. Chincarini, et al., "The REM-IR camera: high quality near infrared imaging with a small robotic telescope," in *Instrument Design and Performance for Optical/Infrared Ground-based Telescopes*, vol. 4841 of *Proceedings of SPIE*, pp. 627–638, 2002.
- [8] G. Tosti, M. Bagaglia, C. Campeggi, et al., "The REM optical slitless spectrograph (ROSS)," in *Ground-Based Instrumentation for Astronomy*, vol. 5492 of *Proceedings of SPIE*, pp. 689–700, June 2004.
- [9] A. Riva and P. Spanò, "Compact multi-band visible camera for 1m-class fast telescopes," in *Ground-Based and Airborne Instrumentation for Astronomy II*, vol. 7014 of *Proceedings of SPIE*, pp. 1–9, Marseille, France, June 2008.

Research Article

Robotic and Non-Robotic Control of Astrophysical Instruments

Gerd Küveler,¹ Van Dung Dao,¹ Axel Zuber,¹ and Renzo Ramelli²

¹ Hochschule RheinMain, Institut für Automatisierungsinformatik, Am Brückweg 26, 65428 Rüsselsheim, Germany

² Istituto Ricerche Solari Locarno, Via Patocchi, 6605 Locarno, Switzerland

Correspondence should be addressed to Gerd Küveler, gerd kueveler@hs-rm.de

Received 2 June 2009; Revised 20 October 2009; Accepted 24 December 2009

Academic Editor: Taro Kotani

Copyright © 2010 Gerd Küveler et al. This is an open access article distributed under the Creative Commons Attribution License, which permits unrestricted use, distribution, and reproduction in any medium, provided the original work is properly cited.

We present a system of device control programs, developed for the solar observatory at Locarno/Switzerland (IRSOL). Because these programs are implemented as servers—clearly separated from the higher levels—scientific instruments, for example, telescopes, can be operated both in a user-controlled mode (GUI, *telnet*) and in a fully automated mode by use of a script. Astronomical instruments such as telescopes or spectrographs will be responded to by ASCII command strings, which are the same for all clients. In case a device control software does not support multiclient operation or in case it is used together with other devices in a complex measuring procedure, it is worthwhile implementing an intermediate layer that relieves the individual device control servers of routine tasks and provides for a safer operational sequence. In addition, the system may make use of an easy-to-learn script language specialised for controlling fully automated processes.

1. Introduction

An automation of technical procedures generally leads to

- (i) a discharge of routine tasks,
- (ii) a higher operating speed,
- (iii) more reliability and precision,
- (iv) easier handling,
- (v) avoidance of costs and damage.

At large automation effects a higher productivity.

For scientific laboratories, here particularly in astrophysical observatories, some of these reasons may be specified.

- (i) If the different levels of automation are clearly separated, it is possible to operate the various instruments (telescope(s), spectrograph(s), cameras(s), etc.) via graphical user interfaces (GUI) and text-based interfaces such as *telnet* or *netcat* at the same time.
- (ii) The observer is able to combine several instruments of an observatory (or even several observatories) in order to perform a complex measurement procedure by making use of scripts.

- (iii) An automatic execution of calibration procedures and of routine jobs (e.g., telescope and dome to target or home position) saves time and avoids maloperation and possible damage (e.g., moving the telescope while the shelter is not sufficiently opened).

The following features are not primary intentions of automation but desirable properties:

- (i) It is advantageous to separate the various levels of automation in order to design a system more clearly arranged and in order to facilitate the exchange of defect or out-of-date components (hardware and software) without affecting the overall system.
- (ii) If possible, industrial hardware standards should be used in order to avoid costs and to preserve a good chance of external support.
- (iii) The same is true for using standard and easily portable programming languages (like C, C++, Java) and software tools (like LabVIEW). Furthermore, it will be easier to find the programmer's successor.
- (iv) The higher levels of automation software (GUI, scripts, etc.) should run under the standard operating systems Windows and UNIX/Linux.

- (v) Standard information transfer and data communication protocols should be used.
- (vi) It is possible to create detailed logs (files, databases, etc.) that enable keeping track of what happened during the data acquisition in a very reliable way.

In this paper, we describe an automation system, developed for the Istituto Ricerche Solari Locarno (IRSOL), a solar observatory which meets the demands mentioned above. It consists of device control programs that operate the various instruments at their low level, of the *command server* which coordinates the interaction between several instruments and the user interfaces. Moreover, the *command server* is able to absorb numerous routine tasks, such as authorisation and syntax check. A special script language (AMI) was developed to allow for an easy assembly of complex measuring procedures. Our new telescope control software will be used as an example for a device control program.

2. Robotic and Non-Robotic Control

Ideally, automated devices will work in both a robotic and a non-robotic modes. This means that an instrument may be handled by a human user (non-robotic mode) as well as by a script in order to run a measurement procedure, optionally also in cooperation with other instruments (robotic mode). This can be achieved by means of a complete separation of the actual control hardware and software from the higher levels. If there are no special real-time requirements given, the communication with user interfaces or scripts of all kinds should follow the standard data communication protocol TCP/IP. Any control software should be designed as an automat with a definite number of functions. All of these functions can be activated through certain commands transferred via Ethernet from a remote computer. Due to modern programming languages and today's powerful hardware, any control function may be performed in a parallel mode, provided that there are no conflicts. Commands may be binary based or consist of ASCII-strings. Statistically, binary numbers are more compact than ASCII numbers but binaries have some important disadvantages with respect to data exchange: not all programming languages and tools use the IEEE format for the internal representation of floating point numbers. Misunderstandings whether a date is float (real, 32 bit) or double (64 bit) may arise and even integer numbers which are longer than one byte can lead to confusion because Intel processors—as opposed to most others—use byte swapping. In contrast, ASCII-strings are unique, independent of software and hardware. Moreover, ASCII-strings allow easy testing of commands by using a standard text-based interface such as *telnet*. Consequently, by using ASCII-strings, the access from all kinds of user interfaces and scripts is the same.

In this paradigm, any device control software is a server. Ideally, the server should be capable of handling multiple clients. This means that more than one high-level interface may simultaneously communicate with the control device, for example, a script and a GUI and *telnet*.

3. Command Server

Control programs for different instruments have many functions in common. Moreover, problems may arise if several clients communicate with the same device at the same time or if a device is involved in a complex procedure, jointly with other devices. For this reason, we developed a program system which generates an intermediate layer between the device control layer and the high-level layer (user interface, client). This program system we call *command server* (*cs*). It is written in Java and thus executable on each computer on that the Java Runtime Environment (JRE) is installed. The *cs* is divided into the modules *command* (which exists only once) and *dispatcher* (which will be created for any application that connects to the *cs*). Between these modules a system of buffers will be established, one for each application.

The *cs* communicates with all applications currently active via TCP/IP. The application is typically a *device control* software. Every application first needs to register at the *cs* in order to get an application number or name as a link to its socket (IP address and port number). Subsequently, the *cs* creates a command buffer (*queue*) and a *dispatcher* for this application in a separate thread.

The server-module *command* of the *cs* looks for commands dispatched by a user interface or by a script. Each command will be checked for formal validity and, if the check succeeded, will be distributed to the addressed application. If a valid status query or an abort commands occurs it will be directed immediately to the *device control* program. Commands effecting an action (e.g., “telescope go to set point”) will be buffered and delayed upon completion of the previous command. Queued commands are prioritised (all priority 0 commands will be executed prior to the first priority 1 commands). Many commands are management commands. These are merely dedicated to the *cs*, not to an application (e.g., “add a new application,” “remove a command from the queue,” “ask for a completion report of a previously given command”). Each command will be confirmed immediately. Syntactically wrong or illegal commands will be sent back to the client with an error byte.

The *dispatcher* sends the next command from the *queue* to its application and waits for the completion report. A command to an application must adhere to the format

application no. or name | *priority* | *command name* |
arbitrary string (may be lacked) | “<CR>”

“|” represents a blank.

All commands usually consist of ASCII-characters found on any computer keyboard. In exceptional cases, binary parameters are possible as well. The different components of a command are always separated by at least one blank. Any command string and receipt should be terminated by a carriage return. Other terminators can be declared in a setup-file.

The *dispatcher* only sends the command name and the following string to the application, for example, *klambda 08 630.2123* (spectrograph go to wavelength 630.2123 nm, grid order 8). The report, returned by the application upon execution of the command, will also be stored in the queue

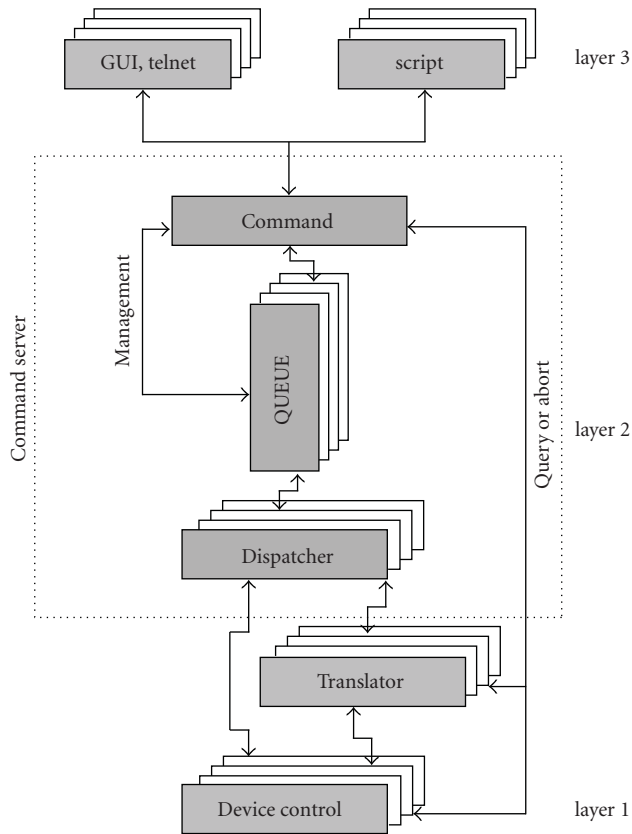


FIGURE 1: Three-layer-model of automation.

and may be requested by any client at any time. If one cannot exert influence on the kind of communication of the *device control*, for example, because it is a commercial product, a *translator* may be necessary. This will be the case, for example, if the device communicates via an industrial field bus or if a digital output bit is set instead of sending a completion report. Therefore, a *translator* is always a very individual software, sometimes supplemented by a special hardware, and thus not part of the *command server*.

Figure 1 shows our three layer automation model and illustrates the functioning of the *command server*.

The major properties of the *command server* are the following.

- (i) Clear separation of the different levels of automation.
- (ii) A central server coordinates and supervises all distributed activities of a scientific measurement procedure, with various instruments participating.
- (iii) Uniform communication structure between command level (clients) and device control level.
- (iv) Communication via TCP/IP.
- (v) Standard mechanisms such as command priorities and queues, execution reports, premature aborts, and status commands do not need to be invented anew for each application.

- (vi) Multiple clients may communicate with the same application at the same time.
- (vii) Simple ASCII command structure which is accessible by each conceivable interface (consoles such as *telnet* or PuTTY (Windows), *script*, GUI).
- (viii) A crash of one of the applications currently controlled will be noticed immediately.
- (ix) A password protection distinguishes between normal users with restricted rights and system managers being allowed to administrate users and to change setup settings.
- (x) Parameter check of a command if a parameter range was specified before.
- (xi) Status broadcasts every few seconds (adjustable) keep all clients informed that are connected with the same application.
- (xii) Instances (e.g., different observatories scattered over the world, which accomplish a joint observation program) share a uniform communication interface for all tasks of automation.
- (xiii) Possibility of chatting with other active users.
- (xiv) Written in Java and thus largely independent of the operating system (Windows, Linux/UNIX, ...).

The *cs* commands are not intended to be given directly in ASCII format by a human user, aside from testing purposes. Such commands typically are hidden behind a GUI or they are elements of a script.

4. Script Language

Whereas the *command server* is still being tested and improved, the development of a script language called AMI convenient to run full automatic measurement procedures and permanent robotic applications is already completed [1]. Of course it is possible to use other script languages like Perl in order to communicate with the *cs* but AMI is much easier to learn for technicians or astronomers who are less familiar with programming. Furthermore, it has some features of interprocess communication and functions for easy conversion of all data types, especially to and from strings, which make AMI appropriate for its main purpose.

AMI means Automation Macro Interpreter and is a "C"-like script language for the operating systems Windows and UNIX/Linux. The language contains statements, functions, and control structures which are explained in a help file. A variable must be declared with its data type (see below) before its first usage. The language supports commands to the shell in wait and no-wait modes with parameter passing. A result string can be returned via an unnamed pipe allocated by AMI, but pipes work only if the remote process runs on the same computer. The AMI-function *tcpclient()* is of much more importance, because it is able to send messages also to a distributed remote process via TCP/IP. The syntax for sending such commands is


```
tcpclient < IP-address >, < port >,
< message string >, < return variable >;
```

The *message string*, for example a command, will be sent to the remote process, for example, the telescope control. Afterwards *tcpclient* waits for the report and stores it within the string variable *return variable*. Thus AMI is able to keep contact with all distributed processes in an easy way and to coordinate them.

AMI needs no special installation. Only the executable program and the help file are required. One may download these files together with some short examples of AMI scripts (*.ami) from our web page [2].

The most important properties of AMI are the following

- (i) An AMI script <macro.ami> will be started by input of *ami < macroname >< parameters >*.
- (ii) Input of *ami -?* shows a short but complete description of AMI.
- (iii) \$[1-10] mark the external parameters which are passed to the AMI script from the shell.
- (iv) It is possible to start an AMI-script via internet browser. The transfer of parameters via CGI-interface will be supported.
- (v) Comments have to be initialised and terminated by the character '#'.
- (vi) AMI-variables must be declared initially. Valid data types are *string*, *int*, *float*, *complex*, *date*, and *time*.
- (vii) AMI provides functions to read and write (console and files).
- (viii) There are many functions to change data types.
- (ix) AMI has C-like loop- and-if-structures which may be nested.
- (x) AMI has the arithmetic operators +, −, *, /, % and ^ (power).
- (xi) AMI has the usual mathematical functions.
- (xii) AMI has a UNIX-like test-function in order to test properties of files and strings.
- (xiii) AMI is able to start programs via shell in wait and no-wait (parallel) modes with parameter passing.
- (xiv) AMI supports pipes in order to return result-strings from a remote process.
- (xv) AMI provides a client (-command) in order to send commands via TCP/IP to a remote process and to receive confirmation of operation (report) as a string.
- (xvi) AMI returns a message in case of a syntax error.
- (xvii) AMI versions exist for UNIX/Linux and Windows.

5. Primary Image Guider as an Example of a Device Control

The control system of the main solar telescope of the Istituto Ricerche Solari Locarno (IRSOL) [3] is over ten years old and was in need of renovation for some reasons. Whereas the sensor-system [4] has remained unchanged due to its continually satisfying performance [5], the revision was prompted by outdated computer hardware and by increased demands regarding communication with other hardware and software. Ten years ago the GUI of the old control system called “Primary Image Guider (PIG)” was the most important user interface [6], whereas today the remote access via TCP/IP from different clients—occasionally at the same time—becomes ever more important.

In its former version, the telescope control part and the GUI of PIG were integrated in the same LabVIEW program. The digital outputs to send signals to the telescope control hardware were part of an ISA bus plug-in card within the PIG PC. This outdated combination of components gave reason to establish a new version of PIG with more functions and complete separation of the different levels of automation.

The new hardware we used to perform our telescope control program is a Compact Real-Time PowerPC Controller (cRIO-9012) from National Instruments. Bundled with the I/O-Modules needed for this project, it is integrated in a small chassis of $18 \times 9 \times 9 \text{ cm}^3$. The new telescope control software now running on this module is also written in LabVIEW. All software for this module has to be developed on a Windows PC and accordingly downloaded via TCP/IP in conjunction with a small real-time operating system. Thus the postulation of using industry standards is satisfied.

The control software is split up into a number of functions which all run parallel in separate threads. They can be called by the ASCII-commands. We do not like to describe the various functions of a solar telescope control system here in detail and refer to [4, 7]. An actual listing of all present PIG commands is specified in Table 1. The syntax has been chosen in order to be compatible with the software used by the Zurich Imaging Polarimeter (ZIMPOL) system, which is largely used at IRSOL [8] and which is also intended to be used with the new GREGOR solar telescope at Tenerife.

Since the functions have been designed independently, subsequent programmers will find it easy to create new ones. Higher level functions such as “position on the solar disk in other coordinates than (x, y)” or “store object position in a table” are requirements of a client. A GUI for Windows and UNIX/Linux which provides such higher level functions has also been written in LabVIEW. Since the PIG control software has been designed as a multiserer, it may be accessed by multiple clients simultaneously. If a command prompts physical access to the telescope motors, these are temporarily locked for other clients. Simple applications may be executed without the assistance of the *command server*. In cooperation with other device controllers PIG may be integrated in fully automatic measurement procedures guided by a script, which may be written in AMI. Especially if the procedure is complex, possibly with other observatories involved via the internet, the employment of the *command server* is very

TABLE 1: Commands and functions of the telescope control system.

pigoff	Turn off guiding, release motor
pigxr?	Query for actual x position [1/10 arcsec]
pigyr?	Query for actual y position [1/10 arcsec]
pigx=%d	Select x position (set point) [1/10 arcsec]
pigy=%d	Select y position (set point) [1/10 arcsec]
pigactu	Let actual position be set position
pigenc=%d	Set guiding mode (0 = sensor, 1 = encoder guiding)
pigenc?	Query for guiding mode (0 = sensor, 1 = encoder guiding)
pigxs?	Query for selected x position
pigys?	Query for selected y position
piggo	Guide to selected position
piggf	Guide to selected position and follow solar rotation
pigrunxy	Go to selected position but do not guide
pigabort	Abort going to selected position (Stop guiding mode)
pigmco=\$m\$nn	Manual control commands [m = speed, nn = direction]
piggmode?	Query for motor status (possible answer 0–6)
	0 = motor is free
	1 = manual control active
	2 = guiding without following solar rotation
	3 = guiding and following solar rotation
	4 = flatfield mode active
	5 = go to sun active
	6 = go to home position active
pigi?	Query for intensity
pigthimin=%d	Set threshold for minimum intensity
pigimin?	Query for minimum intensity
pigthdelta=%d	Set threshold for guiding accuracy [1/10 arcsec]
pigthdelta?	Query for threshold of guiding accuracy [1/10 arcsec]
pigloops=%d	Set number of averagings for position sensor (default is 500)
pigloops?	Query for number of averagings of position sensor
pigffmx=%d	X-length of flatfield area [1/10 arcsec]
pigffmy=%d	Y-length of flatfield area [1/10 arcsec]
pigffms=%d	Flatfield motor speed (1 = slow, 2 = medium)
pigffm?	Query for all flatfield parameters (e.g., 3000,4000,2)
pigstartffm	Start flat field mode
piggosun	Telescope go to sun
piggohome	Telescope go to home position
pigsb?	Query for status

The prefix “pig” may be omitted. Formats of replies (examples):

Command: pigoff

Reply: pigoff:done

Command: pigxr?

Reply: pigxr = 2342.

helpful. Figure 2 illustrates the integration of the telescope control system into the observatory environment.

6. Conclusions

In most cases, the ubiquitous Ethernet with TCP/IP protocol is sufficient for the networking of automated astronomical devices. On this level, real-time problems rarely arise. The actual device control (sometimes real-time) software

should be designed as (multi)server(s). Accordingly, the user interfaces are clients. Between these two layers, we implemented an additional layer which relieves the lower layer and provides for additional security. Besides, this layer (*command server*) is capable of joining different institutions, such as observatories, to combined measuring programs. Safety precautions must be met, even though they are not as extensive as in commercial applications because the transmitted contents are not sensitive.

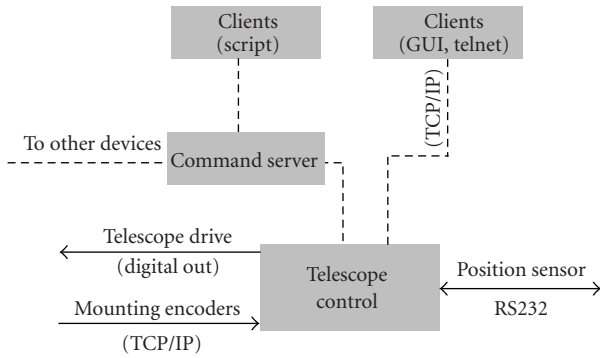


FIGURE 2: Integration of the telescope control system into the observatory environment.

Finally we would like to suggest that programs doing calculations of potential interest to many persons, such as conversion of coordinates or positions of objects, should be arranged as servers accessible via Internet sockets (a sort of astronomical “cloud computing”) or via download. Unfortunately, many interesting web applications are currently only available in an interactive mode.

References

- [1] G. Küveler and A. Zuber, “Eine Prozedursprache zur Steuerung vollautomatischer Prozesse,” *Automatisierungstechnische Praxis*, vol. 46, no. 8, pp. 20–23, 2004.
- [2] <http://www.iai.fh-wiesbaden.de/ami/>.
- [3] M. Bianda, R. Ramelli, A. Feller, J. O. Stenflo, and G. Küveler, “Instrumental developments at the Gregory-Coudé telescope at IRSOL,” in *Proceedings of the Workshop on Modern Solar Facilities—Advanced Solar Science*, F. Kneer, K. G. Puschmann, and A. D. Wittmann, Eds., Göttingen, Germany, 2007.
- [4] G. Küveler, E. Wiehr, D. Thomas, et al., “Automatic guiding of the primary image of solar Gregory telescopes,” *Solar Physics*, vol. 182, no. 1, pp. 247–255, 1998.
- [5] G. Küveler, E. Wiehr, and M. Bianda, “Automatic guiding of solar Gregory telescope,” in *From the Gregory-Coudé. Telescope to GREGOR: A Development from Past to Future*, F. Kneer, E. Wiehr, and A. D. Wittmann, Eds., vol. 324 of *Astronomische Nachrichten*, no. 4, p. 308, 2003.
- [6] G. Küveler, E. Wiehr, and M. Bianda, “Eine sensorgestützte Computersteuerung für Sonnentelkope,” *Automatisierungstechnische Praxis*, vol. 42, no. 7, pp. 50–54, 2000.
- [7] <http://www.mnd-umwelttechnik.fh-wiesbaden.de/pig/>.
- [8] A. M. Gandorfer, H. P. Povel, P. Steiner, et al., “Solar polarimetry in the near UV with the Zurich Imaging Polarimeter ZIMPOL II,” *Astronomy and Astrophysics*, vol. 422, no. 2, pp. 703–708, 2004.

Research Article

The Photometry Pipeline of the Watcher Robotic Telescope

A. Ferrero,¹ L. Hanlon,¹ R. Felletti,¹ J. French,¹ G. Melady,¹ S. McBreen,¹ P. Kubánek,² M. Jelinek,² B. McBreen,¹ P. Meintjes,³ J. Calitz,³ and M. Hoffman³

¹Space Science Group, School of Physics, University College Dublin, Ireland

²Instituto de Astrofísica de Andalucía, C/ Bajo de Huétor 50, ES 18008 Granada, Spain

³Physics Department, University of the Free State, Bloemfontein 9301, South Africa

Correspondence should be addressed to A. Ferrero, alejandro.ferrero@ucd.ie

Received 30 June 2009; Accepted 2 December 2009

Academic Editor: Alberto J. Castro-Tirado

Copyright © 2010 A. Ferrero et al. This is an open access article distributed under the Creative Commons Attribution License, which permits unrestricted use, distribution, and reproduction in any medium, provided the original work is properly cited.

The Watcher robotic telescope was developed primarily to perform rapid optical follow-up observations of Gamma-Ray Bursts (GRBs). Secondary scientific goals include blazar monitoring and variable star studies. An automated photometry pipeline to rapidly analyse data from Watcher has been implemented. Details of the procedures to get image zero-point, source instrumental measurement, and limiting magnitude are presented. Sources of uncertainty are assessed and the performance of the pipeline is tested by comparison with a number of catalogue sources.

1. Introduction

Robotic telescopes offer full automated control of an observatory and its instruments. The key ability of a robotic system is that it can observe without any human intervention. The system generates its own observing schedule according to the priority established from user-specified criteria, such as the altitude of the target. Scheduling is flexible, responding to new requests or events as necessary, or to feedback from environmental monitoring sensors. The system can also be accessed and controlled remotely if required and provide remote users with access to data.

A large proportion of the effort in developing new ground-based astronomy facilities has traditionally been directed towards building larger aperture telescopes. However, at the other end of the scale, an increasing number of scientific programmes are being carried out by smaller instruments operated in an automated or robotic manner. Research goals requiring long time baselines or rapid response times are hampered by the inflexibility and limited availability of observing time at large telescopes. Considerable effort is therefore currently being devoted to developing robotic systems better suited to the specific scientific requirements of such programmes. Robotic telescopes have become increasingly sophisticated due to a variety

of technological advances, in particular the Internet, the widespread availability of powerful, affordable computers since the early 1990s and the increasing sophistication of the amateur community, which has opened up new markets for manufacturers of components such as telescope mounts. Reviews of the technological and scientific advances made in robotic telescope astronomy at various times since the mid-1990s are given in [1–4].

The main advantage of robotic telescopes lies in their flexibility, which allows variability to be studied in ways that are not possible with traditional facilities [5]. Studies of active galactic nuclei [6], variable stars [7], and extra-solar planetary transits [8] greatly benefit from long-term monitoring programmes that robotic facilities can carry out so effectively. In addition, their rapid, automated response capabilities make them ideally suited to observations of transient sources like supernovae and γ -ray bursts (GRBs). Whereas manually operated telescopes can respond on timescales of minutes at best, robotic telescopes can begin observing the target in seconds, opening up a previously unexplored regime in the time-domain study of GRBs [9]. Other areas in which robotic telescopes excel are cosmological surveys [10] and calibration tasks such as extinction monitoring.

2. The Watcher Robotic Telescope

The goal of the Watcher project was to develop a fully robotic optical telescope system capable of responding to GRB alerts generated by orbiting satellites, in particular the *Swift* and *INTEGRAL* missions. The main design drivers from the science point of view were that the system should be fast and sensitive enough to explore associated optical emission in the early-time regime, tens of seconds or less after the initial trigger, ideally while the burst is still active in γ -rays. The technical challenges in carrying out such observations have meant that very early-time optical emission had been very sparsely studied in the pre-*Swift* era, and as a result poorly understood. The unprecedented rate, speed, and accuracy of GRB positions from *Swift* [11] and *INTEGRAL* [12] allows for extensive study of their early optical emission. While a number of robotic telescopes dedicated to GRB follow-ups were already in operation, a world-wide network of such instruments is required in order to maximise coverage of the night sky and gather as much early-time optical data as possible. A suitable instrument located at an appropriate site could contribute significantly to these studies.

2.1. Boyden Observatory. The site selected for Watcher was the Boyden Observatory situated at an altitude of 1387 m in South Africa's Highveld region, 26 km from the city of Bloemfontein at coordinates 29° 02' 20'' South, 26° 24' 20'' East. Boyden was initially established as Harvard University's southern observatory in Peru in 1889 and was relocated to South Africa in 1927. After a number of years of being operated solely by Harvard, the observatory was subsequently run by an international consortium, including Ireland's Dunsink Observatory, until 1976, when it was presented to the University of the Free State (UFS). Following some years of decline, Boyden has been revitalised in recent years thanks to the efforts of the University's Physics Department and the Friends of Boyden organisation. The original 1.5 m telescope has been refurbished and is actively engaged in research. Construction of the Boyden Science Centre Auditorium was completed not long before Watcher was installed, providing space for talks as well as a night sky viewing platform on its roof. The Observatory has a very active educational and public outreach program, frequently holding open evenings and school visits which make use of the refurbished 13'' refractor, the solar telescope, and Watcher.

Several factors contributed to this choice of site. In order to maximise opportunities for observing GRB optical counterparts from the ground, a globally distributed network of instruments which can provide round the clock coverage of the entire night sky is required. Since sky coverage with dedicated robotic telescopes at southern latitudes is relatively sparse, and only one other system is in operation in Africa (ROTSE-IIIc at the HESS site in Namibia), Boyden was a natural choice. Atmospheric conditions at the site are generally very stable, particularly in the winter as the region's dominant high-pressure systems act as a barrier to moisture streams. However during the summer high surface temperatures and streams of warm moisture-laden air from the Indian Ocean can result in cloud formation

and occasional violent thunderstorms [13]. Though the site is at a relatively high altitude and is sufficiently remote to avoid major light pollution problems, it is still very accessible, which facilitates installation, upgrades, and any necessary maintenance. The seeing is typically $\sim 2''$, about 2.5 times the pixel scale.

2.2. Instrument Overview. Watcher began observing in March 2006, and operated in fully automated mode from May until early October that year, when some control electronics were damaged by a lightning strike. It was back in operation in January 2007 until October 2008, when a major upgrade began. The optical tube is a 40 cm Classical-Cassegrain on a Paramount ME robotic mount. The detector is an Apogee AP6e CCD, with a KAF-1001e $1k \times 1k$ chip. The field of view is $14.5' \times 14.5'$, with a plate scale of $0.85''/\text{pixel}$. Bessell BVRI filters are housed in an Optec IFW filter wheel, and automatic focussing is provided by a Robofocus stepper-motor, located at the secondary mirror. A Davis Vantage Pro weather station monitors weather conditions and can shut down Watcher in the event of rain or thick cloud cover. The motorised roll-back roof mechanism is controlled by custom-made electronics. Watcher is controlled by two Linux PCs running RTS2 software, a powerful, open-source package for complete management of a remote observatory [14]. This software automatically manages all the hardware, schedules observations of targets in a local database and can respond to GCN alerts for rapid GRB follow-up observations. A full description of Watcher is in preparation [15].

3. The Photometry Pipeline

A customised pipeline has been implemented for the consistent, reliable, and rapid analysis of Watcher data. Rapid dissemination of new information is particularly important in the case of GRB observations where newly identified afterglows can act as triggers for Target of Opportunity override programmes on larger telescopes.

A flow-chart of the steps involved in the photometry pipeline is shown in Figure 1. Apart from the CCD reduction, for which IRAF is used, all procedures are implemented in Matlab/Octave, providing greater flexibility in the data processing.

3.1. CCD Reduction. The CCD reduction is accomplished in IRAF in the usual way according to

$$I_{\text{red}} = \frac{I_{\text{raw}} - I_{\text{dark}}}{F}, \quad (1)$$

where I_{red} is the reduced image, I_{raw} is the raw image, I_{dark} is the dark image. F is the flatfield correction factor, calculated according to

$$F = \text{median} \left(\frac{I_{\text{ff},i} - I_{\text{dark}}}{\langle I_{\text{ff},i} - I_{\text{dark}} \rangle} \right), \quad (2)$$

where $I_{\text{ff},i}$ is the i th-flatfield image and the median is obtained over the number of flatfields taken for a given filter. It is

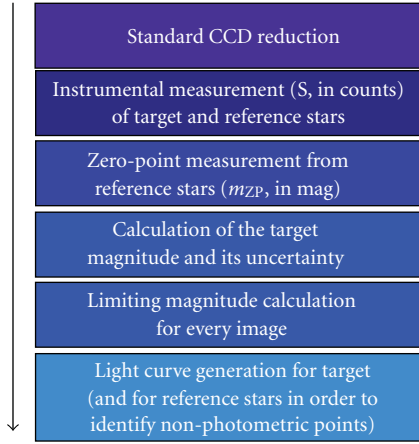


FIGURE 1: Flowchart of Watcher's photometry pipeline.

important that the target and dark images are taken at the same temperature (within $\pm 1^\circ\text{C}$) to keep the dark current and bias values sufficiently stable. In the event that the flatfield image is of poor quality, as can happen in the case of some GRB observations, adequate photometry can still be obtained by eliminating the flatfield correction since the nonuniformity of the image field is only $\sim 2\%$.

3.2. Source Magnitude and Uncertainty Calculation. The source magnitude, m_{target} , is calculated according to

$$m_{\text{target}} = m_{\text{ZP}} - 2.5 \log S, \quad (3)$$

where m_{ZP} is the zero-point uncertainty, S is the source count and $m_{\text{ins}} = -2.5 \log S$ is the instrumental magnitude of the source.

The uncertainty on the calculated magnitude is then given by

$$u(m) = \sqrt{u_{\text{ZP}}^2 + 1.1788 \left(\frac{u_{\text{S+sky}}^2 + u_{\text{sky}}^2}{S^2} \right)}, \quad (4)$$

where u_{ZP} is the zero-point uncertainty, $u_{\text{S+sky}}$ is the source plus sky uncertainty, and u_{sky} is the sky uncertainty. Equations (3) and (4) are applied to all sources of interest (targets and reference stars). The measured magnitudes of a number of reference sources versus catalogue magnitudes for a test Watcher image are shown in Figure 2. The slope of this graph shows that the Watcher clear filter corresponds reasonably closely to the USNO-B1, R2 filter.

3.2.1. Instrumental Measurement of a Source. Conventional aperture photometry is used to calculate S from $(S + \text{sky}) - \text{sky}$. The typical aperture radius used is 1.75 FWHM. The uncertainty in the instrumental measurement of the source is given by:

$$u_S = \sqrt{u_{\text{S+sky}}^2 + u_{\text{sky}}^2}. \quad (5)$$

The standard deviation per pixel (σ_{sky}) is calculated from the sky annulus pixels. When the value of a pixel deviates

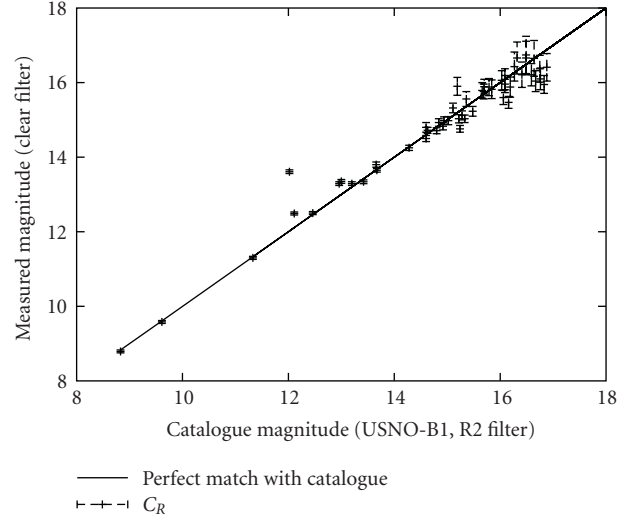


FIGURE 2: Measured magnitudes of reference stars versus catalogue magnitudes for a Watcher test image.

by more than $2\sigma_{\text{sky}}$ from the sky average, it is rejected in order to avoid contamination of the sky measurement due to neighbouring sources. The uncertainty in the sky measurement is given by

$$u_{\text{sky}} = \sigma_{\text{sky}} \frac{N_{\text{ap}}}{\sqrt{N_{\text{ann}}}}, \quad (6)$$

where N_{ap} is the number of pixels in the aperture and N_{ann} is the number of pixels in the sky annulus. The uncertainty on the source plus sky measurement, $u_{\text{S+sky}}$, is given by

$$u_{\text{S+sky}} = \sqrt{\frac{S}{G} + \sigma_{\text{sky}}^2 N_{\text{ap}}}, \quad (7)$$

where G is the conversion factor of the CCD from counts to electrons. Readout noise is already included in σ_{sky} . If N_{ann} is large enough, u_{sky} is negligible compared to $u_{\text{S+sky}}$.

3.2.2. Zero-Point Measurement of an Image. The zero-point is assumed to be constant across the image. This is verified by comparing the temporal evolution of the magnitudes of different stars within an image. Instrumental measurements of all catalogued stars in a radius of 300 arcsec from the target are determined. Instrumental magnitudes are then calculated for each star, where $\text{SNR} > 10$, from catalogued magnitudes and instrumental measurements. Points deviating by more than 1σ are removed from the distribution of calculated zero-points. The standard deviation of the average ($\sigma_{\text{ZP}}/\sqrt{N}$) of the new distribution is the uncertainty of the zero-point (u_{ZP}). A larger number of stars used for the zero-point determination naturally results in lower uncertainty. No weighting is used in the averaging.

3.3. Limiting Magnitude Measurement. Reliable determination of the limiting magnitude in an image is important, particularly for GRB observations where the source can

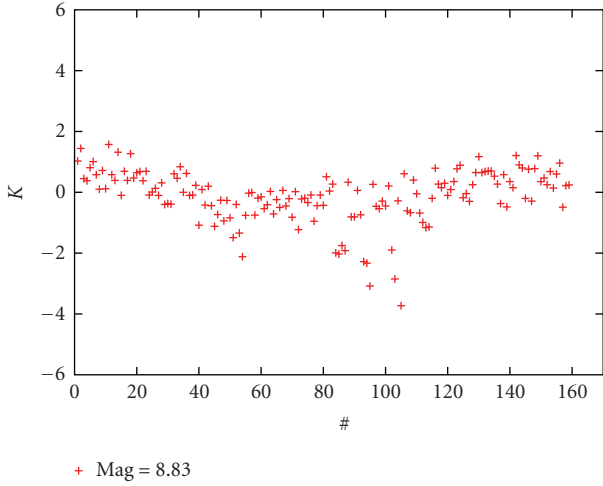


FIGURE 3: Bright source: uncertainty limited by the zero-point measurement.

fluctuate strongly and its brightness may be close to the limit of a small telescope's capabilities.

The limiting magnitude should be expressed as a measurement, since due to the uncertainty in the catalogue values, it is calculated from a distribution.

For all sources with SNR between 1 and 10, $\log \text{SNR}$ is linearly fitted to the corresponding catalogue magnitude. From the resultant equation, the limiting magnitude corresponding to a $\text{SNR} = 2$ is calculated. The uncertainty on the limiting magnitude is then calculated from the uncertainty of the best-fit parameter.

4. Test of Photometry Performance

To assess the performance of the pipeline, 159 images of two specific nonvariable stars were selected and the statistical behaviour examined using a χ^2 test, with $\chi^2 = \sum^N k^2$, where $k = (m_{\text{ins}} - m_{\text{average}})/u(m)$. The first star's derived magnitude is 8.83 where the uncertainty is limited by the zero-point measurement. In this case, χ^2/ν is 0.77 (122.1/158), suggesting that the uncertainty on the zero-point is slightly overestimated. The second star is a faint source (magnitude = 17.15), whose uncertainty is limited by the instrumental measurement. In this case χ^2/ν is 1.03 (162.4/158). The index k for both stars is plotted in Figures 3 and 4 as a function of the image number (#).

5. Preliminary Results: GRB 080905B

Watcher observations of GRB 080905B began 44.3 s after the trigger, with images being acquired without filter (clear, R_C), with exposures of 10 seconds (44.3 s–656.3 s), 30 seconds (660.3 s–3591.3 s), and 60 seconds (3718.3 s–7264.3 s). The zero-points of the measurements were calculated by comparison with the R2 magnitude in the USNO B.1 catalogue. The 2MASS galaxy, 2MASX J20065732–6233465, is located 4 arcsec from the GRB. The galaxy contribution was subtracted from the data by calculating the flux of

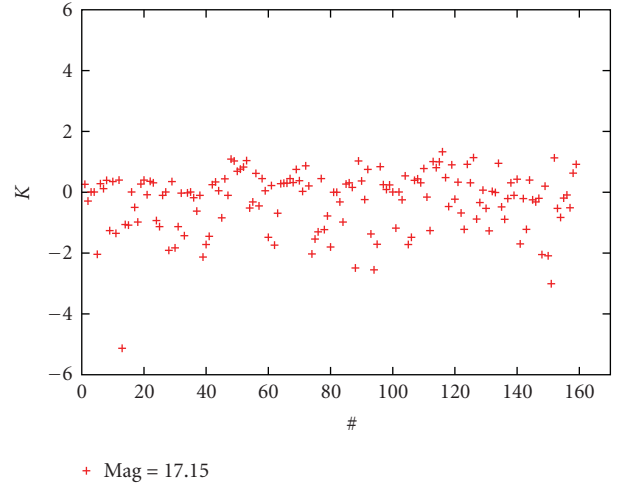


FIGURE 4: Faint source: uncertainty limited by the instrumental measurement.

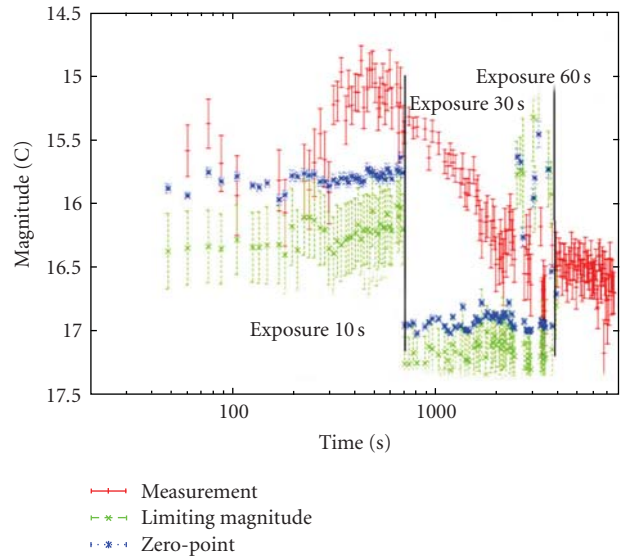


FIGURE 5: The Watcher light curve of the prompt and early afterglow emission from GRB 080905B in the clear filter band with the time quoted relative to the GRB trigger time. The zero-point and limiting magnitude for every exposure are also shown. Since the value of the zero-point is related to the total number of counts per exposure time unit, its temporal evolution is correlated with the limiting magnitude evolution and the exposure time.

photons in the aperture from a set of long exposure images (120 s) that were acquired a long time after the trigger, when the contribution of the optical transient to the flux was negligible. In the Watcher light curve, the prompt optical emission and optical afterglow are clearly separated (Figure 5). The origin of the peaks in limiting magnitude at around 3000 s is most likely due to intermittent cloud. The separation of the optical components shows their temporal relationship and relative strength and will be presented in more detail in a future publication [16].

6. Conclusions

The Watcher photometry software provides a robust, automated pipeline for the automated processing of large sets of CCD data. In particular for GRB observations, it permits limiting magnitudes to be properly calculated for each exposure setting, so that in the absence of an afterglow detection, a reliable upper limit can be rapidly disseminated.

Acknowledgment

The authors acknowledge the support from the Science Foundation Ireland under Grant 07-RFP-PHYF295.

References

- [1] G. W. Henry and J. A. Eaton, Eds., *Robotic Telescopes: Current Capabilities, Present Developments, and Future Prospects for Automated Astronomy*, vol. 79 of *Astronomical Society of the Pacific Conference Series*, Astronomical Society of the Pacific, San Francisco, Calif, USA, 1994.
- [2] M. F. Bode, Ed., *Robotic Observatories*, Wiley-Praxis Series in Astronomy and Astrophysics, John Wiley & Sons, New York, NY, USA, 1995.
- [3] W. P. Chen, C. Lemme, and B. Paczynski, Eds., *Small Telescope Astronomy on Global Scales*, vol. 246 of *Astronomical Society of the Pacific Conference Series*, Astronomical Society of the Pacific, San Francisco, Calif, USA, 2001.
- [4] T. D. Oswalt, Ed., *The Future of Small Telescopes in the New Millennium*, Kluwer Academic Publishers, Dordrecht, The Netherlands, 2003.
- [5] J. A. Eaton, W. Henry, and F. C. Fekel, "Advantages of automated observing with small telescopes," in *The Future of Small Telescopes in the New Millennium*, T. D. Oswalt, Ed., vol. 2, pp. 189–207, Kluwer Academic Publishers, Dordrecht, The Netherlands, 2003.
- [6] I. G. van Breda, "Monitoring of active galactic nuclei," in *Robotic Observatories*, M. F. Bode, Ed., Wiley-Praxis Series in Astronomy and Astrophysics, pp. 101–105, John Wiley & Sons, New York, NY, USA, 1995.
- [7] L. Szabados, "Variable star research with small telescopes," in *The Future of Small Telescopes in the New Millennium*, T. D. Oswalt, Ed., vol. 3, pp. 207–223, Kluwer Academic Publishers, Dordrecht, The Netherlands, 2003.
- [8] C. H. McGruder, S. B. Howell, and M. E. Everett, "The detection extrasolar planets via the transit method," in *The Future of Small Telescopes in the New Millennium*, T. D. Oswalt, Ed., vol. 3, pp. 173–187, Kluwer Academic Publishers, Dordrecht, The Netherlands, 2003.
- [9] M. I. Andersen and H. Pedersen, "Gamma-ray burst optical follow ups with robotic telescopes," *Astronomische Nachrichten*, vol. 325, no. 6–8, pp. 490–495, 2004.
- [10] J. Huchra, "The importance of small telescopes to cosmological research," in *The Future of Small Telescopes in the New Millennium*, T. D. Oswalt, Ed., vol. 3, pp. 343–354, Kluwer Academic Publishers, Dordrecht, The Netherlands, 2003.
- [11] N. Gehrels, G. Chincarini, P. Giommi, et al., "The *Swift* gamma-ray burst mission," *Astrophysical Journal*, vol. 611, no. 2, pp. 1005–1020, 2004.
- [12] C. Winkler, T. J.-L. Courvoisier, G. Di Cocco, et al., "The INTEGRAL mission," *Astronomy & Astrophysics*, vol. 411, no. 1, pp. L1–L6, 2003.
- [13] A. H. Jarrett, "Meteorology at Boyden observatory from 1980–1985," *Monthly Notes of the Astronomical Society of South Africa*, vol. 46, p. 11, 1987.
- [14] P. Kubánek, M. Jelínek, S. Vitek, A. de Ugarte Postigo, M. Nekola, and J. French, "RTS2: a powerful robotic observatory manager," in *Advanced Software and Control for Astronomy*, H. Lewis and A. Bridger, Eds., vol. 6274 of *Proceedings of SPIE*, Orlando, Fla, USA, May 2006.
- [15] J. French, et al., "The Watcher robotic telescope system description," in preparation.
- [16] A. Ferrero, et al., "Watcher observations of the prompt and early afterglow emission from GRB080905B," in preparation.

Research Article

The Data Reduction Pipeline of the Hamburg Robotic Telescope

**Marco Mittag, Alexander Hempelmann, José Nicolás González-Pérez,
and Jürgen H. M. M. Schmitt**

Hamburger Sternwarte, Universität Hamburg, Gojenbergsweg 112, 21029 Hamburg, Germany

Correspondence should be addressed to Marco Mittag, mmittag@hs.uni-hamburg.de

Received 25 June 2009; Accepted 7 September 2009

Academic Editor: Lorraine Hanlon

Copyright © 2010 Marco Mittag et al. This is an open access article distributed under the Creative Commons Attribution License, which permits unrestricted use, distribution, and reproduction in any medium, provided the original work is properly cited.

The fully automatic reduction pipeline for the blue channel of the HEROS spectrograph of the Hamburg Robotic Telescope (HRT) is presented. This pipeline is started automatically after finishing the night-time observations and calibrations. The pipeline includes all necessary procedures for a reliable and complete data reduction, that is, Bias, Dark, and Flat Field correction. Also the order definition, wavelength calibration, and data extraction are included. The final output is written in a fits-format and ready to use for the astronomer. The reduction pipeline is implemented in IDL and based on the IDL reduction package REDUCE written by Piskunov and Valenti (2002).

1. Introduction

The HRT [1] was built by Halfmann Teleskoptechnik GmbH (Germany) and installed at Hamburg Observatory in 2005. This Cassegrain-Nasmyth F/8 type telescope has a 1.2 m aperture, an Alt/Az mounting, and final direct drives with high-precision absolute encoders. The only instrumentation of the HRT is the Heidelberg Extended Range Optical Spectrograph (HEROS). It is connected with the telescope via a polymicro FVP 50/70 μ fused silica fibre, equipped with microlenses on both sides of the fibre to adapt the HRT-HEROS F-ratios. At present, only the blue channel of HEROS (380–570 nm) is operating, while the red channel will start its operations in July 2009. The spectral resolution of the device is $R = 20000$. The telescope is designated for long-time monitoring of active stars at its final location Guanajuato in Mexico.

2. Reduction Pipeline

The reduction pipeline is provided as fully automatic reduction pipeline including an automated wavelength calibration. It is started by the Central Control Software of the HRT system after the observations and calibrations have been finished. The reduced data are stored in an archive. This pipeline is implemented in IDL (Interactive

Data Language) and uses the reduction package REDUCE, by Piskunov and Valenti [2]. REDUCE is a powerful package providing the required functionality for the HEROS pipeline.

In the following the main reduction steps of the pipeline are described and these are represented in flow charts.

2.1. Preparation of the Reduction. Before the main reduction starts, it is necessary to prepare the reduction. The flow chart in Figure 1 shows the main steps of this part.

The first step of the preparation is the definition of the directory holding the raw data. Also a temporary directory and the directory are created, where results are saved on disk.

Thereafter the parameters and file names for reduction procedure are defined. All reduction parameters are supplied with the same values to all routines called by the pipeline at the different steps of the reduction. This is made for consistency in the reduction. The parameter values are read out from the parameter file for the blue channel.

2.2. Building the Master Calibration Images. The HRT system takes several calibration images: Bias, dark, and flat fields, before and after the observations. The respective images are averaged and then used as master calibration images. The main steps to build the master image are similar for bias,

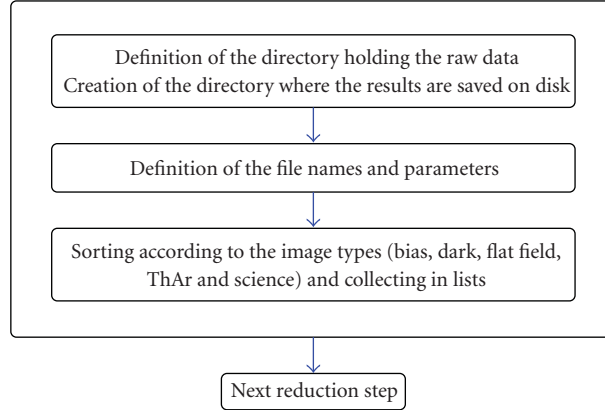


FIGURE 1: Flow chart with the main steps of the preparation of the reduction.

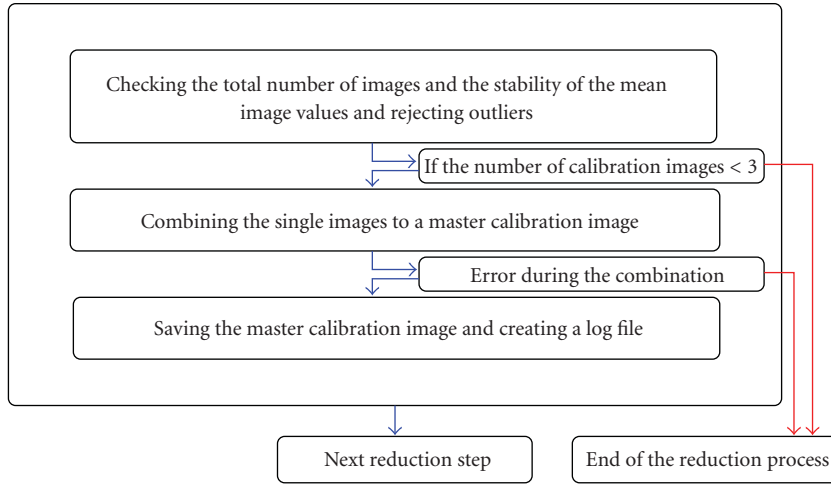


FIGURE 2: Flow chart with the main steps of building the master calibration images.

dark, and flat field. The flow chart in Figure 2 shows the main steps in this part.

The first step is a check of the variation in the calibration images. The percentage of relative variation rv_i between the arithmetic mean of the single images $\langle im_i \rangle$ and the median of this values $\text{median}(\langle im_1 \rangle \cdots \langle im_n \rangle)$ is calculated as

$$rv_i = \left(\frac{\langle im_i \rangle - \text{median}(\langle im_1 \rangle \cdots \langle im_n \rangle)}{\text{median}(\langle im_1 \rangle \cdots \langle im_n \rangle)} \right) \cdot 100. \quad (1)$$

For the calculation of rv_i for the darks the single images are corrected by bias and for the rv_i for the flats by bias and dark. The percentage of relative variation is plotted in a log file.

The calibration images are split in two lists. If the same number of images is taken before and after the observation, then in the first list the images taken at the start of the observation are collected and in the second list those taken after the observation. Then, the percentage of relative variations of the images are checked for both lists. If the percentage of relative variation is higher than a threshold, the corresponding image is not used for building the master calibration image. Normally the total number of images in

both lists after the check of rv_i is greater or equals 3. The standard deviations of the percentage of relative variation of images, Equation (1), are calculated for both lists and used as the thresholds to build the master calibration image. If the standard deviation is less than 3.5, then it is reset to the default value 3.5. This is the minimum threshold to find outliers in the images.

If the total number of images in one list is less than 3, an error message is obtained and the images are collected in a new list. The content of this new list is checked. Now there are 3 possibilities.

- (1) The total number of images is <3 . The reduction ends, because one needs at least 3 calibration images to build a master calibration image.
- (2) The total number of images is <6 . The new list is not split, because in the list must be at least 3 images.
- (3) The total number of images is ≥ 6 . The new list is split in two lists.

Thereafter the single calibration images are averaged. As next step it is checked if an error arose during the combination of

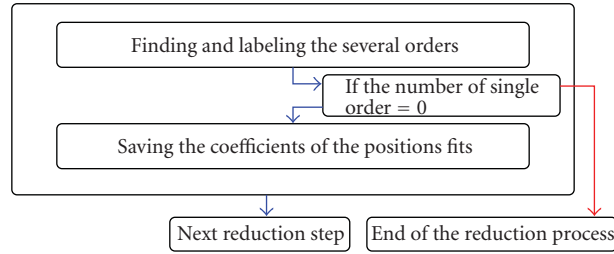


FIGURE 3: Flow chart with the main steps of the order definition.

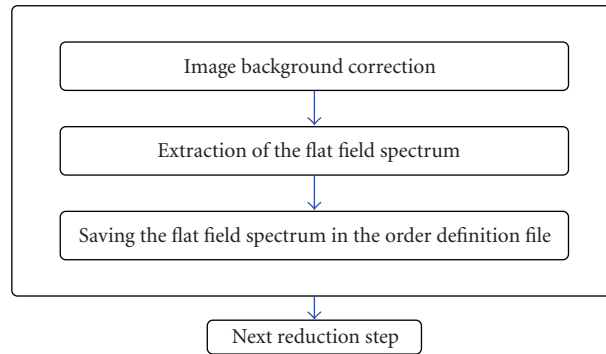


FIGURE 4: Flow chart with the main steps of the blaze extraction.

the single calibration images. In this case the pipeline stops and an error message is written to a file.

The master bias is subtracted from the average dark and flat field and additionally the flat field is corrected from the dark contribution. The dark correction is not performed, if the arithmetic mean of master dark is smaller than a predefined threshold for the dark correction, because in this case a dark contribution is negligible. After the subtraction of the master bias, the dark is time normalised.

The results are saved as master calibration images (hereafter, bias, dark, and flat field). To monitor long-term changes, the arithmetic mean of the single images and the corresponding standard deviation are saved in a log file. Also the standard deviation of both lists and the arithmetic mean, the median, and the standard deviation of the master calibration images are saved.

2.3. Order Definition. The flat field is used for the order definition. The central positions of the individual spectral orders are located and defined in this step of the reduction pipeline. If a single order is not found, then the pipeline stops and an error message is written to a file. The results of the order definition are saved in the order definition file. The flow chart in Figure 3 shows the main steps in this reduction part.

2.4. Blaze Extraction. During the next step in the reduction pipeline the spectrum of the flat field lamp is extracted. The flow chart in Figure 4 shows the main steps in this part of the pipeline. This spectrum (hereafter, blaze) can be used as blaze

function. The blaze is used to eliminate the blaze function in the science spectrum and to correct for the difference in quantum efficiency of the pixels (Section 2.6). After the background correction the blaze is extracted like a science spectrum. The counts in the blaze are converted in electrons and the blaze is normalised by the exposure time. Finally the blaze is saved in the order definition file.

2.5. Wavelength Calibration. The spectrum of the ThAr lamp is used for the wavelength calibration. One ThAr image will be taken before and one after the observations. The flow chart in Figure 5 shows the main steps in this part. The flow of the wavelength calibration can be split in two parts: the spectrum extraction and the new wavelength solution.

ThAr Spectrum Extraction. The two ThAr spectra are reduced consecutively. The bias is subtracted from the ThAr image. If the arithmetic mean of dark is above the threshold for dark subtraction, then the dark is also subtracted from the ThAr image. Thereafter the ThAr spectrum is extracted and saved on disk.

Wavelength Solution. For the automatic wavelength calibration a reference ThAr spectrum with 1D wavelength solutions of the several orders is used. The extracted spectra are compared with the reference spectrum. The shifts are calculated for each order via a cross correlation. After that the order shifts of the two ThAr spectra are averaged for each order.

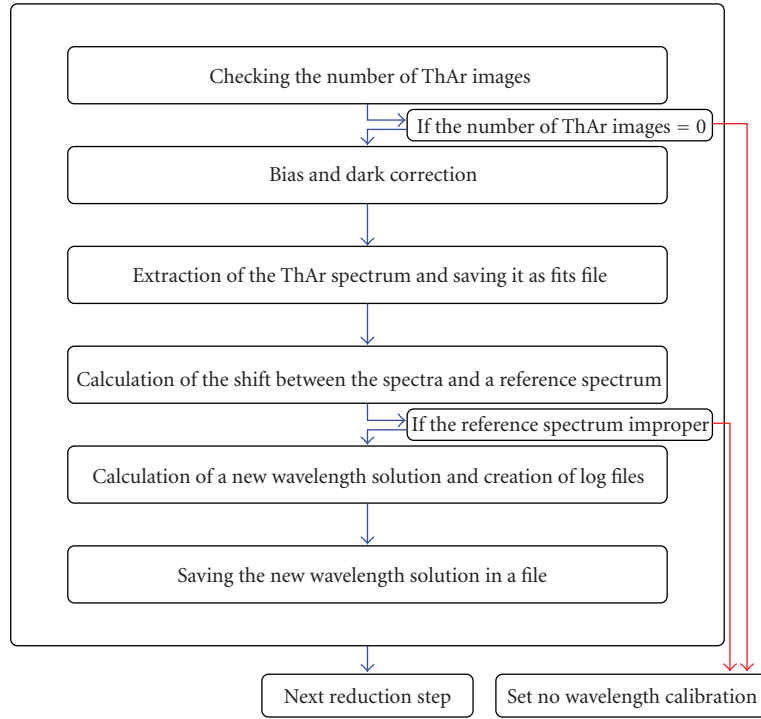


FIGURE 5: Flow chart with the main steps of the wavelength calibration.

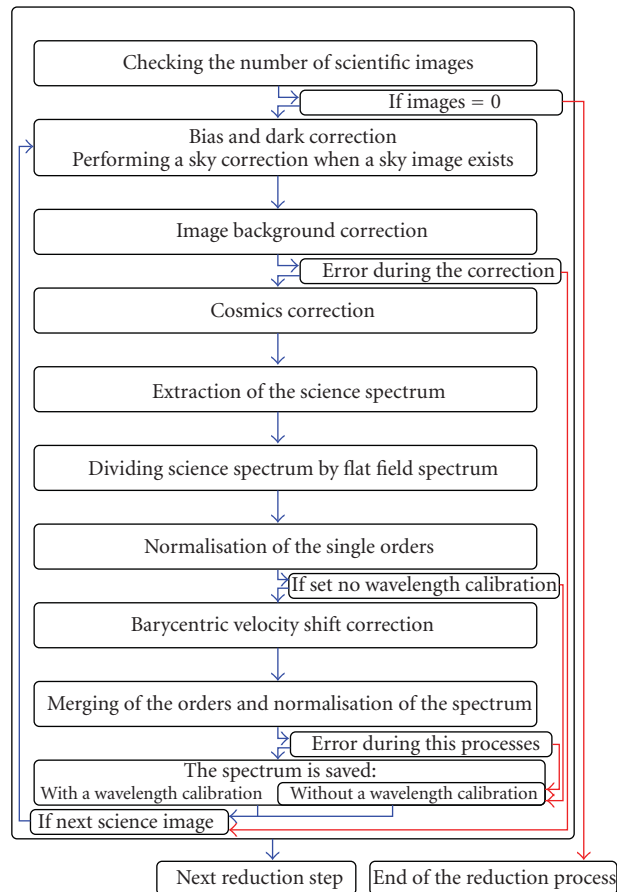


FIGURE 6: Flow chart with the main steps of the spectrum extraction form the single science image.

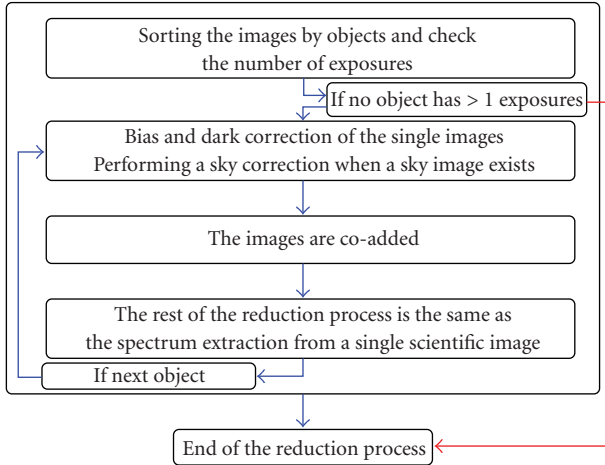


FIGURE 7: Flow chart of the first steps of the spectrum extraction of the coadd science images.

The new 1D wavelength solutions of all orders are determined with the shifts and the 1D wavelength solution of the reference spectrum. Finally, the results, the shifts, and the spectral resolution of the reference ThAr spectrum are saved in a wavelength file.

To check the results, the pipeline creates plots with the residuals of the 1D wavelength solutions fits and a file containing the arithmetic mean and standard deviation of the shifts and the residuals of the 1D wavelength solution.

2.6. Spectrum Extraction. The final part of the pipeline is the extraction of the actual spectra. First, the spectra of all images are extracted. The images of the same object are coadded and then a summed spectrum is created.

Spectrum from the Single Science Image. The flow chart in Figure 6 shows the main steps in this part of the pipeline. The science images were collected in a list. The bias is subtracted from the science image, and if the arithmetic mean of dark is greater than a threshold for dark subtraction, the dark is also subtracted from the science image. If sky images from this image (object) exist, then the average of two sky images is created and subtracted from the science image. Next, a background correction is performed. After the background correction the pipeline identifies outliers in the science image and these are flagged. Thereafter, the spectrum is extracted, the counts in the spectrum are converted to electrons, and the spectrum is time normalised. In the following, the spectrum is divided by the blaze [3]. This step eliminates the blaze function. Simultaneously the correction for the quantum efficiency is achieved. If the keyword `noautocal` is not set, then the wavelengths for the individual objects are corrected by the corresponding barycentric velocity shifts. Finally the spectra are saved in fits file.

Spectrum from the Coadded Science Images. This is the last part of the reduction pipeline. Here the spectrum from the summed science images of the same object is extracted. This

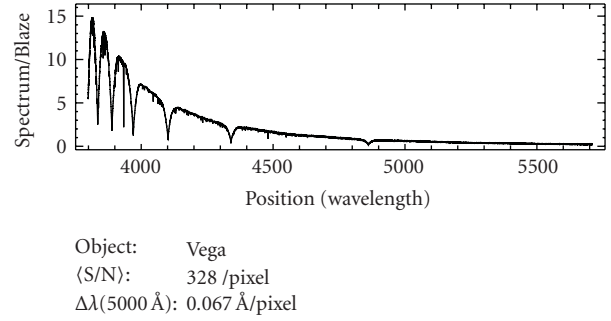


FIGURE 8: A sample result: Vega spectrum relative to the flat field spectrum and normalised to Figure 9.

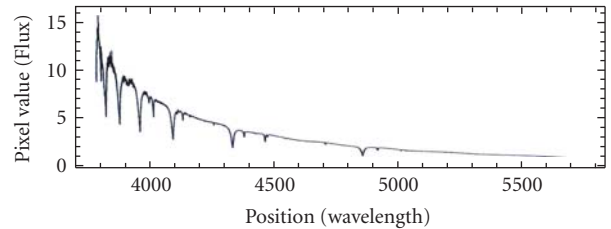


FIGURE 9: A comparative spectrum: Alcaid spectrum [3].

reduction procedure is similar to the procedure of extraction the spectrum from the single science image, but additionally at first the images are coadded. The flow chart in Figure 7 shows the first steps in this reduction part. The rest is similar to the spectrum extraction a single science image.

The first difference between the both reduction steps is a check which objects have more than one exposure. These objects are collected in a list.

Another difference is the coaddition of the single images for the same object, after the bias and, if necessary, a dark and sky correction. The mean Julian date for the summed image and the barycentric velocity shift are computed.

3. Conclusions

The data reduction pipeline for the blue channel works fully automatically and stably. In case of an error in some positions in the reduction flow, a message is written in a file. Also log files are written during the reduction. With these error and log files the astronomer can check the reduction flow. In Figure 8 an example of the final output of the pipeline is shown. A spectrum of Alcaid taken with HEROS and extracted with MIDAS [3] is shown in Figure 9 for comparison only.

One problem in the reduction pipeline is the identification of faint outliers in the science image. Also the continuum normalisation process of late types stars may have problems in order to find the quasicontinuum segments of the spectrum.

A future task will be the creation of the data reduction pipeline for the red channel. In general this pipeline will have the same structure as the pipeline for the blue channel has.

Finally, the optimisation and regular support of both pipelines are important to obtain the best possible outputs.

References

- [1] <http://www.hs.uni-hamburg.de/DE/Ins/Per/Hempelmann/HRT/index.html>.
- [2] N. E. Piskunov and J. A. Valenti, “New algorithms for reducing cross-dispersed echelle spectra,” *Astronomy and Astrophysics*, vol. 385, no. 3, pp. 1095–1106, 2002.
- [3] P. Škoda and Šlechta, “Reduction of spectra exposed by the fiber-fed echelle spectrograph HEROS,” *ASCR*, vol. 90, pp. 40–60, 2002.

Research Article

High-Speed and Wide-Field Photometry with TORTORA

G. Greco,¹ G. Beskin,² S. Karpov,² S. Bondar,³ C. Bartolini,¹ A. Guarnieri,¹ and A. Piccioni¹

¹ *Astronomy Department, Bologna University, 40126 Bologna, Italy*

² *Special Astrophysical Observatory of Russian Academy of Science, 369167 Nizhnij Arkhyz, Russia*

³ *Institute for Precise Instrumentation, 369167 Nizhnij Arkhyz, Russia*

Correspondence should be addressed to G. Greco, giuseppe.greco2@studio.unibo.it

Received 8 July 2009; Accepted 24 September 2009

Academic Editor: Alberto J. Castro-Tirado

Copyright © 2010 G. Greco et al. This is an open access article distributed under the Creative Commons Attribution License, which permits unrestricted use, distribution, and reproduction in any medium, provided the original work is properly cited.

We present the photometric analysis of the extended sky fields observed by the TORTORA optical monitoring system. The technology involved in the TORTORA camera is based on the use of a fast TV-CCD matrix with an image intensifier. This approach can both significantly reduce the readout noise and shorten the focal length following to monitor relatively large sky regions with high temporal resolution and adequate detection limit. The performance of the system has been tested using the relative magnitudes of standard stars by means of long image sequences collected at different airmasses and at various intensities of the moon illumination. As expected from the previous laboratory measurements, artifact sources are negligible and do not affect the photometric results. The following analysis is based on a large sample of images acquired by the TORTORA instrument since July 2006.

1. Introduction

The complete randomness of the angular distribution of the γ -ray bursts (GRBs) in the sky, along with their typical short duration, suggested us to monitor large sky regions with high temporal resolution in order to increase the probability to catch optical emissions simultaneous with the γ -ray prompt events. To perform such a task, we have proposed different search strategies [1–6] and the high-speed and wide-field FAVOR [7] and TORTORA cameras represent the more recent and promising developments. Presently TORTORA (Telescopio Ottimizzato per la Ricerca dei Transienti Ottici Rapidi) is mounted on top of the REM robotic telescope at La-Silla Observatory in Chile and has been operating since May 2006 [8].

2. Short Technical Description

The camera consists of a main objective, an image intensifier used to down-scale and amplify the image, a transmission optics, and a fast low-noise TV-CCD matrix based on the Sony ICX285AL chip. The TV-CCD matrix is an interline-transfer CCD with microlens raster to compensate the loss of surface area. It can operate at 7.5 frames per seconds with

negligible gaps between consecutive exposures. This frame-transfer regime is typical for CCDs and does not bring any significant artifacts in the image. The main objective and the transmission optics focusing unit are controlled through the PC parallel port interface. In Table 1 are reported the main technical parameters of the TORTORA camera.

The resulting data flow rate is about 20 MB/s. The raw data are stored on a RAID array until the next observational night and are processed in real time by a dedicated software for detection and classification of optical transient events [9].

The difference between an ordinary imaging with a CCD camera and fast imaging with a CCD equipped with an image intensifier tube is very significant [10]. The intensifier converts each photon, detected by the photocathode, into a luminous spot on the phosphor screen that preserves the (x, y) location of the event. This approach produces an efficient amplification of the intensity of the image afterwards recorded by the CCD. High gain of the image intensifier, which may be expressed as the number of resulting CCD counts per photon on the photocathode leads to effective reduction of the readout noise down to a subelectron values. Furthermore, the image intensifier is able to down-scale the image reducing the focal length and consequently increasing the field of view for a fixed CCD size. The gain of the image

TABLE 1: Main parameters of the TORTORA camera.

Main objective		Intensifier		CCD	
Diameter	120 mm	Photocathode	S20	Dimensions	1388×1036 pix
Focal length	150 mm	Diameter	90 mm	Pixel scale	$81''/\text{pix}$
Focal ratio	1/1.2	Gain	150	Exposures	0.13 s
Field of view	$24^\circ \times 32^\circ$	Scaling factor	5.5	Pixel size	6.5 micron
		Quantum efficiency	10%	Readout noise	$6 e^-/\text{pix}$

intensifier tube employed in TORTORA is 150, and the focal length is reduced from 150 mm down to 27 mm. However, the drawback of image intensifier is the decrease of the system quantum efficiency (Section 4.1) to a value defined by the characteristics of the photocathode, which is only 10% for an S20 photocathode used here.

3. Data Reduction

The real-time data processing pipeline is based on a fast *differential imaging* algorithm described in [10]. More detailed time series analysis may be performed a posteriori studying the images stored on the RAID array.

3.1. Preliminary Analysis. The first step of the postprocessing analysis is the dark current noise subtraction and flat-fielding to compensate vignetting due to the objective design. The low-noise TV-CCD matrix employed in TORTORA operates at room temperature. The dark current component is originated from thermally generated charge in the photocathode before the amplification stage and then it will be also amplified (the dark current in image intensifiers was traditionally called the Effective Background Illumination (normally abbreviated to EBI)). The dark current is generally not an issue if short time exposures are planned. Practically thermal noise has a negligible effect on the signal-to-noise ratio of the frames acquired by TORTORA, therefore no cooling is applied to the CCD camera.

The next step is the measure of the CCD frames taking into account the distribution of the background level and the statistics of photoelectrons.

3.2. Background Estimate. Faint stars at the limit of detection, photons of scattered light by the environment, satellites trails, cosmic-rays, or bad pixels can produce random fluctuations in a single frame. The variable background brightness is initially treated identifying pixels which are significantly higher than the surrounding one. The pixels deviating by a specified statistical amount are replaced by the median value. The nonuniformity of the frame background was reduced by approximately 15% in accordance with external conditions. This procedure is done on the whole frame, subsequently the background signal is determined within the circular shell of inner radius annulus and outer radius annulus surrounding the object without including other astronomical objects within this shell. The measured standard deviation in the stack of images is higher than that expected from pure

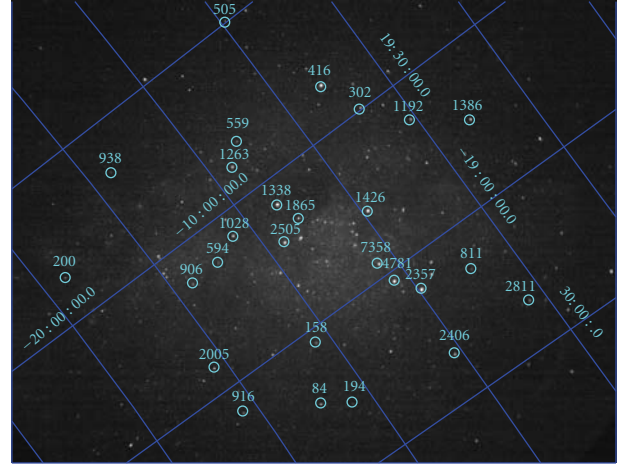


FIGURE 1: Image acquired by the TORTORA camera with an exposure time of 0.13 seconds. The selected stars are labeled using the identification number (id number) as tabulated in Tycho-2 catalogue. They have been chosen as reference stars to test the linearity and the homogeneity of the instrument (see text for more details). The center coordinates of the image are at the position: RA(J2000) = 18 h : 37 m : 05.28 s, DEC(J2000) = -06 d : 29' : 38.04''. Real time images of the TORTORA system are available using the public graphical user interface at the following address: <http://polaris.merate.mi.astro.it/trem/>.

Poisson noise especially at large count rates. Although the image intensifier overcomes the problem of readout noise, images acquired with an image intensifier suffer from gain noise. Intensifier noise is mainly caused by the discrete nature of the electron amplification process. Each photon entering the image intensifier will induce a large number of photons leaving the phosphorus screen. The variation in the gain for each incoming photon and the correlation in time of the output photons are the source of the noise. A single input photon yields a burst of output photons. The departure times of these output photons are strongly correlated in time. As a consequence, the Poisson process at the input of the intensifier yields a non-Poisson process at the output, which has an increased variance compared to ordinary Poisson-distributed noise. The number of photoelectrons generated at the photocathode depends on the binomial statistics:

$$P(r) = \binom{N}{r} p^r (1-p)^{(N-r)}. \quad (1)$$

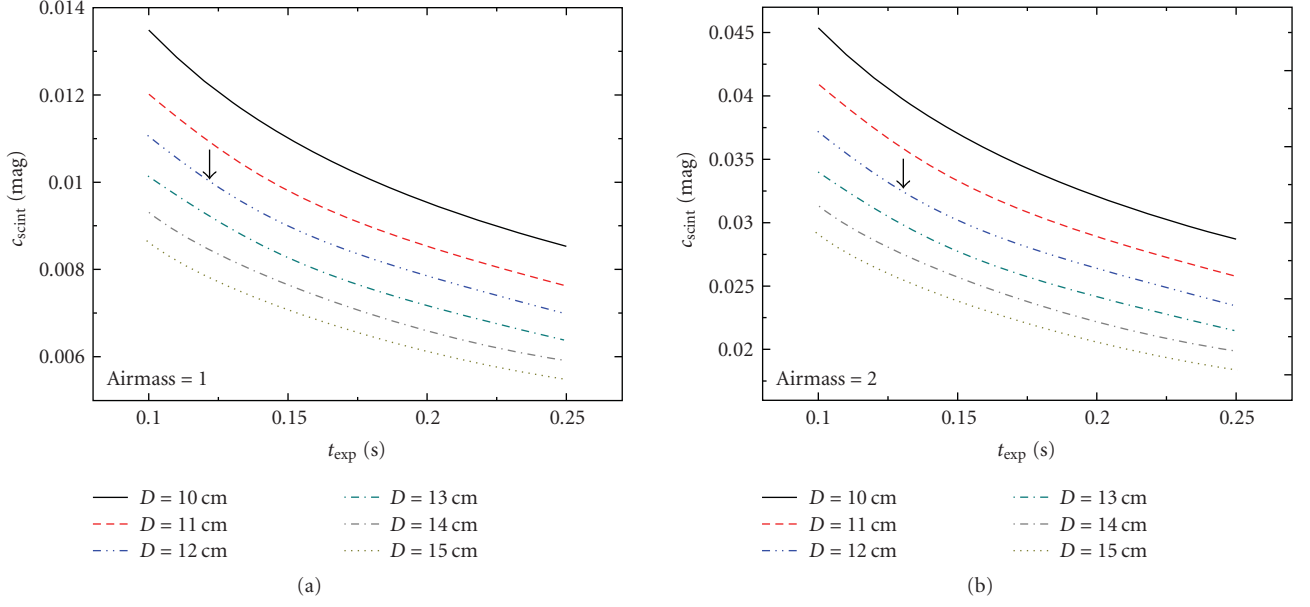


FIGURE 2: c_{scint} versus short exposure times $t_{\text{exp}} < 0.25$ seconds for different size of telescopes ($10 \text{ cm} \leq D \leq 15 \text{ cm}$) at a fixed values of airmass: $X = 1$ (a) and $X = 2$ (b). The arrows indicate the typical scintillation noise in TORTORA observations.

$P(r)$ is the probability of obtaining r photoelectrons for N photons given a quantum efficiency of p . The mean is $\mu = Np$, and the variance is $\sigma^2 = Np(1 - p)$.

3.3. Scintillation Noise. Additional uncertainty arises from atmospheric transmission variability. Scintillation is a dimensionless measure of the flux variation of a source observed through a finite aperture due to fluctuations in the refractive index of the atmosphere. Atmospheric scintillation adds an effective constant error term to the photometry. This error can be estimated from [11] as

$$c_{\text{scint}} = 0.09 \frac{X^{7/4}}{D^{2/3} \sqrt{2t_{\text{exp}}}} \left(\frac{\lambda}{550} \right)^{-7/12} \exp\left(\frac{h}{8000} \right), \quad (2)$$

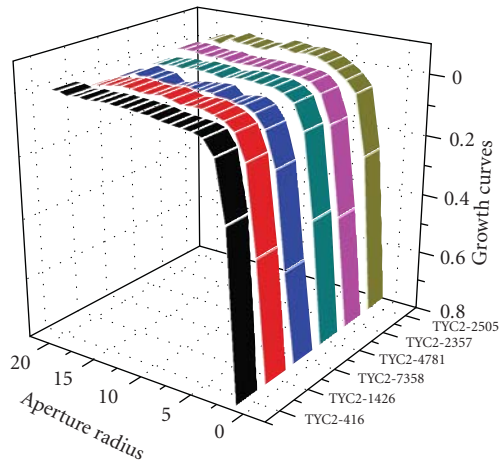
where D is the telescope diameter in centimeters, X is the airmass, h is the observatory altitude in meters, t_{exp} is the exposure time in seconds, λ is the wavelength in nanometers, and c_{scint} is the scintillation noise in magnitudes. The precise value of the exponent of the airmass X depends on the wind direction; it is equal to 2 when observing in the same direction as the wind and to 1.5 when observing perpendicular to it. Young [12] was able to show that for moderate airmass, the scintillation standard error is proportional to the 1.75 power of airmass but becomes asymptotically proportional to the 3/2 power for very large airmass.

The $D^{-2/3}$ dependence may be applied only to exposures long enough to ignore all high-frequency content. Ryan and Sandler [13] have derived a $D^{-1.1 \pm 0.1}$ dependence for exposure times ≤ 0.25 seconds, which agrees with Ellison and Seddon's [14] experimental data and Reiger's theoretical equations [15]. We adopt this diameter dependence in (2) to describe the scintillation noise in TORTORA photometry.

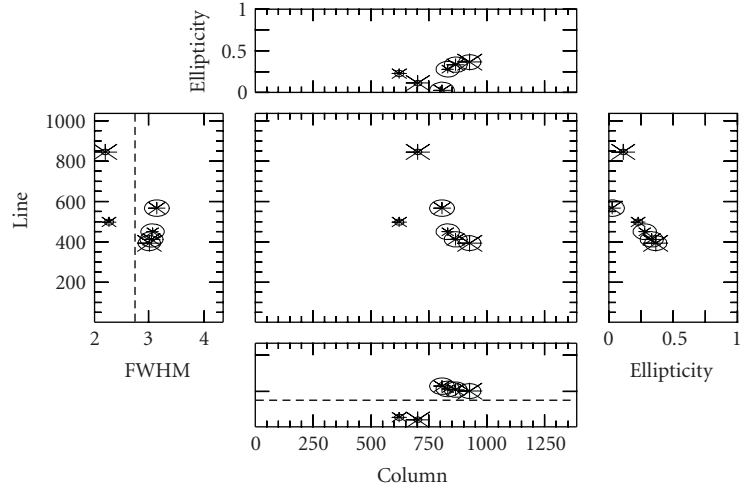
Taking into account the altitude of ESO Observatory ($h = 2400 \text{ m}$) and the aperture diameter of TORTORA telescope ($D = 12 \text{ cm}$), the estimated amount of scintillation is $0.01 \lesssim c_{\text{scint}} \lesssim 0.03$ magnitudes for moderate sky conditions with an airmass value X between 1 and 2 in 0.13-seconds photometric measurements (Figure 2).

4. Photometry of the TORTORA Fields

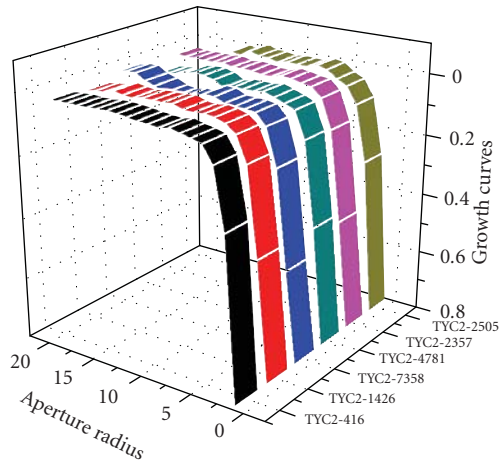
Circular aperture photometry of the TORTORA images was performed with PHOT/DAOPHOT function in IRAF (IRAF: Image Reduction and Analysis Facility; <http://iraf.noao.edu/>). Typically, the optimal radius of aperture was chosen to be 5 pixels for bright sources after the experiments with growth curves. Determining an appropriate aperture size to measure a total instrumental magnitude can be done by building up a light growth curve of the object. The light growth curve is the object's flux as a function of aperture radius. The adopted aperture would then reflect the point in the light growth curve where it flattens out. This optimal aperture size, which produces the smallest photometric error, contains also the spatially varying PSF due to geometric distortions present in the final images. A temporal sequence of contiguous light growth curves for as well as the values of the ellipticity and the Full Width at Half Maximum (FWHM) of the best fit Moffat profile is displayed in Figure 3. The growth curves were calculated selecting bright and isolated stars in different location of the wide-field image. The images were acquired with a continuous exposures time of 0.13 seconds per frame under moderate sky condition. The values of the affective air mass and the seeing are estimated to be ~ 1.30 and $\sim 0.8''$, respectively (<http://www.la.eso.org/lasilla/dimm/>). At the corresponding time the percent of the Moon illuminated is 6% at a distance



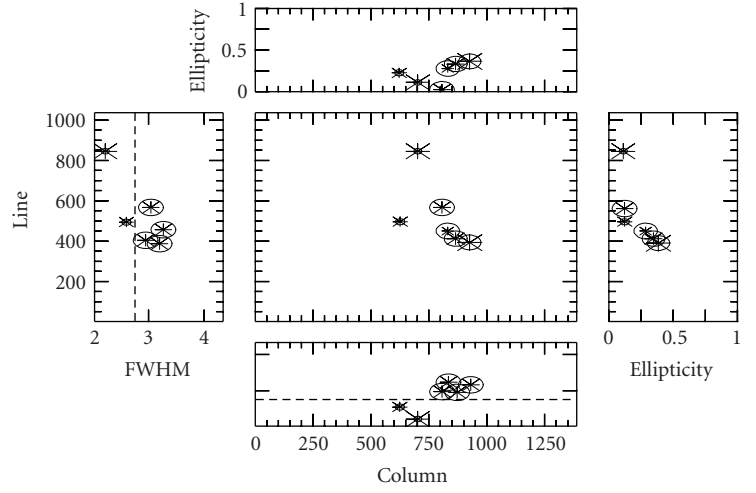
(a)



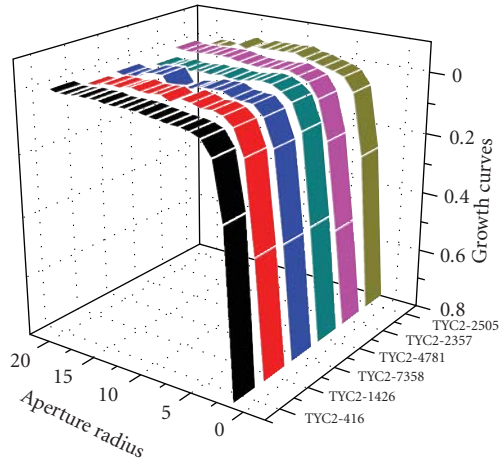
(b)



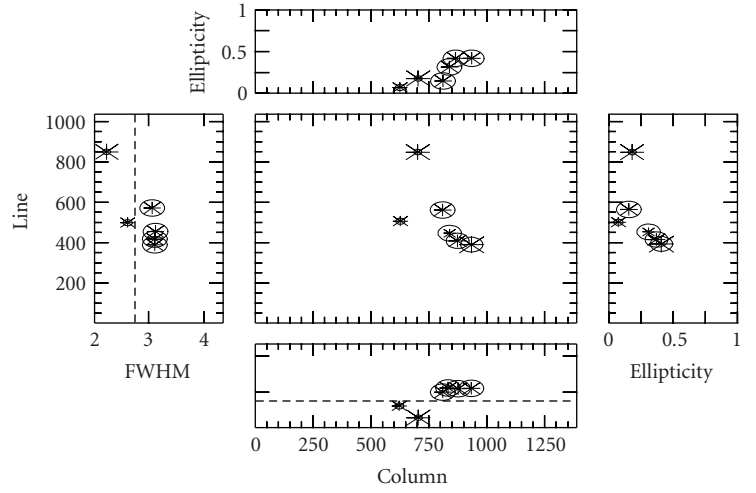
(c)



(d)



(e)



(f)

FIGURE 3: Continued.

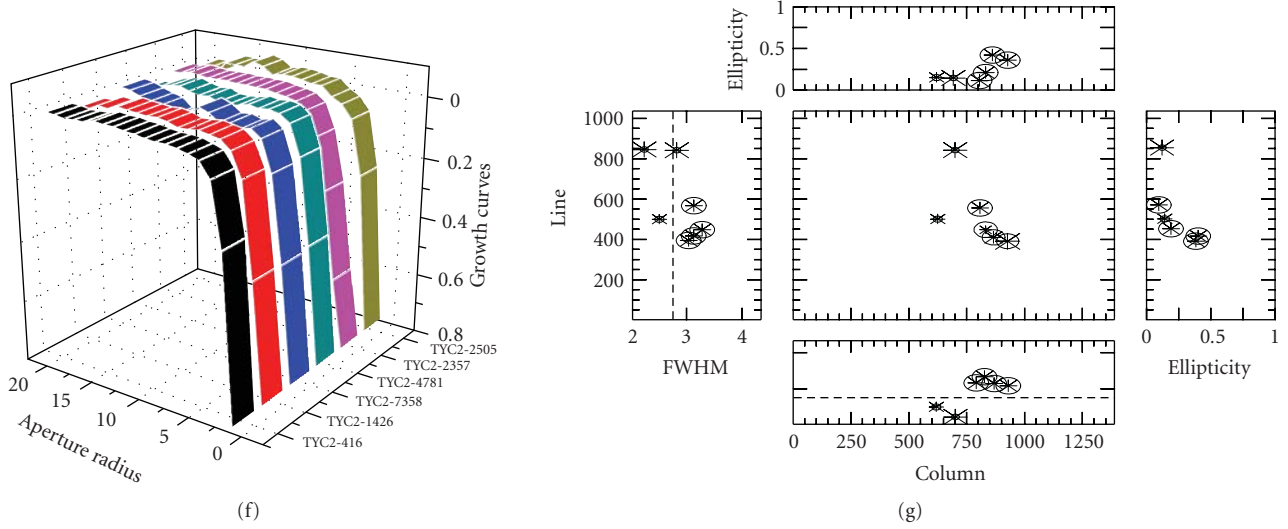


FIGURE 3: Example of growth curves acquired with a continuous exposure time of 0.13 seconds per frame, under moderate sky condition (see values in the text). The position of the stars may be found in the sky field of Figure 1 reading the Tycho-2 identification number (id number) labeled in y -axis. For each star are reported the values of the ellipticity, the FWHM using as best fit a Moffat profile, and the pixel coordinates.

of 126° from the target. The position of the star may be found in the sky field displayed in Figure 1 reading the Tycho-2 identification number (id number) labeled in y -axis. The total flux of the stars is contained within well-determined radius showing a good homogeneity of image intensifier and CCD response. The asymptotic value is immediately apparent and constant with a satisfactory degree of accuracy. The short sequence collected here shows that the stability of the TORTORA system is enough to assure the reliability of the detected short-lived periodicity in the ultra-fast optical photometry.

The correction for the finite size of the aperture is called the aperture correction. It is defined simply as the magnitude difference between the asymptotic magnitude and the magnitude at the given aperture. Corrections for the amount of missing flux from the source outside the optimal aperture size were done using a correction factor estimated from the method proposed by Stetson [16] and implemented under *IRAF* task *mkapfile*. The aperture correction is typically of order 0.10 mag at the center of the image ($10^\circ \times 10^\circ$), while it reaches a maximum value of 0.20 mag at the edges of the frame in which the field has less sharpness due to the vignetting. Proper correction factor is systematically added to our photometry. Finally, by the use of very large circular apertures we test that extra-scattered light contribution around the source is so low that it can be neglected.

Sufficiently accurate results are also obtained under relatively suboptimal sky conditions. Figure 4 shows a contiguous sequence of standard stars detected within the limits of observability permitted by the instrument before the automatic protection shutdown. The images were acquired with a continuous exposures time of 0.13 seconds per frame. The plots combine an image, a surface plot of the image data and a contour plot of the images data in a single tri-level

display. The x -axis and y -axis indicate the pixel coordinates place in the center of the FOV, and the z -axis represents the signal intensity. The values of the effective air mass and the seeing are estimated to be ~ 2.61 and $\sim 0.9''$, respectively. At the corresponding time the percent of the Moon illuminated is 98 at a distance of 58° from the target. We emphasized that the autofocusing system is stable, and the stars retain their original position without emerging distortion effects.

4.1. Linearity and Dynamic Range. The spectral response of the system is primarily determined by the photocathode type used in the image intensifier. TORTORA was developed for ground optical observation, and a multialkali (S20) photocathode is employed. Its typical spectral response peaks near 440 nm (Figure 5). No photometric filter has been used with it.

By comparing the instrumental magnitudes with the standard stars tabulated in Tycho-2 catalogue (<http://archive.eso.org/ASTROM/>), we may test the linearity and the fractional coincidence loss of the instrument for a wide range of fluxes. Figure 6 shows the dependency of the measured instrumental magnitude and the standard V magnitude. This result spotlights a good linearity of the instrument. Furthermore, the fractional coincidence loss caused by dead time is negligible for the fluxes under consideration in TORTORA system. The stars with color index $(B-V) > 1$ and $(B-V) < 1$ are plotted with square and circle symbols, respectively. The reference Tycho-2 stars used to check the linear response of the camera are labeled in Figure 1. The values of the linear best-fits for the two samples (see the upper right box in Figure 6) are statistically comparable due to the large color term across the passband. Finally, using the linear fit equations reported in Figure 6, the photometry performed in instrumental system was converted to the V magnitudes of the Tycho-2 star catalogue.

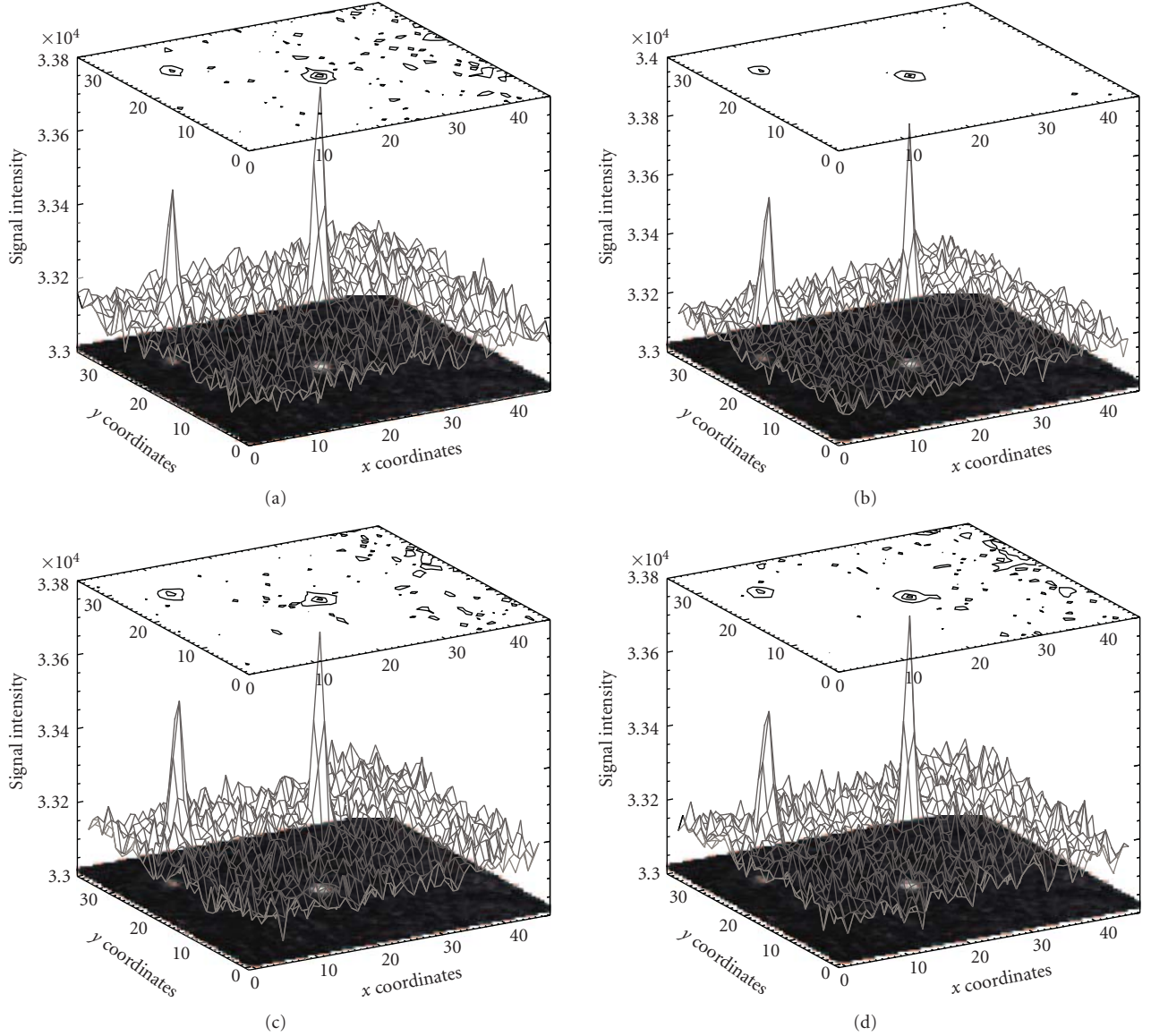


FIGURE 4: An example of observations acquired with continuous exposures time of 0.13 seconds per frame, under relative extreme sky conditions. The plots combine an image (image size: $2.5^\circ \times 2.5^\circ$), a surface plot of the image data, and a contour plot of the images data in a single tri-level display. The x-axis and y-axis indicate the pixel coordinates place in the center of the image frame at the position: RA(J2000) = 14 h : 31 m : 40.7 s, DEC(J2000) = 36 d : 18' : 14.7'' and the z-axis represents the signal intensity. The values of the affective air mass and the seeing are estimated to be ~ 2.61 and $\sim 0.9''$, respectively. At the corresponding time the percent of the Moon illuminated is 98% at a distance of 58° from the target.

The calibration of the TORTORA instrumental magnitude to the visual band is preferable than the blue filter because the empirical correlation has a lower degree of dispersion and the dependence of color index is negligible.

5. Discussion and Conclusion

The photometric accuracy of the wide sky fields observed by the high speed TORTORA CCD camera equipped with an image intensifier is analyzed. The typical potential sources of instrumental artifacts such as (i) the spatial deformation

of the image produced by the electron-optical input system (after electrons are ejected from the photocathode, they are collected and focused by the electric field of an electrodes configuration), (ii) blurring introduced by imperfections in the transmission optics between the phosphor screen and CCD, (iii) broadening of the light pulse produced by a fraction of photons emitted by the phosphor screen that travel parallel to the surface and scatter, (iv) stray light that arrives to the camera through multiple reflections from various detector components in the optical interface are negligible and do not affect the photometric results as expected from the previous laboratory measurements. Long

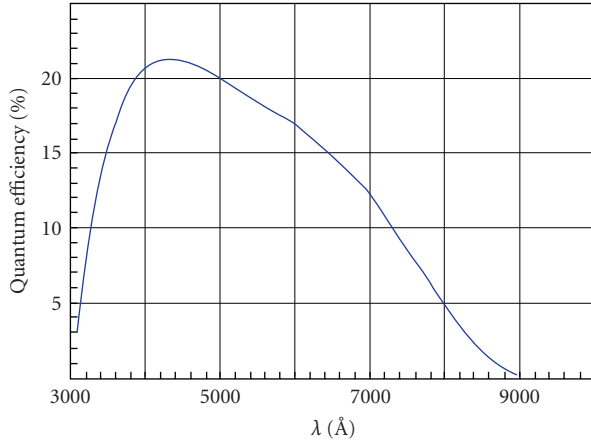


FIGURE 5: Spectral sensitivity curve of the multialkali (S20) photocathode employed in TORTORA.

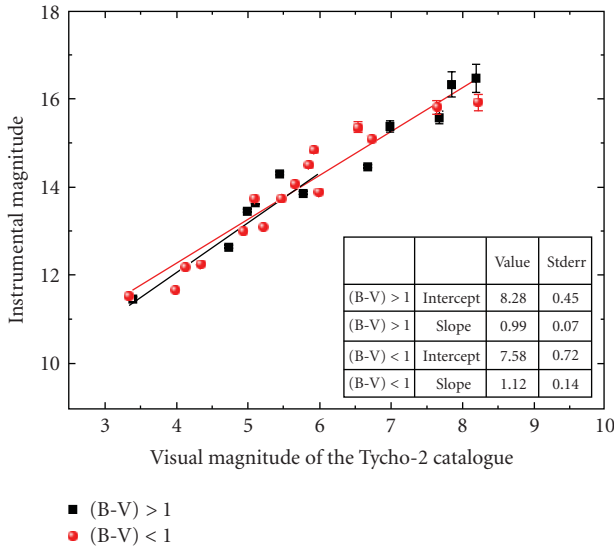


FIGURE 6: Instrumental magnitude versus standard Visual magnitude. The stars with color index $(B-V) > 1$ and $(B-V) < 1$ are plotted with square and circle symbols, respectively. The reference stars under consideration are labeled in Figure 1 using the Tycho-2 identification number (id number). The values of the linear best-fits are reported in the right upper box.

sequences of growth curves of bright and isolated standard stars show that the flux is contained within a well-determined and constant radius. Sequences of surface plot indicate that (x, y) location of the event is preserved without appreciable degradation of its intensity profile. The example given here shows the performance of the TORTORA camera within the limits of observability permitted by the instrument before the automatic protection shutdown. However proper extra-Poissonian fluctuations caused by statistical variations produced by gain variation across the image intensifier have to be considered for the reliability of the detected short-lived periodicity (Section 3.2).

Since May 2006 we accumulated approximately 200 nights of observations. The fields of the GRB 060719 [17], GRB 061202 [18], and GRB 061218 [19] were observed 59 seconds, 92 seconds, and 118 seconds after the satellite trigger, respectively. Fourier analysis was performed to search for upper limit for periodic signal at the GRB position. In the remarkable case of the GRB 080319B, TORTORA began taking data 26 minutes before the satellite trigger and observed the optical flux coincident with the γ -ray emission with unprecedented level of accuracy, collecting ~ 13320 images. Long and short time-scale variability was detected during the naked-eye prompt emission [20].

One of the important results of our routine observation is the estimation of the detection rate of the short-lived orphan transients (in preparation). Currently the prompt optical transient detection rate determined by observations of TORTORA is less than $8 \times 10^{-9} \text{ deg}^{-2} \text{ sec}^{-1}$ for transients that are brighter than 10.5^m on 0.13 seconds timescale.

Acknowledgments

This work was supported by the University of Bologna Progetti Pluriennali 2003, by grants of CRDF (no. RP1-2394-MO-02), RFBR (no. 04-02-17555, 06-02-08313, and 09-02-12053), INTAS (04-78-7366), and by the Presidium of the Russian Academy of Sciences Program. The authors thank the referee for his/her diligent work and for providing several suggestions that have helped to clarify the results.

References

- [1] A. Piccioni, C. Bartolini, A. Guarnieri, G. Pizzichini, J. M. Poulsen, and S. R. Rosellini, "A fast imaging photometer and the detection of optical flashes from gamma-ray burst sources," in *Vulcano Workshop 1988: Frontier Objects in Astrophysics and Particle Physics*, pp. 217–224, 1989.
- [2] A. Piccioni, C. Bartolini, A. Guarnieri, and G. Pizzichini, "FIP—a fast imaging photometer for optical flash observations," in *Gamma-Ray Bursts—Observations, Analyses and Theories (A93-20206 06-90)*, pp. 148–154, 1992.
- [3] A. Piccioni, C. Bartolini, F. Cortecchia, G. Cosentino, A. Guarnieri, and G. Pizzichini, "FIP: a fast imaging photometer for the optical study of gamma ray bursts," *Memorie della Societa Astronomia Italiana*, vol. 67, pp. 569–575, 1996.
- [4] G. M. Beskin, V. Plokhotnichenko, C. Bartolini, et al., "Catching the light curve of flaring GRBs: the opportunity offered by scanning telescopes," *Astronomy and Astrophysics Supplement Series*, vol. 138, no. 3, pp. 589–590, 1999.
- [5] G. Beskin, C. Bartolini, A. Guarnieri, et al., "Simultaneous detection of the high energy and optical transients by Čerenkov telescopes," in *Gamma-Ray Bursts in the Afterglow Era: Proceedings of the International Workshop*, E. Costa, F. Frontera, and J. Hjorth, Eds., ESO Astrophysics Symposia, 2001, pp. 387–389, Springer, Rome, Italy, October 2000.
- [6] A. Piccioni, C. Bartolini, A. Guarnieri, and G. Beskin, "Search for optical high energy transients by large light collectors," in *Presented at the IHP-Users Workshop*, 2001.
- [7] S. Karpov, G. Beskin, A. Biryukov, et al., "Optical camera with high temporal resolution to search for transients in the wide field," *Nuovo Cimento della Societa Italiana di Fisica C*, vol. 28, no. 4-5, pp. 747–750, 2005.

- [8] E. Molinari, S. Bondar, S. Karpov, et al., “TORTOREM: two-telescope complex for detection and investigation of optical transients,” *Nuovo Cimento della Societa Italiana di Fisica B*, vol. 121, no. 12, pp. 1525–1526, 2006.
- [9] A. Biryukov, G. Beskin, S. Bondar, et al., “Software for detection of optical transients in observations with rapid wide-field camera,” *Astronomische Nachrichten*, vol. 325, no. 6–8, p. 676, 2004.
- [10] S. Karpov, G. Beskin, S. Bondar, et al., “Wide and fast. Monitoring the sky in sub-second domain,” in *Proceedings of Workshop on Robotic Autonomous Observatories*, Malaga, Spain, May 2009.
- [11] D. S. Birney, G. Gonzalez, and D. Oesper, *Book-Review of Observational Astronomy*, Cambridge University Press, Cambridge, UK, vol. 101, 2nd edition, 1991.
- [12] A. T. Young, “Observational technique and data reduction,” in *Methods of Experimental Physics*, N. Carleton, Ed., pp. 123–192, 1974.
- [13] P. Ryan and D. Sandler, “Scintillation reduction method for photometric measurements,” *Publications of the Astronomical Society of the Pacific*, vol. 110, no. 752, pp. 1235–1248, 1998.
- [14] M. A. Ellison and H. Seddon, “Some experiments on the scintillation of stars and planets,” *Monthly Notices of the Royal Astronomical Society*, vol. 112, pp. 73–87, 1952.
- [15] S. H. Reiger, “Starlight scintillation and atmospheric turbulence,” *Astronomical Journal*, vol. 68, pp. 395–406, 1963.
- [16] P. B. Stetson, “On the growth-curve method for calibrating stellar photometry with CCDs,” *Publications of the Astronomical Society of the Pacific*, vol. 102, pp. 932–948, 1990.
- [17] A. Guarnieri, C. Bartolini, G. Beskin, et al., “GRB 060719: TORTOREM optical upper limits,” GRB Coordinates Network, Circular Service, 5372, 1, 2006.
- [18] S. Karpov, G. Beskin, S. Bondar, et al., “GRB 061202: TORTOREM optical upper limits,” GRB Coordinates Network, Circular Service, 5897, 1, 2006.
- [19] S. Karpov, G. Beskin, S. Bondar, et al., “GRB 061218: TORTOREM optical upper limits,” GRB Coordinates Network, Circular Service, 5941, 1, 2006.
- [20] G. Beskin, S. Karpov, S. Bondar, et al., “Fast optical variability of Naked-Eye Burst—manifestation of periodic activity of internal engine,” <http://arxiv.org/abs/0905.4431>.

Research Article

Automated Detection of Short Optical Transients of Astrophysical Origin in Real Time

Marcin Sokołowski,¹ Katarzyna Małek,² Lech W. Piotrowski,³ and Grzegorz Wrochna¹

¹ *The Andrzej Soltan Institute for Nuclear Studies, Hoża 69, 00-681 Warsaw, Poland*

² *Center for Theoretical Physics, Polish Academy of Sciences, Al. Lotników 32/46, 02-668 Warsaw, Poland*

³ *Institute of Experimental Physics, Faculty of Physics, University of Warsaw, Hoża 69, 00-681 Warsaw, Poland*

Correspondence should be addressed to Marcin Sokołowski, msok@fuw.edu.pl

Received 29 June 2009; Revised 11 November 2009; Accepted 4 January 2010

Academic Editor: Taro Kotani

Copyright © 2010 Marcin Sokołowski et al. This is an open access article distributed under the Creative Commons Attribution License, which permits unrestricted use, distribution, and reproduction in any medium, provided the original work is properly cited.

The detection of short optical transients of astrophysical origin in real time is an important task for existing robotic telescopes. The faster a new optical transient is detected, the earlier follow-up observations can be started. The sooner the object is identified, the more data can be collected before the source fades away, particularly in the most interesting early period of the transient. In this the real-time pipeline designed for identification of optical flashes with the “Pi of the Sky” project will be presented in detail together with solutions used by other experiments.

1. Introduction

The first robotic telescopes were designed to work autonomously and without too much human supervision. The development of these devices was strongly stimulated by optical observations of Gamma-Ray Bursts (GRBs) ([1–3]). These powerful explosions, discovered by VELA satellites in the late 60s [1], take place on very short timescales, ranging from a fraction of second up to hundreds of seconds. In the early days chances for observation of optical counterparts were very limited due to large errorboxes of burst positions. Bursts localizations were typically provided a long time after the event, thus early optical observations in the most interesting period of these processes were practically impossible. The idea of automatic identification of optical transients (OT) was born as an answer to the above problems. In the 90s the Burst And Transient Source Experiment (BATSE) detector on board of the Compton Gamma Ray Observatory (CGRO) [4] was providing real-time alerts with the positional accuracy of the order of 5°. Alerts were distributed in almost real-time via the Gamma-ray bursts Coordinates Network (GCN) [5]. Optical system covering large field of view (FOV) together with the pipeline automatically identifying transients would allow

find optical counterparts of BATSE bursts. In 1997 the first optical counterpart of the gamma-ray burst was observed, triggering rapid development of robotic telescopes. In 1999 great milestone was achieved by the ROTSE robotic telescope [6], which for the first time observed the optical emission simultaneously with the γ -rays emission (GRB 990123). Since that time many automatic robotic telescopes have been built in order to quickly react to GCN alerts [5] and observe prompt optical signal as early as possible. During the last decade these devices became more and more sophisticated. Many of them are fully automatic and autonomous telescopes, not requiring too much human attention. The standard approach is to wait for the GCN alert and, when it comes, quickly move to the burst position, reaching it normally in less than 60s. Nowadays, real-time alerts are mostly provided by Swift [7] and Fermi [8] satellites, but only Swift gives positional accuracy of the order of 3 arcminutes. The basic requirements for fast robotic telescopes have already been achieved, but new challenges are coming.

Nowadays, robotic telescopes and their associated data pipelines are expected to perform automated data analysis, find interesting events, and send alerts to the community so that larger telescopes can observe such objects as soon

as possible. Since the very beginning robotic telescopes were producing a lot of optical data which was generally analysed off-line. Successful implementation of a real-time pipeline requires that additional conditions are fulfilled, some of them specific for a particular detector architecture: stable hardware and software for data acquisition, good efficiency of algorithms, and sufficient CPU power to handle data while it is collected. Usually it requires also effective data management systems (i.e. databases) to catalogue reduced data and analyse it in real time. As it can be clearly seen from the example of gamma-ray bursts, offline or late identification of the phenomena is insufficient and does not guarantee a chance of follow-up observations which could allow the collection of important early data. Real-time discovery, alert distribution, and immediate reaction of large telescopes and other detectors are needed to successfully investigate short timescale astrophysical phenomena.

The regime of short timescale (scaled in seconds and less) is a relatively unexplored area. The examples of GRBs, blazars, and Active Galactic Nuclei (AGNs) show that the most violent and interesting astrophysical processes occur on very short timescales. Thus many interesting discoveries can be expected in this regime. This includes optical transients related to GRBs, as it was already confirmed by observations of prompt optical emission from at least a few GRBs (990123 [6], 080319B [9]), these processes may have even very bright optical counterparts. Particularly the case of GRB080319B showed that the brightness of prompt optical flashes from the GRB can reach 5^m which makes them accessible even for a naked eye and certainly for wide field detectors. This further confirms the necessity and suitability of building wide field systems for observations of prompt optical signal from GRBs. It also motivates for developing real-time pipelines, able to self-trigger follow-up observation even without GCN alerts. It has to be noted, however, that except for the two cases mentioned above (GRB 990123 and 080319B) observed optical counterparts are typically fainter than 13^m ([10, 11]). On the other hand, there is a very limited number of optical observations of GRBs in the very beginning of the burst.

Currently we have solid proof that such short time optical transients can even reach brightness of the order of 5^m . Wide field arrays of photo camera lenses and even fish-eye cameras can be effective tools for automatic identification of such events in real time. The “Pi of the Sky” system will be able to reach magnitudes of the order of $14\text{--}15^m$ for combined images, a magnitude range largely unexplored for OTs. Discovered events should be immediately distributed via global communication networks (like VOEventNet [12], Heterogeneous Telescope Networks (HTN) [13] or other), which could become viable extensions of the GCN network.

The most important and interesting processes that could be detected with this kind of analysis are untriggered GRBs or orphaned afterglows. Current GRB models predict that optical emission may be less collimated than high energy emission and thus there may be more optical flashes related to GRBs than γ -ray flashes. The observation of such events would probably be one of the milestones in GRB understanding.

Most of optical observations are related to so called long GRBs, but there are also short GRBs, with very short time scales (time durations $\Delta T < 2\text{ s}$). Optical counterparts of short GRBs have been observed only in very few cases and in relatively long time after the outburst. Optical observations of short GRBs in the early phase would therefore give important input to the theoretical understanding of these processes.

In addition to GRBs there are other processes which should be identified as fast as possible in order to allow deeper investigations. These can be supernovae explosions (SN), cataclysmic variables like novae or dwarf nova explosions, but also activities of AGNs and blazars. Very similar tools are useful also for the automatic identification of Near Earth Objects (NEOs), Potentially Hazardous Asteroids (PHAs) or Space Debris, which has recently become a serious problem for all modern space missions.

Every time technology allows to enter new regimes, new types of phenomena can be discovered. It is very probable that on the timescales of seconds and less there are optical processes in the Universe which were not yet classified or even observed. In order to systematically study such kind of processes, effective pipelines for real-time identification are required. Typically, they are implemented in wide field systems, but the synergy between wide field and large telescopes would allow the good coverage of optical light curves. Recently similar pipelines have been developed also for large telescopes and this direction is also very promising, giving chances for the detection of fainter OTs.

Finally there are practical reasons for development of such pipelines, as astronomical experiments produce more and more data. In certain points they can reach amounts which will not be possible to store permanently. They may almost approach the amounts produced by the high energy experiments and thus it may be necessary to use similar methods for reducing the stream of data by using on-line selection algorithms. Real time analysis pipelines can identify interesting event candidates in the images and store only raw data related to these events ignoring the rest of the data. It may be necessary to develop specific triggers for specific types of phenomena, exactly like in particle physic experiments. Today it is not yet a very crucial problem, but it may become an issue in the near future, when experiments like Large Synoptic Survey Telescope (LSST) [14] or the Panoramic Survey Telescope & Rapid Response System (Pan-STARRS) [15] will start to collect 30 TB of data per night.

2. Methods of Identification of Optical Transients in Short Timescales

In this section, we give an overview of methods used for the identification of optical flashes. We concentrate on short ($\leq 10\text{ s}$) optical flashes, but also methods for detecting events with longer timescales will be described. Depending on the type of experiment and especially on exposure times, different methods of flash recognition have to be implemented. The exposure time is the main limitation for the complexity of image analysis. A new image has to be analyzed

while the next one is being collected, therefore time and CPU consuming algorithms cannot be used. The situation is different in the case of longer exposures where much more sophisticated algorithms can be implemented. Typical methods will be described in the first subsection. In the second subsection methods used in the pipeline developed for the “Pi of the Sky” experiment will be presented.

2.1. Identification of New Objects in the Sky. The main purpose of the algorithm looking for optical transients is to analyze new images of the sky and find new objects which were not present in the previous images nor in the star catalogues. The purpose is to find candidates for optical flashes with high efficiency, but also to effectively reduce the background so that the amount of events requiring visual inspection is reasonable. The first step is to compare the new image with the reference image. The type of the reference image depends on the realization of the algorithm. It may be a series of previous images taken in similar conditions just a moment ago or it may be a reference image resulting from a combination of best images of the same field of the sky taken before at very good observing conditions. Another way is to compare a new image with the reference catalogue of astrophysical objects. It is also possible to combine both solutions to obtain the most satisfying result.

The implementation of the method depends on the specific needs and characteristics of the experiment. Typically, experiments collect subsequent images and the time period for the analysis of a new image is limited by the exposure time: new image should be analyzed before the next image is read out. In case of the short time scale (≤ 10 s) surveys, like for example “Pi of the Sky” (10-second exposures), this may be a strong limitation, imposing requirements on the type of analysis methods that can be implemented. Therefore the image subtraction method is widely used. Images are taken under almost the same conditions, so the previous image can be subtracted from the new one, exhibiting changes in the sky. A precise and exact method of image subtraction was described in [16]. However, in many applications this method can be too time consuming, thus very simple, pixel based subtraction is applied. In case of sub second exposures, like in the case of the TORTORA experiment ([17, 18]) it is probably the only method that can be used. There are many variations of this method, in some cases a reference image or median of images from earlier observations (i.e., taken at very good observing conditions) is used for subtraction. After the subtraction, when the image revealing changes in the sky is obtained, the list of flash candidates is usually built by a selection of pixels, where the signal exceeds certain threshold (5σ or so). However, one has to be aware of several types of artifacts which appear in the image after the subtraction. For example Point Spread Functions (PSF) of stars fluctuate and the subtraction can produce a false signal at the edges of the stars PSF. The suppression of this type of false alerts (by, e.g., rejection of alerts close to edges of stars or division by a variability map) is one of the main tasks of flash selection algorithm. After this step a list of flash candidates is produced and subsequent steps are introduced

to reject background events. A typical background that has to be handled at this stage by subsequent cuts of the algorithms is mainly due to

- (i) sky background fluctuations,
- (ii) fluctuations of faint stars,
- (iii) fluctuations of PSF of bright stars,
- (iv) saturated stars,
- (v) cosmic rays hitting a CCD chip,
- (vi) defects of the CCD matrix (hot pixels, bad columns, etc.),
- (vii) artifacts (e.g., strip due to permanently opened shutter),
- (viii) flashes due to artificial satellites,
- (ix) flashes due to planes.

In case of observations in longer timescales (≥ 30 s) the situation is usually easier. The time is long enough to implement more sophisticated algorithms. In such a situation exact photometry can be performed. The *sExtractor* package [19] is usually applied as one of the fastest photometric programs, many other photometric packages are also in use. After the photometric analysis a list of stars in the new image is produced and it is compared with the reference list of stars in the observed field. A catalogue of reference stars is stored in the computer’s memory (or on hard drive) and indexed (spherical index or bucket index), allowing very fast binary searches, so that every star in the new image can be verified very fast. The reference list can be obtained from external star catalogues like USNO, Guide Star Catalog (GSC) or SIMBAD depending on the limiting magnitude of the survey. It can also be obtained from the self-produced star catalogue or it may be a list of stars extracted from the reference image which was collected at very good observing conditions. After the comparison of the two lists of stars, a list of new objects in the sky is produced. They are candidates for optical transients and have to be verified by a more sophisticated analysis.

The usage of exact photometry has many advantages over the simple pixel based image comparison. First of all it produces a list of stars and if the photometry takes the stars’ PSF properly into account, the problem of star image fluctuations can be easily avoided. In case of longer exposures most of the background types listed above are irrelevant. Typically a few (≥ 2) images with exposure time $T \geq 30$ s are collected within an interval of a few hours and new objects are required to be visible on at least 2 images. Such a requirement rejects all background events due to cosmic-ray hits, flashing satellites and planes. However, it rejects also short optical transients.

2.2. Identification of Short Optical Flashes in the “Pi of the Sky” Experiment

2.2.1. Pi of the Sky experiment. The “Pi of the Sky” system is designed for observations of a large fraction of the sky with a temporal resolution of the order of ≤ 10 s. The system

TABLE 1: Maximal distance from the Earth allowing for the rejection of artificial satellites with the parallax, for the angular size of a pixel of 36 arcsecond.

Site separation [km]	Maximum distance [km]
18	103,000
50	286,000
100	572,000

will consist of two farms of 16 cameras (Figure 1 in [20] in these proceedings), installed in a distance of several dozens of kilometers. Each camera will cover a field of view (FOV) of $20^\circ \times 20^\circ$, which will result in a total sky coverage of 2 steradians for a single set of 16 cameras. This corresponds to the field of view of Swift BAT [7] and Fermi LAT [8] detectors. Every GRB detected by the Swift satellite, when followed by the “Pi of the Sky” system, will already be in its field of view. The presented algorithms will analyze images in real time, in search for short optical flashes. The two sets of 16 cameras will observe the same part of the sky. The large distance between two sets is needed to use parallax for rejection of short optical flashes caused by artificial satellites and other near Earth sources (Table 1).

The design and construction of the prototype was the first step towards the final “Pi of the Sky” system. The prototype was installed in Las Campanas Observatory (LCO) in Chile in June 2004. It consists of two custom designed cameras (almost the same as built for the final system) [21] installed on an equatorial mount. Each camera has a CCD with 2000×2000 pixels of $15 \times 15 \mu\text{m}^2$ and is equipped with CANON EF $f = 85 \text{ mm}$, $f/d = 1.2$ photo lenses, covering FOV $\approx 20^\circ \times 20^\circ$ and resulting in a pixel scale of 36 arcsec/pixel. The cameras continuously collect 10 s images of the same field in the sky with 2 s breaks for the CCD readout.

The typical astrometric error of a star position is ≤ 10 arcsec. Large angular size of pixels can be a cause of source confusion, particularly in dense fields. However, it is not a problem for identification of optical transients as astrometric precision is sufficient for source identification with larger instruments (e.g., in cases of discovered nova stars). It becomes more important issue in the case of variable star analysis. Therefore lightcurves of stars possibly affected by blending have to be excluded from the analysis.

The values of a limiting magnitude for the prototype are the same as expected for the final system: 12^m on a single 10 s exposure and $14\text{--}15^m$ on 20 averaged images. It was estimated that $\approx 1/5$ of the Swift’s GRBs will occur in the FOV of the system during good weather (75% of observational nights assumed). Based on the observed optical lightcurves of GRBs, it was estimated that at least 1–2 bursts per year should be bright enough for a positive or marginal detection. For the rest of bursts, optical limits for the moment of the onset will be determined. Hopefully, first optical limits or detections of short GRBs in the very moment of the burst will also be obtained. More details about the prototype and final design of the system can be found in [10, 20, 22].

2.2.2. First Level Trigger—Identification of Flashes from a Single Camera. The aim of this algorithm is to find optical flashes occurring in a single image (time scale < 10 s). The signature of such events is the following: an object appears in a new image of the sky in the position where nothing was present in the previous images of the same field. In the “Pi of the Sky” experiment a new image is compared to a series (typically 7) of images collected just before it.

The first step of the analysis is the subtraction of a dark frame. In the next step, the image is transformed by a custom designed transformation, called `laplace` (because it resembles a discrete version of Laplace operator). The value of each pixel is calculated as a simple function of several surrounding pixels as illustrated in Figure 1. Values of pixels just around the transformed pixel (black squares in Figure 1) are summed and values in further pixels (opened squares) are subtracted with proper weight. This transformation is equivalent to the calculation of a simple aperture brightness for every pixel. The distribution of pixel values after such a transformation is centered around zero (Figure 2). The transformation allows for easy identification of pixels significantly brighter than the local background level. For every collected image a Gaussian curve is fitted to this distribution and the threshold required for signal T_n is calculated as a multiplicity of the dispersion value (σ_B), typically $T_n = 5\text{--}6\sigma_B$.

Several types of filters which were tested are shown in Figure 1. Images before and after applying the `g54_laplace` filter (aperture 4 in Figure 1) are shown in Figure 2. After comparing efficiencies and false event rates for different filters, `laplace_12` (aperture 12 in Figure 1) was chosen for the current optical setup.

At this stage, algorithm must handle the highest data rate, of the order of the number of the CCD pixels ($4 \cdot 10^6$), so it must be very fast and simple. It should preserve most of the signal and reject big fraction of non-interesting measurements. The algorithm does not require astrometry to be performed on every image, it is enough to run it every ten images or so. The algorithm takes advantage of the fact that the constant mount rotation is compensating very efficiently for the Earth rotation. However, it was not clear in the beginning whether it would be the case, so an image shift determination was also implemented and could be eventually used (e.g. for a fixed mount setup). At this stage flash-like events in a single camera are identified. The following two criteria are required to select candidates for new objects in the sky.

(i) T_n —this cut selects stars in the new image by requiring a signal in the analyzed pixel. The condition for the signal presence is $N(x, y) > T_n$, where $N(x, y)$ is the value of pixel (x, y) on the `laplace` transformed image, T_n —denotes signal threshold and N stands for the new image. The threshold T_n is specified by configuration parameters in multiplicities of the σ_B value. Usually it is set to $5\sigma_B$, but for full moon nights it is automatically increased to $6\sigma_B$. The goal of this cut is the identification of all pixels belonging to stars or other point like objects in the new image.

(ii) T_v —this cut rejects objects present on previous images. It requires that there is no signal on the previous frame. “Previous frame” in this case means not just one

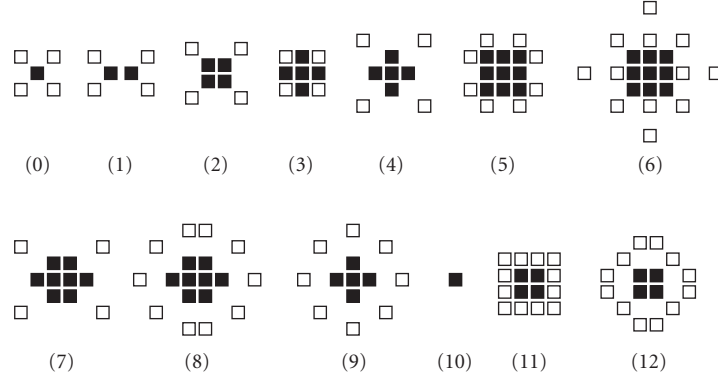


FIGURE 1: Different laplace “apertures” tested for on-line flash recognition algorithms. Full black squares denote image pixels added with positive signs and opened squares denote those which are subtracted with proper weight.

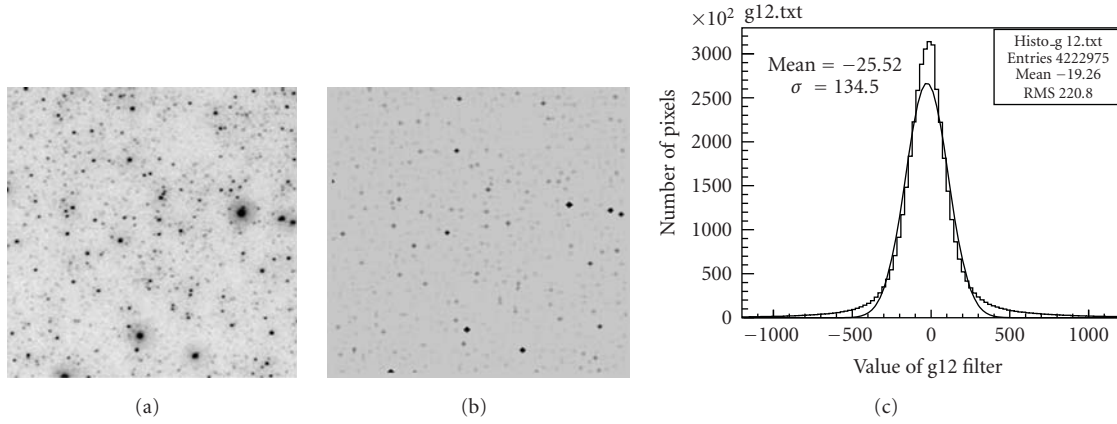


FIGURE 2: Sky image before (a) and after (b) applying the laplace filter, and the distribution of pixel values after laplace filter is applied (c).

single image, but the average of several previous images. The condition imposed on the value of a pixel in the reference image is the following: $P(x', y') < T_v$, where $P(x', y')$ is the maximum value in the surrounding of pixel (x, y) on the average of N_{aver} previous images, T_v —denotes veto threshold and P stands for “previous images”. The pixel (x', y') is usually chosen from 9 pixels (3×3 square) around (x, y) . It allows to avoid an influence of small mount tracking inaccuracies and fluctuations of edges of brighter stars. Mount tracking ensures that in most cases an object falls in the same 3×3 pixels square on the new image. Pixels remaining after this cut should be new objects which appeared on the new image and were not present on previous images. Typically less than 100 such objects are identified per image.

After these two cuts the list of flash candidates is created. Most of them are still due to the background which can be rejected by the following criteria:

(i) *MinLaplace*—rejects pixels which have a value on the previous image lower than the minimum allowed value (T_{MinLap}). This cut allows to reject edges of bright stars where the values of pixels after laplace filter often become negative, but can also vary to values exceeding T_n .

(ii) *IfMoreAfterTv*—rejects the whole image if the number of pixels accepted after T_v cut exceeds a certain limit N_{MaxTv} . This cut allows to reject images with a big number of events which are usually due to system errors, moonlight or clouds. If the image is flagged as bad, all events are certainly false, so they are rejected and no further analysis of this image is performed. In the final version of the project it will be possible to use cloudmeter in order to reject cloudy images, but it is not yet available for the prototype system.

(iii) *SkipOverlaps*—checks the number of pixels accepted in a certain radius R_{overlap} around the current pixel. The algorithm keeps only one event and removes the overlapping ones. This reduces the number of pixels to be analyzed, related to the same object, to a single one.

(iv) *Shape*—the object shape indicator S is calculated as:

$$S = \frac{S_{\text{cluster}}}{S_{\text{circle}}}, \quad (1)$$

where S_{cluster} is the area of a cluster and S_{circle} is the area of the smallest circle circumscribed on this cluster. The cluster is defined as a group of pixels around the current pixel with values satisfying $N(x, y) \geq T_{\text{cluster}}$ (usually set to $2\sigma_B$). Elongated events, which are probably due to moving objects,

result in small S values. These are rejected by the requirement $S > T_{\text{shape}}$ (usually set to value 0.2).

(v) *BlackPixels*—this cut rejects pixels which have signal much smaller than neighboring pixels. In case such a pixel is one of the “minus” pixels in the laplace filter (Figure 1), the resulting value of the filter is too high and would produce false alerts.

(vi) *HotPixels*—due to CCD chip defects some pixels can give a much higher signal than normal “good” pixels. Such effects should generally be eliminated by the dark image subtraction. However, sometimes new hot pixels can appear temporarily during a night and become quiet again later. Two ways of rejecting such events have been implemented. The first one is the calculation of the average value in a pixel on previous images, pixels with sky background should have this value close to the average value of the laplace filter (i.e., close to zero). Hot pixels and stars will have a large average value on previous images, in case it is larger than $3.5\sigma_B$, the pixel is rejected. The second antihotpixel cut is the rejection of pixels by the list of known hot-pixels. This list is updated regularly when new defects are found.

After the above selection cuts, the list of event candidates from a single camera is created, usually it consists of not more than several tens of events per image.

2.2.3. Second Level Trigger: Transient Verification. The goal of the second level trigger is to confirm events from a single camera and reject background events, which at this stage are mostly due to cosmic-ray hits, satellites and planes. The action at this level depends on the type of the system setup. Generally three configurations are possible.

(i) Two cameras on a single mount working in coincidence. In this configuration events found by the first camera are verified in the corresponding image from the second camera. Only events present in images from both cameras are accepted. This configuration is realized by the prototype system in LCO.

(ii) Confirmation of an event on the next images. It is also a very effective way of rejecting flashing satellites and cosmic-ray hits. However, short optical flashes are also rejected by such a requirement, thus this is not the best way to fulfill all the requirements for the ideal algorithm. Formerly it was used when only one camera of the prototype was operational.

(iii) Two cameras in distant locations working in coincidence. This will be realized in the final version of the “Pi of the Sky” system. Cameras will be paired, and each pair will observe the same field in the sky. Spatial and time coincidence of the flash in both cameras will be required.

In any case coincidence requirement is one of the most important cuts. The main goal is the rejection of cosmic rays hitting the CCD chip and imitating astrophysical flashes. In many cases cosmic-ray hits have a PSF completely different than the PSF of stars and they could be rejected by a shape recognition procedure. However, in some cases they are very similar to PSFs of the stars. Even if this is a very small fraction of all cosmic ray events this would cause all flashes found by the algorithm to be uncertain. The probability that different cosmic ray particles will hit two chips in the same

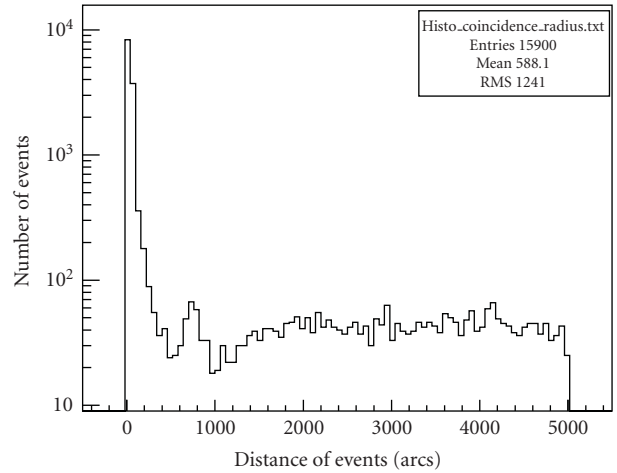


FIGURE 3: Distribution of angular distances between all event candidate pairs from images collected by cameras k2a and k2b during night 2006-05-28/29. Number of event candidates from single camera is typically of the order of 10^4 - 10^5 , which results in a combinatorial background at distances ≥ 500 arcsec.

time and in the same positions (with respect to stars) is negligible. Coincidence is also a very effective way of rejecting background events due to sky background fluctuations, edges of bright stars and clouds. In the prototype version, the collection of images by two cameras is synchronized so the only parameter is the maximum allowed angular distance of events in both cameras. The value $R_{\text{coinc}} = 150$ arcsec is used in the current setup. It was determined from the distribution of angular distances of events in both cameras (Figure 3).

After the coincidence requirement the remaining events are real optical transients coming from the sky. However, most of them are still background events, mainly due to flashing satellites. In order to reject most of these events databases of orbital elements in Two Lines Element (TLE) format are retrieved from the Internet every evening. They are combined to a single larger database containing ≈ 13000 orbital elements. For every image, positions of all satellites in the database are calculated (using the predict package [23]) and every flash candidate is verified, it is rejected, if it is closer than $R_{\text{sat}} = 0.5^\circ$ from any of the satellites. The rejection radius was determined from the distribution of angular distances from flashes to the closest satellite from the database which is clearly peaked around zero (Figure 4).

The red dots on the plot represent the distance distribution for randomly generated flashes to the closest satellite from the catalogue and illustrate the size of combinatorial background.

The orbital elements databases are not complete and many satellites are not included there. In order to reject those, event candidates from many consecutive images are examined against track conditions. If it is possible to fit a track to the set of events from different images and the velocity of the object is constant, all events on the track are rejected. This rejects a big fraction of flashing satellites and

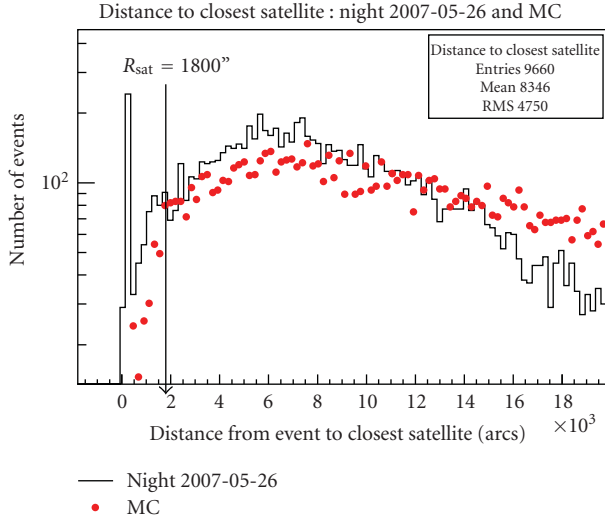


FIGURE 4: Distribution of the distance from flash event candidate to the closest satellite from the catalogue, for events found by coincidence algorithm during night 2004.10.28/29. For comparison distances from randomly generated flashes to the nearest satellite are shown as red dots—combinatorial background is nicely reproduced. For the purpose of this analysis signal threshold was decreased to have more accidental coincidences.

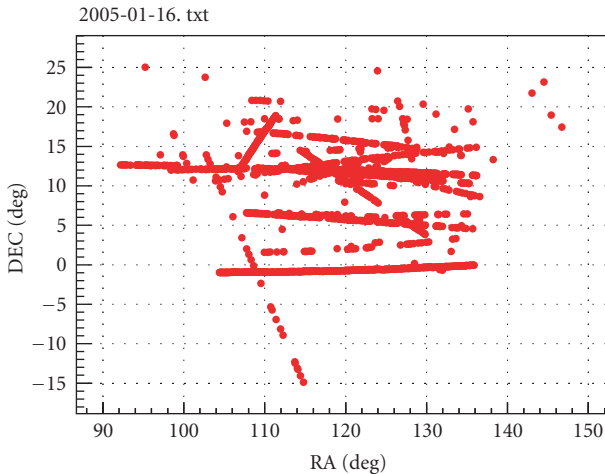


FIGURE 5: Events rejected by track cut during single night 2005-01-16/17.

planes (Figure 5); however, it is possible that rarely flashing (rotating) satellites can still survive this cut.

Artificial satellites orbiting the Earth may rotate and sometimes reflect the sunlight towards the apparatus causing flash-like events. The most problematic are those entering the FOV of the telescope and flashing once or twice. Another problem is that verifying whether an event belongs to a track or not requires a collection of some images after the flash. In order to confirm the event, the program must wait for some time and therefore it is not a real time transient identification any more.

A better solution allowing for efficient rejection of satellites in real time is a coincidence between cameras installed in distant locations. In such a configuration, it is possible to reject near Earth flashing objects by using a parallax (Figure 1 in [20], these proceedings). In the prototype version of the experiment two cameras are installed on a single mount. Nevertheless, this method was tested by coincidence with the RDOT experiment [24] located at La Silla at a distance of ≈ 30 km. The final design of the “Pi of the Sky” experiment will consist of the two subsystems in a distance of several dozens of kilometers.

Table 1 shows a maximum distance to which artificial satellites can be rejected, assuming optics and CCD chip used for the final design of the “Pi of the Sky” experiment (pixel angular size of 36 arcsec). The distance of ≈ 100 km would be optimal and would allow to reject all objects even further than the orbit of the moon. Building such a wide field systems is a large project. However, the number of robotic systems looking for optical transients is rapidly growing, thus another promising possibility may be looking for coincidences of transients in co-operation with other experiments. Development and joining networks like VOEventsNet [12] allow to correlate events from different experiments (not only optical) in almost real time.

2.2.4. Third Level Trigger: Final Confirmation and Classification. The first two levels of trigger retain a very small number of events. On average it is not more than 20 per night. It depends strongly on weather conditions and in case of cloudy night this number can reach hundreds. However, in the final system the number of events will be 16 times larger reaching 300–400 per night which would be much more difficult to be inspected. For this reason the third level of the trigger (TLT) has been implemented. It checks the final events accepted by the previous levels which ensures that only a small number of events have to be examined. Therefore it is possible to implement more sophisticated and time consuming algorithms to check every event. The current implementation of the TLT consists of several cuts. As an example, criteria developed for rejection of plane and meteor-like events will be described. A simple Hough transform (Hough transform from (x, y) to cylindrical (r, ϕ) coordinates in order to find particular shapes in an image) can be applied to a small image part surrounding the event. It finds pixels with signal above a certain level T_{hough} and creates the distribution of their polar angle ϕ ($\phi = \text{atan}((y - y_0)/(x - x_0))$). A significant peak in the distribution means that the event looks like a “straight line” which is most probably due to a plane or a satellite (Figure 6).

The event will be considered as “straight line” due to a plane if the maximum of this distribution is larger than certain threshold above the mean value (Figure 6). More details about criteria implemented in the TLT, can be found in [10].

2.2.5. Testing and Results. The “Pi of the Sky” prototype in Las Campanas Observatory has been collecting data

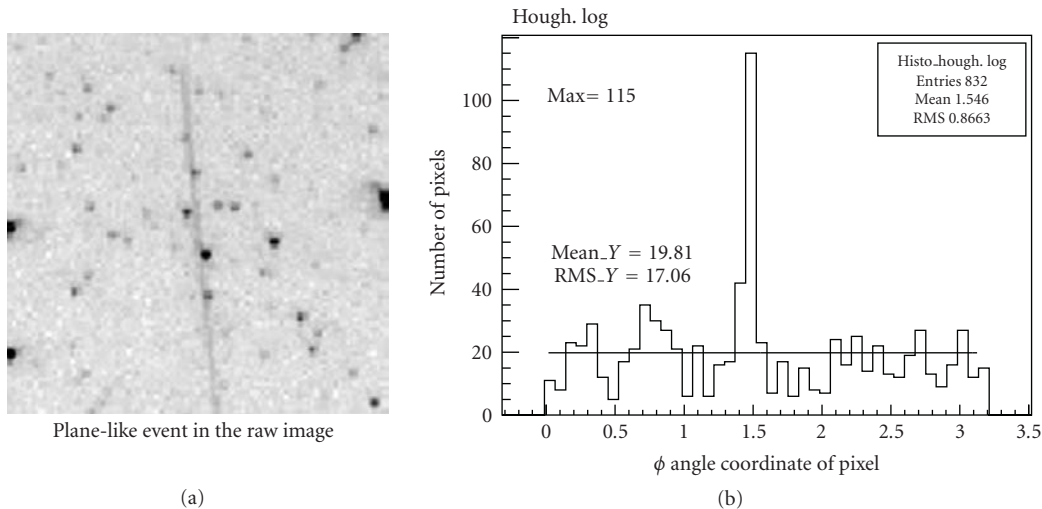


FIGURE 6: The original image of the event (a) and the distribution of the ϕ angle coordinate for the plane-like event (b).

since June 2004. The algorithm works every observational night. The efficiency of the flash recognition was determined by simulating optical flashes and counting how many of artificial stars added to real sky images were identified and how many of them were wrongly rejected. This efficiency is typically of order of 70%–80% for cloudless nights and objects brighter than 11^m . Overall efficiency of the algorithm for stars brighter than 12^m is $\approx 35\%$. Further improvements of the algorithm are planned for the final system.

The greatest success of the experiment, but also of the real-time pipeline for optical transients was automatic discovery of the OT from GRB080319B [9]. Another interesting event was automatic identification of the outburst of flare star CN Leo (RA = $10^h56^m29^s$, Dec = $+7^\circ01'$) on 2005.04.02 1:13:40 UT [25]. There were also a few events which were observed on 2 consecutive 10 s images, but only on a single camera (second one was not working then). And there were more than 200 events visible on single 10 s exposure by both cameras simultaneously. None of them was positively correlated with any astrophysical events or signal from other experiments. Most of them are probably due to rarely flashing satellites which could not be rejected by the algorithm. However, some of them can be due to interesting astrophysical processes. In the near future OTs discovered by the “Pi of the Sky” detector will be automatically published via the VOEventNet network. Based on statistics of the optical transients identified by the prototype preliminary, upper limits for the number of OTs brighter than 11^m on the whole sky were determined.

- (i) Number of OTs of time duration $\Delta T < 10$ s is $N < 300 \text{ events}/4\pi/\text{day}$.
- (ii) Number of OTs of time duration $\Delta T > 10$ s is $N < 2 \text{ events}/4\pi/\text{day}$.

3. Implementation of Real Time Pipelines in other Experiments

The number of telescopes and wide field systems is rapidly growing. In many cases the main goal is strictly related to GRBs, but covers also other short time scale processes, especially optical transients (OTs). It is impossible to present all experiments which developed pipelines searching for OTs or other processes in the real time. The choice of experiments presented in this contribution had to be subjective. The idea was to present several experiments focused on different areas of astrophysical processes and present a variety of applications in which real-time pipelines are already very important tools. Most of the experiments presented here collect images with exposures times ≥ 30 s, in many cases a few images of a given field are collected and later after a few hours the next set of images of the same field is collected. In most cases algorithms require object to be visible on at least 2 images from a single or both sets of images. Thus several problems, typical for algorithms acting on ≤ 10 s images are irrelevant (see Section 2).

Perhaps one of the most advanced systems for wide field observations is the RAPTOR experiment [26]. It already consists of two sites RAPTOR-A and RAPTOR-B separated by a distance of 38 km. The single site consists of 4 wide field cameras covering FOV of $40^\circ \times 40^\circ$ and a fovea telescope which is used for followup observations. The parallax gives a possibility of rejecting near Earth objects. Integration time is typically 30 s, the algorithm compares new images with self-produced star catalogue. The catalogue is started from the GSC star catalog and extended when a new data is collected. The system is planned to be extended to a large array of wide field cameras.

Another very advanced project from the opposite site of the Earth is MASTER system in Russia ([27–29]). According to author’s knowledge it already consists of 6 wide field cameras, each covering FOV of $25.5^\circ \times 39.8^\circ$. The experiment

covers timescales >0.15 s, reaching $13''$ for 5 s exposures. The real time pipeline was implemented and successfully searches for supernovae explosions, several events have been discovered automatically. The important components of the system are 40 cm telescopes for followup observations of the detected transients.

The ROTSE system ([6, 30]) was so far probably one of the most important robotic telescopes in the history. It was the first experiment to observe optical emission contemporaneous with the γ -ray emission from GRB 990123. Since that time ROTSE changed its strategy from the wide field system to a narrow field ($1.85^\circ \times 1.85^\circ$) telescopes located in 4 sites around the Earth. Typical exposure times are 20–60 s. The pipeline for an automatic identification of OTs was implemented and about 30 supernovae events and few OTs of unknown origin per year are identified.

The TORTORA project ([17, 18]) is a wide field system which for the first time observed optical signal from a GRB (GRB080319B) with a sub-second time resolution ([9]). The camera covers $24^\circ \times 32^\circ$ FOV and collects 1/7 s images, which are analyzed in real time in search for optical transients. Such a high time resolution system results in an enormous amount of the produced data, making implementation of real-time analysis inevitable.

The first Polish robotic telescope and one of the first in the world is the All Sky Automated Survey (ASAS) ([31]). The system is located in Las Campanas Observatory in Chile and also in Maui at Hawaii Islands. It consists of wide field cameras covering $8^\circ \times 8^\circ$. They typically collect 2–3-minute exposures on each field. The system scans the entire sky every 1–2 days. New objects in the sky are identified in real-time by a comparison of list of stars from new images with the own star catalogues resulting from previous observations. The main goal of the experiment is creation of complete catalogue of variable stars. However, pipeline designed for optical transients discovered many new cataclysmic variable stars and also several comets.

Perhaps one of the first real-time pipelines ever implemented was the one developed for the Optical Gravitational Lensing Experiment (OGLE) experiment [32]. It is not robotic telescope, but the pipeline for automatic discovery of optical gravitational lensing events is a very successful one and is definitely worth presenting here. Analysis of this type of phenomena requires good coverage of optical lightcurve so early detection and distribution of alert in the community is a very important issue. In order to find brightening due to gravitational lensing, differential photometry technique is used [16]. The cumulative reference image of the same field observed in previous seasons is subtracted from the new image in order to find brightness variations. The OGLE group has also developed a pipeline dedicated for OTs (NOOS system—New Objects in OGLE Sky) which discovered some supernovae events. OGLE microlensing events are already distributed via the VOEventNet network in almost real-time.

Recently real-time pipelines for OTs have been implemented and tested on the data from several large telescopes. One of the examples can be Catalina Real-Time Transient Survey (CRTS) [33] which uses images from Catalina Sky

Survey (CSS) in order to find optical transients. The telescope observes $8^\circ \times 8^\circ$ FOV and collects four 30 s exposures of a given field every 30 minutes. The real-time pipeline based on an image subtraction technique has been implemented. The transients are also verified against star catalogues USNO-B, the Sloan Digital Sky Survey (SDSS) and Palomar Quest (PQ) survey. The survey has detected 350 events in 6 months. They were mostly supernovae, cataclysmic variables, UV Ceti flare stars, blazars, and Near Earth Objects (NEOs). An important feature of the experiment is that events are already published in real-time through the VOEventNet network.

A similar example is the Palomar Transient Factory [34] which uses 1.2 m telescope in Palomar Observatory. It covers $\text{FOV} \approx 7.8^\circ \times 7.8^\circ$ and reaches limiting magnitude of $21''$ on 30s exposures. The real-time pipeline for OTs has been developed in order to search for SNs and also exotic optical transients of unknown origin.

The Liverpool Telescope Transient Rapid Analysis Pipeline (LT-TRAP) is an interesting example of the pipeline for real-time GRB analysis. It was originally designed for 2 m Liverpool Telescope (LT) [35], which reacts to GCN alerts. The main purpose of LT-TRAP pipeline is to automatically identify afterglow candidates in images collected just after the telescope had been re-pointed to the GRB position. The real-time analysis results in the decision on the strategy of the OT observations. It must quickly decide whether polarimetry and spectroscopy should be performed or rather multi-color imaging and so forth. The LT-TRAP pipeline has also been deployed on other facilities (i.e., Faulkes Telescopes).

There are currently many efforts to implement and deploy real-time pipelines on large telescopes. In several cases the main goal is to study the discovery potential of such devices in the short time scale regime and background studies. They provide a science-driven testbed for future projects such as the Large Synoptic Survey Telescope (LSST) which is planned to start collecting data in 2014 [14]. The LSST will be 8.4m telescope, with FOV of $3.5^\circ \times 3.5^\circ$ and 3.2 gigapixel CCD mosaic. It will cover time scales > 10 s scanning the whole sky every 3–4 days. One of the important points of the scientific program is discovering OTs in real-time. The experiment will produce up to 30 TB of data per night, the amounts which will probably have to be analyzed in real-time.

Another large scale future project for wide field multi-band observations is Pan-STARRS [15]. It is now in the prototype phase PS1 (one mirror) and is intended to be fully operational in the next few years. Its main goal is identification of moving Solar System objects, especially Potentially Hazardous Asteroids (PHAs) and Near Earth Objects (NEOs). However, identification of other varying sources will also be covered. Single exposure (typically 30 s) will have a size of 2 GB, making real-time data analysis pipeline a must. The cumulative master image of every observed field will be produced. It will be used by the pipeline to be subtracted from the new image in order to find moving or varying sources. Only the most interesting data will be stored longer for further analysis.

On the other side there are plenty of fish-eye cameras observing night sky all around the world. Since the famous GRB080319B it is already clear that even such a small devices can be successful and provide interesting scientific results. In many cases real-time pipelines were implemented and search for optical transients. For example CONtinuous CAMera (CONCAM) system [36] consists of 11 stations all around the world. They collect 180 s images of the whole sky reaching limiting magnitude of 6.8^m . The algorithm analyzes only good quality images, compares them to the reference images collected at good conditions and automatically rejects false alerts due to planets or variable stars. An interesting optical transient OT060420 of unknown origin and brightness of $\approx 5.5^m$ was identified and reported in [37].

4. Conclusions

The number of experiments implementing real-time pipelines is rapidly growing. They span from the very small fish-eye all sky cameras, through complex wide field systems to very large, not only robotic telescopes. They cover time scales from fraction of second up to hours and days. The areas of scientific interest also form a reach variety. There are many interesting and successful solutions in the field. Probably the best solution is stereo observation with the two systems in distant locations. This allows real-time rejection of near Earth objects, especially flashing artificial satellites. The problem is that this doubles the costs of the system. The main problem with many optical transients discovered in different experiments is that they lack confirmation from other projects. Therefore attention should also be paid to joining networks (like VOEventNet). They allow the distribution of alerts about optical transients and the correlation with other experiments in almost real-time. In a certain moment a number of observatories may reach the point where correlation with other experiments will be as efficient as stereo double-systems. The data streams from optical telescopes are becoming larger and larger, this will also imply necessity of fast real-time data analysis tools. The creation of good standard solutions, widely used and tested by the community, would save many future efforts. The implementation of pipelines for the identification of short optical transients in the “sPi of the Sky” data was presented. It successfully works on the data from the prototype system in LCO. The algorithm automatically identified a bright optical transient related to GRB080319B and many short OTs of unknown origin. It is intended to be used in the final design of the system. The final system will correlate OTs from two farms of wide field cameras, separated by a distance of several dozens of kilometers. It will be able to credibly identify optical transients of astrophysical origin in real-time.

Acknowledgments

The authors are very grateful to G. Pojmanski for giving access to ASAS dome and sharing his experience with us. They would like to thank the staff of the Las Campanas

Observatory for their help during the installation of the apparatus. This work was financed by the Polish Ministry of Science in 2005–2009 as a research project.

References

- [1] R. W. Klebesadel, I. B. Strong, and R. A. Olson, “Observations of γ -ray bursts of cosmic origin,” *The Astrophysical Journal*, vol. 182, pp. 85–88, 1973.
- [2] P. Meszaros, “Gamma-ray bursts,” *Reports on Progress in Physics*, vol. 69, pp. 2259–2321, 2006.
- [3] E. Nakar, “Short-hard γ -ray bursts,” *Physics Reports*, vol. 442, no. 1–6, pp. 166–236, 2007.
- [4] W. S. Paciesas, C. A. Meegan, G. N. Pendleton, et al., “The fourth BATSE γ -ray burst catalog (revised),” *Astrophysical Journal*, vol. 122, no. 2, pp. 465–495, 1999.
- [5] S. Barthelmy, et al., The GCN, <http://gcn.gsfc.nasa.gov/>.
- [6] C. Akerlof, R. Balsano, S. Barthelmy, et al., “Observation of contemporaneous optical radiation from a γ -ray burst,” *Nature*, vol. 398, no. 6726, pp. 400–402, 1999.
- [7] S. D. Barthelmy, L. M. Barbier, J. R. Cummings, et al., “The burst alert telescope (BAT) on the SWIFT midex mission,” *Space Science Reviews*, vol. 120, no. 3–4, pp. 143–164, 2005.
- [8] W. B. Atwood, A. A. Abdo, M. Ackermann, et al., “The large area telescope on the fermi γ -ray space telescope mission,” *Astrophysical Journal*, vol. 697, no. 2, pp. 1071–1102, 2009.
- [9] J. L. Racusin, S. V. Karpov, M. Sokolowski, et al., “Broadband observations of the naked-eye γ -ray burst GRB 080319B,” *Nature*, vol. 455, no. 7210, pp. 183–188, 2008.
- [10] M. Sokolowski, *Investigation of astrophysical phenomena in short time scales with “Pi of the Sky” apparatus*, Ph.D. thesis, The Andrzej Soltan Institute for Nuclear Studies, Warsaw, Poland, 2008, <http://arxiv.org/abs/0810.1179>.
- [11] L. W. Piotrowski, L. Mankiewicz, M. Sokolowski, G. Wrochna, and A. F. Zarnecki, “Limits on GRB early optical emission from “ π of the Sky” system,” in *Photonics Applications in Astronomy, Communications, Industry, and High-Energy Physics Experiments 2006*, vol. 6347 of *Proceedings of SPIE*, Wilga, Poland, May–June 2006.
- [12] VOEventNet project, <http://voeventnet.caltech.edu/>.
- [13] R. R. White and A. Allan, “An overview of the heterogeneous telescope network system: concept, scalability and operation,” *Astronomische Nachrichten*, vol. 329, no. 3, pp. 232–236, 2008.
- [14] M. Strauss, “Towards a Design Reference Mission for the LSST,” <http://www.lsst.org/Meetings/CommAccess/abstracts.html>.
- [15] N. Kaiser, H. Aussel, B. Burke, et al., “Pan-STARRS—a large synoptic survey telescope array,” in *Survey and Other Telescope Technologies and Discoveries*, vol. 4836 of *Proceedings of SPIE*, pp. 154–164, Waikoloa, Hawaii, USA, August 2002.
- [16] C. Alard and R. H. Lupton, “A method for optimal image subtraction,” *Astrophysical Journal*, vol. 503, no. 1, part 1, pp. 325–331, 1998.
- [17] S. Karpov, et al., Volume 2010 (2010), Article ID 784141, 8 pages.
- [18] G. Beskin, et al., these proceedings.
- [19] E. Bertin and S. Arnouts, “SExtractor: software for source extraction,” *Astronomy and Astrophysics Supplement Series*, vol. 117, no. 2, pp. 393–404, 1996.
- [20] K. Malek, et al., “Pi of the Sky detector,” Volume 2010 (2010), Article ID 194946, 9 pages.
- [21] G. Kaspruwicz, H. Czyrkowski, R. Dabrowski, et al., “New low noise CCD cameras for “Pi of the Sky” project,” in *Photonics*

- Applications in Astronomy, Communications, Industry, and High-Energy Physics Experiments 2006*, vol. 6347 of *Proceedings of SPIE*, Wilga, Poland, May-June 2006.
- [22] M. Cwiok, L. Mankiewicz, K. Nawrocki, M. Sokolowski, and G. Wrochna, "PiMan—system manager for "Pi of the Sky" experiment," in *Photonics Applications in Astronomy, Communications, Industry, and High-Energy Physics Experiments IV*, vol. 6159 of *Proceedings of SPIE*, Wilga, Poland, May-June 2006.
 - [23] Predict package, <http://www.qsl.net/kd2bd/predict.html>.
 - [24] H. Pedersen, "Rene Descartes Optical Telescope," <http://www.astro.ku.dk/~holger/rdot.html>.
 - [25] M. Cwiok, W. Dominik, G. Kaspruwicz, et al., "Search for GRB optical counterparts with "Pi of the Sky" apparatus," in *Astrophysical Sources of High Energy Particles and Radiation*, vol. 801 of *AIP Conference Proceedings*, pp. 143–144, Torun, Poland, June 2005.
 - [26] W. T. Vestrand, P. R. Wozniak, J. A. Wren, et al., "A link between prompt optical and prompt γ -ray emission in γ -ray bursts," *Nature*, vol. 435, no. 7039, pp. 178–180, 2005.
 - [27] MASTER project, <http://observ.pereplet.ru/>.
 - [28] V. Lipunov, et al., Volume 2010 (2010), Article ID 349171, 6 pages.
 - [29] E. Gorbovskoy, et al., these proceedings.
 - [30] C. Akerlof, et al., "ROTSE," these proceedings.
 - [31] G. Pojmański, "The all sky automated survey," *Acta Astronomica*, vol. 47, no. 4, pp. 467–481, 1997.
 - [32] A. Udalski, "The optical gravitational lensing experiment. Real time data analysis systems in the OGLE-III survey," *Acta Astronomica*, vol. 53, no. 4, pp. 291–305, 2003.
 - [33] A. J. Drake, S. G. Djorgovski, A. Mahabal, et al., "First results from the Catalina real-time transient survey," *The Astrophysical Journal*, vol. 696, no. 1, pp. 870–884, 2009.
 - [34] G. Rahmer, R. Smith, V. Velur, et al., "The 12kx8k CCD mosaic camera for the palomar transient factory," in *Ground-Based and Airborne Instrumentation for Astronomy II*, vol. 7014 of *Proceedings of SPIE*, Marseille, France, June 2008.
 - [35] C. Guidorzi, A. Monfardini, A. Gomboc, et al., "The automatic real-time gamma-ray burst pipeline of the 2 m Liverpool Telescope," *Publications of the Astronomical Society of the Pacific*, vol. 118, no. 840, pp. 288–296, 2006.
 - [36] CONCAM project, <http://nightskylive.net/index.php>.
 - [37] L. Shamir and R. J. Nemiroff, "OT 060420: a seemingly optical transient recorded by all-sky cameras," *Publications of the Astronomical Society of the Pacific*, vol. 118, no. 846, pp. 1180–1185, 2006.

Research Article

Transient Detections and Other Real-Time Data Processing from MASTER-VWF Wide-Field Cameras

Evgeny Gorbovskoy,¹ Kirill Ivanov,² Vladimir Lipunov,¹ Victor Kornilov,¹ Alexander Belinski,¹ Nikolaj Shatskij,¹ Dmitry Kuvshinov,¹ Nataly Tyurina,¹ Pavel Balanutsa,¹ Vadim Chazov,¹ Artem Kuznetsov,¹ Petr Kortunov,¹ Andrey Tlatov,³ Alexander Parkhomenko,³ Vadim Krushinsky,⁴ Ivan Zalozhnyh,⁴ Alexander Popov,⁴ Taisia Kopytova,⁴ Sergey Yazev,² and Alexander Krylov¹

¹ Sternberg Astronomical Institute, Moscow State University 13 Univeristetskij pr-t, Moscow 119991, Russia

² Irkutsk State University, 1 Karl Marks street, Irkutsk 664003, Russia

³ Kislovodsk Solar Station, P.O. Box 145, 100 Gagarina street, Kislovodsk 357700, Russia

⁴ Ural State University, 51 Lenina pr-t, Ekaterinburg 620083, Russia

Correspondence should be addressed to Evgeny Gorbovskoy, gorbovskoy@gmail.com

Received 2 July 2009; Revised 8 October 2009; Accepted 10 March 2010

Academic Editor: Joshua S. Bloom

Copyright © 2010 Evgeny Gorbovskoy et al. This is an open access article distributed under the Creative Commons Attribution License, which permits unrestricted use, distribution, and reproduction in any medium, provided the original work is properly cited.

Construction of robotic observatories has developed into an important and thriving field of astronomy. Their large field of view combined with the capability to be pointed at any direction makes robotic astronomical systems indispensable for tasks involving searches for transients like GRB, supernovae explosions, novae, and so forth, where both the time and direction of the search are impossible to predict. This paper describes prompt GRB observations made with MASTER-VWF wide-field cameras and the methods of image analysis and classification of transients used for real-time data processing. During seven months of operation six synchronous observations of gamma-ray bursts have been made using MASTER VWF facilities deployed in Kislovodsk and Irkutsk. In all cases high upper limits have been obtained.

1. Introduction

1.1. Very Wide-Field Telescopes. Currently, several dozen robotic telescopes are operated worldwide, each of them usually meant for certain dedicated tasks. A special case of these instruments is superWide-Field telescopes with fields of view ranging from hundreds to thousands square degrees. It is impossible to make a very Wide-Field system with a large aperture using now available CCDs and optical systems, and that is why the apertures of very Wide-Field cameras are limited to 5–15 cm. All very Wide-Field cameras are designed to record various optical transients. Most of the optical transients are of circumterrestrial origin meteors and satellites; however, very wide-field cameras may also provide valuable data on the prompt emission of cosmological GRBs. A striking example is the incredibly successful observation of GRB080319B that was performed

within the framework of the Russian-Italian experiment TORTORA [1] and Polish experiment “Pi of the Sky” [2]. All transients are highly variable and therefore snapshots must be taken at intervals of several seconds or even less. Hence solutions capable of operating without dead time (such as the time needed for CCD readout), like MASTER-VWF [3], TORTORA, and others (see Table 1), have an important advantage over other systems.

The operation of any automatic astronomical facility is supported by a dedicated software package, which also performs primary image processing and data storage. Which software to use for an automatic astronomical system depends on the particular task the facility is meant to perform, and multipurpose solutions are therefore unsuitable in such cases. Classical universal techniques are even less suited for superwide-Field observations, because of the problems due to the field curvature and very large data amount.

TABLE 1: Comparative characteristics of super Wide-Field systems.

Project	FOV	Exposure [s]	Limiting magnitude [Mag(V)]
WIDGET [4]	$44^\circ \times 44^\circ \times 3$	5	10^m
RAPTOR	$40^\circ \times 40^\circ$	60	12^m
Pi of the Sky [2]	$22^\circ \times 22^\circ$	10	11.5^m
Yatsugatake Cameras	$85^\circ \times 70^\circ$	8	5^m
FAVOR [5]	$16^\circ \times 24^\circ$	0.13	11.5^m
TORTORA [6]	$24^\circ \times 32^\circ$	0.13	10.5^m
MASTER-VWF (1) [3]	$18^\circ \times 25^\circ$ or $28^\circ \times 45^\circ$	0.3–10	12^m (5-s) 9.5^m (0.3 s)
MASTER-VWF (4) [7]	$4 \times 28^\circ \times 42^\circ$	0.3–10	11.5^m (5-s) 9.5^m (0.3 s)

1.2. MASTER—Mobile Astronomical System of the Telescope Robot. MASTER was the first robotic telescope of this kind constructed in Russia. It was built and tested by students, postgraduate students, and lecturers of SAI MSU in 2002 (<http://observ.pereplet.ru>). MASTER has evolved into a broad network of telescopes spread across the entire country. A detailed description of the MASTER facility can be found in [7]. Below we discuss the basic properties of MASTER wide field cameras (MASTER-VWF).

The main task of the MASTER-VWF experiment is to perform continuous all-sky monitoring with the aim to detect all objects absent in the available astronomical catalogues. This includes, in particular the following:

- (i) prompt detection of GRB emission synchronously with gamma-ray space observatories,
- (ii) search for star-like transients of unknown origin and orphan bursts,
- (iii) detection of meteors and determination of their basic parameters: brightness (photometry), velocity (astrometry), and altitude of combustion in the atmosphere (triangulation),
- (iv) detection of satellites and space debris and determination of their basic parameters—astrometry, velocity, brightness, and altitude above the earth’s surface.

For these purposes, a completely robotic MASTER-VWF4 facility with four wide-field cameras and a total field of view of 4000 square degrees (deg^2 below) has been deployed at the MSU Caucasian Mountain Astronomical Observatory near Kislovodsk (2075 m). Another facility—MASTER-VWF2 (two cameras and 2000 deg^2 field of view)—has been deployed near Irkutsk. In Kislovodsk cameras are set on parallactic mounts in pairs 702 meters apart (see Figure 2). Each mount has an automated dome and two fast and powerful (11 Megapixels) Prosilica GE 4000 CCD cameras with Nikkor 50 mm ($f/1.2$) lenses. The camera is capable of continuous imaging with a speed of one frame in 0.2 to 60 seconds with no time gaps. The 702 m baseline allows the facility in Kislovodsk to determine the parallaxes of circumterrestrial objects and reconstruct their altitudes from the results of astrometric reduction.

All telescopes operate in a fully autonomous mode: at night, if the weather conditions permit (a “Boltwood Cloud Sensor” provides the current weather report updated every

three seconds), the cameras begin to automatically survey the sky. The frames taken are then processed and stored in a special data storage device. Because of the very large data flow (up to 700 Gb per night), the images can be kept only for several days and then most of them have to be erased, except for some images with objects of special interest like meteors, candidate optical transients, and satellites. We also keep the images taken simultaneously with GRBs. Nevertheless we save the coadd images, with total exposure from a minute and more. Thereby we form archive, which soon will be available to the community.¹ The survey is halted and the telescope dome is closed every time when the weather deteriorates or at dawn. The operation of the entire MASTER-VWF4 facility is controlled by seven computers (see Figure 3): four computers to control the operation of the Prosilica GE 4000 CCD camera and perform source extraction, two computers to control the operation of the dome and mount, and one big quad-core server to process and store the data obtained and publish it in the Web.

The majority developed in the project software products are grouped in independent applications (astrometry, transient events classification, batch pipeline data processing) which at certain upgrade can be used and in other projects, operations on such upgrade are carried on.

The facility is a complex engineering system, which needs sophisticated and powerful software to control it, perform observations and data processing. The data flow can be as high as several Terabytes/day (in the case of very short exposures on the order of 0.2 s), requiring highly optimized software, powerful data storage facilities, and interfaces. With 5-second long exposures the limiting is 11.5–12 on each frame depending on weather conditions. Thus every image contains about 10–15 thousand objects, resulting in a data flow that is impossible to store and has to be processed in real-time.

A special software package has been developed for this purpose. It allows the coordinates of all objects and their photometric characteristics (profile, magnitude) to be determined in real-time, and is also capable of finding and analysing optical transients. MASTER-VWF can measure the coordinates of the objects with an error smaller than 10 arcseconds. The system is supplied with a daily updated database of the ephemerides of artificial satellites and a program developed to identify the satellites in real-time. The program is capable of finding new artificial satellites, to

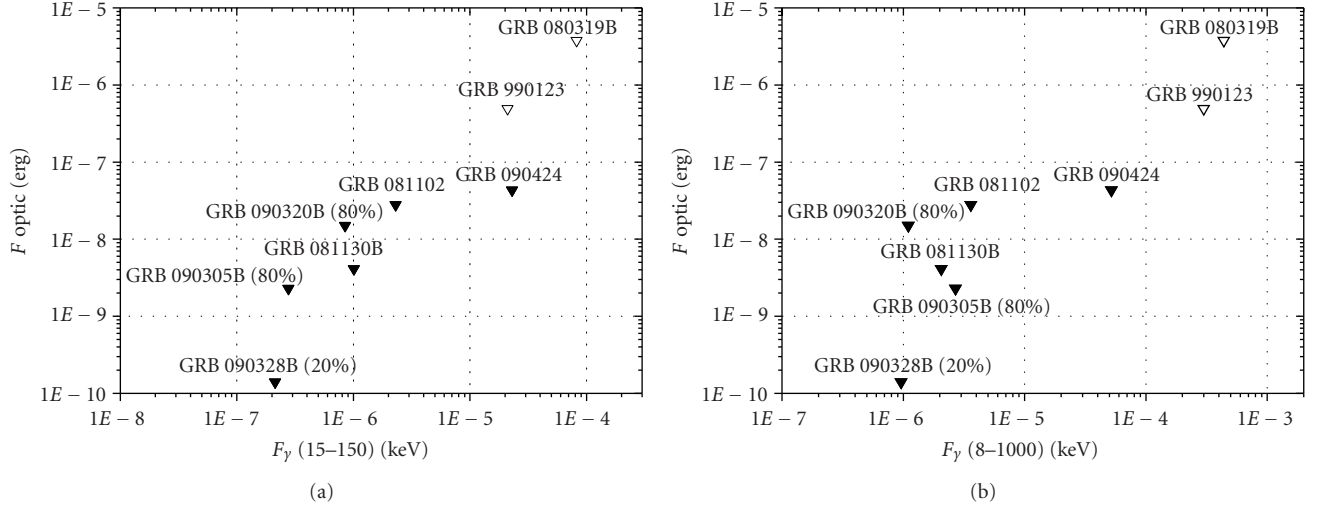


FIGURE 1: Summary results of synchronous observations of a gamma-ray burst: dependence plotted as a function of gamma-ray fluence in the soft (15–150 keV) and hard (8–1000 keV) energy interval.

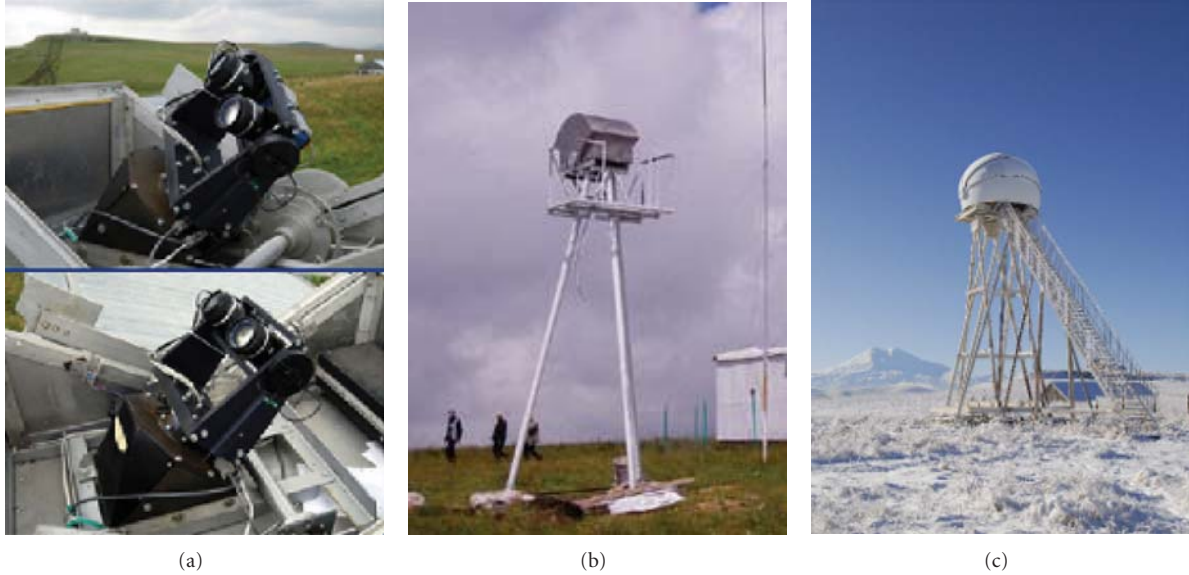


FIGURE 2: The equipment of the MASTER facility deployed at the MSU Caucasian Mountain Astronomical Observatory near Kislovodsk. From the left to right: (a) the East and West cameras of the MASTER-VWF4 northern installation, (b) the main tower and shelter of the southern MASTER-VWF4 installation, and (c) the main tower of the MASTER-2 telescope [7].

observe the destruction of known artificial satellites and not only to control space debris but also observe the process of its formation. Sometimes unknown or lost objects are recorded. For example, on October 20, 2008 MASTER-VWF recorded the debris of the American military satellite USA114Deb (see Figure 4).

A total of six synchronous observations of gamma-ray bursts have been made by MASTER-VWF in Kislovodsk and Irkutsk during seven months of their operation. In all cases high upper limits have been determined (see Table 2 and Figure 1).

In the following sections we describe these and other results in more detail.

2. Primary Reduction in Wide-Fields: Astrometry and Photometry

Let us consider the methods of astrometric and photometric reduction of a Wide-Field in more detail. The identification of the field of view and calculation of the coordinate grid for the image is based on the table of Cartesian image-plane coordinates (X, Y) produced by program used for the extraction of objects (SExtractor) and the Tycho-2 astrometric catalogue, which contains exact coordinates for most of the stars down to a limiting magnitude of $11^m \cdot 5$. To perform this task, the program should meet high requirements in terms of speed of processing (10–15 seconds

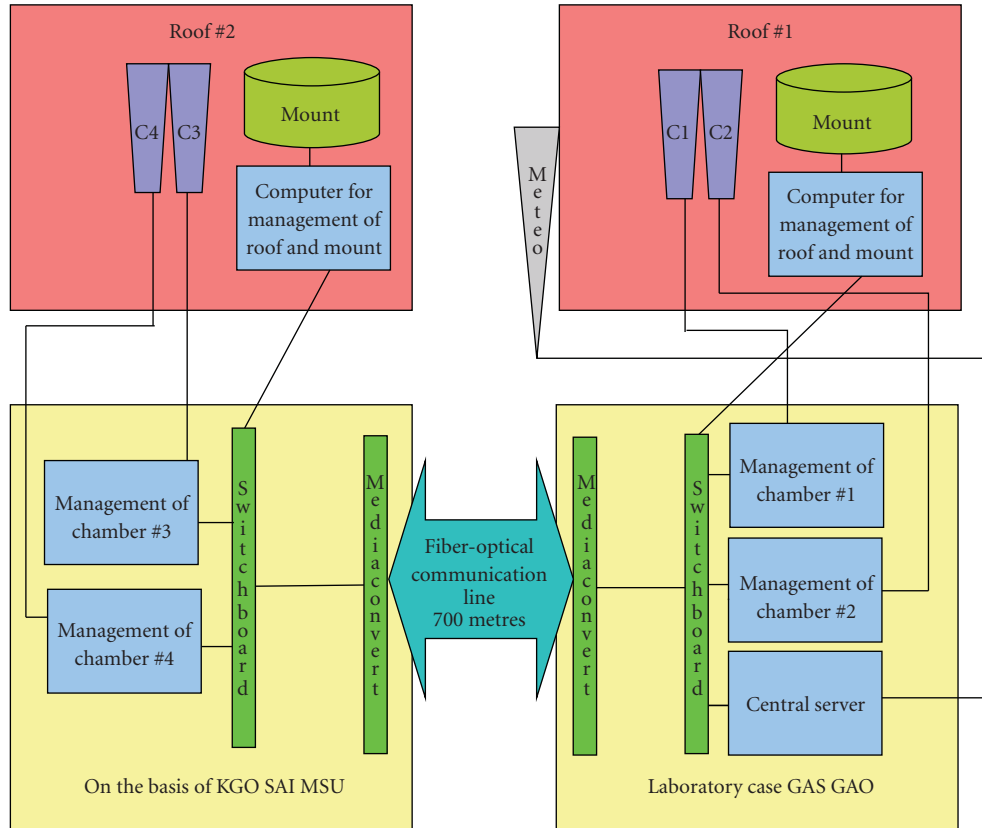


FIGURE 3: Schematic diagram of the layout of the equipment in the MASTER-VWF4 experiment.

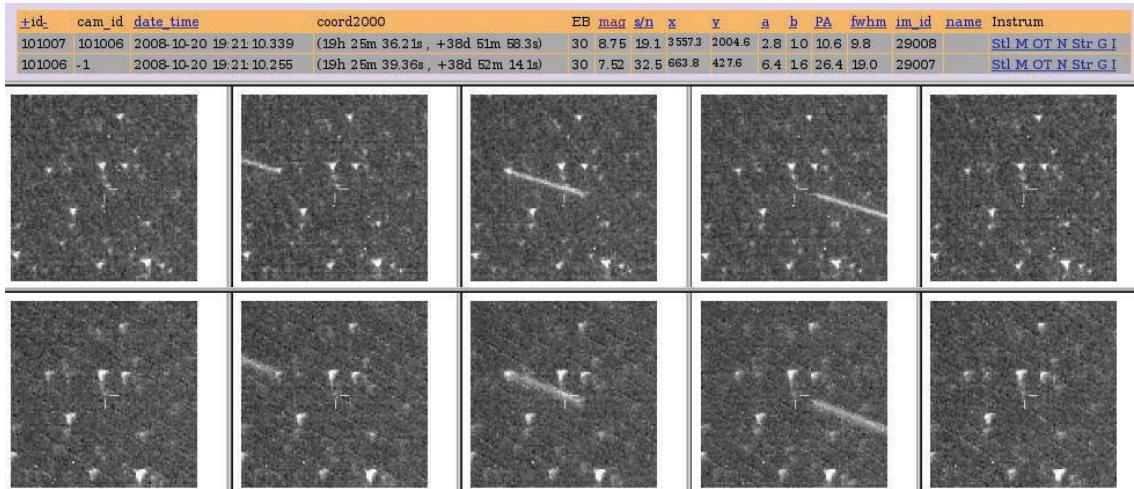


FIGURE 4: Debris of the American military satellite USA114Deb found via the web interface of the MASTER system. The top and bottom rows of the images are taken by the Northern and Southern cameras, respectively. The parallax shift is apparent even to an unaided eye. The measured parallax implies a height of 4000 ± 200 kilometers.

and less) for a field containing about 10000 stars, ensure high probability of identification (more 99%), be applicable to various fields ranging in size from narrow (tens of square minutes) to superwide (thousand deg^2) fields, allow for a certain freedom in the telescope parameters, because the focal length and other parameters may change in the course

of the year due to the variation of the outside temperature, and be capable of operating with approximate initial midfield coordinates provided that they are within the field of view.

All processing in MASTER experiments is performed under Linux OS and hence no ready-made software was likely to be found. The current implementation of the

TABLE 2: Prompt grb observations.

GRB	Satellite	Site	V	Optical fluence	Gamma-ray fluence (15–150 keV)	Gamma-ray fluence (8–1000 keV)	
GRB990123	BeppoSAX	Konus-Wind	ROTSE-I	8.9 ^m	4.9 · 10 ^{−7}	2.1 · 10 ^{−5}	3.0 · 10 ^{−4}
GRB080319B	Swift	Pi-of-the-sky	TORTORA	5.3 ^m	3.7 · 10 ^{−6}	8.3 · 10 ^{−5}	4.4 · 10 ^{−4}
GRB081102	Swift	MASTER	Kislovodsk	<13.0 ^m	<2.8 · 10 ^{−8}	2.3 · 10 ^{−6}	3.6 · 10 ^{−6}
GRB090424	Swift	MASTER	Irkursk	<9.7 ^m	<4.3 · 10 ^{−8}	2.3 · 10 ^{−5}	5.2 · 10 ^{−5}
GRB0901130B	FERMI	MASTER	Kislovodsk	<11.0 ^m	<4.1 · 10 ^{−9}	1.0 · 10 ^{−6}	2.0 · 10 ^{−6}
GRB090305B (80% part)	FERMI	MASTER Kislovodsk	<9.5 ^m	<2.3 · 10 ^{−9}	2.7 · 10 ^{−7}	2.7 · 10 ^{−6}	
GRB090320B (80% part)	FERMI	MASTER Kislovodsk	<11.0 ^m	<1.5 · 10 ^{−8}	8.5 · 10 ^{−7}	1.1 · 10 ^{−6}	
GRB090328B (20% part)	FERMI	MASTER Irkursk	<9.1 ^m	<1.4 · 10 ^{−10}	2.1 · 10 ^{−7}	9.6 · 10 ^{−7}	

“astrom”² program is based on the algorithm of pairing similar triangles of bright stars in the image and in the catalogue. This program works perfectly with the most different images from those taken under poor weather conditions and containing a few dozen stars (typical situation for alert observations) to images in the Milky-Way fields taken during a good observing night and containing up to 100000 objects. The root-mean-square error of the measured coordinates ranges from 1/4 of arcsecond (scale 2.1''/pixel) for most of the images taken with the basic telescope of the MASTER system to about 7–8 arcseconds for very wide-field cameras (scale 36''/pixel) (see Figure 2).

The system may also operate in a “fast” astrometry mode to process consecutive frames of the same area taken with wide-field cameras. In this mode the software uses a priori information about the field of view based on the previous frames, allowing the operating time to be reduced to less than 0.2 second. There is also a dedicated mode for more accurate determination of the coordinates of special objects (gamma-ray bursts, supernovae, asteroids, meteors, and others) with the local coordinate adjustment computed only in the field of the object searched using 10–25 nearest stars with well-accurate coordinates. Our experience shows that this mode provides a factor of two improvement of the accuracy of the inferred coordinates.

Our program for extracting objects from images is based on the SExtractor software package written for the TERAPIX [8] project. SExtractor is written in the C language and offers sufficiently high performance. We adapted this program to the task of reducing images taken with MASTER, and describe our version of the program in the following chapter. The main parameter used by the extraction program is the threshold signal-to-noise ratio. This value directly affects both the program execution time and the accuracy of the results obtained. We adopt $S/N = 2$ for primary selection, whereas at the subsequent stages of processing we select from the initial list only the objects with higher S/N values.

2.1. Photometric Calibration. Practically all wide-field systems operate without filters. MASTER-VWF is not an exception. This poses the problem of the calibration of the

photometric band of the measurements. It is clear that our instrumental photometric band is limited to a certain extent by the CCD sensitivity curve and lens transmission curve. Our task is therefore to determine instrumental magnitudes based on the magnitudes of the reference stars adopted from photometric catalogues.

To this aim, colour-colour diagrams are analysed, which relate the difference between the instrumental magnitude and the magnitude in any of the modelled bands (or combinations thereof) to a chosen colour index for each detected star. The closer is the modelled band to the instrumental band, the more horizontal appears the cloud of points on the diagram. Figure 6 shows the corresponding colour-colour diagrams for the MASTER-VWF-4 system consisting (in its photometric part) of a Nikkor 50 mm $f/1.4$ lens and Prosilica GE4000 CCD. The instrumental photometric band can be described fairly well by the V_{TYCHO2} filter. The absolute accuracy of photometric measurements made with wide-field cameras is, on the average, of about $\Delta m_{\text{abs}} \sim 0.25\text{--}0.35^m$. Note that the relative accuracy of measurements is substantially better with errors as low as $\Delta m_{\text{rel}} 3\text{--}5\%$.

2.2. Automatic Determination of the Limiting Magnitude of an Image. Automatic determination of the limiting magnitude for the images taken is an important part of the operation of modern automatic sky surveys. An automatic survey must naturally include automated quality control. The automatically determined limiting magnitude may serve as some kind of objective quality assessment for the images obtained. Furthermore, the determination of the limiting magnitude is also needed for gamma-ray burst observations.

The task of the determination of the limiting magnitude can be addressed formally by setting the limiting magnitude of the frame equal to the magnitude of the faintest object. This approach; however, has a number of shortcomings. First, when the system is operated with a low extraction threshold, most of the faintest objects are noise artifacts. If the sky is covered with clouds, no real faint objects can be seen and practically all objects at the visibility limit are chance fluctuations of cloud brightness. Moreover, because of the large number of such false objects some of them

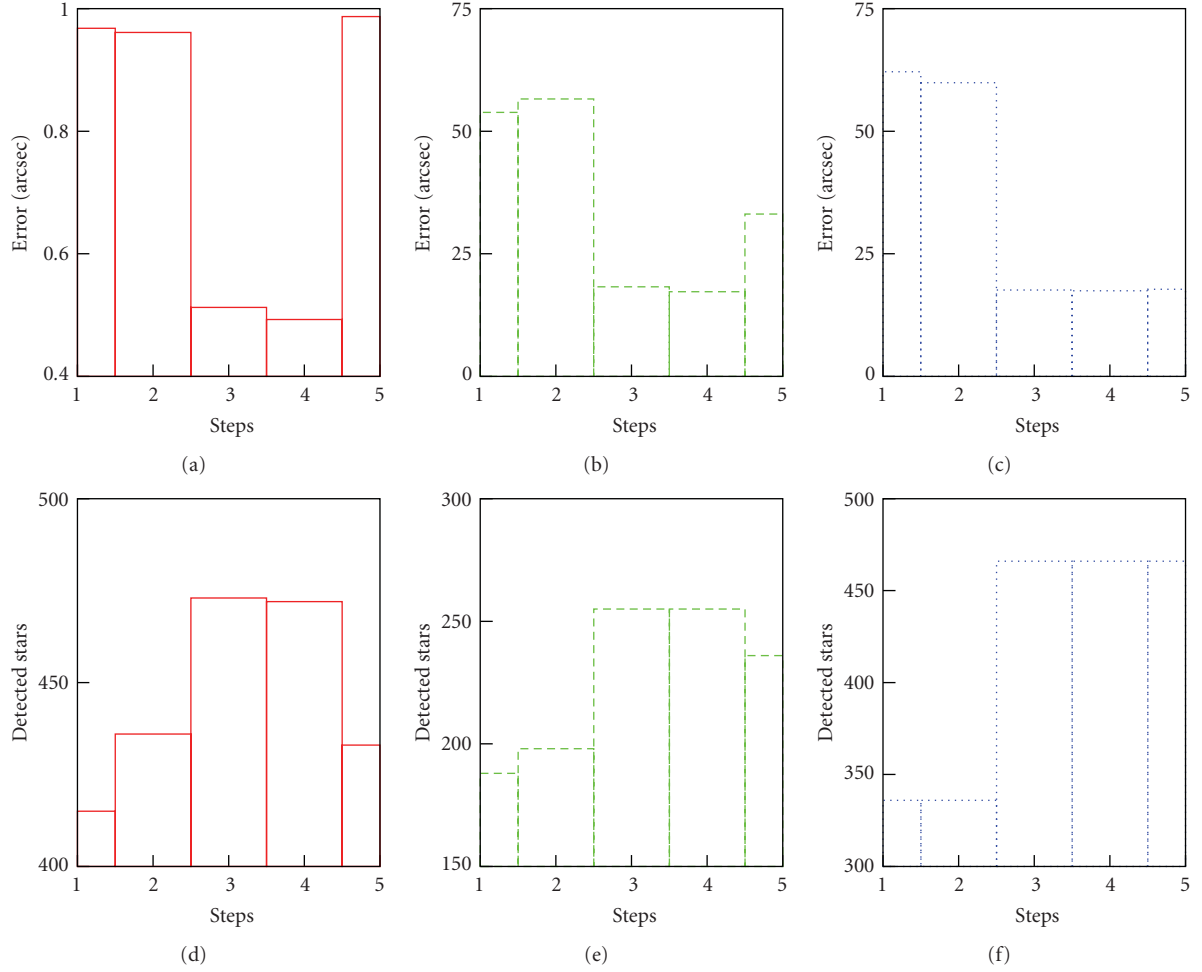


FIGURE 5: Average error (a, b, c) and the number of identified stars (d, e, f) as functions of the degree of the polynomial used. The dependences are shown for three different optical systems. Red (a) and (d) Rigter-Slefogt (MASTER) with a field of view of 6 deg^2 , Nikkor 50 mm $f/1.2$ (b) and (e) with a field of view of 1000 deg^2 , and Nikkor 50 mm $f/1.4$ (c) and (f) with a field of view of 1000 deg^2 . The histograms are based on arbitrary frames from various sky areas. A third-to-fourth-degree polynomial approximation can be seen to provide optimum solution (95–99 percent of stars are identified with the minimum average error). A more detailed analysis shows that the third-degree fit yields slightly better results. That is logical, because most of the known aberrations (e.g., distortion) depend on the third power of radial distance.

may be identified with real stars and hence the situation cannot be remedied by restricting the list to objects identified with catalogued stars. Second, this approach allows one to estimate the limiting magnitude only within a local area and the quantity inferred does not characterise the entire image and is therefore unsuitable for quality control.

These problems can be addressed as follows. All stars of the reference catalogue that are located within the field considered are subdivided into magnitude bins of fixed width. For each bin the fraction of identified stars to the total number of catalogued stars is computed, and the corresponding histogram is drawn (see Figure 7). One can see that the ratio decreases sharply when the average magnitude of the bin approaches the limiting magnitude. In practice, it is convenient to adopt a certain threshold ratio and define the limiting magnitude as the magnitude at which the curve reaches this threshold. The thresholds of

$\sigma_{\text{lim}} = 25\%$ and $\sigma_{\text{lim}} = 50\%$ have been shown empirically to correspond to objects with $S/N \approx 9\text{--}11\sigma$ and $S/N \approx 14\text{--}15\sigma$, respectively.

Note that for robust operation of the algorithm the limiting magnitude of the reference catalogue should be fainter than that of the frame studied. Otherwise the method becomes inapplicable because the catalogue lacks stars of the given magnitude. However, the USNO-B1 catalogue is sufficient for most of the modern wide-field surveys, whereas very wide-field surveys can be reduced successfully even with the TYCHO-2 catalogue (and this is very convenient).

3. Automatic Classification and Analysis of Astronomical Transients

3.1. Extraction of Objects and Data Transfer to the Server. The search for and classification of transients starts once

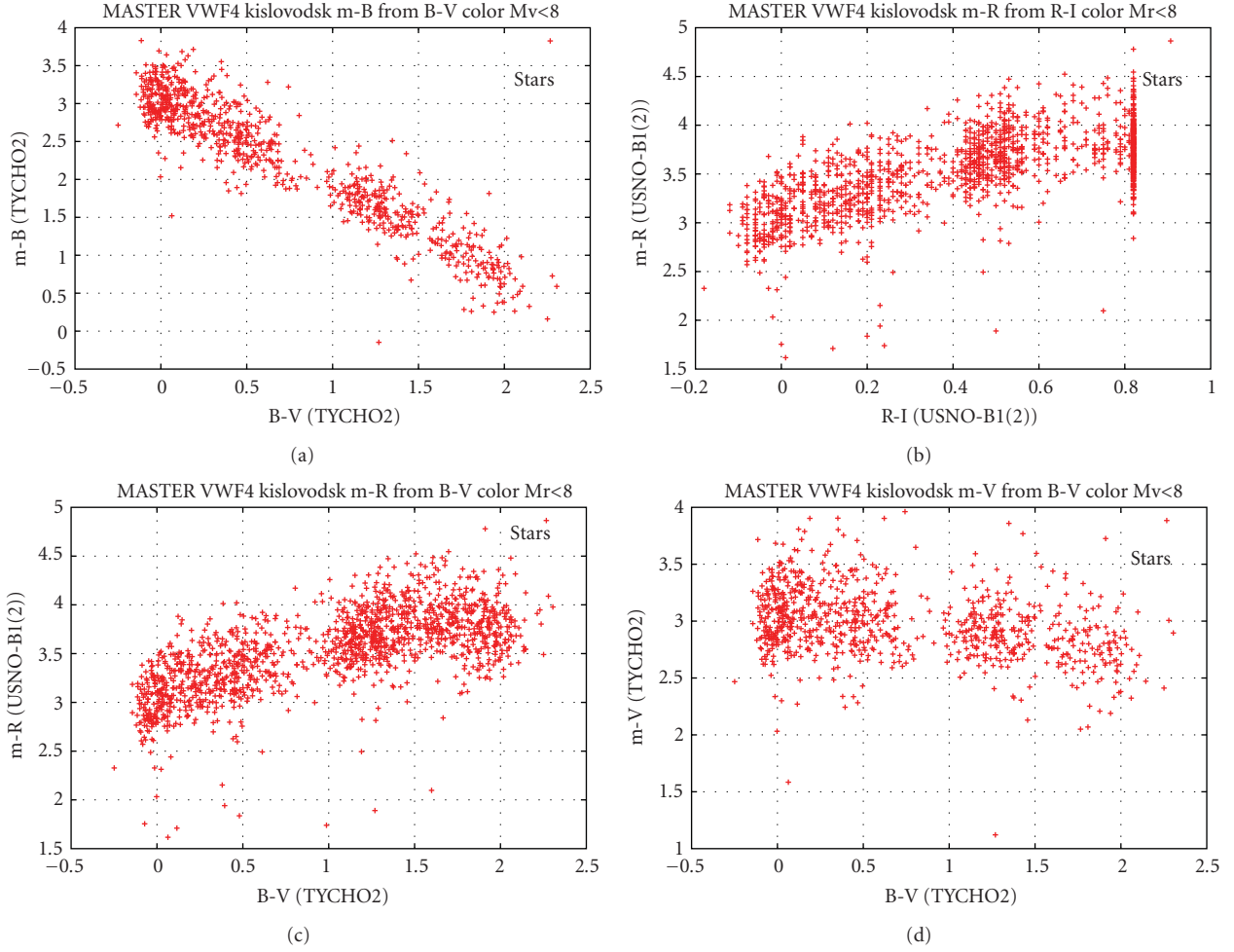


FIGURE 6: Color-color diagrams are used to calibrate instrumental magnitudes. On these plots $m = 2.5 \lg(F_{\text{inst}})$ and the zero point is of no importance and cannot be determined at this stage. Note that the width of the sequences is real and due to the fact that stars have different spectral types, and not due to measurement errors. $R-I = 0.82$ clustered connected with non very w.

the primary reduction of the image is finished. All transient events in frames can be subdivided into two classes: star-like objects as strips,³ which differ substantially in the methods used for primary reduction. All rapidly moving objects are usually classified as strips: low-altitude satellites and meteors. All transients of stellar or extragalactic nature (novas and supernovas, orphan bursts, stellar flares) and geostationary satellites (see, e.g., Figure 18) are Star-like. Star-like objects are much easier to process, because the program of object extraction and instrumental photometry (SExtractor, described above) has been developed to analyse such objects. Therefore all main parameters of Star-like objects (flux and magnitude, FWHM, Cartesian frame coordinates (X , Y), and semiaxes (a , b)) are determined very reliably.

Extraction of strip-shaped objects is fraught with serious problems. First, a fine adjustment of SExtractor's additional internal parameters is necessary. Second, a change of these parameters strongly affects the image processing time. Furthermore, strip-shaped objects contribute appreciably to the background within the small area suitable for identification of stars. Fine adjustment of all parameters allowed us

nevertheless not only to identify strips in the image, but also achieve high speed of operation (half exposure time) (see Figure 8). However, SExtractor algorithm cannot identify strips in the frame, to say nothing about performing their high-quality photometry. To this end, a special program had to be developed, which we describe below.

To reduce the server load, identification of objects in the image can be physically performed not only by the server, but also by the control computer of each particular camera (see Figure 3). Note that the resulting catalogue of detected objects should have higher priority for the transmission to the server compared to the images that are to be stored in the database.

3.2. Primary Reduction of Astronomical Transients. After the objects identification the next step is their astrometric and photometric calibration. A catalogue of objects with calibrated coordinates and photometry is produced.⁴ All unidentified objects (identification is performed using both coordinate and photometric criteria: usually $\Delta S = 20 - 30''$

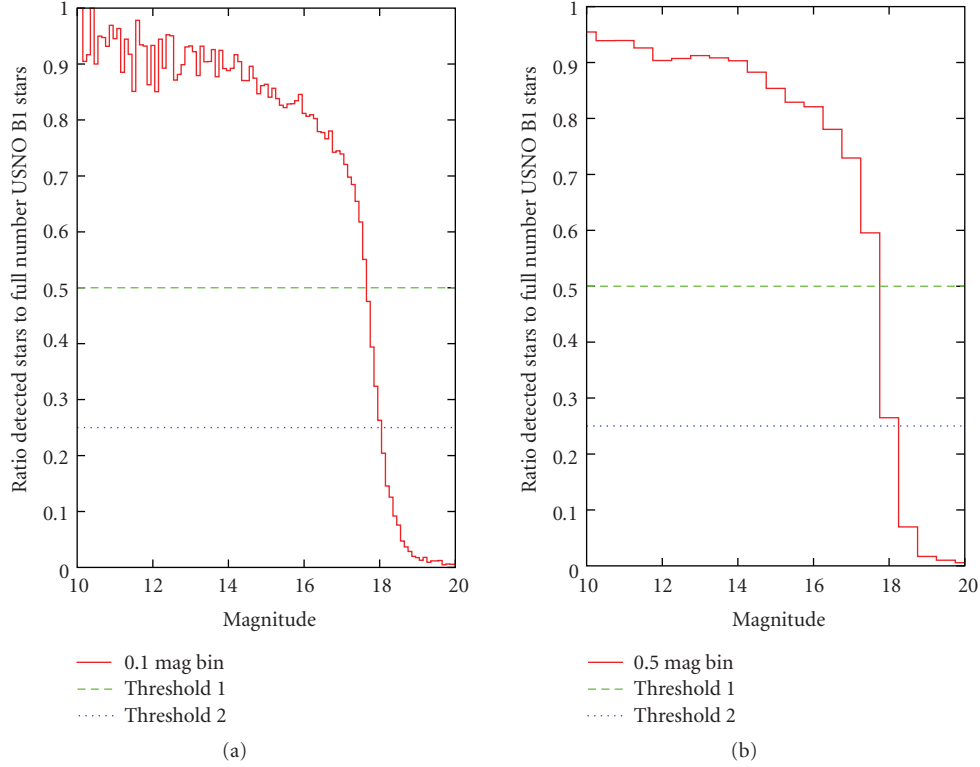


FIGURE 7: The number of identified stars as a function of magnitude. The straight lines indicate the $\sigma_{\text{lim}} = 50\%$ and $\sigma_{\text{lim}} = 25\%$ thresholds. Averaging was made within 0.5^m and 0.1^m bins in the right and left histograms, respectively. The right (coarser binned) histogram is smoother, resulting in reduced probability of accidentally reaching the threshold at a bright magnitude. It is therefore convenient to determine the limit on the coarsely binned histogram and then refine it on the finer-binned curve.

and $\Delta m = 1.5^m$) are viewed as possible optical transients. This approach allows us to identify stellar flares as transients and to a certain extent prevent spurious identifications with fainter and hence more numerous stars. To filter noise, objects that could not be identified with the catalogue are correlated with the objects of several (usually 2-3) previous sets. An object is considered to be a candidate transient if it could not be found either in the catalogue or in the previous frames. All candidate transients are then passed through a number of special filters. For example, if the semiminor axis of the object, which should typically be of about $b \sim 0.7\text{--}2$ pixels, exceeds $b \sim 4\text{--}5$ pixels, it must be a trail of a cloud with a probability of 95%.⁵ If $\text{FWHM} < 1$ pixel, we must be dealing with a hot pixel or a cosmic-ray hit. We also set for all transients the trigger threshold, which is always higher than the extraction threshold. Currently, the trigger threshold is $S/N > 10\sigma$. We consider a candidate found on two or more consecutive frames to be a trustworthy transient.

Preliminary classification of transients is performed after the objects are passed through all filters. First, all objects are searched for possible identifications in the catalogue of artificial satellites and all identified objects are included into the database of satellites. The remaining ones are subdivided into Star-like and strip-shaped objects. The object is classified as a strip-shaped if $a/b > 3$; otherwise it is considered to be Star-like (here a and b major and minor semiaxis). All Star-like objects are then passed through the

coincidence circuit, and strip-shaped objects are. Objects are provisionally subdivided into meteor candidates and unknown artificial satellites. If each of three successive frames contains a candidate transient such that the three objects lie on a straight line, all of them are considered to be the images of an artificial satellite. The remaining objects are considered to be meteor candidates.

3.3. Coincidence Scheme of and Determination of Heights. All the procedures described above are performed for each of the four cameras in real-time mode. Real-time processing ends here if the cameras operate in uncoupled (alert) mode. In the case of survey observations, when two cameras point to the same sky area, all Star-like transients are passed through the coincidence scheme, and all strip-shaped objects have their heights determined (see Figures 9 and 10). To improve the accuracy of identification, special transformation is applied to the frame taken with the Northern camera to convert it to the coordinate frame of the Southern camera. This transformation is based on the same principles as astrometric reduction. It takes little time to compute (~ 0.2 seconds) and improves the accuracy (and hence reduces the correlation radius and the number of chance identifications) by more than a factor of 2.5 compared to the accuracy of the results obtained in the case of identification by celestial coordinates. Should a real Star-like transient be found, an alert can be

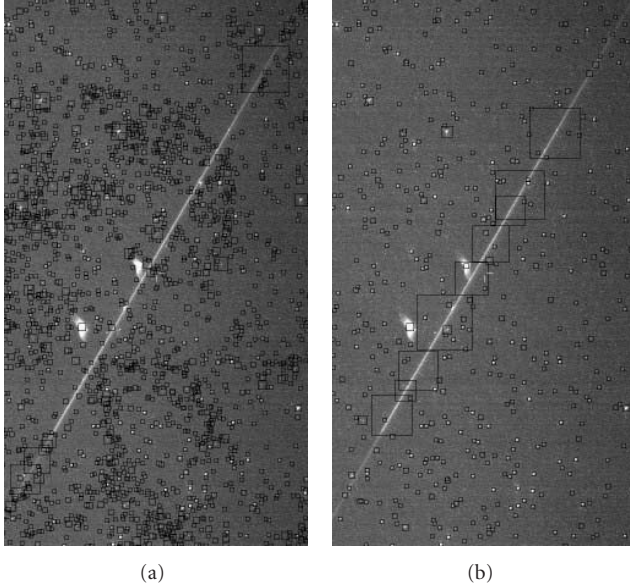


FIGURE 8: A $5^\circ \times 9^\circ$ image with a bolide. The black squares indicate objects extracted from the frame. The side of the square corresponds to the FWHM of the object. (a) shows a frame with objects extracted using standard SExtractor parameters (with the extraction threshold of $S/N > 1.5$) with no filters applied. As a result, the program identified all Star-like objects, heaps of faint garbage, hot pixels, and simply random noise, that is, virtually everything except the bolide. (b) shows the result of extraction made using the currently adopted refined custom parameters. Several bright elongated objects are extracted on the bolide image and the noise level is appreciably lower.

immediately issued to larger (45-cm) MASTER telescopes (located near Moscow, in Kislovodsk and in the Urals) to study the event in more detail. However, this mode is currently in the stage of development, mostly because of the debris of high-orbital satellites, which often contaminate the frames (see Figures 4 and 18).

3.4. Analysis of Strips. As we pointed out above, SExtractor computes only the approximate position of a strip, breaking it into several bright elongated objects. To perform complete photometry of a strip, determine the coordinates of its centre and ends and other parameters, a special program is used dedicated to the analysis of strips on astronomical images. To prevent server overload, this program is run only when cameras are idle (in the afternoon or during bad weather). The program starts with the coordinates of any location inside the strip determined at the previous stage. The working area of the given size (usually 512×512 pixels, which is sufficient for the analyses of any satellite or meteor trails) is chosen around this initial point. The size of the working area is automatically increased when a very bright and long bolide is to be analysed.

Determination of Background. To determine the background, we subdivide the working area into subareas of the given size. For each subarea the median and standard

deviation are computed twice: the first time over almost all pixels in the given subarea, and the second time more precisely, after discarding the pixels that deviate strongly (by more than $6-10\sigma$) from the preliminary background estimate. We number all these subareas—there are a total of N_{zone} of them (currently $N_{\text{zone}} = 256$)—and compute the background and standard deviation at a given pixel as

$$\begin{aligned} \text{Bg}(i, j) &= \sum_{k=1}^{k < N_{\text{zone}}} \frac{1}{r_k^2} \cdot \text{Med}(k), \\ \Sigma(i, j) &= \sum_{k=1}^{k < N_{\text{zone}}} \frac{1}{r_k^2} \cdot \Sigma(k), \end{aligned} \quad (1)$$

where $\text{Bg}(i, j)$ is the background at the point with coordinates (i, j) ; $\text{Med}(k)$ is the median in k th area; Σ is the standard deviation within the corresponding subarea, r_k is the distance between the point (i, j) and the centre of k th area. Such simple map suffices for the primary analysis. In a consequence more detailed analysis with more exact background definition (e.g., by SExtractor algorithm [8]) can be made. Figures 11: 3-4 show the corresponding background maps.

Extraction of Strips. To extract a strip, we first compute the map of bright pixels exceeding the background level by $n_\sigma \cdot \Sigma(i, j)$ or more. The optimum threshold has been shown empirically to be $n_\sigma = 1.5$. The corresponding points are shown by black shade on the map (see Figure 11: 2).

A recursive search algorithm for connected area is then used starting at the centre found by SExtractor. Once the connected area is found, the main parameters of the object (the position of the centre, a , b , and the angle θ between the axis of the object and the X axis) are determined. The standard deviation σ_{line} from the straight line drawn at angle θ through the centre of the object is computed if the object found can be classified as a strip ($a/b > 3$). The recursive algorithm of searching for connected area is then started again, this time within $2-3\sigma_{\text{line}}$ of the straight line just mentioned. The algorithm is allowed to jump over one to two faint pixels within $2\sigma_{\text{line}}$ of the straight line. Thus the second pass yields a completely extracted strip including faint edges in the case of meteors.

The program then attempts to find objects located on the extension of the strip line on the subsequent and previous frames. If such object can be found, the strip is classified as a satellite; otherwise, as a meteor. The brightness profiles along the strip are then computed both for satellites and meteors (see Figure 12). Portions of images are kept for all transients.

4. Synchronous Observations of Prompt GRB Emission

In this section we discuss synchronous GRB observations. Note that during two years of the operation of the single-channel wide-field Kislovodsk camera we have made over 20 faster than 1-minute alert pointings published in the corresponding GCN-telegrams GRB 070224 (gcn 6139),

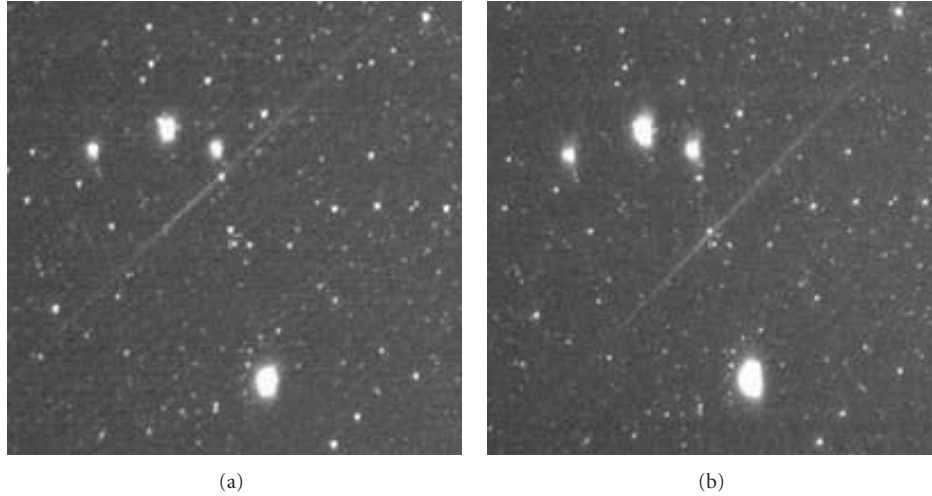


FIGURE 9: MASTER-VWF4 frames of a $5^\circ \times 5^\circ$ sky area taken with the Northern and Southern cameras. The parallax of the meteor is immediately apparent. Triangulation yields a height of $H_{\text{meteor}} = 72 \pm 2$ km.

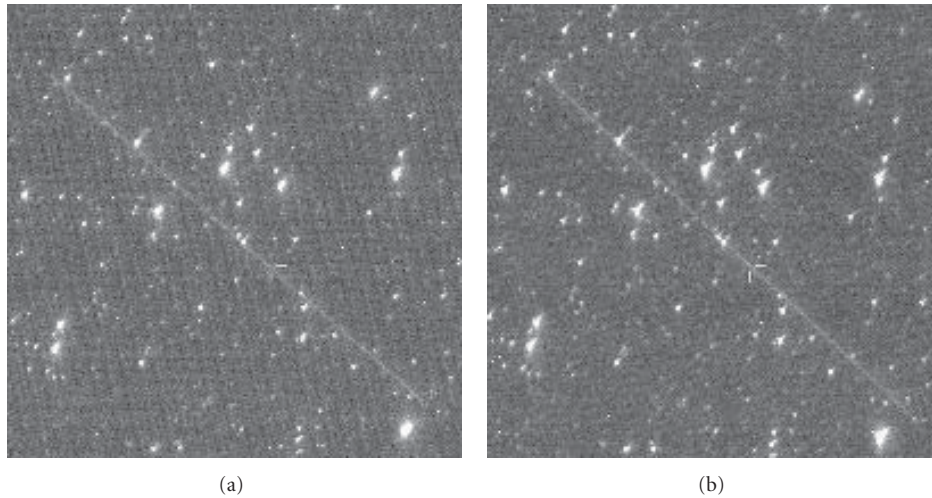


FIGURE 10: Parallax of an artificial satellite. Here we show the $4^\circ \times 4^\circ$ frames of a sky area taken with the MASTER-VWF4 Northern and Southern cameras. Triangulation yields a height of $H_{\text{satell}} \sim 4500$ km. Given the accuracy of astrometric measurements for strip-shaped objects, $\sigma_{\text{astrom}}^{\text{line}} \sim 20''$, and the baselength of $\Delta l = 702$ m, the maximum height that can be determined via triangulation is $H_{\text{max}} = \Delta l * \arcsin(\sigma_{\text{astrom}}^{\text{line}}) \sim 10000$ m.

GRB 070223 (gcn 6131), GRB 070219 (gcn 6113), GRB 061213 (gcn 5915), GRB 061002 (gcn 5677), GRB 060929 (gcn 5657), and others [9].

4.1. The Importance of Synchronous Observations. As is well known, optical GRB glow can be roughly subdivided into two parts: prompt emission and afterglow. We do not discuss the afterglow phenomenon here, because it has already been thoroughly studied and it is not the target of Wide-Field observations. Let us now consider prompt emission.

Prompt optical GRB emission is the emission that appears simultaneously with gamma rays detected by various space-based gamma observatories (HETE2, Swift, Fermi). Unlike afterglow, it bears information about the object

that gives birth to GRB, and not about its environment. There are two ways to detect prompt optical GRB emission: synchronous observations and very quick alert pointing. To date, about a dozen [10] optical prompt GRB have been made and most of them were alert based. That is to say, when prompted by a quick trigger from a gamma-ray observatory, a robotic optical telescope points at the object within several tens of seconds after the corresponding gamma-ray event is detected. If the GRB is long enough, its prompt emission is still detectable by this time. Another, less common type of observations, are synchronous wide-field camera observations. Perhaps the most amazing example of the latter is the prompt GRB 080319B detection [1]. Synchronous observations are much more efficient than alert observations for at least two reasons. First, alert observations

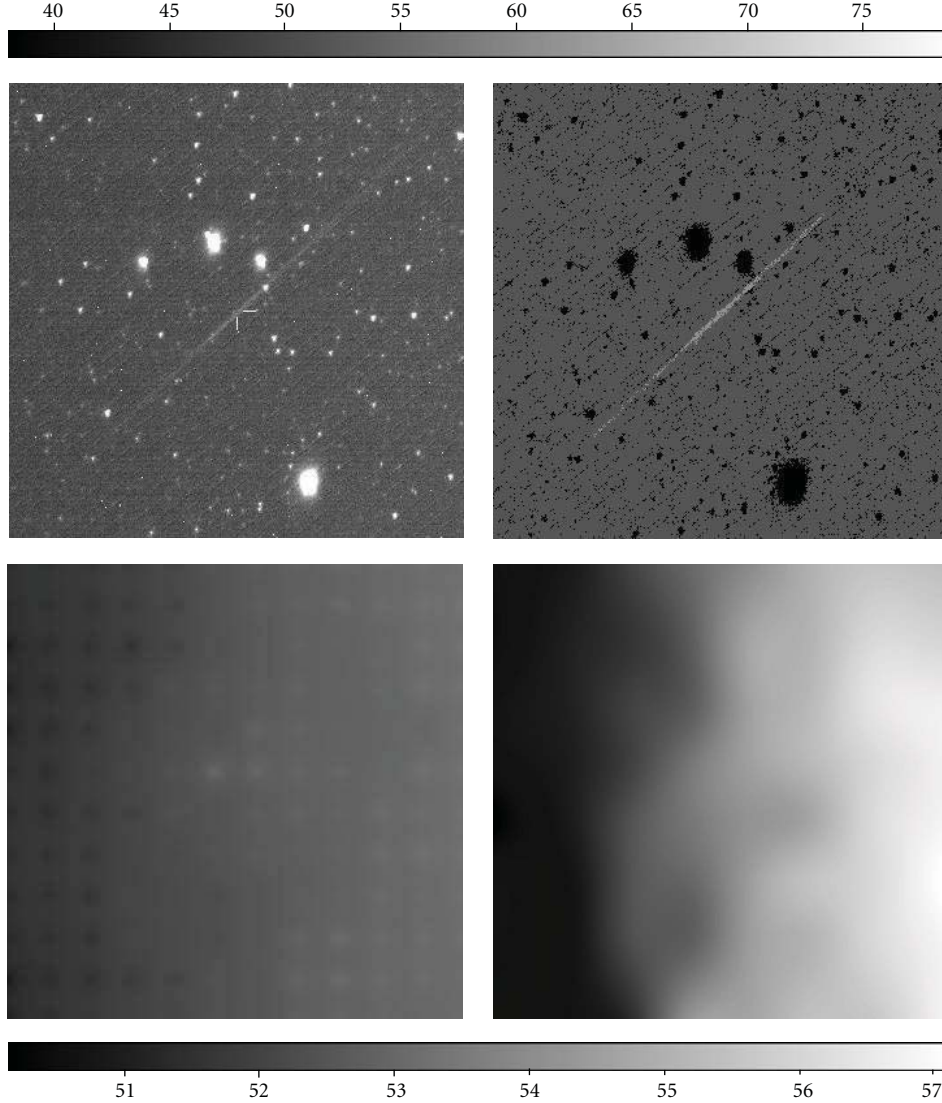


FIGURE 11: (1) Image of a meteor on a $3^\circ \times 3^\circ$ frame ($F(i, j)$). (2) Extraction map. Black shade shows the points with $F(i, j) > n_\sigma \cdot \Sigma(i, j)$; white shade indicates the points included into the object under study. Grey shade indicates the background. (3) Background map—($Bg(i, j)$) (bottom left). (4) More exact map of a background use SExtractor background estimation algorithm [8].

are subject to selection effects. The point is that an alert may result in the detection of prompt emission only if the GRB lasts longer than 30–40 seconds, because of the delay due to the time it takes to perform data processing on-board the space telescope, transmit the signal to the ground, and point the optical telescope. Hence alerts cannot be used to detect prompt optical emission from short GRBs. It is significant that this kind of emission has never been observed and moreover, it has never had its upper limit measured.

4.2. Energy Calibrations of the MASTER-VWF4 Photometric Passband. To make any conclusions about the brightness of objects not just in terms of relative magnitudes, but also in terms of energy units, we must calibrate the MASTER-VWF4 zero-point. Let us determine the energy flux (in the units of $\text{erg}/\text{cm}^2/\text{s}$) produced by a zero-magnitude star

(e.g., Vega). The MASTER-VWF4 band is close to the V band of the Tycho2 catalogue. Figure 13 shows the spectrum of Vega and the same spectrum folded with the lens passband and sensitivity curve of the CCD. Integration over the entire spectrum finally yields the flux produced within the MASTER-VWF4 band by a zero-magnitude star:

$$F^{\text{Vega}} = \int_0^\infty f_v(\nu) \cdot \nu \cdot d\nu = 6.4 \pm 0.1 \cdot 10^{-6} \text{ erg}/\text{cm}^2/\text{s}. \quad (2)$$

4.3. Synchronous GRB Observations with MASTER-VWF Very Wide-Field Cameras. MASTER-VWF cameras perform nightly monitoring of the sky with the aim to detect optical transients. These cameras may operate in two different modes. In the first mode, which is meant for searching for optical transients, two cameras are pointed to the same

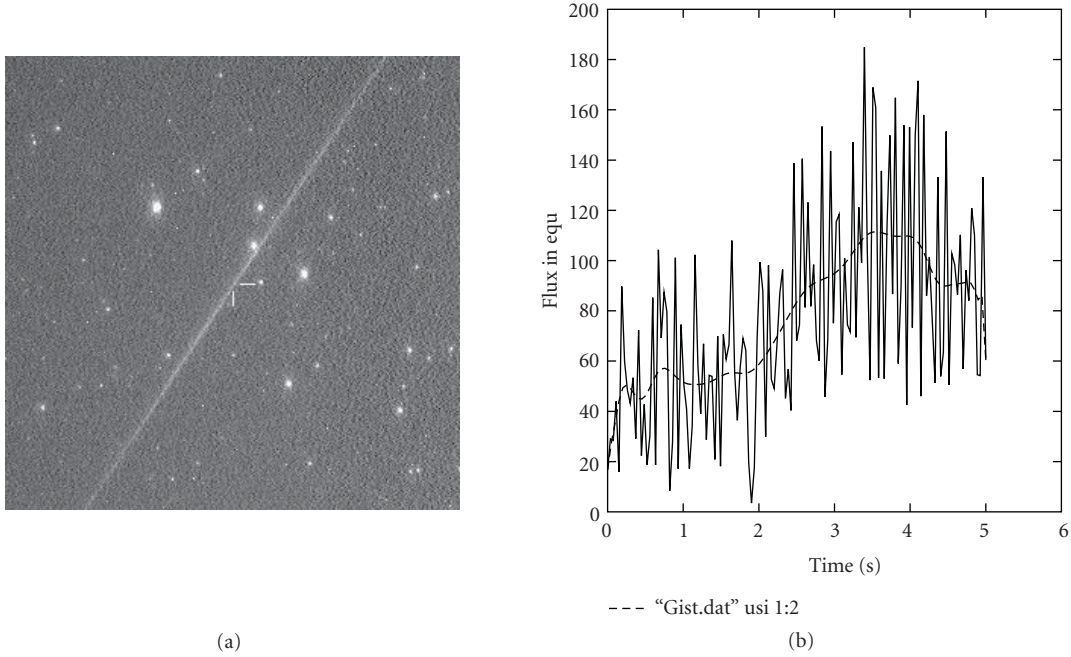


FIGURE 12: Meteor and its automatically determined brightness profile, FOV is about $5^\circ \times 5^\circ$ here.

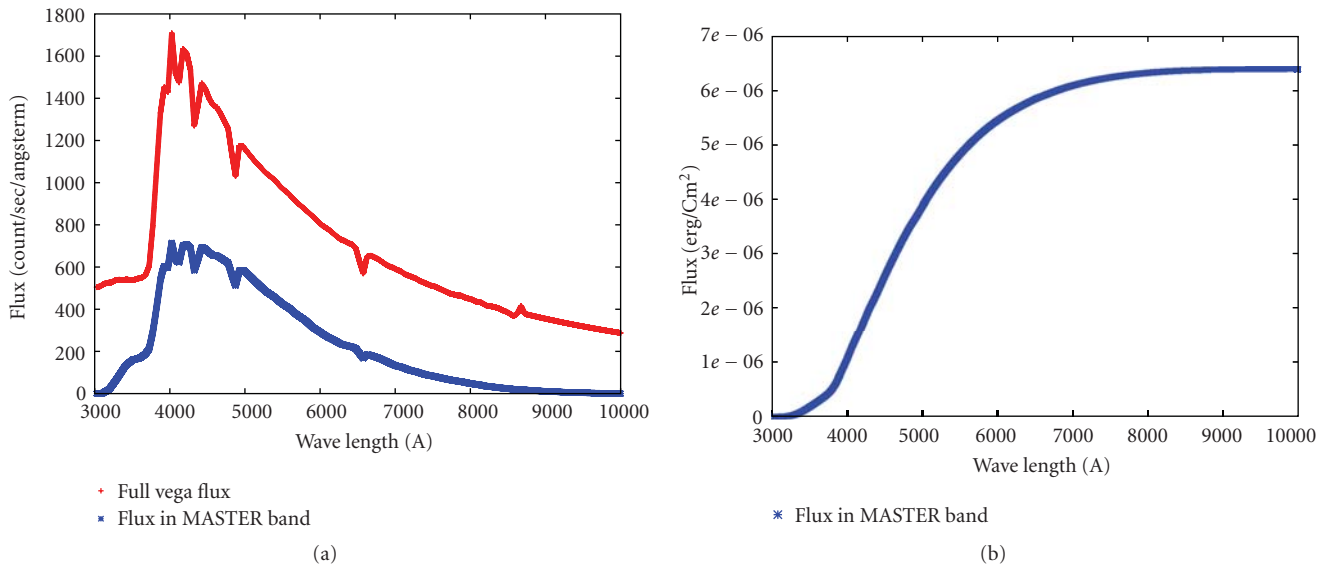


FIGURE 13: The spectrum of Vega and the same spectrum as observed after passing through the MASTER-VWF band (a). The cumulative curve of this spectrum in power units (b).

sky area in order to implement the coincidence scheme (see Figures 9 and 10). In the second mode the fields of view of the cameras are set apart as far as possible in order to provide a combined field of view of more than 4000 and 2000 deg^2 for the Kislovodsk and Irkutsk observatories, respectively. The second mode is dedicated for synchronous observations of gamma-ray bursts.

4.3.1. The GRB081102 and GRB090424 Gamma-Ray Bursts Recorded by Swift Spacecraft. GRBs recorded by the Swift

gamma-ray observatory satellite have very accurate coordinates, allowing the location of the burst origin on very wide-field cameras to be determined with the highest precision possible (i.e., to within less than one-pixel large error box).

Long Gamma-Ray Burst GRB081102. (see Figure 14) [15] Although it was a typical long ($T_{90} = 63$ s) gamma-ray burst, the telegram from Swift was issued only after 15 minutes. This delay prevented early observations by automated telescopes. However, MASTER-VWF-4 in Kislovodsk covered

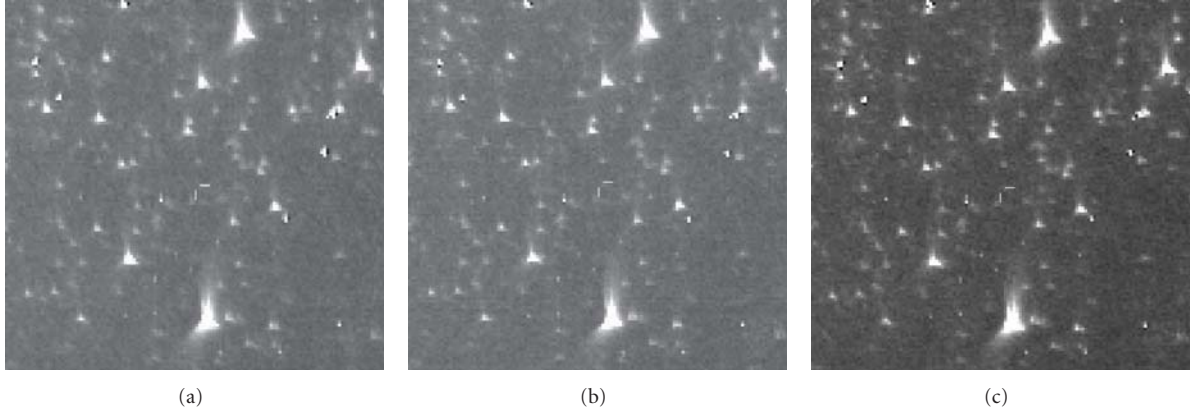


FIGURE 14: Coadded images taken 30 seconds before (a), during (b), and 30 seconds after (c) GRB081102. Each frame is a coadd of 12 images (six images from each camera)—60 seconds exposure for each frame. FOV $3^\circ \times 3^\circ$ on the frame edge. So strange stars shape is connected with off-axis aberrations. Animation is available here: http://observ.pereplet.ru/images/GRB081102/grb_film.html.

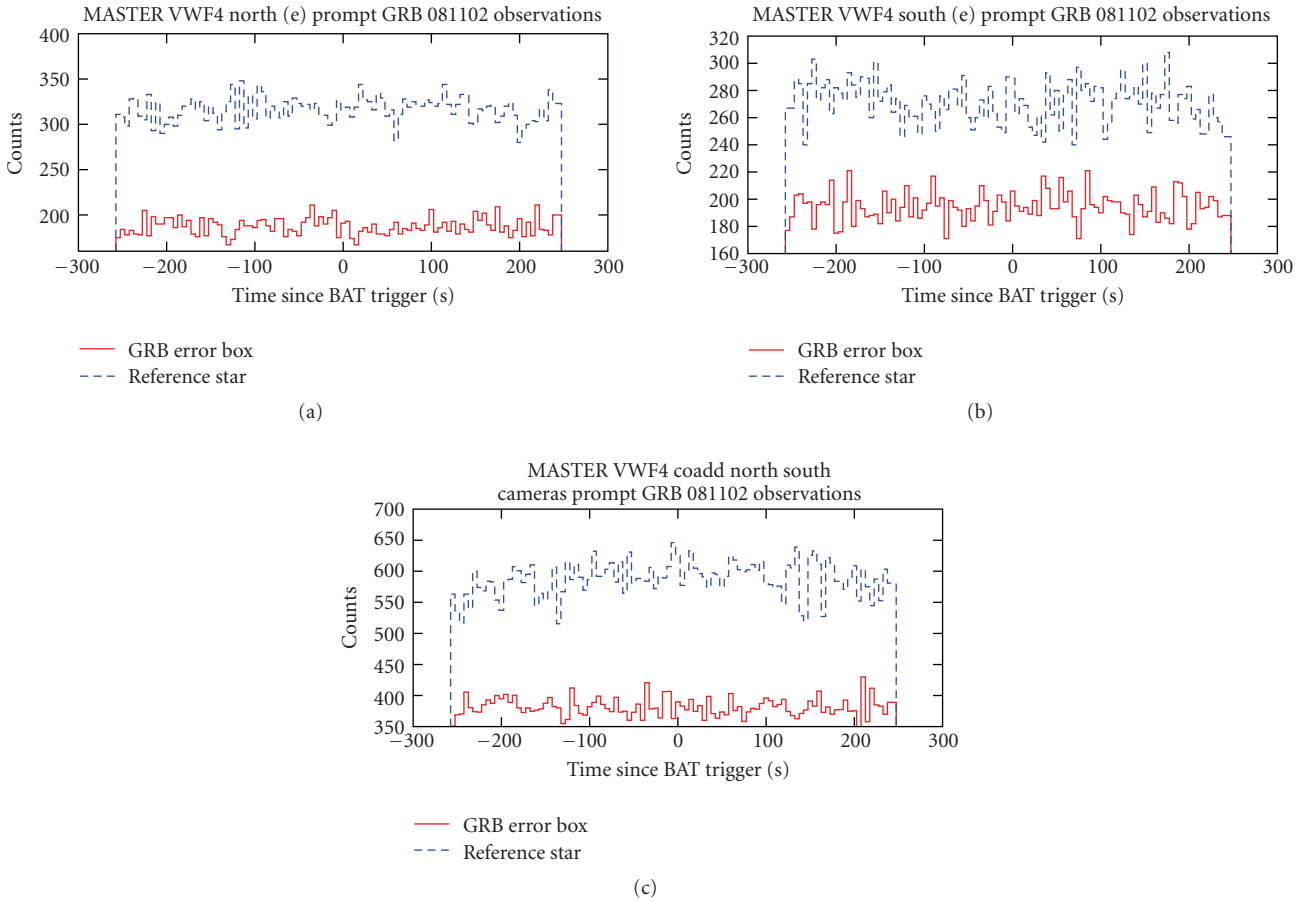


FIGURE 15: GRB081102. Hash (red) from the Northern and Southern cameras and from the two cameras simultaneously inside the GRB081102 error-box and the signal from the $V_{\text{ref}} = 11.5^m$ reference star (blue).

the entire error box at the edge of its field of view. MASTER-VWF-4 operated in the survey mode with aligned cameras, allowing the grb error-box to be recorded simultaneously in two channels. This area has been observed for two hours before and seven hours after the grb with no time gaps [16].

Unfortunately, no optical counterpart was detected from this burst (see Figures 14 and 15). The lack of optical counterpart may have been due to extremely strong absorption toward the burst (formula 4). However, a very high upper limit (for synchronous (!) observations with very wide-field

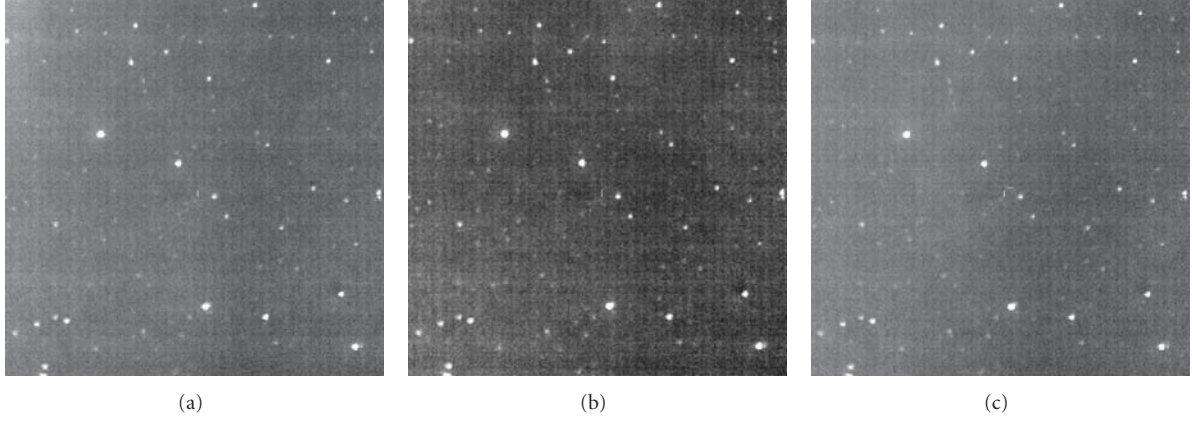


FIGURE 16: A $6^\circ \times 6^\circ$ field around the GRB090424 Swift XRT position. One-minute exposure images taken before, during, and after T_{GRB} . Clouds can be seen on the images, resulting in the optical limit of $V < 9.7^m$ on each frame. Animation is available here: http://observ.pereplet.ru/images/film_grb.html.

cameras) of $V_{\text{grb081102}} < 13.0^m$ has been obtained, which is the highest synchronous upper limit so far [17].

Let us now compare GRB081102 with GRB080319B from which bright prompt optical emission $V = 5.3^m$ [1] has been recorded. Consider the F_{opt}/F_γ ratio (where F_{opt} and F_γ are the optical and gamma-ray flux, resp.) for both bursts. The gamma-ray spectrum is known for all bursts discussed in this paper and therefore we reduce F_γ to the flux in the 15–150 keV energy interval for the sake of uniformity.

Let us estimate $F_{\text{opt}}^{\text{grb081102}}$. The V-band extinction can be estimated by the following simple empirical formula [18]:

$$\tau_V = 5.2 \cdot 10^{-22} N_H. \quad (3)$$

Given the known hydrogen column density toward GRB081102, $N_H = 4.9 \cdot 10^{21} \text{ cm}^{-2}$ [19], we can use the inferred optical depth and Pogson's formula to estimate $F_\gamma^{\text{grb081102}} = 2.3 \cdot 10^{-6} \text{ erg/cm}^2$ [20] or

$$\begin{aligned} \tau_V^{\text{grb081102}} &= 5.2 \cdot 10^{-22} \cdot 4.9 \cdot 10^{21} = 2.548 \Rightarrow \delta m = 2.8^m, \\ \frac{F_{\text{opt}}^{\text{grb081102}}}{F_\gamma^{\text{grb081102}}} &< \frac{2.512^{m_{\text{Vega}} - (m_{\text{grb081102}} - \delta m)} \cdot F_{\text{Vega}} \cdot T_{90}^{\text{grb081102}}}{F_\gamma^{\text{grb081102}}}, \\ \frac{F_{\text{opt}}^{\text{grb081102}}}{F_\gamma^{\text{grb081102}}} &< \frac{2.512^{0-13.0+2.8} \cdot 6.4 \cdot 10^{-6} \text{ erg/s/cm}^2 \cdot 63\text{s}}{2.3 \cdot 10^{-6} \text{ erg/cm}^2} = \frac{1}{83}. \end{aligned} \quad (4)$$

The “less than” sign is used because only the upper limit could have been determined for grb081102. For GRB080319B the column density is $N_H = 9.2 \cdot 10^{20} \text{ cm}^{-2}$ [1], that is, five times lower than toward GRB081102 $\tau_V^{\text{grb080319B}} = 0.48$, $F_\gamma = 8.25 \cdot 10^{-5} \Rightarrow \delta m = 0.5^m$. Hence

$$\frac{F_{\text{opt}}^{\text{grb080319B}}}{F_\gamma^{\text{grb080319B}}} = \frac{1}{22}. \quad (5)$$

It thus follows that the fraction of prompt optical emission for GRB081102 is at least four times smaller than for grb080319B.

The Long Gamma-Ray Burst GRB090424. At that time MASTER-VWF-2 in Irkutsk operated in the alert mode (with cameras pointed apart) and GRB090424 happened to be at the centre of the field of view of one of the cameras (Figure 16). It was also a typical long ($T_{90} = 48 \text{ s}$) gamma-ray burst and UVOT detected the afterglow with unfiltered magnitude of about 15.3^m 167 seconds after the burst [21]. MASTER-VWF-2 observed the grb error-box without time gaps for 1.2 hours before, during and 1.5 hours after the gamma-ray burst with 1-second exposures. Unfortunately, weather conditions were far from favourable, resulting in a not so high upper limit of $V_{1s} < 8.0^m$ and $V_{60s} < 60.0^m$ for a coadd of 60 images (see [22] and [23]). According to both Swift/BAT [24] data and FERMI observatory data converted to the 15–150 keV energy interval [25], $F_\gamma^{\text{grb090424}} = 2.1 \cdot 10^{-5}$, implying that

$$\frac{F_{\text{opt}}^{\text{grb090424}}}{F_\gamma^{\text{grb090424}}} < \frac{1}{530}. \quad (6)$$

Note that despite the rather modest upper limit the burst was very powerful and even such an upper limit restricts substantially the possible flux.

4.3.2. Gamma-Ray Bursts Recorded by FERMI Observatory.

Unlike Swift, the FERMI observatory does not specialise in gamma-ray burst observations. Its on-board equipment allows the burst coordinates to be determined only to within several degrees or even worse. FERMI currently issues two to three times more alerts than Swift and is capable of recording harder (up to 10 MeV) radiation (Swift has an upper sensitivity limit of about 300 keV), and responds to short hard gamma-ray bursts, whose prompt optical or IR emission has not been detected so far. Given the large error of the coordinate measurement, gamma-ray bursts detected by FERMI observatory may at present (and, very likely, also in the future) have their prompt emission observed only with wide-field cameras, such as MASTER-VWF.

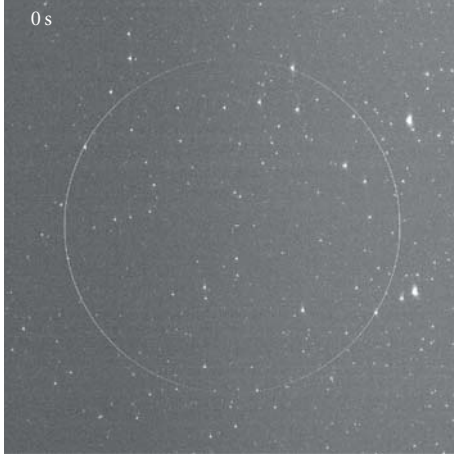


FIGURE 17: The most recent error box of GRB081130B $\alpha = 00^h56^m20^s$ $\delta = +04^\circ12'$, error-box radius is $R = 3.5^\circ$ [11]. The centre of the field of view of the camera that which recorded the burst pointed at $\alpha = 01^h01^m56^s$ $\delta = +19^\circ20'38''$. The image size is $10^\circ \times 10^\circ$. Animation available here: <http://observ.pereplet.ru/images/GRB081130B/grb.film.html>.

Until now (July, 1 2009), a total of five FERMI GRB error boxes have overlapped with the MASTER-VWF field of view, and two more (GRB081215 and GRB090526) proved to be outside the field of view after a very substantial final refinement of their coordinates.

GRB081130. GRB081130 was the first burst recorded by FERMI and synchronously observed by the MASTER-VWF4 facility in Kislovodsk. Its coordinates and error-box have been refined repeatedly (with a characteristic scatter of $\pm 10^\circ$), but always fell within the field of view of our cameras. Figure 17 shows the final localisation of this gamma-ray burst. The error box of grb081130 has been observed without time gaps for several hours before, during, and for hours after the grb.

No proper candidates could have been found inside the error box. However, given the rather large uncertainty of the coordinates measured by FERMI, we extended the search area for transient candidates to the entire frame. As a result, a very interesting object resembling a grb optical counterpart has been found 14 degrees from the localisation centre synchronously with grb (Figure 18). However, after cross identification with the catalogue of artificial satellites this transient was found to coincide with a high-orbit satellite, which occasionally produces such flashes. Thus a rather high upper limit of $V_{\text{grb081130B}} > 12^m.0$ has been obtained again after the coadd of four images ($T_{\text{grb081130B}} = 15\text{--}20$ s taken in different channels [11]) [26].

When converted to the 15–150 keV energy interval, the gamma-ray fluence from GRB081130 is $F_{\gamma}^{\text{grb081130B}} = 1.01 \cdot 10^{-6}$ erg/cm². We then apply the same procedures as in the case of GRB081102 to infer $F_{\text{opt}}^{\text{grb081102}} = 3.82 \cdot 10^{-9}$ erg/cm², implying a flux ratio of $F_{\text{opt}}^{\text{grb081130B}}/F_{\gamma}^{\text{grb081130B}} < 1/245$ [27].

GRB090305B. The gamma-ray burst GRB090305 (Figure 19) was recorded by FERMI [12]. MASTER-VWF-4 in Kislovodsk operated in the alert mode (with cameras apart) and observed 80% of the GRB090305 error-box at the edge of the field of view of one of the cameras. Despite of its rather short duration ($T_{90} = 2$ s) [12], GRB090305 was nevertheless a rather long and bright gamma-ray burst. However, even the final position estimate has a large error-box ($\alpha = 10^h20^m$, $\delta = 68^\circ06'$ $R_{\text{sigma}} = 5.4^\circ$) and therefore no alert observations have been made. MASTER-VWF-4 has observed the error-box of this GRB without time gaps for 3.5 hours before, during and for two hours after the with 1-second exposures. No optical transients close to T_{GRB} could be found and we obtain an upper-limit of $V_{1s} < 9.5^m$ [28]. $F_{\text{opt}}^{\text{grb090305B}}/F_{\gamma}^{\text{grb090305B}} < 1/121$.

GRB090320B. The MASTER-VWF-4 system in Kislovodsk observed synchronously 80% of the GRB090320B error-box (see Figure 20). This moderately bright burst has been detected by FERMI observatory at $\alpha = 12^h15^m.3$, $\delta = 57^\circ33'$ with an uncertainty of 12.6 degrees (this includes the 3° systematic error) [13]. No optical candidates could be found for this burst, which was long enough ($T_{90} = 60$ s) for its upper-limit $V < 11^m$ to be estimated on 60-s. exposure sets [29].

On the whole, this burst turned out to be rather faint with $F_{\text{opt}}^{\text{grb090320B}}/F_{\gamma}^{\text{grb090320B}} < 1/57$.

GRB090328B. Finally, GRB090328B is the last of the bursts considered here to deserve a separate discussion. It had 20% of its error box observed by MASTER-VWF-2 in Irkutsk (Figure 21). GRB090328B was short compared to all other long bursts and it is the first short gamma-ray burst to have been synchronously observed.

This faint burst has been recorded FERMI observatory at 19:13:46.1 UT on 20 March 2009 at $\alpha = 10^h22^m.8$, $\delta = 33^\circ24'$ with with an uncertainty of 26.82° (including the 3° systematic error) [26, 30]. It is the faintest burst so far recorded by our cameras and had therefore its coordinates determined with large errors. We found its upper limit to be $V < 9.1^m$ on 1 s images and $F_{\text{opt}}^{\text{grb090328B}}/F_{\gamma}^{\text{grb090328B}} < 1/1527$ [14].

5. Summary

Figure 1 and Table 2 summarise the results of observations of prompt emission of gamma-ray bursts. Even a cursory analysis of Figure 1 demonstrates that optical emission is better correlated with soft rather than hard gamma-ray emission. The gamma-ray burst GRB090424 is located in a remarkable position in Figure 1. One can see that the upper limit for its optical emission is about one order of magnitude lower than the flux from the famous gamma-ray burst GRB990123, a pattern that may be indicative of irregular conversion of gamma-ray emission into optical radiation from one burst to another. On the whole, it is safe to conclude that more observations are required for a detailed analysis. The example of GRB090424 gamma-ray

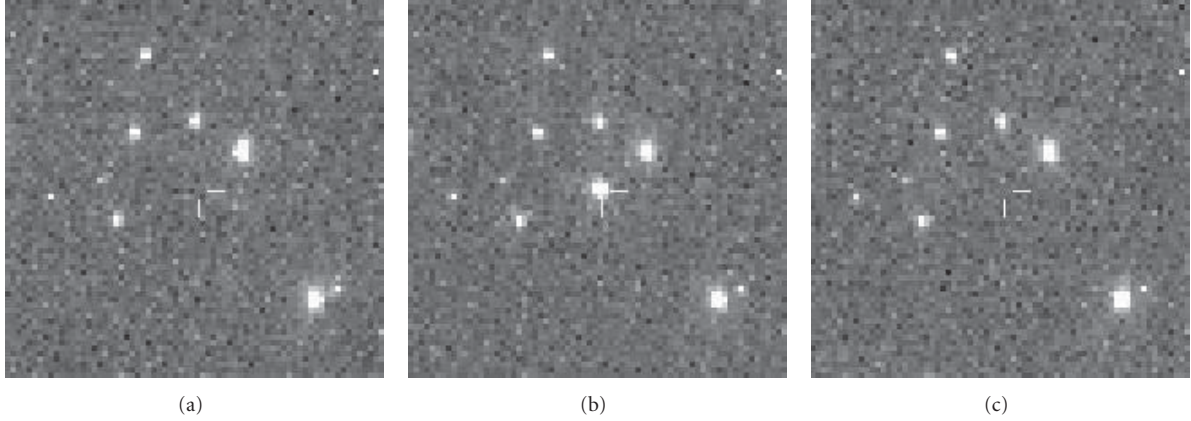


FIGURE 18: Transient object found simultaneously with GRB081130B at $\alpha = 01^h 10^m 20^s$ $\delta = +18^\circ 44' 35''$, 14 degrees from the centre of its last GRB081130B localisation. A detailed analysis showed the object to be a short flash produced by the “MOLNIYA” high-orbit satellite.

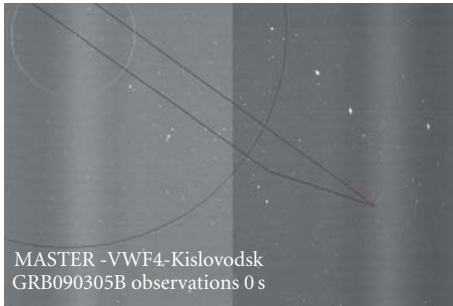


FIGURE 19: MASTER-VWF4 Kislovodsk GRB090305B follow-up observation. This is a $40^\circ \times 24^\circ$ full-frame image. The white and black circles show the error boxes corresponding to the 1 and 3 sigma FERMI error limits plus the 3° systematic error [12] ($R_{\text{sigma}} = 5.4^\circ$). The black rectangle shows the IPN triangulation error-box. Animation is available here http://observ.pereplet.ru/images/GRB090305B/GRB090305B_full2.gif.



FIGURE 21: MASTER-VWF4 follow-up observations of GRB090328B in Kislovodsk. This is a $40^\circ \times 24^\circ$ full-frame image. The black circle shows the error box corresponding to the 3 sigma FERMI error limits plus the 3° systematic error ($R = 12.6^\circ$) [14]. Animation is available here http://observ.pereplet.ru/images/GRB090320B/GRB090320B_60sec.gif.

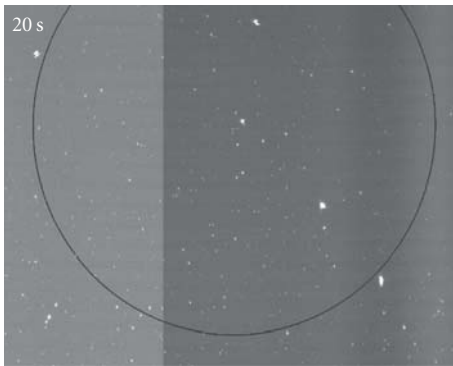


FIGURE 20: MASTER-VWF4 Kislovodsk GRB090320B follow-up observation. This is a $40^\circ \times 24^\circ$ full-frame image. The black circle shows the error box corresponding to the 3 sigma FERMI error limits plus the 3° systematic error ($R = 12.6^\circ$) [13]. Animation is available here http://observ.pereplet.ru/images/GRB090320B/GRB090320B_60sec.gif.

burst indicates that even the measured optical limit may constitute a result of real importance and that this burst deserves separate analysis.

In this article we describe the methods of observation and analysis of images taken with very wide-field cameras, and their application to synchronous observations of prompt gamma-ray burst emission in the MASTER-VWF experiment. We finally recall that the renowned astrophysicist Bohdan Paczynski [31] pointed out in his last paper the exceptional astrophysical significance of robotic telescope networks, which, like MASTER, are composed of Wide-Field searching cameras and larger telescopes. Now his and our ideas at last become reality.

Acknowledgment

This work was supported by the Ministry of Science of the Russian Federation (state contract no. 02.740.11.0249).

Endnotes

1. The information about archive opening will be accessible on our website and will published separately.
2. Original program is delivered by E. Gorbovskoy and A. Belinskii.
3. As Star-like I name objects with $1.5 < \text{FWHM} < 4\text{--}5$ and the small semiaxes ratio $a/b < 2\text{--}3$. Limiting the relation of semiaxes it is so great because objects at frame edges have naturally prolated the form (see stars form on Figure 8 or 14).
4. For pipeline processing we use only dark and bias calibrations. Long and more computationally difficult flat-calibration is used only necessarily (GRB case for an example).
5. Semimajor axis (a) unused here because it can change in vast limits for real objects. From 1.5–3 for stars to 100 for fast satellites.

References

- [1] J. L. Racusin, S. V. Karpov, M. Sokolowski, et al., “Broadband observations of the naked-eye γ -ray burst GRB 080319B,” *Nature*, vol. 455, no. 7210, pp. 183–188, 2008.
- [2] M. Ćwiok, W. Dominik, K. Małek, et al., “Search for GRB related prompt optical emission and other fast varying objects with “Pi of the Sky” detector,” *Astrophysics and Space Science*, vol. 309, no. 1–4, pp. 531–535, 2007.
- [3] V. M. Lipunov, V. G. Kornilov, A. V. Krylov, et al., “Optical observations of gamma-ray bursts, the discovery of supernovae 2005bv, 2005ee, and 2006ak, and searches for transients using the “MASTER” robotic telescope,” *Astronomy Reports*, vol. 51, no. 12, pp. 1004–1025, 2007.
- [4] K. Onda, T. Tamagawa, M. Tashiro, et al., “Ultra wide-field telescope WIDGET for observing GRB,” *Nuovo Cimento della Societa Italiana di Fisica B*, vol. 121, no. 12, pp. 1549–1550, 2006.
- [5] S. Karpov, G. Beskin, A. Biryukov, et al., “Optical camera with high temporal resolution to search for transients in the wide field,” *Nuovo Cimento della Societa Italiana di Fisica C*, vol. 28, no. 4–5, pp. 747–750, 2005.
- [6] E. Molinari, S. Bondar, S. Karpov, et al., “TORTOREM: two-telescope complex for detection and investigation of optical transients,” *Nuovo Cimento della Societa Italiana di Fisica B*, vol. 121, no. 12, pp. 1525–1526, 2006.
- [7] V. Lipunov, V. Kornilov, E. Gorbovskoy, et al., “Master robotic net,” *Advances in Astronomy*, vol. 2010, Article ID 349171, 6 pages, 2010.
- [8] E. Bertin, “SExtractor: software for source extraction,” *Astronomy and Astrophysics Supplement*, vol. 117, no. 2, pp. 393–404, 1996.
- [9] N. Tyurina, V. Lipunov, and K. Victor, “MASTER prompt and follow-up GRB observations,” *Advances in Astronomy*. In press.
- [10] A. Panaitescu, “Prompt GeV emission in the synchrotron self-compton model for gamma-ray bursts,” submitted, <http://arxiv.org/abs/0811.1235v1>.
- [11] A. J. van der Horst, “GRB 081130B: Fermi GBM detection,” *GCN Circular*, no. 8593, 2008.
- [12] C. A. Wilson-Hodge, “GRB090305B: Fermi GBM detection,” *GCN Circular*, no. 8972, 2009.
- [13] P. N. Bhat, “GRB 090320B: Fermi GBM detection,” *GCN Circular*, no. 9020, 2009.
- [14] K. Ivanov, S. Yazev, E. Gorbovskoy, et al., “GRB 090328B: MASTER-Irkutsk prompt optical short burst observations,” *GCN Circular*, no. 9065, 2009.
- [15] V. Mangano, B. Sbarufatti, V. La Parola, and T. Ukwatta, “GRB 081102: Swift-XRT refined analysis,” *GCN Circular*, no. 8470, 2008.
- [16] V. Lipunov, V. Kornilov, E. Gorbovskoy, et al., “GRB 081102: MASTER prompt optical limit,” *GCN Circular*, no. 8471, 2008.
- [17] E. Gorbovskoy, V. Lipunov, V. Kornilov, et al., “GRB 081102: MASTER refind and final results,” *GCN Circular*, no. 8516, 2008.
- [18] A. V. Zasov and K. A. Postnov, *General Astrophysics*, Vek 2, Fryazino, Russia, 2006.
- [19] P. M. W. Kalberla, W. B. Burton, D. Hartmann, et al., “The Leiden/Argentine/Bonn (LAB) survey of Galactic HI. Final data release of the combined LDS and IAR surveys with improved stray-radiation corrections,” *Astronomy & Astrophysics*, vol. 440, no. 2, pp. 775–782, 2005.
- [20] E. E. Fenimore, S. D. Barthelmy, W. H. Baumgartner, et al., “GRB 081102: Swift-BAT refined analysis,” *GCN Circular*, no. 8468, 2008.
- [21] P. Schady and J. K. Cannizzo, “Swift/UVOT observations of GRB 090424,” *GCN Circular*, no. 9234, 2009.
- [22] E. Gorbovskoy, V. Lipunov, V. Kornilov, et al., “GRB 090424: MASTER-Net prompt optical limit,” *GCN Circular*, no. 9252, 2009.
- [23] E. Gorbovskoy, V. Lipunov, V. Kornilov, et al., “GRB 090424: MASTER-Net prompt optical observations,” *GCN Circular*, no. 9233, 2009.
- [24] T. Sakamoto, S. D. Barthelmy, W. H. Baumgartner, et al., “GRB 090424: Swift-BAT refined analysis,” *GCN Circular*, no. 9231, 2009.
- [25] V. Connaughton, “GRB 090424: Fermi GBM observation,” *GCN Circular*, no. 9230, 2009.
- [26] E. Gorbovskoy, V. Lipunov, V. Kornilov, et al., “GRB 081130: MASTER VWF prompt optical observations Fermi GRB,” *GCN Circular*, no. 8585, 2009.
- [27] E. Gorbovskoy, V. Lipunov, V. Kornilov, et al., “GRB 081130B: MASTER prompt optical observations,” *GCN Circular*, no. 8597, 2008.
- [28] E. Gorbovskoy, V. Lipunov, V. Kornilov, et al., “GRB090305B: MASTER-net prompt optical short burst observations,” *GCN Circular*, no. 9004, 2009.
- [29] E. Gorbovskoy, V. Lipunov, V. Kornilov, et al., “GRB 090320B: MASTER-Net prompt optical observations,” *GCN Circular*, no. 9038, 2009.
- [30] A. Goldstein, “GRB 090328B: Fermi GBM detection,” *GCN Circular*, no. 9056, 2009.
- [31] B. Paczynski, “Astronomy with small telescopes,” *The Publications of the Astronomical Society of the Pacific*, vol. 118, no. 850, pp. 1621–1625, 2006.

Research Article

The Data Big Bang and the Expanding Digital Universe: High-Dimensional, Complex and Massive Data Sets in an Inflationary Epoch

Meyer Z. Pesenson,¹ Isaac Z. Pesenson,² and Bruce McCollum¹

¹IPAC, California Institute of Technology, m/c 220-6, Pasadena, CA 91125, USA

²Department of Mathematics, Temple University, Philadelphia, PA, USA

Correspondence should be addressed to Meyer Z. Pesenson, misha@ipac.caltech.edu

Received 15 June 2009; Revised 21 October 2009; Accepted 12 January 2010

Academic Editor: Joshua S. Bloom

Copyright © 2010 Meyer Z. Pesenson et al. This is an open access article distributed under the Creative Commons Attribution License, which permits unrestricted use, distribution, and reproduction in any medium, provided the original work is properly cited.

Recent and forthcoming advances in instrumentation, and giant new surveys, are creating astronomical data sets that are not amenable to the methods of analysis familiar to astronomers. Traditional methods are often inadequate not merely because of the size in bytes of the data sets, but also because of the complexity of modern data sets. Mathematical limitations of familiar algorithms and techniques in dealing with such data sets create a critical need for *new paradigms* for the representation, analysis and scientific visualization (as opposed to illustrative visualization) of heterogeneous, multiresolution data across application domains. Some of the problems presented by the new data sets have been addressed by other disciplines such as applied mathematics, statistics and machine learning and have been utilized by other sciences such as space-based geosciences. Unfortunately, valuable results pertaining to these problems are mostly to be found in publications outside of astronomy. Here we offer brief overviews of a number of concepts, techniques and developments that are vital to the analysis and visualization of complex datasets and images. One of the goals of this paper is to help bridge the gap between applied mathematics and artificial intelligence on the one side and astronomy on the other.

1. Introduction

Astronomy is undergoing a rapid, unprecedented and accelerating growth in both the amount and the intrinsic complexity of data. This results partly from past and future large sky surveys: the Sloan Digital Sky Survey [1], the Large Synoptic Survey Telescope (LSST) [2, 3], ESA's GAIA mission [4], Pan-STARRS [5, 6], the Palomar Transient Factory [7], LAMOST [8], and the Palomar-Quest Survey [9]. Smaller surveys and catalogs comprised of $\sim 10^3$ – 10^4 objects appear annually. The increasing availability of multiple-object spectrographs deployed at ground-based observatories enables observers to obtain spectra of hundreds of objects in a single exposure [10–16]. Million-object spectrographs have been proposed and are undergoing design studies (e.g., [17, 18]). All together, and sometimes individually, such projects are creating for astronomy massive multitemporal

and multispectral data sets comprised of images spanning multiple wavebands and including billions of objects. Furthermore, the Virtual Observatory (VO) is undertaking to combine existing historical data from all wavelengths into what will be, from the user's perspective, a single data set of gigantic size and unprecedented complexity (<http://www.ivoa.net/>).

In addition, mathematically new (for astronomy) forms of data are starting to appear, such as those of the ESA Planck mission in which the cosmic microwave background (CMB) is characterized by a 2×2 matrix at each point in the sky [19].

Other great challenges arise from the so-called three-dimensional (3D) reconstructions. For example, a very important and difficult problem of solar astrophysics is 3D reconstruction of coronal mass ejections [20]. The resulting reconstruction problem cannot be solved via classical methods and must be addressed by more modern

image processing methods like compressed sensing (see Section 5). Another example of tomographic reconstruction is coming from the neutral hydrogen mapping using the redshifted 21 cm line that has recently emerged as a promising cosmological probe. A number of radio telescopes are currently being proposed, planned or constructed to observe the redshifted 21 cm hydrogen line from the Epoch of Reionization (e.g., Fast Fourier Transform Telescope, [21]).

The richness and complexity of new data sets will provide astronomy with a wealth of information and most of the research progress expected from such sets inherently rests in their enormity and complexity. In order to take full advantage of immense multispectral, multitemporal data sets, their analysis should be *automated*, or at least *semi-automated*, and should consist of the following steps: *detection*, *characterization* and *classification* of various features of interest, followed, if necessary, by *automated decision-making* and possibly by *intelligent automatic alerts* (e.g. for follow-up observations or data quality problems). Moreover, a *real-time processing* may be required. Complex data also call for scientific visualization rather than ordinary illustrative visualization. By scientific visualization we mean visualization that does not simply reproduce visible things, but makes the things visible, thus enabling extraction of meaningful patterns from multiparametric data sets and ultimately facilitating analysis. All this requires the development and adaption of modern methods for data representation, analysis and visualization. Methods now standard in astronomy are often ineffective because the data sets are too large and too complex for existing tools to be scaled in a straightforward way from handling several parameters up to dozens or more. There are also important limitations inherent in the mathematical algorithms familiar to astronomers. Scientific visualization, dimensionality reduction, and non-parametric methods in general are among the least-advanced categories of tools in astronomy because until this century there have not been data sets requiring new approaches related to those aspects of the data. All this not only creates a critical need for new sophisticated tools, but moreover urgently calls for *new paradigms* for the analysis, visualization and organization of heterogeneous, multiresolution data across application domains.

The astronomical community is becoming increasingly aware of the fact that new and advanced methods of applied mathematics, statistics and information technology should be developed and utilized. Three of the State of the Profession Position Papers submitted to the Astronomy and Astrophysics Decadal Survey strongly emphasized astronomy's need for new computational and mathematical tools in the coming decade [22–24] (see: http://sites.nationalacademies.org/bpa/BPA_049492). A variety of individual and organizational initiatives and research projects have been proposed or are underway to at least partially address this looming challenge by developing or implementing a new generation of methods of data representation, processing and visualization.

However, there is a large communication gap between astronomy and other fields where adequate solutions exist or are being developed: applied mathematics, statistics and artificial intelligence.

The principal objectives of this paper are twofold. First, we wish to bring attention to some specific needs for new data analysis techniques. Second, we describe some innovative approaches and solutions to some of these problems and give examples of novel tools that permit effective analysis, representation, and visualization of the new multispectral/multitemporal data sets that offer enormous richness if they are mined with the appropriate tools. The extensive amount of relevant work already accomplished in disciplines outside of astronomy does not allow us to offer a complete review of all aspects of these complex topics and problems, but we have selected a number of important examples.

The structure of the paper is as follows. In Section 2 we discuss challenges related to semi-automated processing of low-dimensional images and describe briefly our framework for advanced astronomical image processing. Section 3 describes problems posed by complex astronomical data sets; Section 4 addresses some of these problems and presents some innovative methods for nonlinear dimension reduction, sampling on graphs and manifolds; it also describes briefly a new unifying method for image segmentation and information visualization that is based on physical intuition derived from synchronization of nonlinear oscillations; Section 5 reviews some recent approaches to the challenges posed by high-dimensional, complex data sets and their importance for cosmological and astrophysical problems; in particular, we briefly discuss in this part a new tool called *needlets* for processing data that is laying on the sphere, applications of needlets to the analysis of CMB data, and a generalization of the wavelet-like transforms to Riemannian manifolds. The paper ends with a conclusion.

2. Framework for Processing and Visualizing Astronomical Images

Vast data sets demand automated or semi-automated image processing and quality assessment of the processed images. Indeed, the sheer number of observed objects awaiting analysis makes obvious the need for sophisticated automation of object detection, characterization and classification. Adapting recent advances of computer vision and image processing for astronomy and designing and implementing an image processing framework (see below) that would utilize these continuing achievements, remains, however, a major challenge.

Developers and users alike have realized that there is more to creating an application than simple programming. The objective of creating a flexible (see below) application is customarily achieved by exploiting the object-oriented paradigm [25, 26]. In computer science such systems are called frameworks [27]. Frameworks are flexible, and users can extend frameworks' capabilities by installing plug-ins without having to rewrite the basic code. An application framework consists of computational (processing) modules, data, and an interactive interface. Frameworks are extendable (i.e., they can easily adopt software products to changes of specification) and reusable (the software elements are able to serve for construction of many different new applications).

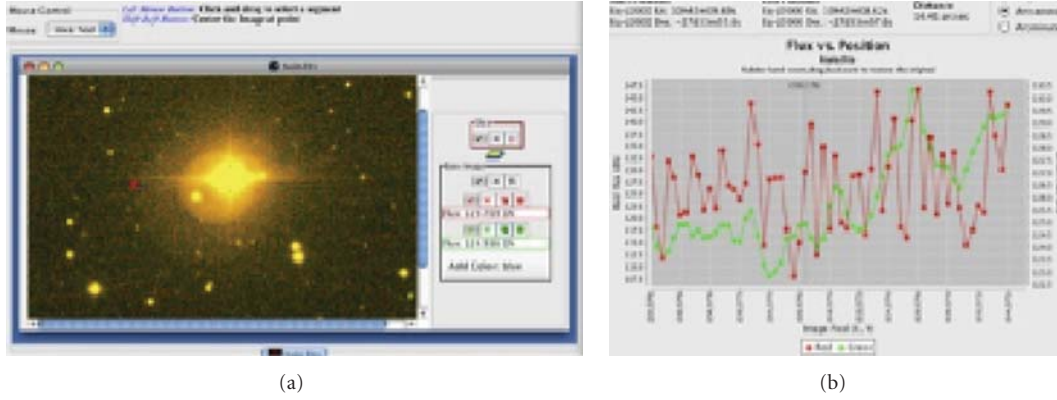


FIGURE 1: ESO-La Silla; courtesy of A. Grado, INAF-Osservatorio Astronomico di Capodimonte. (a) overlaid pre- and post-processed images; the red cross shows approximately the edge of the diffuse halo. (b) Flux-cut through the overlaid pre- and post-processed images (red and green, resp.); the vertical grey line (close to the center of the plot) corresponds to the red cross in the plot on the left; after the preprocessing the average level “outside” of the halo is lower than the average level “inside”, thus enabling a better automated separation of the diffuse halo from the background.

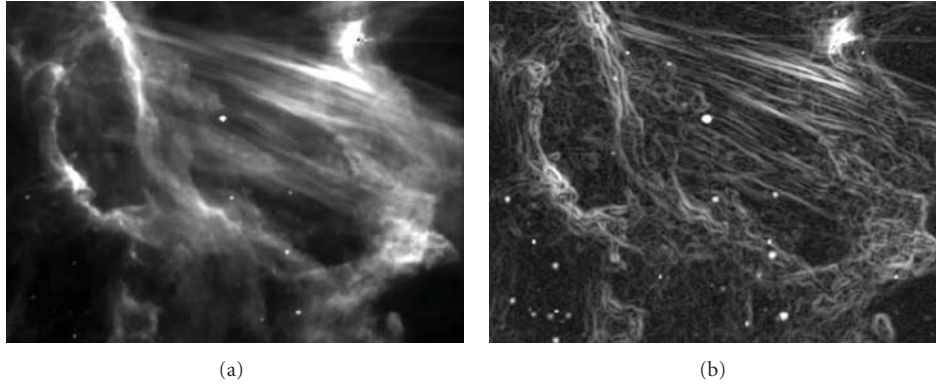


FIGURE 2: Morphology unveiling [28]. (a) IC 405, *Spitzer* IRAC camera $8.0\mu\text{m}$ image (France et al. [29]); filaments and a bow shock near HD34078 (see the red cross “x” in Figure 3(a)). The brightness is proportional to the flux (logarithmic scale). (b) Brightness is proportional to the module of the gradient of flux (logarithmic scale); this way of looking at astronomical images facilitates analysis of nebular morphology, outflows, jets, embedded sources, and shock fronts.

The keystone elements of a system that unifies a wide range of methods for astronomical image processing should be computational and visualization modules. Such a platform-independent framework with an integrated environment was described in Pesenson et al. [28]. It provides many common visualization features plus the ability to combine these images (overlays, etc.) in new and unique ways. The framework has a very intuitive GUI that allows the user to set up a custom pipeline interactively and to process images singly or in a batch mode. The final products, as well as the results of each step, are viewable with the framework. It also provides access to different data archives and can easily incorporate custom modules written in any programming language. Figures 1–4 give a few self-explanatory examples that demonstrate some of the framework’s functionality.

The framework deals primarily with image regularization and segmentation. These are fundamental first steps for the detection and characterization of image elements or objects and as such they play principal roles in the realization

of automated computer vision applications. Image segmentation can roughly be described as the process that subdivides an image into its constituent parts (objects) and extracts those parts of interest. Since the inception of image segmentation in the 1960s, a large number of techniques and algorithms for image segmentation have been developed.

However, due to revolutionary advances in instrumentation, the complexity of images has changed significantly: the extension of grey level images to multi- and hyperspectral images, from 2D images to 3D, from still images to sequences of images, tensor-valued images (polarization data), and so forth. Some modern, cutting-edge methods for image processing have been developed lately, and are being developed today, by information scientists outside of astronomy. The substantial progress in this direction made by the image processing and computer vision communities [30, 31], has found multiple applications in physics, technology, and biomedical sciences. Unfortunately, for the most part these advances have not yet been utilized by the astronomical community.

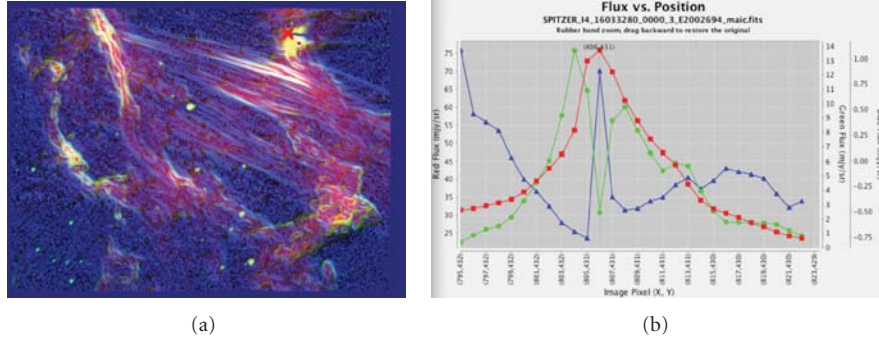


FIGURE 3: Overlaid pre- and postprocessed images [28]. (a) Three overlaid images of IC 405: *Spitzer* IRAC camera 8.0 μm image, the module of its gradient, and the angle of its gradient (red, green, and blue, resp.). The line through the red cross “x” indicates the crosscut. (b) Three profiles for the crosscut through “x”. The crosshair goes through the ridge point and a local minimum of the module of the gradient. Note the different scales on the left and right vertical axes.

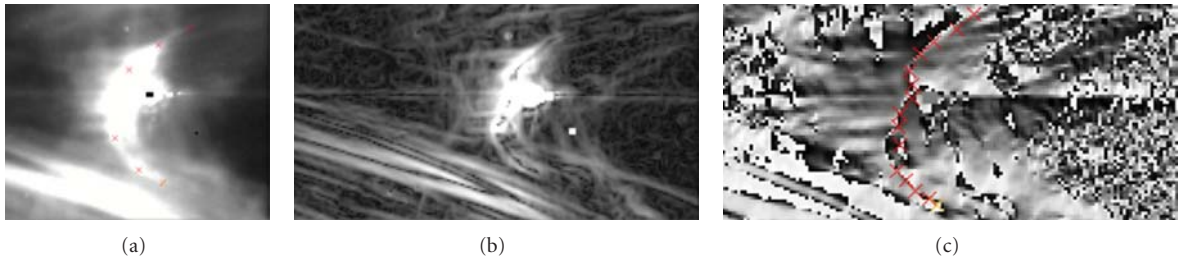


FIGURE 4: Three different visualizations of the bow shock structure [28]. (a) IC 405, *Spitzer* IRAC camera 8.0 μm image, the bow shock (red crosses) near HD 34078. The brightness is proportional to the flux (logarithmic scale). (b) The bow shock area where the brightness is proportional to the module of the gradient of flux (logarithmic scale). (c) The bow shock area where the front of the bow shock is immediately apparent as a curve of 1 pixel width (red crosses); the brightness is proportional to the angle of the gradient of flux (logarithmic scale).

Multiscale image representation and enhancement are such approaches. They have become important parts of computer vision systems and modern image processing. The multiscale approach has proven to be especially useful for image segmentation for feature, and artifact detection. It enables a reliable search for objects of widely different morphologies, such as faint point sources, diffuse supernova remnants, clusters of galaxies, undesired data artifacts, as well as unusual objects needing detailed inspection by a scientist. It is well known that in astronomical images one often sees both point sources and extended objects such as galaxies embedded in extended emission (see, e.g., Figures 2, 6 and 7). Because of the issue of robustness with respect to noise (Section 4), a careful preprocessing is required before one can safely apply image segmentation or dimension reduction. So, an adequate way of preprocessing is what needs to be addressed first.

One effective approach to denoising is based on partial differential equations and may be seen as the local adaptive smoothing of an image along defined directions that depend on local intensities. One wants to smooth an image while preserving its features by performing a local smoothing mostly along directions of the edges while avoiding smoothing orthogonally to these edges. Many regularization schemes have been developed so far for the case of

simple two-dimensional scalar images. An extension of these algorithms to vector-valued images is not straightforward. For a gray-scale image, the gradient is always perpendicular to the level set objects of the image; however, in the multi-channel case, this quality does not hold. Applying nonlinear diffusion to each channel or spectral band separately is one possible way of processing multi- and hyperspectral cubes; however, it does not take advantage of the richness of the multi/hyperspectral data. Moreover, if the edge detector acts only on one channel, it may lead to an undesirable effect, such as color blurring, where edges in color images are blurred due to the different local geometry in each channel. Hence, a coupling between image channels should appear in the equations through the local vector geometry. We achieve this by implementing a nonlinear diffusion on a weighted graph, thus generalizing the approach adopted by Pesenson et al. [28]. The governing equation is linear, but the nonlinearity enters through the weights assigned to the graph edges. This algorithm respects the local smoothing geometry and thus serves well as a preprocessing step required for dimension reduction (Section 4).

Our framework handles two-dimensional scalar images and paves the way to the semi- and automated image processing and image quality assessment. However, the ability to extract useful knowledge from high-dimensional

data sets is becoming more and more important (Section 3). It is closely related to finding complicated structural patterns of interrelated connections and heavily depends on the ability to reduce dimensions of the raw data. This problem constitutes a big challenge for the scientific and technology communities. To extend the framework's functionality to high-dimensional images and data sets we have been developing novel, practical algorithms for dimension reduction. In the next section we describe some of the challenges presented by modern, high-dimensional data sets.

3. Complex, Massive Data Sets

Astronomy has long found the use of multiple data dimensions to be crucial aids to progress. For example, surveys of H-alpha sources when cross-correlated with spectral types guided astronomy to discover interesting new types of objects such as Herbig AeBe stars [32]. Cross-comparison of brightnesses, redshifts, and optical object morphologies led to the discovery of quasars. X-ray emission proved to be a highly efficient method of identifying pre-main sequence objects in a large field of view (e.g., review [33]). The fact that the same object (SS 433) was noticed to exhibit H-alpha emission and strong radio and optical variability led astronomers to investigate further and thus discover the existence of microquasars [34–36]. Other discoveries from the use of multidimensional data using just a few dimensions include such things as Be X-ray binaries and soft gamma ray repeaters.

Simple color-magnitude diagrams are another traditional tool taking advantage of multiple data dimensions (e.g., cataloging YSO candidates from Spitzer survey data, Whitney et al. [37]). In addition, it is well known that simple color-color plots using four colors provide ways to efficiently and fairly reliably classify into physical types a large number of objects (IRAS data, e.g., [38, 39]; 2MASS data, e.g., [40] MSX data, e.g., [41, 42]; *Spitzer* data, e.g., [43]) as well as to discover interesting new objects as outliers (e.g., Luminous Red Novae, [44, 45]). The meaning and usefulness of more complicated multiwavelength cross-correlations across widely-separated wavelength domains remain a nontrivial but fruitful challenge still being explored (e.g., microquasars identified by comparing radio, IR, and X-ray properties [46]).

As multiwavelength data have become available for huge numbers of objects in the past few decades, the number of data dimensions for a typical object has grown beyond what can be visualized and studied using classical color-color plots and correlations using only a few dimensions. For example, Egan et al. [41] write “six-dimensional data are difficult to represent; in addition, it is not clear that all of the colors yield completely independent information” (see Figure 5).

While Figure 5 successfully permits one to identify meaningful patterns, it is easily imagined that attempting to display a much larger number of data dimensions by simply using many more colors and symbols overlaid on the same plot and same region of parameter space would not be a useful form of scientific visualization. Also, two-dimensional

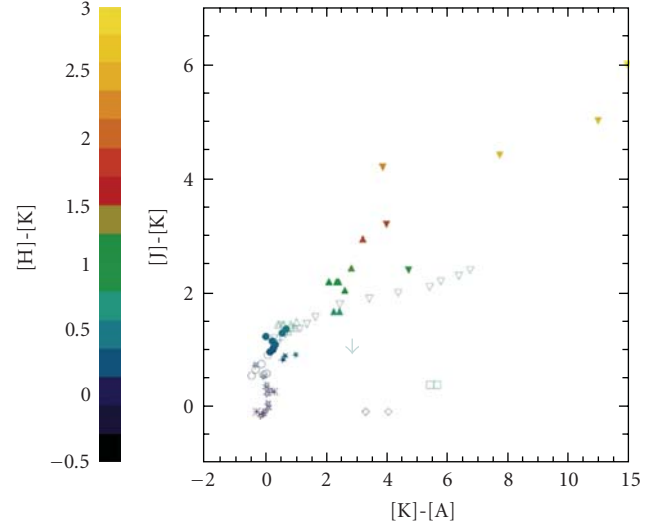


FIGURE 5: Color-color plots are a familiar form of scientific visualization. This example (from [41]) shows, simultaneously, infrared color-color information for several different categories of objects. Different object classes are represented by different symbols or different hues. Thus several data dimensions (the four IR colors and the several classes of object) are represented.

plots are obviously not useful for expressing relationships among more than four colors. Effective scientific visualization of a large number of data dimensions requires new techniques.

The catalog information available for a great many objects already includes such information as magnitude, several optical and IR colors, metallicities, spectral types, and so on. A galaxy catalog would of course include other parameters such as morphology and redshift. When spectra are considered and compared in detail, the huge number of emission and absorption features obviously compounds the problem vastly. Still more complexity is added when one attempts to correlate a large grid of models with a large data set having many dimensions (e.g., the YSO analysis [37]) in order to create feedback for models based on statistically significant samples rather than on a few putative prototypes.

Other examples of high-dimensional data include, but are not limited to, multiparametric data sets (e.g., the manifold of galaxies, [47, 48]), multitemporal, multispectral and hyperspectral data sets and images, and high-resolution simulations on massively parallel computers. The magnitude of the computational challenge for pattern recognition and classification algorithms is suggested by the fact that the VO will contain billions of data points each having hundreds of dimensions [49].

All these examples clearly demonstrate that the automated and semiautomated processing required by the unprecedented and accelerating growth in both the amount and the complexity of astronomical data demands new ways of information representation. In the next section we discuss such approaches and describe some of the original algorithms we have developed in the course of this ongoing work.

4. Dimensionality Reduction and Sampling for Complex and Large Data Sets

Because approaches to complex data require advanced mathematics, astronomers who wish to take advantage of them will need at least some basic knowledge of new, unfamiliar mathematical concepts and terminology. The full practical adoption of such methods requires interdisciplinary scientists who understand the new approaches in depth and are interested in working with astronomers to adapt and apply the methods to astronomical data sets. This is already happening as part of some research. The first step for a “neophyte” astronomer, however, is to learn “what is out there” as a basis for further investigation and consideration of the utility of various methods. The goal of this section is to offer a very basic introduction and explanation of some of these unfamiliar concepts.

Machine learning [50] is becoming increasingly important in astronomy (see extensive reviews [51, 52]). The main objectives of machine learning are clustering (automatic identification of groups of similar objects), and classification (assigning labels to instances). However, high dimensionality complicates machine learning and can easily thwart the entire effort. It also becomes a formidable obstacle in computing numerical solutions in Bayesian statistics for models with more than a few parameters.

Bellman [53] coined the term “curse of dimensionality”, to describe how difficult it was to perform high-dimensional numerical integration. For example, 100 evenly-spaced sample points suffice to sample a unit interval with no more than 0.01 distance between points; an equivalent sampling of a 10-dimensional unit hypercube with a lattice with a spacing of 0.01 between adjacent points would require 10^{20} sample points. Thus, in some sense, the 10-dimensional hypercube can be said to be a factor of 10^{18} “larger” than the unit interval. *Obviously, this will make many computational tasks intractable for high-dimensional data sets.*

Euclidian spaces are usually used as models for traditional astronomical data types (scalars, arrays of scalars). Another *general manifestation* of high dimensionality is the fact that in a high-dimensional Euclidean space, volume expands far more rapidly with increasing diameter than it expands in lower-dimensional spaces. Indeed, if one compares the size of the unit ball with the unit cube as the dimension of the space increases, it turns out that the unit ball becomes an insignificant volume relative to that of the unit cube. Thus, in some sense, nearly all of the high-dimensional space is “far away” from the center. This is called the “empty space phenomenon” [54, 55]: the high-dimensional unit space can be said to consist almost entirely of the “corners” of the hypercube, with almost no “middle”. One more important example of the unexpected properties of high-dimensional Euclidean spaces is the following behavior of the Gaussian distribution in high dimensions: the radius of a hypersphere that contains 95% of the distribution grows as the dimensionality increases.

These sorts of problems demonstrate that in order to make practical the extraction of meaningful structures

from multiparametric, high-dimensional data sets, a low-dimensional representation of data points is required. Dimension reduction (DR) is motivated by the fact that the more we are able to reduce the dimensionality of a data set, the more regularities (correlations) we have found in it and therefore, the more we have learned from the data. Data dimension reduction is an active branch of applied mathematics and statistics [50]. It consists of methods for finding lower-dimensional representation of high-dimensional data, without losing a significant amount of information, by constructing a set of basis functions that capture patterns intrinsic to a particular state space. DR methods greatly increase computational efficiency of machine learning algorithms, improve statistical inference and enables effective scientific visualization and classification. From a large set of images obtained at multiple wavebands, effective dimension reduction provides a comprehensible, information-rich single image with minimal information loss and statistical details, unlike a simple coadding with arbitrary, empirical weights (see a simple four-wavelength example in Figures 6 and 7).

Classical approaches to dimension reduction not unfamiliar to astronomy are principal components analysis (PCA) [56] and multidimensional scaling [57]. Although first applied to astronomy by Bijaoui [56] in 1974, PCA was not commonly used until the 1990’s [58, 59]; see also a general introduction to PCA in [60]. It has been used for such things as classification of galaxies and quasars [59, 61], photometric and spectroscopic redshift estimation (e.g., [62, 63], sky subtraction [64] and optical spectral indicators [65]. PCA has been used for the simultaneous analysis of dozens of data parameters for each member of a sample of 44 active galactic nuclei [66], which appears to be the largest number of parameters yet analyzed using PCA in an astronomical study.

PCA has a serious drawback in that it does not explicitly consider the structure of the manifold on which the data may possibly reside. In differential geometry an n -dimensional manifold is a metric space that on a small scale resembles the n -dimensional Euclidean space; thus a circle is a one-dimensional manifold, while a sphere is a two-dimensional manifold. PCA is intrinsically linear, so if data points form a nonlinear manifold, then obviously, there is no rotation & shift of the axis (this is what a linear transform like PCA provides) that can “unfold” such manifold. In other words, if the data are mainly confined to an almost linear low-dimensional subspace, then simple linear methods such as PCA can be used to discover the subspace and estimate its dimensionality. If, on the other hand, the data lie on (or near) a highly nonlinear low-dimensional submanifold, then linear methods are not effective in capturing the fine meaningful structures in the data. A blind application of linear methods may result in a complete misrepresentation of the data.

We have recently developed some advanced, original methods for performing nonlinear DR, which do not suffer from the limitations of PCA. In what follows, we briefly describe these methods. First, we introduce some more concepts and methods that have proved to be effective in the area of machine learning.

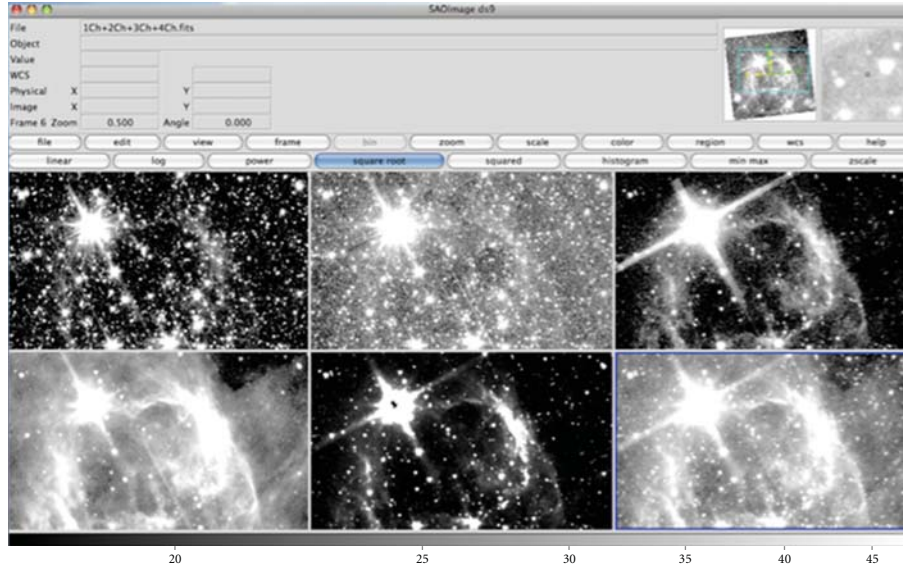


FIGURE 6: *Spitzer* IRAC camera $8.0\ \mu\text{m}$ image, 1–4 channels. Upper row: channels 1–3. Lower row: channel 4; the result of applying dimension reduction; sum of the channels 1–4.

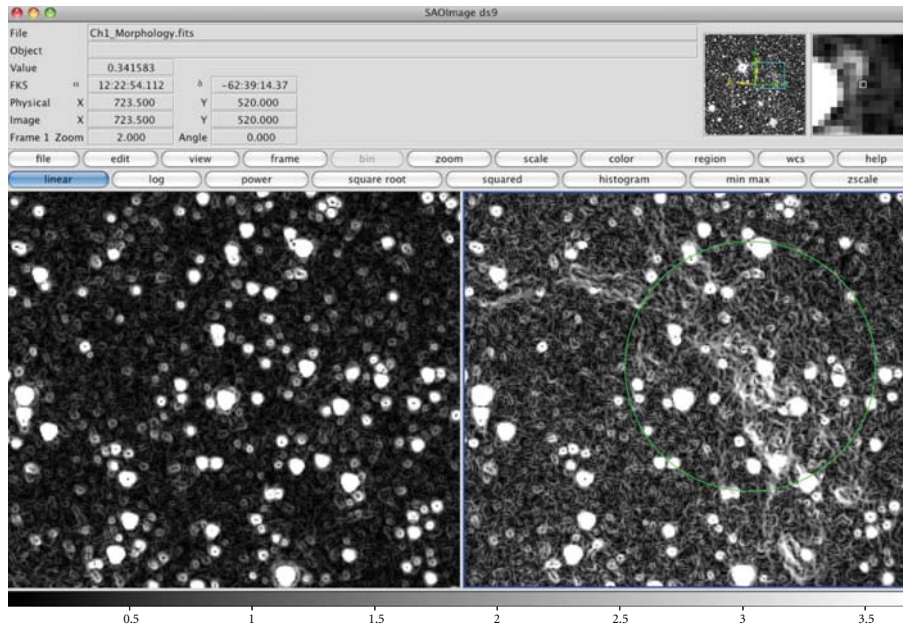


FIGURE 7: *Spitzer* IRAC camera $8.0\ \mu\text{m}$ image, Left: channel 1, morphology unveiling following [28]. Right: morphology unveiling performed on the reduced image from Figure 6. It demonstrates that dimensionality reduction retains the important features from all channels. This is especially useful for dealing with large numbers of images.

4.1. Graphs. In the context of data retrieval and processing, dimensionality reduction methods based on *graph theory* have proved to be very powerful. In mathematics and computer science, graph theory is the study of mathematical structures to model relations between objects [67]. Graph theory has been successfully applied to a wide range of very different disciplines, from biology to social science, computing and physics. Among many applications, graphs and manifolds have been used to address mining databases, Internet search engines, computer graphics, computation reordering, image processing, and so forth. In what follows

we discuss various data structure and algorithms that we have already developed and are developing.

The graph representation of structured data provides a fruitful model for the relational data mining process. A graph is a collection of nodes and links between them; the nodes represent data points and the weights of the links or edges indicate the strength of relationships. A graph in which each graph edge is replaced by a directed graph edge is called a directed graph, or diagraph [67]. Diagraphs are used for context-sensitive browsing engines and for ranking hyper-linked documents for a given query.

The modern approach to multidimensional images or data sets is to approximate them by graphs or Riemannian manifolds. The first important, and very challenging, step is to convert such a data cloud to a weighted finite graph. The next important problem is the choice of “right” weights that should be assigned to edges of the constructed graph. The weight function describes a notion of “similarity” between the data points and as such strongly affects the analysis of the data. The weights should entirely be determined by application domain. The most obvious way to assign weights is to use a positive kernel like an exponential function whose exponent depends on the local Euclidean distance between data points and a subjectively chosen parameter called “bandwidth”. (There are also other ways of assigning weights, which depend on more complex mathematics than we discuss in this article.)

Next, after constructing a weighted graph, one can introduce the corresponding combinatorial Laplace operator [67, 68]. In machine learning, methods based on graph Laplacians have proved to be very powerful [50]. The eigenfunctions and eigenvalues of the Laplacian form a basis, thus allowing one to develop a harmonic or Fourier analysis on graphs. By further developing harmonic analysis on graphs and manifolds [69–81], we have devised innovative algorithms for data compression and nonlinear data dimension reduction. These results enable one to overcome PCA’s limitations for handling nonlinear data manifolds and also allow one to deal effectively with incomplete data (such as missing observations or partial sky coverage).

4.2. Hypergraphs. Most existing data mining and network analysis methods are limited to pairwise interactions. However, sets of astronomical objects usually exhibit multiple relationships, so restricting analysis to the dyadic (pairwise) relations leads to loss of important information and to missing discoveries. Triadic, tetradic or higher interactions offer great practical potential. This has led to the approach based on hypergraphs (e.g., [82]). Hypergraphs constitute an important extension of graphs that allow edges to connect more than two vertices simultaneously. Thus hypergraphs provide a more comprehensive description of feature relations and structures. Hypergraphs furnish a much more adequate approach to real world data sets and allow one to deal with clustering and classifications using higher order relations. It has been shown that, in general, there does not exist a graph model that correctly represents the cut properties of the corresponding hypergraph (Ihler et al. [83]). Thus new mathematical methods are required to take advantage of the richness of information available in hypergraphs. In order to provide means for analysis of databases with multiple relationships, we are currently developing extensions of the original methods described in the previous subsection.

4.3. Fractals. Data sets having fractional dimensions (“fractals”: Mäkelä [84]; Schroeder [85]; Faloutsos [86]) have been suggested to represent many phenomena in astronomy.

Examples include star formation on galactic scales [87], the stellar initial mass function [88], galaxy distributions in space [89, 90], cloud distributions in active galactic nuclei [91], the cosmic microwave background [92], thermonuclear flame velocities in Type Ia supernovae [93], and the mass spectrum of interstellar clouds [94]. Such data sets exhibit a dimensionality which is often much lower than the dimension of the Euclidean space they are embedded into. For example, the distribution of galaxies in the universe has dimension $D \sim 1.23$. The difference between the two dimensions occurs because the fractal dimensionality is intrinsic. The intrinsic dimension of a graph reflects the intrinsic dimension of the sampled manifold.

Obviously, an important first step in practical dimensionality reduction is a good estimate of the intrinsic dimension of the data. Otherwise, DR is no more than a risky guess since one does not know to what extent the dimensionality can be reduced. To enable analysis of astronomical data sets that exhibit a fractal nature, we are currently developing a practical concept of spectral dimensionality, as well as original algorithms for sampling, compression and embedding fractal data.

4.4. The Petascale Connection. The approaches described above dealt with compact manifolds and finite graphs. However, massive data sets are more adequately described by noncompact manifolds and infinite graphs. In order to deal with extremely large data sets we extended dimension reduction to *non-compact* manifolds and *infinite* graphs. We are also working on generalizing the Fourier analysis to *non-compact* Riemannian manifolds and *infinite* quantum and combinatorial graphs, directed graphs, hypergraphs and some fractals. Implementation of these algorithms, and incorporation of them into the framework described in Section 2, will enable a more adequate analysis of massive data sets.

4.5. Robustness of Dimension Reduction Algorithms with Respect to Noise. Despite the important and appealing properties of the above mentioned dimension reduction algorithms, both linear and nonlinear approaches are sensitive to noise, outliers, and missing measurements (bad pixels, missing data values). Because noise and data imperfections may change the local structure of a manifold, locality preservation means that existing algorithms are topologically unstable and not robust against noise and outliers [95].

This is obviously a serious drawback because astronomical data are always corrupted by noise. Budavári et al. [96] presented a robust version of PCA and applied it to astronomical spectra. Their approach addressed the issues of outliers, missing information, large number of dimensions and the vast amount of data by combining elements of robust statistics and recursive algorithms that provide improved eigensystem estimates step by step. However, as it was mentioned earlier, the PCA method is intrinsically linear and cannot be applied to data points residing on a nonlinear manifold.

Thus the practical usage of dimension reduction demands careful improvement of signal-to-noise ratio without smearing essential features. Implementing a nonlinear diffusion on weighted graphs (Section 2) enables us to apply dimension reduction to noisy data sets as well.

4.6. Image Segmentation, Unsupervised Learning and Information Visualization. In what follows we briefly describe a new, original unifying approach to segmentation of images in particular and pattern recognition and information visualization in general. Image segmentation (see Section 2) plays a principal role in the realization of automated computer processing, as a previous stage for the recognition of different image elements or objects.

Solutions to the manifold learning problem can be based on intuition derived from physics. A good example of this is the approach of Horn and Gottlieb [97] that is based on the Schrödinger operator, where they constructed an approximate eigenfunction, and computed its corresponding potential. The clusters were then defined by the minima of the potential.

We developed [98] an alternative that is also based on physical intuition, this one being derived from synchronization of nonlinear oscillations [99, 100]. Approximating a multidimensional image or a data set by a graph and associating a nonlinear dynamical system with each node enables us to unify the three seemingly unrelated tasks: image segmentation, unsupervised learning and data visualization. Pattern recognition may benefit significantly from new methods of visualization and representation of data, since they may uncover important relationships in multidimensional data sets. Bringing out patterns by setting data points into oscillatory motion is a very effective way of visualizing data [101]. Our method is a feature-based, multilevel algorithm that finds patterns by employing a nonlinear oscillatory motion. At the same time, the oscillatory motion reveals to the eye patterns by making them oscillate coherently with a frequency different from the rest of the graph. Patterns are detected recursively inside the graph, and the found features are either collapsed into single nodes, forming a hierarchy of patterns or can be zoomed in and studied individually. This method can be described as a precomputed animation and it enables both qualitative (by eye) and quantitative discovery of correlations (see Figure 8).

The approaches presented in this section enable interpolation, smoothing and immersions of various complex (dozens or hundreds of useful parameters associated with each astronomical object) and large data sets into lower-dimension Euclidean spaces. Classification in lower dimensional space can be done more reliably than in high dimensions. Thus, DR can be significantly beneficial as a pre-processing step for many existing astronomical packages, such as for example, the popular source extractor SExtractor [102]. Incorporating into our framework (Section 2) the graph/manifold-based tools described in this section, will allow to address multiple pattern recognition (clustering) tasks as well as visualization of multidimensional data. Altogether, these approaches provide important generalizations

of the tools for spectral clustering and dimensionality reduction, and enable more adequate representation, effective data retrieval and analysis of complex, modern astronomical data sets.

5. Some Recent Approaches to the Challenges of Data Intensive Astronomy

Data intensive astrophysics requires an interdisciplinary approach that will include elements of applied mathematics [67, 103], modern statistical methods [104, 105], machine learning [50], computer vision [31] and image processing [30]. The breadth and complexity of the work relevant to modern astronomical data challenges is large, and does not permit a full treatment here. However, it is valuable to briefly mention a number of important problems, approaches and efforts that have been pursued.

The problem of processing data that lay on a manifold is very important for cosmological data analysis. The standard, powerful data analysis package HealPix [106] processes data on a two-dimensional manifold—the sphere. The concept of needlets (second generation spherical wavelets) has recently attracted a lot of attention in the cosmological literature. The first application of needlets to cosmological data was provided by Pietrobon et al. [107]. They analyzed cross-correlation of Wilkinson Microwave Anisotropy Probe (WMAP) CMB data with NRAO VLA Sky Survey (NVSS) radio galaxy data. The approach based on needlets enabled more accurate statistical results related to the dark energy component. The investigation of needlets from the probabilistic viewpoint and their relevance for the statistical analysis of random fields on the sphere was done for the first time by Baldi et al. [108]. A thorough presentation of the spherical needlets for CMB data analysis is given by Marinucci et al. [109]. Various issues related to CMB, such as spectrum estimation, detection of features and anisotropies, mapmaking were addressed by Faÿ et al. [110], Pietrobon et al. [111] (see also references there). The CMB models are best analyzed in the frequency domain, where the behavior at different multipoles can be investigated separately; on the other hand, such problems as missing observations or partial sky coverage make impossible the evaluation of spherical harmonic transforms. The needlets allow for a very efficient simple reconstruction formula that enables one to perform frequency analysis by using only partial information about data and providing means for handling masked data. Besides, needlets exemplify other important properties that are not generally shared by other spherical wavelet constructions: they do not rely on any kind of tangent plane approximation; they have good localization properties in both pixel and harmonic space; and needlet coefficients are asymptotically uncorrelated at any fixed angular distance (which makes their use in statistical procedures very promising). All these unique properties make needlets a very valuable tool in various areas of CMB data analysis. Recently, Geller and Marinucci [112] introduced spin needlets as a tool for the analysis of spin random fields. Geller et al. [113] adopted the spin needlet approach for the analysis of CMB polarization

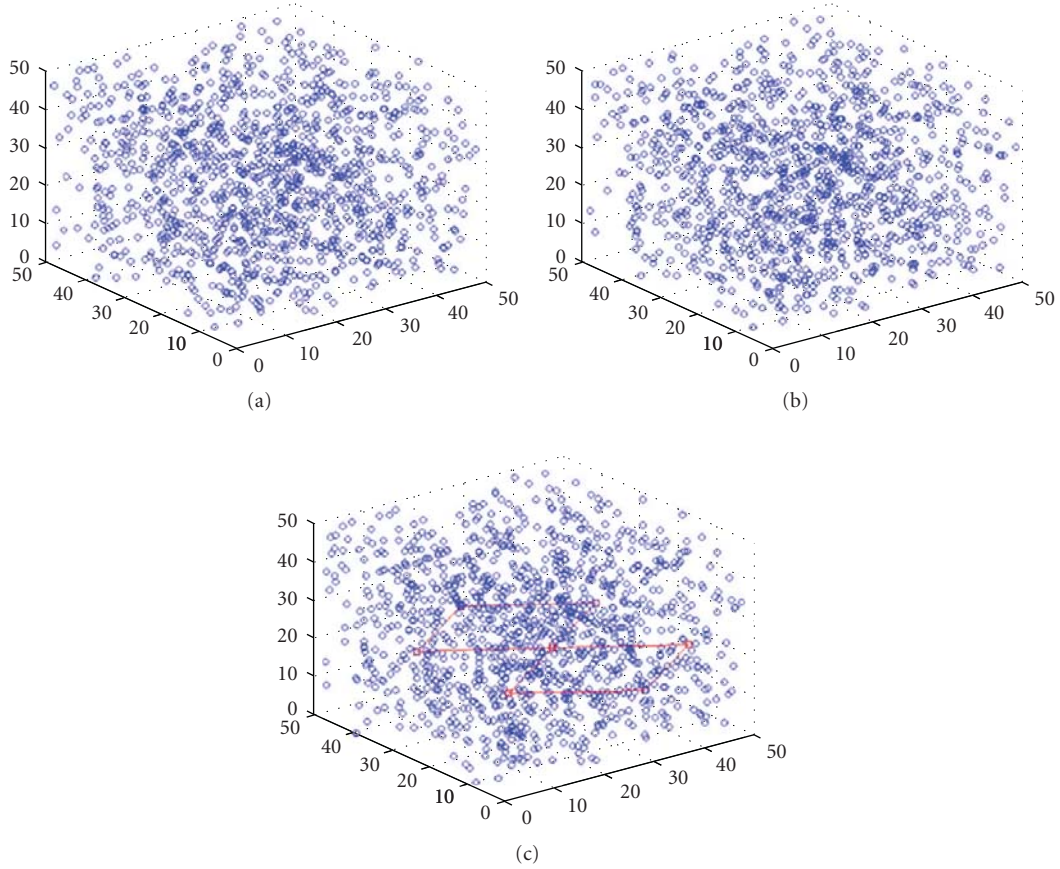


FIGURE 8: Testing the algorithm on synthetic data. A simulated three-dimensional set of a thousand uniformly distributed random points with a double-diamond pattern created by assigning large weights to the edges connecting the points in the pattern (while the rest of the weights are negligible). (a) and (b): two screen shots from a running animation—each point in the set oscillates (in this case in three dimensions) with its own, random frequency. (c) Synchronization of the points that are connected with high-weight edges allows to reveal the pattern visually (to avoid extra clutter, the edges are not displayed in the animation), or automatically, by selecting synchronized points and highlighting them.

measurements. Lately Geller and Mayeli [114] constructed continuous wavelets and nearly tight frames (needlets) on compact manifolds.

The essential part of the general analysis based on the wavelet-like constructions is sampling of bandlimited functions. The mathematical foundations of sampling on arbitrary Riemannian manifolds of bounded geometry were laid down by Pesenson [115, 116]. Recently Geller and Pesenson [117], constructed bandlimited and highly concentrated tight frames on compact homogeneous manifolds. These results can be considered as an extension of the wavelet-like transforms to Riemannian manifolds, thus enabling one to reconstruct information from incomplete data defined on an arbitrary manifold.

Multiscale data analysis has proved to be a very powerful tool in many fields. Applications of multiscale image analysis to astronomy were pioneered by Starck et al. [118] and Starck and Murtagh [119].

Spectral methods and diffusion maps have recently emerged as effective approaches to nonlinear dimensionality reduction [120–122]. The diffusion maps approach has

successfully been applied to analysis of astronomical spectra by Richards et al. [123].

Manifold learning may be seen as a DR procedure aiming at capturing the degrees of freedom and structures (clusters, patterns) within high-dimensional data. Manifold learning nonlinear algorithms such as isometric mapping (ISOMAP) by Tenenbaum et al. [124] and local linear embedding (LLE) by Roweis and Saul [125] project high-dimensional manifold data into a low-dimensional space by preserving the local geometric features. Ball and Brunner [51] provide a very broad review of the current state of machine learning and data mining in astronomy.

The AstroNeural collaboration group [52] implemented tools based on neural networks, fuzzy-C sets and genetic algorithms, and applied them to perform complex tasks such as unsupervised and supervised clustering and time series analysis. D’Abrusco et al. [126] present a supervised neural network approach to the determination of photometric redshifts. D’Abrusco et al. [127] describe a method for the photometric selection of candidate quasars in multiband surveys based on the probabilistic principal surfaces. Pasian

TABLE 1: Examples of complex data types and some of the methods for their representation and processing.

Data Types	Some Astronomical Applications	Traditional Approaches to Data Representation & Processing	Advanced Approaches to Data Representation & Processing
Vector Data	(1) Multiwavelength observations.	(1) Linear dimension reduction: PCA and its modifications.	(1) Spectral methods, eigenmaps, diffusion maps, LLE, ISOMAP.
	(2) Multitemporal observations.		(2) Sampling on graphs.
	(3) VO.		(3) Methods based on nonlinear dynamics.
	(4) Spectra.		(4) Neural networks, fuzzy-C sets. (5) Genetic algorithms. (6) Scientific visualization. (7) Compressed sensing.
Manifold-Valued and/or Manifold-Defined	(1) Polarization measurements (CMB).	(1) Various sampling distributions on the sphere.	(1) Healpix (data on 2D sphere).
	(2) Gravitational lensing.		(2) Needlets.
	(3) Solar astrophysics.		(3) Sampling on manifolds.
			(4) Scientific visualization.

et al. [128] give a general review of the development of tools to be subsequently used within the international VO.

Comparato et al. [129] show how advanced visualization tools can help the researcher in investigating and extracting information from data. Their focus is on VisIVO, a new open-source graphics application that blends high performance multidimensional visualization techniques and up-to-date technologies to cooperate with other applications and to access remote, distributed data archives.

Draper et al. [130] discuss the GAIA application for analyzing astronomical image and show how the PLASTIC protocol has been used to inter-operate with VO enabled applications.

The Center for Astrostatistics (CASt) at Pennsylvania State University provides a wealth of resources (codes, data, tutorials, programs, etc.) related to challenges in statistical treatments of astrophysical data: <http://astrostatistics.psu.edu/>.

A large amount of practical and up-to-date information (texts, tutorials, preprints, software, etc.) related to Bayesian inference in astronomy and other fields is provided by T. Loredo on the website Bayesian Inference for the Physical Sciences (BIPS) at <http://www.astro.cornell.edu/staff/loredo/bayes/index.html>.

The International Computational Astrostatistics (InCA) Group at Carnegie Mellon University develops and applies new statistical methods to inference problems in astronomy and cosmology, with an emphasis on computational non-parametric approaches (see for details <http://www.stat.cmu.edu/~inca/index.html>).

The AstroMed project at Harvard University's IIC is dedicated to the application of medical image visualization to 3D astronomical data [131].

Compressed sensing and the use of sparse representations offer another promising new approach. Traditionally it has been considered unavoidable that any signal must be sampled at a rate of at least twice its highest frequency in

order to be represented without errors. However, a technique called compressed sensing that permits error-free sampling at a lower rate has been the subject of much recent research. It has great promise for new ways to compress imaging without significant loss of information, thus ameliorating analysis limitations deriving from limitations of computing resources. The power of compressed sensing was strikingly illustrated when an object was successfully imaged in some detail by a camera composed of a *single pixel* [132]. Bobin et al. [133] discuss recent advances in signal processing that use sparse representations. Relatively nontechnical introductions to compressed sensing may be found in Candes and Wakin [134] and Romberg [135]. The first astronomical results in the literature based on the use of compressed sensing are that of Wiaux et al. [136].

Various data types together with methods used for their representation are briefly summarized in Table 1. The table is not comprehensive, but it provides a quick overview of what was discussed above.

6. Conclusion

Extremely large data sets, as well as the analysis of hundreds of objects each having a large number of data dimensions, present astronomy with unprecedented challenges. The challenges are not only about database sizes in themselves, but about how intelligently one organizes, analyzes, and navigates through the databases, and about the limitations of existing data analysis approaches familiar to astronomy. The answers to these challenges are not trivial, and for the most part lie in complex fields of research well outside the training and expertise of almost all astronomers. Fortunately, other disciplines such as imaging science and earth sciences have for many years been grappling with the same sorts of problems. Fruitful interdisciplinary work has already become a regular feature of research in those other disciplines, and has resulted in applications of crucial value to other sciences

seeking to take advantage of complex, giant data sets in their respective fields. This work has brought about many helpful applications and promising paths for further progress that potentially have significant value to astronomy.

Multidimensional image processing, image fusion (combining information from multiple sensors in order to create a composite enhanced image) and dimension reduction (finding lower-dimensional representation of high-dimensional data) are effective approaches to tasks that are crucial to multi-temporal, multiwavelength astronomy: study of transients, large-scale digital sky surveys, archival research, and so forth. These methods greatly increase computational efficiency of machine learning algorithms and improve statistical inference, thus facilitating automated feature selection, data segmentation, classification and effective scientific visualization (as opposed to illustrative visualization). Dimensionally reduced images also offer an enormous savings in storage space and database-transmission bandwidth for the user, without significant loss of information, if appropriate methods are used.

To effectively use the large, complex data sets being created in 21st Century astronomy, significant interdisciplinary communication and collaboration between astronomers and experts in the disciplines of applied mathematics, statistics, computer science and artificial intelligence will be essential. The concepts and approaches described in this paper are among the first steps in such a broad, long-term interdisciplinary effort that will help bridge the communication gap between astronomy and other disciplines. These concepts, and the approaches derived from them, will help to provide practical ways of analysis and visualization of the increasingly large and complex data sets. Such sophisticated new methods will also help to pave the way for effective automated analysis and processing of giant, complex data sets.

Acknowledgments

The authors would like to thank Alanna Connors for stimulating discussions and useful suggestions. They would also like to thank the referee for constructive suggestions that led to substantial improvements of the article. The first author would like to thank Michael Werner for support. This work was carried out with funding from the National Geospatial-Intelligence Agency University Research Initiative (NURI), Grant HM1582-08-1-0019, and support from NASA to the California Institute of Technology and the Jet Propulsion Laboratory.

References

- [1] D. York, J. Adelman, J. Anderson, et al., "The Sloan digital sky survey: technical summary," *Astronomical Journal*, vol. 120, pp. 1579–1587, 2000.
- [2] J. Tyson, C. Roat, J. Bosch, and D. Wittman, "LSST and the dark sector: image processing challenges," in *Proceedings of the 17th Annual Conference on Astronomical Data Analysis Software and Systems (ADASS '08)*, J. Lewis, R. Argyle, P. Bunclark, et al., Eds., vol. 394 of *ASP Conference Series*, ASP, London, UK, 2008.
- [3] A. S. Szalay, J. Gray, and J. Van den Berg, "Petabyte scale data mining: dream or reality?" in *Survey and Other Telescope Technologies and Discoveries*, vol. 4836 of *Proceedings of SPIE*, pp. 333–338, 2002.
- [4] M. A. C. Perryman, "GAIA: an astrometric and photometric survey of our galaxy," *Astrophysics and Space Science*, vol. 280, no. 1–2, pp. 1–10, 2002.
- [5] K. W. Hodapp, N. Kaiser, H. Aussel, et al., "Design of the Pan-STARRS telescopes," *Astronomische Nachrichten*, vol. 325, no. 6–8, pp. 636–642, 2004.
- [6] P. Price, E. Magnier, and J. Hobbitt, "Processing petabytes for Pan-STARRS, AAS Meeting 210," *Bulletin of the American Astronomical Society*, vol. 38, p. 183, 2007.
- [7] N. M. Law, S. R. Kulkarni, R. G. Dekany, et al., "The palomar transient factory: system overview, performance, and first results," *Publications of the Astronomical Society of the Pacific*, vol. 121, no. 886, pp. 1395–1408, 2009.
- [8] G. Zhao, Y. Q. Chen, J.-R. Shi, et al., "Stellar abundance and Galactic chemical evolution through LAMOST spectroscopic survey," *Chinese Journal of Astronomy and Astrophysics*, vol. 6, no. 3, pp. 265–280, 2006.
- [9] S. G. Djorgovski, C. Baltay, A. A. Mahabal, et al., "The Palomar-Quest digital synoptic sky survey," *Astronomische Nachrichten*, vol. 329, no. 3, pp. 263–265, 2008.
- [10] S. C. Barden and T. Armandroff, "Performance of the WIYN fiber-fed MOS system: Hydra," in *Fiber Optics in Astronomical Applications*, S. Barden, Ed., vol. 2476 of *Proceedings of SPIE*, pp. 56–67, Orlando, Fla, USA, April 1995.
- [11] B. C. Bigelow, A. M. Dressler, S. A. Shectman, and H. W. Epps, "IMACS: the multi-object spectrograph and imager for the Magellan I telescope," in *Optical Astronomical Instrumentation*, S. D'Odorico, Ed., vol. 3355 of *Proceedings of SPIE*, pp. 225–231, 1998.
- [12] I. J. Lewis, R. D. Cannon, K. Taylor, et al., "The Anglo-Australian observatory 2dF facility," *Monthly Notices of the Royal Astronomical Society*, vol. 333, no. 2, pp. 279–298, 2002.
- [13] R. M. Sharples, R. Bender, M. Lehnert, et al., "KMOS: an infrared multiple object integral field spectrograph for the ESO VLT," in *Ground-Based Instrumentation for Astronomy*, A. F. M. Moorwood and I. Masanori, Eds., vol. 5492 of *Proceedings of SPIE*, pp. 1179–1186, 2004.
- [14] R. Mark Wagner, "An overview of instrumentation for the Large Binocular Telescope," in *Ground-Based and Airborne Instrumentation for Astronomy*, I. S. McLean and I. Masanori, Eds., vol. 6269 of *Proceedings of SPIE*, 2006.
- [15] K. Freeman and J. Bland-Hawthorne, "Panoramic high resolution spectroscopy," in *Proceedings of the Panoramic Views of Galaxy Formation and Evolution*, T. Kodama, T. Yamada, and K. Aoki, Eds., vol. 399 of *ASP Conference Series*, p. 439, 2008.
- [16] S. Eto, T. Maihara, K. Ohta, et al., "The fiber multi-object spectrograph (FMOS) for the Subaru Telescope III," in *Ground-Based Instrumentation for Astronomy*, A. F. M. Moorwood and I. Masanori, Eds., vol. 5492 of *Proceedings of SPIE*, pp. 1314–1318, 2004.
- [17] S. C. Barden, A. Dey, B. Boyle, and K. Glazebrook, "KAOS: kilo-aperture optical spectrograph," in *Ground-Based Instrumentation for Astronomy*, A. F. M. Moorwood and I. Masanori, Eds., vol. 5492 of *Proceedings of SPIE*, pp. 364–372, Glasgow, UK, June 2004.
- [18] T. D. Ditto and J. M. Ritter, "Million object spectrograph," in *Advanced Optical and Mechanical Technologies in Telescopes*

- and *Instrumentation*, E. Atad-Etchedgui and D. Lemke, Eds., vol. 7018 of *Proceedings of SPIE*, pp. 70182R.1–70182R.12, 2008.
- [19] M. Zaldarriaga and U. Seljak, “All-sky analysis of polarization in the microwave background,” *Physical Review D*, vol. 55, no. 4, pp. 1830–1840, 1997.
 - [20] R. Frazin, M. Jacob, W. Manchester, H. Morgan, and M. Wakin, “Toward reconstruction of coronal mass ejection density from only three points of view,” *Astrophysical Journal*, vol. 695, no. 1, pp. 636–641, 2009.
 - [21] M. Tegmark and M. Zaldarriaga, “Fast Fourier transform telescope,” *Physical Review D*, vol. 79, no. 8, Article ID 083530, 2009.
 - [22] T. Loredó, A. Accomazzi, J. Bloom, et al., “The astronomical information sciences: a keystone for 21st-century astronomy,” submitted to the *The Astronomy and Astrophysics Decadal Survey*.
 - [23] K. Borne, “Scientific data mining in astronomy,” in *Next Generation of Data Mining*, H. Kargupta, J. Han, P. S. Yu, R. Motwani, and V. Kumar, Eds., pp. 91–114, CRC Press, 2009.
 - [24] H. Ferguson, P. Greenfield, T. Axelrod, et al., “Astronomical data reduction and analysis for the next decade,” submitted to the *The Astronomy and Astrophysics Decadal Survey*.
 - [25] M. Grand, *Patterns in Java v.1*, Addison-Wesley, New York, NY, USA, 1998.
 - [26] G. Booch, J. Rumbaugh, and I. Jacobson, *The Unified Modeling Language User Guide*, Addison-Wesley, Reading, Mass, USA, 2005.
 - [27] M. Fayad, R. Johnson, and D. Schmidt, *Building Application Frameworks: Object Oriented Foundations of Framework Design*, John Wiley & Sons, New York, NY, USA, 1999.
 - [28] M. Pesenson, W. Roby, and B. McCollum, “Multiscale astronomical image processing based on nonlinear partial differential equations,” *Astrophysical Journal*, vol. 683, no. 1, pp. 566–576, 2008.
 - [29] K. France, S. McCandliss, and R. Lupu, “A Cometary Bow Shock and Mid-Infrared Emission Variations Revealed in *Spitzer* Observations of HD 34078 and IC 405,” *The Astrophysical Journal*, vol. 655, no. 2, pp. 920–939, 2007.
 - [30] A. Bovik, Ed., *Handbook of Image and Video Processing*, Elsevier, Amsterdam, The Netherlands, 2005.
 - [31] N. Paragios, Y. Chen, and O. Faugeras, *Handbook of Mathematical Models in Computer Vision*, Springer, Berlin, Germany, 2006.
 - [32] G. Herbig, “The spectra of Be- and Ae-TYPE stars associated with nebulosity,” *Astrophysical Journal Supplement*, vol. 4, p. 337, 1960.
 - [33] E. D. Feigelson and T. Montmerle, “High-energy processes in young stellar objects,” *Annual Review of Astronomy and Astrophysics*, vol. 37, no. 1, pp. 363–408, 1999.
 - [34] D. H. Clark and P. Murdin, “An unusual emission-line star/X-ray source/radio star, possibly associated with an SNR,” *Nature*, vol. 276, no. 5683, pp. 44–45, 1978.
 - [35] P. Feldman, C. Purton, T. Stiff, and S. Kwok, “H-alpha-Emission Object SS 433,” *IAU Circulars*, no. 3258, 1978.
 - [36] B. Margon, H. Ford, J. Katz, et al., “The bizarre spectrum of SS 433,” *Astrophysical Journal*, vol. 230, pp. L41–L45, 1979.
 - [37] B. A. Whitney, M. Sewilo, R. Indebetouw, et al., “*Spitzer* sage survey of the large magellanic cloud. III. Star formation and 1000 new candidate young stellar objects,” *The Astronomical Journal*, vol. 136, no. 1, pp. 18–43, 2008.
 - [38] W. van der Veen, H. Habing, and T. Geballe, “Objects in transition from the AGB to the planetary Nebula stage,” *Astronomy & Astrophysics*, vol. 226, pp. 108–136, 1989.
 - [39] W. van der Veen and H. Habing, “Far evolved AGB stars in the galactic bulge,” *Astronomy & Astrophysics*, vol. 231, no. 2, pp. 404–418, 1990.
 - [40] K. Finlator, Z. Ivezić, X. Fan, et al., “Optical and infrared colors of stars observed by the Two Micron All Sky Survey and the Sloan Digital Sky Survey,” *The Astronomical Journal*, vol. 120, no. 5, pp. 2615–2626, 2000.
 - [41] M. P. Egan, S. D. Van Dyk, and S. D. Price, “MSX, 2Mass, and the large magellanic cloud: a combined near- and mid-infrared view,” *The Astronomical Journal*, vol. 122, no. 4, pp. 1844–1860, 2001.
 - [42] R. Ortiz, S. Lorenz-Martins, W. J. Maciel, and E. M. Rangel, “Evolution from AGB to planetary nebula in the MSX survey,” *Astronomy & Astrophysics*, vol. 431, no. 2, pp. 565–574, 2005.
 - [43] S. V. Ramirez, R. G. Arendt, K. Sellgren, et al., “Point sources from a *Spitzer* IRAC survey of the galactic center,” *Astrophysical Journal*, vol. 175, no. 1, pp. 147–164, 2008.
 - [44] U. Munari, A. Henden, S. Kiyota, et al., “The mysterious eruption of V838 Mon,” *Astronomy & Astrophysics*, vol. 389, no. 2, pp. L51–L56, 2002.
 - [45] H. E. Bond, A. Henden, Z. G. Levay, et al., “An energetic stellar outburst accompanied by circumstellar light echoes,” *Nature*, vol. 422, no. 6930, pp. 405–408, 2003.
 - [46] J. A. Combi, J. F. Albacete-Colombo, and J. Martí, “A new search strategy for microquasar candidates using NVSS/2MASS and XMM-Newton data,” *Astronomy & Astrophysics*, vol. 477, no. 1, pp. 125–132, 2008.
 - [47] P. Brosche, “The manifold of galaxies. Galaxies with known dynamical parameters,” *Astronomy & Astrophysics*, vol. 23, pp. 259–268, 1973.
 - [48] S. Djorgovski and M. Davis, “Fundamental properties of elliptical galaxies,” *Astrophysical Journal*, vol. 313, p. 59, 1987.
 - [49] S. Djorgovski, R. Brunner, A. Mahabal, R. Williams, R. Granat, and P. Stolorz, “Challenges for cluster analysis in a virtual observatory,” in *Statistical Challenges in Astronomy*, E. Feigelson and G. Babu, Eds., pp. 127–141, Springer, Berlin, Germany, 2003.
 - [50] S. Haykin, *Neural Networks and Learning Machines*, Prentice Hall, Upper Saddle River, NJ, USA, 2009.
 - [51] N. Ball and R. Brunner, “Data mining and machine learning in astronomy,” *International Journal of Modern Physics D*, vol. 18, no. 17, pp. 1–53, 2009.
 - [52] G. Longo, C. Donalek, and G. Raiconi, “Artificial intelligence tools for data mining in large astronomical databases,” in *Globular Clusters-Guides to Galaxies*, p. 1431, Springer, Berlin, Germany, 2004.
 - [53] R. Bellman, *Adaptive Control Processes*, Princeton University Press, Princeton, NJ, USA, 1961.
 - [54] D. Scott, *Multivariate Density Estimation: Theory, Practice and Visualization*, Wiley Series in Probability and Mathematical Statistics, John Wiley & Sons, New York, NY, USA, 1992.
 - [55] J. Matousek, *Lectures on Discrete Geometry*, Springer, New York, NY, USA, 2002.
 - [56] A. Bijaoui, “Astronomical application of information compression,” *Astronomy & Astrophysics*, vol. 30, p. 199, 1974.
 - [57] I. Borg and P. Groenen, *Modern Multidimensional Scaling: Theory and Applications*, Springer, New York, NY, USA, 2005.

- [58] T. A. Boroson and R. F. Green, "The emission-line properties of low-redshift quasi-stellar objects," *Astrophysical Journal*, vol. 80, no. 1, pp. 109–135, 1992.
- [59] P. J. Francis, P. C. Hewett, C. B. Foltz, and F. H. Chaffee, "An objective classification scheme for QSO spectra," *Astrophysical Journal*, vol. 398, no. 2, pp. 476–490, 1992.
- [60] P. Francis and B. Wills, "An introduction to PCA," in *Quasars and Cosmology*, G. Ferland and J. Baldwin, Eds., vol. 162 of *ASP Conference Series*, p. 363, ASP, San Francisco, Calif, USA, 1999.
- [61] A. J. Connolly, I. Csabai, A. S. Szalay, D. C. Koo, R. G. Kron, and J. A. Munn, "Slicing through multicolor space: galaxy redshifts from broadband photometry," *The Astronomical Journal*, vol. 110, no. 6, pp. 2655–2664, 1995.
- [62] K. Glazebrook, A. R. Offer, and K. Deeley, "Automatic redshift determination by use of principal component analysis. I. Fundamentals," *Astrophysical Journal*, vol. 492, no. 1, pp. 98–109, 1998.
- [63] C. W. Yip, A. J. Connolly, D. E. Vanden Berk, et al., "Spectral classification of quasars in the sloan digital sky survey: eigenspectra, redshift, and luminosity effects," *The Astronomical Journal*, vol. 128, no. 6, pp. 2603–2630, 2004.
- [64] V. Wild and P. C. Hewett, "Peering through the OH forest: a new technique to remove residual sky features from sloan digital sky survey spectra," *Monthly Notices of the Royal Astronomical Society*, vol. 358, no. 3, pp. 1083–1099, 2005.
- [65] V. Wild, G. Kauffmann, T. Heckman, et al., "Bursty stellar populations and obscured active galactic nuclei in galaxy bulges," *Monthly Notices of the Royal Astronomical Society*, vol. 381, no. 2, pp. 543–572, 2007.
- [66] J. Kuraszkiewicz, B. Wilkes, G. Schmidt, and P. Smith, "Principal component analysis of the spectral energy distribution and emission line properties of red 2Mass active galactic nuclei," *Astrophysical Journal*, vol. 692, no. 2, pp. 1180–1189, 2009.
- [67] J. Gross and J. Yellen, Eds., *Handbook of Graph Theory*, CRC Press, Boca Raton, Fla, USA, 2004.
- [68] F. Chung, "Spectral graph theory," in *Conference Board of the Mathematical Sciences*, American Mathematical Society, Providence, RI, USA, 1997.
- [69] I. Pesenson, "Poincaré-type inequalities and reconstruction of Paley-Wiener functions on manifolds," *Journal of Geometric Analysis*, vol. 14, no. 1, pp. 101–121, 2004.
- [70] I. Pesenson, "An approach to spectral problems on Riemannian manifolds," *Pacific Journal of Mathematics*, vol. 215, no. 1, pp. 183–199, 2004.
- [71] I. Pesenson, "Variational splines on Riemannian manifolds with applications to integral geometry," *Advances in Applied Mathematics*, vol. 33, no. 3, pp. 548–572, 2004.
- [72] I. Pesenson, "Band limited functions on quantum graphs," *Proceedings of the American Mathematical Society*, vol. 133, no. 12, pp. 3647–3655, 2005.
- [73] I. Pesenson, "Polynomial splines and eigenvalue approximations on quantum graphs," *Journal of Approximation Theory*, vol. 135, no. 2, pp. 203–220, 2005.
- [74] I. Pesenson, "Analysis of band-limited functions on quantum graphs," *Applied and Computational Harmonic Analysis*, vol. 21, no. 2, pp. 230–244, 2006.
- [75] I. Pesenson, "Frames for spaces of Paley-Wiener functions on Riemannian manifolds, integral geometry and tomography," in *Contemporary Mathematics*, vol. 405, pp. 135–148, American Mathematical Society, Providence, RI, USA, 2006.
- [76] I. Pesenson, "Sampling in Paley-Wiener spaces on combinatorial graphs," *Transactions of the American Mathematical Society*, vol. 360, no. 10, pp. 5603–5627, 2008.
- [77] I. Pesenson, "Variational splines and Paley-Wiener spaces on combinatorial graphs," *Constructive Approximation*, vol. 29, no. 1, pp. 1–21, 2009.
- [78] I. Pesenson, "Paley-Wiener approximations and multiscale approximations in Sobolev and Besov spaces on manifolds," *Journal of Geometric Analysis*, vol. 19, no. 2, pp. 390–419, 2009.
- [79] I. Pesenson and M. Pesenson, "Sampling of bandlimited functions on combinatorial graphs," in *Proceedings of the 8th International Conference on Sampling Theory and Applications*, Marseille, France, 2009.
- [80] M. Pesenson, I. Pesenson, and B. McCollum, "Facing 'the Curse of Dimensionality': image fusion and nonlinear dimensionality reduction for advanced data mining and visualization of astronomical images," in *Proceedings of the 214th AAS Meeting*, 2009.
- [81] I. Pesenson and M. Pesenson, "Eigenmaps, minimal and bandlimited immersions of graphs into Euclidean spaces," *Journal of Mathematical Analysis and Applications*, vol. 366, no. 1, pp. 137–152, 2010.
- [82] D. Zhou, J. Huang, and B. Scholkopf, "Beyond pairwise classification and clustering using hypergraphs," Tech. Rep. 143, Max Planck Institute for Biological Cybernetics, Tübingen, Germany, 2005.
- [83] E. Ihler, D. Wagner, and F. Wagner, "Modeling hypergraphs by graphs with the same min cut properties," *Information Processing Letters*, vol. 45, no. 4, pp. 171–175, 1993.
- [84] B. Mabelbrot, *Fractal Geometry of Nature*, W.H. Freeman, New York, NY, USA, 1977.
- [85] M. Schroeder, *Fractals, Chaos, Power Laws*, W. H. Freeman, New York, NY, USA, 1991.
- [86] C. Faloutsos, "Next generation data mining tools: power laws and self-similarity for graphs, streams and traditional data," in *Proceedings of the 7th European Conference on Principles and Practice of Knowledge Discovery in Databases*, vol. 2838 of *Lecture Notes in Artificial Intelligence*, pp. 10–15, 2003.
- [87] B. G. Elmegreen and D. M. Elmegreen, "Fractal structure in galactic star fields," *The Astronomical Journal*, vol. 121, no. 3, pp. 1507–1511, 2001.
- [88] R. Larson, "Towards understanding the stellar initial mass function," *Monthly Notices of the Royal Astronomical Society*, vol. 256, no. 4, pp. 641–646, 1992.
- [89] J. Einasto, M. Einasto, M. Gramann, and E. Saar, "Structure and formation of superclusters. XIII—the void probability function," *Monthly Notices of the Royal Astronomical Society*, vol. 248, p. 593, 1991.
- [90] T. Kurokawa, M. Morikawa, and H. Mouri, "Scaling analysis of galaxy distribution in the Las Campanas Redshift Survey data," *Astronomy & Astrophysics*, vol. 370, no. 2, pp. 358–364, 2001.
- [91] M. Bottorff and G. Ferland, "Fractal quasar clouds," *Astrophysical Journal*, vol. 549, no. 1, pp. 118–132, 2001.
- [92] E. M. de Gouveia dal Pino, M. Elisabete, A. Hetem, et al., "Evidence for a very large scale fractal structure in the universe from COBE measurements," *Astrophysical Journal*, vol. 442, no. 2, pp. L45–L48, 1995.
- [93] C. R. Ghezzi, E. M. de Gouveia dal Pino, and J. E. Horvath, "Asymmetric explosions of thermonuclear supernovae," *Monthly Notices of the Royal Astronomical Society*, vol. 348, no. 2, pp. 451–457, 2004.

- [94] B. G. Elmegreen and E. Falgarone, "A fractal origin for the mass spectrum of interstellar clouds," *Astrophysical Journal*, vol. 471, no. 2, pp. 816–821, 1996.
- [95] M. Balasubramanian and E. L. Schwartz, "The isomap algorithm and topological stability," *Science*, vol. 295, no. 5552, p. 7a, 2002.
- [96] T. Budavári, V. Wild, A. S. Szalay, L. Dobos, and C.-W. Yip, "Reliable eigenspectra for new generation surveys," *Monthly Notices of the Royal Astronomical Society*, vol. 394, no. 3, pp. 1496–1502, 2009.
- [97] D. Horn and A. Gottlieb, "Algorithm for data clustering in pattern recognition problems based on quantum mechanics," *Physical Review Letters*, vol. 88, no. 1, Article ID 018702, 4 pages, 2002.
- [98] M. Pesenson and I. Pesenson, "Image segmentation, unsupervised manifold learning and information visualization: a unified approach based on nonlinear dynamics," submitted.
- [99] Y. Kuramoto, *Chemical Oscillations, Waves and Turbulence*, Springer, Berlin, Germany, 1984.
- [100] A. Pikovsky, M. Rosenblum, and J. Kurths, *Synchronization*, Cambridge University Press, Cambridge, UK, 2001.
- [101] C. Ware and R. Bobrow, "Supporting visual queries on medium sized node-link diagrams," *ACM Transactions on Applied Perception*, vol. 1, pp. 3–18, 2004.
- [102] E. Bertin and S. Arnouts, "SExtractor: software for source extraction," *Astronomy & Astrophysics*, vol. 117, no. 2, pp. 393–404, 1996.
- [103] J. Goodman and J. O'Rourke, Eds., *Handbook of Discrete and Computational Geometry*, Discrete Mathematics and Its Applications, Chapman & Hall/CRC, 2004.
- [104] E. Feigelson and J. Babu, *Statistical Challenges in Astronomy*, Springer, Berlin, Germany, 2003.
- [105] J. Silk, "An astronomer's perspective on SCMA III," in *Statistical Challenges in Astronomy, III*, E. D. Feigelson and G. J. Babu, Eds., p. 387, Springer, New York, NY, USA, 2003.
- [106] M. Gorski, E. Hivon, A. J. Banday, et al., "HEALPix: a framework for high-resolution discretization and fast analysis of data distributed on the sphere," *Astrophysical Journal*, vol. 622, no. 2, pp. 759–771, 2005.
- [107] D. Pietrobon, A. Balbi, and D. Marinucci, "Integrated Sachs-Wolfe effect from the cross correlation of WMAP 3 year and the NRAO VLA sky survey data: New results and constraints on dark energy," *Physical Review D - Particles, Fields, Gravitation and Cosmology*, vol. 74, no. 4, Article ID 043524, 2006.
- [108] P. Baldi, G. Kerkycharian, D. Marinucci, and D. Picard, "High frequency asymptotics for wavelet-based tests for Gaussianity and isotropy on the torus," *Journal of Multivariate Analysis*, vol. 99, no. 4, pp. 606–636, 2008.
- [109] D. Marinucci, D. Pietrobon, A. Balbi, et al., "Spherical needlets for cosmic microwave background data analysis," *Monthly Notices of the Royal Astronomical Society*, vol. 383, no. 2, pp. 539–545, 2008.
- [110] G. Faÿ, F. Guillaoux, M. Betoule, J.-F. Cardoso, J. Delabrouille, and M. Le Jeune, "CMB power spectrum estimation using wavelets," *Physical Review D*, vol. 78, no. 8, Article ID 083013, 2008.
- [111] D. Pietrobon, A. Amblard, A. Balbi, P. Cabella, A. Cooray, and D. Marinucci, "Needlet detection of features in the WMAP CMB sky and the impact on anisotropies and hemispherical asymmetries," *Physical Review D*, vol. 78, no. 10, Article ID 103504, 2008.
- [112] D. Geller and D. Marinucci, "Spin wavelets on the sphere," <http://arxiv.org/abs/0811.2935>.
- [113] D. Geller, F. K. Hansen, D. Marinucci, G. Kerkycharian, and D. Picard, "Spin needlets for cosmic microwave background polarization data analysis," *Physical Review D*, vol. 78, no. 12, 2008.
- [114] D. Geller and A. Mayeli, "Continuous wavelets on compact manifolds," *Mathematische Zeitschrift*, vol. 262, no. 4, pp. 895–927, 2009.
- [115] I. Pesenson, "Lagrangian splines, spectral entire functions and Shannon-Whittaker theorem on manifolds," Temple University Research Report 95/87, 1995.
- [116] I. Pesenson, "A sampling theorem on homogeneous manifolds," *Transactions of the American Mathematical Society*, vol. 352, no. 9, pp. 4257–4269, 2000.
- [117] D. Geller and I. Pesenson, "Band-limited localized Parseval frames and Besov spaces on compact homogeneous manifolds," to appear in *Journal of Geometric Analysis*.
- [118] J.-L. Starck, F. Murtagh, and A. Bijaoui, *Image Processing and Data Analysis: The Multiscale Approach*, Cambridge University Press, Cambridge, UK, 1998.
- [119] J.-L. Starck and F. Murtagh, *Astronomical Image and Data Analysis*, Springer, Berlin, Germany, 2002.
- [120] M. Belkin and P. Niyogi, "Towards a theoretical foundation for Laplacian-based manifold methods," in *Learning Theory*, vol. 3559 of *Lecture Notes in Computer Science*, pp. 486–500, Springer, Berlin, Germany, 2005.
- [121] R. R. Coifman and S. Lafon, "Diffusion maps," *Applied and Computational Harmonic Analysis*, vol. 21, no. 1, pp. 5–30, 2006.
- [122] S. Lafon and A. B. Lee, "Diffusion maps and coarse-graining: a unified framework for dimensionality reduction, graph partitioning, and data set parameterization," *IEEE Transactions on Pattern Analysis and Machine Intelligence*, vol. 28, no. 9, pp. 1393–1403, 2006.
- [123] J. Richards, P. Freeman, A. Lee, and C. Schafer, "Exploiting low-dimensional structure in astronomical spectra," *Astrophysical Journal*, vol. 691, pp. 32–42, 2009.
- [124] J. B. Tenenbaum, V. de Silva, and J. C. Langford, "A global geometric framework for nonlinear dimensionality reduction," *Science*, vol. 290, no. 5500, pp. 2319–2323, 2000.
- [125] S. T. Roweis and L. K. Saul, "Nonlinear dimensionality reduction by locally linear embedding," *Science*, vol. 290, no. 5500, pp. 2323–2326, 2000.
- [126] R. D'Abrusco, A. Staiano, G. Longo, et al., "Mining the SDSS archive. I. Photometric redshifts in the nearby universe," *Astrophysical Journal*, vol. 663, no. 2, pp. 752–764, 2007.
- [127] R. D'Abrusco, G. Longo, and N. A. Walton, "Quasar candidates selection in the Virtual Observatory era," *Monthly Notices of the Royal Astronomical Society*, vol. 396, no. 1, pp. 223–262, 2009.
- [128] F. Pasian, U. Becciani, and S. Cassisi, "VObs.it—the Italian Virtual Observatory," *Highlights of Astronomy*, vol. 14, p. 631, 2007.
- [129] M. Comparato, U. Becciani, A. Costa, et al., "Visualization, exploration, and data analysis of complex astrophysical data," *Publications of the Astronomical Society of the Pacific*, vol. 119, no. 858, pp. 898–913, 2007.
- [130] P. Draper, M. Currie, T. Jenness, et al., "GAIA 3D; visualizing data cubes," in *Proceedings of the 16th Annual Conference on Astronomical Data Analysis Software and Systems (ADASS '07)*, R. Shaw, F. Hill, and D. Bell, Eds., vol. 376 of *ASP Conference Series*, pp. 695–698, Tucson, Ariz, USA, 2007.

- [131] M. Borkin, A. Goodman, and M. Halle, "Application of medical imaging software to 3D visualization of astronomical data," in *Proceedings of the 16th Annual Conference on Astronomical Data Analysis Software and Systems (ADASS '07)*, R. Shaw, F. Hill, and D. Bell, Eds., vol. 376 of *ASP Conference Series*, pp. 621–624, Tucson, Ariz, USA, 2007.
- [132] W. L. Chan, K. Charan, D. Takhar, K. F. Kelly, R. G. Baraniuk, and D. M. Mittleman, "A single-pixel terahertz imaging system based on compressed sensing," *Applied Physics Letters*, vol. 93, no. 12, Article ID 121105, 2008.
- [133] J. Bobin, J.-L. Starck, and R. Ottensamer, "Compressed sensing in astronomy," *IEEE Journal on Selected Topics in Signal Processing*, vol. 2, no. 5, pp. 718–726, 2008.
- [134] E. J. Candes and M. B. Wakin, "An introduction to compressive sampling," *IEEE Signal Processing Magazine*, vol. 25, no. 2, pp. 21–30, 2008.
- [135] J. Romberg, "Imaging via compressive sampling," *IEEE Signal Processing Magazine*, vol. 25, no. 2, pp. 14–20, 2008.
- [136] Y. Wiaux, L. Jacques, G. Puy, A. M. M. Scaife, and P. Vanderghelynst, "Compressed sensing imaging techniques for radio interferometry," *Monthly Notices of the Royal Astronomical Society*, vol. 395, no. 3, pp. 1733–1742, 2009.

Research Article

Multiple Depth DB Tables Indexing on the Sphere

Luciano Nicastro¹ and Giorgio Calderone²

¹ *Istituto Nazionale di Astrofisica, IASF Bologna, Via P. Gobetti 101, 40129 Bologna, Italy*

² *Istituto Nazionale di Astrofisica, IASF Palermo, Via U. La Malfa 153, 90146 Palermo, Italy*

Correspondence should be addressed to Luciano Nicastro, nicastro@iasfbo.inaf.it

Received 30 June 2009; Revised 13 October 2009; Accepted 12 January 2010

Academic Editor: Joshua S. Bloom

Copyright © 2010 L. Nicastro and G. Calderone. This is an open access article distributed under the Creative Commons Attribution License, which permits unrestricted use, distribution, and reproduction in any medium, provided the original work is properly cited.

Any project dealing with large astronomical datasets should consider the use of a relational database server (RDBS). Queries requiring quick selections on sky regions, objects cross-matching and other high-level data investigations involving sky coordinates could be unfeasible if tables are missing an effective indexing scheme. In this paper we present the Dynamic Index Facility (DIF) software package. By using the HTM and HEALPix sky pixelization schema, it allows a very efficient indexing and management of spherical data stored into MySQL tables. Any table hosting spherical coordinates can be automatically managed by DIF using any number of sky resolutions at the same time. DIF comprises a set of facilities among which SQL callable functions to perform queries on circular and rectangular regions. Moreover, by removing the limitations and difficulties of 2-d data indexing, DIF allows the full exploitation of the RDBS capabilities. Performance tests on Giga-entries tables are reported together with some practical usage of the package.

1. Introduction

Astronomical projects need to manage data which are directly or indirectly related to sky coordinates. As larger and larger datasets are collected by detectors at all wavelengths, it is more and more crucial to efficiently manage those data to speed up and optimize their exploitation. Modern database servers (RDBS), being highly optimized for managing large amounts of data, are the best available choice for today's astronomical project. The SQL language used to access the data provides several high-level functionalities; still it could be not enough since some scientific, in particular, Astronomy specific capabilities and tools are missing. Speed and flexibility of a query are strongly dependent on the indexing used for the underlying DB table(s). Even simple and in principle little resource-demanding tasks can become highly inefficient if performed on poorly indexed archives. Typically DB servers offer efficient indexing of one or more 1-d data using the so-called B-tree structure. However data produced by an astronomical experiment are typically related to sky coordinates which span a 2-d space. Although it is possible to index such data using one or two simultaneous 1-d indexes like RA and Dec, the queries performance will be

very poor since the search criteria on a 2-d space can be much more complex than on a union of two independent 1-d space. Indeed the only possible queries that take advantages of such indexes will involve range checking along the two coordinates like $\alpha_1 \leq \alpha \leq \alpha_2$ and $\delta_1 \leq \delta \leq \delta_2$. In some cases, the RDBS provides built-in capabilities to manage 2-d coordinates into index files using the R-tree structure. This would allow search criteria like "Find all objects within 2 arcsec of a given location." However these functionalities are far from being a standardized feature of RDBS; furthermore, there is room for optimization and specialization for astronomical usage.

Fast data access is, for example, required by tasks like cross-matching between two full-sky optical or IR catalogs. Another example is the automatic fast astrometry of a field aimed at quickly identifying transient sources, for example, gamma-ray bursts optical transients. This is a typical task of robotic telescopes. The transient source coordinates can then be automatically communicated to larger instruments in order to perform a more detailed study through spectral or polarimetric observations. One more example is the quick production of the map of a sky region showing some physical or statistical property of the underlying DB entries. This should be possible by using a simple, SQL standard query.

Web-based tools managing large-area surveys would greatly benefit from fast RDBS response time too.

Luckily, like the amount of data, also DB servers power and flexibility increase with time making possible to dream, actually to start thinking about a DB table with sub-arcsec sky resolution, that is, comparable to a CCD pixel. We will see that DIF is just ready for this! Building a Stellarium-like (<http://www.stellarium.org/>) or GoogleSky-like (<http://www.google.com/sky/>) tool to browse an astronomical data archive would then be the natural choice, with the obvious difference being that the user can retrieve or work interactively with scientifically meaningful data. Discussing the technical and financial problems of such an ambitious project is beyond the scope of this paper. We only mention the ESO VirGO project (<http://archive.eso.org/cms/virgo/>) as a possible initial pathfinder.

The open-source package DIF (Dynamic Indexing Facility) [1] is a combination of a C++ library, a Perl script, and SQL stored procedures allowing the automatic indexing of MySQL tables hosting sky coordinates. The approach adopted was to “discretize” a 2-d space and map it onto 1-d space using a pixelization scheme. Each pixel is then tagged with a unique integer ID so that an index can be created using the standard B-tree. The usage of MySQL was a natural choice as it was the only open-source RDBS which allowed us to add a custom “DB engine” to the server. At the moment it remains the only RDBS supported by DIF.

2. DIF Motivation and Architecture

The motivations for an efficient management of DB tables hosting data with spherical coordinates are not different from those of any other type of data. Exploiting large datasets and performing complex types of queries are unfeasible, in a reasonable amount of time, without an effective indexing. Typically indexes are not just used to quickly select entries within a given table, but also to define a “relation” with the content of other tables in the DB. The capability to perform “joined” queries is a key feature of *relational* databases. As mentioned, indexing 2-d data (in order to allow spatial queries) is quite different from the 1-d case because any “sequential” data ordering, for example, along one direction, inevitably causes data close in space to be distant in a table, or disk file. Consider, for example, a catalog of objects; in this case one can slice the sphere along the declination (latitude) axis and sort in right ascension (longitude) within each strip. Objects in each strip can be stored into a separate table. Let us now assume that, upon a user request, a dedicated task exists which identifies the stripes of interest. If only one strip is affected by the query, then, depending on how many objects are stored in that table/file, the task of identifying and delivering the requested data is relatively easy. In the case that several strips are to be searched, the task will simply access and search all the affected tables. Of course if the slicing is also performed along the RA axis, the amount of data per table reduces, as does the response time of such task. Moreover, instead of this geographic-like grid, one can adopt any kind of sky slicing and manage

the requests accordingly. All this would work fairly well for a cone-search service. Actually this method is adopted by several catalog search tools (e.g., the VizieR service, vizier.u-strasbg.fr) with acceptable performance. Of course the search efficiency depends on the relative size of the queried region with respect to that of the slice. The closer the better. Also the average number of objects falling into a slice must be not too small nor too large. For example, the 1 billion objects USNO-B1.0 catalog uses strips of $0.^{\circ}1$ in declination, which means that an average of half-million objects is present in each strip.

But what about importing those tables into a RDBS to exploit its capabilities? For example, the usage of an RDBS would allow to easily perform spatial joins on various catalogs. Not to mention the fact that a standard language (SQL) is used to perform queries. This offers an infinitely greater flexibility compared to a custom program which performs a limited number of tasks, only works on a given catalog, requires maintenance, and probably has little portability. As already been said, once the data have been inserted into a DB, one has to find an efficient indexing method for 2-d data. A simple 1-d indexing on declination could be investigated in order to estimate the RDBS performance with respect to the previous custom management. We have not done so and we do not expect a significant leap in performance when compared to the custom case. In particular the RDBS optimizer would be unable to take advantage of the index to perform spatial joins. However other advantages of using an RDBS remain.

The next step is then to find a method to cover the sphere with cells (pixels) and number them. The resulting set of integers can then be indexed using the conventional B-tree and therefore the whole potential of the RDBS can be exploited. So what we need is a 2-d to 1-d mapping function: each entry in the table will have one single integer ID and a sky area maps to a set of integers. A further step is identifying the most appropriate pixel size. Likely this is project dependent, but we will see that having some thousands entries per pixel could be a good choice. Among the various available functions, those implemented by the Hierarchical Triangular Mesh (HTM) [2] and the Hierarchical Equal Area isoLatitude Pixelization (HEALPix) [3] tessellation schema are the most suitable to our aim for a number of reasons; for example, (1) they cover the sky uniformly with no singularities at the poles, (2) the algorithm to compute the pixel IDs is very fast, (3) they implement, or allow to easily implement, tasks to work with the pixel IDs, (4) they are commonly used in Astronomy, and (5) they are available as open-source C++ libraries (see <http://www.sdss.jhu.edu/html/> and <http://healpix.jpl.nasa.gov/>). See Section 3 for more details.

The DIF core is represented by a MySQL DB engine implemented into a C++ class. Functions to perform region selection (and other tasks) use the HTM and HEALPix libraries to calculate the IDs of the pixels included or touched by the requested region. From the user point of view a dynamic table is generated which contains only the entries falling in the region. A DIF-managed table can be queried as any DB table with the additional possibility to perform queries on circular and rectangular sky regions, and so forth (see below). In other words DIF extends the SQL language

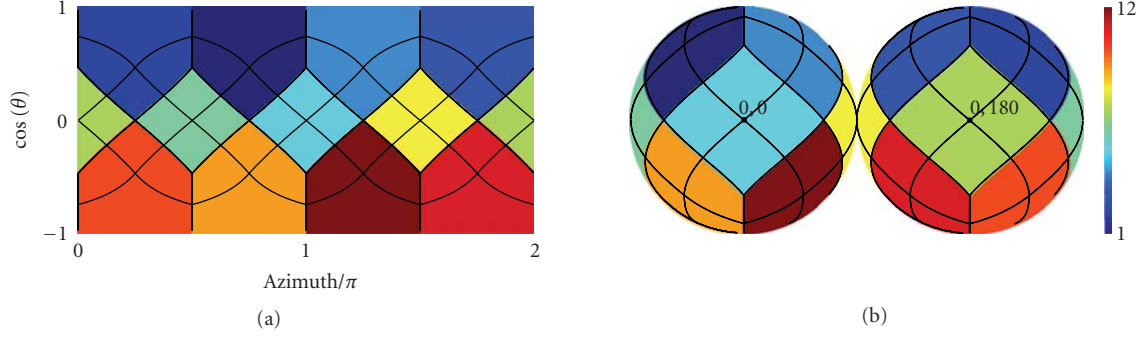


FIGURE 1: The 12 HEALPix base pixels color coded for the “ring” scheme. Overplotted the pixel boundaries for $k = 1$ which gives 48 pixels.

and removes the need to write complex procedures or to use temporary tables to perform 2-d selections. Notably, the current version of the package has no limitations on the number and type of simultaneous pixelizations applicable to a table and the user can choose between two possible types of select queries on spatial regions: (1) give the region of interest in each query string, and (2) first define the region of interest, eventually selecting a specific pixelization depth, then perform any number and type of query on the DIF created view (see examples below). Which one is more convenient depends on the type of interaction of the DB client application and complexity of the query one needs to perform. What is important to note is that in the latter case the selected region is retained until a new region selection command is issued or the region selection is cleared. This property could be useful in the future to implement more complex selections involving union or intersection of regions.

Additionally DIF offers (a) useful User-Defined Functions (UDFs) mainly derived from the HTM and HEALPix libraries, (b) standalone programs to create fake test tables with spherical coordinates, and (c) HEALPix-specific IDL library which allows the user to obtain the result of a query as a sky map. So who should use it? Potential users are those wishing to manage in an automatic and effective way large datasets of astronomical data, of whichever kind: objects catalogs, observation logs, photon lists collected by space-based high-energy detectors, single pixel counts of low-medium resolution wide-field cameras, and so forth.

3. HEALPix and HTM

The HEALPix pixelization scheme [3] uses equal-area pseudo-square pixels, particularly suitable for the analysis of large-scale spatial structures. The base pixels are 12 with two different shapes: four identical ones are centered along the equator at 90° step starting from $(0, 0)$; the remaining eight, all identical, are centered at 45° longitude offset and at a fixed poles distance of $z \equiv \cos \theta = \pm 2/3$ (θ is the colatitude), four in the northern and four in the southern hemispheres (see Figure 1). The region in the range $-2/3 < z < 2/3$ is referred to as the equatorial zone, with the two remaining regions being the polar caps. Recursive subdivision of these pixels is performed keeping their centers equally distributed

TABLE 1: Relevant parameters for the HTM and HEALPix sphere pixelization.

	HTM	HEALPix
N_{pix}^{\dagger} :	8×4^d	$12 \times N_{\text{side}}^2$ (where $N_{\text{side}} = 2^k$)
ID range:	$[N_{\text{pix}}, 2 \times N_{\text{pix}} - 1]$	$[0, N_{\text{pix}} - 1]$
Max N_{pix} :	$\simeq 9.0 \times 10^{15}$	$\simeq 3.5 \times 10^{18}$
Max res. $^{*}(\prime\prime)$:	$\simeq 1 \times 10^{-2}$	$\simeq 4 \times 10^{-4}$ ($\Omega_{\text{pix}} = \pi / (3 \times N_{\text{side}}^2)$)

$^{\dagger} d$ (depth): $[0, 25]$; k (order \leftrightarrow resolution parameter): $[0, 29]$

* For HTM the maximum resolution is derived from the trixel minimum side, for HEALPix assuming a square-pixel equivalent area.

along rings of constant colatitude. Rings located in the equatorial zone are divided into the same number of pixels, the remaining rings contain a varying number of pixels. The two rings closest to the poles always have 4 pixels and going toward the equator the number of pixels increases by four at each step. The resolution of the HEALPix grid is parameterized by $N_{\text{side}} = 2^k$, where k assumes integer values being 0 for the base pixelization. It is called the “resolution parameter” or *order*. It is then $N_{\text{pix}} = 12 \times N_{\text{side}}^2$. Table 1 shows the relevant pixelization parameters (see Górski et al. [3] for more details). The HEALPix library implements a recursive quad-tree pixel subdivision which is naturally nested. The resulting pixel numbering scheme is then referred as the *nested* scheme. Alternatively the *ring* scheme simply counts the pixels moving down from the north pole to the south pole along each isoLatitude ring (see Figures 1 and 2). The usage of the ring scheme is not recommended to index tables like objects catalogs which are typically queried on small sky regions. In fact in this case a data sorting will not result into an efficient “grouping” like that obtainable for the nested scheme where to “close-on-sky” pixels correspond “close-on-disk” data. This is important because data seek time is the main issue to face when very large tables are considered.

The C++ library released in HEALPix version 2.10 uses 64-bit long integers to store the pixels IDs. This allowed us to push the resolution of the pixelization to $\simeq 4 \times 10^{-4}$ arcsec. However, because of 64-bit floating point arithmetics limitations (e.g., minimum appreciable angular distance), this limit is not applicable for all the DIF implemented functions.

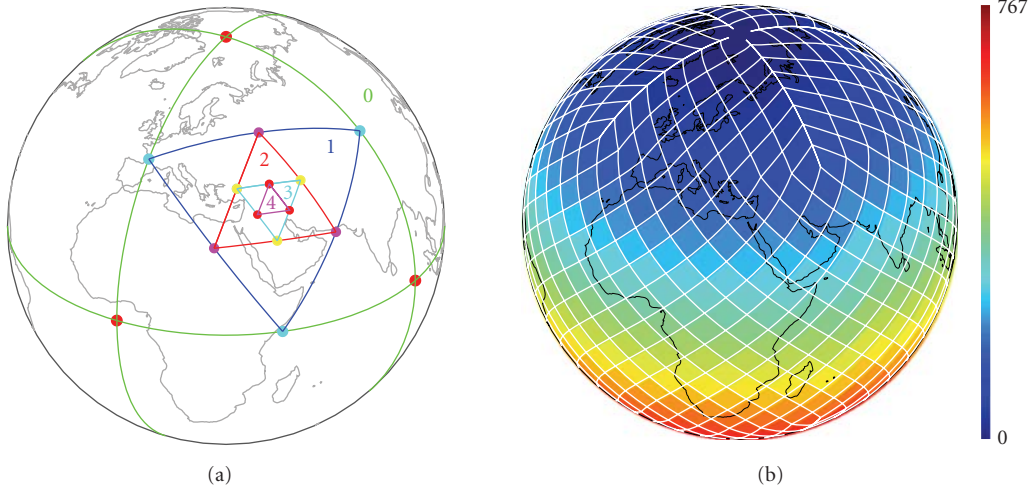


FIGURE 2: (a) The 8 HTM base pixels and recursive subdivisions on Earth surface. The “depth” d of the *trixels* is marked. (b) HEALPix tessellation at order $k = 3$ giving 768 pixels whose colors encode their actual IDs in the “ring” scheme.

The HTM sphere pixelization scheme [2] uses triangular pixels which can recursively be subdivided into four pixels. The base pixels are 8, 4 for each hemisphere. They are obtained by the intersection on the sphere of 3 major big circles. On Earth they can be represented by the equator and two meridians passing at longitudes 0° and 90° (see Figure 2). These base spherical triangles all have the same area. Each of them can then be further divided into four spherical triangles, or *trixels*, by connecting the three sides middle points using great circle segments. As can be seen from Figure 2, from the first subdivision onward the resulting trixels are no longer equal area. The scatter of the trixels area remains within the $\pm 70\%$ of the mean area, which is $2\pi/4^{d+1}$, with d being the *depth* or level (step of recursive subdivision) of the trixel. For a given depth the number of trixels is $N_{\text{pix}} = 8 \times 4^d$. The minimal side length is $\pi/2^{d+1}$ and the maximal is $\approx \pi/2$ times the minimal length. The HTM indexing algorithm performs recursive subdivisions on a unit sphere using a quad-tree nested scheme and can identify each trixel both by integer and string IDs which refer to the vertices of the parent trixel counted counterclockwise (see Kunszt et al. [4] for more details). This algorithm has proven to be very efficient for selecting point sources in catalogs and was specifically developed for the Sloan Digital Sky Survey (see <http://www.sdss.jhu.edu/> and [5]). Table 1 shows the relevant pixelization parameters. Note that, similarly to the HEALPix case, the depth 25 limit is imposed by the 64-bit floating point calculations. It can be lifted up to 30 if 128-bit variables and functions will be introduced in the source code.

Unless one needs to access a large fraction of a table and perform spatial analysis and map plot, we suggest to prefer the HTM pixelization because it offers a larger set of functions with respect to HEALPix. We will see below that the HEALPix IDs of any set of selected rows can still be computed using the DIF functions at query execution time.

4. Using DIF

Here we give a brief technical description of the DIF components and its capabilities. Installation instructions and other details can be found in the user manual distributed with the package and available at the MCS(My Customizable Server, ross.iasfbo.inaf.it/MCS/) website. The DIF source code can be downloaded from the same place as a compressed tar file. Note that being the DIF DB engine an extension to the MySQL server, it requires that MySQL was/is installed using the source package and that the path to the source code location is supplied in the configuration step. DIF adds the following components to a MySQL server:

- (1) A DIF database with the two tables: *dif* and *tbl*. The first is a *dynamic* table listing pixel IDs; the second retains all the information about the managed tables.
- (2) A set of SQL stored functions useful to get information from the *tbl* table. Users can use them as an example to implement their own functions/procedures.
- (3) A set of SQL callable C++ utility functions usable independently from the table type or query executed. Most of these external UDFs make use of the HTM and HEALPix libraries.
- (4) The DIF DB engine, which feeds the DIF. *dif* table, and a set of DIF specific sky region selection functions. They are the compound of a C++ class plus functions which rely on the HTM and HEALPix libraries to dynamically, and transparently, compute the pixel IDs of the region of interest.
- (5) The *dif* Perl script used to perform various management tasks. It requires the DBD::mysql Perl library to work (see Section 4.1).
- (6) For each DIF indexed table, a number of views and triggers will be created.

Note that `DIF.dif` is a table whose content is dynamically generated by the DIF DB engine each time it is accessed, transparently to the user, based on query search criteria. A simple “`SELECT * from DIF.dif`” without the usage of one of the DIF specific sky region/pixels selection functions will result in an “Empty set.” The `DIF.tbl` table hosts all the necessary information about the DIF-managed tables, like pixelization schema, depth/order, and name of the fields with the coordinates. However, the only DIF components a user needs to know about are two: (1) the `dif` script (for a DB administrator) and (2) the DIF functions accessible within MySQL queries. They are listed in Table 2. A detailed description is reported in the user manual.

4.1. The `dif` Script. As mentioned, this section is of interest only for a DB administrator. All the various actions related to the management of a table via the DIF package are performed using a Perl script: `dif`. Its parameters and flags can be viewed typing `dif --help`. Its usage is straightforward and we give here a partial list of examples.

Let us assume that a DB `MyDB` with a table `MyTab` exists, that the sky coordinates of the entries are reported as cent-arcsec, and that the field names are `RAcs` and `DECcs`. To index the table with an HTM tessellation with depth = 8, the command to give is

```
dif --index-htm MyDB MyTab 8
"RAcs/3.6e5" "DECcs/3.6e5",
```

and the result will be the following

- (1) a column named `htmID_8` of type `MEDIUMINT UNSIGNED` (3 bytes) and default value 0 will be added to the `MyTab` table,
- (2) the column will be filled with the IDs of the trixel where that entry falls,
- (3) an index is created on the `htmID_8` column,
- (4) a new entry is inserted into the table `DIF.tbl` with the values:

```
MyDB MyTab 1 0 8 RAcs/3.6e5 DECcs/3.6e5,
```

- (5) a view named `MyDB.MyTab_htm` is created. It contains the appropriate `INNER JOIN` of the `htmID_8` column with the dynamically populated column `DIF.dif.id` plus other statements (see the manual),
- (6) a trigger named `MyDB.difi_MyTab` is created. It is used to automatically calculate the `htmID_8` value when an `INSERT` query is executed.

Moreover, if two or more pixelization depths are to be applied to the table, they can be given simultaneously as a comma-separated string. For example, to apply depths 8 and 12, the command would have been

```
dif --index-htm MyDB MyTab "8,12"
"RAcs/3.6e5" "DECcs/3.6e5".
```

A spatial query on the `MyTab_htm` view performed via `DIF.HTMCircle` or `DIF.HTMRect/HTMRectV` will make use

of all the available depths simultaneously by performing a recursive “erosion” of the requested region. Let us say that we have three indexes, 8, 10, and 12, then the algorithm will find, in this order, that (1) the $d = 8$ trixels fully contained in the region, (2) the $d = 10$ fully contained trixels in the remaining area, and (3) the $d = 12$ fully and partially contained trixels in what is left of the region. It could happen that no $d = 8$ or/and $d = 10$ trixel is found.

Sometimes it could be convenient to use only one of these pixelizations, for example, when the queried region size is close to the trixel size of one of the available depths. In this case the user can issue the command

```
dif --single-index-views MyDB MyTab
```

which will create views like `MyDB.MyTab_htm_8` suitable to directly perform queries using one single pixelization depth. Of course this makes sense only if more than one pixelization was applied (see below how to perform sky regions `SELECT` queries on these views). To use a HEALPix tessellation with “nested” scheme, $k = 8$, the command would have been

```
dif --index-healpix-nested MyDB MyTab 8
"RAcs/3.6e5" "DECcs/3.6e5".
```

The added column name will now be `healpID_1.8` (`healpID_0.8` if the “ring” scheme was used) and the view will be `MyTab_healp_nest`. To remove an index and the related DIF facilities from a table, use a command like this the following:

```
dif --drop-index-htm MyDB MyTab 8
```

which refers to the first of the two examples above. If one wishes just to remove all the views and triggers from a table but keeping indexes and columns created with a `dif` command, then simply he/she can use `dif --drop-views MyDB MyTab`.

4.2. UDFs: SQL Routines and SQL Callable C++ Utilities. SQL stored functions are linked to the DIF database and give access to the information stored in the `DIF.tbl` table. They are usable in any query and are accessible to all MySQL users. For example, to find out which are the table columns used to get sky coordinates (in degrees!), one can execute the query

```
SELECT DIF.getRa("MyDB", "MyTab"),
DIF.getDec("MyDB", "MyTab");
```

SQL callable functions are MySQL “external” function; still they can be used in any `SELECT` statement exactly like any DB server built-in function. Apart from the spherical distance calculation performed by `Sphedist`, they make available to the user HTM and HEALPix related functions. Note that the parameters “RA” and “Dec” are constants *or* the table column names corresponding to spherical coordinates. As mentioned, they must be in *degrees*; therefore conversion factors can be present, for example, `RAcs/3.6e5`. For example, to get the HTM IDs at $d = 6$ of the neighbors of the pixel where the point $(100^\circ, -20^\circ)$ falls, the command “select

TABLE 2: DIF functions available in MySQL.

SQL stored routines	SQL callable C++ utilities
DIF.getHTMDepth (db, tab)	HTMLLookup (d, Ra, Dec)
DIF.getHEALPOrder (db, tab)	HEALPLookup (s, k, Ra, Dec)
DIF.getHEALPNested (db, tab, k)	HTMBary (d, ID)
DIF.getRa (db, tab)	HTMBaryC (d, Ra, Dec)
DIF.getDec (db, tab)	HTMBaryDist (d, ID, Ra, Dec)
<i>Sky region/pixels selection</i>	HTMNeighb (d, ID)
DIF.HTMCircle (Ra, Dec, r)	HTMNeighbC (d, Ra, Dec)
DIF.HTMRect (Ra, Dec, S1, [S2])	HEALPBary (s, k, ID)
DIF.HTMRectV (Ra1, Dec1, Ra2, Dec2)	HEALPBaryC (s, k, Ra, Dec)
DIF.HEALPCircle (Ra, Dec, r)	HEALPBaryDist (s, k, ID, Ra, Dec)
DIF.HTMNeighbC (Ra, Dec)	HEALPNeighb (s, k, ID)
DIF.HEALPNeighbC (Ra, Dec)	HEALPNeighbC (s, k, Ra, Dec)
DIF.setHTMDepth (d)	Sphedist (Ra1, Dec1, Ra2, Dec2)
DIF.setHEALPOrder (s, k)	<i>Auxiliary functions</i>
DIF.Sphedist (Ra1, Dec1, Ra2, Dec2)	DIF_useParam (d or k)
DIF.FineSearch (var)	DIF_cpuTime ()
	DIF_clear ()

Note: in DIF.HTMRect if S2 is omitted it is assumed = S1, that is, query a square; s is the HEALPix schema switch: 0 for ring, 1 for nested.

HTMNeighbC(6, 100, -20)" will return the string:

```
37810, 37780, 37781, 37783, 37786, 37788,
37808, 37809, 37811, 37817, 37821, 37822,
37823.
```

The first of the 13 IDs is always the one containing the input coordinates. Similarly to get the IDs of the neighbors starting from a given pixel ID, use "selectHTMNeighb(6, 37810)," which gives the same string above excluding the first ID, that is, 12 IDs. Note that for HEALPix the number of neighbors is not constant! More utility functions will be added in the future.

4.3. The DIF Specific Region/Pixels Selection Functions. These functions are those that allow the user to select the desired subset of table rows making a (transparent) use of the columns with the HTM and HEALPix IDs. They must be used either in the query WHERE clause or as the only argument of a SELECT statement to initialize the DB engine (see below). The pixel neighbors and region selection functions (the DIF.HTM... and DIF.HEALP..., see Table 2) only give results if applied to the corresponding HTM or HEALPix views as they produce a list of IDs in the dynamic table DIF.dif, which is then used as a reference table to join the managed table. For these functions, "RA" and "Dec" are the table column names corresponding to the sky coordinates. Also in this case, to have them in degrees, conversion factors can be present. Note how these functions do not require the pixelization parameters as they are directly managed by the views they apply to. For example, DIF.HEALPNeighbC only requires the coordinates column names, compared to the UDF HEALPNeighbC which also requires scheme ID and order k . This dynamic management of the table is a specific capability of the DIF DB engine. Some query examples with

direct region selection are

```
SELECT * FROM MyTab_htm WHERE
    DIF.HTMCircle(33,44,30);

SELECT * FROM MyTab_healp_nest WHERE
    DIF.HEALPCircle(33,44,30);

SELECT * FROM MyTab_htm_8 WHERE
    DIF.HTMRect(33,44,40);
```

The first two queries return all the entries in a circular region centered at $\alpha = 33^\circ$ and $\delta = 44^\circ$ with radius $30'$. The third will select entries in a pseudo-square region with same center and sides length of $40'$ along RA and Dec.

Alternatively one can initialize the region of interest once and then execute any number of queries on the resulting entries. If multiple indexing has been applied (either HTM or HEALPix), then one can also choose to use only one depth/order, for example, $d, k = 8$. In this case the function DIF_useParam must be used. A typical sequence of queries, for example, on an optical sources catalog, is:

```
SELECT DIF_useParam(8);
SELECT DIF.HTMCircle(5,3,60);
SELECT COUNT(*) AS Nobj, AVG(B-V) AS
    C1r FROM MyTab_htm;

SELECT HEALPLookup(0,8,
    RAcs/3.6e5,DECcs/3.6e5) FROM
    MyTab_htm;
```

The first two SELECT just set DIF internal parameters returning 1 on success. The next query shows number and

average “color” of the sources within 1° around $\alpha = 5^\circ, \delta = 3^\circ$. The last query will calculate and return the HEALPix IDs (order 8, ring scheme) of these sources. Note that cent-arcsec coordinates are assumed. Omitting to use `DIF.useParam` or giving it the value 0 would instruct DIF to use all the available depths (or orders) to perform the selection. This is the default. Also note that the region selection query can be followed by *any* number of queries on *any* table view. Only the rows falling into the selected region will be affected by these queries until a new region selection command is issued. A `DIF.clear()` can be issued to reset all the internal parameters. The MySQL server is a multithread process which means that it creates a new work environment for each client connection. DIF functions, being part of the server, set thread-specific parameters like any other MySQL intrinsic function. Their status and values are retained until the connection is closed. When a new connection with the server is established, the initial status of a DIF parameter is unpredictable (like the value of an uninitialized variable in a program).

An example which makes use of all the three described functions typs is:

```
SELECT  DIF.getRa("MyDB", "MyTab") as
RAdeg,
        DIF.getDec("MyDB", "MyTab") as
DECdeg,
        HTMNeighbC(6, RAdeg, DECdeg)
FROM MyDB.MyTab_htm.6 WHERE
        DIF.HTMCircle(10,20,5);
```

The result will be the list of neighbors for each object ID in the given circular region. Of course if more than one object falls in one pixel, the output will present several identical rows. It is trivial to modify the query to avoid this.

What about alternatives to DIF and in particular to the DIF DB engine and related UDFs? One could, for example, write a stored procedure which performs a cone search. First of all the table must have been created with a column suitable to receive, for example, HTM IDs at a given depth. For a given cone, one needs to write a function to calculate the IDs of the fully and partially covered trixels, then search the table for all the entries with these IDs excluding those falling outside the cone. The usage of a temporary table to store the IDs is unavoidable. This could pose efficiency problems but it is affordable. The usage of views and/or tables join would certainly help. Additionally one has to manually manage the insertion of new entries to calculate their IDs. The usage of triggers could help. We can continue with the reasoning requiring further facilities and tools and we will likely end up with a system with an architecture which resembles the DIF one, but is lacking the efficiency and flexibility intrinsic to DIF.

5. Benchmarks

In order to perform benchmarks on access time of DIF-managed tables, we used several tables with fake entries. Some of them were produced generating fully random

TABLE 3: Parameters for the HTM and HEALPix pixelization used in the tests.

d / k	N_{pix}	$\langle \text{Area} \rangle$ (arcmin ²)	Rows/Pix.	Bytes*
HTM				
6	32,768	1.26 [†]	89,290	2
8	524,288	283	5,580	3
10	8,388,608	18	348	3
12	134,217,728	1	21	4
HEALPix				
6	49,152	0.84 [†]	59,526	2
8	786,432	189	3,720	3
10	12,582,912	12	232	3
12	201,326,592	0.7	14	4

[†](deg²); *additional disk storage per row needed.

coordinates; this means that the sky distance between two sequentially generated entries could be anything in the range $[0^\circ, 360^\circ]$. It also means that a set of “close-on-sky” entries could be spread all over the disk data file. Other tables had their entries generated following a $\sim 1^\circ$ sky pixelization schema. This means that the data spread within the disk files is reduced by a factor equal to the number of pixels used to split the sky. For simplicity and analogy with the GSC 2.3 catalog (see below) we generated the entries over 32768 pixels corresponding to the HTM of depth 6 grid. Tables with average objects/pixel density in the range ~ 10000 – 90000 were produced (i.e., containing 0.4–3 billion entries). We also produced and performed tests on “pixelized” and RA sorted (within each pixel) table. The 3 billion entries tables gave disk files size of ~ 120 GBytes. All the tables were created using the MyISAM DB engine. We avoided to split tables, and then the data files, by using the MERGE DB engine or the PARTITION BY option as, apart from management convenience, we do not expect any significant performance improvement on machines not equipped with a large number of disks. Region selections were performed using coordinates in degrees and cent-arcsec. Because the HEALPix library does not allow rectangular selections, for homogeneity reasons the selections were only performed on circular regions (also referred to as “disc” or “cone”). Four different pixelization depths/orders were used both for HTM and HEALPix (nested scheme) and the queries involved only one of them at the time. The results of benchmarks using the multidepth facility on very large tables will be reported elsewhere. The relevant parameters are reported in Table 3. We used a custom program to monitor the system resources usage by the select queries on DIF-managed tables. As expected, the most important hardware component determining the overall query execution time is the hard disk, in particular its data seek and access time. The higher the data contiguity the faster the query execution time. The used query implied calculations on the rows content; this is in order to force the load of the data into memory and not to have just a row counting. For each pixelization

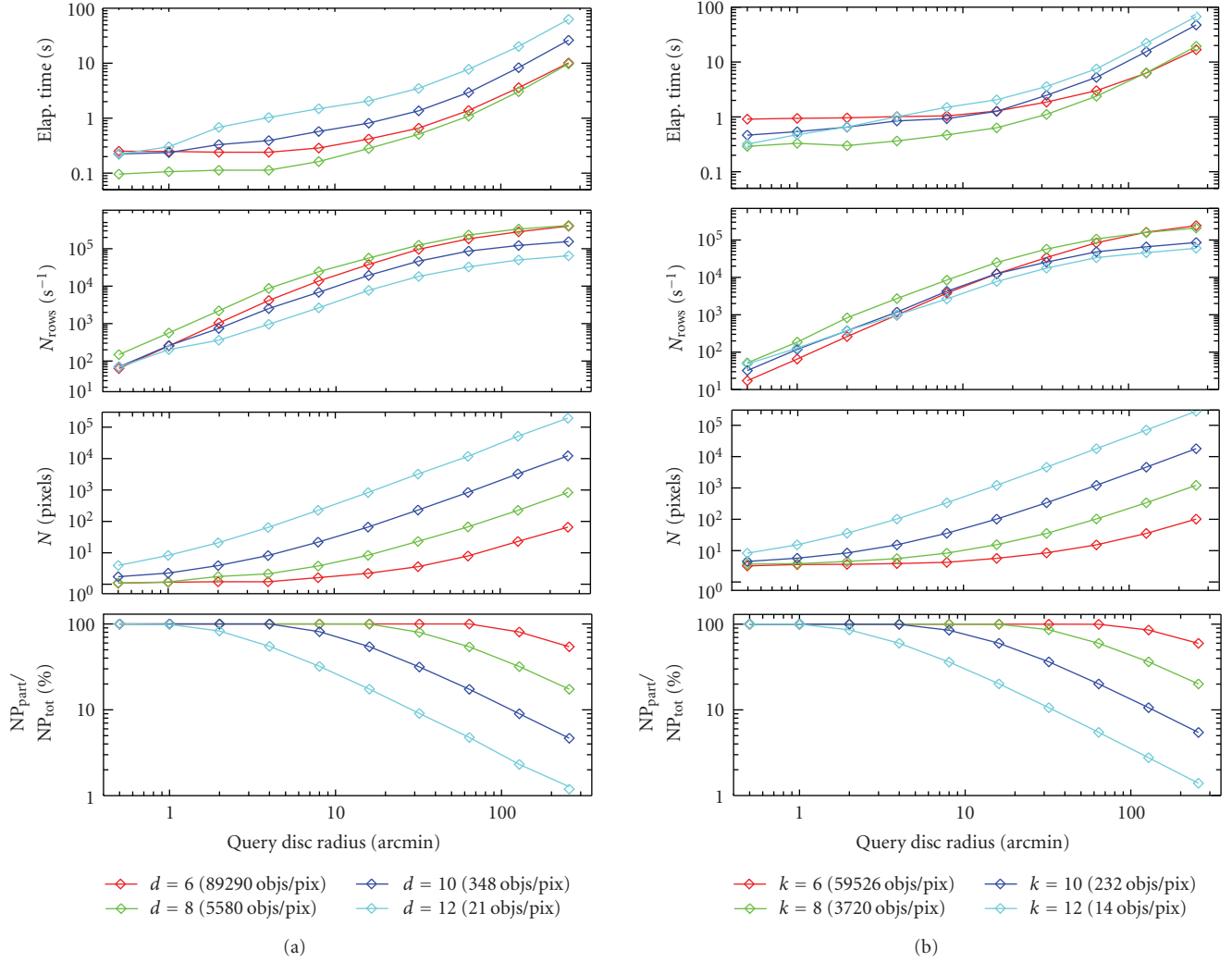


FIGURE 3: Select query execution times and other parameters for a DIF-managed table with ~ 3 billion entries as a function of the disc radius. Results for four different pixel scales are reported both for HTM (a) and HEALPix (b). Each point represents the average of the results from 50 queries performed on random sky positions.

Figure 3 shows, in a log-log scale, respect to the queried disc radius (top to bottom): (1) query execution times, (2) number of processed rows per second, (3) number of pixels involved, and (4) number of partially covered pixels respect to the total at a given depth/order. The used machine main characteristics are OS: Linux kernel 2.6.22.19 SMP x86_64, CPU: bi-proc. dual-core Intel Xeon 5130 @ 2 GHz, RAM: 8 GBytes DDR2-667 166 MHz, and Disk: RAID 1 on a 3 Ware Raid 9550SX-8 LP controller with two SATA2, 500 GBytes, 7200 rpm, 3 Gbits/s, reiserfs. The MySQL version used is 5.1.32 with `key_buffer = 384M`, `myisam_sort_buffer_size = 64M`, `query_cache_size=32M`. The main results are as follows.

(a) For the fully random tables, query execution times are quite long because to fast index lookups corresponds slow disk file seeking (not scanning) which could affect the entire data table. Times grow in a quasi-linear way with respect to the region size and it is of ~ 100 rows s^{-1} . This

makes clear that, even though it is better than having, for example, a simple declination indexing, the usage of DIF on such sort of table is of very limited help. On the other hand, any real data would almost never be produced in a fully random way, but rather in a sequential way over sky “spots” or “stripes”. This is, for example, the case of all-sky surveys performed in point-and-stare or slewing mode. A possible solution is to perform data clustering by sorting over the DIF index with lower depth/order using `myisamchk -R index` (see `myisamchk` manual).

(b) The HTM depth 6 sorted tables behave quite differently and show better performance when pixels with area of $\sim 200\text{--}300$ arcmin 2 (HTM depth = 8 and HEALPix order = 8) are used to index the tables. This is particularly true for the table with ~ 3 billion rows we used, where we have some thousands entries per pixel (see Figure 3). Having a look to the curves measuring query execution time and number of processed rows per second as a function of the region size, we

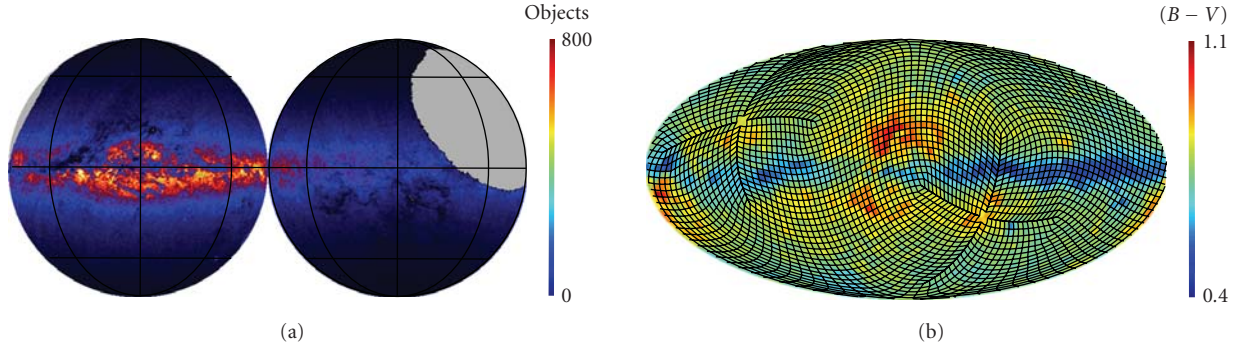


FIGURE 4: UCAC 2.0 full sky objects density map (a) and ASCC 2.5 objects average $B - V$ (b).

note that the behavior is similar for all the depths. However the point where the bending becomes more significant is depth dependent being shifted toward larger number of rows for higher depth pixelizations. As a consequence of this, we also note that, when some 1×10^5 rows are involved, $d = 6$ starts to perform like $d = 8$. The rows/s processing limit is $\sim 5 \times 10^5$. For tables with ~ 1 billion rows or less we found that higher resolution pixelizations ($d, k = 10, 12$) perform not too differently from the $d, k = 8$ case. The reasons for this are not so simple to investigate considering the many parameters involved. We note that for a given region size, when the pixel size reduces, the number of joins on pixel IDs in the query increases but the number of entries falling into partially covered pixels, for which a direct distance calculation from the center of the circle is required, decreases. It is likely that, depending on DB server and machine characteristics, the performance can vary with pixel density and number of join operations required. However, as already been mentioned, we do not note any significant dependence of the query execution time on the total CPU usage time, which is negligible. So, once again, the attention should fall on the data seek/access time and consequently its impact for the various pixel densities. Let us assume that a given circular region only partially covers 1 trixel at $d = 8$; this is typically the case for a $\sim 1'$ radius region. In this trixel entries coordinates are randomly distributed. However we will access all of them on disk, so, in some way, they are accessed quite efficiently having a “contiguity factor” $f_c = 1/16$ (being the data clustered on $d = 6$ trixels and for each depth step there is a factor four increase in the number of trixels). It is not a constant, but let us say that at $d = 10$ the very same region partially covers two subtrixels of that trixel. The number of entries to seek/access reduces by a factor eight. Considering that the various processes involved will likely put in cache memory adjacent data, we can assume that there is one single data seek operation to access these rows. However now it is $f_c = 1/256$, that is, the data are a factor eight more fragmented. Now if we half the entries density, the benefit of the reduced seek time is a factor eight greater for $d = 10$ respect to $d = 8$. This explanation seems to us sufficient to account for the measured query performance as a function of pixel density and size; still other possibilities could be investigated.

(c) Adding (in our case) the RAcS column to a given table index and sorting the data on disk with this new combined index reduce the query execution time by a variable, still not very significant amount of time. On the other hand, time reduces by up to an order of magnitude if one uses directly in the WHERE clause of the query the RAcS column to delimit a range. This is what we did in the customized catalogs used for astrometry and objects matching in the REM [6] produced images (see below). Moreover, if one makes use of the buffering capabilities of the MySQL server by performing more than one query on the same sky region, the queries other than the first one will be executed in a very fast way. This strategy can easily be implemented in robotic telescopes software, for example, for GRB alerts!

(d) The usage of the “ring” scheme for HEALPix indexed tables is not recommended because any table sorting which makes use of such index will give for adjacent on sky pixels not adjacent position on disk. This effect is less relevant in the extreme cases when a few or the majority of the pixels are interested by a selection. Because of the poorer performance measured and because the calculation of the HEALPix IDs of table entries can be computed at query execution time, for a general purpose table we suggest to use always the HTM indexing.

6. MCS-IDL Contributed Library

MCS offers a client interface to the IDL language. We have implemented a library useful to interact in a very simple way with the MySQL server from this language. A further library useful to plot data on the sphere using the HEALPix IDL library is available too. DIF-managed tables data are easily plottable using this library. It is enough to put them on the user’s IDL path together with the HEALPix library. These libraries are retrievable from the web. Here we show their usage on customized optical and IR catalogs.

6.1. Optical and IR Catalogs Sky Maps. For our tests on real data we used catalogs which are routinely used for real-time objects identification in images taken by the IR/optical robotic telescope REM (see Molinari et al. [6]). Among them are GSC 2.3, GSC 2.2 (~ 18 th mag threshold), USNO B1.0,

2MASS, UCAC 2.0, and ASCC 2.5 (see the websites: www.gsfc.stsci.edu/, www.nofs.navy.mil/, www.ipac.caltech.edu/ad.usno.navy.mil/, cdsarc.u-strasbg.fr/). Using DIF, we have indexed these catalogs with various pixelizations. The performed tests confirm the results obtained for the fake tables, that is, the fastest access time is achieved by using pixels of size $\sim 1'$. We recall that the GSC 2.3 is distributed as 32768 FITS files, each covering a $d = 6$ HTM trixel, whereas USNO B1.0 and 2MASS are split in files covering $0^\circ.1$ in Dec, RA ordered in the slice. To further speed up the region lookup, which for REM is $10' \times 10'$, we added coordinates indexing. For optimization and disk space-saving reasons, coordinates were converted into cent-arcsec and therefore packed into 4-byte integers. Then a "unique" combined index was created on HTM ID plus coordinates. As already noticed in [1], with such an index and the usage of coordinate ranges in the WHERE clause to further reduce the number of rows to seek/access, queries on regions of size $10' - 30'$ take ~ 20 ms.

Using IDL routines to visualize as sky maps data read from MySQL tables is quite straightforward. As said, the HEALPix pixelization schema and routines can be used to this aim. For example, in Figure 4 we show the UCAC 2.0 sky objects density in galactic orthographic projection. The map was built using $k = 8$, that is, a pixel size of $\simeq 14'$. The sky region not covered by the catalog is shown in grey. In the same figure the average $B - V$ of the ASCC 2.5 objects in pixels of area 13.4 deg^2 is shown in galactic mollview projection. A simple (and basic) IDL program to produce the first map is:

```
@mcs_healplib
COMMON HEALPmap, $
    hp_nested, hp_nside, hp_order, $
    hp_npix, hp_emptypix, hp_npixok, $
    hp_map_nocc, hp_map_sum
hp_order = 8
Query = "select healpID_0.8 from UCAC_2orig"
DBExec_Qry("MyDB_name", "User_name", $
    "Password", Query)
healp_MapFill()
orthview, hp_map_nocc, rot=[45,45], $
    coord=["C","G"], /grat, col=5
```

Note: (1) `mcs_healplib(.pro)` has all the high-level routines needed to build and save HEALPix maps; it also loads `mcs_usrlib` which is used to access MySQL tables. (2) The common block `HEALPmap` is used to pass the map parameters among the various routines. (3) If the `UCAC_2orig` table does not have the `healpID_0.8` column (e.g., it is not indexed), then simply change the query into `"select HEALPlookup(0,8, RAcs/3.6e5,DECcs/3.6e5) from UCAC_2orig"` which will calculate the IDs for $k = 8$ on the fly. (4) `healp_MapSave()` can be used to write the map into

an FITS file. On the MCS website some demo programs are available to help write custom programs and routines.

7. Conclusions

We presented the DIF software package, its capabilities, and the results of benchmarks over very large DB tables. We have shown that for tables with billion entries a sky pixelization with pixel size of the order of $\sim 15'$ (HTM $d = 8$) gives best performance for select queries on regions of size up to several degrees. At this spatial resolution some thousands of entries fall in each of the $\sim 1/2$ million pixels; these entries have the same ID assigned in the DB table. We stress the fact that these results apply only in case some sky coordinates ordering is applied to the disk data file. If not, the disk seek time becomes so dominant to make the use of DIF, or any other indexing approach, meaningless. We also note that, in all cases, the CPU time accounts for only a few percent of the total query execution time; therefore great care must be put in choosing and designing the data storage. We have also shown the usage of HEALPix IDL libraries allowing the visualization and saving of sky maps obtained executing SQL queries directly from IDL.

The package is distributed under the GNU GPL and we encourage everybody to use it for their astronomical projects, in particular to manage object catalogs and large archives of data of any sort. We believe that the Virtual Observatory could certainly benefit by adopting a DIF-like approach and we hope that VO software developers will consider it. It is worth to note that not only Astronomy can benefit of the usage of DIF. It can be used by any project dealing with spherical data. Research fields like geology, geodesy, climatology, oceanography, and so forth all deal with geographical data. Those data can be stored into a DB, indexed on coordinates using DIF, and then efficiently retrieved, visualized, and used for a variety of purposes. Some new type of automatic navigation system having a DBS behind could also find more convenient a DIF indexing approach.

More capabilities and improvements are under development among which are cross-match UDF for automatic matching of objects in a circular or rectangular region selected from two different tables and the full porting to Mac OS. Other types of selection region, like regular and irregular polygons, rings, and so forth, or the adoption of commonly used region definition strings will be considered too. Though widely tested, the package is periodically update to remove bugs, improve performance, add new facilities, make it compatible with new MySQL versions, and so forth. Any comment or feedback is welcome. Users willing to contribute to the package development or testing are kindly asked to contact us. Please visit the website: ross.iasfbo.inaf.it/MCS/.

The now available DIF version 0.5.2 introduced some changes with respect to the version used when writing this paper. The reader is asked to read the user manual available with the software package at the mentioned website.

Acknowledgments

The authors acknowledge support from the astrometry group of the Turin Astronomical Observatory to have given

us access to the various optical and IR catalogs. DIF makes use of the HEALPix [3] and HTM [2] packages. They also thank the referee for his/her helpful comments.

References

- [1] L. Nicastro and G. Calderone, “Indexing astronomical database tables using HTM and HEALPix,” *Astronomical Society of the Pacific Conference Series*, vol. 394, pp. 487–490, 2008, Edited by R. W. Argyle, P. S. Bunclark, and J. R. Lewis.
- [2] P. Z. Kunszt, A. S. Szalay, and A. R. Thakar, “The hierarchical triangular mesh,” in *Proceedings of the MPA/ESO/MPE Workshop—Mining the Sky*, A. J. Banday, S. Zaroubi, and M. Bartelmann, Eds., pp. 631–637, Springer, Garching, Germany, 2001.
- [3] M. Górski, E. Hivon, A. J. Banday, et al., “HEALPix: a framework for high-resolution discretization and fast analysis of data distributed on the sphere,” *The Astrophysical Journal*, vol. 622, no. 2, pp. 759–771, 2005.
- [4] P. Z. Kunszt, A. S. Szalay, I. Csabai, and A. R. Thakar, “The indexing of the SDSS science archive,” *Astronomical Society of the Pacific Conference Series*, vol. 216, pp. 141–144, 2000, Edited by N. Manset, C. Veillet, and D. Crabtree.
- [5] J. Gray, A. S. Szalay, A. Thakar, et al., “Data mining the SDSS SkyServer database,” in *Proceedings of the 4th International Workshop on Distributed Data and Structures (WDAS '02)*, W. Litwin and G. Levy, Eds., pp. 189–210, Carleton Scientific, Paris, France, 2002.
- [6] E. Molinari, S. Covino, S. D’Alessio, et al., “REM, automatic for the people,” *Advances in Astronomy*. In press.

Research Article

The REM Observing Software

Mauro Stefanon,¹ Stefano Covino,² Dino Fugazza,² Emilio Molinari,^{2,3} Francesco D'Alessio,⁴ Giuseppe Malaspina,² Luciano Nicastro,⁵ Vincenzo Testa,⁴ Gino Tosti,^{6,7} and Fabrizio Vitali⁴

¹ *Edifici Instituts d'Investigació, Observatori Astronòmic Universitat de València, Polígon La Coma, Paterna, 46980 València, Spain*

² *INAF-Osservatorio Astronomico di Brera, Via E. Bianchi 46, 23807 Merate, Italy*

³ *INAF-Telescopio Nazionale Galileo, Fundación Galileo Galilei, INAF, Rambla José Ana Fernández Pérez, 7, 38712 Breña Baja, Spain*

⁴ *INAF-Osservatorio Astronomico di Roma, Via di Frascati, 33, 00040 Monte Porzio Catone, Italy*

⁵ *INAF-IASF, Via P. Gobetti 101, 40129 Bologna, Italy*

⁶ *Istituto Nazionale di Fisica Nucleare, Sezione di Perugia, 06123 Perugia, Italy*

⁷ *Dipartimento di Fisica, Università degli Studi di Perugia, 06123 Perugia, Italy*

Correspondence should be addressed to Mauro Stefanon, mauro.stefanon@uv.es

Received 26 June 2009; Accepted 12 January 2010

Academic Editor: Joshua S. Bloom

Copyright © 2010 Mauro Stefanon et al. This is an open access article distributed under the Creative Commons Attribution License, which permits unrestricted use, distribution, and reproduction in any medium, provided the original work is properly cited.

The Rapid Eye Mount (REM) is a 60 cm robotic telescope located at La Silla, Chile. Its Observing Software (REMOS) is constituted by a set of distributed intercommunicating processes organized around a central manager. Together they grant the system safety, automatically schedule and perform observations with two simultaneous cameras of user-defined targets, and drive fast reaction to satellite alerts. Subsequent data reduction is left to pipelines managed by each camera.

1. Introduction

The discovery in the last decades of astrophysical processes which develop on timescales of few seconds to few minutes has given rise to the necessity of instruments capable of collecting as much information as possible on those timescales. On the other side, the technological developments in informatics of the last 20–30 years have enabled the astronomical community to develop telescopes with a high degree of autonomy. The scientific needs of rapid response to astrophysical processes have thus obtained one of the required tools, that is, *robotic telescopes* which can manage to acquire photons coming from a precedent unknown source position in a completely unattended way.

The Rapid Eye Mount (hereafter REM) telescope is one of the main robotic telescopes dedicated to the study of Gamma Ray Bursts (GRBs) afterglow. Its implementation allows to automatically point towards a new GRB in 30 seconds from the reception of the alert.

The system has already been described in [1–3]. In the following paragraph we outline its overall design. The next section describes all the strategies implemented in the

software, while Sections 5 to 12 report on the technical implementation issues.

2. Scientific Aim

REM was installed at La Silla in June 2004 and became fully operational in the second half of 2005. Since its commissioning, the scientific drive of the project was the study of the early phases of GRB afterglows. This concretized into the realization of a software system able to analyze in real time all the alerts coming from the satellites, like HETE II, INTEGRAL, SWIFT, and, recently, Fermi, and to rapidly and automatically point the telescope to the source location. When no alerts are active, REM in realtime draws and executes the schedule for the night based on *secondary science* targets.

Starting from October 2006 REM has also become an Italian national facility under INAF (Istituto Nazionale di Astrofisica). Within this new context, REM is now offered to the scientific community with two Calls for Proposals per year.

Since the operations involved in the observations are quite different depending on the fact that the system is reacting to satellite alerts or not, it is thus natural to divide the kind of observations in two classes:

- (i) satellite alert fast reaction,
- (ii) observation of known-position sources. A generalization of this point is the possibility of activating a Target of Opportunity (ToO) request. This will be discussed in Section 6.

3. General Description of the System

3.1. Telescope. The Rapid Eye Mount REM is a 60 cm robotic fast slewing telescope located at La Silla site of the ESO La Silla Paranal Observatory, in the Chilean Andes.

It has a classical Ritchey-Cretien optical scheme, with a primary mirror of 60 cm diameter at $f/2.2$ with a total equivalent focal ratio of $f/8$ on the focal plane.

The mount is a compact alt-azimuth with two Nasmyth stations. One station hosts two instruments, a high-efficiency IR camera (REMIR) and an optical slitless spectrograph (ROSS), which can operate simultaneously thanks to a beam splitting dichroic mirror; the second Nasmyth focus is currently not used by any instrument. The compact design of the mount allows the telescope to slew as fast as 10 degrees per second. Although the telescope is not equipped with a guiding systems, the high precision ETEL encoders allow to track for about five minutes keeping the stellar spot within its average 2 arcsec full width half maximum (fwhm).

The telescope enclosure is composed by a two-sided roof, which can slide apart, leaving the telescope able to point to a minimum altitude of 5 degrees above the horizon.

3.2. Cameras. The REM Infrared Camera ([4, 5]) is equipped with a Rockwell 512×512 pixels, $18 \mu\text{m}$ pitch HgCdTe array, and cooled by liquid nitrogen. An optical system allows to obtain a FoV of $9.9 \times 9.9 \text{ arcmin}^2$. The camera has a 10-position filterwheel, with standard J, H, Ks plus y, and H2 filters.

The REM Optical Slitless Spectrograph (ROSS [6]) is a commercial Apogee CCD camera, with a $1 \text{ K} \times 1 \text{ K}$ detector. The optics allow to cover almost exactly the same field of the IR camera (namely, $9.54 \times 9.54 \text{ arcmin}^2$ FoV). Apart from standard Johnson V, R, I filters, the filterwheel also holds an Amici prism, which allows to obtain slitless spectra of all the objects in the field down to a magnitude of $R \approx 14$ for an exposure of 300 s and $S/N = 5$.

Since August 2006, REM is also hosting the TORTORA camera ([7, 8] this proceeding). The instrument is dedicated to the early discovery and study of optical transients; mounted in parallel to the REM optical tube, it is constituted by a wide field ($20 \text{ deg} \times 10 \text{ deg}$) fast photometry photomultiplied optical camera, allowing to obtain the photometry of the observed region of sky every second down to $R \approx 9$.

4. Overall View of the Software Structure

The diverse operations performed by REM translate to a great number of algorithms necessary to their implementation. In fact, as a robotic telescope, REM does not only automatically perform a set of observations, but it also continuously monitors itself and, to some degree, it can also self-diagnose and react to malfunctions, allowing, in some cases, to automatically continue the observation although in a degraded mode.

The complexity of operations is on the other part efficiently implemented through a set of intercommunicating programs, each one dealing with one (or in the most complex cases, even only a part) of the many aspects of the REM activities.

Another advantage of the adoption of a modular organization of the tasks is that in case of software failure, only the corresponding module is affected, leaving all the other programs running, thus minimizing the risks deriving from such problems.

Figure 1 represents a general scheme of all the processes constituting the REM Observing Software. They can be divided into logic groups: management of dome, management of meteorology data, management of cameras, management of satellite alerts, management of the telescope, system logging and communication with home, and synchronization of all the operations. Each one of these units will be described in the following sections.

As a general idea, all the modules relate to a specific one, named the REM Manager (REMMNGR). This program collects the data coming from the other modules, processes all the relevant information, and takes a decision about the next operation to perform. The number of actions includes the following: observe new sources, evaluate the figure of merit for a GRB alert, and interrupt an ongoing observation as a response to a transient alert.

Figure 2 shows a block-diagram of the idle cycle of the REMNGR process. The system is continuously listening for new alerts. While no alert is received and the environmental conditions are good enough, a target selected from the accepted scientific programs is observed. As soon as a new alert is received, any possible ongoing observation is interrupted and the telescope is pointed towards the new source.

The complete list of all the processes together with a brief description is available in Table 1.

The vast majority of the modules have been implemented with the python language, with only few exceptions (REMSCHDLR, REMOBS) which are entirely written in ANSI C.

Despite the fact that most of the modules run on the same machine, communication among them is achieved through the TCP/IP protocol; in particular the YAMI [9] library has been chosen for its portability (it is available under all the most common OS), its availability for many common programming languages (C/C++, python, Tcl), its compactness, and for the low amount of resources required for running it.

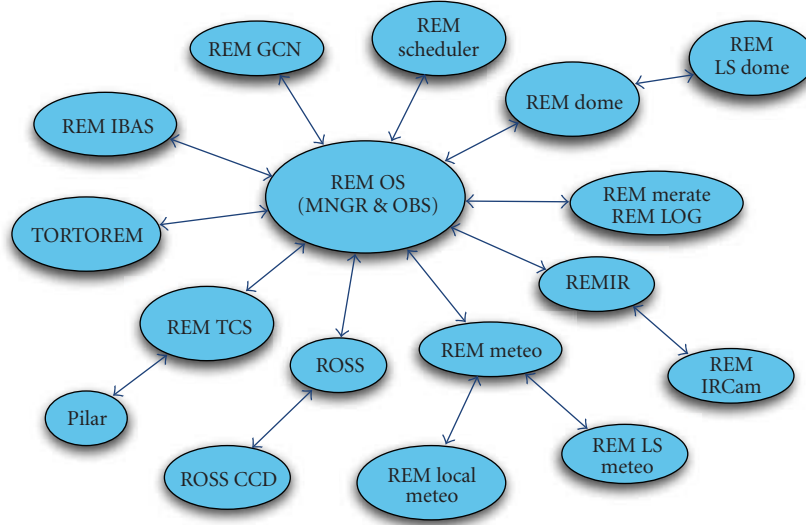


FIGURE 1: The set of all the REMOS processes can be organized into several groups: management of dome (REMDM, REMLSDM), management of meteorology data (REMMT, REMLSMT), management of cameras (REMROSS, REMIR), management of satellite alerts (REMGCN, REMIBAS, TORTOREM), management of the telescope (REMTCS), system logging and communication with home (REMMRT, REMLOG), and synchronization (REMMNGR).

TABLE 1: List of all the modules which constitutes the REMOS system.

Module name	Purpose
REMGCN	GCN network connection
REMIBAS	IBAS network connection
REMSCHDLR	Short-term scheduling of observations
REMDOME	REM dome management
REMLSDOME	Status of the La Silla domes
REMLOG	Logging management and alert routines
REMIR	NIR camera management
ROSS	Optical camera management
REMMT	Local environmental parameters management
REMLSMT	La Silla meteorological station connection
REMTCS	Connection with the Telescope Control System (TCS)
REMMNGR	General manager of operations
REMOBS	Drive ongoing observations
REMLR	Evaluation of the status of the low-level telescope software
TORTOREM	Communication with the TORTORA camera

5. Alert Management

Since one of the main features of REM is the ability of rapid reacting to satellite alerts, great care has been put into the management of all the kinds of alerts sent by the number of high-energy satellites available to date.

The main source of alerts is the GCN system. This system is in charge of providing alerts generated by the HETE II and Swift satellites. Communication with this system is achieved by the REMGCN process. This program encapsulates the always active socket server necessary to receive the different classes of messages dispatched by the GCN central engine over a TCP/IP network connection, and to communicate the receipt of the alert to the REM central

manager, which will chose its action depending on various parameters.

The other permanent source of alerts is the IBAS network, developed for the Integral satellite. The process in charge of keeping the communication with this system is REMIBAS; in this case, the socket connection follows the UDP standard and makes extensive usage of a public library developed by the Integral Team [10] and with whom REM also actively collaborated as beta tester.

Apart from merely listening for new alerts, both the modules above incorporate algorithms capable of detecting network failures and of recovering from these classes of problems, trying to reestablish the corresponding connection as soon as the conditions are restored.

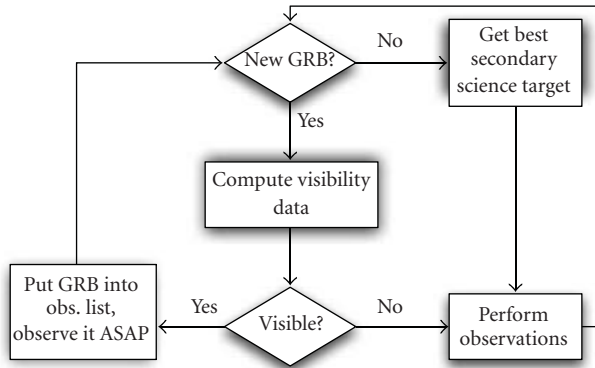


FIGURE 2: Block diagram of the idle cycle of REMNGR.

6. Source Observation

Since REM is now a national facility available to the scientific community, the common way REM operates is through the submission of a proposal for observation. The rapid reaction to satellite alerts is managed at this phase just as one of the observing modes offered by the telescope.

As a first step, the proposal submitted by the PI will be judged by the same INAF panel evaluating proposals for all the other Italian astronomical facilities, like the Telescopio Nazionale Galileo. Once the proposal has been accepted, for each required target a corresponding target is created and added to the queue. Here two processes are in charge of selecting which target to observe during a specific night at a given time: *OB manager* (REMOBS) and *short-term scheduler* (REMSCHDLR).

6.1. Target Archiving and Organization. The way the REM system manages the observation is through what is called *Observation Block* (hereafter OB). OBs are the unit of information for the observation and they can be considered as an adaptation of the ESO P2PP OB scheme. (The Phase II Proposal Preparation (P2PP) is an ESO program used to create and manage Observation Blocks for all ESO instruments.) As such, the information they carry can be organized into 5 categories: source type, telescope preset, instrument setup, observing conditions, and PI information.

The *source type* section contains data about the kind of target (e.g., if it is a star, AGN, GRB, etc.) and the origin of the target information (e.g., GRB alert, manual insertion of target, etc.). This influences the way targets are considered by the observing software; that is, they act as a first-level target priority.

Telescope preset data encapsulates all the relevant data needed, in the most general case, for deciding if pointing the telescope to the given position or not; in particular, this class of data includes information on Right Ascension and Declination, the equinox to which the coordinates refer and the error box of the coordinates. While this last parameter is generally not used for fixed, previously known objects, it is of fundamental importance for targets coming from satellite alerts. In fact, the central algorithm applies a figure of merit

on each alert which excludes from following those alerts whose error box is much bigger than the field of view of the REM cameras.

The way images are collected is defined in the *instrument setup* section. Here it is possible to define which sequence of filters to use, the exposure time, and the number of desired repetitions.

The conditions under which each target should be observed are organized in the *observing conditions* parameter set. These include both information on the sky conditions (like moon fraction, sky transparency, and airmass) and constraints on the allowed epoch during which the target should be observed. In addition, it is also possible to set a periodicity of observation and to link two or more targets in order to get them observed during the same night (grouped targets). Finally, each target is assigned a priority which drives the order in which targets are observed during the night. Section 6.3 explains in more detail this process.

After the completion of each observation, REM automatically informs the PI of the program via email with a preview of the acquired (for the optical camera) and prereduced (for the IR camera) images. The data necessary for this is stored in the *PI information* fields.

Each OB is initially ingested into a general PostgreSQL database physically located on a machine in Italy and duplicated on the corresponding machine in the dome. This database thus archives all the targets foreseen for the running public proposal period (AOT). A process, called REMOBS and described in the next section, has the duty of selecting, by putting them into a shorter archive, those targets which are best observable in the following 3–5 nights and which will be used by the short-term scheduling software to draw the night of observation schedule.

6.2. OB Manager. To make the scheduling operations of REM telescope easy, the REM team has developed a password protected interface that provides the insertion of an OB through a web form. This interface allows to perform the most common activities on the OB database, namely, list all the OBs currently in the archive, insert and remove OBs, and modify existing OBs (see Figure 3), in the view of a mid to long-term scheduling.

The main activities which can be executed through the web interface are as follows.

- (i) *Seasonal optimization*: this includes automatic selection of all and only OBs relevant for the ongoing AOT.
- (ii) *Syncopal scheduling*: although the short-term scheduler, presented in the coming section, is capable of allocating targets with a fixed periodicity during any number of nights, for some targets it may be advantageous to allocate them with nonconstant (syncopal) periodicities.
- (iii) The third one is the reallocation of already observed targets whose constraints were not properly satisfied during the execution.

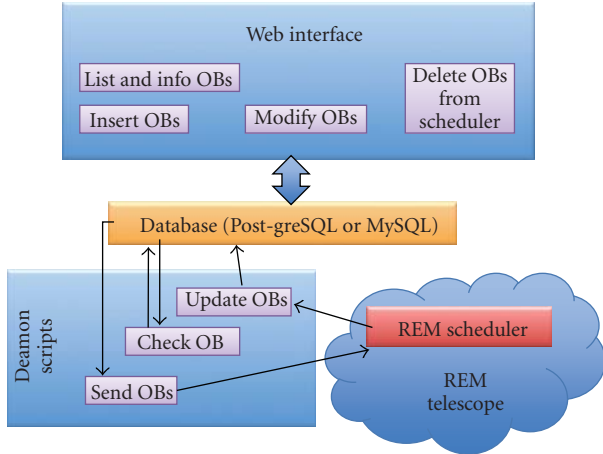


FIGURE 3: Schematic view of REMOBS operations.

The synchronization between the general and the local database is maintained by three processes (REMOBS_performed, REMOBS_send, and REM_ntimes), which are run daily in an automatic way through daemon scripts from the server located in Merate. The REMOBS_performed module is in charge of collecting all the information on the observations performed during the previous night, while the REMOBS_send sends the updated list of OBs to the local archive. Finally, the REM_ntimes process checks for synodal periodicities of the OBs and acts as *garbage collector* for the general archive, removing targets already observed a preestablished number of times.

The whole system is based on different perl scripts interfaced with a PostgreSQL database and Common Gateway Interface (CGI) library. The web form is dynamic and all the options are modified depending on the selected semester Call for Proposal. After inserting the password, the REM team can choose which interface to work with and the operation to use (see Table 2).

6.3. Short-Term Scheduling. The decision about the observation of any specific target during the current night is taken by the REMSCHDLR module. This process is called by the REMMNGR at the beginning of the night, before and after the observation of each target and every time a new target is inserted into the archive. The output of this process is an ordered and time-defined list of targets for the current night.

The REMOS system is able to automatically detect camera malfunctioning and this information is also intercepted by the scheduling software which can select in real time only those targets which do not need the temporary unavailable camera. A further benefit of having a dynamic scheduling against a static one, computed once at the beginning of the night, is that it allows to schedule targets which most take advantage of the changing sky conditions.

Figure 4 shows the block diagram of the central engine of the scheduler. The basic idea is to try to allocate each target when it is best visible, and respecting all the timing and visibility constraints, as defined by the user.

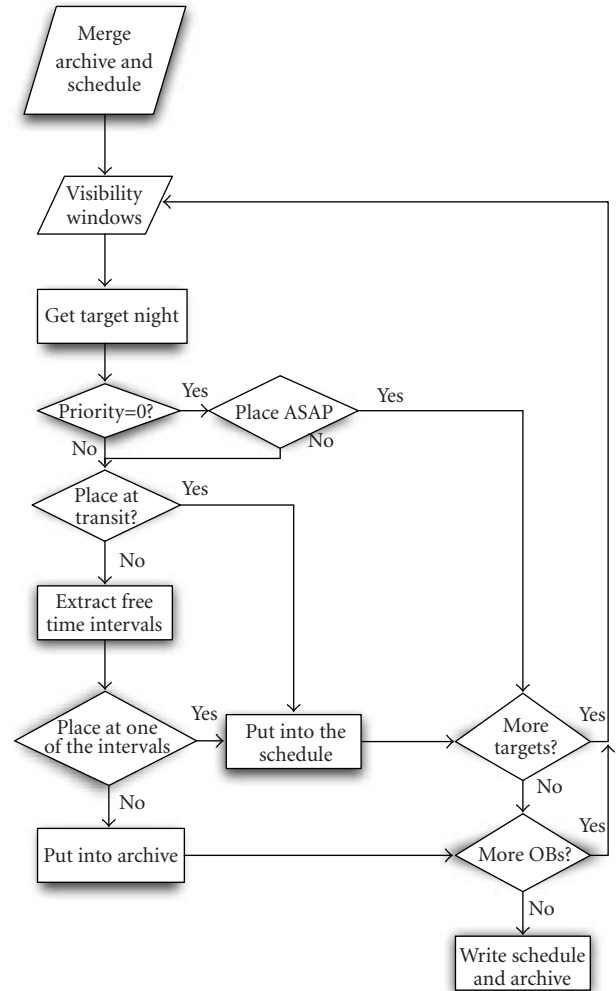


FIGURE 4: Block diagram of the REMSCHDLR core.

As a first step, the current short-term archive and schedule are merged and targets are sorted according to their priority. The algorithm then collects all the time intervals which are wide enough to allow the whole observation and which also satisfy all the visibility constraints. If the target has the highest priority, then the chosen time interval is the one which follows the *observe-as-soon-as-possible* strategy. This is the typical case for observations of GRBs whose location in the sky was not immediately reachable by the telescope at the time of the alert. For all the other priorities, the program sorts the collected time interval according to their distance from the time of transit through the meridian and tries to allocate the target starting from the interval closer to the transit time.

Starting from 2006 REM also accepts Target of Opportunity (ToO) requests. In the spirit of robotic operations, ToO is also completely managed in a fully unattended way. The activation of a ToO consists in an email sent by the PI to a machine located in the REM dome and containing all the information necessary to create the corresponding OB. A dedicated process then creates the OB in the archive; the

TABLE 2: The list of the possible operations with REMOBS interface.

Interface	Operation
List OBs	Visualize OBs status for the chosen programme.
Modify OBs	Modify OBs previously inserted for the chosen programme.
Insert OBs	Insert new OBs for the chosen programme.
Delete OBs	Delete OBs from REMSCHDLR.

schedule is computed as soon as the ongoing observation is completed and the target observed as soon as possible.

Apart from dealing with scientific targets, the scheduler is also capable of managing some classes of calibrations, namely, sky flat field, standard star fields, and focus fields. In these cases, the REMSCHDLR program only allocates the time for the observations, leaving the choice of the particular field to the REMFIELDS, REMSTD, and REMFCS, respectively, for the sky flat field, the standard star field and the focus field. In particular, flat fields are observed every morning, with the strategy left to each of the camera, although a typical session consists in taking 3 sky flats per filter; for standard stars are allocated once per night with 2 optical standards and one for the infrared and the focus field is observed once per night. The detailed strategy for focusing is explained in the next section.

6.4. Focusing. Good focus is a nontrivial task for a robotic facility; in the case of REM this is complicated by the fact that there are two cameras which observe at the same time and thus need to both have a good focus position. This is achieved through a double procedure.

- (i) The infrared camera focus is directly managed by moving the M2 mirror.
- (ii) Focus for the optical camera is adjusted via a series of neutral optical elements in the pupil and with different optical lengths, with the effect of shifting the focal plane.

Each night a set of 11 *focus frames* are taken, each one with a different M2 offset value, distributed around what is considered the best value. This set is then analyzed during the following morning and the focus value is obtained by fitting a parabola to the $3\text{-}\sigma$ clipped fwhm values of the star along the major and minor axis of the stellar image. The value obtained for the focus position is then archived in a database together with the environmental temperature; the full dataset contained in the database is finally used to update the parameters of the temperature-focus relation via a minimum χ^2 fit and after applying a $3\text{-}\sigma$ clip to the data.

Immediately before the beginning of each observation, the REMMNGR process sets the value of the focus position according to the environmental conditions.

As a further possibility, for the observation of very bright objects, the definition of a focus offset for source defocussing is also offered.

7. Cameras Management

Each camera is controlled by a dedicated computer (instrument machine) on which the low-level C/C++ software runs.

One of the most important features of REM is the ability to synchronize the observations with the two cameras. The synchronization is managed by the REMMNGR process which sends the relevant information to REMIR and ROSS modules, respectively. These two modules have a corresponding *twin* module on the instrument machine whose purpose is twofold.

- (i) Dispatch the observation information from and to the low-level software of the camera. In general, this includes sending the beginning of the observation, waiting for its completion and, in case an alert is received, sending an abort message to the camera, in order to stop the current observation and start the sequence which best fits the kind of source of the alert.
- (ii) Keep a constant check on the status of the camera. In case an erroneous state is detected, the main manager is immediately informed and subsequent operations are taken in accordance to the new status.

Being an external project, the impact on the software side of the TORTORA telescope is minimal, although necessary. The TORTOREM process is in charge of constantly informing the main TORTORA software about the ongoing observing conditions and in particular the position REM is pointing to and if a GRB alert is active.

8. Telescope Control System

The intermediate and low-level controls of the telescope are provided by the *Pilar* software, produced by the German company 4PI Systems GmbH and running on a dedicated machine. This software provides a socket server with all the high-level commands necessary to point the telescope to a given coordinate set, start/stop the tracking of the telescope, and move the derotator to the desired angle.

Similarly to the way communication with the cameras is implemented, also for the telescope control system a dedicated process, REMPILAR, runs on the telescope machine. This python-written module both manages the communication of the commands to and from the Pilar server and it also periodically checks that Pilar is correctly running. When this is not the case, the module automatically tries to restart Pilar and, if after a number of attempts the problem still persists, it sends an email informing the team of the problem;

an analogous algorithm is implemented by REMPLR also for the detection of the general telescope safety activation which may occur when local technicians from the observatory need to access the telescope for routine mechanical and cryogenic maintenance.

9. Meteorology

The acquisition and analysis of weather conditions is one of the fundamental activities to keep the observatory in a safe status, especially when operations are managed in an autonomous way.

REM is continuously checking meteorology data coming from two distinct sources; in fact, apart from having its own meteorology station, it can also access the data of La Silla weather station. To this aim, the two processes REMLSMT and REMMT are collecting data every 5 minutes, respectively, from La Silla meteorology data and the REM local station. These processes are in charge of merely collecting the data, leaving the decision process to the central engine of the system, that is, the REMMNGR tasks.

The possibility of accessing an external, but still local, meteorology station, like the one of La Silla, has a double advantage: on one side it provides an independent estimate of the meteorological conditions and on the other side it offers the necessary level of redundancy in case of failures of the REM local station.

The local weather station is a Davis Vantage Pro device, with sensors measuring the temperature and humidity inside and outside the dome, the wind speed, and direction and the rain rate.

For weather conditions being considered safe, both REMLSMT and REMMT processes implement the following limits which must be satisfied at the same time.

- (i) Rain rate must be zero.
- (ii) Wind speed must stay below 15 m/s.
- (iii) The relative humidity inside and outside the dome must be below 90%.

The decision algorithm implemented in the REMMNGR considers meteorological conditions as safe for operations if the above limits are entirely respected by at least one of the two sources of information.

10. Dome

Since the telescope does not implement any kind of protection for the primary mirror, the dome is the only way the REM observatory has to keep its instrumentation safe from environmental conditions. Great care has thus been put in the algorithms which control its opening and closing phases. Furthermore, the design of the dome is such that it is possible to open and close it without the need of having the telescope in a particular position, assuring the fastest reaction to sudden changes of weather conditions.

In addition to the constant check of the meteorology conditions, the REM system relies on the status of the domes of the other telescopes at La Silla. The REMLSDOME module is

in fact able to gather the data about the opening status of the ESO DIMM, NTT, 3p6, 2p2, and the Swiss Heuler telescopes.

A figure of merit based on the status of the above telescopes is then applied in order to establish if the REM dome can be opened. Apart from satisfying the meteorological constraints described in the previous section, the REM dome can be opened when.

- (i) the DIMM protection is open;
- (ii) at least another dome appears as open.

As a last aid to the safety of the telescope, if, for any reason, the REMLSDOME process can not access the status of La Silla dome, then the REM dome is kept closed and everything is automatically resumed as soon as the status can be accessed again.

11. GPS and Time

The accuracy of time measurement is a fundamental issue for a robotic observatory like REM for two reasons. In fact, a correct timing not only is essential for an accurate pointing and tracking of the telescope but also has a scientific value.

The ability of rapidly reacting to satellite alerts for astrophysical processes whose typical times are of the order of few seconds means that the information stored together with the observations must allow to perform an as much accurate as possible timing analysis of the phenomenon itself. Hence information such as the time of the reception of the alert and the time of beginning and end of each observation must reflect this need.

To satisfy the need of accuracy, the REM observatory adopts a double source for time synchronization. On one side, the GPS antenna installed on the external wall of the dome provides an accurate time signal through the *Pilar* program. On the other side, all the machines in the dome are synchronized to the La Silla time server via the *Network Time Protocol*. On top of these two methods, the module REMGPS continuously checks that the time provided by the GPS antenna is compatible with the one on the computers. In case a difference greater than 8 seconds is found, the process sends an email to the team informing of the problem.

This procedure already allowed to discover, and correct, an anomaly with the GPS antenna.

12. System Data Logging

Although the software system implements many algorithms which allow to limit the operations in case of problem and, for the best cases, also to automatically recover from an error state, a detailed system logging is fundamental tool of diagnosis for all the other cases.

Each REMOS process sends its logging information to a central module, the REMLOG, which locally archives the log data and immediately also duplicates it to an external server located in Merate, Italy.

Another fundamental aspect is the supervision of all the parameters of the instruments and of the telescope, that is, the *system telemetry*. The *tREMometer* (see Molinari et al.,

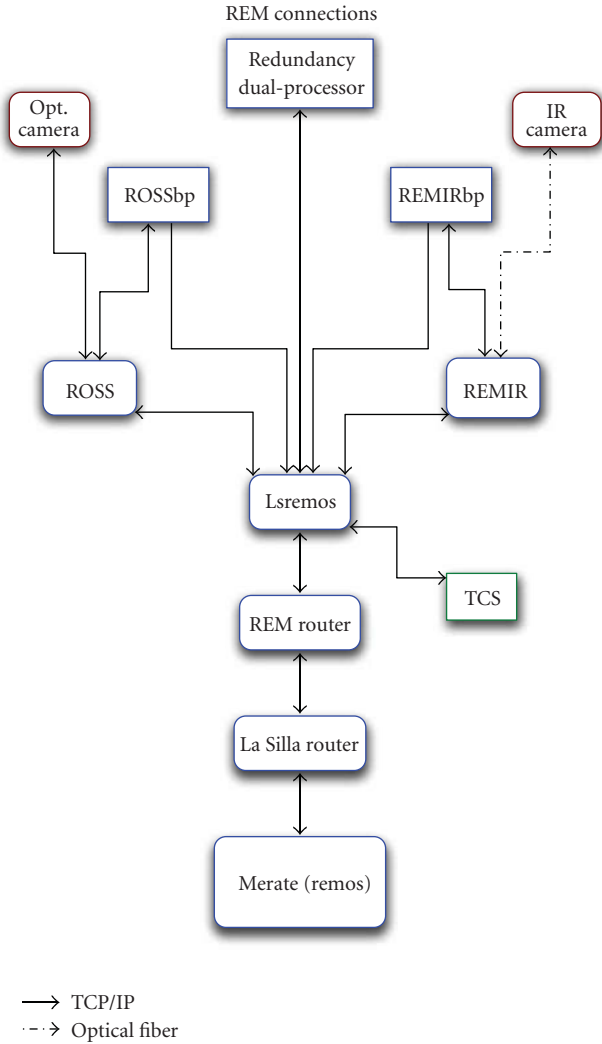


FIGURE 5: Organizational chart of the REM local network.

this issue [11]) is an articulated software which checks the status of the instruments and of the REM software and generates a publicly available almost real-time resume.

13. System Hardware

Figure 5 shows the organization of the running hardware inside the dome. The REMOS software has demonstrated to be capable of being easily run on commercial machines, which makes maintenance an easy task.

Most of the modules run on the same machine, an AMD i686 single processor with Linux Fedora 8. The optical and infrared camera are managed by a dedicated dual processor each, to grant the speed necessary for the real-time prereduction pipelines.

Communication with serial devices is implemented through two MOXA devices, which provide an ethernet access to serial ports.

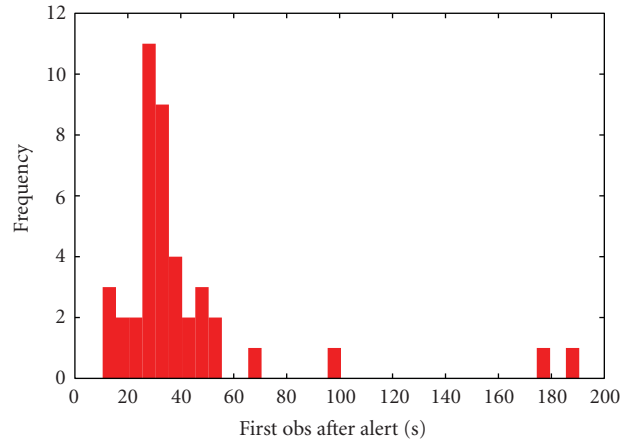


FIGURE 6: Histogram of the time necessary to REM to point a new GRB alert. The median time is of 30 seconds.

14. Results and Conclusions

Figure 6 shows the histogram of the pointing time for all the GRB alerts received by REM in 2007. The median value is 30 seconds; this value mostly raises during the accelerating and decelerating phases of the pointing. This result is a confirmation that, on the software side, a strict real-time implementation is not necessary, being most of the dead-time on the electromechanical part.

To date, more than 100 GCN have been published reporting prompt observation of GRB made automatically by REM. This is also made possible by the high level of stability reached by the whole software operating the telescope.

In this article the software managing the observations of the REM telescope has been presented. The requirement of autonomously reacting to satellite alert together with the necessity of synchronizing the observations of two independent cameras makes the software requirements more demanding than in other cases. The strategy for the implementation was to keep as much separate as possible the distinct kinds of operations of the telescope. The results obtained so far by REM are the clearest proof of the effectiveness of the adopted solutions.

Acknowledgment

The authors wishes to thank Maciej Sobczak for providing the YAMI library and for his continuous support to it.

References

- [1] F. M. Zerbi, G. Chincarini, and G. Ghisellini, "The REM telescope: a robotic multiwavelength facility," in *Ground-Based Instrumentation for Astronomy*, A. F. M. Moorwood and M. Iye, Eds., vol. 5492 of *Proceedings of SPIE*, pp. 1590–1601, Glasgow, UK, June 2004.
- [2] G. Chincarini, F. Zerbi, A. Antonelli, et al., "The last born at La Silla: REM, the rapid eye mount," *The Messenger*, vol. 113, pp. 40–44, 2003.

- [3] S. Covino, M. Stefanon, and G. Sciuto, “REM: a fully robotic telescope for GRB observations,” in *Ground-based Instrumentation for Astronomy*, A. F. M. Moorwood and M. Iye, Eds., vol. 5492 of *Proceedings of SPIE*, pp. 1613–1622, Glasgow, UK, June 2004.
- [4] P. Conconi, R. Cunniffe, F. D’Alessio, et al., “The commissioning of the REM-IR camera at La Silla,” in *Ground-Based Instrumentation for Astronomy*, A. F. M. Moorwood and M. Iye, Eds., vol. 5492 of *Proceedings of SPIE*, pp. 1602–1612, Glasgow, UK, June 2004.
- [5] F. Vitali, F. M. Zerbi, G. Chincarini, et al., “The REM-IR camera: high quality near infrared imaging with a small robotic telescope,” in *Instrument Design and Performance for Optical/Infrared Ground-Based Telescopes*, M. Iye and A. F. M. Moorwood, Eds., vol. 4841 of *Proceedings of SPIE*, pp. 627–638, Waikoloa, Hawaii, USA, August 2002.
- [6] G. Tosti, M. Bagaglia, C. Campeggi, et al., “The REM optical slitless spectrograph (ROSS),” in *Ground-Based Instrumentation for Astronomy*, A. F. M. Moorwood and M. Iye, Eds., vol. 5492, pp. 689–700, Glasgow, UK, June 2004.
- [7] Grigory Beskin, Sergey Bondar, Sergey Karpov, et al., “From TORTORA to MegaTORTORA—Results and Prospects of Search for Fast Optical Transients,” *Advances in Astronomy*, vol. 2010.
- [8] S. Karpov, et al., “Wide and fast monitoring the sky in subsec domain,” *Advances in Astronomy*. In press.
- [9] M. Sobczak, “YAMI: a simple orb library,” *C/C++ Users Journal*, vol. 21, 2003.
- [10] D. Cremonesi, S. Mereghetti, and J. Borkowski, “The INTEGRAL burst alert system,” in *Gamma-Ray Bursts in the Afterglow Era*, F. Frontera, E. Costa, and J. Hjorth, Eds., p. 434, Springer, New York, NY, USA, 2001.
- [11] E. Molinari, et al., “REM: automatic for the people,” *Advances in Astronomy*. In press.

Research Article

REM: Automatic for the People

**Emilio Molinari,^{1,2} Stefano Covino,¹ Francesco D'Alessio,³ Dino Fugazza,¹
Giuseppe Malaspina,¹ Luciano Nicastro,⁴ Mauro Stefanon,⁵ Vincenzo Testa,³
Gino Tosti,⁶ and Fabrizio Vitali³**

¹ INAF-Osservatorio Astronomico di Brera, Via Bianchi 46, 23807 Merate, Italy

² INAF-Telescopio Nazionale Galileo, Rambla José Ana Fernández Pérez, 7 38712 Breña Baja, Spain

³ INAF-Osservatorio Astronomico di Roma, Via di Frascati, 33 00040 Monte Porzio Catone, Italy

⁴ INAF-IASF Bologna, Via Gobetti 101, 40129 Bologna, Italy

⁵ Observatori Astronòmic de la Universitat de València, Edifici Instituts d'Investigació, Polígon La Coma,
46980 Paterna, València, Spain

⁶ Dipartimento di Fisica, Facoltà di Scienze MM. FF. NN., Università degli Studi di Perugia, Via A. Pascoli, 06123 Perugia, Italy

Correspondence should be addressed to Emilio Molinari, molinari@tng.iac.es

Received 16 June 2009; Revised 27 November 2009; Accepted 18 December 2009

Academic Editor: Alberto J. Castro-Tirado

Copyright © 2010 Emilio Molinari et al. This is an open access article distributed under the Creative Commons Attribution License, which permits unrestricted use, distribution, and reproduction in any medium, provided the original work is properly cited.

We present the result of a year-long effort to think, design, build, realize, and manage the robotic, autonomous REM observatory, placed since June 2003 on the cerro La Silla, ESO Chile. The various aspects of the management and control are here surveyed, with the nice ideas and the wrong dead ends we encountered under way. Now REM is offered to the international astronomical community, a real, schedulable telescope, automatic for the People.

1. Half a World Away

REM (Rapid Eye Mount) was thought and realized in order to catch fast optical and infrared transient phenomena, correlated with high-energy events signaled by orbiting observatories, mainly GRB discovered by then recently launched Swift satellite. Its realization resulted in a workbench for various other existing and wish-list telescopes [1–3] (see also <http://www.rem.inaf.it/>).

The statistics of pre-Swift bright GRB optical transient led to a 60 cm diameter telescope, equipped with VIS/IR cameras, fast enough to follow Swift acrobatics and to acquire images, process them fast, and detect the transient with good accuracy to alert larger telescopes' spectrographs. We decided, in order to put it far from existing or proposed robotic telescopes, half a world apart in the southern hemisphere, on the Chilean Andes in the ESO site of La Silla.

2. Losing My Religion

In order to fulfill the requirements the telescope should have had the capabilities to react immediately to alerts, see the

afterglow of the GRBs, and classify it to estimate the redshift by photometry. To this extent the mechanics of the telescope should have been robust and fast enough, the size of the mirror should have been large enough, and the photometry was needed in both visible and infrared. On the software side we should be able to control the telescope, command both cameras and analyze the images, and at the end also alert the rest of the world. Were we good at this? Unfortunately the belief that GRB afterglows were bright enough for our chosen size of 60 cm as primary mirror revealed false, and the mean, dim luminosity of the transients de facto prevented REM, as most of the other robotic telescopes of the same class, to observe a large fraction of the afterglows following Swift satellite alerts. In those early times, before we could enhance the REM pointing capabilities to observe down to 5 degrees above horizon, only 5% of the GRB alerts could be reached by REM pointing. Our lack of ability to detect precise coordinates in due time also led to abandon the finalization of the transient detection and alert software, which remained at the still remarkable level of producing automatic astrophotometry for good quality images.



FIGURE 1: The REM Observatory: *one dome, two telescopes, three instruments*. Under the main telescope body is the Tortora telescope with its wide field, fast photometer. On the left Nasmyth focus the are the visible (ROSS) and infrared (REMIR) cameras, partially hidden in the photo.

The robotic nature also revealed to be somewhat tricky and we had to add to our system a full self-telemetry of vital signal of the various subsystems which was also able to send SMS and e-mail to real people. A team of trained real people on-site was also required and we received the help and collaboration from ESO-La Silla technical staff, which is now able to intervene in case of need or emergency.

After we added the funded possibility to use REM as a laboratory for new technologies and finally offered the nonalert time to the astronomical community via the classical systems of call for proposals, we finally completed the REM Observatory, working regularly and autonomously every night since 4 semesters (a full photo in Figure 1).

3. All the Right Friends

The companies and developers involved in the REM realization were both from the private industry and from public research institutions. Halfmann Teleskoptechnik designed together with our group the telescope body and main reflecting Zeiss optics, coated by Sagem with protected silver to enhance the performances in the infrared. The main near infrared REMIR camera [4, 5] was designed by the gOlem group of the Brera Astronomical Observatory and assembled in the US-based Infrared Lab. An engineering Hawaii I chip from Rockwell was used in its best quadrant, with 512×512 pixels on a 10×10 arcmin field of view. The visible camera and spectrograph ROSS [6], also designed by gOlem, hosts SILO optics in a mechanical assembly manufactured by Perugia University and Brera Observatory workshops. The same field of view of REMIR is imaged by means of ZaoT coated dichroic with a 1 m cut on a 1 K \times 1 K ALTA camera by Apogee. In Figure 2 the same field of view is observed with both cameras.

4. Daysleeper

The REM dome is positioned in the ESO La Silla premises and can profit of all the (still, at date of writing) existing infrastructures and facilities. ESO provides power, UPS, and network connections, as well as liquid nitrogen refilling every 4 days. In every assembling phase the availability of a mechanical workshop and a clean room for the infrared detector assistance proved to be essential and both time sparing and mission proved to be critical.

The dome realization was performed by ESO general services and has two sliding roof which leave completely clear the sky without the need to have any movement during the observations (see a CAD rendering in Figure 3). Notre Dome opens when the Sun is below the horizon and all the safety parameters are within the limits; otherwise the telescope room is air conditioned and telescope parked in home position. The temperature inside the dome follows nevertheless the day/night cycle and a better thermal insulation would be required. The inner relative humidity never hits the excess of outer values and no dew point conditions were so far recorded. We finally rely on ESO and local meteorological measurements to define safety conditions. Humidity below 90%, wind speed lower than 17 m/s, external temperature above 0°C , and Sun below horizon are the main safety parameters, although a check on the open status of other domes in the La Silla site revealed to be a good choice, so that we will perform normal operations only when two other telescopes are observing.

5. Imitation of Life

The way REM acts is badly an imitation of autonomous machine. It needs a daily check from Italy in order to catch in with its many unforeseen situations and also, although now rare, unrecoverable stops in its sequences of jobs. In fact, we experienced some dome blockings, few main computer crashes and network halts, as well as some CCD driver timeouts. Many of these we recovered by remote commands but in some cases we had to wait for human help in La Silla.

Nevertheless its main sign of activity is the reaction to inputs. The main information flux starts from the Observing Block Scheduler which enters in the REM Observing Software (REM-OS, cfr. Stefanon et al. in this volume [7]) the sequence of targets, which is reorganized should a GRB alert or other boundary conditions occur (e.g., high airmass due to delayed observations). The flux eventually ends delivering a series of outputs: the raw data and processed photometric catalogues are immediately sent to the Bologna REM database, where PIs can retrieve their data and the general public can browse the complete observing log and retrieve all calibrations and standard stars. In the meantime a continuous cross-talk between REM-OS and the in situ internal telemetry database as well as the controls of telescope and cameras allow the images to be acquired safely.

A series of (mainly) python programs run autonomously in the various machines in the dome to get the status of the sensors, encoders, and so forth, and fill the proper SQL tables in the REM-OS machine.



FIGURE 2: NGC3606 imaged by the REM cameras. (a) The color composite of the REMIR J, H, and K filters. (b) Photo the composition of the ROSS V, R, and I images.

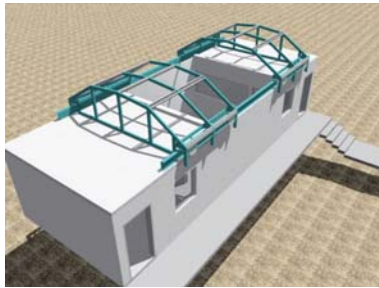


FIGURE 3: *Notre Dome de La Silla* as designed by ESO. A control room and a warehouse complete the REM building. An IP subnet is reserved for the REM operations and internet access is controlled by ESO internal firewalls. Its sliding roof is also used as a crane to mount and dismount instrumentation.

The control python program is the tREM-o-meter which runs every 2 minutes. The tREMometer collects the relevant data from archive, fills in the missing values, produces a public web page with the status of the telescope and all subsystems and performed observations, and, finally, checks for malfunctions and sends e-mail and SMS alerts. In case the conditions become dangerous in the infrared Dewar (the most delicate area), it is able to autonomously interrupt all IR data acquisitions. We in fact allow a small range in IR chip temperature as safe operational range: should the sensor get heated more than 105 K, the IR camera is turned off, returning to normal operations only after its temperature is lower than 100 K.

6. Until the Day Is Done

The information you can see in the tREMometer well summarizes the observatory life cycle. In Figures 4 and 5 we show the tREMometer content and the capability of the REM observatory in operation.

Figure 4 at a glance gives to the human control people the instant situation of the alarm status (checking temperature and pressure in the infrared Dewar and also the telescope

control hardware for failure to respond to Remos command) and the job REM is actually performing in the night. The scheduled targets are listed in the sequence they will be observed. Such schedule is continuously recomputed after every observation because the optimal conditions for the next target may be affected by some misbehavior during the last acquisition (delays, repeated frames, etc.). When the night is done, all blue dots will disappear and soon a new schedule for the next day is arranged. After every observing night every PI involved in recent observations is noticed by an automatic e-mail from the REM archive.

The monitoring of the dome opening together with shutter-open time of every acquired image is the content of Figure 5. The La Silla domes monitoring proved essential to the security of the REM operations, as we ended opening the dome only when our meteo station gives good measures, as well as the ESO one, and two other domes are open in the site. We are thus able to produce independent meteo statistics for the ESO La Silla site as well as our own efficiency rate (Figure 6).

Other plots in the tREMometer include the status of the cryostat, temperatures, and meteo data from REM meteo station. Also, the program offers a Gantt graph of the past night, allowing the REM team to check for inconsistencies in the programmed observations. The degraded, small image previews are then posted on the web site for PI and public access.

During the following morning, every PI whose observations were continued in the previous night receives a detailed e-mail directly from the database in Bologna.

Furthermore, the Remos machine produces weekly reports which are sent to a restricted set of people: first, a report on a 4-month timeline of the pressure in the REMIR Dewar and the daily consumption of the liquid nitrogen supply. These are very useful to program mid term maintenance, such as repumping the vacuum in the cryostat and in the nitrogen lines.

The last information sent by the Remos system is the status of the observing programs accepted by the Italian Time

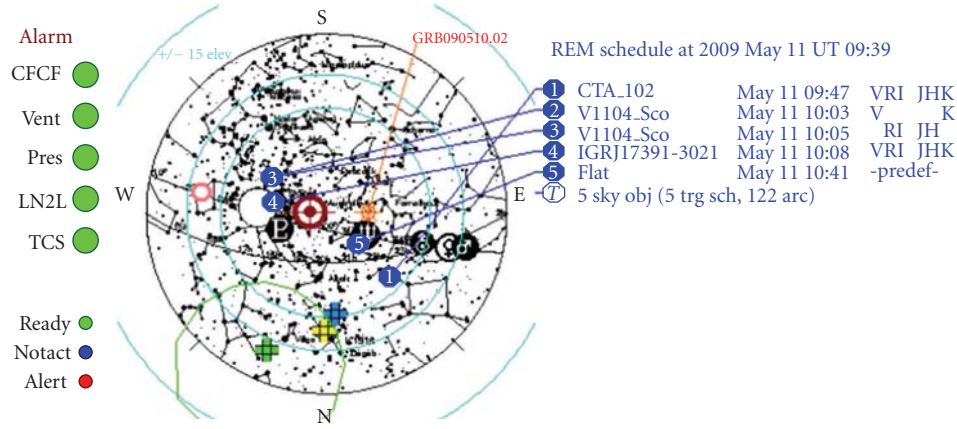


FIGURE 4: *tREMometer* first glance at <http://www.ls.eso.org/lasilla/rem/> offers the alarm status (on the left, here all is green and working) and the working night sky over La Silla. All remaining targets for the night, listed on the right, are positioned in the sky hemisphere as blue, numbered dots. Other important information includes the actual telescope pointing, the Swift (green), INTEGRAL (yellow), and AGILE (cyan) current pointing. Also the position of the last alerted GRB (orange) is shown.

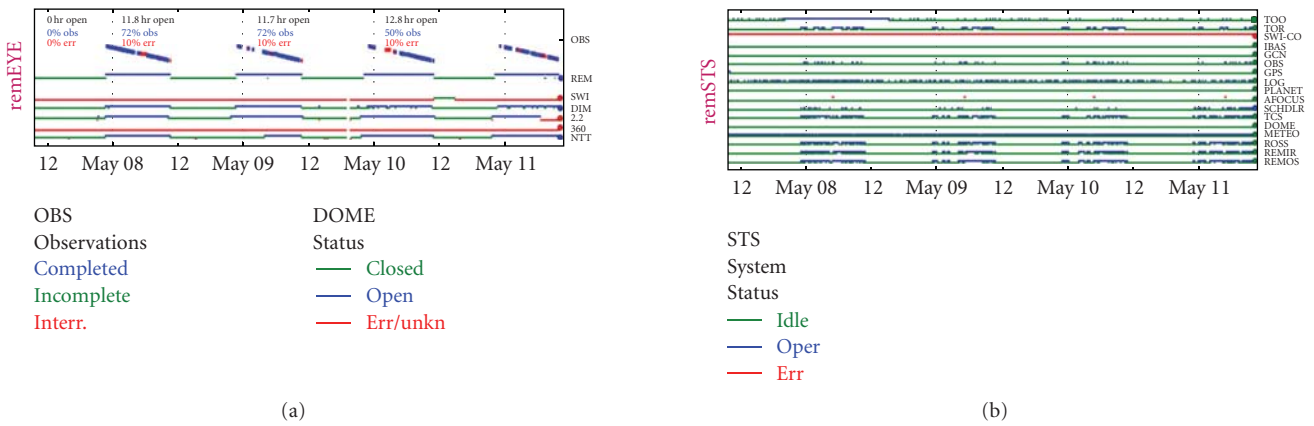


FIGURE 5: (a) The status of every dome in La Silla is monitored and is used as one of the safety parameters we include in our opening decision algorithm. Also an automatic statistics is computed after each night in order to keep track of real night length (useful for meteo + technical downtime statistics) as well as the effective use of the open time. Percentages report shutter-open time in the night. Errors (in red) are noncompleted observing blocks that need to be repeated. (b) The log of every subsystem status.

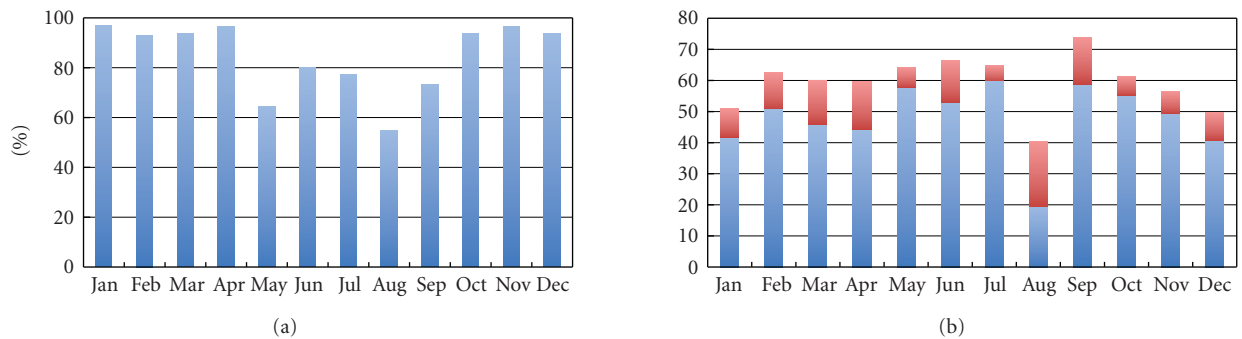


FIGURE 6: La Silla good nights of year 2008. (a) The percentage of nights with more than 6 hours of opening for REM dome: it may be considered very close to good weather nights in La Silla. (b) The shutter-open time percentage for REM cameras: red portions are the Observing Blocks ending with some error status which are to be repeated. No overheads have been included in this plot. The month of August included a two-week maintenance mission which makes those data inconsistent.

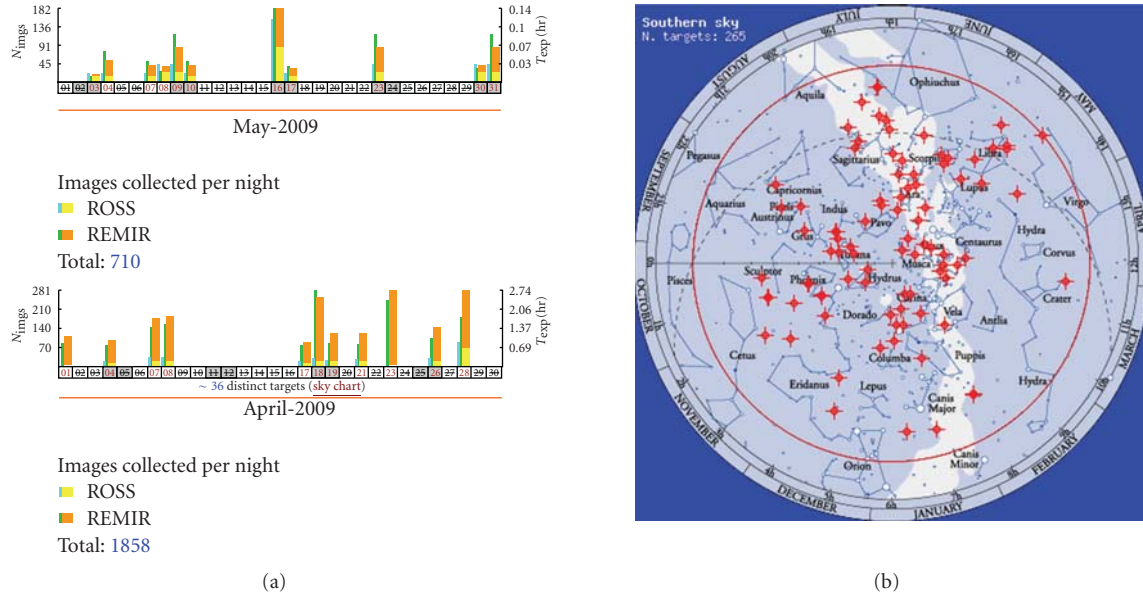


FIGURE 7: The REM archive browser allows PI and general public to select and retrieve observed targets. A limited statistical analysis can be performed on the fly: on the upper part of (a) all the flat field frames in the month of May 09, in the lower part of (a) the GRB observations during April 09. The sky chart on (b) the position in the southern hemisphere of all GRBs in the year 2008.

Allocation Committee, allowing to follow the completion of the requested observations. In the last completed call (AOT18) all programs were well above 80%, not counting the ToO which did not use all their time.

7. 1 000 000

The final repository for all the REM images is the REM Archive in Bologna. After an image is written on disk in Chile by the cameras, it is processed for quick astrophotometry and then sent to the database together with other data. In May 2009 the number of entries in the archive overcame 1 000 000. The archive web browser allows identified users to use a password layer to access their private data as well as all the public calibration frames.

Various preset types of query can be used to select and then retrieve the wanted images, and as well a custom SQL WHERE clause may be entered by the user.

It is also possible to perform basic on-line analysis on the observations, grouping by date or type, and showing the object position on the sky as shown in Figure 7.

Among the 1 million images many have found their place in high ranked scientific papers, both in GRB science [8] and in other topics such as blazars [9]. In fact, even if GRBs are fainter than thought, the fast reaction time of REM allowed us to observe the onset of the infrared afterglow, leading to the measure of the expansion velocity of the fireball. The mean elapsed time for REM observing after a satellite alert is 30 seconds as shown in [7] and the time resolution can be as fast as 1 second when the afterglow is bright enough.

8. Everybody Hurts

Even the most exciting project comes to a regime cycle that can hurt the creativity of a research group. REM Team

to avoid becoming a managing and maintenance unit for yet another telescope turned the REM observatory into a working laboratory for experimenting new devices.

The first was the change in cooling system for the REMIR camera. The on-board Stirling cryocooler by Leibold Vacuum presented a series of problems ending in a serious instability of the system. The main problem was the underdimensioned power for our heat removal needs, but the Leibold company itself admitted that the maintenance of such cryocooler was so difficult that at the end they dismissed the production. Thus we adopted an ad hoc modified Continuous Flow Cryostat, a cryogenics system developed by ESO and extensively used in ESO instrumentation, whose main characteristic is that the LN2 vessel is separated from the cryostat, allowing a greater LN2 tank, then really improving the hold time [10]. We are now able to run continuously the telescope with one LN2 tank change every 4/5 days. In normal conditions this is the only human intervention REM needs to work.

A completely new experiment was also conceived in collaboration with IASF-Bologna, University of Bologna and SAO (Russia). TORTORA [11, 12] is a separated telescope hosted in parallel to REM, mechanically fixed in the same mount (see Figure 1). The aim was to study short stochastic optical flares of different objects (GRBs, SNs, etc.) of unknown localization. To this purpose it is necessary to monitor large regions of sky with high time resolution and we developed a wide-field camera (FOW is 400–600 sq.deg.) using TV-CCD with time resolution of 0.13 second to record and classify optical transients. The photometer can reach mag 10.5 in one single 0.13 second exposure. Together with REM cameras it forms the telescope complex TORTOREM, operated from May 2006 by the joint teams of REM and SAO. The main result was the serendipitous observation of

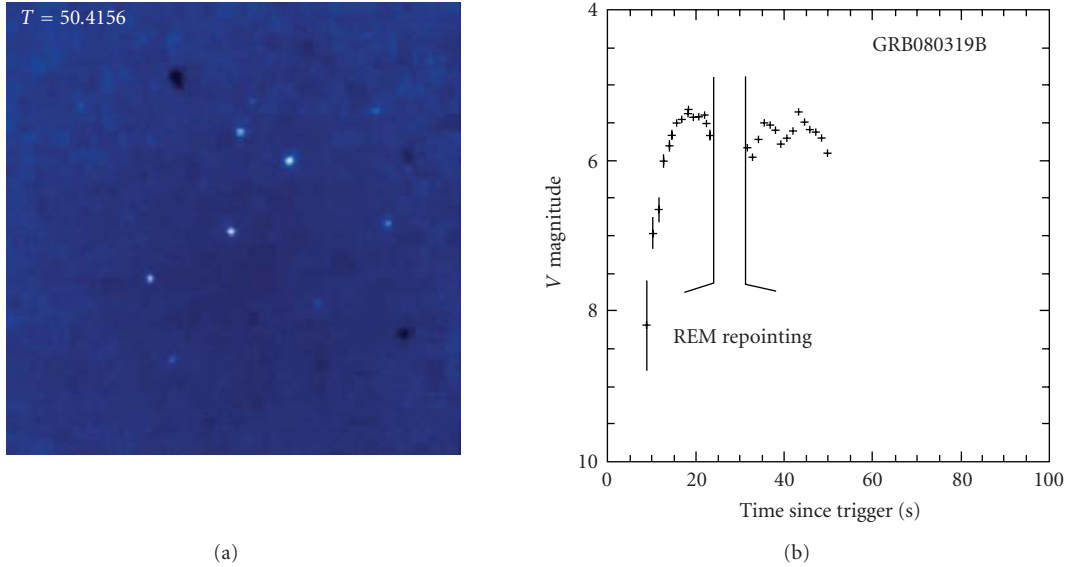


FIGURE 8: (a) A subframe of the wide field image centered on the optical transient 50 seconds after Swift trigger. The light curve (b) of GRB080319B measured by the TORTORA camera.

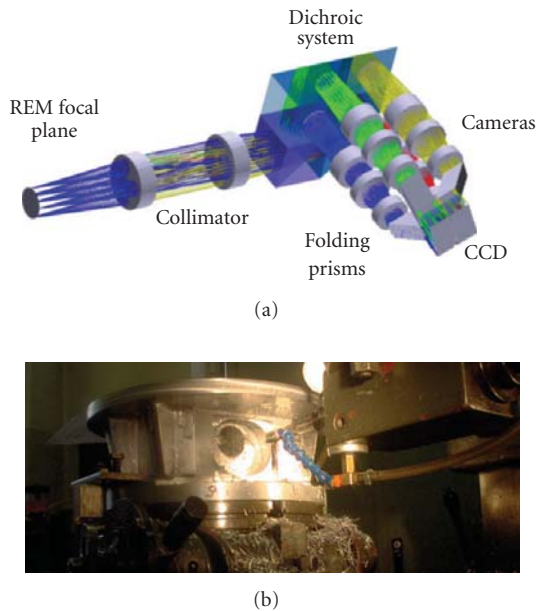


FIGURE 9: (a) ROSS2 visible camera optical layout: 4 separated images in four passbands will be recorded on a single $2K \times 2K$ CCD. (b) The manufacturing of the mechanical interface for ROSS2 and REMIR.

GRB080319B, a naked-eye burst whose light curve could be monitored in high time frequencies [13] as reported in Figure 8.

The future step of the REM lab will be the complete replacement of the optical camera ROSS. ROSS2 will have better optical quality which revealed not being optimized in the present camera and will produce 4 simultaneous images in the Sloan passbands g' , r' , i' , and z' . Figure 9 sketches the optical design which makes heavy use of dichroics.

9. The Great Beyond

The experience of this project will not be lost. Our team is now deeply involved in the conceptual design of a 4-meter class telescope which will have a simultaneous camera like ROSS2 which extends into the infrared up to K' band. Its response time after alerts will be comparable with REMs, aiming to the target within well under one minute [14]. Its capabilities will be coupled with a battery of wide field, fast photometer telescopes which in principle should cover the whole sky or a great portion of it and be able to generate alerts instead of reacting to satellites.

Acknowledgments

The authors acknowledge the effort from all people which made REM possible; in particular the four ESO musqueteers in La Silla which helped and collaborated with them since the beginning and without their skill the project could have been in serious troubles. Also, they thank the American rock band R.E.M. for their prophetic song titles which have been used in this article.

References

- [1] F. M. Zerbi, G. Chincarini, G. Ghisellini, et al., "The REM telescope, a robotic multiwavelength facility," in *Ground-Based Instrumentation for Astronomy*, A. F. M. Moorwood and M. Iye, Eds., vol. 5492 of *Proceedings of SPIE*, pp. 1590–1601, Glasgow, UK, June 2004.
- [2] G. Chincarini, F. Zerbi, A. Antonelli, et al., "The last born at La Silla: REM, The Rapid Eye Mount," *The Messenger*, vol. 113, pp. 40–44, 2003.
- [3] S. Covino, M. Stefanon, G. Sciuto, et al., "REM: a fully robotic telescope for GRB observations," in *Ground-Based Instrumentation for Astronomy*, A. F. M. Moorwood and

- M. Iye, Eds., vol. 5492 of *Proceedings of SPIE*, pp. 1613–1622, Glasgow, UK, June 2004.
- [4] P. Conconi, R. Cunniffe, F. D'Alessio, et al., "The commissioning of the REM-IR camera at La Silla," in *Ground-Based Instrumentation for Astronomy*, A. F. M. Moorwood and M. Iye, Eds., vol. 5492 of *Proceedings of SPIE*, pp. 1602–1612, Glasgow, UK, June 2004.
 - [5] F. Vitali, F. M. Zerbi, G. Chincarini, et al., "The REM-IR camera: high quality near infrared imaging with a small robotic telescope," in *Instrument Design and Performance for Optical/Infrared Ground-Based Telescopes*, M. Iye and A. F. M. Moorwood, Eds., vol. 4841 of *Proceedings of SPIE*, pp. 627–638, August 2002.
 - [6] G. Tosti, M. Bagaglia, C. Campeggi, et al., "The REM optical slitless spectrograph (ROSS)," in *Ground-Based Instrumentation for Astronomy*, A. F. M. Moorwood and M. Iye, Eds., vol. 5492 of *Proceedings of SPIE*, pp. 689–700, Glasgow, UK, June 2004.
 - [7] M. Stefanon, et al., "The REM observing software," accepted in *Advances in Astronomy*.
 - [8] E. Molinari, S. D. Vergani, D. Malesani, et al., "REM observations of GRB060418 and GRB060607A: the onset of the afterglow and the initial fireball Lorentz factor determination," *Astronomy & Astrophysics*, vol. 469, no. 1, pp. L13–L16, 2007.
 - [9] A. Giuliani, F. D'Arrimando, S. Vercellone, et al., "AGILE observation of a gamma-ray flare from the blazar 3C 279," *Astronomy and Astrophysics*, vol. 494, no. 2, pp. 509–513, 2009.
 - [10] F. Vitali, J. L. Lizon, G. Ihle, et al., "The REMIR cryogenics restyling," in *Ground-Based and Airborne Instrumentation for Astronomy*, I. S. McLean and M. Iye, Eds., vol. 6269 of *Proceedings of SPIE*, Orlando, Fla, USA, May 2006, 626954.
 - [11] S. Karpov, et al., "Wide and fast monitoring the sky in subsec domain," accepted in *Advances in Astronomy*.
 - [12] E. Molinari, G. Beskin, S. Bondar, et al., "Ground-based complex for detection and investigation of fast optical transients in wide field," in *Ground-Based and Airborne Telescopes II*, L. M. Stepp and R. Gilmozzi, Eds., vol. 7012 of *Proceedings of SPIE*, Marseille, France, June 2008, 70122S.
 - [13] J. L. Racusin, S. V. Karpov, M. Sokolowski, et al., "Broadband observations of the naked-eye γ -ray burst GRB 080319B," *Nature*, vol. 455, no. 2008, pp. 183–188, 2008.
 - [14] F. Vitali, et al., "A path to the stars: the evolution of the species," accepted in *Advances in Astronomy*.

Research Article

PiMan: System Manager of the “Pi of the Sky” Experiment

Krzysztof Nawrocki,¹ Maria Ptasinska,² Marcin Sokołowski,³ Janusz Użycki,³
and Marcin Zaremba²

¹ Department of High Energy Physics, The Andrzej Soltan Institute for Nuclear Studies, Hoza 69, 00-681 Warsaw, Poland

² Faculty of Physics, Warsaw University of Technology, Koszykowa 75, 00-662 Warsaw, Poland

³ Laboratory of Astrophysical Instrumentation, The Andrzej Soltan Institute for Nuclear Studies, Hoza 69, 00-681 Warsaw, Poland

Correspondence should be addressed to Krzysztof Nawrocki, krzysztof.nawrocki@fuw.edu.pl

Received 30 June 2009; Accepted 20 December 2009

Academic Editor: Taro Kotani

Copyright © 2010 Krzysztof Nawrocki et al. This is an open access article distributed under the Creative Commons Attribution License, which permits unrestricted use, distribution, and reproduction in any medium, provided the original work is properly cited.

This paper describes PiMan, a CORBA-based system manager of the “Pi of the Sky” experiment, whose prototype consisting of two cameras on parallactic mount is running at Las Campanas Observatory in Chile. We discuss in detail all software components of the “Pi of the Sky” system, interactions between them, and the architecture of the PiMan system. PiMan extension and other system software that will control and monitor final system being under construction, consisting of two sites with 16 CCD cameras installed on three mounts per site, is also described in this paper.

1. Introduction

The prototype of the “Pi of the Sky” [1] experiment, which was custom designed and made, located at Las Campanas Observatory in Chile, searches for rapidly changing optical objects such as Gamma Ray Bursts (GRBs). The prototype system is composed of two CCD cameras located on parallactic mount and operated by a PC equipped with the dedicated and highly specialized software which is divided into modules that correspond to hardware or logical components. The software system controls all aspects of data collection and online data analysis. The PiMan assures communication and interoperation between all modules, coordinates their behaviour, and gives possibility to operate the system automatically and to control it remotely over low bandwidth and/or unstable link. The implemented solution, based on CORBA, is described in the presented paper.

2. Overview of the “Pi of the Sky” Experiment

Perhaps the most powerful cosmic processes ever observed are gamma ray bursts (GRBs) which are 0.1–100 seconds short pulses emitted by extragalactic sources. The energy of the typical burst is estimated to be of the order of 10^{51} erg.

The intensity of the burst is often higher than the total background from all other sources in the sky in gamma rays.

In order to proceed with understanding the physics of GRB one needs to observe them in wavelengths different than gamma rays. It is natural to expect that GRB should be accompanied by optical flashes. Systematic study of optical flashes accompanying GRB can impose important limits for theories explaining burst mechanisms and their energy engines. Perhaps not every GRB is accompanied by a bright optical flash.

We propose to build a system consisting of a number of CCD cameras covering as wide field of view as possible. The cameras continuously monitor the sky by taking relatively short (5–10 seconds) exposures. The data are analyzed online, in search for optical transients.

The design assumes that a large part of the sky is observed continuously. This is to be achieved by two sets of 16 CCD cameras per site (in the starting phase of the final stage of the experiment, each site will be equipped with 12 cameras. One additional mount per site will be added later), with each camera covering $20^\circ \times 20^\circ$ field of view (FOV).

Each set of 16 cameras will be organized in such a way that 4 cameras will be installed on single mount and each site will have 4 mounts. Cameras in separate sites will be

paired and each pair will observe the same field of the sky, a coincidence of cosmic events in both cameras will be required. Sites will be separated by distance of ~ 100 km which will allow to reject near Earth objects up to 30000 km orbit thanks to the parallax.

The apparatus is to be controlled and the data are to be analysed by a cluster of PCs. The system will be fully autonomous, but also fully controllable via Internet. During the normal operation the system will run autonomously according to the preprogrammed schedule. Dedicated script language has been developed to make the schedule programming easy and flexible. Every evening script is automatically generated according to satellite pointing information available on WWW. For most of the time the cameras follow the field of view of the SWIFT [2] satellite. When it is not possible to observe any of the satellites, another location in the sky is chosen. The system is also listening to GCN alerts. Should an alert arrive that is located outside the current FOV arrive, the mount automatically moves towards the target and exposures are being taken. Twice a night all sky scanning is performed.

3. “Pi of the Sky” as a Software System

As mentioned earlier the “Pi of the Sky” software consists of several modules that control main hardware components such as cameras and mount. The main modules are the following.

- (i) Data Acquisition (DAQ) module: responsible for controlling the cameras, reading data streams and on-line data analysis.
- (ii) Mount module: responsible for controlling the parallactic mount.
- (iii) GRB Coordinates Network (GCN) module: a module that listens for messages from the GCN network, interprets them, and requests other “Pi of the Sky” modules to react, if necessary.
- (iv) Satellite FOV module: this module is responsible for reading information about the current field of view (FOV) of satellites and providing this information to the system.
- (v) PiMan module: module responsible for communication and coordination between all other modules.

A more detailed description of PiMan is presented in the following sections.

The overview of the “Pi of the Sky” software system and its interactions is presented in Figure 1.

As can be seen in the Figure 1, PiMan accepts several methods for controlling the system by the system operator:

- (i) the PiMan execution shell (Pishell),
- (ii) the cron to execute periodic commands,
- (iii) scripts for the execution of several of commands (e.g., describing observation program for a given period),
- (iv) runscript for execution of scripts from the operating system level (Unix).

PiMan supports a two-way communication with other modules: PiMan can send commands to be executed by modules and modules can send messages to be interpreted by PiMan. The system to perform observations continuously has to be monitored at all levels, starting from low level hardware and ending on all software components. The complexity of the full system consisting of two sites, each one built of 16 CCD cameras installed on 4 parallactic mounts, equipped in many dedicated electronic and software systems, and operated by a cluster of PC computers will grow substantially with respect to the prototype experiment that is operated in Las Campanas Observatory and consisting of two cameras in one mount.

Therefore a new approach to system monitoring fulfilling the following goals:

- (i) modularity and scalability,
- (ii) operational reliability,
- (iii) easy configuration,
- (iv) intuitive and interactive Graphical User Interface

had to be worked out.

The system, based on very well-established standards such as CORBA [3], embedded Linux systems, Django [4], AJAX or Nagios [5] and able to fulfill all goals described above, is being presented in the following chapters.

4. PiMan Architecture

Several assumptions had to be taken into account when designing PiMan.

- (i) The system had to operate automatically and be controlled remotely over low bandwidth and possibly unstable link.
- (ii) The fact that the system consisted of several modules designed by different developers required clearly defined interfaces.
- (iii) Because the system serves as a prototype of the bigger system, the commands and messages had to be easy to modify and add.
- (iv) In addition, a two-way communication with modules, “special” operation modes (e.g., GCN alert mode) and thread safety was required.

As a consequence of the above conditions well-tested solutions were chosen as system components:

- (i) CORBA (MICO [6] implementation) for intermodule communication
- (ii) Boost C++ libraries [7] and STL [8] as base for critical components,
- (ii) Readline [9] was used as the library for Pishell, the PiMan interactive shell.

The internal structure of PiMan is presented in Figure 2.

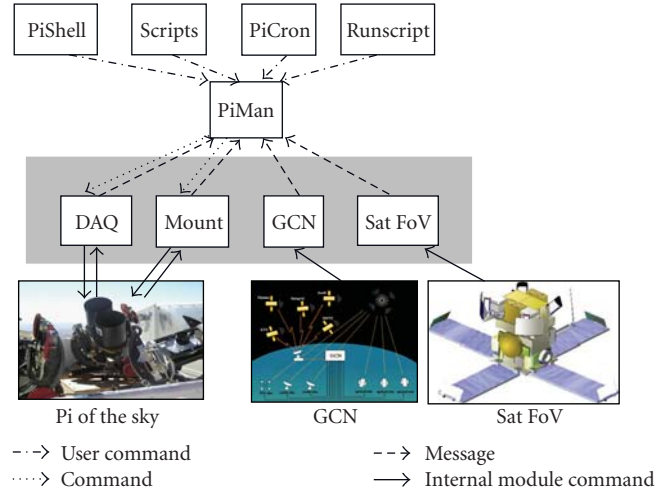


FIGURE 1: Overview of the “Pi of the Sky” software system.

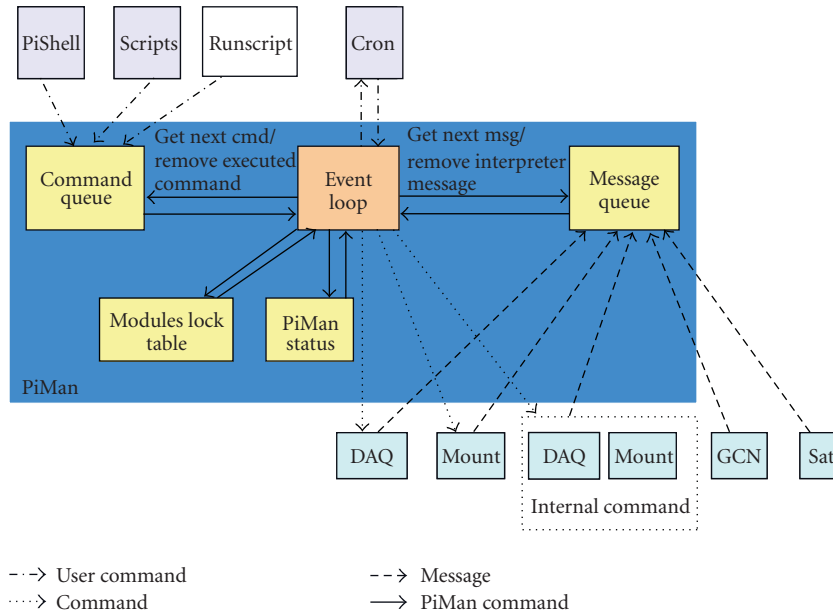


FIGURE 2: The internal structure of PiMan.

PiMan consists of the following.

- (i) A command Queue containing commands to be send to modules for execution.

The syntax for a PiMan command is the following:

```
[module_name] [execution_time] [command]
([parameters]),
```

where: `execution_time` format is MMddhhmm and `execution_time` less or equal 0 means “now.” Lower (more negative) values are used for higher priority.

- (ii) Message Queue containing messages received from modules to be interpreted by PiMan.

- (iii) Modules’ Locks object containing matrix of modules dependencies (e.g., a module’s command locks itself, *internal* command locks DAQ and mount, etc.).

- (iv) PiMan Status object that controls PiMan behavior (e.g., enforces mount to automatically follow the SWIFT satellite FOV, enforces PiMan to execute cron, automatically correct mount position from astrometry, sets PiMan to “alert mode”, etc.).

- (v) Event Loop responsible for reading Command and Messages Queues (in two threads) and sending commands that are ready for execution to respective modules.

There are several special PiMan features. Some of them are the following.

- (i) Locking mechanism to avoid sending commands to busy modules.
- (ii) “Internal module” used in case a command uses several modules in one PiMan command (e.g., DAQ and Mount). This module locks all modules concerned, until all commands of the internal module are finished.
- (iii) Alert Mode that blocks execution of ordinary commands until a command tagged as “forced” arrives. This mode is activated for example when a GCN alert arrives.
- (iv) Scripts can be executed in asynchronous mode, when several commands can be executed in parallel, or in synchronous mode, where all commands from a script wait for previous command to finish. For this feature to work a `thread_id` is assigned to each command. Commands with the same `thread_id` are executed synchronously.

The Command Queue is implemented as STL’s priority queue. Commands sent to PiMan are first checked for syntax validity and then put in the Command Queue. If the `execution_time` is expressed as `MMddhhmm` or `hhmm` (in this case the current night’s date is assumed) then it is converted to the corresponding `unix_time` value. The lower the value the higher the priority assigned to the command. The Event Loop reads a command with the highest priority from the Command Queue and if the command’s `unix_time` is equal or greater than the current `unix_time`, the current PiMan Status object state does not prohibit its execution. If the requested command does not use a module that currently executes another command then the command is sent for execution.

PiMan State in the current state of the system has the following flags:

- (i) `ignoreCmds`—to run PiMan in the “GCN alert mode” and suppress execution of standard commands,
- (ii) `manualMode`—to give an operator full control of the system by suppressing automatically executed commands,
- (iii) `updateCron`—to reread the PiMan cron file,
- (iv) `updateConfig`—to reread main PiMan config file,
- (v) `sunIsAboveHorizon` and `mountIsParked`—self-explaining,
- (vi) `cronPointHete`—to update mount position periodically according to HETE FOV,
- (vii) `autoAG`—to decide if the system is to run in the auto-guiding mode, that is, to correct mount movement by data from the astrometry procedure,
- (viii) `controlCamIdx`—to chose main camera for astrometry.

Commands sent for execution are analyzed by the PiMan’s command interpreter and are sent to respective modules by

calling modules’ CORBA methods. Executed commands are removed from the Command Queue.

As can be seen in Figure 2, the cron can be used to execute periodic commands. The Event Loop reads the cron file that contains commands for execution and their repeating interval. The cron execution can be suppressed by setting the PiMan state `manualMode` on.

Communication from modules to PiMan is implemented as STL’s queue. The syntax of a message is the following: `[module_name] [message] ([parameters])`.

Messages, in contrast to commands, are interpreted instantly. For example, a GCN module can send a message:

`gcn trigger (type_of_trigger, trigger_id, trigger_sub_id, trigger_unix_time, trigger_ra, trigger_dec, trigger_likelihood, moving.decision)`.

Such message is put in the Message Queue, read by the PiMan Event Loop and interpreted. In the case of sending the above message, the system reacts by putting an internal command `gcn_trigger` in the Command Queue for immediate execution.

PiMan, from the very beginning, was designed to be fully scalable, so migration from the prototype to the final system is straightforward. Every mount with four cameras of the final system will be controlled by one, very well tested in the prototype in Las Campanas Observatory, PiMan instance. As seen in Figure 3, the only new component needed is an additional layer controlling all PiMan instances at one site called PimanMaster (each Piman communicates with PimanMaster using CORBA protocol). This module is responsible for receiving operator’s commands, interpreting GRB alerts, and generating scripts for all PiMan modules present at one site.

The only case when communication between DAQ processes bypasses PimanMaster is the `checkFlash` function (remotely called by CORBA) that is used for comparing flash information with data from other site for satellite and cosmic muon background rejection. Direct communication is used here for performance reasons.

5. External Tools

There are several external tools of the “Pi of the Sky” system which enhance PiMan’s functionality:

- (i) the generator used to create scripts for a given time period (e.g., one night) to program “Pi of the Sky” system behaviour,
- (ii) script checker that can be used to check scripts for syntax errors. The checker dynamically learns the PiMan syntax based on the PiMan sources,
- (iii) during the operation of the “Pi of the Sky” a watchdog checks if the whole system works properly. In case of problems a human operator is informed by email or SMS
- (iv) the new integrated monitoring system is being developed for the final system.

Below we describe in detail the script generator, which is the system component crucial for the autonomous operation of “Pi of the Sky” experiment and the new monitoring system.

5.1. Script Generator. The script generator is a component responsible for generation of PiMan scripts for a given night. The example of such script is presented at the address http://grb.fuw.edu.pl/pi/papers/piman_script_malaga09.txt. The script generator is launched an hour before the system starts its night work. It retrieves pointing information of INTEGRAL, HETE, and SWIFT satellites available on the Web and programmes mount movements and data collection according to it. The generator calculates times of sunset and sunrise for choosing the time of system start-up, shutdown, and the time for the evening and morning scan of the whole sky.

The generator adds commands to the scripts to perform the following tasks.

- (i) Initialize modules—make mount calibration, start cameras cooling immediately after the system startup.
- (ii) Start dark frames collection—15 minutes before the Sun sets 10° below horizon.
- (iii) Perform evening and morning scan of the sky when the Sun is 15° below horizon. Subscripts `scan_evening.pish` and `scan_morning.pish` are generated for this purpose and executed at the proper time in the main script.
- (iv) Observe field of view of a satellite that searches for GRBs—SWIFT, HETE, or INTEGRAL, strategy of choosing satellite and position to observe is described in detail later.
- (v) Shutdown of the system—5 minutes after the Sun sinks 10° below the horizon.

The system observes only fields from a predefined list of $30^\circ \times 30^\circ$ fields overlapping by 15° . Scan scripts are generated according to odd fields from the list on one day and according to even fields on next day. Normal observations obey FOV of one of the satellites. It is realized in the following way.

- (i) The program chooses the celestial position, according to the following algorithm.
 - (a) Satellites on the list (currently SWIFT, HETE, and INTEGRAL) are checked if the altitude of their FOV is at least $h_{\min} = 30^\circ$ above the horizon and in such case the position is chosen.
 - (b) Otherwise, the satellite with the biggest part of FOV above horizon is chosen, but it is preferable that the satellite FOV is rising rather than setting.
 - (c) In case it is not possible to find any field according to the above rules the generator can choose an alternative object (like Large Magellanic Cloud (LMC) or Small Magellanic

Cloud (SMC)) or choose a position above the horizon in place where soon one of the satellites will appear after rising above the horizon.

- (d) The chosen field is checked against the calculated position of the Moon and in case it is closer then the minimal distance allowed (depends on the Moon phase, for full Moon it is equal to 30°) it is rejected and another object and position must be determined.
- (e) There are several options for observing any object one wanted. For example, it is possible to define favorite fields which will be followed always when above horizon, define favorite fields to follow in case they overlap with the FOV of the satellite selected to follow or define position and time at which it should be observed.

- (ii) The program finds the closest field from the predefined list, adds a command to follow this field.
- (iii) The program calculates the time when the last followed field will be lower then 30° and a new position must be determined for this moment.

In case of any problems with script generation, for example due to unavailability of pointing information an email describing the problem is generated and sent to a human system operator.

5.2. Integrated Monitoring and Control System. This part of the paper describes the architecture of the monitoring and control system of all components of the “Pi of the Sky” experiment. The experiment is totally remotely controlled so all information about its state (both hardware and software components) has to be collected. One of the main goal of the monitoring system is to present the state of the experiment in user-friendly and intuitive way and to detect and solve emerging problems automatically using an artificial intelligence system if possible or alert operators otherwise.

5.2.1. Low Level Hardware Monitoring. The low level hardware monitoring plays a fundamental role in keeping the detector hardware in an operational state. Due to the fact that whole detector has been constructed as modular and scalable system, the low level hardware monitoring part should reflect the detector architecture. Therefore a modular hardware called “PiMon” for monitoring any physical quantity has been developed.

The core of the “PiMon” hardware called “PiMon-d” module is based on ARM microcontroller with embedded operational system.

Additional measurement modules for voltage (“PiMon-k” and “PiMon-m”), temperature (“PiMon-t”) and cooling fan rotation speed (“PiMon-w”) monitoring are connected to main digital modules; see Figure 4.

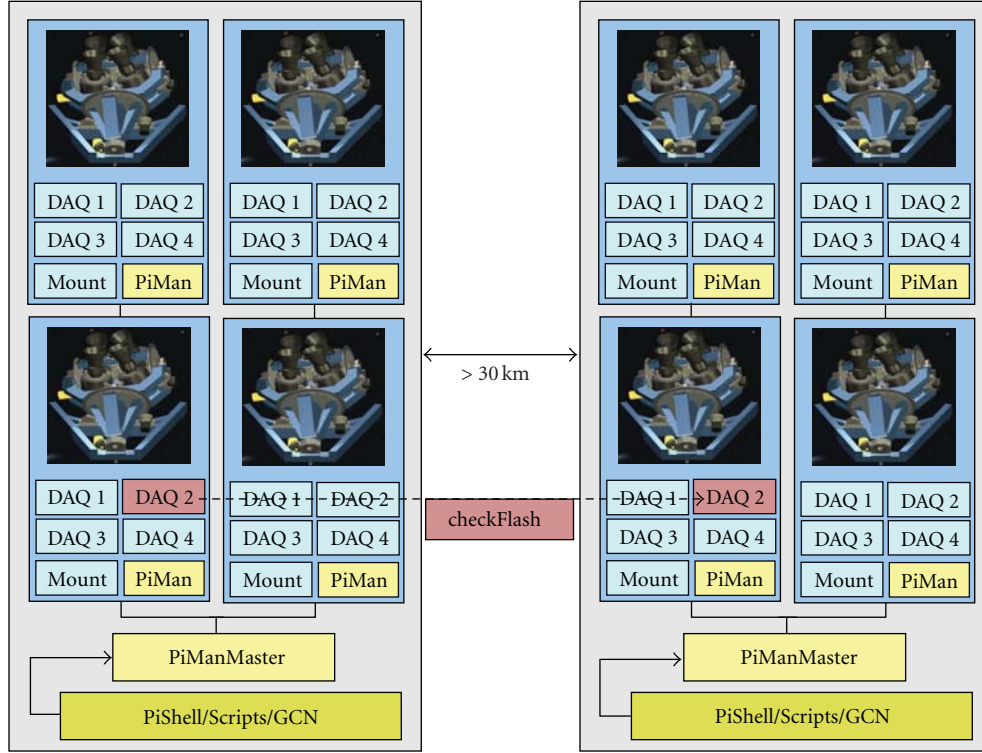


FIGURE 3: Software architecture of the final system. A new function, checkFlash, described in the text is shown in red.

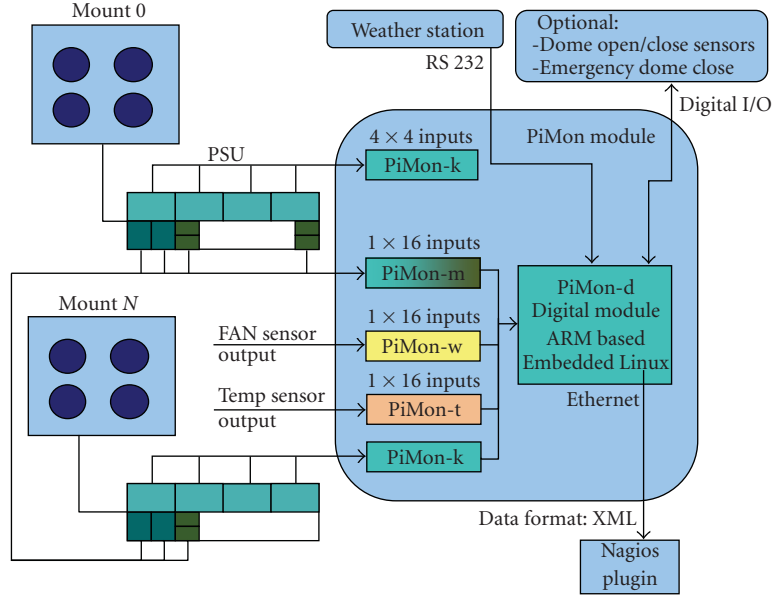


FIGURE 4: Low level hardware monitoring architecture—"PiMon" hardware.

As "PiMon-d" a common, the ready-to-use microprocessor system based on AT91SAM9260 micro-controller [10] and equipped with necessary operational memory (SDRAM) and data storage memory (NAND Flash) was used. Modularity was achieved by adapting the module to well-defined mechanical standard with an electrical interface. For this purpose VME mechanical standard was used. The

communication with the central control system was implemented using an Ethernet interface (with possible additional communication through USB as backup). Additional two RS232 ports are used for debugging/maintenance purposes and for communication with the weather station.

Each measurement module sends data on demand to the master ("PiMon-d" module) through SPI bus. The maximal

number of modules is 255 irrespective of its type. The type of the measurement module defines the physical quantity being measured. In case of “Pi of the sky” hardware three types are needed to have full information about its status. These are

- (i) “PiMon-k” and “PiMon-m” for cameras’ and mounts’ power supplies monitoring,
- (ii) “PiMon-t” for temperature monitoring in critical points,
- (iii) “PiMon-w” for cooling fan rotation speed measurement.

“PiMon-k” and “PiMon-m” have 16 independent differential inputs for voltage measurement with low noise amplifier and low-pass filter at each input to avoid ground loops. Each module includes two 12 bit AD converters with SPI interface to communicate with the digital module. The measurement resolution and range of each input channel depend on the amplification of the input stage selected during assembly (e.g., from 3 mV for 0–12 V range to 7 mV for 0–28 V range). An additional rectifier for AC measurement is required. One “PiMon-k” module can measure voltage from 4 cameras PSU (4×4 inputs— 4×1 DC and 4×3 AC) therefore one module per one mount is required. One “PiMon-m” module can measure all voltages from mount engines, encoders, and eth/can converters PSU (16 DC inputs) therefore one module per one “site” is required.

5.2.2. Software Monitoring and Data Exchange. The main software is based on OpenWRT Linux [11] distribution designed for embedded devices. Each measurement input module has a different communication set of messages sent through SPI bus being defined in the particular software modules. The main program reads out measured data from each module and stores them in memory. The refresh rate of data depends on the input modules count.

Stored data can be read out by the central system through Ethernet interface using TCP/IP protocol. The special module written for embedded Linux sends data on demand in XML format. Measurement data were grouped in logical blocks. Each element of the real system has its representation in the XML document which simplifies reading its state.

For example, one “Site” element (<xs:complexType name=“Site”>) includes information about itself and time of read out information:

```
<xs:attribute name="location" type="xs:string"/>
<xs:attribute name="date" type="xs:date"/>
<xs:attribute name="time" type="xs:time"/>
```

...

and further other elements such as

```
<xs:element name="Mount" minOccurs="1"
  maxOccurs="4" type="Mount"/>
```

```
<xs:element
  name="EthCANconverterPwrSupp"
  type="TwoOutputPwrSupply"
  minOccurs="1" maxOccurs="1"/>
```

....

Nagios Plugin described below reads out data every defined period of time and after parsing XML data stores them in central database where they can be used for further processing.

5.2.3. Central Monitoring and Error Recovery System. The most important assumptions taken into account when developing the monitoring system for the final setup were the following.

- (i) Modularity and scalability—these are the most important issues for the system due to the fact that the experiment is still underway and it was essential to consider its future developments.
- (ii) Operational reliability—it goes without saying that system that controls another system should be more reliable than the latter. If it works fine all information will be collected in one place. It will not be necessary to look for information how the system works in a separate log file what would take a lot of time.
- (iii) Easy system configuration—the system should be fully configurable at the interface level allowing administrators to easily define components being monitored and define the way the information is presented.

The general architecture of the monitoring system is presented in Figure 5.

It consists of the following logical modules.

- (i) Nagios—main data collector which collects the data from all defined sources and write them to the MySQL [12] database using NDOutils library.
- (ii) Nagios plugins—software utilities used to communicate with all monitored components, able to read their state and deliver it to Nagios. The following Nagios plugins classes are present:

- (a) electronic hardware plugin—able to read and parse information about PSUs, weather station, dome position, and so forth, delivered in XML format (already described in the previous chapter),
- (b) PC-s, routers, UPS-es plugins—to monitor state of computers, network equipment and UPS. Ready plugins obtainable with Nagios are being used,
- (c) software components such as PiMan, DAQ, Mount server, GCN server, that control various aspects of the system. Custom plugins that communicate with software modules using CORBA protocols are being used.

- (iii) Recovery System—module to perform recovery actions in case Nagios triggers predefined system failure (such as mount slide, computer failure, software module problem, etc.) and/or notice system operators through email/sms.

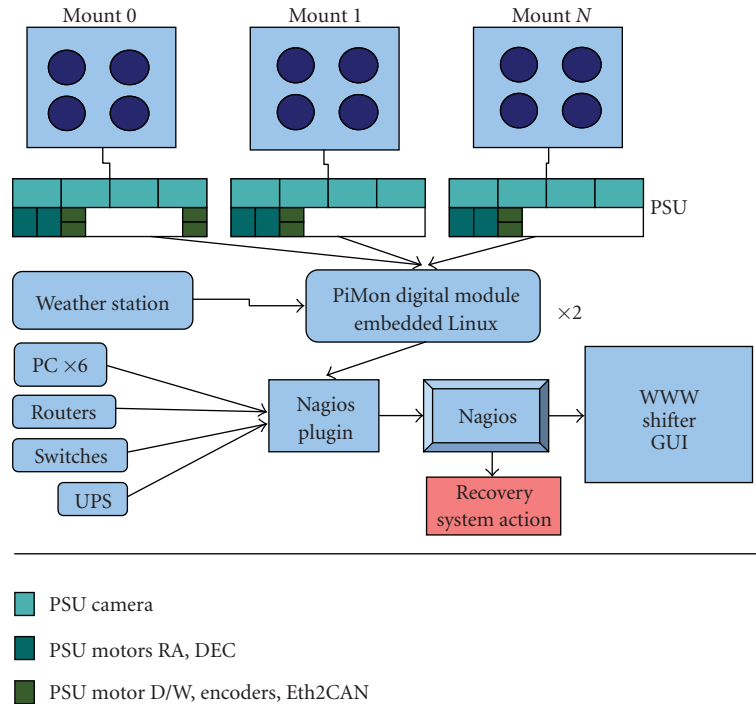


FIGURE 5: Overview of the data flow in the monitoring system.

- (iv) Shifter GUI—user-friendly WWW interface for system operators (shifters), described later.

Details of the system GUI system are given below. The monitoring and controlling system is based on Apache server, Nagios, MySQL database, Django framework, JQuery JavaScripts library, SimpleJson, and AJAX.

Every observation post has its own Nagios server and its own MySQL database where information about the states of the devices is collected. All monitored components of the “Pi of the Sky” experiment have their own tables in database. Structure of table is described in model.py Django file.

This solution guarantees ease of maintenance of the tables. Ease of adding new components to the monitoring panel is an important element of system. It is of crucial importance due to the ongoing development of the project. Adding new parts to the system is performed by adding new interface elements, that is, by filling the relevant table in the database.

The user interface to control and monitor devices consists of a web site with fully dynamic content. The data (i.e., monitoring information) contained in the database are simultaneously displayed by the functions written with the use of JQuery libraries. The data are also simultaneously updated using AJAX technology. When monitored system failures are being detected the operator is immediately informed by alerts on the monitoring web page. Another important part of the monitoring system is the administration panel that enables graphical access to low level database monitoring data.

6. Conclusions

PiMan as the “Pi of the Sky” system manager tool turned out to be very stable, predictable, and easy to extend in many developers’ environment. This was achieved by using mature and high level standards like CORBA. In the future the PiMan will be extended to be used in the next phase of the “Pi of the Sky” experiment, as the number of cameras and mounts and the overall system complexity will grow significantly.

Acknowledgments

The authors are very grateful to G. Pojmanski for access to the ASAS dome and sharing his experience with us. The authors would like to thank the staff of the Las Campanas Observatory for their help during the installation and maintenance of their detector. This work has been financed by the Polish Ministry of Science in 2005–2009 as a research project.

References

- [1] A. Burd, M. Cwiok, H. Czyrkowski, et al., “Pi of the Sky— all-sky, real-time search for fast optical transients,” *New Astronomy*, vol. 10, no. 5, pp. 409–416, 2005.
- [2] SWIFT mission, <http://heasarc.gsfc.nasa.gov/docs/swift/swiftsc.html>.
- [3] CORBA, <http://www.corba.org/>.
- [4] Django project, <http://www.djangoproject.com/>.
- [5] Nagios project, <http://www.nagios.org/>.

- [6] MICO, <http://www.mico.org/>.
- [7] Boost C++ libraries, <http://www.boost.org/>.
- [8] STL, <http://www.sgi.com/tech/stl>.
- [9] Readline—library, <http://cholm.home.cern.ch/cholm/misc/rlmm>.
- [10] AT91SAM, http://www.atmel.com/dyn/products/product_card.asp?part_id=3870.
- [11] OpenWRT project, <http://openwrt.org/>.
- [12] MySQL database, <http://www.mysql.com/>.

Research Article

The Software for the Robotization of the TROBAR Telescope

Mauro Stefanon

Edifici Instituts d'Investigació Polígon La Coma, Observatori Astronòmic Universitat de València, Paterna, 46980 València, Spain

Correspondence should be addressed to Mauro Stefanon, mauro.stefanon@uv.es

Received 26 June 2009; Accepted 30 October 2009

Academic Editor: Taro Kotani

Copyright © 2010 Mauro Stefanon. This is an open access article distributed under the Creative Commons Attribution License, which permits unrestricted use, distribution, and reproduction in any medium, provided the original work is properly cited.

The Telescopi ROBotic de ARas (TROBAR) is a new robotic facility built at Aras de Los Olmos (Valencia, Spain). This is a 60 cm telescope equipped with a $4k \times 4k$ optical camera, corresponding to 30×30 arcmin² FoV, and it will be primarily used for a systematic search of Ha emitting stars in the Galactic Plane to a depth of ≈ 14 mag. Both data acquisition and reduction will be performed automatically. The robotization of data acquisition is now entering its final coding phase while the development of the data reduction pipeline has just started.

1. Introduction

Galactic H α emitting objects are tracers of pre- and postmain-sequence stars as well as of nebulae, cataclysmic variables, Be stars, and other more exotic objects like Luminous Blue Variables (LBVs) and Wolf-Rayet stars. IPHAS [1–4], the most complete survey of the galactic plane carried out so far, is complete in the magnitude range $r' = 13$ to 20 for $-5 < |b| < 5$. The classical surveys, mostly based on objective-prism photographic observations, are complete up to magnitude 9 (see, e.g., [5, 6]). In this context, the main aim of our project is to carry out a photometric survey covering the existing gap down to $r' \approx 14$ with observations and data reduction automatically performed.

2. Telescope and Location

TROBAR is located at the Observatori Astronòmic de Aras (OAA), approximately 100 Km north-west of Valencia, at an altitude of 1330 m, in a region of low light pollution. The telescope, realized by Teleskoptechnik Halfmann, has a main mirror of 60 cm in diameter, with a classical Ritchey-Chrétien optical scheme; a Nasmyth focus is present, to which an optical camera is attached. The telescope can slew as fast as 10 deg/sec allowing to point any region of the sky in less than a minute. A filterwheel hosts standard Sloan u, g, r, i, z , Strömgren u, b, y, v plus two H α filters (one narrow and one medium-band). Table 1 lists the main features of the telescope.

Low level control of telescope pointing capabilities is done by the *Pilar* software provided by 4II Systems Gmb company, which supplies a socket interface to the TCS commands.

The optical detector is a Fairchild Peregrine 486 back-illuminated CCD, providing an array of 4096×4096 pixels of $15 \mu\text{m} \times 15 \mu\text{m}$ read by four amplifiers; the readout noise is $4e^-$.

The telescope can be both remotely controlled and robotically operated and a set of commands also allows to perform almost all the operations via scripting procedure. Here we will outline its robotic capabilities.

3. System Description

The operations which can be performed by the telescope comprise the acquisition of calibration frames (bias, darks, sky flat field, and focus) and the observation of scientific targets.

All the software is written in python, with the Object Oriented paradigm. All astronomical calculations are performed through the pyephem libraries (<http://rhodessmill.org/pyephem/>).

The routine operations are managed by a set of 3 main programs, in communication one with the other through TCP/IP connection. The adoption of the TCP/IP paradigm allows a complete independence of the software from the running machine, hence allowing fast replacing of hardware in case of problems. These high level programs communicate

TABLE 1: TROBAR main features.

Device	Value
M1 diameter	60 cm
Focal length	4800 mm
Mount	Alt-az—Nasmyth focus
Camera	Fairchild 4K × 4K optical camera
FoV	30' × 30'
Filters	Sloan u, g, r, i, z; Strömgren u, b, v, y; H α (narrow + medium band)

with low-level processes managing the corresponding device (see Figure 1).

The organization into three main programs directly reflects what are the main duties an autonomous observatory should accomplish, namely, check meteorological conditions, safely manage the dome opening and, when all the conditions are good enough, send an observation to the telescope. In the following sections the realization of each one of these processes will be described.

3.1. Meteorology Manager. Meteorological information is collected by a DAVIS Vantage Pro meteorology station, installed on a pillar located 10 m away from the dome; it is equipped with sensors for measuring air pressure, inner and outer air temperature and relative humidity, wind speed and direction, solar radiation and rain rate.

Meteorological data is collected by a dedicated process, called *meteo_man*. This program reads the meteorology station every 5 minutes during the day and every minute during the night. Apart from reading data, it also checks if current meteorological conditions are to be considered safe for operations; this requirement is achieved when all the following conditions are satisfied

- (i) External humidity must be below 85%.
- (ii) Difference between the dew point and current external temperature as absolute value must be greater than 3 degrees Celsius.
- (iii) Wind speed must not exceed 15 m/s. If the speed is between 12 m/s and 15 m/s then an azimuth limitation flag is raised, meaning that the telescope should avoid to point directly into the wind and to the 180 degrees around it.
- (iv) Atmospheric pressure must be above 870 hPa.
- (v) Rain rate must be equal to zero.

If any of the above conditions is not satisfied, then the *bad meteo condition* flag is raised. Since the evaluation of safe meteorological conditions is a very delicate task for any autonomous robotic telescope, particular prudence has been implemented in the algorithm evaluating the meteorological conditions. Thus, when conditions are not satisfied, in order to consider meteorological conditions good again, these must satisfy for 30 minutes the above rules with stronger constraints, namely, humidity must stay below 80%, wind speed below 12 m/s, pressure above 880 hPa and, of course, no rain.

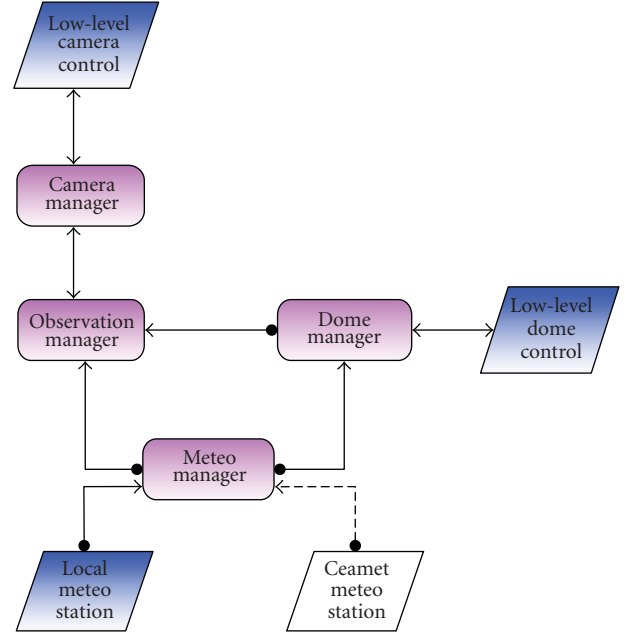


FIGURE 1: Flux diagram of the main cycle of the observation manager.

3.2. Dome Manager. The enclosure of the telescope is a classical hemispheric dome with two vertical sliding doors. The dome can rotate at a maximum speed of 6 degrees per second, which, during the pointing, translates to an average delay of 30 seconds respect to the telescope, so that the pointing of the telescope is poorly affected by the dome and it is not a concern at all for the scope of the scientific project.

The program *dome_man*, which is in charge of managing the dome has two main duties.

- (i) To provide a socket interface to the dome actions: although for robotical operations the dome is kept synchronized to the telescope position, so that it is not necessary to reposition the dome before each observation, its status is continuously monitored by another process, running on a different machine, which detects malfunctions and informs the team accordingly.
- (ii) As autonomous process, it continuously acquires the meteorological conditions and decides to open or close the dome depending on meteorological conditions and sun altitude. Currently, the dome is allowed to stay opened when the sun is below -5 degrees of altitude.

3.3. Observation Manager. The third main process, *obs_man*, is the one which is in charge of managing the observations. Figure 2 shows the diagram of the main activities. The system continuously checks if there is a target suitable for observations, if meteorological conditions are fulfilled and if the dome is open. If this is the case, then the observation process starts. This is composed of two threads, one checking the tracking status of the telescope during all the exposure

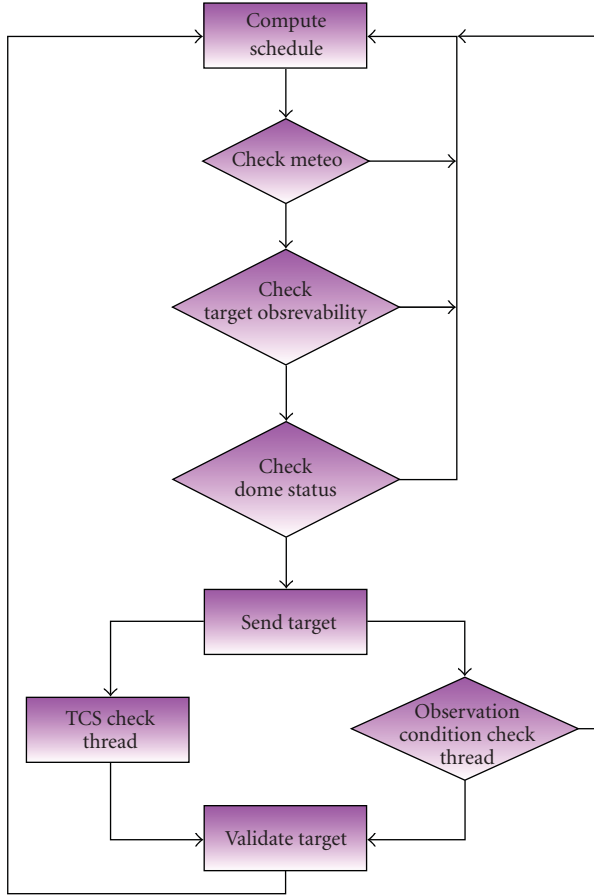


FIGURE 2: Flux diagram of the main cycle of the observation manager.

and the other checking that all the environmental conditions are valid during the whole observation.

Due to a limitation in the low level software controlling the camera provided by the camera company, it is currently not possible to interrupt an ongoing observation. The information collected by the two threads is then used at the end of the exposure for validating the observation; if at least one of the two threads reported an error, then the target is ingested back into the archive for subsequent reobservation.

Although the scheduling software already takes into account constraints whose dissatisfaction can reveal dangerous for the telescope, the observation manager, before starting each target, performs a bunch of checks which prevent the telescope from directly pointing towards the sun, the moon and towards those directions which cannot be reached by the telescope and would thus send the telescope to its limit switches.

Each one of the above processes is coupled to an isAlive program. This is a crontab regulated job periodically checking that the corresponding process is running and, if this is not the case, restarting it.

3.3.1. Target Archive and Scheduling. The set of targets is organized in a MySQL table. Each target can be associated

to a user-defined priority value with the logic that the lowest is the value, the highest is the priority; in addition the definition of all the most common constraints under which each target should be observed, such as the maximum moon fraction and distance, minimum and maximum airmass, and periodicity of observation is implemented.

The fundamental idea behind the scheduling algorithm is to try to observe each target when it is closest to its minimum airmass (either because it is transiting through the meridian or because the user set a greater value in the minimum airmass field). This is achieved in the following two steps:

(i) the scheduling software makes a first pass through all the targets, selecting only those whose constraints are satisfied from that moment and through all the exposure time;

(ii) a figure of merit (FoM) is then applied to each of the selected targets. This FoM is a generalization of the $e^{-|x|}$ mathematical function, where x here stands for the whole set of parameters. This is done in order to have a strong peak when all the conditions are best satisfied. The complete adopted function is

$$h(p, f_a, f_t, f_d) = p \left(1 - \exp \left(- \left(\frac{f_a}{f_t} \right)^{1/2} \right) + f_d \right), \quad (1)$$

where $p \in \mathcal{N}$ is an integer number specifying the priority, with the value of 0 denoting the highest priority; the normalized difference between the current and the minimum airmass f_a is given by

$$f_a = \frac{a(0) - \min(a)}{\min(a)}, \quad (2)$$

where $a(0)$ is the airmass at the time of the computation and $\min(a)$ is the maximum between the minimum airmass the object can reach on the sky and the user requirements for the minimum airmass; f_t is the ratio between the total time an object is above its horizon (as defined by the airmass constraints) and the required exposure time. Finally f_d is the normalized distance of the object from the celestial pole. Explicitly, the expression for f_d is

$$f_d = \frac{n(\delta - \min(\delta))}{90.0 - \min(\delta)}. \quad (3)$$

Here δ is the declination of the object, $\min \delta$ is the minimum declination which is visible from the site for a given airmass, and is n a factor to reduce f_d values to a suitable range of values of the whole h function.

The f_d term has the effect of giving higher priority to those objects with low declination, which typically are the objects whose time for observation is shorter than that of objects at higher declinations. Finally, the $1/2$ exponent to the argument of the exponential function has been introduced in order to smooth the wings of the FoM.

Figure 3 shows the value of the result of applying the FoM described above to three targets with the same Right Ascension but with Declination $\delta = +10, +30$, and $+60$, respectively.

Note that targets with $p = 0$ will always have the lowest value of h (in fact $h \equiv 0$ independently of the value of

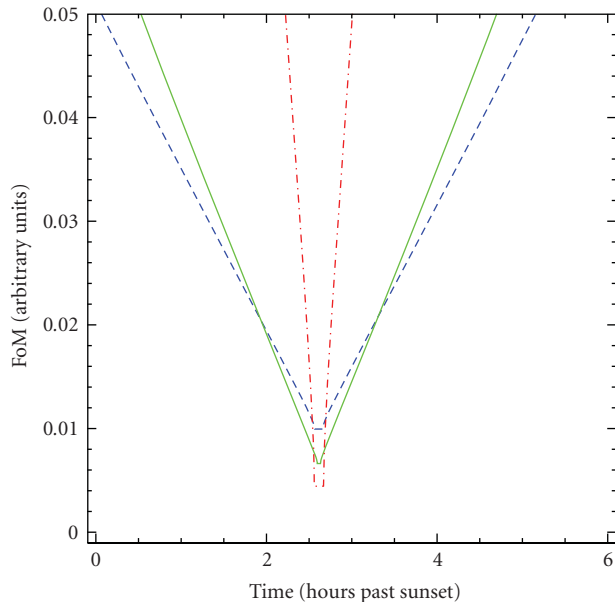


FIGURE 3: Scheduler FoM for objects with the same priority = 1, RA = 15h and $\delta = +10$, +30, and +60 for red dot-dashed, green solid and blue long dashed line, respectively.

the other constraints), which translates into allocating the 0-priority target as soon as possible.

The FoM expression can of course be generalized by introducing multiplicative parameters with the effect of shifting in time the points where the FoMs of targets with the same RA but different δ intersect (cf. Figure 3), in order to better suite arising scheduling needs. This optimization will be done during the commissioning phase.

3.4. Hardware. All the software runs on almost of the shelf hardware, without any particular need for high-speed processing, with a total number of three computers. The only exception is the machine with the obs_man program which is running on a quad-core linux. This is due not because of the supposedly high demanding software of the observation manager, but because this machine is shared with another experiment which need real-time data analysis.

In addition, each machine has its own UPS system granting power supply to the computers in case of shortages. A UPS for the dome is also foreseen to be installed in the near future.

4. Current Status and Future Prospects

The coding is now complete at the 80% level and we foresee to complete it by the end of the year. In particular one of the tasks we still need to implement is the procedure of automatic focusing. This will be achieved by a single exposure, tentatively at the beginning of the night, on which a bright star is imaged with different focus offset and by slightly moving the telescope between one acquisition and the next. The image will then be analyzed using SExtractor [7] and the fwhm of the star fitted by a parabola.

In parallel we started to develop a pipeline for the reduction of the survey data. This will make extensive use of the pyraf environment for the prereduction processes (bias subtraction, flat field correction, etc.). Detection of the objects on each image will be managed by SExtractor; its mag.auto value will be used as a first estimation of the flux, which will then be used by DoPhot [8] to derive psf magnitudes.

5. Conclusions

We described the software for the robotization of TROBAR, with the aim of performing a survey of the Galactic Plane, looking for H α emitting objects. The system is able to allocate and observe the targets in a MySQL archive when they are best visible and depending on observing constraints. The code is now almost complete and we foresee to start robotic operations by the end of the present year.

References

- [1] J. E. Drew, R. Greimel, M. J. Irwin, et al., “The INT Photometric H α survey of the northern Galactic plane (IPHAS),” *Monthly Notices of the Royal Astronomical Society*, vol. 362, no. 3, pp. 753–776, 2005.
- [2] M. Corradi, R. Rodríguez-Flores, A. Mampaso, et al., “IPHAS and the symbiotic stars: I. Selection method and first discoveries,” *Astronomy & Astrophysics*, vol. 480, no. 2, pp. 409–419, 2008.
- [3] A. R. Witham, C. Knigge, J. E. Drew, et al., “The IPHAS catalogue of H α emission-line sources in the northern Galactic plane,” *Monthly Notices of the Royal Astronomical Society*, vol. 384, no. 4, pp. 1277–1288, 2008.
- [4] E. A. González-Solares, N. A. Walton, R. Greimel, et al., “Initial data release from the INT Photometric H α survey of the northern Galactic plane (IPHAS),” *Monthly Notices of the Royal Astronomical Society*, vol. 388, no. 1, pp. 89–104, 2008.
- [5] L. Kohoutek and R. Wehmeyer, “Catalogue of H-alpha emission stars in the Northern Milky Way,” *Astronomy and Astrophysics Supplement Series*, vol. 134, no. 2, pp. 255–256, 1999.
- [6] L. R. Wackerling, “A catalogue of early-type stars whose spectra have shown emission lines,” *Monthly Notices of the Royal Astronomical Society*, vol. 149, p. 405, 1970.
- [7] E. Bertin and S. Arnouts, “SExtractor: software for source extraction,” *Astronomy and Astrophysics Supplement Series*, vol. 117, no. 2, pp. 393–404, 1996.
- [8] P. L. Schechter, M. Mateo, and A. Saha, “DOPHOT, a CCD photometry program: description and tests,” *Publications of the Astronomical Society of Pacific*, vol. 105, p. 1342, 1993.

Research Article

RTS2—The Remote Telescope System

Petr Kubánek^{1,2}

¹Image Processing Laboratory (IPL), Universidad de Valencia, 46010 Valencia, Spain

²Instituto de Astrofísica de Andalucía-Instituto del Consejo Superior de Investigaciones Científicas (IAA-CSIC),
18008 Granada, Spain

Correspondence should be addressed to Petr Kubánek, petr@iaa.es

Received 30 June 2009; Revised 25 November 2009; Accepted 29 January 2010

Academic Editor: Lorraine Hanlon

Copyright © 2010 Petr Kubánek. This is an open access article distributed under the Creative Commons Attribution License, which permits unrestricted use, distribution, and reproduction in any medium, provided the original work is properly cited.

RTS2 is an open source observatory manager. It was written from scratch in the C++ language, with portability and modularity in mind. Its driving requirements originated from quick follow-ups of *Gamma Ray Bursts*. After some years of development it is now used to carry tasks it was originally not intended to carry. This article presents the current development status of the RTS2 code. It focuses on describing strategies which worked as well as things which failed to deliver expected results.

1. Introduction

RTS2 originates from RTS, the Remote Telescope System. RTS was written during years 1999 and 2000 as a team project for Computer Science courses [1] by students of Mathematics and Physics faculty of Charles University in Prague.

RTS2 is primarily developed on the *Ubuntu Linux* distribution. It is known to run on a wide variety of Linux distributions, the *Solaris* operating system and partially on *Microsoft Windows* and *Mac OS X*.

Project source code can be obtained from the Web site <http://rts2.org/>. The project Wiki pages on <http://rts2.org/wiki/> list group experiences with various fully autonomous observatory projects.

The outline of this paper is as follows: the first section is this introduction. The next section describes goals and history of the project development. The third section focus is a description of how various tasks inside RTS2 are divided. The fourth summarises communication protocol. The next section describes approaches used during development. The sixth section forms the core of the article—it lists currently added features. The seventh section informs readers about currently running RTS2 systems. The eighth is a reminder about our experiences with restarting failed devices. The contribution concludes with a section about expected developments.

2. Project Goals and Its Development

The original goal of the RTS2 development was to produce software for a small robotic telescope, devoted to study Gamma Ray Burst (GRB) transients. The requirements of the project were

- (i) must be fully autonomous,
- (ii) must react as fast as possible to incoming GRB alerts,
- (iii) must perform regular observations during periods with no GRB observation to verify system readiness,
- (iv) must be modular to enable easy switching of the instruments.

Those requirements were laid in early 2000. They share similarities with other projects, notably *AudeLA* [2] and the *Liverpool Telescope System* [3]. At the time, open-source projects of similar scale did not exist. Available commercial, closed-source solutions were either associated with a single instrument, with questionable portability to others telescopes, or did not fulfill the requirement for fast switching between targets. It is worth noting that even today it is not easy to implement this requirement. It forms a strong entry barrier for those who would like to become GRB observers.

As the project advanced, additional requirements were added. They reflected experiences gained during development, and particularly pains and problems associated with early porting of the system to the other observatories:

- (i) system must be robust enough to continue operations even when non-critical part(s) fail;
- (ii) observer must have possibility to remotely interact with observations;
- (iii) system must be fully configurable using configuration files;
- (iv) system must provide clear description of what its components are performing;
- (v) observer must be presented with a list of devices which failed;
- (vi) the code should include dummy device drivers for testing the software without hardware.

Creation of dummy environments brings great benefits during system development. They enable developers to debug the system before it is deployed. There are still cases when errors and bugs are detected only during night runs. But as the project matures, the number of those cases significantly decreases—and there are recorded cases when new software, with significant new features, was deployed and it just worked, without any debugging.

As the number of observatories running *RTS2* grows, their management, fixing various small glitches, as well as their scheduling and data processing started to saturate staff time. We are aware of this, and we are in progress of creating tools which will allow us to manage network operations using a smaller amount of operators' time.

3. RTS2 Quick Overview

RTS2 is based on the “*plug and play*” philosophy. The parts which constitute the system can be started, restarted or stopped anytime, without affecting system performance. Special care is taken of resolving all possible blocking states, so the system will always respond to requests in reasonable time.

The whole system is user-space-based and except for drivers provided either by hardware manufacturers or by our group, it does not require any kernel-space-based components.

Code is designed around a central *select* system call, which picks any incoming messages. If there is no incoming message, class *idle* method is called. The code uses extensive hierarchy of its own C++ classes.

The *RTS2* system consists of the processes summarised in Table 1. Figure 1 shows processes and connections used on an example observatory, which includes three CCDs, two domes, and a single weather station serving both domes. For a detailed description please see [4].

TABLE 1: RTS2 processes.

Process	Description
Centrald	Central component of the <i>RTS2</i> system. It provides three main services—a list of devices and services present in the system, system state changes and synchronisation among devices.
Devices	Corresponds to hardware attached to the observatory system. Different classes of devices are provided. They represents hardware coming from different manufacturers.
Services	Represents execution logic of the system. They provide functions for the end-user—carry observations, receive GCN and other alerts, enables XML-RPC (XML-RPC web site: http://www.xmlrpc.com/) based access to the system.
Clients	Provides information to end-user. They are usually run in interactive mode, with end-user interacting with the program. They include an interactive monitor and simple tools to execute observation scripts.

4. Communication Protocol

RTS2 employs its own communication protocol. A detailed protocol description can be found in [5]. The protocol is based on sending ASCII strings over TCP/IP sockets. It is fast, simple and robust. Among its important features are

- (i) sending of “*I am alive traffic*,” disconnecting connection if reply is not received—this removes connections to dead components,
- (ii) ability to switch to binary mode for data transfer, to transfer images and other large data items,
- (iii) traffic speed-up values which were not changed are not transported.

The protocol supporting libraries provides developers with a flexible and simple way to use common parts of the system. This results in a robust, transparent code, which can be easily extended. This greatly enhances software reuse. There are reasonable hopes and claims that the interfaces are simple enough to be understood by developers unfamiliar with the project.

5. Coding Style and Philosophy

It is widely rumoured that there are as many approaches to coding as there are software developers. This section aims to list rules and customs used during *RTS2* development. Although most of them are widely known we hope they are worth mentioning.

The best documentation for the code is the code itself. Readers of this article are encouraged to check out the system and study it. Code with complexity of the *RTS2* project cannot be made completely transparent. It is not expected that the developer will understand code on the first encounter. It is important that he/she find interfaces being

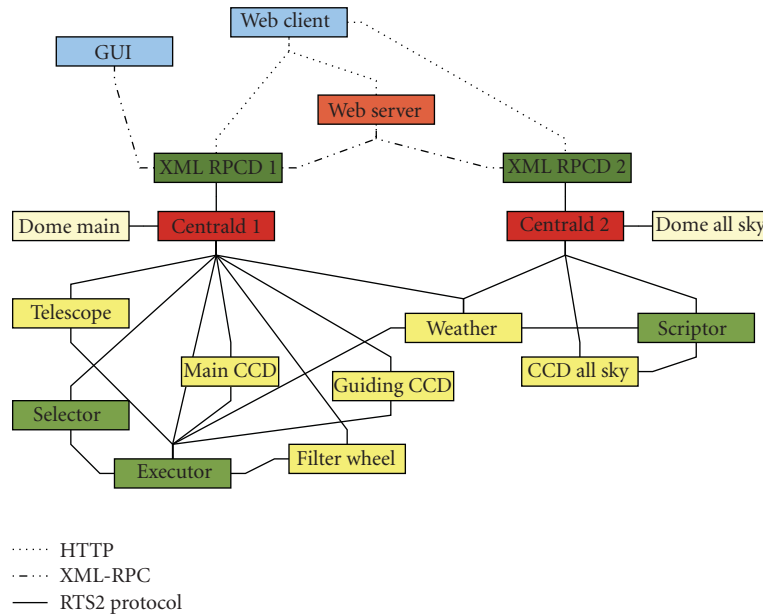


FIGURE 1: Example RTS2 environment. Two basic setups are present on the site—a telescope with a guiding CCD and a main CCD equipped with a filter wheel, and an all sky camera. There are two domes (one for telescope, second for all sky camera), three CCD detectors, *executor* and *selector* services controlling telescope setup and *scriptor*, a simplified *executor* service, controlling the all sky camera. Both observatories offer external access through XML-RPC protocol, provided by *XMLRPCD*. This is used by the Graphical User Interface and the Web server. *XMLRPCD* also provides a Web browser with direct access to some functions. Access to XML-RPC and Web functions can be protected with a password.

used. Later he/she can continue progressing towards system core classes.

5.1. Track Software Changes in Version Control System. The project is tracked in Subversion (Subversion web site—<http://subversion.tigris.org/>) tracking system. Previously version tracking relied on Concurrent Version System (CVS). (CVS web site—<http://www.nongnu.org/cvs/>). We have to admit that switch of the version control system to Subversion provides significant improvements, and we were really surprised with Subversion capabilities. Subversion really provides simply resolution for situations which were difficult or impossible to handle with CVS.

5.2. Code Releases. As the project is still under active development, a release formalism is yet not well established. There are usually two big releases during a year. All observatories are running Subversion code—code is regularly updated from Subversion and put to use. This way version management is also used for software distribution. We expect to calm this pace and establish a formal release mechanism.

5.3. Development Cycle-Release Early. Changes are usually committed to Subversion as soon as they compile without any errors. Before each commit, difference between new code and code in repository is reviewed. Sense and purpose of committed lines is examined once again.

This approach tracks vast majority of bugs right before they make it to the version control repository. After all changes are committed, and at least some documentation

which explains new features is provided, behavior of the code is tested once again. It is up to developer, where tests will be performed. Usually the system is tested on dummy devices, before moving to a real observatory. But small changes, which should introduce predictable results, are tested directly on observatories.

5.4. Follow Common Practices. The common practices can be summarized by a few sentences, such as: Think twice, code once. Discuss with others, inform users about changes. Try to design a generic solution instead of a simple additions for new problems. Add new features slowly and test them before implementing another. Divide a complex problem to simpler subproblems, implement and test the solution for them first, and then integrate the code to solve the complex problem. Keep in mind that the best developers are able to design, code, test, and release no more than 100 lines per working day—try to keep number of lines small by reusing what is already available either in your code or in C++ libraries.

6. Current Developments

This section deals with features which were recently added to RTS2. The list provided below is not complete—please see project change-logs for a more in-depth description.

6.1. State Machines. RTS2 uses state machines. The states represents various states of the hardware, for example camera can have idle, exposing, and readout state.

The states were originally used for coding purposes, to distinguish various states of the code. They were displayed in monitoring applications, so the user was informed what the device should do.

Later state use was expanded toward synchronisations. States prevent the camera from taking exposures during telescope movement, and unwanted telescope movements during camera exposures. They are displayed on users displays, allowing observes to identify which device is blocking the next exposure or the next telescope movement. The use of states for synchronisation is depicted in Figure 2.

6.2. Default Configuration. Originally RTS2 did not change configuration of devices prior to observations. That leaves the user responsible for device configuration. He/She can do that using either a monitor application or a script for observation.

This handling was later extended by RTS2 remembering default values. The command *script_ends* was added to the protocol. It loads back all changed values.

This code was successfully used for focusing. The system was able to change back to the last known good focuser position even when a focusing run was interrupted. But it starts to show its bottlenecks, notably

- (i) unpredictable behavior for the end user—he/she changes something, and suddenly another value appears in acquired images;
- (ii) unknown default values—system unfortunately does not show which values were changed;
- (iii) the system was quite hard to code, and as a consequence, quite hard to maintain.

Various solutions were considered to resolve those bottlenecks. The following was selected as the best one:

- (i) when appropriate, the system offers default value and various offsets. The default value can be changed only on user request, and is never changed by the system. Offsets can be changed by user and/or system. Offsets are zeroed before beginning of the next observation;
- (ii) or default values are provided only for values written in devices default configuration file.

Both cases can be best understood from an example. The first case can be best demonstrated on the new focuser interface and the second on handling mode settings on CCD.

6.2.1. Offsets, Default and Target Values. The interface provides end user with the following values:

- (i) *current value*, which is read from focuser;
- (ii) *target value*, equal to sum of values listed below;
- (iii) *default value*, set by the user;
- (iv) *focusing offset value*, settable by the user;
- (v) *temporary focusing offset value*, settable by the user, zeroed at the end of the observing script.

Changes of the last three values are used for user focuser interaction. The default value is changed when the user would like to significantly change focuser position. For example the offset can be set for different optical thickness of the filters. And temporal focusing offset is used in the focusing script to change the focuser position during focusing runs.

If a focusing run is interrupted, the focusing script finished, or the focusing program is disconnected, the temporal focusing offset is set by focuser driver to zero. Then a focuser new target value is calculated and used.

Similar control is used for the telescope. There offsets are used to command dithering from the target position.

6.2.2. Camera Acquisition Modes. New modern cameras provide various settings. Some of the combinations of settings are very good for astronomy, while some are pretty bad. A desired behaviour of the system is to allow the user to set only good settings, avoiding the bad ones, while still leaving an option to set all variables manually.

A desired behaviour of the system will also switch the camera at the end of the script to a default mode so that the next script will be able to use camera, without changing any variable.

This functionality is provided by setting the camera mode back to default at the end of the script. A camera mode file provides various modes. The first is the default one, which is used to set camera. An example configuration file is included in the software distribution.

6.3. Observatory Scheduling. It is widely known that observatory scheduling is not a trivial problem. Scheduling is known to belong to NP-hard class of problems, which does not make the problem easier. On top of that, it is not always clear what exactly should be observed in order to maximise the scientific output of the observatory.

RTS2 currently provides users with three scheduling modes: dispatch scheduling, queue scheduling and preprogrammed night plan. The advanced, genetic algorithm scheduling, which should be able to schedule full night runs, is in the late integration phase. The scheduling modes are described in the following sections.

6.3.1. Dispatch Scheduling. Dispatch scheduling is the kind of scheduling used on most, if not all fully autonomous observatories. Each observable target is assigned a merit function, its expected benefits. Dispatch scheduling then calculates merits for all targets, picks the one with the best merit, and observes it. After this target is finished, the scheduler recalculates merit functions, and picks a new target. This approach is discussed by multiple authors, notably [6, 7]. RTS2 provides this mode in the *selector* component.

6.3.2. Queue Scheduling. Queue scheduling schedules targets with the human-night observer in the loop. The night observer is presented with a list of possible targets, which are worth observing. Based on the current conditions,

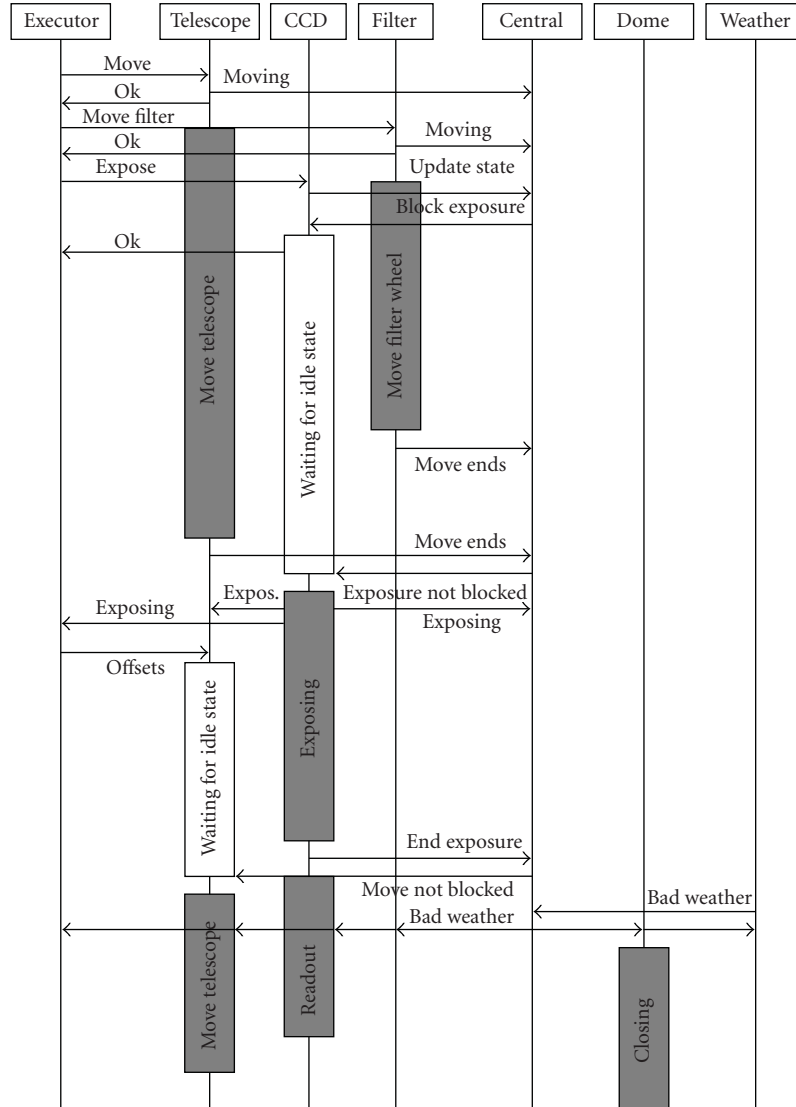


FIGURE 2: Interactions of devices using states for synchronisation. Note how various block are placed to keep telescope from moving and camera from exposing. The observation is interrupted by bad weather reported from a weather sensor, which closes the roof.

instrument setup and astronomer preferences, he/she picks a queue and executes its observation. After the target is finished, a new target is picked from the queue, or the queue is changed by the observer.

This scheduling is used by current big observatories, for example, by ESO VLT [8], CAHA, and IAC telescopes.

The observer can fill a queue of targets in the *RTS2* *executor* component. There are plans to provide automatic selection from those targets, so the observer enters them in the evening, and the system will observe them during the night at optimal weather and time.

6.3.3. Night Plan. Another option is to provide a detailed night plan, which will list sequence of observations, their time and how images should be handled. Although *RTS2* does provide support for night plan, it does not provide any interfaces for plan creation and its management. The

observer must fill a text file and load it into a database. Because of the complexity of this operation and lack of support tools this option is not widely used.

6.3.4. Genetic Algorithm-Based Scheduling. None of the scheduling modes discussed above is optimal. Dispatch scheduling lacks predictability and is short-sighted—it produces schedules which search for a local maxima, instead of focusing on long-term gains. Queue scheduling and night planning requires nontrivial involvement of the observer.

We proposed and implemented scheduling based on genetics algorithms (GA). The problem is described in full depth in [9]. Here is outline of this approach.

Observation targets can list various constraints and merits. The algorithm then searches for the Pareto optimal front [10]—a set of schedules which does not violate any constraints and their respective merit functions are at least

comparable to the other best schedules. The search for this front is performed with NSGA-II [11].

Experimental implementation of GA scheduling is part of the current RTS2 developer branch. The main benefits of GA scheduling are a simple addition of new constraints and merits. Ease of its reuse is demonstrated in [12].

The plan is either to provide the observer with Pareto front schedules and let him/her pick the one he/she likes, or to have system select autonomously during night the path which will be followed.

6.4. Weather Blocking. It is very important to close the observatory roof when conditions are hostile for its normal operations and keeping it closed as long as those conditions prevail. Our records clearly indicate that having the roof open with bad weather over it produces significant problems as soon as the wrong roof state is detected.

The following sections deal with this problem. First the original approach is described. This is followed by a detailed description of current hardware and software setup, which is protecting equipment against the elements.

6.4.1. Original Weather Reporting. Keeping track of observatory conditions was originally a job of the dome module. It was regarded as a single point of failure. Dome code was handled with extreme care, and dome software was carefully tested after each software upgrade. Each device which might indicate bad weather sends information about weather state directly to the dome module. The dome module puts them together, decides if weather is favourable for the observation, and reacts accordingly—if all conditions were satisfied, it switched the system to “on” mode. If a single condition was not met, the dome control module tried to close the roof and switch the system to “standby” mode.

This solutions has the following problems:

- (i) dome software testing is time consuming;
- (ii) in case of a serious computer hardware problem the dome can be left open;
- (iii) every new weather sensor requires modifications to dome control software and extensive testing before being put in operation.

6.4.2. Design of the State-Based Weather Handling. As different new sensors were added to the observatory setup, it becomes clear that weather reporting deserves special attention. The following requirements were put for the new algorithm:

- (i) it must be easy to add new sensors for weather reporting;
- (ii) it must be possible to configure the system to include various sensors;
- (iii) the system must report bad weather in the event of a sensor failure.

Apart from those software requirements, additional requirements were put on the hardware responsible for roof operations:



FIGURE 3: Roof control box switches. Switching roof to manual or stop also stops autonomous observations. Unlike (graphical) user interfaces running on computers, it is very unlikely that this panel will fail. Watcher telescope, Boyden Observatory, Republic of South Africa.

- (i) it must run independently from controlling computer,
- (ii) it will be as reliable as possible,
- (iii) it will be as simple as possible,
- (iv) it must close the roof on its own when it loses connection to its controlling computer,
- (v) it must report to the computer the states of all sensors connected to it.

The software and hardware implementation which fulfills all those requirements is described in the next section.

6.4.3. Current Weather Blocking. RTS2 centrald and all devices have a state. When changed, the state is propagated to all connections.

One of the bits in the state represents bad weather. If that bit is set, it means that the component (in case of device) or whole system (in case of centrald) reports violation of observing conditions, and therefore asks for controlled system shutdown.

Centrald also holds a list of devices which are mandatory for observation. If any of the mandatory devices is not present, or do not reply to centrald requests, the system is switched to bad weather state. This presents developers with a very simple way to add a new weather sensor to the system. They can use methods for weather state manipulation provided in *SensorWeather* class.

The ultimate weather protection element is on most systems a programmable logic controller (PLC). The inputs of this hardware are connected to the various sensors carrying information about the roof state. The outputs of the relay are connected to the motors responsible for roof operations. The PLC is conservatively programmed. It is actually harder to open the roof than to close it.

PLC can be controlled manually with switches. For an image of actual roof control panel please see Figure 3.

If the computer would like to open the roof it must send signals every few seconds to the PLC, to check that it is alive.

TABLE 2: RTS2 installations.

Name	Location	Year	D
BART	Ondřejov, Czech Republic	2001	25 cm
BOOTES 1	INTA El Arenosillo, Spain	2002	30 cm
BOOTES 2	La Majora, Spain	2003	60 cm
FRAM	Pierre-Auger South, Argentina	2004	30 cm
Watcher	Bloemfontein, South Africa	2005	40 cm
BOOTES IR	OSN, Sierra Nevada, Spain	2005	60 cm
LSST CCD testing	BNL, New York, USA	2007	
Columbia	UC, New York, USA	2007	
D50	Ondřejov, Czech Republic	2008	50 cm
BOOTES 3	Blenheim, New Zealand	2009	60 cm
CAHA 1.23 m	CAHA, Spain	2009	1.23 m
LSST CCD testing	LPNHE Paris, France	2009	

The PLC is programed to close the roof if this “*I am alive*” signal is not received.

The critical failure points of this setup are motor failure, failure of power wire to motors and signals to PLC, PLC failure or power failure.

We do not have capability to make motors redundant. PLCs are designed for harsh industrial conditions. The PLC program is relatively simple and is very carefully tested. As its installation requires the presence of the person installing it on site, it is not sensitive to usual bugs introduced by system upgrades. Power backup is provided by UPS capable of closing the roof. The UPS state is monitored by RTS2 and the roof is commanded to close if the remaining UPS uptime or battery level drops below a predefined values.

PLCs are also commodity value. In the unlikely event that the PLC is damaged or destroyed, a new can be purchased without significant problems on almost any place of the planet and installed within a few days from time the failure was detected.

Source code of the PLC program is available from RTS2 subversion repository. As was shown by installing it on multiple sites, this setup is fully replicable and quite modular.

7. RTS2 Installations

Table 2 provides list of the current RTS2 installations together with the year they started using RTS2 and current diameter of the primary optic. The full listing of RTS2 installations is provided on project web pages.

The system is currently being considered for various new and refurbished telescopes. Please note that 1.23 m at CAHA is currently operated in semiautomatic mode, and RTS2 is not on controls only during a few nights. More details about this can be found in [13].

8. Coding Strategy—To Restart or to Code Properly?

At the beginning of the project, we sometimes employed a “last chance” strategy where if something fails (which in our case usually means “produces core dump”), the system

will notice it, wait for a while and restart the failed part. Although this looked as very wise approach, it turned out that it hides potential serious problems and can affect system performance. Moreover, with errors in certain places it can produce situations when devices will keep restarting, produce a few lines in the system log, and exit.

Our experience is that the *if it fails, let system restart it and hope for the best* strategy is contraproductive and should not be employed. After fixing the most important bugs in the code, the programmes run on some setups for months without need for a single restart. If a problem is encountered, its root cause is found and fixed. A fixed driver is then installed and started with the remote ssh access.

The following things are vital for this strategy to work: compile all code with debugging option, change ulimit for core dumps to unlimited and knowledge of how to use *gdb* (GDB web site—<http://www.gdb.org/>) to find cause of the core dump. If all of the previous fails, have *valgrind* (Valgrind web site—<http://www.valgrind.org/>) or a similar memory profiler installed, with knowledge of how to use it to find memory allocation problems.

Once the coder has managed all those issues, not only will the system operate smoothly, but he/she also will not be tempted to switch to some language with a garbage collector (which promises to free developers from memory allocation problems—the most probable reason for failure of the C++ code). That is not to say that high-level languages are not fine for some jobs—we do use Python for GUI and Java/PHP for Web pages. But in our experience, for low-level, hardware control algorithms, nothing beats properly designed and coded C/C++ code.

9. Expected Project Changes

Although RTS2 is able to control autonomous observatories, there is still a lot which deserves more attention, some solutions and some coding. These items are presented in the following list.

9.1. Image Quality Monitoring. The system currently provides some basic quality checks. Those includes results of a plate solving routine provided by Jibaro [14] and/or Astrometry.net (Astrometry.net web site: <http://www.astrometry.net/>) packages, so observers knows if telescope is pointing towards the expected position.

The system lacks real-time display of various image quality parameters—average and median values, minimal and maximal values, number of detected objects (stars) in the image, and so on. Those are calculated and saved to the image header. Our experience shows that those should be easily accessible in real-time displays, as well as in tool for navigation through the image archive.

9.2. Image Processing. Image processing can be configured as an external script, providing relative photometry and other services. We would like to better integrate it with the system by

- (i) adding calibration image database, and providing tools to maintain and use this database;

- (ii) providing observations-to-paper solutions for pre-defined well understood problems, among others observatorion of planetary transit occultations and microlensing events.

9.3. Better User Interfaces. The system is primarily controlled through an ncurses based interface. While this is sufficient for experienced users, the interface is not well suited for occasional users.

Development of both Web and X-Windows Graphical User Interfaces is currently in initial phases. Plans also call for addition of applets for GNOME and other desktops environments, so we will be able to track telescope operations world-wide from a single desktop.

9.4. Network Management. The System currently lacks a central management console. Observatories are usually managed and monitored through ssh connections. While this approach is feasible, it quickly grows beyond the capabilities of a single maintainer.

There is a need for application, which will

- (i) show states of individual observatories in the network,
- (ii) list unresolved problems of individual telescopes, keeping track of actions to fix the problem, and the results of those actions,
- (iii) enable scheduling of the whole network,
- (iv) synthesise results obtained by network members.

It would be nice to have those features backed by simple, low-level, Internet interface. There is work in progress on an XML-RPC interface which will do just this.

9.5. Archive Access. RTS2 keeps all important information in a database. Information about executed observations, and images acquired, together with basic image characteristics (which includes WCS coordinates, fitted by Jibaro and/or Astrometry.net) is recorded for quick retrieval.

Current archive access is provided primarily through console-based utilities. Without doubt in this is a bit too old fashioned in the graphical user interfaces age.

There were PHP scripts for Web-based archive access, which even included cut-out service. Unfortunately they were not very well designed. As the project matures and introduces changes to the database, those scripts cease to function, to the point when it was ruled to be too expansive to make them work again, as is the usual case with simple small fast PHP and other scripts.

Up to now multiple attempts to provide better solutions were made. Yet till now each of them has failed to deliver usable results.

Current attempts include a Google Web Toolkit XML-RPC-backed application. We have reasonable hopes that this will deliver promised results, although not in a short timescale.

10. Conclusions

This article presented an open-source system for robotic observatory control. It provides an overview of rationales for its development, its composition and its main features. It then focused on a list of recent improvements. The article concludes with lists of development items still left on the agenda.

Acknowledgments

The author would like to acknowledge generous financial support provided by Spanish *Programa de Ayudas FPI del Ministerio de Ciencia e Innovaci (Subprograma FPI-MICINN)* and European *Fondo Social Europeo*. Work on RTS2 was supported, influenced and encouraged by numerous people, whose list would be too large for this article. Persons from this list which according to author deserve to be mention explicitly are Martin Jelínek, Alberto Castro-Tirado, Antonio de Ugarte Postigo, Ronan Cuniffe, Michael Prouza, René Hudec, Víctor Reglero and Beatriz Sánchez Félix. The article was carefully reviewed by two anonymous referees, whose suggestions significantly improved it. Stephen Bailey made final gramatical improvements to the article.

References

- [1] T. Jílek, et al., “Detekce astronomických objektů s proměnnou intenzitou za pomoci robotického teleskopu,” Team project, Praha, UK, 2000.
- [2] A. Klotz, F. Vachier, and M. Boër, “TAROT: robotic observatories for gamma-ray bursts and other sources,” *Astronomische Nachrichten*, vol. 329, no. 3, pp. 275–277, 2008.
- [3] S. N. Fraser and I. A. Steel, “Object oriented design of the Liverpool Telescope Robotic Control System,” in *Advanced Telescope and Instrumentation Control Software II*, vol. 4848 of *Proceedings of SPIE*, pp. 443–454, Waikoloa, Hawaii, USA, August 2002.
- [4] P. Kubánek, M. Jelínek, S. Vitek, A. De Ugarte Postigo, M. Nekola, and J. French, “RTS2: a powerful robotic observatory manager,” in *Advanced Software and Control for Astronomy*, vol. 6274 of *Proceedings of SPIE*, Orlando, Fla, USA, May 2006.
- [5] P. Kubánek, M. Jelínek, J. French, et al., “The RTS2 protocol,” in *Advanced Software and Control for Astronomy II*, vol. 7019 of *Proceedings of SPIE*, Marseille, France, June 2008.
- [6] S. N. Fraser, “Scheduling for Robonet-1 homogenous telescope network,” *Astronomische Nachrichten*, vol. 327, no. 8, pp. 779–782, 2006.
- [7] Y. Tsapras, R. Street, K. Home, et al., “RoboNet-II: follow-up observations of microlensing events with a robotic network of telescopes,” *Astronomische Nachrichten*, vol. 330, no. 1, pp. 4–11, 2009.
- [8] A. M. Chavan, G. Giannone, D. Silva, T. Krueger, and G. Miller, “Nightly scheduling of ESO’s very large telescope,” in *Astronomical Data Analysis Software and Systems VII*, vol. 145 of *ASP Conference Series*, 1998.
- [9] P. Kubánek, *Genetic Algorihm for Robotic Telescope Scheduling*, Máster en Soft Computing y Sistemas Inteligentes, Universidad de Granada, Granada, Spain, 2008.
- [10] V. Pareto, *Manual di Economia Politica*, MacMillan, New York, NY, USA, 1906.

- [11] K. Deb, A. Pratap, S. Agarwal, and T. Meyarivan, "A fast and elitist multiobjective genetic algorithm: NSGA-II," *IEEE Transactions on Evolutionary Computation*, vol. 6, no. 2, pp. 182–197, 2002.
- [12] F. Förster, N. López, J. Maza, P. Kubánek, and G. Pignata, "Scheduling in targeted transient surveys and a new telescope for CHASE," *Advances in Astronomy*, vol. 2010, Article ID 107569, 8 pages, 2010.
- [13] J. Gorosabel, P. Kubanek, M. Jelinek, et al., "Recent GRBs observed with the 1.23m CAHA telescope and the status of its upgrade," *Advances in Astronomy*. In press.
- [14] A. de Ugarte Postigo, M. Jelínek, J. M. G. Urquía, et al., *JIBARO: un conjunto de utilidades para la reducción y análisis automatizado de imágenes*, Astrofísica Robótica en España, Ed. Sirius, Madrid, Spain, 2005.

Research Article

Identification and Analyses in Optical Light of Gamma-Ray Sources with Astronomical Archival Plates

René Hudec^{1,2} and Miloš Klíma²

¹ *Astronomical Institute, Academy of Science of the Czech Republic, 25165 Ondřejov, Czech Republic*

² *Faculty of Electrical Engineering, Czech Technical University in Prague, 16636 Prague, Czech Republic*

Correspondence should be addressed to René Hudec, rene.hudec@gmail.com

Received 13 June 2009; Accepted 2 September 2009

Academic Editor: Alberto J. Castro-Tirado

Copyright © 2010 R. Hudec and M. Klíma. This is an open access article distributed under the Creative Commons Attribution License, which permits unrestricted use, distribution, and reproduction in any medium, provided the original work is properly cited.

The ESA INTEGRAL satellite (International Gamma Ray Laboratory) launched in October 2002 continues to deliver valuable data about the gamma-ray sky. Nearly 450 gamma-ray sources have been detected so far mainly by the IBIS onboard instrument, and others are expected in the future. The first 3.5 years of INTEGRAL public and Core Program data have revealed more than 400 sources and this number is expected to increase to more than 500 in the future (Bird et al. 2007). Alternative method to identify and to analyze INTEGRAL gamma-ray sources using optical light and astronomical archival plates is described, together with additional results from analyses of high-energy sources in these databases.

1. Identification of High-Energy Sources

Only a fraction of the newly detected INTEGRAL hard X-ray/gamma-ray sources are either known sources or have been identified and classified already. From the 56 newly by- INTEGRAL detected sources (IGR sources), only 20% have already firm classification, mostly with Cataclysmic Variables (CVs), AGN, High Mass X-ray Binaries, Low Mass X-ray Binaries, Black Hole Candidates, and Anomalous X-ray Pulsars [1]. One of the methods applied in the past is the identifications by spectroscopy, which proved recently some new and interesting identification of INTEGRAL gamma-ray sources such as newly detected symbiotic and cataclysmic variables (e.g., [2]).

2. Limitations of Spectroscopic Method

Although successful, this method based on optical and/or NIR spectroscopy has some limitations. First, it can be hardly applied for particular types of transients and even recurrent transients. Secondly, it requires access to dedicated large

aperture telescopes and spectrographs and this is mostly limited, and expensive. Moreover, it can be laborious in the cases of large error box and crowded field, and this is quite a common situation as most of the INTEGRAL fields indeed lie in the Galactic Plane region. And in some specific cases, only the spectral information alone is sometimes not enough for reliable classification of the objects.

3. The Photometric Alternative

In this paper, we discuss an alternative method to identify the still nonclassified INTEGRAL gamma-ray sources and newly detected INTEGRAL sources in the future (and of other high-energy satellites in general). This method is based on the fact that (1) many of gamma-ray sources identified and classified so far do have optical counterparts, in many cases brighter than magnitude 18, and (2) a significant fraction of these sources is variable both in gamma-rays as well as in optical wavelengths. Both CCD images covering the error boxes of the sources taken preferably by robotic telescopes over at least few months time interval and archival sky patrol plates can be used in this case.

4. The Motivation

The ESA INTEGRAL satellite focuses on the Galactic Centre region as well as on Galactic Plane Scans (GPS). Numerous new gamma-ray sources have been found in these regions by INTEGRAL, and only a fraction of these sources was successfully identified. The identification of INTEGRAL sources indicates that most of them have variable optical counterparts brighter than magnitude 18. The recent progress in classification of newly detected INTEGRAL sources has indicated that the fraction of Cataclysmic Variables and Symbiotic Stars is larger than originally expected (32 at the time of writing this paper). These sources are usually optically bright with magnitudes 10–18 and can be easily and effectively studied at optical wavelengths by ground-based telescopes or, alternatively, by archival databases as described in this contribution. In addition to identification and classification, another goal is to provide light curves for more detailed scientific analyses. This is also an important task as the newly identified IGR sources only rarely have an optical light curve available.

5. Suitable Databases

The Sonneberg Field Patrol and Leiden/Johannesburg Franklin Adams Plates represent a suitable database for identification and analysis of INTEGRAL sources (see Figure 1). They both provide numerous data for regions along the Galactic Plane. In addition, the southern sky patrol plates located at the Bamberg Observatory, Germany, represent a suitable additional source of data.

6. Sonneberg Field Patrol

The Sonneberg Observatory Field Patrol covers selected northern regions along the Galactic Plane (but, also, other fields) by numerous (typically 50–500) astrograph plates. Typical Field of View (FOV) is 10×10 deg and the typical limiting magnitude is $B \sim 17$. In exceptional cases, also low-dispersion spectral plates are available. This kind of data is valuable for analyses related to the ESA Gaia project, as it will provide BP and RP photometric data in the form of ultra-low dispersion spectra. The Sonneberg plates can be scanned as the observatory possesses plate scanners, and, moreover, the plate catalogue is available as a file, hence searches in the plate catalogue are easily based on developed software package.

7. Leiden/Johannesburg Franklin Adams Plates

These plates were taken in Johannesburg by the high quality Franklin Adams refractor (Taylor, 1904) in years 1923–1952 within the project originated by Professor E. Hertzsprung and are located in Leiden. The plates cover selected fields along the southern Galactic Plane as well as the Galactic Centre. The typical number of plates per field is 300–400; FOV is 10×10 deg and limiting magnitude 17.

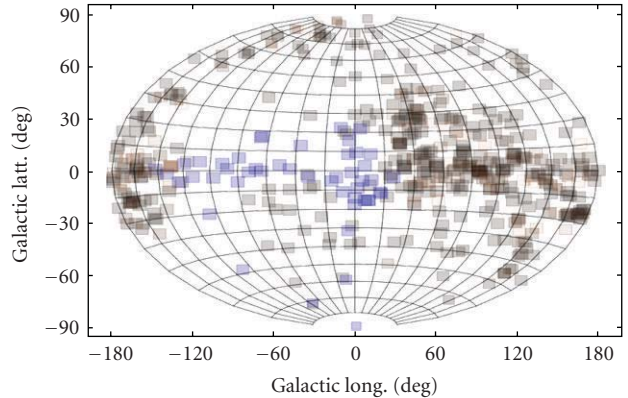


FIGURE 1: Distribution of Sonneberg Field Patrol Fields and Franklin Adams Fields (blue) in Galactic coordinates. The densely covered fields are darker.

Unfortunately, the plate catalogue is available only as a hard copy at the Leiden Observatory, and, moreover, there is no dedicated plate scanner available.

8. Bamberg Observatory Plates

The third most suitable plate archive is located at the Bamberg Observatory in Germany, and represents a systematic southern sky patrol up to limiting magnitude 15 to 15.5. Hence all objects are covered within this limiting magnitude, and the typical number of plates available for particular position is about 200. The preference is plate catalogue as searchable file as well as available plate scanner.

9. The Plate Analysis

Using the data material mentioned here, the optically identified INTEGRAL sources with objects brighter than mag 17 can be investigated for long-term changes covering 10–50 years. In addition, these data can be used to search for new optical identifications of nonclassified INTEGRAL sources on hand of their optical variability. The same is valid also for optical counterparts of other high-energy (HE) sources.

For plate analyses, various methods can be used. As most of the plate archives were not yet fully scanned, the most effective method at moment is combination of on site analyses, for example, by an optical plate microscope (transmitted light), with computer analyses of digitized plates, depending on the nature of the task to be performed.

A few additional prospects are listed as follows: analyzing the light curves for flares and flaring activity, trying to fit the flare profiles, trying to look for possible periodicities and recurrences, studying of colours and colour changes with time, with consequent physical discussions and interpretations. Correlations with other objects, with related conclusions toward physical processes and physical models.

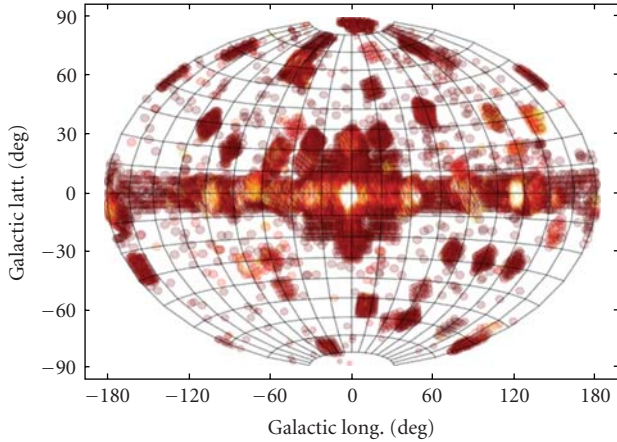


FIGURE 2: The coverage of INTEGRAL IBIS for revolutions 1–430.

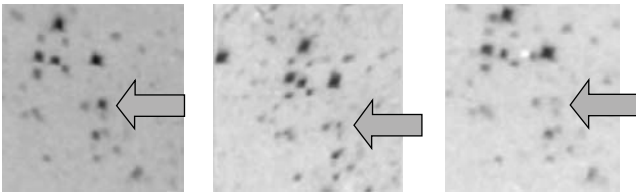


FIGURE 3: IGR J12349-6434 = RT Cru, hard X-ray symbiotic star, on Leiden Franklin Adams Plates. INTEGRAL gamma-ray source visible on astronomical plates taken by 100 years old optical telescope. Violent (amplitude 3 magnitudes) optical brightness variations about 80 years ago.

10. Galactic Centre

A particular interest is to be devoted to regions close to Galactic Centre where the INTEGRAL satellite coverage is large and where numerous HE sources are located, and still new sources are discovered (see Figures 2–5). This area is also heavily covered by archival plates at particular observatories (e.g., Leiden, Franklin Adams plates taken in Johannesburg). On the other hand, the crowded nature of fields near the Galactic Centre represents an additional problem especially in case of deep plates/images.

11. GRBs Analyses

The archival astronomical plates can be used also for study of optical afterglows (OAs) and optical transients (OTs) related to gamma-ray bursts (GRB). However, it should be taken into account that not only X-ray and gamma, but also the optical sky is highly variable even on short-term timescales. Not only do optical transients and optical afterglows of GRBs contribute but also a rich variety of transient astrophysical phenomena resulting in fast optical transients—such as flare stars, flares on AGN, novae and other types of variable stars, SNe, and so forth—appeal on astronomical emulsion. Some of them are rare events and their detection requires wide fields (20 deg^2 or more) and prolonged (>1 year of total cumulative time) monitoring intervals.

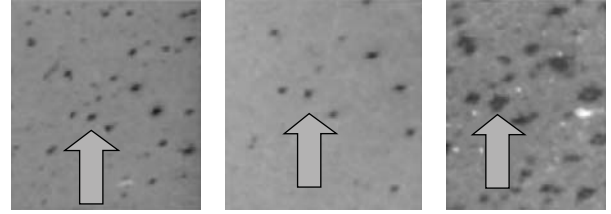


FIGURE 4: IGR J10109-5746, hard X-ray symbiotic star. Optical variability on Franklin Adams plates, field 10, Leiden, year 1928.

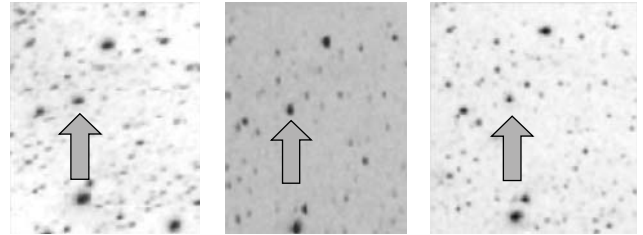


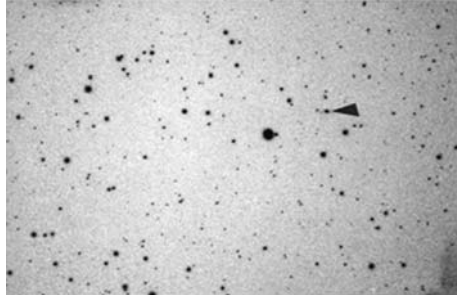
FIGURE 5: IGR J11215-5952 High-Mass X-ray Binary detected in gamma-rays by INTEGRAL and visible in optical light on historical F. A. plates (various epochs).

11.1. OTs on Astronomical Archival Plates. What is the origin of OTs found within the astronomical plate analyses of GRB error boxes? At least some of them were confirmed as real astrophysical triggers. On the other hand, relation to GRB was not confirmed. However, some of them represent very probably rare large, amplitude flares of faint AGNs.

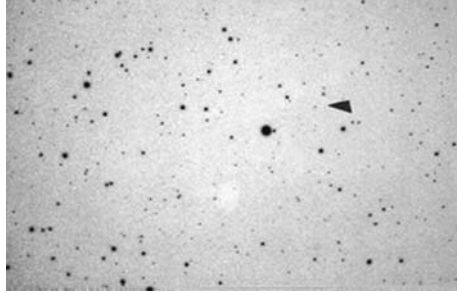
There is unprecedented large time coverage of used plates: up to 3.2 years of continuous monitoring of a particular position collected and analysed—more than any other astrophysical search before. A question arises, namely: could indeed no relation to GRBs be established? In recent understanding, the GRB origin is in star forming regions (SFR) in distant galaxies. GRBs are not confirmed as recurrent events. However, the historical OTs found at positions of GRBs may represent another triggers from the same SFR or the same galaxy, separated in time by more than 50 years. Below we discuss some objects found on astronomical emulsions during archival GRB searches.

11.2. OT Triangulum (Figure 6). The OT Triangulum represents an example of OT of unknown origin found by a chance on astronomical archival plates: $B = 10.5 \text{ mag}$, more than 6 mag above the plate limit, according to Hudec et al. [3]. Despite of the possible presence of plate faults, there are developed methods (such as reflected light or confocal microscopy) able to reliably exclude these false triggers. One has to be careful in elimination of background triggers such as aircraft and satellite glints, and so forth. However, the OT shown here exhibits all attributes of a real OT of an astrophysical origin.

11.3. OT GRB781119. This object was discovered by B. Schaefer inside the error box of GRB781119 as the first possible OT related to a gamma-ray burster (Schaefer, 1981



(a)



(b)

FIGURE 6: The OT Triangulum. Above the discovery plate with the OT (estimated magnitude $B \sim 10.5$) indicated, below a comparison plate with no object at the position. Astrograph plate from the Sonneberg Observatory archive, limiting magnitude 17.

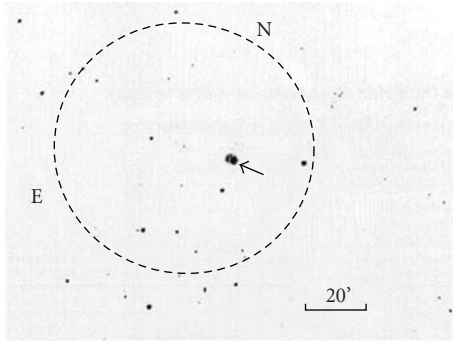


FIGURE 7: The OT inside the error box of GRB910219.

[4]). Later, there were doubts by Zytkov pointing out the alternative explanation as a plate fault. To explain this controversy, the original plate was investigated in detail by reflected light microscopy and was confirmed as real object by Hudec et al. [5, 6]. The object relation to GRB is not clear. In fact, the OT could be caused by a blue large amplitude flare from a nearby 18 magnitude quasar.

11.4. OT GRB790325b. This object represents multiple OT from the position close to GRB790325b. It was found on astronomical archival plates (5000 plates used with total cumulative exposure time 7000 hrs). The OT was confirmed as real object by method of grain depth distribution [7]. A faint blue object was found on the OT position,

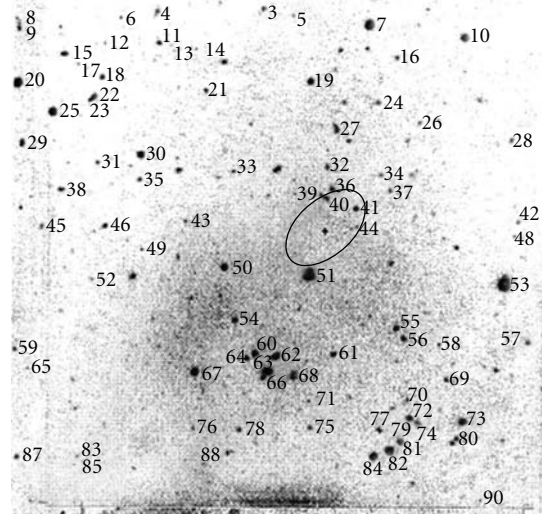


FIGURE 8: The deep sky objects inside and around the error box of the OT GRB910219.

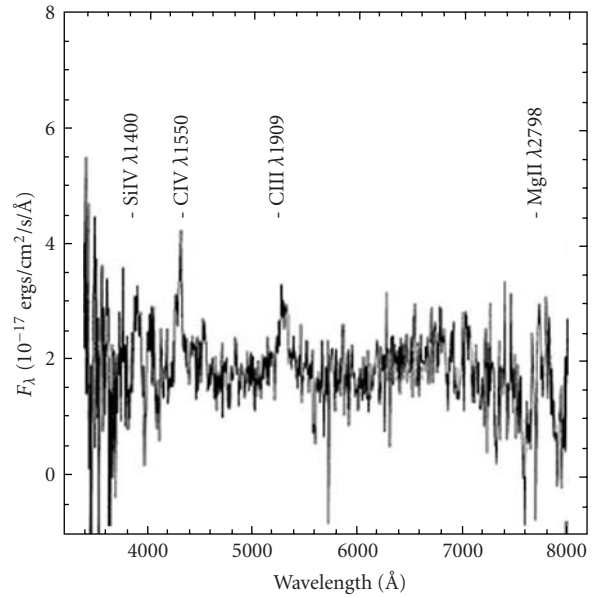


FIGURE 9: The spectrum of the object 41 inside the OT error box from previous figure. This is a candidate object for the OT, probably a faint QSO.

very probably faint AGN [8]. Possible explanation: large amplitude flares from faint AGN.

11.5. OT GRB910219 (Figures 7–9). This OT was found on the Harvard College Observatory (HCO) archival plate in the error box of GRB910219 [5, 6]. The image probably represents a large amplitude flare of a faint QSO at the OT position. Altogether 3.2 years of continuous optical monitoring (by archival plates) were used to reveal this object.

There still are many open questions related to the studies of GRB positions on astronomical plates. Before OTs of GRBs

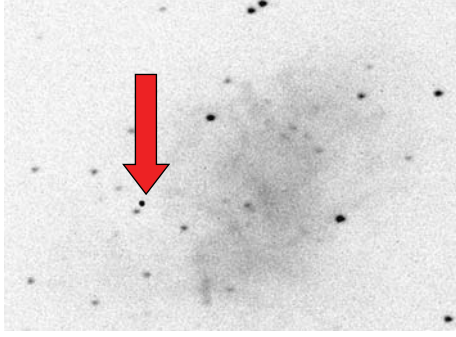


FIGURE 10: The OT of unknown nature: object detected on a sequence of CCD images (field M1) by the 60 cm telescope of the Brno Observatory by Filip Hroch. The estimated duration is less than 20 sec and the magnitude $R = 11$.



FIGURE 11: Plate scanning efforts at the Sonneberg Observatory, the largest European plate collection (280 000 plates). More than 200 000 plates were digitized already.

found by BeppoSAX, there were extended dedicated efforts to detect the optical emission of GRBs by taking Schmidt telescope plates hours to dozens of hours after GRBs triggers. No OTs or OAs were found at that time in relevant GRB error boxes with limiting magnitude between 16 and 22. Why? In recent understanding, there should be a positive detection at least in few cases.

11.6. OTs with CCD Detections. OTs with unknown origin were found not only on photographic plates but also on CCD images as shown in Figure 10.

12. Future Prospects

Over the last years, extended efforts were done at several major plate centres, such as Sonneberg, HCO, or PARI (see Figure 11). What is new in data mining in astronomical plate archives: (1) wide digitization of the plates and easy access to data recorded in astronomical emulsions, (2) specially designed and commercially available flatbed scanners, (3) dedicated programs to search in plate logs and catalogues, and (4) dedicated computer programs to evaluate data.

In the near future, we plan some additional improvements in the procedures and analyses described above, based

on novel methods of image analysis (not only for direct images but also for spectral ones as well as multiple images), in particular,

- (1) the evaluation of source image data from real image detector, that is, the data deconvolution for the compensation of distortions caused by the properties of the image sensor and optical and archiving (e.g., [9]),
- (2) postprocessing of input image data (improving the signal/noise ratio, etc.),
- (3) extraction of required data (data mining) from the images (e.g., analysis of spectral lines etc., e.g., [10]),
- (4) statistical evaluation of obtained data,
- (5) compression of image data for transfer and archiving (e.g., [11]),
- (6) simulations of some parts of imaging/detecting chain (e.g., [12]),
- (7) the program selection and recognition of important image information and comparison of their quantitative characteristics and reliability of the analysis based on analyses of series of multispectral images,
- (8) statistical evaluation of large sets of multispectral image data sets, including those focused on particular triggers,
- (9) the correlation of characteristics, selection of similar or belonging to the same type objects, automated searches for analogous objects on series of images. Possibility of stereoscopic analysis taking the astrometric results into account,
- (10) improvements also includes development of algorithms and codes for automated analyses of low dispersion spectra, automated classifications, analyses of spectra lines, spectral continuum distributions, searches for spectral variability (both lines and continuum), and searches for objects with spectral variability and with peculiar spectra, and so forth [10, 13].

13. Conclusions

An alternative cost-effective method for classification and optical identification of INTEGRAL sources (and gamma-ray and hard X-ray sources in general) was discussed with some examples. This method can be applied both to detailed analyses of already identified sources as well as to identification of nonclassified new sources. Dedicated software programs are in design and development. The astronomical archival plates represent, due to large FOVs and large time coverage, an important data source for the monitoring of transient universe in general. For a given sky region, a total cumulative time of more than 3 years can be easily analysed on plates from several plate archives, impossible by any other method. Due to large FOV of astronomical archival plates, such large time coverage can be obtained for many of the celestial positions. The novel methods of image analyses and

dedicated software packages are expected to further improve the importance of these data.

Acknowledgments

The authors acknowledge the support provided by ESA PECS 90823 and the Grant Agency of the Czech Republic, grants 205/08/1207 and 102/09/0997. The plate analyses were supported also by MSMT project ME09027. The investigation of Bamberg sky patrol plates is supported by DAAD-25-CZ4/08 project DAAD-AVCR.

References

- [1] A. J. Bird, A. Malizia, A. Bazzano, et al., “The third IBIS/ISGRI soft gamma-ray survey catalog,” *Astrophysical Journal, Supplement Series*, vol. 170, no. 1, pp. 175–186, 2007.
- [2] N. Massetti, et al., “Unveiling the nature of INTEGRAL objects through optical spectroscopy. V. Identification and properties of 21 southern hard X-ray sources,” *Astronomy & Astrophysics*, vol. 459, no. 1, pp. 21–30, 2006.
- [3] R. Hudec, et al., “Possible optical transient in Triangulum and its relation to the gamma-ray burst sources,” *Astronomy & Astrophysics*, vol. 225, p. 411, 1989.
- [4] B. E. Schaefer, “Probable optical counterpart of a γ -ray burster,” *Nature*, vol. 294, no. 5843, pp. 722–724, 1981.
- [5] R. Hudec, et al., “OT 1928: A real candidate for GRB 781119,” *Astronomy & Astrophysics*, vol. 284, p. 499, 1994.
- [6] R. Hudec, et al., “Optical studies in the fields of gamma ray burst sources. 2: GRB 910219 and the detection of flashing optical counterpart,” *Astronomy & Astrophysics*, vol. 284, p. 839, 1994.
- [7] R. Hudec, et al., “Grain depth distribution and the reality of optical transient candidates near the GRB 790325b position,” *Astronomy & Astrophysics*, vol. 270, p. 151, 1993.
- [8] C. Motch, R. Hudec, and C. Christian, “Quiescent candidates for the repeating optical transient OT 1809 + 31,” *Astronomy & Astrophysics*, vol. 235, no. 1-2, pp. 185–196, 1990.
- [9] M. Klíma, J. Pazderák, and K. Fliegel, “Examples of subjective image quality enhancement in multimedia,” in *Applications of Digital Image Processing XXX*, A. G. Tescher, Ed., vol. 6696 of *Proceedings of SPIE*, pp. 1–9, San Diego, Calif, USA, August 2007.
- [10] L. Hudec, *Algorithms for spectral classification of stars*, BSc thesis, Charles University Prague, Prague, Czech Republic, 2007.
- [11] P. Pata, et al., “PCA Based Compression Technique for the BOOTES Image Data,” in *Proceedings of the 5th INTEGRAL Workshop on the INTEGRAL Universe (ESA SP-552 '04)*, V. Schönfelder, G. Lichti, and C. Winkler, Eds., p. 883, Munich, Germany, February 2004.
- [12] M. Reřábek, P. Páta, K. Fliegel, J. Švihlík, and P. Koten, “Space variant point spread function modeling for astronomical image data processing,” in *Astronomical Adaptive Optics Systems and Applications III*, R. K. Tyson and M. Lloyd-Hart, Eds., vol. 6691 of *Proceedings of SPIE*, pp. 1–10, San Diego, Calif, USA, August 2007.
- [13] R. Hudec, V. Šimon, and L. Hudec, “The GRB Investigations by ESA Satellite Gaia, in GAMMA-RAY BURST: Sixth Huntsville Symposium,” in *AIP Conference Proceedings*, vol. 1133, pp. 52–54, 2009.

Research Article

Detection of GRBs and OTs by All-Sky Optical and SID Monitors

R. Hudec,^{1,2} M. Spurny,³ M. Krizek,⁴ P. Pata,² R. Slosiar,⁵ M. Rerabek,² and M. Klima²

¹ *Astronomical Institute, Academy of Sciences of the Czech Republic, 251 65 Ondrejov, Czech Republic*

² *Faculty of Electrical Engineering, Czech Technical University in Prague, Technicka 2, 166 27 Prague 6, Czech Republic*

³ *Karlovy Vary Observatory, K Letisti 144, 360 01 Karlovy Vary, Czech Republic*

⁴ *Charles University, Astronomical Institute, 180 00 Prague, Czech Republic*

⁵ *Partizanske Observatory, 958 04 Partizanske, Slovakia*

Correspondence should be addressed to R. Hudec, rhudec@asu.cas.cz

Received 13 June 2009; Accepted 15 November 2009

Academic Editor: Taro Kotani

Copyright © 2010 R. Hudec et al. This is an open access article distributed under the Creative Commons Attribution License, which permits unrestricted use, distribution, and reproduction in any medium, provided the original work is properly cited.

We report on two alternative simple methods to detect counterparts of cosmic gamma-ray bursts (GRBs) and optical transients (OTs). We report on the development and tests of an alternative optical all-sky monitor recently tested at the Karlovy Vary Observatory. The monitor is based on a Peleng 8 mm fish-eye lens (1:3.5–1:16) and CANON EOS 350D digital CCD camera. This type of monitor represents a low-cost device suitable for easy replication and still able to detect brighter optical transients simultaneously to GRB triggers. Such OTs have been observed for some of the GRBs such as GRB990123, GRB060117, or recently GRB080319 indicating that some fraction of GRBs can generate optical transient emission accessible by simple small aperture instrumentation as described here. These efforts are accompanied by development of dedicated programmes to access and to evaluate all-sky images; these efforts will be also briefly described. The All-Sky Monitor is a space variant optical system and its point spread function (PSF) has not uniform shape in the field of view. The processing and measuring of image data is complicated, and sophisticated deconvolution algorithms are used for image restoration. The second method is the GRB detection based on their ionospheric response.

1. Bright Prompt Optical Emission of GRBs

The fast response is required to investigate the optical prompt emission of GRBs. However, even the fastest optical follow-up telescopes cannot access the times close or identical to times of GRBs, and the time domain before GRB remains completely hidden. These time domains can be accessed only by optical wide-field monitors (as the position of the GRB is unpredictable). The all-sky monitors offer the best sky coverage. An alternative approach is to monitor the FOVs of recent GRB satellites with optical WF cameras. Some of the all-sky monitors operated on daily basis are based on the use of photographic emulsion (allowing long exposures and fine spatial resolution of few microns). However, the photographic emulsion is not very sensitive to short optical flares and has some additional disadvantages. The alternative digital all-sky monitoring is provided by the CONCAM system. However, the limiting magnitudes are not very deep, so one can hardly expect that such system will be able to

detect optical transients (OTs) of GRBs. The brightest OTs related to GRBs observed so far were observed at magnitudes 6–10 (e.g., GRB990123, GRB060117, GRB080319) [1, 2]. For GRB060117, the optical transient was followed due to technical reasons from 2 minutes after the GRB trigger and already declining, so one can deduce that the peak brightness probably exceeded magnitude 8 [3]. We hence need monitors able to detect short OTs with duration of about 1 minute and fainter than magnitude 8. Some optical all-sky monitors are in operation already such as the EN photographic network managed by the Ondrejov Observatory (Figures 5, 6, and 7) and CCD-based sky monitor was tested at the Sonneberg Observatory (Figure 4).

2. The Optical All-Sky Monitor

We report on an alternative low cost all-sky monitor. The used instrumentation is simple and low-cost. The camera

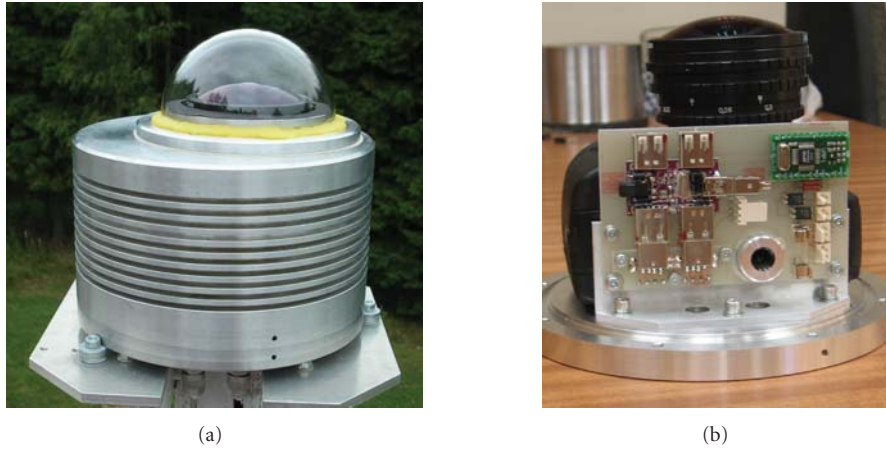


FIGURE 1: The assembled all-sky camera in observing conditions (a) and the camera with control electronic board (b).



FIGURE 2: The picture and the schema of the used Peleng fish-eye lens. It should be noted that the lens consist of 10 glass elements. Although no detailed measurements about spectral efficiency of the lens, by analogy with similar lenses, one can expect that there will be no or very little response below 400 nm.

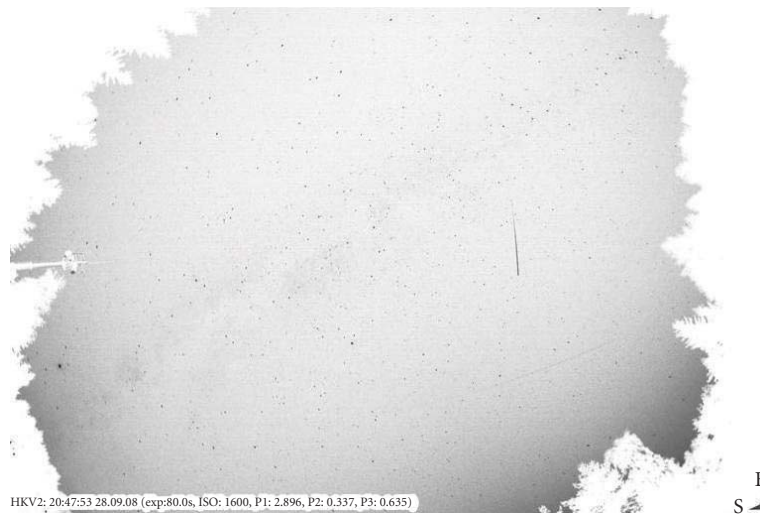


FIGURE 3: An example of raw nonguided image taken by the camera illustrated in Figure 1, exposure time 80 seconds (converted to negative).

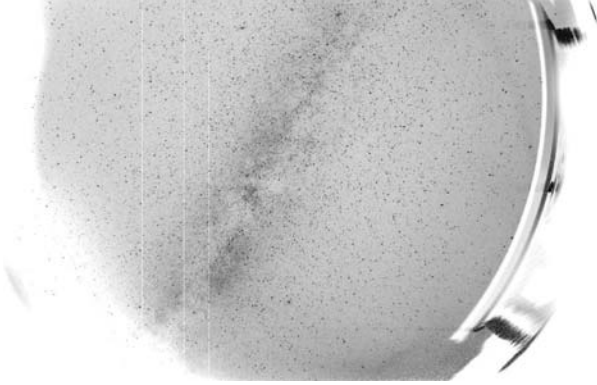


FIGURE 4: Sonneberg Observatory All-Sky 7k \times 4k CCD camera, 10 minutes exposure, 4 \times 4 binning (converted to negative).

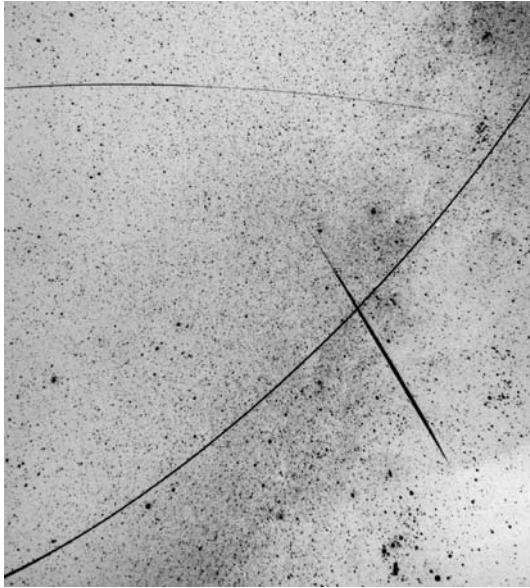


FIGURE 5: Ondrejov Observatory EN network photographic plate, central part (converted to negative). The EN network uses fish-eye lenses F-Distagon 3.5/30, and the images are recorded on planfilms 90 \times 120 mm; sky diameter is 80 mm and typical exposure time 3 hours resulting in limiting magnitude 11.

has two parts, namely, the Peleng 8 mm fish-eye lens (1 : 3,5–1 : 16, Figure 2) that provides a 24 mm circular 180 field of view (Figure 3), and a CANON EOS 350D digital CCD camera (Figure 1). The total cost of the hardware is around 1500 USD, that is, one order less than the CONCAM system. One can hence expect the system to be easily and cheaply replicated to numerous sites. One can consider the alternative type of the digital camera, such as Canon EOS 5D with a larger CCD chip (but somewhat larger pixel size) hence covering the whole FOV of the fish-eye lens. We plan to improve the performance of the system by designing, in collaboration with the Czech Technical University in Prague, especially dedicated mount and miniature dome for the camera. Use of another lens can provide deeper magnitudes but smaller FOV (Figure 8).



FIGURE 6: The automated EN sky patrol photographic camera operated by the Ondrejov Observatory, Department of Interstellar Matter.

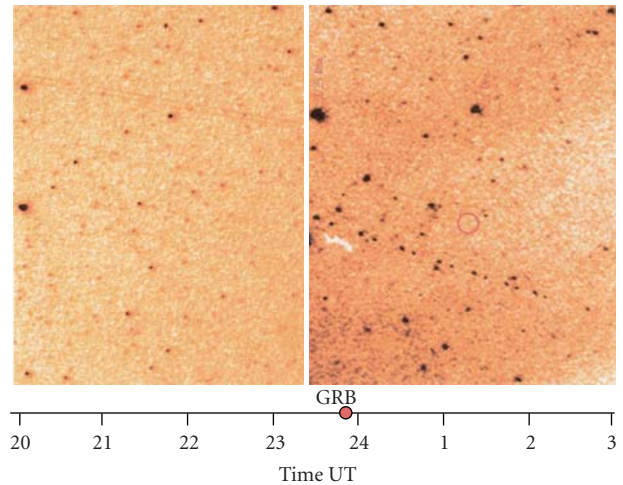


FIGURE 7: The area of the GRB000926 on the photographic plates of the EN network. Left: preburst image (end of exposure 29 minutes before the GRB trigger), lim magnitude 10. Right: simultaneous image, lim magnitude 8. The position of the GRB is indicated by a circle. Both images contain airplane trails/lights.

3. Simulation and Evaluation of Images from Optical All-Sky Systems

As shown in Figure 2, the all-sky fish-eye lenses consist of 10 glass elements. This type of optics influences the focal images. Any reliable scientific use and evaluation of images from these systems must take this into account. There are two related problems in WFC and UWFC optical systems: (1) optical aberrations, and (2) space variant systems. The motivation for the simulation is as follows:

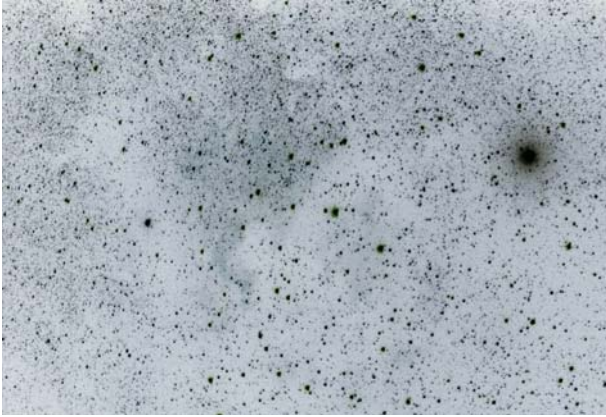


FIGURE 8: An example of image taken by Canon EOS 350D digital CCD camera with nonfish eye lens Soligor 2.8/105 mm (converted to negative) at Sonneberg Observatory. Then the limiting magnitude amounts to 15 over a smaller FOV of order of 10×10 degrees.

(1) modelling of optical system used in all-sky monitors and their transfer characteristics aberrations and distortion, (2) UPSF image restoration and deconvolution of acquired image data removal, and (3) enhancement of measurement precision.

Real UWFC image data and their evaluation are related with the following problems: (1) objects on ultra-wide-field images are very small (a few pixels per object dimension). (2) Optical aberrations and distortions in UWFC systems, see Figure 11, (3) influence of optical aberrations increases at the edges of FOV and, (4) these aberrations distort the PSF of optical system and rapidly cut the accuracy of measurements. (5) Objects on the frontier of field of view are not used for analysis in astrometry because a lot of aberrations. Above we show several preliminary results obtained in this direction (Figures 9, 10, and 12).

4. The VLF Detections of GRBs

The method of indirect detections of GRBs at Very Low Frequency (VLF) has been described already before [4], however only very few positive records are known. Previously reported VLF detections of GRBs are as follows. (i) GRB830801: a first observation of an ionospheric disturbance from a gamma-ray burst reported [4]. The burst, occurred at 22:14:18 UT on August 1, 1983, and was one of the strongest ever observed at that time. The total fluency was 0.002 erg/sq cm, most of which occurred in the first 4 seconds of the burst. Simultaneously, a change was observed in the amplitude of a VLF radio signal from a transmitter in Rugby, England indicative of an ionospheric disturbance. Weaker disturbances were also recorded at the same receiving site on signals from VLF stations in Annapolis, Maryland and Lualualei, Hawaii. The times of the burst and the disturbances are coincident within the 10-second resolution of the VLF recording system. No similar disturbances were observed within 60 hours around the time

of the burst. (ii) SGR1806: detection of a Sudden Ionospheric Disturbance [5], (iii) GRB030329 observed as a Sudden Ionospheric Disturbance (SID) [6]. Although there were numerous efforts to detect GRBs by VLF and despite the fact that the necessary instrumentation is inexpensive, this field still remains little exploited [7].

The instrumentation used in obtaining the results discussed below consists of a loop radio antenna and a 2-channel VLF radio receiver (Figure 13). The motivation is an alternative and inexpensive approach to detection and investigation of GRBs.

5. Physics of Ionospheric Detection

The solar particle stream, solar wind, shapes and controls the Earth's magnetic envelope—the magnetosphere—and increases heat in the aurora zones. But not all ionospheric variability is caused by solar or geomagnetic disturbances. The ionosphere is not a constant “mirror in the sky.” The E layer (100–200 km aboveground) and the F1 layer (170–200 km) usually behave in regular, solar-controlled way, but the F2 layer (250–350 km) does not. It is the F2 layer, which has the greatest density of free electrons, and is potentially the most effective reflector of radio waves (see [7]).

The ionospheric D layer plays in the GRB detections an important role, as the detection of X-ray and gamma-ray triggers is based on the measurement (monitoring) of reflected radio waves from this layer. The ionospheric D layer is not transparent for radio VLF waves (frequencies 3 kHz to 30 kHz) and behaves like a mirror. If the transmitter is at large distance (800 to 2000 km) then the radio waves are guided like in a waveguide consisting of the D layer and the earth surface. Any change in the quality of this waveguide results then in the signal change in the SID monitor. The change can be positive but in some cases such as the sudden phase anomaly also negative.

6. VLF Detections of GRBs

We present below examples of our VLF/SID detection of GRBs in three cases: GRB 060124A (Figure 14), GRB080319D and GRB080320A (Figure 15), as well as an indication for detection of GRB induced propagating ionospheric waves (Figure 15).

7. Conclusions

An alternative low-cost (~1.5 kUSD) optical digital all-sky monitoring system has been assembled and it is tested recently. The preliminary results indicate the limiting magnitude even for nonguided system and for one image with exposure of 30 seconds amounts to mag 8. Deeper magnitudes are expected for guided system and longer or cumulated exposures, then the expected limiting magnitude can reach the magnitude 9–10 range. This makes the system suitable for wide-field monitoring in the sky for brighter optical transients. Using nonfish-eye lenses, the limiting

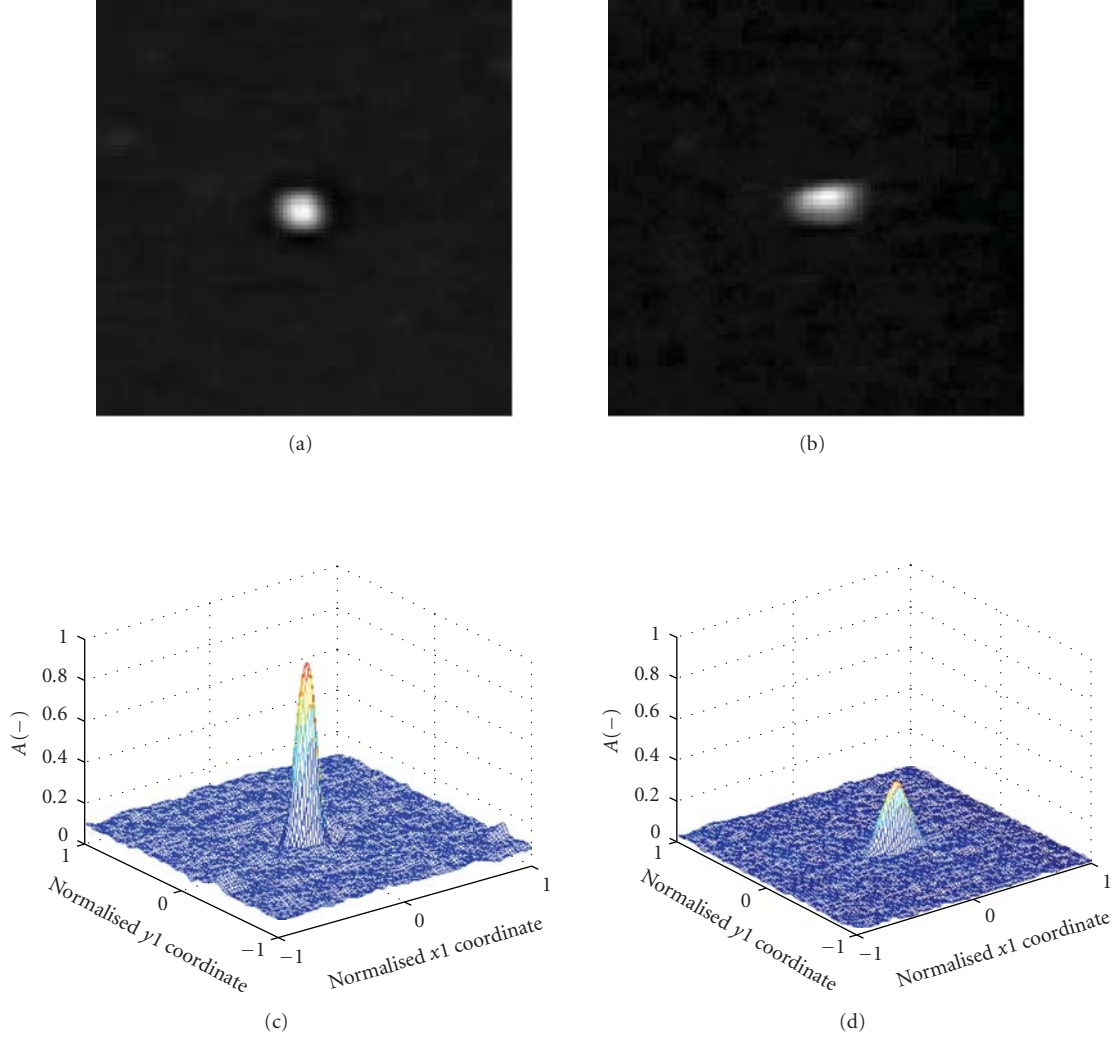


FIGURE 9: The ellipticity of star profiles (simulation). Profiles of stars also are not circular but rather elliptical, especially for worse objectives and greater distance from the middle of the image. The ellipticity is qualified by sigma x and sigma y (while considering the Gaussian function), where sigma x and sigma y are the distance from the centre of the Gaussian in which the Gaussian is equal to $\exp(-0.5)$ of its central value. Sigma x and sigma y are the major and minor half-axis of the ellipse, perpendicular to each other. The ellipticity in radial direction can significantly grow with the angle distance from the middle of the image, especially for wide-angle images.

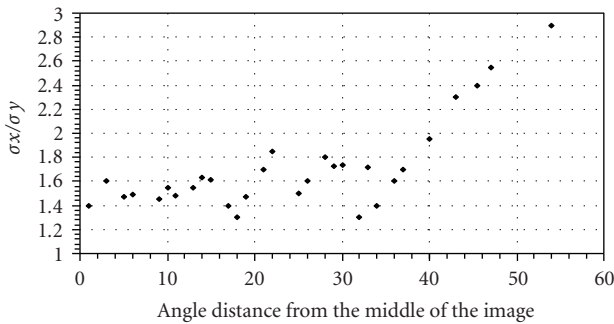


FIGURE 10: Ellipticity (an ideal PSF deformation) of stars' profiles as a function of angle distance from the middle of an all-sky image.

magnitude can reach 15 over a smaller (10×10 degrees) FOV. The system can be very easily duplicated to numerous

sites. Future improvements are planned such as design of a miniature camera mount and dome to allow guided images and development of dedicated control and evaluation software. The algorithms for evaluation of images from all-sky monitors were developed and tested.

The independent and indirect detection of GRBs by their ionospheric response (SID) observed at VLF is feasible. We presented and discussed examples of such VLF/SID detection in three cases: GRB 060124A, GRB080319D, and GRB080320A. In addition, these measurements are in agreement with the scenario of propagating ionospheric waves triggered by the relevant GRBs. Although few such detections have been already reported in the past, the capability of such alternative and indirect investigations of GRBs, as well as the possible contribution to analyses of GRBs, still remains to be investigated in more details.

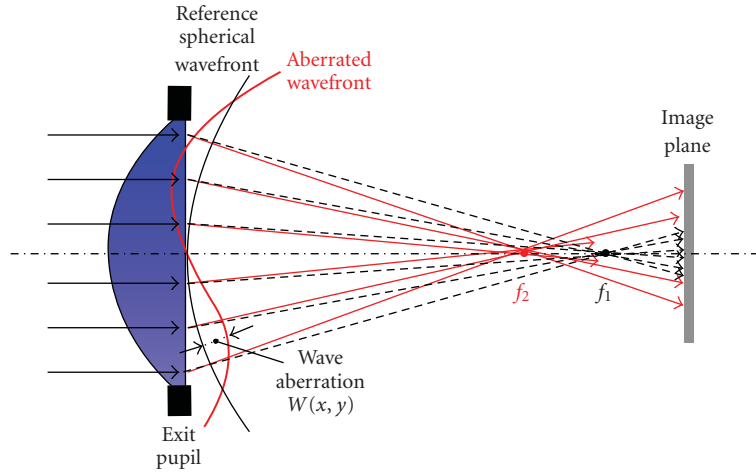


FIGURE 11: Optical aberration can be described using the so-called wave aberration function. The wave aberration function is defined as the distance (in optical path length) from reference sphere to the wave front in the exit pupil measured along the ray. Optical aberrations negatively affect the image quality, imaging system transfer characteristics, and cut precision of other measurements.

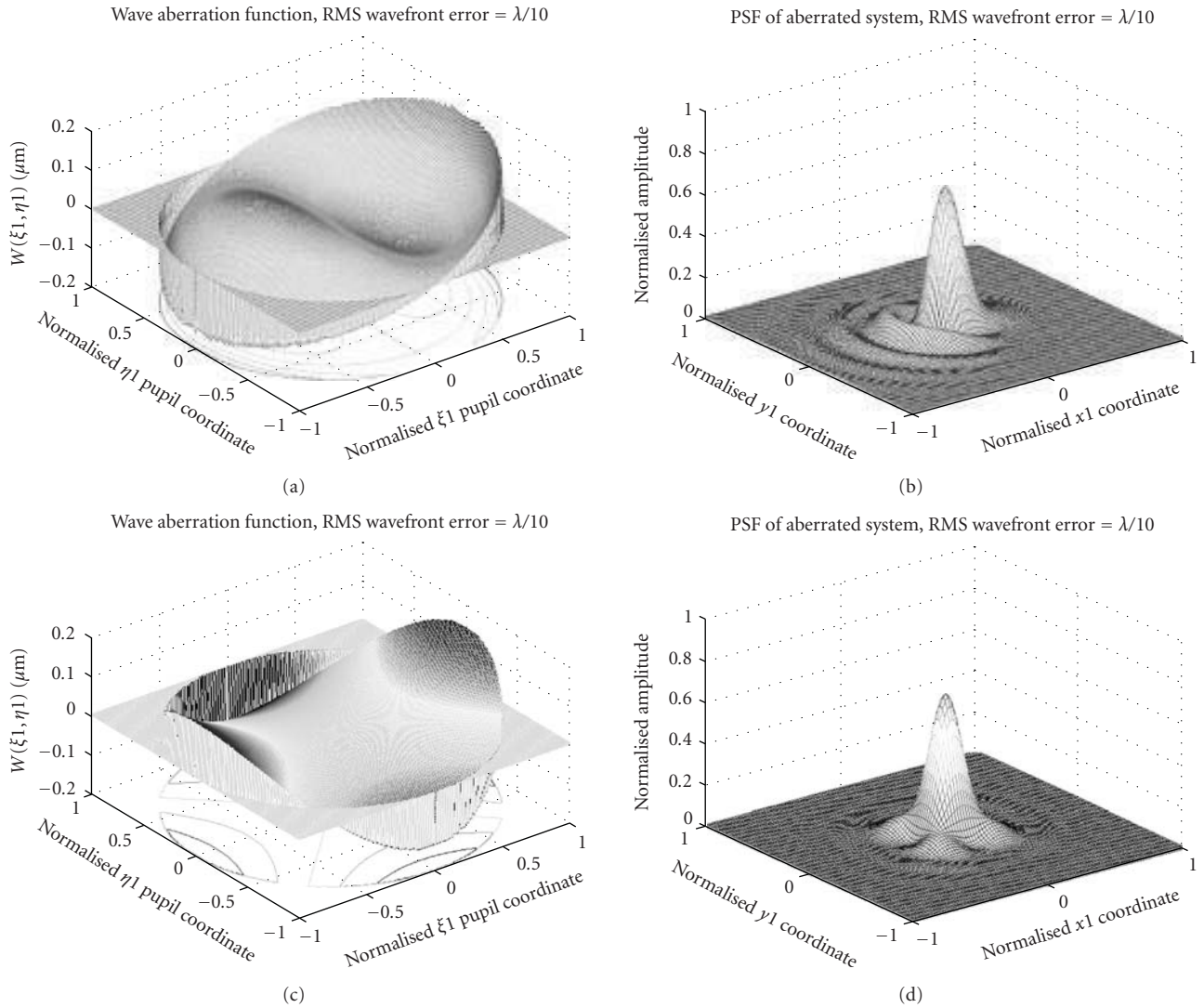


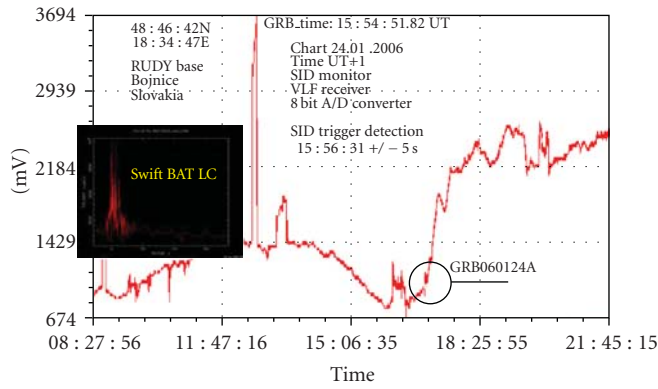
FIGURE 12: Examples of modelling of optical aberrations in optical all-sky monitors.



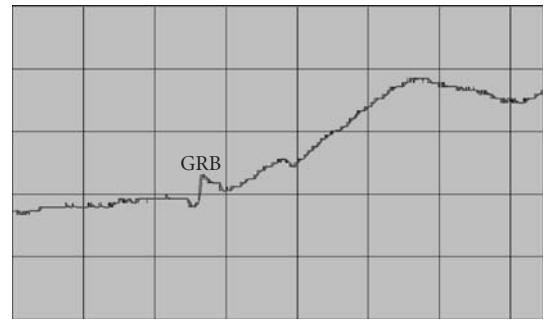
(a)



(b)

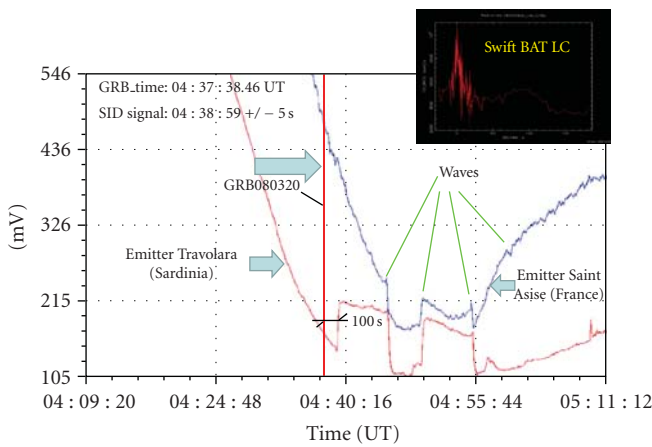
FIGURE 13: The loop antenna (size 75×75 cm) and a 2-channel radio VLF receiver used for SID detection of GRBs.

(a)

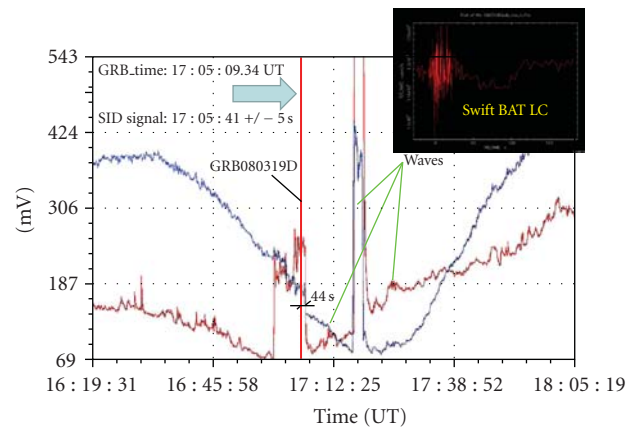


(b)

FIGURE 14: The detection of GRB 060124A.



(a)



(b)

FIGURE 15: The probable detection of GRB080319D (a) and GRB080320A (b) with indicated probable propagating ionospheric waves caused by the GRB.

Acknowledgments

The GRB analyses described here are linked to the GRB analyses within the ESA PECS INTEGRAL Project 98023. Some parts are related to the grant of the Grant Agency of the Czech Republic 205/08/1207 and 102/09/0997. The analyses of GRBs in optical range are newly supported by MSMT KONTAKT Project ME09027.

References

- [1] C. Akerlof, R. Balsano, S. Barthelmy, et al., “Observation of contemporaneous optical radiation from a γ -ray burst,” *Nature*, vol. 398, no. 6726, pp. 400–402, 1999.
- [2] J. L. Racusin, S. V. Karpov, M. Sokolowski, et al., “Broadband observations of the naked-eye γ -ray burst GRB 080319B,” *Nature*, vol. 455, no. 7210, pp. 183–188, 2008.
- [3] M. Jelínek, M. Prouza, P. Kubánek, et al., “The bright optical flash from GRB 060117,” *Astronomy and Astrophysics*, vol. 454, no. 3, pp. L119–L122, 2006.
- [4] G. J. Fishman and U. S. Inan, “Observation of an ionospheric disturbance caused by a γ -ray burst,” *Nature*, vol. 331, no. 6155, pp. 418–420, 1988.
- [5] P. Campbell, M. Hill, R. Howe, et al., “SGR1806: detection of a sudden ionospheric disturbance,” GCN GRB Observation Report 2932, GRB Coordinates Network, AAVSO, Cambridge, Mass, USA, 2003.
- [6] P. W. Schnoor, D. L. Welch, G. J. Fishman, and A. Price, “GRB030329 observed as a sudden ionospheric disturbance (SID),” GCN GRB Observation Report 2176, GRB Coordinates Network, AAVSO, Cambridge, Mass, USA, 2003.
- [7] H. Rishbeth, I. C. F. Müller-Wodarg, L. Zou, et al., “Annual and semiannual variations in the ionospheric F2-layer. II. Physical discussion,” *Annales Geophysicae*, vol. 18, no. 8, pp. 945–956, 2000.

Research Article

Scheduling in Targeted Transient Surveys and a New Telescope for CHASE

Francisco Förster,¹ Nicolás López,¹ José Maza,¹ Petr Kubánek,² and G. Pignata¹

¹Departamento de Astronomía, Universidad de Chile, Camino el Observatorio, 1515 Las Condes, Chile

²Image Processing Laboratory, Universidad de Valencia, Polígono La Coma s/n, Paterna, 46980 Valencia, Spain

Correspondence should be addressed to Francisco Förster, fforster@das.uchile.cl

Received 28 June 2009; Accepted 21 September 2009

Academic Editor: Alberto J. Castro-Tirado

Copyright © 2010 Francisco Förster et al. This is an open access article distributed under the Creative Commons Attribution License, which permits unrestricted use, distribution, and reproduction in any medium, provided the original work is properly cited.

We present a method for scheduling observations in small field-of-view transient targeted surveys. The method is based on maximizing the probability of detection of transient events of a given type and age since occurrence; it requires knowledge of the time since the last observation for every observed field, the expected light curve of the event, and the expected rate of events in the fields where the search is performed. In order to test this scheduling strategy we use a modified version of the genetic scheduler developed for the telescope control system RTS2. In particular, we present example schedules designed for a future 50 cm telescope that will expand the capabilities of the CHASE survey, which aims to detect young supernova events in nearby galaxies. We also include a brief description of the telescope and the status of the project, which is expected to enter a commissioning phase in 2010.

1. Introduction

With a new generation of observatories dedicated to studying the time domain in astronomy [1–4], our understanding of astrophysical transient phenomena will be significantly improved. The diversity of known families of transient events will be better understood thanks to improved sample sizes and better data, and new types of transient events will be likely discovered.

These observatories will include not only large field-of-view, large aperture telescopes, which will scan the sky in a relatively orderly fashion, but also networks of small field-of-view, small aperture robotic telescopes that will scan smaller areas of the sky in a less predictable way.

The smaller robotic telescopes are ideal for studying very short-lived transients, for example, gamma ray bursts (GRBs), and also for doing detailed follow up studies of longer lived galactic (e.g., cataclysmic variables, planetary systems) and extragalactic (e.g., supernovae) transient events. Moreover, they constitute a relatively inexpensive tool to obtain reduced cadences, of the order of days, in relatively small areas of the sky which are of special interest, for example, nearby galaxies.

Here, we present a scheduling strategy that maximizes the probability of finding specific types of transient phenomena, or the expected number of events, at different times since occurrence. In Section 2 we derive the probability of finding one or more of these events, as well as the expected number of events. In Section 3 we show the results obtained with this method and discuss its implications. Finally, in Section 4 we give an overview of the future 50 cm telescope that will expand the capabilities of the CHASE survey and which will use the scheduling method presented in this work.

2. Detection Probabilities of Transient Events

This discussion will be limited to well-known types of events in targets with known distances. We assume that the light curves of every transient event is composed of a monotonically increasing early component, followed by a monotonically decreasing late component. We will show how to compute detection probabilities for individual difference observations, as well as for sequences of observations to predefined targets. With this information, we will discuss how to build observational plans that maximize the detection of events with certain characteristics.

Expected Numbers versus Probabilities. The probability of having exactly k occurrences of an event, in a time interval where λ occurrences are expected, is

$$P(k, \lambda) = \frac{\lambda^k e^{-\lambda}}{k!}, \quad (1)$$

which means that the probability of zero occurrences of the event is

$$P(0, \lambda) = e^{-\lambda}, \quad (2)$$

which we would like to minimize. Note that for small values of λ , the probability of detecting at least one event should be a better indicator of a good schedule than the total expected number, but since $1 - e^{-\lambda} \approx 1 - (1 - \lambda) = \lambda$, in practice this can be ignored. For big values of λ the total expected number of events should be most of the time a better indicator of a good schedule than the probability of finding at least one event. For the purpose of this discussion we will use probabilities, but it is easy to change the formulation to the expected number of events, as we will show later.

Detection Probabilities of Individual Events. Let us assume that the events remain detectable for a time τ and that their rate of occurrence is R . Consider also the case when we look at a target twice to generate a difference image, with a time interval or *cadence*, Δt .

If each event remains visible for τ years, we would like to know what is the interval where an event which was not seen in the first observation could occur and be detected in the second observation.

Let us also assume that the event was not seen in the first observation, performed at time t_1 , and that we make a second observation with a cadence Δt , that is, at time $t_2 = t_1 + \Delta t$. Defining $\Delta t'$ as the minimum between Δt and τ , then the time interval where new transients can occur and be detectable in the second observation will span from $t_2 - \Delta t'$ and t_2 . This is because short-lived transients only have a time τ to remain visible, which could be smaller than Δt . Hence, the expected number of new events that can be detected will be the rate of occurrence times the former time interval. Using (2), the probability of no events occurring in this interval and no detections being made, P_{ND} , will be

$$P_{\text{ND}} = \exp\{-R \min(\Delta t, \tau)\}. \quad (3)$$

Let us now assume that the event can only be detected a time t_0 after its occurrence, that it remains visible for a time τ and that we are only interested in events younger than τ_{age} (see Figure 1).

The event will be detectable younger than τ_{age} only if $\tau_{\text{age}} \geq t_0$. If this is the case, the time period where events not seen in the first observation could occur and be detected in the second observation will now be the minimum between Δt , $\tau_{\text{age}} - t_0$, and τ (see Figure 2).

Thus, the probability of no events occurring in this time interval and no detections being made, $P_{\text{ND}}^{\text{age}}$, will be

$$P_{\text{ND}}^{\text{age}} = \exp\left[-R \min\left\{\Delta t, \max(\tau_{\text{age}} - t_0, 0), \tau\right\}\right]. \quad (4)$$

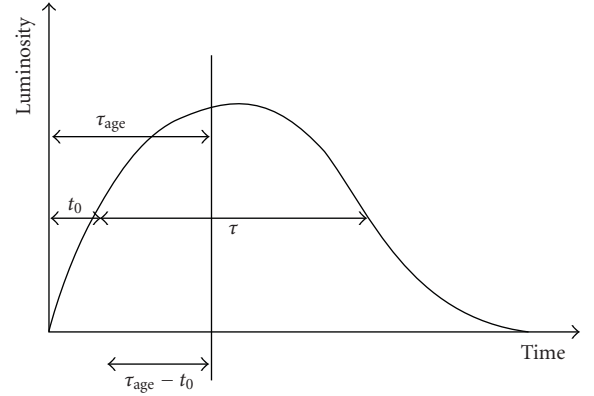


FIGURE 1: The different variables used in this calculation. t_0 is defined as the time when the luminosity is above a certain threshold value which makes the object detectable; τ is defined as the time period where the transient can be detected, and τ_{age} is an arbitrary age since explosion, with $\tau_{\text{age}} - t_0$ being the time period where events younger than τ_{age} can be detected.

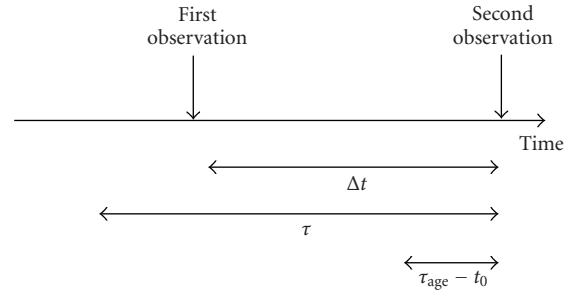


FIGURE 2: Example of how the detection probabilities are calculated. Δt is the cadence; τ is the time period when the transient remains detectable and $\tau_{\text{age}} - t_0$ is the time period when the transient remains detectable while it is younger than τ_{age} . In this case, the cadence is shorter than τ , which means that some transient events of the type of interest could have already been seen in the first observation, but $\tau_{\text{age}} - t_0$ is shorter than the cadence, which means that all events younger than τ_{age} could not have been seen in the first observation. The minimum between these three quantities should be multiplied by the rate of events in order to compute the expected number of events and compute the detection probabilities.

With this information, the probability of detecting one or more events in the second observation will be simply $1 - P_{\text{ND}}^{\text{age}}$.

Cadence Choice. Using the formula above, we could try maximizing the probability of detection. For a fixed target, this can only be done by decreasing the cadence, Δt , as long as the number of targets that are observed in the sample is not compromised significantly.

It is easy to see that, if $\tau_{\text{age}} > t_0$, increasing Δt from zero to larger values will increase the probability of detection only while $\Delta t < \min(\tau_{\text{age}} - t_0, \tau)$. For bigger cadences the probability will stay constant. Thus, a natural choice for the cadence would be $\Delta t = \min(\tau_{\text{age}} - t_0, \tau)$.

If larger cadences were chosen, the probability of detecting events younger than τ_{age} would not change, but not all detected events would be guaranteed to be younger than τ_{age} , which could be a problem if a fast age estimation is required. On the other hand, larger cadences would increase the probability of detecting older events, up to when $\Delta t > \tau$, when the probability of detecting an event of any age would remain constant too.

Choosing $\Delta t = \min(\tau_{\text{age}} - t_0, \tau)$ has the added benefit that if τ_{age} is smaller than the rise time and the object type was known, the absolute magnitude of the event could be used as an age estimator. This is because the event would be guaranteed to be rising at detection time and the magnitude-age relation would be single valued. In reality, there could be events of different types simultaneously occurring which would make the age determination only useful in a statistical sense.

In general, Δt will be not only a function of the distance and light curve of the variable object to be detected, but also of the desired age of detection, τ_{age} . Hence, for young and bright objects with extended light curves, the cadence should be set to at least $\tau_{\text{age}} - t_0$ if we want to increase the cadence while maximizing the detection of events with a given age.

However, it is not always easy to repeat the observations with a fixed cadence. Bad weather, the change of position of the targets throughout the year, or the appearance of other objects of interest, among many reasons, may cause the cadence between observations to vary.

An alternative strategy is to let the cadence adapt individually in a sequence of observations in order to maximize the detection probabilities.

Detection Probabilities for a Sequence of Observations. Now, we compute the probability of not detecting any new events in a sequence of observations, $P_{\text{ND, Total}}^{\text{age}}$.

We note that for no events to be detected, each individual observation must result in negative detections, that is, we have

$$\begin{aligned} P_{\text{ND, Total}}^{\text{age}} &= \prod_i \exp\left[-R^i \min\{\Delta t^i, \max(\tau_{\text{age}} - t_0^i, 0), \tau^i\}\right] \\ &= \exp\left[-\sum_i R^i \min\{\Delta t^i, \max(\tau_{\text{age}} - t_0^i, 0), \tau^i\}\right], \end{aligned} \quad (5)$$

where the indices indicate different targets. Thus, the probability of detecting one or more new events will be

$$P_{\text{D, Total}}^{\text{age}} = 1 - \exp\left[-\sum_i R^i \min\{\Delta t^i, \max(\tau_{\text{age}} - t_0^i, 0), \tau^i\}\right]. \quad (6)$$

With this formula, we recover the expected number of events in the entire observational sequence, which is the term inside the exponential, that is, in $P_{\text{D, Total}}^{\text{age}} = 1 - \exp(-\lambda_{\text{D, Total}}^{\text{age}})$,

$$\lambda_{\text{D, Total}}^{\text{age}} = \sum_i R^i \min\{\Delta t^i, \max(\tau_{\text{age}} - t_0^i, 0), \tau^i\} \quad (7)$$

is the expected number of new detected events with the required age. Thus, we can use either (6) or (7) to determine

TABLE 1: For a desired detection age (τ_{age}) we show a possible choice of cadence in days (Δt), the maximum sample size consistent with this cadence, and the approximate detection rate if the suggested cadence and maximum sample sizes were used. t_0 corresponds to the time for the transient events to become visible since its occurrence; N_{exp} is the number of observations per night, and R is the rate of events expected in each field. We assume that in all cases the time that a transient remains visible, τ , is bigger than the cadence chosen. For the opposite case, Δt can be replaced by τ in the last two columns below.

Age	Reference cadence	Sample size	Approx. detection rate
τ_{age}	$\Delta t = \langle \tau_{\text{age}} - t_0 \rangle$	$f N_{\text{exp}} \Delta t$	$f N_{\text{exp}} \Delta t \langle R \rangle$

the *fitness* of individual schedules, but we recommend using (7).

Limited Number of Targets. It is possible that the number of targets available for detecting new events with a given age is too small, that is, assuming a fixed exposure time and cadence for all observations, that the number of visible targets where $\tau_{\text{age}} > t_0$ is smaller than the length of the night divided by the exposure time.

For very short-lived transient surveys this is not a problem, even with relatively small cadences $\Delta t > \tau$, and the probability of detection in an individual observation would be $p \approx R\tau$, that is, it would be almost independent of the cadence or how many times we observe a target per night.

In relatively long-lived transient surveys, that is, time-scales of days or longer, we would not want to repeat targets in a given night. This is because when $\Delta t < \tau_{\text{age}} - t_0$, the probability of detection in an individual observation is $P \approx R\Delta t$. Thus, many observations to a given target in a given night would be almost equivalent to observing the target once per day or once every few days in terms of probabilities, but with a significantly higher cost on the resources and preventing the telescope from observing other targets.

In general, the number of targets for a given cadence should be of the order of the fraction of time that we want to spend in that sample per night, f , times the total number of observations per night, N_{exp} , times the cadence, Δt . The detection rate would be approximately the multiplication of this number with the typical rate of occurrence, R .

Hence, a possible strategy would be to order targets by the time that it takes for the events of interest to be detectable, t_0 , depending on their distance and extinction, select a detection age according to scientific criteria, and then group the targets according to the resulting cadence and sample sizes. This is summarized in Table 1.

2.1. Genetic Algorithm. As discussed above, one can let the cadence vary from observation to observation and from object to object. For an ideal schedule, we would like to select the optimal combination of cadences that can adapt to unexpected changes of the observational plan. For this, we use the probability of detection, or the expected number of events of a sequence of observations as the *fitness* indicator

and we use a genetic algorithm to find the best available observational plan for the following night. This can reflect unexpected changes to the observational plan in a daily basis, and can be extended to fractions of a night optimizations if necessary.

We have used the genetic algorithm implemented in RTS2 [5], taking into account the cadence to each target (Δt) and the distance, event rate, height above the horizon, and sky brightness, all of these reflected in the quantities t_0 and τ , to build the observational plan.

The distance between targets is also taken into account indirectly. If it is too big, the number of visited targets per night or the number of terms in (7) will be reduced and the probability of detection will decrease accordingly. Similarly, when the targets are too distant or too close to the horizon, or the sky too bright, t_0 will increase and τ will decrease, decreasing the detection probabilities too. The bigger the event rate in every target, the bigger the detection probability, which will favour those targets with the biggest intrinsic rates. Finally, the time since last observation will determine the cadence, changing the detection probabilities as well.

In these calculations, the time between targets is computed using the maximum between the slew time and the readout time, which effectively defines a disk around each target where the time penalty is constant. Reaching the outer circumference of this disk would take exactly the readout time assuming that the CCD can read out electrons while simultaneously slewing in the most efficient trajectory. This is regularly accomplished by RTS2, since it optimizes observations by reading out electrons and moving to a new position simultaneously.

For instance, a readout speed of about 2 sec and a slew speed of 5 deg sec⁻¹ define a disk around the previous target of about 10 deg in the sky where the time penalty for new targets is the same. In most telescopes the slewing movement is accomplished with two independent motors, which makes the size and shape of this disk really depend on the initial configuration of the telescope before slewing, and whether an equatorial or altazimuthal mount is used.

The details of the genetic optimizer, based on the NSGAI algorithm [6], are described in detail in [7]. It is worth mentioning that the genetic algorithm can handle multiple objectives, which can be used to find the Pareto front of optimal values instead of a single solution, for example, look for multiple detection ages, which we have also implemented (see Figure 4).

The Pareto front is the locus of solutions in a multi-objective optimization problem where one objective cannot be improved without compromising the other objective functions. For example, in an optimization problem with two objective functions, for every value of one of the two objective functions there is an optimal value for the remaining objective function, that is, the Pareto front can be composed by infinite solutions.

2.2. Calculation of t_0 and τ . In the previous sections we did not include the calculation of the time for an event to become

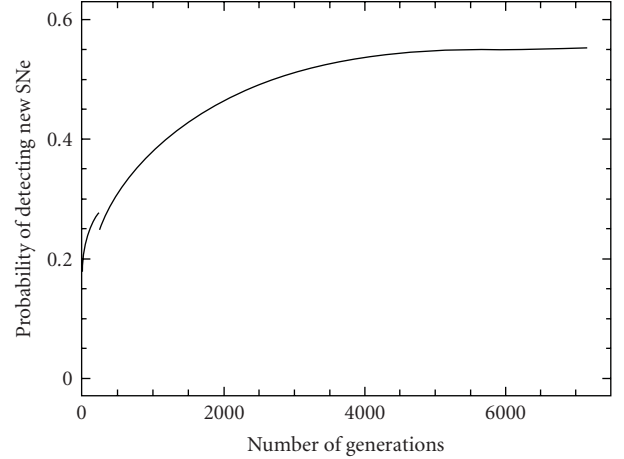


FIGURE 3: Evolution of the probability of detecting new supernova with the number of generations. In this example, every generation consists of a population of 1,000 observational plans, where each observational plan contains hundreds of 60 sec exposures to different targets. For the simulation, we have used the gold sample of galaxies of the CHASE survey [8], where the distances were computed from recession velocities. Event rates were created randomly at the beginning of the simulation to reproduce the typical rates expected for supernova explosions. The cadences were randomly generated to reproduce the typical values expected in the CHASE survey.

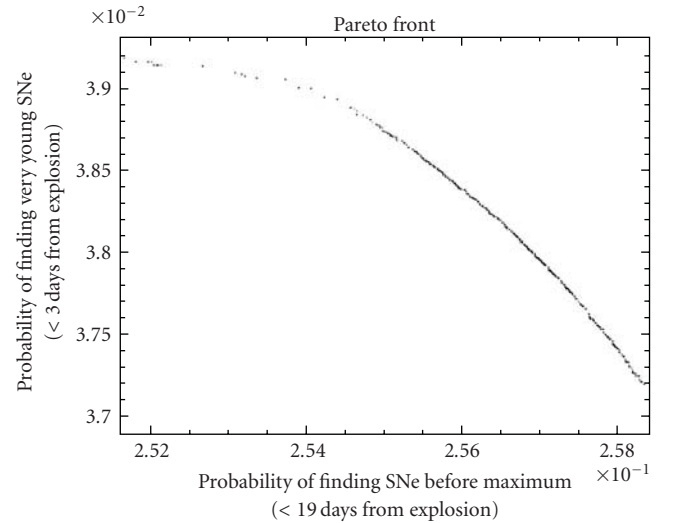


FIGURE 4: Locus of Pareto-optimal solutions, or Pareto front, using two objective functions: the probability of finding SNe before maximum (abscissa) and the probability of finding SNe no later than three days after the explosion (ordinate). In this example we have evolved 10,000 generations of 1,000 observational plans each, similar to the simulation shown in Figure 3, but with two objectives instead of only one. Absolute numbers should not be trusted, since the simulated cadences are too big for the values expected in a survey looking for SNe as young as three days after explosion. Individual points represent individual observational plans, and the set of points are only an approximation to the Pareto front. Once the Pareto front is computed, one observational plan from the set of solutions can be chosen according to arbitrarily defined criteria.

detectable, t_0 , and the time that an event remains detectable, τ . These terms can be computed from empirical light curves of the particular event to be detected, and can be stored as functions of the critical luminosity above which the object can be detected.

Thus, the problem is reduced to computing the flux above which the object can be detected. To do this, we solve the signal to noise equation for an arbitrary value above which we define an object to be detected, for example, $S/N = 5$. This equation is

$$\frac{S(t)}{N(t)} = \frac{\gamma_{\text{TE}}^{\text{CCD}}(t)T}{\left[\gamma_{\text{TE}}^{\text{CCD}}(t)T + \gamma_{\text{sky}}^{\text{CCD}}T n_{\text{pix}} + \gamma_{\text{RN}}^2 n_{\text{pix}}\right]^{1/2}}, \quad (8)$$

where $S/N(t)$ is the signal to noise ratio as a function of time; $\gamma_{\text{TE}}^{\text{CCD}}(t)$ are the photons per unit time detected by the CCD from the transient event as a function of time; T is the exposure time; $\gamma_{\text{sky}}^{\text{CCD}}$ are the photons per unit time coming from the sky and detected in one pixel of the CCD; n_{pix} is the number of pixels used to do photometry, and γ_{RN} is the readout noise per pixel of the CCD. In general, n_{pix} is a function of the seeing at the zenith and the angle from the zenith.

Solving the previous quadratic equation for $\gamma_{\text{TE}}^{\text{CCD}}(t)$ with a given value of S/N and choosing the positive root gives the following result:

$$\gamma_{\text{TE}}^{\text{CCD}}(t) = \frac{S/N^2}{2T} \left[1 + \left(1 + \frac{4n_{\text{pix}}}{S/N^2} \left\{ \gamma_{\text{RN}}^2 + \gamma_{\text{sky}}^{\text{CCD}}T \right\} \right)^{1/2} \right]. \quad (9)$$

Now, we can include the effect of distance, collecting area, spectral shape, and CCD characteristics in the following equation:

$$\gamma_{\text{TE}}^{\text{CCD}}(t) = \frac{A}{4\pi D^2} \int \gamma_{\text{TE}}^{\nu}(t) \eta_{\nu} d\nu, \quad (10)$$

where A is the collecting area of the telescope; D is the distance to the object; $\gamma_{\text{TE}}^{\nu}(t)$ is the number of photons per unit time, per unit solid angle and per unit frequency of the transient event as a function of time since occurrence; η_{ν} is the efficiency with which the photons are captured as a function of frequency, which depends on the reflecting surfaces, intervening lenses, CCD quantum efficiency, and filters.

We can write a similar equation for the photons coming from the sky in every pixel of the CCD:

$$\gamma_{\text{SKY}}^{\text{CCD}}(t) = \frac{\Delta\Omega A}{\cos z} \int \gamma_{\text{SKY}}^{\nu}(t) \eta_{\nu} d\nu, \quad (11)$$

where $\Delta\Omega$ is the solid angle of one pixel of the CCD; z is the angle from the zenith, and $\gamma_{\text{SKY}}^{\nu}$ is now the number of photons coming from the sky per unit time, per unit area, per unit solid angle and per unit frequency.

Thus, if we compute $\gamma_{\text{TE}}^{\text{CCD}}(t)$, assuming the object is at a distance D from the observer, $\gamma_{\text{TE},D}^{\text{CCD}}(t)$, and $\gamma_{\text{SKY}}^{\text{CCD}}$ assuming the object is at a given angle z from the zenith, $\gamma_{\text{SKY}}^{\text{CCD}}(z)$, for a given sky brightness and for a particular telescope configuration, we can simply scale the results as follows:

$$\gamma_{\text{TE},D}^{\text{CCD}}(t) = \gamma_{\text{TE},D_0}^{\text{CCD}}(t) \left(\frac{D_0}{D} \right)^2 \quad (12)$$

$$\gamma_{\text{SKY}}^{\text{CCD}}(z) = \frac{\gamma_{\text{SKY}}^{\text{CCD}}(0)}{\cos z}, \quad (13)$$

thus, we can now compute the times when the object becomes detectable and when it is no longer detectable, t_0 and $t_0 + \tau$:

$$t_0, t_0 + \tau = \left(\gamma_{\text{TE},D_0}^{\text{CCD}} \right)^{-1} \left\{ \left(\frac{D}{D_0} \right)^2 \frac{S/N^2}{2T} \times \left[1 + \left(1 + \frac{4n_{\text{pix}}}{S/N^2} \left\{ \gamma_{\text{RN}}^2 + \frac{\gamma_{\text{sky}}^{\text{CCD}}(0)}{\cos z} T \right\} \right)^{1/2} \right] \right\}, \quad (14)$$

where $(\gamma_{\text{TE},D_0}^{\text{CCD}})^{-1}$ is the inverse of the function computed in (12), which should have two solutions for a transient which is composed by an early monotonically increasing component followed by a monotonically decreasing late component. Importantly, the inversion of $\gamma_{\text{TE},D_0}^{\text{CCD}}$ must be performed only once, and can be stored numerically in a table, for example, in logarithmic intervals of photons per unit time.

Thus, for a given signal to noise ratio (S/N), which we arbitrarily define as the value that gives a detection, a given distance from the source (D), exposure time (T), sky brightness (c.f. $\gamma_{\text{SKY}}^{\text{CCD}}$), seeing (c.f. n_{pix}), readout noise per pixel (γ_{RN}), and angle from the zenith (z), we can compute t_0 and τ , which are necessary for the calculation of the expected number of events and the probabilities of detection in an individual target and a sequence of observations.

It is important to note that the detection of objects is sometimes performed using individual pixels, in which case we can set n_{pix} to one, and multiply the term $\gamma_{\text{TE}}^{\text{CCD}}(t)$ in (8) by the fraction of photons that fall in the central pixel in the position of the object, depending on the seeing conditions, which would result in the following modified equation:

$$t_0, t_0 + \tau = \left(\gamma_{\text{TE},D_0}^{\text{CCD}} \right)^{-1} \left\{ \left(\frac{D}{D_0} \right)^2 \frac{S/N^2}{2fT} \times \left[1 + \left(1 + \frac{4}{S/N^2} \left\{ \gamma_{\text{RN}}^2 + \frac{\gamma_{\text{sky}}^{\text{CCD}}(0)}{\cos z} T \right\} \right)^{1/2} \right] \right\}, \quad (15)$$

where f is the fraction of the light from a point source that would fall in one pixel in the position of the object, generally

a function of the seeing at the vertical, the angle from the zenith, and the frequency of the photons to be detected.

3. Results and Discussion

In Figures 3 and 4 we present example implementations of the scheduling strategy presented in this work with the genetic algorithm used in RTS2.

Figure 3 shows the probability of finding supernova with a reference 50 cm telescope in an observational plan composed of 60 sec individual exposures, with simulated cadences and supernova rates in each field. We can see the probability increasing with each generation of observational plans and then staying constant. Each generation is formed by a population of 1,000 different observational plans and the initial iteration consisted of a series of randomly generated targets for each observational plan of the population, which were crossed and mutated to obtain the best observational plans.

Figure 4 shows the space of optimal solutions when two objective functions are used. This is, the Pareto front of nondominated solutions or the space of solutions where one variable is at its optimal value without compromising the other variables. In this simulation we use the objective functions: (1) probability of finding supernovae before maximum and (2) the probability of finding supernova younger than three days from explosion, using similar parameters to those used in the simulation shown in Figure 3.

Interestingly, we have used the already implemented genetic scheduler from RTS2 to find the schedule that maximizes the average height above the horizon for our list of targets, or that minimizes the typical distance between targets. For both cases, we have found that the probability of detection of the resulting schedule is smaller by more than a factor of two with respect to our method, which suggests that our strategy is significantly better for finding transient objects.

Thus, the implemented scheduling strategy based on maximizing the probability of finding new transient events is able to obtain significantly higher detection probabilities than alternative methods. We were able to build observational plans for every night to maximize the probability of detecting particular events, or similarly, the expected number of detections. These plans were based on predefined samples of targets that have characteristic cadence and exposure times, and that can easily adapt to unforeseen changes in the scheduled observations.

In order to compute the observational plans with the highest detection probabilities, we used the genetic algorithm implemented in the telescope control system RTS2, where a multiobjective algorithm selects the optimal sequence of observations for our purposes.

We expect to be able to extend this work to scheduling of coordinated networks of robotic telescopes looking for specific types of transient events, or looking for many different phenomena if multiobjective optimization is used. We also expect to release the implementation in a future version of RTS2 (<http://rts2.org/>).

An important question is whether this method is able to recompute the optimal observational plan when unexpected changes in the sequence of observations occur. In a single computer, with the current implementation of the code, we cannot think of simple ways of achieving this, since it normally takes many hours to find the optimal observational plan or set of Pareto-optimal plans in a single PC. However, with faster computers, precalculating detection probabilities for every target at every time in the night, and given that genetic algorithms can be relatively easily parallelised, we expect this to be feasible in the near future.

Alternatively, one could switch from using optimized observational plans to computing the detection probabilities for every available target and choose the one with the highest detection probability every time the telescope has finished integrating, taking into account the slew and readout time by subtracting the expected cost of slewing in terms of detection probabilities per unit time for the corresponding slewing times.

Finally, it should be noted that this method is not exclusive for supernova transients, but to any transient with well-characterized light curves and with well-understood target fields.

4. Application to the New 50 cm Robotic Telescope for CHASE

The CHASE survey [8] is the most prolific nearby supernova search in the southern hemisphere. It finds more than 70% of the nearby ($z < 0.3$) supernova in the southern hemisphere, with discovery ages much younger than competing surveys (see Figure 5). CHASE uses a fraction of the time available in four of the six PROMPT telescopes [1] located in CTIO.

In order to expand the capabilities of CHASE and to have a better control over the scheduling of the observations, we are in the process of purchasing and installing a 50 cm robotic telescope that will join the other PROMPT telescopes for the SN survey and follow up.

The telescope will be a 50 cm automated telescope: composed of an optical tube, a CCD camera with a set of filters, a mount, a meteorological station, a dome, and computers for controlling and analyzing the data. It will be located in CTIO and remotely controlled from Cerro Calán (Santiago, Chile). It will observe hundreds of targets every night with the aim of doubling the observing capabilities of the CHASE survey and to try new observing strategies with new associated scientific goals.

The optical tube of the telescope will be a 50 cm aperture Ritchey-Chretien design, with a focal ratio of 12, in an open truss carbon fiber tube purchased from the Italian company Astrotech. The camera will be a 2kx2k pixels Finger Lakes Proline camera, with a back illuminated, UV enhanced, 95% peak quantum efficiency Fairchild 3041 CCD. The pixel size will be $0.52''$ and the field-of-view will be $17.6'$ in side. The camera will be equipped with a 12-slot filter wheel with the filters u'g'r'I, Johnson B and V and WFCAM Z, purchased from Asahi-Spectra (see transmission curves in Figure 6).

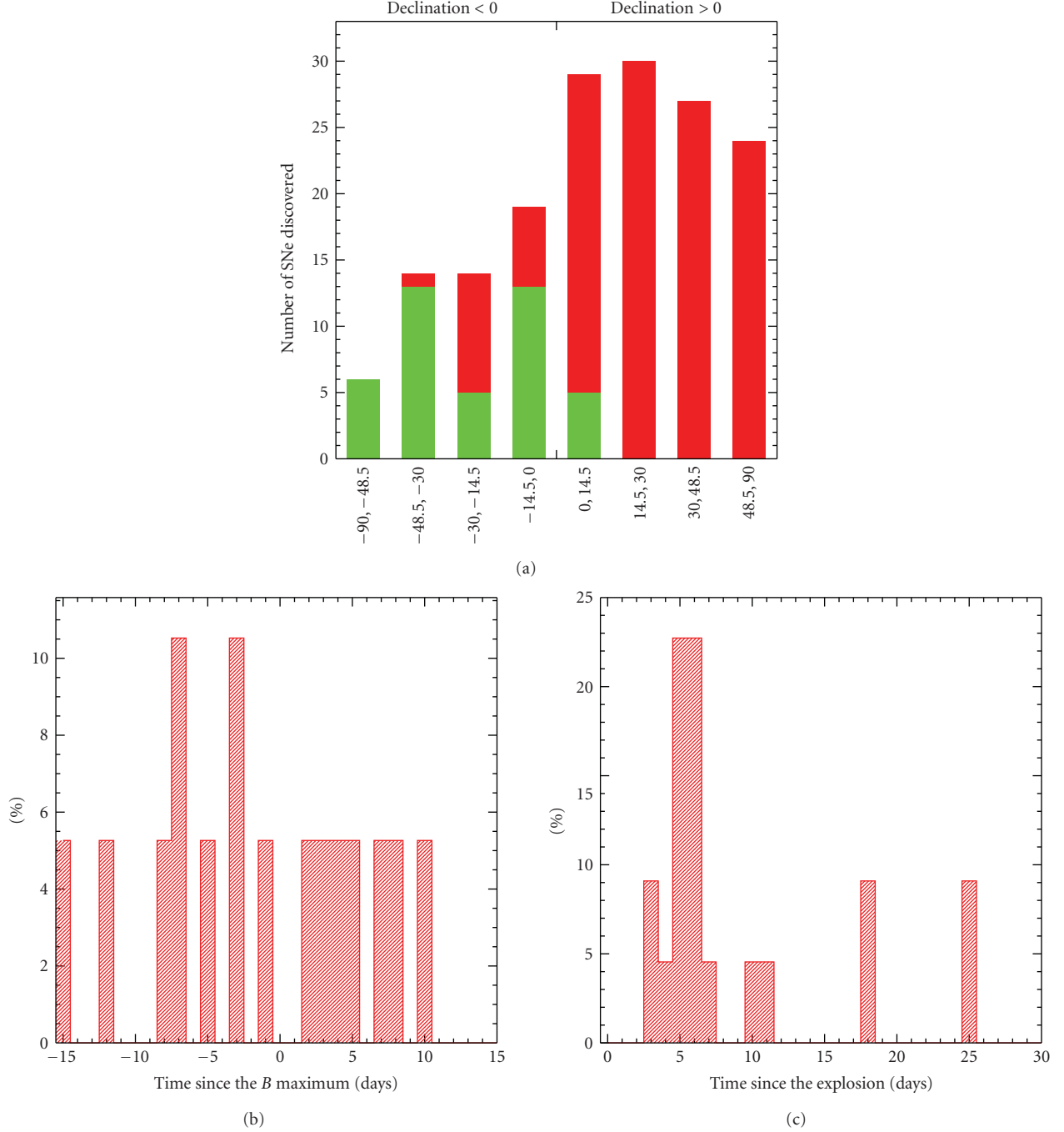


FIGURE 5: CHASE survey results. (a) the distribution of supernova with declination in bins of equal solid angle. Red bins correspond to all nearby SNe found in 2008, and green bins correspond to SNe discovered by CHASE in 2008. (b) the distribution of discovery ages of Type Ia SNe in CHASE. About half of the SNe were discovered before maximum. (c) the distribution of discovery ages of Type II SNe in CHASE. The median discovery age was about 5 days after explosion. (G. Pignata, private communication).

The camera was chosen to avoid the potential presence of residual images in the imaging of targets, which currently dominate our SN candidate lists with the PROMPT telescopes, to obtain a relatively big field-of-view, which would allow us to image enough reference stars to do an accurate image alignment and subtraction, but also to obtain the best available quantum efficiency, which is a cost-effective way of collecting more photons per target.

The mount will be the Astro-Physics 3600GTO “El Capitán” model, which is a German equatorial mount with sub-arcmin pointing errors, and a slew speed of about 5 deg sec^{-1} . The dome of the telescope will be built in Chile and is currently in the design phase.

The scheduling of the observations will be done with the strategy presented in this work, and we expect to start collaborations with other groups using this scheduler in an

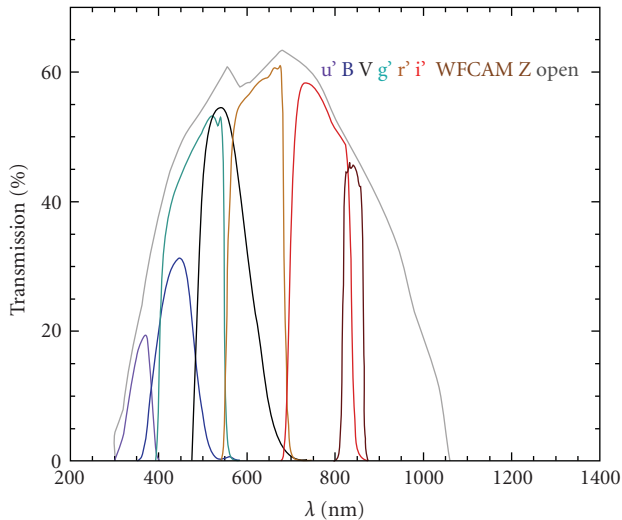


FIGURE 6: Approximate transmission curves for the filters implemented in our future 50 cm telescope. “Open” corresponds to no filters, and includes the effects of atmospheric extinction, mirror reflectivity and CCD quantum efficiency. The supernova search will be likely performed in “Open” mode or with a clear filter, but for the follow-up program we will use the filters shown here. It is possible that in the future we will include additional filters.

integrated fashion. For more information please contact the authors.

Acknowledgments

The authors acknowledge an anonymous referee whose help and guidance lead to significant improvements of the manuscript. F. F. acknowledges partial support from GEMINI-CONICYT FUND. G. P. acknowledges partial support from the Millennium Center for Supernova Science through Grant P06-045-F funded by “Programa Bicentenario de Ciencia y Tecnología de CONICYT” and “Programa Iniciativa Científica Milenio de MIDEPLAN”.

References

- [1] D. Reichart, M. Nysewander, J. Moran, et al., “PROMPT: panchromatic robotic optical monitoring and polarimetry telescopes,” *Nuovo Cimento C Geophysics Space Physics C*, vol. 28, pp. 770–767, 2005.
- [2] S. C. Keller, B. P. Schmidt, M. S. Bessell, et al., “The SkyMapper telescope and the southern sky survey,” *Publications of the Astronomical Society of Australia*, vol. 24, no. 1, pp. 1–12, 2007.
- [3] T. M. Brown, et al., “Las cumbres observatory global telescope,” in *Proceedings of the American Astronomical Society Meeting*, vol. 214, 2009, paper no. 409.14.
- [4] Z. Ivezić, J. A. Tyson, T. Axelrod, et al., “LSST: from science drivers to reference design and anticipated data products,” *Bulletin of the American Astronomical Society*, vol. 41, p. 366, 2009.
- [5] P. Kubánek, et al., “RTS2—remote telescope system, 2nd version,” in *Gamma Ray Bursts: 30 Years of Discovery: Gamma*

Ray Burst Symposium, vol. 727 of *AIP Conference Proceedings*, pp. 753–756, 2004.

- [6] K. Deb, A. Pratap, S. Agarwal, and T. Meyarivan, “A fast and elitist multiobjective genetic algorithm: NSGA-II,” *IEEE Transactions on Evolutionary Computation*, vol. 6, no. 2, pp. 182–197, 2002.
- [7] P. Kubánek, *Genetic algorithm for robotic telescope scheduling*, M.S. thesis, Universidad de Granada, Granada, Spain, 2007.
- [8] G. Pignata, J. Maza, R. Antezana, et al., “The Chilean automatic supernova search (CHASE),” in *Probing Stellar Populations Out to the Distance Universe*, vol. 1111 of *AIP Conference Proceedings*, pp. 551–554, 2009.

Research Article

Wide and Fast: Monitoring the Sky in Subsecond Domain with the FAVOR and TORTORA Cameras

Sergey Karpov,¹ Grigory Beskin,¹ Sergey Bondar,² Adriano Guarnieri,³ Corrado Bartolini,³ Giuseppe Greco,³ and Adalberto Piccioni³

¹Special Astrophysical Observatory, Russian Academy of Sciences, Nizhnij Arkhys, 369167, Russia

²Institute for Precise Instrumentation, Nizhnij Arkhys, 369167, Russia

³Astronomy Department, Bologna University, Bologna 40126, Italy

Correspondence should be addressed to Sergey Karpov, karpov@sao.ru

Received 29 June 2009; Accepted 1 December 2009

Academic Editor: Lorraine Hanlon

Copyright © 2010 Sergey Karpov et al. This is an open access article distributed under the Creative Commons Attribution License, which permits unrestricted use, distribution, and reproduction in any medium, provided the original work is properly cited.

In order to detect and investigate short stochastic optical flares from a number of variable astrophysical objects (GRBs, SNe, flare stars, CVs, X-Ray binaries) of unknown localizations as well as near-earth objects (NEOs), both natural and artificial, it is necessary to perform the systematic monitoring of large regions of the sky with high temporal resolution. Here we discuss the criteria for a system that is able to perform such a task and describe two cameras we created for wide-field monitoring with high temporal resolution—FAVOR and TORTORA. Also, we describe basic principles of real-time data processing for the high frame rates needed to achieve subsecond temporal resolution on a typical hardware.

1. Introduction

The systematic study of night sky variability on subsecond time scales still remains an important, but practically unsolved problem. Its necessity for the search of non-stationary objects with unknown localization has been noted by Bondi in [1]. Such studies have been performed [2, 3], but due to technical limitations it has only been possible either to reach high temporal resolution of tens of milliseconds in monitoring of 5'–10' fields, or use 5–10 seconds time resolution in wider fields. The wide-field monitoring systems currently in operation, such as WIDGET [4], RAPTOR [5], BOOTES [6] and π of the Sky [7], while having good sky coverage and limiting magnitude, lack temporal resolution, which significantly lowers their performance in the study of transient events of subsecond duration.

Optical transients of unknown localization may be very short. For example, the rise times of flashes of some UV5 Cet-like stars may be as short as 0.2–0.5 seconds [8], 30% of GRBs have the duration shorter than 2 seconds, and details of their light curves may be seen on time scales shorter than 1 ms [9]. Also, of great interest are the observations of very fast meteors which may be of extra-Solar system origin [10].

One more task which requires wide-field observations with high temporal resolution is the monitoring of near-Earth space. There are a number of satellites, as well as a vast amount of small space debris pieces, which have rapidly evolving trajectories, and so are difficult to observe by typical satellite tracking methods. High temporal resolution is needed here due to the fast motion of such objects on the sky.

To study the variability of large sky areas on such time scales, it has been proposed [11, 12] to use large low-quality mosaic mirrors of air Cerenkov telescopes. However, in [13, 14] we demonstrated that it is possible to achieve the subsecond temporal resolution in a reasonably wide field with small telescopes equipped with fast CCDs, to perform fully automatic searching and classification of fast optical transients. Moreover, a two-telescope scheme [15, 16], able to study such transients in a very short time after detection, has been proposed. According to these ideas, we created the prototype fast wide-field camera called FAVOR [14] and the TORTORA camera as part of the TORTOREM [17] two-telescope complex, and operated them over several years.

The recent discovery of the brightest ever GRB, GRB080319B (the Naked-Eye Burst [18]), by several wide-field monitoring systems—TORTORA [19], RAPTOR [20] and Pi of the Sky [21]—and the subsequent discovery of its fast optical variability [22] on time scales from several seconds down to a subsecond time scale [23] demonstrated that the ideas behind our efforts in fast temporal resolution wide-field monitoring are correct.

In this article we describe these basic ideas, covering both the selection of optimal hardware parameters and the principles of real-time data processing for such high temporal resolution observations.

2. General Requirements for Wide-Field Monitoring

Typical followup observations, performed for the detailed study of newly discovered transients, require no more than a good robotic telescope with fast repointing. Such instruments, however, will inevitably only begin to capture data after the first few seconds or tens of seconds of the event. To get information from the start of the event, which is essential for understanding the nature and properties of transients, one needs to observe the position of the transient before it appears. And, as transients occur in unpredictable places, the systematic monitoring of large sky regions becomes an important task.

For such monitoring, one needs to select the optimal set of mutually exclusive parameters—the angular size of the field of view, the limiting magnitude and the temporal resolution. Indeed, the area of the sky Ω , covered by an objective with diameter D and focal length F , equipped with an $N \times N$ pixels CCD with pixel size of l and exposure time of τ seconds, is

$$\Omega \propto \frac{N^2 l^2}{F^2} \quad (1)$$

while the faintest detectable object flux, for a sky background noise dominating over the CCD read-out noise, is

$$\text{Flux}_{\min} \propto \left(\frac{D}{F}\right) D^{-2} l \tau^{-1/2}. \quad (2)$$

For the case of CCD read-out noise σ domination, the limit is

$$\text{Flux}_{\min} \propto \frac{\sigma}{D^2 \tau}. \quad (3)$$

The number of detectable events, uniformly distributed in Euclidean space, is

$$\text{Number} \propto \Omega \cdot \text{Flux}^{-3/2} = D \left(\frac{D}{F}\right)^{1/2} \tau^{3/4} N^2 l^{1/2} \quad (4)$$

when the duration of the event T is longer than the exposure, and

$$\text{Number} \propto \Omega \cdot \text{Flux}^{-3/2} \left(\frac{\tau}{T}\right)^{-3/2} = D \left(\frac{D}{F}\right)^{1/2} T^{3/2} \tau^{-3/4} N^2 l^{1/2} \quad (5)$$

TABLE 1: Wide-field monitoring cameras currently in operation. For FAVOR and TORTORA the limits correspond to 3σ detection on a single frame, and differ from their real-time operational values.

Name	Field of view (degrees)	Temporal resolution (seconds)	Limit (magnitudes)
WIDGET	62×62	5	10^m
RAPTOR A/B	40×40	60	12^m
RAPTOR Q	180×180	10	10^m
BOOTES	16×11	30	12^m
π of the Sky	33×33	10	11.5^m
AROMA-W	25×35	5–100	10.5^m – 13^m
MASTER-VWF	20×21	5	11.5^m
MASTER-Net	30×30	1	9^m
FAVOR	16×24	0.13	10^m – 11.5^m
TORTORA	24×32	0.13	9^m – 10.5^m

when it is shorter—as Flux_{\min} decreases, one can detect a larger number of events in a greater volume. High temporal resolution, thus, is essential in the detection and analysis of short optical transients. On the other hand, it requires the application of fast CCD matrices, which usually have large read-out noise, that limits the detection of a faint objects.

Most of the general-purpose wide-field monitoring systems currently in operation, listed in Table 1, chose a large of field of view while sacrificing the temporal resolution to achieve decent detection limit. Our cameras, FAVOR and TORTORA, in contrast, chose high temporal resolution as a key parameter.

Several examples of various hardware configurations leading to different sizes of field of view for a fixed temporal resolution are shown in Figure 1.

3. FAVOR and TORTORA Cameras

It is obvious that realization of an ideal wide-field system combining both wide field, high temporal resolution and a good detection limit is very difficult. One possible variant of such a project, the Mega TORTORA one, based on a multi-objective design and fast, low-noise EM-CCDs, is presented elsewhere [24]. For our cameras, we have used a simpler and cheaper approach, described in [14]. Its main idea is the application of an image intensifier to both effectively reduce the focal length by downscaling the image, and to overcome the read-out noise of a fast TV-CCD by the high amplification factor of the intensifier. Technical parameters of the cameras are listed in Table 2, and their images are shown in Figure 2. Compared to FAVOR, TORTORA has a somewhat smaller aperture and focal length, as well as cruder pixel scale, but a significantly greater field of view and slightly sharper PSF FWHM.

Both cameras use custom $f/1.2$ objectives, refractive in FAVOR and reflective in TORTORA, and are equipped with image intensifiers and fast CCDs based on the Sony ICX285AL chip. The TORTORA camera is also equipped with two motors for automatic focusing of the main objective

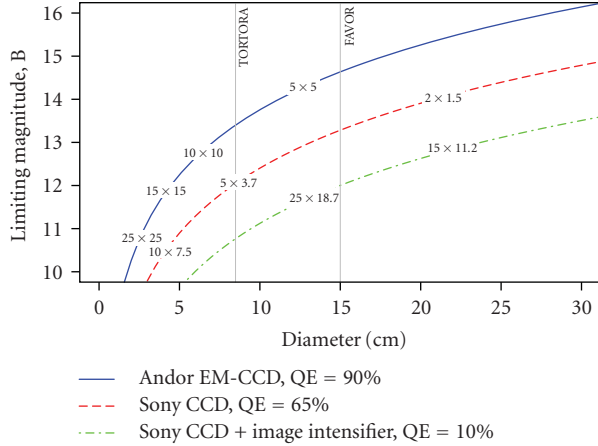


FIGURE 1: Limiting magnitudes for various configurations of objective diameter and CCD used. The Sony ICX285AL 1388×1036 CCD with $6.5 \mu\text{m}$ pixels and $6e^-$ read-out noise, without and with the image intensifier used to effectively shorten the focal length 7.7 times, is compared to the Andor iXon^{EM} + 888×1024 EM-CCD with $13 \mu\text{m}$ pixel and $0.5e^-$ read-out noise. The objectives are assumed to have $D/F = 1/1.2$. Vertical gray lines mark the objective sizes of FAVOR and TORTORA cameras. Numbers inside the lines represent the corresponding sizes of the field of view. The limiting magnitudes are in B band for 0.13 s exposure. For TORTORA camera, the effective diameter is shown, which is $\sqrt{2}$ times smaller than the input window size due to multi-mirror objective design which reflects back approximately 50% of incoming light. The variant with a low-noise EM-CCD is obviously the best in sensitivity, while the one with the image intensifier is far superior in a size of field of view.

and transmission optics, while FAVOR is focused manually. The FAVOR camera is placed on a dedicated equatorial mount, while the TORTORA is mounted on top of the Italian REM telescope, which has an alt-azimuthal mount design (it leads to the field rotation during the observations). The cameras, when possible, are pointed to the regions of the sky observed by the Swift telescope according to its real-time pointing information distributed through GCN network [25].

4. Data Acquisition

The cameras are operated by a cluster of three PCs connected via a dedicated Gigabit Ethernet network. The first one is equipped with a TV5 frame-grabber; it acquires the data from a TV-CCD at a 7.5 frames per second rate, attaches a timestamps to them and supplies them to the network as a set of broadcast UDP packets. Any number of clients on this network can collect and process these data. In a typical scheme, one of clients is the RAID array which continuously stores all broadcast data for possible detailed future investigation. The size of the RAID array has to be chosen carefully to be able to store at least the amount of data collected during one or two nights; for an 8-hour long acquisition it corresponds to 580 Gb of data. The RAID PC

TABLE 2: Technical parameters of the FAVOR and TORTORA cameras.

	FAVOR	TORTORA
<i>Main objective</i>		
Diameter	150 mm lens	120 mm mirror
Focal length	180 mm	150 mm
Focal ratio	1/1.2	1/1.2
<i>Image intensifier</i>		
Photocathode	S20	S20
Diameter	90 mm	90 mm
Gain	150	150
Scaling factor	7.7	7.7
Quantum efficiency	10%	10%
<i>CCD</i>		
Model	VS-CTT285-2001	VS-CTT285-2001
Frame size	1388×1036	1388×1036
Pixel scale	$57''/\text{pix}$	$81''/\text{pix}$
Exposure	0.13 s	0.13 s
Pixel size	$6.5 \mu\text{m}$	$6.5 \mu\text{m}$
Read-out noise	$6 e^-/\text{pix}$	$6 e^-/\text{pix}$
Star FWHM	$3.1'$	$2.7'$
Mount	Equatorial	Alt-azimuthal
Focus	manual	automatic

also hosts the network service which is able to extract any given frame from the RAID array and send it to the client.

One more client connected to the local network performs the real-time data processing, extracting the information on transients and performing their basic classification during the observations. Then, during day time, it performs the detailed analysis of these events. Also, this PC hosts the software controlling the whole cluster and, in the case of the TORTORA system, communicating with the REM telescope. A schematic view of the complete set of interacting network services inside the TORTORA system is presented in Figure 3.

5. Real-Time Data Processing

The fast TV-CCD camera with 1388×1036 pixels operating at a 7.5 Hz frame rate produces 20.5 megabytes of data each second. The processing of such an enormous data flow is complicated. A typical data processing pipeline, for example, SExtractor-based [26], requires at least one second on a modern PC to extract all objects from a single frame and perform their comparison with the catalogue. As this is an order of magnitude slower than needed for our task, we decided to use simpler data processing, aimed at the detection of variable objects only. This approach, often named “the differential imaging” method, is based on a statistical analysis of pixel values for a sequence of images. During the data acquisition, an “average frame” is being constantly updated, representing the mean values for each pixel over some number of previous frames (100 frames seems to be the optimal amount, since on longer



FIGURE 2: Images of prototype fast wide-field FAVOR camera, located in the Special Astrophysical Observatory of Russian Academy of Sciences at North Caucasus, and the TORTORA camera, mounted on top of the REM robotic telescope in La-Silla Observatory, ESO, Chile.

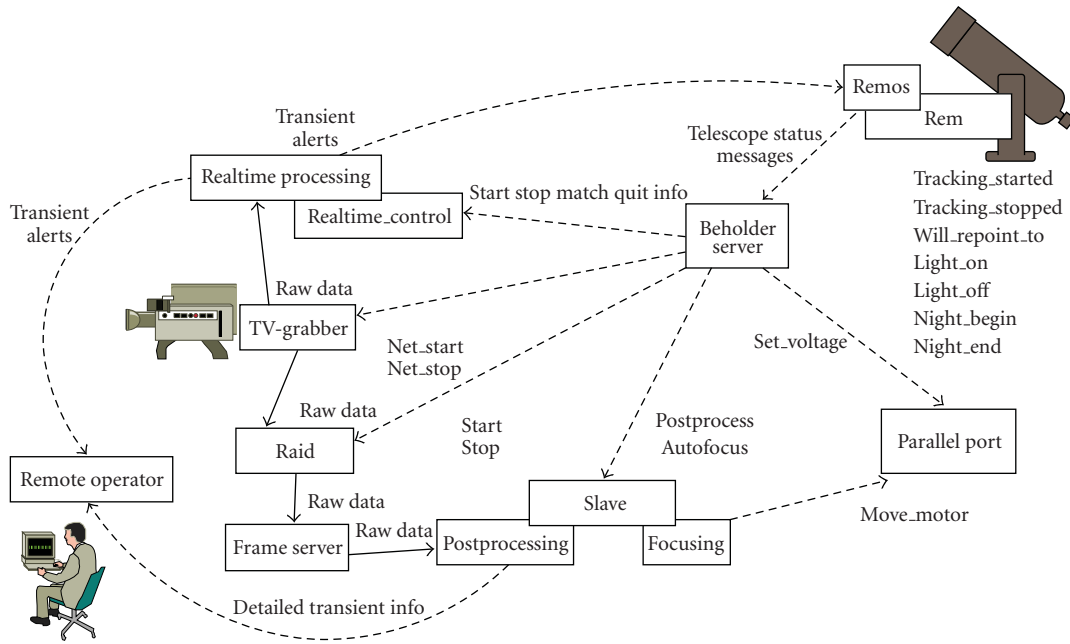


FIGURE 3: Schematic view of interoperation of various TORTORA subsystems with the REM telescope. The data are distributed from TV-CCD through the local Gigabit Ethernet network to a RAID array for a temporary storage and to a real-time processing software. All subsystems are controlled by a dedicated service connected to the REM operating software and responsible for the management of the image intensifier high voltage power supply, auto-focusing subsystem, and so forth.

scales the atmospheric variations become significant). Also, the “dispersion frame” is being formed in a similar way, representing the estimated standard deviations of each pixel over the same number of previous frames.

Then, for each consecutive frame we subtract “average frame” to cancel the spatial variations across the frame related to inhomogeneities of both CCD and image intensifier sensitivities, and of the sky due to bright stars and Milky Way. Then, the resulting residual frame is divided by the “dispersion frame” to compensate for different levels of stationary variability—star PSF wings are more variable

than the background, while CCD defects are mostly not variable. Finally, the thresholding is performed to locate pixels deviating significantly (i.e., greater than 3σ) from the mean level. The process is illustrated in Figure 4. A fast clustering algorithm is then used to locate continuous areas of interest on the frame—the so-called “events”. A 4σ pixel connected with a 3σ one is regarded as the minimal acceptable event. Assuming Gaussian statistics, this leads to a 0.5 purely stochastic false events per frame; in real operation, the number of such events is found to be 2–4 due to non-Gaussian nature of image intensifier noise, caused by

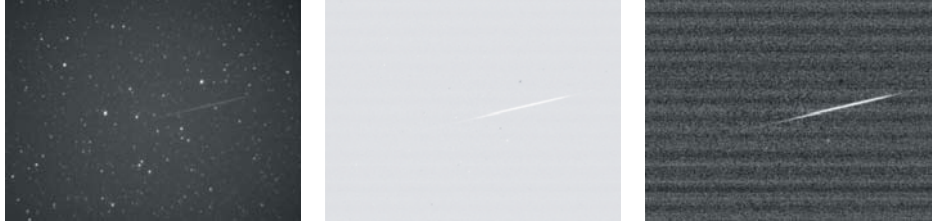


FIGURE 4: Differential imaging method applied to a meteor track. Left pane: original frame imaged by the FAVOR camera. Middle pane: image with the “average frame” (the mean values of each pixel over the last 100 frames), subtracted. There are residual signatures of stars due to higher level of fluctuations in the wings of star PSFs, as well as regions with very low fluctuation levels due to CCD defects and dust in the focal plane. Right pane: residual image divided by a “dispersion frame” (standard deviations for each pixels estimated over last 100 frames). The only significant deviations from the zero level are due to the fast transient, which may be located and extracted by a thresholding on a $3\text{--}4\sigma$ level.

stochastic nature of electron multiplication process as well as by thermal and ion events.

Thus, the marginally detected event has a 7σ flux, which corresponds to $V = 10.5^m - 11.5^m$ for FAVOR and $V = 9.5^m - 10.5^m$ for TORTORA, depending on the sky conditions.

It is worth mentioning that the dispersion estimation used in differential imaging corresponds to the temporal variations of a pixel value, not spatial variations of values across the single frame. The noise behaviour is generally non-ergodic—temporal and spatial dispersions may significantly differ, and the differential imaging limit may deviate from a single-frame “classical” detection limit by up to 0.5^m in both directions.

The differential imaging method is not universal. The estimation of a “null hypothesis” statistical properties of each pixel over previous frames becomes biased when the transient is sufficiently long and bright—its flux on the first frames where it occurs influences the mean and dispersion values for the next frames. This is demonstrated in Figure 5 for the case of the 60-seconds-long Naked-Eye Burst as well as a 2-seconds long artificial event with the same temporal structure and peak brightness. It is obvious that differential imaging is ineffective for a long and slowly-changing transients (which may be well studied by another methods on longer time scales); it is, however, extremely powerful in the detection of highly-variable or fast-moving ones (as fast motion implies rapid changes in pixels on the object edges). Also, due to this feature of the differential imaging, it is also insensitive to a slow variations of atmospheric conditions.

In spite of these problems, the application of differential imaging method solves the “bottleneck” problem in real-time data processing in a high frame-rate case. The extraction of all events from a single frame, deviating significantly from the average one, requires only ~ 10 ms on a typical PC.

6. Detection and Classification of Fast Optical Transients

Detection of a continuous region significantly deviating from the average frame level is not enough to draw a conclusion on its nature—it may be a meteor, satellite, flash of a star-like object or just a noise event. Therefore, some additional steps

are then needed to check whether the object is real, and to determine its type.

In our software, we use a simple three-stage algorithm. It is based on the determination of the parameters of object motion—its direction and speed. As a first step, after the initial detection of each event on the first frame, we form a circular region of expectation for its appearance on the next one, by assuming that its speed is below some reasonable value (for FAVOR and TORTORA, we chose 1 degree per second as an upper limit for the speed). Then, on the second frame, for all events inside this region, we form a set of hypotheses about the possible directions and speeds of the object; for each hypothesis errors of coordinate determinations for the first and second events define a new, smaller elliptical region of expectation for the next frame. Finally, on the third frame, we check whether the object is detected in the positions predicted by each hypothesis, and usually only one hypothesis survives. This three-stage process is illustrated in Figure 6. The object for which no suitable events appeared on the second frame, is assumed to be a noise event, and is rejected. Objects with no suitable events on the third frame may be optionally checked on the fourth one. Objects with detected and confirmed motion may be tracked while they are staying inside the field of view, constantly adding events from new frames to their trajectories and light curves, which allows their motion parameters to be determined with increasing accuracy; a typical satellite passing over the FAVOR site may be seen on a set of up to 500 consecutive frames.

Immobility is just an extremal kind of a motion—the motion with a zero speed. So, if the object is detected during three consecutive frames, and its speed is estimated to be no more than its statistical error, it is assumed to be an immobile transient, probably at a galactic or cosmological distance. Slowly moving satellites, however, may produce flares due to rotation, and the duration of the flares may be too short to measure their speed. An example of such a flare is shown in Figure 7. Such events may be identified with known satellites by examining the catalogue of satellite orbital elements [27] and pre-computing their trajectories over the observatory field of view. It is, unfortunately, not always possible to identify such flashes as not all satellites (and large enough

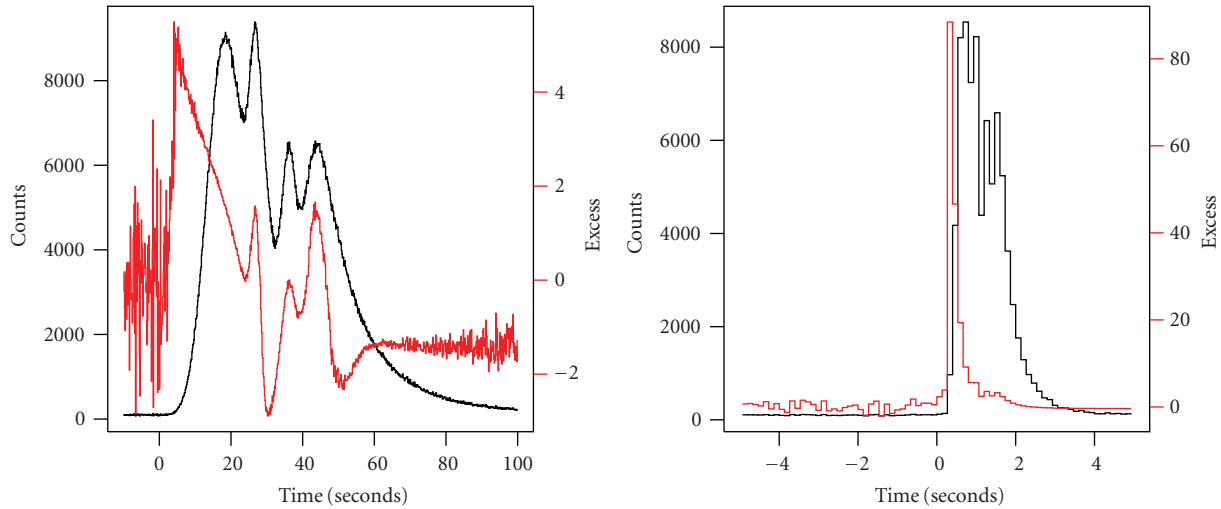


FIGURE 5: Response of the differential imaging method to the Naked-Eye Burst, as seen by the TORTORA camera software. Left pane: original burst light curve in counts (black line), and corresponding deviations from the mean value over 100 previous points in units of the standard deviation estimated over the same interval (red line). The response is highly non-linear due to the influence of the burst itself on the estimation of the mean and standard deviation. The deviation never exceeds 5σ . Right pane: response to a burst with the same temporal structure and brightness, but 30 times shorter than Naked-Eye Burst (2-second duration). There is a sharp $\sim 90\sigma$ peak in deviation.

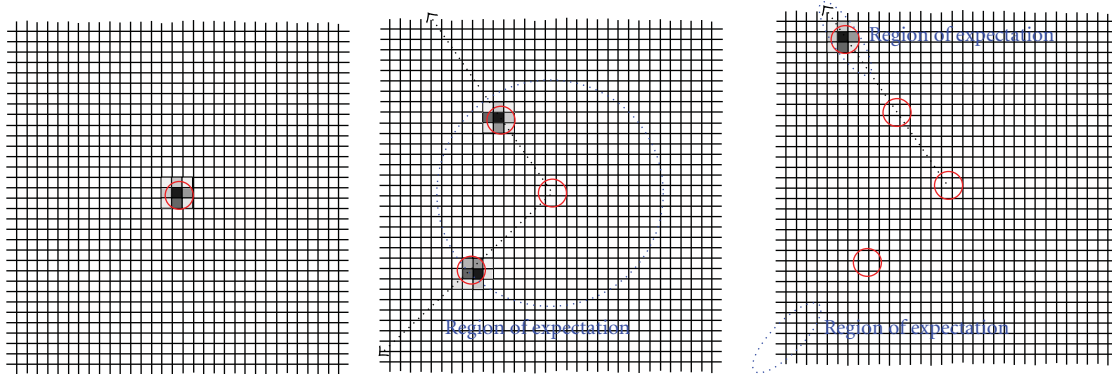


FIGURE 6: Motion hypotheses formulation. Three stages of a detection and classification of a transient. From left to right: the initial detection of the event on a first image, formation of a circular region of expectation based on assumption about some reasonable maximal speed of expectation; the formation of a set of hypotheses on object motion direction and speed based on an appearance of events inside this region on a second frame; the rejection of failed and acceptance of successful hypotheses based on events seen on a third frame. Objects not detected on a second frame are immediately rejected as a probably noise events; objects with determined motion parameters are tracked until their disappearance from field of view or fading out below the detection limit. For FAVOR and TORTORA systems with 0.13 s temporal resolution, this three-stage algorithm is completed in less than 0.4 seconds, resulting in nearly real-time detection and classification of transient.

pieces of cosmic debris) are in the database. However, they may be identified if their flashes are repeating while they pass through the camera field of view.

Meteors cannot be reliably detected by the algorithm, as they move too fast, forming significantly non-point-like tracks on the frames, and they are often visible for only one or two frames. However, bright ones can be extracted by purely geometrical criteria on each frame, and then combined together on a postprocessing stage. Then, classical methods like the Hough transform may be used to estimate the direction of the meteor track, to get their intensity profiles and—in the case of events lasting several frames—to

measure their velocities. An example of a fast meteor detected by the FAVOR camera is shown in Figure 8.

The algorithm described above can detect a transient and measure its motion parameters in a three consecutive frames, which for the FAVOR and TORTORA cameras corresponds to less than 0.4 seconds. Then the nature of the transient may be guessed based on this information and by comparing its position and time of appearance with the catalogue of satellite passes over the site. At that point, any event not showing signatures of motion and not present in the satellites database, may become the targets of a follow-up and detailed investigation by robotic telescopes [17].

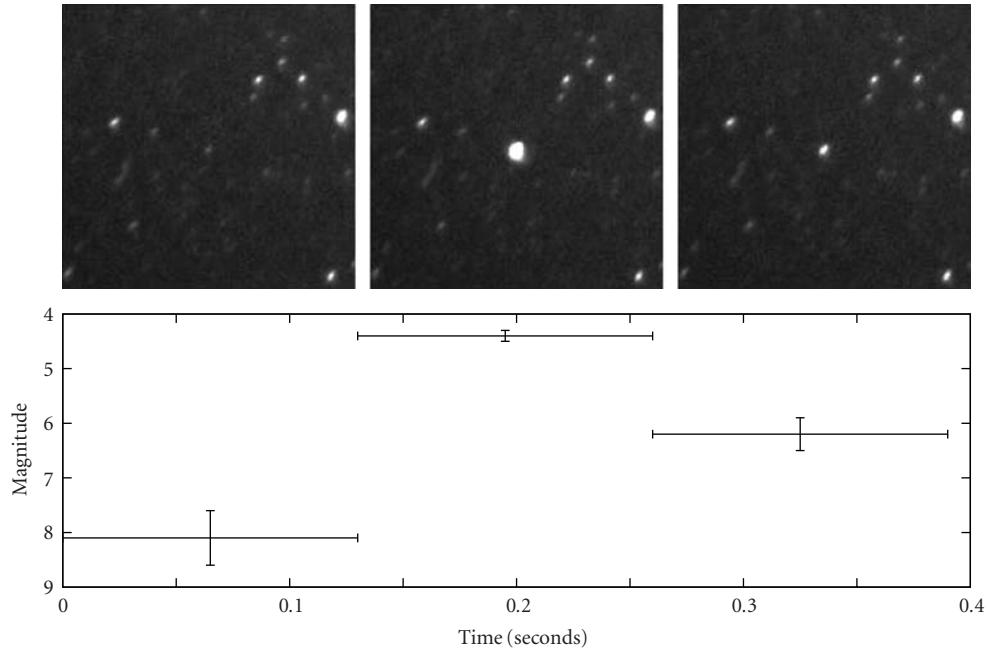


FIGURE 7: Example of a short flare detected by the FAVOR camera. The total length of the event is 0.4 seconds (seen on 3 successive frames), and the object motion speed is too low to be detected. This is identified as a satellite event by checking the database of satellite orbital parameters.

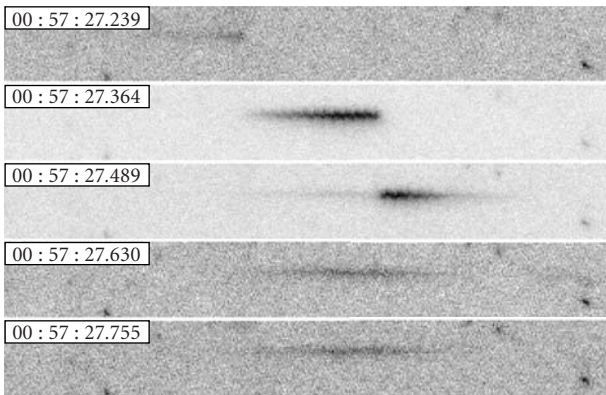


FIGURE 8: Example of a fast (flight time approximately 0.3 seconds) and bright ($V_{\text{peak}} \approx 3$) meteor detected by the FAVOR camera. Sub-frame brightness variations, as well as long-lasting trail, are clearly seen.

7. Conclusions

The importance of wide-field monitoring is obvious. High temporal resolution must be an essential part of such monitoring, as it has been demonstrated by the discovery of the fast optical variability of the Naked-Eye Burst. The real-time data processing is also important, as it allows the detected transient information to be distributed to robotic telescopes or, in the case of a Mega TORTORA-like complex [24], to reconfigure the system for a detailed investigation of the event. We have demonstrated that it is not too difficult to both construct the cameras able to perform such monitoring,

and organize the real-time detection and classification of fast optical transients.

Acknowledgments

This work was supported by the Bologna University Progetti Pluriennali 2003, by grants of CRDF (no. RP1-2394-MO-02), RFBR (no. 04-02-17555, 06-02-08313 and 09-02-12053), INTAS (04-78-7366), and by the Presidium of the Russian Academy of Sciences Program. The first author has also been supported by grant of President of Russian Federation for federal support of young scientists.

References

- [1] H. Bondi, "Astronomy of the future," *Quarterly Journal of the Royal Astronomical Society*, vol. 11, pp. 443–450, 1970.
- [2] B. Schaefer, "Celestial optical flash rate—predictions and observations," *Astronomical Journal*, vol. 90, pp. 1363–1369, 1985.
- [3] B. E. Schaefer, H. Pedersen, C. Gouiffes, J. M. Poulsen, and G. Pizzichini, "Optical flash background rates," *Astronomy & Astrophysics*, vol. 174, no. 1–2, pp. 338–343, 1987.
- [4] T. Tamagawa, F. Usui, Y. Urata, et al., "The search for optical emission on and before the GRB trigger with the WIDGET telescope," *Nuovo Cimento della Societa Italiana di Fisica C*, vol. 28, no. 4–5, pp. 771–774, 2005.
- [5] K. N. Borozdin, S. P. Brumby, M. C. Galassi, et al., "Real-time detection of optical transients with RAPTOR," in *Astronomical Data Analysis II*, J.-L. Starck and F. D. Murtagh, Eds., vol. 4847 of *Proceedings of the SPIE*, pp. 344–353, Waikoloa, Hawaii, USA, August 2002.

- [6] A. J. Castro-Tirado, J. Soldán, M. Bernas, et al., “The burst observer and optical transient exploring system (BOOTES),” *Astronomy and Astrophysics Supplement Series*, vol. 138, no. 3, pp. 583–585, 1999.
- [7] A. Burd, M. Cwiok, H. Czyrkowski, et al., “Pi of the sky—all-sky, real-time search for fast optical transients,” *New Astronomy*, vol. 10, no. 5, pp. 409–416, 2005.
- [8] V. F. Shvartsman, G. M. Beskin, R. E. Gershberg, V. L. Plakhotnichenko, and L. A. Pustilnik, “Minimum rise times in Uv-Ceti type flares,” *Soviet Astronomy Letters*, vol. 14, no. 2, p. 97, 1988.
- [9] S. McBreen, F. Quilligan, B. McBreen, L. Hanlon, and D. Watson, “Temporal properties of the short gamma-ray bursts,” *Astronomy & Astrophysics*, vol. 380, no. 2, pp. L31–L34, 2001.
- [10] V. L. Afanasiev, V. V. Kalenichenko, and I. D. Karachentsev, “Detection of an intergalactic meteor particle with the 6-m telescope,” *Astrophysical Bulletin*, vol. 62, no. 4, pp. 301–310, 2007.
- [11] G. M. Beskin, V. Plohotnichenko, C. Bartolini, et al., “Catching the light curve of flaring GRBs: the opportunity offered by scanning telescopes,” *Astronomy and Astrophysics Supplement Series*, vol. 138, no. 3, pp. 589–590, 1999.
- [12] D. Eichler and G. Beskin, “Optical search for extraterrestrial intelligence with air Cerenkov telescopes,” *Astrobiology*, vol. 1, no. 4, pp. 489–493, 2001.
- [13] I. Zolotukhin, G. Beskin, A. Biryukov, et al., “Optical camera with high temporal resolution to search for transients in the wide field,” *Astronomische Nachrichten*, vol. 325, no. 6–8, p. 675, 2004.
- [14] S. Karpov, G. Beskin, A. Biryukov, et al., “Optical camera with high temporal resolution to search for transients in the wide field,” *Nuovo Cimento della Societa Italiana di Fisica C*, vol. 28, no. 4–5, pp. 747–750, 2005.
- [15] S. Karpov, D. Bad’in, G. Beskin, et al., “FAVOR (FAst Variability Optical Registration)—two-telescope complex for detection and investigation of short optical transients,” *Astronomische Nachrichten*, vol. 325, no. 6–8, p. 677, 2004.
- [16] G. Beskin, V. Bad’in, A. Biryukov, et al., “FAVOR (FAst Variability Optical Registration)—a two-telescope complex for detection and investigation of short optical transients,” *Nuovo Cimento della Societa Italiana di Fisica C*, vol. 28, no. 4–5, pp. 751–754, 2005.
- [17] E. Molinari, S. Bondar, S. Karpov, et al., “TORTOREM: two-telescope complex for detection and investigation of optical transients,” *Nuovo Cimento della Societa Italiana di Fisica B*, vol. 121, no. 12, pp. 1525–1526, 2006.
- [18] J. L. Racusin, S. V. Karpov, M. Sokolowski, et al., “Broadband observations of the naked-eye γ -ray burst GRB 080319B,” *Nature*, vol. 455, no. 7210, pp. 183–188, 2008.
- [19] S. Karpov, G. Beskin, S. Bondar, et al., “GRB 080319B: RAPTOR observations of a naked eye burst,” GCN 7452, GRB Coordinates Network Circular, 2008.
- [20] P. Wozniak, W. Vestrand, J. Wren, and H. Davis, “GRB 080319B: RAPTOR observations of a naked eye burst,” GCN 7464, GRB Coordinates Network Circular, 2008.
- [21] M. Cwiok, W. Dominik, G. Kaspruwicz, et al., “GRB 080319b prompt optical observation by Pi-of-the-sky,” GCN 7439, GRB Coordinates Network Circular, 2008.
- [22] G. Beskin, S. Karpov, S. Bondar, et al., “TORTORA discovery of naked-eye burst fast optical variability,” in *Nanjing Gamma-ray Burst Conference*, Y.-F. Huang, Z.-G. Dai, and B. Zhang, Eds., vol. 1065 of *AIP Conference Proceedings*, pp. 251–254, 2008.
- [23] G. Beskin, S. Karpov, S. Bondar, et al., “Fast optical variability of naked-eye burst—manifestation of periodic activity of internal engine,” <http://arxiv.org/abs/0905.4431>.
- [24] G. Beskin, S. Karpov, S. Bondar, et al., “From TORTORA to Mega-TORTORA—results and prospects of search for fast optical transients,” *Advances in Astronomy*, vol. 2010, article ID 171569, 2010.
- [25] S. D. Barthelmy, “Observing strategies using GCN,” in *Proceedings of the 4th Hunstville Symposium on Gamma-Ray Bursts*, C. A. Meegan, R. D. Preece, and T. M. Koshut, Eds., vol. 428 of *AIP Conference Proceedings*, pp. 129–133, 1998.
- [26] E. Bertin and S. Arnouts, “SExtractor: software for source extraction,” *Astronomy and Astrophysics Supplement Series*, vol. 117, no. 2, pp. 393–404, 1996.
- [27] Database of satellite orbital parameters of US Department of Defence, <http://www.space-track.org/>.

Review Article

Protocols for Robotic Telescope Networks

Alain Klotz^{1,2}

¹ *Observatory of Haute-Provence, Route de l'observatoire, 04870 Saint-Michel l'Observatoire, France*

² *CESR, University of Toulouse, 9 avenue Colonel Roche, 31028 Toulouse Cedex 4, France*

Correspondence should be addressed to Alain Klotz, alain.klotz@free.fr

Received 11 June 2009; Accepted 28 December 2009

Academic Editor: Alberto J. Castro-Tirado

Copyright © 2010 Alain Klotz. This is an open access article distributed under the Creative Commons Attribution License, which permits unrestricted use, distribution, and reproduction in any medium, provided the original work is properly cited.

Autonomous robotic observatories can use modern communications to receive pertinent information from institutes that generate events to observe (e.g., supernovae, near-earth asteroids, gravitational lensings, and gamma-ray bursts). This paper is addressed to astronomers who are not specialists in computer science. We give explanations of some basic and advanced protocols to receive events and how to implement them in a robotic observatory software. We describe messages such as GCN notices, VOEvents or RTML, and protocols such as CGI, HTTP, SOAP, RSS, and XMPP.

1. Introduction

Autonomous robotic observatories (AROs) use complex software to control devices and to check the security conditions (weather, power supply, and mechanical sensors). This software must exchange messages with its different parts and with external resources. When an ARO is not connected to another one, the messages can use any language, but for decade, there have been coordinated efforts to standardize communication protocols [1]. The ultimate goal is to send alert messages to telescope networks that can be understandable by any observatory within the network. The scientific goal of observatory networks is to maximize the observation efficiency in order to characterize the nature of objects recently discovered (e.g., asteroids, supernova, gamma-ray bursts) or to perform optimized follow-ups (e.g., gravitational lensing and variable stars). In this paper, we focus on protocol techniques usually used by telescope networks in the context of the Virtual Observatories (VOs). These protocols are mostly defined and maintained by the International Virtual Observatory Alliance (<http://www.ivoa.net/>) (IVOA) and the scope of this paper is to present them to the astronomers that are not specialists in computer science.

2. Agents, Servers, Clients

In the context of VO, we define an agent as a software or a library that carries out a predefined task of an ARO (e.g., in

[2]). For example, the telescope agent is a software which can drive the telescope mount.

Generally, agents are slaves, that is, waiting for basic orders. In the context of computer science, they are named servers. A server is an agent that waits forever until an order is received. When an order is received, the corresponding task is executed, and the agent returns to the waiting loop. All server agents are managed by a more intelligent agent that collects the status of the observatory and the schedule of observations and decides to send orders to the server agents. This intelligent agent is a client in the context of the computing science (see Figure 1). First, the intelligent agent establishes client connexions to the server agents. Second, the intelligent agent sends messages to server agents in an order corresponding to the sequence of observations scheduled. A good example of ARO agents is the suite RTS2 [3] which can be adapted to many hardware configurations. An example of a more complex telescope network and its agents (RoboNet-II) is described in [4].

3. What Is a Protocol?

Computer science uses the concept of Open Systems Interconnection Reference Model (hereafter OSI model) to define how to communicate between computers. The OSI model defines seven layers: physical, data link, network, transport, session, presentation, and application. The three first layers are related to the media used to send data (Internet Protocol,

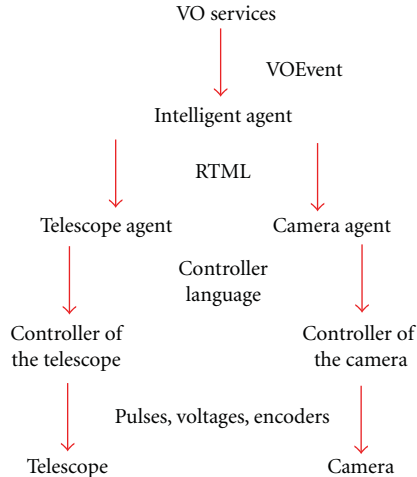


FIGURE 1: Simple schema of agents used in an autonomous robotic observatory.

Point to Point Protocol, cables, hubs, etc.). The four last layers concern how data are managed in the computer. ARO agents use protocols defined essentially in the application layer. In this paper, we will use the following protocols: CGI, HTTP, SOAP, RSS, and XMPP.

The application layer protocols define how the messages are transported to the other agents, but the contents of the messages are written in a given language. In this paper, we use the following languages: HTML and XML.

The combination of the application layer protocol and the message language defines the protocol as defined in the title of this paper. Let us take an example. The telescope agent is waiting for a message using an event loop which is based on a TCP socket server. At a time, the TCP socket receives the following message from the intelligent agent:

```

<Coordinates>
  <RightAscension>41.25</RightAscension>
  <Declination>+22.5</Declination>
</Coordinates>
  
```

This message is written in the eXtensible Markup Language (XML) and is understandable by an astronomer. This is a text language with a syntax rule based on start-tags (<>) and corresponding end-tags (</>). The tag `Coordinates` implies that the following coordinates stand for the next target to observe. The parameters are the Right Ascension and the Declination. The corresponding values lie in the start/end tags `RightAscension` and `Declination` respectively. The tag `Declination` could be given before that of `RightAscension` without any difference of interpretation. If the telescope controller is based on the LX200 Meade protocol, the telescope agent must convert the coordinates to the language of the controller (the full list of the LX200 Meade commands can be found in <http://www.meade.com/support/CommandSet.html>):

```

:Sr02:45:00#
:Sd+22*30:00#
  
```



FIGURE 2: Web form of the Minor Planet Center ephemeris center as seen using a browser.

Then, these two commands must be sent to the RS232 socket of the telescope controller. These low level commands depend on the manufacturer of the telescope controller and the role of the telescope agent is to transform commands from a standard form (cf. the XML text above, and see Section 6 for the RTML definition) to the low level command language specific to the telescope controller (e.g., the LX200 Meade language).

4. Protocols to Prepare Observations

In a full ARO, the schedule of observations is generated by a schedule agent that sorts the observations to maximize a criterion related to the scientific results [5]. It is also important to simplify human data inputs of observation requests to avoid human errors when entering target coordinates. For example, it is preferable to ask for an asteroid name rather than ask for its coordinates that change all the time. In this section, we show how to incorporate two simple name solver codes in an ARO agent.

4.1. CGI and HTTP. In this section, we present a classical web service delivered by the Minor Planet Center (MPC). MPC provides on-line ephemeris for minor planets. First, connect to the MPC server using a web browser (Figure 2). The Uniform Resource Locator (URL) is the address of the MPC server computer that delivers the web page. This page is written in Hyper Text Language Markup (HTML) which is based on start and end tags (e.g., `<HTML>` and `</HTML>`). In the case of the MPC web service, an excerpt of the web form is defined by the HTML code in Algorithm 1.

The interpretation of this code by the browser gives what can be seen on Figure 2. The main tag is `<FORM>`. It defines web gadgets (hereafter widgets) as buttons, radio buttons, text areas, and so forth. The contents of these widgets will be sent to the URL associated parameter `ACTION` in the tag `FORM` using the method `POST`. This URL triggers a Common Gateway Interface script (CGI) in the MPC server when the user pushes the submit button. To summarize, data format is CGI-POST and the protocol is HTTP.

```

<FORM
METHOD=POST
ACTION="http://scully.cfa.harvard.edu/~cgi/MPEph2">
<input type=submit value="Get ephemerides/HTML page">
<input type=reset value="Reset form"><br>
<input type="radio" name="ty" VALUE="e" CHECKED>
<input type="radio" name="ty" VALUE="s">
Return <a href="#summary">summary</a>
Return ephemerides
<input type="radio" name="ty" VALUE="h">
Return HTML page<br>
Objects may be identified by designation or by name.
Enter a list of designations or names below (one
entry per line, excess entries will be ignored):<br>
<textarea name="TextArea" cols=17 rows=5></textarea>
<br>Ephemeris start date: <input name="d" maxlength=20 size=17 VALUE="">
<br>Title for document: <input name="tit" maxlength=60 size=40>
<br>Base URL for document: <input name="bu" maxlength=80 size=40>
</FORM>

```

ALGORITHM 1

Obviously, an ARO must be able to send a CGI form without any human action (i.e., without a web browser). How to do it? The software of the ARO must use a code that simulates the web form displayed by the browser. The corresponding code to obtain ephemeris of Ceres is given by the seven following lines written in the Tcl script language (see Algorithm 2) (documentation available at <http://www.tcl.tk/>. Tcl/Tk is installed in most Linux distributions. Type `tclsh` to launch a Tcl interpreter.):

At the end of the script, the variable `html_text` contains the HTML code of the result. The next action to do is to parse the HTML text to extract the coordinates of the minor planet.

4.2. SOAP and HTTP. The Simple Object Access Protocol (SOAP) is close to the CGI-POST. It can be used with HTTP. Let us take an example. We want to use the web service of the Centre de Données Stellaires (CDS) to find coordinates associated to an object name. This name solver is not usable by a browser because the SOAP protocol has no graphical interface in a web browser. Nevertheless, SOAP is easy to use in an ARO agent and SOAP can be better than CGI-POST for many technical reasons that are outside the scope of this paper. As an example, the following lines are written in the Tcl script language to solve the coordinates of Messier 51 (see Algorithm 3).

At the end of the script, the variable `xml_text` contains the XML code of the result. The next action is to parse the XML text to extract the coordinates of the galaxy. The lines in Algorithm 4 display the XML code returned in the variable `xml_text`.

The URL defined in the parameter `xsi:noNamespaceSchemaLocation` gives the structure of the tags used in the document. The coordinates in decimal form lie in the tags `jradeg` and `jdedeg`. XML format is much more easy to parse than the HTML code like that returned by the CGI-POST of Section 4.1 because the coordinates to extract from

the HTML code is not necessary defined inside start/end tags and the structure of the returned HTML code is not auto-documented as it is the case for XML.

5. Protocols to Receive Events

Just after the discovery of Gamma-Ray Burst (GRB) optical afterglows in 1997 [6] BACODINE was created, an internet message distribution service that became later the Gamma-ray burst Coordinate Network (GCN, [7]). The data input of this service is information delivered by satellites that are equipped by a real-time localizer of GRBs (e.g., Swift, Integral, and Fermi). The useful output of the GCN for ARO is notices. (see <http://gcn.gsfc.nasa.gov/invitation.html> for a complete description) For each GRB triggered by a satellite, the GCN builds a notice that indicates coordinates, error box and summarizes miscellaneous informations about the characterization of the burst. These notices are generated automatically when a new trigger appears. The distribution is done freely by a simple TCP socket connexion to any ARO that asks to receive notices.

5.1. GCN Notices and TCP Sockets. A TCP socket is one of a simplest way to exchange messages between software. The principle is based on the client-server connexion. First, the software that wants to receive messages opens a port. This is the server and the port is an integer number between 0 and 65535. The other software that will send messages opens a connexion to the Internet Protocol (IP) number at the port number of the server. This is the client. For the GCN service, ARO are the servers and the GCN opens client connexions and sends notices by this way. The GCN must know who are servers to reach. So, it is mandatory to register the IP+port numbers of the ARO agent to the GCN. Then, the ARO agent opens the server socket port and waits for the GCN notices. Note that the port number is attributed by the GCN (the list


```

set minor_planet "ceres"
set url "http://scully.cfa.harvard.edu/~cgi/MPEph2"
package require http
set query [::http::formatQuery TextArea \
"$minor_planet" ty "e" d "" tit "" bu ""]
set token [::http::geturl $url -query "$query"]
upvar #0 $token state
set html_text $state(body)

```

ALGORITHM 2

```

package require SOAP
set name "M51"
set resultType "xp"
set server "http://cdswww.strasbourg.fr/axis/services/Sesame"
SOAP::create sesame -uri $server -proxy $server \
  -action "urn:sesame" \
  -params { "name" "string" "resultType" "string" }
set xml_text [sesame $name $resultType]

```

ALGORITHM 3

of registered ARO is <http://gcn.gsfc.nasa.gov/sites.cfg.html> (e.g., port=5134 for the TAROT telescope).

In GCN notices delivered by TCP sockets, data are coded in a binary stream of 40 integers of 4 bytes each. So, a total of 160 bytes must be received before beginning to decode the notice parameters. The corresponding code in Tcl script is shown in Algorithm 5.

In this code, the procedure `socket_accept` is called when the TCP channel is opened. Note that this channel is configured to be activated only when 160 bytes are received. The `fileevent` function creates a call back to the procedure `socket_read` when data are arrived in the opened channel:

```

proc socket_read { channel } {
  set line [read $channel 160]
  if {[eof $channel]} {
    close $channel
  } elseif {![fblocked $channel]} {
    binary scan $line I* longs
    set datas [notice_parser $longs]
    return $datas
  }
  return ""
}

```

The procedure `socket_read` reads the data in the channel and stores them in the variable `line`. Then it transforms this line into 40 integers in the list variable `longs`. Now one must call the procedure `notice_parser` to retrieve the celestial coordinates of the GRB (see Algorithm 6).

The rules of parsing are defined in a GCN document. (the notice definition can be download at http://gcn.gsfc.nasa.gov/sock_pkt_def_doc.html.) The type of notice (`pkt_type`) is the most important parameter to decode. The type is related to the source of the trigger (e.g., Swift BAT triggers are of

`pkt_type=61`). The procedure `notice_parser` returns the minimal informations: the type of the notice and celestial coordinates. Obviously, a real implementation of the parser should include other informations from the notice in order to conclude if the trigger deserves to be observed or not. The last Tcl function `vwait forever` must be used to activate the event loop of the socket listener.

5.2. Limitations of Using GCN Notices with TCP Sockets. The advantage of using TCP sockets is that the code is easy to write in any programming language. Almost all the early optical emissions of GRBs were found thanks to this system. However, there are several disadvantages:

- (1) Most institutes do not authorize the opening of the GCN port due to security reasons. The network administrator of the institute must configure the firewall to authorize only the IP numbers of the GCN (128.183.16.187, 128.183.96.236, and 128.183.96.237) to connect on the server port. Unfortunately, not all institute authorize to do that. One can skirt the problem by using of a Virtual Private Network (VPN).
- (2) Parsing the GCN notice parameters depends on each type of alert (more than 100 are defined in 2009). The parser must treat all cases to be robust. The arrival of a new satellite implies to add codes.
- (3) The GCN computer must verify connections to tens of computers. This excellent work is made by Scott Barthelmy but it is almost impossible to extend the system to thousands ARO.

```
<?xml version="1.0" encoding="UTF-8"?>
<Sesame xmlns:xsi="http://www.w3.org/2001/XMLSchema-instance"
  xsi:noNamespaceSchemaLocation=
    "http://vizier.u-strasbg.fr/xml/sesame_4.xsd">
<Target>
  <name>M51</name>
  <Resolver name="S=Simbad (CDS, via client/server)">
    <otype>Sy2</otype>
    <jpos>13:29:52.36 +47:11:40.8</jpos>
    <jradeg>202.46820833</jradeg>
    <jdedeg>47.19466667</jdedeg>
    <refPos>1999ApJS..125..409C</refPos>
    <errRAmas>10800</errRAmas><errDEmas>10800</errDEmas>
    <Vel><v>600</v><q>D</q><r>2004A&A...422...39S</r></Vel>
    <MType>Sc</MType>
    <oname>4C 47.36A</oname>
    <nrefs>2092</nrefs>
  </Resolver>
</Target>
</Sesame>
```

ALGORITHM 4

```
set channel [socket -server socket_accept 5134]

proc socket_accept { channel ip port } {
  fconfigure $channel -buffering full -translation binary
  fconfigure $channel -encoding binary -buffersize 160
  fileevent $channel readable [list socket_read $channel]
}
```

ALGORITHM 5

The solution is to replace the 160 byte notices by an XML file designed specifically to define an event. In the context of VO, these are VOEvents.

5.3. GCN Notices versus VOEvents. A VOEvent is an XML file (<http://www.ivoa.net/cgi-bin/twiki/bin/view/IVOA/Ivoa-VOEvent>). VOEvent specifications are maintained by the IVOA. The structure of a VOEvent is

```
<voe:VOEvent>
  <Who></Who>
  <What></What>
  <WhereWhen></WhereWhen>
  <How></How>
  <Why></Why>
  <How></How>
</voe:VOEvent>
```

Applied to the GCN notices, a VOEvent should indicate the notice type in the tag What:

```
<What>
  <Param name="Packet_Type" value="61"/>
</What>
```

The celestial coordinates lie in the tag WhereWhen; see Algorithm 7.

The access to the coordinates seems not trivial but the rules of decoding are stored in a file defined in the tag voe:VOEvent by the parameter xsi:schemaLocation (see Section 4.2 for a similar case). A complete parser of VOEvent is difficult to develop but there is no need to update it when a new type of notice is sent.

5.4. VOEvents and XMPP. VOEvents could be broadcasted using TCP socket but it does not solve the problem of managing thousands of connexions by the broadcaster nor the authorization problems. There are many solutions in computer science but the main constrain is that ARO agents must open a client instead of a server connexion to solve the problems of authorizations. However, in this case, the problem is that the broadcaster (i.e., the GCN) cannot connect itself to the ARO agents. One must find a mechanism that allows ARO agents to be informed when a new VOEvent can be downloaded somewhere.

One solution is to use Really Simple Syndication (RSS). The ARO agent download, periodically, a file defined in a fixed URL (for GCN an RSS URL is <http://www.estar.org.uk/voevent/GCN/GCN.rdf>). This is an XML file that contains two important informations: the tag PubDate which indicates when the last notice was created, and the tag

```

proc notice_parser { longs } {
    set pkt_type [lindex $longs 0]
    set burst_ra [expr [lindex $longs 7]*0.0001]
    set burst_dec [expr [lindex $longs 8]*0.0001]
    return [list $pkt_type $burst_ra $burst_dec]
}

vwait forever

```

ALGORITHM 6

```

<WhereWhen>
  <ObsDataLocation>
    <ObservationLocation>
      <AstroCoord coord_system_id="FK5-UTC-GEO">
        <Position2D unit="deg">
          <Name1>RA</Name1>
          <Name2>Dec</Name2>
          <Value2>
            <C1 pos_unit="deg">189.0740</C1>
            <C2 pos_unit="deg">32.9846</C2>
          </Value2>
        </Position2D>
      </AstroCoord>
    </ObservationLocation>
  </ObsDataLocation>
</WhereWhen>

```

ALGORITHM 7

link that indicates the URL of the last VOEvent file to download. In the case of GRBs, the ARO agent should to be informed with a frequency higher than 1 Hz. This is generally a frequency too high for an RSS flux (but RSS remains a good solution for low frequency events as gravitational lensing, e.g.).

A better solution comes from the eXtensible Messaging and Presence Protocol (XMPP). This is an open protocol used for instant messaging. This is not very different than for the popular Skype or MSN Messenger but XMPP is open source! An ARO agent opens a client connexion to an XMPP server. The XMPP client is identified and must subscribe to a feed. There is such a server at Caltech (see informations in <http://voeventnet.caltech.edu/software/index.html>). This server also proposes a Java client named `voeclient.jar` that can be included easily in any code. A configuration file allows to choose the GCN notices in a VOEvent format; (see Algorithm 8).

The XMPP client is run using a Java Runtime Environment (JRE) available for any operating systems. Before starting, one must create an account by:

```
java -jar voeclient.jar -n myname
      mypassword client.properties
```

And one must subscribe to the GCN VOEvents by

```
java -jar voeclient.jar -s home/moriori.
      cacr.caltech.edu/egcn \
```

`client.properties`

Then, the following call starts the listener of VOEvents:

```
java -jar voeclient.jar -r
      client.properties
```

`voeclient.jar` generates the file `feed.log` where one can follow the arrival of new VOEvents. Unfortunately, the original code of `voeclient.jar` does not write the VOEvent itself on the disk but the code is open source and it is easy to write code just after the comment “// ADD CODE HERE TO PROCESS PACKETS” of the `VOEventJabberClient.java` code. Note that this code is also able to send a VOEvent.

6. RTML

Remote Telescope Markup Language (RTML, see (<http://www.astro.physik.uni-goettingen.de/hessman/>) [8, 9]) is usually used to communicate between agents of a given ARO. RTML defines an XML syntax to describe observation parameters like instrument setup. RTML is different from VOEvent. VOEvents define the science case of objects to observe. Then, a VOEvent must be treated by an agent who parse the astronomical parameters to generate RTML messages knowing the instrument characteristics of the observatory. In the case of a telescope network, this agent must generate RTML messages for each telescope. The power

```
# Properties file for VOEventJabberClient
jabber.id=ARO Agent
jabber.server=moriori.cacr.caltech.edu
jabber.feed=home/moriori.cacr.caltech.edu/egcn
user.name=myname
user.pass=mypassword
packet.validate=false
schema.location=c:/d/voeventnet/VOEvent-v1.1.xsd

# Properties for logging
log4j.rootLogger = INFO, stdout, logfile
log4j.appender.stdout=org.apache.log4j.ConsoleAppender
log4j.appender.stdout.layout=org.apache.log4j.PatternLayout
log4j.appender.stdout.layout.ConversionPattern=%d [%t] %-5p %c - %m%n
log4j.appender.logfile=org.apache.log4j.DailyRollingFileAppender
log4j.appender.logfile.File=feeds.log
log4j.appender.logfile.DatePattern='.'yyyy-ww
log4j.appender.logfile.layout=org.apache.log4j.PatternLayout
log4j.appender.logfile.layout.ConversionPattern=%d [%t] %-5p %c - %m%n
```

ALGORITHM 8

of the combination of VOEvents and RTML is that the agent can optimize observations knowing a preexisting observation strategy of an heterogeneous telescope network (HTN). To summarize, a VOEvent defines the astronomical characteristics of a target and RTML defines the telescope setup to observe this target. The protocol to send and to receive RTML messages can be whatever we want (e.g., TCP socket, and SOAP) but it must be adapted to the constraints of the ARO or of the HTN.

In Section 3, we took an example of an intelligent agent that sends an RTML message to the telescope agent:

```
<Coordinates>
  <RightAscension>41.25</RightAscension>
  <Declination>+22.5</Declination>
</Coordinates>
```

This is just an excerpt of the RTML message focused on the tag Coordinates. RTML can be used also from a telescope agent to inform the intelligent agent that a task is done.

7. Conclusions

Protocols for robotic telescope networks just begin to be available for few years and their development is not fully completed. Today, the most important heterogeneous telescope network is eSTAR which is also a development platform for VOEvents and RTML [10]. In the next years, thousands of VOEvents are believed to be broadcasted by large digital survey projects (LSST (<http://www.lsst.org/>) and Pan-Starrs (<http://pan-starrs.ifa.hawaii.edu/>). It is important to incorporate these protocols into ARO agents as soon as possible, especially in small telescope networks, because they will thus benefit from the VOEvents generated by the large surveys, enabling them to participate actively in the astronomical science of the twenty-first century.

Acknowledgments

The author thanks Matthew Graham and Joshua Bloom for helpful discussions and the CNRS-INSU GDR PCHE for funds provided via the Figaro collaboration.

References

- [1] R. R. White and A. Allan, "An overview of the heterogeneous telescope network system: concept, scalability and operation," *Astronomische Nachrichten*, vol. 329, pp. 232–236, 2008.
- [2] C. J. Mottram and S. N. Fraser, "Robonet-1.0," *Astronomische Nachrichten*, vol. 329, no. 3, pp. 317–320, 2008.
- [3] P. Kubánek, M. Jelínek, and J. French, "The RTS2 protocol," in *Advanced Software and Control for Astronomy II*, vol. 7019 of *Proceedings of SPIE*, p. 92, Marseille, France, June 2008.
- [4] Y. Tsapras, R. Street, K. Horne, et al., "RoboNet-II: follow-up observations of microlensing events with a robotic network of telescopes," *Astronomische Nachrichten*, vol. 330, pp. 4–11, 2009.
- [5] T. Granzer, "What makes an automated telescope robotic?" *Astronomische Nachrichten*, vol. 325, no. 6–8, pp. 513–518, 2004.
- [6] J. van Paradijs, P. J. Groot, T. Galama, et al., "Transient optical emission from the error box of the γ -ray burst of 28 February 1997," *Nature*, vol. 386, pp. 686–689, 1997.
- [7] S. D. Barthelmy, T. L. Cline, P. Butterworth, et al., "GRB Coordinates Network (GCN): A status report," in *Gamma-Ray Bursts*, C. Meegan and R. Preece, Eds., vol. 526 of *AIP Conference Proceedings*, pp. 731–735, Springer, Berlin, Germany, 2000.
- [8] C. Pennypacker, M. Boer, R. Denny, et al., "RTML—a standard for use of remote telescope enabling ubiquitous use of remote telescopes," *Astronomy and Astrophysics*, vol. 395, pp. 727–731, 2002.

- [9] F. V. Hessman, “Remote telescope markup language (RTML),” *Astronomische Nachrichten*, vol. 327, no. 8, pp. 751–757, 2006.
- [10] A. Allan, T. Naylor, and E. S. Saunders, “Autonomous software: myth or magic?” *Astronomische Nachrichten*, vol. 329, pp. 266–268, 2008.

Research Article

Making Preliminary GRBs Real-Time Astronomical Reports

Sebastián Castillo-Carrión¹ and Alberto Javier Castro-Tirado²

¹ Department of EVLT, University of Malaga, Campus de Teatinos, 29071 Malaga, Spain

² Department of Stellar Physics, Institute of Astrophysics of Andalusia, Camino bajo de Huetor 50, 18008 Granada, Spain

Correspondence should be addressed to Sebastián Castillo-Carrión, scastillop@uma.es

Received 9 June 2009; Accepted 15 September 2009

Academic Editor: Lorraine Hanlon

Copyright © 2010 S. Castillo-Carrión and A. J. Castro-Tirado. This is an open access article distributed under the Creative Commons Attribution License, which permits unrestricted use, distribution, and reproduction in any medium, provided the original work is properly cited.

We present a standalone software tool which makes reports for analysis and evaluation of GRBs. Recently, analysis and evaluation of GRBs were done without help of semiautomated tools or routines; so the time elapsed from the detection until getting all the information produced (DSS-2 data: Digitized Sky Surveys, elevation diagrams in each observatory, etc.) could be 30 minutes. The software presented allows to reduce the time elapsed to 30 seconds, getting an email, web, and sms reports.

1. Introduction

Gamma ray bursts (GRBs) were first reported by Klebesadel et al. [1] as they studied data acquired by the VELA spacecraft [2]. GRBs are the most luminous events known in the Universe. They are flashes of gamma rays, coming from seemingly random places on the sky and at random times, that last from milliseconds to many minutes. They are often followed by afterglow emission at longer wavelengths (X-ray, UV, optical, IR, and radio).

The longest GRBs are followed by an X-ray afterglow emission. GRB events take place in random sky coordinates, and their prediction are not possible. The majority of observed GRBs appear to be due to supernova explosion (longer GRBs) and binary systems collapse (shorter GRBs). GRBs can only be detected from space because the Earth's atmosphere absorbs gamma rays and therefore we cannot observe them from the ground, although afterglow emission is possible to be observed.

2. Recent GRB Follow-up Systems

Following the *BeppoSAX* [3] and the *High-Energy Transient Explorer 2 (HETE-2)* [4] results in the field, other space observatories like *Chandra* [5] and *XMM-Newton* [6] are pinpointing the X-ray afterglow emission that follow the gamma-ray events. Recently, the *International Gamma Ray Astrophysics Laboratory (INTEGRAL)*, from ESA [7],

The Fermi Gamma-ray Space Telescope (FERMI) [8], and *Swift*, (a NASA Midex Mission) [9] are increasing the number of GRB detections to about 100/yr.

The GRB afterglow emission can only be observed for few days; so, the time elapsed from GRB detection until its observation must be minimized. Once a GRB has been detected by one of the satellites mentioned above, rapidly analysis and evaluation of the alert info and external conditions need to be done. This helps to determine whether any reasonable followup effort is feasible, which helps making “Target of Opportunity” (ToO) proposals. Observations are scheduled if a transient event covered by the proposal occurs during the scheduling cycle. Analysis and evaluation of GRB were initially made by hand (observatories, instrumentation, elevation diagrams, Sun and Moon position in each observatory, etc.). This makes the time elapsed between the reception of the GRB alert and the production of this “followup” output as large as 30 minutes. However, it is possible to make them semiautomated with new technologies, taking not more than 30 seconds, which helps starting to obtain images, in several occasions, 3 minutes after the burst commenced [10].

Similar to *Rapid Response Analysis of GRB Optical Afterglows* [11], this work has been directed towards optimizing ToO techniques. Semi-automated programs and routines have been developed to facilitate faster and more efficient GRB follow-up. They are used in conjunction with other real time, online, automatic data analysis system: BOOTES [12].

3. Realtime Astronomical Report Software

One of the key issues in GRB followup observations is response time. The rapid fading of the GRB optical afterglow can make it fade below visibility within hours, which sets heavy demands on quick response times of any followup observations.

In order for the GRB ToO run to be successful, a number of conditions must be met. Here are listed some of the common problems that must be considered or solved during a run:

- (i) visibility: whether the GRB field is observable at the telescopes, distance to Sun/Moon, and so forth;
- (ii) telescope availability: it must be determined which telescopes are actually available for ToO activation: night reserved for technical time, outside the time of the approved ToO programme, and so forth;
- (iii) size of error-field: the size of error-field can be dramatically different from one burst localization to the next, making it necessary to consider carefully;
- (iv) extinction: the position on the sky of the GRB-field with respect to the plane of the Milky Way is very important for evaluating the chances of a successful follow-up;
- (v) to provide the observer with charts of the GRB-field, to ensure that the position observed is the correct one.

An application which makes GRBs reports has been developed at the Instituto de Astrofísica de Andalucía [13]. It streamlines and automates some of the previous procedures involved in GRB ToO operations. This application provides fast and detailed information on a given GRB on basis of a satellite localization alert. It helps to form a reliable basis for quick decision making regarding whether a ToO activation should be performed.

This application supports the ToO research projects BOOTES-1 [14], BOOTES-2 [15], and BOOTES-IR [16].

It is a public domain software, although there is currently no web-site to download the software, but an email can be sent to scastillop@gmail.com to get the source/application, detailed instruction for installing, deploying and running, and any kind of support.

The details of software specification, design, and implementation are given next.

3.1. Specification. Functionality and requirements of software are listed.

(1) Input Data

- (i) Type of alert: identified by a number
- (ii) Right ascension and declination of GRB
- (iii) GRB alert start time
- (iv) Error Box
- (v) GRB Id (grb trigger).

Input data are provided by another software: *rts2* [17], which receives alerts from satellites through sockets [18] and makes the input data which are stored into a relational database.

(2) Output Data

- (i) Report title according to alert type:

INTEGRAL_WAKEUP, SWIFT_XRT_POSITION,
INTEGRAL_OFFLINE, FERMI_GMB_GND_POS,
SWIFT_BAT_GRB_POSITION, FERMI_LAT_GRB_POS_UPD.
SWIFT_FOM_OBSERVE,

- (ii) Report time
- (iii) Time elapsed from GRB detection to report generation
- (iv) GRB galactic coordinates
- (v) Value from Lambert-projection maps: E(B-V), Au, Ab, Av, Ar, Ai, Aj, Ah, Ak
- (vi) Moon and Sun right ascension and declination; Sun-GRB and Moon-GRB distance, Moon phase
- (vii) Observatories with approved Spanish ToO programme, telescopes, instrumentation, and so forth
- (viii) GRB altitude-azimuth diagrams in each observatory
- (ix) FITS and JPEG images of ESO Online Digitized Sky Survey using the Digitized Sky Survey (2n version, dss-2 [19]) (red, ir, blue) tool.

All report information will be available through web page, email, and sms (not so detailed).

3.2. Design and Implementation. This application is running in GNU/Linux 2.6.16.9 i686. In a basic diagram, general working of software is shown (Figure 1): when a grb is detected, this application is executed by *rts2* (which provides the input data) and outputs three types of reports.

The system is composed of several modules. Some of them can run simultaneously; others need data to be received from other modules.

The most relevant modules of the system are the following:

- (i) Make Title Report: Given type of GRB, it reports title of grb;
- (ii) Galactic Coordinates: it reports galactic coordinates from grb equatorial coordinates;
- (iii) Distance Sun-Moon to GRB: given equatorial coordinates of Sun and Moon, computes distance from GRB to Sun and Moon;
- (iv) Moon, Sun RA, and DEC: Computes equatorial coordinates of Sun and Moon;
- (v) elevation graph in observatories: computes, for each observatory of the database (with known latitude and longitude), grb elevation graphs;

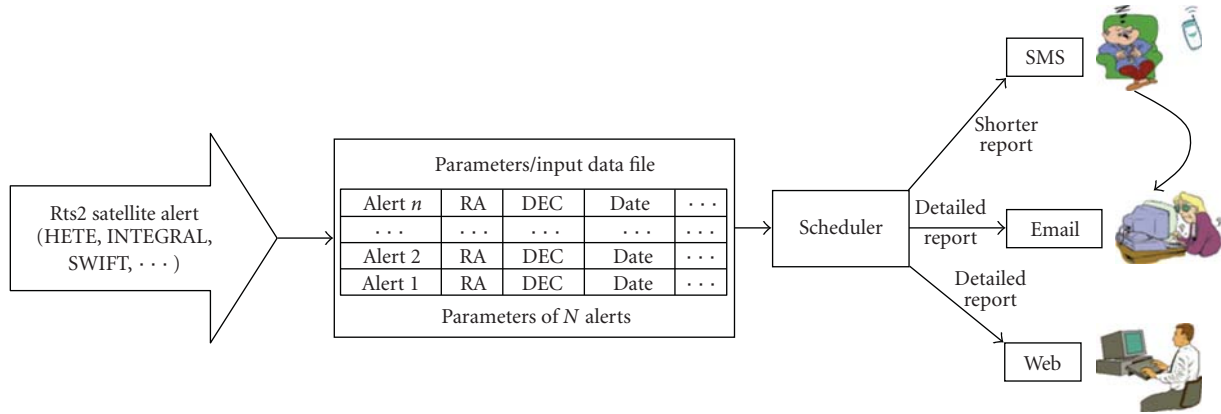


FIGURE 1: Basic working.

- (vi) moon phase: given date and time, it reports Moon phase;
- (vii) list observatories, instrumentation, and so forth: Given a date and time, it reports, for every telescope of each observatory, who is the observer, instrument mounted, approved ToO programme, and so forth;
- (viii) dss-2: given equatorial coordinates and field of view, it returns digital sky image of that area;
- (ix) report time: it returns date and time when report has just been created;
- (x) dust_getval: it computes $E(B-V)$ extinction value;
- (xi) database observatories, instrumentation, and so forth: it is not a module, just a database which provides data to other modules;
- (xii) time elapsed GRB detection-report generation: time elapsed from detection of grb to creation of this report.

Execution order of modules is shown in Figure 2. An arrow indicates dependency between two modules: it leaves the module that provides the data and ends in the module which uses them. A module with no arrows mean that it does not need data and neither provides them to others.

Next, a more detailed working of above diagram is shown in Figure 3. It gives additional information of each module: technology used is reported within brackets, graphs paths of inputs and outputs, and so forth. Each *module* takes input data from left and generates output data to right. Input data of the application are on the left side of the diagram, and reports produced are on the right one.

Database stores all observers/researchers, instrumentation, telescopes, observatories, and country time observation in different tables and interrelationships between them in “Schedule timetable.” These data determine which telescopes are actually available for ToO activation for the coming night.

The most important entity is “Schedule timetable,” which establishes spatial and time entity relations between data stored in the other tables. So, when a GRB is detected, the application will query the database and make a detailed

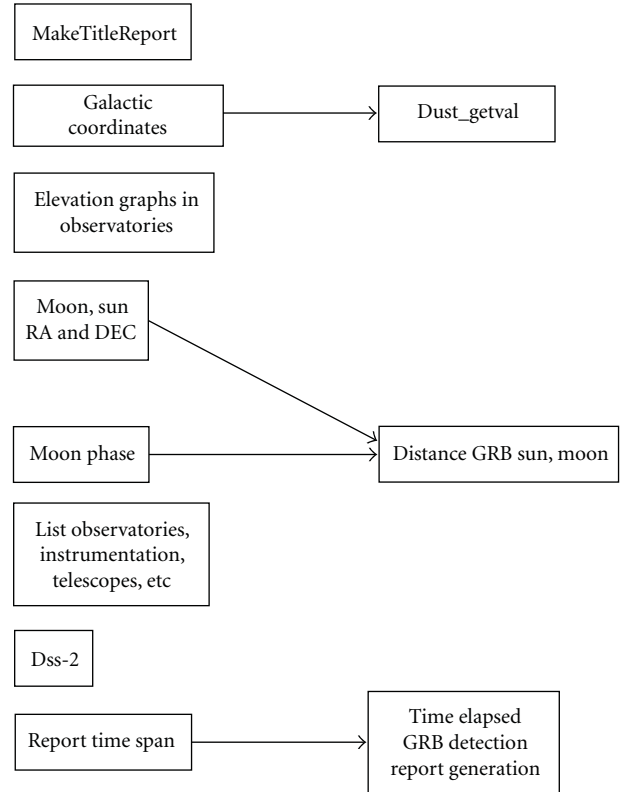


FIGURE 2: Execution order of modules.

report for all telescopes of each observatory: observer, instrument mounted, ToO programme, and so forth. Figure 4 shows simplified entity relationship model:

Below, there is a list of *libraries* and software required by this tool, with brief description of the actions performed by each one of them.

- (i) rts2, Remote Telescope System, is an integrated open source package for remote observatory control under the Linux operating system. It runs the software presented in this work and provides input data (see Section 3.1). The software presented is not provided with rts2.

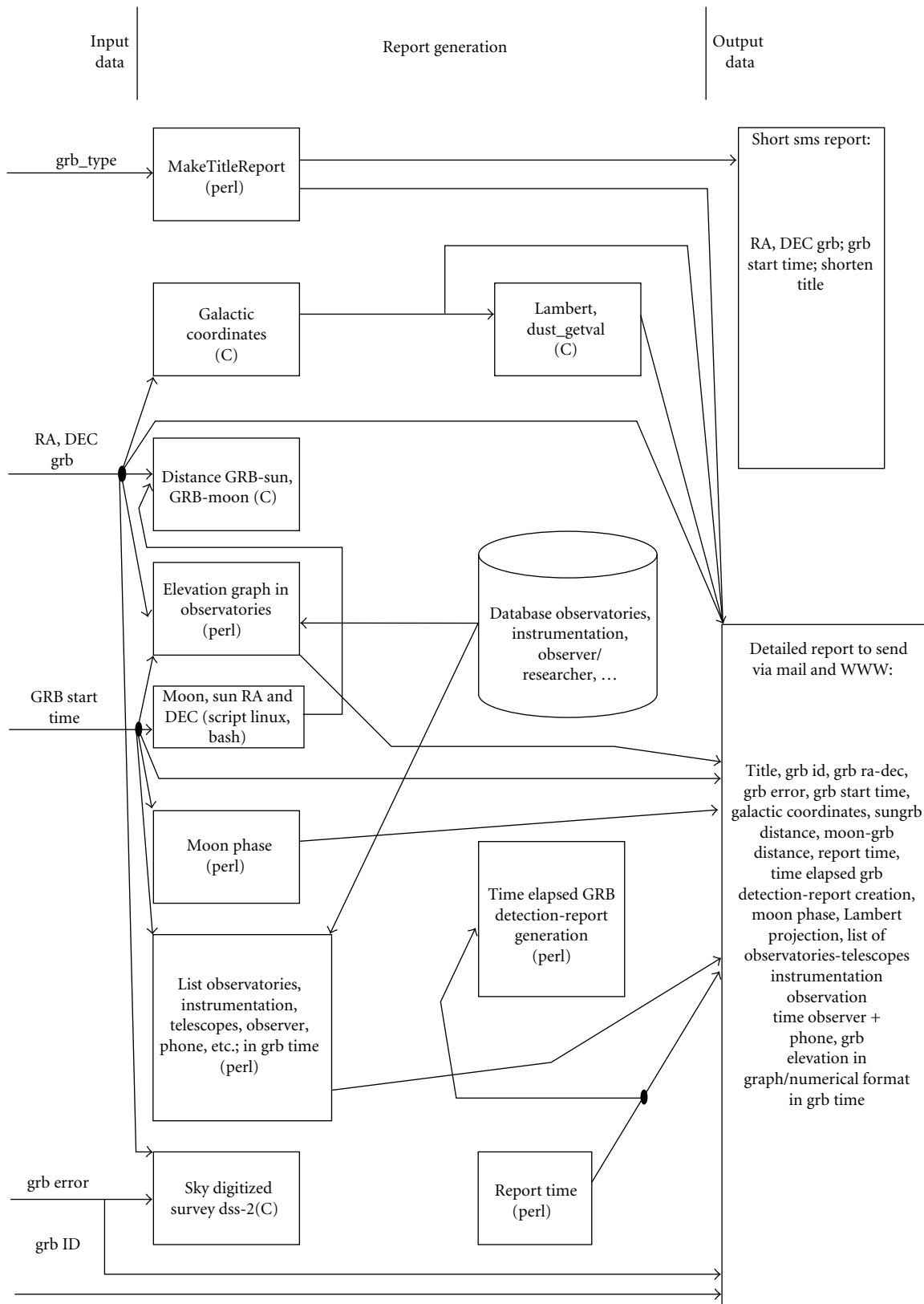


FIGURE 3: Detailed operation of the software.

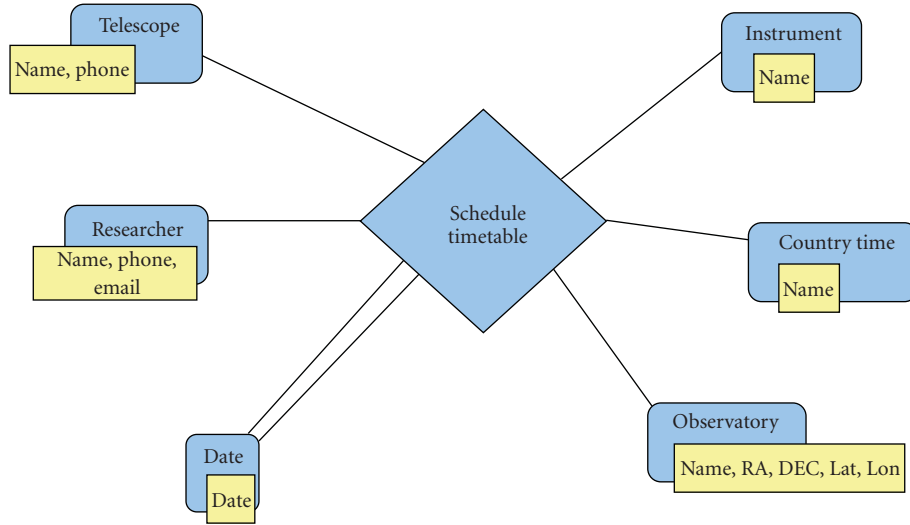


FIGURE 4: Entity relationship model.

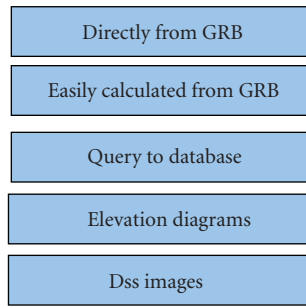


FIGURE 5: Output report format.

- (ii) Perl [20]: it is a high-level, general-purpose, interpreted, dynamic programming language. Perl borrows features from other programming languages including C, sh, awk, and sed. It is intended to be practical and support programming paradigms. Quick startup, powerful features, and true flexibility are some reasons for choosing this programming language to implement the system. The main module (and almost all the system, ~80%) is written in perl, and also secondary or auxiliary functions (extract arguments from shell outputs, make base or main report, elevation diagrams, etc.).
- (iii) Astro: MoonPhase [21]: returns information about the phase of the Moon at a given time.
- (iv) Libnova for C,C++ [22]: general purpose, double precision, celestial mechanics, astrometry, and astrodynamics library. In this work it is used to calculate distance from grb to Sun and Moon, Sun position, Moon position, Moon phase, Horizontal and Equatorial Coordinates of objects (grb, Sun, Moon), and so forth.

(v) dss-2 (sky digitized survey): the ESO/ST-ECF digitized sky survey (dss) application is a remote client program that extracts random sky section from the DSS image server installed at ESO, which covers the entire sky. The extracted images are delivered in standard FITS format and contain all header keywords needed to visualize proper celestial coordinates for any pixel position. This remote client application enables the creation of batch jobs to be integrated into other application software. So, once rts2 provides equatorial coordinates and size of error of the grb, the software presented executes this remote client to get images from dss which help to identify the grb in the sky.

(vi) dust_getval [23]: given galactic longitude and latitude, it returns the reddening value $E(B-V)$.

3.3. Output Report Format. Output report is divided into five sections (see Figure 5):

- (i) *Directly from GRB.* In this section the data are extracted directly from input provided from rts2; so basically the software only produces well-formatted text: equatorial coordinates of grb, type, trigger num, error, date, and time.
- (ii) *Easily calculated from GRB.* Data received from rts2 are used to calculate other parameters without undue complexity.
- (iii) *Query to database.* Database returns, for each telescope of each observatory, observer/staff member responsible for the telescope, instrument mounted on, approved ToO programme, phone and contact information.
- (iv) *Elevation Diagrams.* Knowledge on the pointing restrictions of the individual telescopes is quite vital, especially when planning longer duration ToO observations.

GRB20070704 200831

070704 220908

TITLE:
TRIGGER NUM:
GRB_RA:
GRB_DEC:
GRB_ERROR:
GRB_TIME:
GRB_DATE:
GAL_COORDS:
SUN_DIST:
MOON_DIST:
T_INF:
GRB_TIME-T_INF:
MOON_PHASE:
DUST MAP:

SWIFT_XRT_POSITION
283791
23h 37m 55.0799997600s
+66d 17` 3.1200000000 ``
0.001900 [arcmin radius, statistival only]
20:08:31 UT
2007/07/04
115.62374, 4.46119 [deg] lat, lon of the burst
76.405660
77.235307
2007/7/4 20:9:8 (UT)
0/0/0 0:0:37
0.80
E(B-V) = 1.80438
Au = 8.99
Ab = 7.43
Av = 5.77
Ar = 4.31
Ai = 2.8
Aj = 1.62
Ah = 1.01
Ak = 0.65

OBSERVATORIO	TELESCOPIO	INSTRUMENTO	T_OBSERV	INVESTIGADOR	TLF
LA_PALMA	TNG	—	—	—	922-40_55_35

CURVAS DE ELEVACION

OBSERVATORIO	UT (LA FECHA ES EN LA	AZIMUTH QUE SE PRODUJO EL	ALTURA(grb) GRB)	AZIMUTH	ALTURA (sol)
LA_PALMA	18 : 00 : 00	180.01	5.04	102.77	26.61
LA_PALMA	19 : 00 : 00	186.03	5.73	108.71	13.92
LA_PALMA	20 : 00 : 00	191.75	7.78	115.22	1.82
LA_PALMA	21 : 00 : 00	196.89	11.05	122.93	-9.71
CALAR_ALTO	17 : 00 : 00	180.12	13.51	98.60	27.96
CALAR_ALTO	18 : 00 : 00	186.3	14.18	106.67	16.28
CALAR_ALTO	19 : 00 : 00	192.22	16.11	114.99	5.08
CALAR_ALTO	20 : 00 : 00	197.66	19.21	124.03	-5.23

FIGURE 6

(v) *DSS images*. They help the observer to identify grb or new objects on the sky.

3.4. Example of Output Data. Some examples of report generated email and sms alerts are presented for GRB 070704 (see Figures 6 and 7). Report generated web page is close similar to email with different paragraph formats, and so web example is not included in this section.

An sms message issued for GRB 070704 will be received from phone number “SX233755s+661703_20:08, 04/07”, with the following encoding:

SX : simplified GRB title. The simplified GRB titles are

INTEGRAL_WAKEUP → IO;

INTEGRAL_OFFLINE → IF;

SWIFT_BAT_GRB_POSITION → SB;

SWIFT_XRT_POSITION → SX;

SWIFT_FOM_OBSERVE → SF;

FERMI_GBM_GND_POS → FG;

FERMI_LAT_GRB_POS_UPD → FL.

233755: right ascension in hours, minutes, and seconds.

+661703: declination in degrees, minutes, and seconds.

20:08: UT GRB time.

04/07: GRB Date (it is supposed to be the present year).

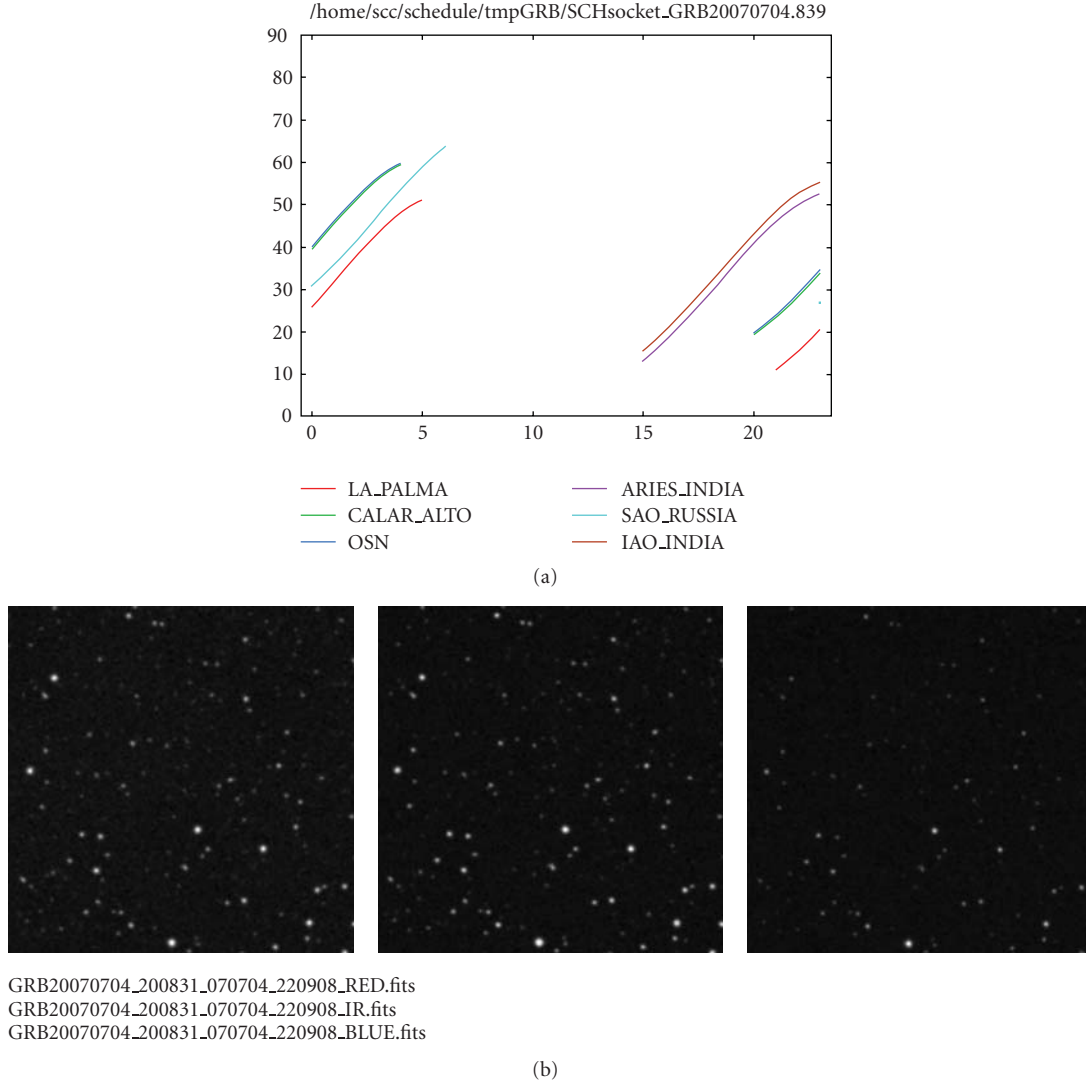


FIGURE 7: Example of report received for GRB 070704.

4. Conclusions

Due to the transient and inherent unpredictable nature of gamma-ray bursts, it is of singular importance to minimize ToO response and ToO preparation times in advance of an alert. At the same time it is necessary to have easy access to all relevant information in order to rapidly devise the most efficient observation strategy in the limited time available.

A successful ToO system has been developed, which allows to achieve this through automation of the time-critical processes: Alert, Information retrieval, and ToO preparation and activation.

The automated system has effected in a much improved response time. It decreases the minimum delay from alert to ToO-activation. This system also reduces the significant overhead time required for evaluating the ToO-feasibility for each alert, frees up a lot of resources formerly used to consider, and rejects unsuitable alerts for follow-up.

It allows rapid GRB alert response and follow-up, with minimum delay from alert to ToO-activation, accessing to all relevant information and rejecting unsuitable alerts.

Acknowledgments

The authors thank J. Gorosabel, Jelínek, P. Kubánek, and A. de Ugarte Postigo for fruitful discussions. This work was supported by the Spanish Ministry of Science and Technology's projects AYA 2004-01515 and AYA 2007-63677.

References

- [1] R. W. Klebesadel, I. B. Strong, and R. A. Olson, "Observations of gamma-ray bursts of cosmic origin," *Astrophysical Journal Letters*, vol. 182, pp. L85–L88, 1973.
- [2] R. W. Klebesadel and J. T. Bonnell, "A brief history of the discovery of cosmic gamma-ray bursts," in *Proceedings of the 3rd Huntsville Symposium on Gamma-Ray Bursts*, vol. 384, pp. 977–980, Los Alamos, NM, USA, August 1996.

- [3] <http://www.asdc.asi.it/bepposax/>.
- [4] <http://space.mit.edu/HETE/>.
- [5] <http://chandra.harvard.edu/>.
- [6] <http://xmm.esac.esa.int/>.
- [7] C. Winkler, T. J.-L. Courvoisier, G. Di Cocco, et al., "The INTEGRAL mission," *Astronomy & Astrophysics*, vol. 411, no. 1, pp. L1–L6, 2003.
- [8] <http://fermi.gsfc.nasa.gov/>.
- [9] <http://swift.gsfc.nasa.gov/docs/swift/swiftsc.html>.
- [10] J. M. Castro Cerón, A. Castro-Tirado, J. Soldán, et al., "Search for gamma ray burst quasi simultaneous optical emission with BOOTES-1," in *Proceedings of the 4th Reunión Científica de la Sociedad Española de Astronomía*, pp. 37–40, Santiago de Compostela, Spain, September 2001.
- [11] B. L. Jensen, *Rapid response analysis of GRB optical afterglows*, Ph.D. thesis, Astronomical Observatory, NBIfAFG, University of Copenhagen, Copenhagen, Denmark.
- [12] J. M. Castro-Cerón, A. J. Castro-Tirado, J. Soldán, et al., "The BOOTES experiment as support to the Gran Telescopio Canarias (GTC) in the study of the high energy Universe," in *Proceedings of the Conference of Science with the GTC*, Granada, Spain, February 2002.
- [13] <http://www.iaa.es>.
- [14] A. J. Castro-Tirado, J. Soldán, M. Bernas, et al., "The burst observer and optical transient exploring system (BOOTES)," *Astronomy and Astrophysics Supplement Series*, vol. 138, no. 3, pp. 583–585, 1999.
- [15] T. J. Mateo-Sanguino, A. J. Castro-Tirado, A. de Ugarte Postigo, et al., "Desarrollos técnicos en BOOTES-1 y BOOTES-2," in *Proceedings of the I Reunión Nacional de Astrofísica Robótica, Astrofísica Robótica en España*, A. J. Castro-Tirado, B. A. de la Morena-Carretero, and J. Torres Riera, Eds., pp. 189–200, Huelva, Spain, May 2004.
- [16] A. J. Castro-Tirado, R. Cuniffe, A. de Ugarte Postigo, et al., "BOOTES-IR: a robotic nIR astronomical observatory devoted to follow-up of transient phenomena," in *Ground-Based and Airborne Telescopes*, L. M. Stepp, Ed., vol. 6267 of *Proceedings of SPIE*, Orlando, Fla, USA, May 2006.
- [17] P. Kubanek, M. Jelinek, S. Vitek, A. de Ugarte Postigo, M. Nekola, and J. French, "RTS2: a powerful robotic observatory manager," in *Advanced Software and Control for Astronomy*, H. Lewis and A. Bridger, Eds., vol. 6274 of *Proceedings of SPIE*, Orlando, Fla, USA, May 2006.
- [18] http://gcn.gsfc.nasa.gov/gcn_describe.html.
- [19] <http://archive.eso.org/dss/eso-dss.html>.
- [20] <http://www.perl.org/>.
- [21] <http://search.cpan.org/~brett/Astro-MoonPhase/MoonPhase.pm>.
- [22] <http://libnova.sourceforge.net/>.
- [23] <http://www2.nbi.ku.dk/side33966.htm>.

Research Article

Double-Station Automatic Video Observation of the Meteors

Stanislav Vítek,¹ Pavel Koteň,² Petr Páta,¹ and Karel Fliegel¹

¹ Faculty of Electrical Engineering, Czech Technical University in Prague, Technická 2, 166 27 Prague, Czech Republic

² Interplanetary Matter Department, Astronomical Institute AV CR, Friova 298, 251 65 Ondřejov, Czech Republic

Correspondence should be addressed to Stanislav Vítek, viteks@fel.cvut.cz

Received 30 June 2009; Accepted 26 October 2009

Academic Editor: Alberto J. Castro-Tirado

Copyright © 2010 Stanislav Vítek et al. This is an open access article distributed under the Creative Commons Attribution License, which permits unrestricted use, distribution, and reproduction in any medium, provided the original work is properly cited.

The double station observation of the meteors by means of sensitive image intensifier technique started at the Ondřejov Observatory 10 years ago. The sensitivity of such instrumentation allows detection of the meteors down to masses of fractions of gram. Moreover, video technique provides us with a time resolution of the meteor events. On the other side, the precision of the video data is lower in comparison with the photographic data. We are introducing technological progress on the project—replacing of the S-VHS camcorders with gigabyte, ethernet cameras and making the whole process of video observation automatic.

1. Introduction

Using the double station data of the meteor we can calculate its atmospheric trajectory and the heliocentric orbit. The meteor light curve provides us with information about the mass of the original particle. Both the shape of this curves as well as the height interval where the meteor radiates correspond to the structure of the parent meteoroid.

Observations are usually made on the following bases:

- (i) Ondřejov ($14^{\circ}46'48.8''$ E, $49^{\circ}54'36.8''$ N, 524 m)
- (ii) Kunžak ($15^{\circ}12'2.8''$ E, $49^{\circ}6'27.2''$ N, 652 m)

Separation of the stations is 92.5 km, and the azimuth of the second station is 340° (south = 0°); see Figure 1.

2. Current System

Both stations are currently equipped with S-VHS commercial Panasonic camcorders connected to second generation of Mullard XX1332 image intensifiers and Arsat 1.4/50 mm or Jupiter 2/85 mm lenses (see Figure 2). The diameter of the field of view is about 25 and 32 for Arsat and Jupiter lenses respectively. The limiting magnitude of the system is about +5.5.

Limits of S-VHS recording system are known, introduced in June 1987, using analog recording to tapes with horizontal

resolution of 420 lines per picture. Video recordings are not suitable for scientific purposes due to mechanical movement of tape (jitter).

2.1. Image Processing. The records are currently stored on S-VHS tapes. The meteors are detected using the recognition software MetRec [1]. Then the interesting events are transformed using PC frame-grabber into 8-bit monochrome images with time resolution of 0.04 second and spatial resolution of 768×576 pixels. Measurement is done using original software MetPho [2]; see Figure 3.

Photometric procedure includes flat-fielding, dark image subtraction and noise reduction. Then the identification of the stars follows. The signal of the star is computed as the sum of pixel intensities in the area of interest. The calibration curve is computed as a plot of the stars catalogue brightness against their signal intensities logarithm.

Similarly, the signal of the meteor is measured as the sum of pixel intensities in the area of interest on each frame of the record. The background value is subtracted and the apparent magnitude of the meteor is determined using the calibration curve. Position of the meteor on each frame is measured simultaneously.

The atmospheric trajectories and heliocentric orbits of the simultaneous meteors are computed from the measured data as well as the photometric mass of the meteor and these meteor properties are analysed consequently.

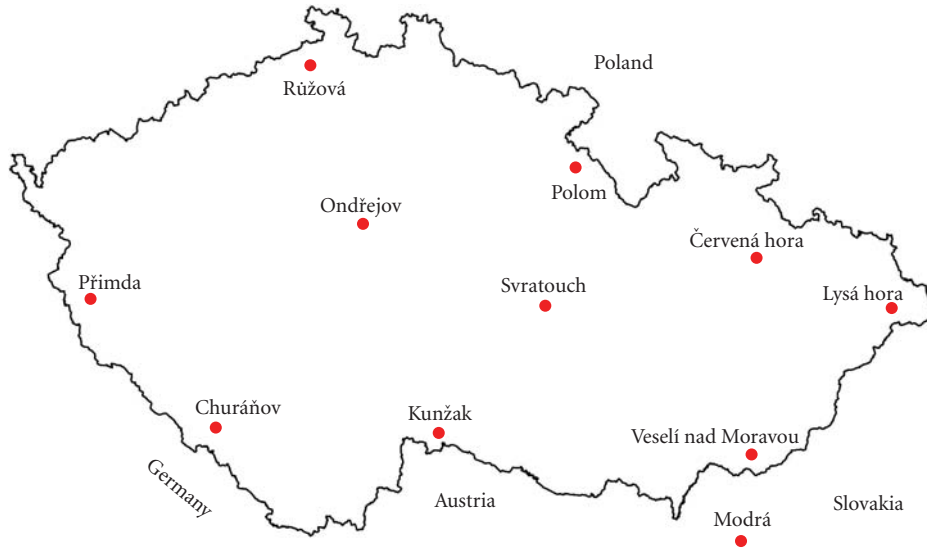


FIGURE 1: Location of the station within the Czech fireball network (Image courtesy of Pavel Spurný).



FIGURE 2: Current device used on both stations in Kunžak and Ondřejov S-VHS camcorder equipped with image intensifier and wide-field lens.

3. Proposed System

For the novel version of automatic system, we are proposing gigabit ethernet camera JAI CM-040 or similar with resolution of $767(h) \times 582(v)$ pixels ($1/2''$ progressive scan IT CCD) and maximum frame-rate of 60 fps.

With given resolution and frame-rate the proposed system has bit-rate, 400 Mbps (400 Mbps for 10 bit depth, 300 Mbps for 10 bit depth and “packed mode” and 200 Mbps for 8 bit depth); it means total amount of data of 2.06 TB per night. Due to this fact massive data reduction is extremely important. Data reduction has two phases: during first phase image data are basically calibrated, if any interesting objects are found on images, data from both stations are compared during second phase; see Figure 4.

3.1. Controlling Software. Because the system deals with simultaneous observations of the same optical events so it is not necessary to ensure synchronous work of the processes



FIGURE 3: Composite image of bright Leonid meteor recorded by the video camera on November 18th, 2001 during the Leonid meteor storm.

running on both stations. However, stations should work independently. Control is proceeding in four levels:

Camera Driver. Camera driver is dedicated to take care of readout of camera and set of parameters of observation (time and length of exposition). The camera has two modes of work: one image per request or continuous stream of image data (TV mode).

Main Control Program. Start and end of observation and getting and storing of the data are key objectives of the main control program. As an additional function, this part of software is taking care of getting of the dark frames and the flat fields, asking for the criteria of select and making log of operations. As is written above, the system is designed

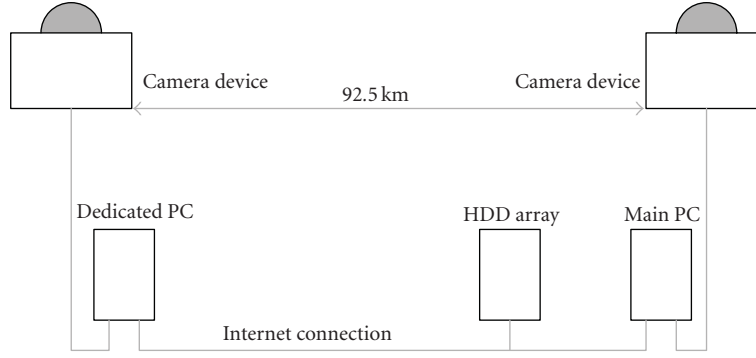


FIGURE 4: Configuration of the proposed system.

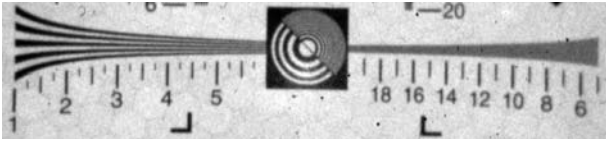


FIGURE 5: Fragment of the MTF test captured with image intensifier.

to work simultaneously, but particular devices should work independently.

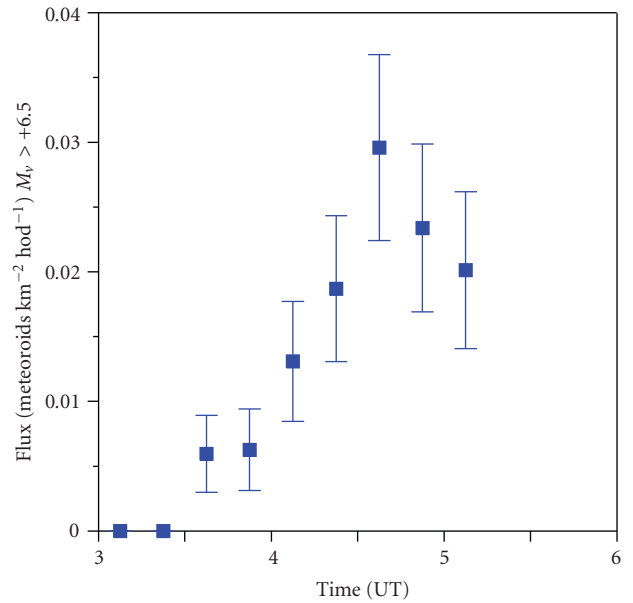
Basic Image Processing. This part of software is dedicated to evaluation of actual weather conditions, detection and classification of interesting objects and phenomena, calibrations (flat-fielding and dark frames subtraction).

Advanced Image Processing. This is a pipeline doing photometric and astrometrical calibration, advanced image processing like noise suppression, and interpretation of data.

3.2. Device Housing. For the first version of the automatic video-system, we expect to use transparent acrylic hemisphere-shaped dome, allowing us at first to observe any weather conditions, decreasing hazards of the weather controlling subsystem at second, and allowing us have housing without any moving parts, which are typical source of the problems (moreover with moving parts we have to provide emergency power supply). The solution has a disadvantage in potential decrease of total sensitivity limit of device.

3.3. Image Quality. Image processing algorithms will be very difficult. Not only because of high bitrate, but because of image quality also. We believe that the most limiting device of system is image intensifier. Figure 5 provides example of image acquired on the output of image intensifier.

We can see high level of noise, optical aberrations and resolution limit for about 6 lines/mm relative to height of image. With expected size of object around 10 pixels, right design of algorithms will be very important.

FIGURE 6: Flux of the meteoroids per km² per hour as detected at the Kunžak station during the 2006 Leonid outburst.

4. Results

The most important papers based on the video observations:

- (i) properties of the Perseid, Orionid, Leonid, Geminid and Taurid meteor showers [3],
- (ii) survey of meteor spectra and orbits [4],
- (iii) quadrantid meteor shower and implications for its parent body [5],
- (iv) radiation of the meteors above 130 km [6],
- (v) draconid meteor shower [7, 8].

As an example of results of old analogue system we present graph of flux of the meteoroids during Leonid outburst (see Figure 6) and beginning heights as function of the photometric mass of the meteoroids compared with the sporadic meteor of similar velocity (see Figure 7).

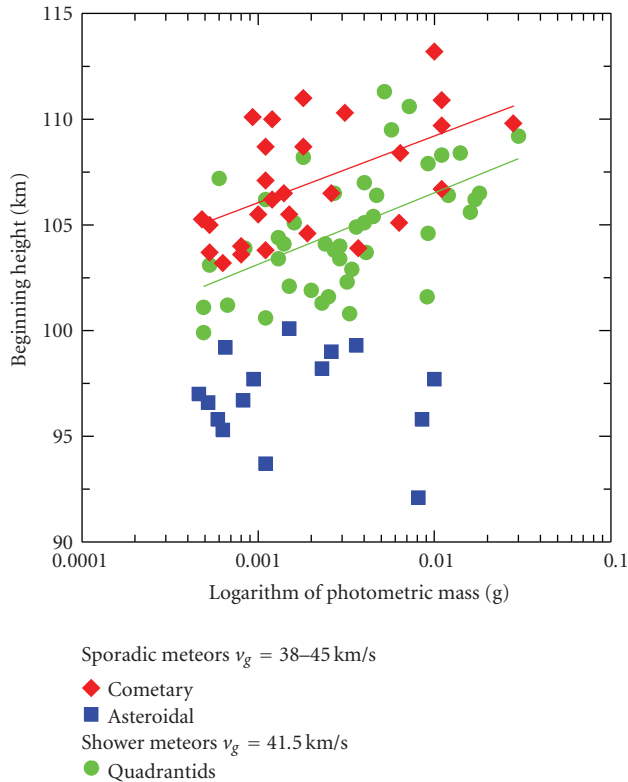


FIGURE 7: Beginning heights as function of the photometric mass of the meteoroids compared with the sporadic meteor of similar velocity.

5. Conclusions

Simultaneous long-term video observations of the night sky are a very efficient way of getting important data for study of the meteors properties. The main goal of our project is to have high-time resolution allowing us to calculate three-dimensional trajectories when the meteors with very high precision. During past decade of the system worked with technically limited device, we got couple of interesting results and they are promising for the proposed instrumentation. With automatic double-station video observations we expect to observe sporadic meteors and new meteoric outbursts.

Acknowledgments

This work is supported by Grant no. 205/09/1302 of the Grant Agency of the Czech Republic. The authors also acknowledge grant no. 102/09/0997 by the Grant Agency of the Czech Republic.

References

- [1] S. Molau, "The meteor detection software MetRec," in *Proceedings of the Meteoroids Conference*, W. J. Baggaley and V. Poruban, Eds., p. 131, 1999.
- [2] P. Koteň, "Software for processing of meteor video records," in *Proceedings of the ACM Conference on Asteroids, Comets and*

Meteors, pp. 197–200, Technical University, Berlin, Germany, 2003, ESA SP-500.

- [3] P. Koteň, J. Borovička, P. Spurný, H. Betlem, and S. Evans, "Atmospheric trajectories and light curves of shower meteors," *Astronomy and Astrophysics*, vol. 428, no. 2, pp. 683–690, 2004.
- [4] J. Borovička, P. Koteň, P. Spurný, J. Boček, and R. Štork, "A survey of meteor spectra and orbits: evidence for three populations of Na-free meteoroids," *Icarus*, vol. 174, no. 1, pp. 15–30, 2005.
- [5] P. Koteň, J. Borovička, P. Spurný, S. Evans, R. Štork, and A. Elliott, "Double station and spectroscopic observations of the Quadrantid meteor shower and the implications for its parent body," *Monthly Notices of the Royal Astronomical Society*, vol. 366, no. 4, pp. 1367–1372, 2006.
- [6] P. Koteň, P. Spurný, J. Borovička, et al., "The beginning heights and light curves of high-altitude meteors," *Meteoritics and Planetary Science*, vol. 41, no. 9, pp. 1305–1320, 2006.
- [7] J. Borovička, P. Spurný, and P. Koteň, "Atmospheric deceleration and light curves of Draconid meteors and implications for the structure of cometary dust," *Astronomy and Astrophysics*, vol. 473, no. 2, pp. 661–672, 2007.
- [8] P. Koteň, J. Borovička, P. Spurný, and R. Štork, "Optical observations of enhanced activity of the 2005 Draconid meteor shower," *Astronomy and Astrophysics*, vol. 466, no. 2, pp. 729–735, 2007.

Research Article

Automated Observations of the Earthshine

P. R. Goode,¹ S. Shoumko,¹ E. Pallé,² and P. Montañés-Rodríguez²

¹ Big Bear Solar Observatory, New Jersey Institute of Technology, Newark, NJ 07102, USA

² Instituto de Astrofísica de Canarias, Vía Lactea s/n, La Laguna, E38200 Tenerife, Spain

Correspondence should be addressed to E. Pallé, epalle@iac.es

Received 16 June 2009; Accepted 9 November 2009

Academic Editor: Taro Kotani

Copyright © 2010 P. R. Goode et al. This is an open access article distributed under the Creative Commons Attribution License, which permits unrestricted use, distribution, and reproduction in any medium, provided the original work is properly cited.

The overall reflectance of sunlight from Earth is a fundamental parameter for climate studies. We have designed and implemented small aperture, remote control telescopes in Big Bear Solar Observatory in California and in Tenerife in the Canary Islands. These telescopes observe the earthshine to obtain a global mean terrestrial reflectance utilizing a coronagraph-like design for long exposures of the dark of the Moon and have internal moving parts in the optical train, which presented some design and control problems.

1. Introduction

For a decade, we have been measuring the Earth's reflectance by observing the earthshine, which is sunlight reflected from the Earth to the Moon and retroflected to the nighttime Earth. These observations provide an absolutely calibrated measure of the terrestrial albedo—a fundamental climate parameter.

For our observations, we have utilized a terrestrial determination of the Earth's global albedo from an old, and largely forgotten method. That is, an absolutely calibrated, large-scale albedo can be determined by measuring the amount of sunlight reflected from the Earth and in turn, back to the Earth from the dark portion of the face of the Moon (earthshine) and taking the ratio of that to the brightside (moonshine) signal; see Figure 1 [1, 2]. In Figure 1, the fiducial points used in the measurements are shown in a single image in which the brightside is heavily filtered. The most important historical program of earthshine measurements was carried out by Danjon [3, 4] from a number of sites in France. Danjon estimated his uncertainty at roughly 5% (ignoring his appreciable systematic error from an incorrect determination of the Moon's reflectivity). Our measurements are about an order of magnitude more precise than his estimates, in large part because we have better measurement technologies. We have also eliminated his systematic error by correctly measuring

the scattering from the Moon as a function of the phase of the Moon [1]. At about 1% precision on individual nights, our terrestrial estimates of the Earth's albedo have a precision comparable to that from satellites like ERBE with around the same value [5], and to those of the CERES instrumentation, of around 1% [6] making our method sufficiently precise to usefully complement satellite measurements.

The earthshine observations reveal a large decadal variability in the Earth's reflectance [7], which is yet not fully understood, but which is in line with other satellite and ground-based global radiation data (see [8, 9] and references therein). In order to continue to contribute to a better understanding of the Earth's radiation budget continuous observations from a global network of robotic telescopes are necessary.

The modern earthshine observations began in Big Bear Solar Observatory (BBSO) using a small-aperture telescope requiring an operator who controlled the swapping between observations of the brightside of the Moon (moonshine) with very short exposures, and the dark side (earthshine) with very long exposures. Changing to a highly automated, remotely operated telescope was more difficult than one might imagine because of the internal moving parts in the optical train operating during the near continuous switching between moonshine and earthshine observations, and the continuous variation of the lunar phase.

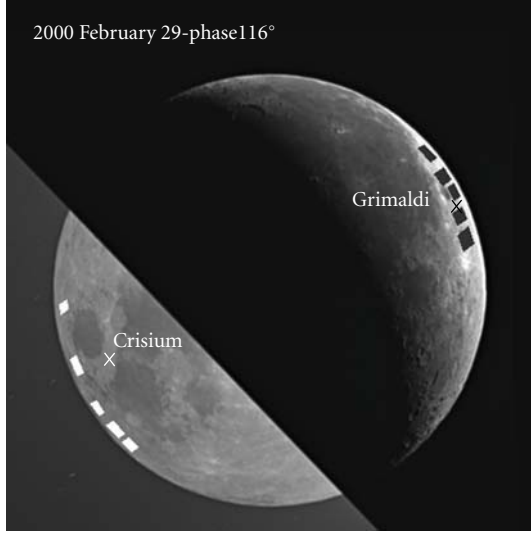


FIGURE 1: The moon showing the brightside and the earthshine. The Grimaldi side is in the moonshine (brightside) and the Crisium side is in the earthshine. Our ten highlands fiducial patches used in the observations made from BBSO are indicated. The crosses give the approximate positions of Danjon's [3, 4] fiducial patches. Goode et al. [11] used one fiducial patch on each side, and on the Crisium side it is the one closest to the white cross, while on the Grimaldi side, it is the one immediately above the black cross. In the image, the lunar phase is $115^\circ.9$, near a declining quarter moon. Unlike the moonshine, the earthshine is flat across the disk. The flatness is due to the uniform, incoherent back-scattering (non-Lambertian), in contrast to the forward scattering of sunlight occurring in the sunlit lunar crescent surface.

The telescope needs to function like a coronagraph because of stray light problems associated with long exposures to collect earthshine images. We now have built, tested, calibrated, and deployed two automatic telescopes for observing the earthshine. The first is in Big Bear Solar Observatory at 2 km above sea level in Southern California, while the second is in the Observatorio del Teide in the Canary Islands; see Figure 2. Two sites widely spaced in longitude are necessary to obtain global coverage. For instance, the BBSO telescope cannot see much of the North America or longitudes near the Europe-Asia boundary. A third site is working in Crimea Observatory, in Ukraine, but it is not a robotic, but a manually operated telescope. However that site has already allowed us a first comparison of data from two separate locations [10]. If funding is available we plan to increase our network to a maximum of 6–8 telescopes.

2. Why Earthshine Photometry Matters for Climate

The net power deposited in the terrestrial atmosphere and surface depends on the solar irradiance and the Earth's short-wavelength (0.15–4.9 microns) albedo

$$P_{\text{in}} = C\pi R_e^2(1 - A), \quad (1)$$



FIGURE 2: Earthshine dome in the Canaries. Part of the German Gregor dome may be seen in the background.

where C is the solar constant (adjusted for the Sun-Earth distance), R_e is the Earth's radius, and A is the short-wavelength Bond albedo (the amount of sunlight reflected back to space by the atmosphere and surface of the Earth). Subsequently, the short-wavelength, incoming power is reradiated back into space at thermal or long-wavelengths (peaks near ~ 10 – 15 microns), where

$$P_{\text{out}} = 4\pi R_e^2 \sigma T_{\text{toa}}^4, \quad (2)$$

and where σ is the Stefan-Boltzmann constant and T_{toa} (~ 255 K) is the effective temperature of the Earth (defined with unit emissivity). T_{toa} is a physically averaged long-wave emission temperature at about 5.5 km height in the atmosphere (this “top of the atmosphere” or “toa” temperature depends on wavelength and cloud cover; altitudes from 0 to 30 km contribute to this emission). One can relate that temperature to a more relevant global climate parameter like the globally averaged surface temperature T_{sur} by introducing a greenhouse forcing parameter G [W/m²], which is defined as the difference between the emission at the top of the atmosphere and the surface. The forcing G increases with an increasing concentration of greenhouse gasses. After Raval and Ramanathan [12], one can define the normalized greenhouse effect g as $g = G/\sigma T_{\text{sur}}^4$. Then the outgoing power can be written as

$$P_{\text{out}} = 4\pi R_e^2 \sigma (1 - g) T_{\text{sur}}^4. \quad (3)$$

If the planet is in radiative equilibrium, $P_{\text{in}} = P_{\text{out}}$, then we have

$$T_{\text{sur}}^4 = \frac{C}{4\sigma(1 - g)}(1 - A). \quad (4)$$

This means that the Bond albedo, together with solar irradiance and the greenhouse effect, directly controls the Earth's temperature. Global warming would result if either A decreased or g or C increased.

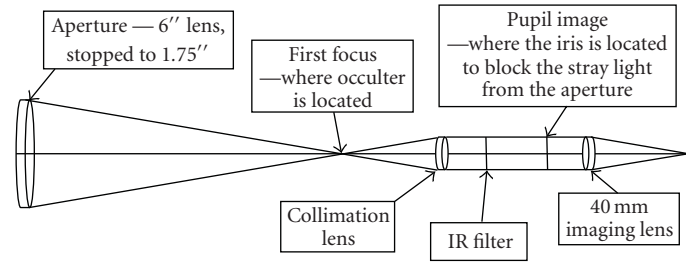


FIGURE 3: Schematic of the earthshine telescope optical train. At prime focus during the earthshine exposures, the moonshine blocker translates and rotates to its proper position to shield out the brightside. At the image of the pupil, the edges of the entrance aperture are blocked to reduce stray light. The earthshine camera chip is at the second focus.

3. Observational Challenges to Automate an Earthshine Telescope

A schematic of the the robotic telescopes is shown in Figure 3. Building the first robotic telescope required some care because it needs to translate/rotate in and out a blocking filter that blocks the scattered light from the sunlit moon during exposures on the earthshine side of the moon. The blocking filter is located at the first telescope focus. The second telescope focus is at the camera. In between, the telescope has a Lyot stop at the pupil image to block the stray light introduced by the edge of the entrance aperture. The telescope needs this “anticonoragraphic” structure to reduce stray light during very long exposures (~ 1 minute of the earthshine, as opposed to the ~ 10 ms exposures of the brightside). The source of the stray light in the dark side observations is light from the brightside of the Moon scattered by the atmosphere. The telescope was designed and built with stray light contamination in mind. In fact, we tested bright lights inside the dome and they only had a measurable effect if they were directed straight into the telescope along the path of the moonlight. A picture of the box housing the earthshine hardware in the Canaries is shown in Figure 4.

The dome, telescope, and coronagraph-like features are all under remote control. One can remotely open the dome, take flat fields, point the telescope, and then observations go on their own along the night, but can also be closed down from afar if conditions call for it.

4. The Earthshine Telescope

4.1. Controlling the Earthshine Telescope. The Earthshine robotic telescope and its dome have several hardware parts that are under software-control. These are the following.

(1) The camera: we use a Princeton Instruments Photon-Max 512 camera (512×512 pixels, 8.2×8.2 mm CCD size, 16 bit, high efficiency camera).

(2) The shutter: we use a 6 mm Vincent Associates UniBlitz LS6 shutter. This shutter can operate in the range from 2 ms up.

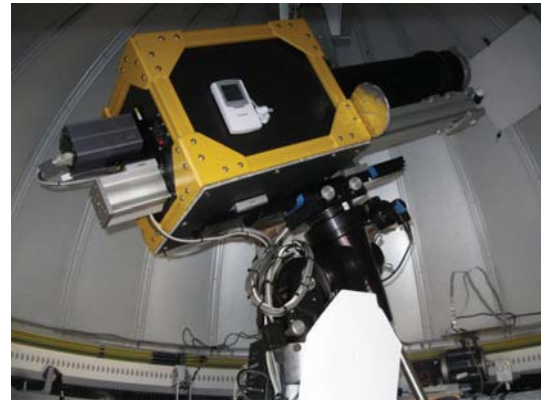


FIGURE 4: The earthshine telescope shown inside its dome. The light-shielding yellow box extends about one-half meter along the optical axis.

(3) The occulter stages: we installed two Standas motorized stages, one is rotational with 50 mm aperture and another is translation stage. The occulter is mounted on the rotation stage and the rotation stage is in turn mounted on the translation stage.

(4) The dust cap at the end of the telescopes tube.

(5) The dome: the dome consists of three controllable parts: azimuth motor (dome rotation), the lower shutter door, and the upper shutter. To read the position of the dome we use a barcode tape (with barcodes evenly spaced approximately every inch) mounted on moveable part of the dome and a barcode scanner.

(6) The telescope mount: the telescope is installed on a Losmandy Titan equatorial mount.

To control various hardware parts, we use three Galil Motion Control's controllers. Two of them are 4-axis DMC-2132 and one is an IO board IOC-7007. One of the DMC-2132's controls the occulter stages and another one controls the cap. The IOC-7007 is used to control the dome's shutter, both the door and the upper shutter. We also use a relay board installed inside of the earthshine computer. The relay board controls the dome's azimuth motor. The computer's serial ports are used to set and trigger exposure via a UniBlitz

shutter, to set various options on the camera and to control the mount. We also use two remotely controlled (via web interface) power switches to turn on/off power on various pieces of hardware, including the computer. If the main control computer hangs, we can reboot it remotely with the power switches. We installed several web cameras to watch and see that everything is working nominally.

The earthshine telescope software controls consist of two programs: ESCameraControl, which controls everything on the telescope with the exception of the dust cap and DomeControl, which controls the dome and the dust cap.

4.2. Remote Observing Sequence. The earthshine telescope is a remotely controlled telescope rather than a fully robotic telescope. This means that an observer (whose physical presence is not required) needs to send the commands to setup and start the observations. There are several steps in the remote observing sequence.

(1) Open the dome with the help of the DomeControl program, the remote “observer” initializes the azimuth control (read current position of the dome) and starts the dome’s automatic movement. The dome will position the shutter opening according to the positions of the Moon and the telescope thus the moonlight shines on the camera.

(2) Remotely start the ESCameraControl program and open the dust cap.

(3) Observer points the telescope at the Moon (the program calculates position of the Moon) and put camera in the “live image” mode making sure that the Moon is in the field of view.

(4) With the help of the occulter control window, using linear and rotational movements of the stages find two positions of the occulter, occulter “in” and occulter “out.” In the “out” position, the occulter is completely out of the field of view. Then set “in” position such that the occulter blocks illuminated side of the Moon (moonshine) and leaves earthshine side visible (like in Figure 1).

(5) After setting the “in” and “out” positions (which do not differ much from night to night) start-so-called “cycle”. During one cycle of observations, the software first moves the occulter “out” and takes 10 moonshine images, then moves the occulter “in” and takes 1, longer, earthshine image. The program repeats this cycle until stopped by the operator. The program automatically adjusts exposure time so the image counts stay in the same range. After 30 images the program also takes dark frames for both exposures (moonshine and earthshine).

(6) At the end of observations the operator stops the cycle, parks the mount, and rotates the dome to some predefined position so the telescope is pointed toward a white screen mounted on the surface of the dome. Then the operator turns on the flat field lights mounted on the end of the telescope and takes flat field images.

(7) After the observations are completed for the evening, the observer closes the dome shutter and turns off the hardware, including the camera. All of the above steps are done remotely by the observer, using a remote desktop control software called UltraVNC. We installed the UltraVNC server

on the earthshine computer and the UltraVNC client on the operator’s controlling computer.

Steps (1)–(5) take about 15 minutes at the beginning of the observations each night. After which, the remote observer may largely ignore his/her control computer. The computer has an alarm system that sounds and shows red on the screen, if a problem arises. The observations will stop automatically if the warnings are ignored. Steps (6)–(7) take about 10 minutes at the end of observations each night. This remote observing sequence is ideal for the Canary Islands where observers remotely control several synoptic type telescope each night from a remote mountaintop control room a few hundred meters from the earthshine dome.

5. Conclusions

Future observations of the earthshine from a planned global network of robotic telescopes will provide an even more valuable tool, complementary to satellite data, for the study of changes in the short-wave forcing of the Earth’s climate. We plan to expand our two station remote-control network to a global one with several stations.

Acknowledgments

P. R. Goode and S. Shoumko gratefully acknowledge the support from NASA-NNX08BA22G. Research by E. Pallé was supported by a “Ramon y Cajal” fellowship.

References

- [1] J. Qiu, P. R. Goode, E. Pallé, et al., “Earthshine and the Earth’s albedo: 1. Earthshine observations and measurements of the lunar phase function for accurate measurements of the Earth’s Bond albedo,” *Journal of Geophysical Research D*, vol. 108, no. D22, article 4709, pp. 1–22, 2003.
- [2] E. Pallé, P. R. Goode, V. Yurchyshyn, et al., “Earthshine and the Earth’s albedo: 2. Observations and simulations over 3 years,” *Journal of Geophysical Research D*, vol. 108, no. D22, article 4710, pp. 1–17, 2003.
- [3] A. Danjon, “Recherches sur la photométrie de la lumière cendrée et l’albedo de la terre,” *Annales de l’Observatoire de Strasbourg*, vol. 2, pp. 165–180, 1928.
- [4] A. Danjon, “Albedo, color, and polarization of the Earth,” in *The Earth as a Planet*, G. P. Kuiper, Ed., pp. 726–738, University of Chicago Press, Chicago, Ill, USA, 1954.
- [5] E. F. Harrison, P. Minnis, B. R. Barkstrom, V. Ramanathan, R. D. Cess, and G. G. Gibson, “Seasonal variation of cloud radiative forcing derived from the Earth Radiation Budget Experiment,” *Journal of Geophysical Research*, vol. 95, no. D11, pp. 18687–18703, 1990.
- [6] S. Kato, N. G. Loeb, and C. K. Rutledge, “Estimate of top-of-atmosphere albedo for a molecular atmosphere over ocean using Clouds and the Earth’s Radiant Energy System measurements,” *Journal of Geophysical Research D*, vol. 107, no. 19, p. 4396, 2002.
- [7] E. Pallé, P. R. Goode, P. Montañés-Rodríguez, and S. E. Koonin, “Changes in Earth’s reflectance over the past two decades,” *Science*, vol. 304, no. 5675, pp. 1299–1301, 2004.
- [8] E. Pallé, P. Montañés-Rodríguez, P. R. Goode, S. E. Koonin, M. Wild, and S. Casadio, “A multi-data comparison of shortwave

- climate forcing changes,” *Geophysical Research Letters*, vol. 32, no. 21, Article ID L21702, 4 pages, 2005.
- [9] E. Pallé, P. R. Goode, and P. Montañés-Rodríguez, “Interannual variations in Earth’s reflectance 1999–2007,” *Journal of Geophysical Research*, vol. 114, Article ID D00D03, 2009.
- [10] E. Pallé, P. R. Goode, P. Montañés-Rodríguez, S. E. Koonin, and V. Remyantsev, “Toward a global earthshine network: first results from two stations,” *Geophysical Research Letters*, vol. 32, no. 11, Article ID L11803, 4 pages, 2005.
- [11] P. R. Goode, J. Qiu, V. Yurchyshyn, et al., “Earthshine observations of the Earth’s reflectance,” *Geophysical Research Letters*, vol. 28, no. 9, pp. 1671–1674, 2001.
- [12] A. Raval and V. Ramanathan, “Observational determination of the greenhouse effect,” *Nature*, vol. 342, no. 6251, pp. 758–761, 1989.

Research Article

The STELLA Robotic Observatory on Tenerife

**Klaus G. Strassmeier, Thomas Granzer, Michael Weber, Manfred Woche,
Emil Popow, Arto Järvinen, Janos Bartus, Svend-Marian Bauer, Frank Dionies,
Thomas Fechner, Wilbert Bittner, and Jens Paschke**

Cosmic Magnetic Fields, Astrophysical Institute Potsdam, An der Sternwarte 16, D-14482 Potsdam, Germany

Correspondence should be addressed to Klaus G. Strassmeier, kstrassmeier@aip.de

Received 23 June 2009; Accepted 5 October 2009

Academic Editor: Alberto J. Castro-Tirado

Copyright © 2010 Klaus G. Strassmeier et al. This is an open access article distributed under the Creative Commons Attribution License, which permits unrestricted use, distribution, and reproduction in any medium, provided the original work is properly cited.

The Astrophysical Institute Potsdam (AIP) and the Instituto de Astrofísica de Canarias (IAC) inaugurated the robotic telescopes STELLA-I and STELLA-II (STELLar Activity) on Tenerife on May 18, 2006. The observatory is located on the Izaña ridge at an elevation of 2400 m near the German Vacuum Tower Telescope. STELLA consists of two 1.2 m alt-az telescopes. One telescope feeds a bench-mounted high-resolution echelle spectrograph while the other telescope feeds a wide-field imaging photometer. Both scopes work autonomously by means of artificial intelligence. Not only that the telescopes are automated, but the entire observatory operates like a robot, and does not require any human presence on site.

1. Introduction

STELLA is a robotic observatory with two 1.2 m fully automatic telescopes located at the Teide Observatory in Tenerife, Spain [1, 2]. Not only the telescopes are automatic but also the entire observatory; no human presence is needed for observing, data reduction, and archiving. The STELLA Echelle spectrograph (SES) on STELLA-I is in robotic operations mode for three years now, and produced approximately 20,000 spectra of the entire optical range between 390 and 900 nm at a spectral resolution of 55,000 with a peak shutter-open time of 93% [3]. (The time during a night that is used for science exposures.) Although we do not use an iodine cell nor an actively stabilized chamber or simultaneous Th-Ar wavelength calibration, its radial velocity precision over the past two years was 30 m/s rms depending on target. The Wide-Field STELLA Imaging Photometer (WiFSIP) is currently being tested and is scheduled to enter operation in early 2010 on STELLA-I when the SES fiber will be moved to STELLA-II.

The central scientific objective of STELLA is to understand the structure and dynamics of stellar surface activity and its impact on stellar evolution. The magnetic fields that permeate stellar atmospheres affect the transport of energy

and momentum and give rise to surface features similar to the spots and plagues we observe on the Sun. These features change with time as a function of the cyclic behaviour of magnetic activity. Reconstructing the spatial distribution of these features from high-resolution spectra—by means of a tomographic technique called Doppler imaging—is still a great challenge and requires simultaneous photometric and spectroscopic observations over the rotation period of a star without significant data gaps. Together with a systematic determination of rotational periods in open clusters as a function of age, time-series Doppler imaging of active stars is the core science program of STELLA.

2. A Bit of History and Lessons Learned

Six years of hard work led to the first stellar spectrum taken by STELLA-I from the star α Tauri (K5III) on September 9, 2005. In late May 2006, STELLA-I started its first robotic operation. By mid September 2009 a total of 18,000 echelle spectra were obtained (Figure 1). The STELLA-II telescope is now expected to enter operation with SES in early 2010.

Several problems had and still are to be solved on the way to a functioning observatory (see Granzer et al., *this proceedings*). The building was, for example, occupied

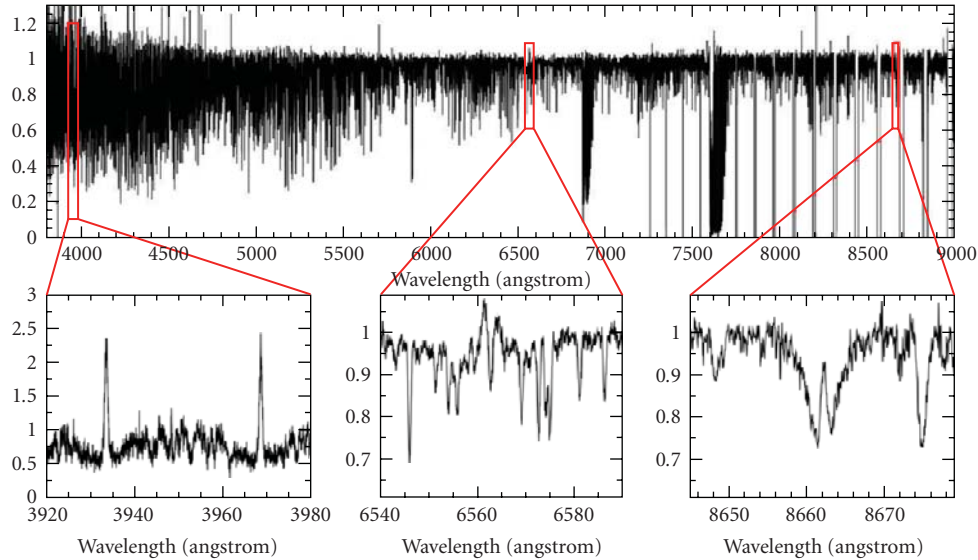


FIGURE 1: An example spectrum from the SES. What is shown is the $V = 9.0$ mag K0III RS CVn binary XX Triangulum. Exposure time was 1 hour, spectral resolution is 55,000, an S/N ratio of 120 : 1 was achieved. The top panel shows the full spectrum (note the increasing order gaps redwards of 725 nm). The lower panels zoom into the Ca II H&K region, Balmer $H\alpha$, and one of the Ca II infrared triplets.

by worms which could not find their way out anymore and passed away throughout all the electronics cabinets in the observatory. Chemicals now keep the worms off the building. Frequent ice storms during the winter, as well as one major electromagnetic storm, damaged the building and its electronics. An elaborate control system and a new uninterrupted power supply solve the problem today. Sensors distributed over the entire building continuously report about the environmental conditions inside and outside the building, the telescopes, the scientific instruments, and the many auxiliary systems. The STELLA control system [4–6] linked with an all-sky camera predicts now critical weather conditions such as humidity five minutes in to the future and closes the observatory roof in case of an upcoming storm. A dust monitor was installed just a few months ago to cope with the extremes of the Sahara sand (Calima) and an IR cloud monitor will be installed in early 2010.

3. The STELLA Control System (SCS)—Building, Telescope, Instrument, and Data Control and Scheduling

The basic command structure includes always a command caster and a command listener with precomputed acknowledge times for every task, the latter driven by the hardware response time provided by the various manufacturers. The real advantage of this concept is that it allows for efficient error handling. However, it comes with increased network requirements which are standard though and easily handled with 100 Mbit/s networks. The principle is laid out in Figure 2. When a command is sent, for example, switch guiding on, a listener receives the command and computes an acknowledge time for that particular task and sends this

together with the known execution time to the caster which is waiting for that time to receive the done acknowledge from the listener that, in the meantime, ordered to execute the command or subcommand. Once the listener receives the done from its hardware controller it forwards it to the caster which then decides whether it was done in the precomputed time or not. If not, something went wrong and an error handler is loaded where all messaging is logged. If ok, the caster closes this particular command as being executed successfully. Retrials are done automatically for many but not all processes.

The building is an integrated part and slaved to two redundant weather stations running in coincidence and controlled via the SCS. It was designed to allow full view of the sky for both telescopes at the same time, and to allow emergency closing of the roof at any possible telescope position. This latter feature is a necessity for a secure unattended operation of the system. The roof subsystem is operating autonomously; that is, the power for the roof drives is backed up by a UPS system, and a watchdog makes sure the roof will close if the control computer or the corresponding communication infrastructure fails. All crucial electronics components are backed up by batteries for at least 30 minutes, as are the telescopes. The hydraulic oil pumps for the azimuth bearings are supported by an emergency pressure reservoir, which holds the pressure up until the telescopes come to a complete stop.

Another novel feature is the SCS's weather prediction capability. Meteorology tells us that if the barometric pressure is low the humidity is usually high, and cloudiness is likely. The SCS now learns from the time dependency of the local environmental database how likely this really is. (The database has been built up from the readout of two redundant weather stations with five parameters

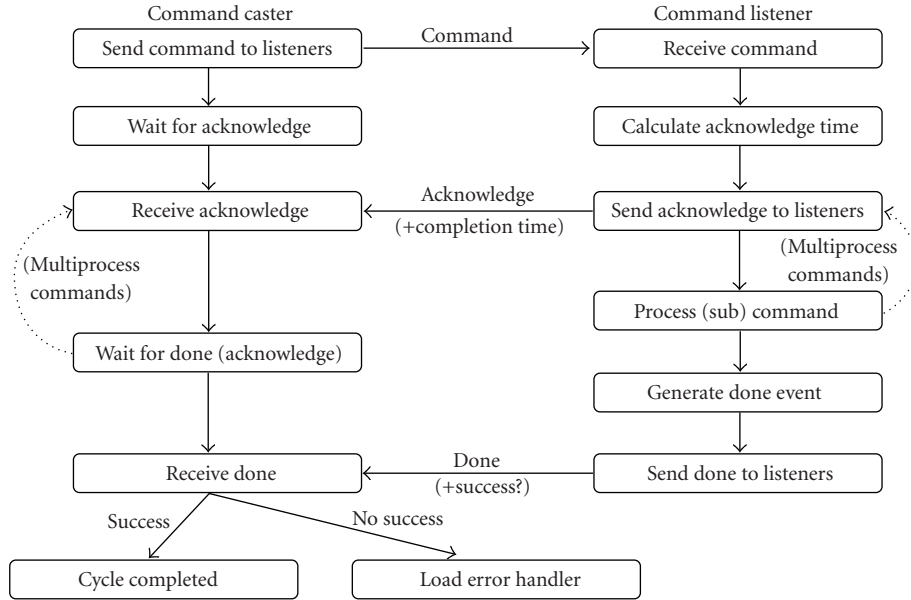


FIGURE 2: The basic messaging system of the STELLA control system (SCS).

each and a full log is available via a Web interface (see <http://www.aip.de/stella>.) It predicts the humidity increase from the gradient of the decrease of the barometric pressure and temperature two minutes into the future. Figure 3 depicts an example with various extrapolation curves depending on how many data points and what functionals are used. STELLA is located on the Izaña rim at 2400 m altitude that first gently and then steeply falls down to sea level. This allows clouds to creep up from “underneath” and go unnoticed because the all-sky cloud monitor sees clear sky. Fortunately, the clouds announce their coming by increased humidity and, so far, the system did not fail.

We employ a dispatch scheduler for target-load distribution [6]. This is used nowadays on most commercial robotic systems, for example, for air traffic controlling. It runs in real time, allows easy reaction on weather changes, and allows targets to be picked according to actual conditions. The STELLA approach is to split the merit function into a time-slot variable, ts_j , for long-term merit and a gain variable, g_j , for short-term merit. The ts variable sets the type of observation, for example, periodic pick, phase-dependent pick, or pick at a predefined time while the g variable sets the immediate priority, for example, by taking into account the air mass during an upcoming integration.

4. The Telescopes

Both telescopes were manufactured by Halfmann Teleskop-technik in Neusäß near Augsburg, Germany (Figure 4(a)). They feature an Alt/Az mount and an aperture of 1.2 m. STELLA-I is an f/8 Cassegrain system with two Nasmyth foci and a field of view of 30 arcmin. The second telescope (STELLA-II) is equipped with a high-precision spherical mirror with a prime-focus corrector that feeds the optical fiber for the SES at f/8.4 with a field of view of 2 arcmin. A

third telescope, identical to STELLA-I but with an aperture of 0.8 m, is located at the AIP in Potsdam-Babelsberg and serves as a testbed for STELLA instrumentation and interface software as well as for educational purposes (see <http://www.aip.de/groups/robotel/>).

All telescopes rest on hydrostatic azimuth bearings driven by a single stage oil pump. The altitude axis features a ball bearing. The two telescope axes are moved by direct-drive motors from ETEL with optical Heidenhain encoders. One increment on the encoder corresponds to 36 arcsec, which is interpolated at a resolution of 11 bits, which translates to a theoretical pointing and tracking accuracy of the drives of 0.18 arcsec. If STELLA does not find a target, it assumes that it is not there; that is, no spiral search is done to correct for pointing errors, it then moves on to the next target. After three consecutive failures a set of predefined bright targets distributed over the sky will be moved at and, if not found, the telescope goes to sleep for 30 minutes and then retries if the weather station permits. We have not recorded a case yet where this was not due to clouds.

The acquisition and guiding unit (AG unit) of a robotic telescope is naturally more complex than for a manual telescope. Guiding on STELLA-I is currently done using a grey beam splitter in the AG-unit. The back-reflected light from an aluminized glass plate with a pinhole for the fiber is simultaneously imaged onto the guiding camera, which allows an estimate of the amount of light reaching the fiber. The diameter of the pinhole is 120 μm , which corresponds to approximately 2.5 arcsec on the sky. The guiding images are recorded on disk and, after the exposure, averaged and archived for later review if needed. Figure 4 shows the accumulated repositioning of the telescope during a 1-hour stellar integration on a 50 μm diameter core of the SES fiber.

Focusing of the telescope is done using a focusing pyramid. At the beginning of operation, a relationship between

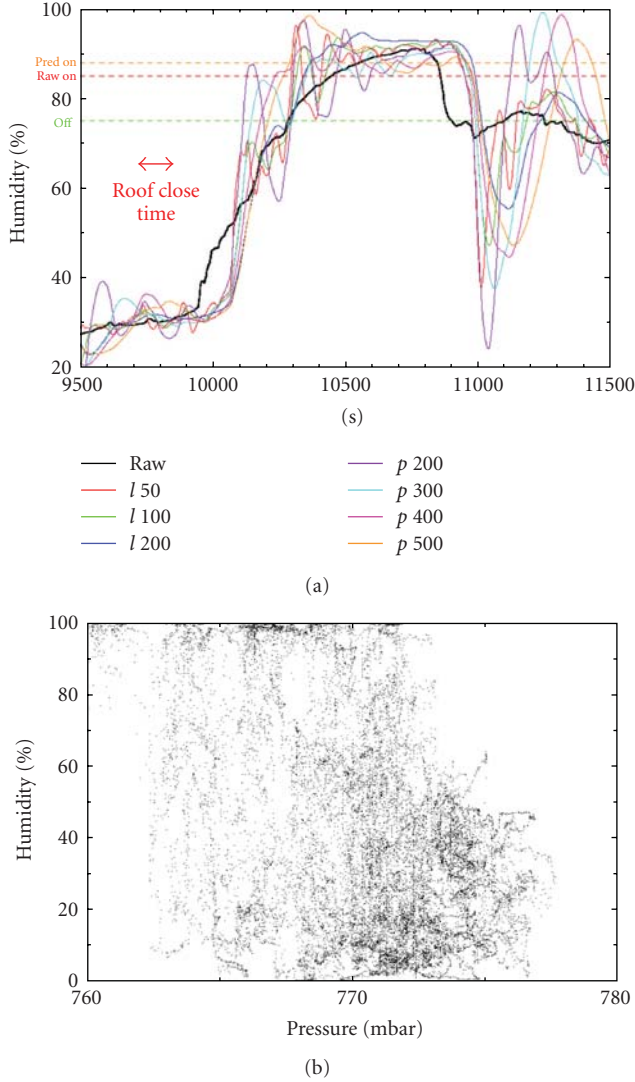
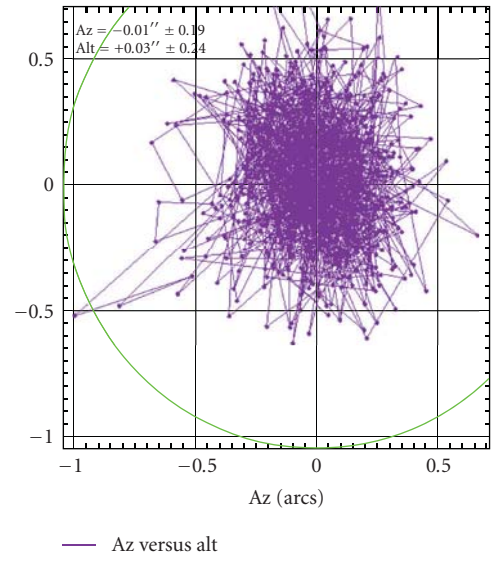


FIGURE 3: The SCS local cloud predictor. (a) The thick line represents measurements of a sudden humidity increase; that is, a cloud was moving across the STELLA weather stations. The x-axis is in seconds and the 2-minute slot needed to close the observatory roof is indicated. The predictor needs in about that time to predict the increase to the actual future value. For the incidence shown this was already the case when the humidity level was still low (50–60% in this case at $t = 10100$ seconds) and the roof closed well before the cloud could have been trapped inside the observatory bay. (b) The basis for that prediction is the (local) relation between humidity and barometric pressure. This relation is not strict but the likeliness of low humidity, that is, good weather, is high when the pressure is also high, that is, when the data fall within the lower right of above diagram.

the distance of the four images produced by the focusing pyramid and the focus position of the telescope was established. This was used to construct a master-focus relation which is just a function of temperature. For bright targets down to 8th magnitude, the optimal focus is determined before the observation starts, for fainter targets the master temperature calibration is applied (see [3] for more details).



(a)



(b)

FIGURE 4: (a) STELLA-I in the foreground with its AG-unit (black box) in the right Nasmyth focus (with the fiber cable making a loop). STELLA-II is in the background. (b) Accumulated guiding corrections for a 1-hour exposure with the SES on STELLA-I. The dots are the individual alt-az pointings. The circle indicates the fiber entrance diaphragm of $120 \mu\text{m}$ (2.5 arcsec). The guiding rms was 0.19 arcsec in azimuth and 0.24 arcsec in altitude.

At the beginning of routine operation of STELLA-I, fatal failures of the telescope system during the night were rather frequent. It usually meant the loss of the remaining night since recovery after a fatal failure required a hard reset of the telescope electronics which takes its time. Most failures in the first year of observations were caused by such errors. In the meantime, the telescope runs without problems for weeks due to proper error handling, and almost all errors can be treated by the control system in an automated way. Nevertheless, the hard reset capability that we introduced to handle the problems in the beginning, still prove to be useful in solving exceptional problems.

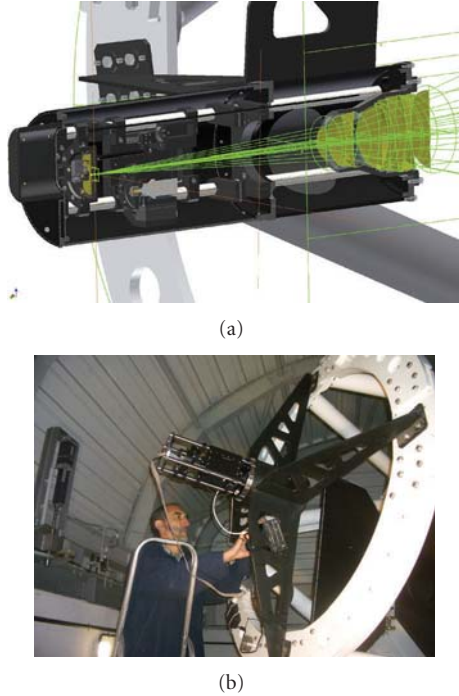


FIGURE 5: Design and installation of STELLA-II's prime focus unit. (a) The CAD drawing shows the reflected beam through the five-lens corrector optics (right), an ADC, and a fiber viewing unit. (b) Emil Popow during installation of the unit in the prime focus.

Another important feature is the capability to execute pointing models remotely. The error handler of the SCS realizes when certain regions in the sky experience increased acquisition aborts or even unnatural large offsets. This can be the case when the telescope is out of balance and the azimuth bearing requests higher oil pressure when pointing to a certain region in the sky, for example, always west of the meridian and when the alt position is low. If so, the operator in Potsdam can decide to dedicate a good night to redo the pointing model (see [6, 7] and Granzer et al., *this proceedings*).

STELLA-II is a highly specialized telescope as compared to STELLA-I. Its sole purpose is to feed as much light as possible into a 50 μm -diameter fiber. This actually does not mean it is a simple telescope. We chose to build the telescope around a space-quality, light-weighted, spherical $f/1.95$ primary mirror from ZEISS Jena and designed a 5-lens prime-focus corrector unit to achieve a PSF matching the fiber entrance f -ratio for optimal injection (see Figure 5). The fiber coupling is done through a microlens based on the EFO-Quartz concept (the microlens is cast and polished by molding the fiber end to a drop). We expect a threefold increase of the light-collection efficiency as compared to the AG-unit on STELLA-I (the current location of the SES fiber until the end of 2009). Acquisition and guiding of the telescopes is currently done with a 150 mm refracting telescope mounted piggyback to the telescope truss. It includes a V -filter and an Audine-based AIP-built guiding camera with a KAF-3200 CCD detector.

5. STELLA Instrumentation

5.1. SES—The STELLA Echelle Spectrograph

5.1.1. The 2006–2009 Version. The current version of the SES is a white-pupil spectrograph with a fixed wavelength format of 388–882 nm. The instrument is located in a separated, thermally controlled room on a stabilized optical bench (see Figure 6) and is fed with a 15 m-long optical fibre. Currently, a 50- μm core-diameter fibre enables an instrumental resolution of $\lambda/\Delta\lambda \approx 55,000$ (0.01 nm or ≈ 5 km/s), corresponding to an entrance aperture of 2.1 arcsec on the sky. Its heart is 31 lines per mm R2 grating from RGL. Two off-axis parabolic collimators, one folding mirror, and two prisms as cross-disperser transport the light into the $f/2.7$ katadioptric camera with a 20 cm corrector and a 40 cm spherical mirror. Beam diameter is 130 mm. The CCD camera is based on a top-grade thinned E2V42-40 device with 2048×2048 13.5 μm pixels. Its nominal quantum efficiency is 90% at 650 nm, and 65% at 400 nm and 800 nm, respectively, with a full-well capacity well above 100,000 electrons. Together with a second-generation CUO (Copenhagen) controller the read-out noise is 3–4 electrons rms. A closed cycle cooler keeps the detector cooled to -130° Celsius. A rotating shutter with a propeller-like blade is located just in front of the CCD-entrance window (our “Salami cutter”).

The main problem with the current set up is the low overall efficiency (3%). This is because we used already pre-existing components from another spectrograph that do not fully cope with the modern instrument design. For example, the Schmidt camera has a folding mirror on the optical axis that is not matched to the fiber exit and thus diffracts up to 40% of the light. Furthermore, the cross-disperser is red optimized and is rather inefficient short of 400 nm. Its dispersion is also inadequate for the large wavelength coverage which makes stray-light reduction a tedious software issue and will never be perfect (we estimate an average 5% stray-light contribution which is mostly taken out during the data reduction). The cross-disperser is also not matched to the size of the CCD so that the CCD starts to cut the orders on both ends redwards of 725 nm and does not leave enough space between adjacent echelle orders. Therefore, an upgrade of the spectrograph was planned all along once the observatory enters routine operation.

5.1.2. The 2010+ Version. Figure 7 summarizes the new SES. The setup remains to be a white-pupil spectrograph with an R2 grating and the two off-axis main and transfer collimators. The Schmidt camera is replaced by an all refractive 7-lens camera with an aperture of 150 mm. It is matched to a thinned and back-illuminated Semiconductor Technology Associates (STA) $4\text{ k} \times 4\text{ k}$ 15 μm -pixel CCD. Its controller is a modified AIP-built Magellan controller and enables four-port readout of the device at ≈ 5 electrons read-out noise in 30 seconds. Its full-well capacity is 70,000 electrons and its cosmetics are excellent. A new cross-disperser will consist of two prisms that optimally distribute the echelle orders across the CCD field of view. The STELLA-I AG-unit does not contain an atmospheric dispersion

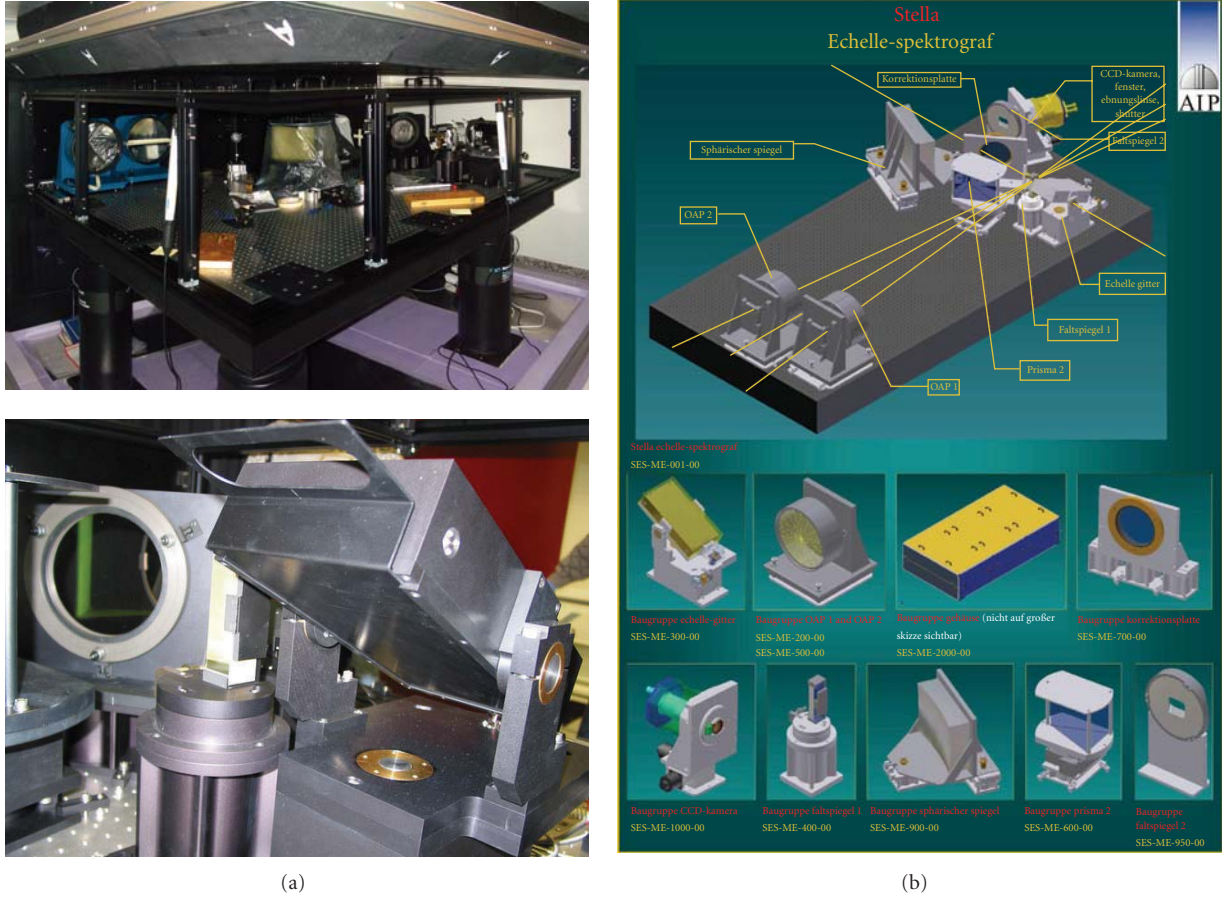


FIGURE 6: The STELLA Echelle Spectrograph (SES). (a) top: The instrument is mounted on a Newport optical bench on four gas-damped legs on a pier separated from the building. The table and its optical and mechanical components are enclosed with a dust cover made of anodized aluminium sheets (partly removed in this picture). This cover together with the bench legs is additionally enclosed in a thermal insulation chamber (also partly removed). This chamber is in a dedicated room with active temperature control. (a) bottom: The heart of the spectrograph, the R2 31-l/mm echelle grating (covered). (b) Overview of the opto-mechanical design and its components.

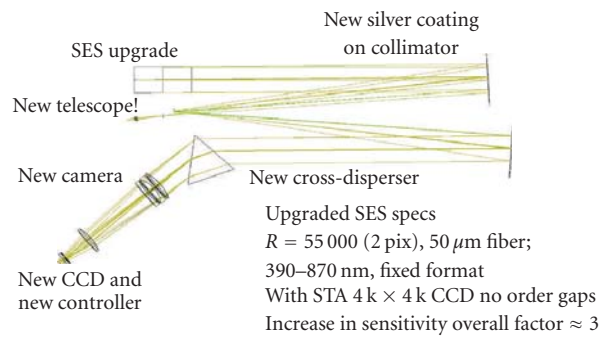


FIGURE 7: Layout of the 2010+ version of the SES. The fiber connection remains to be based on a $50\,\mu\text{m}$ Polymicro fiber and the EFO-Quartz principle. The resolution and wavelength coverage remain, the latter without any gaps due to the larger CCD and new cross-disperser. The overall efficiency shall be increased by a factor of three to $\approx 10\%$ (all inclusive) compared to the current SES version.

corrector (ADC) which added extra losses in the extreme blue and red ends of the spectrum. This will be compensated for in the STELLA-II prime-focus unit. A novel feature of the upgrade will be the simultaneous light feed from a (first) Th-Ar cathode lamp that will be replaced later

by a Fabry-Perot halogen lamp. This enables ultra-precise wavelength calibration approaching a radial-velocity stability of (hopefully) few m/s without the insertion of an iodine cell that basically ruins the spectrum for other purposes than velocity measurements.

5.2. WiFSIP—The Wide-Field STELLA Imaging Photometer. WiFSIP is a CCD photometer and imager with off-axis guiding. The CCD is a four-port 4096×4096 $15\ \mu\text{m}$ -pixel back-illuminated CCD from STA and was thinned and antireflection coated at Steward Imaging Technology Lab. It is a twin system of the upgraded SES CCD version. Its controller is optimized for speed though and its current read-out noise is 15 electrons rms in 12 seconds read-out time per port. This is sufficient for high-precision photometry. The instrument is currently mounted on RoboTel (see Section 4 and Figure 8) and is being prepared for deployment to Tenerife in late 2009.

The field of view with a 3-lens field corrector on STELLA-I is an unvignetted 22×22 arcmin with a scale of $0.32''/\text{pixel}$ (see Figure 9). The photometer is equipped with 90 mm sets of Strömgen-*uvby*, narrow and wide $H\alpha$ and $H\beta$, Johnson-Bessell *UBVRI*, and Sloan *ugriz* filters. A high-speed, double-bladed “Bonn shutter” enables a vibration-free 10 milliseconds exposure with still photometric precision due to counterbalancing the blade’s motion. The telescope’s limiting magnitude is well below 20th magnitude while it will be difficult to image anything brighter than 10th magnitude due to CCD saturation unless significant telescope defocus. We expect sub-mmag precision for defocused time-series photometry down to 13th magnitude. However, external error sources like telescope jitter are still to be determined and properly handled (robotically of course). Other issues are the low-light level behaviour of the CCD, its quadrant photon mirroring due to the four amplifier architecture of the chip, its (radio) signal pick up suppression, and other telescope interface issues.

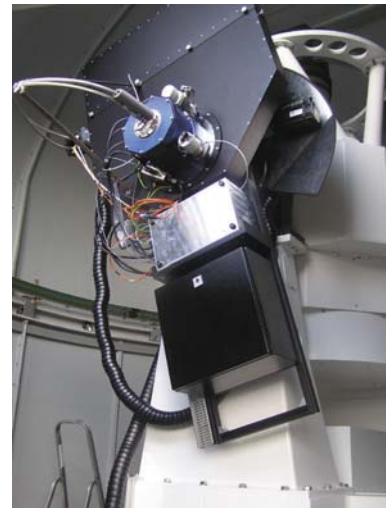
6. Data Handling

We transfer all raw data including the acquisition frames, the stacked guider frames, and the guiding offsets plus the environmental and status database to the STELLA communication center in Potsdam. Currently, we accumulate about 500 MB of compressed data each day from the SES plus the database contents, which requires an average data rate of 50 kbit/s. An SQL database acts as the central storage pool. Once WiFSIP is operable the data rate will increase at least tenfold due to the much higher cycle time for photometry compared to spectroscopy. Currently, only the SES calibration and data-reduction pipeline are in operation.

6.1. The SES Data Pipeline. The automatic data-reduction pipeline for SES is based on the NOAO Image Reduction and Analysis Facility (IRAF). It consists of a number of IRAF-CL scripts which are invoked by a master script (for more details see [3]). The reduction process is started automatically after the morning calibration exposures are finished and the raw data transferred to Potsdam. The first and largest part contains the bad-pixel correction, bias subtraction, scattered-light subtraction, cosmic-ray correction, flat fielding, and aperture extraction. Because the orders from about 600 nm and shorter overlap, we use the program HAMSCAT [8] to fit the scattered light and the light pollution from adjacent



(a)



(b)

FIGURE 8: The Wide-Field STELLA Imaging Photometer WiFSIP. (a) The large 24-hole filter wheel during manufacture in the AIP workshop. (b) The instrument during first tests mounted on the 0.8m RoboTel Nasmyth focus. The box with the filter wheel is now located on the top with the CCD dewar in blue connected to a closed-cycle cryocooler (not shown). The middle box contains the CCD controller in a thermally insulated aluminium enclosure. The lower black box contains the remaining electronics. Note that the instrument is flanged to an image derotator and is turning to compensate for the field rotation due to the alt-az mount.

orders and remove it. Order extraction is done using IRAF’s optimal extraction. The current wavelength calibration uses a predefined Th-Ar line list and interpolates between two Th-Ar exposures closest in time before and after the science observation. The raw FITS images along with the end products of the data reduction pipeline are then moved to a backup server. The second part consists of continuum fitting which is currently not automated but will be once the SES upgrade is installed (see Figure 1 for a spectrum example).



FIGURE 9: The WiFSIP CCD field of view on RoboTel ($30' \times 30'$).

Once the spectra are reduced and properly back upped, an automated analysis of the reduced spectra is launched. It currently includes radial velocity measurements with both a template spectrum computed from a model atmosphere appropriate for the star in question and with a radial velocity standard star spectrum. Template spectra are tabulated with metallicities between -1 dex and $+0.5$ dex in steps of 0.5 dex, logarithmic gravities between 0 and 5 in steps of 0.5 , and temperatures between 3500 K and $50,000$ K in steps of 250 K for a wavelength range of 380 – 920 nm. The user can choose the velocity that gives the most consistent result for his/her particular type of target. The next and final step is the determination of the best-fit effective temperature T_{eff} , gravity $\log g$, and metallicity $[\text{Fe}/\text{H}]$ of the target star. This is done with the program PARSES [9] by fitting atmospheric models to the spectral region containing $\text{H}\beta$. For this purpose, the SES spectra are degraded to a resolution of $\approx 7,000$ because PARSES in its current version neglects rotational line broadening. An update will be implemented soon and then the full resolution in five spectral orders will be used.

6.2. The WiFSIP Data Pipeline. As for the spectrograph, data reduction for WiFSIP will be done in Potsdam once the raw data has been transferred. For flat fielding of the science data, sky flats are taken at morning and evening twilight. The high number of available filters inhibits a procedure where flats for all filters are taken during twilight. Thus, during twilight only flats for a single photometric set (Johnson, Strömgren, or Sloan) are taken. The SCS tries to anticipate within the evening twilight which filter set is the one with the most urgent need, depending on flat history, flat stability, and filters to be used in the upcoming night, a decision that could be refined later during dawn twilight. Once all data has been transferred to the AIP, a preparatory pipeline assures that for any given night, the most recent bias and flat calibration frames are available. Depending on the secured flat-field stability, a warning is issued if the flats in proximity to the night in question are too far off in time in order to assure a pixel-to-pixel stability exceeding 10^{-3} . The science pipeline itself is based on the ICAT-pipeline ([10]; see also Colomé et al., *this proceedings*), which, in

turn, utilizes NOAO-IRAF for bias and dark subtraction and flat fielding. Astrometric calibration is done using WCSTools [11]. For photometry, two methods are available, the aperture-photometry package SExtractor [12], and the PSF-modelling package DAOPHOT [13]. The instrumental magnitudes along with the astrometric data are collected in a database. From there, time-series of ensembles of images can be extracted using a modified version of the ENSEMBLE4 package [14]. The current development focuses on the incorporation of standard stars to gain full-sky absolute photometric solutions.

7. Early Results

Currently, STELLA-I/SES carries out 12 programs from German, Spanish, U.S., and Hungarian investigators on a private communication basis and without further quality control. Until the SES is upgraded, we dub this phase the science demonstration time. A few auxiliary programs are highlighted in what follows.

7.1. HD 1—The Number One Star in the Sky. HD 1 = HIP 422 is among the few rather bright stars ($V = 7.4$ mag) of which we basically know nothing except some very basic parameters. It is thus a well suited target for a data demonstration and we have randomly chosen HD 1 to be our first science verification target. We find the star to have a systematically variable radial velocity and suggest it be a single-lined spectroscopic binary in a very long and eccentric orbit. It appears to be a K2 bright giant of luminosity class III-II with $\approx 300 L_{\text{Sun}}$ at an age of 130 Myr, a mass of $4 \pm 1 M_{\text{Sun}}$, and a radius of $\sim 27 R_{\text{Sun}}$.

7.2. ϵ Aurigae Entering Its Next Eclipse after 27 Years. ϵ Aur is a binary star system that eclipses once every 27.1 years. The next eclipse is currently ongoing and began in July 2009. The eclipse is flat-bottomed and lasts nearly two years. A mid-eclipse brightening was seen by several observers, including observations from space, and many models appeared for its explanation. Among them a neutron stars with a warped semiopaque disk. Photometry of the primary F star appears to show pulsational variability with at least eight periods ranging from >570 days to 48 days [15]. Our STELLA SES data show short-term radial velocities variations with a peak-to-peak amplitude of up to 25 km/s consistent with the photometry.

7.3. Capella—Two Active Giants in a 104-Day Orbit. Astrophysical parameters of giant stars are uncertain because there are just a few such stars that can be studied in spectroscopic binary systems. The present position of the G1III component of α Aur in the Hertzsprung gap, where it is approaching the base of the giant branch, indicates that violent changes are taking place in its internal structure; the mass of the convection zone increases rapidly as does also the total stellar moment of inertia while the other component is likely already helium burning. We may expect that this has an impact on the overall magnetic activity of the system. We

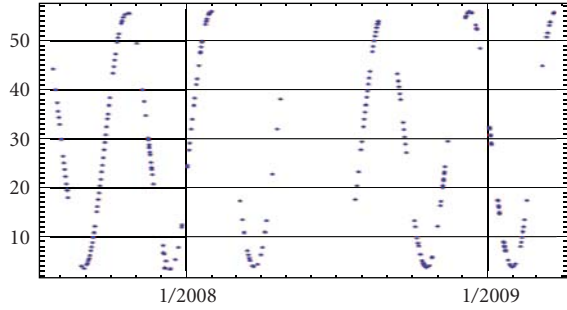


FIGURE 10: Radial velocities for the primary giant of the Capella binary system. Note that the orbital period is 104 days and that the total time coverage is three years. Gaps are mostly due to the observing season but also due to the various weather-related and technical down times.

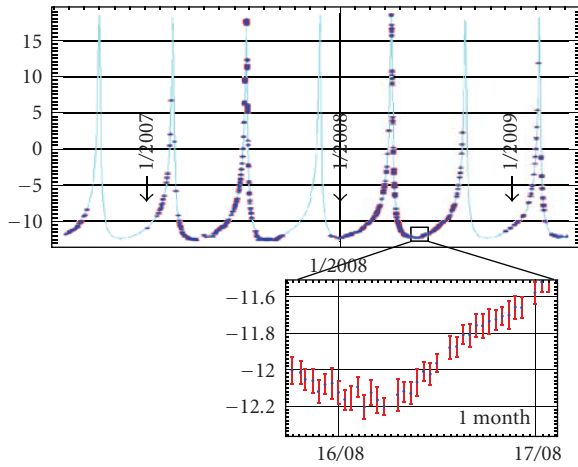


FIGURE 11: Radial velocities and orbit for HD123351. The star turned out to be a very eccentric single-lined spectroscopic binary with a period of 148 days. Note that its rotational period can be seen in the radial velocities due to the asymmetric distribution of its starspots.

monitor the Capella system with one spectrum every clear night. Its radial velocities from the SES data pipeline are shown in Figure 10.

7.4. The Surprising Radial Velocities of HD123351. Another extreme magnetically active star is HD123351. Known to be a K2IV star it was assumed to be single due to constant radial velocities. Soon after we started monitoring with STELLA-I it turned out to be a binary in a very eccentric 148-day orbit. The eccentricity is 0.81 and the semiamplitude near 15 km/s. The radial velocities and a preliminary orbit are shown in Figure 11. Note that the radial velocities are also rotationally modulated!

7.5. The Exoplanet 51 Pegasi b. For demonstration purposes we also monitored the famous exoplanet system 51 Pegasi. Figure 12 shows the radial velocities and a clear detection of the star's hot Jupiter planet. The overall rms of the data is

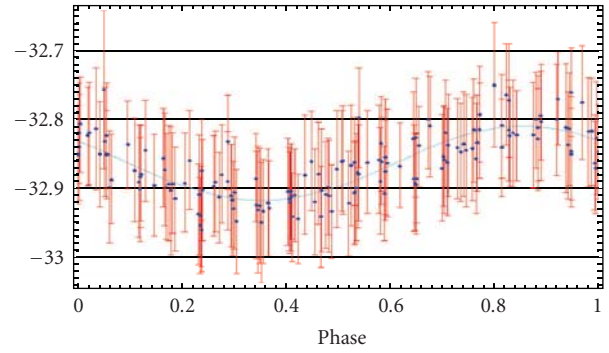


FIGURE 12: The planet of 51 Pegasi with STELLA-I/SES. The orbital period of the planet is 4.23 days ($e = 0$; continuous line) and the velocity amplitude is ≈ 100 m/s. Our overall rms of the data is 30 m/s, an individual measurement error is ≈ 70 m/s. The data span between May and August in 2008 and are plotted directly from the SES pipeline. Note that no other measures than the thermal and mechanical stabilization of the spectrograph were taken.

30 m/s. Note that no iodine cell or simultaneous Th-Ar light or template cross correlation is involved.

7.6. Doppler Imaging of FK Comae. Early on, we participated in a simultaneous observing campaign with ESO's VLT to map the magnetic field of the active rapidly rotating giant FK Comae. The STELLA/SES data were used to obtain a Doppler image from an inversion of its photospheric line profiles ([16]; see Figure 13). Simultaneously, a dynamic spectrum of the accompanying $H\alpha$ line profiles suggested a close relation with the photospheric spots and the phases of strongest magnetic field.

7.7. Beteigeuze's Convective Motion Pattern. Hydrodynamic "star-in-a-box" simulations show Beteigeuze with a very coarse and time-variable granulation pattern [17]. Roughly 20 granulation cells at a time are covering this $800-R_{\text{Sun}}$ M supergiant with a typical life time of a "few years." We monitor the star's radial velocities with high precision in order to detect the granulation signature and to compare it with numerical model predictions.

7.8. Active Star Binary Orbits. Magnetically very active stars in binaries are thought to modulate the orbital period due to a feedback on the gravitational quadrupole moment from a magnetic activity cycle induced rearrangement of internal angular momentum. STELLA-I/SES monitors approximately 50 active stars, most of them previously unknown binaries.

7.9. Gliese 586A—Monitoring the Most Eccentric Binary Orbit Known. Two cool M dwarfs revolve around a common center of mass with a period of 890 days and a record eccentricity of 0.975 [18]. Despite the long period, the periastron where the radial velocity reverses its sign is passed in just 24 hours and spans 70 km/s at 5 km/s per hour. So far, STELLA covered one periastron passage in 2007 but the next passage is coming up in 2009. Figure 14 shows the current status of the

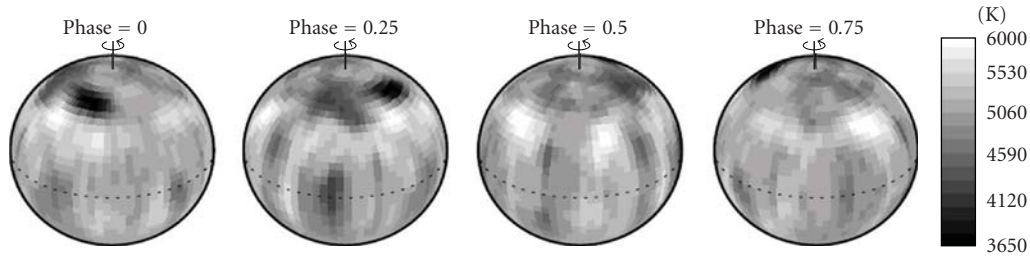


FIGURE 13: Doppler image of the rapidly rotating G giant FK Comae based on STELLA-I SES data. The map plots surface temperature according to the scale. It was taken from [16].

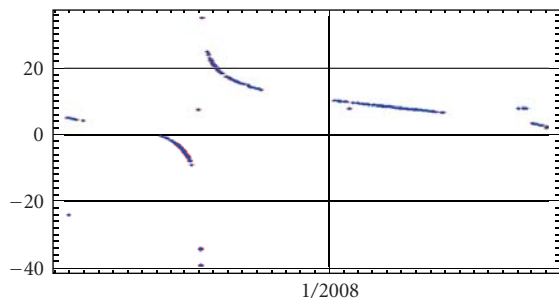


FIGURE 14: Radial velocities in km/s of Gliese 586A. The time coverage in this plot is ≈ 900 days, that is, one full orbital period of Gl586A. The gaps are the seasons when the target is unobservable. Also note some misidentifications at a constant velocity of 8 km/s (likely one of the other visual binary components, Gliese 586C or D; *tbd*).

monitoring program. Only the brighter of the two M dwarfs is shown in this preliminary radial-velocity plot.

Acknowledgments

STELLA is funded by AIP through the State of Brandenburg and the Federal Ministry for Education and Science in Germany. It is operated jointly by AIP and the Instituto de Astrofísica de Canarias (IAC) at the Teide Observatory of the IAC. The authors thank the staff of the IAC for their great and continuous support to run STELLA.

References

- [1] K. G. Strassmeier, T. Granzer, M. Weber, et al., “The STELLA robotic observatory,” *Astronomische Nachrichten*, vol. 325, no. 6–8, pp. 527–532, 2004.
- [2] K. G. Strassmeier, T. Granzer, M. Weber, et al., “STELLA: two new robotic telescopes for binary-star research,” *Astrophysics and Space Science*, vol. 304, no. 1–4, pp. 397–400, 2006.
- [3] M. Weber, T. Granzer, K. G. Strassmeier, and M. Woche, “The STELLA robotic observatory: first two years of high-resolution spectroscopy,” in *Advanced Software and Control for Astronomy II*, vol. 7019 of *Proceedings of SPIE*, Marseille, France, June 2008.
- [4] T. Granzer, “Generic control of robotic telescopes,” in *Advanced Software, Control, and Communication Systems for Astronomy*, vol. 5496 of *Proceedings of SPIE*, pp. 667–678, Glasgow, UK, June 2004.
- [5] T. Granzer, M. Weber, and K. G. Strassmeier, “Automation hardware and software for the STELLA-I robotic telescope,” *Astronomische Nachrichten*, vol. 322, no. 5–6, pp. 295–302, 2001.
- [6] T. Granzer, “What makes an automated telescope robotic?” *Astronomische Nachrichten*, vol. 325, no. 6–8, pp. 513–518, 2004.
- [7] K. G. Strassmeier, K. Agabi, L. Agnoletto, et al., “Telescope and instrument robotization at Dome C,” *Astronomische Nachrichten*, vol. 328, no. 6, pp. 451–474, 2007.
- [8] C. W. Churchill and S. L. Allen, “A treatment for background correction on the Hamilton Echelle Spectrograph,” *Publications of the Astronomical Society of the Pacific*, vol. 107, no. 708, pp. 193–198, 1995.
- [9] C. Allende Prieto, “Automated analysis of stellar spectra,” *Astronomische Nachrichten*, vol. 325, no. 6–8, pp. 604–609, 2004.
- [10] J. Colomé and I. Ribas, “ICAT: a general purpose image reduction and analysis tool for robotic observatories,” in *Astronomical Data Management, 26th meeting of the IAU, Special Session 6*, Prague, Czech Republic, August, 2006, SPS6, #11.
- [11] D. Mink, “WCSTools 4.0: building astrometry and catalogs into pipelines,” in *Astronomical Data Analysis Software and Systems XV*, C. Gabriel, Ch. Arviset, D. Ponz, and E. Solano, Eds., vol. 351 of *Astronomical Society of the Pacific Conference Series*, p. 204, 2006.
- [12] E. Bertin and S. Arnouts, “SExtractor: software for source extraction,” *Astronomy and Astrophysics Supplement*, vol. 117, pp. 393–404, 1996.
- [13] P. B. Stetson, “DAOPHOT—a computer program for crowded-field stellar photometry,” *Publications of the Astronomical Society of the Pacific*, vol. 99, pp. 191–222, 1987.
- [14] E. Distefano, S. Messina, G. Cutispoto, et al., “ARCO: a program for automatic reduction of CCD observations,” N. Epchtein, et al., Ed., vol. 25 of *EAS Publications Series*, pp. 165–169, Roscoff, France, 2007.
- [15] K. G. Strassmeier, P. Reegen, and T. Granzer, “On the rotation period of Capella,” *Astronomische Nachrichten*, vol. 322, no. 2, pp. 115–124, 2001.
- [16] H. Korhonen, S. Hubrig, S. V. Berdyugina, et al., “First measurement of the magnetic field on FK Com and its relation to the contemporaneous star-spot locations,” *Monthly Notices of the Royal Astronomical Society*, vol. 395, no. 1, pp. 282–289, 2009.

- [17] B. Freytag, M. Steffen, and B. Dorch, “Spots on the surface of Betelgeuse—results from new 3D stellar convection models,” *Astronomische Nachrichten*, vol. 323, no. 3-4, pp. 213–219, 2002.
- [18] A. Duquennoy, M. Mayor, J. Andersen, J.-M. Carquillat, and P. North, “Duplicity in the solar neighbourhood. VI. The highly eccentric spectroscopic binary Gl 586A and associated multiple system,” *Astronomy and Astrophysics*, vol. 254, no. 1, pp. L13–L16, 1992.

Review Article

Monitoring of X-Ray Sources in the Optical Spectral Region

Vojtěch Šimon

Astronomical Institute, Academy of Sciences of the Czech Republic, 25165 Ondřejov, Czech Republic

Correspondence should be addressed to Vojtěch Šimon, simon@asu.cas.cz

Received 11 June 2009; Revised 17 November 2009; Accepted 19 November 2009

Academic Editor: Lorraine Hanlon

Copyright © 2010 Vojtěch Šimon. This is an open access article distributed under the Creative Commons Attribution License, which permits unrestricted use, distribution, and reproduction in any medium, provided the original work is properly cited.

We review current results and perspectives of the photometric monitoring of the optical counterparts of X-ray sources of various kinds (binary X-ray sources (cataclysmic variables and low-mass X-ray binaries, supersoft X-ray sources, microquasars), gamma-ray bursts). We discuss the problems of the monitoring of the individual kinds of objects in the optical and X-ray passbands. We show the importance of multifilter monitoring to obtain a deeper understanding of the physical processes and to resolve between the individual emission mechanisms. We also show that there are brief, unique, and little understood phenomena which are very promising targets for the optical monitoring, for example, flares in intermediate polars.

1. Introduction

This review deals with the observations of the optical counterparts of sources of high-energy emission. Since the research field of the high-energy sources is already very broad, we have to limit this topic. We will concentrate on the systems which contain a compact object with the mass comparable with the stars, that is, excluding supermassive black holes present in active galactic nuclei. Furthermore, we will concentrate on the systems and events in which the optical emission radiated by the accreting matter dominates. Our review is focused on binary X-ray sources (cataclysmic variables (CVs), low-mass X-ray binaries (LMXBs), supersoft X-ray sources, microquasars), gamma-ray bursts (GRBs). These objects are very important laboratories for the study of the physical processes occurring in extreme conditions. However, their activity on long timescales of months, years, and even decades remains little studied, although it is very important for our understanding of the relevant physics. A search for and analysis of rare dramatic variations of activity like outbursts of various kinds which reflect huge changes of the physical processes are particularly exciting.

Study of the long-term activity requires monitoring of the individual objects (if they are already identified), or even

monitoring of the large fields of the sky to search for the events like optical afterglows of GRBs.

2. Binary X-Ray Sources

CVs and LMXBs are binary systems in the phase of mass exchange (e.g., [1, 2]). They contain a compact object (white dwarf in CVs, neutron star, or black hole in LMXBs) which accretes matter from its Roche lobe-filling companion (the so-called donor). The donor is usually a late type main-sequence star, but also rare cases where it is a subgiant or a white dwarf are known (the type of the donor depends on the orbital period ranging from several minutes to several days, mostly several hours). These systems are emitters of radiation over a very broad range of wavelengths, from high energy (X-ray, sometimes even gamma-ray) to the optical and infrared, in some cases even to the radio. In most cases and spectral passbands, the luminosity of these systems is dominated by the light originating from the transferring matter, not from the stellar components. The accretion process is thus the dominant source of their luminosity. These systems are extremely active in real time over a very broad range of timescales, from seconds to decades, not speaking about their evolutionary changes. This activity is directly related to the

physical processes in the transferring matter and its accretion onto the compact object.

2.1. Mechanisms for the Long-Term Activity in CVs and LMXBs. Several mechanisms can cause the long-term variations of brightness in CVs and LMXBs (e.g., [1]).

- (a) Changes of the mass transfer rate \dot{m} from the donor onto the compact object. They occur on the timescale of days, weeks, months, and years. They give rise to the luminosity of the accretion disk and hence to the fluctuations of the brightness of the system, including the transitions between the high and low states in both CVs and LMXBs. The amplitude of these variations can be several magnitudes.
- (b) Thermal-viscous instability of the accretion disk. It gives rise to the outbursts in CVs and LMXBs. These outbursts have the typical optical amplitudes between 2 and 5 mag in CVs called dwarf novae and between 3 and 7 mag in LMXBs called soft X-ray transients (SXTs). The typical recurrence time T_C (cycle-length) of these outbursts is weeks and months in dwarf novae. However, it is often years and decades in the case of SXTs. The typical length of the outburst is days and weeks in dwarf novae, but weeks and months in SXTs.
- (c) Hydrogen burning on the white dwarf. Episodic burning leads to the classical nova explosion. The amplitude of the explosion is very high, about 12 mag, with the duration of the event being from weeks to months. Steady-state burning is thought to explain supersoft X-ray sources (a unique type of CVs with a very high \dot{m} [3]). Such objects are also luminous in the optical passband. Some of them undergo fluctuations of brightness and high/low state transitions with the amplitude of 1–2 mag on the timescales of weeks and months.

This very brief overview of the mechanisms clearly shows that CVs and LMXBs with their wild activity are very attractive targets for the monitoring. Some of these variations and events may be cyclic, but they are not periodic. In additions, dramatic changes of the activity on the timescale of years and decades were observed in some systems, so our understanding of a given object can hardly be satisfactory if the physical processes which control its long-term activity are not taken into account.

2.2. Problems in the Long-Term Coverage. The different X-ray/optical intensity ratios of the individual categories of binary X-ray sources impose problems on the long-term coverage of their activity.

LMXBs are often bright in X-rays at least in their outburst. Several tens of them are easily observable by the X-ray monitors onboard the satellites, but they are often faint in the optical passband. They are usually fainter than 16–18 mag except infrequent outbursts, so the existing optical data are often fragmentary or even absent.

CVs are often relatively bright in the optical passband, so good long-term coverage is available at least for some of them. Nevertheless, more deep observations are needed in quiescence between outbursts and in the episodes of the low state, since the brightness of some of these systems is below the detection limit of the usually used visual observations in these states of activity. The X-ray data of CVs are often fragmentary because most of these systems are too faint for the X-ray monitors.

Transitions between the activity states (e.g., outbursts, high/low state transitions) are often fast and unpredictable. Monitors are thus needed to resolve them. Occasional pointing is not enough because of several reasons: many pieces of information on the time evolution are lost; time allocation has to be justified (search for unexpected behavior of the object is usually not approved).

2.3. Properties of the Outburst Light Curves in Dwarf Novae. Investigation of any more general properties of outbursts in dwarf novae deserves coverage of several outbursts in a given binary. Monitoring is necessary to obtain a sufficient number of the well-mapped outbursts to collect a meaningful ensemble of outbursts. The typical duration of the outburst is from several days to one or two weeks, while the recurrence time T_C of outbursts is from several weeks to several months, although exceptions exist (e.g., [1]). A single observation per night may thus be sufficient to cover the profile of outburst, although denser coverage is desirable for the often steep rising branch. The case of DX And can serve as an example of the long-term activity [4] (Figure 1(a)). The peak magnitude of outbursts turns out to be variable by 1.3 mag_{vis}. While the slope of the rising branches of the outbursts was found to be largely dependent on the peak magnitude (brighter outbursts having steeper rises), the decaying branches remain stable and very similar for most outbursts. Shifting the individual outbursts along the time axis to match the decay branch of the template then enabled to investigate the properties of the profiles of the light curves of the ensemble. The relation between the peak magnitude of the outburst and the slope of its rising branch (Figure 1(b)) can thus be established. This can be used for testing the thermal-viscous instability model (e.g., [5]), particularly for the discrimination between the case A (outside-in) and case B (inside-out) outbursts.

The determination of the location where the outburst starts, that is, case A versus case B event, is important for the study of the physics of outbursts in a large ensemble of dwarf novae with various system parameters like the orbital period, and so forth. Clearly, the outbursts in more systems have to be studied in a similar way as DX And.

The magnetic field of the white dwarf in intermediate polars (CVs with a magnetized white dwarf (e.g., [1])) can influence the profile and recurrence time (cycle-length) T_C of their outbursts caused by the thermal-viscous instability [7]. This results in short and infrequent outbursts like in DO Dra (e.g., [8]). It is thus quite possible that many such outbursts in CVs which may be intermediate polars remain unobserved due to insufficient coverage by the data. Clearly, more attention to monitoring of intermediate polars and the

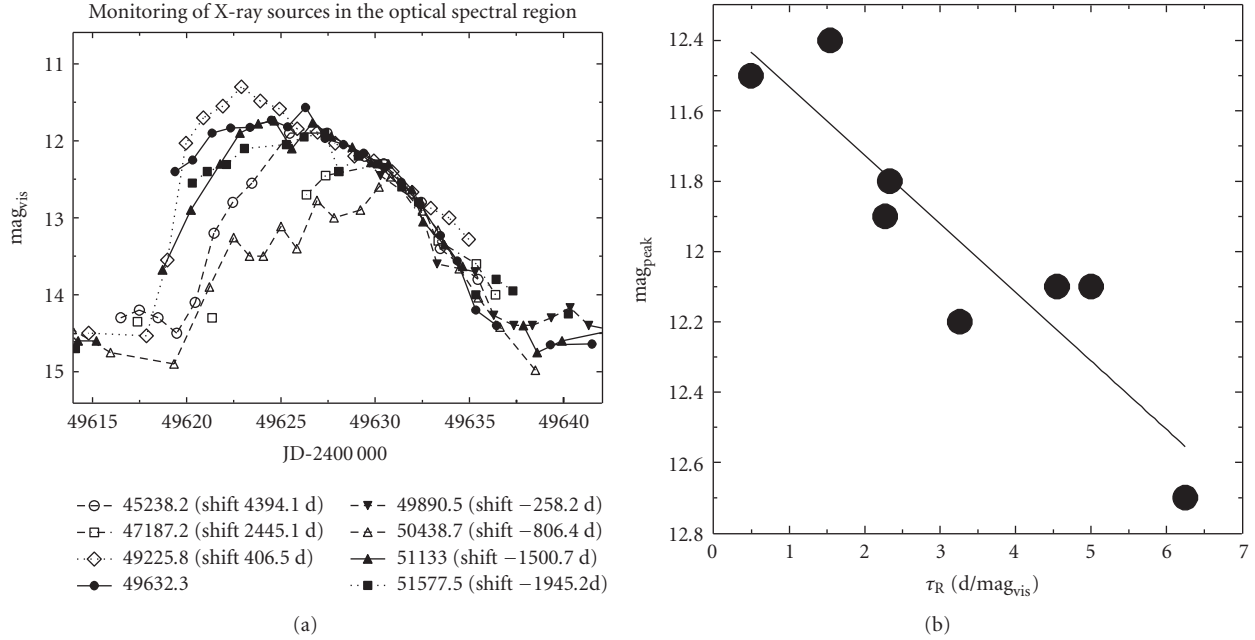


FIGURE 1: (a) Profiles of the outbursts in the dwarf nova DX And (observations from the AFOEV database). One-day means were connected by a line in densely covered parts for convenience. The individual outbursts were shifted along the time axis to match the decaying branch of the template—the time of crossing 12.8 mag_{vis} and the shifts with respect to the template are listed. (b) The relation between the peak magnitude mag_{peak} of the outburst and the slope of its rising branch in DX And. The slope (rate of rise τ_R) is expressed in days $\text{mag}_{\text{vis}}^{-1}$. Adapted from [4].

investigation of the properties of their outbursts should be paid.

Some dwarf novae display the cyclic variations of the brightness in quiescence, with the typical cycle-length of several years, which was attributed to the solar-type cycles of activity of the donor [9]. The typical brightness of many dwarf novae in quiescence $\sim 14\text{--}17 \text{ mag(V)}$ enables to monitor such systems and to investigate these variations and their relation to the outburst parameters.

The state of the long-term activity of at least some CVs is affected by their classical nova explosions. The large influence of these events can be apparent even decades after the explosion. At least some CVs which were observed to explode as classical novae display a complicated evolution of their activity after return to quiescence. The intermediate polar GK Per (Nova Per 1901/A 0327+43) [10] is an important example in this regard (e.g., [6, 11, 12]). Fluctuations of its brightness by about 1 mag on the timescale of months appeared after return to quiescence. Later, they developed into the discrete 2–3 mag optical outbursts which recur on timescales of hundreds of days. Their amplitude and recurrence time tend to increase. A similar behavior is observed in V446 Her (Nova Her 1960) [13]. The behavior of such systems can be caused by the decrease of the temperature of the white dwarf in the decades following the nova explosion. The irradiation of the disk by the very hot white dwarf helps the disk remain in the hot, luminous state, so no outbursts occur. The cooling of the white dwarf can lead to the evolution of the thermal-viscous instability of the disk and to the appearance of the outbursts.

Current results show that the relation between the profiles of the outburst of dwarf nova in the optical and X-ray passbands is very complicated, as shown by the pointed observations of SS Cyg by [14, 15]. Such studies of a larger ensemble of dwarf novae are important because these multifrequency observations enable us to investigate the behavior of various parts of the system; X-rays come from the close vicinity of the white dwarf, while the optical emission originates from a large area of the accretion disk. Indeed, the observations of [14, 15] show that the boundary layer changes from the optically thin, geometrically thick to the optically thick, geometrically thin during outburst. However, the problem is the low ratio of the X-ray to the optical intensity of many CVs and the complicated variations of the X-ray intensity during outburst. Only a very few CVs were detected by the X-ray monitor ASM/RXTE. The X-ray intensity of SS Cyg in the 1.5–12 keV passband of ASM/RXTE decreases below its quiescent level during outburst [16]. The X-ray intensity of GK Per observed by this instrument rises only slightly during the optical outburst, and the profile of the X-ray and optical light curve largely differ from each other in the time of the peak optical brightness [6] (Figure 2). The start of the X-ray outburst can precede the start of the optical one by up to 40 days [17, 18]. Figure 2 shows the optical and X-ray profile of a well-mapped outburst. The optical data used for Figure 2(a) were fitted by the code HEC13 written by [19]. The code is based on the method of [20, 21]. This method can fit a smooth curve to the data no matter what their profile is. The resulting fit consists of the mean points, calculated to the individual observed

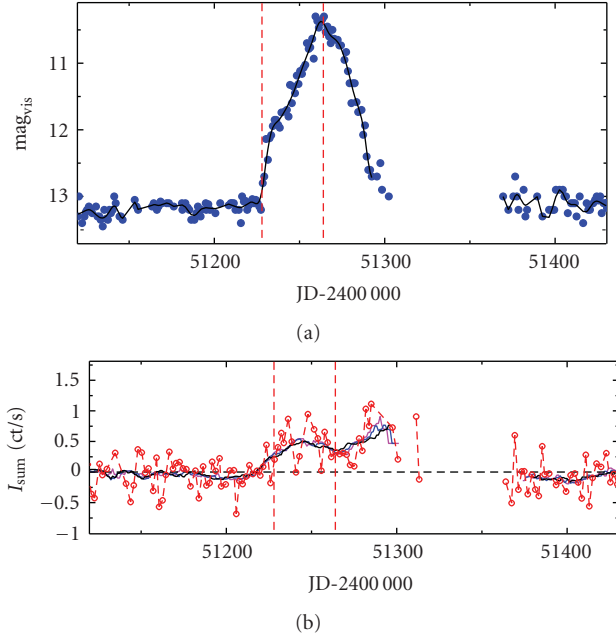


FIGURE 2: Relation between the outburst light curves of GK Per in the optical (a) and X-ray (1.5–12 keV) (b) passbands. The optical data are from the AFOEV database, while the X-ray ones were obtained by ASM/RXTE. The smooth line in (a) represents the fit by the code HEC13. The thick lines in (b) denote the smoothing by the moving averages. The dashed vertical lines mark the times of the onset and the maximum light of the outburst in the optical region. Adapted from [6]. See Section 2.3 for details.

points of the curve. A set of fits to the data with the different input parameters ϵ and ΔT was generated and submitted to inspection. It was found that the fit with $\epsilon = 0.1$, $\Delta T = 5$ d reproduces the main features of the light curve and enhances the visibility of the main profile. It is true that this method is somewhat subjective but it enables us to find a compromise between a curve running through all the observed values and an ideal smooth curve. The X-ray signal in Figure 2(b) was smoothed by the moving averages with the filter half-widths of 10 d, 12 d, and 15 d. They reproduce the main features of the light curve and significantly enhance the visibility of the main profile.

We can see that the analysis of the properties of outbursts in dwarf novae gives us the possibilities to investigate various phenomena. Even in a single system, the individual outbursts can display largely different profiles. Search for the common features is thus needed. Also a search for the relation between the outburst properties and the long-term activity of a given system is very important.

2.4. Variations of the Outburst Recurrence Time in Dwarf Novae. It is known that the recurrence time T_C of outbursts in dwarf novae can vary by a large amount. However, analyses using the method of the O–C residuals from a trial period [22, 23] have shown that the variations of T_C are not chaotic and that well-defined trends can be found in the O–C curves. The relation between the O–C curve and T_C is as follows: a

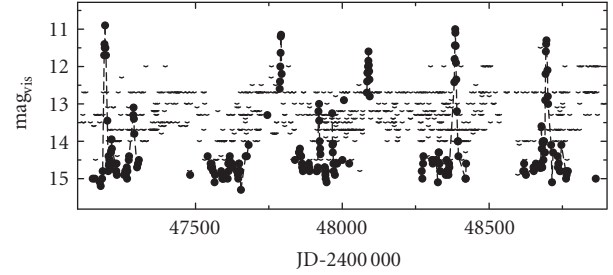


FIGURE 3: (a) Part of the light curve of the dwarf nova CH UMa showing the bright and faint outbursts (AFOEV data). Closed circles denote detections. Upper limits are marked by \vee . Adapted from [23].

linear profile of the O–C curve, no matter what its slope is, implies a constant T_C . A parabolic profile of the O–C curve implies a linear change of T_C (T_C is increasing/decreasing if the parabola is curved upward/downward). This method can work even if some outbursts are missing due to the gaps in the data, if the profile of the O–C curve is not too complicated. Monitoring is thus needed to avoid or at least diminish the gaps in the data.

Variations of T_C in CH UMa can serve as an example. This system displays two types of outburst (bright and faint) (Figure 3). Evolution of the peak magnitude of these outbursts is displayed in Figure 4(a) while the accompanying O–C variations can be seen in Figure 4(b). The observed long-term trends in the O–C curves suggest that the individual outbursts depend on each other in a given system. T_C shows large jumps and/or cyclic variations, but the precise profile of the O–C curve depends on the given system. The episodes or intervals of both increase and decrease of T_C in a given dwarf nova are not explicable by the evolutionary processes in the system. Extensive analysis of the relation between T_C and the outburst parameters is needed to find the physical mechanisms (e.g., variations of \dot{m} or the disk viscosity) which control the activity of these systems.

2.5. Supersoft X-Ray Sources. As mentioned in Section 2.1, supersoft X-ray sources are a unique type of X-ray sources. They are usually close systems, with their orbital periods of the order of hours to a few days, in which the mass transfer onto a white dwarf occurs at a very high rate ($\dot{m} \approx 10^{-7} M_\odot \text{ yr}^{-1}$). This allows a steady-state hydrogen burning on the surface of the white dwarf [3]. This burning is the source of intense soft X-ray radiation, but its detectability depends on the interstellar extinction and metallicity of the source. The optical radiation originates mostly from the reprocessing off the X-rays in the disk and the donor star [24]. The known supersoft X-ray sources are mostly located in the Magellanic Clouds and in M31, because soft X-rays are easily absorbed in the interstellar medium in our Galaxy. In addition to these supersoft X-ray sources, there are several groups of objects that could be their close relatives. V Sge stars display very similar properties in the optical passband as the above mentioned supersoft X-ray sources. The potential members were listed by [25]. The work in [26] revealed

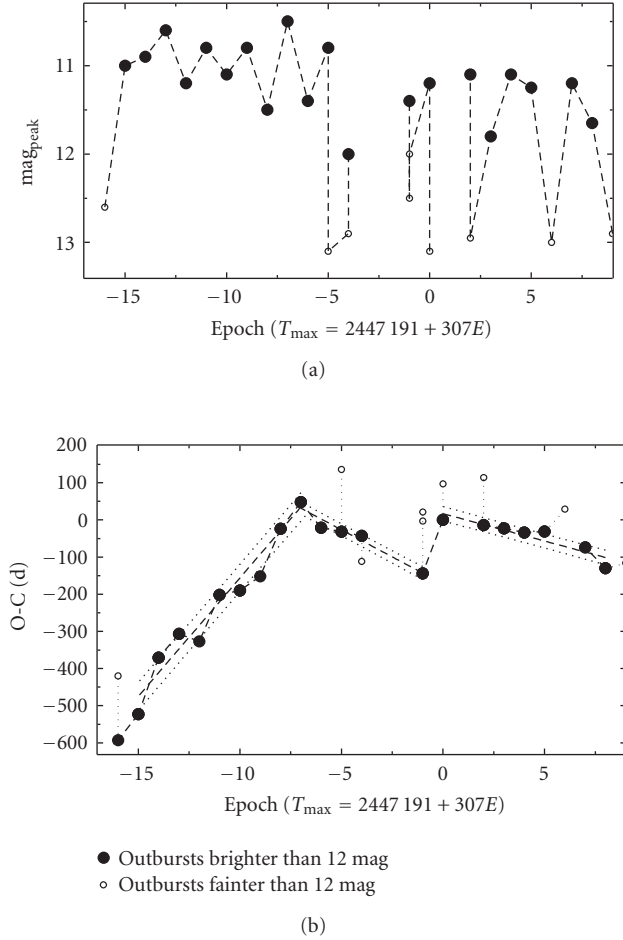


FIGURE 4: (a) Evolution of the peak magnitude of the outbursts in CH UMa. The bright and faint outbursts are marked by closed and open circles, respectively. (b) The O-C diagram (defined in Section 2.4) for the outbursts in CH UMa. The ephemeris is included in the title of the abscissa. The bright and faint outbursts are resolved. The O-C values of the faint outbursts are negative (positive) if they occurred before (after) the following (preceding) bright outburst. The faint outbursts are connected with the bright outburst, having the same epoch number, by a line for clarity. Adapted from [23].

that V Sge is a luminous, very soft X-ray source during the optical low state, turning into a faint hard source in the optical high state due to a variable amount of circumstellar matter. The optical changes are thus in antiphase with those in X-rays, in a similar way as in another supersoft X-ray source, RX J0513.9-6951 [27]. V Sge is a very active system; it displays a complicated long-term activity, whose character changed considerably during about 40 years (e.g., [28]). Some symbiotic systems can be supersoft X-ray sources, too (e.g., [29, 30]). They usually contain a white dwarf, accreting matter from its red giant companion via a strong stellar wind or Roche lobe overflow. They often display strong and complicated long-term activity, with the typical amplitude exceeding 1-2 mag. Some peculiar symbiotic novae may be related to supersoft X-ray sources, too.

2.6. Polars. Polars are CVs with a strongly magnetized white dwarf accretor (e.g., [1]). Streaming matter is threaded through the accretion column onto the magnetic pole(s) of the white dwarf because the strong magnetic field of the white dwarf prevents formation of the accretion disk. This transferring matter is usually the dominant source of radiation in the optical and X-ray spectral regions in the high state. Since the disk is missing, the variations of the mass transfer rate are rapidly reflected in the luminosity of the polar. The matter falling onto the white dwarf forms an accretion column above its surface. This column is a source of radiation via several mechanisms. Cyclotron emission is dominant in the optical and UV passbands, while the medium and hard X-ray emission is due to bremsstrahlung. Also soft X-ray excess, probably caused by the thermal emission from the surface of the white dwarf heated by the impact of matter, can be present (e.g., [1]). Some polars occasionally enter a low state (e.g., [31]) because of a transient reduction or cessation of the mass transfer. Only when the polar enters this low state, the light contribution of the donor and the white dwarf becomes significant. The X-ray luminosity fades substantially in this time period because neither the white dwarf nor the donor is strong X-ray emitters.

An example of the complicated relation between the optical and X-ray (1.5–12 keV) intensity in the individual high states of AM Her is displayed in Figure 5. Investigation of this relation enables us to relate the processes responsible for the emission in these spectral regions. AM Her is one of a very few CVs detected by ASM/RXTE. Nevertheless, the X-ray signal is weak, hence displaying a significant scatter. The data were therefore fitted by the code HEC13 (see Section 2.6 for details). It was found that the fits with $\epsilon = 1$, $\Delta T = 25$ d, and $\Delta T = 35$ d reproduce the main features of the light curve and significantly enhance the visibility of the main profile. This procedure also shows that the optical to X-ray intensity ratio differs considerably for the individual episodes of the high state (Figure 5(c)).

2.7. Possibility to Detect and Identify Rare Phenomena in CVs. Some intermediate polars, that is, CVs with a mildly magnetized white dwarf (e.g., [1]), were observed to display rare, peculiar brief flares with an amplitude larger than 1 magnitude. TV Col undergoes rare flares with an amplitude of about 2 mag. The duration of such an event is uncertain because of the gaps in the coverage, but it is likely to be shorter than one day (e.g., [32, 33]). The temperature of the inner disk region increased during this event [32]. Two flares, one of them represented by only a single point, were observed in V1062 Tau [34]. Also V1223 Sgr was observed to undergo two flares. The first one was sufficiently covered to show that it lasted only for several hours [35]. The second flare was found on a photographic plate (see below). The brevity of such flares makes their study very difficult. It is not known how frequent these flares can be because only a few such events have been observed in a given system due to fragmentary data. Monitoring of a large sample of systems can shed more light on the parameters of such events

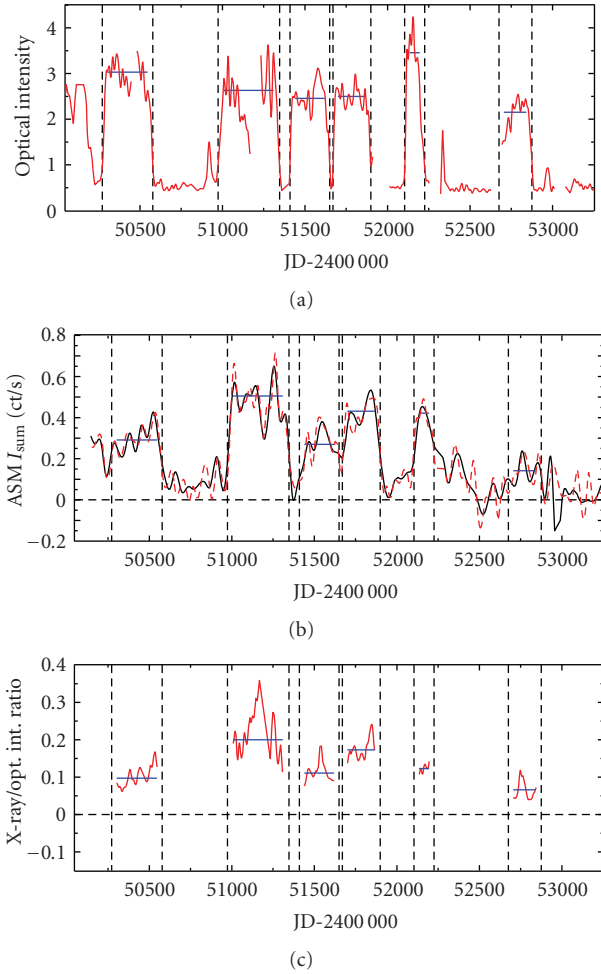


FIGURE 5: The light curve of the polar AM Her in the optical (a) (AFOEV data) and X-ray band (b) (ASM/RXTE data). The ratio of the X-ray to the optical intensity is shown in (c). Only HEC13 fits are shown. The dashed vertical lines denote the crossing of the level of 14.3 mag_{vis}. Solid horizontal lines denote the average intensity of the given high state. See Section 2.6 for details.

(amplitude, duration, recurrence time, variations of the color indices, relation of these events to the state of the long-term activity). Observing this sample can also help us reveal what system parameters are needed to give rise to such flares (orbital period, magnetic field, and spin period of the white dwarf...).

Also investigation of the relation of the flares to the long-term activity is important. Between the flares, the B magnitude of TV Col was at ~ 14.5 mag(B), without any fluctuations larger than several tenths of mag [33]. V1062 Tau displayed both high and low states and the observed flare occurred shortly after return to the high state [34]. V1223 Sgr represents an important example. Analysis of the Bamberg Observatory plates (one plate per night) (Figure 6(a)) clearly shows the importance of monitoring. Although the sampling of these data does not allow to determine the profile of the flare, the long-term coverage by the plates enables us to study the relation of the flare to the surrounding activity.

The statistical distribution of the brightness of V1223 Sgr is helpful in this case (Figure 6(b)). The marginally double-peaked distribution caused by the “common” variability of this system with the peak-to-peak amplitude of about 1.2 mag is clearly visible. It is defined by most measurements. Notice the sharp edge of this distribution at about 12.3 mag. The largely deviating point marked with an arrow represents the outburst in JD 2439 383. This point is not a simple continuation of the “common” variability. The outburst, albeit defined only by a single data point and representing thus only slightly more than 1 percent of the observations, significantly affects the skewness and excess of the statistical distribution. On the other hand, the mean magnitude and its standard deviation are affected by the outburst only marginally. These outbursts thus can be responsible for the “outliers” in the long-term light curve, although their profiles remain unresolved due to the sampling.

2.8. Properties of the Outburst Light Curves in SXTs. Since SXTs are often intense X-ray emitters during outbursts, these events are usually discovered by the X-ray monitors onboard the satellites. Nevertheless, the optical monitoring is important also in this case. The typical duration of the outburst is from several weeks to more than a month, while the recurrence time T_C of outbursts is more than a year, although exceptions exist (e.g., [2]). A single observation per night may thus be sufficient to cover the profile of outburst, although denser coverage is desirable for the often steep rising branch. The rise of the optical emission to the peak magnitude may even be of the order of a day. In the case of GRO J1655-40, the 1996 outburst begun sooner in the optical passband than in X-rays [36]. It is important to note that the observed relation between the profile of the optical and X-ray light curve differs not only for the individual SXTs, but also for a single binary if more of its outbursts were observed. The issue of what comes first, that is, X-rays or optical emission, remains ambiguous. Simultaneous observations of a series of outbursts of Aql X-1/V1333 Aql in the optical and X-ray passbands by [37] revealed that the duration of the outburst in various passbands and the X-ray/optical intensity ratio differ substantially for the individual events. The optical versus soft X-ray correlation during a set of outbursts revealed that two kinds of outbursts exist in this system. In addition, Aql X-1 displayed a peculiar flare with the reddening of the $B-V$ index during its 1978 outburst [38]. Its nature is unclear. Since the duration of this flare was considerably shorter than the outburst itself, monitoring in various filters during the outburst is very important.

The conditions in the disk of SXTs, reflected in the light curves of the outbursts, are affected by the presence of a very hot inner disk region; it acts as irradiating source during outburst and is thought to modify the disk structure [39, 40]. Nevertheless, the observations show that the relation between the optical and X-ray flux, hence irradiation of the disk, is more complicated than thought previously [41]. The parameters of irradiation of the disk can be studied by analysis of the profile of the light curve of the outburst. In order to obtain a meaningful ensemble of outbursts,

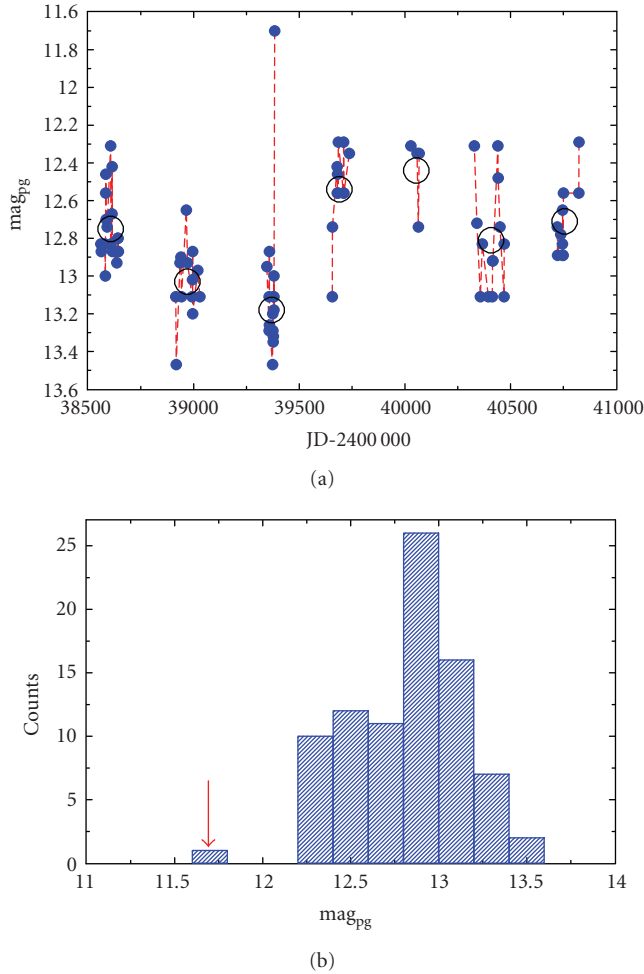


FIGURE 6: (a) Segment of the long-term light curve of the intermediate polar V1223 Sgr on the Bamberg photographic plates. The intervals of missing data are seasonal gaps. Closed circles represent the individual observations. The data in the densely covered segments are connected by a line to guide the eye though the complicated profile of the light curve. Large open circles denote the annular averages. The largely deviating point in JD 2439 383 represents a flare and is not included in the annular mean. (b) Statistical distribution of the brightness in the long-term light curve. The largely deviating point marked with an arrow represents the flare.

monitoring is necessary to obtain a sufficient number of the well-mapped outbursts in a given SXT. Also spectroscopic observations are important in this regard. Although it is difficult to arrange a spectroscopic monitoring of such relatively faint sources like SXTs, rapid communication of the outburst to the spectroscopists will be certainly helpful.

At least some SXTs display significant variations of their quiescent optical brightness. The long-term optical variations of GS 1354-64/BW Cir observed by [42] had the amplitude of about 1 mag. Since SXTs are very faint in quiescence (~ 20 mag(V)), their optical monitoring is a difficult task. Dense series of the multifilter observations are

needed to determine the profile of such variations (small outbursts, gradual waves?) and to resolve among the individual emission mechanisms (e.g., thermal or synchrotron).

2.9. Variations of the Outburst Recurrence Time in SXTs. The recurrence time T_C of outbursts in SXTs in which a series of outbursts was observed varies by a large amount in a similar way as in dwarf novae [43] (Section 2.4). In some extreme cases, the mean T_C of some SXTs can even be as short as those in dwarf novae with long orbital period (CH UMa, DX And, GK Per). The available observations suggest that the individual outbursts in a given system are dependent on each other. T_C shows large jumps and/or cyclic variations, but the precise profile of the O–C curve depends on the given system. The episodes or intervals of both increase and decrease of T_C in a given SXT are not explicable by the evolutionary processes. It emerges that the disk of SXT is not considerably depleted in outburst, but that a lot of matter remains (at least in some systems). A gradual accumulation and redistribution of matter in the outer disk region plays a large role in the observed activity.

2.10. Optically Bright Persistent LMXBs. Although studies of the long-term optical activity of persistent X-ray binary sources are rare, the available findings show strong and mostly unexplored activity.

HZ Her/Her X-1 is an LMXB with the orbital period of 1.7 days. It consists of a neutron star and a main sequence donor (e.g., [44]). The principal source of the optical variability is the changing aspect of the secondary's hemisphere, facing the neutron star and strongly heated by X-rays. The usual kind of the optical activity of HZ Her with the large orbital modulation (active state) is occasionally interrupted by the intervals of inactive states. In that time, the heating disappears and the system remains near the minimum brightness of the orbital modulation (e.g., [45]). All episodes of the inactive state were discovered only on archival plates and were shown to recur on a time scale of about 10 years in the first half of the 20th century [46], prior to the onset of the X-ray satellite era.

The long-term light curve of HZ Her composed of the photographic observations is displayed in Figure 7(a). Both the active state and two episodes of the low, inactive state were captured. The remarkably different profiles of the orbital modulation in both states can be seen in Figure 7(b). Notice the much smaller amplitude, appearance of the secondary minimum lagging behind phase 0.5, and the flat profile outside the primary and secondary minima. It can be seen that even one plate per night is enough to reveal the character of the activity in HZ Her.

Sco X-1 is an optically bright (~ 12.5 – 13.5 mag(V)) and hence easily observable LMXB. Its long-term light curve in blue light made of measurements on archival photographic plates [48] displayed fluctuations by about 1 mag, with a trend of fading. This system is also significantly variable on short timescales, during a single night [49]. Its optical brightness is related to the complicated variations of the X-ray spectrum [50].

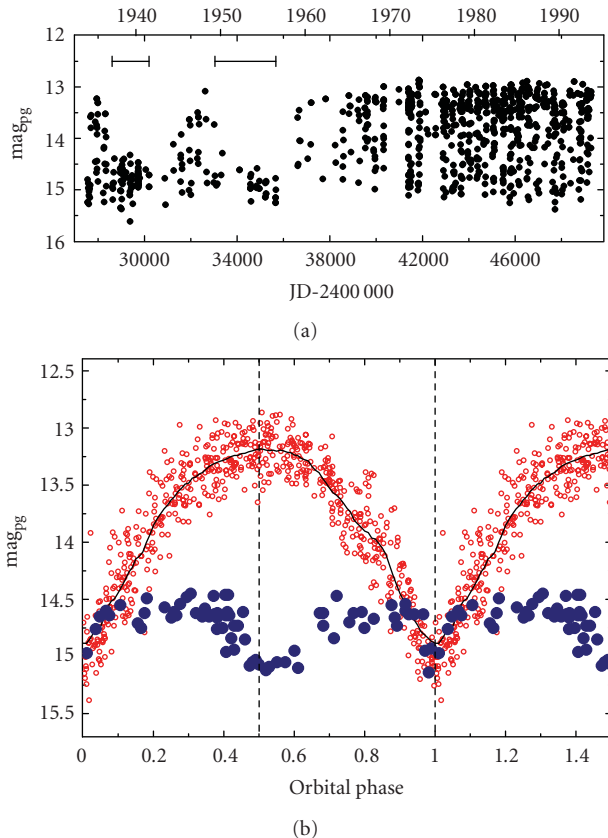


FIGURE 7: (a) The optical light curve of HZ Her/Her X-1, composed of 807 observations obtained with the D 40 cm and D 17 cm astrographs of the Sonneberg Observatory. The intervals of inactive states are marked by the horizontal bars. Adapted from [47]. (b) The orbital modulation of HZ Her. Open circles denote the extended active state between February 1959 and October 1993 [47]; the smooth line represents the moving averages of these data. Closed circles mark the orbital modulation in the low state observed by [45].

2.11. Microquasars. Microquasars are X-ray binaries with relativistic jets [51]. This category comprises both high- and low-mass systems [52], including some SXTs (e.g., GRO J1655-40 [53]) mentioned in Section 2.8. Here, we point the attention to two relatively bright, peculiar systems which displayed large-amplitude outbursts seen in the X-ray, optical, and radio bands. Relativistic jets were launched during these events.

CI Cam (XTE J0421+560) underwent an intense outburst in 1998. Its characteristics are quite atypical among X-ray transients (e.g., [54]). The X-ray outburst was accompanied by a strong brightening in the optical and radio. It can be explained by the thermal-viscous instability of the accretion disk, analogous to the outbursts of SXTs [55, 56]. This event influenced both the photometric and spectroscopic properties of the system (e.g., [57, 58]). The compact object is most likely a black hole or a neutron star [55, 59]. The photometric history during the years 1928–1939 and 1989–2004 is shown in Figure 8. Notice the difference in the activity before and after the outburst.

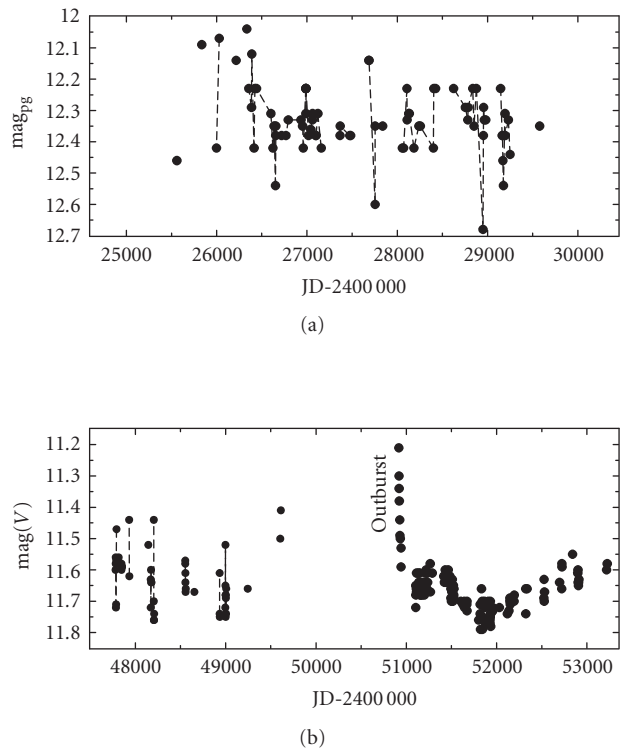


FIGURE 8: (a) Photometric history of the microquasar CI Cam according to the Bamberg photographic observations in the blue band (similar to the B band) (1928–1939). Points are connected by a line in the densely covered segments. Typical uncertainty is 0.05 mag. (b) The activity in the V passband in 1989–2004. The peak of the 1998 outburst is out of the scale. Adapted from [58, 60].

The postoutburst activity of CI Cam (1999–2004) displayed significant variations of the continuum, as suggested by the changes of the color indices. This activity was interpreted by [57, 58] as due to several superposed spectral components, with the division of their dominant contributions near $\lambda = 550$ nm: free-free emission from the wind and/or envelope in the red and near-IR, and a (pseudo)photospheric emission in the blue region. Hysteresis of the shifts in the color-color diagram can be ascribed to the $H\alpha$ changes which are not any simple variations of the combined continuum and weaker emission lines at stable $H\alpha$ emission. The $H\alpha$ region evolves on the timescale of hundreds of days [58].

Huge changes of the extinction in X-rays and no detectable extinction variations in the optical passband suggest that the X-ray emission comes from the close vicinity of the mass-accreting black hole (refilling of the disk after the outburst?), not from the giant donor [58].

We can thus see that this system is clearly active even in quiescence and especially the large change of the character of its activity after the outburst deserves further careful monitoring over a broad spectral range.

V4641 Sgr (SAX J1819.3-2525) represents another example of a microquasar (B9III donor and a black hole [61]) with a major outburst in September 1999, observed in X-rays,

optical, and radio. Radio structures suggest superluminal jet ejection [62]. Several smaller peculiar outbursts with the multipeak structure followed the 1999 event. Their mean T_C was 377 days, with a trend of a decrease (e.g., [63]). They were interpreted as cyclo-synchrotron emission associated with magnetic flares [64]. The preoutburst observations on the Bamberg photographic plates (1964–1967) reveal ongoing activity of the system. It displayed low-amplitude fluctuations on the timescale of several weeks, independent on the orbital phase [63].

2.12. Optical Afterglows of GRBs and Their Color Indices.

The relativistic jet radiating the synchrotron emission is the dominant source of emission of GRB and its afterglow from gamma-ray to the optical, infrared, and radio spectral region [65]. While the duration of the gamma-ray emission is typically from less than a second to several minutes, optical afterglow lasts much longer (days). Optical emission can be therefore searched for even using untriggered observations. The intensity of the emission depends on the inclination angle of the jet with respect to the observer; the jet has to point almost exactly to the observer.

Deep observations are needed to detect optical afterglow in later phases after the gamma-ray trigger, since most of them are fainter than 18 mag(R) at $t - T_0 \approx 1$ day, although some of them can be brighter than 14 mag(R) in their early phase, at $t - T_0 \approx 0.01$ day [66]. The profile of the light curves suggests that most optical afterglows are the brightest immediately after gamma-ray trigger, and display a power-law decay later on. Many observed optical afterglows display striking similarities in both their time evolution and spectra (Figure 9—ensemble of optical afterglows [67, 68], optical afterglow of GRB 060218 [69–71]). Their absolute R magnitudes M_{R_0} were k -corrected according to [67] and corrected for the Galactic extinction according to [72]. The profiles of these curves are mutually similar although M_{R_0} of the individual afterglows can differ by about 4 mag at a given time since the gamma-ray trigger in rest frame, $(t - T_0)_{\text{rest}}$.

spite of the scatter in magnitude, the individual events display remarkably similar color indices with negligible changes during the first several days, which is important for discriminating them from other kinds of objects. Photometric observations using the commonly available filters provide us with important information on the spectral profiles of optical afterglows. Color-color ($B-V$ versus $V-R$) diagram of optical afterglows from Figure 9 is displayed in Figure 10. It contains the color indices in the observer frame. Only observations within $t - T_0 < 10$ days were plotted. Multiple indices of the same optical afterglow are connected by lines for convenience. They were corrected for the Galactic reddening, so only reddening in the host galaxies of these GRBs could remain. Notice a very strong clustering of the color indices of most afterglows. The same clustering was also obtained for the $V-R$ versus $R-I$ diagram. This suggests that although these events possess a large range of redshifts z (they are at $z < 3.5$), they display very similar spectra. Besides the astrophysical analysis, these specific color indices give us

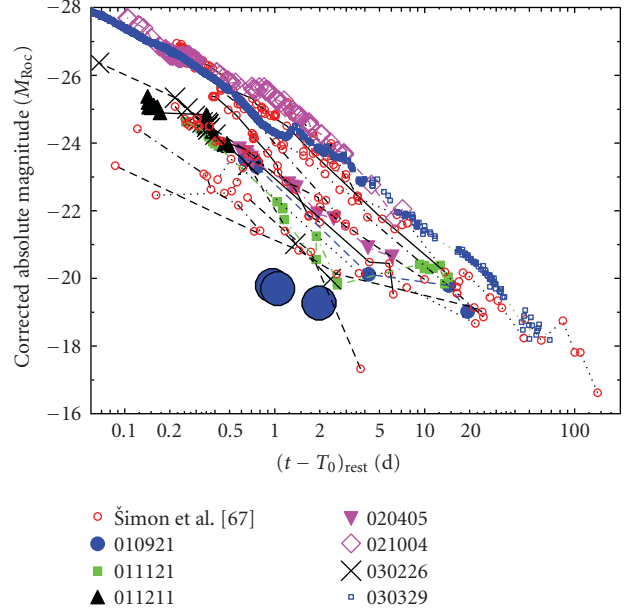


FIGURE 9: k -corrected absolute R magnitudes of the ensemble of optical afterglows of long GRBs from [67, 68]. The magnitudes of the early phase of optical afterglow of GRB 060218 are plotted as large closed circles. Rest frame time interval $(t - T_0)_{\text{rest}}$ is used for the abscissa.

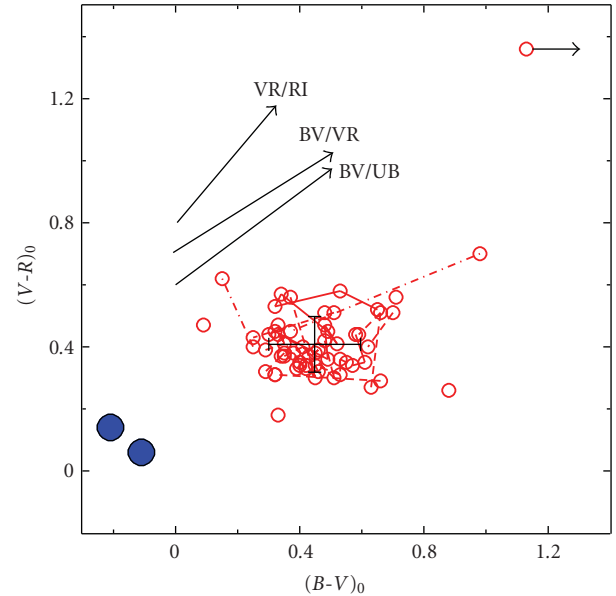


FIGURE 10: Color-color ($B-V$ versus $V-R$) diagram of optical afterglows of long GRBs. The color indices were corrected for the Galactic reddening. Multiple indices of the same optical afterglow are connected by lines for convenience. Optical afterglows of the ensemble [67, 68] are denoted by open red circles. The mean colors (centroid) of the whole ensemble, including the standard deviations, are marked by the large cross. The outlying optical afterglow of GRB 060218 (closed blue circles) is not included in the calculation of the centroid. The representative reddening paths for $E_{B-V} = 0.5$ are shown. Adapted from [67, 68], where a detailed information can be found.

a hope to resolve whether an optical transient event is related to a GRB even without available gamma-ray detection. Of course, a trivial case is that a GRB occurs outside the field of view of the gamma-ray telescopes of the operating satellites, so only optical transient can be detected by the observer on the Earth. Nevertheless, the missing gamma-ray emission can indicate the so-called orphan afterglow. These events represent an important challenge for astrophysics. They can be caused by several mechanisms. Gamma-ray emission from many GRBs cannot be observed because the jet is not pointing to the observer, but the late-time afterglow is less beamed and can reach us [73]. Failed GRBs [74] are another possibility. According to [74], the number of failed GRBs may even be much larger than that of successful bursts and so there should be many orphan afterglows. Deep optical monitoring can decide between these possibilities. Multifilter observations are important to help discrimination between optical afterglows and other kinds of transients. Since these events are extragalactic, the magnitude of a given transient can be corrected for the reddening caused by the dust in our Galaxy according to [72]. Nevertheless, the extinction and reddening caused by the dust in our Galaxy are not serious if the parts of the sky far from the Galactic plane are monitored. The scatter of the color indices of the individual optical afterglows is therefore expected to be small even without such a correction.

3. Conclusions

We can see that the dense series of observations are necessary to investigate the properties of the long-term activity of the X-ray sources. Especially resolving the profiles of the state transitions, like the rising and decaying branches of outbursts, is important for our understanding of the relevant physical processes involved. It is also important to place these events in the context of the long-term activity of a given system. Only a long observing series can enable us to form a representative ensemble of events (e.g., outbursts) in (a) a given system, (b) in a type of systems. Of course, the exciting search for the unexpected and unique phenomena can be carried out only by monitoring. The optical monitoring is important for the investigation of the systems containing a compact object which, although the source of X-ray emission, may not be detected in X-rays due to the beaming and/or big intrinsic extinction.

We emphasize the very important role of the X-ray monitors like ASM onboard the *RXTE* satellite on our understanding of the processes operating in X-ray sources. We argue in favor of the development of more sensitive X-ray monitors that will be able to detect the long-term activity of CVs to enable analysis of the simultaneous behavior in the X-ray and optical passbands.

In addition, the current results of the analysis of the rare and/or unexpected phenomena show that unique transient brightenings also occur in systems which are relatively bright even in quiescence and hence easy to monitor. This means that observation of transient activity including large-amplitude outbursts can be carried out even with small

aperture monitoring telescopes. The microquasars CI Cam and V4641 Sgr can serve as examples.

Acknowledgments

The support by the Grant 205/08/1207 of the Grant Agency of the Czech Republic and the projects D-25-CZ4/08-09 DAAD and PECS 98058 Gaia is acknowledged. This research has made use of the observations from the AFOEV database operated in Strasbourg, France. The authors thank the variable star observers worldwide whose observations contributed to this analysis. They acknowledge using the curve-fitting code HEC13 written by Professor. P. Harmanec; the Fortran source version, compiled version, and brief instructions on how to use the program can be obtained at this URL: <http://astro.troja.mff.cuni.cz/ftp/hec/HEC13/>. This research has made use of the observations provided by the ASM/*RXTE* team.

References

- [1] B. Warner, *Cataclysmic Variable Stars*, Cambridge University Press, Cambridge, UK, 1995.
- [2] W. H. G. Lewin, J. van Paradijs, and E. P. J. van den Heuvel, *X-Ray Binaries*, Cambridge University Press, Cambridge, UK, 1995.
- [3] E. P. J. van den Heuvel, D. Bhattacharya, K. Nomoto, et al., "Accreting white dwarf models for CAL 83, CAL 87 and other ultrasoft X-ray sources in the LMC," *Astronomy & Astrophysics*, vol. 262, no. 1, pp. 97–105, 1992.
- [4] V. Šimon, "Activity of DX Andromedae—the dwarf nova with a very long recurrence time of outbursts," *Astronomy & Astrophysics*, vol. 364, no. 2, pp. 694–700, 2000.
- [5] J. Smak, "Accretion in cataclysmic binaries. IV—Accretion disks in dwarf novae," *Acta Astronomica*, vol. 34, p. 161, 1984.
- [6] V. Šimon, "Dramatic change of the recurrence time and outburst parameters of the intermediate polar GK Persei," *Astronomy & Astrophysics*, vol. 382, no. 3, pp. 910–920, 2002.
- [7] L. Angelini and F. Verbunt, "The effect of the white dwarf magnetic field on dwarf nova outbursts," *Monthly Notices of the Royal Astronomical Society*, vol. 238, pp. 697–708, 1989.
- [8] V. Šimon, "Outburst activity of the intermediate polar DO Draconis (3A 1148+719)," *Astronomy & Astrophysics*, vol. 360, no. 2, pp. 627–632, 2000.
- [9] A. Bianchini, "Solar-type cycles in close binary systems," *Astronomical Journal*, vol. 99, no. 6, pp. 1941–1952, 1990.
- [10] M. G. Watson, A. R. King, and J. Osborne, "The old nova GK Per: discovery of the X-ray pulse period," *Monthly Notices of the Royal Astronomical Society*, vol. 212, pp. 917–930, 1985.
- [11] F. Sabbadin and A. Bianchini, "The old-nova GK Per (1901). IV. The light curve since 1901," *Astronomy & Astrophysics*, vol. 54, pp. 393–403, 1983.
- [12] R. Hudec, "Optical properties of X-ray stars. I—X-ray system GK Per A 0327+43. II—the secular brightness," *Bulletin of the Astronomical Institute of Czechoslovakia*, vol. 32, no. 2, pp. 93–120, 1981.
- [13] M. R. Schreiber, B. T. Gänsicke, and J. K. Cannizzo, "On the occurrence of dwarf nova outbursts in post novae," *Astronomy & Astrophysics*, vol. 362, no. 1, pp. 268–272, 2000.

- [14] M. H. Jones and M. G. Watson, "The EXOSAT observations of SS Cygni," *Monthly Notices of the Royal Astronomical Society*, vol. 257, no. 4, pp. 633–649, 1992.
- [15] P. J. Wheatley, C. W. Mauche, and J. A. Mattei, "The X-ray and extreme-ultraviolet flux evolution of SS Cygni throughout outburst," *Monthly Notices of the Royal Astronomical Society*, vol. 345, no. 1, pp. 49–61, 2003.
- [16] K. E. McGowan, W. C. Priedhorsky, and S. P. Trudolyubov, "On the correlated X-ray and optical evolution of SS Cygni," *Astrophysical Journal*, vol. 601, no. 2, pp. 1100–1108, 2004.
- [17] A. R. King, M. J. Ricketts, and R. S. Warwick, "The detection of an X-ray outburst from the old nova GK Per," *Monthly Notices of the Royal Astronomical Society*, vol. 187, pp. 77P–81P, 1979.
- [18] A. Bianchini and F. Sabbadin, "the old-nova GK per (1901): evidence for a time-delay between its X-ray and optical outbursts," *Information Bulletin on Variable Stars*, vol. 2751, p. 1, 1985.
- [19] P. Harmanec, 1992, <http://astro.troja.mff.cuni.cz/ftp/hec/HEC13/>.
- [20] J. Vondrák, "A contribution to the problem of smoothing observational data," *Bulletin of the Astronomical Institute of Czechoslovakia*, vol. 20, p. 349, 1969.
- [21] J. Vondrák, "Problem of smoothing observational data II," *Bulletin of the Astronomical Institute of Czechoslovakia*, vol. 28, p. 84, 1977.
- [22] N. Vogt, "The SU UMa stars: an important sub-group of dwarf novae," *Astronomy & Astrophysics*, vol. 88, no. 1-2, pp. 66–76, 1980.
- [23] V. Šimon, "Outburst parameters and the long-term activity of the dwarf nova CH Ursae Majoris," *Astronomy & Astrophysics*, vol. 354, no. 1, pp. 103–111, 2000.
- [24] R. Popham and R. di Stefano, "Accretion disks in supersoft X-ray sources," in *Supersoft X-Ray Sources*, vol. 472 of *Lecture Notes in Physics*, p. 65, Springer, New York, NY, USA, 1996.
- [25] J. E. Steiner and M. P. Diaz, "The V Sagittae stars," *Publications of the Astronomical Society of the Pacific*, vol. 110, no. 745, pp. 276–282, 1998.
- [26] J. Greiner and A. van Teeseling, "On the X-ray properties of V Sge and its relation to the supersoft X-ray binaries," *Astronomy & Astrophysics*, vol. 339, no. 1, pp. L21–L24, 1998.
- [27] J. Reinsch K., A. van Teeseling, A. R. King, and K. Beuermann, "A limit-cycle model for the binary supersoft X-ray source RX J0513.9-6951," *Astronomy & Astrophysics*, vol. 354, p. L37, 2000.
- [28] V. Šimon and J. A. Mattei, "The peculiar binary V Sagittae: properties of its long-term light changes," *Astronomy & Astrophysics*, vol. 139, no. 1, pp. 75–88, 1999.
- [29] U. Mürset, S. Jordan, and B. Wolff, "X-ray properties of symbiotic stars: I. The supersoft symbiotic novae RR Tel and SMC3 (=RX J0048.4-7332)," in *Supersoft X-Ray Sources*, vol. 472 of *Lecture Notes in Physics*, p. 251, Springer, New York, NY, USA, 1996.
- [30] J. Greiner, K. Bickert, R. Luthardt, et al., "The UV/X-ray emission of the symbiotic star AG Draconis during quiescence and the 1994/1995 outbursts," *Astronomy & Astrophysics*, vol. 322, no. 2, pp. 576–590, 1997.
- [31] R. Hudec and L. Meinunger, "Active and inactive state of AM Her = 3U 1809+50," *Information Bulletin on Variable Stars*, vol. 1184, p. 1, 1976.
- [32] P. Szkody and M. Mateo, "An unprecedented UV/optical flare in TV Columbae," *Astrophysical Journal*, vol. 280, pp. 729–733, 1984.
- [33] R. Hudec, V. Šimon, and J. Skalický, "Outbursts of the intermediate polar TV Col," *The Astrophysics of Cataclysmic*, vol. 330, p. 405, 1984.
- [34] Y. M. Lipkin, E. M. Leibowitz, and M. Orio, "Photometry of V1062 Tau: low states, short outbursts and period switching," *Monthly Notices of the Royal Astronomical Society*, vol. 349, no. 4, pp. 1323–1330, 2004.
- [35] S. van Amerongen and J. van Paradijs, "Detection of a brief outburst from the intermediate polar V 1223 SGR," *Astronomy & Astrophysics*, vol. 219, no. 1-2, pp. 195–196, 1989.
- [36] J.-M. Hameury, J.-P. Lasota, J. E. McClintock, and R. Narayan, "Advection-dominated flows around black holes and the X-ray delay in the outburst of GRO J1655-40," *Astrophysical Journal*, vol. 489, no. 1, pp. 234–243, 1997.
- [37] D. Maitra and C. D. Bailyn, "Outburst morphology in the soft X-ray transient aquila X-1," *Astrophysical Journal*, vol. 688, no. 1, pp. 537–549, 2008.
- [38] P. A. Charles, J. R. Thorstensen, S. Bowyer, et al., "The 1978 X-ray and optical outburst of Aquila X-1 /4U 1908+00/," *Astrophysical Journal*, vol. 237, p. 154, 1980.
- [39] J. Van Paradijs, "On the accretion instability in soft X-ray transients," *Astrophysical Journal*, vol. 464, no. 2, pp. L139–L141, 1996.
- [40] G. Dubus, J.-M. Hameury, and J.-P. Lasota, "The disc instability model for X-ray transients: evidence for truncation and irradiation," *Astronomy & Astrophysics*, vol. 373, no. 1, pp. 251–271, 2001.
- [41] E. S. Rykoff, E. M. Cackett, and J. M. Miller, "Swift monitoring of Cygnus X-2: investigating the NUV-X-ray connection," <http://arxiv.org/abs/0909.3804>.
- [42] J. Casares, J. A. Orosz, C. Zurita, et al., "Refined orbital solution and quiescent variability in the black hole transient GS 1354-64 (= BW Cir)," *Astrophysical Journal*, vol. 181, no. 1, pp. 238–243, 2009.
- [43] V. Šimon, "On the recurrence time and outburst properties of the soft X-ray transient Aquila X-1," *Astronomy & Astrophysics*, vol. 381, no. 1, pp. 151–167, 2002.
- [44] W. Forman, C. A. Jones, and W. Liller, "Optical studies of UHURU sources. III. Optical variations of the X-ray eclipsing system HZ Herculis," *Astrophysical Journal*, vol. 177, p. L103, 1972.
- [45] R. Hudec and W. Wenzel, "Observations of HZ Her/Her X-1 on Sonneberg astrograph plates," *Bulletin of the Astronomical Institute of Czechoslovakia*, vol. 27, p. 325, 1976.
- [46] C. A. Jones, W. Forman, and W. Liller, "Optical studies of UHURU sources. IV. The long-term behavior of HZ HERCULIS=HERCULES X-1," *Astrophysical Journal*, vol. 182, p. L109, 1973.
- [47] V. Šimon, P. Kroll, P. Neugebauer, et al., "Characteristics of the photometric modulation of HZ Her/Her X-1 in active states over a very long time interval," *New Astronomy*, vol. 7, no. 6, pp. 349–358, 2002.
- [48] R. Hudec, "Optical properties of X-ray stars. 2. The secular brightness variations of the X-ray system V 818 Sco/Sco X-1," *Bulletin of the Astronomical Institute of Czechoslovakia*, vol. 32, p. 108, 1981.
- [49] T. J. Moffett, G. Grupsmith, and P. A. Vanden Bout, "High-speed UBV photometry of Scorpius X-1 flares," *Publications of the Astronomical Society of the Pacific*, vol. 85, no. 504, p. 177, 1973.
- [50] T. Augusteijn, K. Karatasos, M. Papadakis, et al., "Coordinated X-ray and optical observations of Scorpius X-1," *Astronomy & Astrophysics*, vol. 265, no. 1, pp. 177–182, 1992.

- [51] I. F. Mirabel and L. F. Rodríguez, "Sources of relativistic jets in the Galaxy," *Annual Review of Astronomy & Astrophysics*, vol. 37, no. 1, pp. 409–443, 1999.
- [52] J. M. Paredes, "Microquasars as high-energy gamma-ray sources," *Chinese Journal of Astronomy & Astrophysics*, vol. 5, pp. 121–132, 2005.
- [53] R. M. Hjellming and M. P. Rupen, "Episodic ejection of relativistic jets by the X-ray transient GRO J1655-40," *Nature*, vol. 375, no. 6531, pp. 464–468, 1995.
- [54] F. Frontera, M. Orlandini, L. Amati, et al., "Multifrequency observations of XTE J0421+560/CI Cam in outburst," *Astronomy & Astrophysics*, vol. 339, no. 3, pp. L69–L72, 1998.
- [55] E. L. Robinson, I. I. Ivans, and W. F. Welsh, "High-dispersion spectroscopy of the X-ray transient RXTE J0421+560 (= CI Camelopardalis) during outburst," *Astrophysical Journal*, vol. 565, no. 2, pp. 1169–1182, 2002.
- [56] V. Šimon, C. Bartolini, A. Piccioni, and A. Guarnieri, "Interpretation of the 1998 outburst of the unique X-ray transient CI Camelopardalis (XTE J0421+560)," *Monthly Notices of the Royal Astronomical Society*, vol. 369, no. 1, pp. 355–359, 2006.
- [57] J. S. Clark, A. S. Miroshnichenko, V. M. Larionov, et al., "Photometric observations of the radio bright B[e]/X-ray binary CI Cam," *Astronomy & Astrophysics*, vol. 356, no. 1, pp. 50–62, 2000.
- [58] V. Šimon, C. Bartolini, A. Guarnieri, A. Piccioni, and D. Hanžl, "Photometric activity of the unique X-ray transient CI Camelopardalis (XTE J0421+560)," *New Astronomy*, vol. 12, no. 7, pp. 578–589, 2007.
- [59] A. J. Mioduszewski and M. P. Rupen, "CI camelopardalis: a shell-shocked X-ray nova," *Astrophysical Journal*, vol. 615, no. 1, pp. 432–443, 2004.
- [60] V. Šimon, C. Bartolini, A. Piccioni, et al., "Long-term activity and outburst of the microquasar CI Cam (XTE J0421+560)," in *Proceedings of the 7th Microquasar Workshop: Microquasars and Beyond*, p. 108, Foca, Turkey, September 2008.
- [61] J. A. Orosz, E. Kuulkers, M. van der Klis, et al., "A black hole in the superluminal source SAX J1819.3-2525 (V4641 Sgr)," *Astrophysical Journal*, vol. 555, no. 1, pp. 489–503, 2001.
- [62] R. M. Hjellming, M. P. Rupen, R. W. Hunstead, et al., "Light curves and radio structure of the 1999 September transient event in V4641 Sagittarii (= XTE J1819-254 = SAX J1819.3-2525)," *Astrophysical Journal*, vol. 544, no. 2, pp. 977–992, 2000.
- [63] V. Šimon and A. Henden, "Long-term optical activity of the microquasar V4641 Sgr," in *Proceedings of the 7th Microquasar Workshop: Microquasars and Beyond*, p. 111, Foca, Turkey, September 2008.
- [64] M. Uemura, T. Kato, R. Ishioka, et al., "Rapid optical fluctuations in the black hole binary V4641 Sagittarii," *Publications of the Astronomical Society of Japan*, vol. 54, no. 5, pp. L79–L82, 2002.
- [65] R. Sari, T. Piran, and R. Narayan, "Spectra and light curves of gamma-ray burst afterglows," *Astrophysical Journal*, vol. 497, no. 1, pp. L17–L20, 1998.
- [66] B. Zhang, "Gamma-ray bursts in the Swift era," *Chinese Journal of Astronomy & Astrophysics*, vol. 7, no. 1, pp. 1–50, 2007.
- [67] V. Šimon, R. Hudec, G. Pizzichini, and N. Masetti, "Colors and luminosities of the optical afterglows of the γ -ray bursts," *Astronomy & Astrophysics*, vol. 377, no. 2, pp. 450–461, 2001.
- [68] V. Šimon, R. Hudec, G. Pizzichini, et al., "Colors of optical afterglows of GRBs and their time evolution," in *Gamma-Ray Bursts: 30 Years of Discovery: Gamma-Ray Burst Symposium*, vol. 727 of *AIP Conference Proceedings*, pp. 487–490, 2004.
- [69] S. Campana, V. Mangano, A. J. Blustin, et al., "The association of GRB 060218 with a supernova and the evolution of the shock wave," *Nature*, vol. 442, no. 7106, pp. 1008–1010, 2006.
- [70] P. J. Brown, P. W. A. Roming, D. E. Van den Berk, S. T. Holland, S. Immler, and P. Milne, "Swift UVOT observations of core-collapse SNe," in *Supernova 1987A: 20 Years after: Supernovae and Gamma-Ray Bursters*, vol. 937 of *AIP Conference Proceedings*, pp. 386–390, Aspen, Colo, USA, February 2007.
- [71] N. Mirabal, J. P. Halpern, D. An, J. R. Thorstensen, and D. M. Terndrup, "GRB 060218/SN 2006aj: a gamma-ray burst and prompt supernova at $z = .0335$," *Astrophysical Journal*, vol. 643, no. 2, pp. L99–L102, 2006.
- [72] D. J. Schlegel, D. P. Finkbeiner, and M. Davis, "Maps of dust infrared emission for use in estimation of reddening and cosmic microwave background radiation foregrounds," *Astrophysical Journal*, vol. 500, no. 2, pp. 525–553, 1998.
- [73] J. E. Rhoads, "How to tell a jet from a balloon: a proposed test for beaming in gamma-ray bursts," *Astrophysical Journal*, vol. 487, no. 1, pp. L1–L4, 1997.
- [74] Y. F. Huang, Z. G. Dai, and T. Lu, "Failed gamma-ray bursts and orphan afterglows," *Monthly Notices of the Royal Astronomical Society*, vol. 332, no. 3, pp. 735–740, 2002.

Research Article

Robotic Astronomy with the Faulkes Telescopes and Las Cumbres Observatory Global Telescope

Fraser Lewis,^{1,2,3} Rachel Street,³ Paul Roche,^{1,2,3} Vanessa Stroud,^{1,2,3} and David M. Russell⁴

¹ Faulkes Telescope Project, School of Physics and Astronomy, 5, The Parade, Cardiff CF24 3AA, UK

² Department of Physics and Astronomy, The Open University, Milton Keynes MK7 6AA, UK

³ Las Cumbres Observatory Global Telescope, 6740 Cortona Drive, Suite 102, Goleta, CA 93117, USA

⁴ Astronomical Institute “Anton Pannekoek”, University of Amsterdam, P. O. Box 94249, 1090 GE, Amsterdam, The Netherlands

Correspondence should be addressed to Fraser Lewis, lewisf@cf.ac.uk

Received 30 June 2009; Accepted 2 December 2009

Academic Editor: Alberto J. Castro-Tirado

Copyright © 2010 Fraser Lewis et al. This is an open access article distributed under the Creative Commons Attribution License, which permits unrestricted use, distribution, and reproduction in any medium, provided the original work is properly cited.

We present results from ongoing science projects conducted by members of the Faulkes Telescope (FT) team and Las Cumbres Observatory Global Telescope (LCOGT). Many of these projects incorporate observations carried out and analysed by FT users, comprising amateur astronomers and schools. We also discuss plans for the further development of the LCOGT network.

1. Introduction

The Faulkes Telescope Project (<http://www.faulkes-telescope.com/>) is based in Cardiff, Wales, and is an educational and research arm of LCOGT (<http://lcogt.net/>), based in Goleta, California. Presently, the network has two operational 2-metre optical telescopes, located at Haleakala on Maui, Hawaii (FT North) and Siding Spring in New South Wales, Australia (FT South).

The FT provides telescope time free of charge to all UK schools, as well as other educational groups, and is able to provide its users with science and imaging projects [1]. Many of these projects relate to the UK school's curriculum, and some of them allow the schools to collaborate with researchers within the FT Team, and externally.

2. The Telescopes

Both FT North and FT South are 2-metre, fully autonomous, robotic Cassegrain-type reflectors with Richey-Chretien hyperbolic optics on an alt-azimuth mount. Both telescopes employ a Robotic Control System (RCS) [2].

They are currently operated in the following two modes.

(i) UK (and some overseas) schools use a “real-time interface” (RTI) mode, where each user has exclusive control of the telescope for 30 minutes at a time. During this time, the users are able to select co-ordinates, filters, and exposure

times. Many educational users participate in data gathering for research programmes.

(ii) The “offline” mode of the telescope lends itself more easily to science observing, using a Graphic User Interface (GUI). In this instance, users may specify “flexible” (observe when most suitable), “fixed-time” (for specifically timed transient events), or “monitor” (repeat these observations every few days/weeks) type observations. For either mode, the telescopes also have an over-ride capability for Target of Opportunity (ToO) events such as gamma-ray bursts.

All observations are pipeline-processed to take account of flat-fielding and debiasing, with the finished images in 2×2 binned FITS format available typically 24 hours after the observing run.

The telescopes are equipped with a $4.6' \times 4.6'$ field of view Merope camera [3] featuring SDSS $u'g'r'i'z'$, Bessel BVRI, Pan-STARRS Z,Y broad-band filters in addition to $H\alpha$, $H\beta$ and O III narrow-band filters. The cameras use an E2V CCD42-40DD CCD with 2048×2048 pixels.

A second camera has recently been installed, known as the Spectral camera, possessing a wider field of view of $10.5' \times 10.5'$. The Spectral cameras have an improved readout time of ~ 5 seconds. The CCD on this camera is a Fairchild CCD 486 with 4096×4096 pixels.

It is planned that all future telescopes within the LCOGT network (i.e., 0.4 m and 1.0 m) will have similar filter sets.

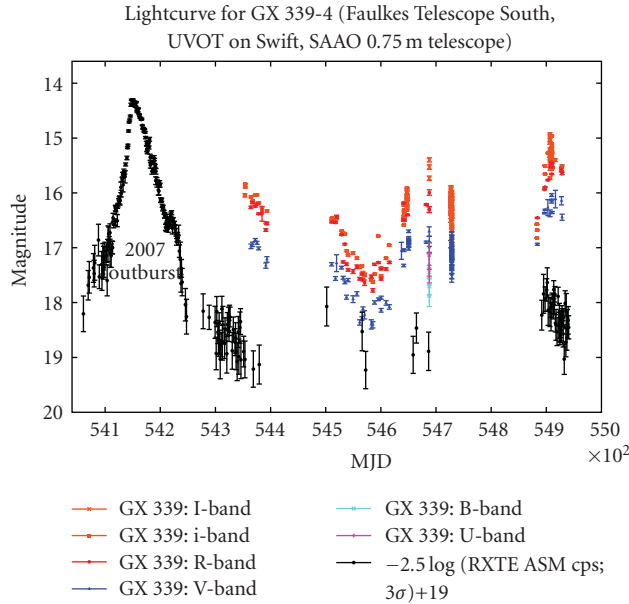


FIGURE 1: FT (V, R, i'), RXTE ASM, Swift, UVOT (U, B), and SAAO (I) band from 2007 to present.

3. Scientific Results

3.1. LMXB Monitoring. The Black Hole X-ray Binary, GX339-4. X-Ray binaries (XRBs) consist of a pair of stars orbiting each other; however unlike “normal” binary stars, one of the components is a compact object. This compact object is either a neutron star or a black hole. There are currently ~ 300 XRBs in the Milky Way, split into two broad categories based on the mass of the normal component of the system, namely, Low-Mass and High-Mass (LMXBs and HMXBs).

XRBs possess accretion discs of matter (at temperatures of up to millions of Kelvin), which has been drawn from the “normal” donor star. As well as supernovae, XRBs are also closely linked with phenomena such as Gamma Ray Bursts (GRBs) and as potential sources of gravitational waves.

Initial detections of XRBs are usually made at X-ray wavelengths, a signature of the highly energetic processes involved. They are also observed at other wavelengths, such as the optical regime that the FTs operate within. They can often increase in optical brightness by factors of 1000 or more in a matter of days (known as outbursts) and often display variability on the order of seconds (flickering or flaring).

The low-mass systems (LMXBs) form around 50% of the overall population—they contain a compact object and a K or M type donor star of up to ~ 1 solar mass.

Since early 2006, we have been observing a subset of 30 LMXBs with the two FTs [4]. The telescopes are an ideal vehicle with which to monitor these objects, since they allow us the flexibility to change both the frequency and intensity of our observing, subject to changes in the behaviour of our targets. No other survey of LMXBs has covered this many systems so comprehensively or over this time period.

The initial aims of the project are twofold.

(i) We wish to identify outbursts. It is known that many of these systems show increases in brightness at optical

wavelengths before being detected in X-rays. Associated with this is the fact that our monitoring is often more sensitive to the initial phase of outburst than typical X-ray monitoring instruments. Identifying these outbursts before other observers allows us to alert the wider astronomical community to initiate multiwavelength follow-up observations (e.g., [5, 6]).

(ii) Secondly, most XRBs spend a larger fraction of their time as “quiescent” systems rather than in outburst. We wish to constrain this duty cycle and also to compare behaviour in these two states.

On several occasions, we have been able to involve schools and other users in helping us to collect and analyse data. This has led to the schools’ contribution being acknowledged in journal papers (e.g., [7, 8]). As well as contributing to professional science, studying XRBs allows students to gain a better understanding of the life cycle of stars, as studied in the science curriculum for schools in the UK.

For systems in outburst, we have been able to collect extensive datasets, incorporating supplementary data at other wavelengths from colleagues, including observatories such as the Very Large Telescope, the Very Large Baseline Array, and the Swift and RXTE X-ray satellites.

One notable target for FT South is the transient black hole binary, GX339-4. This system went into outburst in late 2006 (\sim MJD 54150), steadily declining in brightness over the following months. The outburst was noted at X-ray [9], optical/infrared [10], and radio wavelengths [11].

Our optical observations (Figure 1) show a continuing decline in V, R, and i' bands until \sim MJD 54585, at which time the source began to increase back to its previous brightest level ($i' \sim 16$) over ~ 80 days.

More recent observations (\sim MJD 54900) show a continued brightening of the source to $i' \sim 15$. On several occasions, we have observed rapid flaring in the i' and V bands, with changes of 0.3–0.4 magnitudes in periods of 140 seconds. Our ATel [12] triggered multiwavelength follow-ups with SALT, VLT, Swift and RXTE.

3.2. Observing Massive Stars and Open Clusters: Cyg OB2-B17. Massive stars play an important role in the structure and evolution of galaxies. They are the principal source of heavy elements and UV radiation. They are also the progenitors of energetic phenomena such as X-ray binaries and gamma-ray bursts. However, our understanding of their formation and evolution is still unclear. This is due to their short lifetimes and rapid evolutionary stages, and dust extinction making them difficult to observe during early formation phases.

Some variable massive stars include the following.

(i) OB binaries—the brightest and most massive stellar objects found in galaxies. They are the only direct way to measure the masses and radii of stars, making them the perfect test beds for studying the evolution of massive stars.

(ii) Be Stars—rapidly rotating Be stars which have circumstellar discs at some points during their lives. These are characterised by infrared excess and emission lines. How these discs are formed is still poorly understood. By studying Be stars, we can obtain information on stellar rotation and mixing.

(iii) Luminous Blue Variables (LBVs)—massive stars close to the upper luminosity limit, causing instabilities in the stellar envelope which results in sporadic mass ejections.

We have been looking for photometric variability of massive stars in the Magellanic Clouds. This survey will be combined with multiepoch spectroscopic data from the VLT-FLAMES study (e.g., [13]).

This search has been divided into the following two main parts.

(i) Looking at lightcurves derived from the MACHO microlensing survey [14]. This survey was carried out between June 1992 and December 1999. A 50 inch telescope at Mt. Stromlo, Australia, was used with a dichroic, obtaining simultaneous blue and red observations.

(ii) Photometric monitoring with Faulkes Telescope South. Since October 2007 we have been obtaining offline observations of the clusters NGC2004 (field covered by 5 FTS Merope camera mosaics), and N11 (8 mosaics) in the LMC and NGC346 (1 mosaic) in the SMC. A similar monitoring campaign is now monitoring 30 Doradus in the LMC, where we are obtaining observations using both offline and real-time modes. Much of the real-time data will be collected by schools.

Our aims are to look for the following.

- (i) Eclipsing binaries—in order to determine the masses of the components, along with the orbital parameters.
- (ii) Variability in Be stars—gaining or losing circumstellar discs.
- (iii) Variability due to sporadic mass ejections in Luminous Blue Variables.
- (iv) Any transients or new phenomena within the clusters.

The photometric follow-up in the Magellanic clouds is intended to reveal further systems similar to the massive binary, B17 [15].

It is an eclipsing, double-lined spectroscopic binary in the Cyg OB2 association, with two supergiants having preliminary spectral classifications of O7 and O9. The lightcurve reveals a semicontact binary with an orbital period of 4.0217 ± 0.0004 days (Figure 2) and indications of mass transfer.

B17 appears to have progenitor masses of ~ 60 solar masses, being consistent with the preliminary spectral types of both components as well as the age and stellar population of Cyg OB2. Assuming that the system avoids merger, it is likely to evolve through an extreme B supergiant/LBV phase into a long period Wolf-Rayet + Wolf-Rayet binary configuration, as mass loss via stellar winds increases the orbital separation.

Open clusters are groups of tens to thousands of loosely gravitationally bound stars, formed from the same original molecular cloud. Since the stars within a cluster essentially have the same chemical composition, age, and distance, open clusters are important in the study of stellar evolution.

We have collected observations of many previously unstudied open clusters, as we encourage schools and other

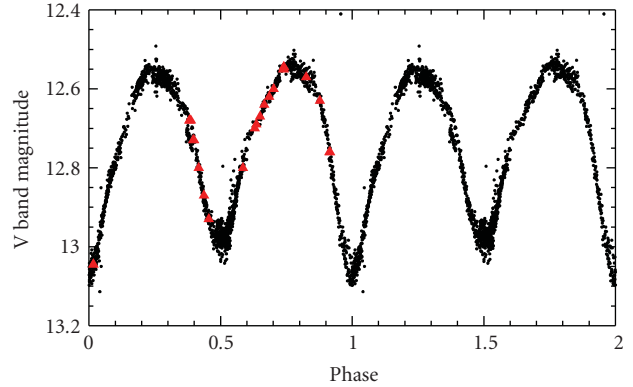


FIGURE 2: Folded lightcurve of B17 obtained by amateur astronomers. The red triangles show the phases where spectra were obtained [15].

users to analyse. In doing this, they are able to create colour-magnitude diagrams, and search the clusters for H α bright objects, such as Be stars. Further, they are encouraged to image the clusters themselves to search for variable objects.

3.3. Microlensing Events. LCOGT supports a professional programme to observe microlensing events in the direction of the Galactic Bulge, with the aim of discovering new exoplanets. The observations we provide help to characterise the systems.

With hundreds of events every year, this program relies on a robotic system to prioritise those events which offer the most sensitivity to the presence of planets. In this season, the microlensing team has established a website to provide Faulkes Telescope Project contributors with an updated list of current targets, with advice on making observations of the events using the Real-Time Interface [16]. The images taken by the schools are gathered automatically for processing and combined with data taken by astronomers around the world. This pilot program has received an encouraging response from FT users in its first year.

4. Future Plans

LCOGT is expanding its network to include 1-metre and 0.4-metre telescopes running in conjunction with the 2-metre FTs [17]. In addition to the imaging capability of the FTs, LCOGT is commissioning a Medium Resolution Echelle Spectrograph and a Low Resolution Spectrograph. LCOGT is designing and building a set of 1-metre telescopes, primarily for use in the LCOGT science program, but with possibly limited time available for educational use. Currently, 12–15 telescopes are planned across 6 sites, each housed in its own custom-made dome. Sites currently being planned are Siding Spring (Australia), Cerro Tololo (Chile), Mauna Loa (Hawaii), Sutherland (South Africa), Tenerife (Canary Islands) and San Pedro Martir (Mexico), with the prototype being despatched to Cerro Tololo in early 2010.

Currently in production at LCOGT headquarters in Goleta, California, the 0.4 m telescopes are based around

an off-the-shelf Meade telescope with a custom equatorial mount, and high specification CCD cameras. It is anticipated that these telescopes will mainly be available for the education community and other nonprofessional astronomers to use. Despite their relatively small size, they will be installed at dark sites in pairs or sets of fours, allowing high-quality imaging with wider fields of view ($\sim 30' \times 20'$) than those of the larger aperture telescopes. They will feature the SBIG STL-6303 with a Kodak KAF 6303E CCD with 2048×3072 pixels.

Two of these telescopes are now located inside the enclosures of each FT. Two to four telescopes will be installed at the other 1.0 m sites. When fully commissioned, they will become available to the user community. With the exception of those 0.4 m telescopes housed within the FTs, the remainder of the 0.4 m network will be placed within their own Aqawan enclosures, each capable of housing two telescopes [18].

Acknowledgments

The first and the fourth authors acknowledge the financial support from the Dill Faulkes Educational Trust and The Open University. The fifth author acknowledges the support from a Netherlands Organization for Scientific Research (NWO) Veni Fellowship. ASM/RXTE data are provided by the ASM/RXTE team.

References

- [1] F. Lewis and P. Roche, "Not just pretty pictures," in *Astronomy: Networked Astronomy and the New Media*, R. J. Simpson and D. Ward-Thompson, Eds., 2009.
- [2] Y. Tsapras, R. Street, K. Home, et al., "RoboNet-II: follow-up observations of microlensing events with a robotic network of telescopes," *Astronomische Nachrichten*, vol. 330, no. 1, pp. 4–11, 2009.
- [3] <http://lcogt.net/en/network/camera/merope-llc-merope>.
- [4] F. Lewis, D. M. Russell, R. P. Fender, P. Roche, and J. S. Clark, "Continued monitoring of LMXBs with the Faulkes Telescopes," in *Proceedings of the 7th Microquasar Workshop: Microquasars and Beyond*, 2008.
- [5] F. Lewis, M. Linares, D. M. Russell, R. Wijnands, and P. Roche, "Renewed optical and X-ray activity in IGR J00291+5934," *ATel*, no. 1726, 2009.
- [6] D. M. Russell and F. Lewis, "Optical and hard X-ray detections of an outburst from Aquila X-1," *ATel*, no. 1970, 2009.
- [7] P. Elebert, M. T. Reynolds, P. J. Callanan, et al., "Optical spectroscopy and photometry of SAX J1808.4-3658 in outburst," *Monthly Notices of the Royal Astronomical Society*, vol. 395, no. 2, pp. 884–894, 2009.
- [8] M. R. Burleigh, T. R. Marsh, B. T. Gänsicke, et al., "The nature of the close magnetic white dwarf + probable brown dwarf binary SDSS J121209.31+013627.7," *Monthly Notices of the Royal Astronomical Society*, vol. 373, no. 4, pp. 1416–1422, 2006.
- [9] H. A. Krimm, L. Barbier, S. D. Barthelmy, et al., "Swift-BAT detects a bright hard X-ray outburst from GX339-4," *ATel*, no. 968, 2006.
- [10] M. Buxton and C. Bailyn, "Latest optical and infrared observations of GX 339-4," *ATel*, no. 1027, 2007.
- [11] S. Corbel, T. Tzioumis, C. Brocksopp, and R. Fender, "ATCA radio observations of GX339-4," *ATel*, no. 1007, 2007.
- [12] D. M. Russell, D. Altamirano, F. Lewis, P. Roche, C. B. Markwardt, and R. P. Fender, "Unusual optical and X-ray flaring activity in GX339-4," *ATel*, no. 1586, 2008.
- [13] C. J. Evans, D. J. Lennon, S. J. Smartt, and C. Trundle, "The VLT-FLAMES survey of massive stars: observations centered on the Magellanic Cloud clusters NGC 330, NGC 346, NGC 2004, and the N11 region," *Astronomy and Astrophysics*, vol. 456, no. 2, pp. 623–638, 2006.
- [14] C. Alcock, R. A. Allsman, D. R. Alves, et al., "Calibration of the MACHO photometry database," *The Publications of the Astronomical Society of the Pacific*, vol. 111, no. 766, pp. 1539–1558, 1999.
- [15] V. E. Stroud, S. Clark, I. Negueruela, P. D. Roche, A. J. Norton, and F. Vilardell, "Discovery of the eclipsing of supergiant binary, Cyg OB2-B17," submitted to *Astronomy & Astrophysics*, <http://arxiv.org/abs/1002.0707>.
- [16] <http://microlensing.lcogt.net>.
- [17] M. G. Hidas, E. Hawkins, Z. Walker, T. M. Brown, and W. E. Rosing, "Las Cumbres Observatory Global Telescope: a homogeneous telescope network," *Astronomische Nachrichten*, vol. 329, no. 3, pp. 269–270, 2008.
- [18] <http://lcogt.net/en/blog/egomez/how-keep-telescope-dry>.

Research Article

Robotic Monitoring of Gravitationally Lensed Quasars

Luis J. Goicoechea,¹ Vyacheslav N. Shalyapin,² and Aurora Ullán³

¹Departamento de Física Moderna, Universidad de Cantabria, Avda. de Los Castros s/n, 39005 Santander, Spain

²Institute for Radiophysics and Electronics, National Academy of Sciences of Ukraine, 12 Proskura Street, Kharkov 61085, Ukraine

³Robotic Telescopes Group, Centro de Astrobiología (CSIC-INTA), Ctra de Ajalvir, km 4, Torrejón de Ardoz, 28850 Madrid, Spain

Correspondence should be addressed to Luis J. Goicoechea, luis.goicoechea@unican.es

Received 22 June 2009; Accepted 23 November 2009

Academic Editor: Joshua S. Bloom

Copyright © 2010 Luis J. Goicoechea et al. This is an open access article distributed under the Creative Commons Attribution License, which permits unrestricted use, distribution, and reproduction in any medium, provided the original work is properly cited.

We report on the first observational phase of the Liverpool Quasar Lens Monitoring (LQLM) project. This mainly consisted of the optical follow-up of three lensed quasars using the 2 m Liverpool Robotic Telescope. The observational subprogram started in January 2005 and was completed in July 2007. We also describe our photometric approaches (including two pipelines to extract accurate and reliable fluxes of images of lensed quasars), the performance of the telescope when taking modest nightly exposures of lens systems, and the main scientific results from the observed light curves. The LQLM archive and the current status of the project (second phase) are also outlined.

1. Introduction

If there is a massive galaxy (or an association of galaxies) between a background quasar (QSO) and the observer, the QSO is seen as a multiple system consisting of several images A, B, C, ... (see, e.g., [1]). In the simplest case, the gravitational deflector produces two bright images (A and B) of the same distant QSO. As the ray paths are different for the two images of the double QSO, the corresponding magnifications and travel times do not agree with each other. Thus, each flare in the distant source is observed in A and B with different flux peak (magnitude offset) and arrival time (time delay). Time delays of gravitationally lensed QSOs are basically related to the present expansion rate of the Universe (Hubble constant) and mean surface densities of main lensing galaxies [2, 3] as well as flaring regions where the luminosity fluctuations occur [4, 5]. Moreover, delays between intrinsic variations observed at different wavelengths could unveil the origin of QSO flares. Structure function analyses also allow one to quantify typical luminosity fluctuations at different rest-frame lags. Hence, these analyses may reveal important aspects of the mechanism of intrinsic variability in QSOs [6, 7]. Apart from intrinsic variations, extrinsic signals are detected in

some lensed QSOs (see, e.g., [8]). These extrinsic events are very probably due to small-scale substructures in main lensing galaxies, that is, stars and other collapsed objects (gravitational microlensing), or clouds of dust (variable transmission). The study of extrinsic variability has a great interest, since one can obtain information about the nature of sources (QSOs), as well as the composition of intervening galaxies (see, e.g., [9–11]).

Accurate measurements of time delays (ranging from days to years) obtained from optical intrinsic events (timescales of weeks-months) require intensive long-term monitoring campaigns, that is, nightly observations over relatively long periods. An intensive long-term sampling is also required for detailed studies of structure functions or extrinsic variations. Moreover, bright-lensed QSOs have image separations and visual fluxes of $\Delta\theta \sim 1\text{--}10''$ and $m_V \sim 17\text{--}20$ mag [12]. Taking these values into account, one also needs high-performance telescopes (good angular resolutions, relatively large primary mirrors, reliable instruments, etc.). Unfortunately, space and largest ground-based telescopes are not available for observational programs involving such exigent samplings. Only some 1–3 m conventional telescopes and the 2 m Liverpool Robotic Telescope (LRT) are being used for systematic monitoring of lensed QSOs.

TABLE 1: LQLM I optical frames.

Target	z	$\Delta\theta_{AB}$ (")	g -band frames	r -band frames	i -band frames
SBS 0909 + 532	1.38	1.1	237	214	—
QSO 0957 + 561	1.41	6.2	286	264	—
FBQ 0951 + 2635	1.24	1.1	—	—	259

The LRT [13, 14] at the Roque de los Muchachos Observatory (Canary Islands, Spain) is one of the world's largest fully robotic telescopes, and it is ideally suited for monitoring lens systems and for deriving light curves of their components. In this paper we review the Liverpool Quasar Lens Monitoring (LQLM) project, which is being conducted by us. In Section 2, we give a brief description of the phase I (LQLM I) observations. In Section 3, we discuss the photometric methods and focus on two pipelines that are specially designed for the analysis of large sets of frames of lensed QSOs. In Section 4, we give an overview of the observed light curves and the behaviour of the telescope (effective sampling and photometric accuracy). In Section 5, we summarize the main scientific outputs of the LQLM I subproject. In Section 6, we present the LQLM archive and the current status of the project (phase II).

2. LQLM I Observations

The first phase of the nightly long-term observational program with the LRT began in January 2005 and finished in July 2007. This LQLM I subprogram was carried out with the RATCam optical CCD camera on the LRT, using *gri* Sloan filters. The field of view and the pixel scale (binning 2×2) were $\sim 4.6' \times 4.6'$ and $0.278''$, respectively. The subprogram mainly focused on the optical follow-up of three bright double QSOs at $1 \leq z \leq 2$: SBS 0909 + 532, QSO 0957 + 561 and FBQ 0951 + 2635 (see [12] for HST frames, basic properties, and references). During our 2.5-year monitoring campaign, we obtained 1260 individual frames with exposure times ranging from 100 to 200 seconds. The distribution of frames is shown in Table 1.

While SBS 0909 + 532 and QSO 0957 + 561 were monitored in the g and r Sloan bands over two years (until January 2007) and the whole 2.5-year period, respectively, the monitoring campaign of FBQ 0951 + 2635 in the i Sloan band only lasted four months (in 2007). The long-term follow-up of SBS 0909 + 532 and QSO 0957 + 561 is characterised by two important seasonal gaps. These are a consequence of the simultaneous annual occultation of both lens systems. For SBS 0909 + 532 and QSO 0957 + 561, in most observation nights we got one exposure in each filter (sometimes two or three exposures were taken with the LRT). With respect to FBQ 0951 + 2635, each observation night consisted of five exposures of 100 seconds in the i band, using a dither cross pattern.

3. Photometric Approaches and Pipelines

The LRT preprocessing pipeline included bias subtraction, trimming of the overscan regions, and flat-fielding. We also performed other basic instrumental reductions: cosmic rays cleaning, bad pixel correction, and defringing (i -band frames). The next step was a preselection, based on individual inspection of frames and headers. We initially removed all frames that either do not include the lens systems or are characterised by an anomalous image formation or have large seeing discs (FWHMs). For example, only QSO 0957 + 561 frames verifying $\text{FWHM} < 3''$ and FBQ 0951 + 2635 frames with $\text{FWHM} \leq 2''$ were considered for subsequent analyses. Note that our FWHM limits are not consistent with each other, since the constraint on QSO 0957 + 561 ($\text{FWHM} < \Delta\theta_{AB}/2$) is consistent with an upper limit of $0.5''$ for the compact systems (see the corresponding angular separations in Table 1). Unfortunately, at present there are no available facilities to carry out intensive long-term monitoring projects of compact-lensed QSOs under such extremely good seeing conditions. For FBQ 0951 + 2635, all preselected frames in each night (≤ 5) were combined; that is, they were aligned and then averaged.

SBS 0909 + 532 consists of two images of the same distant QSO ($z = 1.38$), which are separated by about $1''$ (see Table 1). The lensing galaxy is not apparent in optical frames, even using the HST [12]. Thus, a simple photometric model (with only two close stellar-like sources, i.e., two empirical PSFs) is able to describe the whole crowded region associated with the QSO images. Our second target was the first gravitationally lensed QSO: QSO 0957 + 561 or Twin QSO. It also consists of two bright images (A and B) of a QSO at $z \sim 1.4$. However, in this case, the separation between both QSO images is of about $6''$, and there is a relatively bright lensing galaxy near to B ($1''$ apart). This giant elliptical galaxy is clearly detected in HST optical frames [12]; so it is taken into account when modelling the system. The photometric model incorporated two empirical PSFs (to fit both QSO images) and a de Vaucouleurs profile convolved with the empirical PSF (to fit the lensing elliptical galaxy). The third target FBQ 0951 + 2635 is compact (like SBS 0909 + 532) and includes a relatively bright lens galaxy very near to the B QSO image (only $0.2''$ apart). It is not possible (or very difficult) to separate the galaxy signal from the B signal and to resolve the system into three individual contributions under normal seeing conditions, that is, $\text{FWHM} = 1\text{--}2''$. Despite efforts to quantify the galaxy signal in LQLM I frames, we inferred meaningless results. Therefore, we adopted a simple photometric model (two empirical PSFs), where the B flux represents the true flux of B plus some contamination by galaxy light.

For a given target, once the most suitable photometric model (including associated procedures and constraints) is decided, the corresponding crowded-field photometry pipeline (CPP) does photometry of bright field stars and QSO images. This pipeline is written in Python programming language and incorporates the capabilities of IRAF, through the PyRAF interface, and IMFITFITS software [15], as well as additional numerical and graphical tools.

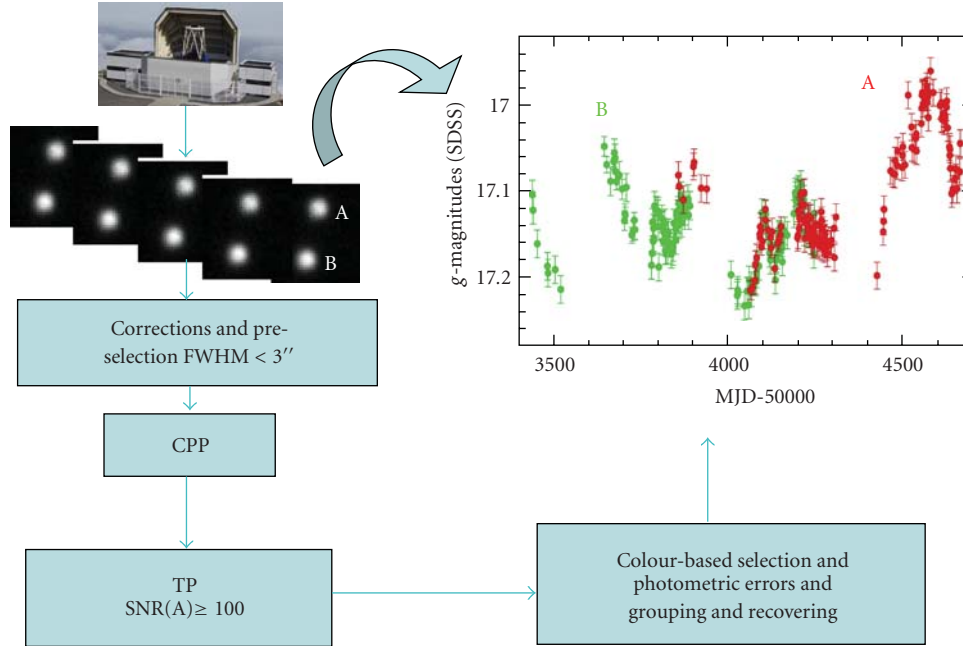


FIGURE 1: Photometric scheme for QSO 0957 + 561: from LRT frames in the g band to SDSS magnitudes of both images (see main text for details).

The IMFITFITS software has been developed to analyse gravitational lens systems. We also used a transformation pipeline (TP; in Python programming language) to obtain SDSS magnitudes from instrumental magnitudes that are corrected for systematic effects. The transformation model incorporates zero-point, colour, and inhomogeneity corrections.

For example, the photometric scheme for QSO 0957 + 561 in the g band is outlined in Figure 1 (see also [16]). The TP was initially applied to frames with signal-to-noise ratio (SNR) ≥ 100 over the A image (both images have similar brightness). This automatic task fits the deviations between instrumental and standard (SDSS catalogue) magnitudes of several reference stars to the transformation model. The zero-point term and the colour coefficient are allowed to vary over time, and the inhomogeneity term contains linear and quadratic coefficients (see, e.g., [17, 18]). From the TP output, we derived two relevant results: (a) there are some dates in which the colour coefficient very strongly deviates ($\sim 100\%$) from its average value, and (b) the 2D inhomogeneity pattern has an amplitude of about 80 mmag, and so the inhomogeneity correction plays an important role in getting accurate fluxes. The extreme deviations in the colour coefficient were very probably related to atmospheric-instrumental problems, and so the associated frames were removed from the dataset (colour-based selection). Sometimes an atmospheric-instrumental perturbation produces an anomalous behaviour of the colour coefficient that is associated with a systematic artifact in the fluxes of all images of a lensed QSO. Thus, we must be careful when interpreting the origin of short-timescale variations in lensed QSOs.

We used the standard deviation between adjacent magnitudes (time separation ≤ 3 days) as an error estimator. This works with stellar records, and moreover, QSO 0957 + 561 is not an optically violently variable QSO. We obtained self-consistent uncertainties for stars and QSO images. The final step consisted of grouping pairs or trios of magnitudes measured on the same night. These final light curves in the g band are incorporated in our current LQLM I data-tools release. However, during the analysis of the time delays of the Twin QSO, we recovered some critical frames ($80 < \text{SNR}(A) < 100$) to improve the information on the time evolution of A [16]. The A light curve in Figure 1 includes these additional fluxes. In Figure 1, we also shift the A record by +417 days (time delay) and -0.089 mag (magnitude offset) to better assess the origin of the observed variability.

4. LQLM I Light Curves and Performance of the LRT

Several LQLM I light curves have been presented in recent months [7, 16, 19]. For example, the r -band records of SBS 0909 + 532 from January 2005 to June 2006 are based on 153 original frames. However, a useful database containing 92 frames (after corrections and preselection) was used to make the light curves [7]. Hence, the success rate (useful frames/original frames) was 60%, which is really impressive if one rethinks the observational procedure, that is, photometric exposures taken in a fully automatic (robotic) way; so one cannot correct the telescope pointing (when it fails), adapt the exposure time to the atmospheric-moonlight conditions, and so forth. This means an effective sampling

TABLE 2: Performance of the LRT when taking modest nightly exposures of double QSOs with images A and B.

Target/filter	Sampling period (days)	$\sigma(m_A)$ (mmag)	ε_A (%)	$\sigma(m_B)$ (mmag)	ε_B (%)
SBS 0909 + 532/ <i>r</i>	4	14	1.3	18	1.7
QSO 0957 + 561/ <i>g</i>	3.7	16	1.5	16	1.5
QSO 0957 + 561/ <i>r</i>	4.3	12	1.1	12	1.1
FBQ 0951 + 2635/ <i>i</i>	5-6	14	1.3	—	—

period (excluding the ~ 120 -day seasonal gap) of about 4 days, that is, ~ 2 useful 120 seconds exposures per week (see Table 2). Although pipelines and other posterior refinements were not considered in this first part of the project, we checked the time evolution of the QSO images by means of a parallel *R*-band monitoring at the Maidanak Observatory. The photometric uncertainties were $\sigma(m_A) \sim 14$ mmag ($m_A \sim 16.4$ mag) and $\sigma(m_B) \sim 18$ mmag ($m_B \sim 17$ mag), and we unambiguously detected 50–100 mmag intrinsic variations. The corresponding photometric accuracies were $\varepsilon_A \sim 1.3\%$ and $\varepsilon_B \sim 1.7\%$ ($\varepsilon = \sigma(F)/F = 0.921\sigma(m)$, where F is the physical flux). In Figure 2, we show SDSS magnitudes of the A image in the 2005–2006 season (from October 2005 to June 2006). The *r*-band record (red triangles) traces a 50 mmag intrinsic gradient around day 3800. This is also detected in the *g* band record (green circles) of the brightest image A. To properly compare the behaviours in both bands, the bluer (*g*-band) record is shifted by -0.57 mag.

All LQLM I frames of QSO 0957 + 561 were fully analysed using the photometric scheme in Figure 1. After corrections and preselection ($\text{FWHM} < 3''$), the global database contained 199 frames in the *g* band and 210 frames in the *r* band. This means that $\sim 75\%$ of the original LRT frames were selected as input for the CPP (see previous section). Before applying the TP, we removed the frames with $\text{SNR}(A) < 100$. The database was also rechecked for anomalies in the image formation, which led to the rejection of the *r*-band exposures taken during the first semester of 2005. The initial high-quality database consisted of 170 *g*-band and 167 *r*-band frames (TP input), that is, about 60% of the original ones. We then found some anomalous values of the colour coefficients (TP output). These are due to atmospheric-instrumental perturbations at some epochs; so the associated frames must also be removed from the database. The final records were based on 163 *g*-band and 142 *r*-band useful exposures of 100–200 seconds [16]. The average magnitudes and photometric uncertainties were $m_A \sim m_B \sim 17.2$ mag (*g*-band) and $m_A \sim m_B \sim 17$ mag (*r*-band), and $\sigma(m_A) \sim \sigma(m_B) \sim 16$ mmag (*g*-band) and $\sigma(m_A) \sim \sigma(m_B) \sim 12$ mmag (*r*-band). Thus, photometry to the 1%–2% was achieved for the lensed QSO. All these results appear in Table 2. With respect to the observed variability, we found several 100–200 mmag intrinsic events and gradients. The final light curves of the A image in the 2005–2006 and 2006–2007 seasons are displayed in Figure 3. We present both the *g*-band (green circles) and *r*-band (red triangles) curves, where the redder (*r*-band) record is shifted by $+0.229$

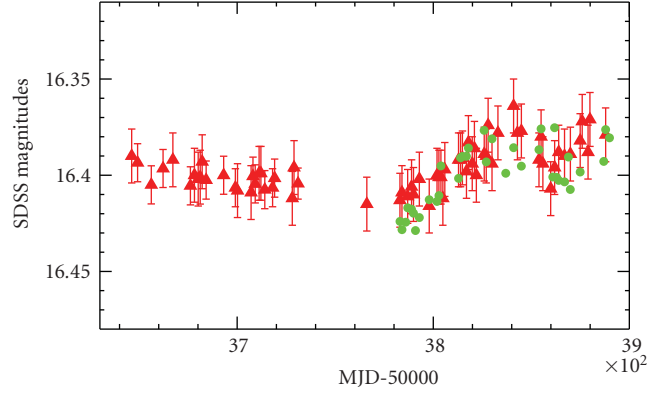


FIGURE 2: LRT light curves of SBS 0909 + 532A from October 2005 to June 2006. The whole *r*-band record (red triangles) is compared to the *g*-band curve (green circles) over the second half of the 2005–2006 season (it is shifted by -0.57 mag).

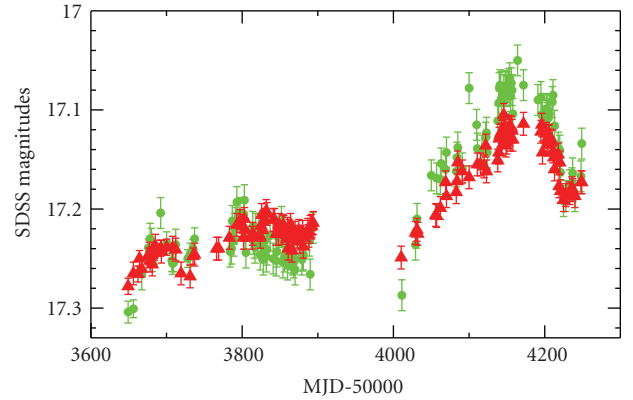


FIGURE 3: LRT light curves of QSO 0957 + 561A from October 2005 to June 2007. The *r*-band (red triangles) and *g*-band (green circles) curves are compared with each other. To make the comparison easier, the *r*-band magnitudes are shifted by $+0.229$ mag.

mag (average *g-r* colour). The *r*-SDSS record from October 2005 to June 2007 (two whole seasons) incorporates different prominent features that are also seen in the *g*-SDSS curve (see Figure 3), with the *g*-SDSS features having a larger amplitude.

After running the CPP, the combined frames of FBQ 0951 + 2635 in the *i* band were selected on the basis of their image quality: $\text{FWHM} < 1.5''$ and $\text{SNR}(S3) > 50$, where the S3 field star has a magnitude similar to that of the faintest QSO image B ($m_A \sim 17.5$ mag and $m_B \sim 18.6$ mag). Therefore, the TP was exclusively applied to 22 combined exposures of mostly 400–500 seconds [19]. Unfortunately, we could not achieve 1%–2% level photometry for B even using frames with $\langle \text{FWHM} \rangle \sim 1.2''$ and $\langle \text{SNR}(S3) \rangle \sim 80$. Some deviations between fluxes of adjacent nights were very large (see green triangles in Figure 4), and we did not try to improve the B record (subtracting galaxy contaminations, looking for outliers, grouping adjacent fluxes, etc). The light curve of A is much less noisy, and so an accurate trend could be obtained by grouping four pairs of adjacent fluxes

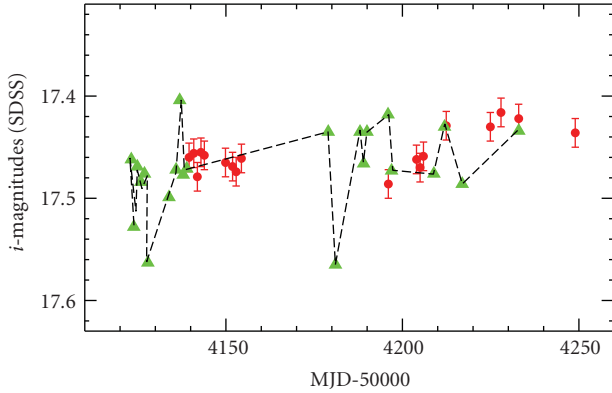


FIGURE 4: LRT *i*-band light curves of FBQ 0951 + 2635 in February-May 2007. We compare the record of the A image (red circles) and the time- and magnitude-shifted light curve of the B image (green triangles; the noisy brightness record of B is shifted in time and magnitude, using the 16-day time delay of the system and an average magnitude difference of 1.094 mag). There is a reasonable agreement between both trends, and so we do not find evidence of short-timescale extrinsic variability.

(showing significant differences between pair members). The final record of A (18 data points; see red circles in Figure 4) is characterised by a typical uncertainty $\sigma(m_A) \sim 14$ mmag, and it shows a 60 mmag gradient.

As a general conclusion, the LRT works reasonably well when monitoring the 17-mag *r*-band images of two of the brightest double QSOs. Nightly 120 seconds exposures permit us to get accurate and reliable fluxes, approximately 2 times per week. Although this sampling efficiency is partially due to weather, technical factors play also a role (see Section 6). While the fluxes of the images of the wide-separation system ($\Delta\theta_{AB} \gg 1''$) have 12 mmag errors ($\sim 1\%$ accuracy in physical flux), the study of the compact system leads to larger uncertainties ($\sim 2\%$ accuracy in physical flux). In the current (second) phase of the LQLM project, we are trying to characterise the performance of the LRT when monitoring fainter (18–19 mag) *r*-band images of double and quadruple QSOs from nightly exposures of 300–600 seconds (see Section 6).

5. Main Scientific Outputs

5.1. Time Delays. The accurate *r*-band light curves of SBS 0909 + 532 allowed us to confirm the time delay of the system (about 50 days) [7]. On the other hand, the QSO 0957 + 561 records led to accurate time delays between QSO images and optical bands [16]. These new delays (together with previous ones obtained by the Princeton group and collaborators [20]) suggested the existence of reverberation in the accretion disc around the central black hole (BH; see Figure 5). High-energy (EUV/X-ray) flares are generated within or close to the jet and later reprocessed by the disc in two different emission rings (blue and red rings in Figure 5, corresponding to the *g* and *r* observation bands, resp.). The fluctuations at shorter wavelengths (inner ring) are then

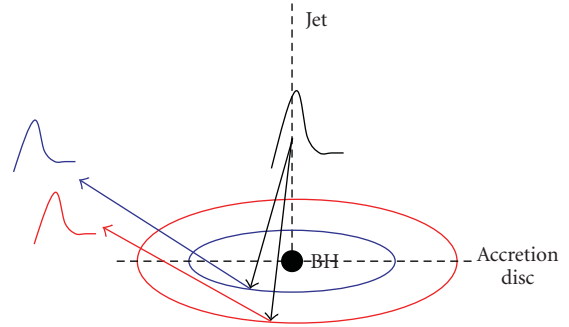


FIGURE 5: Reverberation in the accretion disc around the central BH of QSO 0957 + 561.

produced and observed before than those similar variations at larger wavelengths (outer ring).

5.2. Structure Functions. The brightness records of SBS 0909 + 532 (*r* band) and QSO 0957 + 561 (*g* and *r* bands) are important tools to better understand the mechanism of intrinsic variability in QSOs at $1 < z < 2$. Both double QSOs have similar redshift ($z \sim 1.4$), BH mass ($M_{BH} \sim 2\text{--}4 \times 10^9 M_\odot$), and luminosity [21]; so similar fluctuations might be produced in both distant sources. In the first study of the structure function of SBS 0909 + 532, no simple model was able to accurately reproduce the typical luminosity fluctuations at rest-frame lags shorter than 100 days [7]. However, if we compute more realistic uncertainties in the structure function, that is, considering that not all pairs of data in a given time lag bin are independent [22], 100-day time-symmetric flares can account for the fluctuations at $\lambda_{rest} \sim 2600 \text{ \AA}$ (reduced $\chi^2 \sim 1$).

We also obtained the structure functions of the QSO 0957 + 561 luminosity at $\lambda_{rest} \sim 2100 \text{ \AA}$ (*g* band) and 2600 \AA (*r* band) [23]. In Figure 6, we show the three LQLM I structure functions. For QSO 0957 + 561, we did not find clear evidence of a chromatic mechanism of variability, since the fluctuations at the two rest-frame wavelengths were explained from the production of 100-day time-symmetric and 170-day time-asymmetric flares. A time-asymmetric flare refers to a shot with very different rise and decay times, whereas a time-symmetric flare has symmetric rise and decay. Although there are subtle differences between the two structure functions of QSO 0957 + 561 (see Figure 6), these are likely caused by the difference between time coverages, gaps, and artifacts in the *g* ($\lambda_{rest} \sim 2100 \text{ \AA}$) and *r* ($\lambda_{rest} \sim 2600 \text{ \AA}$) bands [23]. Besides of the time delay measurements, our structure function analysis also supports a reverberation scenario (see Figure 5). As time-symmetric flares lasting ~ 100 days are also generated in SBS 0909 + 532 (see above), this fact suggests a unified scheme. In other words, the SBS 0909 + 532 flares at $\lambda_{rest} \sim 2600 \text{ \AA}$ may be due to high-energy symmetric fluctuations similar to those occurring in QSO 0957 + 561. High-energy asymmetric fluctuations (lasting ~ 170 days) would be produced in an intermittent way, since they are not detected in our SBS 0909 + 532 records and

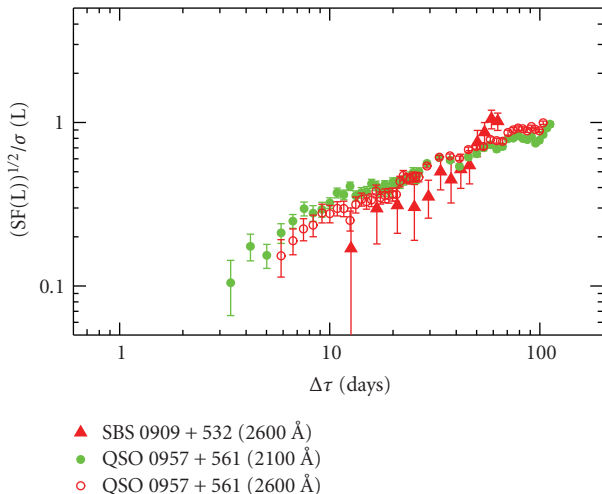


FIGURE 6: LQLM I structure functions of the UV variability of two lensed QSOs.

previous records of QSO 0957 + 561 (that were obtained 10 years before).

The on-going monitoring of QSO 0957 + 561 will permit us to very accurately trace the structure at $\Delta\tau \leq 100$ days as well as to properly address the structure at rest-frame lags exceeding $\Delta\tau \sim 100$ days. In a forthcoming analysis, from a longer monitoring period, we will describe the UV variability at rest-frame lags ≤ 1 year.

5.3. Extrinsic Variations. We have not detected any kind of extrinsic signal. If the light curves of SBS 0909 + 532, QSO 0957 + 561, and FBQ 0951 + 2635 incorporate extrinsic variations, these should be very weak (undetectable in our experiments). Thus, we indeed put constraints on the possible extrinsic signals. These constraints can be used to obtain information on the composition of the lensing halos and the structure of the distant sources (see Introduction and [7, 16, 24]).

6. Archive and LQLM II Subproject

All LQLM I optical frames are publicly available at the Liverpool Quasar Lens Monitoring archive [25] on the German Astrophysical Virtual Observatory (GAVO). This archive is part of a larger optical database of gravitationally lensed QSOs. The whole collection of frames consists of exposures from three telescopes in the North Hemisphere: 3.5 m ARC Telescope at the Apache Point Observatory (USA), 2.0 m LRT at the Roque de los Muchachos Observatory (Canary Islands, Spain), and 1.5 m AZT-22 at the Maidanak Observatory (Uzbekistan). We point out that much of these frames at the global Lens Image Archive on the GAVO are not in the public domain, but the person-in-charge of the Maidanak database could make them available upon request.

In the LQLM public archive, for example, you may select a target and a filter and then get details on observation dates, labels of FITS files (frames), exposure times (in s),

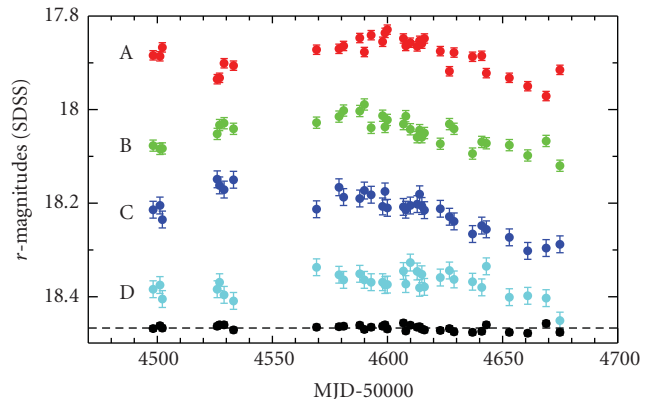


FIGURE 7: LRT light curves of the four images A–D of H 1413 + 117 (Cloverleaf QSO). These r -band records correspond to the LQLM II observational subprogram.

file sizes, air masses, Moon illuminations (fractions), lunar distances (in deg), backgrounds (in counts s^{-1}), and seeing values (in $''$). We also manage a website incorporating information on the status of the LQLM project. In particular, the LQLM I data-tools release [26] includes a link to the archive as well as public access to some photometric pipelines and their outputs (quality of images, instrumental fluxes, transformation coefficients, calibrated and corrected magnitudes, etc.). The data-tools release also contains final light curves and references.

The second observational phase of the LQLM project started in February 2008, and it will be completed in the middle of 2010 or early 2011. This LQLM II observational subprogram is designed to take frames for a broad range of lensed QSOs. The main targets are the very bright doubles observed during the first phase as well as other bright double and quadruple QSOs. For example, the Cloverleaf QSO (H 1413 + 117) consists of four images A–D of a QSO at $z = 2.55$ [12]. A photometric model with four close stellar-like sources, that is, four empirical PSFs, is able to fully describe the compact lens system. From this photometric model, we infer the light curves in Figure 7. The LQLM II records in Figure 7 are based on 300 seconds r -band exposures taken over a semester (February–July 2008). Apart from the curves of the four quasar images (A–D), the light curve of a control (non-variable) star is also plotted for comparison (black circles and dashed horizontal line; the stellar brightness is shifted by +0.3 mag). We remark that the QSO records from our best 33 frames, that is, from a set of exposures having $\langle \text{FWHM} \rangle \sim 1.2''$ and $\langle \text{SNR}(\text{star}) \rangle \sim 200$, are characterised by small observational noises: $\sigma(m_A) \sim 10$ mmag ($m_A \sim 17.9$ mag), $\sigma(m_B) \sim 12$ mmag ($m_B \sim 18$ mag), $\sigma(m_C) \sim 18$ mmag ($m_C \sim 18.2$ mag), and $\sigma(m_D) \sim 18$ mmag ($m_D \sim 18.4$ mag).

The LRT performance has improved during the last observing semesters (LQLM II period), and this is a promising result to make a high-quality r -band database (QSO images with $m_r \leq 19$ mag) leading to 1%-2% accuracy and reasonable sampling. Excluding two relatively long gaps in the light curves of H 1413 + 117 (see Figure 7), the effective

sampling period is about 4 days. For the very bright and widely separated double QSO (0957 + 561), we have obtained an effective sampling period of about 2.4 days over the first semester of 2008 and the 2008–2009 season (from November 2008 to June 2009). This represents a sampling efficiency significantly better than the previous one (see Table 2).

Acknowledgments

The authors are grateful to the organizers (LOC and SOC) of the workshop on Robotic Autonomous Observatories held in Malaga from 18 to 21 May 2009, who prepared a useful meeting showing current robotic facilities as well as the efforts of several groups in different fields and some ongoing projects. They thank several members of the Liverpool Telescope staff (M. Bode, C. Moss, R. Smith, and I. Steele) for guidance in the preparation of their robotic monitoring project and kind interaction during the last five years. The Liverpool Telescope is operated on the island of La Palma by Liverpool John Moores University in the Spanish Observatorio del Roque de los Muchachos of the Instituto de Astrofísica de Canarias with financial support from the UK Science and Technology Facilities Council. They thank R. Gil-Merino and B. McLeod for different kinds of support during the first stages of the LQLM project. Their LQLM project is being developed in parallel with a similar project at the Maidanak Observatory. They also thank T. Akhunov, B. Artamonov, O. Burkhanov, E. Koptelova, S. Nuritdinov, A. Sergeyev, and A. Zheleznyak for collaboration, discussion and exchange of information on common targets. They use information taken from the Sloan Digital Sky Survey (SDSS) Web site, and they are grateful to the SDSS team for doing that public database. This research has been financially supported by the Spanish Department of Education and Science Grants AYA2004-08243-C03-02 and AYA2007-67342-C03-02, and University of Cantabria funds.

References

- [1] P. Schneider, J. Ehlers, and E. E. Falco, *Gravitational Lenses*, Springer, Berlin, Germany, 1992.
- [2] S. Refsdal, "On the possibility of determining Hubble's parameter and the masses of galaxies from the gravitational lens effect," *Monthly Notices of the Royal Astronomical Society*, vol. 128, pp. 307–310, 1964.
- [3] C. S. Kochanek, P. Schneider, and J. Wambsganss, *Gravitational Lensing: Strong, Weak & Micro*, Springer, Berlin, Germany, 2006.
- [4] A. Yonehara, "Source size limitation from variabilities of a lensed quasar," *Astrophysical Journal*, vol. 519, no. 1, pp. L31–L34, 1999.
- [5] L. J. Goicoechea, "Multiple delays in QSO 0957+561: observational evidence and interpretation," *Monthly Notices of the Royal Astronomical Society*, vol. 334, no. 4, pp. 905–911, 2002.
- [6] T. Kawaguchi, S. Mineshige, M. Umemura, and E. L. Turner, "Optical variability in active galactic nuclei: starbursts or disk instabilities?" *The Astrophysical Journal*, vol. 504, no. 2, pp. 671–679, 1998.
- [7] L. J. Goicoechea, V. N. Shalyapin, E. Koptelova, R. Gil-Merino, A. P. Zheleznyak, and A. Ullán, "First robotic monitoring of a lensed quasar: intrinsic variability of SBS 0909+532," *New Astronomy*, vol. 13, no. 3, pp. 182–193, 2008.
- [8] D. Parafiez, J. Hjorth, I. Burud, P. Jakobsen, and Á. Elíasdóttir, "Microlensing variability in time-delay quasars," *Astronomy and Astrophysics*, vol. 455, no. 1, pp. L1–L4, 2006.
- [9] J. Wambsganss, *Gravitational microlensing*, Ph.D. thesis, Munich University, Munich, Germany, 1990.
- [10] C. S. Kochanek, "Quantitative interpretation of quasar microlensing light curves," *The Astrophysical Journal*, vol. 605, no. 1, pp. 58–77, 2004.
- [11] R. Gil-Merino, J. González-Cadelo, L. J. Goicoechea, V. N. Shalyapin, and G. F. Lewis, "Is there a caustic crossing in the lensed quasar Q2237+0305 observational data record?" *Monthly Notices of the Royal Astronomical Society*, vol. 371, no. 3, pp. 1478–1482, 2006.
- [12] C. S. Kochanek, E. E. Falco, C. Impey, et al., "Gravitational Lens Data Base," 2009, <http://www.cfa.harvard.edu/castles/>.
- [13] I. A. Steele, "The Liverpool robotic telescope," *New Astronomy Reviews*, vol. 45, no. 1–2, pp. 45–47, 2001.
- [14] I. A. Steele, R. J. Smith, P. C. Rees, et al., "The Liverpool telescope: performance and first results," in *Ground-based Telescopes*, vol. 5489 of *Proceedings of SPIE*, pp. 679–692, Glasgow, UK, June 2004.
- [15] B. A. McLeod, G. M. Bernstein, M. J. Rieke, and D. W. Weedman, "The gravitational lens MG 0414+0534: a link between red galaxies and dust," *The Astronomical Journal*, vol. 115, no. 4, pp. 1377–1382, 1998.
- [16] V. N. Shalyapin, L. J. Goicoechea, E. Koptelova, A. Ullán, and R. Gil-Merino, "New two-colour light curves of Q0957+561: time delays and the origin of intrinsic variations," *Astronomy and Astrophysics*, vol. 492, no. 2, pp. 401–410, 2008.
- [17] J. Manfroid, F. Selman, and H. Jones, "Achieving 1% photometric accuracy with the ESO Wide Field Imager," *The Messenger*, vol. 104, pp. 16–20, 2001.
- [18] E. A. Magnier and J.-C. Cuillandre, "The Elixir system: data characterization and calibration at the Canada-France-Hawaii Telescope," *The Publications of the Astronomical Society of the Pacific*, vol. 116, no. 819, pp. 449–464, 2004.
- [19] V. N. Shalyapin, L. J. Goicoechea, E. Koptelova, et al., "Microlensing variability in FBQ 0951+2635: short-timescale events or a long-timescale fluctuation?" *Monthly Notices of the Royal Astronomical Society*, vol. 397, pp. 1982–1989, 2009.
- [20] T. Kundić, E. L. Turner, W. N. Colley, et al., "A robust determination of the time delay in 0957+561A, B and a measurement of the global value of Hubble's constant," *The Astrophysical Journal*, vol. 482, no. 1, pp. 75–82, 1997.
- [21] C. Y. Peng, C. D. Impey, H.-W. Rix, et al., "Probing the coevolution of supermassive black holes and galaxies using gravitationally lensed quasar hosts," *The Astrophysical Journal*, vol. 649, no. 2, pp. 616–634, 2006.
- [22] S. Collier and B. M. Peterson, "Characteristic ultraviolet/optical timescales in active galactic nuclei," *The Astrophysical Journal*, vol. 555, no. 2, pp. 775–785, 2001.
- [23] L. J. Goicoechea, V. N. Shalyapin, R. Gil-Merino, and A. Ullán, "Structure function of the UV variability of Q0957+561," *Astronomy and Astrophysics*, vol. 492, no. 2, pp. 411–417, 2008.
- [24] R. Schmidt and J. Wambsganss, "Limits on MACHOs from microlensing in the double quasar Q0957+561," *Astronomy and Astrophysics*, vol. 335, no. 1, pp. 379–387, 1998.
- [25] <http://dc.zah.uni-heidelberg.de/liverpool/res/rawframes/q/form>.
- [26] http://grupos.unican.es/glendama/LQLMI_DR.htm.

Review Article

BART: The Czech Autonomous Observatory

**Martin Nekola,¹ René Hudec,¹ Martin Jelínek,² Petr Kubánek,^{2,3}
Jan Štrobl,¹ and Cyril Polášek¹**

¹ *Astronomical Institute, The Academy of Sciences of the Czech Republic, Fričova 298, CZ–251 65 Ondřejov, Czech Republic*

² *Instituto de Astrofísica de Andalucía (CSIC), Camino Bajo de Huétor, 50, 18.008 Granada, Spain*

³ *Laboratorio de Procesado de Imágenes, Parque Científico del Campus de Paterna, Institutos de Investigación, Universidad de Valencia, edificio 3, planta 3, Polígono Industrial La Coma, s/n, 46.980 Paterna, Spain*

Correspondence should be addressed to Martin Nekola, ford@asu.cas.cz

Received 30 June 2009; Revised 30 November 2009; Accepted 16 January 2010

Academic Editor: Alberto J. Castro-Tirado

Copyright © 2010 Martin Nekola et al. This is an open access article distributed under the Creative Commons Attribution License, which permits unrestricted use, distribution, and reproduction in any medium, provided the original work is properly cited.

The High Energy Astrophysics group of the stellar department of the Astronomical Institute in Ondřejov operates two small aperture robotic telescopes called BART and D50. Both telescopes are capable of making automatic followup observation of gamma-ray burst optical counterparts. This paper deals with the smaller telescope BART.

1. Introduction

An increasing use of microprocessors in different professions has also touched an astronomical instrumentation like a telescope guiding, or even controlling of a whole observatory including an observation scheduling. Nowadays there is roughly one hundred robotic telescopes throughout the world. A degree of robotization level differs. Only few of them reach the level of complete independence. Generally the term robotic telescope stand for any telescope using advanced information technologies—a computer is at least able to guide a telescope to given position and take images or is capable of more complicated tasks. The term autonomous observatory means a robotic telescope and dome are computer controlled in such manner, that all indispensable actions of observation are done automatically, including processing of weather conditions, dome driving, choosing objects to observe, exposing by cameras or other optical sensors, taking calibration images, and so forth. No human interaction nor activity is necessary for observation.

2. BART

The Burst Alert Robotic Telescope (BART) is an independent robotic observatory, employing an 0.25 m optical telescope, dedicated to monitoring of objects interesting for high energy astrophysics like X-ray stars, supernovae, active

galactic nuclei (AGN), blazars, cataclysmic variable stars (CV), quasars and to Gamma-Ray Burst (GRB) follow-up.

BART has been since the beginning designed as an autonomous robotic observatory. Thanks to the effort of our team lasting few years we achieved the required level of automation. It is operated by High Energy Astrophysics group of the Stellar department of the Astronomical Institute in Ondřejov. It is the first autonomous observatory in the Institute and the first observatory controlled by Remote Telescope System (RTS) software [1–3].

The space telescopes and orbital observatories working in sundry energy ranges represent an important tool of modern astrophysics with many valuable inputs for the different fields of astronomy and astrophysics. There are scientific applications where the support by ground-based robotic telescopes can substantially improve the scientific value of satellite data. Examples of such objects are *INTEGRAL* gamma-ray sources, CV or blazars. Also simultaneous optical data for various satellite campaigns are needful. The ground-based telescopes with immediate response to satellite observations have been designed mostly for immediate optical GRB observations. The system can be applied also for other types of astrophysical objects requiring immediate ground-based observations, like flares of TeV sources or blazars. Our telescope BART can perform observing of objects without human interaction including immediate reaction to GCN (GRB Coordinates Network [4]) alert or long term

monitoring of selected objects, for example GK Per, TT Ari, OJ 287.

Another application of robotic telescopes is for example, monitoring of various celestial objects for their activity states, like CV, AGN and blazars. It can then provide inputs for following satellite observations during active states of these sources (ToO—targets of opportunity). Another possibility is a simultaneous observation providing complementary optical data as well as good sampling over long time interval, for example. *INTEGRAL* gamma-ray sources with optical counterparts where mostly the optical light curve is not available for comparison with gamma-ray light curves. The software RTS2 allows planning of observation of such objects with user defined priority and procedure of observation.

BART is made of devices easily available on market (mount, optical telescope assembly, CCD camera, focuser, filter wheel). It is relatively easy to build it and reproduce it.

BART was also serving as a platform for developing and testing of software package RTS. An advantage of BART is the availability of location from the capital Prague, where is located the Charles University. Students can come to observatory and learn how to observe with BART and how to process acquired data.

3. History of BART

Using of inexpensive instrumentation supplemented by dedicated software was first time considered in 1992. Further idea was to equip the telescope by attached wide field (WF) camera covering the error box of the *BATSE* satellite. There was also an additional idea of using the attached WF camera as a testing device. It had similar parameters to the optical monitoring camera (OMC) onboard the *INTEGRAL*—17 arc seconds/pixel and limiting magnitude about 15.

At the beginning we had 254 mm (10") telescope Meade LX200 with fork mount, CCD cameras SBIG, Meopta lens f 109 mm/d 82.5 mm, PC, observing room, so we did not search ideal unique place with good weather, dark night sky and electric power, optical telescope assembly with the best quality optics and stable construction, stable and fast mount for used telescope capable of accurate positioning and tracking and guide cables from devices like cameras and so forth. We used what we had.

We needed to develop or to get many things like a controlling software, a computer controlled roof, weather sensors, Internet connectivity, an uninterruptable power source, photometric filters and a computer controlled carousel and a focuser and so forth. We faced to many problems, for example avoiding of collision of telescope with roof or other things in vicinity, broken cameras, guiding cables from cameras and so forth, bad optics fixing, dew at optics, stray light, weather data acquisition and processing, useful calibration images, logical archive system, data processing and reduction, and so on.

The first controlling software for telescope BART was developed by Jan Soldán. Software for controlling of autonomous observatory RTS was later developed by students of Faculty of Mathematics and Physics of Charles University in Prague, mainly by Petr Kubánek. Later it was rewritten.

The current version of RTS is number 2 (RTS2). During development of BART various approaches and methods were tested.

Observation began in 2001. BART was a robotic telescope capable of fast follow-up observation of GCN alerts. It was not yet an autonomous observatory. Man had to manually open and close the roof, switch on and off the mount, manually to do focusing, watch a weather conditions and check the controlling software. It is necessary never again. During BART's lifetime we changed CCD cameras, the mount, WF lenses, a focusing, photometric filters and software. BART later generated daughter experiments such as BOOTES and FRAM.

We plan to preprocess the data archive for a better accessibility of the data and provide a preview of a light curve of an examined object.

4. A Contemporary BART Configuration

BART consists of the following devices:

- (i) optical telescope assembly: 10" Schmidt-Cassegrain Meade LX 200—an amateur astronomers classic,
- (ii) FLI digital focuser,
- (iii) color filter wheel FLI CFW-1,
- (iv) CCD camera FLI MaxCam CM2-1 with back-illuminated chip,
- (v) equatorial mount of German type Losmandy Titan + Gemini GoTo guiding system,
- (vi) wide field camera attached to the Meade: teleobjective Rubinar, CCD camera FLI IMG6303,
- (vii) room with sliding roof at solar building; it can be opened remotely; room was inherited from another experiment; It was necessary to do some improvements,
- (viii) precipitation detector Meteoservis RDM1,
- (ix) cloud meter based on measurement of thermal radiation,
- (x) Polaris watcher-CCD camera with small chip and Meopta lens f 109 mm/d 82.5 mm.

Main parameters of the telescope and the attached wide field camera you can find in the Table 1. BART is shown in the Figure 1.

5. Software

BART uses the following software:

- (i) GNU/Linux: an operating system,
- (ii) RTS-2: a GNU GPL licensed software package for controlling of autonomous observatory,
- (iii) PostgreSQL: an open source SQL database.

RTS2 is an integrated open source package for remote telescope control running under the Linux operating system. It can control various cameras, photometers, mounts and

TABLE 1: BART parameters.

	Telescope	WF camera
optical setup	Schmidt-Cassegrain	Maksutov-Cassegrain
focal length	1600 mm	500 mm
aperture	254 mm	89 mm
field of view	28×28 arc minutes	3.1×2.1 arc degree
CCD sensor resolution	1024×1024 of $13 \mu\text{m}$ pixels	3088×2056 of $9 \mu\text{m}$ pixels
photometric filters	Johnson B, V, R, i, z	—
limiting magnitude	17.5 at 3σ for 60 s in R	16.2 at 3σ for 60 s
slew speed	6 arc degrees/s	—

dome controllers. RTS2 can perform a whole observation from choosing targets from a database, opening and closing roof, changing position of a telescope, setting photometric filters, taking exposures and calibration images by cameras, processing images and storing their coordinates and other data to the SQL database. RTS2 uses the FITS data format for storing images all time. Now it writes also coordinates in the FITS WCS (World Coordinate System) to the image header. FITS and WCS are well known standards.

Every target object in our database has its own identification number and observing script. The script describes the length and number of expositions and used photometric filters for one observation of an object. A number of observations can belong to one object.

RTS2 can choose targets during a night by calculating a merit function of all observable targets during every last exposition of actual script or can perform queue scheduling or direct entering of targets. There is also a module for receiving and processing of GCN alerts. It interrupts execution of actual script and guides the telescope to the coordinates received by the GCN alert message and starts the observation according to a script for GRBs.

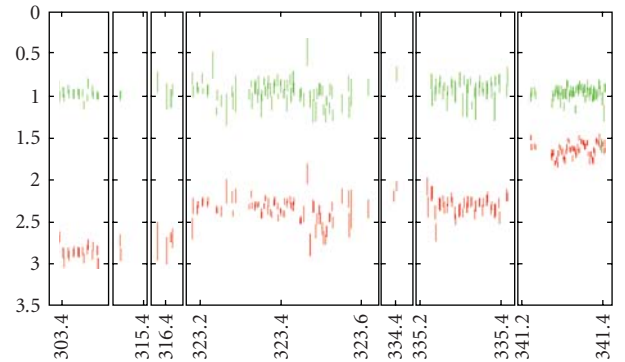
RTS2 is capable of remote supervision by a secure shell (ssh) remote login and by a program `rts2-mon`, which is a part of the package allowing to see a state of all devices and daemons and to change selected state parameters of the running system. RTS2 also includes several utilities for adding new targets and their observing scripts to the SQL database, generating a list of targets stored in the database or showing information about selected target or image and for selecting images from archive according to entered criteria. In the past there was a website for accessing the database of targets and preview images using any web browser. There is an informative website about BART <http://lascaux.asu.cas.cz/en>.

6. Science with BART

GRBs are most energetic known explosions in the universe. BART has observed many GRB positions as a prompt reaction to GCN alerts. It had seen optical afterglows of GRB-GRB060218, GRB060512. Measurements of negative observations gave magnitudes, that were published at GCN circulars [5]. A part of them you can see in the Table 2. In the Table 3 you can see BART reactions to GCN alerts



FIGURE 1: Burst Alert Robotic Telescope; wide field camera at left top.

FIGURE 2: An example of photometric light curve of GK Per obtained from BART's data; x -axis shows time in JD-2453000.0.

shorter than one hour after an alert in years 2005–2007. BART has been observing more high energy sources, for example cataclysmic variable star GK Per. Its light curve is shown in the Figure 2. There were published numerous papers about BART, mostly dealing with GRBs, telescope setup, RTS2 and observational results [6–15] and a few with respect to another type of high energy objects [16, 17].

TABLE 2: Overview of BART GRB reactions 2002–2005.

GRB	GRB Δ	GCN Δ	comment
020124	11 h 30 m	10 h 20 m	R > 14 mag
020305	10 h 30 m	30 m	R > 14 mag
020317	58 m	90 s	R > 13,5 mag
020331	5 h 30 m	5 h 20 m	R > 12,5 mag, bad weather
030824	1 h 50 m	30 m	R > 14,3 mag
031111A	1 h 10 m	30 s	disturbing Moon
031111B	10 m	30 s	R > 14,5 mag, I > 14,2 mag
040403	93 m	—	preburst limit
040606	5 h 30 m	—	I > 12 mag
050505	9,5 m	29 s	V > 11,5 mag, poor cond.
050509A	79 s	62 s	V > 14,9 mag
050520	15 m	14 m	V > 14 mag
050525	10 m	16 s	V ~ 15 mag
050824	10 m	31 s	V > 12 mag

TABLE 3: Overview of BART GRB reactions 2005–2007.

GRB	GRB Δ	GCN Δ
GRB 070613	53.927 s	21.539 s
GRB 070502	01 m 42.696 s	27.092 s
GRB 070429	13 m 35.885 s	12 m 05.614 s
GRB 070412	11 m 21.490 s	07.903 s
GRB 070411	52.225 s	12.446 s
GRB 070411	01:03:42.425	58 m 26.233 s
GRB 070406	19:50:48.262	04.412 s
GRB 070314	56.758 s	37.045 s
GRB 070306	54 m 11.582 s	53 m 07.358 s
GRB 061019	01 m 10.642 s	33.251 s
GRB 060929	02 m 36.382 s	02 m 33.236 s
GRB 060926	57.920 s	44.080 s
GRB 060901	04:02:02.340	04 m 54.359 s
GRB 060522	02 m 36.118 s	32.778 s
GRB 060512	13 m 44.794 s	33.761 s
GRB 060507	01 m 00.563 s	40.254 s
GRB 060421	33.695 s	19.397 s
GRB 051112	06 m 49.959 s	02 m 11.065 s
GRB 051109	49.531 s	21.104 s
GRB 051013	−06 m 21.183 s	16 m 36.237 s
GRB 051011	01 m 05.765 s	22.718 s
GRB 051011	17 m 50.197 s	31.649 s
GRB 051011	01 m 06.120 s	44.372 s
GRB 051008	11 m 58.140 s	21.769 s
GRB 050922	05 m 57.392 s	02 m 24.348 s
GRB 050807	27.617 s	20.170 s

7. Conclusions

BART is a good instrument for monitoring of objects with limiting magnitude 17.5 in R filter and for student's practice. RTS2 is well designed to take advantage of networking. There is certain probability to observe an optical counterpart

of GRB considering a weather in our region and limiting magnitude of BART.

Acknowledgments

The authors acknowledge support by ESA PECS *INTEGRAL* Project 98023 and by the Grant Agency of the Czech Republic 205/08/1207. The third author was supported by Spanish Ministry of Education and Science Grant no. AP2003-1407. The authors would like thank everyone who help with BART for his/her help.

References

- [1] P. Kubánek, M. Jelínek, S. Vítek, A. De Ugarte Postigo, M. Nekola, and J. French, “RTS2: a powerful robotic observatory manager,” in *Advanced Software and Control for Astronomy*, H. Lewis and A. Bridger, Eds., vol. 6274 of *Proceedings of SPIE*, Orlando, Fla, USA, May 2006, 62741V.
- [2] P. Kubánek, “Remote Telescope System—2nd version,” November 2008, <http://rts2.org>.
- [3] P. Kubánek, M. Jelínek, M. Nekola, et al., “RTS2—remote telescope system, 2nd version,” in *Gamma-Ray Bursts: 30 Years of Discovery: Gamma-Ray Burst Symposium*, vol. 727 of *AIP Conference Proceedings*, pp. 753–756, 2004.
- [4] GCN, “The Gamma-Ray bursts Coordinates Network,” November 2009, <http://gcn.gsfc.nasa.gov>.
- [5] GCN circulars 1236, 1265, 1278, 2456, 2491, 3431, 3481, 3498, 3500, 3854, 4319, 4535, 4536, 4617, 4675, 4986, 5092, 5658, 6335, 7651, 7689, 8092, November 2009, http://gcn.gsfc.nasa.gov/gcn3_archive.html.
- [6] P. Kubánek, M. Jelínek, S. Vítek, et al., “Status of robotics telescopes driven by RTS2 (BART, BOOTES, FRAM and Watcher),” *Nuovo Cimento della Societa Italiana di Fisica B*, vol. 121, no. 12, pp. 1501–1502, 2006.
- [7] P. Kubánek, M. Jelínek, R. Hudec, M. Nekola, and J. Štrobl, “BART: real time follow-up of GRBs since 2001,” in *Gamma-Ray Bursts in the Swift Era: Sixteenth Maryland Astrophysics Conference*, vol. 836 of *AIP Conference Proceedings*, pp. 684–687, 2006.
- [8] M. Jelínek, P. Kubánek, R. Hudec, M. Nekola, M. Topinka, and J. Štrobl, “BART—burst alert robotic telescope,” in *The Astrophysics of Cataclysmic Variables and Related Objects*, J.-M. Hameury and J.-P. Lasota, Eds., vol. 330 of *Proceedings of ASP Conference*, p. 481, Astronomical Society of the Pacific, 2005.
- [9] M. Jelínek, P. Kubánek, and M. Nekola, “BART 2001–2004: an intelligent robotic observatory,” *Nuovo Cimento della Societa Italiana di Fisica C*, vol. 28, no. 4-5, pp. 735–738, 2005.
- [10] M. Jelínek, P. Kubánek, M. Nekola, and R. Hudec, “BART: an intelligent GRB and sky monitoring telescope (2000–2004),” *Astronomische Nachrichten*, vol. 325, no. 6–8, p. 678, 2004.
- [11] M. Jelínek, P. Kubánek, M. Nekola, and R. Hudec, “GRB optical prompt followup with BART,” in *Third Rome Workshop on Gamma-Ray Bursts in the Afterglow Era*, M. Feroci, F. Frontera, N. Masetti, and L. Piro, Eds., vol. 312 of *ASP Conference Series*, p. 213, Astronomical Society of the Pacific, 2004.
- [12] M. Jelínek, R. Hudec, P. Kubánek, et al., “BART—recent status,” in *Gamma-Ray Burst and Afterglow Astronomy 2001: A Workshop Celebrating the First Year of the HETE Mission*, vol. 662 of *AIP Conference Proceedings*, pp. 520–522, 2003.
- [13] M. Jelínek, P. Kubánek, M. Nekola, et al., *Robotic Telescope BART*, vol. 16, Odessa Astronomical, 2003.

- [14] R. Hudec, M. Nekola, P. Kubánek, C. Polášek, and A. J. Castro-Tirado, “The status of the Ondřejov BART experiment,” in *Gamma-Ray Bursts in the Afterglow Era*, E. Costa, F. Frontera, and J. Hjorth, Eds., *Eso Astrophysics Symposia*, p. 396, Springer, London, UK, 2001.
- [15] R. Hudec, J. Soldán, V. Hudcová, et al., “Optical observations of GRBs: EN, BART, and OMC,” in *Proceedings of the 5th Huntsville Symposium on Gamma-ray Bursts*, vol. 526 of *AIP Conference Proceedings*, pp. 265–269, September 2000.
- [16] J. Soldán, R. Hudec, M. Němeček, and T. Rezek, “Burst alert robotic telescope (BART) and monitoring of selected AGNs,” in *BL Lac Phenomenon Poster Session*, p. 103, Turku, Finland, June 1998.
- [17] R. Hudec, M. Jelínek, M. Nekola, and P. Kubánek, “BART robotic telescope and blazar monitoring,” in *High Energy Blazar Astronomy*, L. Takal and E. Valtaoja, Eds., vol. 299 of *ASP Conference Series*, pp. 193–196, Astronomical Society of the Pacific, San Francisco, Calif, USA, 2003.

Research Article

Four Years of Real-Time GRB Followup by BOOTES-1B (2005–2008)

Martin Jelínek,¹ Alberto J. Castro-Tirado,¹ Antonio de Ugarte Postigo,² Petr Kubánek,^{1,3} Sergey Guziy,¹ Javier Gorosabel,¹ Ronan Cunniffe,¹ Stanislav Vitek,⁴ René Hudec,^{4,5} Victor Reglero,³ and Lola Sabau-Graziati⁶

¹*Instituto de Astrofísica de Andalucía (IAA CSIC), 18008 Granada, Spain*

²*Instituto Nazionale di Astrofisica, 23807 Milano, Italy*

³*Image Processing Laboratory, Universitat de Valencia, 46980 Valencia, Spain*

⁴*Fakulta Elektrotechnická, ČVUT, 16627 Praha, Czech Republic*

⁵*Astronomický ústav Akademie věd (ASÚ AV ČR), 251 65 Ondřejov, Czech Republic*

⁶*Instituto Nacional de Técnica Aeroespacial, 28850 Torrejón de Ardoz, Spain*

Correspondence should be addressed to Martin Jelínek, mates@iaa.es

Received 25 July 2009; Revised 18 November 2009; Accepted 12 January 2010

Academic Editor: Joshua S. Bloom

Copyright © 2010 Martin Jelínek et al. This is an open access article distributed under the Creative Commons Attribution License, which permits unrestricted use, distribution, and reproduction in any medium, provided the original work is properly cited.

Four years of BOOTES-1B GRB follow-up history are summarised for the first time in the form of a table. The successfully followed events are described case by case. Further, the data are used to show the GRB trigger rate in Spain on a per-year basis, resulting in an estimate of 18 triggers and about 51 hours of telescope time per year for real-time triggers. These numbers grow to about 22 triggers and 77 hours per year if we include also the GRBs observable within 2 hours after the trigger.

1. Introduction

BOOTES-1B (see also [1, 2]) is an independent robotic observatory with a 30 cm aperture telescope dedicated primarily to followup of gamma-ray burst (GRBs). Since 2003, it has used RTS2 [3] as an observing system. It is located at the atmospheric sounding station (Estación de Sondeos Atmosféricos—ESAt, INTA) of El Arenosillo in Andaluca, Spain (at lat: 37°06′16″ N, long: 06°43′58″W). A nearby, older dome (BOOTES-1A) is used for complementary wider angle instruments (Figure 2).

We present results of our GRB follow-up programme. In a large table, we show a 4-year long follow-up log of BOOTES-1B GRBs—including all triggers available in real time which were or should have been received and processed by the system. This selected sample of GRBs is then used to provide a basic idea of how much time is needed at the telescope to observe GRB optical afterglows.

2. Robotic Telescope Configuration

The telescope is built mostly from commercially available components—a Paramount ME from Software Bisque and a $D = 30$ cm Schmidt-Cassegrain optical tube assembly from Meade. Over time, four distinct system configurations were used, including also two 8-inch S-C telescopes (Figure 1).

2.1. Original Meade—Stereoscopic System. The original BOOTES project idea of a new generation of robotic telescopes was very simple, BOOTES-1B would—simultaneous with an identical setup at BOOTES-2 for parallax ability—look for optical transients in an extended area of the sky with wide field cameras. Both systems would use a commercial 12-inch Meade LX-200 “robot.” The wide-field cameras were considered a primary instrument, while the ability to followup with a large telescope was an option. Between 1998 and 2002 the wide-field system provided simultaneous

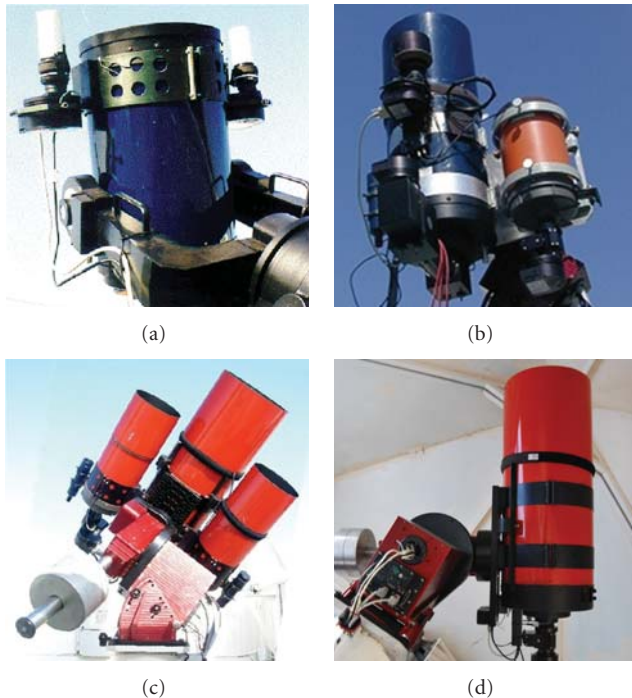


FIGURE 1: Four historic BOOTES-1B configurations.

limits for several *CGRO/BATSE* and *BeppoSAX* GRBs, most notably the candidate afterglow for the short GRB 000313 [4]. The 30 cm telescope was successfully used to followup GRB 030329.

Although we made the original system able to observe, it kept having problems. It required an operator presence several times per week and, despite a notable effort, the fork mount's electronics had to be exchanged several times. Because of that, we decided to purchase another mount.

2.2. The Prototype. The new incarnation of BOOTES-1B was in preparation since mid-2002, and the first prototype was put together in November 2002 in order to follow-up *INTEGRAL* bursts. The most important change was the mount to be used—the Paramount ME from Software Bisque. The system was still carrying a wide field camera, but a shift had been made in priorities—the wide field camera performed monitoring of satellite field of view and the telescope pointed when a trigger was received. The early stage was, however, plagued with technical and organizational problems which eventually delayed the first real-time real-GRB follow-up until early 2005.

The prototype carried three instruments on a large aluminium base plate: the 30 cm telescope with a field spectrograph [5] plus an SBIG-ST8 camera, the 20 cm Meade (originally BOOTES-1A) telescope with an SBIG-ST9 camera observing in a fixed V-band filter, and an unfiltered wide-field 18 mm/1 : 2.8 with an SBIG ST-8 CCD ($43^\circ \times 29^\circ$).

BOOTES-1B was operating with this setup for about a year—on June 2004, it was dismantled and sent to the Workshop in Ondřejov for a definitive solution.



FIGURE 2: The building of ESAt with domes of BOOTES-1A and BOOTES-1B (2002).

2.3. Triple Telescope. The prototype was very heavy and from the beginning had some problems. In September 2004 BOOTES-1B finally received an upgrade—together with the 30 cm telescope, there were also two 20 cm telescopes (One of them lent personally by AJCT) for direct imaging in different filters. The system was completely redesigned with many mechanical improvements and was built to be as light as possible to allow the mount working at its maximum slewing speed. In belief that the rapid dissemination and fast followup after the launch of *Swift* would lead into relatively frequent detections of bright optical counterparts, the 30 cm telescope was equipped with a field spectrograph and two 20 cm telescopes with fixed V&I-band filters. The limiting magnitude of all three instruments was $V \sim 16$ for a 60-second exposure. The wide-field cameras were moved from BOOTES-1B to BOOTES-1A.

Later, during the telescope operation, it became clear that the GRB optical transients were not as bright as had been expected and so the spectrograph on the 30 cm telescope was replaced with a direct imaging CCD with R-band filter—improving the limiting magnitude but losing the spectroscopic ability.

On April 23, 2006, The ESAt building was struck by lightning during a storm, destroying a major part of BOOTES-1B electronics. It took more than a year to get BOOTES-1B definitively back online.

2.4. Single 30 cm Telescope. During the lengthy reconstruction of BOOTES-1B, the follow-up strategy was reconsidered: in the interest of detecting more optical transients, the filter(s) were abandoned ($\sim 2.5\times$ or 1 magnitude gain in sensitivity). The limiting magnitude of an unfiltered 120 s exposure would be about 18.0—effectively doubling the likelihood of getting an optical transient in comparison with the R-band imaging (cf. Figure 4). Both 20 cm telescopes were dropped because of lack of suitable CCD cameras available for them. Since then, BOOTES-1B has only a single 30 cm telescope.

Any observations obtained after June 15, 2007 have been obtained without filter (*W* for white). We calibrate them against *R*-band, which, in the case of no color evolution of the optical counterpart, is expected to result in a small constant offset in magnitude.

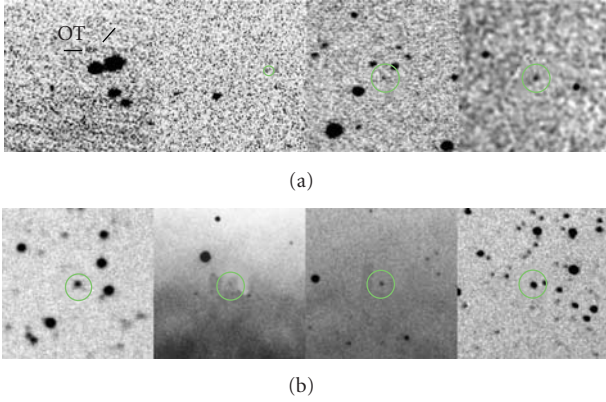


FIGURE 3: GRB optical transient detections by BOOTES-1B: (a) GRB 050824, GRB 050922C, GRB 051109A, GRB 080330. (b) GRB 080413B, GRB 080430, GRB 080602B, GRB 080605.

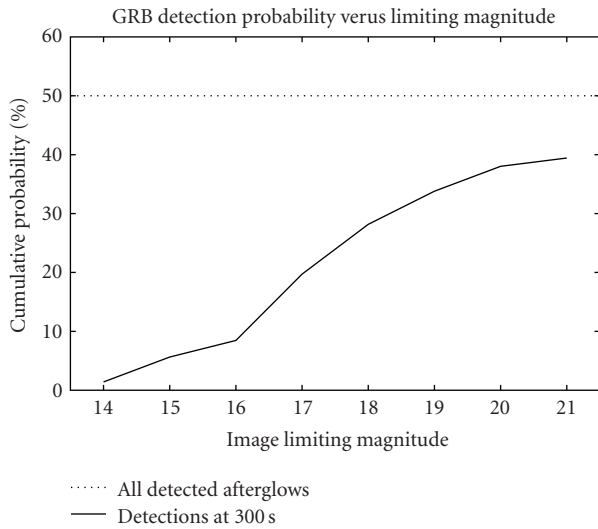


FIGURE 4: The graph (based on T_{300} data from Table 3) showing the likelihood of detection of an optical afterglow of a GRB as a function of the magnitude the telescope can detect (in the time interval discussed here). The dotted line delimits 50%—the ratio of GRBs in our data for which there was eventually discovered an optical transient.

3. Real-Time GRB Followup

BOOTES-1B could have received during the past 4 years (since January 2005 until December 2008) 86 GRB triggers via GCN, which could have been followed in real time or would become observable within the following two hours. Table 3 summarizes these triggers, noting, among BOOTES-1B status of the followup, also the brightness of the GRB optical counterpart if it is known. The magnitude estimation search was done with a heavy use of GRBLog [6]. Successful followups are summarized in Table 1, the detected optical transients also in Figure 3. We use these data to construct a “limiting magnitude versus likelihood of detection” graph (Figure 4).

3.1. GRB Triggers Followed by BOOTES-1B

(a) *GRB 050215B*. GRB was discovered by *Swift*/BAT at 02:33:43.2 UT. BOOTES received the notice, but because of a software error waited with the slew until ~ 22 minutes after the GRB. We coadded 600 s exposures taken by both 20 cm telescopes to obtain limits of $V > 16.5$ and $I > 15.0$ [7].

(b) *GRB 050505*. First image of this *Swift*-discovered GRB [8] was obtained at 23:32:30 UT, that is, 609 s after the trigger and 70 s after receiving the coordinates. No optical afterglow was detected [9].

(c) *GRB 050509A*. At the time of this trigger, the dome was still operating independently on the rest of the system; we obtained the first image 23 s after the GRB trigger (6 s after receiving the alert). The dome was closed due to what we consider a false trigger on the rain sensor. The first useful 10 s exposure was obtained 63.8 minutes after the burst and has a limiting magnitude of $V > 14.9$. A coadd of first 112×10 s exposures with an exposure mean time of 88.0 minutes after the GRB has a limit of $V > 18.1$.

(d) *GRB 050509B*. This was a *Swift*-detected short gamma-ray burst [10]. Starting 62 s after the trigger, BOOTES-1B seems to have obtained the world-first data set of this short duration GRB. However, bad luck caused that the location of the GRB on the sky coincided with the tip of a nearby antenna and its signalling light. The limiting magnitude is thus seriously degraded. The first 10-second exposure has a limiting magnitude of $V > 11.5$; a combination of the first 12×10 s exposures provides $V > 12.5$.

(e) *GRB 050525A*. GRB 050525A [11] was the first BOOTES-1B burst for which a detection was obtained. The telescope started the first exposure 383 s after the GRB trigger (28 s after receiving the notice). An optical afterglow with $V \simeq 15.0$ was detected.

(f) *GRB 050528*. We observed the errorbox [12] at 04:07:56 UT, that is, starting 71 s after the burst and 28 s after receiving the trigger in a light twilight, setting the limit to the possible GRB counterpart to $V > 13.8$ and $I > 13.0$ during the first 60 s after the beginning of our observation [13].

(g) *GRB 050730*. Located at 19:58:23 UT, this GRB was very low above horizon in real time; BOOTES-1B obtained few exposures starting 233.4 s after the GRB, when the system failed. The images did not provide detection of the 17.0 mag optical transient discovered by both *Swift*/UVOT [14] and 1.5 m telescope at OSN [15].

(h) *GRB 050805B*. This short burst was localized by *Swift* at 20:41:26 UT; BOOTES obtained first images 62.2 s after the trigger (7.2 s after receiving the trigger). No optical transient was detected. The first 10-second exposure has a limiting magnitude of $R > 16$, a combination of first five images

(exposure mean time 118 s after the GRB) has a limit of $R > 17.0$.

(i) *GRB 050824*. The optical afterglow of this GRB was discovered with the 1.5 m telescope at Sierra Nevada [16, 17]. BOOTES-1B was, however, the first telescope to observe this optical transient, starting 636 s after the trigger with $R \simeq 17.5$. The weather was not stable and the focus not perfect, but BOOTES-1B worked as expected. Eventually, several hours of data were obtained.

(j) *GRB050904*. BOOTES-1B reacted to this GRB, starting 124 s after the trigger. There was a hot pixel close to the GRB location, which made us believe we might have a detection in the R -band, which was issued in the first BOOTES-1B circular. Later, the observation revised as a limit ($R > 18.2$) which was used to compute the record redshift of this GRB [18]. The I -band camera of the 20 cm telescope, unluckily, failed.

(k) *GRB 050922C*. This bright burst was detected by *Swift*/BAT at 19:55:50 UT. BOOTES was not very lucky; the weather on the station was bad. Instead of a limiting magnitude of ~ 17.0 for a 30-second exposure, we got 12.9. The afterglow was eventually detected with the R -band camera (at the 30 cm telescope) on few occasions between flying clouds. The first weak detection was obtained 228 s after the GRB trigger gave $R \simeq 14.5$.

(l) *GRB 051109A*. This is the only GRB ever detected by BOOTES-1B simultaneously in more than one filter. The first images were obtained 54.8 s after the burst in R and I bands [19].

(m) *GRB 051211B*. Observation of this burst started 42 s after the burst. A 30-second R -band exposure was obtained, but the camera failed after getting this image. Only useless defocused I -band images were taken with the 20 cm telescope [20].

(n) *GRB 051221B*. This GRB was detected by *Swift*/BAT at 20:06:48 UT [21]. BOOTES-1B slewed to the position and started obtaining images 27.8 s after receiving the alert (234.8 s after the burst). We did not find any new source in our images [22]. 30 minutes after the trigger, a faint 21 magnitude afterglow was discovered elsewhere [23].

(o) *GRB 060421*. BOOTES-1B reacted to this GRB within 61 s after the trigger. Images were not of a great quality, yielding a limit of $R > 14$ for the first 10-second exposure and $R > 16$ for the combination of 30 images (exposure mean time was 547 s after the trigger).

(p) *GRB 061110B*. The GRB was detected by *Swift*/BAT at $T_0 = 21:58:45$ UT, but the notices were delayed by 626 s because *Swift* was performing downlink. BOOTES-1B started to slew immediately after reception of the trigger,

obtaining the first image 698 s after the burst (72 s after the GCN notice). When seven 60-second exposures were obtained, a communication error with the mount occurred. The communication was later restored and further 19 images were obtained starting 22:49:49 UT (0.85 hour after burst). Last image was obtained at 23:36:20 (1.62 hours after burst).

Combination of the first 7 images (limiting magnitude ~ 17.2 mag each) with the exposure mean time of 938 s after the GRB trigger was found to have a magnitude limit of ~ 18.0 . Combination of 11 images obtained between 22:49:49 UT and 23:03:45 UT (lim ~ 16.9 mag each) yields a limit of ~ 18.2 with mean time $T_0 + 3452$ s.

(q) *GRB 071101*. In the process of reconstruction, the 30cm telescope from BOOTES-1B was re-installed at the BOOTES-2 site in La Mayora (Málaga). This GRB was the first event successfully observed by the repaired telescope at this site. The GRB trigger [24] was at 17:53:46 UT. BOOTES started imaging 54.8 s after the burst (23.3 s after receiving the coordinates). No afterglow was detected, an unfiltered, R -band calibrated limit of $W > 17.0$ was estimated [25].

(r) *GRB 071109*. *INTEGRAL* detected this GRB at 20:36:05 UT [26]. BOOTES followed up 58.5 s after the GRB (30.9 s after receiving the alert). Because of high altitude clouds, the telescope performance was reduced, yielding an unfiltered limit of ~ 13.0 in the first 10 s exposure [27].

(s) *GRB 080330*. This GRB [28] happened during the first day of recomissioning of BOOTES-1B after its move from BOOTES-2 site in La Mayora. The GCN client was not yet operational and at the time of the GRB we were focusing the telescope. First image was obtained 379 s after the GRB trigger and the optical afterglow was detected with magnitude ~ 16.3 on the first image. A bug in the centering algorithm caused a loss of part subsequent data. Further detections were obtained starting 21 minutes after the GRB when the problem was fixed.

(t) *GRB 080413A*. BOOTES-1B started obtaining images of the GRB 080413A [29] starting 60.7 s after the trigger (46.3 s after reception of the alert). A $W \simeq 13.3$ magnitude optical afterglow was found [30].

(u) *GRB 080430*. BOOTES-1B obtained the first image of this GRB [31] 34.4 s after the trigger. An optical transient was found with a magnitude of $W \simeq 15.5$ [32].

(v) *GRB 080603B*. This GRB happened at BOOTES-1 site during sunset. We obtained first useful images starting one hour after the trigger. An $W \simeq 17.4$ optical transient was found.

(w) *GRB 080605*. GRB 080605 was observed starting 41.9 s after the trigger. A rapidly decaying optical afterglow with $W \simeq 14.8$ was found [33].

(x) *GRB 081003B*. *INTEGRAL* detected this GRB at 20:36:05 UT [34]. BOOTES started obtaining unfiltered images at 20:48:49 UT (41 s after the GRB trigger and 17.4 s after the GCN notice); single images have a detection limit of $W > 14$ mag. The combination of the first 32 images with an exposure mean time of 80 s after the GRB has a limit of $W > 17.6$ mag (calibrated against GSC2). Neither shows any new sources within the GRB errorbox [35].

4. Implications

4.1. Success Rate. Of the 89 triggers, 45 were processed in realtime and observed if possible; in 44 cases the system could not respond. This makes the overall failure rate quite high (50%). 29 triggers were, however, lost due to long-term failures resulting from the telescope being struck by lightning. 8 more triggers failed during the first 6 months of operation, when the system was not yet fully stable and one was lost during maintenance (and followed manually). 6 triggers out of 47 (13%) were lost unexpectedly during the 963 nights of telescope operation if we do not count the first semester of 2005.

4.2. Planning. When specifying the GRB follow-up needs, the number of nights (hours) spent observing GRBs has to be estimated. Under various follow-up strategies, we may derive different results.

Due to various instrumental effects (like a passage through the South Atlantic Anomaly) related to the satellite *Swift*, an offset from the overall triggering statistic which would depend on a geographical location could be found.

In Table 3, the fourth column has the time in hours until the first set of the event location below 10° of altitude or until the Sun rises above -15° of altitude. For nonrealtime events, this is the time the location spends on the night sky; for real-time triggers, it is the time between the trigger and the moment when the target becomes unobservable.

For a small telescope, we assume that once the GRB is real-time triggered, it is unlikely to detect it the following night (i.e., after ~ 24 hours); so we assume the following simple follow-up strategy: Let the telescope observe the GRB once it becomes accessible for the first time (which is immediately for real-time triggers) and let it observe until the GRB sets or the night ends. Do not observe any further nights. Under the given assumptions, we get the following observing needs (assuming perfect weather).

(y) *Real-time triggers.* There have been 72 real-time triggers during the studied 4 years; during their first nights they accumulated 202 hours.

So if we allow only real-time followable triggers to be observed, we would need ~ 18 triggers per year (once per 20 days) and on average 2.8 hours (max. 8.0 hours) of observing time per trigger, 50.5 hours per year. Such a program would consume about 2% of the telescope time.

(z) *Extended set.* In the extended set, we assume that GRBs that would become observable within 2 hours after the event

TABLE 1: Summary of GRBs successfully followed by BOOTES-1B.

GRB	$T_{\text{obs}} - T_{\text{trigger}}$	$T_{\text{obs}} - T_{\text{notice}}$	mag
050215B	22 min		$V > 16.5, I > 15.0$
050505	609 s	70 s	$V > 14.0$
050509A	63.8 min		$V > 18.1$
050509B	62 s	48 s	$V > 12.5$
050525A	383 s	28 s	$V \approx 15.0$
050528	71 s	28 s	$V > 13.8, I > 13.0$
050730	233 s	172 s	$R > 16$
050824	636 s	55.8 s	$R \approx 17.5$
050805B	62 s	17 s	$R > 16.0$
050904	124 s	43 s	$R > 18.2$
050922C	228 s	62.3 s	$R \approx 14.5$
051109A	54.8 s	27 s	$R \approx 16.2$
051211B	42 s	48.4 s	$I > 14.0$
051221B	234.8 s	27.8 s	$V > 13.3$
060421	61.2 s	47.6 s	$R > 16.0$
061110B	698 s	72 s	$R > 18.0$
071101	54.8 s	23.3 s	$W > 17.0$
071109	58.5 s	30.9 s	$W > 13.0$
080330	379 s		$W \approx 16.3$
080413A	60.7 s	46.3 s	$W \approx 13.3$
080430	34.4 s	22.1 s	$W \approx 15.5$
080603B	60 min		$W \approx 17.4$
080605	41.9 s	29.3 s	$W \approx 14.8$
081003	41 s	17.4 s	$W > 14.8$

TABLE 2: Results of the GRB-planning statistic.

	Real time only	Up to 2 hours
triggers/year	18	22
hours/year	50.5	78.5
hours/trigger	2.8	3.5
days/trigger	20.3	16.6

would also be followed. We would need ~ 22 triggers per year, each with an average length of 3.5 hours. In total we would need 78.5 hours per year, or about 3% of the telescope time. Summary of the triggering statistic cf. Table 2.

4.3. Optical Afterglow Brightnesses. As a representative value of GRB optical transient brightness, important for real-time followup, we have chosen its magnitude at 300 s after the trigger. It turns out that it is not easy to find a uniform sample, and available magnitudes and limits are a mixture of different passbands, mainly V, R and unfiltered CCD magnitudes. For a general idea of how bright an OT could be this is, however, good enough. Figure 4 shows a cumulative probability of detecting an OT five minutes after the trigger with a telescope is able to detect a given magnitude. For many GRBs, the brightness at this early time is unknown, or only a limit from small telescopes has been established, so this curve is actually a slight underestimation.

TABLE 3: The Great Table of BOOTES-1B GRBs. “Target” is the RTS2 target number at BOOTES-1B. t_1 is the time delay between the GRB trigger and the possible start of observation. t_{obs} is the amount of time for which the GRB can be followed until it sets for the first time. m_{300} is the known brightness of the GRB optical transient 300 s after the event. dT is the delay of BOOTES-1B followup.

Object	Target	t_1 [h]	t_{obs} [h]	m_{300} [mag]	dT	observation status
050128	—	+0.0	1.8	—	—	No link to GCN
050208	—	+0.0	4.2	—	—	No link to GCN
050215B	5064	+0.4	10.0	$\gtrsim 16^\dagger$ [36]	22 m	V, I limits [7]
050306	5075	+0.2	1.8	>16 [37]	86 s	w/roof closed
050416B	5109	+0.0	2.8	—	—	grbd failure
050421	5112	+0.0	0.2	>18.4 [38]	—	hw problems
050502A	—	+0.0	1.8	16.3 [39]	—	grbd failure
050505	5123	+0.0	2.2	$—^\dagger$	609 s	clouds, V, I limits
050509A	5129	+0.0	2.2	>18.2 [40]	23 s	hw problems, later limit
050509B	5130	+0.0	0.0	>20.8 [41]	62 s	OK, $V > 12.5$, antenna hit!
050520	—	+0.0	3.6	>16.6	—	GCN connection lost
050525A	5136	+0.0	3.6	14.7 [42]	383 s	OK, V-band lightcurve
050714A	1037	+0.0	3.6	$—^\dagger$	10 m	manually, later limit
050730	50008	+1.2	1.6	17.4 [14]	1 h 40 m	limits
050805B	50015	+0.2	7.2	—	62 s	Limits
050824	50032	+0.0	5.2	17.5 [17]	636 s	detection [17]
050904	50055	+0.0	2.8	$—^\dagger$	124 s	R-band limit [18]
050922C	50090	+0.0	6.2	15.5 [43]	228 s	detections between clouds
051109A	50126	+0.0	1.4	16.8	54.8 s	detection in R,I
051111	—	+0.0	4.6	14.9 [44]	—	GCN connection lost
051211A	50144	+0.0	3.2	$—^\dagger$	—	CCD failure
051211B	50146	+0.0	4.8	>14.0	50 s	OK, limits [20]
051221B	50151	+0.0	3.8	>18.2 [45]	235 s	OK, limits [22]
051227	50155	+1.6	10.6	>19.2 [46]	59 m	bad weather
060111A	50162	+0.0	2.0	>18.3 [47]	296 s	during maintenance, limit
060121	—	+0.0	7.8	$—^\dagger$	—	telescope OFF
060123	50171	+0.0	7.6	—	—	bad weather
060130	50173	+0.0	1.2	—	—	bad weather
060203	—	+0.0	6.2	—	—	bad weather+no GCN
060204C	—	+0.0	9.6	>18.7 [48]	—	bad weather+no GCN
060206	—	+0.0	1.4	16.5 [49]	—	GCN connection lost
060219	50185	+1.0	6.0	>18.6 [50]	—	bad weather
060319	50190	+0.0	4.4	$>19^\dagger$ [51]	—	bad weather
060418	50207	+0.0	1.4	14.2 [52]	—	bad weather
060421	50208	+0.0	3.8	>16.8 [53]	61.2 s	Limit
060424	—	+0.0	0.0	$—^\dagger$	—	hw failure
060502A	—	+0.0	1.0	18.7 [54]	—	hw failure
060507	—	+0.0	2.0	$>15.5^\dagger$ [55]	—	hw failure
060512	—	+0.0	4.6	17.15 [56]	—	hw failure
060515	—	+0.0	1.4	>16.2 [57]	—	hw failure
060522	—	+0.0	1.6	19.65 [58]	—	hw failure
060602A	—	+0.0	1.2	$>15^\dagger$ [59]	—	hw failure
060602B	—	+0.0	3.6	—	—	hw failure
060712	—	+0.2	3.0	>14.5 [60]	—	hw failure
060814	—	+0.0	0.8	>17.4 [61]	—	hw failure
060825	—	+0.0	1.4	>18.3 [62]	—	hw failure
060901	—	+1.6	5.2	$—^\dagger$	—	hw failure
060904A	—	+0.0	0.2	>19.5 [63]	—	hw failure
060904B	—	+0.0	2.2	~ 17 [64, 65]	—	hw failure

TABLE 3: Continued.

Object	Target	t_1 [h]	t_{obs} [h]	m_{300} [mag]	dT	observation status
060929	50212	+0.0	1.2	>17.0 [66]	—	bad weather
061019	50220	+0.0	1.0	>14.8 [†] [67]	—	bad weather
061110B	50228	+0.0	2.2	> 17.8 [†] [68]	11 m 38 s	>18.1 OK
061217	50240	+0.0	2.6	>19.2 [69]	—	mount failure
061218	50242	+0.0	2.0	>18.6 [70]	—	mount failure
061222B	50245	+0.0	0.6	18.0 [71]	—	mount failure
070103	50246	+0.0	2.8	>19.6 [72]	—	mount failure
070129	50253	+0.0	0.4	>19.2 [†] [73]	—	mount failure
070219	—	+0.0	4.8	>20.0 [74]	—	mount failure
070220	50258	+0.0	1.2	>19.6 [75]	—	mount failure
070223	50259	+0.0	4.6	>21.4 [†] [76]	—	mount failure
070224	50260	+1.4	8.0	>20.1 [†] [77]	—	mount failure
070406	50277	+0.0	4.0	—	—	mount failure
070411	—	+0.0	3.2	~18.3 [78]	—	mount failure
070412	—	+0.0	3.2	>20.7 [79]	—	mount failure
070429A	50286	+1.6	1.0	>18.0 [80]	—	mount failure
070531	—	+0.0	1.4	>19.9 [81]	—	mount failure
070610	—	+0.4	6.2	~19 [82]	—	mount failure
070704	—	+1.4	6.2	>21.2 [83]	—	manually disabled
070714A	50010	+0.0	1.0	— [†]	52 s	bad weather
071025	50033	+0.0	0.4	17.3 [84]	—	bad weather
071101	50038	+1.0	10.6	>19.7 [85]	56 s	limit [25]
071109	50040	+0.0	1.0	>15.5 [86]	59 s	thick cirrus, limit [27]
071112C	50044	+0.4	11.0	17.5 [87]	64 s	bad weather
080320	50076	+0.0	0.6	>20 [88]	—	bad weather
080330	50079	+0.0	1.2	16.8 [89]	400 s	manual, detection
080413A	50082	+0.0	1.6	15.0	60.7 s	detection [29]
080430	50090	+0.8	7.4	17.5	34 s	detection [31, 32]
080517	50098	+0.0	2.4	>18.5 [90]	3 h 22 m	weather delay
080603B	50113	+1.6	6.4	16.5 [91]	1 h 15 m	detection
080605	50115	+0.0	3.8	17.9 [92]	43 s	detection [33]
080727C	—	+0.0	4.8	>19.9 [93]	—	dome failure
080903	—	+0.0	4.4	19.2 [94]	—	dome failure
081001	50159	+0.0	1.4	—	—	bad weather
081003B	50167	+0.0	3.6	>17.6 [35]	41 s	OK, limit [35]
081126	50181	+0.0	4.0	>18.0 [95]	—	bad weather
081128A	50184	+1.2	9.8	20.9 [96]	—	bad weather
081210	50188	+0.0	8.0	19.9 [97]	45 m	weather delay, out of focus
081228	50195	+0.0	2.0	19.8 [98]	—	bad weather
081230	50197	+0.0	3.2	19.1 [99]	—	bad weather

[†] denotes discovered optical counterparts where there are not enough data to estimate the brightness 300 s after the GRB.

For example BOOTES-1B, which could detect mag ~ 18 at an unfiltered 60 s exposure, may detect an OT in about one third of the GRB triggers.

5. Conclusions

We have shown in a small historical retrospective the evolution of the telescope of BOOTES-1B, as it developed

from the wide-field survey telescope to a dedicated GRB follow-up telescope.

Four years of BOOTES-1B GRB follow-up history are summarised for the first time transparently in the form of a table, which includes not only the observation status of BOOTES-1B, but also the time for which the object could have been observed, and a magnitude (or a limit) of the GRB optical afterglow 5 minutes after the trigger found in the literature. Every existing GRB trigger which was, or could

have been observed by BOOTES-1B within 2 hours after the trigger is included. Twenty four successfully followed events are described case by case in a separate chapter. Many of these are published for the first time.

The data collected are also used to show the GRB trigger rate in Spain. By simply counting the triggers and the days during which they were collected, we estimate 18 triggers and about 50.5 hours of telescope time per year for real-time triggers. These numbers grow to about 22 triggers and 78.5 hours per year if we include also the GRBs observable within 2 hours after the trigger. We also derive the likelihood of the optical afterglow detection five minutes after the GRB trigger depending on the limiting magnitude of the telescope.

Acknowledgments

The Spanish side was supported by Spanish Ministry of Science and Technology by projects AYA 2004-01515, AYA 2007-63677, AYA2007-67627-C03-03, AYA2008-03467/ESP, and AYA2009-14000-C03-01. The Czech participation is supported by Grants of the Grant Agency of the Czech Republic 205/08/1207, 102/09/0997, and PECS 98023. Martin Jelínek was supported by the Ministry of Education and Science (MEC) Grant AP2003-1407.

References

- [1] A. J. Castro-Tirado, J. Soldán, M. Bernas, et al., “The burst observer and optical transient exploring system (BOOTES),” *Astronomy & Astrophysics*, vol. 138, pp. 583–585, 1999.
- [2] A. J. Castro-Tirado, M. Jelínek, T. J. Mateo Sanguino, and A. de Ugarte Postigo, “BOOTES: a stereoscopic robotic ground support facility,” *Astronomische Nachrichten*, vol. 325, no. 6–8, p. 679, 2004.
- [3] P. Kubánek, M. Jelínek, S. Vitek, A. de Ugarte Postigo, M. Nekola, and J. French, “RTS2: a powerful robotic observatory manager,” in *Advanced Software and Control for Astronomy*, vol. 6274 of *Proceedings of SPIE*, Orlando, Fla, USA, 2006.
- [4] A. J. Castro-Tirado, J. M. Castro Cerón, J. Gorosabel, et al., “Detection of an optical transient following the 13 March 2000 short/hard gamma-ray burst,” *Astronomy & Astrophysics*, vol. 393, no. 3, pp. L55–L59, 2002.
- [5] A. de Ugarte Postigo, “Antonio de Ugarte Postigo, Gamma-ray burst afterglows and instrumentation for their study: From BOOTES to X-shooter,” Ph.D. thesis, Universidad de Granada, Granada, Spain, 2007.
- [6] R. Quimby, E. McMahon, and J. Murphy, “GRBLog: a database for gamma-ray bursts,” *Astrophysics*, vol. 727, pp. 529–532, 2003.
- [7] M. Jelínek, et al., “GRB 050215b, BOOTES-1B optical limit,” GRB Coordinates Network, Circular Service, 3023, 2005.
- [8] M. Jelínek, et al., “Swift-BAT detection of GRB050505,” GRB Coordinates Network, Circular Service, 3360, 2005.
- [9] A. de Ugarte Postigo, M. Jelínek, and J. Gorosabel, “GRB 050505: early time observations,” GRB Coordinates Network, Circular Service, 3376, 2005.
- [10] A. J. Castro-Tirado, A. de Ugarte Postigo, J. Gorosabel, et al., “GRB 050509b: the elusive optical/nIR/mm afterglow of a short-duration GRB,” *Astronomy & Astrophysics*, vol. 439, pp. L15–L18, 2005.
- [11] D. Band, J. Cummings, M. Perri, et al., “GRB 050525: Swift detection of a bright, possibly short burst,” GRB Coordinates Network, Circular Service, 3466, 2005.
- [12] S. T. Holland, “Swift-BAT detection of possible GRB 050528,” GRB Coordinates Network, Circular Service, 3496, 2005.
- [13] M. Jelínek, et al., “GRB050528: BOOTES optical candidate (retraction),” GRB Coordinates Network, Circular Service, 3500, 2005.
- [14] A. J. Blustin, et al., “Swift/UVOT photometry of GRB050730,” GRB Coordinates Network, Circular Service, 3717, 2005.
- [15] S. A. Pandey, A. J. Castro-Tirado, S. McBreen, et al., “Multi-wavelength afterglow observations of the high redshift GRB 050730,” *Astronomy & Astrophysics*, vol. 460, p. 415, 2006.
- [16] S. Campana, S. Barthelmy, D. Burrows, et al., “GRB050824: Swift-BAT detection of a burst,” GRB Coordinates Network, Circular Service, 3866, 2005.
- [17] J. Sollerman, J. P. U. Fynbo, and J. Gorosabel, “The nature of the X-ray flash of August 24 2005,” *Astronomy & Astrophysics*, vol. 466, no. 3, pp. 839–846, 2007.
- [18] J. B. Haislip, M. C. Nysewander, D. E. Reichart, et al., “A photometric redshift of $z = 6.39 \pm 0.12$ for GRB 050904,” *Nature*, vol. 440, no. 7081, pp. 181–183, 2006.
- [19] M. Jelínek, et al., “GRB 051109a: BOOTES R & I-band detection of the early afterglow,” GRB Coordinates Network, Circular Service, 4227, 2005.
- [20] M. Jelínek, et al., “GRB 051211A and GRB051211B: BOOTES simultaneous observations,” GRB Coordinates Network, Circular Service, 4333, 2005.
- [21] P. Boyd, et al., “Swift-BAT detection of a possible burst,” GRB Coordinates Network, Circular Service, 4376, 2005.
- [22] A. de Ugarte Postigo, et al., “GRB 051221B: BOOTES optical observations,” GRB Coordinates Network, Circular Service, 4379, 2005.
- [23] J. P. Halpern and S. Tyagi, “Possible GRB 051221B: MDM optical detection,” GRB Coordinates Network, Circular Service, 4381, 2005.
- [24] S. McBreen, et al., “GRB 071101: Swift detection of a burst,” GRB Coordinates Network, Circular Service, 7030, 2007.
- [25] M. Jelínek, et al., “GRB 071101: BOOTES-2 prompt optical observations,” GRB Coordinates Network, Circular Service, 7032, 2007.
- [26] S. Mereghetti, et al., “GRB 071109: a long GRB detected by INTEGRAL,” GRB Coordinates Network, Circular Service, 7046, 2007.
- [27] A. de Ugarte Postigo, et al., “GRB 071109: BOOTES-2 prompt optical observations,” GRB Coordinates Network, Circular Service, 7047, 2007.
- [28] J. Mao, et al., “GRB 080330: Swift detection of a burst with an optical counterpart,” GRB Coordinates Network, Circular Service, 7537, 2008.
- [29] P. Kubánek, et al., “GRB 080413A Bootes observation,” GRB Coordinates Network, Circular Service, 7603, 2008.
- [30] M. Jelínek, et al., in preparation.
- [31] M. Jelínek, et al., “GRB 080430: Bootes observation,” GRB Coordinates Network, Circular Service, 7648, 2008.
- [32] A. de Ugarte Postigo, et al., in preparation.
- [33] M. Jelínek, et al., “GRB080605: observation by BOOTES,” GRB Coordinates Network, Circular Service, 7837, 2008.
- [34] D. Gotz, et al., “GRB 081003B: a long GRB detected with INTEGRAL,” GRB Coordinates Network, Circular Service, 8317, 2008.

- [35] M. Jelínek, et al., “GRB081003B: optical limits from Spain,” GRB Coordinates Network, Circular Service, 8320, 2008.
- [36] S. A. Yost, et al., “GRB050215B: ROTSE-III optical observations,” GRB Coordinates Network, Circular Service, 3022, 2005.
- [37] R. M. Quimby, et al., “GRB 050306: ROTSE-III early limits,” GRB Coordinates Network, Circular Service, 3107, 2005.
- [38] E. S. Rykoff, S. A. Yost, and H. Swan, “GRB 050421: ROTSE-III optical limits,” GRB Coordinates Network, Circular Service, 3304, 2005.
- [39] C. Guidorzi, A. Monfardini, A. Gomboc, et al., “The early multicolor afterglow of GRB 050502a: possible evidence for a uniform medium with density clumps,” *The Astrophysical Journal*, vol. 630, pp. L121–L124, 2005.
- [40] T. Poole, et al., “GRB050509a: Swift UVOT observations,” GRB Coordinates Network, Circular Service, 3394, 2005.
- [41] P. Wozniak, et al., “GRB 050509b: RAPTOR deep, early limits,” GRB Coordinates Network, Circular Service, 3414, 2005.
- [42] A. J. Blustin, D. Band, S. Barthelmy, et al., “Swift panchromatic observations of the bright gamma-ray burst GRB 050525a,” *The Astrophysical Journal*, vol. 637, pp. 901–913, 2006.
- [43] S. D. Hunsberger, et al., “GRB050922C—Swift UVOT preliminary analysis,” GRB Coordinates Network, Circular Service, 4041, 2005.
- [44] C. G. Mundell, et al., “Faulkes Telescope R-band detection of GRB051111,” GRB Coordinates Network, Circular Service, 4250, 2005.
- [45] A. Klotz, et al., “GRB 051221B: TAROT optical limits,” GRB Coordinates Network, Circular Service, 4386, 2005.
- [46] P. Roming, et al., “GRB 051227: Swift/UVOT upper limits (Possible U-band),” GRB Coordinates Network, Circular Service, 4411, 2005.
- [47] A. Klotz, et al., “GRB 060111: TAROT optical observation,” GRB Coordinates Network, Circular Service, 4483, 2006.
- [48] A. Melandri, et al., “GRB 060204C: Liverpool Telescopes optical limit,” GRB Coordinates Network, Circular Service, 4665, 2006.
- [49] C. Guidorzi, et al., “GRB060206: Liverpool Telescope observation,” GRB Coordinates Network, Circular Service, 4693, 2006.
- [50] A. Breeveld and A. Moretti, “GRB 060219: Swift/UVOT upper limits,” GRB Coordinates Network, Circular Service, 4798, 2006.
- [51] A. Melandri, et al., “GRB060319: Liverpool Telescope optical limit,” GRB Coordinates Network, Circular Service, 4889, 2006.
- [52] M. Jelínek, et al., “GRB 060418: FRAM early afterglow observation,” GRB Coordinates Network, Circular Service, 4976, 2006.
- [53] V. Lipunov, et al., “GRB(?) 060421: MASTER optical limit,” GRB Coordinates Network, Circular Service, 4988, 2006.
- [54] T. S. Poole and V. La Parola, “GRB 060502A: Swift/UVOT source detection,” GRB Coordinates Network, Circular Service, 5068, 2006.
- [55] M. Jelínek, et al., “GRB 060507: BART limit,” GRB Coordinates Network, Circular Service, 5092, 2006.
- [56] M. D. Pasquale and J. Cummings, “Swift/UVOT observations of GRB060512,” GRB Coordinates Network, Circular Service, 5130, 2006.
- [57] A. Klotz, M. Boer, and J. Atteia, “GRB 060515: TAROT optical observation,” GRB Coordinates Network, Circular Service, 5134, 2006.
- [58] S. T. Holland, “GRB 060522: Swift/UVOT observations of the optical Afterglow,” GRB Coordinates Network, Circular Service, 5158, 2006.
- [59] S. Viték, et al., “GRB060602A: bootes-IR observations,” GRB Coordinates Network, Circular Service, 5201, 2006.
- [60] V. Lipunov, et al., “GRB060712: MASTER optical observation,” GRB Coordinates Network, Circular Service, 5303, 2006.
- [61] A. Klotz, M. Boer, and J. Atteia, “GRB 060814: TAROT optical observations,” GRB Coordinates Network, Circular Service, 5448, 2006.
- [62] A. Gomboc, “GRB060825: Liverpool Telescope optical observations,” GRB Coordinates Network, Circular Service, 5476, 2006.
- [63] A. Klotz, M. Boer, and J. Atteia, “GRB 060904: TAROT optical observations,” GRB Coordinates Network, Circular Service, 5506, 2006.
- [64] E. S. Rykoff, et al., “Looking into the Fireball: rotse-III and swift observations of early gamma-ray burst afterglows,” *The Astrophysical Journal*, vol. 702, pp. 489–505, 2009.
- [65] M. Jelínek, et al., in preparation.
- [66] M. Nekola, et al., “GRB 060929: BART observation,” GRB Coordinates Network, Circular Service, 5658, 2006.
- [67] A. Klotz, et al., “GRB 061019: TAROT La Silla observatory optical observations,” GRB Coordinates Network, Circular Service, 5731, 2006.
- [68] H. Mikuz, et al., “GRB061110B: optical observations at Crni Vrh,” GRB Coordinates Network, Circular Service, 5808, 2006.
- [69] A. Klotz, et al., “GRB 061217: TAROT Calern observatory optical observations,” GRB Coordinates Network, Circular Service, 5942, 2006.
- [70] P. D’Avanzo, et al., “GRB 061218: REM prompt observations,” GRB Coordinates Network, Circular Service, 5937, 2006.
- [71] A. de Ugarte Postigo, et al., “GRB 061222B: BOOTES-IR optical observations,” GRB Coordinates Network, Circular Service, 5968, 2006.
- [72] S. T. Holland and T. Sakamoto, “GRB 070103: Swift/UVOT upper limits,” GRB Coordinates Network, Circular Service, 5993, 2006.
- [73] M. M. Chester and O. Godet, “GRB 070129: Swift/UVOT upper limits,” GRB Coordinates Network, Circular Service, 6066, 2007.
- [74] A. Breeveld and T. Sakamoto, “GRB 070219: Swift/UVOT upper limits,” GRB Coordinates Network, Circular Service, 6111, 2007.
- [75] M. Stamatikos, et al., “GRB 070220: Swift detection of a burst,” GRB Coordinates Network, Circular Service, 6114, 2007.
- [76] W. Landsman, et al., “GRB070223: Swift/UVOT refined analysis,” GRB Coordinates Network, Circular Service, 6134, 2007.
- [77] S. T. Holland, et al., “GRB 070224: Swift/UVOT upper limits,” GRB Coordinates Network, Circular Service, 6152, 2007.
- [78] H. Mikuz, et al., “GRB 070411: optical photometry at Crni Vrh,” GRB Coordinates Network, Circular Service, 6288, 2007.
- [79] H. Mikuz and B. Dintinjana, “GRB 070412: optical observations at Crni Vrh,” GRB Coordinates Network, Circular Service, 6284, 2007.
- [80] E. S. Rykoff, et al., “GRB 070429: ROTSE-III optical limits,” GRB Coordinates Network, Circular Service, 6356, 2007.
- [81] M. de Pasquale and C. B. Markwardt, “Swift/UVOT refined analysis of GRB070531,” GRB Coordinates Network, Circular Service, 6481, 2007.

- [82] A. Stefanescu, et al., “GRB 070610: OPTIMA-Burst high-time-resolution optical observations,” GRB Coordinates Network, Circular Service, 6492, 2007.
- [83] A. Meshcheryakov, et al., “GRB 070704: RTT150 optical observations,” GRB Coordinates Network, Circular Service, 6617, 2007.
- [84] E. S. Rykoff, et al., “GRB 071025: ROTSE-III refined analysis,” GRB Coordinates Network, Circular Service, 6992, 2007.
- [85] M. Uemura, et al., “GRB071101: optical and NIR upper limits by KANATA,” GRB Coordinates Network, Circular Service, 7037, 2007.
- [86] A. Klotz, et al., “GRB 071109: TAROT Calern observatory optical observations,” GRB Coordinates Network, Circular Service, 7052, 2007.
- [87] B. Dintinjana, et al., “GRB 071112C: optical observations at Crni Vrh,” GRB Coordinates Network, Circular Service, 7078, 2007.
- [88] G. G. Williams and P. A. Milne, “GRB 080320: early super-LOTIS observations,” GRB Coordinates Network, Circular Service, 7492, 2008.
- [89] A. Klotz, et al., “GRB 080330: TAROT Calern observatory optical observations,” GRB Coordinates Network, Circular Service, 7543, 2008.
- [90] A. M. Parsons, et al., “GRB 080517: Swift detection of a burst,” GRB Coordinates Network, Circular Service, 7742, 2008.
- [91] N. P. M. Kuin, et al., “GRB 080603B: Swift/UVOT detection of the afterglow,” GRB Coordinates Network, Circular Service, 7808, 2008.
- [92] V. Rumyantsev, et al., “GRB080605: optical observations,” GRB Coordinates Network, Circular Service, 7833, 2008.
- [93] E. A. Hoversten and A. M. Parsons, “GRB 080727C: Swift/UVOT upper limits,” GRB Coordinates Network, Circular Service, 8043, 2008.
- [94] F. E. Marshall, et al., “GRB 080903: Swift/UVOT observations,” GRB Coordinates Network, Circular Service, 8179, 2008.
- [95] B. Gendre, et al., “GRB 081126: TAROT Calern observatory optical observations,” GRB Coordinates Network, Circular Service, 8555, 2008.
- [96] L. P. Xin, et al., “GRB 081128: optical observation of xinglong TNT,” GRB Coordinates Network, Circular Service, 8572, 2008.
- [97] S. Immler, et al., “GRB 081210: Swift/UVOT refined analysis,” GRB Coordinates Network, Circular Service, 8654, 2008.
- [98] P. Afonso, et al., “GRB 081228: GROND confirmation of the optical/NIR afterglow,” GRB Coordinates Network, Circular Service, 8752, 2008.
- [99] F. Yuan, et al., “GRB 081230: ROTSE-III detection of optical counterpart,” GRB Coordinates Network, Circular Service, 8754, 2008.

Research Article

MASTER Prompt and Follow-Up GRB Observations

**Nataly Tyurina,¹ Vladimir Lipunov,¹ Victor Kornilov,¹
Evgeny Gorbovskoy,¹ Nikolaj Shatskij,¹ Dmitry Kuvshinov,¹ Pavel Balanutsa,¹
Alexander Belinski,¹ Vadim Krushinsky,² Ivan Zalozhnyh,² Andrey Tlatov,³
Alexander Parkhomenko,³ Kirill Ivanov,⁴ Sergey Yazev,⁴ Peter Kortunov,¹
Anatoly Sankovich,¹ Artem Kuznetsov,¹ and Vladimir Yurkov⁵**

¹ Sternberg Astronomical Institute, Moscow State University, 13, Univeristetskij pr-t, Moscow 119991, Russia

² Ural State University, 51, Lenina pr-t, Ekaterinburg 620083, Russia

³ Kislovodsk Solar Station, P.O. Box 145, 100, Gagarina st., Kislovodsk 357700, Russia

⁴ Irkutsk State University, 1, Karl Marks ul., Irkutsk 664003, Russia

⁵ Blagoveschensk Pedagogical State University, 104, Lenina ul., Blagoveschensk 675000, Russia

Correspondence should be addressed to Nataly Tyurina, tyurina@sai.msu.ru

Received 3 November 2009; Revised 12 February 2010; Accepted 10 March 2010

Academic Editor: Alberto J. Castro-Tirado

Copyright © 2010 Nataly Tyurina et al. This is an open access article distributed under the Creative Commons Attribution License, which permits unrestricted use, distribution, and reproduction in any medium, provided the original work is properly cited.

We presented the results of last years GRB observations obtained on the MASTER robotic telescope, which is the only telescope of its kind in Russia. These results include 5 prompt observations of GRB in 2008 and 2009, follow-up observations of 15 other GRBs in 2008-2009, the first observations in different polarization angles of optical emission from the gamma-ray bursts GRB091020, and observations in different polarization angles for GRB091127 and GRB090820.

1. Introduction

The construction of robotic telescopes, which not only automatically acquire but also automatically process images and choose observing strategies, is a rather new and vigorously developing area in modern astronomy. MASTER (Mobile Astronomy System of Telescope Robots, <http://observ.pereplet.ru>), which is the first and still unique robotic telescope network in Russia, was started through the efforts of scientists at the Sternberg Astronomical Institute of Moscow State University and the Moscow "Optika" Association in 2002 and continues to be developed to the present MASTER-NET [1–3].

MASTER is dedicated to the observation and detection of optical transients on time scales from few seconds to several days. The emphasis is on gamma-ray bursts (GRBs), the most powerful explosions in our Universe. A special program package for image reduction in real-time has been created, making it possible not only to carry out astrometry and photometry of a frame but also to recognize objects lacking in astronomical catalogs: supernovae, new asteroids, optical transients, and so forth. This software allowed us to discover

several supernovae: SN2008gy, SN 2006ak, SN2005ee, and SN 2005bv [4].

We observed 20 error boxes of gamma-ray bursts in 2008-2009 and report the results obtained. There are a total of five prompt observations made with very-wide-field cameras (VWFC) during the past half-year after we mounted these cameras in Kislovodsk and Irkutsk in autumn 2009.

2. MASTER System

MASTER network currently consists of six facilities deployed near Moscow (MASTER-Moscow), Kislovodsk, Irkutsk, Ekaterinburg (MASTER-Ural system), and Blagoveshensk (MASTER-Amur one) [3]. We have distant observatories for only a year and a half, and for about five years, observations have been made only with the Moscow telescope facility located in a village near Domodedovo airport. Its location close to Moscow State University allowed us to design, test, and modify the robot system, repair eventual technical faults, and develop reduction software with no financial support from the state. But the negative side is that we had to observe under poor weather conditions near megalopolis (less than



FIGURE 1: MASTER-II system in Kislovodsk observatory ($D = 400$ mm).

70 clear nights per year and most of them are summer white nights). However, we observed several tens of error boxes during five years (HETE and Swift epochs), and in most of the cases our observations were the earliest [2].

MASTER characteristics [3] are the closest to those of the American ROTSE-III network [5] (<http://www.rotse.net/>). MASTER differs in that its facilities have a larger field of view and several telescopes mounted on a single axis, allowing images to be taken at several different wavelengths simultaneously, as in the case of MASTER-Ural and MASTER-Kislovodsk observations.

Until 2008, most of the GRB observations were made with the MASTER-Moscow system, and we therefore report here its main properties.

The main telescope (with a 355 mm aperture) takes images in white light and serves as the main searching unit of the system. It has an Apogee Alta U16 (4096×4096 pixels) camera mounted on it, making it possible to obtain images in a six-square-degree field. In addition, MASTER has a very-wide-field camera ($50^\circ \times 60^\circ$) that covered the field of view of the HETE orbiting gamma-ray telescope and made it possible to obtain simultaneous observations with HETE down to a limiting magnitude of 9 m using a separate automated scheme. This wide-field facility is capable of searching for bright, transient objects exclusively.

MASTER-Kislovodsk allows us to take images of observed GRB in different wavelengths or in different polarizations simultaneously. This system has 2 main telescopes ($D = 400$ mm, [3], Figure 1) with filters. And we have very wide-field cameras (Figure 2) on the Mountain Solar Station of the Pulkovo Main Astronomical Observatory, allowing us to continuously monitor a 420-square-degree sky field down to 13 m with five-second exposures. We have also installed such cameras in *Irkutsk* and *Tunka systems*. MASTER-Tunka has also a main telescope ($D = 400$ mm). And now we have MASTER-Amur with a 200 mm aperture.

Tunka and Amur systems were mounted in October and November of 2009.

The Kislovodsk, Moscow, Ural, Irkutsk, and Amur facilities are linked via the Internet and are able to respond to the detection of uncatalogued objects (optical transients) within several tens of seconds (processing time included). The results of observations using the MASTER network will be reported separately.

All MASTER facilities can operate in a fully automated mode based on the ephemerides (sunset) provided there are satisfactory weather conditions: (the control computer is continuously attached to a weather sensor), the roofs (above the main mount and wide-field camera) are opened, the telescopes are pointed at bright stars, and pointing corrections are applied, and then, depending on the seeing, the facility either goes into a standby regime or begins a survey of the sky using a specialized, fully automated program.

Thus, observations are conducted in two modes: survey and “alert” (e.g., observations of the already obtained coordinates of the gamma-ray bursts). In the former case, the main telescope automatically takes three frames of an arbitrary region in succession with exposures ranging from 30 to 60 s, moves to a neighboring region 2° away, performs the same procedure, and so on, repeating a given set of three frames every 40–50 minutes. Such a procedure makes it possible to avoid artefacts in the data processing and locate moving objects.

The alert mode is supported by a continuous connection between the control computer and the GCN international gamma-ray burst (GRB) network (<http://gcn.gsfc.nasa.gov/>). After detection of a GRB by a space gamma-ray observatory (Swift, Konus, Fermi etc.), the telescope receives the coordinates of the burst region (coordinate error box), automatically points to this direction, takes an image of this region, reduces the image, and identifies all objects not present in the computer catalogs. If a GRB is detected during the day, its coordinates are included in the observing program for the next night.

A special program package for image reduction in real-time has been developed, which is capable not only of performing astrometric and photometric reduction of a frame but also of recognizing objects not contained in astronomical catalogs: supernovae, new asteroids, optical transients, and so forth. Since the start of its operation, the MASTER system has taken the images for a lot of GRB error boxes (see the results of 2002–2006 observations in [1, 2, 4]). In half of the cases, these observations were the first in the world.

3. GRB Observations

We have observations of 20 GRBs in 2008–2009. The results of our prompt and follow-up observations are listed in Table 1.

We observed 80 GRB error boxes from 2002 to 2009 (20 in 2008–2009, 5 in 2007, 17 in 2006, 17 in 2005, 13 in 2004, 7 in 2003, and 1 in 2002). They represent the only 9 cases with optical counterpart. The reasons are the following: at the beginning of our observations we have a lot of technical problems (like with the Internet in our Moscow village with MASTER-I), then for about 5 years we observed only from Moscow region (with very bad astroclimatic conditions), and most of GRB in the first years of observations (mostly HETE results) came only in our day, so we could observe error-boxes only several hours later. But although we have the earliest observations in Europe of **GRB030329** and have 8 hours of continuous observations, we took the earliest images of **GRB050824**.



FIGURE 2: There are 4 MASTER VWFs located at Kislovodsk observatory.

TABLE 1: GRB observations by MASTER system in 2008-2009.

Burst	Optical limits, m	Comments (observatory, time after trigger information, exposures, circular number, etc.)
GRB091130B	15	MASTER-Amur, unfiltered image, 10-s exposures. The time delay is 40 s after the notice time (65 s after the GRB time). There is no OT brighter than 15 m at the Swift XRT position [6].
GRB091130	14.5	MASTER-Amur observations. 23 seconds after the notice time (7 min 22 s after the GRB time). We do not see OT brighter than 14 mag in BAT error box [7].
GRB091127	~14 mag	MASTER-II-Kislovodsk observed 9 seconds after notice time (91 s after the GRB time). OT images in both polarizations [8].
GRB091020	17.9 R	MASTER-II-Kislovodsk <i>has optical transient polarimetry</i> observed OT 3422 s after the GRB time in R and unfiltered. There are images in different polarization angles [9].
GRB090820	11	MASTER-Kislovodsk and Irkutsk VWF responded to Fermi trigger 272421498, 9 s after the GRB time. We took 1300 images with 5-second exposition <i>in different polarization angles</i> [10].
GRB090715B	20	MASTER-Moscow observations, 19 s after the GCN notice time (8 m 04 s after the burst). 160 images with 30-second expositions. No OT [11].
GRB090528B	R > 19.0 V > 18.1	MASTER-URAL, 7 hours after GRB, 180-s exposures in R and V filters. Our images cover 30% last 1- σ Fermi error box. No OT [12].
GRB090424	~8, ~9	<i>Prompt observations</i> by 6 MASTER VWF in Kislovodsk and Irkutsk with common FOW = 6000 sq·deg., 1-s exposures. Unfiltered images (close to V band). No OT [13].
GRB090408B	17	MASTER-URAL, R and V 60-s exposure, starting after sunset (87 min after trigger time). No OT [14].
GRB090328B	9.1	<i>Prompt observations</i> at MASTER VWF located at Irkutsk. 1-s exposures during night: before, during, and after GRB. No OT [15].
GRB090320B	V ~ 9.0	<i>Prompt observation</i> by MASTER VWF located at Kislovodsk. We observed ~80% 1- σ Fermi error box with 1-s exposure during all night: before, during, and after GRB time. No OT [16].
GRB090305B	V ~ 9.5	<i>Prompt observation</i> by MASTER VWF located at Kislovodsk observed ~80% 1- σ Fermi error box with 1-s exposure 7 hours before, during, and 1 hour after GRB time [17].
GRB081215A	V ~ 11	MASTER VWF located at Kislovodsk observed Fermi trigger (SGR 0044+42) during all night with 5-s expositions [18].
GRB081130B	V ~ 12	<i>Prompt observation</i> . MASTER VWF located at Kislovodsk observed Fermi trigger with 5-s exposures. No OT [19].
GRB081110	19	MASTER-Moscow observed error box 6 hours 42 minutes after the GRB time. We have 89 images with limit for coadded one up to 19 m (S/N = 4). No OT [20].
GRB081102	V ~ 13	2 of MASTER VWF at Kislovodsk observed this error box with 5-s exposures during all night. There are two separated (~702 m) mount with double cameras [21]
GRB080822B	18.8	MASTER-Moscow observed his gamma-ray burst 18 m 43 s after the GRB time with 30-s exposures. Each image has 17 m. Summary image (25 \times 30 s) has 18.8 m. The unfiltered images are calibrated relative to USNO A2.0 (0.8 R + 0.2 B) [22].
GRB080605	R ~ 11.5	MASTER VWF at Kislovodsk observed it 46 s after the GRB time (12 s after the notice arrival time) with a series of 5-s exposures. Unfiltered (close to V). No OT [23]
GRB080319D	V ~ 11.5	MASTER VWF at Kislovodsk observed Swift-BAT trigger with a series of 5-s exposures starting 92 s after notice arrival time (708 s after GRB time). Unfiltered (close to R, i.e., another camera). No OT [24].
GRB080205	19.5	MASTER-Moscow observed it 481 minutes after the GRB time. No OT [25].

TABLE 2: The result of the unfiltered polarization.

West-telescope			East-telescope		
GRB time, hour	OT mag	error	GRB time, hour	OT mag	error
1.605	18.65	0.10	1.605	18.60	0.06
1.983	18.91	0.08	1.983	18.46	0.06
2.286	19.04	0.08	2.286	19.14	0.09
2.563	19.28	0.11	2.563	19.11	0.09
2.840	19.36	0.09	2.840	19.56	0.10
3.117	19.32	0.08	3.117	19.38	0.09
3.395	19.35	0.06	3.395	19.70	0.17
3.672	19.23	0.10	3.672	19.53	0.11
3.949	20.07	0.16	3.949	19.92	0.16
4.227	20.67	0.28	4.227	20.03	0.19
4.505	20.07	0.22	4.505	19.99	0.16

TABLE 3: The results of observations in 2007.

Burst	Optical limits, m	Comments (observatory, time after trigger information, exposures, circular number, etc.)
GRB071122	16	MASTER-Moscow observed it 151 s after the GRB time (61 s after notice time). No OT [35]
GRB070810.8	14.8	MASTER-Moscow observed it 125 s after the GRB time. No OT [36].
GRB070224	13	MASTER VWFC observed error box in Kislovodsk with series of 5-s exposures starting 2 s after notice arrival time. Unfiltered (close to R). No OT.
	18	MASTER-Moscow observed error box 51 s after notice arrival time. Unfiltered. No OT [37].
GRB070223	13	MASTER VWFC observed error box in Kislovodsk 5-s exposures starting 1 s after notice arrival time. No OT. Unfiltered (close to R) [38].
GRB070219	13.5	MASTER VWFC observed error box in Kislovodsk 5-s exposures starting 76 s after the GRB time and 15 s after notice arrival time. No OT [39].

We obtained a total of 5 *prompt* observations with the very-wide-field cameras in Irkutsk and Kislovodsk stations during the past half-year (after we had mounted several VWFC cameras there): GRB090424, GRB090328B, GRB090320B, GRB090305B, and GRB081130B. We found no optical candidate in the reduced images, and we give only the optical limits for GRBs. And we have several GRB's observations *in different polarization angles* (**GRB091127**, **GRB091020**, and **GRB090820**).

If we found no optical counterpart in the reduced images, we give only the optical limits for GRBs, that is, there is no optical transient brighter than this limit.

Kislovodsk and Irkutsk VWFC had different cameras during 2008, and that is why we give V- and R-band data in the second column of the table. We have unfiltered images from these cameras, but they are the closest to V and R bands, and we calibrated them using Tycho catalogue [26]. We also calculate the ratio of optical to gamma fluence [26] for GRBs.

We detected several interesting GRBs during this two years, and we now briefly discuss them.

3.1. GRB091127. MASTER-II robotic telescope located at Kislovodsk has early optical transient polarimetry of this burst. System responded to the GRB 091027 [27] 9 seconds

after notice time and 91 s after the GRB time at very large zenith distance (~ 4 degrees up to horizon). We have bright optical counterpart (~ 14 mag, 91–111 seconds after the GRB time) at Liverpool position [28] in both polarizations. We have ~ 20 images with synchronous exposition in two polarizations before GRB setting with growing exposition from 20 to 160 seconds. And we had possible brightening around 2 minutes (after GRB Time).

3.2. GRB091020. MASTER-II robotic telescope located at Kislovodsk was pointed to the GRB 091020 [29] by the Internet 3422 s after the GRB time. The large delay was caused with technical problems on site [30].

We have 2 *first images in different polarization angles* (East telescope and West one, Figure 3).

The first 7 images was taken in R-band. The exposure of each image is 180 s.

The result of the unfiltered polarization is in Table 1.

Using all our polarized magnitudes, we find that the light curve is very well described by a single power-law decay with $\alpha = 1.2 \pm 0.1$, that is in good agreement with the following observations [31].

The light curve of our observations is available at <http://observ.pereplet.ru/images/GRB091020/grb.html>.

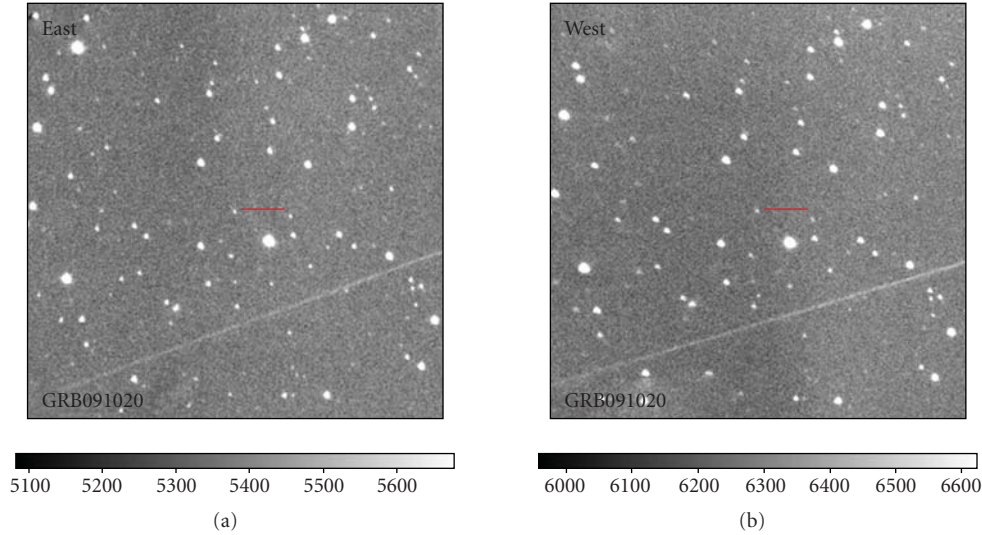


FIGURE 3: GRB091020 images.

3.3. *GRB 090820*. We had MASTER-Net optical polarization observations.

There are 6 MASTER very-wide-field cameras located at Kislovodsk and Irkutsk with common FOW = 2000 + 1680 square degrees observed this bright Fermi trigger [32].

MASTER VWFC, located in Kislovodsk, has produced images beginning at 9 s after the GRB time (first alert notice). We have 1300 images with 5-second exposition in *different polarization angles*. Individual images have limiting magnitudes ~ 11 . Our unfiltered images are calibrated relative to Tycho stars (V) and very close to V-band.

3.4. *GRB090715B*. MASTER robotic telescope located at Moscow ($D = 355$ mm, Apogee Alta U16) responded to the GRB 090715B (Swift trigger, [33]). We have images beginning at 19 s after the GCN notice time. An automated response took the first image at 21:11:18 UT, 8 m 04 s after the burst, under summer Moscow sky.

We have 160 images with 30-second exposition each. These unfiltered images are calibrated relative to USNO 08.R + 0.2B (Usno A2.0). Individual images have limiting magnitudes ranging from 17.8 to 17.0.

No optical transient was found brighter 20.0.

3.5. *GRB090305B-MASTER-Net Prompt Optical Short Burst Observations*. We observed this burst by 6 MASTER very-wide-field cameras located at Kislovodsk and Irkutsk with common FOW = 6000 square degrees. One of the four MASTER very-wide-field Cameras located at Kislovodsk ($D = 50$ mm, 4×1000 square degrees, 11 Mpx) has observed $\sim 80\%$ 1-sigma Fermi error box [34] with 1-s exposure during all night: 7 hours before, during, and 1 hour after GRB time without time gap between images.

Our unfiltered images were calibrated relative to Tycho stars (V). The magnitude limit of each image is ~ 9.5 m at the edge of FOW. We do not detect OT inside the part of

the error box brighter than 9.2 mag before and after trigger time. So we conclude (in the case that GRB is inside our FOW) that the optical fluence during the short 2-s GRBburst is limited by $\sim 1 \times 10^{-8}$ erg/cm² (excluding possible host galaxy absorption).

3.6. *Summary*. There were 5 observations in 2007 with no optical counterpart, because we observed them by Moscow telescope and only VWFC in Kislovodsk, that was just mounted and worked in a half-tested mode.

4. Conclusions

We presented the results of last years GRB observations obtained on the MASTER robotic telescope, which is the only telescope of its kind in Russia. These results include 5 prompt observations of GRB in 2008 and 2009, follow-up observations of 15 other GRBs in 2008-2009, the *first* observations in *different polarization angles* of optical emission from the gamma-ray bursts GRB091020, and observations in *different polarization angles* for **GRB091127** and **GRB090820**.

Our experience of two years of operation of the MASTER wide-field robotic telescope has demonstrated its unique capabilities. We hope that new MASTER telescopes at Kislovodsk and Ural stations and also new Irkutsk and Blagoveschensk systems will justify our hopes. We have 3 optical counterparts in the last half of 2009. When such systems will be installed at suitable sites at various hour angles across Russia, they would provide unique information via continuous monitoring of both the near and distant cosmos.

Acknowledgment

The authors thank the General Director of the “OPTIKA” Association S.M. Bodrov for providing the MASTER project with necessary expensive equipment.

References

- [1] V. M. Lipunov, A. V. Krylov, V. G. Kornilov, et al., “MASTER: the mobile astronomical system of telescope-robots,” *Astronomische Nachrichten*, vol. 325, no. 6–8, pp. 580–582, 2004.
- [2] V. M. Lipunov, V. G. Kornilov, A. V. Krylov, et al., “The master mobile astronomical system. Optical observations of gamma-ray bursts,” *Astrophysics*, vol. 48, no. 3, pp. 389–399, 2005.
- [3] V. M. Lipunov, V. G. Kornilov, E. Gorbovskoy, et al., “Master robotic net,” *Advances in Astronomy*, vol. 2010, Article ID 349171, 6 pages, 2010.
- [4] V. Lipunov, V. G. Kornilov, A. V. Krylov, et al., “Optical observations of gamma-ray bursts, the discovery of supernovae 2005bv, 2005ee, and 2006ak, and searches for transients using the “MASTER” robotic telescope,” *Astronomy Reports*, vol. 51, no. 12, pp. 1004–1025, 2007.
- [5] S. A. Yost, F. Aharonian, C. W. Akerlof, et al., “Status of the ROTSE-III telescope network,” *Astronomische Nachrichten*, vol. 327, no. 8, pp. 803–805, 2006.
- [6] S. Sergienko, V. Yurkov, E. Gorbovskoy, et al., “GRB 091130B: MASTER observations,” *GCN Circular*, no. 10216, 2009.
- [7] S. Sergienko, V. Yurkov, E. Gorbovskoy, et al., “GRB 091130: MASTER observations,” *GCN Circular*, no. 10213, 2009.
- [8] A. Belinski, E. Gorbovskoy, V. M. Lipunov, et al., “GGRB 091127: MASTER early optical transient polarimetry,” *GCN Circular*, no. 10203, 2009.
- [9] E. Gorbovskoy, V. Lipunov, V. Kornilov, et al., “GRB 091020: MASTER-Net optical polarization observations,” *GCN Circular*, no. 10231, 2009.
- [10] E. Gorbovskoy, V. Lipunov, V. Kornilov, et al., “GRB 090820: MASTER-Net optical polarization observations,” *GCN Circular*, no. 9830, 2009.
- [11] D. Kuvshinov, V. Lipunov, V. Kornilov, et al., “GRB 090715B: MASTER optical limit,” *GCN Circular*, no. 9681, 2009.
- [12] V. Krushinski, I. Zalognikh, J. Popov, et al., “GRB 090528B: MASTER-II Kourovka optical limit,” *GCN Circular*, no. 9468, 2009.
- [13] E. Gorbovskoy, V. Lipunov, V. Kornilov, et al., “GRB 090424: MASTER-Net prompt optical limit,” *GCN Circular*, no. 9252, 2009.
- [14] V. Krushinski, I. Zalognikh, T. Kopytova, et al., “GRB 090408B: MASTER II-Kourovka optical observations,” *GCN Circular*, no. 9111, 2009.
- [15] K. Ivanov, S. Yazev, E. Gorbovskoy, et al., “GRB 090328B: MASTER-Irkutsk prompt optical short burst observations,” *GCN Circular*, no. 9065, 2009.
- [16] E. Gorbovskoy, V. Lipunov, V. Kornilov, et al., “GRB 090320B: MASTER-Net prompt optical observations,” *GCN Circular*, no. 9038, 2009.
- [17] E. Gorbovskoy, V. Lipunov, V. Kornilov, et al., “GRB090305B: MASTER-net prompt optical short burst observations,” *GCN Circular*, no. 9004, 2009.
- [18] E. Gorbovskoy, V. Lipunov, V. Kornilov, et al., “Fermi Trig Num 251059717 = SGR 0044+42: MASTER prompt optical observations,” *GCN Circular*, no. 8674, 2008.
- [19] E. Gorbovskoy, V. Lipunov, V. Kornilov, et al., “GRB 081130B: MASTER prompt optical observations,” *GCN Circular*, no. 8597, 2008.
- [20] D. Kuvshinov, E. Gorbovskoy, V. Lipunov, et al., “GRB 081110: MASTER: first optical observations Fermi GRB,” *GCN Circular*, no. 8518, 2008.
- [21] E. Gorbovskoy, V. Lipunov, V. Kornilov, et al., “GRB 081102: MASTER refind and final results,” *GCN Circular*, no. 8516, 2008.
- [22] D. Kuvshinov, V. Lipunov, V. Kornilov, et al., “GRB 080822B: MASTER optical observation,” *GCN Circular*, no. 8123, 2008.
- [23] D. Kuvshinov, V. Lipunov, V. Kornilov, et al., “GRB 080605: MASTER VWF 46 s AT observation,” *GCN Circular*, no. 7836, 2008.
- [24] V. Lipunov, V. Kornilov, D. Kuvshinov, et al., “GRB 080319D: MASTER-VWF-Kislovodsk optical observation,” *GCN Circular*, no. 7455, 2008.
- [25] D. Kuvshinov, V. Lipunov, V. Kornilov, et al., “GRB 080205: MASTER optical observation,” *GCN Circular*, no. 7261, 2008.
- [26] E. Gorbovskoy, et al., *Advances in Astronomy*. In press.
- [27] E. Troja, S. Barthelmy, J. Wren, W. Baumgartner, et al., “GRB 091127: Swift detection of a burst,” *GCN Circular*, no. 10191, 2009.
- [28] R. Smith, S. Kobayashi, C. Guidorzi, et al., “GRB 091127: Liverpool Telescope afterglow candidate,” *GCN Circular*, no. 10192, 2009.
- [29] J. Racusin, S. Barthelmy, A. Beardmore, et al., “GRB 091020: Swift detection of a burst with an optical afterglow,” *GCN Circular*, no. 10048, 2009.
- [30] E. Gorbovskoy, D. Kuvshinov, V. Lipunov, et al., “GRB 091020: MASTER optical transient polarimetry,” *GCN Circular*, no. 10052, 2009.
- [31] D. Kann, U. Laux, M. Roeder, and H. Meusinger, “GRB 091020: early TLS multicolor detections, red afterglow,” *GCN Circular*, no. 10076, 2009.
- [32] V. Connaughton, “GRB 090820: Fermi GBM Detection of a bright burst,” *GCN Circular*, no. 9829, 2009.
- [33] L. Vetere, A. P. Beardmore, N. Gehrels, et al., “GRB 090715B: Swift detection of a burst with a possible optical counterpart,” *GCN Circular*, no. 9668, 2009.
- [34] C. Wilson-Hodge and Fermi GBM Team, “GRB090305B: Fermi GBM detection,” *GCN Circular*, no. 8972, 2009.
- [35] V. Lipunov, V. Kornilov, D. Kuvshinov, et al., “GRB 071122: MASTER optical observation,” *GCN Circular*, no. 7129, 2008.
- [36] V. Lipunov, V. Kornilov, D. Kuvshinov, et al., “GRB 070810: MASTER optical observation,” *GCN Circular*, no. 6752, 2008.
- [37] V. Lipunov, V. Kornilov, D. Kuvshinov, et al., “GRB 070224: MASTER-Net refind analysis,” *GCN Circular*, no. 6140, 2008.
- [38] V. Lipunov, V. Kornilov, N. Shatskiy, et al., “GRB070223: MASTER-VWF-Kislovodsk observations,” *GCN Circular*, no. 6131, 2008.
- [39] V. Lipunov, V. Kornilov, N. Shatskiy, et al., “GRB070219: MASTER-VWF-Kislovodsk observations,” *GCN Circular*, no. 6113, 2008.

Research Article

Recent GRBs Observed with the 1.23 m CAHA Telescope and the Status of Its Upgrade

Javier Gorosabel,¹ Petr Kubánek,^{1,2} Martin Jelínek,¹ Alberto J. Castro-Tirado,¹ Antonio de Ugarte Postigo,³ Sebastián Castillo-Carrión,⁴ Sergey Guziy,¹ Ronan Cunniffe,¹ Matilde Fernández,¹ Nuria Huélamo,⁵ Víctor Terrón,¹ Nicolás Morales,¹ José Luis Ortiz,¹ Stefano Mottola,⁶ and Uri Carsenty⁶

¹ Instituto de Astrofísica de Andalucía (IAA-CSIC), 18008 Granada, Spain

² Imaging Processing Laboratory (IPL), University of Valencia, 4610 Valencia, Spain

³ INAF/Brera Astronomical Observatory, Via Bianchi 46, Lecco, 23807 Merate, Italy

⁴ Universidad de Málaga, 29071 Málaga, Spain

⁵ LAEX-CAB (INTA-CSIC), LAEFF, P.O. Box 78, Villanueva de la Cañada, 28691 Madrid, Spain

⁶ Institute of Planetary Research, DLR, 12489 Berlin, Germany

Correspondence should be addressed to Javier Gorosabel, jgu@iaa.es

Received 2 July 2009; Revised 22 October 2009; Accepted 4 January 2010

Academic Editor: Taro Kotani

Copyright © 2010 Javier Gorosabel et al. This is an open access article distributed under the Creative Commons Attribution License, which permits unrestricted use, distribution, and reproduction in any medium, provided the original work is properly cited.

We report on optical observations of Gamma-Ray Bursts (GRBs) followed up by our collaboration with the 1.23 m telescope located at the Calar Alto observatory. The 1.23 m telescope is an old facility, currently undergoing upgrades to enable fully autonomous response to GRB alerts. We discuss the current status of the control system upgrade of the 1.23 m telescope. The upgrade is being done by our group based on the Remote Telescope System, 2nd Version (RTS2), which controls the available instruments and interacts with the EPICS database of Calar Alto. (Our group is called ARAE (Robotic Astronomy & High-Energy Astrophysics) and is based on members of IAA (Instituto de Astrofísica de Andalucía). Currently the ARAE group is responsible to develop the BOOTES network of robotic telescopes (Jelínek et al. 2009).) Currently the telescope can run fully autonomously or under observer supervision using RTS2. The fast reaction response mode for GRB reaction (typically with response times below 3 minutes from the GRB onset) still needs some development and testing. The telescope is usually operated in legacy interactive mode, with periods of supervised autonomous runs under RTS2. We show the preliminary results of several GRBs followed up with observer intervention during the testing phase of the 1.23 m control software upgrade.

1. Introduction

The 1.23 m telescope is at the German-Spanish observatory of Calar Alto (CAHA) in the province of Almería, Southeast of Spain. The observatory's altitude (2168 m), mean seeing (0.9"; see [1]), and a large fraction (65%) of clear nights make Calar Alto one of the most competitive observatories in Europe in the optical and near-infrared bands. The observatory harbours five telescopes, but only three are currently operative: the 1.23 m, 2.2 m, and 3.5 m telescopes. Figure 1 shows a view of the Calar Alto observatory. The arrow indicates the position of the 1.23 m telescope.

The 1.23 m telescope is a Ritchey-Crétien telescope built in 1975 by Carl Zeiss. The focal ratio of the telescope is f/8 with a total field of view of 90' and a focal plane scale of $\sim 20.9''/\text{mm}$. The aberrationfree field of view is limited to $\sim 15'$. The German mount of the telescope is driven by a mechanical and hydraulic system renovated in 2008 by the observatory staff. Figure 2 shows a drawing and a picture of the 1.23 m CAHA telescope.

Two instruments are available for the 1.23 m, the MAGIC near-infrared camera and the $2\text{ k} \times 2\text{ k}$ SITE#2b optical CCD. Currently, most of the time ($\sim 95\%$) only the optical CCD is used, as the MAGIC camera, one of the first



FIGURE 1: View of the Calar Alto observatory. The picture shows the five telescopes of Calar Alto and the staff building (lower-right corner). The arrow shows the localization of the 1.23 m telescope.

near-infrared cameras ever built, was superseded by modern instruments on larger telescopes. In addition to the offering of the MAGIC near-infrared camera, CAHA is considering the possibility of installing visitor instruments on the 1.23 m telescope.

The field of view of the optical CCD camera is $17' \times 17'$ with a pixel size of $24 \mu\text{m}$. That translates to a pixel scale of $0.5'$ per pixel. The readout time of the whole chip in 1×1 binning mode is very long, close to 4 minutes. For this reason rapid followup observations of transients like Gamma-Ray Bursts (GRBs) are usually carried out trimming the window and/or binning the CCD by 2×2 pixels. Using this technique, the readout time is usually kept below one minute.

The CCD chip is refrigerated using liquid nitrogen, which makes dark current negligible, fewer than 2 electrons per hour. The readout noise is also low, about 7 electrons. However, the chip has several bad columns which RTS2 (see next section and [2]) must avoid at the time of a GRB alert (see the vertical lines on the image of GRB 090628, Figure 6). The optical camera is equipped with a *BVRI* filter wheel. A Wollaston prism can be also mounted in the filter wheel, which makes the 1.23 m telescope suitable also for polarimetric studies.

2. Upgrading the 1.23 m Control Software with RTS2

A call for proposals was issued by CAHA in 2008 for the use of the 1.23 m telescope over 4 years. Six teams obtained observing time, having the following scientific drivers: Solar System bodies, Binary stars, Transits of exoplanets, T Tauri stars, and GRBs. The 1.23 m is also scheduled for public outreach purposes, usually associated to high schools.

The ARAE (Robotic Astronomy & High-Energy Astrophysics) group of IAA (Instituto de Astrofísica de Andalucía, partner in the CAHA operations) agreed to contribute to CAHA by providing the control system of

the 1.23 m telescope. (See <http://www.iaa.es/arae/> and <http://www.iaa.es/bootes/index.php> for more details.) The ARAE group was granted 26 GRB triggers per year with an average duration of 0.5 nights per trigger. The upgrade of the telescope and its instrument control system is currently being carried out based on RTS2 (see [2] and references therein). One of the key requirements of the upgrade is to keep the existing telescope software and hardware untouched. The system must remain operational every night throughout the upgrade.

As none of the telescope instruments, nor their control electronics and software was developed by our group, we are kept away from the complex details of their construction and internal operation. As described later, we exclusively communicate with the control interfaces of the existing software.

The existing control system is an adapted version of that currently used by the 3.5 m Calar Alto telescope. It allows the observer to control the instruments through graphical user interface (GUI) programs running on two main observatory computers—one for the telescope control and the other for the camera. The observer is responsible for preparing the observing plan, opening and closing of the dome, taking care of executing exposures, inspecting images for good pointing and their quality, and synchronizing the telescope and the filter wheel movements with the CCD exposures. The major drawbacks of this approach are obvious: the observer spends most of the night working hard to get the data and keep the system running, and the system is prone to human errors when the observer is tired. Moreover, the observing logs are either hard to extract from the technical log or are not created by the system at all, and the interruption of the observation to react on a quickly evolving target of opportunity requires observer presence and attention.

In contrast, RTS2 was designed to create an autonomous observatory environment. The observer is allowed to interact with the system, and at worst case to take full manual control. The system is able to guide the observatory through the night, taking care of closing and opening the dome, acquiring sky flats, darks, and last, but not least, keeping detailed logs of the images acquired, judging pointing accuracy and producing preliminary results.

RTS2 device drivers are responsible for handling any errors that occur during their operation. If possible, the device is reset, and another attempt to get it operating is made. The RTS2 *rts2-xmllrpcd* component is responsible for communicating the errors to the users and custom scripts, which allows for the execution of more complicated scenarios. One of the core principles is to avoid restarting drivers that have failed. If the driver produces a core dump, it is safely removed from the system and it is up to the observer to restart it. This feature also allows RTS2 to be quite flexible—for example, a configuration without any telescope, just with a camera and other instrumentation, can be made without changing a single line of code. More information on handling the errors and other related issues is provided in [3].

The autonomous capabilities of the RTS2 system reside in a generic layer, with underlying hardware-specific drivers

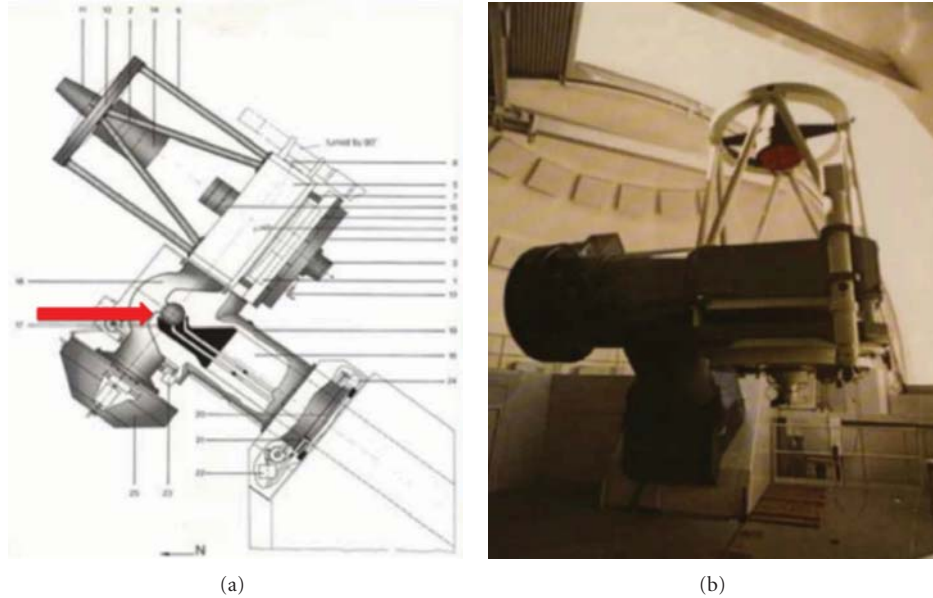


FIGURE 2: The 1.23 m telescope of Calar Alto. (a) The drawing shows the mechanics and the hydraulic system of the 1.23 m telescope of Calar Alto. One of the mechanical peculiarities of the telescope is the presence of a steel sphere (indicated by a red arrow) which, by means of a high-pressure hydraulic system, supports all the weight of the telescope. (b) Picture of the 1.23 m inside the dome. As seen, the instrumentation is always located in the Cassegrain focus. Note the German mount of the telescope.

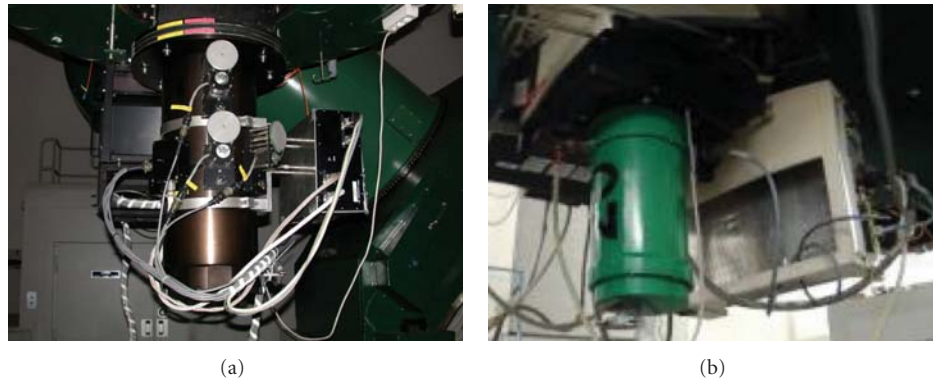


FIGURE 3: The MAGIC near-infrared and optical CCD cameras of the 1.23 m telescope, both in the Cassegrain focus of the telescope. (a) shows MAGIC near-infrared camera. The MAGIC detector is a 256×256 pixel HgCdTe array, providing a field of view of $4' \times 4'$. The filter wheel of MAGIC allows *JHK* broad-band imaging. The instrument is only mounted by special request, so it is not usually available. (b) shows optical CCD camera running on the 1.23 m telescope of Calar Alto. The optical CCD camera is based on a $2k \times 2k$ SITE#2b chip. The green tube is the dewar and the white box is the electronic system associated to the camera. The filter wheel is located in the black flange just on the detector dewar.

and communication via the TCP/IP network stack. So in an ideal world, once the provided skeleton drivers are used to write low-level RTS2 drivers for the hardware, every telescope can be made fully autonomous. To our knowledge, this is a big step forward from the traditional, incremental way of how observatory control software has been developed. Instead of being written primarily as a set of controls for the hardware, with some subsequent autopilot features, RTS2 was designed from the start to provide autonomous capabilities. Secondly RTS2 also provides a way for the observer to interact directly with the hardware.

2.1. Current State of the Upgrade. Development of the first version of the RTS2 drivers was a question of a few days (and nights), since the RTS2 drivers were being written by the main author of RTS2 (with the assistance of the CAHA staff). The major obstacle which we had to face was running RTS2 on an old Solaris operating system, which is used to run the 1.23 m control computers. As RTS2 was written in quite portable C++ on Linux, and using GNU Autotools (GNU Autotools website: <http://www.gnu.org/software/autoconf>) for build control, the porting process involved changing a few unavailable functions (and renaming the variables

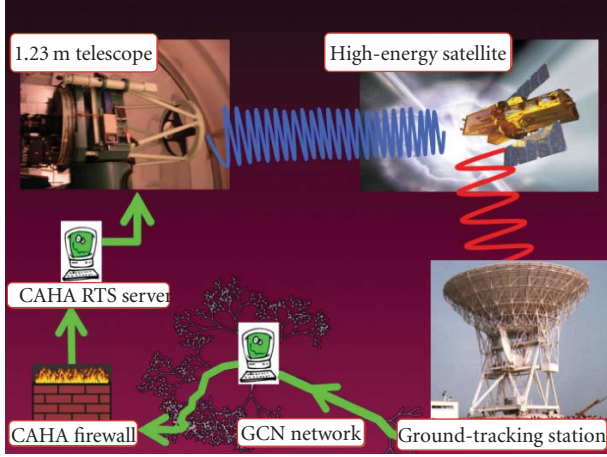


FIGURE 4: Flow diagram of the GCN network and the response mode of the 1.23 m telescope. The whole process can take up to 4 minutes, depending on the position of the GRB on sky. The time needed to receive the coordinates from the high-energy satellite in the RTS2 server takes just a few seconds (usually less than 15 seconds). Currently most of the delay is due to the slow pointing of the 1.23 m, which could take up to 4 minutes in the worst case.

called “sun”; “sun” is a defined symbol on Solaris systems). The system is now able to operate the same as any other observatory using RTS2.

The remaining obstacle is the lack of a natural incorporation of the autoguider in the RTS2 environment. This fact prevents us from taking images with long exposure times. Tests performed with the 1.23 m showed that exposures longer than 300 s produce elongated Point-Spread-Functions (PSFs), especially under sub-arc-second seeing conditions. The guider is an old instrument, with a quite complicated interface, without any autonomous capabilities. Thus, some time will be needed before we will be able to perform observations with the guider smoothly integrated in RTS2.

Currently the 1.23 m is able to respond to GRB alerts generated by the GRB Coordinates Network (GCN). The maximum slew time of the 1.23 m telescope is 4 minutes for the most unfavourable move. Usually the response time is below 3 minutes. The response time is limited by the speed of the current engines/mechanics moving the dome and the telescope. Given that the existing telescope/dome mechanical parts are strong and reliable, CAHA does not plan to renew them, so we do expect to overcome the slew-time limitation in the near future. The RTS2 Gamma-Ray Burst Daemon (*rts2-grbd*) of the 1.23 m is continuously linked via TCP/IP network socket to the GCN server at Goddard Space Flight Center (GSFC). In order to react to GCN alerts, it was necessary to accommodate the GCN connection in the CAHA firewall. Figure 3 shows a working scheme of the 1.23 m response mode to GCN alerts under RTS2.

When a high-energy satellite (usually the *Swift* mission with its BAT [4] detector) localizes a GRB, the position is dumped in a few seconds from the GRB occurrence to ground-tracking stations and distributed by the GCN to

its subscribers. In our case the GCN packet reaches the CAHA *rts2-grbd* server. Then the ongoing observations are interrupted and the 1.23 m is pointed towards the GRB position in order to start a series of short exposures (usually with the CCD windowed and binned in order to save readout time). Interrupting an observing run is a standard mechanism in RTS2 (see details in [3]). The interruption can be either hard, which interrupts the current exposure, or soft, which waits for the current exposure to finish. The rules governing this choice will be decided by the observers once the system is fully operational.

The RTS2 control system stores most of the data in a *Postgresql* database (*Postgresql* website: <http://www.postgresql.org/>). It includes tools for retrieving and manipulating information from the database. New targets can be entered through command line tools, autonomously from various triggering systems, or from the RTS2 Web interface.

The system has a powerful internal scripting engine, which enables users to define the observing strategy. By tracking devices states, the system handles synchronization among instruments, so the user does not have to know the details of the execution of the underlying observation. Scripting enables the user to specify all image parameters, dithering strategy, selected filters, and much more. For example, the following script runs observations in *I* band, based on a series of 9 dithered images with an exposure time (per frame) of 240 seconds, with a 1×1 CCD binning and trimming the CCD to a subwindow of 500×400 pixels [$x_1 = 600$, $x_2 = 1100$, $y_1 = 300$, and $y_2 = 700$]:

```
FW0.filter = I READT = (600, 500, 300, 400) binning
              = 1 E 240
T0.WOFFS = (-72 s, +36 s)
for 3{for 3{E 240 T0.woffs+ = (16 s, -54 s)}
      ×T0.woffs+ = (0, +3m)}.
(1)
```

Note that the syntax for the subwindow in the above example is (x_1 , $x_2 - x_1$, y_1 , $y_2 - y_1$). We have incorporated in RTS2 a call to the automatic astrometric calibration package described in [5]. This “on-the-fly” astrometric calibration corrects the telescope pointing, so the object can be placed on the desired (x , y) coordinates of the detector. The optical distortion on the CCD is negligible (less than one tenth of a pixel), so we decided to make a simple (and hence fast) fit considering a rotation term and a center field shift. The astrometric calibration is done on every frame. Polynomial fit is not used. The typical astrometric error (using ~ 20 stars) is below $0.5''$, good enough to correct the 1.23 m pointing. The typical standard deviation in the inferred rotation angle is ~ 0.1 degrees when ~ 20 field stars are used in the fit. The success rate of the “on-the-fly” calibration is above 95%. The astrometric calibration of the remaining images is done manually afterwards.

In the near future we plan to provide also a rough photometric calibration based on the USNO-B catalogue [6]. Simultaneously to the telescope triggering an e-mail is sent to

the 1.23 m users to warn them on the occurrence of the GRB. Additionally the GCN alert triggers the creation of an e-mail and an SMS for the ARAE group with relevant information of the GRB (coordinates, Galactic reddening, finding chart, elevation curves, and other information). Please see [7] for more details about this system.

Further improvements on this status are likely doable, so we feel confident that, under the current limitations (for instance, the telescope slew speed), we could reduce the GRB response times. This might allow us to detect the prompt optical emission associated to the gamma-ray event.

Another potential upgrade of the 1.23 m telescope could be the incorporation of MAGIC in RTS2. Rapid response observations with MAGIC would make the 1.23 m telescope very competitive in the GRB field. Currently this is beyond our scopes (and also beyond the CAHA manpower maintenance capabilities), but we do not discard it since the flexibility of RTS2 to accommodate new devices would allow us to integrate MAGIC (and new possible visitor instruments) quickly.

2.2. Integration of the Legacy Interfaces to RTS2. The following subsections provide descriptions of the legacy interfaces and their interaction with RTS2.

2.2.1. Interaction of RTS2 with the Calar Alto EPICS. The individual operations of the CAHA telescopes are coordinated, and controlled, by the Experimental Physics and Industrial Control System (EPICS website: <http://www.aps.anl.gov/epics/index.php>). The task of EPICS is to provide access and control of all the CAHA telescopes, as well as data from the central weather station and from the seeing and extinction monitors. The seeing and extinction monitors are based on small aperture telescopes located in CAHA whose values are available through EPICS.

The 1.23 m telescope mount, its focuser, and the camera filter wheel are all fully controllable through EPICS. The legacy telescope interface accepts objects coordinates in the J2000 coordinate system, and handles all the required calculations internally, including precession, aberration, reflection, and telescope pointing model offsets. Both the filter wheel and the focuser can be controlled through their own EPICS channels. Other devices in the 1.23 m telescope system do not exist in the EPICS universe: the CCD detector, the auto-guider camera, the dome itself, and various auxiliary switches (e.g., the dome lights).

We use the information provided through EPICS to automate several tasks of the 1.23 m. For instance, the meteorological information available from the EPICS is used to trigger the bad weather state, and hence to close the dome (Based on calculated Sun position through *libnova*, see <http://libnova.sf.net/>) and stop observations. Bad weather is also triggered when both other telescopes are closed—this is the rule imposed on the 1.23 m operations by CAHA. For discussion on how the weather state voting is integrated into RTS2, including its fail-safe capabilities, (Network crashes and other failures (including the EPICS ones) are properly handled inside RTS2. A detailed description on how the

weather voting system works is beyond the scope of this paper. We refer the reader to the extended discussion given in [3].) please see [3].

Yet another possible application lies in coordinating observations with the other Calar Alto telescopes. From the EPICS system, RTS2 can learn what the targets of the other telescopes are, whether they are in the RTS2 database, and depending on the target information can either start their monitoring or remove them from the list of targets which should be observed.

2.2.2. CCD Integration within RTS2. The optical CCD detector is connected to its own control computer. The control computer communicates with the control software, running on a master workstation, over the network. From the available C source code, we created an RTS2 device driver. All the major settings are supported, including binning and partial chip readout. The camera behaves as just another RTS2 supported CCD camera, visible in monitoring software and available for scripting.

2.2.3. Guider Camera and Its Integration in RTS2. The guider is built from a video camera with an image intensifier, fed from a pickoff mirror on a two-axis stage. This allows to place the guider image anywhere in the telescope field of view (FoV), thus eliminating the significant disadvantages of autoguiding-by-astrometry using the main camera: limited detector FoV, low gain, and a requirement for short exposure times. The guider camera has its own control computer, which assumes that the observer is sitting in front of it (e.g., the video output is sent directly to the screen). Partial remote control has since been provided, in part by placing a web camera in front of the guiding screen.

We would like to improve this setup with a fully integrated RTS2 device, which would transparently provide automatic search for bright stars in the FoV, and guiding capabilities. In principle, RTS2 is able to do this, and some promising tests were already carried out on the other RTS2 controlled telescopes. Currently the biggest problem is to figure out how to communicate with the guider, and to implement a full autoguiding loop.

2.2.4. Dome Control and Other Switches. As the dome is a critical component, its control is separate from the EPICS system (although dome status is reported to EPICS). In order to change the dome state, special commands must be run on the dome control computer. Similar commands are available to turn off and on dome lights and to control the telescope drives, the hydraulics, the tracking, and the mirror cover. Those commands are fully interfaced in RTS2, so RTS2 is able to control all those switches.

3. Preliminary Results

Although not fully autonomous, the 1.23 m has already performed followup optical observations of GRBs. None of the results below itemized was acquired by the automatic response mode of the RTS2 package, but some data were

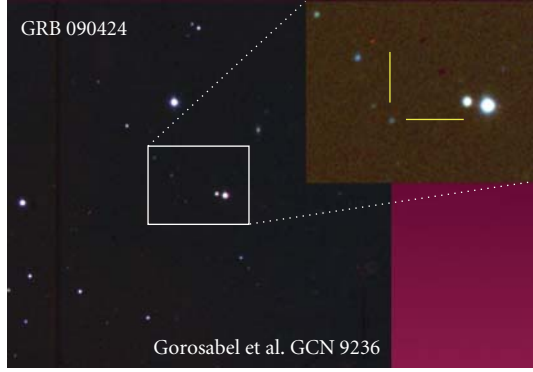


FIGURE 5: The figure shows the optical afterglow of GRB 090424 as detected with the 1.23 m CAHA telescope. The image has been created by combining *BVRI*-band images taken with the $2\text{ k} \times 2\text{ k}$ CCD camera currently in use. The upper right box shows a magnified picture of the afterglow region. The magnitude of the afterglow was $R = 19.3$. The mean observing epoch of the image is April 24.87 UT. North is up and East is right. The field of view of the images is $8' \times 8'$.

manually acquired by using RTS2 as the observing tool. Most of the data were taken by in situ observers, using the currently available GUI.

All the below listed GRBs showed X-ray afterglows which were localized by the XRT X-ray telescope on board *Swift* (see [8] for detailed information on the XRT instrument). So their X-ray afterglows were localized with uncertainties of only a few arc seconds, making the corresponding optical studies much more efficient.

GRB 090313. The optical afterglow of this GRB [9] was observed with the 1.23 m in the *R* band during two consecutive nights one week after the gamma-ray event. The observations were accompanied with *K*-band observations carried out with the 3.5 m telescope of Calar Alto equipped with Omega₂₀₀₀. The data of the afterglow are currently being analyzed and are part of an international monitoring which will be published in [10].

GRB 090424. We detected the afterglow of GRB 090424 [11] in *BVRI* on April 24.87 UT with a magnitude of $R = 19.3 \pm 0.1$. The preliminary results were reported in [12]. In the days following GRB 090424, a long-term monitoring was performed in *R* and *I* bands in order to search for the underlying supernova. Figure 5 shows a colored image constructed with the *BVRI* 1.23 m images taken in April 24.87 UT. The final results have been included in [13].

GRB 090621B. We detected the two afterglow candidates reported for this GRB [16] by Levan et al. and Galeev et al. [14, 15]. The observations were done in the *I* band, 4.14–4.75 hours after the GRB. A deep second epoch observation is pending in order to search for photometric variability of

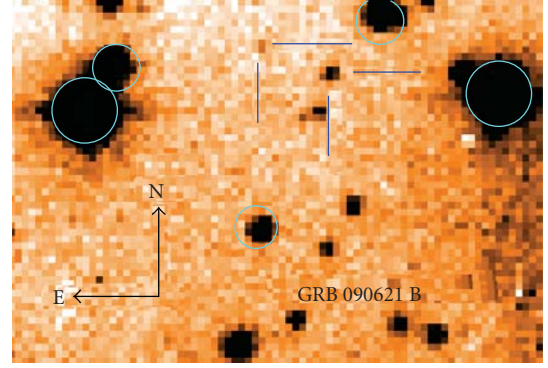


FIGURE 6: The picture shows the coadded *I*-band image taken for GRB 090621B with the 1.23 m telescope of Calar Alto. The faintest of the two objects (the most upper one indicated with tick marks) represents the candidate reported in [14]. Approximately $10''$ towards the Southwest, it is marked the candidate reported by [15], brighter than the one of [14]. The cyan circles show the USNO-A2 catalogue stars used for the astrometric and photometric calibrations. The field of view of the image is $70'' \times 50''$, with North up and East left.

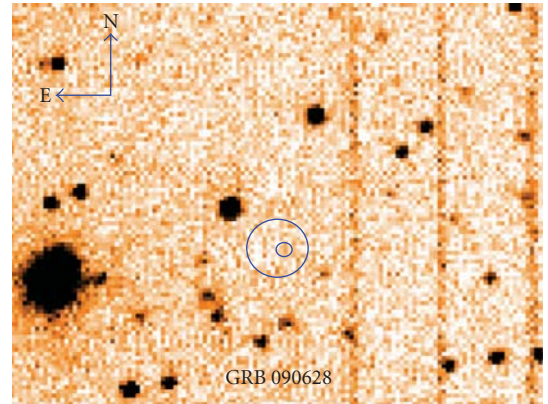


FIGURE 7: Coadded *R*-band image of GRB 090628 taken with the 1.23 m telescope. The large circle represents the preliminary XRT error circle [18], whereas the small one shows the refined one [20] reported for GRB 090628. The field of view of the image is $125'' \times 100''$. The total exposure time is 3120 s. The individual images were taken in June 28.9486–29.0225 UT (1.43–3.20 hours after the gamma-ray event). No objects were found in both error circles down to $R = 22$. More detailed information can be found in [21].

the candidates. The preliminary results were reported in [17]. Figure 6 shows both candidates.

GRB 090628. *R*-band observations of the XRT position [18] were carried out 1.43–3.20 hours after the gamma-ray event. No counterpart was found down to $R = 22$ in the XRT error box. Simultaneous near-infrared observations would have been very helpful in order to discriminate the possible high-redshift nature of this GRB but unfortunately they were not possible. The results of the observations were reported in [19].

GRB 090727. This GRB was observed in July 27.9646–28.0063 UT in the I band, 0.45–1.45 hours after the gamma-ray event. The afterglow reported by [23] was detected with a magnitude of $I \sim 19.4$, using as calibrator the USNO B1.0 star with $I = 18.72$ and coordinates $RA_{J2000} = 21:03:49.099$, $DEC_{J2000} = +64:55:58.23$. The results can be found in [24].

The Discovery of the Optical Afterglow of GRB 090813. GRB 090813 represents the first optical afterglow discovered with the 1.23 m CAHA telescope. I -band observations of the XRT position were initiated 437 s after the GRB trigger, revealing an object with a rough magnitude of $I \sim 17$ coincident with the XRT position. The lack of the object on the DSS strongly suggested its association with the optical afterglow of GRB 090813. The preliminary results were reported in [25].

GRB 090814B. This is the only GRB detected by the INTEGRAL satellite to date that we have followed up with the 1.23 m telescope. We carried out a series of I -band observations with different exposure times ranging from 180 s to 700 s. The total exposure time invested for this GRB was 9520 s, with a mean observing epoch of Aug 14.1259 UT. No optical object was found within the refined X-ray error circle provided hours later by XRT. The 3σ limiting magnitude of the coadded image is $I = 20.6$. A more extended description can be found in [21].

4. Conclusions

The 1.23 m is a wide-purpose telescope which is currently used by six international teams to perform long-term projects with a duration of four years. The ARAE group of IAA is responsible for automating the telescope operations so that such teams can perform their (usually long) observing campaigns without errors, yet enabling quick override observations of GRBs.

The GRB results obtained to date have been mostly taken by night observers. Use of the fully autonomous mode, provided by RTS2, is pending nontrivial integration of the guider. After this is done, we have reasonable hopes to believe that telescope will be able to react to GRB alerts in a few minutes. This could allow us to detect the optical emission at the first stages of the explosion, making the associated GRB science much more attractive for the GRB community.

We acquired images for seven GRBs, detecting the optical afterglows of four of them. The typical reaction time of these observations ranged from ~ 8 minutes up to a few hours. When fully implemented, the autonomous system should be able to react to triggers within 4 minutes. We have reasonable hopes to obtain much more interesting and world-competitive results in the near future.

Acknowledgments

The research of J. Gorosabel, A.J. Castro-Tirado, R. Cunniffe and M. Jelínek is supported by the Spanish programmes AYA2008-03467/ESP, AYA2009-14000-C03-01, and AYA2007-63677. We are very grateful to all of the CAHA

staff and in particular to Ulli Thiele for his excellent support with the 1.23 m telescope. P. Kubánek would like to acknowledge generous financial support provided by Spanish *Programa de Ayudas FPI del Ministerio de Ciencia e Innovación (Subprograma FPI-MICINN)* and European *Fondo Social Europeo*. We also would like to thank the two anonymous referees for their helpful comments.

References

- [1] S. F. Sánchez, J. Aceituno, U. Thiele, D. Pérez-Ramírez, and J. Alves, “The night sky at the Calar Alto observatory,” *Publications of the Astronomical Society of the Pacific*, vol. 119, no. 860, pp. 1186–1200, 2007.
- [2] P. Kubánek, M. Jelínek, S. Vitek, A. de Ugarte Postigo, and M. Nekola, “RTS2: a powerful robotic observatory manager,” in *Advanced Software and Control for Astronomy*, vol. 6274 of *Proceedings of SPIE*, Orlando, Fla, USA, May 2006.
- [3] P. Kubánek, “RTS2—the remote telescope system,” *Advances in Astronomy*. In press.
- [4] S. D. Barthelmy, L. M. Barbier, J. R. Cummings, et al., “The burst alert telescope (BAT) on the Swift midex mission,” *Space Science Reviews*, vol. 120, no. 3–4, pp. 143–164, 2005.
- [5] A. de Ugarte Postigo, et al., “JIBARO: un conjunto de utilidades para la reducción y análisis automatizado de imágenes,” in *Astrofísica Robótica en España*, A. J. Castro-Tirado, B. A. de la Morena, and J. Torres, Eds., p. 35, Madrid, Spain, 2005.
- [6] D. G. Monet, S. E. Levine, B. Canzian, et al., “The USNO-B catalog,” *Astronomical Journal*, vol. 125, no. 2, pp. 984–993, 2003.
- [7] S. Castillo-Carrión and A. J. Castro-Tirado, “Making preliminary GRBs realtime astronomical reports,” *Advances in Astronomy*, vol. 2010, Article ID 102831, 8 pages, 2010.
- [8] D. N. Burrows, J. E. Hill, J. A. Nousek, et al., “The Swift X-ray telescope,” *Space Science Reviews*, vol. 120, no. 3–4, pp. 165–195, 2005.
- [9] R. Chornock, W. Li, and A. V. Filipenko, “GRB 090313 OA candidate,” GRB Coordinates Network, Circular Serv, 8979, 2009.
- [10] A. Melandri, et al., *Astronomy & Astrophysics*. In preparation.
- [11] J. K. Canizzo, S. D. Barthelmy, A. P. Beardmore, et al., “GRB 090424: Swift detection of a burst with an optical counterpart,” GRB Coordinates Network, Circular Serv, 9223, 2009.
- [12] J. Gorosabel, P. Kubánek, M. Jelínek, A. de Ugarte Postigo, and J. Aceituno, “GRB 090424: optical observations from 1.23m CAHA,” GRB Coordinates Network, Circular Serv, 9236, 2009.
- [13] D. A. Kann, S. Klose, B. Zhang, et al., “The afterglows of Swift-era gamma-ray bursts. I. Comparing pre-Swift and Swift era long/soft (type II) GRB optical afterglows,” <http://arxiv.org/abs/0712.2186>.
- [14] A. J. Levan, P. Curran, K. Wiersema, and P. Groot, “GRB 090621B: optical observations,” GRB Coordinates Network, Circular Service, 9547, 2009.
- [15] A. Galeev, I. Bikmaev, N. Sakhibullin, et al., “GRB 090621B: RTT150 optical observations,” GRB Coordinates Network, Circular Serv, 9549, 2009.
- [16] P. A. Currant, S. D. Barthelmy, A. P. Beardmore, et al., “GRB 090621B: Swift detection of a short hard burst,” GRB Coordinates Network, Circular Serv, 9545, 2009.
- [17] J. Gorosabel, P. Kubánek, S. Motolla, et al., “GRB 090621B: I-band observations from 1.23m CAHA,” GRB Coordinates Network, Circular Serv, 9561, 2009.

- [18] B. Sbarufatti, V. Mangano, et al., “GRB 090628: Swift XRT position,” GRB Coordinates Network, Circular Servic, 9586, 2009.
- [19] P. Kubánek, N. Morales, J. L. Ortiz, et al., “GRB 090628: 1.23m CAHA optical observations,” GRB Coordinates Network, Circular Service, 9589, 2009.
- [20] V. Mangano and B. Sbarufatti, “GRB 090628: Swift XRT refined analysis,” GRB Coordinates Network, Circular Service, 9599, 2009.
- [21] J. Gorosabel, A. de Ugarte Postigo, V. Terrón, et al., “GRB 090814B: I-band observations from 1.23m CAHA telescope,” GRB Coordinates Network, Circular Servic, 9808, 2009.
- [22] M. Jelinek, A. J. Castro-Tirado, A. de Ugarte Postigo, et al., “Four Years of Realtime GRB Followup by BOOTES-1B (2005–2008,” *Advances in Astronomy*. In press.
- [23] R. J. Smith and C. G. Mundell, “GRB 090727: Liverpool telescope possible OT candidate,” GRB Coordinates Network, Circular Service, 9719, 2009.
- [24] J. Gorosabel, N. Huélamo, M. Fernández, et al., “GRB 090727: I-band observations from 1.23m CAHA,” GRB Coordinates Network, Circular Servic, 9728, 2009.
- [25] J. Gorosabel, V. Terrón, M. Fernández, P. Kubanek, M. Jelinek, and A. J. Castro-Tirado, “GRB 090813: optical candidate from 1.23m CAHA telescope,” GRB Coordinates Network, Circular Servic, 9782, 2009.

Review Article

Gamma-Ray Bursts in the Era of Rapid Followup

C. G. Mundell,¹ C. Guidorzi,^{1,2} and I. A. Steele¹

¹ *Astrophysics Research Institute, Liverpool John Moores University, Twelve Quays House, Birkenhead CH41 1LD, UK*

² *Physics Department, University of Ferrara, via Saragat 1, 44122 Ferrara, Italy*

Correspondence should be addressed to C. Guidorzi, guidorzi@fe.infn.it

Received 30 June 2009; Revised 9 February 2010; Accepted 5 March 2010

Academic Editor: Joshua S. Bloom

Copyright © 2010 C. G. Mundell et al. This is an open access article distributed under the Creative Commons Attribution License, which permits unrestricted use, distribution, and reproduction in any medium, provided the original work is properly cited.

We present a status report on the study of gamma-ray bursts (GRBs) in the era of rapid followup using the world's largest robotic optical telescopes—the 2 m Liverpool and Faulkes telescopes. Within the context of key unsolved issues in GRB physics, we describe (1) our innovative software that allows real-time automatic analysis and interpretation of GRB light curves, (2) the novel instrumentation that allows unique types of observations (in particular, early time polarisation measurements), and (3) the key science questions and discoveries to which robotic observations are ideally suited, concluding with a summary of current understanding of GRB physics provided by combining rapid optical observations with simultaneous observations at other wavelengths.

1. Introduction

Gamma-Ray Bursts (GRBs) are the most powerful explosions in the Universe and, arguably, represent the most significant new astrophysical phenomenon since the discovery of quasars and pulsars. As their name suggests, GRBs are detected as brief, intense and totally unpredictable flashes of high-energy gamma rays, thought to be produced during the core collapse of massive stars (long-soft bursts, $T_\gamma > 2$ seconds) or the merger of two compact objects such as two neutron stars or a neutron star and a stellar-mass black hole (short-hard bursts, $T_\gamma < 2$ seconds). Although discovered through their γ -ray emission [1], they are now known to emit nonthermal radiation detectable across the electromagnetic spectrum [2–4]. However, despite their enormous luminosity, their unpredictability and short duration limit rapid, accurate localisation and observability with traditional telescopes. Consequently, new ground and space-based facilities have been developed over the past decade; dedicated satellites optimised for GRB detection and followup, such as Swift [5], are revolutionizing GRB studies by locating ~ 100 bursts per year with γ -ray positions accurate to $\sim 3'$ and X-ray positions accurate to $5''$ within seconds or minutes of the burst. Here we describe the automatic ground-based followup of GRBs with the world's

largest robotic optical telescopes that use intelligent software and innovative instruments.

The Era of Rapid Followup: Predictions and Outcomes. Before the launch of current satellites such as Swift, Integral, and Fermi, significant progress in understanding GRBs had been made since their discovery, in particular the general γ and X-ray properties. The first crucial step in disseminating real-time GRB positions to ground observers was triggered by BATSE on the CGRO [6] through the GRB Coordinates Network (GCN) [7] via internet socket connection (no humans-in-the-loop). This drove development of the first generation of wide-field robotic followup ground-based facilities, such as GROCSE, ROTSE, and LOTIS, culminating with the discovery of the optical flash associated with GRB 990123 [8]. BATSE provided an invaluable catalogue of prompt γ -ray profiles, whose isotropic sky distribution and inhomogeneous intensity distribution suggested a cosmological origin [6], and BeppoSAX [9] revolutionised the cosmological study of GRBs by providing subarcmin ($\sim 50''$) localisation of X-ray afterglows that enabled late-time (\sim hours) optical followup with traditional ground-based telescopes and redshift determinations. Collimation of the ejecta (i.e., jets) was inferred from temporal breaks—steepening—of optical light curves at ~ 1 day post burst and

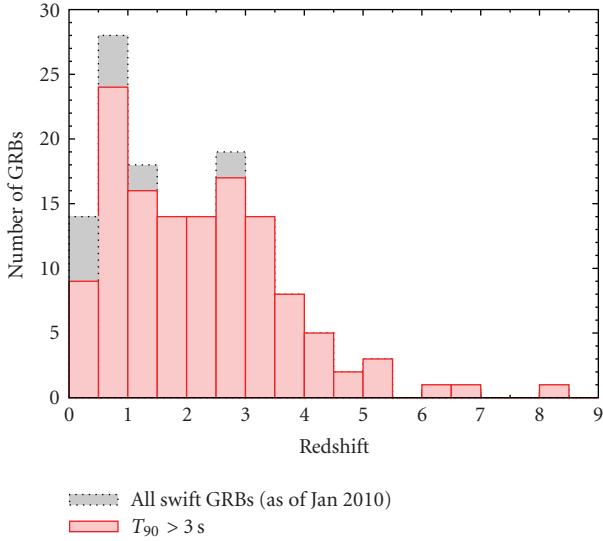


FIGURE 1: Redshift distribution of *Swift* GRBs detected to-date.

the concept of a universal central engine and the use of GRBs as standardisable cosmological candles was introduced [10, 11].

The possibility for great advances with the launch of *Swift* was fully recognised. Optical counterparts were expected to be found for all GRBs with many GRBs expected to exhibit bright optical flashes from reverse shock emission at early-times, similar to GRB 990123 [8]. An increase in the number of GRBs detected would lead to many jet breaks being identified, short GRBs would be easily observed and understood, and identification of GRBs at very high redshift would be routine. Instead, 50% of GRBs remain optically dark, despite deep, rapid followup [12–15]; there is a dearth of bright reverse-shock optical emission [16]; light curves are complex in all bands with a variety of chromatic and achromatic breaks and flares observed (e.g., [17–23]). Jet breaks have proven elusive, short bursts remain technically challenging [24], and only 3 GRBs have been identified to lie at $z > 6$ (Figure 1) [25–28].

2. Robotic Followup and Intelligent Autonomy

The field of GRB research is the most rapidly evolving topic in modern day astrophysics—driven primarily by technological innovation in both hardware and software; most notable is the need for rapid, intelligent, and fully autonomous followup. Within the context of robotic telescopes devoted to searching for optical counterparts to GRBs (e.g., [29–36]), the Liverpool Telescope (LT) offers a unique combination of sensitivity, speed, instrument choice, and real-time reduction pipeline with complexity and flexibility. The LT, owned and operated by Liverpool John Moores University (LJMU), has a 2 m diameter mirror, altitude-azimuth design, final focal ratio $f/10$, a comprehensive suite of instruments, and a fully robotic control system. As shown in Figure 2, it is sited at the Observatorio del Roque de los Muchachos in La Palma. Optimised for robotic followup of transient sources, the LT

TABLE 1: Current instrumentation on the Liverpool and Faulkes telescopes and associated GRB science goals; upcoming instrumentation is shown in *italics*.

Instrumentation	Science goals
Optical Camera (FoV $\sim 5'$) (BVRi'z') (LT/FTN/FTS)	(i) Early multicolour light curves
	(ii) Shock physics/ISM studies
	(iii) Later-time light curves/jet breaks
	(iv) GRB-supernova connection
RINGO2 polarimeter (FoV $\sim 4'$) (LT only)	(i) Early-time polarisation studies 1% polarisation at $r' < 17$ mag in 1 minute
	(ii) Fundamental tests of magnetization
SupIRCam Infrared Camera (FoV $\sim 1'$) (LT only)	(i) High- z “naked” bursts
	(ii) Low- z “obscured” bursts
FRIDOSpec IFU (FoV $\sim 11''$) (LT only)	(i) Early evolution of circumburst medium
STILT (FoV $1^\circ/20^\circ/180^\circ$) (LT only)	(i) Bright bursts/neutrino counterparts
<i>IO—wide-field optical/IR imager (LT-2010)</i>	(i) Deep, simultaneous optical/IR light curves over 2° FoV

was designed to have a fully open enclosure, robustness to wind gusts, and a fast slew rate of $2^\circ/\text{s}$; currently as the fastest telescope for its size, it observes GRBs within 1–3 minutes of receipt of a satellite alert. Although smaller robotic telescopes slew more quickly, the LT is more sensitive to fainter bursts at early-time. Most importantly, the LT can perform unique early-time polarisation measurements (see Section 4).

The LT has five instrument ports: four folded and one straight-through, selected automatically within 30 seconds by a deployable rotating mirror in the Acquisition and Guidance (AG) box. Table 1 describes the instruments available and the related GRB science goals. All GRB followups with the LT begin with RINGO polarimetry exposures before continuing with a sequence of 10-s R -band exposures that are used to automatically identify an optical counterpart, determine its characteristics, and conduct subsequent optimized followup observations with the most appropriate instrument. Guidorzi et al. [36] describe the intelligent software logic—LT-TRAP—developed to perform the real time analysis and followup. Automatic multicolour light curves of optical transients brighter than $R \sim 19$ mag are produced in real-time; transients brighter than $R \sim 15$ mag trigger additional RINGO polarisation observations before continuing with multicolour imaging. Faint OTs or nondetections trigger deep exposures in red filters. The 2 m Faulkes telescopes¹, clones of the LT, provide additional sky coverage, operate the same intelligent LT-TRAP software—apart from small differences due to the different instruments mounted on each facility—and concentrate on multicolour optical imaging (Figure 2 and Table 1). Figure 3 displays the flow chart of the LT-TRAP.



FIGURE 2: The locations of the 2 m robotic Liverpool Telescope and its clones the Faulkes telescopes. GRB triggers from satellites drive prompt automatic followup.

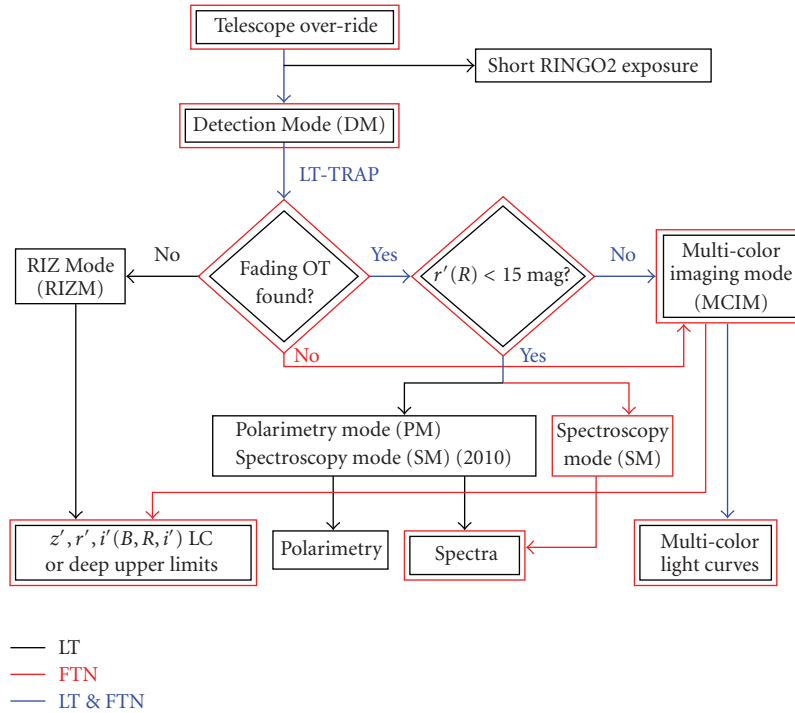


FIGURE 3: Flow chart of the robotic GRB pipeline currently running on the Liverpool and Faulkes Telescopes (adapted from [36]).

3. Characteristics of Multiwavelength Light Curves

A major breakthrough provided by Swift was the discovery of complex light curves at X-ray energies that led to introduction of the so-called canonical light curve [37, 38], characterized by four decay segments: (1) an “early steep decay” with power-law decay indices ~ 3 or even steeper; (2) a “shallow or flat decay” with a typical index around 0.5; (3) a normal decay, with indices around 1.2; and (4) finally, the late steep decay with typical values around 2. In $\sim 50\%$ of cases, flares are also superimposed

[20, 21]. Some complexity is attributed to on-going central engine activity producing different emission components that originate from spatially distinct regions but that are temporally coincident, but alternative explanations invoking an external origin have also been suggested [39, 40]. Unlike other high-energy phenomena such as Active Galactic Nuclei, GRBs will remain spatially unresolved with current and future instrumentation. Model-dependent temporal properties therefore provide a powerful, indirect probe of the expanding fireball and its interaction with the surrounding medium. Polarisation measurements provide a *direct* probe.

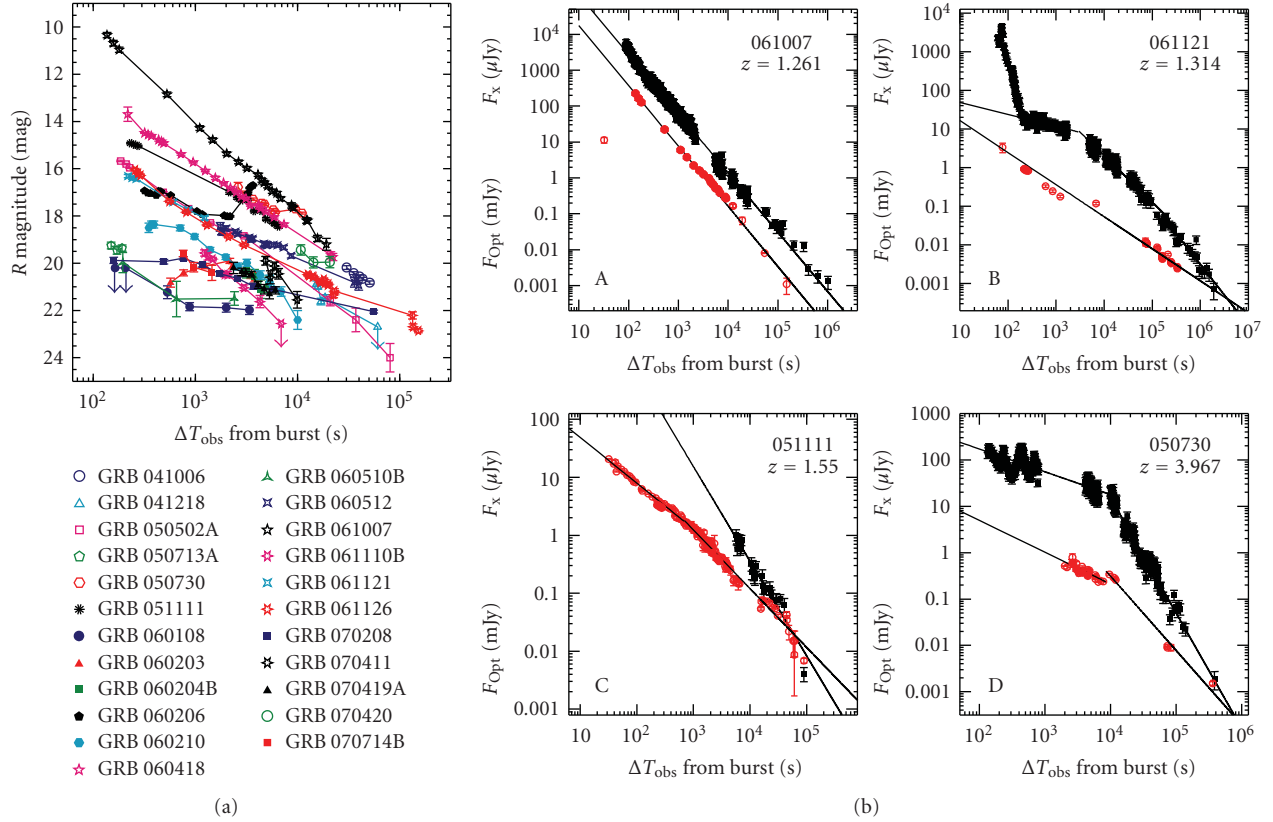


FIGURE 4: (a) Selection of early-time optical light curves from the Liverpool and Faulkes telescopes. (b) Examples of X-ray (black) and optical (red) light curve comparisons leading to classification scheme using synchrotron model breaks [12].

At optical wavelengths, a variety of light curve properties are expected depending on the relative contributions of emission from reverse and forward shocks, the presence of additional energy injection by a long-lived central engine, and the time of the observations with respect to the initial burst.

Melandri et al. [12] classified a sample of 63 bursts via their optical and X-ray light curves. 50% of the sample remained optically “dark” despite rapid, deep observations through red filters. Optical counterparts ranged in brightness from $R \sim 10$ mag to ~ 22 mag in the first minutes after the burst and showed a range of decay behaviours (Figure 4). Flares, although less common in the optical than X-ray band, were present and in some cases (e.g., GRB 060206) showed direct evidence of significant energy injection [41–44].

By comparing optical and X-ray light curves observed from $t = 100$ seconds to $\sim 10^6$ seconds post burst, Melandri et al. [12] introduced a coherent classification of optical/X-ray light curves under the framework of the standard fireball model and synchrotron theory, using the presence or absence of temporal breaks in each band (Figure 4); the temporal location and evolution of chromatic and achromatic breaks depend on typical synchrotron and cooling frequencies with respect to the observing bands. Simply, class A shows no break in optical or X-ray bands because ν_c lies above or between the two bands; class B shows a break in the X-ray but not in the optical band as ν_c passes through the X-ray

band; class C shows a break in the optical but not the X-ray band due to ν_c passing through the optical band; class D has breaks in both bands as energy injection stops or a jet break occurs. 60% of optically detected bursts were explained with the forward shock model, while the remainder required energy injection and/or an ambient density gradient. GRB 070419A required a long-lived central engine (~ 250 seconds in γ and X-rays), a finely tuned energy injection rate and an abrupt cessation of injection (Figure 5).

3.1. Long-Lived Central Engines Explain Bright and Dark Bursts. Large robotic telescopes such as the LT provide deep upper limits at early-times (e.g., $R < 22$ mag), thereby ruling out slow followup as a reason for nondetection of optical afterglows. Observing with red filters, the LT and FTs can identify GRBs at $z < 4$ within the first few minutes after the burst via R -band photometric dropouts; a deep, early upper limit in R -band plus an i' -band detection quickly identified GRB 060927 as a moderately high-redshift source ($z = 5.467$) [46, 47]. Whilst a small fraction of optically undetected GRBs may lie at very high redshift so have their rest frame emission redshifted out of optical observing bands (e.g., GRB 090423 at $z = 8.1$ [27, 28]), others require a physical explanation for their darkness. Some may be explained by a relatively flat optical-to-X-ray spectral index and modest dust extinction (e.g., GRB 060108 [48]; for typical extinction values, see, e.g., [49, 50]). The underlying physical mechanism may be energy

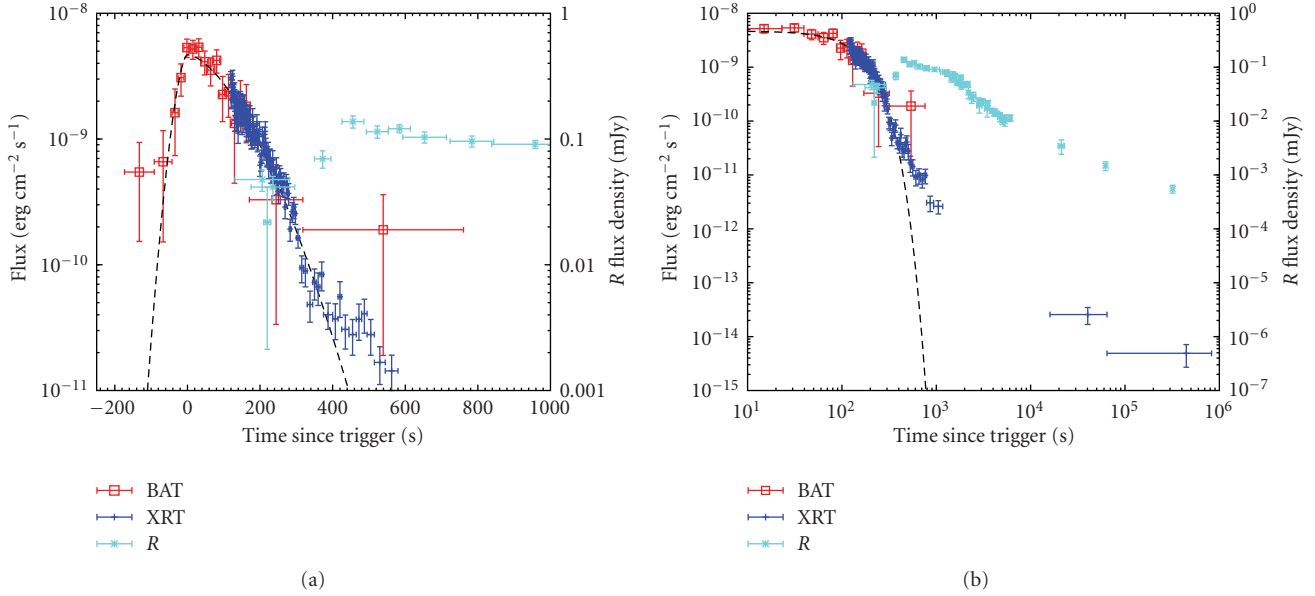


FIGURE 5: γ -ray, X-ray, and optical light curves of GRB 070419A. (a) Early-time light curves plotted on linear-log scale. (b) Later time evolution included and shown on log-log scale (see Melandri et al. [45]).

injection; as discussed above, a long-lived central engine is required to explain the properties of bright bursts but such a model may also provide a self-consistent explanation for dark bursts at intermediate redshift ($z < 6$). Enhanced X-ray emission in the early-time X-ray afterglow due to late-time central engine activity would make the bursts brighter than expected in the X-ray band compared to the optical band [12].

4. Magnetized Fireballs?

The production of synchrotron radiation requires the presence of a magnetic field but the degree of magnetization and the configuration of the magnetic fields remain a matter of debate (e.g., [51–53]). Determination of the magnetic field properties is key to understanding the driving mechanism of the explosion, namely, whether the ultrarelativistic ejecta are dominated by kinetic (baryonic) or magnetic (Poynting flux) energy. The ratio of magnetic and kinetic energy flux, σ , is used to express the magnetization (e.g., [54]) and is large if the magnetic field originates at the central engine and is advected outwards with the relativistic flow (Poynting flux jet). For a baryonic jet, $\sigma \ll 1$ and magnetic fields are assumed to be produced locally in the shock. Magnetization may be inferred from optical light curves, given a variety of assumptions, or determined directly from measurements of the degree of polarisation of the optical afterglow. In both cases, observations at the earliest possible time after the burst—when the magnetic properties of the expanding fireball are still encoded in the emission—are essential to address these issues.

Indirect Observational Tests—Light Curve Evolution. In the standard fireball model (see [55–59] for reviews) a shell of

the relativistically expanding fireball collides with the circumburst medium to produce an external shock that results in the long-lived afterglow emission detectable from X-ray to optical, IR, or sometimes radio frequencies. A reverse shock propagating backwards through the shell may, in some circumstances, produce short-lived but bright optical emission—the so-called optical flash. Figure 6 shows three possible optical light curves with the relative contributions from the reverse and forward shocks identified. The strength of the reverse shock depends on magnetization and whether the typical frequency is close to the optical band [52, 54].

The dearth of reverse-shock optical flashes from Swift GRBs may be explained in the standard model via weak, nonrelativistic reverse shocks and a typical frequency far below the optical band at early-time; the bright optical counterpart to GRB 061007 (Figure 7) illustrates this with its light curve comprising forward shock emission only and the typical frequency of the reverse shock emission being shown to lie in the radio band as early as 137 seconds after the burst [60]. Alternatively, some optical flashes may be suppressed by strong magnetization.

Direct Observational Tests—Polarisation. Synchrotron radiation is intrinsically highly polarised; specific properties of the emitting region may reduce the observed degree of polarisation, (e.g., [63–71]), so detection of significant polarisation at early-time provides a direct signature of large-scale ordered magnetic fields in the expanding fireball [72]. Claims of high levels of polarisation observed in the gamma-ray prompt emission have remained controversial: Coburn and Boggs [73] reported a high degree $P = 80 \pm 20\%$ of linear polarisation of the prompt emission of GRB 021206, but reanalysis of the data showed null polarisation [74, 75]. In other cases, BATSE data of two bursts were reported to

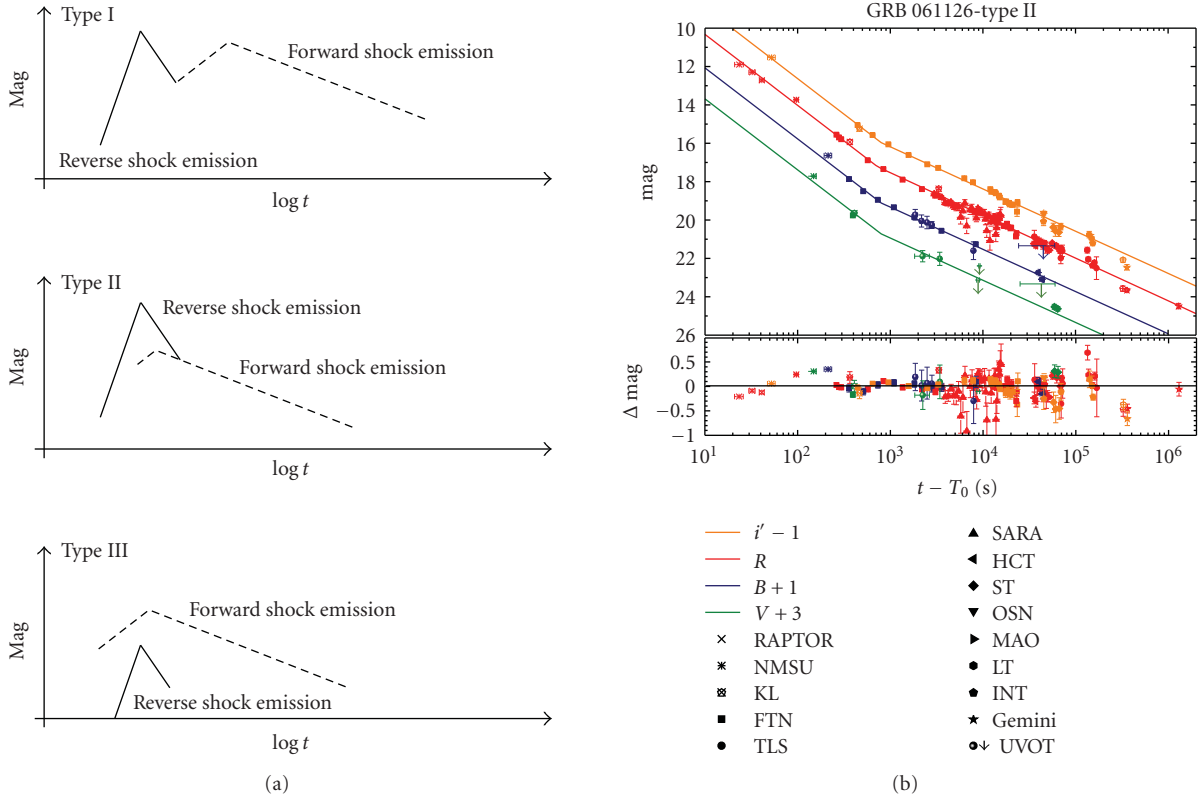


FIGURE 6: (a) Light-curves with different reverse-forward shock contributions. Magnetic energy density determines the relative contributions [61]. (b) Optical light curves of GRB 061126 showing the steep-to-shallow temporal break characteristic of a Type II reverse-forward shock observed after the reverse-shock peak [62].

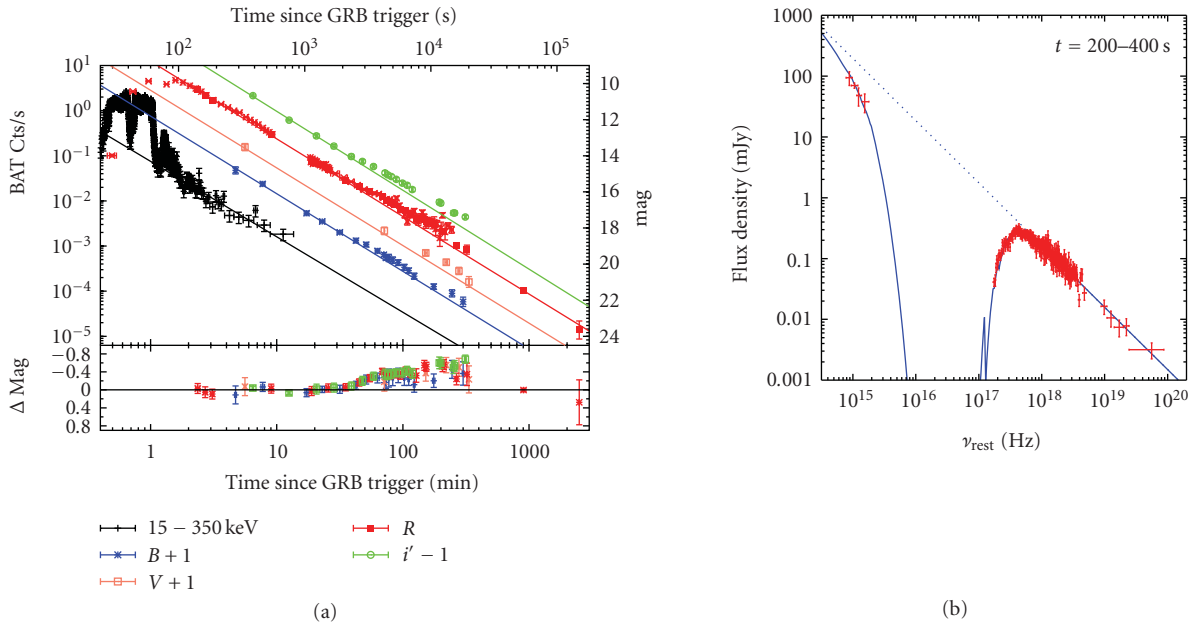


FIGURE 7: (a) γ -ray (black) and optical $BVRi'$ (colour) light curves of GRB 061007 all decaying with a steep power-law index $\alpha \sim 1.7$ from 137 seconds to $\sim 10^6$ seconds. Despite its optical brightness ($R \sim 10.3$ mag at 137 seconds), a reverse-shock optical flash is ruled out (adapted from [23, 60]). (b) Early-time (200–400 seconds) broad-band optical to γ -ray SED fitted with single absorbed power law $\beta(\text{opt-X-}\gamma) = 1.02 \pm 0.05$ and rest-frame extinction $A_V(\text{SMC}) = 0.48 \pm 0.19$ mag (from [60]).

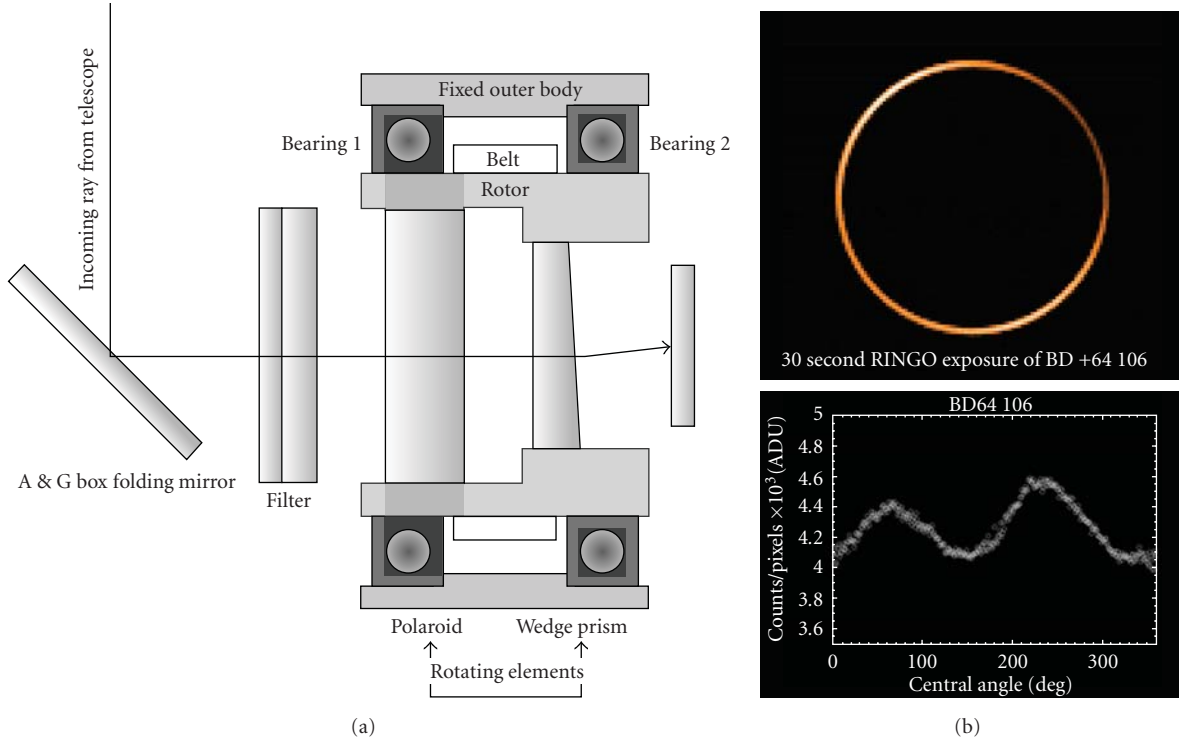


FIGURE 8: (a) Diagram illustrating design of RINGO. (b) Polarised star BD +64 106 observed through RINGO (top panel): calibrated trace around ring showing polarisation signature (from [82]).

show evidence for $P > 35\%$ and $>50\%$ using a GEANT4 model of the Earth albedo [76]. More recently, observations of GRB 041219A with the INTEGRAL imager IBIS show polarization up to 43% with rapid variability of degree and position angle [71], although independent confirmation with spectrometer SPI data remains difficult due to instrumental systematics [77, 78]. In the remaining cases, only upper limits to possible large polarisation degrees have been reported (e.g., [79]). Although careful calibration of instrumental systematics for γ -ray data remains challenging, these measurements show tantalising support for large-scale ordered magnetic fields in the region responsible for the prompt γ -ray production. Measuring the early optical polarisation provides a direct probe of the magnetic field configuration. Optical polarisation observations of GRBs have the advantage that stars in the GRB field of view can be used as simultaneous independent checks on any instrumental systematics. Theoretical models of GRBs predict that mildly magnetized outflows produce strong reverse shock emission that should be polarised [51, 52, 68, 69, 80, 81], making early-time optical polarisation measurements vital for direct determination of the magnetic field structure.

The time-variable nature of optical emission from GRBs, however, makes traditional polarisation instruments unsuitable; we therefore designed the novel RINGO polarimeter on the LT [82], whose overall layout is shown in Figure 8. Its design was based on a novel ring polarimeter concept explored by Clarke and Neumayer [83]. This makes use of a rotating Polaroid to modulate the incoming polarised flux

to be studied and is followed by deviating optics which corotate. A filter equivalent to $V + R$ bands was chosen to optimise the signal to noise ratio, as estimated from the typical GRB colours and to avoid the fringing on the CCD that the I filter would have caused. The result of this design is that each source image is recorded on the CCD as a ring, with the polarisation signal mapped out along the ring in a $\sin(2\theta)$ pattern (Figure 8(b)). One benefit of this design is the reduction of the saturation constraints on high precision photometry, as the flux is spread over the pixels along the ring. The potential problem of many rings overlapping with each other is only a concern for crowded fields which correlate with low galactic latitudes, that is, where GRB optical counterparts are strongly extinguished and therefore observationally already disfavoured. The design was optimised through requirements on (i) the rotation speed, to minimise impact on the polarisation ring profiles; and (ii) the geometry of the deflecting optics, to optimise the ring size. The polarimetric accuracy of RINGO is a few percents for an $R = 15$ -mag object in a 10-second long exposure and decreases to a few 0.1% in a 10-minute exposure. Further details on the RINGO polarimeter and its calibration and data reduction can be found in Steele et al. [82].

RINGO has now measured the optical polarisation of two GRBs (Figures 9, 10, and 11): Mundell et al. reported $P < 8\%$ in GRB 060418 at 203 seconds post burst [84] and Steele et al. 2009 measured $P = 10.2 \pm 1.3\%$ in GRB 090102 at 160.8 seconds post burst [85]. In the standard

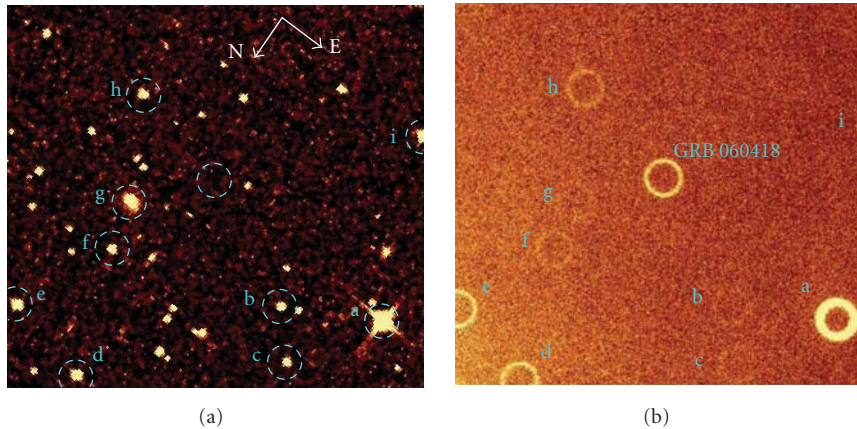


FIGURE 9: (a) DSS image of the field before the occurrence of GRB 060418. (b) RINGO image showing GRB 060418 and other field sources as rings (from [84]).

GRB fireball model both a forward shock, propagating into the circumburst medium, and a reverse shock, propagating into the GRB ejecta, contribute to the observed afterglow emission [61, 86] (Figure 6). The measurement in GRB 060418 was made close to the peak in the optical light curve at the time of deceleration of the fireball associated with the onset of the afterglow, when the reverse and forward shocks contributed equally to the detected light, while GRB 090102 was measured when the light curve was dominated by reverse-shock emission. Below we summarise the observations and suggest a unifying model to reconcile the two results.

Optical Polarisation Measurements of GRB 060418 and GRB 090102. The RINGO images of the fields containing GRB 060418 and 090102 are shown in Figures 9 and 10. GRB 060418 was detected by the Swift Burst Alert Telescope (BAT) on April 18, 2006 and showed a multipulsed gamma-ray profile with a total duration of 52 seconds, followed by a separate small bump at 130 seconds concomitant with a large X-ray flare observed with the Swift X-Ray Telescope (XRT) [87, 88] and probably due to prolonged internal activity (see Figure 11). A number of robotic facilities reacted to the prompt Swift alert and detected the optical and NIR counterpart: in particular, REM detected a smooth optical rise peaking at 153 seconds, interpreted as the onset of the afterglow [89], whereas the X-ray curve was seen to decline from the beginning, apart from the large flare mentioned above (Figure 11). The LT was triggered automatically, starting observations with a 30-second long exposure taken with the RINGO polarimeter at 203 seconds post GRB, that is, simultaneously with the fading tail of the prompt gamma-ray emission (Figure 11) and the close to the X-ray flare. However, the contribution in the optical band from the X-ray flare was estimated to be negligible, thus confirming that RINGO measured the afterglow [84].

Swift detected GRB 090102 on 2 January 2009 at 02:55:45 UT, with a pulse of gamma rays lasting $T_{90} = 27$ seconds and comprising four overlapping peaks starting 14-second

before the trigger time [91]. The automatic localization was communicated to ground-based facilities, and a single 60-second RINGO exposure was obtained starting 160.8 seconds after the burst. Simultaneous with our polarization observation of GRB 090102, a number of automated photometric followups were performed by other facilities [85]. The optical light curve (Figure 11), beginning at 40-second post burst, is fitted by a steep-shallow broken power law $\alpha_1 = 1.50 \pm 0.06$ and then $\alpha_2 = 0.97 \pm 0.03$ after approximately 1000 seconds [90]. In contrast, the X-ray light curve began at 396 seconds post burst and shows a steady decay consistent with a single power law with slope $\alpha = 1.36 \pm 0.01$ and no evidence of flares or breaks up to $t > 7 \times 10^5$ seconds [90]. The absence of additional emission components, for example, from late-time central engine activity, in the optical light curves of GRB 060418 and 090102 allows a straightforward interpretation of their early-time polarisation in the context of current GRB models.

Despite the brightness of the optical afterglow of GRB 060418, no dominant reverse shock was observed, similar to other cases in which the typical frequency is inferred to lie below the optical band at early-time such as GRB 061007 [60]. Instead, the light curve peak is typical of the forward shock. The forward shock peaks either when fireball decelerates or when the typical synchrotron frequency crosses the observed band: the latter was ruled out for GRB 060418, as no colour evolution was observed around the peak, thus supporting the deceleration interpretation with the synchrotron frequency lying below the NIR bands at the peak time [89]. This is also consistent with the steep ($|\alpha| \sim 2.7$) rise observed in the NIR bands (Figure 11), in agreement with the theoretical expectations for the forward shock deceleration [92]. The RINGO measurement of GRB 060418 was made close to the deceleration time at the onset of the afterglow and when any magnetic field would still be present in the emitting region because the detected light contains an equal contribution from forward and reverse shocks, that is, Type III [12, 61] (Figure 6).

In contrast to GRB 060418, GRB 090102 exhibited the steep-shallow optical decay typical of that expected from an

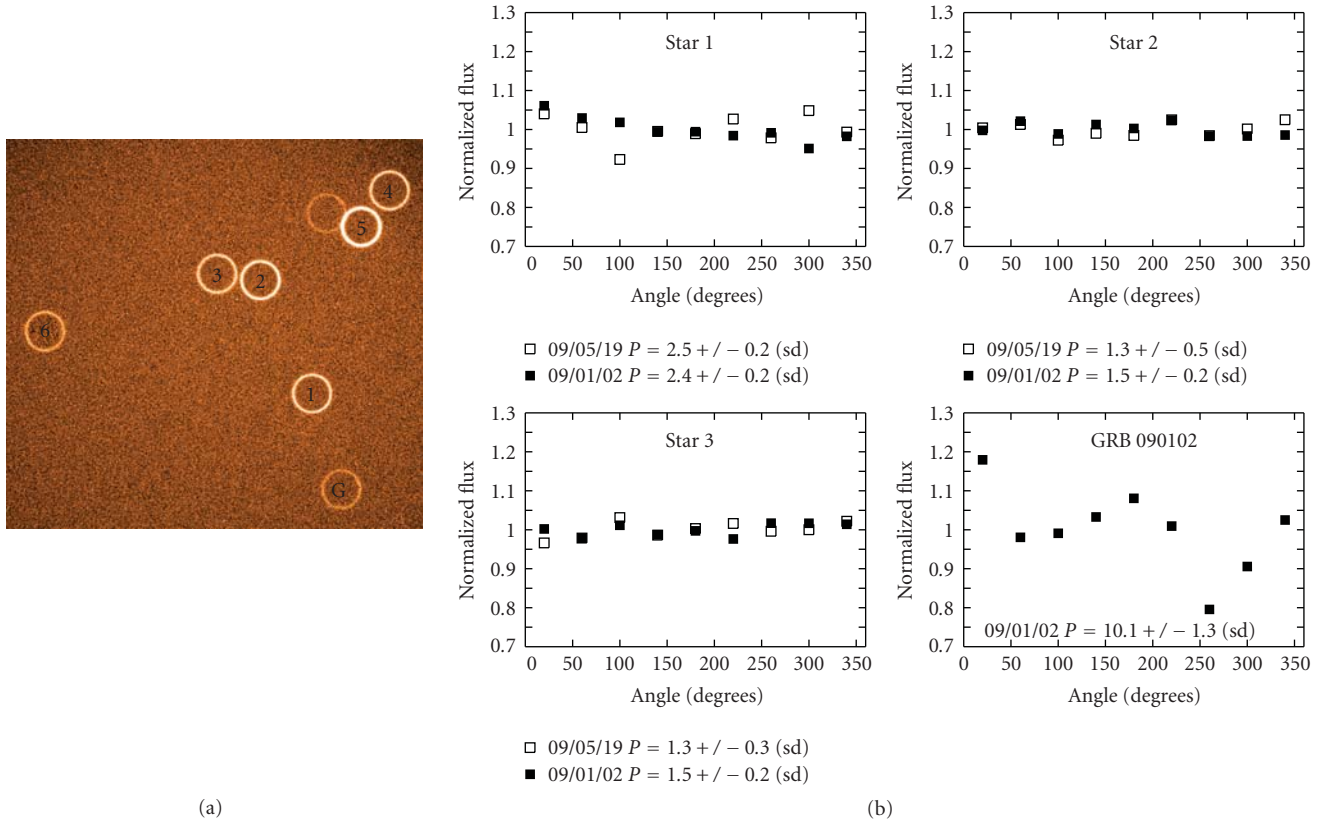


FIGURE 10: (a) RINGO image of field containing GRB 090102 (marked “G”); field stars are also visible. (b) Traces around rings for stars 1, 2, 3 and GRB 090102; derived polarisation % for each is quoted. [85].

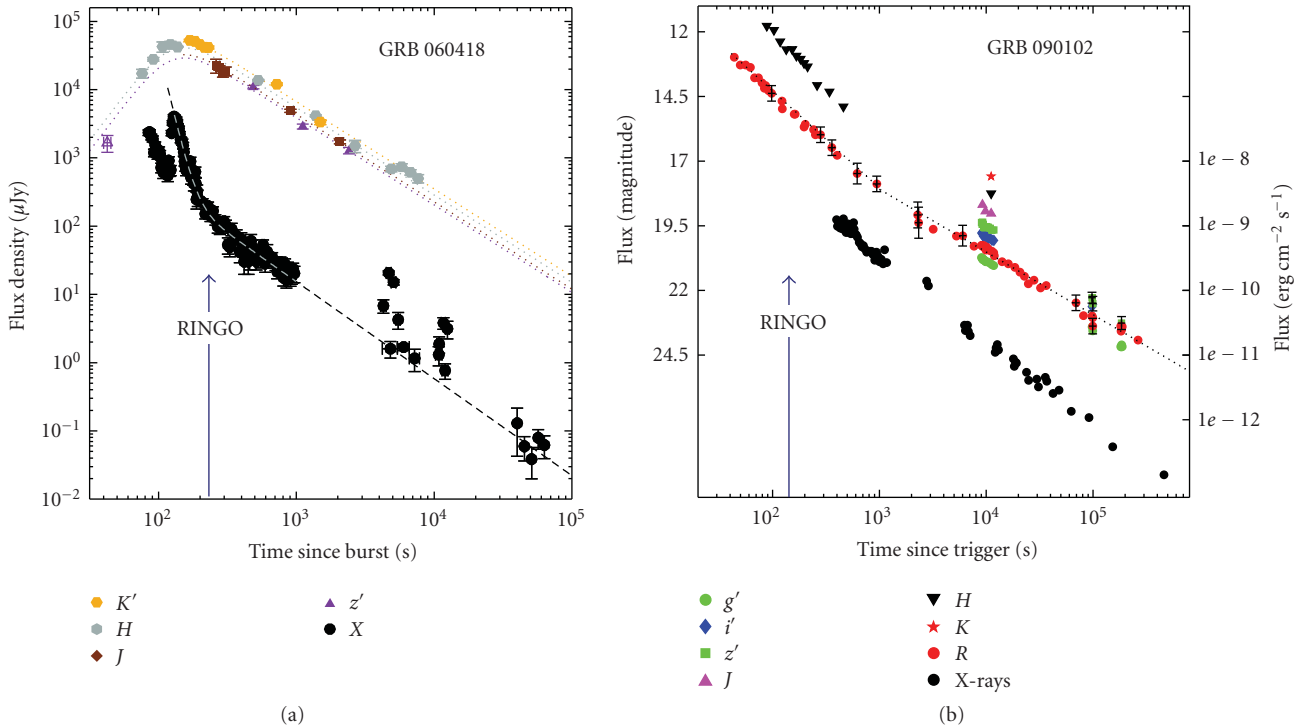


FIGURE 11: Light curves of GRB 060418 and GRB 090102 with time of RINGO observation marked at 203 seconds and 160 seconds (adapted from [89] and [90]), respectively.

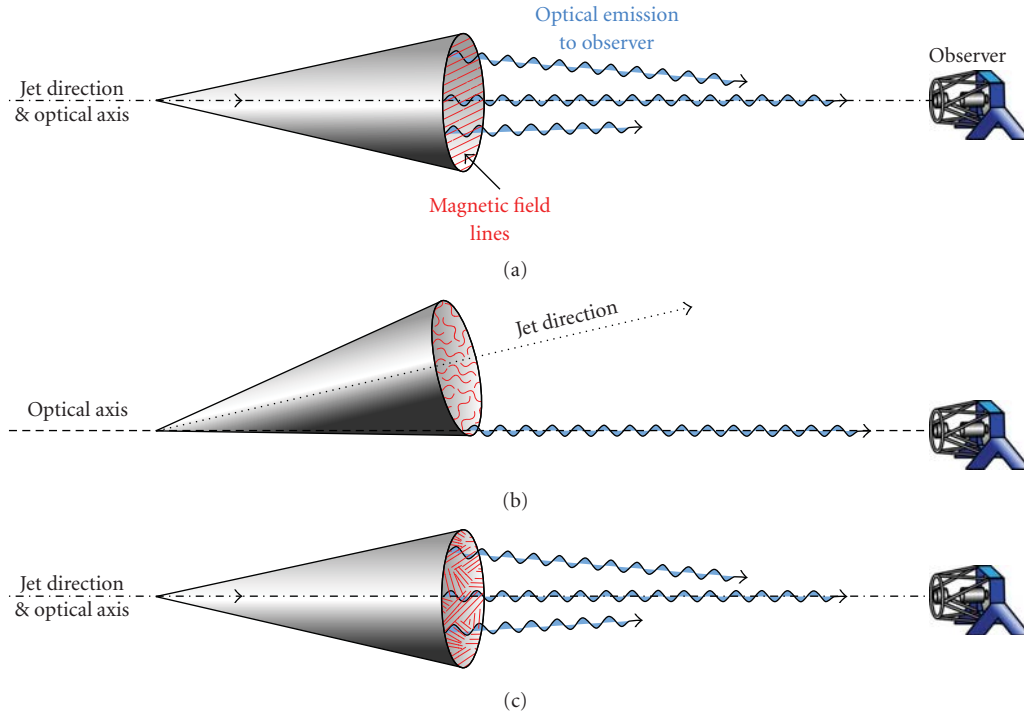


FIGURE 12: Competing models of GRB magnetic field structure for standard fireball model: (a) large-scale ordered magnetic field (favoured for GRB 090102); (b) tangled magnetic field in shock front and line of sight close to jet edge, and (c) shock front contains some independent patches of locally ordered magnetic fields [85].

afterglow whose emission is dominated by the reverse shock emission at early-times (Figure 11); this is the first GRB for which polarized optical light at early-time has been detected and its high level of polarisation $P = 10.2 \pm 1.3\%$ requires the presence of large-scale ordered magnetic fields in the outflow [85] (Figure 12). As the RINGO measurement was made when the reverse shock emission dominated the light curve, the large polarisation signal provides the first *direct* evidence that reverse shocks are produced in the presence of such fields.

Figure 12 shows three competing models of GRB magnetic field structure for the standard fireball model that could produce polarised light: (a) large-scale ordered magnetic field threaded through the GRB outflow—this model is favoured for GRB 090102; (b) tangled magnetic field generated in the shock front and an off-axis line-of-sight close to the jet edge—a scenario ruled out by the optical light curves for which an off-axis jet would require a shallow-to-steep decay, where the opposite is observed in GRB 090102; (c) a shock front containing independent patches of locally ordered magnetic fields—a scenario that is unlikely to account for GRB 090102 because the *maximum* predicted polarisation is 10% under the extreme assumption that the coherence length grows at the speed of light in the local fluid frame after the field is generated.

In summary, the polarisation properties of GRB 060418 and GRB 090102 can be reconciled in a single model in which the outflow is mildly magnetised ($\sigma \sim 1$) and contains large-scale ordered magnetic fields. In GRB 060418, σ slightly

larger than unity is needed to suppress the reverse shock emission (and hence polarisation), while in GRB 090102, σ slightly less than unity will produce the bright polarised reverse shock emission that is observed.

5. Summary and Prospects

Exploring the extreme physics exhibited by GRB explosions is technically challenging due to (a) the unpredictability of their occurrence, (b) their short-lifetime rapidly fading emission, and (c) the wide range of observed brightnesses of optical counterparts, ranging from $R = 5$ to >22 mag within minutes of the burst itself—all drivers of autonomous followup technology. Deep, fast, and multifilter observations are crucial to identify the counterparts to these events that represent the brightest stellar objects observed out to the epoch of reionization. With the advent of Swift, discoveries such as the canonical early X-ray decay, the X-ray flares, the detection of the afterglows of short-duration GRBs, and the recognition that GRB-producing stars exist out at least to $z = 8.2$ keep GRB studies at the forefront of astrophysics.

Efforts continue to understand the complexity of the X-ray versus optical afterglow temporal evolution, the circum-burst environment properties, in particular the dust versus gas content around the GRB progenitor and along the line of sight through the host galaxy, and the origin(s) of optical flares and their possible interpretations (e.g., GRB 080129 [43]: residual collisions in the GRB outflow or hot spots in strongly magnetized ejecta? [93]). Questions remain on

the fundamental nature of the relativistic ejecta, the underlying radiation mechanisms, and the role of magnetic fields. Observational surprises such as the relative lack of GeV emission from many bursts detected by Fermi and the rich variety in optical properties of GRB counterparts continue to drive developments in GRB modelling and observational technology. The 2 m robotic telescopes described here are proving decisive in tackling many of these issues: the variety of light curves has been investigated both on statistical grounds [12] as well as in individual cases of special interests: the dark GRB population and the luminosity function distribution have been characterised over a broad range of apparent brightnesses and the presence and lack of reverse shock emission in specific cases was investigated.

The interplay between forward and reverse shocks within the standard fireball model, as determined by the magnetic properties of the outflow, may yet succeed in explaining the dearth of reverse shocks previously expected from pre-Swift observations. The use of the RINGO polarimeter on the LT, capable of measuring the polarisation of optical counterparts to GRBs as early as a few minutes after the onset of the prompt γ -ray emission, has provided the earliest measurements and detection of GRB polarisation, setting important direct constraints on the magnetic field structure of the fireball and on the jet configuration [84, 85]. Further progress made in understanding the magnetic field structure of the fireball—large-scale ordered fields are currently preferred over locally tangled fields in the shock layer—will contribute to our knowledge of the nature of the outflow along the jets. Time-resolved early-time polarisation light curves (% and PA) from the newly commissioned RINGO2 promise to provide unprecedented diagnostic information on the structure and evolution of the outflow and its magnetic field for a statistically significant sample of GRBs down to $R < 17$ mag and thus allow powerful discrimination between predictions of the hydrodynamical versus magnetised jet models and ultimately constrain the physics of GRB central engines.

Acknowledgments

The authors thank the Liverpool Telescope group for technical, scientific, and artwork support. C. G. Mundell acknowledges financial support from Research Councils U.K. The Liverpool Telescope is located at the Observatorio del Roque de Los Muchachos, La Palma, Canary Islands, Spain. It was designed and built by Telescope Technologies Ltd and is owned and operated by Liverpool John Moores University with financial support from the U.K. PPARC. The Faulkes telescopes, owned by Las Cumbres Observatory, are located in Hawaii (FTN) and Siding Spring, Australia (FTS), and are operated with support from the Dill Faulkes Educational Trust.

Endnotes

1. Now owned by Las Cumbres Observatory, are operated with support from the Dill Faulkes Educational Trust.

References

- [1] R. W. Klebesadel, I. B. Strong, and R. A. Olson, "Observations of gamma-ray bursts of cosmic origin," *Astrophysical Journal*, vol. 525, no. 1, pp. 1214–1217, 1999.
- [2] E. Costa, F. Frontera, J. Heise, et al., "Discovery of an X-ray afterglow associated with the γ -ray burst of 28 February 1997," *Nature*, vol. 387, no. 6635, pp. 783–785, 1997.
- [3] J. Van Paradijs, P. J. Groot, T. Galama, et al., "Transient optical emission from the error box of the γ -ray burst of 28 February 1997," *Nature*, vol. 386, no. 6626, pp. 686–689, 1997.
- [4] D. A. Frail, S. R. Kulkarni, L. Nicastro, M. Feroci, and G. B. Taylor, "The radio afterglow from the γ -ray burst of 8 May 1997," *Nature*, vol. 389, no. 6648, pp. 261–263, 1997.
- [5] N. Gehrels, G. Chincarini, P. Giommi, et al., "The Swift gamma-ray burst mission," *Astrophysical Journal*, vol. 611, no. 2, pp. 1005–1020, 2004.
- [6] W. S. Paciesas, C. A. Meegan, G. N. Pendleton, et al., "The fourth BATSE gamma-ray burst catalog (revised)," *Astrophysical Journal, Supplement Series*, vol. 122, no. 2, pp. 465–495, 1999.
- [7] S. Barthelmy, "GCN and VEvent: a status report," *Astronomische Nachrichten*, vol. 329, no. 3, pp. 340–342, 2008.
- [8] C. Akerlof, R. Balsano, S. Barthelmy, et al., "Observation of contemporaneous optical radiation from a γ -ray burst," *Nature*, vol. 398, no. 6726, pp. 400–402, 1999.
- [9] G. Boella, R. C. Butler, G. C. Perola, L. Piro, L. Scarsi, and J. A. M. Bleeker, "BeppoSAX, the wide band mission for X-ray astronomy," *Astronomy and Astrophysics Supplement Series*, vol. 122, no. 2, pp. 299–307, 1997.
- [10] D. A. Frail, "Beaming in gamma-ray bursts: evidence for a standard energy reservoir," *Astrophysical Journal*, vol. 562, no. 1, pp. L55–L58, 2001.
- [11] G. Ghirlanda, G. Ghisellini, D. Lazzati, and C. Firmani, "Gamma-ray bursts: NEW rulers to measure the universe," *Astrophysical Journal*, vol. 613, no. 1, pp. L13–L16, 2004.
- [12] A. Melandri, C. G. Mundell, S. Kobayashi, et al., "The early-time optical properties of gamma-ray burst afterglows," *Astrophysical Journal*, vol. 686, no. 2, pp. 1209–1230, 2008.
- [13] S. B. Cenko, J. Kelemen, F. A. Harrison, et al., "Dark bursts in the Swift era: the palomar 60 inch—Swift early optical afterglow catalog," *The Astrophysical Journal*, vol. 693, no. 2, pp. 1484–1493, 2009.
- [14] S. R. Oates, M. J. Page, P. Schady, et al., "A statistical study of gamma-ray burst afterglows measured by the Swift Ultraviolet Optical Telescope," *Monthly Notices of the Royal Astronomical Society*, vol. 395, no. 1, pp. 490–503, 2009.
- [15] S. A. Yost, F. Aharonian, C. W. Akerlof, et al., "The dark side of rotse-III prompt GRB observations," *Astrophysical Journal*, vol. 669, no. 2, pp. 1107–1114, 2007.
- [16] P. W. A. Roming, P. Schady, D. B. Fox, et al., "Very early optical afterglows of gamma-ray bursts: evidence for relative paucity of detection," *Astrophysical Journal*, vol. 652, no. 2, pp. 1416–1422, 2006.
- [17] G. Tagliaferri, M. Goad, G. Chincarini, et al., "An unexpectedly rapid decline in the X-ray afterglow emission of long γ -ray bursts," *Nature*, vol. 436, no. 7053, pp. 985–988, 2005.
- [18] D. N. Burrows, P. Romano, A. Falcone, et al., "Astrophysics: bright X-ray flares in gamma-ray burst afterglows," *Science*, vol. 309, no. 5742, pp. 1833–1835, 2005.
- [19] P. T. O'Brien, R. Willingale, J. Osborne, et al., "The early X-ray emission from GRBs," *Astrophysical Journal*, vol. 647, no. 2, pp. 1213–1237, 2006.

- [20] G. Chincarini, A. Moretti, P. Romano, et al., "The first survey of X-ray flares from gamma-ray bursts observed by Swift: temporal properties and morphology," *Astrophysical Journal*, vol. 671, no. 2, pp. 1903–1920, 2007.
- [21] A. D. Falcone, D. Morris, J. Racusin, et al., "The first survey of X-ray flares from gamma-ray bursts observed by Swift: spectral properties and energetics," *Astrophysical Journal*, vol. 671, no. 2, pp. 1921–1938, 2007.
- [22] A. Klotz, M. Boër, J. L. Atteia, and B. Gendre, "Early optical observations of gamma-ray bursts by the TAROT telescopes: period 2001–2008," *The Astronomical Journal*, vol. 137, no. 5, pp. 4100–4108, 2009.
- [23] E. S. Rykoff, F. Aharonian, C. W. Akerlof, et al., "Looking into the fireball: Rotse-III and Swift observations of early gamma-ray burst afterglows," *Astrophysical Journal*, vol. 702, no. 1, pp. 489–505, 2009.
- [24] J. F. Graham, A. S. Fruchter, A. J. Levan, et al., "GRB 070714B: discovery of the highest spectroscopically confirmed short burst redshift," *The Astrophysical Journal*, vol. 698, no. 2, pp. 1620–1629, 2009.
- [25] N. Kawai, G. Kosugi, K. Aoki, et al., "An optical spectrum of the afterglow of a γ -ray burst at a redshift of $z = 6.295$," *Nature*, vol. 440, no. 7081, pp. 184–186, 2006.
- [26] J. Greiner, T. Krühler, J. P. U. Fynbo, et al., "GRB 080913 at redshift 6.7," *The Astrophysical Journal*, vol. 693, no. 2, pp. 1610–1620, 2008.
- [27] R. Salvaterra, M. Della Valle, S. Campana, et al., "GRB 090423 at a redshift of $z \approx 8.1$," *Nature*, vol. 461, no. 7268, pp. 1258–1260, 2009.
- [28] N. R. Tanvir, D. B. Fox, A. J. Levan, et al., "A γ -ray burst at a redshift of $z \approx 8.2$," *Nature*, vol. 461, no. 7268, pp. 1254–1257, 2009.
- [29] F. M. Zerbi, G. Chincarini, G. Ghisellini, et al., "The REM telescope: detecting the near infra-red counterparts of gamma-ray bursts and the prompt behavior of their optical continuum," *Astronomische Nachrichten*, vol. 322, no. 5–6, pp. 275–285, 2001.
- [30] W. T. Vestrand, K. Borozdin, D. J. Casperson, et al., "RAPTOR: closed-Loop monitoring of the night sky and the earliest optical detection of GRB 021211," *Astronomische Nachrichten*, vol. 325, no. 6–8, pp. 549–552, 2004.
- [31] D. Reichart, M. Nysewander, J. Moran, et al., "PROMPT: panchromatic robotic optical monitoring and polarimetry telescopes," *Nuovo Cimento della Societa Italiana di Fisica C*, vol. 28, no. 4–5, pp. 767–770, 2005.
- [32] S. A. Yost, F. Aharonian, C. W. Akerlof, et al., "Status of the ROTSE-III telescope network," *Astronomische Nachrichten*, vol. 327, no. 8, pp. 803–805, 2006.
- [33] A. Klotz, M. Boër, J. Eysseric, et al., "Robotic observations of the sky with TAROT: 2004–2007," *Publications of the Astronomical Society of the Pacific*, vol. 120, no. 874, pp. 1298–1306, 2008.
- [34] S. B. Cenko, D. B. Fox, D.-S. Moon, et al., "The automated palomar 60 inch telescope," *Publications of the Astronomical Society of the Pacific*, vol. 118, no. 848, pp. 1396–1406, 2006.
- [35] J. S. Bloom, D. L. Starr, C.H. Blake, et al., "Autonomous observing and control systems for PAIRITEL, a 1.3 m infrared imaging telescope," in *Astronomical Data Analysis Software and Systems XV*, vol. 351 of *ASP Conference Series*, pp. 751–754, 2006.
- [36] C. Guidorzi, A. Monfardini, A. Gomboc, et al., "The automatic real-time gamma-ray burst pipeline of the 2 m Liverpool Telescope," *Publications of the Astronomical Society of the Pacific*, vol. 118, no. 840, pp. 288–296, 2006.
- [37] A. Nousek, C. Kouveliotou, D. Grupe, et al., "Evidence for a canonical gamma-ray burst afterglow light curve in the Swift XRT data," *Astrophysical Journal*, vol. 642, no. 1, pp. 389–400, 2006.
- [38] B. Zhang, Y. Z. Fan, J. Dyks, et al., "Physical processes shaping gamma-ray burst X-ray afterglow light curves: theoretical implications from the Swift X-ray Telescope observations," *The Astrophysical Journal*, vol. 642, no. 1, pp. 354–370, 2006.
- [39] C. D. Dermer, "Rapid X-ray declines and plateaus in Swift GRB light curves explained by a highly radiative blast wave," *Astrophysical Journal*, vol. 664, no. 1, pp. 384–396, 2007.
- [40] C. D. Dermer, "Nonthermal synchrotron radiation from gamma-ray burst external shocks and the X-ray flares observed with Swift," *Astrophysical Journal*, vol. 684, no. 1, pp. 430–448, 2008.
- [41] A. Monfardini, S. Kobayashi, C. Guidorzi, et al., "High-quality early-time light curves of GRB 060206: implications for gamma-ray burst environments and energetics," *Astrophysical Journal*, vol. 648, no. 2, pp. 1125–1131, 2006.
- [42] C. Guidorzi, S. D. Vergani, S. Sazonov, et al., "GRB 070311: a direct link between the prompt emission and the afterglow," *Astronomy & Astrophysics*, vol. 474, no. 3, pp. 793–805, 2007.
- [43] J. Greiner, T. Krühler, S. McBreen, et al., "A strong optical flare before the rising afterglow of GRB 080129," *The Astrophysical Journal*, vol. 693, no. 2, pp. 1912–1919, 2009.
- [44] T. Krühler, J. Greiner, S. McBreen, et al., "Correlated optical and X-ray flares in the afterglow of XRF 071031," *Astrophysical Journal*, vol. 697, no. 1, pp. 758–768, 2009.
- [45] A. Melandri, C. Guidorzi, S. Kobayashi, et al., "Evidence for energy injection and a finetuned central engine at optical wavelengths in GRB 070419A," *Monthly Notices of the Royal Astronomical Society*, vol. 395, no. 4, pp. 1941–1494, 2009.
- [46] C. Guidorzi, D. Bersier, A. Melandri, et al., "GRB 060927: Faulkes Telescope South observation," GRB Coordinates Network, Circular Service, 5633, 2006, <http://gcn.gsfc.nasa.gov/gcn3/5633.gcn3>.
- [47] A. E. Ruiz-Velasco, H. Swan, E. Troja, et al., "Detection of GRB 060927 at $z = 5.47$: implications for the use of gamma-ray bursts as probes of the end of the dark ages," *Astrophysical Journal*, vol. 669, no. 1, pp. 1–9, 2007.
- [48] S. R. Oates, C. G. Mundell, S. Piranomonte, et al., "Anatomy of a dark burst: the afterglow of GRB 060108," *Monthly Notices of the Royal Astronomical Society*, vol. 372, no. 1, pp. 327–337, 2006.
- [49] D. A. Kann, S. Klose, and A. Zeh, "Signatures of extragalactic dust in PRE-Swift GRB afterglows," *Astrophysical Journal*, vol. 641, no. 2, pp. 993–1009, 2006.
- [50] A. Kann, S. Klose, B. Zhang, et al., "The afterglows of Swift-era gamma-ray bursts. I. Comparing pre-Swift and Swift long/soft (Type II) GRB optical afterglows," submitted, <http://arxiv.org/abs/0712.2186>.
- [51] M. Lyutikov, V. I. Pariev, and R. D. Blandford, "Polarization of prompt gamma-ray burst emission: evidence for electromagnetically dominated outflow," *Astrophysical Journal*, vol. 597, no. 2, pp. 998–1009, 2003.
- [52] Y. Z. Fan, D. M. Wei, and C. F. Wang, "The very early afterglow powered by ultra-relativistic mildly magnetized outflows," *Astronomy & Astrophysics*, vol. 424, no. 2, pp. 477–484, 2004.
- [53] Y. -Z. Fan, D. Xu, and D. -M. Wei, "Polarization evolution accompanying the very early sharp decline of gamma-ray burst X-ray afterglows," *Monthly Notices of the Royal Astronomical Society*, vol. 387, no. 1, pp. 92–96, 2008.
- [54] B. Zhang and S. Kobayashi, "Gamma-ray burst early afterglows: reverse shock emission from an arbitrarily magnetized

- ejecta,” *Astrophysical Journal*, vol. 628, no. 1, pp. 315–334, 2005.
- [55] T. Piran, “Gamma-ray bursts and the fireball model,” *Physics Report*, vol. 314, no. 6, pp. 575–667, 1999.
- [56] B. Zhang and P. Mészáros, “Gamma-ray bursts: progress, problems & prospects,” *International Journal of Modern Physics A*, vol. 19, no. 15, pp. 2385–2472, 2004.
- [57] P. Mészáros, “Gamma-ray bursts,” *Reports on Progress in Physics*, vol. 69, no. 8, pp. 2259–2321, 2006.
- [58] B. Zhang, “Gamma-ray bursts in the Swift era,” *Chinese Journal of Astronomy and Astrophysics*, vol. 7, no. 1, pp. 1–50, 2007.
- [59] T. Piran and Y. -Z. Fan, “Gamma-ray burst theory after Swift,” *Philosophical Transactions of the Royal Society A*, vol. 365, no. 1854, pp. 1151–1162, 2007.
- [60] C. G. Mundell, A. Melandri, C. Guidorzi, et al., “The remarkable afterglow of GRB 061007: implications for optical flashes and GRB fireballs,” *Astrophysical Journal*, vol. 660, no. 1, pp. 489–495, 2007.
- [61] A. Gomboc, S. Kobayashi, C. G. Mundell, et al., “Optical flashes, reverse shocks and magnetization,” in *Proceedings of the 6th Huntsville Symposium on Gamma-Ray Bursts*, vol. 1133 of *AIP Conference Proceedings*, pp. 145–150, 2009.
- [62] A. Gomboc, S. Kobayashi, C. Guidorzi, et al., “Multiwavelength analysis of the intriguing GRB 061126: the reverse shock scenario and magnetization,” *Astrophysical Journal*, vol. 687, no. 1, pp. 443–455, 2008.
- [63] R. Sari, “Linear polarization and proper motion in the afterglow of beamed gamma-ray bursts,” *Astrophysical Journal*, vol. 524, no. 1, pp. L43–L46, 1999.
- [64] A. Gruzinov and E. Waxman, “Gamma-ray burst afterglow: polarization and analytic light curves,” *Astrophysical Journal*, vol. 511, no. 2, pp. 852–861, 1999.
- [65] G. Ghisellini and D. Lazzati, “Polarization light curves and position angle variation of beamed gamma-ray bursts,” *Monthly Notices of the Royal Astronomical Society*, vol. 309, no. 1, pp. L7–L11, 1999.
- [66] E. Waxman, “Astronomy: new direction for γ -rays,” *Nature*, vol. 423, no. 6938, pp. 388–389, 2003.
- [67] J. Greiner, S. Klose, K. Reinsch, et al., “Evolution of the polarization of the optical afterglow of the γ -ray burst GRB030329,” *Nature*, vol. 426, no. 6963, pp. 157–159, 2003.
- [68] J. Granot and A. Königl, “Linear polarization in gamma-ray bursts: the case for an ordered magnetic field,” *Astrophysical Journal*, vol. 594, no. 2, pp. L83–L87, 2003.
- [69] E. M. Rossi, D. Lazzati, J. D. Salmonson, and G. Ghisellini, “The polarization of afterglow emission reveals γ -ray bursts jet structure,” *Monthly Notices of the Royal Astronomical Society*, vol. 354, no. 1, pp. 86–100, 2004.
- [70] A. Sagiv, E. Waxman, and A. Loeb, “Probing the magnetic field structure in gamma-ray bursts through dispersive plasma effects on the afterglow polarization,” *Astrophysical Journal*, vol. 615, no. 1, pp. 366–377, 2004.
- [71] D. Götz, P. Laurent, F. Lebrun, F. Daigne, and E. Bonjak, “Variable polarization measured in the prompt emission of GRB 041219a using ibis on board integral,” *Astrophysical Journal*, vol. 695, no. 2, pp. L208–L212, 2009.
- [72] D. Lazzati, S. Covino, J. Gorosabel, et al., “On the jet structure and magnetic field configuration of GRB 020813,” *Astronomy & Astrophysics*, vol. 422, no. 1, pp. 121–128, 2004.
- [73] W. Coburn and S. E. Boggs, “Polarization of the prompt γ -ray emission from the γ -ray burst of 6 December 2002,” *Nature*, vol. 423, no. 6938, pp. 415–417, 2003.
- [74] R. E. Rutledge and D. B. Fox, “Re-analysis of polarization in the γ -ray flux of GRB 021206,” *Monthly Notices of the Royal Astronomical Society*, vol. 350, no. 4, pp. 1288–1300, 2004.
- [75] C. Wigger, W. Hajdas, K. Arzner, M. Güdel, and A. Zehnder, “Gamma-ray burst polarization: limits from *RHESSI* measurements,” *Astrophysical Journal*, vol. 613, no. 2, pp. 1088–1100, 2004.
- [76] D. R. Willis, E. J. Barlow, A. J. Bird, et al., “Evidence of polarisation in the prompt gamma-ray emission from GRB 930131 and GRB 960924,” *Astronomy & Astrophysics*, vol. 439, no. 1, pp. 245–253, 2005.
- [77] S. McGlynn, D. J. Clark, A. J. Dean, et al., “Polarisation studies of the prompt gamma-ray emission from GRB 041219a using the spectrometer aboard INTEGRAL,” *Astronomy & Astrophysics*, vol. 466, no. 3, pp. 895–904, 2007.
- [78] E. Kalemci, S. E. Boggs, C. Kouveliotou, M. Finger, and M. G. Baring, “Search for polarization from the prompt gamma-ray emission of GRB 041219a with SPI on INTEGRAL,” *Astrophysical Journal, Supplement Series*, vol. 169, no. 1, pp. 75–82, 2007.
- [79] S. McGlynn, S. Foley, B. McBreen, et al., “High energy emission and polarisation limits for the INTEGRAL burst GRB 061122,” *Astronomy & Astrophysics*, vol. 499, no. 2, pp. 465–472, 2009.
- [80] Y. Z. Fan, B. Zhang, and D. M. Wei, “Early optical-infrared emission from GRB 041219a: neutron-rich internal shocks and a mildly magnetized external reverse shock,” *Astrophysical Journal*, vol. 628, no. 1, pp. L25–L28, 2005.
- [81] S. Covino, “A closer look at a gamma-ray burst,” *Science*, vol. 315, no. 5820, pp. 1798–1799, 2007.
- [82] I. A. Steele, S. D. Bates, D. Carter, et al., “RINGO: a novel ring polarimeter for rapid GRB followup,” in *Ground-Based and Airborne Instrumentation for Astronomy*, vol. 6269 of *Proceedings of SPIE*, Orlando, Fla, USA, May 2006.
- [83] D. Clarke and D. Neumayer, “Experiments with a novel CCD stellar polarimeter,” *Astronomy & Astrophysics*, vol. 383, no. 1, pp. 360–366, 2002.
- [84] C. G. Mundell, I. A. Steele, R. J. Smith, et al., “Early optical polarization of a gamma-ray burst afterglow,” *Science*, vol. 315, no. 5820, pp. 1822–1824, 2007.
- [85] I. A. Steele, C. G. Mundell, R. J. Smith, S. Kobayashi, and C. Guidorzi, “Ten per cent polarized optical emission from GRB 090102,” *Nature*, vol. 462, no. 7274, pp. 767–769, 2009.
- [86] S. Kobayashi, T. Piran, and R. Sari, “Hydrodynamics of a relativistic fireball: the complete evolution,” *Astrophysical Journal*, vol. 513, no. 2, pp. 669–678, 1999.
- [87] A. D. Falcone, S. D. Barthelmy, D. N. Burrows, et al., “GRB 060418: Swift detection of a burst with bright X-ray and optical afterglow,” GRB Coordinates Network, Circular Service, 4966, 2006, <http://gcn.gsfc.nasa.gov/gcn3/4966.gcn3>.
- [88] A. D. Falcone, D. N. Burrows, and J. Kennea, “GRB 060418: Swift XRT team refined analysis,” GRB Coordinates Network, Circular Service, 4973, 2006, <http://gcn.gsfc.nasa.gov/gcn3/4973.gcn3>.
- [89] E. Molinari, S. D. Vergani, D. Malesani, et al., “REM observations of GRB060418 and GRB 060607A: the onset of the afterglow and the initial fireball Lorentz factor determination,” *Astronomy & Astrophysics*, vol. 469, no. 1, pp. L13–L16, 2007.
- [90] B. Gendre, A. Klotz, E. Palazzi, et al., “Testing GRB models with the strange afterglow of GRB 090102,” *Monthly Notices of the Royal Astronomical Society*, <http://bit.ly/cvqXIG>, in press.

- [91] T. Sakamoto, S. D. Barthelmy, W. H. Baumgartner, et al., “GRB 090102: Swift-BAT refined analysis,” GRB Coordinates Network, Circular Service, 8769, 2009, <http://gcn.gsfc.nasa.gov/gcn3/8769.gcn3>.
- [92] S. Kobayashi and B. Zhang, “GRB 021004: reverse shock emission,” *Astrophysical Journal*, vol. 582, no. 2, pp. L75–L78, 2003.
- [93] M. Lyutikov, “The electromagnetic model of gamma-ray bursts,” *New Journal of Physics*, vol. 8, article 119, 2006.

Research Article

Master Robotic Net

Vladimir Lipunov,¹ Victor Kornilov,¹ Evgeny Gorbovskoy,¹ Nikolaj Shatskij,¹ Dmitry Kuvshinov,¹ Nataly Tyurina,¹ Alexander Belinski,¹ Alexander Krylov,¹ Pavel Balanutsa,¹ Vadim Chazov,¹ Artem Kuznetsov,¹ Petr Kortunov,¹ Anatoly Sankovich,¹ Andrey Tlatov,² A. Parkhomenko,² Vadim Krushinsky,³ Ivan Zalozhnyh,³ A. Popov,³ Taisia Kopytova,³ Kirill Ivanov,⁴ Sergey Yazev,⁴ and Vladimir Yurkov⁵

¹ Sternberg Astronomical Institute, Moscow State University, 13 Univeristetskij pr-t, Moscow 119991, Russia

² Kislovodsk Solar Station, P.O. Box 145, 100 Gagarina street, Kislovods 357700, Russia

³ Ural State University, 51 Lenina pr-t, Ekaterinburg 620083, Russia

⁴ Irkutsk State University, 1 Karl Marks ul., Irkutsk 664003, Russia

⁵ Blagoveschensk State Pedagogical University, 104 Lenina street, Blagoveschensk 675000, Amur region, Russia

Correspondence should be addressed to Vladimir Lipunov, lipunov@sai.msu.ru

Received 30 June 2009; Accepted 16 November 2009

Academic Editor: Taro Kotani

Copyright © 2010 Vladimir Lipunov et al. This is an open access article distributed under the Creative Commons Attribution License, which permits unrestricted use, distribution, and reproduction in any medium, provided the original work is properly cited.

The main goal of the MASTER-Net project is to produce a unique fast sky survey with all sky observed over a single night down to a limiting magnitude of 19-20. Such a survey will make it possible to address a number of fundamental problems: search for dark energy via the discovery and photometry of supernovae (including SNIa), search for exoplanets, microlensing effects, discovery of minor bodies in the Solar System, and space-junk monitoring. All MASTER telescopes can be guided by alerts, and we plan to observe prompt optical emission from gamma-ray bursts synchronously in several filters and in several polarization planes.

1. Introduction

The MASTER project (Mobile Astronomical System of TElescope Robots) was launched in 2002, when the first Russian robotic telescope was installed near Moscow on an automated mounting with automatic roof, weather station, and alert system (Lipunov et al. [1–3]). By early 2008 we posted about 100 GCN circulars, recorded optical emission from three gamma-ray bursts, and discovered four supernovae (Lipunov et al. [4], Tyurina et al. [5]). Unfortunately, very poor astroclimatic conditions near Moscow made it impossible to demonstrate the potential of our telescope to its full extent. However, we obtained about 80 000 images, each with a size of six square degrees, and used them to successfully develop a software pipeline, which allows us not only to perform in real time the extraction of images and their astrometric and photometric reduction, but also to automatically classify the sources identified; that is, determine which type of astronomical objects (supernovae, minor

planets, comets, man-made satellites, meteors, or optical transients) they belong to (Figures 1 and 2). Moreover, our facility can also be used for alert observations of optical emission of gamma-ray bursts (Tyurina et al. [5]).

Our experience with the operation of robotic telescopes allowed us to develop the wide-field MASTER optical facility with optimum parameters, which can be used to address a wide range of astrophysical tasks. We actually developed a multipurpose optical facility, which is similar in composition to the one independently proposed by Bogdan Paczynski (Paczynski [6]). The first MASTER telescopes and their individual components are already installed at three sites in Russia—near Kislovodsk (Caucasian Mountain Observatory of the Sternberg Astronomical Institute of the Moscow State University), in Urals (Kourovka Observatory of Ural State University), and near Irkutsk (Irkutsk State University Observatory). In summer 2009 we also plan to deploy similar facilities near Irkutsk and Blagoveshchensk.

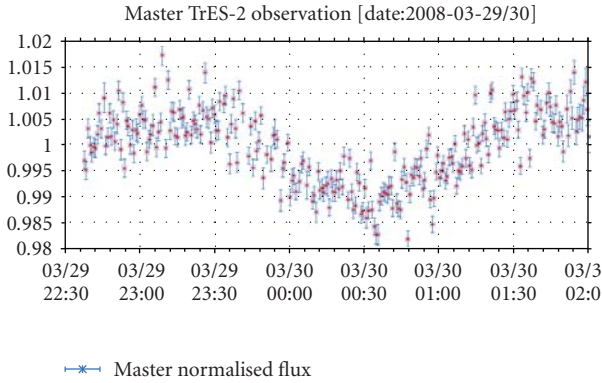


FIGURE 1: Follow-up exoplanet transit observations by MASTER (Moscow).

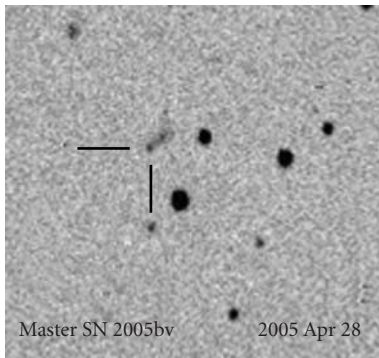


FIGURE 2: The first supernova discovered in Russia (SN2005bv).

2. MASTER Wide-Field Robotic Facility

The MASTER wide-field robotic telescope that we developed is manufactured by OAO Optika Moscow Association. The facility consists of two instruments: MASTER II wide-field optical telescope “Santel 400” and MASTER very wide-field (VWF) cameras.

2.1. MASTER II Wide-Field Robotic Telescope. A single fast German equatorial mounting carries two 1:2.5 focal-ratio symmetrical high-aperture 400-mm catadioptric telescopes (Figure 3). The telescope has an extra degree of freedom, which allows their tubes to be aligned or misaligned, making it possible to double the size of the field of view and, when operating in the alert mode (with collinear tubes), to perform synchronous photometry of rapidly varying objects in standard broad-band filters (B,V,R,I) and their polarimetry at different polarizations (Figure 4).

Table 1 lists the technical parameters of MASTER II telescope. The telescope is equipped with a shell-type automatic shelter, which, when open, allows the entire sky to be observed. This facility is also equipped with a time synchronization system, a weather station, and a cloud cover sensor.

2.2. MASTER VWF Very Wide-Field Camera. V. G. Kornilov developed a robotic very wide-field MASTER VWF camera

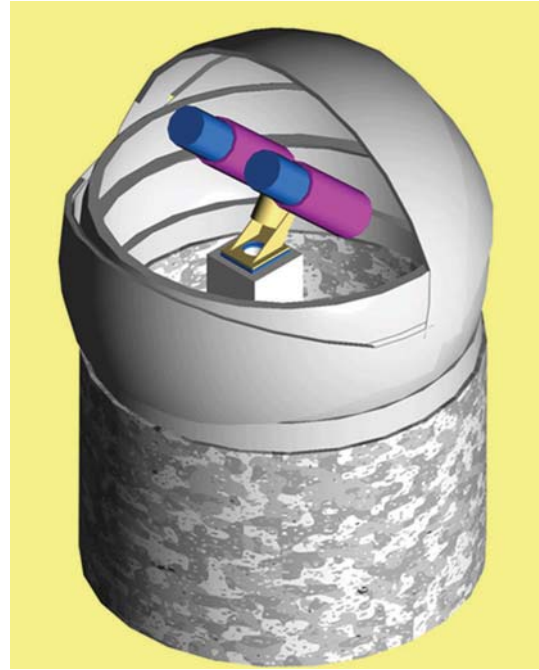


FIGURE 3: MASTER II wide-field robotic telescope (manufactured by OAO Optika Moscow Association). Each tube is equipped with a photometer with a set of B, V, R, I filters and polarizers.

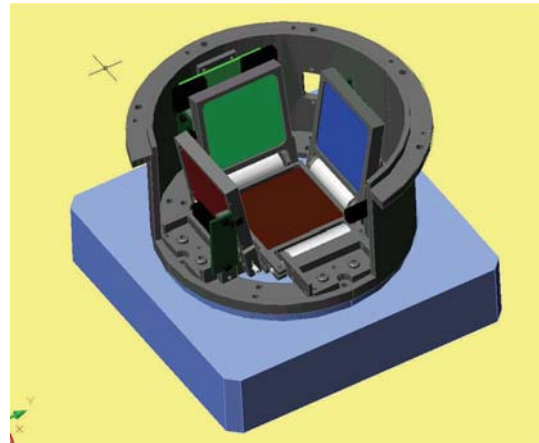


FIGURE 4: Photometer with 3 filters and 1 polarimeter based on an Apogee AltaU16M CCD camera.

with a maximum field of view of 1000 square degrees (Figure 5) for synchronous observations of optical emission from gamma-ray bursts. The facility uses a parallactic fork capable of carrying 2 CCD cameras with up to 10-cm aperture lenses. The facility has an autonomous high-quality roof designed by N. I. Shatskii. Our experience of its operation under extreme conditions of Russian winter (with temperatures as low as -40 degree Celsius) demonstrates good survival potential of all systems. Table 2 lists the specifications of the very wide-field camera. The cameras are adapted to all large-aperture Nikor and Nikor-Ziess lenses.

TABLE 1: Composition and specification of MASTER II telescope.

Item	Parameter	Number	Remark	Special name
Telescope (2 pieces)	Diameter	400 mm	Light-beam diameter	Hamilton system (Santel 400)
	Focus	1 000 mm	—	—
	Weight	50 kg	On each side	—
	Field of view	2×4 square degrees	For an Apogee AltaU16 type CCD camera	—
Mounting	Weight capacity	Up to 100 kg	German	NTM
	Maximum positioning speed	30 deg/s	—	—
Dome	Diameter	3.6 m	—	—
	Weight	500 kg	—	—
2 CCD cameras	Number of pixels	$4K \times 4K$ pix for each	—	—
	Pixel size	9 microns	—	—
	Image scale	1.84'' per pix	—	—
Cloud Sensor	—	—	The Boltwood Cloud Sensor II	—
GPS	Accuracy of synchronization	100 microseconds	—	—
Server	RAM	8 Gb	—	—
	Processor	Xion 54XX	—	—
	HDDs	Rate 10Tb	—	—
Survey rate	—	480 sq. deg/h	—	—
Limiting magnitude for 1-min exposure	—	19 m	under optimum astroclimatic conditions	—

Our facility uses two lenses with the focal distances of 50 and 85 mm. The cameras allow continuous sky imaging with a minimum exposure of 150 milliseconds.

3. Geographic Location of the Stations of the MASTER Network as of May 2009

The locations of the station sites were determined by two factors: (1) sites must be about ~ 2 hours apart in longitude and (2) sites must provide minimum required infrastructure (power supply, Internet, warm room for servers). Such sites can usually be found at university observatories (Figure 6).

The participants to the project already include Moscow State University (Figure 7), Ural State University (Figure 8), Irkutsk State University, and Blagoveshchensk Pedagogical University. The network extends over seven hours in longitude, thereby ensuring virtually continuous 24-hour observations during winter seasons.

When deployed, the first step MASTER II telescope network will have the following parameters



FIGURE 5: MASTER very wide-field camera.

- (i) Total field of view—38 square degrees.
- (ii) Survey rate—2000 square degrees per hour down to a limiting magnitude of 19-20.
- (iii) Alert positioning speed—up to 30 degrees/s.

TABLE 2: Composition and specification of MASTER VWF camera.

Item	Parameter	Value	Remark	Special name
Lens (2 pieces)	Diameter	35.7 mm	Light-beam diameter	Nikor 50 f/1.4
	Focus	50 mm	—	—
	Field of view	1040 square degrees	For a CCD camera with a chip size of 24×36 mm	—
Lens (2 pieces)	Diameter	60.7 mm	Light-beam diameter	Zeiss-Nikor 85/1.4
	Focus	85 mm	—	—
	Field of view	432 square degrees	—	—
Mounting	Weight capacity	Up to 10 kg	Fork	Frictional
	Maximum positioning speed	6 deg/s	—	—
	Positioning accuracy	1 arcmin	—	—
Dome	Diameter	1×1.5 m	—	—
	Weight	30 kg	—	—
CCD cameras (2 pieces)	Number of pixels	12 Mpix	—	—
	Pixel size	9 microns	—	—
	Image scale	$36''$ per pix $20''$ per pix	for f50 for f85	—
Limiting magnitude for 1-min exposure	—	11^m 13^m	for f50 for f85	—

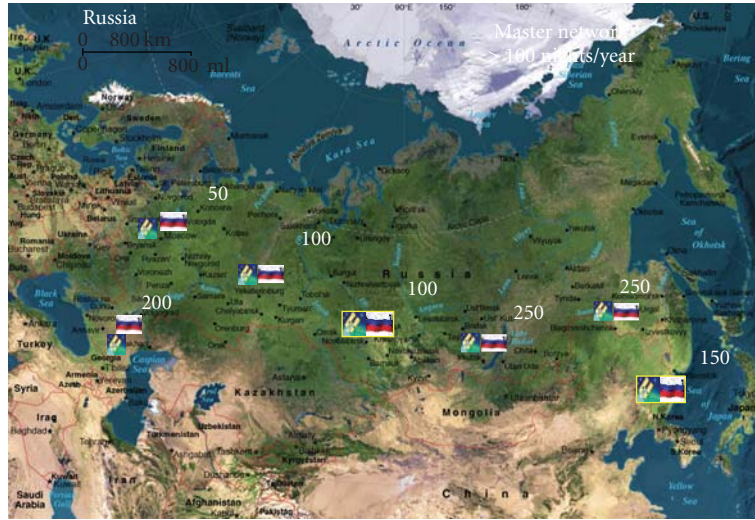


FIGURE 6: Russian robotic network MASTER. The flags indicate the Russian contribution into gamma-ray burst's astrophysic. The yellow rectangles indicate planned sites of network stations and the indicators without rectangles introduce already equipped ones. From West to East: Moscow (MASTER I), Kislovodsk (MASTER II, MASTER VWF-4), Ekaterinburg (MASTER II), Novosibirsk (planned), Irkutsk (MASTER II in Tunka (made in November 2009) and VWF-2), Blagoveshchensk (MASTER-I, made in October 2009), and Ussuriysk (planned). The average annual number of clear nights is indicated near each site.

4. Expected Scientific Results

4.1. GRB Mystery. Observations of the prompt emission of gamma-ray bursts, which is determined by the physical processes in the central engine, are of fundamental importance

for understanding the nature of these bursts (Lipunov and Gorbovskoy [7, 8]).

First and foremost, we expect that MASTER II telescopes will allow us to obtain multicolor photometric and polarimetric follow-up observations for alerts from gamma-ray



FIGURE 7: MASTER II (Kislovodsk, Sternberg Astronomical Institute, Moscow State University). Photo by A. Belinskiy.



FIGURE 8: MASTER II (Kourovka, near Ekaterinburg, Ural State University).

space observatories. We also plan to continue synchronous observations with very wide-field cameras. Recall that we have performed five synchronous observations of gamma-ray error boxes since November 2008 (Gorbovskoy et al. [9]).

4.2. Dark Energy. The first mass observations of type Ia supernovae showed (Reiss et al. [10]; Perlmutter S. et al. [11]) that the Universe expands with acceleration, which may be due to the so-called dark energy. This result follows from observations of several dozen supernovae. On the other hand, present-day search surveys miss most of the supernovae. The first computations of the velocities of explosions of cosmological supernovae performed by Jorgensen et al., [12] showed that the number of supernovae

exploding in our Universe with magnitudes brighter than m can be described by the following formula:

$$N(< m) \sim 10^5 10^{\frac{3}{5}(m-20)} \text{ yrs}^{-1} \quad (15 < m < 22). \quad (1)$$

Note that without the correction for host-galaxy extinction 20^m corresponds to a redshift of $z \sim 0.2-0.3$, where the effect of cosmic energy of vacuum becomes quite appreciable.

This actually means that MASTER can discover several thousand supernovae annually and perform multicolor photometry of these objects.

5. Conclusion

A complete survey of the entire visible sky during a single night will allow to perform a number of tasks with no special observing plan (provided, naturally, proper coordination between the stations of the network):

- (i) search for orphan flares,
- (ii) search for exoplanets,
- (iii) search for dangerous asteroids,
- (iv) search for microlensing effects,
- (v) search for and monitoring of space waste.

Acknowledgment

The authors thank the General Director of the "OPTIKA" Association S. M. Bodrov for providing the MASTER project with necessary expensive equipment.

References

- [1] V. Lipunov, "Mobile astronomical systems of the telescope-robots (MASTER) near the Moscow," *Bulletin of the American Astronomical Society*, vol. 35, p. 766, 2003.
- [2] V. M. Lipunov, A. V. Krylov, V. G. Kornilov, et al., "MASTER: the mobile astronomical system of telescope-robots," *Astronomische Nachrichten*, vol. 325, no. 6–8, pp. 580–582, 2004.
- [3] V. M. Lipunov, V. G. Kornilov, A. V. Krylov, et al., "The master mobile astronomical system. Optical observations of gamma-ray bursts," *Astrophysics*, vol. 48, no. 3, pp. 389–399, 2005.
- [4] V. M. Lipunov, V. G. Kornilov, A. V. Krylov, et al., "Optical observations of gamma-ray bursts, the discovery of supernovae 2005bv, 2005ee, and 2006ak, and searches for transients using the "MASTER" robotic telescope," *Astronomy Reports*, vol. 51, no. 12, pp. 1004–1025, 2007.
- [5] N. Tyurina, V. Lipunov, V. Kornilov, et al., "MASTER prompt and follow-up GRB observations," <http://arxiv.org/abs/0907.1036>.
- [6] B. Paczynski, "Astronomy with small telescopes," *Publications of the Astronomical Society of the Pacific*, vol. 118, no. 850, pp. 1621–1625, 2006.
- [7] V. Lipunov and E. Gorbovskoy, "An extra long X-ray plateau in a gamma-ray burst and the spinar paradigm," *Astrophysical Journal*, vol. 665, no. 2, part 2, pp. L97–L100, 2007.

- [8] V. M. Lipunov and E. S. Gorbovskoy, “Spinar paradigm and the central engine of gamma-ray bursts,” *Monthly Notices of the Royal Astronomical Society*, vol. 383, no. 4, pp. 1397–1412, 2008.
- [9] E. Gorbovskoy, K. Ivanov, V. Lipunov, et al., “Transient detections and other real-time data processing from wide-field chambers MASTER VWF,” <http://arxiv.org/abs/0907.1118>.
- [10] A. G. Riess, A. V. Filippenko, P. Challis, et al., “Observational evidence from supernovae for an accelerating universe and a cosmological constant,” *Astronomical Journal*, vol. 116, no. 3, pp. 1009–1038, 1998.
- [11] S. Perlmutter, G. Aldering, G. Goldhaber, et al., “Measurements of Ω and Λ from 42 high-redshift Supernovae,” *Astrophysical Journal*, vol. 517, no. 2, pp. 565–586, 1999.
- [12] H. E. Jorgensen, V. M. Lipunov, I. E. Panchenko, K. A. Postnov, and M. E. Prokhorov, “Evolution of supernova explosion rates in the universe,” *Astrophysical Journal*, vol. 486, no. 1, pp. 110–116, 1997.

Research Article

Taiwan Automated Telescope Network

**Dean-Yi Chou,¹ Ming-Tsung Sun,² Javier Fernandez Fernandez,¹ Li-Han Wang,¹
Antonio Jimenez,³ Alexander Serebryanskiy,⁴ and Shuhrat Ehgamberdiev⁴**

¹ Department of Physics, National Tsing Hua University, Hsinchu 30013, Taiwan

² Department of Mechanical Engineering, Chang-Gung University, Kwei-San 33302, Taiwan

³ Instituto de Astrofísica de Canarias, 38205 La Laguna, Spain

⁴ Ulugh Beg Astronomical Institute, 100052 Tashkent, Uzbekistan

Correspondence should be addressed to Dean-Yi Chou, chou@phys.nthu.edu.tw

Received 15 June 2009; Accepted 5 October 2009

Academic Editor: Taro Kotani

Copyright © 2010 Dean-Yi Chou et al. This is an open access article distributed under the Creative Commons Attribution License, which permits unrestricted use, distribution, and reproduction in any medium, provided the original work is properly cited.

A global network of small automated telescopes, the Taiwan Automated Telescope (TAT) network, dedicated to photometric measurements of stellar pulsations, is under construction. Two telescopes have been installed in Teide Observatory, Tenerife, Spain and Maidanak Observatory, Uzbekistan. The third telescope will be installed at Mauna Loa Observatory, Hawaii, USA. Each system uses a 9-cm Maksutov-type telescope. The effective focal length is 225 cm, corresponding to an f -ratio of 25. The field of view is 0.62 degree square. The images are taken with a 16-bit 1024×1024 CCD camera. The telescope is equipped with UBVRI filters. Each telescope is fully automated. The telescope can be operated either interactively or fully automatically. In the interactive mode, it can be controlled through the Internet. In the fully automatic mode, the telescope operates with preset parameters without any human care, including taking dark frames and flat frames. The network can also be used for studies that require continuous observations for selected objects.

1. Introduction

The global ground-based telescope network is a way to continuously monitor selected objects. The Hungarian Automated Telescope (HAT) Network, dedicated to the extrasolar planet search, so far has two sites [1]. The Stellar Oscillations Network Group (SONG) is a ground-based network dedicated to measurements of stellar pulsation velocity. It plans to build eight identical telescopes around the globe [2]. Here we introduce the Taiwan Automated Telescope (TAT) Network, which is a ground-based network dedicated to photometric measurements of stellar pulsations to study the structure and evolution of stars. The network will consist of several identical robotic optical telescopes at appropriate longitudes around the globe to continuously measure stellar pulsations with a high duty cycle. The headquarter of the network is located at the Physics Building of National Tsing Hua University, Taiwan, where the electronic devices and software are designed and built. The mechanical devices are designed and built in Chang-Gung University. So far two telescopes have been installed at

Teide Observatory ($28^{\circ}18' \text{ N}$, $16^{\circ}31' \text{ W}$), Tenerife, Spain and Maidanak Observatory ($38^{\circ}41' \text{ N}$, $66^{\circ}56' \text{ E}$), Uzbekistan. Figure 2 shows the picture of the telescope at Maidanak. The third telescope is planned to be installed at Mauna Loa Observatory ($19^{\circ}32' \text{ N}$, $155^{\circ}35' \text{ W}$), Hawaii, USA. The search for the fourth site is underway. Each telescope is fully automated. The telescope can be operated either interactively or fully automatically. In the interactive mode, it can be controlled through the Internet. In the fully automatic mode, the telescope operates with preset parameters without any human care, including taking dark frames and flat frames. The telescope can measure 10-magnitude stars with an error of about 2-3 mmag. The long-term goal of the project is to upgrade the telescopes to ones with a larger aperture.

2. Hardware

The overall structure of the automated telescope is described by a system block diagram shown in Figure 1. The major components are briefly described as follows.

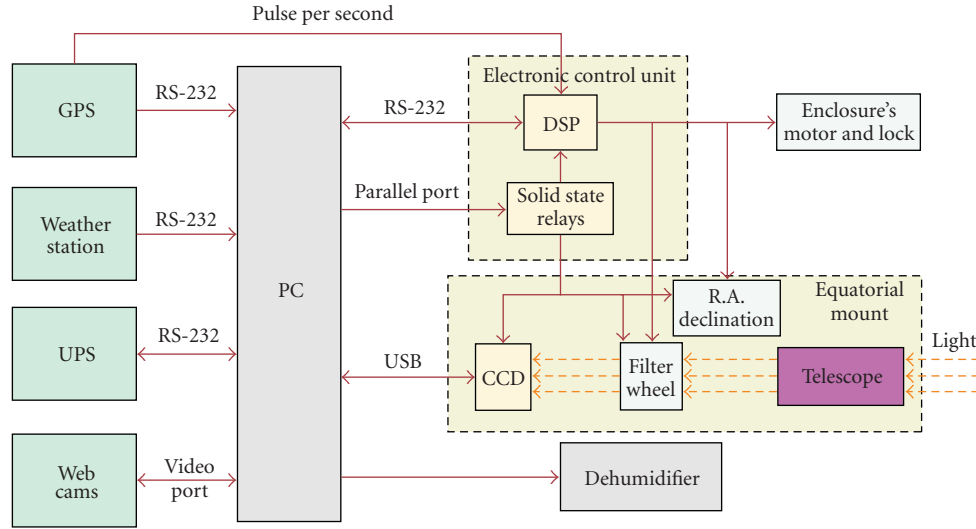


FIGURE 1: Block diagram of the telescope system.



FIGURE 2: Telescope at the Maidanak Observatory, Uzbekistan.

2.1. Computer. The whole system is controlled by a Linux-based industrial personal computer, which allows us to install several interface cards. The computer uses an RAID-1 system to avoid loss of data and for a quick recovery. A digital signal processor (DSP) is used as an interface between the computer and some hardware devices, such as filter wheel, stepping motors, limit switches, and enclosure.

2.2. Optics and CCD. Each system uses a 9 cm (3.5-inch) ruggedized Questar telescope (Maksutov type). The focus of the telescope can be locked with six screws on three rods attached to the main mirror. The field of view can vary by changing the separation between the telescope and the CCD camera. The images are taken with a 16-bit 1024×1024 air-cooled CCD camera, using a Kodak KAF-1001E chip, made by Apogee. The dimension of the chip is 2.45×2.45 cm. The field of view is currently set to 0.62 degree square.

The effective focal length is 225 cm, corresponding to an f -ratio of 25. The telescope and the CCD are mounted on an aluminum beam, and their separation can be changed for the focal length adjustment. A filter wheel with UBVRI filters, covered with a case, is mounted between the telescope and the CCD. The filter wheel is driven by a stepping motor which is controlled by the computer through the DSP.

2.3. Telescope Tracking. The telescope is mounted on a German-type equatorial mount, made by Takahashi. The original two Takahashi step motors of right ascension (RA) and declination (DEC) are replaced by two five-phase stepping motors made by Oriental Motor. The two stepping motors are controlled by the DSP, which is in turn controlled by the computer. Two photo interrupters are used for the reference position of the RA and DEC. The target position is computed relative to this reference position, and the telescope moves to the reference position before moving to the target position [3]. Limit switches are used to prevent the telescope from moving out of range. The telescope tracking is corrected by cross-correlating the current image with a reference image. This correction is carried out after each exposure.

2.4. Enclosure. A rectangular-shape enclosure is used to house the telescope and all equipments except the external weather sensors and webcams and GPS antenna. A rectangular-shape enclosure instead of a conventional dome is used because it can provide a better seal. A dehumidifier is installed inside the enclosure to reduce humidity during nonobserving periods. A heater is used to ensure the function of the dehumidifier and UPS batteries in the winter.

2.5. Monitoring Webcams. Eight to ten webcams are used to monitor the status of the telescope and other equipments. Some of the webcams are installed inside the enclosure. The webcams are equipped with infrared light source for

night monitoring. They are automatically turned off during observations to avoid light pollution. A couple of wide-angle webcams of 150° point to the sky to monitor the sky quality. The video streams from the webcams can be viewed on the webpage of each station.

2.6. GPS. A GPS is used to provide the computer with the precise time/date. It also provides the DSP with the signal of pulse per sec (PPS) because the DSP needs an accurate time reference.

2.7. Weather Station. A weather station is set up near the telescope to provide basic weather data for the autoobserving software to determine whether the observation can start. The weather data are also used to determine the emergency stop during observations. The observing criterion could vary from site to site. It is currently set as the wind speed less than 20 m/s and the relative humidity lower than 70% for Teide and Maidanak sites.

2.8. Uninterrupted Power Supply. An uninterrupted power supply (UPS) of 1500 VA is used to protect the computer and other electrical equipments. The UPS is connected to the computer through a serial port. The UPS will shut down the computer in case of persistent power failure and turn it on again when the power is resumed.

3. Software

3.1. Automatic Control. Each telescope is fully automated. The telescope can be operated either interactively or fully automatically. In the interactive mode, it can be controlled through the Internet. The observer, logging in the computer, can control each component of the system through a user-friendly command menu.

In the fully automatic mode, the telescope operates with a set of preset parameters without any human care. All preset parameters are written in a file, checked by the computer every minute. The parameters include the beginning and end of the observing period, the coordinates of the target, the exposure time, the CCD temperature, and the filter wheel position. The file can contain multiday parameters. When it reaches the preset beginning of observing time and the weather criterion is satisfied, the enclosure is unlocked and opened. The telescope moves to the target star and tracks it. The CCD takes images at the preset rate. At the end of observations, the telescope moves back to the reference position, and the enclosure is closed and locked. If weather conditions change and fail the observing criterion during the observation, the observation will be stopped and the enclosure will be closed immediately. The automatic observing procedure also includes taking dark frames and twilight flat frames before and after observations. The observed images are stored in the hard disk drives and transferred back to the headquarter through the Internet.

3.2. Website. Each station has its own website providing the status and information of the system. Observers can

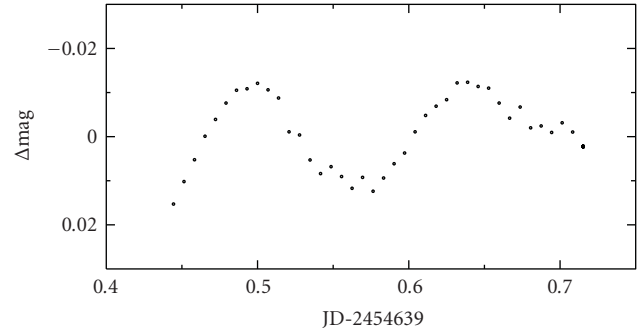


FIGURE 3: Light curves of HD 163032 from data taken on 18 May 2007 at Teide. The exposure time was 560 seconds. No filter was used in this observation. HD 163032 is an A5 star with $m_V = 8$ [10].

monitor the status and obtain information from the website. It includes the life images from all webcams, the history of weather conditions, and the history of UPS status.

4. Scientific Goals and Preliminary Results

The Taiwan Automated Telescope Network will be dedicated to observing stellar pulsations for the study the stellar structure and evolution, although it could be used for other studies that require continuous observations for selected objects. Major information used to study the properties of pulsating stars is the frequency of pulsating modes [4–8]. The advantage of the TAT Network is that it can observe a target star for a long period with high duty cycle. This would increase the S/N and the spectral resolution which would increase accuracy in determining mode frequencies. The long data set provides the opportunity to study temporal variations of mode parameters, such as amplitude, frequency, and line width [6, 9]. The long data set could also be used to search for long-period modes, such as g modes [6]. The data will be available to the community after a certain period.

Although the aperture of the TAT is small, there are still many bright variable stars which could be studied with the TAT. The telescope can measured 10-magnitude stars with an error of about 2-3 mmag with 10-minute exposure. Figure 3 shows an example of the light curve of HD163032 derived from the data taken with the TAT at Teide. It should be mentioned that combining data taken at different sites will be a challenge in data analysis.

Acknowledgment

The authors are supported by NSC of ROC under Grant NSC-96-2112-M-007-034-MY3.

References

- [1] G. Á. Bakos, J. Lázár, I. Papp, P. Sári, and E. M. Green, “System description and first light curves of the Hungarian automated telescope, an autonomous observatory for variability search,” *Publications of the Astronomical Society of the Pacific*, vol. 114, no. 799, pp. 974–987, 2002.

- [2] F. Grundahl, T. Arentoft, J. Christensen-Dalsgaard, S. Frandsen, H. Kjeldsen, and P. K. Rasmussen, “Stellar Oscillations Network Group —SONG,” *Journal of Physics: Conference Series*, vol. 118, no. 1, Article ID 012041, 2008.
- [3] J. Meeus, *Astronomical Algorithms*, Willmann-Bell, Richmond, Va, USA, 2nd edition, 1998.
- [4] C. Aerts, J. Christensen-Dalsgaard, M. Cunha, and D. W. Kurtz, “The current status of asteroseismology,” *Solar Physics*, vol. 251, no. 1-2, pp. 3–20, 2008.
- [5] T. M. Brown and R. L. Gilliland, “Asteroseismology,” *Annual Review of Astronomy and Astrophysics*, vol. 32, no. 1, pp. 37–82, 1994.
- [6] A. Gautschy and H. Saio, “Stellar pulsations across the HR diagram: Part II,” *Annual Review of Astronomy and Astrophysics*, vol. 34, no. 1, pp. 551–606, 1996.
- [7] J. Christensen-Dalsgaard, “Asteroseismology,” *Astrophysics and Space Science*, vol. 261, no. 1–4, pp. 1–12, 1998.
- [8] D. W. Kurtz, “Asteroseismology: from dream to reality,” *Solar Physics*, vol. 220, no. 2, pp. 123–135, 2004.
- [9] P. Moskalik, “Modulation of amplitudes in oscillating stars due to resonant mode coupling,” *Acta Astronomica*, vol. 35, pp. 229–254, 1985.
- [10] ESA, “The Hipparcos and Tycho Catalogues,” ESA SP 1200, ESA, Noordwijk, The Netherlands, 1997.

Research Article

Astrobiology with Robotic Telescopes at CAB

Luis Cuesta, M. Teresa Eibe, Aurora Ullán, Antonio Pérez-Verde, and Jorge Navas

Laboratorio de Astrofísica Estelar y Exoplanetas, Centro de Astrobiología, Torrejón de Ardoz, 28850 Madrid, Spain

Correspondence should be addressed to Luis Cuesta, cuestacl@inta.es

Received 30 June 2009; Accepted 30 October 2009

Academic Editor: Alberto J. Castro-Tirado

Copyright © 2010 Luis Cuesta et al. This is an open access article distributed under the Creative Commons Attribution License, which permits unrestricted use, distribution, and reproduction in any medium, provided the original work is properly cited.

The key objectives of RTRCAB are the identification of new exoplanets and especially the characterization of the known exoplanets by observing photometric and systematic monitoring of their transits. These telescopes, equipped with advanced technology, optimized control programs, and optical and technical characteristics adequate for this purpose, are ideal to make the observations that are required to carry out these programs. The achievement of these goals is ensured by the existence of three separated geographical stations. In this sense, there are several planned missions that have the same objectives among their scientific goals, like *Kepler*, *CoRoT*, *GAIA*, and *PLATO*.

1. Introduction

Robotic telescopes are new tools that are changing many aspects of the way we do astronomy. The use of this type of telescope has been quickly adopted in some of the most prolific fields of this science, including searches for exoplanets, see Figure 1. In this particular field, robotic telescopes have demonstrated an efficiency and agility that would hardly have been obtained with conventional telescopes.

Robotic telescopes are mostly destined to study nearby and brilliant objects but are perfect to support experiments that require constant monitoring of the sky. Also, robotic telescopes are very useful in routine observations that do not require an operator and for which a great amount of data is generated but can be reduced and analyzed automatically.

In addition to the typical scientific uses, robotic telescopes are being used as fundamental pieces in the practical education of astronomy. Numerous institutes and museums have begun to develop their own robotic telescopes to bring astronomy into the classroom, as a way to understand the Universe that surrounds us. By establishing collaborations between institutes in different countries observations can be made in the classroom without a change in school schedules, which has an enormous benefit to the education community.

2. Science with Robotic Telescopes

The study of exoplanets is in the vanguard of the present investigation of astrophysics and is of great interest to the field of astrobiology. The method of transit detection is based on obtaining differential photometry to detect changes in the light curves of stars [1, 2]. For this type of study a great amount of observation time is required.

Robotic telescopes are very useful for discovering new bodies in the Solar System or tracking already discovered objects, in particular near Earth objects (NEOs) [3, 4], see Figure 2. The study of NEOs is fundamental to increasing our understanding of the rates of impacts on planets, something clearly linked to the origin and the evolution of life.

The study of stars similar to the Sun is also important (particularly in terms of astrobiological implications) and has benefited from the use of these telescopes. A study that covers a wide range of star ages and metallicities can provide data that allow us to determine their zones of habitability. Photometric analysis of these stars will connect the microvariability with the chromospheric and magnetic activities of our star.

Systematic observation projects cover an important part of the time of observation with robotic telescopes, such as search for extragalactic supernovae, astrometry of comets and asteroids, variable star, and binary eclipsing photometry.

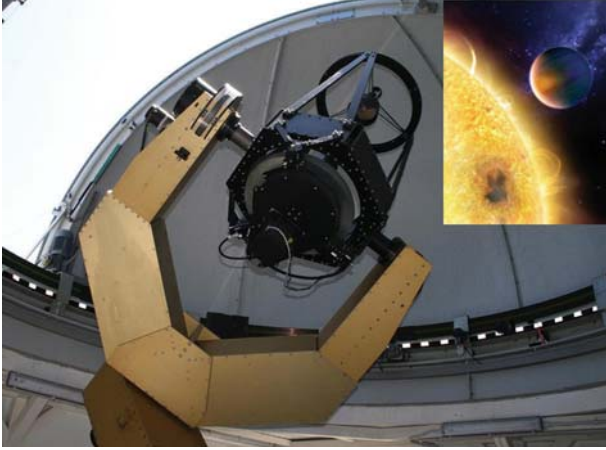


FIGURE 1: Robotic telescopes are one of the best tools for searching exoplanets.

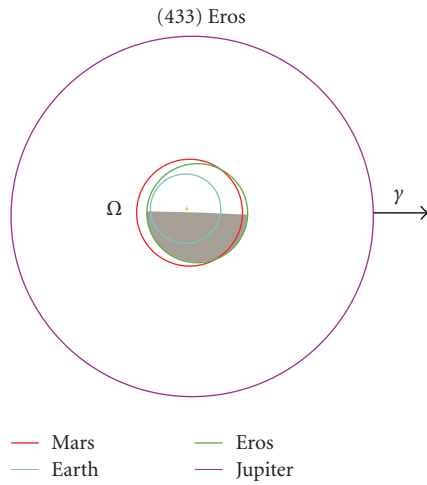


FIGURE 2: Orbit of asteroid Eros.

Also, time is dedicated to targets of opportunity like novae, supernovae, and gamma ray bursts.

3. Exoplanets

Since 1995, when the first exoplanet was discovered by Mayor and Queloz [5, 6], see Figure 3, and Marcy and Butler [7], more than 300 exoplanets (including dozens of multiplanets) have been found. Although a very interesting picture of this rich “zoology” is emerging [8–10], several important questions remain unanswered: what is the diversity of planetary systems, including long periods of planets and exotic systems? What is their dynamical evolution? What are the properties of exoplanets (orbits, masses, and properties of the atmosphere)? What are the frequency and properties of belt planetesimals and what are the implications for the frequency of formation of terrestrial planets, the habitability of planetary systems, and water distribution in the region of the terrestrial planets? How common are planets similar to Earth? These and other questions are of vital importance

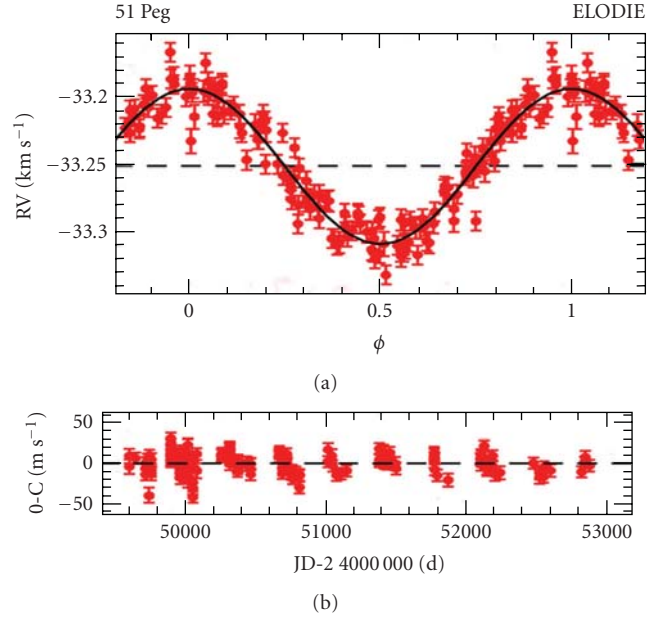


FIGURE 3: Radial velocity curve for 51 Peg where the first exoplanet was detected in 1995 by Mayor and Queloz [5, 6].

from an astrobiological point of view because they can help us to place the evolution of the Solar System and the establishment of basic habitability conditions on at least one of its planets, the Earth, into perspective. This project aims to answer some of these issues by addressing the problem from an observational approach and using this network of robotic telescopes.

During the last two decades there has been an intensive search for exoplanets, and as a result of this effort, there are now more than 300 exoplanets confirmed [11–13], most of them orbiting solar-type stars, with a mass of at least one quarter of the Neptune. Due to bias by instrumental observation techniques (most of the planets have been detected with the radial velocity method, with high-resolution spectrograph in the optical), there is not a census impartial of exoplanets or a full knowledge of their properties. In most cases the exoplanets found are giant and hot, usually found in very early stages of formation, and very close to its star. These properties are closely related to the observational bias introduced by the radial velocity method. The stars with known exoplanets are rich in metals compared to those that do not harbor planets. The number of stars with giant planets around seems to increase with metallicity of the star. For most of the exoplanets found we only know orbital parameters with large errors. Taking advantage of the potential use of the network of robotic telescopes, it is intended to study in depth the parameters of the known exoplanets to follow the curves of light and orbital cycles and phases of maximum and minimum so as to reduce drastically error bars. This will enable us to determine with greater precision the masses, sizes, and distances to the central star of the planets. Thus, we will select in a best approach those that might be within the habitable zone of the star. Also, such an

observation would help to discriminate among the possible causes for the effect of the relationship between metallicity and the presence of planets in a star [14].

From an astrobiological point of view, the study of the atmosphere of exoplanets is of vital importance. The key element is the detection of which can be regarded as traces of the existence of life on earth terms. However, until now, there is not too much work on this topic and the only detections of exoplanet atmospheres have been made from space [15–18]. In the context of this project, we want to use the network of robotic telescopes to identify the presence of such atmospheres. The study is based on a novel analysis of the curves of light during the transit of the exoplanet, see Figure 4. Performing differential photometry during the rapid entry and exit of the transit it is possible to identify the atmosphere through a small change (around 1%) occurred at the beginning and end of the depression in the light curve [19]. The analysis may reveal the presence of the atmosphere that would be subsequently studied in depth with other instruments.

Using the experience of the group in the optical observation and with the extensive existing database, it is expected to cover a substantial number of regions in order to produce a comprehensive census of the characteristics of exoplanets. Depending on the obtained results, we will apply the method of finding exoplanets by its transit to stars with evolutionary stages different of the Sun; for example, M stars or planetary nebulae are ideal candidates for this search. In this last case, the knowledge of their nebular properties, as the inclination or the existence of disks of dust in the nuclear area, provides valuable information to establish in advance the possibility of a transit, if there is an exoplanet, and will help us to interpret much better light curves to establish the properties of the exoplanet.

4. CAB's Robotic Telescopes

The Spanish Instituto Nacional de Técnica Aeroespacial has a network of three telescopes in mainland Spain [20]. The first one is located at some of the best places for astronomy at the Observatorio de Calar Alto in Almería, at an altitude of more than 2100 m, see Figure 5. The second one is near Calatayud in Zaragoza, at the summit of a 1400 m high mountain. The last one is on the campus of the Instituto Nacional de Técnica Aeroespacial (INTA), in Madrid. The three telescopes have a classic Cassegrain configuration, with an aperture of 40–50 cm and motorized and automated equatorial mounts and domes.

Although the Calar Alto Observatory has a high rate of clear nights, the use of three telescopes drastically increases the chances of observation in case of bad weather. Moreover, this way makes possible the simultaneous observation with two telescopes for ultrafast photometry in different filters.

4.1. Mechanics and Optics. The three telescopes, built by Optical Mechanics Inc., are classic Cassegrain telescopes with a parabolic primary and a hyperbolic secondary mirror. The telescopes at Calar Alto and Calatayud both have a diameter

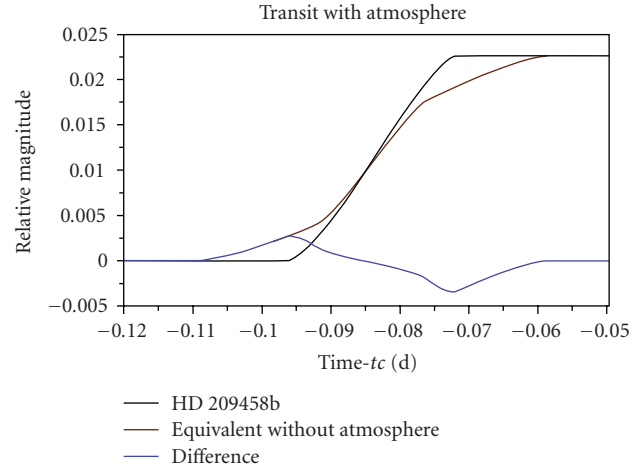


FIGURE 4: Theoretical effect of the presence of an atmosphere in the light curve of an exoplanet transit. The transit was used for HD 209458b, with the slope equivalent to a planet with no atmosphere and the difference between both.



FIGURE 5: Observation station at Calar Alto Observatory. There is an auxiliary building with the wheater station and the control system.

of 50 cm while the third, at INTA, has a diameter of 40 cm. All three telescopes are F/10.

The equatorial fork-mounted system is built from anodized aluminum. Right ascension and declination axes are driven by high-precision zero-lash drive systems. The relative pointing is less than 0.5 arcsecond and the final tracking resolution is less than 0.3 arcsecond using a closed-loop servoactuated system. Nonsidereal rate tracking can be used, see Figure 6.

4.2. Dome. Each telescope is housed in an automatic motorized dome with a window opening from 0° to 90° , see Figure 7. The domes are manufactured by Baader Planetarium.

4.3. Camera. Each telescope is equipped with a 4008×2672 refrigerated CCD Finger Lakes with a pixel size of $9 \mu\text{m}$



FIGURE 6: Complete view of the 0.5 m telescope inside the 3.5 m dome in Calar Alto Observatory.



FIGURE 7: View of the dome for the 0.5 m telescope located in EVA1 El Frasco.

that covers a field of $24' \times 16'$ ($30' \times 20'$ in the case of INTA telescope) with a pixel projection of $0.37''/\text{pix}$, see Figure 8. This is a cooled monochrome interline array manufactured by Kodak (KAI-11002) optimized for speed readout (12 MHz) and a shutter capable of 0.05-second exposures. There is also a filter wheel for each telescope with the typical UBVRI Johnson photometry set, nebula filters (OIII, H α , and H β), and red, green, and blue filters.

4.4. Control System. The LINUX-based control system includes two computers per telescope, one dedicated to telescope control and the other for data analysis. There are some other facilities such as UPS, communications, GPS (for time synchronization), weather station, air conditioning to

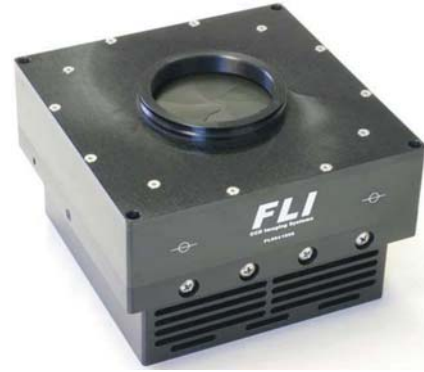


FIGURE 8: CCD Finger Lakes camera installed on the telescopes.

maintain the temperature inside the dome, and remote on-off system.

4.5. Control Programs. To provide complete control over the observatory, some other applications are also available, including sky programs that are used interactively with the telescopes and web cameras to view the status of the telescope and dome remotely.

4.6. Graphical User Interface. The observatories are controlled using the LINUX-based Talon software from Optical Mechanics, Inc. This application controls the entire observatory subsystems including the telescope and all its possible movements, the dome, the filter wheel, the temperature-corrected focus, the weather station, and the CCD camera. There is a separate mode for data acquisition. Talon is operated by a very user friendly graphical user interface, see Figure 9.

4.7. Acquisition of Data. A specific application in Talon is dedicated to the acquisition of data. It controls the important camera settings, including the exposure time, the status of the shutter, the binning factor, subimages, and the temperature. Other tools including photometry, statistics, and a full-width half-maximum (FWHM) calculator are available.

4.8. Operation. There are three operation modes available:

- (i) interactive and onsite, via the console,
- (ii) interactive and remote via a login program,
- (iii) noninteractive and robotic, with automatic preprogrammed tasks.

5. Science with RTRCAB

The main objective of this network is to detect new exoplanets, and especially to characterize the known exoplanets by observing photometric and systematic monitoring of their transits. The telescopes, equipped with advanced technology, optimized control programs, and optical and

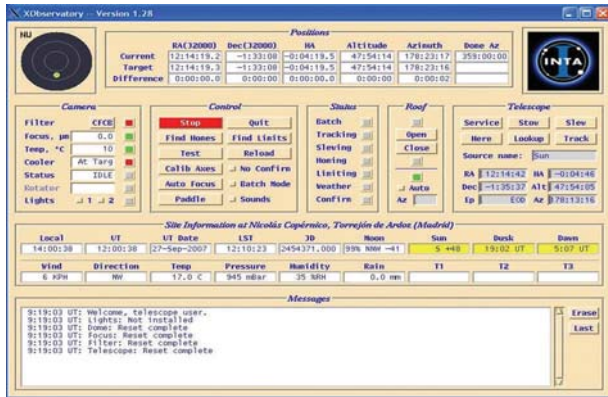


FIGURE 9: Talon graphical user interface for telescope control.

technical characteristics adequate for this purpose, are ideal to make the observations that are required to carry out these programs [21]. The achievement of these goals is ensured by the existence of three separated geographical stations.

But even if the first priority is the detection of exoplanets, a significant fraction of observing time will be available for other scientific projects of interest, objects relatively bright and variable, like Solar System objects, brown dwarfs, variable stars, planetary nebulae, and compact objects in binary systems.

5.1. Characterizing Exoplanets by the Transit Method. The idea of the depth of the project is the scientific exploitation of the RTRCAB from an astrobiological perspective. From this point of view, the detection of new exoplanets is the goal. The working method is to use the RTRCAB for monitoring beforehand selected stars by fast optical photometry. Usually we will work to obtain observational confirmation of the candidates from exoplanet hunter projects such as TrES or SuperWASP. However, we also work over our own select sky fields to find exoplanets. A previous work of selection may be done to know where to look for, the first stage with solar type stars and after that with M type stars or Planetary Nebulae.

Nearly continuous periods observing selected star are needed to try to find some changes in the light from the star. Comparison of photometry data from one night to another will be done to look for the slight variations that could indicate a possible transit. After that, the candidates will be reobserved to confirm results.

But not only is the search for exoplanets important but also the characterization is a goal. In this sense, we will develop a reliable database of parameters for exoplanets. The working method is similar to the previous goal. In this case we will observe stars with known transit exoplanets to obtain a light curve from which information about its parameters may be extracted. The repeated observation of these transits will substantially reduce the error bars and will provide a data set with accuracy so that they can be collated, thus allowing to draw conclusions about the nature of exoplanets and its formation conditions. Previously, we will select the exoplanets with more favorable conditions to be observed

during their transits according to the characteristics of the telescopes: large size, low stellar temperature, low magnitude, and long transit. In this way we will restrict the sample to a particular group of exoplanets, which makes more sense to compare their parameters for their homogeneity.

Finally, the detection of the atmosphere in exoplanets is between our objectives. We will use again fast optical photometry during the transits of exoplanets to detect signs of its atmosphere by slight changes in the slope of entry and exit. Once the atmosphere is detected, we will develop geometric models to infer information about the atmosphere as size, opacity, and composition. We will also select those exoplanets with more favorable conditions for its atmosphere to be detected.

6. Conclusions

The RTRCAB (Red de Telescopios Robóticos del Centro de Astrobiología, Network of Robotic Telescopes at CAB) has three observation stations located in different sites of Spain: campus of INTA, in Torrejón de Ardoz (Madrid), Calar Alto Observatory (Almería), and in EVA1 in El Frasno, near Calatayud (Zaragoza). The network is designed for its use in scientific areas relevant to Astrobiology and, in turn, will support outreach programs and science education.

References

- [1] D. Charbonneau, T. M. Brown, D. W. Latham, and M. Mayor, "Detection of planetary transits across a sun-like star," *The Astrophysical Journal*, vol. 529, no. 1, part 2, pp. L45–L48, 2000.
- [2] M. Konacki, G. Torres, S. Jha, and D. D. Sasselov, "An extrasolar planet that transits the disk of its parent star," *Nature*, vol. 421, no. 6922, pp. 507–509, 2003.
- [3] D. I. Steel and B. G. Marsden, "Astrometry of near-Earth objects using small telescopes," *Earth, Moon and Planets*, vol. 74, no. 2, pp. 85–92, 1996.
- [4] P. R. Holvorcem, M. Schwartz, C. W. Juels, et al., "Astrometry of near-earth asteroids using remotely-operated robotic telescopes," in *Astronomy in Latin America, 2nd Meeting on Astrometry in Latin America and 3rd Brazilian Meeting on Fundamental Astronomy, held on September 2002*, R. Teixeira, N. V. Leister, V. A. F. Martin, and P. Benevides-Soares, Eds., vol. 1 of *ADeLA Publications Series*, pp. 91–100, 2003.
- [5] M. Mayor and D. Queloz, "A search for substellar companions to solar-type stars via precise Doppler measurements: a first Jupiter mass companion detected," in *Proceedings of the 9th Cambridge Workshop on Cool Stars, Stellar Systems and the Sun*, vol. 109 of *ASP Conference Series*, pp. 35–38, 1996.
- [6] M. Mayor and D. Queloz, "A Jupiter-mass companion to a solar-type star," *Nature*, vol. 378, no. 6555, pp. 355–359, 1995.
- [7] G. W. Marcy and R. P. Butler, "A planetary companion to 70 virginis," *The Astrophysical Journal*, vol. 464, no. 2, part 2, pp. L147–L151, 1996.
- [8] D. Charbonneau, T. M. Brown, R. W. Noyes, and R. L. Gilliland, "Detection of an extrasolar planet atmosphere," *The Astrophysical Journal*, vol. 568, no. 1, pp. 377–384, 2002.
- [9] R. Alonso, M. Barbieri, M. Rabus, H. J. Deeg, J. A. Belmonte, and J. M. Almenara, "Limits to the planet candidate GJ 436c," *Astronomy and Astrophysics*, vol. 487, no. 1, pp. L5–L8, 2008.

- [10] G. Basri, “Extrasolar planets: too close for comfort,” *Nature*, vol. 430, no. 6995, pp. 24–25, 2004.
- [11] R. Alonso, T. M. Brown, G. Torres, et al., “TrES-1: the transiting planet of a bright K0 V star,” *The Astrophysical Journal*, vol. 613, no. 2, part 2, pp. L153–L156, 2004.
- [12] D. Pollacco, I. Skillen, A. Collier Cameron, et al., “WASP-3b: a strongly irradiated transiting gas-giant planet,” *Monthly Notices of the Royal Astronomical Society*, vol. 385, no. 3, pp. 1576–1584, 2008.
- [13] C. Moutou, H. Bruntt, T. Guillot, et al., “Transiting exoplanets from the CoRoT space mission: V. CoRoT-Exo-4b: stellar and planetary parameters,” *Astronomy and Astrophysics*, vol. 488, no. 2, pp. L47–L50, 2008.
- [14] G. Israelian, N. C. Santos, M. Mayor, and R. Rebolo, “Evidence for planet engulfment by the star HD82943,” *Nature*, vol. 411, no. 6834, pp. 163–166, 2001.
- [15] A. Ecuivillon, G. Israelian, N. C. Santos, N. G. Shchukina, M. Mayor, and R. Rebolo, “Oxygen abundances in planet-harbouring stars: comparison of different abundance indicators,” *Astronomy and Astrophysics*, vol. 445, no. 2, pp. 633–645, 2006.
- [16] C. J. Grillmair, A. Burrows, D. Charbonneau, et al., “Strong water absorption in the dayside emission spectrum of the planet HD 189733b,” *Nature*, vol. 456, no. 7223, pp. 767–769, 2008.
- [17] A. Vidal-Madjar, A. Lecaveller des Etangs, J.-M. Désert, et al., “An extended upper atmosphere around the extrasolar planet HD209458b,” *Nature*, vol. 422, no. 6928, pp. 143–146, 2003.
- [18] A. Vidal-Madjar, J.-M. Désert, A. Lecavelier Des Etangs, et al., “Detection of oxygen and carbon in the hydrodynamically escaping atmosphere of the extrasolar planet HD 209458B,” *The Astrophysical Journal*, vol. 604, no. 1, part 2, pp. L69–L72, 2004.
- [19] L. Cuesta, “A la búsqueda de exoplanetas,” in *Proceedings of the 8th Scientific Meeting of the Spanish Astronomical Society, Highlights of Spanish Astrophysics V*, J. Gorgas, L. J. Goicoechea, J. I. González-Serrano, and J. M. Diego, Eds., in press.
- [20] L. Cuesta, “Robotic telescopes and their use as an educational tool,” in *Proceedings of Communicating Astronomy with the Public*, L. L. Christensen, M. Zoulais, and I. Robson, Eds., pp. 396–398, Athens, Greece, October 2007.
- [21] L. Cuesta, “The network of INTA telescopes,” in *Proceedings of Communicating Astronomy with the Public*, L. L. Christensen, M. Zoulais, and I. Robson, Eds., pp. 400–402, Athens, Greece, October 2007.

Research Article

A Path to the Stars: The Evolution of the Species

Fabrizio Vitali,¹ Guido Chincarini,^{2,3} Mario Zannoni,² Stefano Covino,³ Emilio Molinari,^{3,4} Stefano Benetti,⁵ Carlotta Bonoli,⁵ Favio Bortoletto,⁵ Enrico Cascone,⁶ Rosario Cosentino,⁴ Francesco D'Alessio,¹ Paolo D'Avanzo,^{2,3} Vincenzo De Caprio,³ Massimo Della Valle,^{6,7} Alberto Fernandez-Soto,⁸ Dino Fugazza,³ Enrico Giro,⁵ Demetrio Magrin,⁵ Giuseppe Malaspina,³ Lech Mankiewicz,⁹ Raffaella Margutti,² Ruben Mazzoleni,³ Luciano Nicastro,¹⁰ Alberto Riva,¹¹ Marco Riva,¹² Ruben Salvaterra,² Paolo Spanò,³ Monica Sperandio,³ Mauro Stefanon,⁸ Gino Tosti,¹³ and Vincenzo Testa¹

¹Istituto Nazionale di Astrofisica, Osservatorio Astronomico di Roma, Via Frascati, 33, Monte Porzio Catone, 00040 Roma, Italy

²Dipartimento di Fisica G. Occhialini, Università degli Studi di Milano - Bicocca, Piazza della Scienza 3, 20126 Milano, Italy

³Istituto Nazionale di Astrofisica, Osservatorio Astronomico di Brera, via Bianchi 46, 23807 Merate, Italy

⁴Istituto Nazionale di Astrofisica, Telescopio Nazionale Galileo, Rambla José Ana Fernández Pérez, 7, 38712 Breña Baja, Spain

⁵Istituto Nazionale di Astrofisica, Osservatorio Astronomico di Padova, Vicolo dell'Osservatorio, 5, 35122 Padova, Italy

⁶Istituto Nazionale di Astrofisica, Osservatorio Astronomico di Capodimonte, Salita Moiariello, 16, 80131 Napoli, Italy

⁷European Southern Observatory, Karl-Schwarzschild-Strasse 2, 85748 Garching bei München, Germany

⁸Instituto de Física de Cantabria (CSIC-UC), Edificio Juan Jorda, Av. de los Castros s/n, 39005 Santander, Spain

⁹Center for Theoretical Physics of Polish Academy of Science, Al. Lotnikow 32/46, 02-668 Warsaw, Poland

¹⁰Istituto Nazionale di Astrofisica, IASF Bologna, via Gobetti 101, 40129 Bologna, Italy

¹¹Istituto Nazionale di Astrofisica, Osservatorio Astronomico di Torino, Via Osservatorio, 20, 10025 Pino Torinese, Italy

¹²Dipartimento Ingegneria Aerospaziale, Politecnico Milano, Via La Masa, 34, 20156 Milano, Italy

¹³Dipartimento di Fisica, Facoltà di Scienze MM. FF. NN., Università degli Studi di Perugia, via A. Pascoli, 06123 Perugia, Italy

Correspondence should be addressed to Fabrizio Vitali, vitali@oa-roma.inaf.it

Received 30 June 2009; Accepted 12 January 2010

Academic Editor: Joshua S. Bloom

Copyright © 2010 Fabrizio Vitali et al. This is an open access article distributed under the Creative Commons Attribution License, which permits unrestricted use, distribution, and reproduction in any medium, provided the original work is properly cited.

During the last years, a number of telescopes have been dedicated to the followup of the GRBs. But after the Swift launch, the average observed intensity of the GRBs showed to be lower than thought before. Our experience with the robotic 60 cm REM telescope confirmed this evidence, with a large number of *lost* GRBs. Then, we proposed to study the feasibility of a 4 m fast pointing class telescope, equipped with a multichannel imagers, from Visible to Near Infrared. In this paper, we present the main result of the feasibility study we performed so far.

1. Introduction

Since the discovery of a dynamic Universe on time scales of hours and seconds it became of paramount importance to have a high sampling frequency of the data. The new epoch started in the late fifties, early sixties with the discovery of short periods in cataclysmic variables. Later on were discovered the X-ray and Gamma-ray radiation very likely due to emissions related to the presence of degenerate matter. Accretion on neutron stars and black holes generate also signals of

very short duration, milliseconds and some time even less, randomly distributed in space and time. These bursts of light made it mandatory to have fast response detectors and fast moving telescopes to detect the event during birth and subsequent rapid evolution: astronomers need large apertures and very efficient instruments to detect the faintest signals and large and efficient telescopes reacting immediately to any alert. In 2003, in the frame of the SWIFT project (that does not provide any coverage in the infrared domain), our group designed and realized the 60 cm robotic visible-infrared

telescope REM, installed in the La Silla mountain, hosted by the ESO facility. Even if the telescope showed to be a very nice robotic machine and gave excellent scientific results, it resulted too small for the weak burst of light coming from the depth of the Universe. Then, we decided to exploit the very positive experience made with REM. We present here the feasibility study of a robotic 4 m class telescope able to point and track everywhere in the visible sky in 30–50 s, equipped with multichannel VIS and NIR imagers, allowing simultaneous observations from 0.4 to 2.5 μm , and visible spectrometer and polarimeter ancillary instruments.

2. The REM Experience

REM is a 60 cm robotic telescope, that has been operating on the La Silla mountain (Chile) since 2003, equipped with a visible imager and spectrometer (ROSS) and a NIR imaging camera (REMIR) [1]. During these years, REM acted as a fruitful laboratory, in which we could operate and learn how to control and manage a remote and automatic telescope: the average response time of the REM telescope to a satellite trigger is ~ 30 s, simultaneous Visible and NIR images can be obtained and all the frames (scientific and technical), all the telescope and instruments parameters are delivered to a database server, which can be queried remotely.

Despite of its small dimensions, REM delivered (and it is still delivering) high quality scientific results, as witnessed, that is, by the two GRBs 060418 and 060607A (see Figure 1), from which a value of the Lorenz factor $\Gamma \approx 400(\eta_{0.2}n_0)^{-1/8}$ has been derived [2].

3. Not Simply a Larger REM

The precious REM experience, allowed us to think about a larger telescope, able to replicate the same performances in terms of fastness and reliability. Then, we asked and received funds from the Italian Research Ministry and Istituto Nazionale di Astrofisica for CODEVISIR (Conceptual Design for a VISible and nIR telescope), a feasibility study to build and operate a fully robotic 4 m class telescope, equipped with VIS and NIR instruments, able to react to a satellite trigger in less than 50 s (with a goal of 30 s). We also applied to the ERC FP7 Call for Ideas on Research, Technological Development and Demonstration—Advanced Grant, for PATHOS (PATH to the Stars).

Taking into account of new scientific hints, we decided to change the instrumental configuration with respect to REM, passing to a multichannel approach. Then, the new instruments will be able to collect simultaneous images in the visible g, r, i, z and NIR J, H and K filters. As for REM, the primary science driver is the follow-up of the GRBs, with the main goal to record the early ($t - t_0 < 50$ s) phase light curve with high temporal resolution and simultaneous multiband imaging, to allow the derivation of the GRB spectral energy distributions and Photo- z , even for high redshift GRBs: as the *naked eye* GRB 080319B has shown [3], micro-variability (sub sec time-scale) during afterglow prompt, that is, in the first tens of seconds, can be a powerful diagnostic tools of

TABLE 1: Configurations.

Alt-Az	Alt-Alt
(i) Blind zenith	(i) Low horizon blind angle
(ii) Unbalanced azimuth motion	(ii) Equilibration on both alt-motions
(iii) Off the shelf	(iii) To be developed

the physical conditions in the emitting region. Moreover, spectroscopy and polarimetry should be performed for the more brilliant GRBs.

When not observing GRBs, the telescope will be devoted to ancillary science programs, spanning from Supernovae to X-Ray Binaries, from Active Galactic Nuclei to Stellar Evolution and Star Formation.

4. The Challenge of the Telescope

The first issue to solve is to build a fast-moving, fully robotic, 4 m class telescope, for which the main requirements are

- (i) pointing rapidity TOO: Required $60^\circ/50$ s, Goal $60^\circ/30$ s;
- (ii) pointing Accuracy: 2-3 arcsec;
- (iii) tracking error: 0.2 arcsec/10 min;
- (iv) minimum Corrected Field of view (FOV): $15'$;
- (v) max PSF degradation on axis: 0.3 arcsec (Active optics, damping and vibration suppression);
- (vi) movements Ranges: Azimuth: $\pm 270^\circ$, Alt: $\pm 90^\circ$, Derotator: 360° .

4.1. Telescope Configuration. We firstly analyzed the best telescope mounting configuration between a classic Alt-z and a less common Alt-Alt (Figure 2). Both configurations have their pros and cons (see Table 1.)

The analysis has shown that the blind zone is not a concern, then, at the moment, we plan to adopt the classical Alt-Az mounting, that has also considerable less costs in term of developing.

4.2. Instrument Location (Nasmyth). We studied also the influence of the instrument location on the overall telescope movements (Figure 3). In Table 2, a comparative study is reported. Currently, our interest is in the Cassegrain configuration, because of the reduced momenta of inertia and minor unbalanced factor.

4.3. The Optical Design. The basic telescope design is based on a classical Ritchey-Chretien, with a $F/10$ equivalent focal ratio (Figure 4). Primary focal ratio is relatively fast, being $F/1.5$, to keep the telescope structure very compact, minimizing moments and overall mass. The unusual location of the focal plane, a bent Cassegrain below the primary mirror, has been selected to allow placement of the dichroic train before the focal plane itself. The flat M3 mirror can rotate, to feed different focal stations.

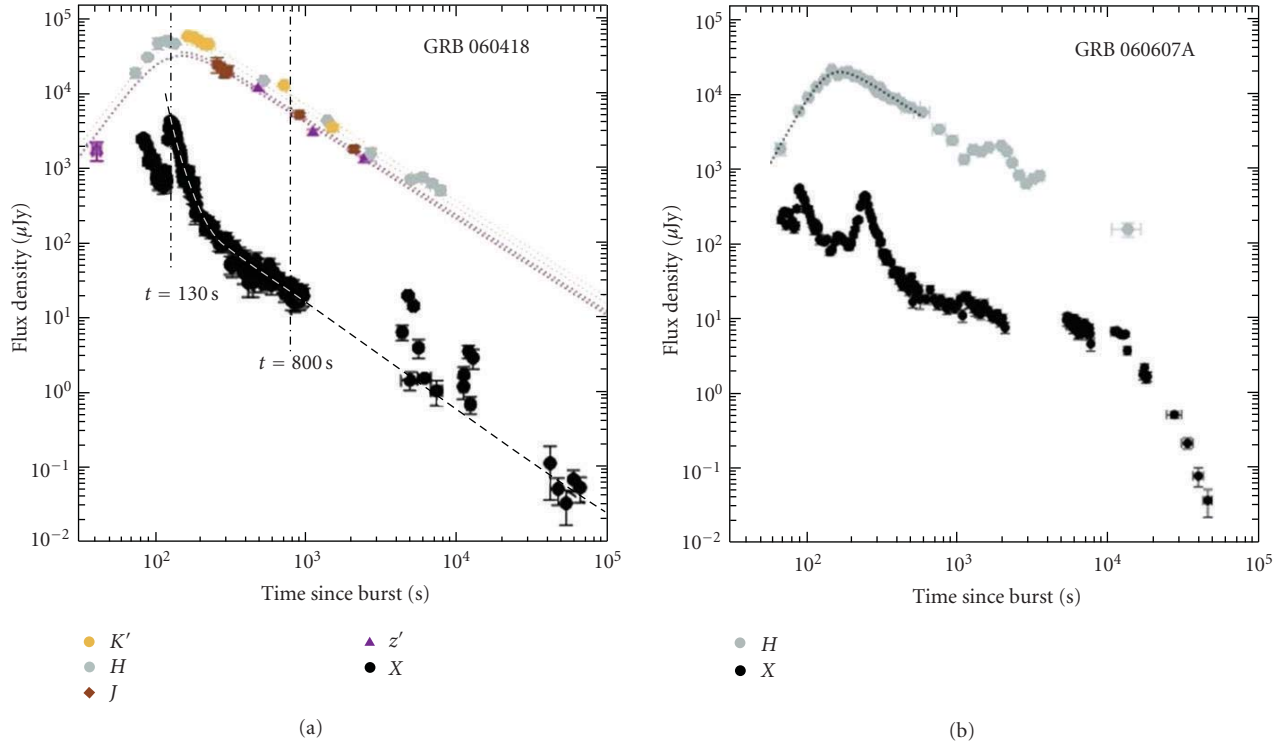


FIGURE 1: NIR and X-ray light curves for GRB 060418 and GRB 060607A.

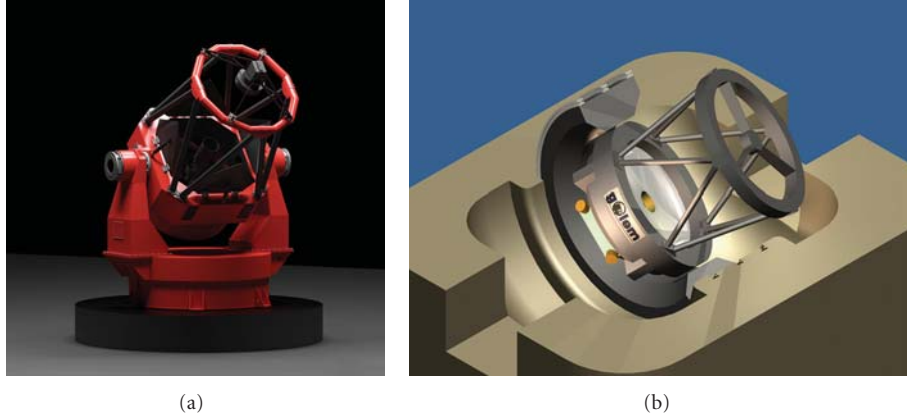


FIGURE 2: The Alt-Az (courtesy by Peter Aniol, Astelco) and Alt-Alt telescope configurations.

TABLE 2: A comparison between the two available foci, Nasmyth and Cassegrain.

Nasmyth		Cassegrain	
M3 between M1 and M2		No M3 and mountings between M1 and M2	
Higher moments of inertia		M1 & Instrs' reduced moments of inertia	
Only two (probably one) derotation		Required a further derotation	
Mass (El stru. + Instr.): 69823 Kg		Mass (El stru. + Instr.) M: 60127 Kg	
Elevation 0°	Izz: 174000 Kgm ² (Az) Ixx: 229000 Kgm ² (Alt)	Elevation 0°	Izz: 128000 Kgm ² (Az) Ixx: 161000 Kgm ² (Alt)
Elevation 90°	Izz: 258000 Kgm ² (Az) Ixx: 229000 Kgm ² (Alt)	Elevation 90°	Izz: 160000 Kgm ² (Az) Ixx: 161000 Kgm ² (Alt)
Unbalance Factor (Az 0°/90°): 1,48		Unbalance Factor Izz (0°/90°): 1,25	

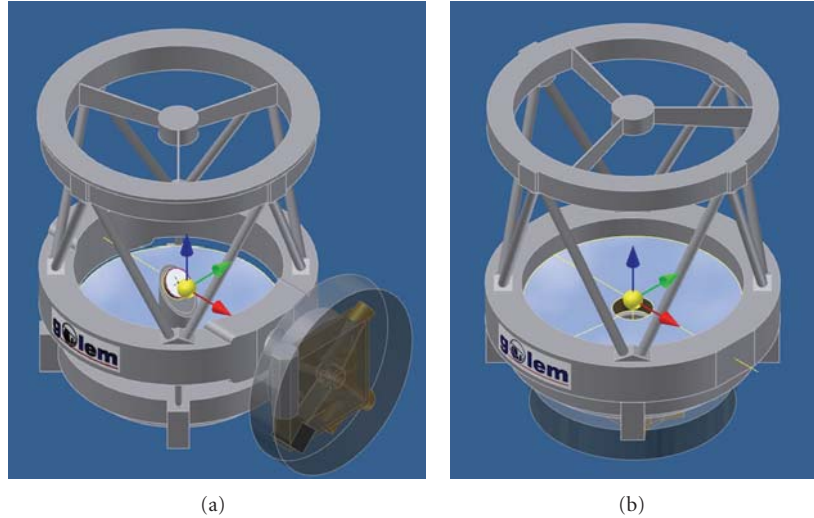


FIGURE 3: The two Nasmyth (a) and Cassegrain (b) Instrument Location.

5. The Instrumentation Suite

Pathos will be equipped with an instrumentation suite able to cover the wavelength range from the Visible (VIS, 400 nm–900 nm) to the Near Infrared (NIR, 1.00–2.5 μm) during the same exposure. This will be allowed by a multichannel imaging configuration, that envisages a detector for each photometric band, delivered through a dichroic cascade along the optical path. The availability of large format arrays, both in the visible and in the infrared wavelength range allows a large flexibility in the optical design, that will ensure a Corrected Field of View of about 10 arcmin for both cameras.

Two ancillary instruments will complete the instrumentation suite, a visible spectrograph and a photopolarimeter, fed by rotating the M3 mirror.

The instrument set up has been thought by integrating optical and mechanical requirements. The mechanical design will be driven mainly by four main requirements:

- (i) extreme light weighting of the structure (the fast pointing nature of the telescope),
- (ii) weight distribution (same reason as above),
- (iii) automation requirement,
- (iv) reliability.

Some complementary items must also be taken into account:

- (i) thermal stabilization,
- (ii) maintenance.

The light weighting is the predominant aspect that will be investigated, both for reducing the overall mass (centrifugal and earthquake passive induced accelerations) and for reducing the thermal inertia of the overall system.

The weight distribution is very critical because of the telescope fast motion requirement. An unbalanced system will induce undesired passive flexions and torsions to the rotating bearings and must be avoided. The best solution is to balance the system just with the payload, (i.e., design of the optical system, location of the nonstructural masses like electronic racks and cables).

The telescope will be remote-managed, that means that all the possible failures must be avoided via proper solutions/redundancy. This implies also an optimization of the maintainability items like handling, accessibility, minimizing of servo-systems, because the absence of the dedicated personnel impose high repairing costs.

The instruments carousel will be organized into 3 systems:

- (1) Multi Color Camera (MCC), VIS camera (g, r, i , and z bands) plus NIR camera (J, H and K),
- (2) Spectrograph (SPEC),
- (3) Fast PhotoPolarimeter (FPP).

The MCC will be continuously fed by the telescope beam (see Figure 5), whereas SPEC and FPP will be selected by properly moving the M3 mirror.

The main idea that is driving the MCC is the simultaneous acquisition. This can be done by considering a single detector for each band (g, r, i, z, J, H and K , see below for a more detailed description). The infrared part of the instrument will be hosted in a cryogenic environment, to avoid the thermal background and to minimize the level of the detectors dark current.

The optical designs of the visible and infrared arms of the MCC are identical, thus allowing a modular design for the opto-mechanical supports and significantly reducing the design-manufacturing costs.

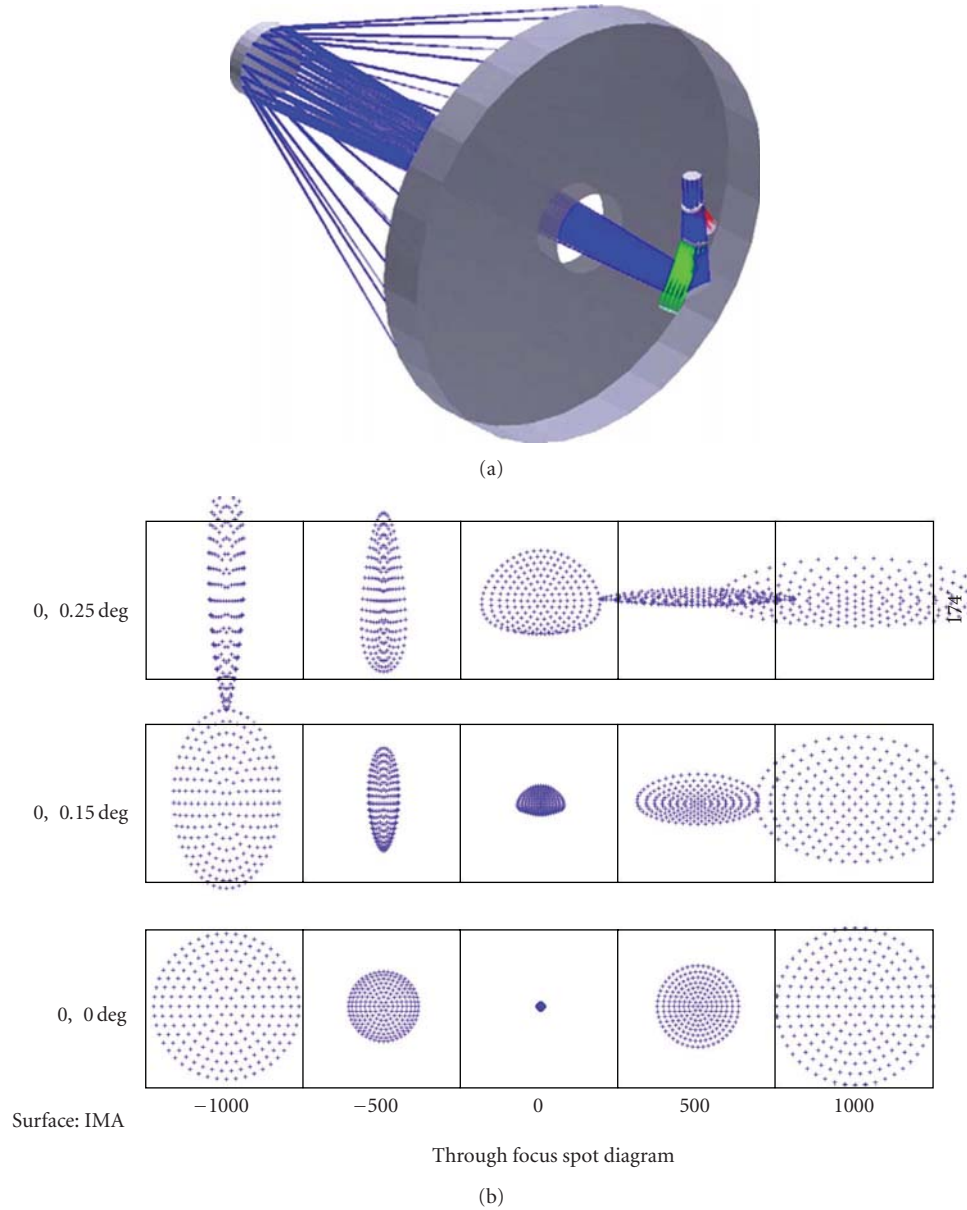


FIGURE 4: The optical scheme of the telescope and the relative spot diagram.

5.1. Mechanics. During the conceptual study, different configurations in terms of main structure and subsystem locations have been analyzed to optimize weight and balancing.

The basic solution (see Figure 6) could be a unique hexagonal bench, where all the active (optical payload) and passive (electronics, calibration units, cryogenics) subsystems are mounted. The main structure rely on a monolithic optical bench, reinforced through radial and hexagonal ribs; the structure is closed up by the derotator connection flange which gives the proper continuity to the structure closing the cell, thus enhancing the overall stiffness. Each subsystem will be connected directly to the main bench, then the design and manufacturing of this structure should pay attention to the overall geometrical tolerances. The overall weight obtained from a 1st order dimensioning of this type of structure, in

aluminum, is about 715 Kg. This instrument set up has the evident advantage of the high accessibility to all subsystems and in addition the space behind M3 is let free and can be used for eventual future add-ons.

Another possible solutions are oriented to minimizing the unbalancing of the overall structure, considering a slightly more compact configuration or a different location of the NIR camera (Figure 7). In this latter case, the NIR subsystem is mounted on a proper truss fixed to the bench; in order to balance the system it is mounted aligned to the main axis of the telescope. The optical beam is directed into the cryogenic system through two pick off mirrors. The other subsystems are mounted on a bench similar to the previous one (hexagonal optical bench with ribs and the closing derotator connection flange).

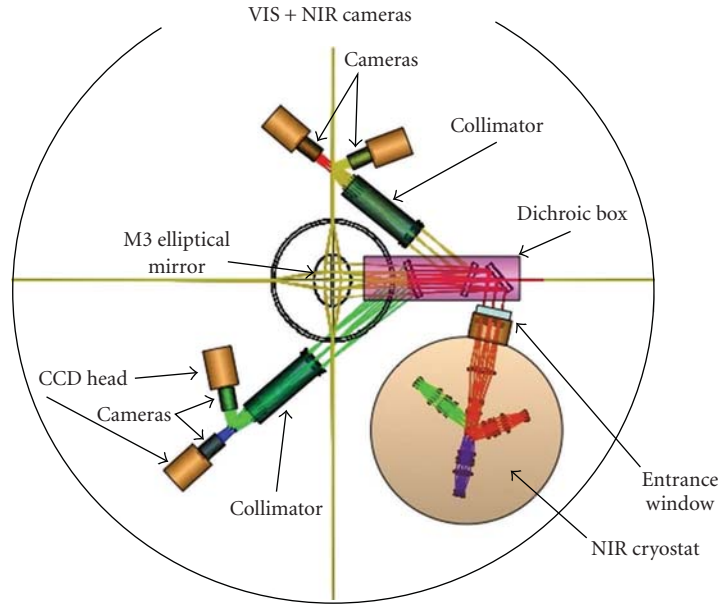


FIGURE 5: The optical scheme of the Pathos focal plane, with the VIS and NIR cameras.

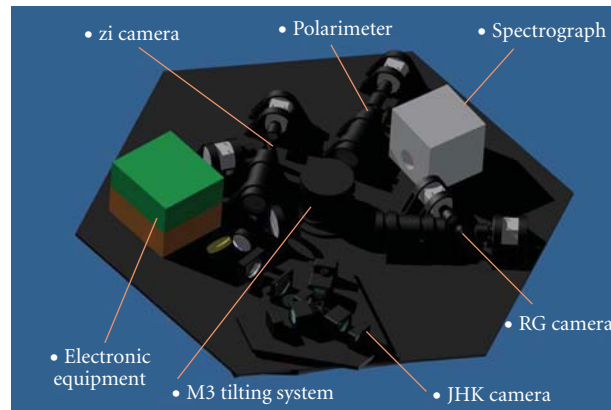


FIGURE 6: The mounting scheme of the Instrumentation at the Cassegrain Focal Plane of Pathos.

This configuration allows a significant reduction of the thickness of both the benches and the ribs. The unbalancing is significant less and can be further optimized by the properly positioning of the electronic systems. The overall weight obtained from a 1st order dimensioning of this type of structure, in aluminum, is about 642 Kg. Nevertheless, in this case the accessibility is reduced in particular for the M3 servo system and for all the components, which are under the truss.

5.2. R&D Composite Material. During this case, it has been investigated also the possible gain deriving from the use of advanced materials like Carbon Fiber Reinforced Panels. The results are interesting and will possible drive the following design following also this opportunity. As an example the second configuration made with typical Carbon Fiber Reinforced Plastic will weight around 550 Kg (-14%) while if

one takes into account an Ultra High Modulus Carbon Fiber Reinforced Plastics it is possible to reach 500 Kg (-20%).

5.3. Optical Design

5.3.1. The Multi Color Camera (MCC). To allow a simultaneous observation of the scientific target, the MCC configuration will envisage four visible arms, covering the Sloan g, r, i and z bands, and three near infrared arms for the J, H and K bands, simultaneously imaged through a dichroics cascade, as shown in Figure 8.

The lens coating, the dichroics and the filters have to ensure the best overall efficiency, then particular care should be taken in the response curve definition and in the prototyping of the most challenging part, as the two main and larger dichroics.

The MCC will be directly linked to an optical bench at the rear of the telescope, to ensure stiffness and alignment during

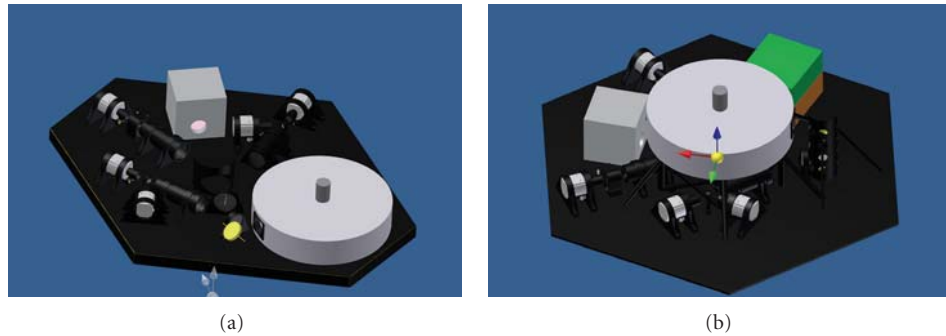


FIGURE 7: The other different Focal Plane Instrument Configurations.

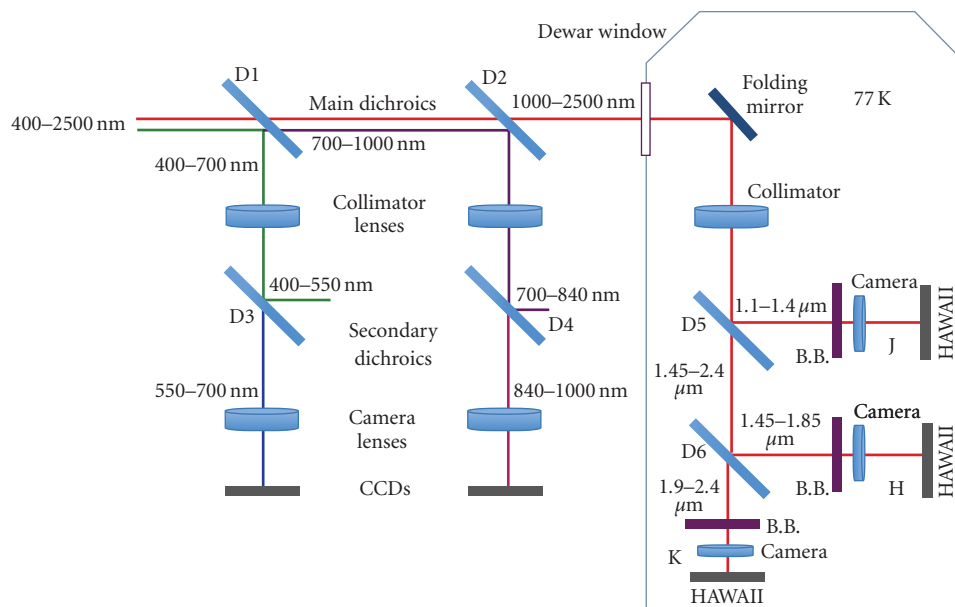


FIGURE 8: The dichroics cascade, feeding the VIS and NIr cameras.

the telescope movements. The configuration of the different parts of the instrument should be optimized also to ensure the best access to the instrumentation for maintenance.

5.3.2. *MCC-VIS*. The VIS cameras will be devoted to the simultaneous observation of the same field of view at four different bands. At least three different dichroics are needed to split wavelengths. They can be put both at a convergent (or divergent) beam, or in a collimated beam. Requirements onto field of view and pixel scale ask for focal reducer system. The large field of view cannot be achieved through classical corrector lenses just in front of the telescope focal plane, so a collimator-camera system is the only choice. Then, some of the dichroics can be put within the focal reduce elements in order to reduce its size and complexity, gaining in space envelope for the overall instrument suite at the same time. So we chose to put a dichroic (D1) in the convergent beam coming from the telescope secondary mirror, and making the second wavelength split in collimated beam (D3 and D4). The other large dichroic D2 is used to split VIS and

NIR light, feeding the NIR cameras. The minimum pixel scale to give good seeing sampling should be large than 3 pixel/arcsec. To cover a 10×10 arcmin onto a $2\text{ K} \times 2\text{ K}$ CCD detector area, the best compromise can be reached with a 3.4 pixel/arcsec plate scale. Because the telescope focal ratio is about $F/10$, an $F/10$ – $F/3.5$ focal reducer is needed. Lens solution classes will give the best performances in term of efficiency, cost and image quality, within a limited space envelope, in order to cope with many arms within the same optical bench assembly. A possible optical design has been done, meeting all those requirements. Only spherical lenses, with maximum diameter of 150 mm, have been adopted, in order to keep overall cost and manufacturing time low. The layout below shows rays crossing all the elements, starting from the telescope focal plane up to the CCD detector plane. Dichroics and filters will be placed near the image pupil of the telescope (in the middle). All the optical train is 70 cm long, and the collimated beam have a 40 mm diameter (Figure 9). This same design will perform very well at all visible (400–1000 nm) wavelengths. This means that

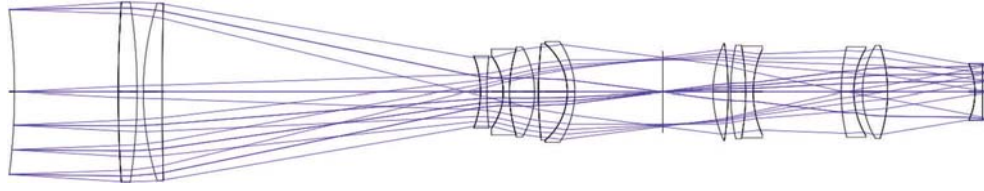


FIGURE 9: The basic optical scheme for the VIS cameras.

multiple arms can be built with just two identical collimators and four identical cameras, decreasing cost and alignment quite a lot.

5.3.3. MCC-NIR. Following the same ideas developed for the VIS channels, NIR wavelengths are split via two dichroics, placed into a collimated beam. A NIR optimized collimator camera system will match the telescope focal ratio to the NIR detector pixel size. Special infrared glasses will be used, to optimize both transmission and image quality. First collimator lens can be used also as cryostat window, reducing the number of air-glass interfaces. In this case, first collimator window will be warm, while all following components will be cooled to 77 K to reduce thermal background, especially in the *K* band. Also dichroics will be optimized to work at low temperatures. To better define spectral bands (JHK), also multilayer filters will be used. A camera prototype will be set up to understand if we need a cryogenic focusing system onto each channel, to improve image quality. This can be possibly realized with a moving lens into the camera assembly, or at the detector level. A proper trade off will be done to make a decision. The *K*-band channel will suffer from thermal emission, then a dithering system will be added, to reduce this effect. A possible solution is to add a folding mirror into the camera assembly that can be moved with cryo motors.

5.4. Ancillary Instruments

5.4.1. Spectrograph. The spectrograph has been designed with the following parameters:

- (i) $R = 800$,
- (ii) CCD: $1\text{ K} \times 1\text{ K}$, 13 μm pixel, BI DD (e.g., Princeton Pixis),
- (iii) Slit: $1\text{ arcsec} \times 4\text{ arcmin}$,
- (iv) Sampling: 4.4 pixel (spectrally), 4.0 pixel/'' (spatially),
- (v) Coverave: 3700–9200 Angstrom (in three exposures),
- (vi) Efficiency: 45% (peak, from entrance slit to detector, including DQE),
- (vii) Movable functions: grating, maybe focus (camera/collimator).

In Figure 10 the optical scheme of the spectrograph and the relative spot diagram are shown. As you can see, the dimension of the spectrograph are relatively small (about 30 cm) and the only movable part is the grating, mounted onto a rotating stage.

5.4.2. PhotoPolarimeter. The polarimeter designed for the CODEVISIR telescope has the following main parameters:

- (i) a field around $4' \times 4'$,
- (ii) a wavelength coverage in the visible band (between 400 and 800 nm),
- (iii) four channels relative to the four Stokes parameters.

Basic scheme of the polarimeter is the classical “collimator/camera” system.

The incoming beam is collimated through lenses. The collimated beam is split into four beams through a combination of Wollaston prisms. This combination takes the name of WeDoWo (WEEdged DOuble WOLLaston) [4]. Following the behavior of the imaging instrument, the aim of WeDoWo is the simultaneous production of four different beams, each one containing the information of one of the Stokes polarization vector parameters (Figure 11).

Each beam is then focused through a camera into the detector. The main possibility is to drive all the four beams into the same detector.

Deeper study arises from the filtering option, where the possibility to cover all the visible spectrum and part of the very near infrared becomes interesting. A filter wheel will be placed in the parallel beam, with at least three positions (standard UBV filters) and an empty slot for white-light observation mode.

One of the auxiliary tasks of the polarimeter can be the guiding system. Indeed, recombining the four channels there will be the possibility to have an immediate field monitor. In principle, due to the small probability of an high polarized guide star, there is the possibility to acquire in real time only one of the four channels, depending on the speed requirements.

5.5. Cryogenics. Differently from visible CCD detectors where only the internally generated dark current must be limited by active cooling, IR detectors working beyond $1\text{--}2\text{ }\mu\text{m}$ are sensitive also to the possible thermal background generated by surrounding surfaces. A limitation to this effect requires the insertion of actively cooled shielding surfaces.

In the past years, large experience has been achieved in the cryogenics field and, in particular in the astronomy field, this is a common practice for this kind of instruments. Then, standard solutions exist, that allow to cool down and keep them cold for a long period, with high thermal stability and reliability. These include cryocoolers constituted by a main compressor linked through a high pressure He line to a smaller cold head, that eventually provide the cryogenic

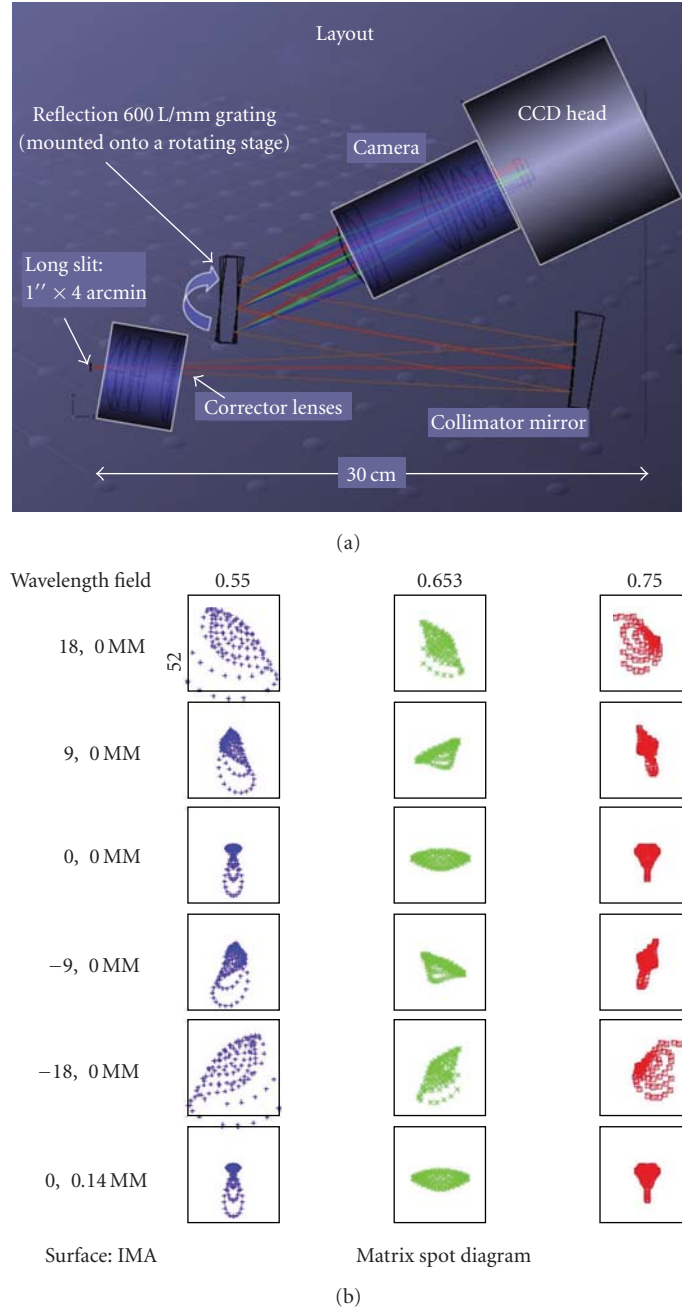


FIGURE 10: The optical layout of the spectrograph and the relative spot diagram at 550, 653 and 750 nm.

temperature to the instrument. These cryocoolers can easily have cryogenic power of tens of Watts @ 77 K (for near infrared instruments). These have been extensively used at the focal plane of telescopes and definitively provided a stable and reliable system.

The current design is based on the Leybold CoolPower 5/100T Cryocooler, a Dual Stage Cold Head that can provide up to 100 W @ 80 K at the 1st stage and 35 W @ 40 K at the 2nd stage. The basic scheme of the cryostat (see Figure 12) envisage an optical bench, on which all the opto-mechanical elements and the NIR arrays rely, surrounded by

two radiation shields, to avoid the direct irradiation from the external 300 K of the external temperature. As usual, a set of standard devices will be hosted in the cryostat, as a Lyot stop (to shield the thermal diffuse light), temperature sensors (to monitor the temperature of the most critical points of the cryostat, as the arrays and the optics), charcoal getters (with their own heaters), heaters (to fine tuning the bench temperature), a dithering mirror and a moving shutter (to perform dark current measurements).

Besides the standard solutions, we will investigate the possible use of mini cryocoolers, that essentially use the same

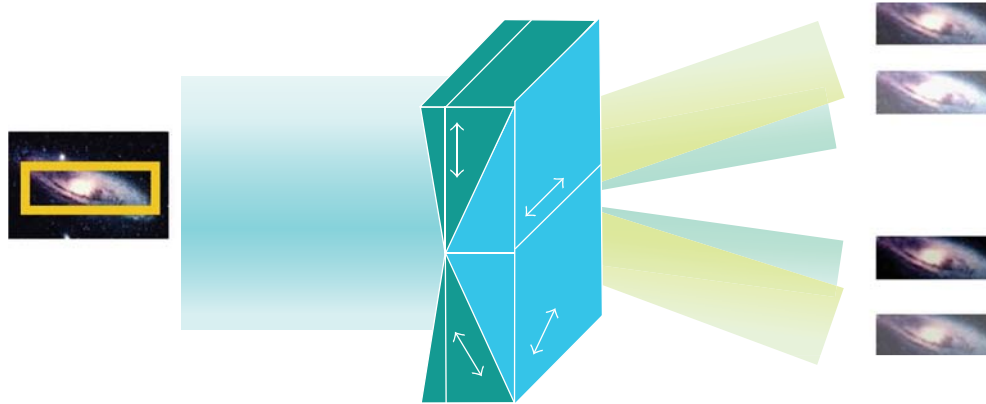


FIGURE 11: The Wedowo scheme for the Pathos Spectrograph.

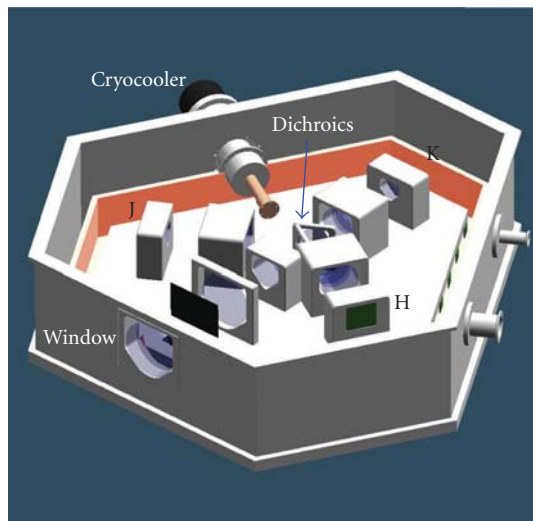


FIGURE 12: The cryomechanical scheme for the NIR camera.

cryogenics concepts but have very small and compact sizes: this would allow to have all the cryogenics device directly at the focal plane of the telescope, thus avoiding the long He line needed for the standard cryocoolers. A fast moving telescope would certainly have benefit of that. Of course, the reduced dimensions reflect in reduced cryogenic power, then pushing the instrument design toward the most compact and light instrument. Anyway, the recent experience in this field with REMIR@REM showed that these devices are sensitive to the telescope movement and then a deep investigation of their performances and a tight collaboration with industry are needed to assess their use at the telescope.

In order to improve reliability, the possibility to avoid the use of servo system into the cryogenic environment will be investigated: this means that the optics should be manually aligned before the cooling and adjust after following heating up cooling down cycles. If this can be achieved there is no needing of differential focus adjustment between the NIR arms because the cryogenic environment is a thermo-elastic stable condition. In addition it will be investigated

the opportunity of stabilize the temperature inside the whole instrument set-up. Doing so the thermo-elastic strain can be eliminated and the focus of each arm can be done directly by a piston motion of the secondary mirror of the telescope. The investigation of this issue will open the possibility of the reduction of the servo-systems, but must be done carefully making a costs versus benefits analysis.

5.6. Detectors

5.6.1. Visible. The VIS image detection system is based on a set of four CCD cameras with $2\text{ K} \times 2\text{ K}$ class detectors. Due to the relatively high background present in the VIS observations (broad-band imaging) the use of autonomous thermoelectrically cooled cameras seems to be the most appropriate solution. With such a choice we will avoid the insertion of more complicated cooling systems (liquid nitrogen or cryo-coolers) in favor of a simple water recycling system.

There is presently an extremely wide market for commercial cameras mounting customized scientific detectors and operating in cooled mode inside a windowed thermally insulated chamber. Even overall dimensions and resulting weight is reduced when compared to classical cryostat based cameras serviced by modular control electronics. Maximum of compactness and system efficiency, even in terms of spare parts, will be obtained making use exactly of the same camera model to populate VIS allowing diversification only for the detector QE specifics in the four bands.

The present reference choice is among two quite similar thermoelectrically cooled cameras (Princeton Pixis2048, in Figure 13, and Andor iKon-L 936) both allowing the insertion of $2\text{ K} \times 2\text{ K}$ CCD detectors (all the standard E2V scientific set with different coating and substrate options is available) with cooling capabilities below -60°C . Insertion on the informatics network taking care of detectors is simplified by the availability of fiber-based USB interfaces.

5.6.2. Near Infrared. At the time of writing, the best NIR detectors available in the market for astronomy are from Teledyne and Raytheon companies, being the former better

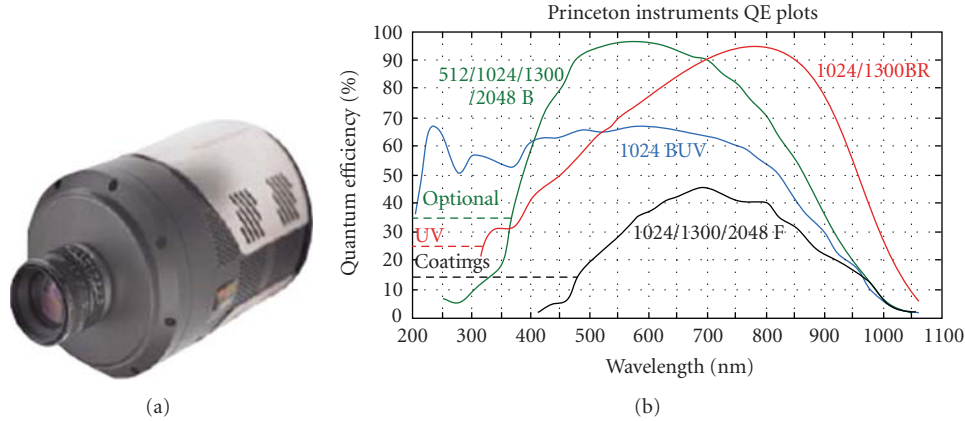


FIGURE 13: Princeton Pixis thermoelectrically cooled cameras and QE curves for the standard set of E3V scientific detectors available.

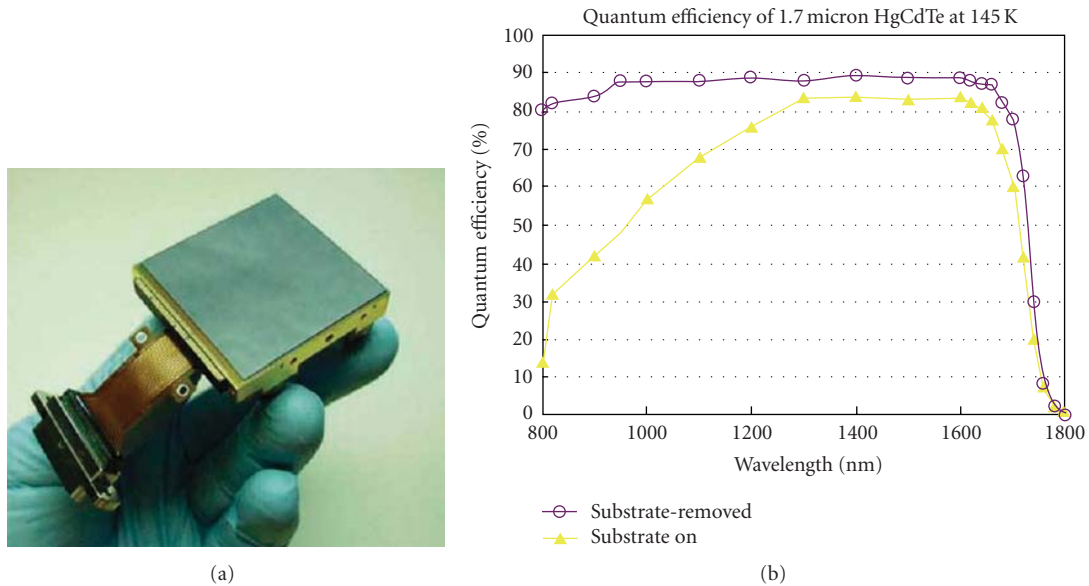


FIGURE 14: The Hawaii-2RG IR array from Teledyne and the predicted QE for 1.7 μm cut-off wavelength. With the substrate removal, the QE curve extends toward the visible domain [5].

in terms of noise and can be delivered together with its own cryogenic control electronics. Anyway, the rapidly evolving technology in the field of NIR detector suggests to be careful in the choice of the final detector and to follow all the evolution of the market in this field. Currently, we are oriented towards the Teledyne Hawaii-RG series of detectors (Figure 14), that can be delivered in different format ($1\text{ k} \times 1\text{ k}$, $2\text{ k} \times 2\text{ k}$ and even $4\text{ k} \times 4\text{ k}$ pixels) and different wavelength coverage (cut-off at 2.5, 1.7 and $5.3\text{ }\mu\text{m}$ are standard), allowing a certain flexibility in the choice of the best detector for each photometric band. These detectors shows the better performances in terms of dark current ($<0.01\text{ e}^-/\text{s/pixel}$ @ 90 K, for a $2.5\text{ }\mu\text{m}$ cut-off wavelength), Read Out Noise ($13\text{--}15\text{ e}^-$ with Single CDS, down to $<3\text{ e}^-$ with multiple sampling) and Quantum Efficiency ($>80\%$) [5, 6].

5.7. Control Electronics. Teledyne is offering a reliable and performing cryogenic electronic for its NIR hybrid detectors, the SIDECAR ASIC, designed as a compact focal plane electronics on a single chip for Teledyne focal plane arrays HAWAIIs, including the $4\text{ k} \times 4\text{ k}$ and the forthcoming $8\text{ k} \times 8\text{ k}$ [5]: it supports all possible modes of operation and can be used in the same cryogenic environment of the detector, thus minimizing the control electronics that generally accompanies such kind of devices (see Figure 15). ESO staff successfully tested this electronics and they are planning to build their own interface for the SIDECAR ASIC (replacing the JADE2 card) and to include the SIDECAR in the standard VLT and E-ELT software environment [7].

Moreover, in principle it could be used also to drive CCDs: very few groups around the world are involved to this aim but it would be worth to open a R&D in this field

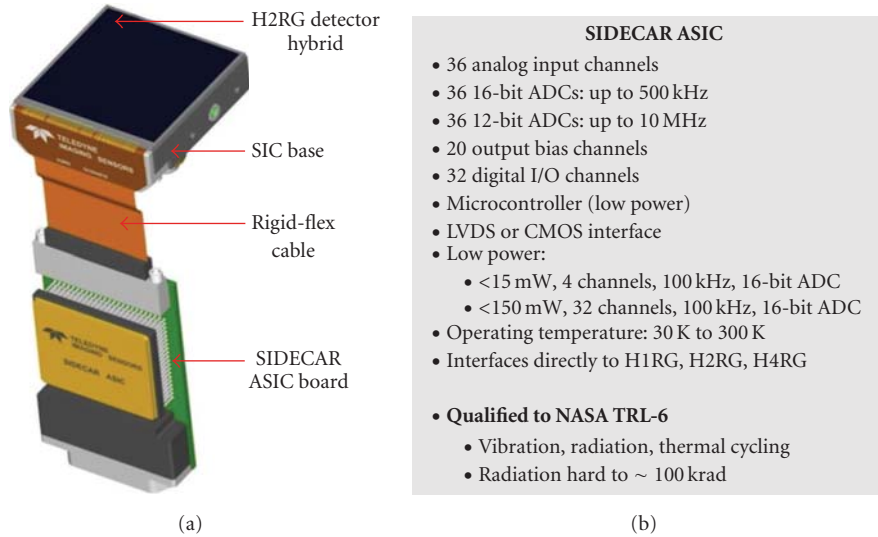


FIGURE 15: The new H2RG-SIDECAR cryogenic packaging and the main characteristics of the SIDECAR electronics.

because the possibility to have a single control electronics for all the detectors in Pathos would increase the reliability of the overall system, even if at higher costs with respect to the standard CCD reading electronics.

6. Control Software and Data Management System

The development of the control software and Data Management System (DMS) will follow an approach similar to that adopted for REM ([1, 8] and reference therein). Operations of the whole system will be managed by a set of processes each one dedicated to a very specific task and in constant inter-communication. A dedicated process will then act as a coordinator of all the above activities.

However some components will require major changes and improvements in order to satisfy all the requirements of the project in terms of (1) safety, (2) reliability, (3) effectiveness. In particular the huge amount of data (scientific and calibration frames, telescope and instruments telemetry, meteo, etc.) will require the DMS to rely on

- (1) reliable internal and external communication network,
- (2) reliable redundant sub-systems,
- (3) relational databases,
- (4) multithread processes using a client/server architecture.

Figure 16 shows the overall s/w architecture. The two core components are the “Observing System” at the telescope site and the “Supervisor System” at a remote site in Italy. The various components will communicate mainly through TCP/IP sockets with processes implementing a client/server scheme. The Observing System will save all the data in a local DB system and will perform all the low-level data reduction.

Data will then be transferred to Italy (in a synchronous or delayed manner) where all the high-level processing will be performed. The general users will have access to the data stored in the latter DB server through an internet accessible server using several types of interfaces ensuring full flexibility. The DB server will be mirrored at least at two sites.

This project has been designed with the explicit main goal to manage unexpected alerts from many sources. There is a large family of astrophysical objects potentially providing events occurring on rapid timescales, that is, comparable or shorter than the typical telescope pointing time (about 30–60 s) as GRBs, XRBs, high-energy transients of various sort, and so forth. We do not discuss here the astrophysical interest of rapid observations of these objects, however it is the case to remind us that optical and near-infrared observations carried out on the occurrence (or with a delay of a few tens of seconds) of high-energy events with a telescope of adequate collecting area are a real novelty and will effectively open a new observational window.

Alerts from astrophysical transient phenomena will likely still come when the telescope will be operational via the GCN system. However, other specialized alert delivering systems already existing (i.e., IBAS, etc.) or future available must also be considered (from neutrino telescopes, extensive air shower experiments, gravitational wave detectors, etc.). In addition, alerts will also be received for transients singled out by other optical instruments, as high-time resolution wide-field telescopes monitors or other robotic telescopes. The management of these families of alerts will be driven by a devoted software component. In general the delivering of these alerts will follow private standard solutions, developed in-house by the missions or experiments delivering them. This code must therefore implement all these solutions and be easy to update and enriched by new alert sources and/or technical solutions which can with time become available. All the received alerts will feed a database and a Figure of Merit (FoM) will be derived. The FoM, essentially, is a priority

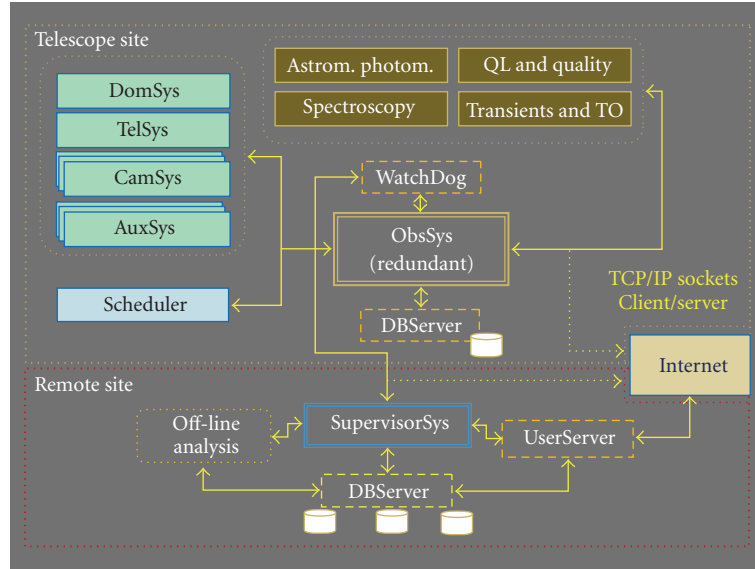


FIGURE 16: A schematic view of the control s/w and DMS.

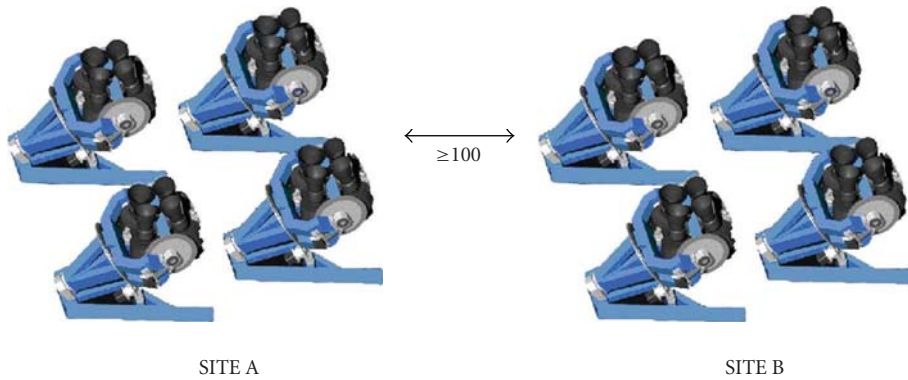


FIGURE 17: Schematic view of architecture of the Wide-Field array.

evaluation based on a multiparametric approach as in the case of the Swift satellite. The final output will be a grade to be compared to the grade of the observation possibly already in progress by the telescope. The FoM will also allow the telescope management system to evaluate a priority among possible multiple subsequent alerts.

7. Wide Field Array

Pathos will be equipped with the most advanced visible Wide Fielded Array ever built, capable to trigger the Pathos observations of rapidly variable phenomena (SNe and GRBs), in absence of satellite γ and X-ray triggers for GRBs. The self-triggering capability will be secured by a construction in collaboration with the “Pi of the Sky” group [9] of a dedicated wide-field (WF) array. Here the main challenges are to considerably shorten the time scale with which the sky will be probed, as compared with already existing projects, and to develop a concept of autonomous CCD camera

equipped with sufficient computing power, memory and GB-ethernet link as to serve as independent unit capable of performing at least primary image processing and analysis, discover candidates for optical transients and exchange corresponding information with other such cameras and wide-field arrays present in the network.

The envisaged architecture assumes 2 sites located at a base distance of about 100 km, as shown in Figure 17. Each site should be equipped with 16 CCD cameras, covering about 2 sr of the sky. Depending on settings, cameras from both sites will work pair wise in coincidence or observe separate FOV's. Note that for short optical transients, elimination of background due to cosmic radiation requires observation of the same FOV by at least 2 units. In addition, sufficiently long baseline allows to eliminate Sun reflections from military, maneuvering satellites with orbital elements which are kept secret to civilian community. In order to filter out background and ultimately to select transients of astrophysical origin in the real time requires development and implementation of very efficient and clever algorithms.

8. Dome

The requirement on the pointing rapidity of the telescope, force us to find a proper solution for the dome, that should follow the velocity of the telescope. Nevertheless, other issues linked to the dome choice have to be taken into evaluation, as feasibility, costs, wind and dust shielding, proper thermalization.

Different dome configurations will be taken into consideration (horizontal or vertical slit, boxes, geodesic, fully retractable) and some simulations have been done to evaluate the impact of the incoming wind on the dome.

9. Conclusions

The evidence that the GRBs are, on average, weaker than thought before, suggested us to exploit our precious experience made with the robotic 60 cm REM telescope in the last 6 years and investigate the possibility to build and operate a larger telescope. We are now completing a feasibility study to build and operate a robotic 4 m class telescope, equipped with a multichannel VIS-NIR camera, able to point on the triggered target in less than 50–30 s.

Acknowledgments

The authors wish to thank MIUR (Italian Ministry of Research) which contributed to the construction of REM and to the present feasibility study, ASI (Italian Space Agency) for its contribution to Swift. The authors would like to thank the ESO La Silla staff, who in the past years collaborated with them in setting up and maintaining the REM telescope and its instrumentation. They would like to thank also Maciej Sobczak, for his useful and skilled software advising.

References

- [1] E. Molinari, S. Covino, F. D'Alessio, et al., "REM, automatic for the people," to appear in *Advances in Astronomy*.
- [2] E. Molinari, S. D. Vergani, D. Malesani, et al., "REM observations of GRB060418 and GRB060607A: the onset of the afterglow and the initial fireball Lorentz factor determination," *Astronomy & Astrophysics*, vol. 469, pp. L13–U16, 2007.
- [3] J. L. Racusin, S. V. Karpov, M. Sokolowski, et al., "GRB 080319B: a naked-eye stellar blast from the distant universe," *Nature*, vol. 455, no. 7210, pp. 183–188, 2008.
- [4] E. Oliva, "Wedge double Wollaston, a device for single shot polarimetric measurements," *Astronomy & Astrophysics*, vol. 123, pp. 589–592, 1997.
- [5] J. W. Beletic, R. Blank, D. Gulbransen, et al., "Teledyne imaging sensors: infrared imaging technologies for Astronomy & Civil Space," in *High Energy, Optical, and Infrared Detectors for Astronomy III*, vol. 7021 of *Proceedings of SPIE*, Marseille, France, June 2008.
- [6] G. Finger, R. Dorn, L. Mehrgan, M. Meyer, and J. Stegmeier, "Evolution of IR detection and possible outcomes for astrophysics," *EAS Publications Series*, vol. 37, pp. 343–353, 2009.
- [7] R. J. Dorn, S. Eschbaumer, D. N. B. Hall, et al., "Evaluation of the Teledyne SIDECAR ASIC at cryogenic temperature using a visible hybrid H2RG focal plane array in 32 channel readout mode," in *High Energy, Optical, and Infrared Detectors for Astronomy III*, vol. 7021 of *Proceedings of SPIE*, pp. 70210Q–1–70210Q, Marseille, France, June 2008.
- [8] M. Stefanon, S. Covino, D. Fugazza, et al., "The REM observing software," to appear in *Advances in Astronomy*.
- [9] K. Malek, T. Batsch, M. Cwiok, et al., "'Pi of the Sky' detector," to appear in *Advances in Astronomy*.

Research Article

From TORTORA to MegaTORTORA—Results and Prospects of Search for Fast Optical Transients

Grigory Beskin,¹ Sergey Bondar,² Sergey Karpov,¹ Vladimir Plokhotnichenko,¹ Adriano Guarnieri,³ Corrado Bartolini,³ Giuseppe Greco,³ Adalberto Piccioni,³ and Andrew Shearer⁴

¹ *Special Astrophysical Observatory of Russian Academy of Sciences, Nizhnij Arkhys 369167, Russia*

² *Arkhyz Branch, Institute for Precise Instrumentation, Nizhnij Arkhys 369167, Russia*

³ *Astronomy Department, Bologna University, 40126 Bologna, Italy*

⁴ *School of Physics, National University of Ireland, University Road, Galway, Ireland*

Correspondence should be addressed to Grigory Beskin, beskin@sao.ru

Received 28 June 2009; Accepted 12 January 2010

Academic Editor: Joshua S. Bloom

Copyright © 2010 Grigory Beskin et al. This is an open access article distributed under the Creative Commons Attribution License, which permits unrestricted use, distribution, and reproduction in any medium, provided the original work is properly cited.

To study short stochastic optical flares of different objects (GRBs, SNs, etc.) of unknown localizations as well as NEOs it is necessary to monitor large regions of sky with high-time resolution. We developed a system consisting of widefield camera with field of view of 400–600 sq.deg. which uses TV-CCD with 0.13 s temporal resolution to record and classify optical transients, and a fast robotic telescope aimed to perform their spectroscopic and photometric investigation just after detection. Such two-telescope complex, combining wide-field camera TORTORA and robotic telescope REM, operated from May 2006 at La Silla ESO observatory. Some results of its operation, including first high time resolution study of optical transient accompanying GRB and discovery of its fine time structure, are presented. Also, prospects for improving the efficiency of such observations are given, and a project of a next generation wide field monitoring system, the MegaTORTORA, is described.

1. Introduction

The efforts for searching and investigation of optical flashes accompanying the Gamma-Ray Bursts were somewhat contradictory from the beginning. The large amount of bursts shorter than 2 seconds (nearly 30%) and the presence of fine temporal structure, down to milliseconds, in their light curves [1] obviously require both continuous optical monitoring of space telescopes fields of view and application of detectors with high temporal resolution [2–4]. But in spite of that until 2002 nearly all studies of GRB optical emission have been performed in a follow-up regime, by pointing a telescope towards burst positions measured by a satellite, and observing with exposures larger than 10 seconds. However, even for the best possible manners of coordinate messages distribution [5], such observations start at least 5–30 seconds after the burst onset and are unable to study the burst temporal structure with resolution comparable to

ones available in gamma-ray band [6–9]. Obviously, optical flashes accompanying short gamma-ray bursts cannot be detected in such a way, while for long bursts it is impossible to compare optical and gamma-ray light curves. Even later, when wide-field monitoring cameras able to detect optical transients independently from satellite triggers, like WIDGET [10], RAPTOR [11], BOOTES [12, 13], and π of the Sky [14], appeared, their low-temporal resolution significantly limited the possibilities of investigating the physical nature of the bursts, and especially—their central engines. Indeed, presently it is widely accepted that GRB central engines are compact relativistic objects—isolated or binary neutron stars [15] or stellar mass black holes [16, 17] interacting with massive accretion disks. Observations in different wavebands with temporal resolution close to time scales of nonstationary processes near the event horizon, from milliseconds to seconds, may be crucial for understanding the physics of such objects.

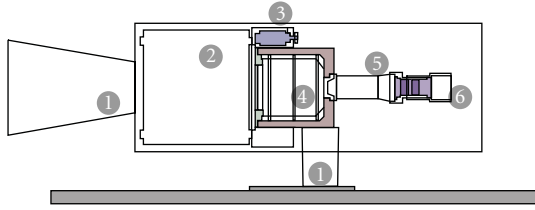


FIGURE 1: Schematic view of a TORTORA design. (1) Protective blend, (2) main objective, (3) main objective focusing unit, (4) image intensifier, (5) transmission optics and CCD focusing unit, and (6) fast CCD.

For that purpose, since late 1990s we are developing the strategy of optical monitoring with high temporal resolution in the wide fields comparable to ones of space-borne telescopes. Initially it has been proposed [18, 19] to use instruments with large mirrors of relatively low quality, air Cerenkov telescopes, or solar concentrators, with phototubes able to operate with temporal resolution down to microseconds. Later, however, we finished the design of a wide-field camera equipped with image intensifier and a fast low-noise CCD. The prototype of such a camera, FAVOR, is operated since 2003 near Russian 6-m telescope [2, 20], while similar Telescopio Ottimizzato per la Ricerca dei Transienti Ottici RAPidi (TORTORA) is mounted since 2006 on top of Italian REM telescope [21] in La-Silla Observatory (ESO, Chile) as a part of a TORTOREM [22] two-telescope complex [23]. The latter camera has detected and studied with unprecedented temporal resolution the optical emission of a Naked-Eye Burst [24–26].

Here we describe the design and implementation of TORTORA camera, present some results of its operation, and propose the project of a next generation wide field monitoring system, the MegaTORTORA, able to catch much fainter transients in a wider field of view, and acquire complete multicolor and polarimetric information on them.

2. Design of TORTORA Wide-Field Camera

Parameters of FAVOR and TORTORA cameras in comparison to other wide-field monitoring systems currently in operation are presented in Table 1. The only cameras combining both wide field of view and relatively high-time resolution are ones presented here.

The schematic view of TORTORA is shown in Figure 1, its technical parameters is listed in Table 2, and the camera photo in Figure 2. The camera consists of the main objective (2), its focusing unit (3), the image intensifier (4) used to downscale and amplify the image, transmission optics (5), and the fast low-noise TV-CCD (6). TORTORA is installed on top of REM robotic telescope, which has alt-azimuthal mounting.

Fast TV-CCD matrix operates at 7.5 frames per second regime with 0.128 s time exposure and gaps between frames negligibly small. The data from CCD is broadcasted through the local gigabit Ethernet network to one terabyte storage

TABLE 1: Typical wide-field monitoring cameras currently in operation. For FAVOR and TORTORA the limits correspond to 3σ detection on a single frame and differ from their real-time operational values.

Name	Field of view (degrees)	Temporal resolution (seconds)	Limit
WIDGET	62×62	5	10^m
RAPTOR A/B	40×40	60	12^m
RAPTOR Q	180×180	10	10^m
BOOTES	16×11	30	12^m
BOOTES-AllSky	180×180	30	10^m
π of the Sky	33×33	10	11.5^m
AROMA-W	25×35	5–100	10.5^m – 13^m
MASTER-VWF	20×21	5	11.5^m
MASTER-Net	30×30	1	9^m
FAVOR	16×24	0.13	10^m – 11.5^m
TORTORA	24×32	0.13	9^m – 10.5^m



FIGURE 2: Photo of a TORTORA camera, mounted on top of REM robotic telescope in La-Silla Observatory, ESO, Chile.

RAID array. The data flow rate for the system is about 20 Mb/s, and so the storage may keep the raw data only for one or two days.

Also, the raw data are transmitted to the real-time processing PC operating the custom pipeline software under Linux OS. The pipeline performs the detection and classification of transient events of various types and tries to recognize already known objects, by comparing the time and position of each events with catalogues of satellites and with star catalogue to minimize the number of false events due to stellar scintillations under bad weather conditions.

3. Detection Methodology

Wide-field monitoring cameras with high temporal resolution may be used for detection and investigation of various classes of transient events—variable stars, supernovae, active galactic nuclei, MACHOs, planetary transits over stars—with fixed, but unknown a priori coordinates. On the other hand, cameras like FAVOR or TORTORA may detect also the

TABLE 2: Technical parameters of TORTORA camera.

Main objective		Intensifier		CCD	
Diameter	120 mm	Photocathode	S20	Model	VS-CTT285-2001
Focus	150 mm	Diameter	90 mm	Dimensions	1388 × 1036 pix
D/F	1/1.2	Gain	150	Image scale	81''/pix
Field of view	24 × 32 deg	Scaling coefficient	7.7	Exposures	0.13–10 sec
		Quantum efficiency	10%	Pixel size	6.45 μm

moving objects—satellites, space debris, comets, asteroids, meteors. For TORTORA, we developed special algorithms able to detect both classes of transients.

Due to very high data flow from the camera, it is impossible to use standard image reduction packages, so we have developed a fast transient detection algorithm based on the “differential imaging” method [27], which implies statistical analysis of temporal behaviour of each pixel over $N = 100$ previous frames, that is, 13 seconds. The current value of the pixel I is being compared with the running mean $\langle I \rangle = \sum I/N$ and standard deviation $\sigma_I = \sqrt{(\sum I^2 - (\sum I)^2/N)/(N-1)}$, and the significance of excess over the mean is computed as $A = (I - \langle I \rangle)/\sigma_I$. Then, all the pixels with deviations over the mean of 3σ and greater are clustered into extended objects. Some objects, like single-pixel ones, are filtered out as they are most likely due to noise.

After the extraction of objects from current frame, the reduction pipeline compares their positions with trajectories of transients seen on previous ones (all objects here are assumed to be moving, but some of them—with zero velocity). Detection of object on three successive frames (in half a second) is enough to classify it into one of three possible classes—“noise,” if the object disappears, moving event, if it has statistically significant motion, or stationary transient. The case of slowly moving geostationary satellites is handled by comparing the event position with regularly updated satellite catalogue [28].

Detection of meteors, however, requires a different approach, as most of them may be seen on single or two successive frames only. Also, their motion is significantly faster than that one of satellites. So, the meteors are selected by geometric length and flux criteria only.

The astrometric and photometric calibration is performed regularly (once per minute in a case of TORTORA camera, as it has an alt-azimuthal mounting with rotating field of view) by means of additional SExtractor-based [29] pipe-line and custom WCS matching code based on Tycho-2 stellar catalogue [30].

So, the real-time pipeline is able to detect and classify any bright optical transient in a 0.4 second (3 frames) since its onset, before it hides from differential imaging algorithm. Example of such short flare is presented in Figure 3. Then, the information on the event may be sent to the robotic telescope to perform its detailed investigation. Also, all the relevant information on the transient, including its light curve, trajectory, and pieces of raw images containing it, is stored for the subsequent offline investigation and statistical analysis.

TABLE 3: Upper limits on the constant flux and sinusoidal variability of gamma-ray bursts, observed by TORTORA wide-field camera in follow-up regime.

Burst	Time since event (seconds)	12 s limit (100 frames)	Variability timescale (Hz)	Variability limit
GRB060719	59	12.4	0.01–3.5	15.3 ^m
GRB061202	92	11.3	0.1–3.5	14.0 ^m
GRB060719	118	11.3	0.01–3.5	16.4 ^m

4. TORTORA Results

TORTORA camera operates since June 2006, approximately half of observational time (when REM is not performing its scheduled programme) it follows up regions of the sky observed by the Swift satellite, according to real-time pointing information distributed through the GCN network [5]. The regime of follow-up observations of transients detected independently by TORTORA with the REM telescope is now in testing stage.

For each observational night, the camera detect approximately 300 meteors and 150 satellites of various brightness.

4.1. Follow-up Observations of Gamma-Ray Bursts. Due to REM telescope operation in follow-up regime in respect to Swift satellite triggers, TORTORA camera has been able to observe the regions of localization of three gamma-ray bursts in a short time since the event [31–33].

The integral data on all these follow-up observations are presented in Table 3. Stationary flux limits have been derived from 100-frame average images (12.8 s effective exposure).

4.2. Observations of Naked-Eye Burst. March 19 and 20, 2008 became the most fruitful days for wide-field monitoring systems around the world. It brought up 5 GRBs in a row, all within 24 hours, one of which, GRB080319B [34], is the brightest ever seen in gamma-rays and optical range, and the first one to be detected by monitoring systems. Its field of view had been images before, during, and after the gamma event by “Pi of the Sky” [35], RAPTOR Q [36], and TORTORA [24] cameras.

We observed the region of GRB080319B [24, 25] since 05:46:22 UT, nearly half an hour before the burst (burst time is 06:12:49 UT), during the event and for several tens of minutes after its end. At 06:13:13 UT till 06:13:20 UT REM telescope performed automatic repointing after receiving the coordinates distributed by Swift [34], which moved

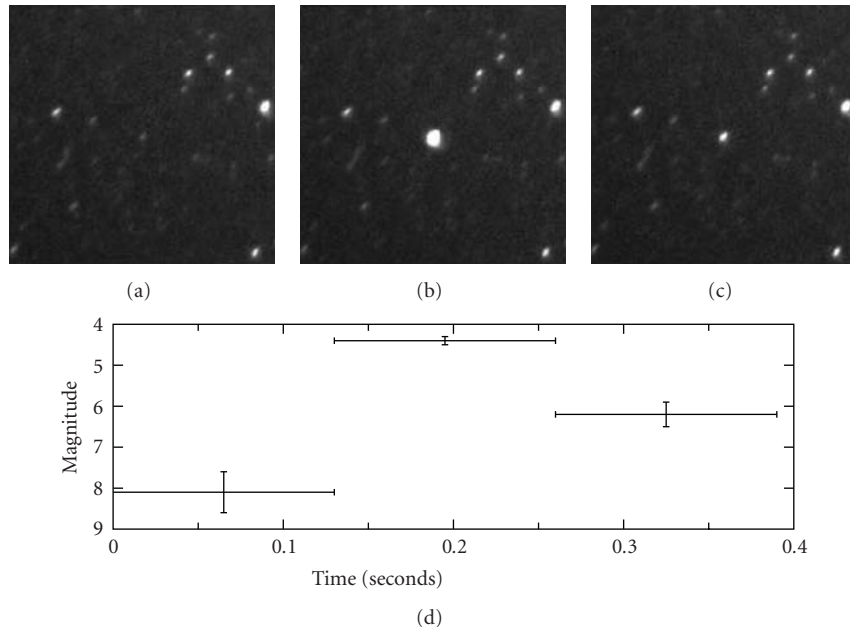


FIGURE 3: Example of a short satellite flare detected by the camera. Total length of the event is 0.4 sec (seen on 3 successive frames).

the position of the burst from the edge of the TORTORA field of view towards its center. Sample images of the burst region at different stages of the event are presented in Figure 4.

The data acquired have been processed by a pipeline including TV-CCD noise subtraction, flat-fielding to compensate vignetting due to objective design, and custom aperture photometry code taking into account non-Poissonian and nonergodic pixel statistics caused by image intensifier. For the REM repointing time interval fluxes have been derived using custom elliptic aperture photometry code after summation of 10 consecutive frames (1.3 s effective exposure) with compensated motion of the stars, therefore no full-resolution measurements (0.13 s exposure) are available for this interval.

TORTORA acquired the data in white light with sensitivity defined by the S20 photocathode used in the image intensifier [2]. Instrumental object magnitudes have then been calibrated to Johnson V system using several nearby Tycho-2 [30] stars. A quick-look low resolution light curve (lacking the data during the REM repointing interval) has been published [24, 25] and has been found to agree with results of other wide-field monitoring cameras which also observed this burst, such as “Pi of the sky” [35] and RAPTOR [36]. Our complete full resolution light curve along with the low resolution one (after the restoring of the gap) is shown in Figure 5.

We clearly detected the transient optical emission since approximately 10 seconds after the trigger. It then displayed fast $\sim t^4$ rise, peaked at $V \approx 5.5^m$, demonstrated 1.5–2 times variations on a several seconds time scale and decayed as $\sim t^{-4.6}$ until went below TORTORA detection limit at about hundred seconds since trigger. The gamma emission itself ended at 57th second.

The light curve clearly shows four peaks with similar amplitudes, durations, and shapes. We decomposed it into four components described by a simple Kocevski [37] profile. We stress that distances between peaks are nearly the same within the errors and are around 8.5 s in observer frame, which corresponds to 4.4 s in the rest frame at $z = 0.937$ [25].

Therefore, for the first time, we have a clear detection of a periodic variations of prompt optical emission on a few seconds time scale.

We then subtracted the smooth curve, formed by four fitted peaks, from the original data and studied the residuals shown in the lower panel of Figure 5. Power spectral analysis of different subintervals of the burst revealed the signature of a periodic intensity variations during the last peak, since $T + 40$ s till $T + 50$ s, shown in Figure 6. No other intervals of the light curve show any variability in 0.1–3.5 Hz (0.3–10 s) range with power exceeding 15% before and 10% after the REM repointing. To exclude artificial nature of these variations we performed analysis of each comparison star separately in the same way as of the object. Neither comparison stars nor background displays any similar periodic feature during either the whole time interval or the last peak.

The significance level of the power density spectrum feature shown in Figure 6 is approximately 1%. The period and amplitude of the corresponding sinusoidal component, derived by means of nonlinear least squares fit, are 1.13 s and 9%, respectively.

To compare the temporal structure of optical and gamma-ray light curves we performed the cross-correlation analysis, using the plateau phase only, excluding the first and last 12 seconds of the burst both in optical and in gamma, which are obviously highly correlated [38] (see Figure 7). The correlation between the full-resolution optical

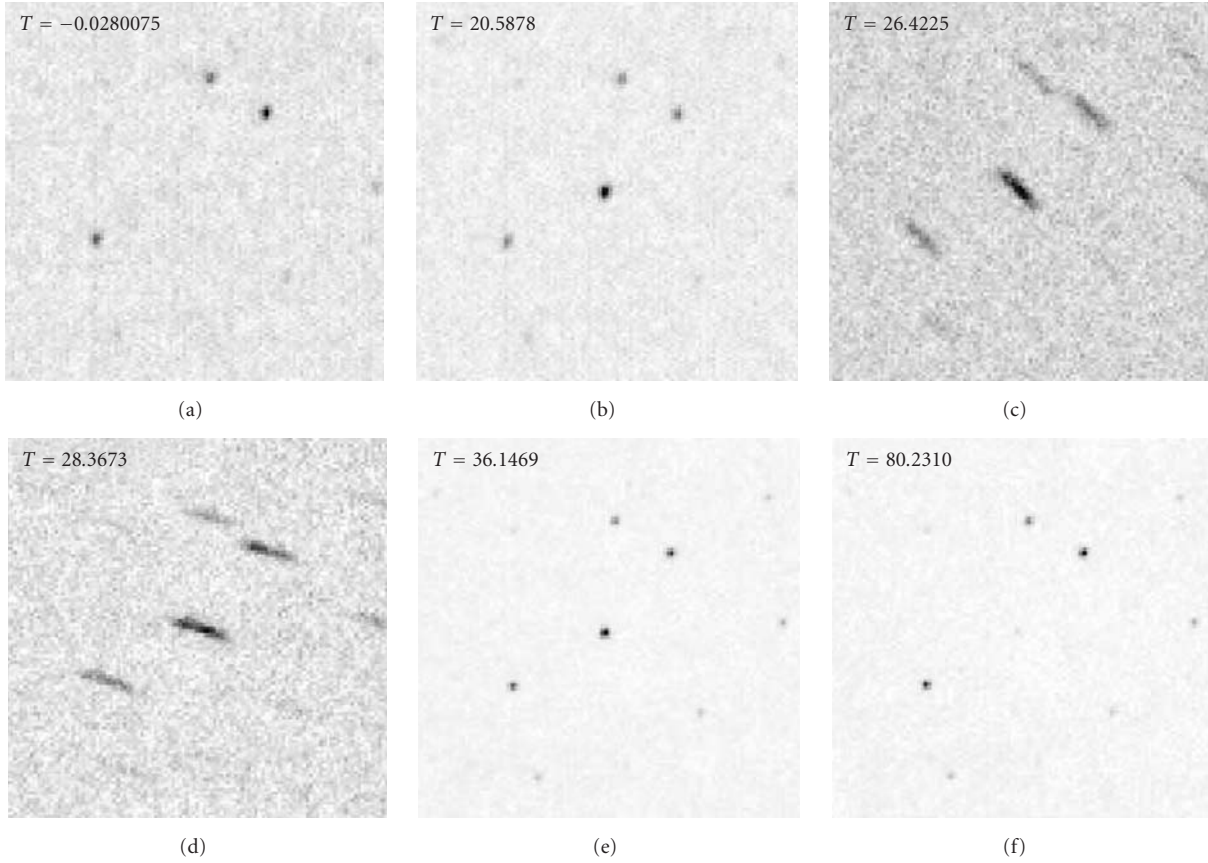


FIGURE 4: The development of prompt optical emission from GRB080319b as seen by TORTORA camera. Sums of 10 consecutive frames with 1.3 s effective exposures are shown for the gamma-ray trigger time ($T = 0$ s), the maximum brightness time during the first peak ($T = 20.5$ s), two middle-part moments ($T = 26.4$ s and $T = 28.4$ s), at the last peak ($T = 36$ s), and during early afterglow ($T = 80$ s) stages. Image size is 2.5×2.5 degrees. The third and fourth images display deformed star profiles as during this time (since $T + 24$ s till $T + 31$ s) REM robotic telescope (which has TORTORA camera mounted on top) repointed after receiving the burst information from Swift. Initially, burst position was on the edge of field of view, as a result of repointing it moved to the center of field of view, which resulted in better data quality.

data and the correspondingly rebinned gamma-ray one is no more than 0.5, due to high level of stochastic component in 0.1–1 s range in both optical (measurements noise) and gamma rays (actual high-frequency variability) [39]. For the low-resolution data, with a 1.3 s binning, the correlation coefficient is, however, as high as 0.82 if the optical light curve is shifted 2 seconds back with respect to gamma-ray one (see Figure 7). Correspondingly rebinned gamma-ray data demonstrate the same four nearly equidistant peaks as optical ones.

This is the first detection of a close relation between the temporal structures of the optical and gamma-ray prompt emission. In our case, the gamma-ray burst itself precedes the optical flash by two seconds. This feature, along with the periodicities we detected, have a serious physical implications for the models of the event, as they clearly contradict most of proposed variants of emission generation [26]. They are, however, inevitably suggest the periodic behaviour of the internal engine, which may be explained by the onset of instabilities and the gravimagnetic precession of the massive accretion disk around the newborn stellar-mass black hole.

5. MegaTORTORA

It is important to develop the methodology of wide-field search for fast optical transients in two directions. The first is the increase of detection threshold by 2–3 magnitudes while keeping the field of view and temporal resolution. It may be achieved by means of multiobjective (or multitelescope) systems, by decreasing field of view of single instrument and, therefore, its pixel scale [40]. To avoid the dominance of CCD read-out noise, the quantum efficiency and amplification of image intensifier have to be increased, or the low-noise fast EM-CCDs may be used instead. The second direction is the acquisition of the spectral, or at least multicolor, and polarimetric information for the transients.

One possible design of a multiobjective monitoring system with EM-CCDs, able to collect multicolor and polarimetric information, is presented below.

5.1. Basic 3×3 Unit. The project utilizes the modular design and consists of a set of basic units, 9 objectives each, installed on a separate mounts (see Figure 8). Each

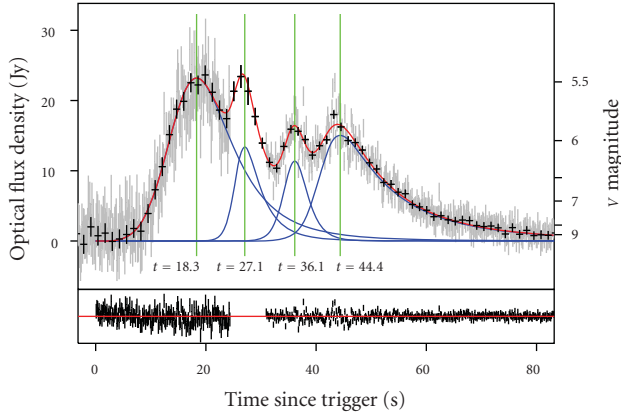


FIGURE 5: The light curve of GRB080319B acquired by TORTORA wide-field camera. The gamma-emission started at $T \approx -4$ s and faded at $T \approx 55$ s. Full resolution (0.13 s exposure, gray lines) data are available for all duration of gamma-emission except for interval of REM telescope repointing ($24.5 \text{ s} < T < 31 \text{ s}$), while low-resolution ones (summation of 10 consecutive frames, 1.3 s effective exposure)—for the whole time. The light curve is approximated by a four nearly equidistant flares; lower panel shows the residuals of such approximation.

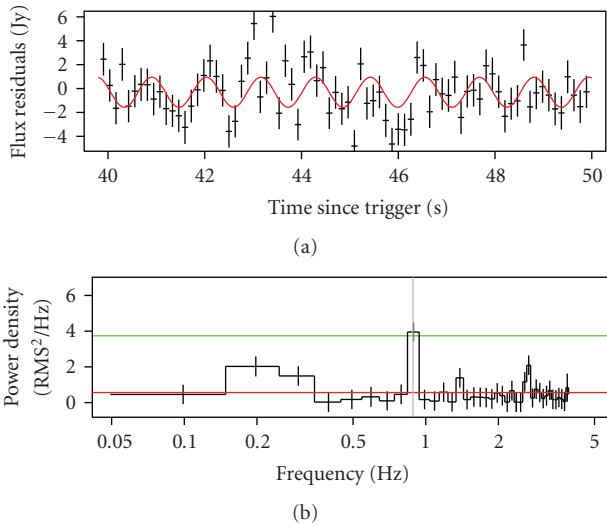


FIGURE 6: (a) Optical flux for a $T + 40 \text{ s} - T + 50 \text{ s}$ interval (last peak) with the approximation shown in Figure 5 subtracted. Smooth line shows the best-fit sinusoidal approximation of the data with $P = 1.13 \text{ s}$ period. (b) Power density spectrum of this data, estimated by bootstrapping method—by generating a large number of sample time series by randomly shuffling the original light curve, what completely destroys its time structure while keeping the distribution of its values, and by studying the distribution and quantiles of resulting power densities. Horizontal lines represent mean noise level (lower) and a level of noise deviations with 10^{-3} significance (upper), estimated by bootstrapping number of time series from the original data set. Vertical line corresponds to the period of the sinusoidal approximation shown in (a), clearly coincided with the peak of power spectrum. The probability of a random appearance of a feature like the one seen in any of 39 frequency bin is ~ 0.01 .

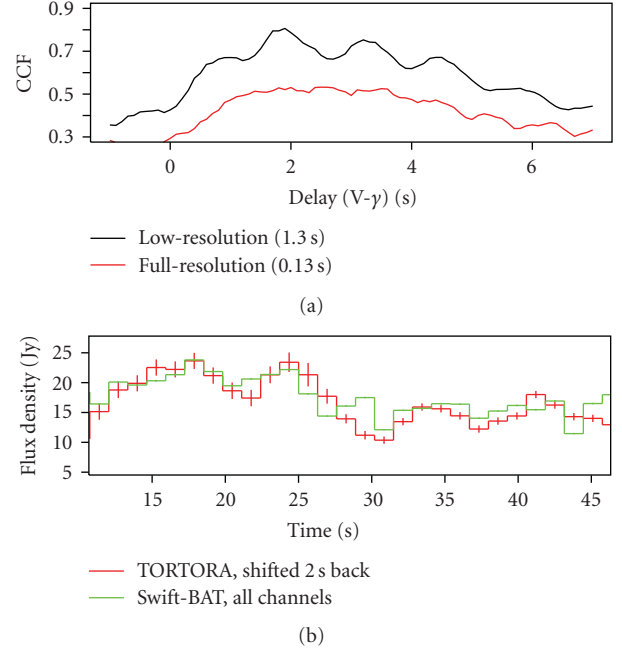


FIGURE 7: (a) Cross-correlation of the Swift-BAT gamma-ray (all energy channels) and TORTORA optical fluxes for the main (plateau) phase of the burst emission. (b) TORTORA optical flux shifted back 2 seconds along with correspondingly rebinned Swift-BAT gamma-ray flux. The correlation is $r = 0.82$ with significance level of $5 \cdot 10^{-7}$. Gamma-ray curve is arbitrarily scaled and shifted for illustrative purposes.

objective in a unit is placed inside the gimbal suspension with remotelycontrolled micromotors, and so may be oriented independently from others. Also, each objective possesses the set of color and polarization filters, which may be installed before the objective on the fly. It allows to change modes of observation on the fly, from routine wide-field monitoring in white light, with no filters installed, to the narrow-field follow-up regime, when all objectives are pointed towards the same point, that is, newlydiscovered transient, and observe it in different colors and for different polarization plane orientations simultaneously, to acquire all possible kinds of information for the transient (see Figure 9). Simultaneous observation of the transient by all objectives in white light is also possible to get better photometric accuracy by coadding frames.

Each objective is equipped with the fast EM-CCD, which has a low readout noise even for a high frame rates when the internal amplification is in effect. Possible variants of a readilyavailable commercial EM-CCDs and objectives are shown in Figure 10.

The data from each channel of such a system, which is roughly 20 megabytes per second, is collected by a dedicated rackmount PC, which stores it in its hard-drive as well as performs its real-time data processing in a way similar to the current processing pipeline of FAVOR and TORTORA cameras, which currently operate under similar data flow rate. The whole system is coordinated by the central server which acquires the transient data from data-processing PCs

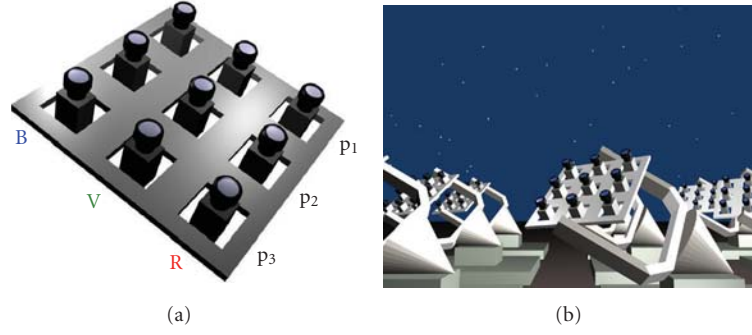


FIGURE 8: (a) Basic 3×3 objective unit. Each objective is able to repoint independently and has installable color and polarization filters. (b) The artistic view of a complete MegaTORTORA system, consisting of a number of basic units on separate equatorial mounts.

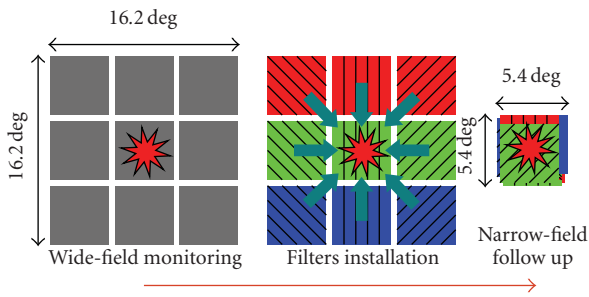


FIGURE 9: Different modes of operation of MegaTORTORA system. Left: wide-field monitoring mode in a white light. Middle: insertion of color and polarization filters as a first step of follow-up routine upon detection of a transient. Right: repointing of all unit objectives towards the transient. In the latter regime of operation the system collects three-color transient photometry for three polarization plane orientations (illustrated by a different stroke directions in figure) simultaneously. Mode transition speed depends on exact hardware parameters (objective and CCD weight, motors used, etc.), but is expected to be less than 0.3 seconds.

and controls the pointing and mode of operation of all objectives in response to them.

Each basic 3×3 unit in wide-field monitoring mode has ~ 260 square degrees field of view and has a $\sim 14.5^m$ limit in a white light for a 0.1 s exposure if a sky background noise prevails over the read-out noise (i.e., in a high gain regime of EM-CCD). Frame coaddition can improve it up to 17^m for effective exposure of 10 s and up to 19.5^m —for 1000 s. In narrow-field follow-up mode, with ~ 30 square degrees field, the limits depend on the selection of color filters and polarizers and are summarized in Table 4. Also, for a bright transients, a very high temporal resolution mode is possible, if the CCD supports the read-out in a small window with greater frame rate (e.g., Andor iXon^{EM}+888 EM-CCD provides the frame rates up to 65 in 128×128 window without binning, and up to 310—with 8×8 binning).

5.2. Complete System. The complete system is a set of basic 3×3 units installed on a separate mounts and operated in

TABLE 4: Detection limits (in stellar magnitudes) of a basic 3×3 unit in narrow-field follow-up mode for a different combinations of color and polarimetric filters in use.

Time scale, s	White/B	B + 3 polarizations	BVR	BVR + 3 polarizations
0.1	15.7	13.0	15.0	12.5
10	18.2	15.2	17.5	15.0
1000	20.7	17.9	20.0	17.5

parallel. The number of units may be arbitrary—the larger the better.

As an example, let us assume 8 unit configuration. It will cover 2100 square degrees of the sky simultaneously in a wide-field monitoring mode, which allows to perform the all sky survey twice per night while staying for half an hour on each region. In a narrow-field mode, by combining the data from all 72 objectives, it will reach 17.2^m to 19.7^m limit for 0.1 to 10 s effective exposures. The amount of data acquired in a night of observations will be around 40 Tb, which will be processed in real time. Such a system is expected to see the light of a GRB once per month. Performance of such a system for observations of different classes of variable objects is shown in Figure 11 in comparison with other wide-field monitoring projects.

As for financial side, assuming the prices as 2 k€ for objective, 45 k€ for EM-CCD, 1 k€ for data-processing PC and 26 k€ for an equatorial mount, a single basic 3×3 unit will costs approximately 500 k€, while the 8 units configuration—approximately 5 millions of Euros.

6. Conclusions

The Naked-Eye Burst has stressed the importance of both wide-field monitoring and high temporal resolution for the search for and investigation of short optical transients of unknown localization. FAVOR and TORTORA cameras, created by our group, achieved significant results in this area,



FIGURE 10: Possible commercially available parts for MegaTORTORA. (a) Andor iXon^{EM}+888 1024 × 1024 EM-CCD with 13 μm pixel size, up to 95% quantum efficiency, 9 frames per second frame rate, and less than 1 e^- read-out noise in high gain regime. (b) Canon EF 85 f/1.2 L USM II objective, which may provide 9×9 degree field of view with $31''$ pixel scale for this CCD. (c) Marshall Electronics 140 mm f/1.0 lens, which will give 5.4×5.4 degree field with $19''$ pixel scale.

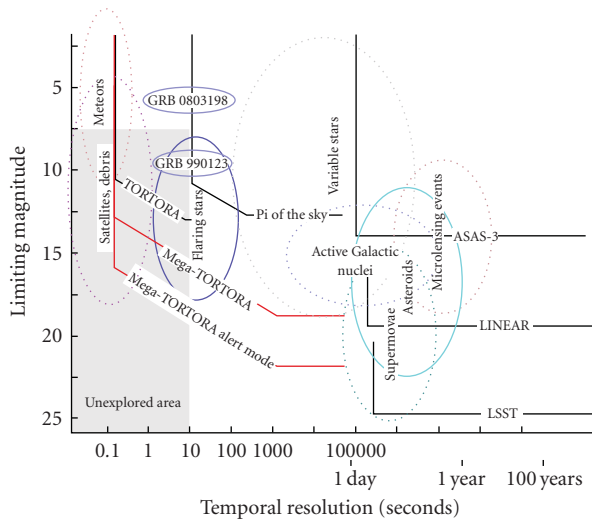


FIGURE 11: Performance of MegaTORTORA, as well as several others typical wide-field monitoring projects both in operation now (ASAS-3, LINEAR, Pi of the Sky, FAVOR/TORTORA) and planned for near future (LSST), in observations of different classes of variable objects.

which allows us to propose the development of such strategy, and formulate the design of a next generation of a wide-field monitoring system—the MegaTORTORA.

Acknowledgments

This work was supported by the Bologna University Progetti Pluriennali 2003, by grants of CRDF (no. RP1-2394-MO-02), RFBR (nos. 04-02-17555, 06-02-08313, and 09-02-12053), INTAS (04-78-7366), and by the Presidium of the Russian Academy of Sciences Program. S. Karpov has also

been supported by a grant from the President of Russian Federation for federal support of young scientists.

References

- [1] S. McBreen, F. Quilligan, B. McBreen, L. Hanlon, and D. Watson, “Temporal properties of the short gamma-ray bursts,” *Astronomy and Astrophysics*, vol. 380, no. 2, pp. L31–L34, 2001.
- [2] S. Karpov, G. Beskin, A. Biryukov, et al., “Optical camera with high temporal resolution to search for transients in the wide field,” *Nuovo Cimento della Societa Italiana di Fisica C*, vol. 28, no. 4-5, pp. 747–750, 2005.
- [3] A. Piccioni, C. Bartolini, C. Cosentino, et al., “An updating about flip: a photometer devoted to the search for optical flashes from gamma-ray bursts,” in *AIP Conference Proceedings*, first-name middle-name M. Friedlander, N. Gehrels, and D. J. Macomb, Eds., vol. 280 of *American Institute of Physics Conference Series*, pp. 1152–1155, 1993.
- [4] B. Paczyński, “Monitoring all sky for variability,” *Publications of the Astronomical Society of the Pacific*, vol. 112, no. 776, pp. 1281–1283, 2000.
- [5] S. D. Barthelmy, “Observing strategies using GCN,” in *Proceedings of the 4th Huntsville Symposium on Gamma-Ray Bursts*, C. A. Meegan, R. D. Preece, and T. M. Koshut, Eds., vol. 428 of *AIP Conference Proceedings*, pp. 129–133, 1998.
- [6] K. L. Page, R. Willingale, J. P. Osborne, et al., “GRB 061121: broadband spectral evolution through the prompt and afterglow phases of a bright burst,” *Astrophysical Journal*, vol. 663, no. 2 I, pp. 1125–1138, 2007.
- [7] S. A. Yost, H. F. Swan, E. S. Rykoff, et al., “Exploring broadband GRB behavior during γ -ray emission,” *Astrophysical Journal*, vol. 657, no. 2 I, pp. 925–941, 2007.
- [8] W. T. Vestrand, P. R. Wozniak, J. A. Wren, et al., “A link between prompt optical and prompt γ -ray emission in γ -ray bursts,” *Nature*, vol. 435, no. 7039, pp. 178–180, 2005.
- [9] C. Akerlof, R. Balsano, S. Barthelmy, et al., “Observation of contemporaneous optical radiation from a γ -ray burst,” *Nature*, vol. 398, no. 6726, pp. 400–402, 1999.
- [10] T. Tamagawa, F. Usui, Y. Urata, et al., “The search for optical emission on and before the GRB trigger with the WIDGET

- telescope,” *Nuovo Cimento della Societa Italiana di Fisica C*, vol. 28, no. 4-5, pp. 771–774, 2005.
- [11] K. Borozdin, S. Brumby, M. Galassi, et al., “Real-time detection of optical transients with RAPTOR,” in *Astronomical data Analysis II*, vol. 4847 of *Proceedings of SPIE*, pp. 344–353, Waikoloa, Hawaii, USA, August 2002.
 - [12] A. J. Castro-Tirado, J. Soldán, M. Bernas, et al., “The burst observer and optical transient exploring system (BOOTES),” *Astronomy and Astrophysics Supplement Series*, vol. 138, no. 3, pp. 583–585, 1999.
 - [13] A. J. C. Tirado, M. Jelínek, S. Vítek, et al., “A very sensitive all-sky CCD camera for continuous recording of the night sky,” in *Advanced Software and Control for Astronomy II*, vol. 7019 of *Proceedings of SPIE*, Marseille, France, June 2008.
 - [14] A. Burd, M. Cwiok, H. Czyrkowski, et al., “Pi of the sky—all-sky, real-time search for fast optical transients,” *New Astronomy*, vol. 10, no. 5, pp. 409–416, 2005.
 - [15] D. Eichler, M. Livio, T. Piran, and D. N. Schramm, “Nucleosynthesis, neutrino bursts and γ -rays from coalescing neutron stars,” *Nature*, vol. 340, no. 6229, pp. 126–128, 1989.
 - [16] S. E. Woosley, “Gamma-ray bursts from stellar mass accretion disks around black holes,” *Astrophysical Journal*, vol. 405, no. 1, pp. 273–277, 1993.
 - [17] B. Paczyński, “Are gamma-ray bursts in star-forming regions?” *Astrophysical Journal*, vol. 494, no. 1, part 2, pp. L45–L48, 1998.
 - [18] G. M. Beskin, V. Plokhhotnichenko, C. Bartolini, et al., “Catching the light curve of flaring GRBs: the opportunity offered by scanning telescopes,” *Astronomy and Astrophysics Supplement Series*, vol. 138, no. 3, pp. 589–590, 1999.
 - [19] D. Eichler and G. Beskin, “Optical search for extraterrestrial intelligence with air Cerenkov telescopes,” *Astrobiology*, vol. 1, no. 4, pp. 489–493, 2001.
 - [20] I. Zolotukhin, G. Beskin, A. Biryukov, et al., “Optical camera with high temporal resolution to search for transients in the wide field,” *Astronomische Nachrichten*, vol. 325, no. 6-8, p. 675, 2004.
 - [21] F. Zerbi, G. Chincarini, M. Rodonò, et al., “REM-Rapid Eye Mount. A fast slewing robotized telescope to monitor the prompt infrared afterglow of GRBs,” in *Proceedings of the 2nd Workshop on Gamma-Ray Bursts in the Afterglow Era*, E. Costa, F. Frontera, and J. Hjorth, Eds., p. 434, 2001.
 - [22] E. Molinari, S. Bondar, S. Karpov, et al., “TORTOREM: two-telescope complex for detection and investigation of optical transients,” *Nuovo Cimento della Societa Italiana di Fisica B*, vol. 121, no. 12, pp. 1525–1526, 2006.
 - [23] G. Beskin, V. Bad’in, A. Biryukov, et al., “FAVOR (FAst Variability Optical Registration)—a two-telescope complex for detection and investigation of short optical transients,” *Nuovo Cimento della Societa Italiana di Fisica C*, vol. 28, no. 4-5, pp. 751–754, 2005.
 - [24] S. Karpov, G. Beskin, S. Bondar, et al., “GRB 080319B: RAPTOR observations of a naked eye burst,” in *GRB Coordinates Network Circular*, vol. 7452, 2008.
 - [25] J. L. Racusin, S. V. Karpov, M. Sokolowski, et al., “Broadband observations of the naked-eye γ -ray burst GRB 080319B,” *Nature*, vol. 455, no. 7210, pp. 183–188, 2008.
 - [26] G. Beskin, S. Karpov, S. Bondar, et al., “Fast optical variability of Naked-Eye Burst—manifestation of periodic activity of internal engine,” <http://arxiv.org/abs/0905.4431>.
 - [27] S. Karpov, G. Beskin, S. Bondar, et al., “Monitoring the sky in sub-second domain,” *Advances in Astronomy*, vol. 2010, Article ID 784141, 8 pages, 2010.
 - [28] American Department of Defense satellite ephemerides database, <http://www.space-track.org/>.
 - [29] E. Bertin and S. Arnouts, “SExtractor: software for source extraction,” *Astronomy & Astrophysics*, vol. 117, no. 2, pp. 393–404, 1996.
 - [30] E. Høg, C. Fabricius, V. V. Makarov, et al., “The Tycho-2 Catalogue of the 2.5 million brightest stars,” *Astronomy & Astrophysics*, vol. 363, no. 1, pp. L27–L30, 2000.
 - [31] A. Guarnieri, C. Bartolini, G. Beskin, et al., “GRB 060719: TORTOREM optical upper limits,” *GRB Coordinates Network, Circular Service*, 5372, 1, 2006.
 - [32] S. Karpov, G. Beskin, S. Bondar, et al., “GRB 061202: TORTOREM optical upper limits,” *GRB Coordinates Network, Circular Service*, 5897, 1, 2006.
 - [33] S. Karpov, G. Beskin, S. Bondar, et al., “GRB 061218: TORTOREM optical upper limits,” *GRB Coordinates Network, Circular Service*, 5941, 1, 2006.
 - [34] J. L. Racusin, N. Gehrels, S. T. Holland, et al., *GRB Coordinates Network Circular*, 7427, 1, 2008.
 - [35] M. Cwiok, W. Dominik, G. Kaspruwicz, et al., “GRB 080319b prompt optical observation by Pi-of-the-Sky,” *GRB Coordinates Network, Circular Service*, 7439, 1, 2008.
 - [36] P. Wozniak, W. T. Vestrand, J. Wren, and H. Davis, “GRB 080319B: RAPTOR observations of a naked eye burst,” *GRB Coordinates Network, Circular Service*, 7464, 1, 2008.
 - [37] D. Kocevski, F. Ryde, and E. Liang, “Search for relativistic curvature effects in gamma-ray burst pulses,” *Astrophysical Journal*, vol. 596, no. 1, pp. 389–400, 2003.
 - [38] G. Beskin, S. Karpov, S. Bondar, et al., “TORTORA discovery of naked-eye burst fast optical variability,” in *Nanjing Gamma-Ray Burst Conference*, Y.-F. Huang, Z.-G. Dai, and B. Zhang, Eds., vol. 1065 of *AIP Conference Proceedings*, pp. 251–254, 2008.
 - [39] R. Margutti, C. Guidorzi, G. Chincarini, F. Pasotti, S. Covino, and J. Mao, “Temporal variability of GRB early X-ray afterglows and GRB080319B prompt emission,” in *Nanjing Gamma-Ray Burst Conference*, Y.-F. Huang, Z.-G. Dai, and B. Zhang, Eds., vol. 1065 of *AIP Conference Proceedings*, pp. 259–262, 2008.
 - [40] G. Beskin, V. de-Bur, S. Karpov, et al., “Search for optical signals from extra-terrestrial intelligence at SAO RAS: past, present and future,” *Bulletin of Special Astrophysical Observatory*, vol. 60-61, pp. 217–225, 2007.

Research Article

Fast Universal Spectrophotopolarimeter for Robotic Telescopes

**Vladimir Plokhotnichenko,¹ Grigory Beskin,¹ Sergey Karpov,¹ Sergey Bondar,²
Vjacheslav de-Boer,¹ Alexandre Lioubetski,³ and Dmitry Badjin⁴**

¹ *Special Astrophysical Observatory, Russian Academy of Sciences, Nizhniy Arkhyz 369167, Russia*

² *Institute for Precise Instrumentation, Nizhniy Arkhyz 369167, Russia*

³ *VOK Industries, Rostov-on-Don 344000, Russia*

⁴ *Sternberg Astronomical Institute, Moscow State University, Moscow 119992, Russia*

Correspondence should be addressed to Grigory Beskin, beskin@sao.ru

Received 28 June 2009; Revised 10 December 2009; Accepted 10 December 2009

Academic Editor: Alberto J. Castro-Tirado

Copyright © 2010 Vladimir Plokhotnichenko et al. This is an open access article distributed under the Creative Commons Attribution License, which permits unrestricted use, distribution, and reproduction in any medium, provided the original work is properly cited.

FUSP is the automatic multimode spectrophotopolarimeter aimed to the study of fast optical transients in the photometric, photopolarimetric (instant measurement of linear polarization), and spectropolarimetric (with or without the slit) modes. The mode change is automatic depending on the transient brightness and the purposes of the observations and may be performed in half a second. The instrument may be equipped with either fast EM-CCD or a position-sensitive detector which may provide temporal resolution up to 1 microsecond. FUSP is the robotic instrument for the robotic telescopes.

1. Introduction

Until now, the gamma-ray bursts, most energetic events in the Universe, remain mysterious. It is, however, clear that they are generated by a compact relativistic objects such as neutron stars or, more probably, the black holes, either isolated or in binary systems. Internal structure and dynamics of the gamma-ray burst internal engine is inevitably reflected in the temporal structure of the burst emission. Indeed, while the duration of bursts varies in 0.01–100 seconds range, their light curves in 80% of cases have substructures, while in 66% the variability time scales are less than 0.1 of total duration of the event [1]. Moreover, light curves of several long bursts display a millisecond temporal structures [2]. At the same time, some models of these events predict the appearance of a significant optical emission along with gamma-ray one, which may reach 8^m–12^m [3–5]. This is especially important as, for a reasonable estimations of a spectral shape, the number of optical photons must be 100–1000 times larger than gamma-ray ones. Unique results of nearly synchronous detection of optical emission from GRB990123 [6] (optical observations started 22 seconds after the burst onset) and completely synchronous from GRB080319B [7] (optical observations

performed by a TORTORA [8] wide-field camera with high temporal resolution, which monitored the position of the burst before the event itself) confirm this conclusion. Therefore, the search for, detection of and the detailed, high temporal resolution investigation of optical transients accompanying gamma-ray burst may provide the decisive information on their nature.

It is clear that such observations have to be performed independently from information from space telescopes, as the delays of their triggers may be unacceptably high. They may be replaced by optical monitoring cameras with significant field of view (larger than 100 square degrees), comparable to the ones of satellites. Such cameras may have small, 15–20 cm, objectives, while the information on optical transients they detect may immediately be passed to a larger, 50–200 cm in diameter, robotic telescope for a detailed investigation which may extract the maximum amount of information on the event—temporal, photometric, spectral and polarimetric. Such a two-telescope complex has been proposed as a result of development of FAVOR prototype fast wide-field optical camera [9] and is being implemented as a combination of TORTORA wide-field camera and REM robotic telescope [8].

Such a complex must satisfy the following set of obvious conditions:

- (i) detection of a transient by a wide-field camera in real-time and formation of a pointing trigger for follow-up instruments in 0.5–1 second since the onset of event,
- (ii) minimal time of distribution of this trigger to one or several robotic telescopes,
- (iii) minimal time of repointing of robotic telescope towards the transient (about 1–2 seconds for angular speed of 5–7°/s),
- (iv) maximal temporal resolution of both instruments—better than 0.5 second for wide-field monitoring camera and better than 0.001 second for follow-up instruments,
- (v) extraction of maximal amount of information by the follow-up instrument—temporal, spatial, photometric, spectral, and polarimetric one for each detected photon; therefore, this instrument has to be the spectropolarimeter,
- (vi) the system must perform completely automatic operation.

Fast Universal SpectroPolarimeter (FUSP) with high temporal resolution is meant to be used on a medium-size telescope as an integral part of a two-telescope complex [8, 10, 11], or any other telescope for observations with high temporal resolution. The instrument is capable of simultaneous measurements of 3 Stokes parameters of object emission in UBV_R bands as well as of objects spectra in a 320–700 nm range, both in slit-less mode and with a spectral slit, with temporal resolution down to 1 microsecond.

Below, we describe the design of this instrument and its use cases inside the two-telescope complex.

2. Modes of Operation and Optical Scheme of FUSP

The instrument can perform observations in one of three modes:

- (i) photopolarimetry with UBV_R filters,
- (ii) slitless spectropolarimetry,
- (iii) spectropolarimetry with slit.

In the first mode, the photometry and the measurement of linear polarizations in one of UBV_R filters are performed for all objects inside 3–5′ instrument field of view. In the second one, four spectra with different orientation of polarization plane are registered for each object, while in the third mode spectra are acquired for the object on the slit only (see Figure 1).

The instrument optical scheme is presented in Figure 2.

The 2″ × 5′ spectral slit is placed in the telescope focal plane, and may be replaced with the field lens to achieve larger field of view. The light reflected from mirrors

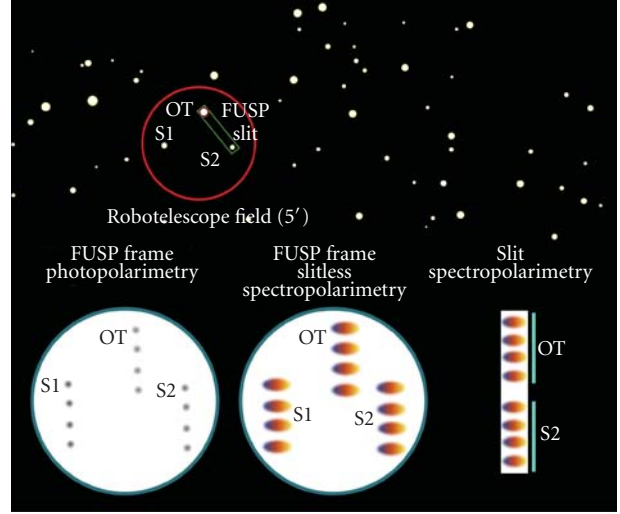


FIGURE 1: Images of FUSP field of view in different operational modes.

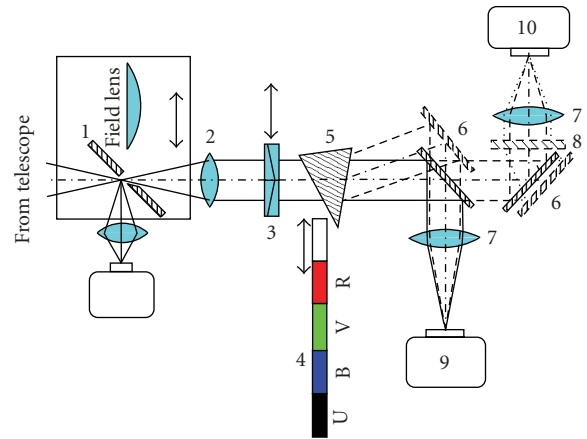


FIGURE 2: Concept of the FUSP. 1: movable mirror with the slit for a transmission of light to TV guiding camera, which may be replaced with the field lens; 2: collimator; 3: double Wollaston prism (polarizer); 4: movable U, B, V, R and white light filters; 5: movable spectral prism; 6: units of light transmission mirrors, movable synchronously with 5 and 8; 7: objectives; 8: diffraction grating; 9: Position-Sensitive detector; 10: EM-CCD. The field lens is used on a telescopes with large relative apertures to achieve wider field of view without vignetting; for systems with smaller D/F ratio it may be omitted.

(1) on edges of the slit is directed towards the guiding camera, aimed for a precise pointing of telescope towards the object. On-axis light beam passes through the collimator (2) and reaches one of two detectors (9, 10). On its way it may be decomposed into spectral (5) and polarimetric (3) components and passed through one of UBV_R color filters (4). All necessary components for that are inserted in the parallel on-axis beam automatically after receiving the information on the source type and brightness according to a mode-selection algorithms.



FIGURE 3: Two possible photodetectors which may be used in FUSP. (a) iXon^{EM}+888 EM-CCD from Andor. (b) Position-Sensitive Detector with GaAs-photocathode, developed at Special Astrophysical Observatory of Russian Academy of Sciences.

All optical parts of the instrument are manufactured from the materials with high UV transparency. The objective (7) focal length is 3 times larger than the collimator one, to cover the whole photocathode of PSD with region of interest in focal plane.

Below are details on several components of the FUSP.

Double Wollaston prism (3) is used in a way similar to one described in [12], to decompose the initial parallel light beam into four ones corresponding to polarization planes separated by 45° . Photometry of four corresponding object images gives three Stokes parameters, that is, linear polarization.

Units of light transmission mirrors (6) allow to equip the instrument with two photodetectors, EM-CCD (10) and Position-Sensitive Detector (9), simultaneously, and use any of them in either imaging or spectral mode, by inserting or removing corresponding units (4, 5). The objective (7) parameters are selected so that the field of view linear size coincides with detector input size. When working in spectral mode, with either prism or diffraction grating, corresponding mirror (6) positions are selected.

3. FUSP Detectors

EM CCD iXon^{EM}+888 is an $1\text{ k} \times 1\text{ k}$ back-illuminated EMCCD produced by Andor [13], and has a single photon detection capability without an image intensifier. The quantum efficiency is up to 90%. The operational frame rates are from 8.9 per second (full frame) till 310 per second (8×8 binning with 128×128 pixels work area). The pixel size is $13\text{ }\mu\text{m}$ (see Figure 3).

Position-Sensitive Detector, developed at Special Astrophysical Observatory of Russian Academy of Sciences, is a vacuum tube with multialkali [14] or GaAs [15] photocathode and microchannel plates to multiply the electron avalanches. Coordinates of incoming photons are measured by means of multisection metallic collector anode. Input area is 18 mm in diameter, with 20–70 μm resulting resolution

element. Quantum efficiency is up to $\sim 30\%$ for GaAs and up to $\sim 15\%$ for multialkali photocathode, and acquisition dead time is about 1 microsecond. The accuracy of photon arrival time measurement is also 1 microsecond, with limiting detection rate of $\sim 10^5$ counts per second from the whole photocathode (see Figure 3).

The microsecond temporal resolution is achieved by means of “Quantochron 4-48” acquisition system [16]—a fast chronometer intended for measurement and acquisition of characteristics of standard discrete event sequences, which is a further development of a data acquisition system described in [17, 18]. It is based on a SPARTAN Field Programmable Gate Array, is programmed in VHDL logical matrices design language, and is designed to interface with acquisition PC through the standard PCI bus. The “Quantochron 4-48” is synchronized with GPS receiver and allows to register the photon time of arrivals with 30-nanosecond accuracy; its internal dead time is also 30-nanosecond, and the limiting flux it able to register without data losses is 10^6 counts per second.

4. Principles of Operation

Upon receiving of a new source coordinates from either gamma-ray telescope or wide-field monitoring camera, the robotic telescope equipped with FUSP is pointed towards it. Inside the instrument, the light is reflected from the mirror edges of the slit towards the TV guide, which may be used to correct the pointing and precisely place the transient onto the slit. Then, if the object is bright enough, the slit opens and the light passes through the optical units towards the photodetectors. If, however, the object is too faint to be localized by TV guide, the slit unit moves out along the slit direction, and the field lens is inserted into the light beam. In this regime, all photons from FUSP field of view sky region may be recorded for a detailed study later.

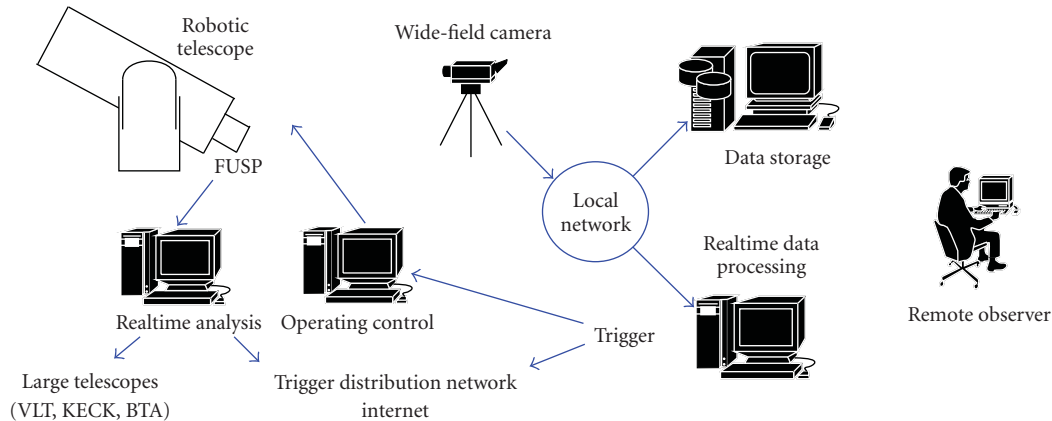


FIGURE 4: General scheme of a two-telescope complex for autonomous detection and investigation of short optical transients. The robotic telescope is equipped with FUSP and is meant to study transients detected by a wide-field monitoring camera in a few seconds after their onset.

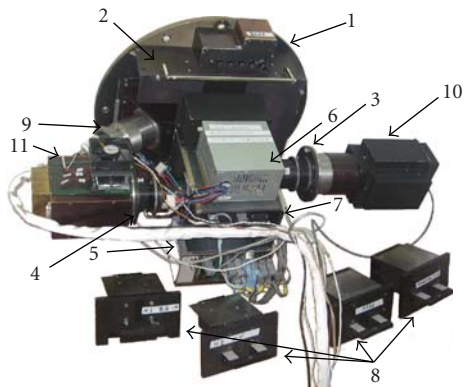


FIGURE 5: Overview of the Multimode Panoramic PhotoSpectroPolarimeter (MPPPP). 1: telescope mounting flange; 2: focal plane unit; 3 and 4: flanges for mounting the Position-Sensitive Detectors or EM-CCDs; 5: instrument state and motors control unit; 6: power supply; 7: mount point for interchangeable light transformation units; 8: set of optical units; 9: TV-CCD guide; 10 and 11: two PSDs, which may be replaced with EM-CCDs.

All the units are configured and inserted into the light beam automatically, according to the brightness of the transient and the program of observations.

5. Desired Performance

The FUSP instrument is supposed to be used on a small-aperture robotic telescopes with relative aperture smaller than 1:4. The spectral range is defined mainly by the type of detector used—for PSD it is from 350 till 700 nm, while for typical CCD it is 400–700 nm. The spectral resolution may vary from 10 to 100 and is defined by the telescope focal length. Temporal resolution is 1 microsecond for PSD photon counter and is down to 1 ms for fast CCDs.

For a typical 60 cm telescope, in photopolarimetric mode the instrument is able to measure 10% linear polarization

(3 Stokes parameters simultaneously) at a 5σ level ($S/N = 5$, polarization measurement accuracy of about 2%) for a $V \approx 13.5^m$ object using 1-second exposure. In slitless spectropolarimetric mode under moderate seeing and sky brightness conditions it is possible to measure a 10%–15% linear polarization at a level of $S/N = 5$ for an object with $V \approx 11.5^m$ – 12^m in 1 second. For a spectropolarimetry with slit the accuracy of polarization measurements for 1-second exposure is about 2% for $V \approx 11.5^m$ – 12^m objects.

6. FUSP inside the Two-Telescope Complex

The FUSP instrument may, in principle, be used alone, for the investigation of objects with known positions, such as black hole candidates, flaring stars, and pulsars and so forth. For gamma-ray bursts, however, the positions are not known in advance; so the instrument must be accompanied by the wide-field monitoring camera, able to perform continuous monitoring of large sky regions, to automatically detect and perform preliminary classification of optical transients, and to pass their positions to FUSP-equipped telescope. Scheme of such two-telescope complex is shown in Figure 4.

The wide-field monitoring camera performs the real-time analysis of its data, detects the appearance of new transients or flux change of previously visible objects, performs the basic classification of such events and, if the transient looks like the flash from GRB, passes its information to robotic telescope equipped with FUSP. Control software then initiates the repointing of robotic telescope and, while it is moving, decides on an optimal mode of operation of the instrument depending on transient brightness, and reconfigures the FUSP accordingly.

7. Current Status of the Instrument

We already built and presently use in observations on a Russian 6-m telescope the prototype of FUSP—the Multimode Panoramic PhotoSpectroPolarimeter (MPPPP) [19].

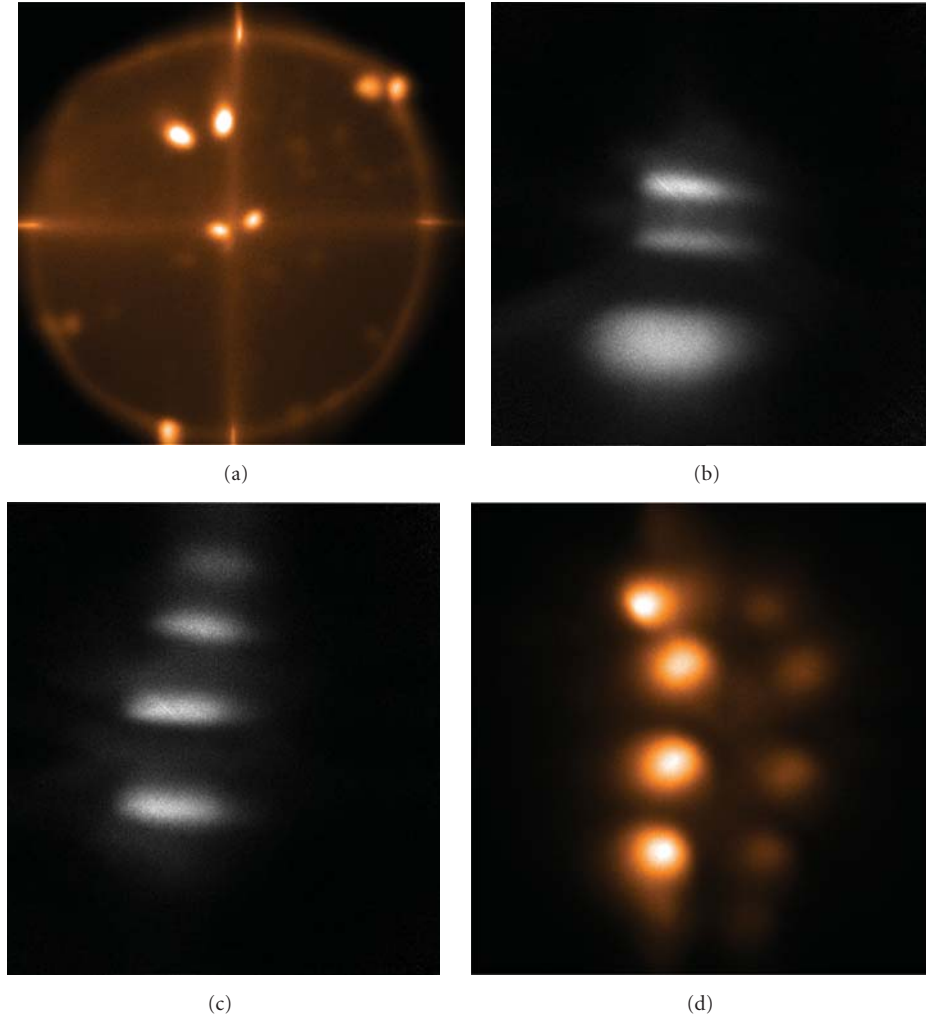


FIGURE 6: The different modes of MPPP operation. (a) One-color photopolarimetric mode with two images of each object in wide field. (b) Spectroscopic mode with low-resolution spectrum of object, along with ones of comparison star and the region of the sky used for calibration. (c) Spectropolarimetric with object spectra in four different polarizations. (d) Multicolor photopolarimetric mode with four images of object in two colors.

The main difference of this instrument is what it is purposed for a preplanned observations, and so it lacks the remotely controlled mode change capability. The needed optical unit is inserted into the light beam before the observations manually. This instrument with the set of optical units, providing different modes of operation is shown in Figure 5. Example images of objects observed with instrument in different regimes are shown in Figure 6.

Acknowledgments

This work was supported by the Bologna University Progetti Pluriennali 2003, by Grants of CRDF (no. RP1-2394-MO-02), RFBR (no. 04-02-17555, 06-02-08313, and 09-02-12053-ofi-m), INTAS (04-78-7366), and by the Presidium of the Russian Academy of Sciences Program. SoKarpov has also been supported by grant of the President of Russian Federation for federal support of young scientists.

References

- [1] T. Piran, "The physics of gamma-ray bursts," *Reviews of Modern Physics*, vol. 76, no. 4, pp. 1143–1210, 2005.
- [2] S. McBreen, F. Quilligan, B. McBreen, L. Hanlon, and D. Watson, "Temporal properties of the short gamma-ray bursts," *Astronomy & Astrophysics*, vol. 380, no. 2, pp. L31–L34, 2001.
- [3] D. Eichler and G. Beskin, "Nonthermal optical transients from relativistic fireballs," *Physical Review Letters*, vol. 85, no. 13, pp. 2669–2672, 2000.
- [4] E. P. Liang, A. Crider, M. Böttcher, and I. A. Smith, "GRB 990123: the case for saturated comptonization," *Astrophysical Journal*, vol. 519, no. 1, pp. L21–L24, 1999.
- [5] X. F. Wu, Z. G. Dai, Y. F. Huang, and T. Lu, "Optical flashes and very early afterglows in wind environments," *Monthly Notices of the Royal Astronomical Society*, vol. 342, no. 4, pp. 1131–1138, 2003.
- [6] C. Akerlof, R. Balsano, S. Barthelmy, et al., "Observation of contemporaneous optical radiation from a γ -ray burst," *Nature*, vol. 398, no. 6726, pp. 400–402, 1999.

- [7] J. L. Racusin, S. V. Karpov, M. Sokolowski, et al., “Broadband observations of the naked-eye γ -ray burst GRB 080319B,” *Nature*, vol. 455, no. 7210, pp. 183–188, 2008.
- [8] E. Molinari, S. Bondar, S. Karpov, et al., “TORTOREM: two-telescope complex for detection and investigation of optical transients,” *Nuovo Cimento della Societa Italiana di Fisica B*, vol. 121, no. 12, pp. 1525–1526, 2006.
- [9] S. Karpov, G. Beskin, A. Biryukov, et al., “Optical camera with high temporal resolution to search for transients in the wide field,” *Nuovo Cimento della Societa Italiana di Fisica C*, vol. 28, no. 4-5, pp. 747–750, 2005.
- [10] S. Karpov, D. Bad’in, G. Beskin, et al., “FAVOR (FAst Variability Optical Registration)—two-telescope complex for detection and investigation of short optical transients,” *Astronomische Nachrichten*, vol. 325, no. 6-8, p. 677, 2004.
- [11] G. Beskin, V. Bad’in, A. Biryukov, et al., “FAVOR (FAst Variability Optical Registration)—a two-telescope complex for detection and investigation of short optical transients,” *Nuovo Cimento della Societa Italiana di Fisica C*, vol. 28, no. 4-5, pp. 751–754, 2005.
- [12] E. Oliva, “Wedged double Wollaston, a device for single shot polarimetric measurements,” *Astronomy and Astrophysics Supplement Series*, vol. 123, no. 3, pp. 589–592, 1997.
- [13] “Andor Technology,” <http://www.andor.com>.
- [14] V. Debur, T. Arkhipova, G. Beskin, et al., “Position-sensitive detector for the 6-m optical telescope,” *Nuclear Instruments and Methods in Physics Research, Section A*, vol. 513, no. 1-2, pp. 127–131, 2003.
- [15] V. de-Bur, A. Terekhov, S. Kosolobov, et al., “Position-sensitive detector with GaAs photocathode and high time resolution,” in *Time Resolution Astrophysics: The Universe at Sub-Second Timescales*, D. Phelan, O. Ryan, and A. Shearer, Eds., vol. 984 of *American Institute of Physics Conference Series*, pp. 186–193, 2008.
- [16] V. L. Plokhotnichenko, A. V. Solin, and A. G. Tikhonov, “The “Quantochron 4–48” facility for registration of random fluxes of multidimensional signals,” *Astrophysical Bulletin*, vol. 64, no. 2, pp. 204–212, 2009.
- [17] A. V. Zhuravkov, A. A. Pimonov, and V. L. Plokhotnichenko, ““QUANTOCHRON”—a multichannel time-to-code converter,” *Bulletin of the Crimean Astrophysical Observatory*, vol. 37, pp. 159–172, 1994.
- [18] V. Plokhotnichenko, G. Beskin, V. Debur, A. Panferov, and A. Panferova, “The multicolor panoramic photometer-polarimeter with high time resolution based on the PSD,” *Nuclear Instruments and Methods in Physics Research, Section A*, vol. 513, no. 1-2, pp. 167–171, 2003.
- [19] V. Plokhotnichenko, G. Beskin, V. de-Bur, et al., “Devices and software for optical panoramic observations with microsecond time resolution,” in *High Time Resolution Astrophysics: The Universe at Sub-Second Timescales*, D. Phelan, O. Ryan, and A. Shearer, Eds., vol. 984 of *American Institute of Physics Conference Series*, pp. 194–201, 2008.

Research Article

Hexasphere—Redundantly Actuated Parallel Spherical Mechanism as a New Concept of Agile Telescope

Michael Valasek,¹ Josef Zicha,² Martin Karasek,¹ and Rene Hudec^{3,4}

¹ Department of Mechanics, Biomechanics and Mechatronics, Faculty of Mechanical Engineering, Czech Technical University in Prague, Technická 4, 166 07 Praha 6, Czech Republic

² Department of Instrumentation and Control Engineering, Faculty of Mechanical Engineering, Czech Technical University in Prague, Technická 4, 166 07 Praha 6, Czech Republic

³ Department of Radioelectronics, Faculty of Electrical Engineering, Czech Technical University in Prague, Technická 2, 166 07 Praha 6, Czech Republic

⁴ Astronomical Institute, Academy of Sciences of the Czech Republic, 251 65 Ondřejov, Czech Republic

Correspondence should be addressed to Rene Hudec, rhudec@asu.cas.cz

Received 1 June 2009; Accepted 11 January 2010

Academic Editor: Alberto J. Castro-Tirado

Copyright © 2010 Michael Valasek et al. This is an open access article distributed under the Creative Commons Attribution License, which permits unrestricted use, distribution, and reproduction in any medium, provided the original work is properly cited.

The paper deals with the description of a new concept for a spherical mechanism for agile telescopes. It is based on redundantly actuated parallel kinematical structure. Due to the three times overactuated structure and application of several further innovative concepts, the Hexasphere achieves the movability of ± 100 degrees. This enables the use of a Hexasphere as the basis for mounts of telescopes. Such telescopes can be optimized for minimum weight or for maximum dynamics. The proposed mechanism is expected to play a role in novel robotic telescopes nowadays used in many fields of astronomy and astrophysics, with emphasis on automated systems for alert observations of celestial gamma-ray bursts.

1. Introduction

There are many mechanisms for the realization of spherical motions. Spherical mechanisms which enable the rotation and orientation of an object in the space are used for many important operations. They are in the mechanisms of swivel heads with spindles for machine tools that create the basis of an absolute majority of machine tools for 5 axes machining. The assemblies of telescopes, that is, the mechanisms for their motion, are also spherical mechanisms. Another group consists of mechanisms for rotation of different antennas. Many applications of spherical mechanisms are for the pointing of optical beams.

The absolute majority of spherical mechanisms are based on the Cardan hinge. Its advantage is high movability, often $\pm 90^\circ$. The first basic disadvantage of Cardan hinges as serial kinematical structures is that they consist of a sequence of successive rotational motions. This leads to the necessity that the subsequent rotations must carry the drive with and

thus increase the mass of the construction. Besides that, the frame of the construction is loaded detrimentally by bending. The consequences are a disadvantageous ratio between mass and stiffness and the smaller dynamic capabilities of the mechanism. The addition of errors in the chain of partial motions leads to a lower positioning accuracy. The second basic disadvantage of Cardan hinges is that the zenith position is singular, making it impossible to carry out a continuous trajectory between all positions in the workspace.

All of these problems were circumvented by the adoption of parallel kinematical structures [1] where the only form of loading is either compression or stress, all motors are situated on the machine frame, and the length of error chains with summed up errors is significantly lower. The disadvantage of simple parallel kinematical structures is that their workspace is limited by singular positions and collisions, the mostly used spherical joints acquire lower stiffness when compared to sliding or rotational joints and nonlinear kinematic transformation between motors and the



FIGURE 1: Telescope HPT Cerro Armazones, Chile.

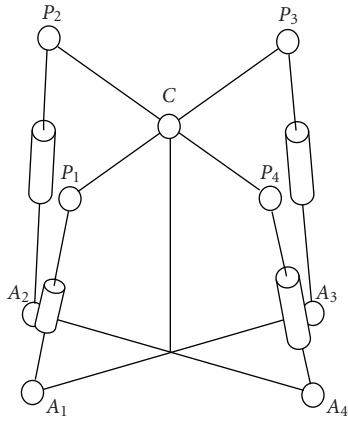


FIGURE 2: Parallel spherical mechanism.

end-effector requires a short sampling period, in order to achieve required accuracy.

The mounts of traditional telescopes both on earth and in orbit (on satellites) are based on the Cardan mechanism. The spherical mechanisms based on Cardan mount as serial mechanisms suffer from the zenith singularity and large mass because of frame loading by bending. This can be improved by mechanisms based on parallel kinematical structure (e.g., Hexapod) where the loading is changed to tension-compression. The recently built hexapod-based telescope HPT (Figure 1) has only 1/5 of the mass of a traditional telescope but can tilt by only $\pm 47^\circ$ before it reaches the singular positions and would collapse [2]. This limitation can be significantly extended if the parallel kinematical structure is redundantly actuated [3, 4]. Based on this idea, a new spherical mechanism suitable for telescope mounts—named Hexasphere—was proposed and a functional kinematical lab model was built. It has demonstrated that Hexasphere

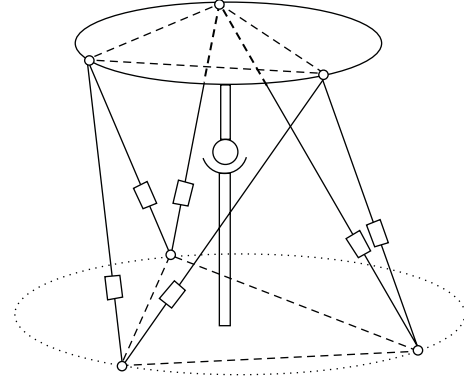


FIGURE 3: Hexasphere kinematical structure.

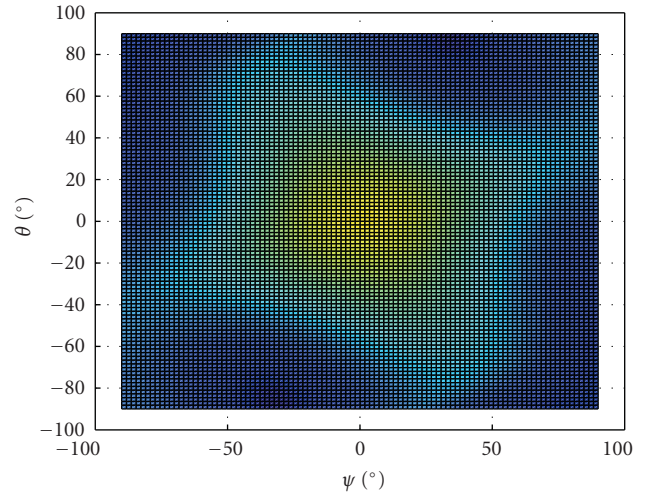


FIGURE 4: The dexterity of spherical mechanism from Figure 2.

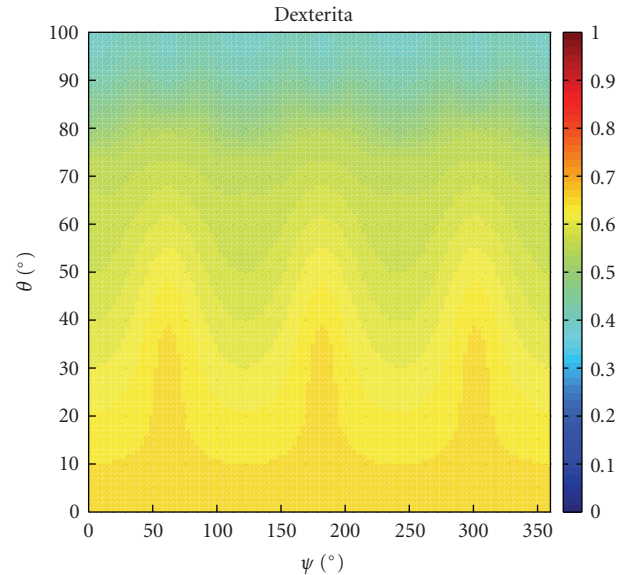


FIGURE 5: The dexterity of Hexasphere.

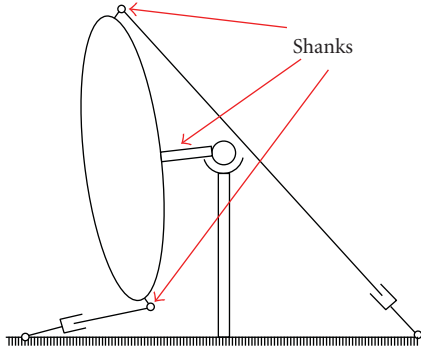


FIGURE 6: Design features of Hexasphere.

can reach the workspace at ± 100 degrees. The experience with parallel kinematical structures is that it can achieve high stiffness and agile dynamics with low masses. The only drawback of limited workspace, due to the kinematical singularities, can be removed by redundant actuation and has been demonstrated by Hexasphere.

2. The Hexasphere Concept

The initial motivation came from [5] where the spherical mechanism in Figure 2 was proposed. The claim was that the problem with singularities (dexterity) had been solved. This structure has been analyzed for the dexterity.

The position of the platform in the space is described by the coordinates q , and the positions of the drives (extensions of struts) are described by the coordinates z . These coordinates are constrained by the constraints

$$f(q, z) = 0. \quad (1)$$

The dexterity is defined as

$$D = \frac{1}{\text{cond}(J_z^{-1}J_q)}, \quad (2)$$

where J_z and J_q are the Jacobians of the constraints (1) with the respect to the coordinates z and q . The dexterity ranges from 0 (the worse value corresponding to the singularity) to 1 (the best value). It expresses the transfer between the input-output velocities and the input-output forces of the mechanism.

Using this approach, the dexterity for the mechanism in Figure 2 has been computed. The range of the dexterity is 0.0065 to 0.6307 (Figure 4). It is nonzero and the workspace is free of singularities but the dexterity changes over a large interval (a factor of a hundred) and the minimum values are very close to zero. It is disadvantageous because the dexterity describes the ratio between the driving force and the acting forces in the end-effector.

To solve these problems, the concept of a Hexasphere [6] has been proposed (Figure 3). The principle of redundant actuation [1] has been applied in order to improve the dexterity. The redundant actuation alleviates the problems associated with parallel kinematics: singularities do not

occur, surprisingly the collisions can be limited, the stiffness and dynamics are significantly increased, kinematic accuracy is improved, and online calibration is possible. The result is that redundantly actuated parallel kinematical structures are functionally equivalent to machines with serial kinematical structures but have significantly improved mechanical properties (stiffness, dynamics, accuracy). This has been successfully demonstrated on the machines Trijoint 900H [7] and Sliding Star [4] for Cartesian translational motion. The remaining kinds of mechanisms with serial kinematical structure are the spherical mechanisms based on Cardan hinges. Although one of the most successful applications of parallel kinematical structures is the parallel swivel head for 5 axes machining, it reaches only limited movability. Finding fully functional equivalent of Cardan hinges with movability $\pm 90^\circ$ using parallel kinematical structures has been an open challenge for a long time.

The concept of a Hexasphere has been used as the basis of the mechanism from Figure 2 and it uses the principle of redundant actuation. The number of redundant struts has been increased. Hexasphere is a combination of Hexapod for actuation and a platform suspension on a passive spherical joint. Hexasphere is three times redundantly actuated. The influence of the high degree of actuator redundancy is very positive on the dexterity. The dexterity of Hexasphere has been analyzed by the same approach: its results are in Figure 5. The dexterity ranges only in the interval from 0.33 to 0.65. The dexterity changes in the whole workspace only twice and its values are quite high. The required actuation forces are just 2-3 times higher than the acting forces in the end-effector.

3. Design of Hexasphere

The mechanism of Hexasphere has the open challenge of parallel spherical mechanism with large tilting angles positively closed. It demonstrates that the redundantly actuated parallel kinematical structure enables the spherical motion now with movability $\pm 100^\circ$ and preservation of all advantages of parallel mechanisms. The new solution principles that enable to create a Hexasphere are the following. The platform is connected to the frame by a central spherical joint. Hence the mechanism has only 3 degrees of freedom and for the motion it would suffice just 3 actuators. However, they enable the motion just in small extent of angles because for large motions the singular positions occur when the platform acquires additional uncontrolled degree of freedom and collapses. Therefore, the platform is suspended on 6 struts. The result is not only the removal of singularities but also very good dexterity in the whole workspace. Another important principle is that the struts are placed on shanks due to which the collisions between the struts and the platform do not happen for large rotations (Figure 6). The other dimensions must be also adjusted accordingly.

Besides the mentioned solution principles of a Hexasphere, the usage of many innovative components was necessary. They are above all the spherical joints with substantially increased mobility. They are realized either

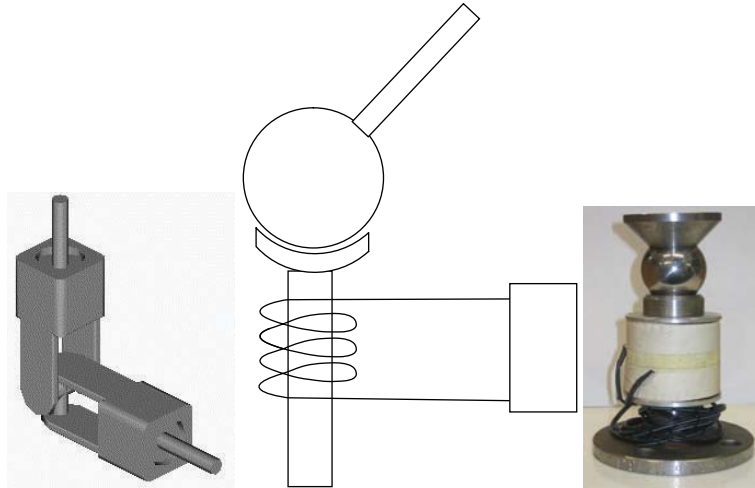


FIGURE 7: Two variants of spherical joint with significantly increased movability.

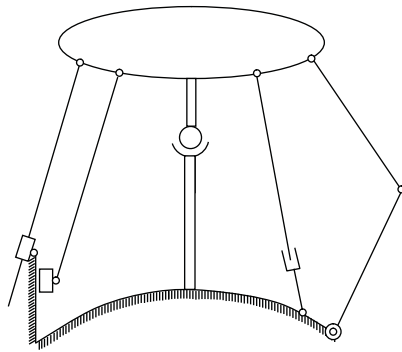


FIGURE 8: Different kinds of strut actuation.

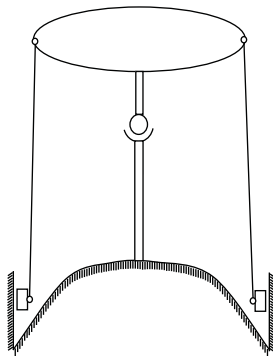


FIGURE 9: Strut concept of functional model.

purely mechanically (but at least with measurement of inner joint motion for calibration if not even with brakes) [8] or by electromagnetic spherical joint (Figure 7) [9].

The struts of Hexasphere can be realized by different ways. They are depicted in the Figure 8. The struts can be with variable length (just extending or telescopic), with fixed length on sliding carriage, or based on robotic arm with rotational joints. The chosen concept of struts for the

manufactured functional model is the strut fixed length on sliding carriage (Figure 9). Using these principles, the design of the functional model of the Hexasphere was carried out and the functional model was manufactured (Figure 10).

4. Applications of Hexasphere for Telescopes

Hexasphere is a new spherical mechanism that can be advantageously used for the design of new telescope mounts. Two such possible concepts are shown in Figure 11. The mechanisms based on Hexasphere concept can be optimized for minimized weight or for maximized dynamics.

The other important property of Hexasphere is the self-calibration that is redundantly actuated and therefore redundantly measured, that is, the capability to determine the dimensions of the whole mechanism just using the internal sensors without any external device. This can be used for online compensation of thermal deformations.

The proposed system is expected to play a role in novel robotic telescopes nowadays used in many fields of astronomy and astrophysics, with emphasis on automated systems for alert observations of celestial gamma-ray bursts. In these systems, there is a need for a fast movability to a sky position which cannot be predicted and is announced by satellite alert systems based on satellites carrying gamma-ray bursts monitors. This position can be hence anywhere on the (visible) sky. The response as fast as possible is essential here, as in some cases prompt optical emission related to gamma-ray burst was observed simultaneously with the gamma-ray burst. The Hexasphere can be considered both for small as well as large telescopes, with still some possible application for wide-field sky monitors including all-sky guided cameras. Here the Hexasphere would be optimized for dynamical applications.

The other applications of a Hexasphere might be the automated telescopes/antennas placed in satellites or Moon or other planets where the weight of the Hexasphere would be optimized.

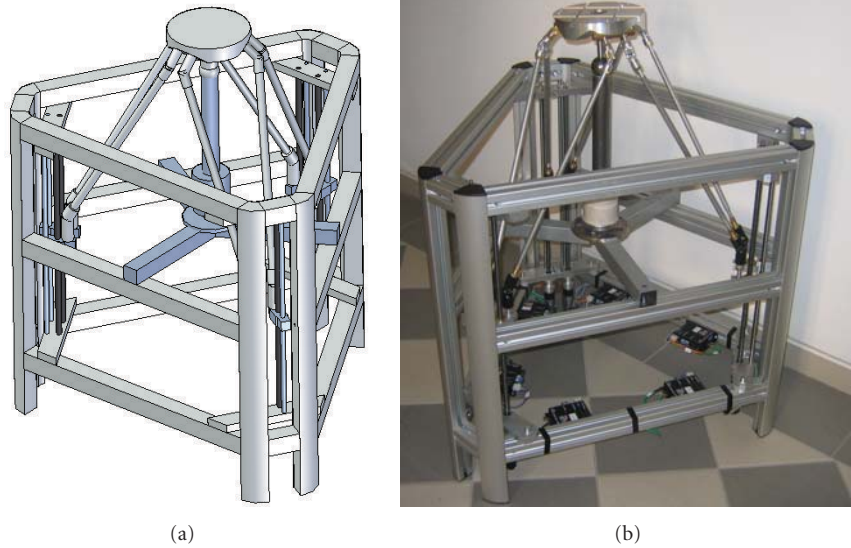


FIGURE 10: Engineering design and functional model of Hexasphere.

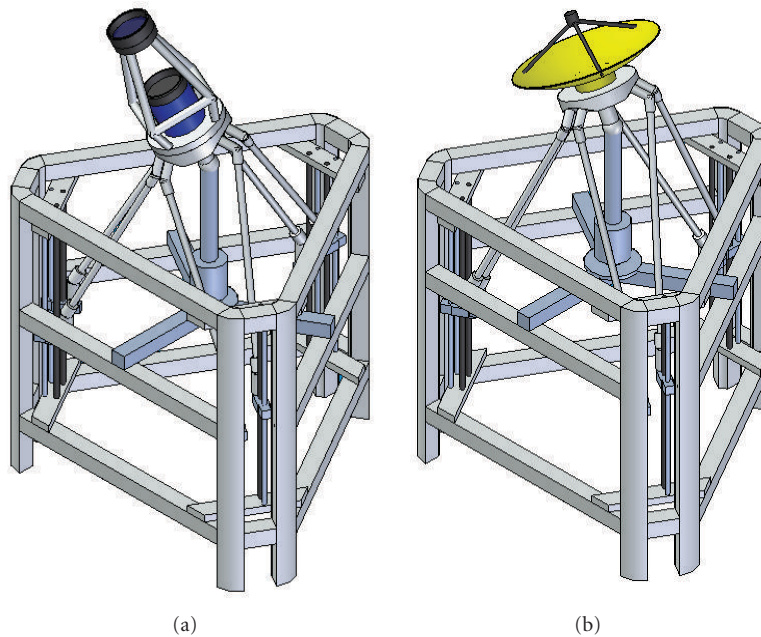


FIGURE 11: Possible applications of Hexasphere as mounts of telescopes.

For the future, it is planned to design, develop, and test a prototype carrying small robotic telescopic system/camera in order to exploit and to test its performance in this application in more detail.

5. Conclusions

The paper has described the new spherical mechanism Hexasphere suitable for mounts of telescopes. The movability of Hexasphere is ± 100 degrees. The mechanisms based on the Hexasphere concept can be optimized for minimized weight or for maximized dynamics.

The proposed system is expected to play a role in novel robotic telescopes nowadays used in many fields of astronomy and astrophysics, with emphasis on automated systems for alert observations of celestial gamma-ray bursts.

Acknowledgments

The authors appreciate the kind support by MSMT project MSM 6840770003, GACR project 101/08/H068, and the Czech Technical University Media Lab Foundation. Rene Hudec acknowledges support by the Grant Agency of the Czech Republic, Grant 102/08/0997.

References

- [1] M. Valášek, “Redundant actuation and redundant measurement: the mechatronic principles for future machine tools,” in *Proceedings of the 3rd International Congress on Mechatronics (MECH2K4 '04)*, pp. 131–144, Praha, Czech Republic, July 2004.
- [2] M. Hustý and H. Eberharter, “Kinematic analysis of the hexapod telescope,” in *Proceedings of the 2nd Workshop on Computational Kinematics*, F. Park and C. Iurascu, Eds., pp. 269–278, Seoul, South Korea, 2001.
- [3] M. Valasek, Z. Šika, V. Bauma, and T. Vampola, “The innovative potential of redundantly actuated PKM,” in *Proceedings of the 4th Chemnitz Parallel Kinematics Seminar (PKS '04)*, pp. 365–384, 2004.
- [4] M. Valášek, V. Bauma, Z. Šika, K. Belda, and P. Piša, “Design-by-optimization and control of redundantly actuated parallel kinematics sliding star,” *Multibody System Dynamics*, vol. 14, no. 3-4, pp. 251–267, 2005.
- [5] R. Kurtz and V. Hayward, “Multiple-goal kinematic optimization of a parallel spherical mechanism with actuator redundancy,” *IEEE Transactions on Robotics and Automation*, vol. 8, no. 5, pp. 644–651, 1992.
- [6] M. Valasek and M. Karasek, “Kinematical analysis of hexasphere,” in *Proceedings of the Conference on Engineering Mechanics*, pp. 1371–1378, Praha, Czech Republic, 2009.
- [7] F. Petru and M. Valasek, “Concept, design and evaluated properties of TRIJOINT 900H,” in *Proceedings of the 4th Chemnitz Parallel Kinematics Seminar (PKS '04)*, pp. 569–584, 2004.
- [8] D. Sulamanidze, *Spherical joints with increased mobility*, Ph.D. thesis, FME CTU, Prague, Czech, 2007.
- [9] M. Valášek, F. Petrů, and J. Zicha, “Magnetic spherical joint,” Patent Pending PV 2008-2058.

Research Article

The Role of Ground-Based Robotic Observatories in Satellite Projects

R. Hudec^{1,2}

¹ *Astronomical Institute, Academy of Sciences, 251 65 Ondřejov, Czech Republic*

² *Faculty of Electrical Engineering, Czech Technical University in Prague, Technická 2, 166 27 Prague 6, Czech Republic*

Correspondence should be addressed to R. Hudec, rhudec@asu.cas.cz

Received 9 June 2009; Revised 25 August 2009; Accepted 20 December 2009

Academic Editor: Alberto J. Castro-Tirado

Copyright © 2010 R. Hudec. This is an open access article distributed under the Creative Commons Attribution License, which permits unrestricted use, distribution, and reproduction in any medium, provided the original work is properly cited.

We discuss the role of robotic telescopes in satellite projects, as well as related strategies. Most satellite projects in space astrophysics focus on high-energy astrophysics from X-rays to gamma-rays. A large fraction of objects of high-energy astrophysics emit also optical light, which is, in many cases, variable. The observation of these sources at optical wavelengths can provide valuable inputs for multispectral analysis of various categories of celestial high-energy (HE) sources. As the magnitudes of numerous objects are bright and can be hence accessed by robotic ground-based observatories, these observations can contribute to investigations and analyses of HE sources. We discuss in detail this possible contribution, with emphasis on the ESA *INTEGRAL* mission. In addition to this, there are also satellite projects outside the high-energy astronomy, in which the robotic telescopes can also play an important role. We will illustrate this on the example of the ESA satellite *Gaia*. In this project, robotic telescopes are expected not only to verify the triggers detected by satellite (such as transients and flares) but also to provide additional (mostly photometric) data for better scientific cases.

1. Introduction

Most satellite projects in space astrophysics focus on high energy astrophysics from X-rays to gamma-rays. A large fraction of objects of high-energy astrophysics emit also optical light, which is, in many cases, variable (Figure 1). The observation of these sources at optical wavelengths can provide valuable inputs for multispectral analysis of various categories of celestial high-energy (HE) sources. As the magnitudes of numerous objects are bright and can be hence accessed by (even small) robotic telescopes, these devices can effectively contribute to investigations and analyses of HE sources.

In addition to this, the robotic telescopes can also play an important role in satellite projects outside high-energy astrophysics. The astrometry mission *Gaia* of European Space Agency ESA can serve here as an example. As it will be shown later, very common is the situation when we have satellite (e.g., HE) monitoring data covering up to \sim years, but we do not have simultaneous optical data. At the same time, the most important goal is to recognize

active states of the sources (flares, high states, etc.) either to trigger the satellite observations, or, alternatively, to be able to concentrate on archival satellite data for those periods. In this aspect, robotic observatories can effectively contribute.

2. The Role of Monitors

Some types of astrophysical objects (e.g., blazars, cataclysmic variables, gamma-ray bursters, flare stars, etc.) exhibit rare flares for which satellite observations are important. These events cannot be monitored by satellites themselves in most cases. These events can be effectively monitored by ground based robotic telescopes (RT) generating ToO (Target of Opportunity) triggers for satellites with ToO regime.

The monitors, in contrast to alert telescopes, can deliver optical photometric data for objects prior and during the active/flaring states—wide-field (WF) coverage is important to cover as many sources as possible. There is a scientifically justified need to have this mode in robotic (i.e., autonomous remotely controlled) telescopes. RT with reasonably large

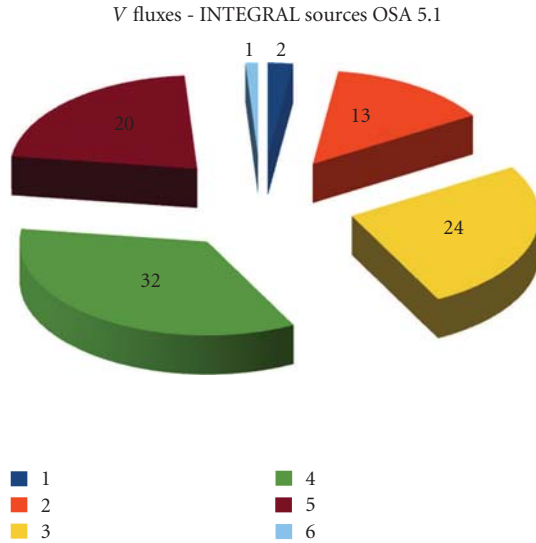


FIGURE 1: The distribution of optical V magnitudes of optically identified *INTEGRAL* gamma-ray sources. Most are brighter than mag 20, and more than half are brighter than mag 15. *Legend* dark blue = mag 2–6, orange = mag 5–10, yellow = mag 10–14, green = mag 14–18, purple = mag 18–22, light blue = mag 22–26. The numbers in the plot indicate number of objects with optical V magnitude within the indicated range.

field of view (FOV), performing regular sky surveys, or with an attached WF camera, can serve as a monitoring device. In some cases, even post-flare monitoring is important as shown by magnetar candidate GRB070610 optical flares [1] in order to (1) detect the optical flares and (2) detect possible recurrence (this is a very difficult task, but important one, which can be performed only by robotic instruments as the recurrence cannot be predicted).

3. The HE Sources as Optical Emitters

The HE sources belong to both galactic as well as extragalactic sources. In the following subsections we will very briefly discuss both groups.

3.1. Galactic HE Sources. There are numerous categories of galactic HE sources, most important ones are listed below:

- (1) Cataclysmic Variables (CVs) and related objects, example: GK Per,
- (2) Low Mass X-ray Binaries (LMXRB), example: HZ Her = Her X-1,
- (3) High Mass X-ray Binaries (HMXRB), example: Cyg X-1,
- (4) X-ray transients,
- (5) New types of sources.

The fact that there are numerous CVs among the gamma-ray sources observed by the ESA *INTEGRAL* satellite (perhaps up to 10% of all *INTEGRAL* gamma-ray sources) represent one of interesting new findings over the last

few years. Moreover, few symbiotic stars (SSs) were also identified with *INTEGRAL* gamma-ray sources.

3.1.1. Are the Optically Variable Galactic HE Sources “Variable Stars”? As many of the HE sources do have optical variable emission, a natural question arises, what is the link between these sources and classical variable stars (VS).

- (1) Yes, some are X-ray and gamma-ray loud cataclysmic variables and symbiotic stars (SS) can serve as examples.
- (2) Some of LMXRB, HMXRB are VS of “non-classical categories”.
- (3) Some are newly detected VS.
- (4) Some are not VS such as the new category of galactic gamma-ray bursts (GRBs).
- (5) The dominant role of CVs is obvious: The contribution of CVs to galactic X-ray background may be greater than assumed before, based on *INTEGRAL* results in hard X-rays (IBIS experiment).

3.2. Extragalactic HE Sources. Numerous celestial HE sources belong to the category of extragalactic sources; the most important types are listed below:

- (1) AGN,
- (2) Blazars,
- (3) Optical Afterglows and Optical Transients of Gamma-Ray Bursts (GRBs),
- (4) SNe,
- (5) LBV (Luminous Blue Variables in external galaxies). They are worth study as they can at some active states mimic the light behaviour of optical afterglows of GRBs.

Several examples of the blazars detected in gamma-rays by the *INTEGRAL* satellite are given and discussed later in this paper.

4. Modes of Observations

There are various modes of optical observations required for the HE sources. The situation is very complex, as the sources belong to various categories.

Satellite Campaigns. One of the most important modes of supporting optical ground-based observations is the response to satellite observing campaigns. While the satellite observation itself usually lasts for several days, the whole observing campaign lasts typically for weeks, as also the time interval before and after the satellite observation needs to be covered. Dense coverage during the satellite observation is required, with less dense coverage before and after. Magnitudes of the targets are typically 12–18 but occasionally can go deeper. Example: satellite campaigns organized by blazar observers.

In addition to that, *planned observations* (mostly known in advance) of optically variable sources by satellites can be supplemented by optical ground based observations, with similar requirements as described above. Example: simultaneous optical observations for targets approved for *Newton*, *Chandra*, *INTEGRAL*.

Monitoring for Triggering Satellite (ToO—Target of Opportunity) Observations. They belong to another important type of optical observations of HE sources. In most cases, moderate sampling of ~ 1 point/day is enough. Magnitudes are typically 12–18. Example: ToO proposal on blazars within *INTEGRAL* project. Here, the blazars included in the approved list are to be optically monitored for possible brightening. Again, about 1 photometric point/day is acceptable for most of the sources.

Providing Optical Data for Non-Triggered Satellite Observations. They represent another category (e.g., providing optical monitoring data for the time span of *INTEGRAL* operation, i.e., 2002–2012). Typically 1 point/day (or even less) is enough. Magnitudes of most of the objects are typically within the range 10–18. This type of observations allows to compare behaviour of gamma-ray sources at various energies and is hence physically important as from such comparison physical interpretations and conclusions may be drawn. Example: Ondrejov D50 RT long-term monitoring of *INTEGRAL* CVs and blazars.

Alert Followup Observations. They represent another important type. They need fast response, better (but not necessarily) automated. However, even a site with non automated instrumentation has chance due to observational/weather constraints. Mostly Gamma-Ray Bursts (GRBs) belong to the group of objects observed this way, but occasionally various types of other flaring and transient targets may be added. Expected magnitudes are 6–22 but in some cases (optically dim GRBs) even fainter. With the ESA *Gaia* satellite, we expect another (*Gaia* project related) type of alerts, which will point on suspicious (mostly flaring) objects detected within *Gaia*. As the *Gaia* itself will have limited ability to confirm the reality of these objects, in most cases the final confirmation and further analyses of *Gaia* alert triggers will rely on ground based (preferably robotic) observers. Example: GRB followup.

Verifying Suggested Identifications. They represent another type of job where robotic observatories may contribute. Typical magnitudes are 10–20. The preferred response is within days or a week. Photometry both with good sampling as well as moderate sampling, photometry with filters, spectroscopy (including low dispersion), are required. Example: confirmation of *INTEGRAL* CV candidates revealed by optical spectroscopy.

Optical Supplementary Analyses. Optical supplementary analyses of HE sources (for complex multispectral analyses) may also add valuable optical data for understanding the

TABLE 1: Cataclysmic variables detected in hard X-rays by *INTEGRAL*.

GCVS Name	Detected CVs		Object Type
	RA (2000)	DEC (2000)	
<u>IGR J00234+6141</u>	00:22:57.63	+61:41:07.8	dq
<u>V709 Cas</u>	00:28:48.84	+59:17:22.3	dq
<u>XY Ari</u>	02:56:08.10	+19:26:34.0	dq
<u>GK Per</u>	03:31:12.01	+43:54:15.4	na/dq
<u>V1062 Tau</u>	05:02:27.47	+24:45:23.4	dq
<u>TV Col</u>	05:29:25.52	−32:49:04.0	dq
<u>IGR J05346−5759</u>	05:34:50.60	−58:01:40.7	vy:
<u>BY Cam</u>	05:42:48.77	+60:51:31.5	am
<u>MU Cam</u>	06:25:16.18	+73:34:39.2	dq
<u>IGR J08390−4833</u>	08:38:49.11	−48:31:24.7	cv
<u>XSS J12270−4859</u>	12:27:58.90	−48:53:44.0	dq
<u>V834 Cen</u>	14:09:07.30	−45:17:16.2	am
<u>IGR J14536−5522</u>	14:53:41.06	−55:21:38.7	dq
<u>IGR J15094−6649</u>	15:09:26.01	−66:49:23.3	dq
<u>NY Lup</u>	15:48:14.59	−45:28:40.5	dq
<u>IGR J16167−4957</u>	16:16:37.20	−49:58:47.5	dq:
<u>IGR J16500−3307</u>	16:49:55.64	−33:07:02.0	dq
<u>V2400 Oph</u>	17:12:36.43	−24:14:44.7	dq
<u>IGR J17195−4100</u>	17:19:35.60	−41:00:54.5	dq:
<u>IGR J17303−0601</u>	17:30:21.90	−05:59:32.1	dq
<u>V2487 Oph</u>	17:31:59.80	−19:13:56.0	na
<u>AM Her</u>	18:16:13.33	+49:52:04.3	am
<u>IGR J18173−2509</u>	18:17:22.25	−25:08:42.9	cv
<u>V1223 Sgr</u>	18:55:02.31	−31:09:49.6	dq
<u>IGR J1 9267+1325</u>	19 26 27.03	+13 22 03.2	cv
<u>V1432 Aql</u>	19:40:11.42	−10:25:25.8	am
<u>V2306 Cyg</u>	19:58:14.48	+32:32:42.2	dq
<u>V2069 Cyg</u>	21:23:44.84	+42:18:01.8	dq:
<u>IGR J21335+5105</u>	21:33:43.65	+51:07:24.5	dq
<u>SS Cyg</u>	21:42:42.80	+43:35:09.9	ugss
<u>FO Aqr</u>	22:17:55.39	−08:21:03.8	dq
<u>AO Psc</u>	22:55:17.99	−03:10:40.0	dq

physics of the sources. The typical magnitudes are 10–20. Again, photometry both with good sampling as well as moderate sampling, photometry with filters, and spectroscopy (including low dispersion) are required. Example: Investigation of gamma-ray loud blazars in optical light.

5. Examples of Ground-Based Observations

5.1. INTEGRAL Cataclysmic Variables. The ESA *INTEGRAL* satellite [2], launched in 2002 and expected to operate at least until 2012, with its 4 onboard telescopes for analyses of gamma-ray sources simultaneously in gamma-ray, X-rays,

TABLE 2: IBIS observations of V1223 Sgr.

JD (24...)	Exp. Time	Flux (15–25) keV [10^{-12} erg s $^{-1}$ cm $^{-2}$]	Flux (25–40) keV [10^{-12} erg s $^{-1}$ cm $^{-2}$]	Flux (40–60) keV [10^{-12} erg s $^{-1}$ cm $^{-2}$]	Flux (60–80) keV [10^{-12} erg s $^{-1}$ cm $^{-2}$]
52 710.38–52 752.01	109.2	161.00 \pm 14.50	57.90 \pm 4.88	<4.93	<6.26
52 917.17–52 926.84	151.1	112.00 \pm 11.30	51.10 \pm 4.19	21.30 \pm 4.24	<5.48
53 082.07–53 119.10	228.1	127.00 \pm 8.90	50.00 \pm 3.28	23.10 \pm 3.48	10.00 \pm 4.54
53 267.41–53 305.97	134.5	126.00 \pm 12.50	55.40 \pm 4.46	25.40 \pm 4.75	27.70 \pm 6.23
53 440.61–53 479.81	90.9	155.00 \pm 15.20	61.30 \pm 5.53	24.10 \pm 5.85	<7.69
53 602.80–53 672.88	409.6	<7.17	31.80 \pm 2.65	<2.82	<3.78
53 781.06–53 809.24	282.1	132.00 \pm 10.00	48.50 \pm 3.50	13.90 \pm 3.56	<4.69
52 710.38–53 809.25	1405.5	103.00 \pm 3.90	46.40 \pm 1.42	15.10 \pm 1.48	12.30 \pm 1.97

TABLE 3: List of blazars observed by the *INTEGRAL* satellite in hard X-rays.

Source	RA	DEC	Gal coord.		z	type
IES 0647+250	06 50 46.6	+25 03 00	190.283	10.996	0.2030	BL Lac
PKS 0823−223	08 26 01.5729	−22 30 27.204	243.990	8.930	0.9100	Possible Q
IES 2344+514	23 47 04.919	+51 42 17.87	112.892	−9.908	0.0440	BL Lac
8C 0149+710	01 53 25.8511	+71 15 06.463	127.920	8.983	0.0220	Q
4C 47.08	03 03 35.2422	+47 16 16.276	144.986	−9.863	0.4750	BL Lac
87GB 02109+5130	01 03 28.1	+43 22 59				BL Lac
BL Lac	22 02 43.2914	+42 16 39.980	92.590	−10.441	0.0688	BL Lac
S5 0716+714	07 21 53.4485	+71 20 36 363	143.981	28.018	0.3000	BL Lac
S5 0836+710	08 41 24.3653	+70 53 42.173	143.541	34.426	2.1720	Q
3C 454.3	22 53 57.7479	+16 08 53.561	86.111	−38.184	0.8590	Q
3C 279	12 56 11.1665	−05 47 21.525	305,104	57.062	0.5362	Q
3C 273	2 29 06.6997	+02 03 08.598	−11.010	4.380	0.1583	Q
PKS1830−211	18 33 39.888	−21 03 39.77	12.166	−5.712	2.5070	Q
Mrk421	11 04 27.3139	+38 12 31.799	179.832	65.032	0.0300	BL Lac
J1656.3−3302	16 56 19.2	−33 01 48	350.604	6.361		?
IGR J22517+2218	22 51 53.498	+22 17 37.29	89.690	−32.750	3.6680	Q
PKS0537−441	05 38 43.5	−44 05 05	250.078	−31.110	0.8960	BL Lac
3C 66A	02 22 39.6115	+43 02 07.799	140.143	−16.767	0.4440	Blazar
Mrk 501	16 53 52.2167	+39 45 36.609	63.600	38.859	0.0336	BL Lac
1ES2344+514	23 47 04.919	+51 42 17.87	112.892	−9.908	0.0440	BL Lac
1ES 1959+650	19 59 59.8521	+65 08 54 653	98.003	17.670	0.0480	Blazar

and (for brighter objects) optical *V* band, is suitable for: (a) detection of the populations of CVs and symbiotics with the hardest X-ray spectra, (b) simultaneous observations in the optical and hard X-ray regions, and (c) long-term observations with Optical Monitoring Camera (OMC)—including a search for rapid variations in observing series during science window (OMC observations also for systems below the detection limit in hard X-rays).

In total, 32 CVs were detected (surprise, more than expected, almost 10% of *INTEGRAL* detections, see Table 1). 28 CVs were seen by IBIS [6–8]—based on correlation of IBIS data and Downes CV catalogue [9]. 4 are CV candidates revealed by optical spectroscopy of IGR sources [10]—new CVs, not in Downes catalogue. They are mainly magnetic

systems: 22 confirmed or propable intermediate polars (IPs), 3 polars, 2 dwarf novae, 4 probable magnetic CVs, 1 unknown. Periods: vast majority $P_{\text{orb}} > 3$ hr, that is, above the period gap (only one <3 h). 5 long period systems with $P_{\text{orb}} > 7$ hr. Some statistics: Intermediate polars represent only ~2% of the catalogued CVs, but they dominate the group of CVs seen by IBIS. More such detections and new identifications can be hence expected. Many CVs covered remain unobservable by IBIS, but new have been discovered. IBIS tends to detect IPs and asynchronous polars: in hard X-rays, these objects seem to be more luminous (up to the factor of 10) than synchronous polars (but detection of more CVs needed for better statistics). A few examples are listed and discussed below.

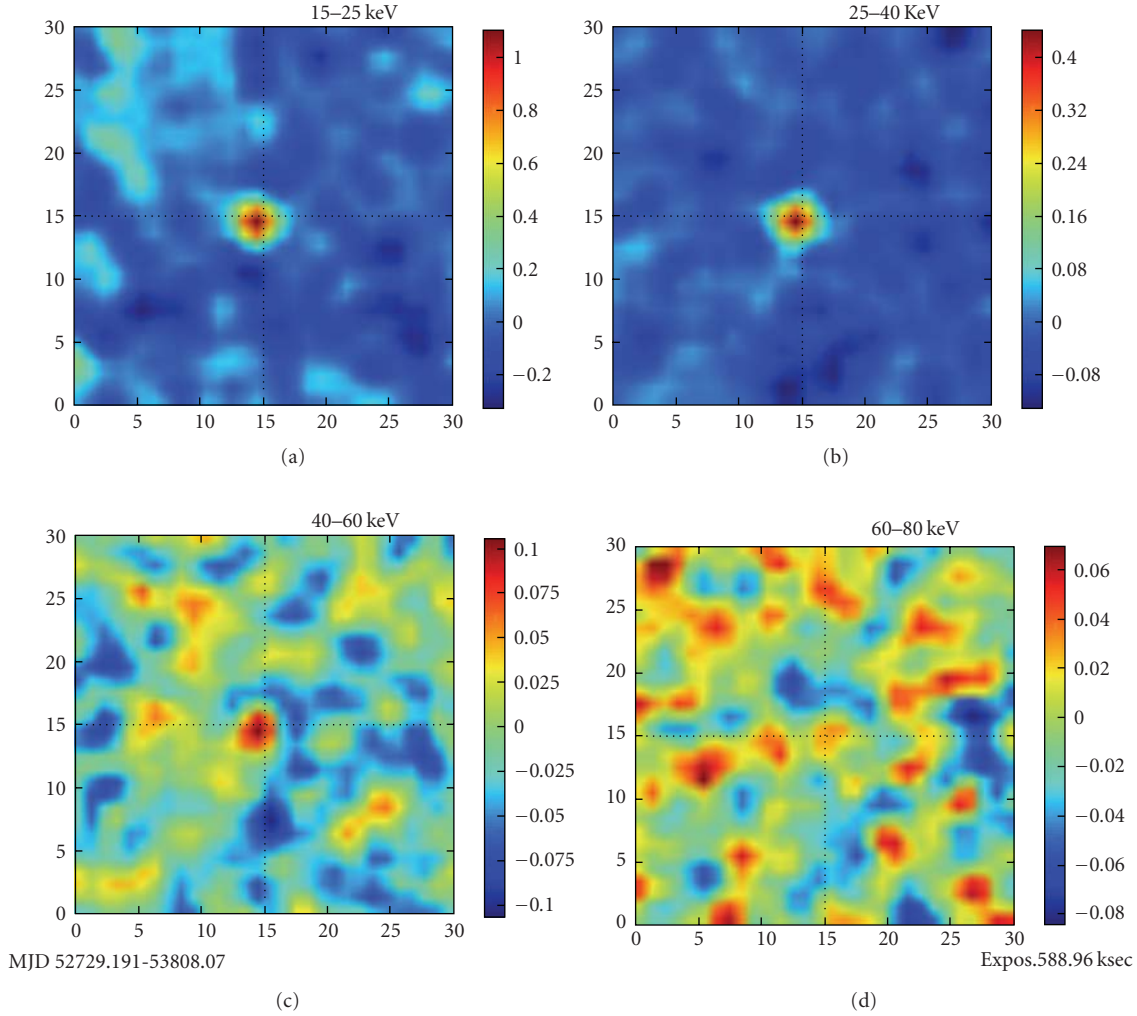


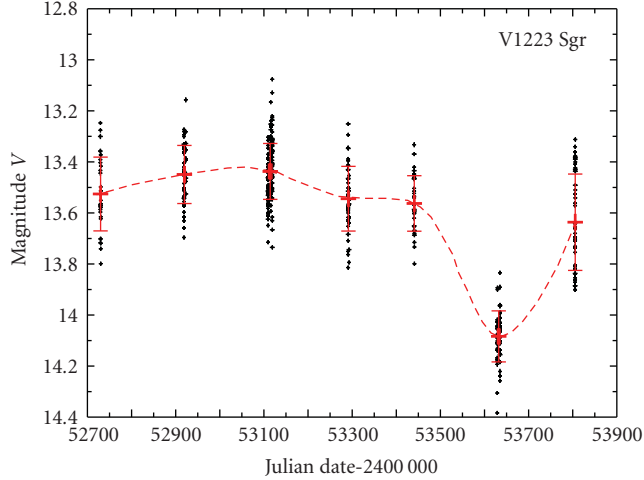
FIGURE 2: V1223 Sgr recent IBIS mosaics (coadded frames) all data (589 ks) intensity maps. The object is in the centre of the images.

V834 Cen. The optical light curve of V834 Cen during the lifetime of *INTEGRAL* shows active and inactive states. V834 Cen is a polar of AM Her class. This polar was probably detected by IBIS since it was in high (active, both optical and gamma-ray) state. This may explain why some CVs have been detected by IBIS and some not. Optical monitoring of sources is important as it can indicate active intervals when the object is expected to be active also in gamma-rays. However, comparing optical and gamma-ray activity is difficult in most cases due to lack of optical data. This is definitely a goal for robotic telescopes (example of monitoring of GK Per is shown in Figure 6).

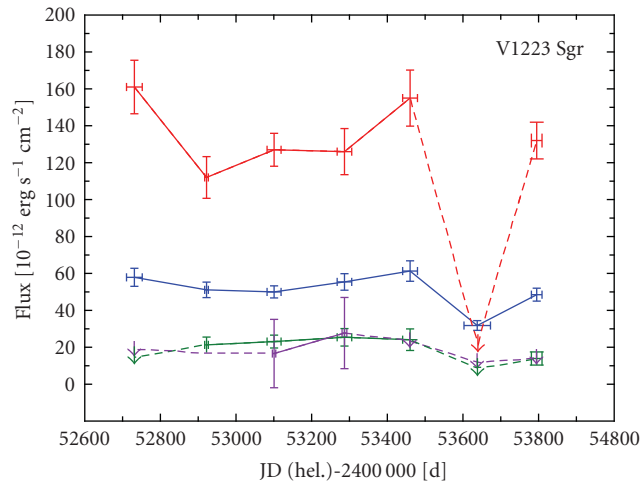
V1223 Sgr. This object is an intermediate polar and represents the most significantly detected CV in the *INTEGRAL* IBIS survey, with a significance of 38 sigma in the 20–40 keV final mosaic (Figures 2, 3, and 4, Table 2). Accretion via disk, bright X-ray source (4U 1849–31). Orbital period: $P_{\text{orb}} = 3.37 \text{ h}$ [11, 12]. Rotational period of the white dwarf: $P_{\text{rot}} = 746 \text{ sec}$ [12]. Beat period (combined effect of P_{orb} and P_{rot}): $P_{\text{beat}} = 794.3 \text{ sec}$ [13].

Prominent long-term brightness variations: (i) outburst with a duration of $\sim 6 \text{ hr}$ and amplitude $> 1 \text{ mag}$ [14], (ii) episodes of deep low state (decrease by several magnitudes) [15]. The object exhibits high-energy flaring activity: seen by IBIS (flare lasting for $\sim 3.5 \text{ hrs}$ during revolution 61 (MJD 52743), peak flux ~ 3 times of the average [6]. Analogous flares were seen also in optical (but at other times) by ground-based instrumentation (duration 6–24 hrs [14]). This confirms the importance of OMC instrument onboard *INTEGRAL*: even with V lim mag 15, it can provide valuable optical simultaneous data to gamma-ray observations.

Similar flares are known also for another IPs in optical, but not in soft gamma rays: Example TV Col [3], where 12 optical flares have been observed so far, five of them on archival southern sky patrol plates from the Bamberg Observatory (Figure 5). TV Col is an intermediate polar and the optical counterpart of the X-ray source 2A0526–328 [16]. TV Col is the first cataclysmic variable (CV) discovered through its X-ray emission. Recently TV Col was detected by *INTEGRAL* IBIS as a hard X-ray source [8]. Physics of the outbursts in IPs is either disk instability or an increase in mass transfer from the secondary.



(a)



(b)

FIGURE 3: The X-ray (IBIS, (a)) and optical (OMC, (b)) light curves for V1223 Sgr. The fluxes especially in (15–25) keV and (25–40) keV bands are long-term variable with significant drop around MJD \sim 53 650. Optical variations are correlated with the changes in (15–25) keV, (25–40) keV and (40–60) keV spectral bands with correlation coefficient 0.81, 0.82, and 0.89, respectively. The fluxes from *INTEGRAL*/JEM-X were persistent within their errors in monitored time period.

5.2. *INTEGRAL* Blazars. From the extragalactic HE sources, blazars belong to the most important and also optically violently variable objects. In Table 3, we list a few examples of blazars analyzed with *INTEGRAL* observations.

1ES 1959+650. This blazar is a gamma-ray loud variable object visible by IBIS in 2006 only, invisible in total mosaics and/or other periods. The optical light curve available for this light curve confirms the relation of active gamma-ray and active optical state (Figures 7 and 8).

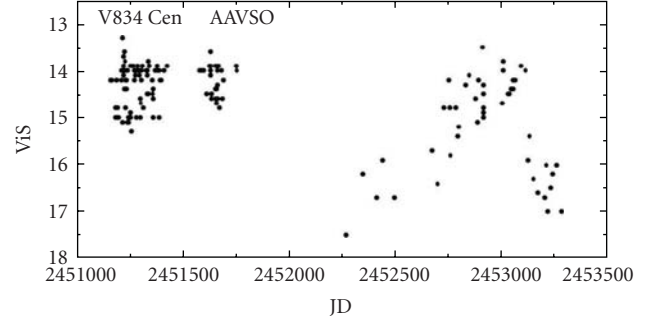


FIGURE 4: The AAVSO light curve for V834, a cataclysmic gamma-ray loud variable detected by the ESA *INTEGRAL* satellite. The active state around JD 2453000 represents the time period when the source was detected in gamma-rays, while it remained undetected at times when the source was in the inactive state.

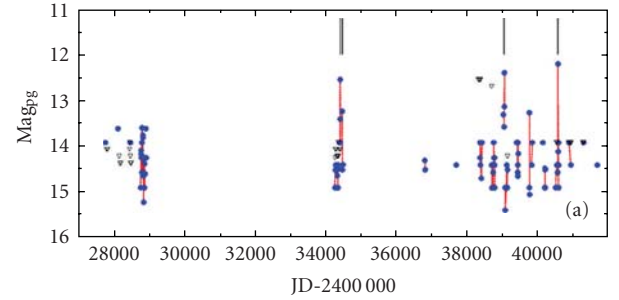


FIGURE 5: Long-term optical light curve of TV Col [3], where 12 optical flares have been observed so far, five of them on archival plates from the Bamberg Observatory. TV Col is an intermediate polar and the optical counterpart of the X-ray source 2A0526-328. This is the first cataclysmic variable (CV) discovered through its X-ray emission. Recently detected also by *INTEGRAL* IBIS.

3C66A. This blazar is visible by IBIS gamma-ray imager onboard *INTEGRAL* only during the optical flare shown below and is invisible other times (Figures 9 and 10). This confirms the importance of monitoring of the object in the optical light.

5.3. Identification and Classification of HE Sources. The RT can also serve as a effective tool in identification and classification of HE sources by optical monitoring and consequent detailed optical analyses of the error box content. Many of the HE are optically variable and hence can be identified (and classified) by their optical variability (Figure 11).

5.4. Poorly Understood Objects. In addition to the main types of HE objects described above, occasionally also objects worth study of another category appear. The variable objects at positions of Ultra High-Energy (UHE) sources can serve as an example, for example, the puzzling poorly investigated variable star at position of UHE source, namely the variable M6 star V347 Aql, with coordinates J2000.0 ICRS position of

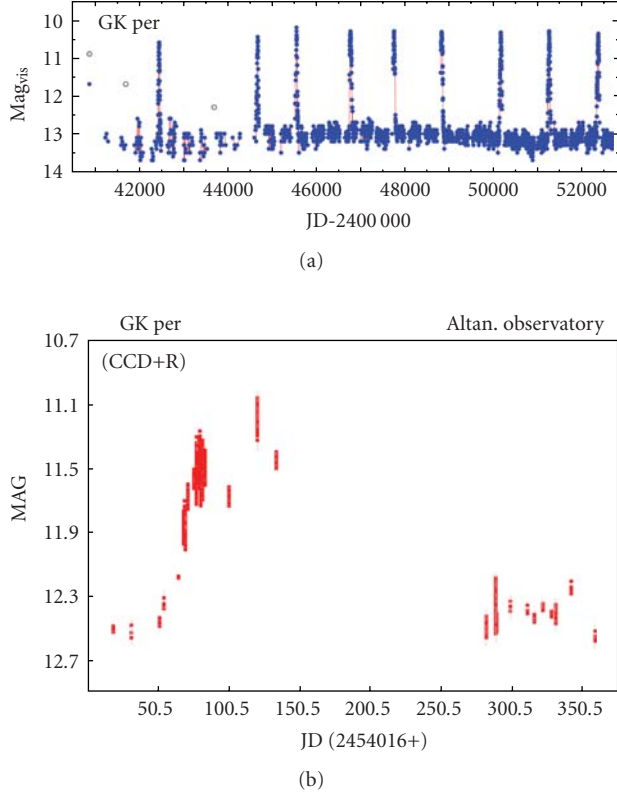


FIGURE 6: The long-term light curve of intermediate polar and *INTEGRAL* source GK Persei (top, source AAVSO) and the recent optical outburst in 2006 (bottom, according to Brat et al. 2006 [4]). The 2006 outburst appeared only 755 days from last outburst. For previous outbursts in 1992, 1996, 1999, 2002, and 2004, the separation was between 1091 and 1333 days, but before that the outburst separation was roughly $N \times 400$ d, $N = 1, 2, 3$ [5].

RA = 19 h 08 m 01.3 s, DEC = +06d18'27, and magnitude $B = 11.5$ mag. The star is within the error box of the new VHE (very high energy) source HESS J1908+063. The nature of this star (which is also an IRAS source) is unknown, previous possible classifications were a possible T Tauri star, or an oxygen rich irregular variable star.

The light curve is unknown, albeit the object magnitude amounts to $B \sim 11$, that is, the star is a good target for small robotic observatories (Figure 12).

5.5. New Types of Optically Variable Objects. There are also newly detected types of optically variable HE sources. The optical counterpart of GRB070610/*SWIFT* J195509+261406 may serve as an example [1, 17]. The basic parameters of this GRB are as follows: detected on 10 June 2007 20:52:26 UT by *Swift*/BAT as a normal burst [18], $T_{90} = 4.6$ s, Photon index 1.76 ± 0.25 , Fluence $(2.4 \pm 0.4) \cdot 10^{-7}$ erg/cm² [19], XRT detected an X-ray counterpart 3100 s later [20] with a column density consistent with the Galactic. Pagani et al. [21] reported the detection of a variable optical counterpart, de Ugarte Postigo et al. [22] confirmed the detection with observations from the 1.5 m OSN. Kann et al. [23] suggested a Galactic origin, based on unusual flaring activity and

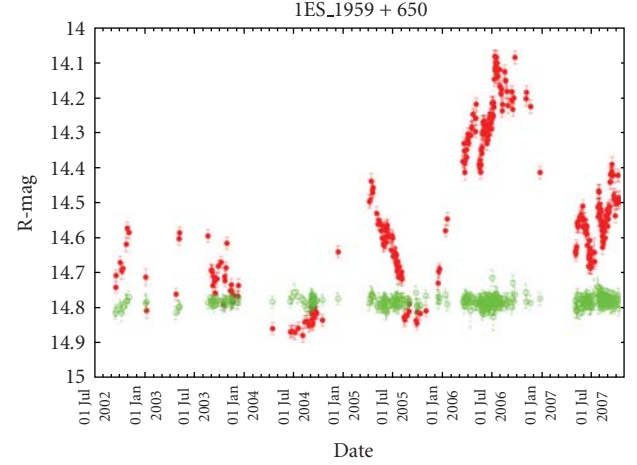


FIGURE 7: Optical light curve of blazar 1ES 1959+650 (in red, Tuorla Observatory blazar monitoring program). The green symbols represent the control measurement of constant star.

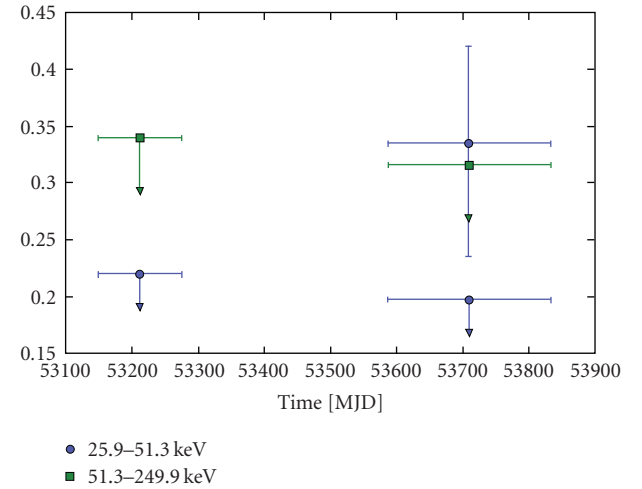


FIGURE 8: IBIS gamma-ray light curve of 1ES 1959+650. Blazar is in *INTEGRAL* gamma-ray imager IBIS visible only in data set corresponding to optical flare.

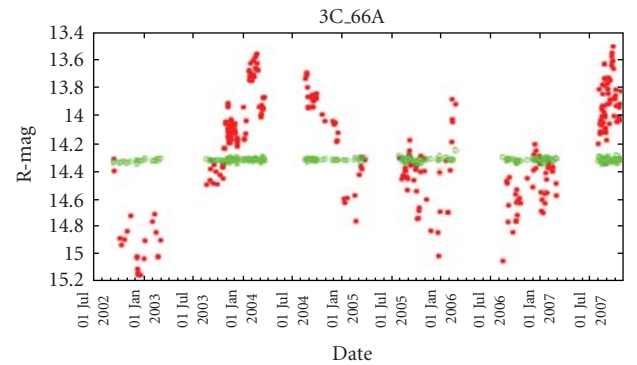


FIGURE 9: Optical light curve of blazar 3C 66A (in red, Tuorla Observatory blazar monitoring program). The green symbols represent the control measurement of constant star.

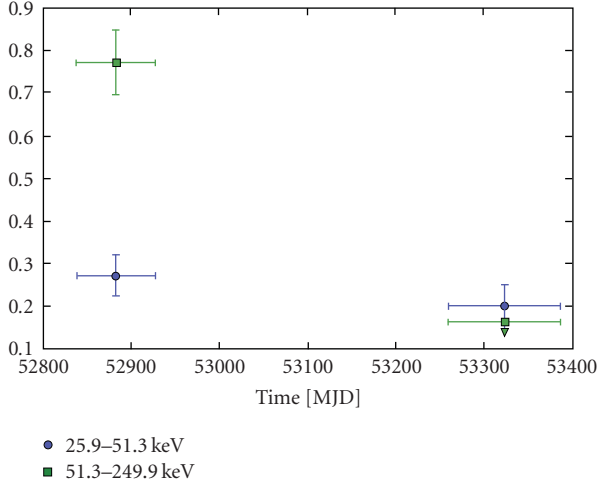


FIGURE 10: IBIS gamma-ray light curve of blazar 3C66A.

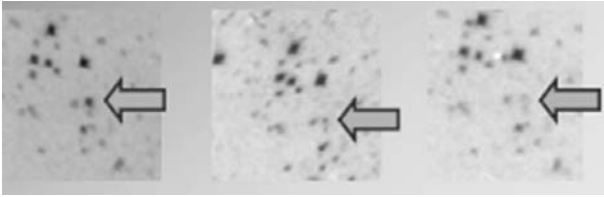


FIGURE 11: An example of appearance of *INTEGRAL* sources in optical light as variable objects. IGR J12349-6434 = RT Cru (hard X-ray symbiotic star) in optical light on Leiden Franklin Adams Plates. The object exhibits violent (amplitude 3 magnitudes) optical brightness variations.

location near the galactic plane: $l = 63.3^\circ$, $b = -1^\circ$. About 40 optical flares peaking at up to I mag 14 as shown on Figure 13. The emission between flares slowly decreased until it disappeared with no detectable quiescent source.

6. Supplementary Optical Data for Non-HE Satellites

Another important role of robotic telescopes is in satellite projects outside high-energy astrophysics. The ESA *Gaia* project may serve as an example. Albeit its main goal is the ultra precise astrometry, *Gaia* will monitor all celestial objects down to magnitude 20 over a 5 years' time period. However, the photometric sampling will not be optimal; hence the supplementary observations provided by ground-based robotic telescopes are expected to provide a valuable contribution. The main goal of these supplementary observations are as follows: (1) confirm triggers (e.g., optical transients, flares, brightenings, etc.) detected by *Gaia* satellite and (2) provide additional photometric data with more dense sampling than provided by the satellite. The HE objects such as LMXRB, HMXRB, and Optical Afterglows and Optical Transients of GRBs can serve here as an example, together with various types of cataclysmic variables including SNe.

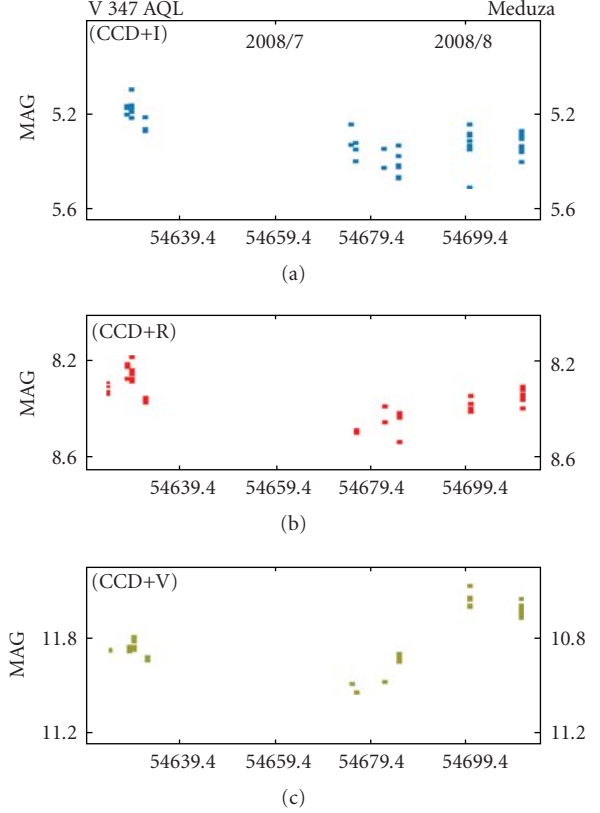


FIGURE 12: The VRI optical light curve V 347 Aql = HESS J1908+063 provided by the Altan Observatory, Czech Republic. The object exhibits both light changes as well as colour variation.

The peculiarity of ESA *Gaia*, where a substantial fraction of data will be as ultra-low dispersion spectra, raises a question about the role of focal devices with dispersive elements, that is, on a spectral alternative. This is fully scientifically justified, as the spectral type of Cepheids, Miras & Peculiar Stars is known to change significantly with time. For example, all classical Cepheids definitely vary their spectral types. At maximum, they all have types around F5–F8. At minimum, the longer the period, the later is the spectral type (to K2) [24]. The long-term behaviour of spectral types of various variable celestial objects (so far only poorly investigated) may be a significant goal not only for ESA *Gaia*, but also for robotic ground-based optical telescopes equipped with corresponding dispersive elements.

7. Supplementary Optical Data for CTA

The CTA (Cherenkov Telescope Array), albeit not being a *satellite*, is in many aspects similar to satellite projects (see also the CTA effort at *INTEGRAL* Science Data Centre ISDC). There is a need for robotic monitoring of VHE (TeV) sources, and alert system for TeV flaring triggers, for example, 1ES1959+650 (TeV blazar at $z = 0.047$). There was an essential progress in Cherenkov telescopes over past years, and nowadays these deliver data analogous to what is known from other energy pass bands (i.e., images and

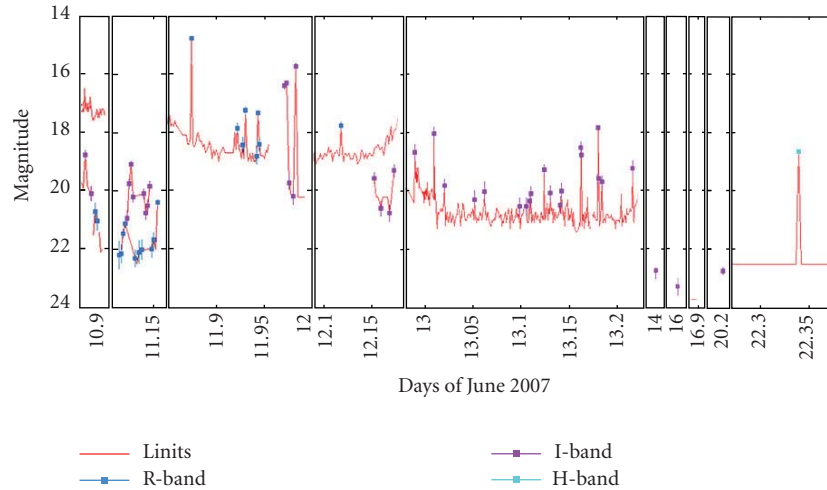


FIGURE 13: Optical light curve of flaring counterpart of GRB070610.

light curves). We propose to implement in Cerenkov systems analogous alert system as those currently used on satellites (i.e., rapid alerts sent to optical and radio observers). But also the opposite way may be essential, as the optical robotic telescopes can monitor TeV sources and report detected flares and active periods to Cerenkov teams.

8. Conclusions

The HE objects in many cases exhibit optical (and mostly variable emission) accessible in some cases even by small robotic observatories. For many of these sources there is a lack of optical data. The optical data provided by automated ground-based optical telescopes are important for multispectral analyses of the sources, contributing of better understanding of related physical processes. Even small apertures may contribute as some sources are brighter than magnitude 12. In addition to that, robotic telescopes may play an important role also in satellite projects outside HE astrophysics, as shown on the example of the ESA *Gaia*, namely as devices confirming the satellite triggers, as well as delivering additional well sampled photometric data for particular objects.

Acknowledgments

The analyses of HE sources by the ESA *INTEGRAL* satellite were supported by ESA PECS project no. 98023, and in optical by grant 205/08/1207 provided by Grant Agency of the Czech Republic. The investigation of high-energy sources and cataclysmic variables by the ESA *Gaia* satellite is supported by the ESA PECS Project no. 98058. The analyses of GRBs in optical light including robotic telescopes are supported by the grant of the Grant Agency of the Czech Republic, 102/09/0997. The investigations of the Bamberg Observatory archival plates are supported by DAAD-AVCR project DAAD-25-CZ4/08 and the analyses of PARI plates by MSMT KONTAKT ME09027.

References

- [1] A. J. Castro-Tirado, A. de Ugarte Postigo, J. Gorosabel, et al., “Flares from a candidate Galactic magnetar suggest a missing link to dim isolated neutron stars,” *Nature*, vol. 455, no. 7212, pp. 506–509, 2008.
- [2] C. Winkler, T. J.-L. Courvoisier, G. Di Cocco, et al., “The *INTEGRAL* mission,” *Astronomy and Astrophysics*, vol. 411, no. 1, pp. L1–L6, 2003.
- [3] R. Hudec, V. Simon, and J. Skaliky, “The astrophysics of cataclysmic variables and related objects,” in *Proceedings of ASP Conference*, J.-M. Hameury and J.-P. Lasota, Eds., vol. 330, p. 405, San Francisco, Calif, USA, 2005.
- [4] L. Brat, J. Strobl, P. Kubanek, et al., “Old nova GK Per in dwarf nova-type outburst,” *The Astronomer’s Telegram*, vol. 965, 2006.
- [5] R. Hudec, “Optical properties of X-ray stars. I - X-ray system GK Per A 0327+43. II—the secular brightness variations of the X-ray system V 818 Sco/Sco X-1,” *Bulletin of the Astronomical Institute of Czechoslovakia*, vol. 32, no. 2, pp. 93–120, 1981.
- [6] E. J. Barlow, C. Knigge, A. J. Bird, et al., “20–100 keV properties of cataclysmic variables detected in the *INTEGRAL*/IBIS survey,” *Monthly Notices of the Royal Astronomical Society*, vol. 372, no. 1, pp. 224–232, 2006.
- [7] A. J. Bird, A. Malizia, A. Bazzano, et al., “The third IBIS/ISGRI soft gamma-ray survey catalog,” *The Astrophysical Journal*, vol. 170, no. 1, pp. 175–186, 2007.
- [8] R. Gális, D. Eckert, S. Paltani, F. Münz, M. Kocka, and R. Hudec, “Hard X-ray emission of cataclysmic variables observed by *INTEGRAL*,” in *Proceedings of the 7th INTEGRAL Workshop*, Copenhagen, Denmark, September 2008.
- [9] R. A. Downes, R. F. Webbink, M. M. Shara, H. Ritter, U. Kolb, and H. W. Duerbeck, “A catalog and atlas of cataclysmic variables: the living edition,” *Publications of the Astronomical Society of the Pacific*, vol. 113, no. 784, pp. 764–768, 2001.
- [10] N. J. Masetti, A. Malizia, A. Dean, A. Bazzano, and R. Walter, “Optical spectroscopic identification of candidate counterparts to four *INTEGRAL* sources,” *The Astronomer’s Telegram*, vol. 957, 2006.
- [11] F. Jablonski and J. E. Steiner, “On the stability of the 13.2 minute oscillation of V1223 Sagittarii,” *The Astrophysical Journal*, vol. 323, pp. 672–677, 1987.

- [12] J. P. Osborne, R. Rosen, K. O. Mason, and K. Beuermann, "New EXOSAT results from the intermediate polar V1223 SGR," *Space Science Reviews*, vol. 40, no. 1-2, pp. 143–149, 1985.
- [13] J. E. Steiner, D. A. Schwartz, F. J. Jablonski, I. C. Busko, M. G. Watson, and J. P. Pye, "Identification of 4U 1849-31 with V1223 Sagittarii and discovery of optical pulsations," *The Astrophysical Journal*, vol. 249, pp. L21–L24, 1981.
- [14] S. van Amerongen and J. van Paradijs, "Detection of a brief outburst from the intermediate polar V 1223 SGR," *Astronomy and Astrophysics*, vol. 219, no. 1-2, pp. 195–196, 1989.
- [15] P. Garnavich and P. Szkody, "Observed low states in DQ Herculis systems," *Publications of the Astronomical Society of the Pacific*, vol. 100, pp. 1522–1528, 1988.
- [16] B. A. Cooke, M. J. Ricketts, T. Maccacaro, et al., "The Ariel V /SSI/ catalogue of high galactic latitude /absolute value of B greater than 10 deg/ X-ray sources," *Monthly Notices of the Royal Astronomical Society*, vol. 182, pp. 489–515, 1978.
- [17] A. de Ugarte Postigo, A. J. Castro-Tirado, J. Gorosabel, et al., "GRB 070610: Flares from a peculiar Galactic," in *GAMMA-RAY BURSTS 2007: Proceedings of the Santa Fe Conference*, vol. 1000 of *AIP Conference Proceedings*, pp. 337–341, Santa Fe, NM, USA, 2008.
- [18] C. Pagani, et al., "GRB Coordinates Network, Circular Service," 6489, 1, 2007.
- [19] J. Tueller, et al., "GRB Coordinates Network, Circular Service," 6491, 1, 2007.
- [20] C. Pagani, et al., "GRB Coordinates Network, Circular Service," 6490, 1, 2007.
- [21] C. Pagani, et al., "GRB Coordinates Network, Circular Service," 6492, 1, 2007.
- [22] A. de Ugarte Postigo, et al., "GRB Coordinates Network, Circular Service," 6501, 1, 2007.
- [23] D. A. Kann, et al., "GRB Coordinates Network, Circular Service," 6505, 1, 2007.
- [24] N. Samus, et al., Private communication, 2008.

Research Article

Photometry and Low Dispersion Spectroscopy with ESA *Gaia*

René Hudec,^{1,2} Vojtěch Šimon,¹ and Lukáš Hudec^{1,2}

¹ Astronomical Institute, Academy of Sciences of the Czech Republic, CZ-251 65 Ondřejov, Czech Republic

² Faculty of Electrical Engineering, Czech Technical University in Prague, CZ-166 27 Prague 6, Czech Republic

Correspondence should be addressed to René Hudec, rhudec@asu.cas.cz

Received 10 June 2009; Accepted 16 December 2009

Academic Editor: Alberto J. Castro-Tirado

Copyright © 2010 René Hudec et al. This is an open access article distributed under the Creative Commons Attribution License, which permits unrestricted use, distribution, and reproduction in any medium, provided the original work is properly cited.

The ESA satellite to be launched in 2012 will focus on highly precise astrometry of stars and all objects down to limiting magnitude 20. Albeit focusing on astrometry related matters, the satellite will also provide photometric and spectral information and hence important inputs for various branches of astrophysics. Within the *Gaia* Variability Unit CU7 and related work package Specific Object Studies there are subwork packages accepted for optical counterparts of celestial high-energy sources and cataclysmic variables. Although the sampling of the photometric data will not be optimal for this type of work, the strength of *Gaia* in such analyses is the fine spectral resolution (spectrophotometry and ultra-low dispersion spectroscopy) which will allow the correct classification of related triggers. We will review the available low dispersion spectral surveys and discuss their use for a simulation and tests of the *Gaia* algorithms and *Gaia* data.

1. Introduction

For many years, the state of art in celestial cartography has been the Schmidt surveys of Palomar and ESO, and their digitized counterparts. *Gaia* will provide the detailed 3-d distributions and space motions of all these stars, complete to mag 20. The measurement precision, reaching a few millionths of second of arc, will be unprecedented [1]. This will allow our Galaxy to be mapped, for the first time, in three dimensions. It is obvious that, with the above briefly described performance, *Gaia* will provide valuable inputs to various research fields of contemporaneous astronomy and astrophysics including the field of high-energy sources. Most of the variable object research will be performed within the *Gaia* Variability Coordination Unit CU7. To study the optical counterparts of celestial high-energy sources, there will be several advantages provided by *Gaia*. First, this will be a deep limiting magnitude of 20 [2], much deeper than most of previous studies and global surveys. For example, no detailed statistics of variable stars has been investigated for magnitudes fainter than 18. Secondly, the time period covered by *Gaia* observations, that is, 5 years, will also allow some studies requiring long-term monitoring, recently provided mostly by astronomical plate archives and small or magnitude-limited sky CCD surveys. But perhaps the most

important benefit of *Gaia* for these studies will surely be the color (spectral) resolution thanks to the low resolution (prism) *Gaia* spectroscope. This will allow some detailed studies involving analysis of the color and spectral changes not possible before. The details of studies of the optical counterparts of high-energy sources have been recently evaluated and are described in more detail mostly by the dedicated sub-workpackages within the workpackage Specific objects studies within the *Gaia* CU7 [3, 4]. The main objective of the sub-workpackage mentioned above is the investigation and analysis of optical counterparts of high-energy astrophysical sources (including High-Mass X-Ray Binaries, Low-Mass X-Ray Binaries, X-Ray Transients, X-Ray Novae, Optical Transients and Optical Afterglows related to X-Ray Flashes and Gamma-Ray Bursts, Microquasars, etc.) based on the *Gaia* data as a complex analysis with additional data.

2. Spectral Coverage by *Gaia*

The G band (in yellow) with GBP, GRP and GRV S of *Gaia* are illustrated on Figure 1. The bands are constructed by multiplying the CCDs QE (red enhanced for RP and RVS, blue enhanced for BP), and the optical transmission curves taken from the *Gaia*ParamDB.

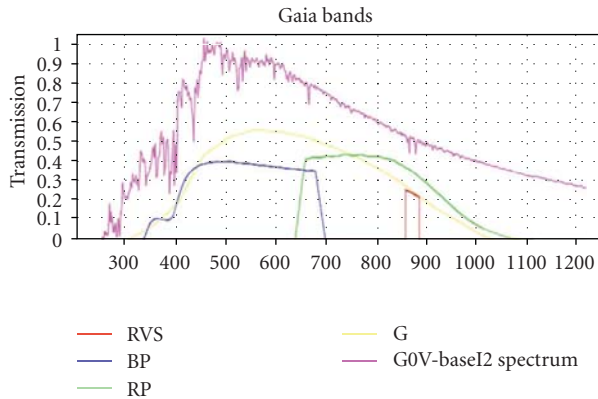


FIGURE 1: The spectral coverage by *Gaia* [5].

The use of dispersive element (prisma) generates ultra low-dispersion spectra. One disperser called BP for Blue Photometer operates in the wavelength range 330–660 nm; the other called RP for Red Photometer covers the wavelength range 650–1000 nm (Figure 1). The dispersion is higher at short wavelengths, and ranges from 4 to 32 nm/pixel for BP and from 7 to 15 nm/pixel for RP [5].

3. Variable Objects by *Gaia*

As already mentioned in Section 1, perhaps the most important benefit of *Gaia* for the variable star studies will surely be the new color resolution. This will allow some detailed studies involving analyses of color and spectral changes not possible before. The details of variable star studies with *Gaia* have been recently evaluated and are described in more detail mostly by the dedicated sub-workpackages within the workpackage Specific objects studies within the *Gaia* CU7. The participation of High Energy Astrophysics (HEA) group at the Astronomical Institute of the Academy of Sciences of the Czech Republic in Ondřejov focuses on *Gaia* CU7 Variability Processing Unit with R. Hudec being a member of *Gaia* CU7 team. Two sub-work packages within the specific object studies on cataclysmic variables (CVs) and optical counterparts of high energy sources have been proposed, evaluated, accepted, and allocated to be managed by R. Hudec. Additional participation is expected in image processing—this includes the algorithms designed for scanned Schmidt spectral plates (simulation of *Gaia* data and variability studies based on Spectrophotometry). The further participation represents direct participation in *Gaia* CU7 Data Processing Center (DPC) as a natural continuation of the participation in *INTEGRAL* ISDC. This includes participation in the software development in a team, and Java and object oriented programming as a natural extension of the participation in *INTEGRAL* ISDC (since 1997). Another participation is represented by the robotic telescopes run with the same RTS2 operating software: BART, BOOTES1, BOOTES2, BOOTES-IR, FRAM, WATCHER, D50 cm CCD telescope (since 2007). Also small and private observatories are expected to participate.

4. Optical Counterparts of High-Energy Sources by *Gaia*

Most high energy sources have also an optical emission, mostly variable and accessible by *Gaia*. The monitoring of this variable optical emission provides important input to understanding of the physics of the source [6, 7]. The idea is to focus on the sources not included in other categories of variable sources (e.g., not on AGNs, CVs, etc.) covered by other sub-workpackages [3, 4]. The investigations and analyses of optical counterparts of high energy sources based on the *Gaia* data also require complex analyses with additional data. Specially, for selected targets, multispectral analyses using *Gaia* and other databases (such as the satellite X-ray and gamma-ray data, optical ground-based data etc.) may be feasible. They will deal with the long-term light changes and their evolution, especially active states, outbursts, and ares. For the selected sources, dedicated complex analyses will be undertaken, including spectrophotometry and investigation of the relation between the brightness and spectrum/color index. This will enable a study and understanding of related physical processes [8]. Also a statistics of the whole sample of objects will be made (Figure 2).

5. Three Observing Modes of *Gaia*

In this paper we focus on the “photometric mode” RP/BP. In reality, this mode generates ultra low-dispersion prism spectra. The use of the dispersive element (prisma) generates ultra low-dispersion spectra. One disperser called BP for Blue Photometer operates in the wavelength range 330–660 nm; the other called RP for Red Photometer covers the wavelength range 650–1000 nm (Figure 3). The dispersion is higher at short wavelengths, and ranges from 4 to 32 nm/pixel for BP and from 7 to 15 nm/pixel for RP.

6. Simulated *Gaia* Low Dispersion Spectra

Gaia’s photometric instrument is based on a dispersive-prism approach such that starlight is not focused in a PSF-like spot but dispersed along the scan direction in a low-resolution spectrum. The instrument consists of two low-resolution fused-silica prisms dispersing all the light entering the field of view (FOV). Two CCD strips are dedicated to photometry, one for BP and one for RP. Both strips cover the full astrometric FOV in the across-scan direction.

All BP and RP CCDs are operated in TDI (time-delayed integration) mode. The CCDs have 4500 (for BP) or 2900 (for RP) TDI lines and 1966 pixel columns (10 × 30 micron pixels). The spectral resolution is a function of wavelength as a result of the natural dispersion curve of fused silica. The BP and RP dispersers have been designed in such a way that BP and RP spectra have similar sizes (on the order of 30 pixels along scan) [5].

BP and RP spectra will be binned on-chip in the across-scan direction; no along-scan binning is foreseen. RP and BP will be able to reach the object densities on the sky of at least

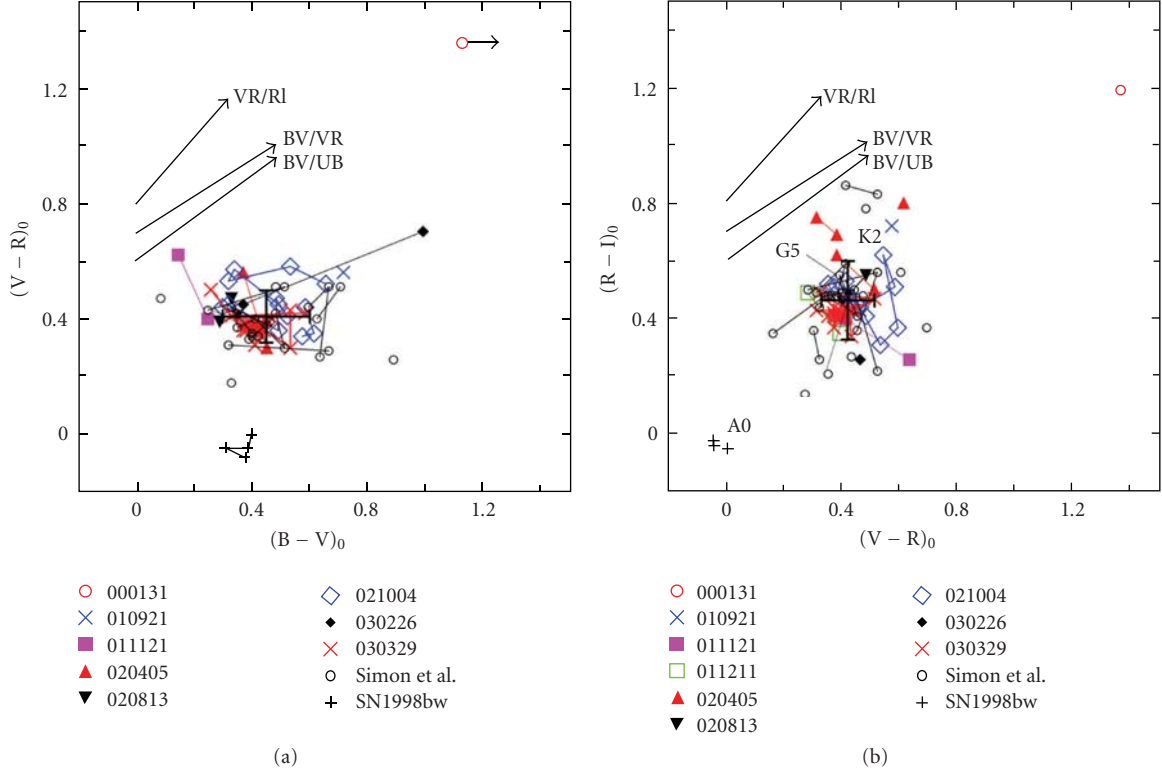


FIGURE 2: Examples of the color diagrams of optical afterglows (OAs) of GRBs. The data for $t - T_0 < 10.2$ d in the observer frame and corrected for the Galactic reddening are displayed. Multiple indices of the same OA are connected by lines for convenience. The mean colors (centroid) of the whole ensemble of OAs (except for GRB000131 and SN 1998bw) are marked by the large cross. The representative reddening paths for $E_{B-V} = 0.5$ and positions of the main-sequence stars are also shown. Adapted from [9–11].

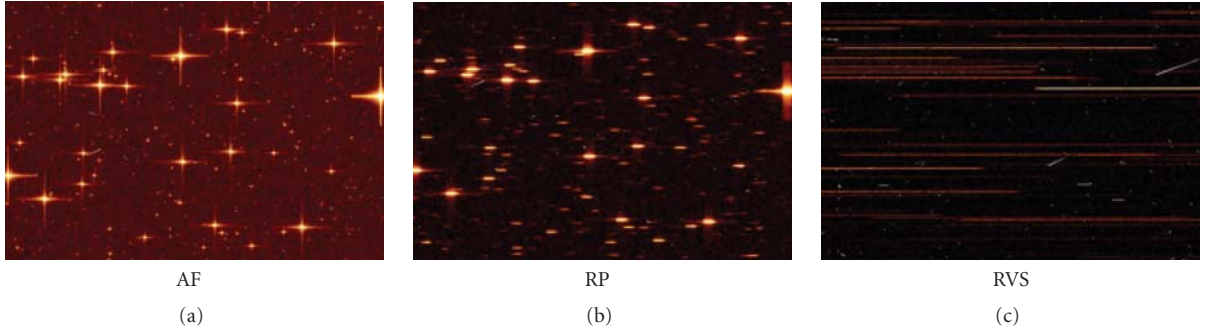


FIGURE 3: Three observation modes of *Gaia*: AF = astrometric, RP = photometric, RVS = spectrophotometric [5].

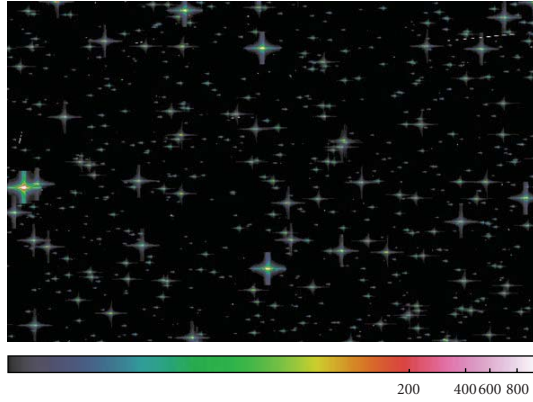
750,000 objects deg^{-2} . The obtained images can be simulated by the GIBIS simulator (see Figure 4).

7. The Spectral Type Variability with *Gaia*

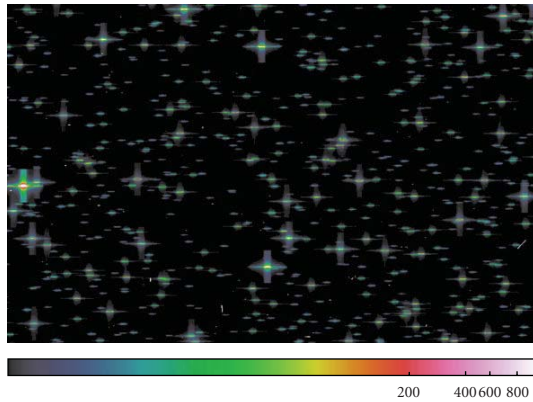
It is known that certain types of variable stars (VS) such as Miras, Cepheids, and peculiar VS exhibit large variations in their spectral types. This field is, however, little exploited, as these studies were very laborious before (plates were mostly visually inspected) and limited. No review on the spectral variability among VS exists (Samus, personal comm. 2008).

The evaluation by computers and dedicated s/w will allow to search and investigate the spectral variability in the *Gaia* data and in digitized spectral plates. For example, the Mira variable X Cam [12] is known to exhibit spectral variations M0 to M6.5, accompanied by the photometric variations with the amplitude 1.4 mag in the R band (Figure 5).

The Cepheid Variables represent another example. Spectral type of all classical Cepheids definitely vary (Figure 6). At maximum, they all have the types around F5-F8. At minimum, the longer the period, the later is the spectral type (to K2) (Samus, 2008). Examples of the related spectral



(a)



(b)

FIGURE 4: BP (a) and RP (b) images simulated by GIBIS simulator, the same sky field.

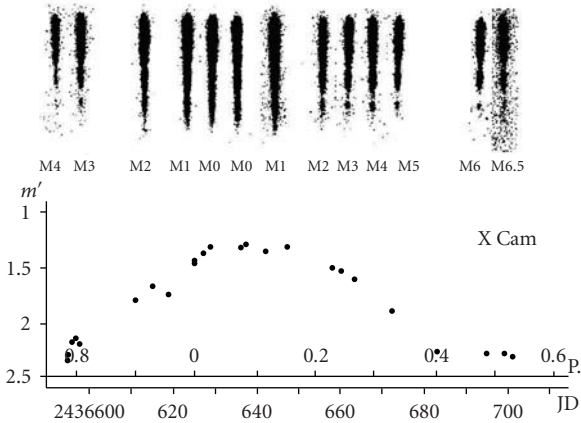


FIGURE 5: Spectral and photometric variability of X Cam [12].

and photometric variations of Cepheids were shown, for example, by Becker 1938 and Shapley 1916 [13, 14]. The spectral type changes of peculiar stars are also known: for example, the variable FG Sagittae changed its spectral type from B to M [15].

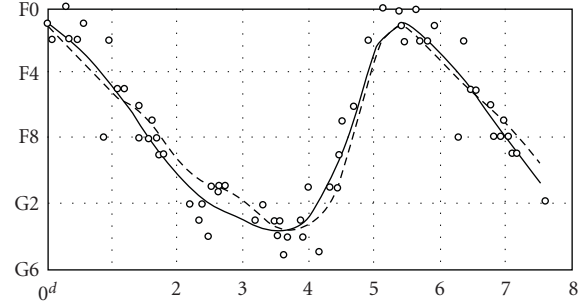


FIGURE 6: Relation of the light curve and spectral type for delta Cephei [13].

8. Suitable Low Dispersion Spectral Databases for *Gaia*

Before *Gaia*, low dispersion spectra were frequently taken in the last century by various photographic telescopes with the objective prisma. Some of them are listed here:

Schmidt Camera Sonneberg. The dispersion ~ 23 nm/mm at Hgamma for the 3 deg prisma. The scan resolution is 0.05 mm/px, thus about 0.5 nm/px. The dispersion ~ 10 nm/mm at Hgamma for the 7 deg prisma. The scan resolution is 0.02 mm/px, thus about 0.2 nm/px.

Bolivia Expedition Spectral Plates. The coverage of the southern sky with spectral and direct plates, Potsdam Observatory, plates stored at the Sonneberg Observatory. Hidden for ~ 75 years. Plates taken ~ 1924 – 1928 , about 70 000 prism spectra estimated and published in Potsdam Publ. 26–19 in 1930 (Figure 7).

Hamburg Quasar Survey. A wide-angle objective prism survey searching for quasars with $B < 17.5$ on the northern sky. The survey plates have been taken with the former Hamburg Schmidt telescope, located at Calar Alto/Spain since 1980. For the survey, the 1.7° prism was used providing unwidened objective prism spectra with a dispersion of 139 nm/mm at Hgamma. Under the conditions of good seeing, the FWHM of the images is $30 \mu\text{m}$ (plate resolution) giving a spectral resolution of 4.5 nm at Hgamma on the objective-prism plates. Online access (Figure 8).

Byurakan Survey. The Digitized First Byurakan Survey (DFBS) is the digitized version of the First Byurakan Survey (FBS). It is the largest spectroscopic database in the world, providing low-dispersion spectra for 20,000,000 objects on 1139 FBS fields = $17,056 \text{ deg}^2$. Online access (Figure 9). Sky coverage: $\text{DEC} > -15^\circ$, all RA (except the Milky Way). Prisma spectral plates by the 1 m Schmidt telescope. Limiting magnitude: 17.5 in V, spectral range: 340–690 nm, spectral resolution 5 nm. Dispersion: 180 nm/mm near Hgamma.

9. Algorithms for Automated Analyses of Digitized Spectral Plates

These algorithms are developed by informatics students [16]. The main goals are as follows: the automated classification of spectral classes, searches for spectral variability (both

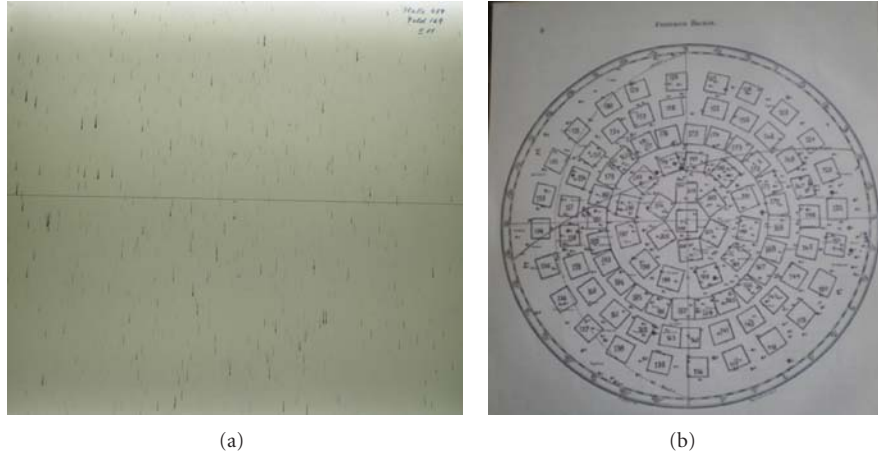


FIGURE 7: Bolivia Expedition spectral plates (a) and the southern sky coverage of the Bolivia Expedition spectral plates (b).

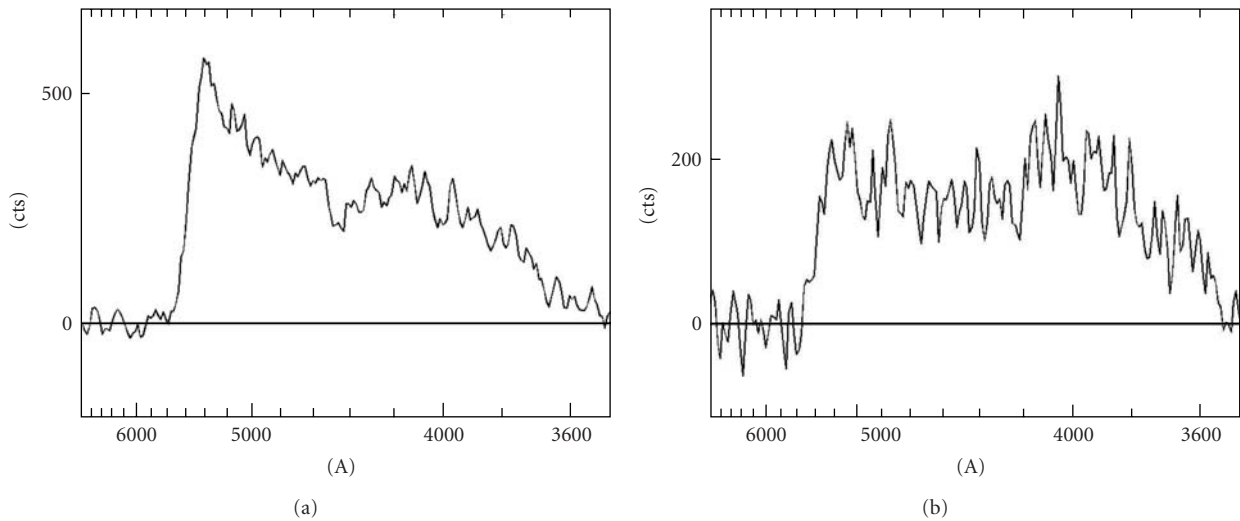


FIGURE 8: Example spectra of cataclysmic variable (a) and blazar (b) (digitized Hamburg Survey).

continuum and lines), searches for objects with specific spectra, correlation of spectral and light ganges, searches for transients, and application for *Gaia*. The archival spectral plates taken with the objective prisma offer the possibility to simulate the *Gaia* low dispersion spectra and related procedures such as searches for the spectral variability and variability analyses based on the Spectrophotometry. We focus on the sets of spectral plates of the same sky region covering long time intervals with good sampling; this enables the simulating of the *Gaia* BP/RP outputs. The main task is the automatic classification of stellar objective prism spectra on digitised plates, a simulation and a feasibility study for the low-dispersion *Gaia* spectra.

The important part here is the algorithm for an automated recognition of a low dispersion spectral image and its comparison with atlas images (specimen of stellar spectra of sample stars with defined spectral type). In addition spectral

changes can be exploited and followed as well as searches for objects with strange spectra.

The algorithms should be able to take into account the background in the photographic emulsion which is not trivial as the background is variable. One method how to solve this is the histogram implementation resulting from digitised plate and reflecting the parameters of a real sky plates, yielding the optimized threshold filter. Then segmentation algorithm follows which recognizes the spectral elongated image. A recursive function is used there, as well as various convolution filters. The function to control the edge-surroundings gradient was also tested and added. The recognized spectral images are then normalized, and consequently the layered neuron network are used to analyze the vectors. The neuron network is then responsible for selection and allocation of model spectra. For more details see [16].

TABLE 1: Comparison of the parameters of *Gaia* BR and RP and of selected plate low dispersion spectra.

	Wavelength range, nm	Limiting magnitude	Dispersion at Hgamma, nm/mm	Spectral resolution, nm
<i>Gaia</i>	330–660, 650–1000	~19	900	~18?
Sonneberg Schmidt	340–650	18	10 and 23	~3
Bolivia Expedition	340–650	14	9	~3
Hamburg	340–540	19	139	4.5
Byurakan	340–690	17.5	180	5

10. The Ultra Low Dispersion Spectral Images by *Gaia*: Comparison of the *Gaia* Low Dispersion Spectra versus Spectral Plates

The dispersion represents an important parameter: (1) *Gaia* BP: 4–32 nm/pixel, that is, 400–3200 nm/mm, 9 nm/pixel, that is, 900 nm/mm at Hgamma, RP: 7–15 nm/pixel, that is, 700–1500 nm/mm. PSF FWHM ~2 px, that is, spectral resolution is ~18 nm (see Figure 10), (2) Plates Schmidt Sonneberg (typical mean value): the dispersion for the 7 deg prisma 10 nm/mm at Hgamma, and 23 nm/mm at Hgamma for the 3 deg prisma. The scan resolution is 0.02 mm/px, thus about 0.2 and 0.5 nm/px, respectively, (3) Bolivia Expedition plates: 9 nm/mm, with calibration spectrum, (4) Hamburg QSO Survey: 1.7 deg prisma, 139 nm/mm at Hgamma, spectral resolution of 4.5 nm at Hg, (5) Byurakan Survey: 1.5 deg prisma, 180 nm/mm at Hgamma, resolution 5 nm at Hgamma (Figure 1). Hence *Gaia* BP/RP dispersion ~5 to 10 times less than typical digitised spectral prism plate, and spectral resolution ~3 to 4 times less. Note that for plates the spectral resolution is seeing-limited hence the values represent the best values (see Table 1). *Gaia* BP/RP dispersion ~5 to 10 times less than typical digitized spectral prism plate, and the spectral resolution ~3 to 4 times less, but on the plates affected by bad seeing only ~2 times less.

The motivation of these studies is as follows: (1) Comparison of the simulated *Gaia* BP/RP images with those obtained from digitized Schmidt spectral plates (both using dispersive elements) for 8 selected test fields, and (2) Feasibility study for application for the algorithms developed for the plates for *Gaia*.

11. The Power of *Gaia* Spectrophotometry for Science

Despite of the low dispersion discussed above, the major strength of *Gaia* for many scientific fields will be the fine spectrophotometry, as the low dispersion spectra may be transferred to numerous well-defined color filters. As an example, the OAs of GRBs are known to exhibit quite specific color indices, distinguishing them from other types of the astrophysical objects [9, 10], hence a reliable classification of optical transients will be possible using this method (see also Figure 2). Colors of Microquasars may serve as another example. The color-color diagram in Figure 11 contains the microquasars of various types: (1) system with

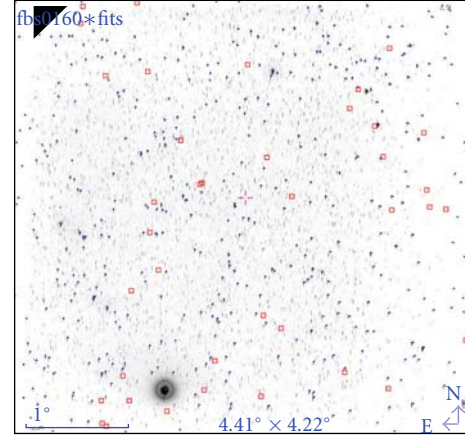
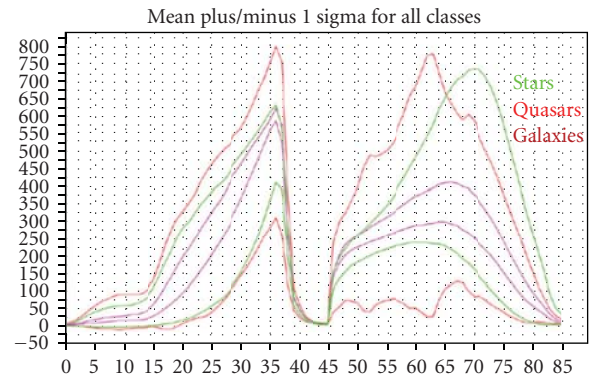


FIGURE 9: An example of the Byurakan Spectral Plate (FOV = 4° × 4°).

FIGURE 10: The simulated 1D low dispersion spectra by *Gaia* according to Bailer-Jones et al., 2008 [17]. The x-axis in pixels covers the BP and RP range, on y-axis is the intensity (arbitrary units). This picture shows that even for very low dispersion spectra without visible spectral lines valuable information can be obtained and scientifically used from the spectral continuum profile.

the optical emission dominated by the high-mass donor-Cyg X-1, (2) persistent systems with the optical emission dominated by the steady-state accretion disk-SS433, Sco X-1, (3) transient low-mass systems in outburst with the optical emission dominated by the accretion disk-GRO J1655-40, XTE J1118+480 (the disk is close to steady-state in outburst), and (3) the high-mass system CI Cam on the decline from its 1999 outburst to quiescence.

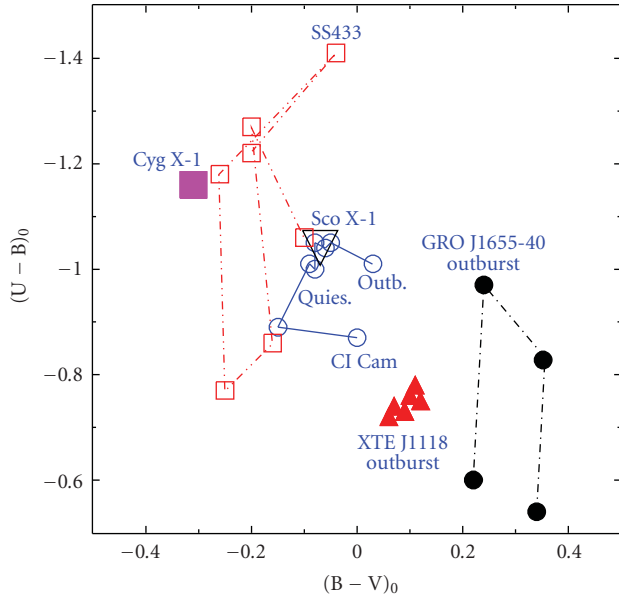


FIGURE 11: The color-color diagram for microquasars.

The systems plotted, irrespective of their types, display blue colors, with a trend of a diagonal formed by the individual objects. This method can be used even for the optically faint, and hence distant objects.

12. Conclusions

The *Gaia* mission of European Space Agency (ESA) will contribute essentially to scientific studies and physical understanding of variable stars in general and of optical counterparts of high energy sources, CVs and related objects in particular. The variability studies based on low-dispersion spectra are expected to provide unique novel data and can use the algorithms recently developed for the automatic analyzes of digitized spectral Schmidt plates. *Gaia* will provide ultra-low dispersion spectra by BP and RP representing a new challenge for astrophysicists and informatics. The nearest analogy is represented by the digitized prisma spectral plates: Sonneberg, Hamburg and Byurakan surveys. These digitised surveys can be used for a simulation and tests of the *Gaia* algorithms and *Gaia* data. Some algorithms have been already tested. Some types of variable stars are known to exhibit large spectral type changes; however, this field is little exploited and more discoveries can be expected with the *Gaia* data as *Gaia* will allows us to investigate the spectral behavior of huge amounts of objects over 5 years with good sampling for spectroscopy.

Acknowledgments

The Czech participation in the ESA *Gaia* project is supported by the PECS project 98058. The scientific part of the study is related to the grants 205/08/1207 and 102/09/0997 provided by the Grant Agency of the Czech Republic. Some aspects of the project described here represent a natural continuation of

the Czech participation to the ESA *INTEGRAL* (ESA PECS 98023). The analyses of digitised low dispersion spectral plates are newly supported by MSMT KONTAKT Project ME09027.

References

- [1] M. A. C. Perryman, "Overview of the *gaia* mission," in *Astrometry in the Age of the Next Generation of Large Telescopes*, vol. 338 of *ASP Conference Series*, p. 3, 2005.
- [2] C. Jordi and J. M. Carrasco, "Photometry with *gaia*," in *The Future of Photometric, Spectrophotometric, and Polarimetric Standardization*, vol. 364 of *ASP Conference Series*, p. 215, 2007.
- [3] R. Hudec and V. Simon, "Specific object studies for cataclysmic variables and related objects," 2007, ESA *Gaia*, Reference Code GAIA-C7-TN-AIO-RH-001-1.
- [4] R. Hudec and V. Simon, "Specific object studies for optical counterparts of high energy sources," 2007, ESA *Gaia*, Reference Code GAIA-C7-TN-AIO-RH-001-1.
- [5] <http://sci.esa.int/gaia/>.
- [6] R. Hudec and W. Wenzel, "Observations of HZ Her/Her X-1 on Sonneberg astrograph plates," *Bulletin of the Astronomical Institute of Czechoslovakia*, vol. 27, p. 325, 1976.
- [7] R. Hudec, "Optical properties of X-ray stars. 2. The secular brightness variations of the X-ray system V 818 Sco/Sco X-1," *Bulletin of the Astronomical Institute of Czechoslovakia*, vol. 32, p. 108, 1981.
- [8] J. E. Rhoads, "How to tell a jet from a balloon: a proposed test for beaming in gamma-ray bursts," *Astrophysical Journal*, vol. 487, no. 1, part 2, pp. L1–L4, 1997.
- [9] V. Šimon, R. Hudec, G. Pizzichini, and N. Masetti, "Colors and luminosities of the optical afterglows of the γ -ray bursts," *Astronomy & Astrophysics*, vol. 377, no. 2, pp. 450–461, 2001.
- [10] V. Šimon, R. Hudec, G. Pizzichini, and N. Masetti, "Colors of optical afterglows of GRBs and their time evolution," in *Gamma-Ray Bursts: 30 Years of Discovery: Gamma-Ray Burst Symposium*, vol. 727 of *AIP Conference Proceedings*, pp. 487–490, 2004.
- [11] V. Šimon, R. Hudec, and G. Pizzichini, "The color evolution of the optical afterglow of GRB 030329 and the implications for the underlying supernova SN 2003dh," *Astronomy & Astrophysics*, vol. 427, no. 3, pp. 901–905, 2004.
- [12] T. Jarzembowski, *Veröffentlichungen der Remeis-Sternwarte zu Bamberg, Veränderlichen-Colloquium*, Bamberg, Germany, 1959.
- [13] F. Becker, "Spektral-Durchmusterung der Kapteyn-Eichfelder des Sudhimmels. V. Zone -15deg," *Publikationen des Astrophysikalischen Observatoriums zu Potsdam*, vol. 28, p. 1, 1938.
- [14] H. Shapley, "The variations in spectral type of twenty Cepheid variables," *The Astrophysical Journal*, vol. 44, pp. 273–291, 1916.
- [15] D. Chalonge, L. Divan, and L. V. Mirzoyan, "Spectrophotometric studies of nonstable stars. III. The spectrum of FG Sagittae in 1968–1973," *Astrophysics*, vol. 13, no. 3, pp. 247–252, 1977.
- [16] L. Hudec, *Algorithms for spectral classification of stars*, BSc. thesis, Charles University, Prague, Czech Republic, 2007.
- [17] C. A. L. Bailer-Jones, K. W. Smith, C. Tiede, R. Sordo, and A. Vallenari, "Finding rare objects and building pure samples: probabilistic quasar classification from low-resolution *Gaia* spectra," *Monthly Notices of the Royal Astronomical Society*, vol. 391, no. 4, pp. 1838–1853, 2008.